

PRE-**Proceedings of the**

ACI-*fib*-RILEM FRC-UHPFRC Workshop 2026

Budapest, Hungary, 28 - 30 September 2026

Edited by

György L. Balázs, Sándor Sólyom, Kálmán Koris, Marco di Prisco, Giovanni Plizzari, Barzin Mobasher

v.24.09.2026a

TABLE OF CONTENTS

Structural applications

Design of post-tensioned SFRC elevated slabs 3
Chiara Gaddi, Matteo Colombo and Marco Di Prisco

Behaviour of a precast steel fiber reinforced concrete thin-walled box structure subjected to cyclic loading 15
Luca Facconi, Fausto Minelli, Andrea Pasetto and Giovanni Plizzari

Distributed Fiber Optic Monitoring in Full-Scale Fiber Reinforced Composite Decks 27
Chidchanok Pleesudjai , Martins Suta , Devansh Patel , Xavier Destree , Gregor Daniel Fischer , Barzin Mobasher

Jointless industrial floor using synthetic macro fibre-reinforced concrete: a Hungarian case study 41
Péter Károly Juhász, Anna Bencze and Márton Kispál

Validation and application of a modified damage plasticity model for fibre-reinforced concrete structures 53
Simone Niccolaini, Paolo Martinelli

Shear strength of SFRC hollow bricks without reinforcement: A Review and Preliminary Analysis 65
Kiran Dabral, Silvia Ientile, Jean-Claude Renaud, Saint-Ange Billo, Damien Suray-Faure, Philippe Robit, François Toutlemonde

Świnoujście tunnel, the largest diameter steel fibre-reinforced road tunnel in Europe 77
Bruno Rossi, Sebastien Wolf

Case Study on the Application of ASTM F2322 to Precast FRC Panels in a Detention Facility 87
Eneas Dosantos, Victoria Olivera, Sofia Martínez, Luis Segura-Castillo

Behavior of steel fiber-reinforced concrete structural walls with simplified detailing under reversed cyclic displacements 97
Gustavo Parra-Montesinos, Osman Carrillo and Jose A. Pincheira

Fibre reinforced concrete and UHPC; their application in structures 105
Jan L. Vítek

Material saving potential by using Steel Fibre Reinforced Concrete for Industrial Floors 117
Efim Griniov, Rewi Sever and Dirk Schlicke

Improving punching shear capacity in flat slabs using SIFCON with 3D steel reinforcing elements 129
Wisam Alzweehm and György L. Balázs

Evidence from slender beam tests on prestressed UHPC for lightweight, durable structures 143
Juan Navarro-Gregori, Yeiner A. Gómez-Velásquez, Juan A. Mateu-Sánchez, Pedro Serna and José R. Martí-Vargas

Fibre-Reinforced Concrete Pile-Supported Foundation Slab for a Building 151
Marco Antonio Carnio, Viviane Visnardi Vaz, Isabela Oliveira Duarte

Behaviour of fibre reinforced concrete in industrial floors: Comparison between the Montevideo test and EN 14651 bending test for an on-site application 165
Carlos Aire, Eneas Dosantos, Luis Segura-Castillo

Finite element analysis of synthetic macro fibre reinforced concrete jointless industrial floors in Latin-America 175
Luis Alberto Leonardo Nolasco, Abraham Hidalgo Bermúdez, Claudio Parada Ibanez, Jesus Munoz Perez, Péter Károly Juhász

Hybrid Fibre-Reinforced Concrete Shear Walls for Seismic-Resilient Structures 191
Alexandru Trandafir

Mechanical Performance and Redundancy of Direct Fastenings in Fiber-Reinforced Concrete: An Experimental Evaluation 201
Alhussain Yousef and Panagiotis Spyridis

Fibres in new types of concrete

Optimization of Fiber Orientation in Steel Fiber Reinforced Concrete by Robotic Extrusion 215
Filippo Medeghini, Ivan Trabucchi, Giulia Brentana, Giuseppe Tiberti, Giovanni Plizzari and Peter Mark

Textile waste as reinforcement fiber for construction panels 227
Diego Carro-Lopez, Belén González-Fonteboa, Carolina Matínez-García

Reducing Cost and Environmental Footprint of 3D-Printed UHPC Using Recycled Tire Steel Fibers 233
Shunyang Yao, Min Zhou, Doo-Yeo Yoo and Behzad Nematollahi

Fibres with no orientation 243
Gyorgy L. Balazs, Wisam K. Tuama, Oscar Pfeffermann, Gábor Kardos, Salem Nehme, Sándor Sólyom

Additively manufactured carbon short-fiber reinforced concrete – non-destructive testing to investigate deteriorations under fatigue 253
Christian U. Grosse, Oliver Fischer, Malte A. Peter, Dirk Volkmer

Design tool for alkali-activated slag-based concrete incorporating single (3D) and multiple (4D, 5D) hooked-end steel fibres 261
Laura Rossi, Maria Paula Zappitelli, Ravi Patel, Frank Dehn

Experimental Investigation of Hemp Fiber-Reinforced Recycled Aggregate Mortar 271
Bojan Poletanovic, Farshad Ameri, Lukas Hausner and Ildiko Merta

Mechanical Performance of Concrete Reinforced with Recycled Tyre-Cord Fibres 281
Peter Czirak and Jaroslav Prokop

Elevated temperature performance of 3D-printed low-carbon alkali-activated UHPC 293
Xiao Zhao, Mehdi Chougan, Ravi Ranade and Behzad Nematollahi

Curing effect on compressive strength of UHPC incorporation Copper Slag 303
Mohammad Mohsin Khan , Subhan Ahmad , Faisal Mukhtar , Mohammed A. Al-Osta

Effect of steel fibre geometry and dosage on the mechanical and post-cracking behaviour of UHPFRC 313
Sándor Sólyom, Anna Szijártó and György L. Balázs

Performance of Date Palm Pedicel and Coir Fibre in Natural Fibre Reinforce Concrete for Sustainable Construction 325
Abdallah Al Abri, Kazi Md Abu Sohel, Sherif El-Gamal and Khalifa Al-Jabri

Design specifications

Beyond superposition: Rethinking fiber bridging in concrete elements with bar reinforcement 341
Viktor Gribniak and Aleksandr Sokolov

Quality Control of Steel Fibre-Reinforced Concrete: Traditional Method versus Innovative Approach 353
Simone Spagnuolo, Alberto Meda and Benoit De Rivaz

Fibers distribution in concrete beams with rebars and steel fibers 363
Mohammad Abu-Ahmad, Yuri Karinski and Avraham Dancygier

Experiences from using Montevideo test for quality control of fibre-reinforced concrete 373
Ingrid Lande, Guillem Rojas and Terje Kanstad

Three-Point Bending Test of UHPFRC with Increased Aggregate Size and Variable Fibre Content 385
Malena Thomassen and Ingrid Lande

Exploring the potential of explicit steel fiber – lattice matrix coupling in high-fidelity simulation of steel-fiber-reinforced composites 397
Saeid Mehrpay, Jelle Billiet, Jan Vorel, Daniele Pelessone, Eskinder Desta Shumuye, Tamon Ueda and Roman Wan-Wendner

Characterization of fiber-reinforced concretes activated at very early ages 407
Benoit de Rivaz and Nicolas Leclere

Lattice Discrete Particle Modeling of Steel Reinforced UHPFRC Members under Eccentric Loading 419
Jiahui Feng, Wenyong Cai and Lin Wan-Wendner

Predictive performance of Eurocode 2 design recommendations for steel-fibre reinforced concrete structures 429
Joaquim Barros and Marcilio Filho

Assessing Fiber Orientation and Mechanical Performance in UHPFRC: A Data-Driven Review and Machine Learning Study 443
Bedirhan Enes Kelek, Olcay Gürabi Aydoğan, Duçem Medya Gündoğmuş, Nilüfer Özyurt

Validity check of punching shear design for steel fiber reinforced flat slabs with shear reinforcement based on new test results 455
Sören Faustmann and Oliver Fischer

Fibre-Reinforced Shotcrete Test Methods: Impact of the Application Process and Analytical–Numerical Correlations 469
Todd Clarke, Peter Schaul and Des Vlietstra

Theorical and Experimental Correlation Between ASTM C1609 and MVD Tests 483
Victoria Olivera, Carlos Aire and Luis Segura-Castillo

A stochastic mixing model for fibre distribution in fibre-reinforced concrete and its implications 495
Péter Károly Juhász

Direct Tensile Tests on Drilled Cores with Different Fiber Orientation: Test Setup and σ-w-Relationships 507
Maximilian Kronau, Roman Wan-Wendner and Oliver Fischer

Blind prediction of steel fiber-reinforced slab punching resistance based on lessons learned from previous contests 519
Jiri Kovar and Jan Cervenka

Statistical approach to quality control of steel fibre reinforced concrete using inductive measurements based on experimental data 531
Nadia Quijano Arteaga, Natividad García Troncoso, Samantha Hidalgo Astudilllo, Stanislav Aidarov and Albert De la Fuente

Effect of fibre orientation and hook type on the tensile response of FRC 543
Ahmed Hamed and Mário Pimentel

Performance optimisation of Hybrid Fiber Reinforced Concrete with macro-synthetic and steel fibers 555
Giovanni Plizzari, Matteo Draconte and Luca Torelli

Performance-Based Design approach for anchorages in Steel Fiber Reinforced Concrete considering concrete related failure modes 567
Norbert Vita, Akanshu Sharma

Brief History and Defining Criteria of Strain Hardening FRC Composites 581
Antonie E. Naaman

Influence of dispersed PVA fibers in the GFRP bar-concrete bond behavior. 597
Veronica Bertolli, Tommaso D'Antino and Christian Carloni

Simplified Flexural Design of FRC Based on Integrated Residual Tensile Stress from Standard Beam Tests 609
Devansh Patel, Chidchanok Pleesudjai and Barzin Mobasher

Design aspects for long term and extreme loads

Long-Term Behavior of FRC with Hybrid Fibers 621
Sergio Carmona , Giovanni Plizzari , Jorge Barraza

Development of probabilistic cracking models for fiber reinforced concrete under static and dynamic loadings 633
Pierre Rossi

Dual-Approach Verification of Enhanced Fatigue Life in Macro Synthetic Fibre Reinforced Concrete Sleepers 643
Christophe Camille, Olivia Mirza, Todd Clarke

On the fatigue performance of ultra-high-performance concrete and strain hardening cementitious composites 653
Vitor Monteiro, Rennan Liberato, Iranildo Silva Junior, Flavio Silva

Thermal Performance of Fibre-Reinforced Concrete with Different Aggregate Types Under Elevated Temperatures 663
Ahmed M. Seyam, Rita Nemes

Enhanced progressive collapse resistance in reinforced concrete frames using polypropylene fibers 669
Rutger Vrijdaghs, Krishnaa Subramanian

High temperature behaviour of strain-hardening ultra-high performance fibre reinforced concretes 683
Péter Ludvig, Anna Szijártó, Bruno Bacelar, Thiago Viana, Salem Nehme

Fatigue Behaviour of High-Performance Fibre Reinforced Concrete (HPFRC): from Experimental Investigations to Design Provisions 695
Gabriele David Bocchino, Nicholas Sergio Burello, Alfredo Alan Flores Gutierrez, Davide Zampini, Liberato Ferrara

Compressive Fatigue Behaviour of Concrete Incorporating Recycled Aggregates and Recycled Glass Fibres from Wind Turbines 711
Nadia Quijano Arteaga, Samantha Hidalgo Astudilllo, Débora Martinello Carlesso, Stanislav Aidarov and Albert De la Fuente

Investigation of different polypropylene fiber contents in ultra-high-performance concretes under temperature increase 723
Thiago Viana, Péter Ludvig, Bruno Bacelar, Isabela Coelho

Effect of Polymer-Fibre-Containing Recycled Concrete Aggregate on the High-Temperature Resistance of Recycled Concrete 735
Viktor Hlavička

Comparative Fatigue Behaviour of Steel Fibre Reinforced Concrete under Flexural and Traffic-Type Loading 749
Sheila Bisika and Humaira Fataar

Flexural Performance of Low-Carbon UHPCs Exposed to Elevated Temperatures 763
M. Mirza Abdillah Pratama, Ravi Ranade, Doo-Yeo Yoo and Behzad Nematollahi

Sustainability, Durability, Serviceability

Durability study of existing SFRC beams subjected to outdoor environmental conditions 775
Gyorgy L. Balazs, Ronny Ramiro Almeida Vasquez, Jorge Luis Campoverde Abril and Katalin Kopecsko

Mechanical and environmental performance of SFRC using fibres made of recycled and renewably produced steel and Limestone Calcined Clay Cement LC3 787
Sébastien Wolf, Lionel Sofia, Beatrice Malchiodi and Karen Scrivener

Mechanical performance of recycled PET fibre-reinforced concrete for sustainable construction 797
Muhammad Ali, Olivia Mirza, Christophe Camille, Fidelis Mashiri

Effect of Residual Tensile Strength on Drying Shrinkage Cracking in Fiber Reinforced Concrete Pavement 809
Chidchanok Pleesudjai, Devansh Patel and Barzin Mobasher

Modeling the compressive behavior and cracking process of plain concrete and fiber reinforced concrete 821
Pierre Rossi

Performance of Date Palm Pedicel and Coir Fibre in Natural Fibre Reinforce Concrete for Sustainable Construction 831
Abdallah Al Abri, Kazi Md Abu Sohel, Sherif El-Gamal, Khalifa Al-Jabri

Time-Dependent Deflection and Crack Width in Polypropylene Fibre Reinforced Concrete Beams: A Review and Preliminary Experimental Results 845
Krishnaa Subramanian, Tom Molkens, Rutger Vrijdaghs

Eco-Resilient (ECORE) FRC Constructions 857
Pierre Rossi

Ultra-High-Performance Concrete (UHPC) as a Sustainable Alternative 867
Ray Hudd and Ralf Winterberg

Evaluation of cracking localization and its effect on load and displacement capacities of R_SFRC beams 875
Yuri S. Karinski and Avraham N. Dancygier

Recycling of steel fiber reinforced concrete 883
Klaus Holschemacher

Fracture model double-K - Concrete with a dose of recycled and industrially produced steel fibers 893
Jaroslav Prokop, Petr Frantík and Ivan Hollý

The role of recycled steel fibers in the sustainability of cementitious composites 903
Alessandro P. Fantilli, Andrea Garda

Retrofitting and strengthening

UHPFRC strengthening of bridge slabs - Towards a better understanding and prediction of failure mode under shear load 917
Jean-Philippe Charron, Espoir Kahama and Martin Pharand

Enhancing the Service Life of Historical Bridge Structures: Experimental Assessment of a CFRP–FRM Retrofit System 927
Anna Bontempi, Nico Di Stefano, Giulio Morandini, Giuseppe Melcangi, Luca Albertario, Fausto Minelli

Tensile Behavior of Fe-SMA Reinforced UHPFRC under Different Activation Methods 943
Xiujiang Shen, Tamás Mészöly, Norbert Randl and Yilin Li

Extended abstracts

Rethinking Wearing Surfaces (WS) for Orthotropic Steel Deck Bridges – SFRC WS for Extending the Bridge Service Life 955
Vellore Gopalaratnam

Hybrid Steel Fibre Reinforced Concrete based on calcium sulfoaluminate binder for precast tunnel segment production 957
Giulia Brentana, Ivan Trabucchi, Stefano Guanziroli, Giuseppe Tiberti and Giovanni Plizzari

Reinforcing 3D-Printed Concrete with Sprayed SHCC Overlay: A Post-Printing Reinforcement Method 959
Min Zhou, Maurizio Guadagnini and Behzad Nematollahi

Energy-based evaluation of ductility and toughness in fibre-reinforced self-compacting natural hydraulic lime concrete 961
Ángel De La Rosa Velasco, Gonzalo Ruiz López, Jesús Rodríguez Pérez

Simultaneous Optimization of Fiber Scheme and Structural Design for UHPC Structures 963
Naser S Alimrani, Jian Zhan and Shao Yi

Behaviour Of Reinforced Concrete Structural Elements Under Fire Exposure – An Integrated Structur-al Interpretation 965
Éva Lublóy , András Biró , György L. Balázs , Viktor Hlavička

Fatigue in compression and indirect tension in a high-tech steel- fiber reinforced concrete 967
Ángel De La Rosa Velasco, Gonzalo Ruiz, Vaibhav W. Masih, Riccardo Zanon

Extension of the Simplified Modified Tension Chord Model to predict cracking and deformation in fibre reinforced concrete 969
Guillem Rojas, Reignard Tan and Terje Kanstad

Fiber orientation effects in thin layers of HPFRC jacketing: a critical discussion of Model Code 2020 provisions. 971
Ivan Beltracchi, Adriano Reggia, Giovanni Metelli and Giovanni Plizzari

Numerical Study on the Strengthening of Pitting-Corroded Reinforced Concrete Dapped-End Beams 975
Elisa Carleschi, Jean-Philippe Charron and Giovanni Plizzari

Systemizing UHPFRC intervention for existing bridges: environmental and economic benefits at the network scale 977
Numa Bertola, Célia Küpfer and Eugen Brühwiler

Structural applications

Design of post-tensioned SFRC elevated slabs

Chiara Gaddi[1], Matteo Colombo[1], Marco di Prisco[1]

[1]: Department of Civil and Environmental Engineering, Politecnico di Milano, Milano, Italy.

Abstract

In the design of statically indeterminate structures, such as elevated slabs, the use of fibre reinforced concrete represents an effective solution to enhance load-bearing capacity, while limiting deflections and improving durability under serviceability conditions. To highlight the design optimization advantages arising from the combination of steel fibre reinforced concrete (SFRC) and post-tensioning, three design alternatives are presented for a case-study of elevated slab. The first option involves the use of traditional flexural reinforcement. The second one combines reinforcement with steel fibres. The third option integrates the use of steel fibres with unbonded post-tensioning only. The design of the three slab alternatives is performed in accordance with the *fib* Model Code 2020, complemented by formulations based on experimental findings for the assessment of the punching shear resistance in slabs without conventional bonded reinforcement. The design predictions obtained can be directly compared with the experimental results in order to assess the safety level of the design approach. A presentation of the results and a critical review of the approach is presented in the paper.

Keywords

Steel fibre reinforced concrete design, elevated slabs, unbonded post-tensioning, punching resistance

1 Introduction

In the design of elevated slabs, the combined use of post-tensioning and steel fibre reinforced concrete (SFRC) enables the development of efficient structural systems, characterised by limited deflections and crack widths under service conditions, enhanced durability and high load-bearing capacity. The statically indeterminate nature of slabs makes fibres particularly effective, allowing the reduction, and in some cases the substitution, of conventional flexural reinforcement, with consequent benefits in terms of reduced steel consumption, simplified detailing, and shorter construction times (Michels et al., 2012; di Prisco et al., 2014; Parmentier et al., 2014; Trygstad et al., 2014; di Prisco et al., 2019). Although the flexural behaviour of SFRC slabs without reinforcement has been extensively investigated, the limited amount of experimental data on their punching shear resistance and the resulting inapplicability of existing design formulations hinder the adoption of this type of structural elements (di Prisco and Felicetti, 1997; Tan and Venkateshwaran, 2019; Gaddi et al., 2026a; Gaddi et al., 2026b).

Regarding the ACI 544.6R (2015) and ACI 318 (2019) provisions, the main limitation lies in their empirical nature. Indeed, although longitudinal reinforcement parameters are not explicitly referenced, the presence of minimum reinforcement to ensure ductile behaviour is implicitly assumed. Consequently, the code equations may overestimate the punching shear capacity of unreinforced or lightly reinforced slabs. In the case of Eurocode 2 (2022) and Model Code 2020 (2023), limitations arise from both the inclusion of flexural reinforcement parameters and the reliance on the Critical Shear Crack Theory (Muttoni et al., 2023). The latter assumes a failure mechanism different from the one observed experimentally in slabs without longitudinal reinforcement (Gaddi et al., 2026a). Therefore, even the use of rotations from nonlinear finite element analyses (NLFEA), allowed by the fourth level of approximation of Model Code 2020, combined with modified analytical failure criteria for SFRC, may lead to inaccurate predictions (Gaddi et al., 2025).

In this context, the paper presents an analytical model for the assessment of the punching shear resistance of post-tensioned SFRC slabs without conventional reinforcement, with the aim of proposing a design approach addressing the current limitations of existing formulations. Building on the experimental results reported by Gaddi et al. (2026a), the proposed approach aims to consistently represent the punching failure modes observed in this type of structural member, namely splitting of the concrete struts and shear-compression failure of the compression chord. The reliability of the model is validated against an experimental dataset including slab specimens with varying fibre contents and post-tensioning (PT) parameters.

The optimisation advantages associated with the use of post-tensioned SFRC slabs are highlighted through the comparison of three alternative design solutions for an elevated slab, in terms of steel consumption and price per unit area. The first solution considers conventional flexural reinforcement only, the second combines reinforcement with SFRC, and the third adopts SFRC in combination with unbonded PT. The design is carried out in accordance with Model Code 2020 provisions, adopting the proposed analytical model for the punching shear verification of the third solution.

2 Punching resistance of SFRC slabs without reinforcement

In contrast to conventional reinforced concrete slabs, where punching failure is governed by

the propagation of flexural tangential cracks that interfere with the concrete struts responsible for shear transfer (Simões et al., 2018; Muttoni et al., 2023), the investigated slabs exhibited punching failure in the absence of tangential cracks (Gaddi et al., 2026a). Circular cracks associated solely with the propagation of the punching cone became visible on the tension side only after failure, whereas diagonal cracks were observed within the slab even at load levels below the punching failure load.

Based on the experimental evidence for slabs without flexural reinforcement (Gaddi et al., 2026a), load transfer is assumed to occur through radial bottle-shaped struts, bounded by radial flexural cracks. Since the propagation of radial cracks affects the stiffness of the struts due to the presence of tensile stresses in the tangential direction, the inclination of the struts is assumed to decrease as flexural cracking progresses. As a result, the load-carrying capacity of the struts is progressively reduced, promoting the onset of splitting cracks.

For slabs with a low fibre content (0.32% by volume in the experimental campaign considered), punching failure coincides with concrete strut splitting, and is therefore associated with diagonal crack openings comparable to those considered by design codes to evaluate the fibre contribution (1.5 mm in Model Code 2020 and 2.5 mm in Eurocode 2). By contrast, for higher fibre contents (0.45-0.57% by volume), the residual tensile strength of the SFRC is sufficient to stabilize the propagation of splitting cracks, with crack openings having a vertical component smaller than 0.35 mm at peak load. This behaviour is consistent with previous experimental observations on both plain concrete and SFRC struts, where an adequate control of cracking, provided by transverse reinforcement or fibres, stabilised crack propagation and prevented strength reduction (Schlaich and Schäfer, 1991; Colombo et al., 2008). Under these conditions, punching failure is governed by the shear-compression failure of the compression chord in the vicinity of the loaded area. In the absence of additional transverse reinforcement, this failure mode represents an upper bound for the punching shear resistance.

In light of these considerations, an analytical model has been developed to predict the punching shear resistance of SFRC slabs without bonded flexural reinforcement. The model involves the calculation of the ultimate load associated with the splitting resistance of the concrete struts and the ultimate load associated with shear-compression failure. The minimum of the two resistances associated with the aforementioned failure mechanisms is taken as the punching resistance of the SFRC slab without reinforcement.

2.1 Splitting failure

With regard to the punching shear resistance associated with splitting failure (V_{sp}), the formation of radial struts with a bottle-shaped geometry in the vicinity of the loaded area is considered. At the top node of the strut, in contrast with existing strut-and-tie models for punching shear (Rizk et al., 2012), due to the absence of longitudinal reinforcement, equilibrium is assumed to be provided by the shear resistance of the upper portion of the slab. For a given strut inclination θ, the geometry of the strut and discontinuity region considered for the evaluation of the splitting resistance, highlighted in red in Fig. 1a, is defined based on trigonometric relationships. The second expression in Equation 3 is adapted from Angotti et al. (2019). The geometrical parameters are defined as follows:

$$a = (r_c \cdot \sin\theta + 2x_C \cdot \cos\theta) \tag{1}$$

$$h = \min\{(H - 2x)/\sin\theta; 2x/\cos\theta\} \tag{2}$$

$$b = \begin{cases} 2x/\cos\theta\,, & h = 2x/\cos\theta \\ h + 0.65a, & h < 2x/\cos\theta \end{cases} \tag{3}$$

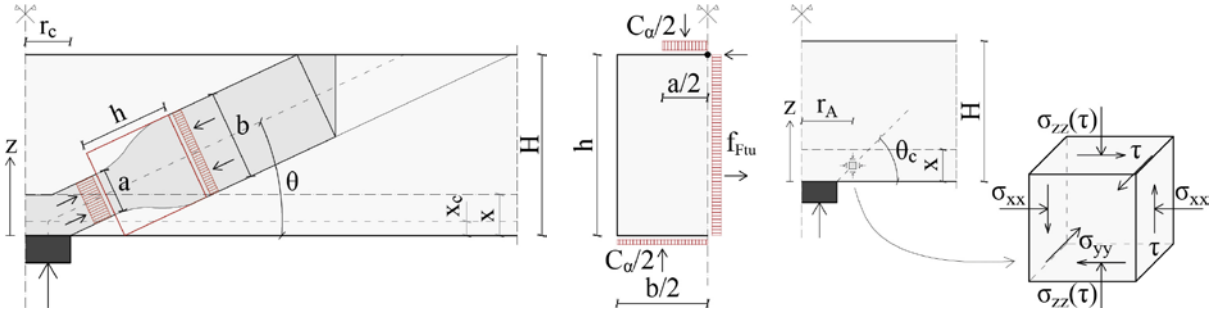
The depth of the compression chord x and the depth x_c, corresponding to the location of the resultant of compressive stresses, are determined by analysing the flexural behaviour of a slab strip representative of the supported area, assuming a crack opening of 0.5 mm at the tension side. This crack opening value is consistent with experimental observations and, for SFRC slabs, can be associated with the onset of flexural failure. For both parameters, the adopted values correspond to the average of those obtained along the two principal slab directions.

The load C_α, associated with the splitting resistance of the concrete strut (Fig. 1a), is determined as follows, by imposing the rotational equilibrium of the discontinuity region and considering the stress distribution shown in Fig. 1b:

$$C_\alpha = \frac{4}{3} \cdot f_{Ftu} \cdot h^2 \cdot \frac{2L(\alpha)+l(\alpha)}{b-a} \tag{4}$$

where $L(\alpha)$ and $l(\alpha)$ are the major and minor dimensions of the discontinuity region, evaluated along the tangential direction to the loaded area for a unit angle α (out-of-plane dimensions with respect to Fig. 1a-1b).

The corresponding splitting resistance V_{sp} is given by the vertical component of the resultant compressive forces in the struts, obtained by integrating the load C_α over the interval [0, 2π].



(a) (b) (c)

Figure 1: Splitting failure: geometry of the concrete strut (a) and equilibrium condition of the D-region at failure (b). Triaxial stress state assumed for shear-compression failure (c).

2.2 Shear-compression failure

The punching shear resistance associated with shear-compression failure (V_{sc}) is assessed based on the triaxial stress state at a representative point located at the centroid of the compression chord ($z = x/2$) and at a distance r_A from the centre of the loaded area (Fig. 1c). The depth of the compression chord x corresponds to the value previously calculated for splitting failure, while the distance r_A is evaluated by assuming a local diffusion of compression at 45° (θ_c).

The stress component σ_{yy}, acting tangentially to the concrete struts, is taken as equal to the average stress in the compression chord, defined by considering only the flexural behaviour of the slab. When the values associated with the two principal slab directions differ, as may occur depending on the adopted PT layout, their average value may be considered. The same value is also adopted, as a simplified assumption, for the stress component σ_{xx}, acting in the radial direction. In contrast to σ_{yy}, however, the evaluation of this stress component cannot be attributed solely to the flexural behaviour of the slab, and further investigation is required.

The vertical stress σ_{zz}, evaluated at $z=x/2$, is computed assuming a uniform distribution of shear stresses ($\tau=\tau_{xz}=\tau_{zx}$) and a decrease in vertical stresses with depth z, reaching zero at the neutral axis. Based on these assumptions, σ_{zz} is computed using the following relations:

$$P = \sigma_{zz(z=0)} \cdot {r_c}^2 \pi = \tau \cdot (2r_c + x/\tan\theta_c) \quad (5)$$

$$P = \sigma_{zz(z=x/2)} \cdot \left(2r_c + \frac{x}{\tan\theta_c}\right)^2 \frac{\pi}{4} = \tau \cdot \frac{x}{2} \cdot [2r_c + x/(2\tan\theta_c)]\pi \quad (6)$$

The resistance V_{sc} is determined from Eq. 5 by computing the value of the shear stress τ such that the stress state lies on the failure surface. The definition of the failure domain is based on the five-parameter model with curved meridians proposed by Willam and Warnke (1974). In the absence of experimental data on triaxial strength, the compression meridian is defined with reference to the high-compression regime stresses reported by Willam and Warnke (1974). The coefficients defining the tension meridian are instead calibrated based on literature data for fibre reinforced concretes with different fibre types and dosages (Lu and Hsu, 2006; Chi et al., 2014; Baghban Golpasand et al., 2021; Kang et al., 2024). Specifically, the coefficients a_0, a_1 and a_2 are assumed equal to 0.0613, -0.8624 and -0.1397, respectively.

2.3 Model validation

To validate the proposed analytical model, the punching resistances associated with splitting and shear-compression failure are compared with the maximum loads observed for slabs without flexural reinforcement (Gaddi et al., 2026a). The slab specimens had dimensions of 200×2000×2000 mm and were cast using self-compacting concrete with maximum aggregate size of 16 mm. Double hooked-end steel fibres with a length of 60 mm and an aspect ratio of 80 were adopted. The reference PT system consisted of straight, unbonded tendons arranged in a uniform-banded layout, resulting in an average compressive stress in the concrete of 0.9 MPa. Variations to the reference PT system and integrity reinforcement are also considered (Table 1), as they were observed to primarily affect the post-punching behaviour.

To estimate the value of the angle θ, the depth of flexural radial cracks under increasing load was evaluated for each slab specimen by means of two-dimensional NLFEA. Details of the adopted numerical models can be found in Gaddi et al. (2025). The angle θ was determined as the tangent to the radial crack profile in the vicinity of the loading area. Since different values were obtained for each slab and no clear correlation with material properties or PT parameters could be identified, a constant value of 25° was adopted for the calculation of the punching resistance. This value corresponds to the average of the angles obtained for the investigated slabs, assuming for each slab the minimum value among those measured along its principal directions, as it is associated with a lower resistance. It should be noted that the adopted value of θ is close to that assumed in the previous Eurocode 2 (2005) for the definition of the punching cone (26.6°). The applicability of this value to slabs with significantly different mechanical properties should be further assessed.

Given the brittle nature of the failure mechanism and the topological variability of the SFRC (Gaddi et al., 2026b), characteristic values of material properties were adopted in the calculation of punching shear resistance. For the same reason, the coefficient k_G was assumed equal to 1. Conversely, the position of the neutral axis and the angle θ were determined using mean values, as they are related to the flexural response of the slab. No partial safety factors were applied, whereas the orientation factor k_0 was taken equal to 1.

Table 1: Experimental and predicted punching shear resistances.

ID	Variation	V_f (%)	f_{ck} (MPa)	SFRC class	P_{exp} (kN)	V_{sp} (kN)	V_{sp}/P_{exp} (-)	V_{sc} (kN)	V_{sc}/P_{exp} (-)
SS25	-	0.32	39.77	3e	481	461	0.96	436	0.91
SS35	-	0.45	41.91	4d	572	573	1.00	549	0.96
SS45	-	0.57	50.51	5e	585	830	1.42	618	1.06
SS35B	Banded tendons	0.45	50.73	3e	599	498	0.83	605	1.01
SS35D	Draped tendons	0.45	51.74	4e	663	723	1.09	605	0.91
SS35G	Bonded tendons	0.45	51.74	4e	618	690	1.12	590	0.96
SS35R	Integrity rebars	0.45	42.45	3.5e	593	599	1.01	513	0.87

The predicted punching shear resistances are reported in Table 1. By considering the minimum value between the resistances associated with splitting failure and shear-compression failure, the average ratio between the predicted punching shear resistance and the experimental ultimate load (P_{exp}) is equal to 0.93, with a coefficient of variation (CoV) of 0.08. The minimum and maximum ratios between predicted resistance and ultimate load are 0.83 and 1.06.

In contrast with the experimental observations, all slabs except specimen SS35B are predicted to fail in shear-compression. However, it is worth noting that, consistently with experimental results, while for slab SS45 there is a clear distinction between the resistances associated with the two failure modes, for the other slabs this difference is less pronounced. Moreover, the resistance values associated with splitting failure are generally consistent with the experimental results. It should be noted that, for slabs with a fibre volume ratio of 0.45%, the experimentally observed failure mode was identified as transitional between splitting failure and shear-compression failure. The tendency toward one failure mode rather than the other was assessed for these specimens solely on the basis of the punching crack opening at peak load.

3 Design of case studies

To highlight the potential advantages arising from the combined use of SFRC and unbonded PT, three alternative design solutions are investigated for the same case study. The reference structure is a square elevated slab with three spans per side, each of them 6 m long, supported by circular columns with a diameter of 300 mm. The non-structural permanent load and the live load are taken as 2.50 kN/m² and 4.00 kN/m², respectively, which are representative of typical loading conditions in multi-storey car parks.

The first solution adopts conventional reinforcement only, whereas the second integrates the use of conventional reinforcement with steel fibres. The third solution involves the use of SFRC in combination with unbonded PT, without any additional passive reinforcement. For each slab configuration, thicknesses ranging from 200 mm to 250 mm are considered, assuming a gross concrete cover of 40 mm. For the plain concrete, the strength class C40/50 is assumed, while for the SFRC slabs, classes C40/50 3e, 4e and 5e are considered. According to Table 1, these classes can be achieved with steel fibre dosages of around 25, 35 and 45 kg/m³, respectively. Steel rebars in class B450 C are considered for the first and second solutions, while tendons characterised by a 0.1% proof stress of 1560 MPa are adopted for the third one. The partial safety factors for concrete in compression (γ_C) and for SFRC in tension (γ_F) are assumed equal to 1.5, while the partial safety factor for reinforcing steel (γ_S) is taken as 1.15.

Given the scope of this study, the design is carried out with reference to the ultimate limit

state only, following the provisions of the Model Code 2020. The flexural capacity of the slabs is assessed according to the Yield Line Theory, assuming a folded plate yield line pattern and a fan failure pattern at column locations. The ratio between positive and negative bending moments is assumed equal to 1.85, corresponding to an elastic distribution of bending moments (di Prisco et al., 2014; fib, 2022). Punching shear resistance is defined according to the capacity-design approach, adopting an overstrength factor equal to 1.

Flexural reinforcement design is performed with reference to the edge spans, whereas punching shear verifications are carried out at the central columns. To ensure a consistent comparison among the three design alternatives, the design process is conducted with the aim of maintaining, as far as possible, a constant safety factor against bending γ_B, defined as the ratio between the ultimate load and the design load.

The results obtained for the three slab types are presented in Tables 2-4, considering all combinations of slab thickness and SFRC strength class. Each slab is identified by a code in which the first number denotes the slab type, while the second indicates the slab thickness in mm. For the SFRC slabs, the strength class is also indicated. The Tables include details on flexural and punching shear reinforcement, as well as the safety factors for bending (γ_B) and for punching without ($\gamma_{P,ws}$) and with shear reinforcement ($\gamma_{P,s}$). These safety factors are defined as the ratio between the punching resistance and the applied shear force.

3.1 Slab type 1: conventional reinforcement

For the flexural reinforcement, the configuration that minimises the total steel volume is selected, considering rebar diameters ranging from 12 to 20 mm. The positive moment reinforcement is distributed uniformly across the bays, whereas the negative moment reinforcement is concentrated at the columns over a square area with a side length equal to half of the span. For punching reinforcement, shear studs with a diameter of 10 mm are considered.

Table 2: Reinforcement and safety coefficients for bending and punching of slab type 1.

ID	Bottom rebars	Top rebars	γ_B (-)	$\gamma_{P,ws}$ (-)	Studs/perimeter	Perimeters	$\gamma_{P,s}$ (-)
1-200	Ø12@150	Ø16@150	1.09	0.33	-	-	0.92
1-210	Ø12@150	Ø14@120	1.12	0.35	-	-	0.98
1-220	Ø12@150	Ø14@125	1.15	0.37	10	4	1.04
1-230	Ø14@240	Ø14@125	1.08	0.41	10	3	1.15
1-240	Ø14@240	Ø14@125	1.12	0.45	10	3	1.25
1-250	Ø14@250	Ø12@100	1.09	0.45	9	3	1.22

For the case study under consideration, punching resistance governs the slab thickness when conventional reinforcement is adopted. Indeed, as shown in Table 2, for slabs 1-200 and 1-210 the maximum resistance associated with the compression strut failure within the support region is lower than the applied shear force. The same failure mechanism is expected for slab 1-220.

3.2 Slab type 2: fibres and reinforcement

The flexural capacity of slab type 2 (Table 3) is evaluated by adopting the rigid-plastic model for SFRC, selecting the reinforcement configuration that minimises steel consumption. The minimum rebar diameter is set to 8 mm. In all calculations, the orientation factor k_0 is taken equal to 1, whereas in the evaluation of punching shear resistance the coefficient k_G is assumed equal to 1, due to the brittle nature of the failure mechanism.

Table 3: Reinforcement and safety coefficients for bending and punching of slab type 2.

ID	Bottom rebars	Top rebars	γ_B (-)	$\gamma_{P,ws}$ (-)	Studs/perimeter	Perimeters	$\gamma_{P,s}$ (-)
2-200-3e	Ø10@200	Ø16@200	1.12	0.64	11	2	1.16
2-200-4e	Ø8@200	Ø16@240	1.10	0.73	11	2	1.25
2-200-5e	Ø8@240	Ø12@240	1.09	0.77	11	2	1.29
2-210-3e	Ø10@240	Ø16@200	1.13	0.70	11	2	1.21
2-210-4e	Ø8@250	Ø16@240	1.13	0.80	11	2	1.31
2-210-5e	Ø8@250	Ø8@150	1.12	0.81	11	2	1.32
2-220-3e	Ø10@250	Ø16@200	1.18	0.76	10	2	1.22
2-220-4e	Ø8@250	Ø12@150	1.17	0.84	10	2	1.30
2-220-5e	Ø8@250	Ø8@250	1.15	0.84	10	2	1.29
2-230-3e	Ø8@240	Ø16@250	1.09	0.77	10	2	1.21
2-230-4e	Ø8@250	Ø10@250	1.09	0.78	10	2	1.22
2-230-5e	Ø8@250	Ø8@250	1.22	0.91	10	2	1.35
2-240-3e	Ø8@240	Ø12@150	1.13	0.81	10	2	1.25
2-240-4e	Ø8@240	Ø8@240	1.12	0.80	10	2	1.24
2-240-5e	Ø8@240	Ø8@240	1.31	0.98	10	2	1.42
2-250-3e	Ø8@200	Ø12@250	1.11	0.76	9	2	1.15
2-250-4e	Ø8@200	Ø8@200	1.24	0.88	9	2	1.26
2-250-5e	Ø8@200	Ø8@200	1.44	1.07	9	2	1.46

In contrast to conventional reinforced concrete slabs, for slab type 2 the addition of two perimetrical lines of shear studs is sufficient to satisfy punching shear verifications. However, it should be noted that neither the Model Code 2020 nor the Annex L of Eurocode 2 explicitly specifies an upper limit to punching shear resistance for SFRC slabs. For the considered cases, if the same limits prescribed for plain concrete slabs were adopted, punching shear verifications would not be satisfied for slabs with a thickness of 200 mm and for slabs 2-230-4e and 2-230-5e.

3.3 Slab type 3: fibres and unbonded post-tensioning

For each combination of slab thickness and SFRC class, the design of the unbonded PT system is performed considering the minimum compressive stress required to achieve the safety factor γ_B obtained for slab type 1. Additionally, as MC2020 does not provide specific requirements for this type of slab, a criterion analogous to that adopted for SFRC slabs with minimum reinforcement is introduced to ensure adequate deformation capacity after cracking (fib, 2023). To this end, the flexural resistance provided solely by the applied axial force is required to exceed 0.5 times the corresponding cracking moment. The PT stress is assumed equal to 1300 MPa for each strand, while the PT losses are conservatively estimated at 30% of the initial stress, accounting for the potential adoption of draped tendons. To limit tendon spacing, 7-wire mono-strand tendons with a nominal area of 200 mm² are adopted. In both slab directions, tendons are arranged in a uniform layout and without vertical eccentricity.

Punching shear verification is performed according to the approach presented in Section 2, assuming an inclination of 25° for the concrete struts. In the absence of experimental data on the punching resistance of post-tensioned SFRC slabs with transverse reinforcement, an additional measure to indirectly enhance punching resistance could be the introduction of draped banded tendons in the column region. Therefore, if the verification is not satisfied, or if the value of $\gamma_{P,ws}$ is lower than γ_B, a draped tendon profile is assumed within the region affected

by punching shear. This allows the applied shear load to be reduced by subtracting the vertical component of the PT force (indicated with V_P in Table 4). For these tendons only, the vertical eccentricity is taken as the slab thickness minus two times the concrete cover.

Table 4: Post-tensioning data, punching shear resistance and safety coefficients of slab type 3.

ID	σ_{cp} (MPa)	**Uniform tendon spacing**	γ_B (-)	V_{Rd} (kN)	V_P (kN)	$\gamma_{P,ws}$ (-)
3-200-3e	1.86	490	1.09	664	-	1.14
3-200-4e	1.42	640	1.09	592	264	1.46
3-200-5e	0.98	930	109	515	264	1.33
3-210-3e	1.70	510	1.13	669	286	1.60
3-210-4e	1.24	700	1.12	585	286	1.46
3-210-5e	0.85	1020	1.13	517	286	1.35
3-220-3e	1.53	540	1.15	667	307	1.60
3-220-4e	1.09	760	1.15	578	307	1.45
3-220-5e	0.84	980	1.22	554	307	1.41
3-230-3e	1.15	690	1.09	582	327	1.47
3-230-4e	0.83	950	1.13	532	327	1.39
3-230-5e	0.83	950	1.30	585	327	1.47
3-240-3e	1.05	720	1.12	589	348	1.48
3-240-4e	0.83	910	1.21	569	348	1.45
3-240-5e	0.83	910	1.39	625	348	1.54
3-250-3e	0.84	870	1.10	548	368	1.42
3-250-4e	0.83	880	1.29	603	368	1.51
3-250-5e	0.83	880	1.48	660	368	1.60

For all the investigated combinations of slab thickness and SFRC class, punching is governed by a shear-compression failure mechanism, and the adoption of a draped tendon profile in the vicinity of the columns is sufficient to ensure the required punching resistance.

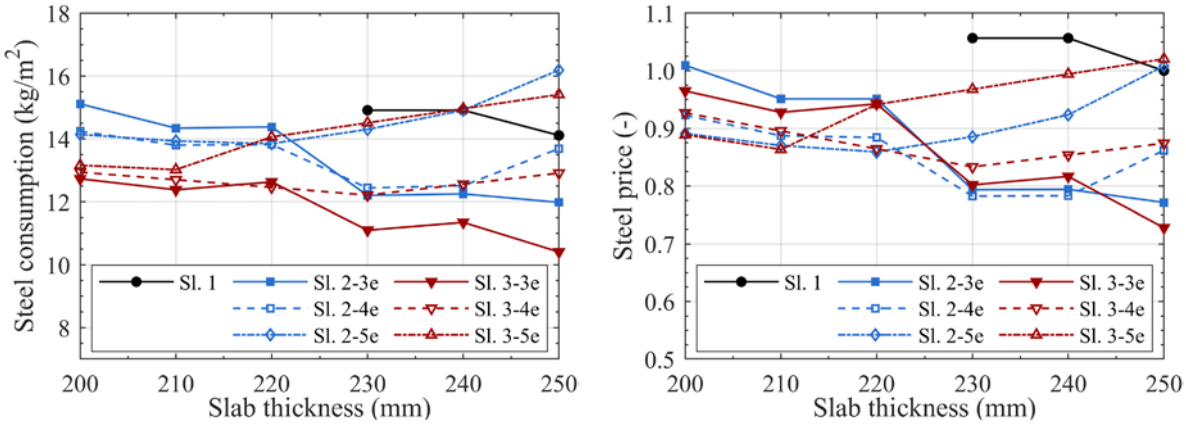
4 Comparison of case studies

The comparison among the three alternative solutions is performed by estimating, for a representative bay, the steel consumption and the price of reinforcement, tendons and fibres. Price estimation is conducted with reference to the price list for public works of Regione Lombardia (2025). Considering the different levels of labour required by the three design alternatives, the adopted unit prices refer to completed works, and therefore include labour costs, site overheads and profit of contractor. Specifically, a unit price of 2.18 €/kg is assumed for the rebars, while the price for PT tendons is taken as 4.77 €/m. The latter value is increased compared with the price list to account for the larger cross-section of the tendon adopted in this study. In the absence of specific data, the same unit price as rebars is assumed for shear studs, while the cost of steel fibres is taken equal to 1.80 €/kg.

The estimated values are reported in Figure 2 as a function of slab thickness and SFRC class. Given the significant fluctuations in steel prices over time, prices are normalized with respect to slab 1-250, which is the most economical among the verified configurations for slab type 1. The price for this slab amounts to 30.76 €/m^2.

The comparison among the three design solutions highlights the advantages of SFRC over conventional reinforced concrete, even when considering strength classes commonly adopted

in practice. Specifically, for a slab thickness of 250 mm, a reduction in steel consumption of up to approximately 15% and 26% can be achieved with respect to slab type 1 for slabs type 2 and 3, respectively. When unit prices are considered, the corresponding reductions amounts to 23% and 27%, respectively. The contribution of steel fibres is particularly evident for slabs with strength class 5e. For these slabs, for thicknesses greater than 210-220 mm, steel consumption and unit prices increase, in contrast to the general decreasing trend observed with increasing thickness. As a result, for thicknesses of 240–250 mm, steel consumption exceeds that of the corresponding slab type 1. This behaviour is mainly related to the need to ensure the minimum reinforcement ratio and PT stress rather than to an actual structural demand, as indicated by the higher safety margins obtained (Tables 3-4). Therefore, when considering the ultimate limit state alone, the benefits associated with higher fibre contents are progressively offset by the ductility requirements.



(a) (b)

Figure 2: Comparison of design alternatives: steel consumption (a) and steel price (b) for unit area.

Regarding the comparison between the SFRC solutions, for the investigated combinations, the use of PT generally results in lower steel consumption for a given SFRC strength class. However, due to the higher price of PT systems compared with conventional reinforcement, the reduction in steel consumption is not always sufficient to offset the additional price of PT. Since the adopted unit prices account only for steel consumption, the differences between slab thicknesses may be compensated by the higher concrete cost per unit area.

5 Concluding remarks

The paper presents three alternative design solutions for the case study of an elevated slab, considering different slab thicknesses and SFRC strength classes to highlight the potential advantages associated with the use of SFRC and unbonded post-tensioning. With reference to the ultimate limit state only, the comparison among the proposed solutions shows that the use of SFRC enables the design of more slender slabs (thickness decreased from 230 to 200 mm) while reducing steel consumption by up to 26% compared with a conventional reinforced concrete slab of the same thickness.

Based on the discussed results, the paper emphasises the need for design provisions capable of assessing the punching shear resistance of unbonded post-tensioned SFRC slabs without traditional reinforcement, in order to enable a more efficient use of material and time resources. To address this, an analytical approach for punching shear resistance is proposed which, despite

some preliminary simplifying assumptions, enables the estimation of the punching shear resistance with an average underestimation of 7% (CoV of 0.08). Given the limited number of experimental results reported in the literature, further experimental investigations are needed to assess the reliability of the proposed model and the validity of the underlying assumptions for slabs with a wider range of thicknesses and concrete strength classes. Furthermore, the experimental results, together with the proposed model, highlight the need to account for an upper limit to punching shear resistance of SFRC slabs, both with and without bonded flexural reinforcement. They also highlight the importance of properly accounting for the interaction between fibres and punching shear reinforcement in the design process.

6 Acknowledgements

The authors gratefully acknowledge Bekaert and CCL for the financial support of the experimental campaign underlying the analytical model presented in this study.

7 References

ACI 318-19, 2019. *Building Code Requirements for Structural Concrete*. American Concrete Institute, Farmington Hills.

ACI 544.6R-15, 2015. *Report on design and construction of steel fiber-reinforced concrete elevated slabs*. American Concrete Institute, Farmington Hills.

Angotti, F., Guglia, M., Marro, P., and Orlando, M., 2019. *Progetto delle strutture in calcestruzzo armato* (in Italian), Second Edition, Hoepli, Italy.

Baghban Golpasand, G., Farzam, M., and Soleymani Shishvan S., 2021. "Experimental and numerical investigation of effect of steel fiber on fiber reinforced concrete under multiaxial compression", *Amirkabir Journal of Civil Engineering*, 53(6), pp2657-2678. doi: 10.22060/ceej.2020.17462.6576

Chi, Y., Xu, L., and Yu, H., 2014. "Constitutive modelling of steel-polypropylene hybrid fiber reinforced concrete using non-associated plasticity and its numerical implementation", *Composite Structures*, 111, pp497-509. doi: 10.1016/j.compstruct.2014.01.025

Colombo, M., di Prisco, M., and Lamperti, M., 2008. "SFRC D-regions: size effect in bottle-shaped struts", Fibre reinforced concrete: design and applications. Proceedings of the 7th RILEM international symposium (BEFIB 2008), Chennai, September 17-19, pp387–398

di Prisco, M., and Felicetti, R., 1997. "Some results on punching shear in plain and fibre-reinforced micro-concrete slabs", *Magazine of Concrete Research*, 49(180), pp201-219.

di Prisco, M., Plizzari, G., and Vandewalle, L., 2014. "Structural design according to fib MC 2010: comparison between RC and FRC elements", *Fibre-reinforced concrete: from design to structural applications. Proceedings of the FRC 2014 joint ACI-fib International Workshop*, Montreal, July 24-25, pp1-16.

di Prisco, M., Colombo, M., and Pourzarabi, A., 2019. "Biaxial bending of SFRC slabs: is conventional reinforcement necessary?", *Materials and Structures*, 52(1), pp1-15. doi: 10.1617/s11527-018-1302-0

EN 1992-1-1, 2005. *Eurocode 2: Design of concrete structures – Part 1-1: General rules and rules for buildings.* European Committee for Standardization, Brussels.

fib, 2022. *Fibre Reinforced Concrete. State-of-the-Art report*. Bulletin 105, Fédération Internationale du Béton, Lausanne. doi: 10.35789/fib.BULL.0105

fib, 2023. *fib Model Code for Concrete Structures 2020*, Final draft. Fédération Internationale

du Béton, Lausanne.

FprEN_1992-1-1, 2022. *Eurocode 2: Design of concrete structures - Part 1-1: General rules - Rules for buildings, bridges and civil engineering structures*, Final Draft. European Committee for Standardisation.

Gaddi, C., Colombo, M., and di Prisco, M., 2025. "Numerical prediction of punching shear in post-tensioned steel fibre reinforced concrete elevated slabs", *Proceedings of the 4th fib Italy YMG Symposium on Concrete and Concrete Structures*, Naples, September 15-16, pp7-14.

Gaddi, C., Colombo, M., and di Prisco, M., 2026a. "Punching shear of unbonded post-tensioned steel fiber reinforced concrete slabs: the fiber contribution", *Structural Concrete* (in press). doi: 10.1002/suco.70579

Gaddi, C., Colombo, M., and di Prisco, M., 2026b. "Punching shear in unbonded post-tensioned steel fibre reinforced concrete slabs: the role of fibre distribution", *Proceedings of the 16th fib International PhD Symposium in Civil Engineering*, Vienna, September 9-11 (in press).

Kang, L., Gong, C., Zhu, H., Ding, W., and Zheng, K., 2024. "Triaxial failure criterion and multi-scale failure mechanism of hybrid steel fiber reinforced self-compacting concrete", *Journal of Building Engineering*, 98, 1113344. doi: 10.1016/j.jobe.2024.111334

Lu, X., and Hsu, T.C.T., 2006. "Behavior of high strength concrete with and without steel fiber reinforcement in triaxial compression", *Cement and Concrete Research*, 36(9), pp1679-1685. doi: 10.1016/j.cemconres.2006.05.021

Michels, J., Waldmann, D., Maas, S., and Zürbes, A., 2012. "Steel fibers as only reinforcement for flat slab construction - Experimental investigation and design", *Construction and Building Materials*, 26(1), pp145–155. doi: 10.1016/j.conbuildmat.2011.06.004

Muttoni, A., Simões, J.T., Faria, D.M.V., and Fernández Ruiz, M., 2023. "A mechanical approach for the punching shear provisions in the second generation of Eurocode 2", *Hormigón y Acero*, 74(299–300), pp61–77. doi: 10.33586/hya.2022.3091

Parmentier, B., Van Itterbeeck, P., and Skowron, A., 2014. "The flexural behaviour of SFRC flat slabs: the Limelette full-scale experiments to support design model codes", *Fibre-reinforced concrete: from design to structural applications. Proceedings of the FRC 2014 joint ACI-fib International Workshop*, Montreal, July 24-25, pp213–222.

Regione Lombardia, 2025. *Prezziario regionale dei lavori pubblici*, 2nd edition. Regione Lombardia, Milano.

Rizk, E., Marzouck, H., and Tiller, R., 2012. "Design of thick concrete plates using strut-and-tie model", *ACI Structural Journal*, 109(5), pp677-686. doi: 10.14359/51684045

Schlaich, J., and Schäfer, K., 1991. "Design and detailing of structural concrete using strut-and-tie models", The Structural Engineer, 69(6), pp113–125

Simões, J.T., Fernández Ruiz, M., and Muttoni, A., 2018. "Validation of the critical shear crack theory for punching of slabs without transverse reinforcement by means of a refined mechanical model", *Structural Concrete*, 19(1), pp191–216. doi: 10.1002/suco.201700280

Tan, K.H., and Venkateshwaran, A., 2019. "Punching shear in steel fiber-reinforced concrete slabs with or without traditional reinforcement", *ACI Structural Journal*, 116(3), pp107-118. doi: 10.14359/51713291

Trygstad, S., Hallberg, M.A., Hansen, H.E., and Kanstad, T., 2014. "Fibre-reinforced SCC in post-tensioned flat slabs: full scale test and design methods", *Proceedings of the 1st Concrete Innovation Conference*, Oslo, June 11-13.

Willam, K.J., and Warnke, E.P., 1974. "Constitutive model for the triaxial behaviour of concrete", *IABSE Seminar on concrete structures subjected to triaxial stresses*, Bergamo, May 17-19.

Behaviour of a precast steel-fibre-reinforced concrete thin-walled box structure subjected to cyclic loading

Luca Facconi[1], Fausto Minelli[1], Andrea Pasetto[2] and Giovanni Plizzari[1]

[1] Università degli Studi di Brescia, via Branze 43, Brescia, Italy

[2] FRAMAR-TMT S.r.l., Via Commercio 2, 25011 Calcinato (BS), Italy

Abstract

Steel-fibre-reinforced concrete (SFRC) is increasingly used in the precast industry for prefabricated elements in industrial and residential buildings. Unlike traditional reinforced concrete (RC), the high post-cracking strength and toughness of SFRC allow conventional reinforcement to be partially, or even completely, replaced, enabling thinner and lighter elements.

Precast RC box structures, such as electrical shelters and water tanks, typically consist of low-rise thin walls internally reinforced with one or more layers of deformed bars and/or welded wire reinforcement. Optimisation through partial replacement of conventional reinforcement with steel fibres can lead to structural walls whose performance is comparable to, or even higher than, that of conventional RC elements. In addition, the use of fibres simplifies fabrication, while the reduction in wall thickness can significantly lower transportation costs.

This paper presents the results of an experimental investigation conducted on a 5.2 x 2.5 x 2.7 m^3 prefabricated box structure consisting of four 70 mm thick perimeter walls and a thin roof slab. Two specimens were tested: one with conventional RC reinforcement and one with hybrid reinforcement, consisting of SFRC with 25 kg/m^3 of steel fibres combined with rebars. Both specimens were subjected to reversed cyclic lateral loading. The comparison of the experimental results shows that, despite the replacement of most of the conventional reinforcement with steel fibres, the SFRC structure exhibited a hysteretic response very similar to that of the RC specimen in terms of strength, deformation capacity and failure mechanism.

Keywords

Steel-fibre-reinforced concrete, precast box structure, thin-walled elements, hybrid reinforcement, cyclic loading, shear behaviour, displacement capacity

1 Introduction

Fibre-reinforced concrete (FRC) has proven to be an effective material for thin-walled prefabricated structures, as it can partially or completely replace conventional reinforcement, which typically consists of welded steel mesh providing distributed reinforcement (Di Prisco et al., 2013). One of the main advantages of steel fibres is their ability to reduce the required thickness of structural elements, since the concrete-cover requirements associated with traditional reinforced concrete can be significantly reduced, or even eliminated, when suitable reinforcement layouts are adopted (Minelli and Plizzari, 2013; Tiberti et al., 2014). This benefit is particularly relevant for modular structures such as precast concrete box shelters, where thinner walls result in lighter modules, thereby facilitating lifting, handling and transportation operations and reducing costs. In addition, the reduced concrete volume required for thin-walled elements, together with the optimisation of production and construction processes, contributes to lowering both environmental impact and energy consumption (Sawadogo et al., 2025).

This work discusses the results of an experimental investigation involving two precast thin-walled box shelters tested under quasi-static cyclic loading, simulating the effects of horizontal actions such as earthquake-induced actions. Consistent with previous experimental research (Facconi et al., 2016), the aim of the tests was to compare the behaviour of conventional reinforcement, used in reinforced concrete (RC), with that of hybrid reinforcement (Facconi et al., 2019), made with a combination of steel fibres and rebars and hereafter referred to as HFRC. To this end, two specimens were constructed and tested: one adopting the traditional RC solution typically used in practice, and the other incorporating the proposed HFRC alternative. The HFRC specimen was designed to exhibit a global response comparable to that of the conventional RC specimen, both in terms of overall strength and displacement capacity. The discussion of the experimental results includes an assessment of the global hysteretic response, together with an analysis of the evolution of crack patterns and the principal damage mechanisms observed during the tests.

2 Experimental programme

The experimental programme consisted of two full-scale box structures with plan dimensions of 5.2 x 2.5 m^2 and a height of 2.7 m, measured from the bottom face of the base slab to the upper face of the roof slab (Figs. 1 and 2). The two specimens, named B-RC and B-HFRC, had identical geometry and structural components, including an 80 mm thick bottom slab, four 70 mm thick walls with rectangular openings, and an 80 mm thick top slab supported by the walls. Both structures were cast in a precast factory using special steel moulds that allowed the concrete to be poured while the structure was positioned upside down. As a result, the bottom slab was monolithically connected to the walls along the entire perimeter of the structure. In contrast, the top slab, which was 60 mm wider and longer than the box, was cast in a separate mould and subsequently connected to the walls using precast steel bolted connections. The two specimens adopted different reinforcement configurations. Specimen B-RC (Fig. 1) replicated a typical reinforced-concrete box shelter currently in production. The reinforcement consisted of two layers of steel mesh formed by 5 mm diameter deformed rebars spaced at 220 mm, placed within the four walls with a concrete cover of approximately 20 mm. In addition to this distributed reinforcement, 8 mm diameter rebars were placed vertically and horizontally in the middle of the walls, particularly near the openings and the corners of the box. This traditional

double-layer reinforcement layout leads to several issues related to both structural design and construction. To ensure adequate durability in accordance with EN 1992-1-1 (2023) provisions, the wall thickness cannot be less than 70 mm, so that minimum concrete-cover requirements are fulfilled. In addition, the amount of reinforcement within such a limited member thickness makes construction time-consuming and challenging, since particular care is required to position the rebars correctly inside the mould.

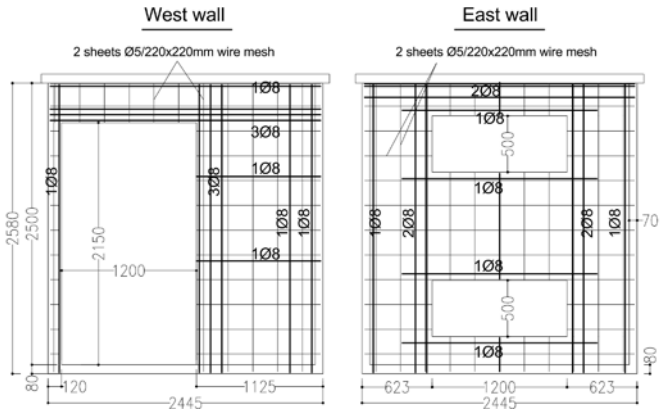
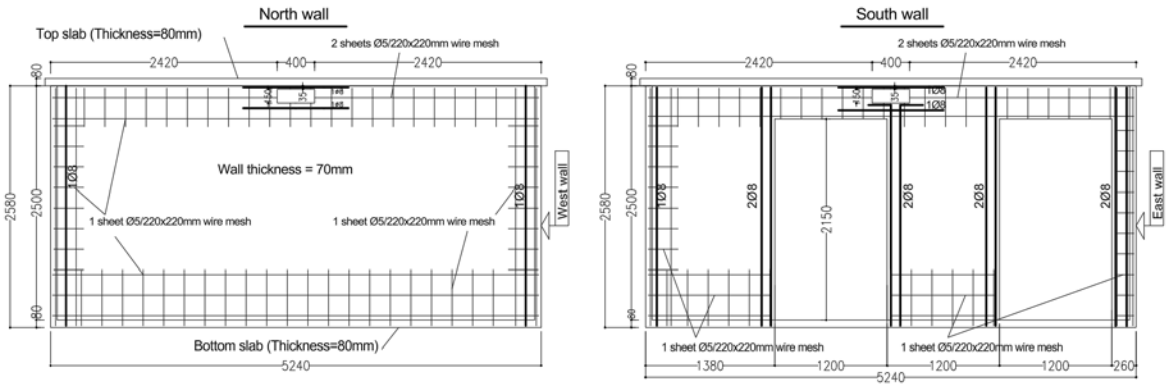
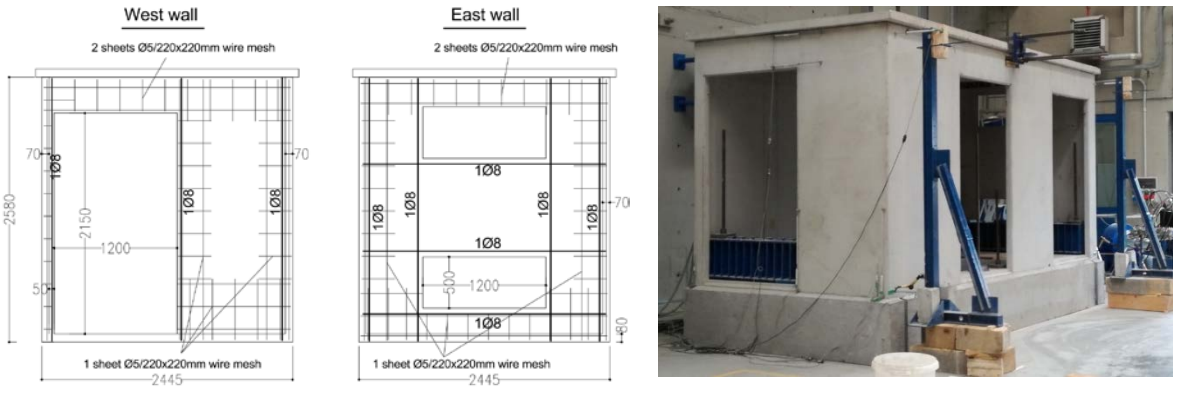


Figure 1: Details of the box structure with conventional reinforcement (B-RC): east and west walls. Dimensions in [mm].



(a)



(b) *(c)*

Figure 2: Details of the box structure with hybrid reinforcement (B-HFRC): (a) north and south walls; (b) east and west walls; (c) view of the specimen before testing. Dimensions in [mm].

Specimen B-HFRC adopted the hybrid reinforcement layout shown in Figs. 2a and 2b, which combines FRC with conventional reinforcement. Unlike B-RC, the walls contained a single reinforcement layer placed at mid-thickness, consisting of a combination of 8 mm diameter (Ø8) rebars and a 220 x 220 mm mesh made with 5 mm diameter (Ø5) welded rebars. The Ø8 rebars were placed vertically near the vertical edges of the openings and along the wall intersections. Additional single rebars were also positioned along the horizontal edges of the openings in the west wall (Fig. 2b). The central areas of the walls were reinforced mainly by fibres, whereas the steel mesh was placed along the wall perimeter to locally enhance tensile capacity in regions where stress concentrations were expected, such as vertical corners and wall spandrels. The mesh sheet located along the base edges of the walls was bent at 90 degrees into two parts, which were embedded within the wall thickness and the base-slab thickness, respectively. This reinforcement detail ensured continuity between the base slab and the walls, resulting in a connection able to transfer both in-plane and out-of-plane bending actions. Fig. 2c shows the B-HFRC specimen before testing.

The B-HFRC specimen was designed to achieve an overall resistance comparable to that of the traditional RC structure. To quantify the actual reduction in steel reinforcement enabled by the use of fibres, the total weight of reinforcement included in specimens B-RC (rebars only: 208 kg) and B-HFRC (rebars + fibres: 78 kg + 70 kg = 148 kg) was normalised with respect to the total concrete volume (2.78 m^3), which was essentially identical for both specimens. The resulting reinforcement indices, equal to 75 kg/m^3 for B-RC and 53 kg/m^3 for B-HFRC, indicate that the incorporation of fibres allowed a reduction of approximately 30% in the total reinforcement amount per unit volume. Moreover, the required conventional reinforcement was reduced from 208 kg to 78 kg, corresponding to a 62% decrease in rebars.

The two specimens were constructed in a precast concrete factory using self-compacting concrete with a mixture containing 370 kg/m^3 of Portland cement 42.5R, 1600 kg/m^3 of aggregates with a maximum size of 12 mm, 280 kg/m^3 of calcium carbonate filler, and 4 L of superplasticiser (i.e., 1.1% by cement mass). A water-to-cement ratio of 0.49 was adopted. To obtain FRC, 25 kg/m^3 (volume fraction = 0.32%) of high-strength hooked-end steel fibres were added to the concrete batch. The fibres had a length of 32 mm, a diameter of 0.4 mm and a tensile strength higher than 2200 MPa. A total of six 150 mm cubes were cast during the construction of each box structure to determine the compressive strength of concrete. The cubes were tested under uniaxial compression according to UNI EN 12390-3:2019. Although the same concrete mixture was used for both box specimens, different compressive strengths were obtained. For specimen B-RC, the mean cube compressive strength ($f_{cm,cube}$) was 51 MPa (CV = 9.8%), corresponding to a cylindrical mean compressive strength (f_{cm}) of 42 MPa. In contrast, the cubes associated with specimen B-HFRC exhibited an $f_{cm,cube}$ of 73 MPa (CV = 5.4%), corresponding to an fcm of 61 MPa. Based on the formulation $E_{cm} = 9500\ f_{cm}^{1/3}$ proposed by clause 5.1.4 of EN 1992-1-1 (2023) for calculating the mean secant modulus of concrete made with quartzite aggregates, the expected modulus of elasticity is 32.9 GPa for B-RC and 37.4 GPa for B-HFRC.

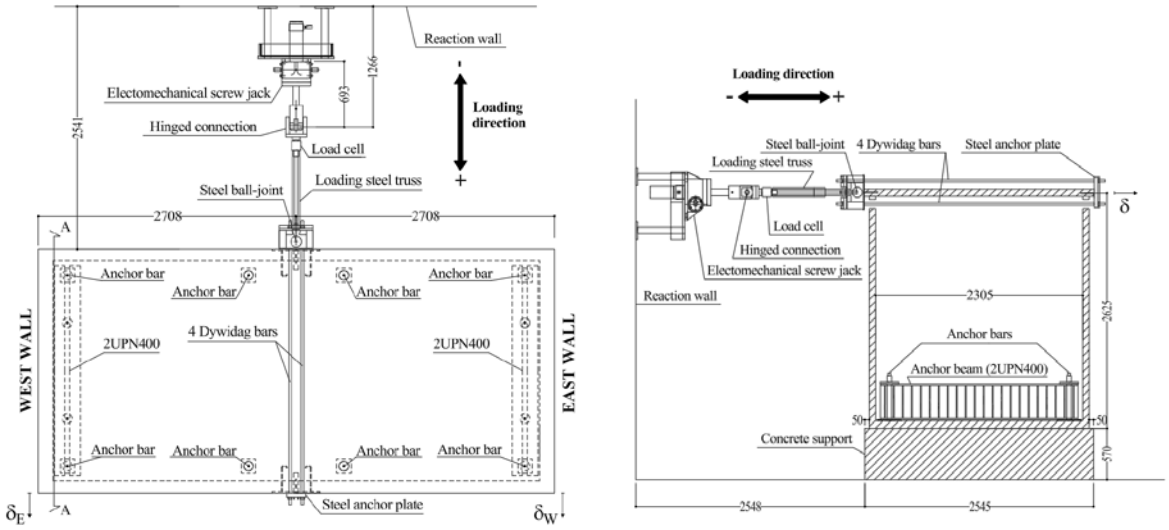
To characterise the tensile behaviour of the FRC, six notched beams measuring 150 x 150 x 600 mm^3 were tested under three-point bending according to EN 14651 (2007). The average nominal stress-CMOD (crack mouth opening displacement) curves obtained from the bending tests allowed the limit of proportionality, f_L (4.66 MPa; CV = 8%), and the residual strengths f_{R1} (3.34 MPa; CV = 24%), f_{R2} (3.81 MPa; CV = 28%), f_{R3} (3.46 MPa; CV = 27%) and f_{R4} (3.14

MPa; CV = 26%) to be determined, corresponding to CMOD values of 0.5, 1.5, 2.5 and 3.5 mm, respectively.

Steel grades B450 A and B450 C were used for the Ø5 and Ø8 reinforcing bars, respectively. The mechanical properties of the two types of reinforcing steel were determined by testing three samples for each steel type according to EN 15630-1 (2019). Based on the results of the uniaxial tensile tests, reinforcing steel B450 A exhibited a mean yield strength (f_y) of 569 MPa (CV = 0.4%), an ultimate strength (f_{tu}) of 639 MPa (CV = 1.8%) and a strain at ultimate strength (A_{gt}) of 3.6% (CV = 4.2%). The corresponding values of f_y, f_{tu} and A_{gt} for B450 C rebars were 519 MPa (CV = 0.5%), 618 MPa (CV = 0.7%) and 13.2% (CV = 0.9%), respectively.

The schematic in Fig. 3 shows the experimental set-up adopted to perform the cyclic tests on the box specimens. Since the tests were designed to assess the behaviour of the box element under lateral actions such as earthquakes, a horizontal load was applied at roof level, with its line of action passing through the centre of gravity of the top slab. The structure was supported by concrete blocks with a total height of 570 mm, positioned beneath the bottom slab along its entire perimeter. To prevent horizontal translation and uplift of the specimen, six anchor bars passing through the thickness of the bottom slab were fixed to the laboratory floor and subsequently post-tensioned. An anchor beam (2UPN400) was installed inside the specimen to fully restrain the base of the short walls, which were subjected to the highest in-plane shear actions because they were oriented parallel to the direction of the applied lateral load. The loading system consisted of a 500 kN electromechanical screw jack connected to the box structure through a double-hinged steel truss equipped with a load cell for continuous monitoring of the cyclic load during the test. The steel hinge connecting the truss to the jack allowed rotation only in the vertical plane. In contrast, the connection between the steel truss and the specimen was provided by a steel ball joint, enabling rotations in both the vertical and horizontal planes. Four Dywidag bars passing through the entire width of the roof transferred the horizontal load from the ball joint to a steel anchor plate positioned on the opposite side of the roof, and vice versa, thereby enabling load reversal.

A total of 24 instruments, including potentiometric and LVDT transducers, were installed to monitor the lateral displacements of the specimen and the crack widths observed in the west and east walls (Fig. 4). For brevity, a detailed description of the instrumentation is omitted. The following discussion focuses mainly on the measurements provided by the LVDTs installed at the top of the structure to measure the lateral displacements of the west wall (δ_W) and east wall (δ_E) (Fig. 3a), both referenced to the laboratory floor. The reversed cyclic tests on the two specimens were performed under displacement control by progressively increasing the imposed lateral displacement until a near-collapse condition was reached. This condition was assumed to occur when a reduction of at least 20% in lateral load capacity was observed in the post-peak response of the structure. The imposed displacement (δ) used as the control parameter of the test was defined as the average of the measured displacements δ_W and δ_E. The same loading history was applied to both specimens, consisting of repeated reversed cycles with stepwise increasing lateral drifts, ranging from a minimum of 0.01% to a maximum of about 2%. As recommended by FEMA 461 (Applied Technology Council (ATC), 2007) for quasi-static cyclic testing, two cycles at each drift amplitude were performed, and 11 drift increments were applied to both specimens. The drift ratio (D) was determined as $D = \delta/h$, where $h = 2440$ mm is the specimen height.



(a) *(b)*

Figure 3: Experimental set-up: (a) plan view; (b) section A-A. Dimensions in [mm].

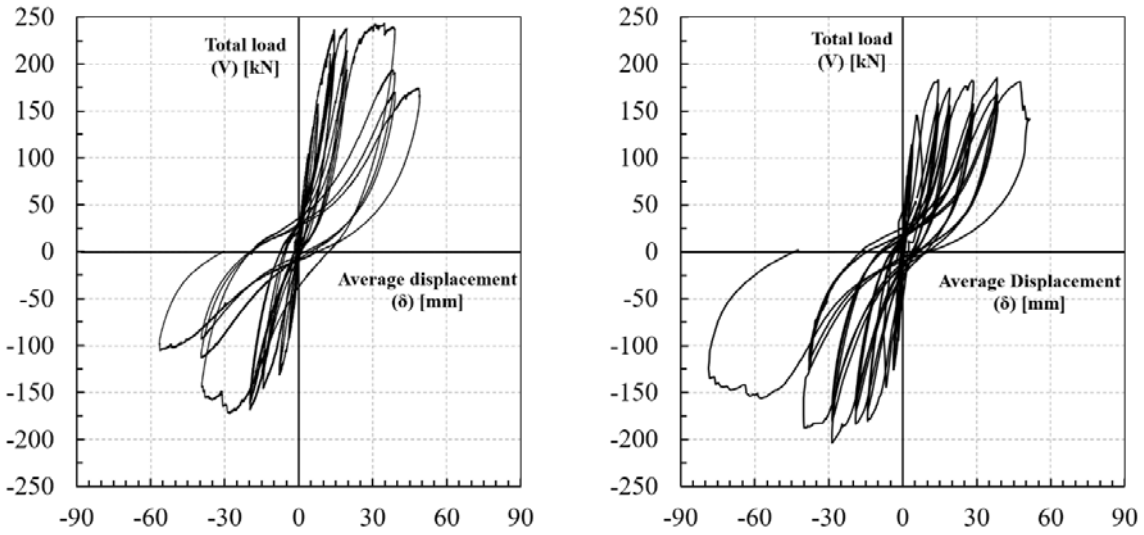


(a) *(b)*

Figure 4: Potentiometric transducers installed on (a) the east wall and (b) the west wall to monitor crack evolution.

3 Test results and comparison

The hysteretic curves in Fig. 5 show the global response of the two specimens in terms of total lateral load (i.e., total base shear, V) versus average lateral displacement (δ). Table 1 summarises the main results of the tests, including the initial secant stiffness (K_i), evaluated in the load range 0-25 kN, the cracking load (V_{cr}), the peak load (V_p) and corresponding displacement (δ_p), the ultimate load (V_u) and corresponding displacement (δ_u), and the displacement at which the load had decreased to $0.8V_p$ ($\delta_{0.8}$). The table also reports the associated drift values (D).



(a) *(b)*

Figure 5: Total lateral load versus average lateral displacement (δ): (a) B-RC; (b) B-HFRC.

Table 1: Main results of the cyclic tests.

Specimen	K_i	V_{cr}	δ_{cr}	D_{cr}	V_p	δ_p	D_p	V_u	δ_u	D_u	$\delta_{0.8}$	$D_{0.8}$
	[kN/mm]	[kN]	[mm]	[%]	[kN]	[mm]	[%]	[kN]	[mm]	[%]	[mm]	[%]
B-RC	+42	+50	+1.3	+0.05	+236	+33	+1.4	+170	+48	+2.0	+46	+1.9
	-45	-40	-0.9	-0.04	-172	-28	-1.1	-103	-55	-2.3	-44	-1.8
B-HFRC	+81	+80	+1.8	+0.07	+185	+38	+1.6	+140	+50	+2.0	+50	+2.0
	-104	-95	-1.8	-0.07	-204	-29	-1.2	-135	-78	-3.2	-54	-2.2

The initial response of specimen B-RC (Fig. 5a) was linear, with similar lateral stiffness in the positive (42 kN/mm) and negative (45 kN/mm) loading directions. The first significant stiffness reduction was observed at loads (V_{cr}) of +50 kN and -40 kN, corresponding to the formation of horizontal flexural cracks at the base of both the east and west walls. At the same time, a crack developed along the right side of the spandrel above the door opening in the west wall, starting from the bottom side. As loading increased, the lateral stiffness gradually decreased due to the activation of additional cracks on both sides of the two openings in the east wall, together with the development and propagation of further flexural cracks within the spandrel of the west wall. In the positive direction, the specimen exhibited a sharp decrease in lateral stiffness at a lateral displacement of +15 mm, corresponding to a load of about +230 kN. After this point, the lateral resistance slightly increased up to a maximum value of +236 kN (δ=+33 mm). Failure occurred at a displacement of +38 mm and a load capacity of +234 kN, when the significant tensile forces acting in the vertical reinforcement at the base of the west wall caused severe cracking at the wall-bottom slab interface. Consequently, the vertical reinforcement of the west wall rapidly lost its ability to transfer tensile forces, as the L-shaped rebars anchoring it to the bottom slab induced splitting of the concrete cover. This resulted in a sudden loss of anchorage capacity and, consequently, a sharp reduction in the overall load-carrying capacity of the specimen. The test was stopped after reaching a maximum

displacement of +48 mm, corresponding to a lateral load of +170 kN, approximately 0.72 times the maximum resistance. In the negative loading direction, a significant stiffness reduction was observed at a lateral displacement of -9.8 mm (V = -123 kN), due to the gradual activation of the previously described horizontal flexural cracks in the squat panels located on both sides of the openings in the east wall, together with propagation of the horizontal crack through the entire length of the west-wall base section. With further increase in lateral displacement, the specimen resistance initially increased as cracking progressively extended across the east wall and new cracks developed along the bottom side of the spandrel in the west wall. After reaching a maximum capacity of -172 kN at a displacement of -28 mm, the lateral resistance gradually decreased until a sudden drop occurred at -40 mm (V = -150 kN), when the vertical reinforcement on the left side of the east wall lost its anchorage to the base slab. This failure mechanism, similar to that observed in the positive loading direction for the west wall, led to collapse of the specimen, which occurred at a maximum displacement of -55 mm and a load of -103 kN. Fig. 6a shows the cracks observed on the east and west walls at the end of the test and highlights the major horizontal crack at the base of both walls, at their interface with the base slab.

The response of specimen B-HFRC (Fig. 5b) was linear, with initial stiffnesses ranging from 81 kN/mm to 104 kN/mm. These stiffnesses were approximately twice those observed for specimen B-RC. This difference may be partly explained by the higher elastic modulus expected for the concrete of specimen B-HFRC, due to the higher compressive strength obtained from the characterisation tests (Section 2). At a lateral load of +80 kN and a displacement of about +1.8 mm, an inclined crack appeared at the base of the west wall and a vertical crack opened through the full depth of the right-side cross-section of the spandrel. These cracks were likely present before the test and rapidly enlarged during the early loading cycles. In the negative direction, the first cracks appeared along the base of the east wall at a load of about -95 kN. After first cracking, the response of the structure remained almost linear up to displacements of +5.5 mm (V = +144 kN) and -3.8 mm (V = -126 kN). At these points, multiple cracks spread over the east wall and a horizontal flexural crack fully developed at the base of the west wall.

The clear stiffness reduction occurring after a lateral displacement of +14.5 mm (V = +180 kN) was likely related to the onset of yielding of the vertical rebars in the west wall. The lateral resistance then slightly increased up to a peak value of +185 kN (δ = +38 mm), followed by a gradual decrease until sudden failure occurred at a displacement of about +50 mm. As observed for specimen B-RC, this failure mechanism was strongly affected by the significant cracks developed at the base of the west wall, which caused the loss of anchorage of the vertical rebars and their resulting inability to transfer tensile actions to the bottom slab. It is worth noting that the spandrel of the west wall developed a very limited crack pattern, mainly formed by the single crack located along the right side of the spandrel. Such crack localisation contributed to limiting the increase in resisting capacity of the west wall. In the negative direction, the lateral resistance increased continuously as new cracks developed over the east wall and the flexural crack at the base of the west wall fully developed. After the maximum resistance was attained (V = -204 kN; δ = -29 mm), a progressive loss of resistance was observed as the horizontal cracks at the base of the west and east walls significantly enlarged, causing failure of the connection with the bottom slab. Compared with specimen B-RC, the maximum resistance attained by B-HFRC was 22% lower in the positive direction and 19% higher in the negative direction. Finally, considering the near-collapse displacement $\delta_{0.8}$ (Table 1), corresponding to

a 20% reduction in lateral capacity in the post-peak response, the displacement capacity of specimen B-HFRC was 10-20% higher than that of B-RC.



(a)



(b)

Figure 6: Ultimate crack patterns detected on the outer surface of the west and east walls: (a) B-RC; (b) B-HFRC.

4 Concluding remarks

This paper reports and discusses the results of reversed cyclic tests performed on two precast thin-walled box shelters reinforced with conventional reinforced concrete (RC) and hybrid reinforcement (HFRC, consisting of rebars and steel fibres), respectively. Based on the experimental findings, the following conclusions can be drawn:

- The maximum lateral resistance of the HFRC specimen was 22% lower than that of the RC specimen in the positive loading direction, whereas it was 19% higher in the negative direction. The discrepancy observed in the positive direction may be attributed, at least in part, to the presence of pre-existing cracks in the west wall of the HFRC specimen. Furthermore, in both specimens, the progressive loss of anchorage of the vertical

reinforcement at the base of the east and west walls limited the development of the full lateral capacity.

- The two specimens exhibited comparable displacement capacities. Considering the near-collapse displacement δ0.8, the displacement capacity of the HFRC specimen was approximately 10–20% higher than that of the RC specimen, indicating that the reduction in conventional reinforcement did not adversely affect the overall deformation capacity.
- The damage evolution observed in the two specimens was similar and predominantly governed by flexural mechanisms. Crack initiation, propagation and final failure mode followed comparable patterns, despite the different reinforcement layouts.
- The adoption of the hybrid reinforcement system enabled a reduction of approximately 62% in the amount of conventional reinforcement compared with the RC specimen. In addition, the simplified reinforcement layout significantly reduced detailing complexity, potentially facilitating fabrication and construction operations.
- Despite the substantial reduction in distributed reinforcement and the reduction of the primary reinforcement (Ø8 bars) around the openings, the HFRC specimen exhibited a global structural response comparable to that of the conventional RC specimen.

Acknowledgements

The authors gratefully acknowledge Eng. Silvia Martini and Eng. Roberto Vecchi for their valuable support during the experimental programme, the reporting phase, and the interpretation of the experimental results. The authors also acknowledge Andrea Del Barba, technician of the Laboratorio Pisa at the University of Brescia, for his valuable assistance during the laboratory testing activities.

5 References

Applied Technology Council (ATC), 2007. Interim Testing Protocols for Determining the Seismic Performance Characteristics of Structural and Nonstructural Components. FEMA 461, Federal Emergency Management Agency, Washington, D.C.

EN 14651:2005+A1:2007. Test Method for Metallic Fibre Concrete — Measuring the Flexural Tensile Strength (Limit of Proportionality (LOP), Residual Strength). European Committee for Standardization, Brussels.

EN ISO 15630-1:2019. Steel for the Reinforcement and Prestressing of Concrete — Test Methods — Part 1: Reinforcing Bars, Rods and Wire. European Committee for Standardization, Brussels.

EN 1992-1-1:2023. Eurocode 2: Design of Concrete Structures — Part 1-1: General Rules and Rules for Buildings, Bridges and Civil Engineering Structures. European Committee for Standardization, Brussels.

Di Prisco, M., Dozio, D., and Belletti, B., 2013. "On the fracture behaviour of thin-walled SFRC roof elements", *Materials and Structures*, 46(5), pp. 803–829.

Facconi, L., Minelli, F., and Plizzari, G. A., 2016. "Steel fiber reinforced self-compacting concrete thin slabs: Experimental study and verification against Model Code 2010 provisions", *Engineering Structures*, 122, pp. 226–237.

Facconi, L., Plizzari, G. A., and Minelli, F., 2019. “Elevated slabs made of hybrid reinforced concrete: Proposal of a new design approach in flexure”, *Structural Concrete*, 20(1), pp. 52–67. https://doi.org/10.1002/suco.201700278

Minelli, F., and Plizzari, G. A., 2013. “On the effectiveness of steel fibers as shear reinforcement”, *ACI Structural Journal*, 110(3), pp. 379–390.

Sawadogo, S. A. S. L., Bui, T. T., Bennani, A., Al Galib, D., Reynaud, P., and Limam, A., 2025. “3D modular construction made of precast SFRC-stiffened panels”, *Infrastructures*, 10(7), 176.

Tiberti, G., Minelli, F., Plizzari, G. A., and Vecchio, F. J., 2014. “Influence of concrete strength on crack development in SFRC members”, *Cement and Concrete Composites*, 45, pp. 176–185. https://doi.org/10.1016/j.cemconcomp.2013.10.004

UNI EN 12390-3:2019. Testing Hardened Concrete — Part 3: Compressive Strength of Test Specimens. Ente Italiano di Normazione, Milan.

Distributed Fiber Optic Monitoring in Full-Scale Fiber Reinforced Composite Decks

Chidchanok Pleesudjai[1], Martins Suta[2], Devansh Patel[1], Xavier Destree[3],

Gregor Daniel Fischer[4], Barzin Mobasher[1]*

[1] *Graduate Research Assistant, School of Sustainable Engineering & the Built Env., Arizona State University, Tempe, AZ, 85281, USA, email: cpleesud@asu.edu*

[1] *Head of Design Department, Primekss SIA, Riga, Latvia, email: martins.suta@primekss.com*

[1] *Graduate Research Assistant, School of Sustainable Engineering & the Built Env., Arizona State University, Tempe, AZ, 85281, USA, email: dpatel52@asu.edu*

[1] *Xavier Destree, Independent Consultant, Brussels, Belgium, email: xavier.destree@gmail.com*

[1] *Associate Professor, Department of Civil and Mechanical Engineering, Technical University of Denmark, Kongens Lyngby, 2800, Denmark, email: grfi@dtu.dk*

[1]* *Professor, School of Sustainable Engineering & the Built Env., Arizona State University, Tempe, AZ, 85281, USA, email: barzin@asu.edu*

Abstract

This study addresses the instrumentation and measurement of strain fields in a full-scale, joint-free composite deck system composed of a corrugated steel deck connected by headed shear studs to the underlying steel framing. A PrimX steel fiber reinforced concrete (SFRC) mixture was cast in two adjacent bays. One bay was additionally reinforced with discrete two-way rebar bands (1000 mm wide) for local load transfer, while the other bay relied on steel fiber alone. Experimental data were acquired by high-resolution distributed fiber optic sensing (DFOS) of the continuous slab under three discrete uniformly distributed load configurations at service level of 10 kN/m². The nominal elastic strain distribution was monitored along the grid of the span in both transverse and longitudinal beam. Both top and bottom positions of the SFRC deck layer. The output providing a continuous spatial map of the through-thickness strain gradient. Experimental results demonstrate the effectiveness of DFOS in continuous monitoring of the flexural strain distribution. Analysis of the continuous strain profiles facilitates the identification of points of moment contraflexure. The experimentally obtained moment distributions support the use of a simplified analytical approach in which the member is idealized as simply supported between points of zero curvature. This confirms the proposed assumptions regarding the effect of internal supports on the determination of an effective span length for simplified structural analysis, as set out in ACI 544.6R.

Finally, the 1-D and 2-D flexural strain distributions have the potential to contribute to the determination of stresses, curvatures, and flexural moments transmitted to the supports. A framework for structural health monitoring is also proposed, utilising a real-time nonlinear analytical solution to derive external load magnitudes, internal moments, and shear-force distributions from the observed strain topologies.

Keywords

Distributed fiber optic sensing; fiber reinforced concrete; composite deck; full-scale monitoring;

1 Introduction

The mechanical response of reinforced and fibre-reinforced concrete is fundamentally heterogeneous and scale dependent [1]. At the cross-section scale, flexural response is commonly interpreted through a linear strain profile across the member depth as curvature develops [2], [3]. At the centimetre scale, however, strain varies locally among hydrated cement paste, aggregate particles, and interfacial transition zones. In steel-fibre-reinforced concrete (SFRC), this variability is further affected by the spatial distribution and orientation of discrete steel fibres, which govern post-cracking stress transfer [1]. At the metre scale, the strain field varies again as the slab transitions between supports, loaded regions, and the surrounding foundation or support system [4]. Conventional instrumentation, such as electrical-resistance strain gauges, vibrating-wire strain gauges and LVDT samples this heterogeneous strain field only at discrete locations with measurement lengths of 10 to 300 mm or over finite gauge lengths depending on the sensor type and mounting configuration [5], [6]. A small number of such sensors, however carefully placed, can therefore return values that are strongly influenced by local composite heterogeneity and by spatial averaging over the gauge length. As a result, peak strains associated with non-uniform shrinkage, strain localisation, and cracking may be attenuated, biasing the interpretation toward local sensor response rather than the global behaviour of the structural system.

Distributed fibre optic sensing (DFOS) replaces this discrete sampling problem with continuous spatial measurement. A single embedded fibre provides readings every few millimetres along its full length [7], [8]. DFOS thereby resolves localised strain features such as fine cracks, bond-transfer zones, and strain concentrations near supports where discrete instrumentation would systematically miss or smear out across its gauge length [9], [10], [11], [12]. In regions with steep strain gradients near macro-cracks, beam-to-slab transitions, or compression-zone discontinuities, DFOS readings may still contain local anomalies such as connector-zone spikes, interrogator drift, and isolated dropouts that arise alongside genuine mechanical features such as bond-transfer and microcracking [13]. Reliable interpretation therefore requires an explicit signal-cleaning step, as described in Section 3.

2 Test Structure and Instrumentation

2.1 Experimental system overview

The experimental area is a two-bay panel within a continuous industrial floor system constructed with the Primekss PrimX steel-fibre-reinforced concrete (SFRC) jointless slab solution. The instrumented region spans 16 m East–West by 15 m North-South. The panel is divided by a continuous central girder (HEA 1000) into two 7.5 m × 16 m bays as Area A (North bay) and Area B (south bay), as shown in Figure 1. Each bay is framed by nine IPE 360 secondary beams running North-South at 2000 mm centres, spanning the full 7.5 m between adjacent main girders.

Both bays were cast with the same PrimX SFRC mix at 200 mm nominal slab depth, comprising a 149 mm PrimX topping over a 51 mm Montana SUPERHOLORIB SHR 51/150 corrugated steel deck. An identical reinforcement detail is provided over each main girder (HEA 1000) line in both Area A and Area B, placed in 1300 mm wide bands centred on the North, Central, and South girders and running the full 16 m East-West extent of the slab. The top mat consists of four Φ16 bars at 200 mm c/c, oriented parallel to the main girder. The bottom mat

consists of Φ16 bars at 200 mm c/c, oriented perpendicular to the main girder, each 1300 mm long. The two bays differ only in the supplemental reinforcement provided over each minor beam. In Area A, a 1000 mm wide two-way rebar band is placed over each of the nine minor-beam (IPE 360) lines, as detailed in Figure 2. The top mat consists of four Φ12 bars at 150 mm c/c, oriented parallel to the minor beam, located 58 mm below the top of the slab. The bottom mat consists of Φ12 bars at 150 mm c/c, oriented perpendicular to the minor beams, located 70 mm below the top of the slab. In Area B, no supplemental reinforcement is provided over the minor beams, and the PrimX steel fibre act alone.

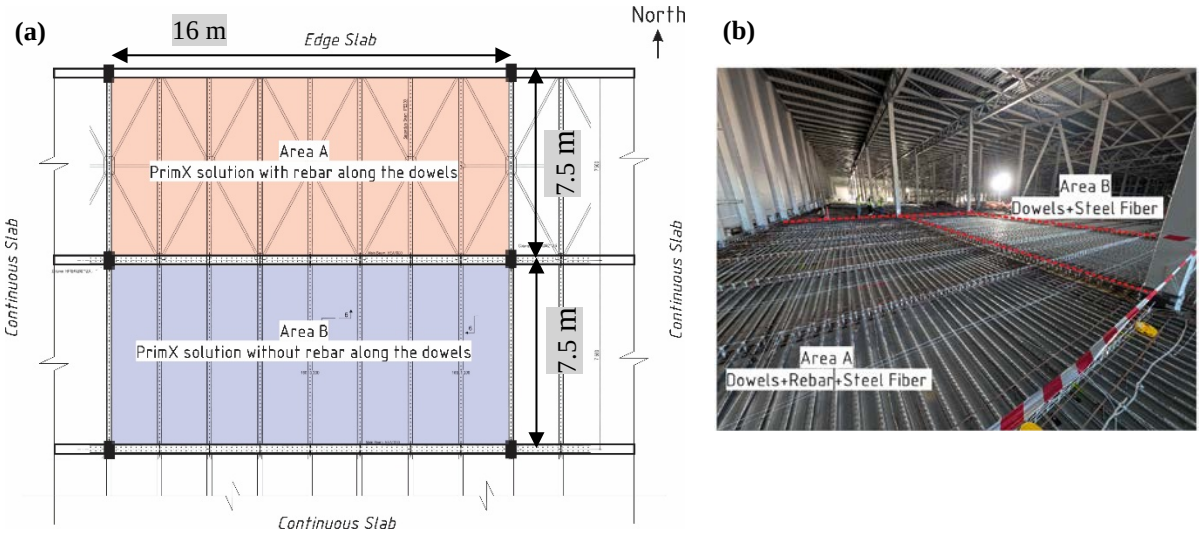


Figure 1: (a) Plan view of the two-bay test panel (16 m × 15 m), divided by the central HEA 1000 girder into Area A and Area B, (b) Montana SUPERHOLORIB SHR 51/150 corrugated deck and reinforcement under the construction process.

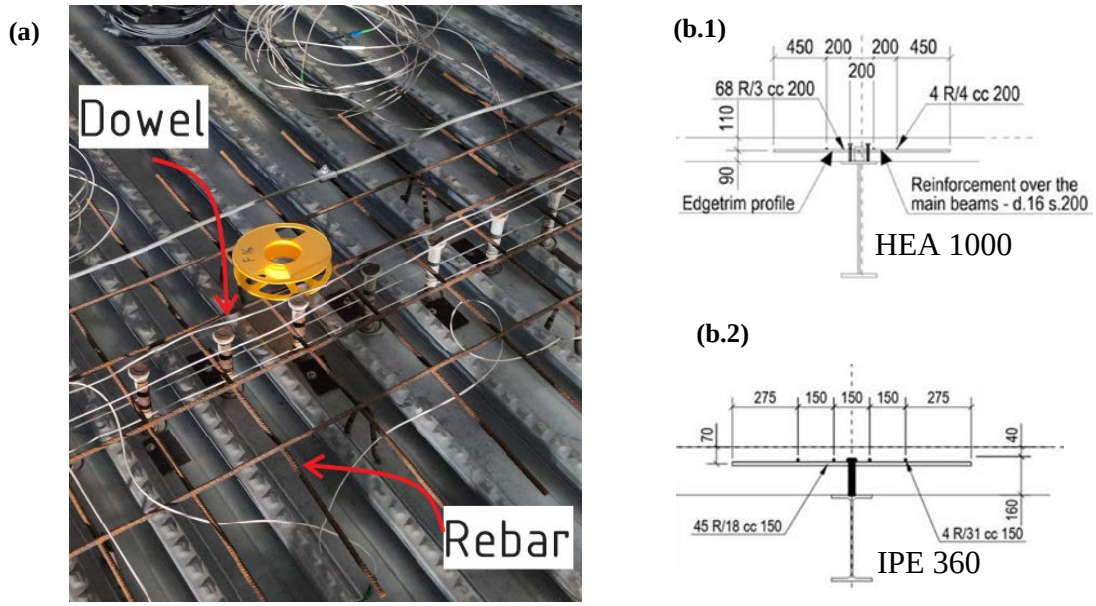


Figure 2: (a) Reinforcement section details: (b.1) over-girder band above each HEA 1000 (1300 mm wide, 4 + 68 Φ16 bars at 200 mm c/c); , (b.1)1000 mm wide, 4 + 45 Φ12 bars at 150 mm c/c).

2.2 Composite slab system

The composite slab is composed of a 51 mm Montana SUPERHOLORIB SHR 51/150 cold-formed steel deck (rib pitch 150 mm c/c, sheet cover width 600 mm) with a 149 mm cast in place PrimX SFRC topping, giving a total slab thickness of 200 mm. Composite action between the steel deck and the concrete topping is achieved by the SUPERHOLORIB top-flange burls embossed at every rib (DIBt approval Z-26.1-45), which engage the concrete continuously at 150 mm c/c without the need for additional shear connectors at the deck to concrete interface (See Figure 2). Steel beam to slab composite action is provided by standard headed shear studs (Nelson type) welded through the deck to the beam top flanges at 150 mm centre to centre along each beam axis. A single row of studs is provided on each minor beam (IPE 360 floor beam), and a double row is provided on each major beam (HEA 1000 girder) to accommodate the higher local shear demand at the supports.

The mechanical properties of the PrimX SFRC topping were characterized at a Latvian laboratory. Compressive strength was determined on six 150 mm cubes from each bay in accordance with EN 12390-3, at an age of 28 days and at a stress rate of 0.6 MPa/s. The mean cube compressive strength $f'c$ was 50.4 MPa (COV=1.3%) for Area A and 45.0 MPa (COV=7.2%) for Area B. Flexural performance was characterized on six notched prismatic specimens (150 × 150 × 550 mm, notch = 25 mm, span 500 mm) tested in three-point bending under crack mouth opening-= displacement (CMOD) control, in accordance with EN 14651. The mean limit of proportionality was f_L=5.7 MPa, and the residual flexural strengths were f_{R1} = 3.4 MPa (CMOD=0.5 mm), f_{R2}=3.6 MPa (CMOD=1.5 mm), f_{R3}=3.6 MPa (CMOD=2.5 mm), and f_{R4}=3.5 MPa (CMOD = 3.5 mm). With $f_{R1} < f_L$ and a ratio f_{R3} / f_{R1} = 1.04, the PrimX SFRC exhibits strain-softening behaviour and falls within the softening class "c" of the fib Model Code 2010 classification.

2.3 Boundary conditions

The slab was assumed continuous across all three HEA 1000 girders since the PrimX steel fiber-reinforced concrete topping was cast in place as a continuous layer. The IPE 360 beams, by contrast, were treated as simply supported bay members. Their ends were released at the HEA 1000 girders through single-plate shear connections. Therefore, continuity across the HEA 1000 girder lines was assigned to the slab only. This slab continuity mobilizes hogging moments over the support lines and provides the structural rationale for the supplemental hogging-moment reinforcement shown in Figure 2(c).

The perimeter idealization was defined from the position of each boundary within the surrounding building. The North Girder was treated as an exterior support because it forms the end of the building. Central Girder remained an interior support within the measured panel. The South Girder was also treated as an interior support, rather than as a free edge or simple support. This condition was preserved by extending the slab one additional bay to the south. Elastic edge springs can be considered at the South edge to represent the restraint provided by the surrounding floor system. The East and West cut lines, located along the I1 and I10 sides, were also treated as internal truncation boundaries within the wider floor plate, as shown in Figure 3. The East and West cut lines along the I1 and I10 sides were treated in the same manner, as internal truncation boundaries within the wider floor plate. Elastic edge springs should be considered rather than pin or free boundaries.

Composite action was represented through two interface assumptions. At the deck-to-concrete interface, the SUPERHOLORIB SHR 51/150 top-flange burls were assumed to engage the PrimX topping at the 150 mm rib pitch. Full displacement compatibility was therefore imposed between the steel-deck shell and the concrete-topping shell within the tributary deck width. At the beam-to-slab interface, the headed shear studs were represented by tied vertical and longitudinal links at 150 mm c/c along each beam axis. A single stud row was assigned to each IPE 360 minor beam, and two stud rows were assigned to each HEA 1000 girder (see Figure 2(b)-(c)). This idealization allowed composite beam-slab curvature to develop while preserving the rotational releases at the IPE 360 beam ends. The applied loads included self-weight, the superimposed dead load corresponding to the test-day construction state, and the 10 kN/m² IBC water-tank patch. The patch covered a 6 m by 15 m area and was placed at the East, West, and Middle positions to reproduce the experimental loading configurations (See Figure 3).

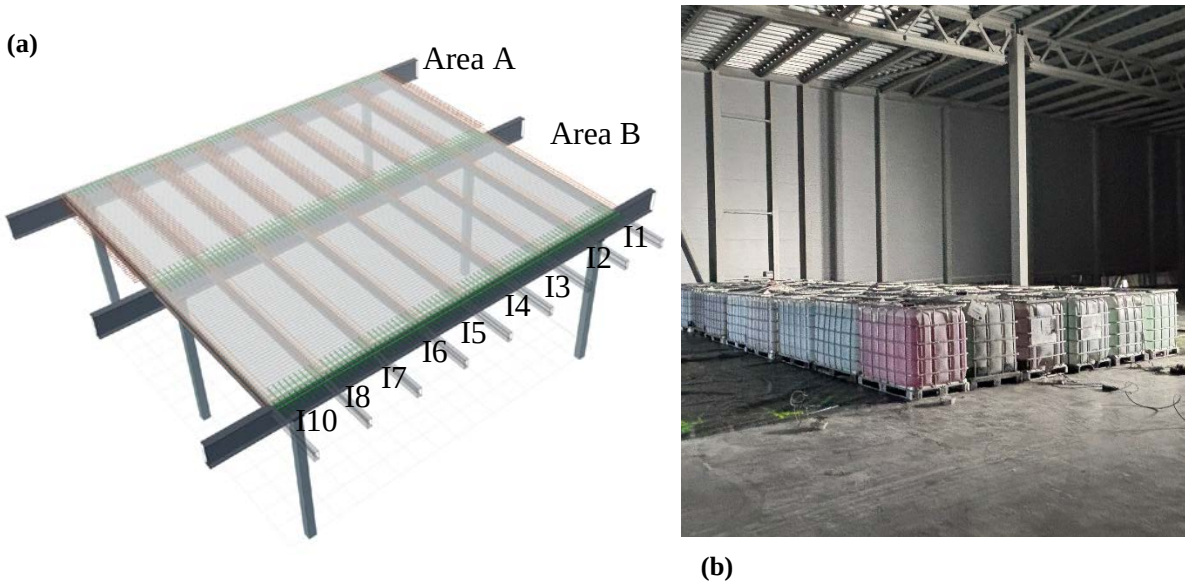


Figure 3: (a) Three-dimensional model of the two-bay NOVO composite deck, (b) IBC water tanks arranged in the 6 m by 15 m loading patch during the field campaign

3 Data Processing

3.1 DFOS data acquisition

The OFDR interrogator records continuous strain along each fibre at sub-centimetre sample spacing of approximately 5 mm. Three measurement batches were acquired across two field campaigns, with each batch corresponding to one load patch position: East, West, or Middle, as described in Section 2. The DFOS grid comprises transverse fibres F1 to F10, running North to South across the panel, and longitudinal fibres F11 to F19, running East to West. Three fibres were excluded due to breakage: F6, F9, and F17. One additional fibre, F15, was excluded because its physical position could not be confirmed. The remaining fifteen fibre fields were retained for processing. Each fibre serpentines between a bottom layer embedded in the PrimX topping just above the steel deck top flange and a top layer located approximately 15 mm above. Every physical point on the panel that a fibre crosses therefore yields two independent strain reading positions, one at each installation depth.

3.2 Outlier cleaning

Raw distributed-strain profiles contain three families of non-mechanical artefacts that violate the smooth spatial variation expected from a flexural strain field. Connector-zone spikes occur at fibre splices where the cable bends sharply outside the slab. Isolated interrogator outliers produce single-sample excursions driven by drift in the Optical Frequency Domain Reflectometry (OFDR) backscatter reference. Dropouts produce short segments of near-zero strain when the local backscatter signal-to-noise ratio falls below the interrogator threshold. A single fixed threshold cannot remove all three families without also distorting genuine flexural peaks.

A distribution-free, two-pass algorithm targets each family separately, as illustrated in Figure 4. Pass 1 applies a both-side gradient check: a sample is flagged if the forward strain gradient on either side exceeds 5000 με/m. This removes connector-zone spikes and isolated step outliers while leaving gradual flexural transitions intact. Pass 2 applies a local neighbourhood check: a sample is flagged if its deviation from the median of a centred 21-point window exceeds 25 με. This targets isolated interrogator outliers and residual dropouts that escape the gradient filter. The two passes are applied iteratively, for up to 10 iterations, until no new outliers are flagged. Flagged samples are then replaced by linear interpolation between the nearest valid bracketing samples. The raw trace is preserved alongside the cleaned trace for every fibre, so the cleaning step is fully auditable.

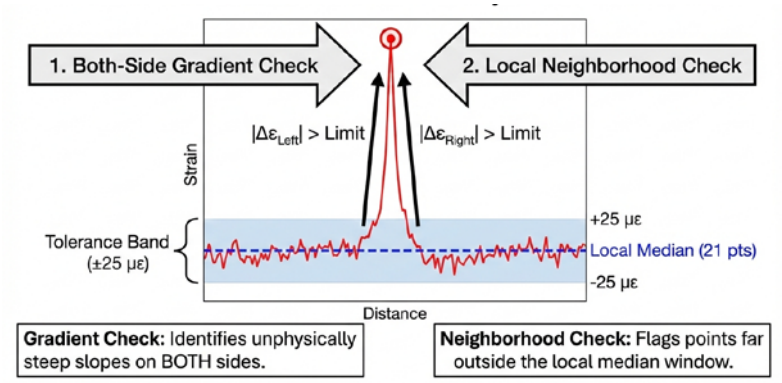


Figure 4: Schematic of the two-pass outlier detection algorithm

4 Results

4.1 Cleaned strain profiles and bending curvature

The cleaning algorithm described in Section 3.2 produced 208 per-route, per-layer strain traces distributed across three load stages and two sensor layers, bottom and top. Each trace covers the physical path of one fibre route on the panel. The two sensor layers are positioned to straddle the neutral axis of the composite slab section. Under downward service loading, the bottom layer experiences tensile strain in mid-bay and compressive strain over the supports, while the top layer experiences the opposite sense. This opposing response provides the basis for extracting bending curvature from the paired measurements. For interpretation in flexural terms, the Bernoulli plane-sections hypothesis was adopted, in which the through-depth strain profile at any cross-section is linear, $\varepsilon(z) = \varepsilon_0 + \varphi_z$, with φ the bending curvature. The curvature

is therefore the slope of the through-depth strain profile, recovered directly from two readings (top and bottom) at known depths;

$$\varphi(x) = \left[\varepsilon_{bot}(x) - \varepsilon_{top}(x)\right] / d_{eff} \tag{6}$$

where $d_{eff} = Z_{BOT} - Z_{TOP} = 15$ mm is the vertical separation between the bottom and top fibre layers (Section 2). The neutral axis depth does not enter Eq. 6 because φ is the slope of a straight line, fixed by any two points on it. The curvature, φ is recovered identically in Area A (PrimX with supplementary rebar) and Area B (PrimX only) without requiring an assumed cracked-section neutral-axis depth that would differ between the two bays. For the sign convention, $\varphi > 0$ corresponds to sagging with top in compression, bottom in tension, $\varphi < 0$ to hogging with top in tension, bottom in compression, and $\varphi = 0$ to a contraflexure point. Throughout Sections 4 and 5, φ is reported in units of 10^{-3} m^{-1}.

Figure 5 shows the cleaned strain profiles of fibre F5 along Route 1 (in-bay, 1.0 m east of the I6 minor beam) at all three load stages. F5 sits at x = 10 m on the E to W axis. Under Load Stage 1 (East), the load patch is cantered at x = 13 m, placing F5 at the western edge of the patch. The slab strip at F5 is therefore only marginally engaged in bending.

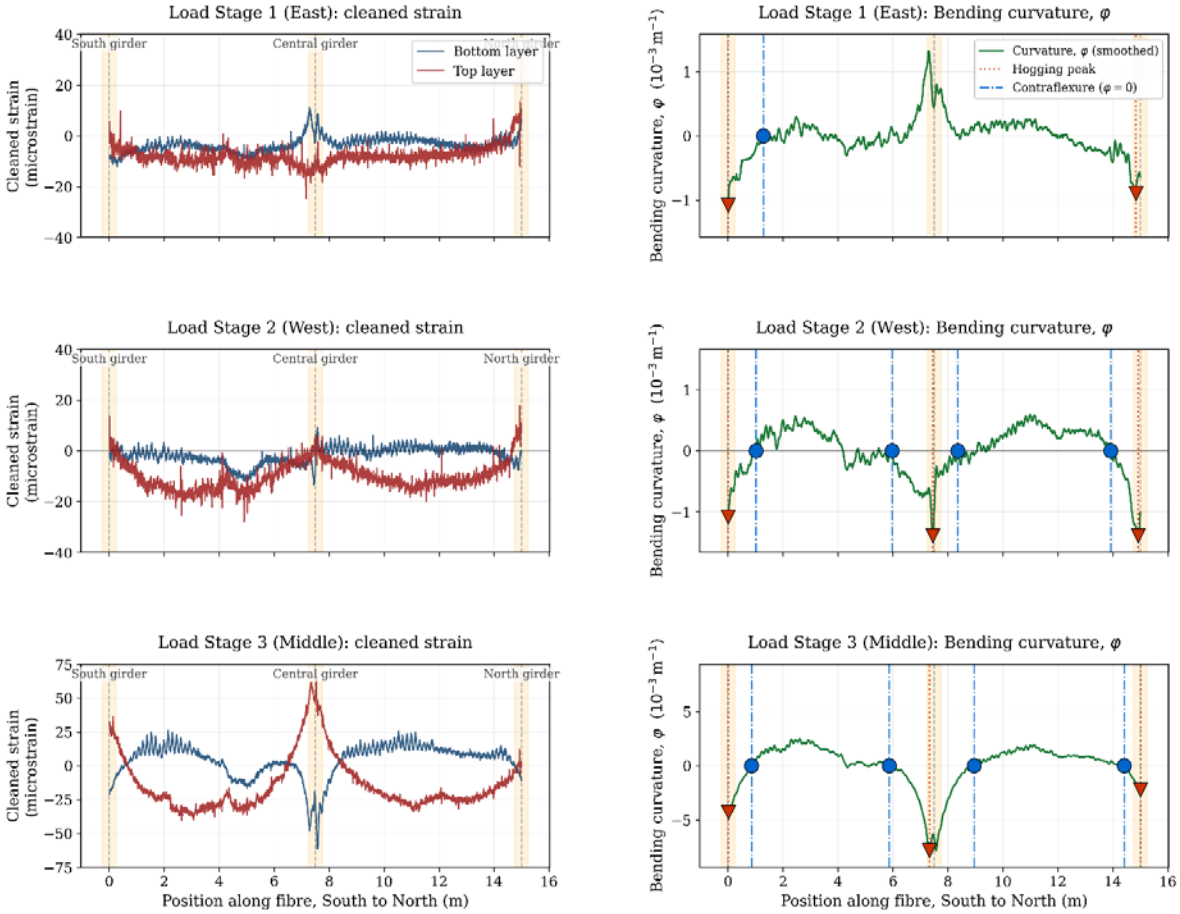


Figure 5: F5 (transverse, in-bay Route 1) cleaned strain profile and bending curvature φ at three load stages.

The Central girder hogging at F5 is therefore weak at $|\varphi_{peak}| = 0.07 \times 10^{-3}$ m^{-1}. Under Load Stage 2 (West) the patch is far from F5 but the slab carries some redistributed moment, giving

moderate hogging at $|\varphi_{peak}| = 1.4 \times 10^{-3}$ m^{-1}. Under Load Stage 3 (Middle), the patch is cantered over F5, the slab strip at F5 is fully engaged, and the hogging signal is strongest at $|\varphi_{peak}| = 7.8 \times 10^{-3}$ m^{-1}. The figure thus shows the load-position dependence of the elastic moment field directly. The bottom layer (blue) and top layer (red) trace approximately mirrored curves around the Central girder under all three load stages. Under Load Stage 3 (Middle), two zero-crossings of φ are visible on either side of the Central girder, at approximately y = 5.9 m and y = 8.9 m. These zero-crossings are the elastic lines of contraflexure where the bending moment passes from sagging in mid-bay to hogging over the support.

Visual inspection of all eight transverse fibres at the same load stage and route (F1, F2, F3, F4, F5, F7, F8, F10) confirmed the same hogging-dip pattern at the Central girder. The dip depth varies smoothly with E to W position, from $|\varphi| = 1.7 \times 10^{-3}$ m^{-1} at F10 to $|\varphi| = 10.7 \times 10^{-3}$ m^{-1} at F5. The qualitative shape of the $\varphi(x)$ curve is consistent across all eight fibres, supporting the conclusion that the curvature signal is a real flexural feature.

4.2 Cleaned strain profiles and bending curvature

The valid DFOS strain readings from both the transverse and longitudinal fibres were resampled onto a 128 by 128 grid spanning the panel using linear interpolation. The grid was split by strain component, with N to S strain ε_{yy} interpolated from transverse fibres and E to W strain ε_{xx} from longitudinal fibres. The two components describe different tensor components and are kept separate. Figure 6a shows the bottom-layer ε_{yy} heatmap for each of the three load stages. The hogging band over the Central girder is visible as a horizontal blue band in all three load stages. Sagging zones appear in red, flanking each girder. The load patch position is visible as a localised concentration of positive bottom-layer strain. For Load Stage 1 (East) the concentration sits on the eastern side of the panel. For Load Stage 2 (West) it sits on the western side. For Load Stage 3 (Middle) it is centred between the bays. The ε_{yy} hogging band is most pronounced at Load Stage 3, consistent with the symmetric load case that generates the largest concentration of negative bending at the interior support.

Figure 6b shows the complementary bottom-layer ε_{xx} heatmap for the same three load stages. The signal is more spatially varied than ε_{yy} because the slab spans only 2 m between adjacent minor beams, giving small-amplitude alternating hogging and sagging zones at each I-beam line crossing. The amplitude is smaller than ε_{yy} under all three load stages, consistent with the slab acting predominantly as a one-way member in the N to S direction between the main girders. The ε_{xx} field is concentrated under the load patch in each case, fading rapidly outside the loaded region.

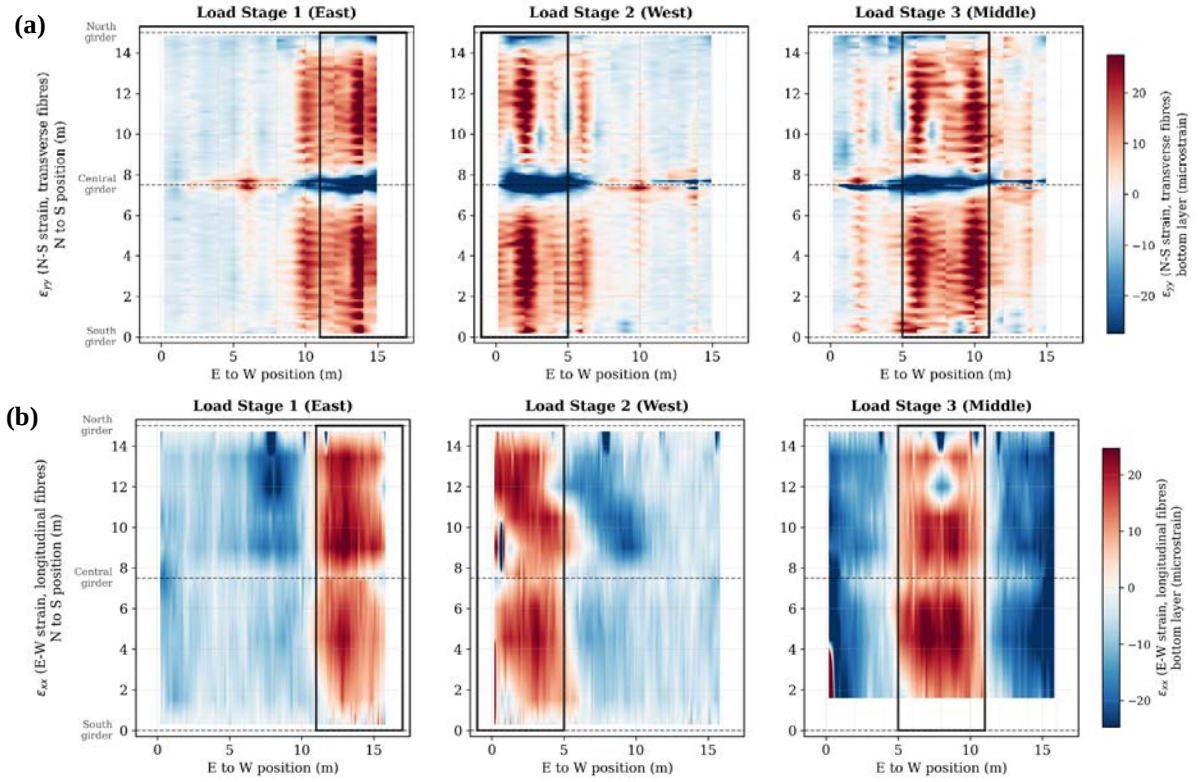


Figure 6: Bottom-layer strain heatmaps for the three load stages. Panel (a) shows the transverse normal strain ε_{yy} and panel (b) shows the longitudinal normal strain ε_{xx}..

4.3 Hogging peak position and line of contraflexure

For each fibre route at each load stage, two distinct geometric features were extracted from the bending curvature profile $\varphi(x)$. These are the position of the elastic hogging peak and the line of moment contraflexure r_s [14], [15]. The extraction procedure is described in Section 5.1. The hogging peak offset is the unsigned distance from the support centreline to the local minimum of $\varphi(x)$ near that support, that is, where the slab is bending most strongly in the hogging sense. The r_s value is the distance from the centreline outward to the first zero-crossing of φ, where the bending moment passes from hogging (over the support) to sagging (in mid-bay) [16], [17]. The two quantities measure different features. The peak offset locates where the plastic hinge would form, while r_s measures how far the elastic hogging zone extends.

Only high-signal routes are included in the statistics, defined as those with peak hogging amplitude $|\varphi_{peak}|$ greater than 3.3×10^{-3} m^{-1} which is equivalent to a strain difference greater than 50 με at d_{eff} = 15 mm. This filter excludes routes too far from the load patch to develop meaningful hogging, on which peak and zero-crossing detection is dominated by noise rather than real flexural features. Only the two interior continuous transverse supports, the South and Central girders, are reported. The North girder is excluded because it is a free building edge. The slab terminates at the North girder centreline and does not develop the symmetric two-sided hogging zone the ACI idealisation assumes.

Across the 64 high-signal routes at the South and Central girders, the hogging peak forms inside the ACI 544.6R ±250 mm yield-line zone in 100% of cases. Mean offsets range from 9 to 151 mm and the worst-case single route is 200 mm (80% of the band half-width, LS2

Central). The plastic-hinge location prescribed by ACI 544.6R is therefore confirmed by the elastic peak position observed at service load. In contrast, the line of contraflexure r_s, which measures the extent of the elastic hogging zone, is substantially larger than the ACI yield-line offset, as shown in Table 1 below.

Table 1. Line of moment contraflexure r_s from DFOS vs reference values from Kinnunen 1960 [14] uncracked elastic theory and ACI 544.6R [18] yield-line theory.

Load stage	Support	DFOS r_s mean (mm)	n	ACI offset (mm)	r_s = 0.22 L (mm)
Load Stage 1 (East)	South girder	1049	6	250	1650
Load Stage 1 (East)	Central girder	1283	9	250	1650
Load Stage 2 (West)	South girder	1028	6	250	1650
Load Stage 2 (West)	Central girder	829	15	250	1650
Load Stage 3 (Middle)	South girder	951	11	250	1650
Load Stage 3 (Middle)	Central girder	773	19	250	1650

Across all six combinations of load stage and interior continuous support, the DFOS-measured r_s sits between the ACI 544.6R yield-line offset (250 mm) and the Kinnunen [14] uncracked elastic value (1650 mm). The DFOS values range from 773 to 1283 mm. Expressed as drift from the ACI 544.6R prediction, DFOS r_s is 3.1 to 5.1 times capered to the ACI value. Relative to the r_s = 0.22L uncracked elastic value, DFOS sits 22% to 53% below (overall mean −40%). This positioning is consistent with a slab in a partially-cracked state. Hogging-side cracking has reduced r_s below the elastic value, but the slab has not reached full yielding [19].

The North girder is a building edge and is idealised in ACI 544.6R as a simple support with no negative yield line and zero offset. The DFOS data shows that the slab develops a small but measurable edge-hogging zone at the North girder. Mean peak $|\varphi|$ values across all transverse routes are 1.4, 1.6, and 1.8 × 10^{-3} m^{-1} at Load Stages 1, 2, and 3, respectively, with a maximum of 4.3 × 10^{-3} m^{-1}. The corresponding line of contraflexure sits 906 to 1346 mm south of the North girder centreline. The peak amplitude is 25 to 30 percent of the Central girder peak. The contraflexure offset is comparable to that of the interior continuous supports. This edge effect is not predicted by the ACI 544.6R simple-edge idealisation but is consistent with the slab having residual rotational restraint at the building boundary.

4.4 Area A versus Area B sub-finding

The two bays of the test panel share the same PrimX SFRC mix and differ only in the supplementary rebar bands provided over each minor beam in Area A. The contribution of these bands was assessed using two metrics. The first is r_s at the Central girder. The second is the local bending curvature $|\varphi|$ measured by longitudinal fibres at mirror positions in the two bays.

At the Central girder, the DFOS-measured r_s does not differ significantly between Area A and Area B. The median ratio of r_s on the Area A side to r_s on the Area B side, computed across 43 paired transverse routes covering all three load stages, is 1.03. The supplementary rebar bands in Area A are localised at each minor beam line and do not alter the global moment-field topology at the main girder centreline.

The longitudinal curvature (E-W) at mirror positions under symmetric loading shows a different result. Fibre F18 in Area A sits at z = +4.5 m north of the Central girder. Fibre F11 in Area B sits at z = −4.5 m south of the Central girder. These two fibres are true mirror pairs about the Central girder centreline. Under Load Stage 3 (Middle), the symmetric load case, F11 measures mean $|\varphi|$ approximately 2.54×10^{-3} m^{-1} along the fibre, and F18 measures 1.27×10^{-3} m^{-1} at the mirror position. The Area A value is 50 percent smaller than the Area B value. Under asymmetric load stages the comparison is confounded by the load patch position rather than the supplementary reinforcement. The two metrics tell a complementary story. The supplement rebar bands do not change the global r_s at the Central girder. The bands are localised at each minor beam and do not affect the slab cross-section between bands. At each minor beam line directly under the rebar band, the local curvature is reduced by 50 percent, reflecting the local stiffening contribution of the supplementary reinforcement.

4.5 Strain to load inversion as a structural-health-monitoring framework

The continuous strain field measured by DFOS opens the possibility of a closed-form inversion from observed strains to applied loads, moments, and shear. The inversion is anchored in the elastic constitutive relation. The bending curvature $\varphi(x)$ at each fibre route directly yields the local moment

$$M(x) = E \cdot I_{eff} \cdot \varphi(x) \tag{7}$$

where E is the elastic modulus of the slab and I_{eff} is the effective moment of inertia per unit width. $\varphi(x)$ is computed from the cleaned DFOS strain difference via Eq. The shear V(x) and the distributed load w(x) are recovered by spatial differentiation. Integration of the load profile across the panel returns an estimate of the total applied load. A proof-of-concept calculation using fibre F5 Route 1 under Load Stage 3 (Middle) and the slab properties of Section 2.2 produces a recovered patch load consistent with the applied 10 kN/m² within measurement and modelling tolerance. The framework is positioned as a proof of concept for real-time structural-health monitoring rather than a fully calibrated SHM tool. The follow-on work will close the gap by combining the DFOS strain field with a calibrated FEM and the multilinear constitutive model for SFRC sections [20], [21].

5 Conclusions

This study deployed distributed fibre optic sensing on a full-scale two-bay composite SFRC deck to measure the elastic moment field at service load. Six conclusions follow.

(1) The two-pass cleaning algorithm of Section 3.2 produces 208 per-route per-layer profiles that resolve continuous strain at sub-centimetre resolution. Connector-zone spikes, isolated outliers, and dropouts are removed without distorting flexural features wider than 100 mm.

(2) The line of moment contraflexure r_s is measured directly from the curvature. The shape of the smoothed and detrended signal is preserved against OFDR baseline drift, and the sign-transition gives a faithful experimental measurement of r_s without any finite-element model.

(3) The DFOS-measured r_s is a service-limit-state quantity. Across all six load-stage and interior continuous transverse-support combinations of Table 1, r_s ranges from 773 to 1283 mm. This range sits between uncracked-elastic SLS value of r_s = 0.22 L = 1650 mm and plastic-

mechanism ULS yield-line offset of 250 mm. The DFOS value sits 22 to 53 percent below r_s value, confirming that the slab is in the partially cracked elastic regime.

(4) The two-part summary of the comparison with ACI 544.6R has two parts. First, the location of the all experimental data elastic hogging peak sits inside the ±250 mm band. Second, the extent of the elastic hogging zone is much wider than the yield-line offset because the elastic and plastic regimes do not place the line of zero moment at the same place. The 250 mm value is a localised plastic-mechanism prescription for ULS reinforcement design, not a prediction of the SLS elastic moment field, and the comparison is therefore between unlike physical quantities. The North girder, idealised by ACI 544.6R as a simple edge with zero offset,

(5) The supplementary rebar bands in Area A do not change the global r_s at the Central girder. The median ratio is 1.03 across 43 paired routes. The local curvature is reduced by 50 percent at mirror positions under symmetric loading, however, reflecting the local stiffening effect of the band.

(6) The strain-to-load inversion framework is feasible as a proof of concept. The closed-form chain from curvature φ to moment to shear to load recovers the applied 10 kN/m² within measurement and modelling tolerance for one fibre under one load stage.

Follow-on work will combine the DFOS strain field with the multilinear constitutive model for strain-softening SFRC sections and a calibrated finite-element model of the test panel. The combination will close the elastic versus plastic gap identified in 4.5 and will provide a calibrated tool for SLS and ULS level monitoring of similar composite SFRC decks.

6 Acknowledgements

The authors gratefully acknowledge Primekss SIA for providing access to the test slab and supporting data, the NOVO optical-fibre interrogator team for the high-resolution DFOS measurements, and the Technical University of Denmark for the field-instrumentation work.

7 References

ACI Committee 544 (2015). ACI 544.6R-15: Report on Design and Construction of Steel Fiber-Reinforced Concrete Elevated Slabs. American Concrete Institute, Farmington Hills, MI.

Barrias, A., Casas, J. R., & Villalba, S. (2016). A review of distributed optical fiber sensors for civil engineering applications. Sensors, 16(5), 748. https://doi.org/10.3390/s16050748

Berrocal, C. G., Fernandez, I., & Rempling, R. (2021a). Crack monitoring in reinforced concrete beams by distributed optical fiber sensors. Structure and Infrastructure Engineering, 17(1), 124–139. https://doi.org/10.1080/15732479.2020.1731558

Berrocal, C. G., Fernandez, I., Löfgren, I., & Rempling, R. (2021b). Distributed optical fiber sensing (DOFS) in reinforced concrete members for reinforcement strain monitoring, crack detection and bond-slip calculation. Engineering Structures, 230, 111385. https://doi.org/10.1016/j.engstruct.2020.111385

Berrocal, C. G., Fernandez, I., & Rempling, R. (2022). Distributed fibre optic sensing: Reinforcement yielding strains and crack detection in concrete slab during column failure simulation. Measurement, 200, 111192. https://doi.org/10.1016/j.measurement.2022.111192

Billon, A., Henault, J.-M., Quiertant, M., Taillade, F., Khadour, A., Martin, R.-P., & Benzarti, K. (2020). Experimental and numerical investigation on the strain response of distributed optical fiber sensors bonded to concrete: Influence of the adhesive stiffness on crack monitoring performance. Sensors, 20(18), 5144. https://doi.org/10.3390/s20185144

Janiak, T., Becks, H., Camps, B., Schmidt, M., Hegger, J., & Reisgen, U. (2023). Evaluation of distributed fibre optic sensors in structural concrete. Materials and Structures, 56, 159. https://doi.org/10.1617/s11527-023-02222-9

Kishida, K., Imai, M., Kawabata, J., & Guzik, A. (2022). Distributed optical fiber sensors for monitoring of civil engineering structures. Sensors, 22(12), 4368. https://doi.org/10.3390/s22124368

Silkans, K., et al. (2025). Fiber optical sensors solutions for concrete construction structural health monitoring. PIERS-Spring 2025. https://doi.org/10.1109/PIERS-Spring66516.2025.11276174

Wan, K. T., & Leung, C. K. Y. (2007). Applications of a distributed fiber optic crack sensor for concrete structures. Sensors and Actuators A: Physical, 135(2), 458–464. https://doi.org/10.1016/j.sna.2006.09.004

Wang, X., Zhang, Q., Sun, L., Chen, R., Bao, Y., & Hou, S. (2024). Distributed fiber optic sensing for internal strain monitoring in full life cycle of concrete slabs with BOFDA technology. Engineering Structures, 305, 117798. https://doi.org/10.1016/j.engstruct.2024.117798

Weisbrich, M., Messerer, D., & Holschemacher, K. (2023). The challenges and advantages of distributed fiber optic strain monitoring in and on the cementitious matrix of concrete beams. Sensors, 23(23), 9477. https://doi.org/10.3390/s23239477

Zhang, H., & Wu, Z. (2008). Performance evaluation of BOTDR-based distributed fiber optic sensors for crack monitoring. Structural Health Monitoring, 7(2), 143–156. https://doi.org/10.1177/1475921708089745

Herbers, M., Richter, B., & Marx, S. (2025). Rayleigh-based crack monitoring with distributed fiber optic sensors: Experimental study on the interaction of spatial resolution and sensor type. Journal of Civil Structural Health Monitoring. https://doi.org/10.1007/s13349-024-00896-5

Imai, M., & Miura, S. (2013). Application of Brillouin optical correlation domain analysis for crack identification in concrete structure. Photonic Sensors, 3(4), 320–328. https://doi.org/10.1007/s13320-013-0134-3

Isaksson, E., Berrocal, C. G., Rempling, R., Tarighat, A., & Fernandez, I. (2021). Measurement and visualization of strains and cracks in CFRP post-tensioned fiber reinforced concrete beams using distributed fiber optic sensors. Automation in Construction, 127, 103604. https://doi.org/10.1016/j.autcon.2021.103604

Monsberger, C. M., & Lienhart, W. (2021). Distributed fiber optic shape sensing of concrete structures. Sensors, 21(18), 6098. https://doi.org/10.3390/s21186098

Berrocal, C. G., Fernandez, I., Bado, M. F., Casas, J. R., & Rempling, R. (2020). Dynamic distributed strain sensing to assess reinforced concrete behaviour. Engineering Structures, 200, 110036. https://doi.org/10.1016/j.engstruct.2019.110036

Catalano, A., Bruno, F. A., Galliano, C., Pisco, M., Persiano, G. V., Cutolo, A., & Cusano, A. (2021). A review of recent distributed optical fiber sensors applications for civil engineering structural health monitoring. Sensors, 21(5), 1818. https://doi.org/10.3390/s21051818

Jointless industrial floor using synthetic macro fibre-reinforced concrete: a Hungarian case study

Péter Károly Juhász[1,2], Márton Kispál[3], Anna Bencze[4]

[1] : Chief engineer in JKP STATIC Ltd, Budapest, Hungary.

[2] : Adjunct lecturer in Budapest University of Technology and Economics, Budapest, Hungary.

[3] : Head of R&D and Design at HelloParks – Futureal Group

[4] : Head of Sustainability at HelloParks – Futureal Group

Abstract

In jointless industrial floors, in addition to conventional service loads, structural behaviour is significantly influenced by tensile stresses induced by concrete shrinkage and by friction between the slab and the subgrade. At present, no generally accepted design guideline exists for the assessment of these effects, and current design practice relies largely on empirical recommendations.

Synthetic macro fibres, even at relatively high dosages, typically exhibit strain-softening behaviour, which raises the question of their effectiveness in mitigating crack localisation in jointless floor slabs. Nevertheless, the economic and sustainability advantages of synthetic fibres are evident, making their application increasingly attractive in industrial floor construction.

The design of the presented jointless industrial floor was preceded by an extensive experimental programme. In addition to determining the residual strength of the fibre-reinforced concrete, the influence of fibres on early-age shrinkage was investigated over a range of fibre dosages. Alongside the mechanical strength parameters of the concrete, the time-dependent shrinkage behaviour was also characterised. Prior to structural design, a finite element parametric study was conducted to analyse crack formation under various loading scenarios and fibre dosages.

Based on the obtained experimental and numerical results, the structural design was carried out for a 24 × 24 m jointless industrial floor slab with a thickness of 190 mm, dimensioned for a predefined rack-leg layout using experimentally derived material parameters. Following construction, continuous diagnostic monitoring is being performed, enabling verification and further development of the numerical model.

This paper presents the design and construction process of the jointless industrial floor, with particular emphasis on the finite element modelling approach and the material parameters employed.

Keywords

Mixing model, stochastic modelling, fibre distribution, fibre-moment, quality control

1 Introduction

From a structural design perspective, industrial floor slabs are generally not classified as primary load-bearing structural elements; therefore, their design is not necessarily required to follow the Eurocode design methodology (Lohmeyer and Ebeling, 1999). Nevertheless, these slabs represent critical components of industrial facilities and must satisfy strict serviceability requirements. In particular, the slab surface must maintain a high level of flatness, while differential movements at joints must remain limited in order to ensure the reliable operation of manufacturing equipment and forklift traffic. In addition, surface crack widths are typically required to remain below approximately 0.2–0.3 mm.

With the increasing application of jointless industrial floors, the risk of deterioration associated with saw-cut contraction joints can largely be eliminated. However, the significantly larger panel dimensions introduce additional challenges, particularly with respect to slab edge curling and the development of larger crack widths.

In the industrial developments of HelloParks, in addition to load-bearing capacity and serviceability requirements, sustainability focused design, construction and operation have become key objectives, with particular emphasis on the reduction of embodied carbon. Based on these requirements, a jointless industrial floor optimisation programme was initiated. As a result, using industrial floor solutions and construction materials available in Hungary, a highly optimised floor structure was developed that satisfies both structural performance and sustainability requirements. The design of the optimised floor system was supported by extensive laboratory material testing and numerical analyses. This paper presents the optimisation methodology and the performance of the constructed floor systems.

2 Designing of industrial floor with advanced finite element analysis

Industrial floor design is governed by several guidelines (e.g. TR34, 2013; ACI360, 2010; ÖVBB, 2008a), which are mainly based on empirical and semi-analytical approaches, considering different load cases (point, line, distributed loads) and support conditions. The design methods can be grouped into manual (guideline-based), linear finite element (FEA), and nonlinear FEA approaches. The main advantage of guidelines is their simplicity and ease of use, but their drawbacks include strong simplifications, conservative assumptions, and limited ability to represent real structural behaviour (e.g. cracking, shrinkage, complex load interactions). In addition, some important phenomena (such as shrinkage effects, joint behaviour, or interaction of multiple point loads) are either poorly addressed or not covered at all.

FEA, on the other hand, allows a more realistic representation of floor behaviour, including subgrade response (e.g. nonlinear springs), material nonlinearity, and cracking. Especially nonlinear FEA can capture post-cracking behaviour and stress redistribution, which guidelines cannot adequately describe. Therefore, FEA is particularly useful for complex loading conditions, high-performance floors, or when optimization (avoiding overly conservative design) is required.

2.1 Material parameters

At HelloParks, particular emphasis is placed on sustainability and reducing the carbon footprint of industrial floor construction. Accordingly, material selection has focused on solutions that provide both high structural performance and low embodied carbon. Fibre-reinforced concrete has a long and well-established track record in industrial flooring, demonstrating reliable performance and broad industry acceptance.

From a sustainability perspective, low-carbon synthetic macrofibres were identified as the most suitable reinforcement option. To support the selection process, a comprehensive comparative testing program was carried out. Mechanical performance was evaluated using three-point bending beam tests (3PBBT) in accordance with EN 14651 (Table 1), while the influence of fibres on crack formation was assessed through ring tests based on the Austrian guideline (ÖVBB, 2008b). Beams were produced using identical concrete mixes and fibre dosages representative of the actual floor application, ensuring direct comparability of results.

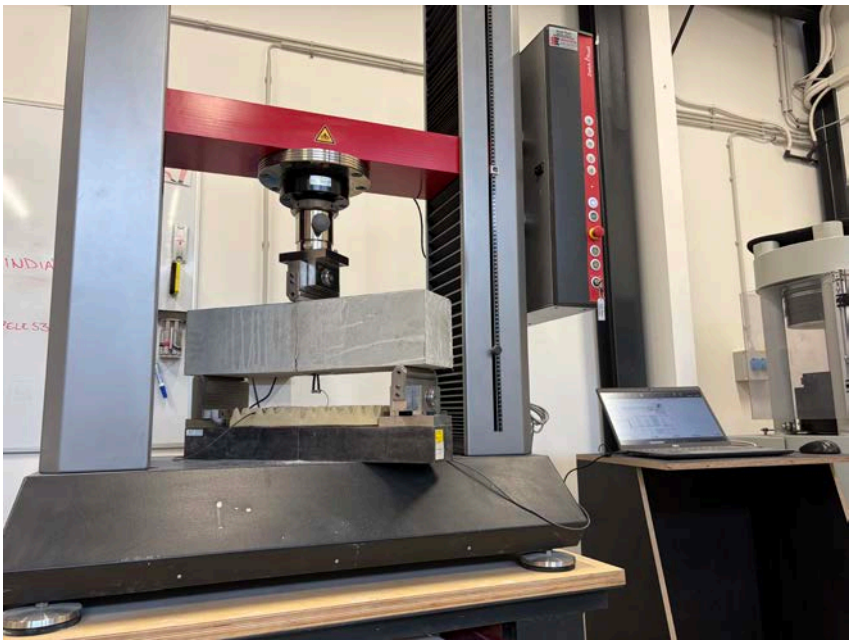


Figure 1. 3PBBT according to EN 14651 in JKP STATIC Concrete Laboratory

The selection criteria included residual strength performance, crack control efficiency, carbon footprint, and practical applicability on site. Based on these combined considerations, BarChip MQ58, a synthetic embossed polyolefin macro fibre, was selected as the optimal reinforcement solution. The adopted dosage of 3 kg/m^3 (approximately 0.33 vol.%) provided the required residual strength while minimizing the embodied carbon of the floor system.

Table 1: Mean flexural tensile and residual strength parameters obtained from EN 14651 three-point bending tests

Parameter	$f_{ct,L}$	$f_{R,1}$	$f_{R,2}$	$f_{R,3}$	$f_{R,4}$
Strength [MPa]	3.3	1.5	1.2	1.2	1.2

The obtained residual strengths satisfied the requirements defined for the proposed industrial floor application and were subsequently used for calibration of the constitutive model.

2.2 Constitutive model

Numerical analyses were performed using the ATENA finite element software (Cervenka Consulting, 2026), which is a well-established and validated tool specifically developed for nonlinear analysis of concrete structures. To improve computational efficiency, double symmetry was applied, allowing a reduction in the total number of finite elements without compromising accuracy.

The modelling approach was initiated with the representation of the subsoil and bedding system. The subsoil beneath the bedding layer was modelled using nonlinear compression-only springs, capturing the stiffness and nonlinear response of the ground. The bedding layer itself was described using a Drucker–Prager material model, enabling a realistic representation of its elastic-plastic behaviour. Material parameters for both soil and bedding were calibrated based on settlement data provided by geotechnical investigations.

The interaction between the concrete slab and the bedding layer was modelled using nonlinear contact elements. This approach allows separation (uplift) of the slab as well as horizontal displacements after detachment, governed by a defined friction coefficient. Such modelling is essential for accurately capturing curling effects and load transfer mechanisms.

The concrete slab was modelled using nonlinear material laws, with the William–Menétrey (1995) failure criterion applied in compression and the Rankine criterion (Cervenka, 2008) in tension. The post-cracking behaviour of fibre-reinforced concrete was incorporated using the modified fracture energy approach (Juhász, 2019; *fib* Bulletin 117, 2025). The constitutive model was calibrated using experimentally determined material properties. In particular, the tensile response was calibrated from the residual flexural strengths and fracture energy obtained from EN 14651 three-point bending beam tests, while the compressive behaviour was defined using the measured compressive strength. Crack development was represented using the crack band theory proposed by Bažant and Oh (1983), ensuring mesh-objective energy dissipation. Compressive strength was measured on cube specimens in accordance with EN 12390-3:2019. Flexural tensile strength and residual tensile strength were obtained from 3PBBT conducted according to EN 14651:2007+A1:2008. The modulus of elasticity and Poisson's ratio were determined based on the provisions of the Eurocode.

Standard isoparametric eight-node linear brick elements with full integration (Gaussian quadrature with eight integration points) were employed. Mesh objectivity was ensured through the crack band approach, where the crack band width was determined as the projection of the finite element size in the direction normal to the crack. As a result, the crack band size varies between integration points depending on the associated concrete volume and crack orientation. The element size of the concrete slab was selected as 5 × 10 × 10 cm. This discretization was determined based on previous studies (Juhász and Schaul, 2023) and validated through mesh sensitivity analyses. The mesh satisfies the requirement of having at least four elements through the slab thickness, while maintaining element aspect ratios below the recommended maximum of 1:4. For the soil domain, two elements were applied through the thickness.

The analysis was carried out in two loading stages. First, the self-weight of the slab and a uniformly distributed load were applied incrementally in 20 steps. Subsequently, shrinkage effects were introduced using an equivalent temperature gradient approach. The temperature load was applied over 300 increments as a linear gradient through the slab thickness, based on the previously conducted shrinkage analysis. The maximum shrinkage strain was 480×10^{-6}, based on previous shrinkage tests conducted in accordance with ASTM C157/C157M.

2.3 Results of numerical analysis

The load-bearing capacity of the floor is difficult to define in terms of the Ultimate Limit State (ULS), as a clearly identifiable failure mode is not straightforward to establish. Therefore, the required slab thickness for the given loading conditions was determined in accordance with the TR34 guideline, considering both bending and shear capacity.

In contrast, deformation and cracking behaviour were evaluated entirely through finite element analysis. As both deformation and crack width are Serviceability Limit State (SLS) criteria, characteristic load values and mean material properties were adopted in the analysis. Accordingly, the finite element model was used primarily to evaluate shrinkage-induced cracking, curling and deformation under serviceability conditions.

The rack system placed on the slab was well defined; therefore, both the positions and dimensions of the rack legs were precisely known. Several loading scenarios were investigated; however, the governing case was identified as the fully loaded slab condition, where all loads act simultaneously. An important aspect of the analysis was the time-dependent application of loads. Shrinkage-induced deformations occurring under unloaded conditions result in lower friction forces; therefore, it is beneficial if operational loads are applied at a later stage, typically after at least three months of curing.

Crack patterns in the slab are presented in Fig. 2a, while vertical displacements are shown in Fig. 2b. The effect of modelling the slab with joints was also investigated, resulting in reduced vertical displacements. The governing criterion was taken as the vertical displacement at the free edge of the slab.

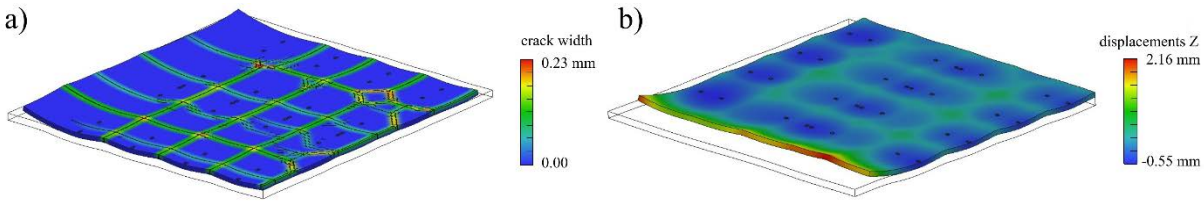


Figure 2. Results of the FEA a) crack width b) displacements

3 Carbon footprint calculation

The real estate sector accounts for approximately 38% of greenhouse gas emissions within the European Union, according to World Green Building Council (2019). As such, it is considered the largest emitting sector, making its decarbonization essential for achieving the climate targets set by the European Union (see European Green Deal).

In the case of buildings, achieving these targets requires assessing the carbon footprint generated throughout the entire life cycle of the asset, with the ultimate goal of reaching carbon neutrality.

The life-cycle carbon footprint can be divided into two main categories: operational and embodied carbon. Operational carbon refers to emissions associated with energy consumption during the use phase of the building. Embodied carbon, on the other hand, arises from the

extraction and production of construction materials, their transportation, the energy demand of construction processes, as well as maintenance, repair, and replacement activities during the life cycle, and finally from demolition, waste treatment, and disposal processes at the end of the building's life.

Over the past decade, regulatory changes have primarily focused on reducing operational carbon, with only limited and mostly indirect consideration of embodied carbon emissions. However, in the case of new buildings – largely due to improved energy efficiency – the balance has shifted significantly towards embodied carbon.

Upcoming European Union regulations will explicitly integrate the assessment and reduction of embodied carbon, representing a major shift in industry priorities. By 2027, all Member States will be required to develop detailed roadmaps for new buildings, including Whole Life Carbon (WLC) targets and limit values, thereby driving continuous reduction across the sector. As a next step, from 2028 onwards, Whole Life-Cycle Global Warming Potential (WLC GWP) calculations will become mandatory for all buildings with a floor area exceeding 1000 m^2, and these results must be incorporated into the building energy performance certificate. Binding national limit values are expected to come into force from 2030.

The construction sector is characterized by long project lead times, with development, design, and execution often spanning several years. As a result, timely preparation for forthcoming regulatory changes is essential. In this context, assessing, understanding, and reducing embodied carbon is a necessary step both to ensure future compliance and to achieve measurable emission reductions. In Hungary, the systematic consideration of embodied carbon is not yet standard practice, therefore early engagement with the topic – such as that undertaken by HelloParks – contributes to its broader recognition and integration into industry practice.

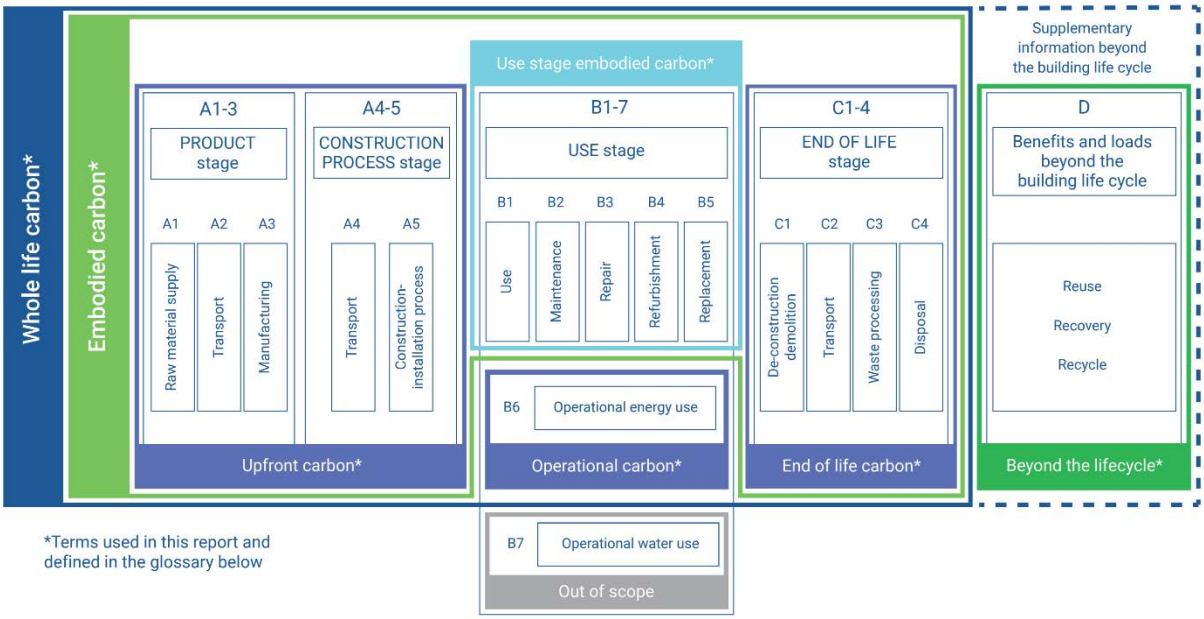


Figure 3. Terminology defined in EN 15978 (World Green Building Council, 2019)

In Europe, the EN 15978 standard defines the methodology for assessing the environmental impacts of buildings over their entire life cycle. The standard divides the building life cycle into the following stages and modules, as shown in Fig. 3 (World Green Building Council, 2019).

In 2022, HelloParks carried out a detailed life-cycle assessment for its standard building typology, which resulted in a distribution of 59% embodied carbon and 41% operational carbon. The following figures present the breakdown by life-cycle stages as well as the temporal distribution of emissions, clearly highlighting the importance of addressing embodied carbon in the case of new buildings.

The analysis further revealed that, considering embodied carbon alone, the largest contributor is the industrial floor, accounting for 13% of the total embodied carbon footprint. It was therefore evident that optimizing the industrial floor and reducing its carbon footprint could yield significant results.

Several carbon reduction measures were identified, and their combined application resulted in a significant 10.62% reduction for a standard building geometry. The achieved savings are attributable to one optimization measure and two interventions related to material type and composition. The full package of measures was gradually implemented during 2023 and 2024 and has since been incorporated into the technical standard.

The optimization of the floor thickness to 19 cm, presented in the previous sections, provides a clear example of reducing unnecessary carbon emissions arising from overdesign (see Table 2). The replacement of steel fibres with synthetic fibres represents a targeted intervention in another carbon-intensive component (see Table 3). The most significant reduction, however, was achieved through the substitution of the cement component in the concrete mix with a higher blast furnace slag content (see Table 4).

Tables 2–4 present the detailed changes in carbon footprint associated with each measure, demonstrating their reduction potential by comparing the standard HelloParks building with the updated standard incorporating the modified technical specifications.

Aggregating the partial results, the three measures together result in a total embodied carbon reduction of 1,925,232.8 $kgCO_2e$ for a standard HelloParks building, corresponding to a decrease of 42.78 $kgCO_2e$ per square metre. This represents a 10.62% reduction compared to the original standard baseline.

The optimisation measures presented in this section were not considered independently but formed the basis of the final floor design described in Sections 2 and 4. The reduction of slab thickness from 200 mm to 190 mm was enabled by the experimentally validated material model and nonlinear FE analysis, while the use of synthetic macro fibres contributed simultaneously to the required structural performance and the reduction of embodied carbon.

Table 2: Optimization – cost savings from reducing industrial floor thickness from 20 cm to 19 cm

Section	Result category	Savings ($kg\ CO_2$)	Savings ($kg\ CO_2/m^2$)	Savings (%)
A1-A3	Construction materials	333 369.43	7.4082	2.09%
A4	Transportation to site	9 781.04	0.2174	1.64%
B1-B5	Material replacement and refurbishment	-	-	0.00%
C1-C4	End of life	11 796.90	0.2622	1.38%
TOTAL		**354 947.37**	**7.8877**	**1.96%**

Table 3: Carbon reduction – 19 cm FRC industrial floor with synthetic fibres instead of steel fibres

Section	Result category	Savings ($kg\ CO_2$)	Savings ($kg\ CO_2/m^2$)	Savings (%)
A1-A3	Construction Materials	529 046.04	11.7566	3.32%
A4	Transportation to site	3 354.85	0.0746	0.56%
B1-B5	Material replacement and refurbishment	-	-	0.00%
C1-C4	End of life	149.17	0.0033	0.02%
TOTAL		**532 550.06**	**11.8344**	**2.94%**

Table 4: Carbon reduction – CEM III/A vs. CEM II/B-S cement

Section	Result category	Savings ($kg\ CO_2$)	Savings ($kg\ CO_2/m^2$)	Savings (%)
A1-A3	Construction Materials	870 014.41	19.3337	5.46%
A4	Transportation to site	-	-	0.00%
B1-B5	Material replacement and refurbishment	-	-	0.00%
C1-C4	End of life	167 720.96	3.7271	19.67%
TOTAL		**1 037 735.37**	**23.0608**	**5.72%**

4 Implementation and construction

Since the founding of HelloParks in 2020, and after the completion of nearly a dozen warehouse buildings with a total floor area exceeding 500,000 m^2, the path that led to the development of the floor design presented in this study has become clearly visible. In the case of HelloParks' first building, the floors were constructed with 20 cm thick slabs in line with standard Hungarian construction practice. However, the sustainability objectives and the continuous optimisation of the technical concept led to the development of the 190 mm thick jointless synthetic macro fibre-reinforced industrial floor presented in this paper.

The floor was completed in April 2024 and consists of 72 jointless panels, each with plan dimensions of 24 × 24 m. Since then, the last three completed projects, with a total floor area of more than 150,000 m^2, have been built using this new industrial floor solution. A completed floor area before installation of the warehouse equipment is shown in Fig. 4.

Achieving a technically sound result requires strict quality control throughout the entire construction process. During the sub-base preparation phase, load tests were carried out at high frequency on every layer, and the laboratory evaluation results were reviewed at multiple levels

during construction. The use of synthetic macro fibres did not require any major modification of conventional industrial floor construction technology. During finishing, the most common technology-related, yet easily remedied, problem is surface defects caused by plastic fibres protruding from the plane of the floor. In some cases, the partially protruding fibres are rotated by the circular motion of the power trowel, creating flower-shaped marks on the surface. These can be removed with a torch without damaging the fresh concrete. No significant fibre-related construction problems, such as fibre balling or segregation, were observed.



Figure 4. Completed jointless industrial floor before installation of warehouse equipment

Approximately two years have elapsed since completion. During this period, no surface cracks visible to the naked eye have been observed on the jointless floor panels, and no detrimental curling has been detected. The only measurable shrinkage-related movement occurred at the steel expansion joints separating the building dilatation units, where an opening of approximately 5 mm was observed, as shown in Fig. 5. This movement occurred at the structural expansion joint rather than within the individual 24 × 24 m jointless panels.



Figure 5. Opening of the steel expansion joint at a column line after shrinkage deformation

The warehouse has since been fully equipped with high-bay racking systems and has been operating under normal service conditions, as illustrated in Fig. 6. No functional limitations or serviceability problems related to the floor have been reported. The observed field performance is therefore consistent with the numerical predictions, which indicated controlled shrinkage deformation without excessive crack width or unacceptable curling.

To further validate the numerical model, a long-term monitoring programme has been initiated on one representative dilatation unit. The monitoring system measures the horizontal movement of the floor with high precision, allowing the time-dependent shrinkage and temperature-related movements to be quantified under real service conditions. These results will be used for further calibration of the finite element model.

The successful performance of the constructed floors confirms that synthetic macro fibre-reinforced concrete can be applied in large jointless industrial floor panels while maintaining the required serviceability performance. The observed field performance also indicates that further optimisation may be possible. In particular, the numerical analyses suggest that a slab thickness of 17 cm may be achievable without compromising comparable load-bearing performance.

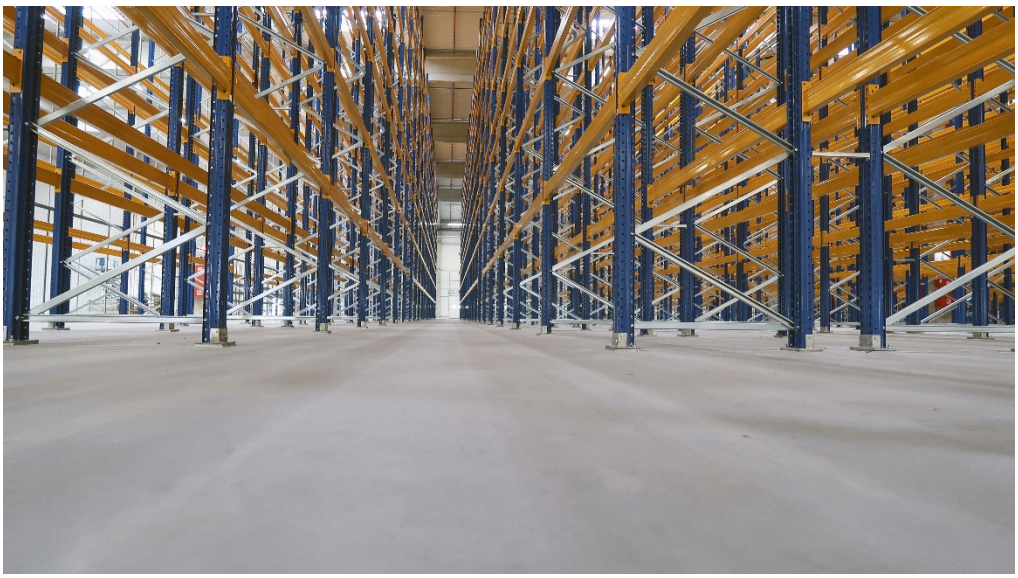


Figure 6. High-bay racking system installed on the jointless industrial floor

5 Concluding remarks

This study demonstrates that industrial floor design can be significantly improved by combining advanced FEA with targeted material optimisation. Nonlinear FEA enables a more realistic representation of structural behaviour, allowing the reduction of conservative assumptions and avoiding overdesign. As a result, slab thickness could be reduced without compromising structural performance or serviceability.

The application of synthetic macro fibres proved to be an effective alternative to conventional steel fibre reinforcement. Despite their strain-softening behaviour, both the EN 14651 test results and numerical results confirmed their suitability for crack control in jointless

industrial floors. In addition, their lower embodied carbon and practical advantages make them a favourable solution from both sustainability and construction perspectives.

From an environmental standpoint, the results highlight that industrial floors represent a key leverage point for reducing embodied carbon in logistics buildings. The combined measures investigated in this study resulted in a meaningful reduction, demonstrating that significant improvements can be achieved through integrated engineering and material decisions.

Overall, the presented approach illustrates that sustainability-driven optimisation does not require compromises in performance. On the contrary, the integration of advanced finite element modelling and innovative materials provides a robust pathway towards more efficient and lower-carbon industrial floor solutions.

The next stage of the research will focus on the further development of the numerical model through a sensitivity analysis of the governing modelling parameters. Particular attention will be paid to the influence of subgrade properties and slab-subgrade interface parameters. The results will be validated against long-term monitoring data collected from the full-scale industrial floor presented in this study.

6 Acknowledgements

The authors would like to express their gratitude to HelloParks for enabling access to project data and supporting the publication of this research. The industrial floor design was carried out by JKP STATIC Ltd., while the laboratory investigations were performed at the JKP STATIC Concrete Laboratory, an accredited testing facility (NAH-1-1902/2022).

7 References

ACI Committee 360, 2010. *Guide to Design of Slabs-on-Ground (ACI 360R-10).* American Concrete Institute, Farmington Hills, MI, USA.

Bazant, Z.P., Oh, B.H., 1983. “Crack band theory for fracture of concrete”, *Materials and Structures* 16, 155–177. https://doi.org/10.1007/BF02486267

Cervenka Consulting (2026), https://www.cervenka.cz/products/atena last accessed 2026/03/28

Cervenka, J., Papanikolaou, V. K., 2008. “Three dimensional combined fracture-plastic material model for concrete”, *International Journal of Plasticity* (24) pp 2192–2220.

fib 2025. *fib Bulletin No. 117: FEM-based approaches for the design of FRC Structures,* Fédération internationale du béton (fib), Lausanne, Switzerland.

Juhász, K.P., 2019. “The effect of the synthetic fibre reinforcement on the fracture energy of the concrete”, in: *IOP Conference Series: Materials Science and Engineering*, vol. 613, p 012037, 4 Nov 2019.

Juhász, K.P., Schaul, P., 2023. “Parametric numerical study on jointless macro synthetic fiber reinforced concrete industrial floors”, in: *FRC2023: Fiber Reinforced Concrete: from Design to Structural Applications – Joint ACI-fib-RILEM International Workshop.*

Lohmeyer, G, Ebeling, K., 1999. *Betonböden im Industriebau: Hallen- und Freiflächen.* Verlag Bau + Technik, Erkrath, Germany.

Menétrey, P., William, K. J., 1995. “Triaxial Failure Criterion for Concrete and Its Generalization”, *ACI Structural Journal* 92 (3) pp 311–318.

Österreichische Vereinigung für Beton- und Bautechnik, 2008a. *Herstellung von faserbewehrten monolithischen Betonplatten*, Wien, Austria.

Österreichische Vereinigung für Beton- und Bautechnik, 2008b. *Richtlinie Faserbeton*, Wien, Austria.

The Concrete Society, 2013. *Concrete Industrial Ground Floors – A Guide to Design and Construction (TR34).* 4th ed., Camberley, UK.

World Green Building Council, 2019. *Bringing Embodied Carbon Upfront: Coordinated action for the building and construction sector to tackle embodied carbon*. London, WorldGBC. https://worldgbc.s3.eu-west-2.amazonaws.com/wp-content/uploads/2022/09/22123951/WorldGBC_Bringing_Embodied_Carbon_Upfront.pdf

Validation and application of a modified damage plasticity model for fibre-reinforced concrete structures

Simone Niccolaini[1], Paolo Martinelli[1]

[1] : Politecnico di Milano, Dep. of Civil and Environmental Engineering, Milan, Italy.

Abstract

Among the various modelling strategies in the literature, damage-plasticity models are widely used to describe the behaviour of plain concrete. However, when applied to fibre-reinforced concrete (FRC), these models often fail to adequately capture the contribution of fibres, particularly in the post-cracking regime. To address this limitation, a Modified Damage Plasticity (MDP) model has been proposed in the literature as an extension of the original formulation. This model incorporates the bridging effect of fibres through the pull-out mechanism into the constitutive relation of SFRC, accounting for both straight and hooked fibres. In this work, the MDP model is validated and applied through a two-scale investigation. First, the model is validated at the material level using numerical simulations of tensile and compressive tests to evaluate its ability to capture the main resistance mechanisms of steel fibre-reinforced concrete. Then, the model is applied at the structural scale to shallow beams reinforced with a combination of conventional steel bars and fibres, as well as to fibre-only beams, assessing its accuracy in predicting the global structural response.

Keywords

fibre-reinforced concrete (FRC); FE analyses; concrete damage-plasticity model; modified damage-plasticity model.

1 Introduction

Fiber-reinforced concrete (FRC) has become a well-established material solution in a wide range of structural applications, including industrial flooring, tunnel linings, and prefabricated elements. In most practical cases, FRC is used in combination with conventional steel reinforcement, following a hybrid reinforcement strategy (reinforced concrete with fibres, R/FRC). In specific applications, such as tunnel linings, FRC can even be employed without traditional reinforcement. The inclusion of fibres enhances crack control, improves post-cracking behaviour, and often leads to a reduction in construction costs when compared to conventional reinforced concrete structures. Moreover, the improved toughness provided by fibres enables the design of thinner structural elements and lightweight systems, contributing to both economic and environmental sustainability.

Despite these advantages, the structural performance of FRC remains strongly dependent on material-related factors that are not yet fully characterized, particularly fibre distribution, orientation, and interaction with the cementitious matrix. Experimental studies have consistently shown that, alongside the concrete mix design, fibre dispersion is a key parameter governing the mechanical response of FRC structures (Mudadu et al. 2018; Martinelli et al. 2021). Among the various types of FRC, steel fibre reinforced concrete (SFRC) is the most widely adopted for structural applications, a fact that is reflected in its recent inclusion in the new Eurocode 2 (CEN, 2023).

In this context, reliable numerical simulations based on the finite element method (FEM) play a fundamental role in exploiting the full potential of fibre reinforcement. Appropriate constitutive models allow engineers to explore innovative and cost-effective structural solutions while significantly reducing the need for extensive experimental campaigns, which can be limited to model calibration and validation purposes. However, recent blind prediction competitions organized by fib Working Group 2.4.1 have highlighted a substantial dispersion in numerical results when simulating the behaviour of SFRC structural members (Barros at al. 2021, 2023). Large discrepancies were observed both in the prediction of flexural response of continuous shallow SFRC beams (Barros et al. 2023) and in the shear behaviour of T-beams (Barros at al. 2021). These outcomes indicate that current modelling approaches may still face challenges in consistently capturing the nonlinear response of SFRC, particularly in the post-cracking regime, and underline the need for constitutive models that are both accurate and robust.

In this framework, the present study provides a first assessment of the Modified Damage Plasticity (MDP) model, originally proposed by Tran et al. (2025), across material and structural scales. It should be noted that part of the material-level response considered herein has already been addressed in previous work (Tran et al., 2025), which focused on validation under standard uniaxial tests. Building on that basis, the present contribution extends the analysis by applying the same modelling framework to structural-scale problems, with particular emphasis on SFRC shallow beams. At this stage, the study represents a preliminary step toward a more comprehensive validation campaign, which will include notched beam tests covering a wider range of material compositions and comparisons with formulations adopted in design codes such as *fib* Model Code 2020.

2 Overview of the modified damage plasticity model for FRC structures

Among the modelling strategies available for reinforced concrete (RC) and FRC structures, damage–plasticity formulations have attracted considerable attention due to their ability to represent both the inelastic behaviour of concrete and the progressive stiffness degradation associated with cracking and crushing. The Concrete Damage Plasticity (CDP) model, originally proposed by Lubliner et al. (1989) and later extended by Lee and Fenves (1998), is one of the most widely adopted approaches. However, its classical formulation is primarily suited to ordinary concrete and does not adequately account for the additional toughness provided by steel fibres, particularly in regimes where fibre bridging and pull-out mechanisms govern the response.

To address this limitation, Tran et al. (2025) recently proposed a Modified Damage Plasticity (MDP) model in which the tensile constitutive behaviour and the evolution of tensile damage are explicitly linked to fibre pull-out mechanisms. This formulation embeds key microstructural effects directly into the macroscopic constitutive law, enabling a more realistic representation of the mechanical contribution of fibres.

The overall modelling and analysis procedure adopted in this work is summarised in Flowchart 1 (Fig. 1). A numerical code implementing the MDP model proposed by Tran et al. (2025) has been developed in a MATLAB environment. The first step consists in defining the input parameters describing both the cementitious matrix and the fibres. The matrix parameters include the cylindrical compressive strength f_c, maximum aggregate size d_a, and water-to-cement ratio. The fibre-related parameters include the fibre length L_f, diameter d_f, Young's modulus E_f, volume fraction V_f, ultimate tensile strength σ_{fu}, snubbing and spalling coefficients f and k, the friction coefficient between fibre surface and concrete μ, the non-dimensional softening parameter β, and the frictional sliding shear stress τ_0 at the debonding tip. For hooked-end steel fibres, additional parameters describing the hook geometry (L_1, L_2, γ_F) and the fibre yield strength σ_y are required. The cementitious matrix properties are derived from the experimental programmes considered in this study and are reported in the corresponding sections describing the validation cases (Sections 3 and 4). Likewise, the geometrical and mechanical properties of the fibres are adopted from the same experimental studies and are summarised in Table 1 for all the cases examined. The compressive and tensile constitutive relationships are derived according to the MDP formulation, whereas the parameters τ_0, β, and σ_y, previously calibrated by Tran et al. (2025), are assumed equal to 1.6 MPa, 0.01, and 600 MPa, respectively, for all simulations. In addition, the fibre–matrix friction coefficient μ is consistently assumed equal to 0.65, following Tran et al. (2025). Readers interested in the physical meaning and role of the parameters τ_0 and β within the MDP formulation are referred to Tran et al. (2025) for further details.

Based on these inputs, the MATLAB code is used to: (i) determine the plasticity parameters of the fibre-reinforced material; (ii) define the compressive stress–strain relationship; (iii) establish the tensile stress–crack opening law, which may exhibit either softening or hardening behaviour; and (iv) derive the compressive and tensile damage evolution laws in a manner consistent with the previously defined constitutive relationships (Flowchart 2, Fig. 1). The resulting material parameters are then implemented in an Abaqus finite element model (Dassault Systèmes 2024) where the structural analysis is performed to

obtain the global response (Flowchart 1, Fig. 1). For a comprehensive description of the MDP model formulation, the reader is referred to Tran et al. (2025).

In the present study, the MDP model is first validated at the material scale by reproducing experimental compressive tests on cylindrical specimens and uniaxial tensile tests available in the literature. Subsequently, the modelling approach is applied to structural elements, namely shallow SFRC beams tested under bending, including beams reinforced with a combination of conventional steel bars and fibres as well as fibre-only beams.

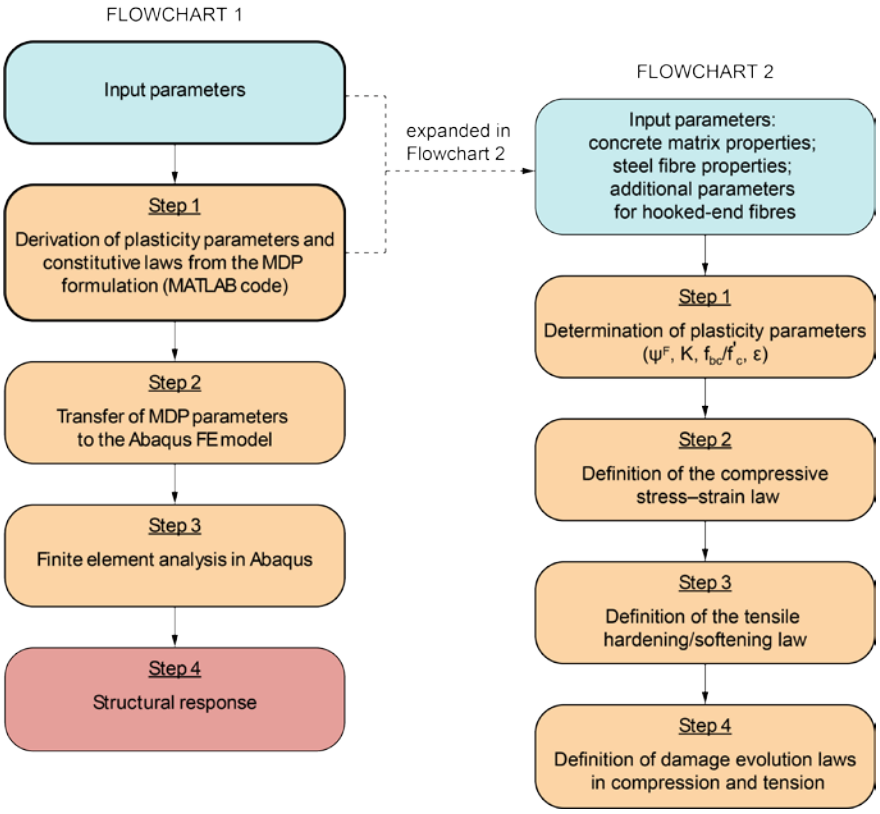


Figure 1:Flowchart 1 illustrates the overall modelling and analysis procedure, while Flowchart 2 provides a detailed description of Step 1, namely the derivation of plasticity parameters and constitutive laws from the MDP formulation.

3 Validation of the MDP model at the material scale

In this section, the numerical approach proposed by Tran et al. (2025) is validated under both compressive and tensile loading conditions. The validation is carried out by comparing numerical results obtained from ABAQUS simulations with experimental data available in the literature. Specifically, the compressive response is calibrated using the cylindrical compression tests conducted by Susetyo (2009), while the tensile behaviour is verified against the uniaxial tension tests reported by Amin et al. (2015). Different fibre volume fractions and fibre geometries are considered to assess the robustness and predictive capability of the proposed approach. Table 1 summarizes the properties of the steel hooked-end fibres required by the MDP model and used in the compression tests (Susetyo, 2009), tensile tests (Amin et al., 2015), and shallow beam tests described in Section 4 (Colombo et al., 2023).

Table 1: Mechanical and geometrical properties of the hooked-end steel fibre. Values are reported for compression tests (Susetyo, 2009), tensile tests (Amin et al., 2015), and shallow beam tests (Colombo et al. 2023).

Parameter	Compression test values	Tension test values	Shallow beam values
L_f (mm)	50	35	60
L_1 (mm)	2.55	2.55	2.55
L_2 (mm)	2.22	2.22	2.22
γ_f (°)	38.3	38.3	45
d_f (mm)	0.62	0.55	0.90
σ_{fu} (MPa)	1050	1340	1900
E_f (GPa)	200	200	200
μ (-)	0.65	0.65	0.65
σ_y (MPa)	600	600	600

3.1 Uniaxial compression tests

The compression tests performed by Susetyo (2009) were conducted on cylindrical specimens with a diameter of 150 mm and a height of 300 mm (Fig. 2a). The compressive cylindrical strength is assumed to be 50 MPa, while the water-to-cement ratio and maximum aggregate size were taken as 0.40 and 12 mm, respectively. Three specimen series were tested, corresponding to fibre volume fractions of 0.5%, 1.0%, and 1.5%. In the following, numerical results are presented only for the 0.5% and 1.0% fibre volume fractions, while those corresponding to the 1.5% case are omitted for brevity. In the numerical simulations, the cylindrical specimens are modelled in ABAQUS using three-dimensional eight-node linear brick elements with reduced integration (C3D8R), as shown in Fig. 2b. A uniform mesh size of 10 mm is adopted. A displacement-controlled loading scheme is adopted, consistent with the experimental set-up.

Using the MDP model, the compressive stress–strain response in the inelastic regime and the associated damage evolution laws are obtained for the three fibre volume fractions (not shown here for the sake of brevity). As expected, an increase in fibre volume fraction leads to higher peak stresses and enhanced ductility. Conversely, lower fibre contents result in a more rapid development of damage, with an earlier degradation of material stiffness. Fig. 3 compares the numerical predictions, obtained with and without damage, with the experimental results reported by Susetyo (2009) for fibre volume fractions of 0.5% (Fig. 3a) and 1.0% (Fig. 3b). Overall, the numerical simulations provide a good representation of the compressive behaviour of the cylindrical specimens, effectively capturing both the mechanical response and the influence of fibre volume fraction observed in the experiments.

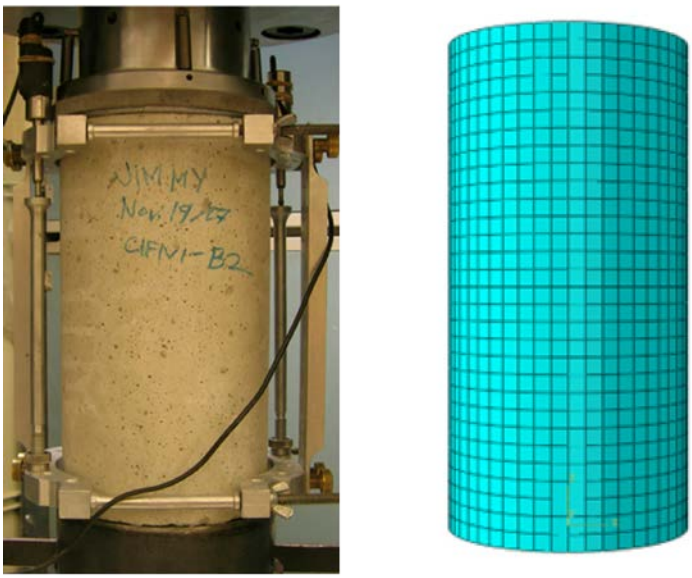


Figure 2: Cylindrical compression tests: (a) experimental set-up (Susetyo 2009), and (b) corresponding mesh view.

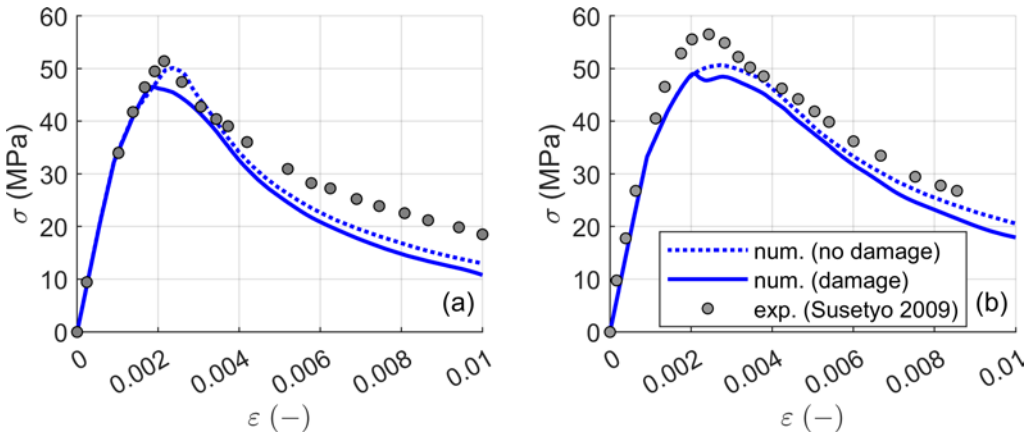


Figure 3: Comparison of numerical and experimental (Susetyo 2009) results from cylindrical compression tests for fibre volume fractions of (a) 0.5% and (b) 1.0%.

3.2 Uniaxial tension tests

The uniaxial tension tests on dog-bone specimens conducted by Amin et al. (2015) were aimed at investigating the tensile behaviour of SFRC under direct tension. The prismatic dog-bone geometry was specifically designed to promote failure within the central region of the specimen and to minimise stress concentrations near the grips. As shown in Fig. 4a, the reduced section has a width and thickness of 125 mm, allowing the development of a nearly uniform uniaxial stress state during testing.

From the entire experimental campaign reported by Amin et al. (2015), four uniaxial tension test series are considered in the present study to assess the influence of fibre geometry and fibre volume fraction on the tensile response of SFRC. Two specimen series were reinforced with straight steel fibres, while the remaining two employed hooked-end fibres. For each fibre geometry, volume fractions of V_f = 0.5% and V_f = 1.0% are examined, enabling

a direct comparison of the mechanical contribution provided by different fibre shapes and dosages in the post-cracking regime. The mechanical properties of the steel fibres adopted in the tests, required for the MDP model, are reported in Table 1. The concrete mix differed slightly among the tests, with cylindrical compressive strengths ranging from 56.2 to 63.7 MPa. The water-to-cement ratio and maximum aggregate size are taken as 0.40 and 10 mm, respectively

In the numerical simulations performed in ABAQUS, the uniaxial tension tests are modelled under plane stress conditions using a two-dimensional mesh composed of 2696 three-node triangular elements (CPS3), as illustrated in Fig. 4b. A refined mesh with an element size of 5 mm is adopted in the central region to accurately capture crack propagation, while a coarser mesh of 15 mm is used elsewhere to improve computational efficiency and numerical stability.

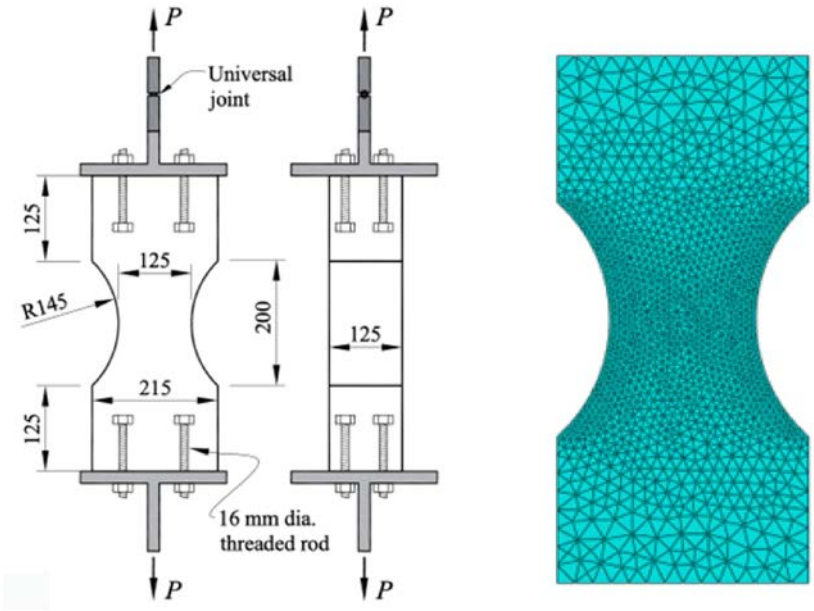


Figure 4: Uniaxial tensile test: (a) experimental set-up (Amin et al., 2015) and (b) corresponding mesh view.

The stress–crack opening relationship in the inelastic regime and the associated damage evolution laws are derived from the MDP model. Figs. 5a and 5b compare the numerical predictions, obtained with and without damage, with the experimental results reported by Amin et al. (2015) for hooked-end fibres with volume fractions of 0.5% and 1.0%, respectively. For V_f equal to 0.5%, the tensile response is well reproduced both with and without damage, whereas for V_f equal to 1.0% the inclusion of damage is essential to accurately capture the experimental behaviour. When damage is considered, the finite element analyses successfully reproduce the residual post-cracking strength and post-peak softening observed in the tests. The tensile response of specimens reinforced with straight steel fibres, characterised by a softening post-peak behaviour, is reproduced with even greater accuracy; these results are omitted here for brevity.

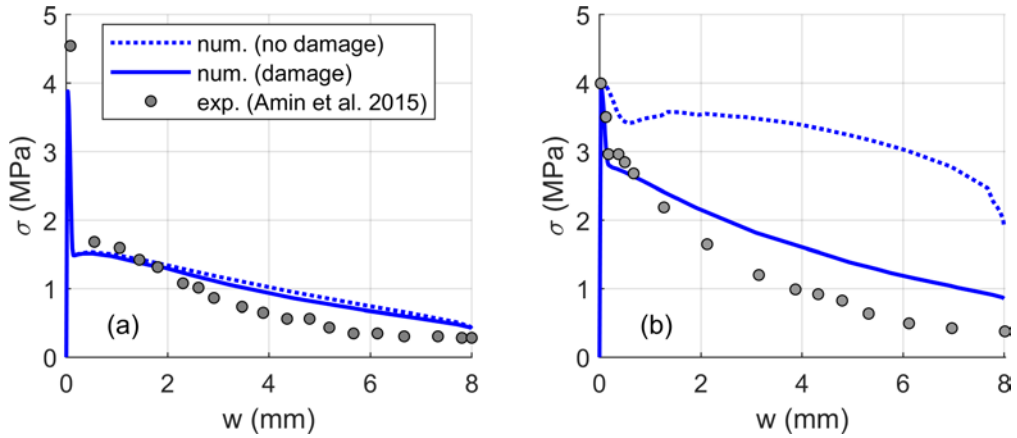


Figure 5: Comparison of numerical and experimental (Amin et al. 2015) results from uniaxial tensile tests for fibre volume fractions of (a) 0.5% and (b) 1.0%, with results referring to hooked-end fibres.

4 Application of the MDP model to shallow beams

In this section, the MDP model described in Section 2 is applied to reproduce and analyse two experimental test series on SFRC shallow beams tested by Colombo et al. (2023). These tests provide a comprehensive dataset on the flexural response of full-scale structural elements and are particularly valuable for assessing both the combined and isolated effects of hooked-end steel fibres and conventional reinforcement, enabling a direct comparison between different reinforcement strategies.

The reference structural element is a shallow beam, 120 mm thick, 3 m long, and 600 mm wide, as shown in Figs. 6a–b. Two reinforcement configurations are investigated (highlighted in red in Fig. 6b): specimens denoted as 55A+R, combining 0.70% hooked-end steel fibres with conventional longitudinal reinforcement (2Ø10), and specimens denoted as 70A, reinforced exclusively with 0.90% hooked-end steel fibres. For each configuration, three nominally identical beams were cast in the same production plant and tested. The compressive cylindrical strength is assumed to be 56 MPa, while the water-to-cement ratio and maximum aggregate size are taken as 0.49 and 15 mm, respectively. The mechanical and geometrical properties of the steel fibres are listed in Table 1.

In the numerical model, the concrete is discretised using three-dimensional eight-node brick elements with reduced integration (C3D8R), while the longitudinal steel reinforcement in specimen 55A+R is modelled using T3D2 truss elements. A uniform element size of 15 mm is adopted for both solid and truss elements, providing a suitable balance between numerical accuracy and computational efficiency. The supports and loading pin are explicitly modelled to closely reproduce the experimental setup and are assumed to behave as linearly elastic steel. Contact interactions between the beam and the supports/loading pin are defined using a hard contact formulation in the normal direction and a Coulomb friction model in the tangential direction, with a friction coefficient equal to 0.5.

The self-weight of all structural beams is included through an initial analysis step, followed by a displacement-controlled loading phase. To reduce computational effort, geometric symmetry is exploited, resulting in the meshed model shown in Fig. 6c. The constitutive parameters adopted in the simulations are derived following the procedure proposed by Tran et al. (2025).

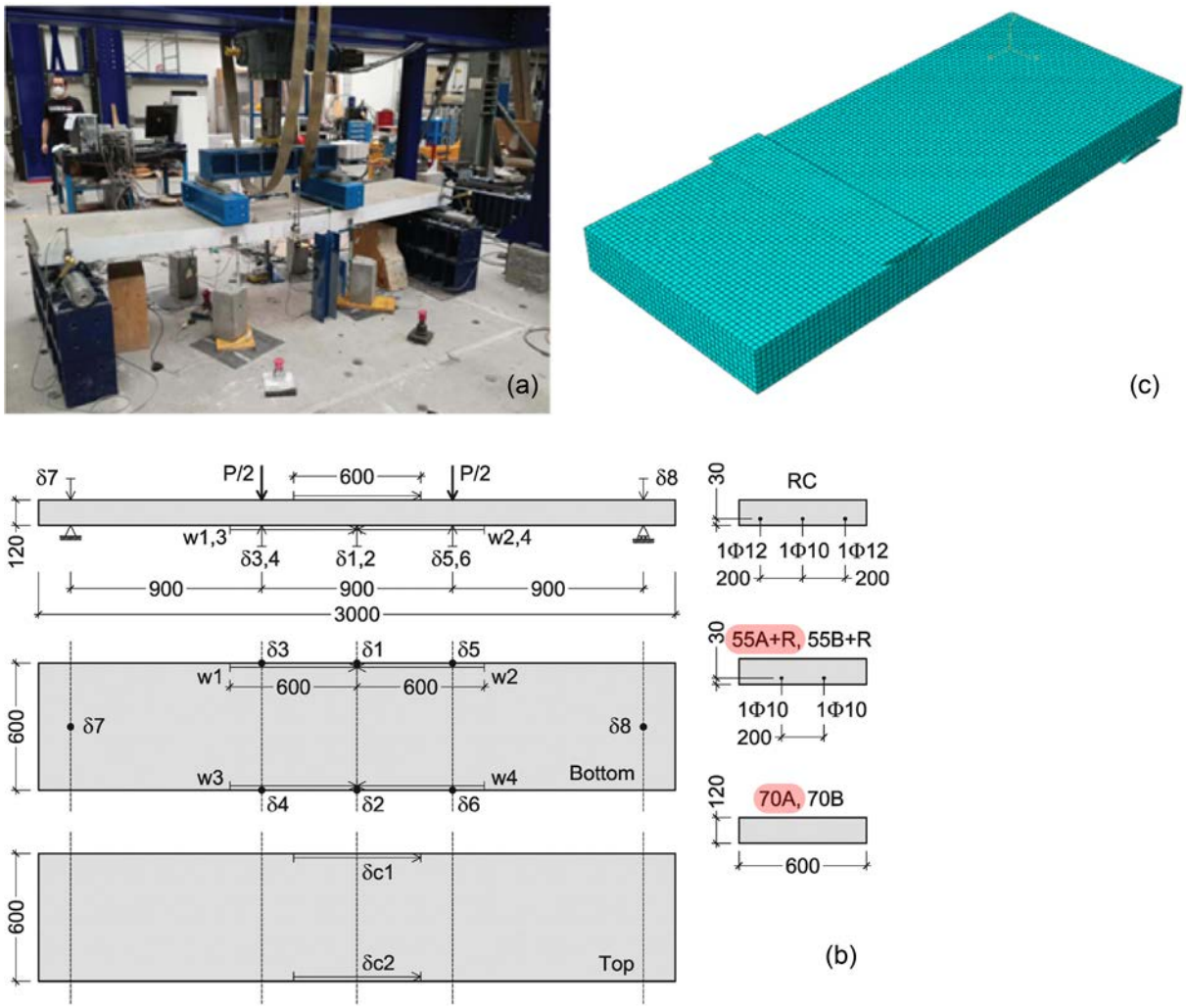


Figure 6: (a-b) Experimental set-up and instrumentation for bending tests on shallow beams (Colombo et al. 2023), and (c) corresponding mesh view of half of the beam.

Fig. 7 compares the numerical predictions with the experimental results for the beams 55A+R. The numerical model shows good agreement with two of the three experimental curves in terms of elastic response, peak load, and overall trend. One specimen (55A+R-1), however, exhibits a markedly different behaviour, deviating not only from the numerical results but also from the other two experimental responses. This discrepancy is also evident in the crack patterns (Fig. 8): specimen 55A+R-1 displays a less pronounced multiple-cracking pattern, resulting in a more brittle response. Such variability may be attributed to differences in fibre orientation and distribution, which can be significant even for specimens cast in the same plant, particularly at relatively low fibre volume fractions.

The numerical model accurately reproduces the crack pattern observed at a midspan deflection of 90 mm, further supporting its reliability. As shown in Fig. 8a, the tensile damage contours closely reflect the experimentally observed multiple-cracking pattern (Fig. 8b). Cracks initiate beneath the loading pin and propagate towards the midspan, with high damage concentrations both under the loading point and in the central region. These zones correspond to either wider cracks or clusters of closely spaced cracks, in agreement with the experimental observations.

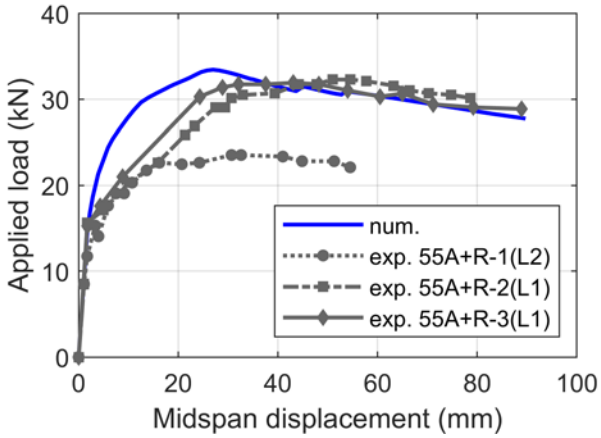


Figure 7: Comparison of numerical and experimental results for 55A+R bending tests on shallow beams (experimental data from Colombo et al. 2023).

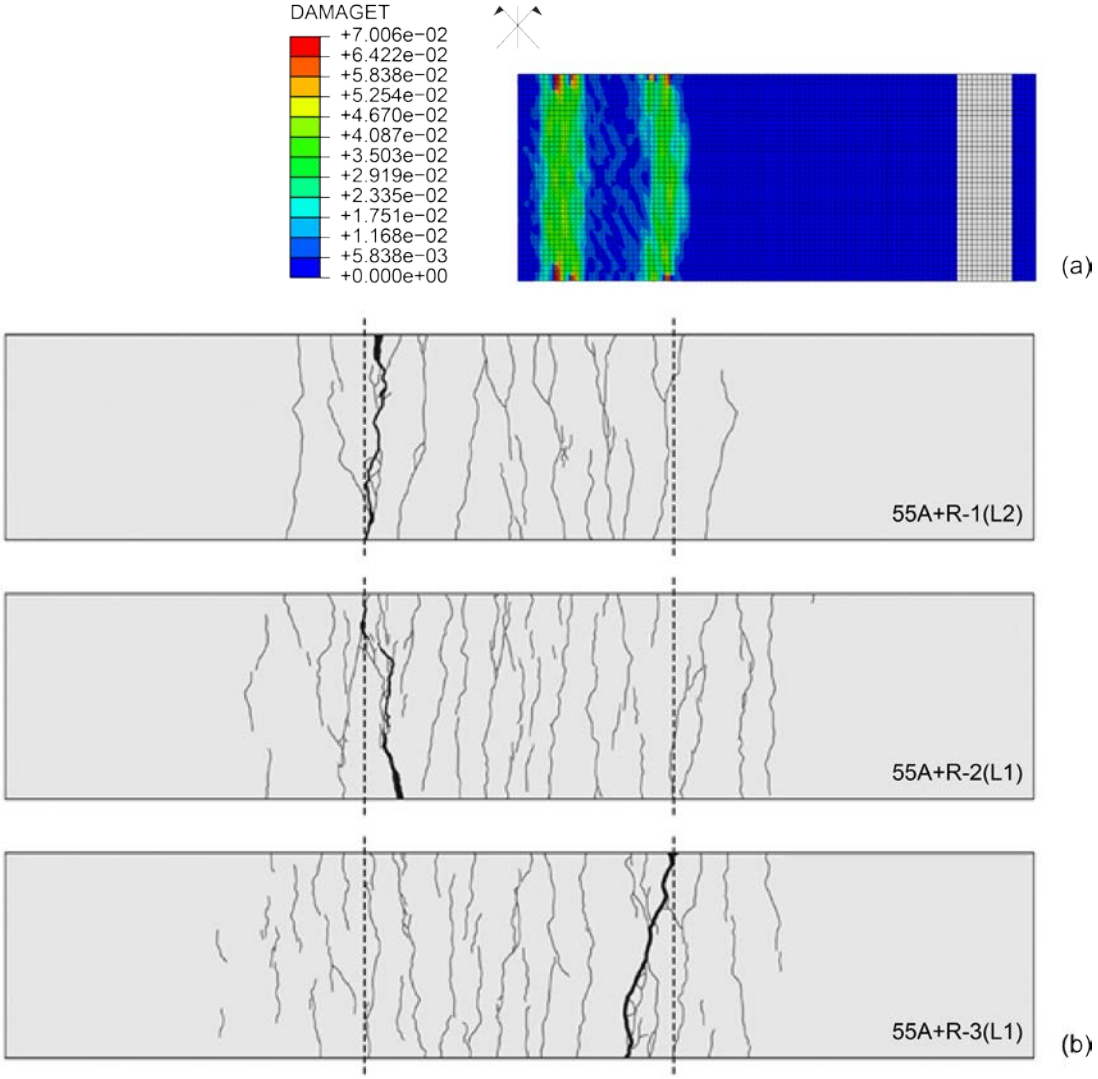


Figure 8: (a) Tensile damage in the numerical model and (b) corresponding crack patterns in 55A+R shallow beams (experimental data from Colombo et al. 2023).

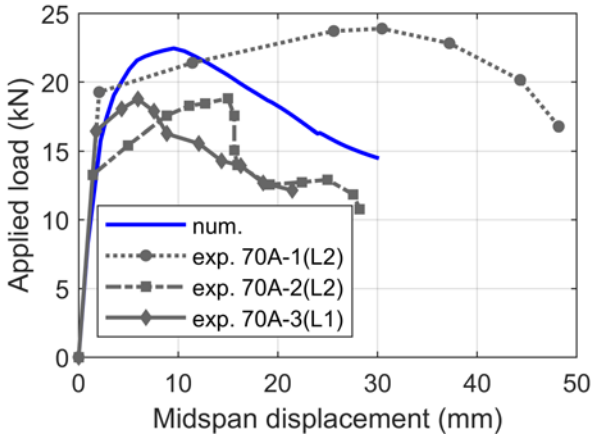


Figure 9: Comparison of numerical and experimental results for 70A bending tests on fibre-only shallow beams (experimental data from Colombo et al. 2023).

Fig. 9 presents the comparison between numerical and experimental results for the fibre-only beams 70A. In this configuration, the structural response is governed solely by the fibres, including their content, distribution, and orientation, leading to significant variability among the experimental specimens. Specimen 70A-1 exhibits a pronounced multiple-cracking pattern extending from the loading pin towards midspan, whereas the other two specimens show a more brittle response, with cracks localised closer to the loading point (crack patterns omitted here for brevity; see Colombo et al. 2023).

The numerical simulations display an intermediate behaviour, both in terms of load–midspan displacement response and crack development. As shown in Fig. 9, the model predicts an initial cracking load of approximately 15 kN, consistent with the experimental results, and a peak load of about 22 kN, lying between the experimental values. The post-peak response is characterised by a pull-out behaviour closer to that observed in specimens 70A-2 and 70A-3. Overall, these results indicate that the proposed modelling strategy can reliably capture both the global structural response and the underlying local damage mechanisms.

5 Conclusions

This study has investigated the performance of a Modified Damage Plasticity (MDP) model for the numerical simulation of steel fibre-reinforced concrete at both material and structural scales. The model, which explicitly incorporates fibre bridging through pull-out mechanisms, has been implemented and validated against experimental tensile and compressive tests, demonstrating its capability to capture the main resistance mechanisms governing the behaviour of SFRC. The application of the model to full-scale shallow beams, including beams reinforced with a combination of conventional steel bars and fibres and fibre-only beams, showed consistency between numerical and experimental results in terms of global load–displacement response and crack pattern development.

A key strength of the proposed approach lies in the consistent incorporation of fibre–matrix interaction and damage evolution within a unified constitutive framework. However, the current formulation is limited to straight and hooked-end fibres, and some input parameters still require calibration. A more comprehensive validation is therefore needed to fully assess the robustness and general applicability of the model, particularly through

notched beam tests covering a wide range of materials and mechanical properties. Future work will focus on extending the validation to notched beams and other structural typologies, such as slabs, using extensive experimental datasets available in the literature. If satisfactory performance is confirmed across a broader range of materials and configurations, the MDP model may represent a reliable tool for the pre-design and assessment of SFRC structures.

6 References

Amin, A., Foster, S. J., & Muttoni, A., 2015. "Derivation of the σ–w relationship for SFRC from prism bending tests", *Structural Concrete*, 16(1), pp93–105. doi: 10.1002/suco.201400018

Barros, J., Sanz, B., Kabele, P., Yu, R. C., Meschke, G., Planas, J., et al., 2021. "Blind competition on the numerical simulation of steel-fiber-reinforced concrete beams failing in shear", *Structural Concrete*, 22(2), pp939–967. doi: 10.1002/suco.202000345

Barros, J., Sanz, B., Filho, M., Figueiredo, F., Kabele, P., Yu, R. C., et al., 2023. "Blind competition on the numerical simulation of continuous shallow steel-fiber-reinforced concrete beams failing in bending", *Structural Concrete*, 24(3), pp3877–3907. doi: 10.1002/suco.202200754

Colombo, M., Conforti, A., di Prisco, M., Leporace-Guimil, B., Plizzari, G., & Zani, G., 2023. "The basis for ductility evaluation in SFRC structures in MC2020: An investigation on slabs and shallow beams", *Structural Concrete*, 24(4), pp4406–4423. doi: 10.1002/suco.202300114

Dassault Systèmes, 2024. Abaqus Analysis User's Manual, Version 2024, Dassault Systèmes.

European Committee for Standardization, 2023. Eurocode 2: Design of concrete structures – Part 1–1: General rules and rules for buildings, bridges and civil engineering structures, FprEN 1992–1–1:2023–04, CEN.

Lee, J., & Fenves, G. L., 1998. "Plastic-damage model for cyclic loading of concrete structures", *Journal of Engineering Mechanics*, 124(8), pp892–900. doi: 10.1061/(ASCE)0733-9399(1998)124:8(892)

Lubliner, J., Oliver, J., Oller, S., & Oñate, E., 1989. "A plastic-damage model for concrete", *International Journal of Solids and Structures*, 25(3), pp299–326. doi: 10.1016/0020-7683(89)90050-4

Martinelli, P., Colombo, M., Pujadas, P., et al., 2021. "Characterization tests for predicting the mechanical performance of SFRC floors: Identification of fibre distribution and orientation effects", *Materials and Structures*, 54, Article 3. doi: 10.1617/s11527-020-01593-7

Mudadu, A., Tiberti, G., Germano, F., Plizzari, G. A., & Morbi, A., 2018. "The effect of fiber orientation on the post-cracking behavior of steel fiber reinforced concrete under bending and uniaxial tensile tests", *Cement and Concrete Composites*, 93, pp274–288. doi: 10.1016/j.cemconcomp.2018.07.012

Niccolaini, S., 2025. "Validation and application of a modified plastic damage model for steel fibre reinforced concrete structures", Master's thesis, Politecnico di Milano.

Susetyo, J., 2009. "Fibre reinforcement for shrinkage crack control in prestressed, precast segmental bridges", Doctoral dissertation, University of Toronto.

Tran, T. T., Pham, T. M., Tran, D. T., Ha, N. S., & Hao, H., 2025. "Modified plastic damage model for steel fiber reinforced concrete", *Structural Concrete*, 26(1), pp13–42. doi: 10.1002/suco.202300640

Shear strength of SFRC hollow bricks without reinforcement: A Review and Preliminary Analysis

Kiran Dabral[1], Silvia Ientile[1], Jean-Claude Renaud[1], Saint-Ange Billo[1], Damien Suray-Faure[1], Philippe Robit[2], François Toutlemonde[1]

[1]: MAST Department, Université Gustave Eiffel, 77420 Champs-sur-Marne, France.

[2]: NGE Fondations, 38420 Domène, France.

Abstract

Diaphragm walls are critical structural elements used to retain earth pressures and ensure stability in underground constructions. Their construction often involves complex placement procedures, slow execution, and risks such as trench instability. This study proposes an alternative modular solution in the form of stackable hollow-core bricks made of steel fiber-reinforced concrete (SFRC) with no conventional longitudinal or transverse reinforcement. Although extensive research has examined the shear strength contribution of fibres in concrete elements, existing studies typically assess contribution of fibres only in the presence of steel reinforcement, thereby conflating the individual contributions of each. In contrast, very limited work has focused on the *pure* shear contribution of fibres in structural elements without steel reinforcement.

This paper investigates the shear capacity provided by concrete and fibres in a hollow-core brick intended for use in modular diaphragm wall construction. The respective contributions of the concrete matrix and the fibres are quantified using the methodologies of Model Code 2010, RILEM TC 162-DF, and other relevant guidelines. Analytical predictions are compared with lower bound of the experimental results obtained from a four-point bending test in which no shear cracking was observed. Using a 0.38 % volume fraction of hooked-end steel fibres, the study examines the shear performance of the proposed brick system. The findings provide insights into the contribution of fibres to shear resistance in the curved section of the brick without any reinforcement, an aspect that remains largely overlooked in prior literature. This study also supports the feasibility of the specific approach to diaphragm wall construction.

Keywords

Shear capacity, fibre contribution, concrete contribution, SFRC, design code, hollow-core slab, unreinforced concrete, web-shear cracking

1 Introduction

Concrete construction is under growing pressure to become more sustainable using less material, cutting carbon emissions, and building structures that last longer with minimal maintenance. Steel fibre-reinforced concrete (SFRC) has emerged as a practical response to these demands. By adding steel fibres to the concrete mix, engineers gain improved crack control, improved ductility, and better overall structural behaviour, all while reducing the need for repair and upkeep over the service life of the structure (Frazão et al, 2022). One application where SFRC shows particular promise is diaphragm walls, these are underground retaining walls used to hold back soil and create space for below-ground construction. Conventionally, these walls are built by excavating a trench supported by bentonite slurry, lowering in a reinforcement cage, and pouring concrete to displace the slurry, a process repeated in panels until a continuous wall is formed. This method is slow and technically demanding, and it carries well-known risks: trench collapse, cage misalignment, bentonite contamination, honeycombing, and poor concrete quality at joints (Abdelhadi et al, 1996). These problems are particularly severe in congested urban sites where space and time are limited (Lei et al, 2019).

The PREFO project, led by NGE Fondations, proposes replacing in-situ casting entirely with prefabricated hollow-core SFRC units, referred to here as "bricks", stacked inside the trench and post-tensioned together to form a continuous wall. Because the bricks are factory-made under controlled conditions, concrete quality and dimensional accuracy are consistent, removing the unpredictability inherent to conventional diaphragm wall construction and significantly reducing material waste. The proposed brick consists of a rigid assembly of hollow cylindrical units forming a 2.0 m long prefabricated block with curved top and bottom surfaces. When stacked and prestressed, the bricks behave as a monolithic structure. A small amount of hooked end steel fibers, 0.38 % by volume were added that provide post-cracking effective capacity and contribute to crack bridging and crack-width control.

The addition of steel fibres fundamentally changes how a concrete element responds to loading. Shear is of particular concern in plain concrete, because it is inherently brittle. Presence of fibres improve this behaviour by bridging cracks as they open, slowing their propagation and improving ductility (fib bulletin no. 105, 2022). This improvement is influenced by how fibres are distributed and oriented in the hardened concrete, which is a consequence of how the mix was designed and placed in the mould and how it flowed during casting (Casanova, 1996).

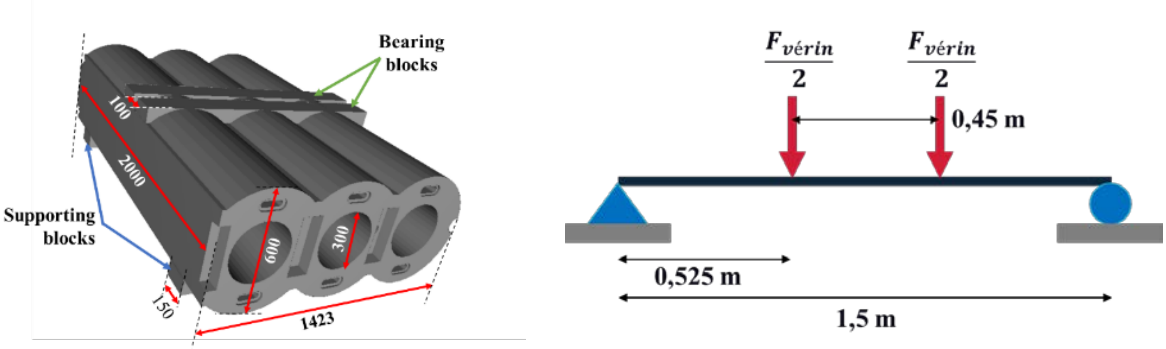
Beyond fibre behaviour, several geometric and material parameters govern the shear capacity of the brick. The cross-sectional height, the hollow versus solid geometry, and the shear-span to effective depth ratio (a/d) influence how shear forces are distributed and where failure initiates. At the material level, the fibre–matrix bond strength and the maximum aggregate size both affect how effectively shear is transferred across a cracked surface. Formwork surface also plays a role that is often overlooked: surface roughness reduces the rate of fluid shearing and thus the tendency of fibres to orient according the concrete flow direction (Švec et al, 2014). The wall effect diminishes with distance from the formwork, meaning the interior of the brick and its outer skin may behave differently under shear, a distinction that becomes significant in hollow-core geometries where wall thickness is limited. The local fibre arrangement at the exact location where a crack initiates and propagates governs the actual structural response, meaning a poorly oriented fibre contributes little to crack bridging regardless of the total fibre content of the concrete matrix (Alberti et al, 2018).

A fundamental limitation of current design codes including *fib* Model Code 2010, Eurocode 2, and ACI 318, is that their shear formulations are built on the assumption that longitudinal reinforcement is always present. The reinforcement ratio ρ appears explicitly or implicitly in nearly every shear capacity expression, meaning that when $\rho = 0$, the formulations either collapse to zero, produce physically meaningless results, or fall outside their stated range of applicability. For a system like the proposed brick, which contains no conventional longitudinal or transverse steel bars, it means that no established code provides a directly applicable design tool. The shear resistance must come entirely from the concrete matrix and the fibres. Sadeghian and Vecchio, 2018 reviewed the inherent complexity of shear assessment in reinforced concrete structures and traced the theoretical development of the Modified Compression Field Theory (MCFT) from its origins through its successive improvements.

This study puts forward a comparative analysis of shear strength estimates for precast SFRC hollow bricks without conventional reinforcement, evaluated using provisions from established structural design codes and other relevant literature. The calculated shear strengths derived from these formulations are compared with the lower bound of shear resistance, obtained from four-point bending tests. This analysis proposes a means of facilitating the structural characterization of the aforementioned SFRC bricks for the structural design of diaphragm walls.

2 Experimental program

A three-dimensional view of the brick geometry is shown in Fig. 1a. Each brick measures 2.0 m in length, 0.6 m in height and 1.42 m in width. The structural section consists of three hollow cylinders, each with an outer diameter of 600 mm and an inner diameter of 300 mm, resulting in a uniform wall thickness of 150 mm. The geometrical ratio of the second moment of inertia to the first moment area is $I/S = 360$mm. Because the brick presents curved contact surfaces, specially fabricated ultra-high-performance fiber-reinforced concrete (UHPFRC) supports with a mean compressive strength of 165 MPa were realized on the upper and lower curved faces to provide stable, planar interfaces for load application and supports. These auxiliary elements were aimed to ensure uniform stress transfer and prevent local crushing during loading. The loading specifications of the four-point bending test are shown in Fig. 1b, where $F_{vérin}$ is the central actuator load.



(a) (b)

Figure 1: (a) 3-D representation of the hollow cylindrical brick (all dimensions in mm), and (b) loading specifications of the 4-point bending test.

The SFRC mix composition consisted of 500 kg/m³ total binder content, 30 kg/m³ hooked-end steel fibers, with a maximum aggregate size of 11.2 mm and a water-to-binder ratio of 0.36. The resulting concrete had a specific gravity of 2543 kg/m³. The SFRC was classified as material strength class 6b, characterized by a residual flexural strength f_{R1} = 6.53 MPa at serviceability limit state and a ratio f_{R3}/f_{R1} = 0.729, where f_{R3} denotes the characteristic residual flexural strength at ultimate limit state (*fib* Model Code 2010). All mechanical properties were evaluated after eight months of curing to ensure the material achieved its long-term strength. Samples from the same production batch as the bricks were used to prepare cylindrical and prismatic specimens for material characterization. Three cylinders with a diameter 112 ± 1 mm and a height of 225 ± 1 mm were tested to determine compressive strength and Young's modulus, in accordance with NF EN 12390-3 and 12390-13, respectively. Six prisms with a length of 550 ± 1 mm and a cross-section of 150 mm ± 1 mm x 150 ± 1 mm were used for flexural tensile testing following NF EN 14651:2007. The bricks were cast using specially designed moulds that promote controlled, progressive placement of the self-compacted concrete along the width of the element, such that each cylinder of the brick was filled sequentially before filling up the next. The test specimens were cast simultaneously with the brick unit to ensure representative material properties. The resulting mechanical properties are summarized in Table 1.

Table 1: Material properties of the SFRC at 240 days of age.

$f_{c,cyl}$ (MPa)	f_{ck} (MPa)	E_{cm} (GPa)	ν	**Flexural strength** (MPa)				
				f_{LOP}	f_{R1}	f_{R2}	f_{R3}	f_{R4}
102.3 ± 2.0	96.6	45.6 ± 0.6	0.22 ± 0.01	5.9 ± 0.5	6.5 ± 1.2	6.0 ± 0.9	4.8 ± 0.8	3.8 ± 0.6

3 Shear capacity formulations from design codes

The general expression for design shear resistance adopted across all major design codes takes the form of a linear superposition of three independent contributions: the uncracked concrete matrix ($V_{Rd,c}$), the steel fibre bridging force ($V_{Rd,f}$), and conventional shear reinforcement ($V_{Rd,s}$). The design condition requires the total resistance to exceed the factored applied shear force V_{Ed}, Eq. 1. For the hollow-core SFRC brick under study, which incorporates no conventional longitudinal or transverse reinforcement, $V_{Rd,s} = 0$. The shear resistance is offered by $V_{Rd,c}$ and $V_{Rd,f}$. The following subsections review the treatment of these two terms in design codes, with particular attention to their applicability at the fully unreinforced condition $\rho = 0$. Table 2 presents the results calculated.

$$V_{Rd} = V_{Rd,c} + V_{Rd,f} + V_{Rd,s} \geq V_{Ed} \quad (1)$$

EN 1992-1-1:2004 and EN 1168:2012. EN 1992-1-1:2004 defines the shear resistance of prestressed members without shear reinforcement through a web-shear cracking criterion: the principal tensile stress at the centroidal axis reaches the design tensile strength of concrete. Section 6.2.2(1) of EN 1992-1-1:2004 gives the shear resistance zero, with a minimum value of the resistance. Applying Mohr's circle to the biaxial stress state at the centroid gives the concrete shear contribution, cf. Eq. 2, where b_w is the smallest width of the web at the centroid of the section, I is the second moment area about the centroidal axis and S is the first moment area above and about the centroidal axis, f_{ctd} is the design tensile strength of the concrete. For

a single PREFO brick, $\sigma_{cp} = 0$ since no axial loading or prestressing is applied then shear strength $V_{Rd,c}$ considers only the first term. Eurocode 2 provides no fibre contribution term.

$$V_{Rd,c} = \frac{I \cdot b_w}{S} \sqrt{{f_{ctd}}^2 + \alpha_1 \cdot \sigma_{cp} \cdot f_{ctd}} \quad (2)$$

EN 1168:2012 for precast prestressed hollow-core slabs, provides a simplified expression that introduces a cross-section reduction factor φ to account for the loss of effective web area in voided sections with $\varphi = 0{,}8$. The modified expression is given in Eq. 3a. For sections deeper than 450 mm, a further 10 % reduction is applied, yielding φ = 0.7, retaining 70 % of the solid-section capacity. For the present brick of total height 600 mm, Eq. 3b governs. *fib* Model Code 2010 adopts the same $\varphi = 0.80$ baseline for hollow-core geometry irrespective of void geometry and section height. Brunesi and Nascimbene (2015) proposed a mechanistically derived corrective coefficient $1/c_s$ that explicitly captures the void geometry through three dimensionless ratios and three constants. Their study was carried out on prestressed hollow core slab units with circular and non-circular voids using finite element simulations. Given in Eq. 3c, where b_1/r is the normalized horizontal web spacing, h_3/r measures the constant web width stretch along the depth and b_2/b_1 quantifies the suddenness of the web-width drop, and results in $c_s = 1{,}1$ for PREFO brick with the values of the constants $c_1 = 1{,}1$, $c_2 = 1$, $c_3 = 1{,}15$ (Brunesi and Nascimbene, 2015). This implies 36 % reduction in shear capacity calculation evaluated using EN 1168:2012 for PREFO brick.

$$V_{Rd,c} = \phi \frac{I \cdot b_w}{S} \sqrt{{f_{ctd}}^2 + \alpha_1 \cdot \sigma_{cp} \cdot f_{ctd}} \quad (3a)$$

$$V_{Rd,c} = 0{,}7 \frac{I \cdot b_w}{S} \cdot f_{ctd} \quad (3b)$$

$$c_s = c_1 \frac{b_1}{r} \cdot c_2 \frac{h_3}{r} \cdot c_1 \frac{b_2}{b_1} \quad (3c)$$

***fib* Model Code 2010.** In section 7.7.3.2, MC 2010 presents the most complete code-level treatment of SFRC shear, and explicitly incorporates a fibre contribution term $V_{Rd,f}$ derived from standardised material characterisation rather than empirical global factors. The concrete contribution $V_{Rd,c}$ follows the same principal-stress criterion as EC2, with the $\varphi = 0{,}8$ hollow-core reduction applied identically. To evaluate $V_{Rd,f}$, MC 2010 gives Eq. 4b, which is sensitive to k_v and is obtained considering the level of strain at section mid-depth and is related to the longitudinal reinforcement. In beams with $\rho = 0$ the limit of the principal tensile stress to be considered is given as lesser than f_{Ftu}/γ_f. The fibre contribution is derived from the residual post-cracking tensile strength at the ultimate limit state, f_{Ftu}, which is obtained using Eq. 4a. $V_{Rd,f}$ can be evaluated using Eq. 4b with $f_{Ftu} = 1{,}59$ MPa and $\gamma_c = 1{,}5$, but it considers the parameter k_v. The formulation for minimum shear strength brought by fibres is shown in Eq. 4c, where k factor considers the size effect, and is $k = 1 + \sqrt{200/d} \leq 2{,}0$, where d is the depth of the section.

$$f_{Ftu} = \frac{f_{R3}}{3} \quad (4a)$$

$$V_{Rd,f} = \frac{1}{\gamma_f} \cdot (k_v \cdot \sqrt{f_{ck}} + k_f \cdot f_{Ftuk} \cdot \cot\theta)\, b_w \cdot z \quad (4b)$$

$$V_{Rd,fmin} = V_{min} \cdot b_w \cdot z \; ; V_{min} = 0.035 \cdot \sqrt{f_{ck}} \cdot k^{1.5} \quad (4c)$$

RILEM TC 162-TDF (2003). This recommendation provides design equations for SFRC valid for concrete up to compressive class C50/60. The concrete contribution $V_{Rd,c}$ follows the EN 1992-1-1 functional form, retaining the longitudinal reinforcement ratio ρ as an explicit parameter. At $\rho = 0$ with no prestressing, $V_{Rd,c}$ vanishes. The more relevant term for the present study is $V_{Rd,f}$, which accounts for the fibre contribution in flanged sections and remains non-zero at $\rho = 0$, given in Eq. 5:

$$V_{Rd,f} = k_f \cdot k_1 \cdot \tau_{fd} \cdot b_w \cdot d \; ; \tau_{fd} = 0{,}12 \cdot f_{eqk,3} \tag{5}$$

where,

$k_f = 1{,}5; k_1 = 1; \tau_{fd} = 0{,}72\ MPa;\ b_w = 150\ mm;\ d = 600\ mm; n = 2; f_{eqk,3} =$ 6 MPa.

ACI 318-14. The code differentiates two independent cracking mechanisms for prestressed members without shear reinforcement: flexure-shear cracking (V_{ci}), initiated when an existing flexural crack becomes inclined under combined shear and moment, and web-shear cracking (V_{cw}), initiated by diagonal tension at the centroidal axis prior to flexural cracking. The design capacity is taken as the lesser of the two. The lower limit of the shear capacity offered by SFRC can be evaluated using Eq. 6a. For the unreinforced, non-prestressed condition ($\rho = 0$, $\sigma_{cp} = 0$) in ACI 318-14 (SI units), Eq. 6a, 6b are given, where b_w is the web width, f_c is in MPa, and $d \geq 0{,}8h$ (h is the height of the section) for circular sections.

$$V_{ci} = 0.17 \cdot \sqrt{f_c} \cdot b_w \cdot d \quad \text{MPa} \tag{6a}$$

$$V_{cw} = 0.29 \cdot \sqrt{f_c} \cdot b_w \cdot d \quad \text{MPa} \tag{6b}$$

AS 3600-2009. This Australian code treats shear in prestressed members without shear reinforcement by distinguishing the same two cracking modes as ACI 318. The maximum crushing limit for any shear design is given by Eq. 7a. The flexure-shear and web-shear cracking capacities are evaluated by Eq. 7b and 7c.

$$V_{u,max} = 0.2 \cdot f_c \cdot b_w \cdot d \tag{7a}$$

$$V_{uc} = \beta_1 \cdot \beta_2 \cdot \beta_3 \cdot b_v \cdot d_0 \cdot f_{cv} \cdot \left[\frac{A_{st}+A_{pt}}{b_v \cdot d_0}\right]^{1/3} + V_0 + P_v \tag{7b}$$

$$V_{uc} = V_t + P_v \qquad V_t = \frac{b_w \cdot I}{Q} \cdot f_{ct}{}' \tag{7c}$$

For the PREFO brick, $V_{uc} = 0$ for $\beta_1 = 1.1$, $\beta_2 = 1$, $\beta_3 = 1{,}0$, $d_0 = 600\ mm$, $A_{st} = 0$, $A_{pt} = 0$, $V_0 = 0, P_v = 0$. Only the web-shear formulation (Eq. 7c) V_t remains valid and is numerically equivalent to the EN 1992 principal-stress criterion (Eq. 2) for $\sigma_{cp} = 0$.

Yang's Method (1994). Yang (1994) proposed a modification to the standard web-shear cracking criterion by relocating the critical stress evaluation point from the centroidal axis to a geometry-dependent position along a line projected from the support centre at $\beta = 35°$ to the bottom face of the hollow-core slab. For sections with circular voids, this critical point coincides with the centroid, and Yang's formulation reduces identically to Eq. (2). For the PREFO brick at $\rho = 0, z_{cp} = 0, N_p = 0$, the capacity reduces exactly to the EN 1992 expression. Yang's principal contribution is therefore the identification of a more conservative critical evaluation

point for non-standard void geometries; for the standard circular-void geometry considered here, no numerical distinction arises.

NF P18-710:2016. These design guidelines were developed for ultra-high-performance fibre-reinforced concrete (UHPFRC) with f_{ck} in the range 150 to 250 MPa, following AFGC recommendations, 2013. Their relevance to the present study lies not in the compressive strength regime but in the mechanical rigour with which the fibre contribution $V_{Rd,f}$ is formulated, an approach transferable to SFRC at $\rho = 0$. The elastic tensile strength $f_{ct,el}$ is derived from four-point bending tests with a depth-dependent correction, shown in Eq. 8a. The shear capacity is equal to the smaller of the $V_{Rd,max}$ and V_{Rd} (the total shear strength considering the contribution term of concrete and fibres). The maximum strut capacity $V_{Rd,max}$ is given in Eq. 8b, where $\alpha_{cc} = 0{,}85$, $\gamma_c = 1{,}3$, $\theta = 30°$, $z = 0{,}7875h$.

$$f_{ct,el} = f_{ct,fl}\frac{\alpha_{fl}.a^{0.7}}{1+\alpha_{fl}.a^{0.7}}, \text{ where } \alpha_{fl} = 0.08 \text{ and } a \text{ is the prism depth in mm} \quad (8a)$$

$$V_{Rd,max} = 2{,}3 \cdot \frac{\alpha_{cc}}{\gamma_c} \cdot b_w \cdot z \cdot (f_{ck})^{2/3} \cdot (tan\theta) \quad (8b)$$

For the non-prestressed, non-reinforced section, the concrete term can be evaluated using Eq. 8c, where $\gamma_c \cdot \gamma_E = 1{,}5$, accounts for the uncertainty in extrapolating the formula calibrated for $f_{ck} \geq 90$ MPa to different strength concrete, and $k = 1$ for $\sigma_{cp} = 0$. In the case of circular sections, $b_w = 0{,}55 \cdot \phi$, giving 660 mm as the total web width of the brick.

$$V_{Rd,c} = \frac{0{,}21}{\gamma_c \cdot \gamma_E} \cdot k \cdot (f_{ck})^{1/2} \cdot b_w \cdot 0{,}875h \quad (8c)$$

The fibre contribution is evaluated from Eq. 8d and 8e, where $A_{fv} = b_w \cdot z$ is the area of a T-section where $z = 0{,}9 \cdot h$; $\sigma_{Rd,f}$ is the fibre bridging stress as a function of crack width derived from the material constitutive law; $\theta \geq 30°$ is the angle of the principal compressive stress to the beam axis, and $K = 1{,}25$ is a fibre orientation efficiency factor, $\gamma_{cf} = 1{,}3$. The code integrates the actual pull-out constitutive response rather than using a single characteristic value, making it the most physically rigorous treatment of $V_{Rd,f}$ reviewed. The calculated values for $V_{Rd,max}$ and $V_{Rd,f}$ are significantly higher than those predicted using other codes in this analysis.

$$V_{Rd,f} = \frac{A_{fv} \cdot \sigma_{Rd,f}}{\tan\theta} \quad (8d)$$

$$\sigma_{Rd,f} = \frac{1}{K \cdot \gamma_c} \cdot \frac{1}{w_{lim}} \cdot \int_0^{w_{lim}} \sigma_f(w) \cdot dw \,, where\ w_{lim} = max(w_u, w_{max}) \quad (8e)$$

The findings of Tawadrous and Morcous, 2018 evaluated predictions from ACI 318-14, *fib* MC2010, AS 3600-2009 and EN 1168-2005 and other standards against experimental hollow-core shear data, fib MC 2010 provided the best agreement with test results, while ACI 318 and EN 1168 yielded the least conservative web-shear predictions.

All the design formulations given above share a common principle: web-shear cracking is governed by the principal tensile stress at a critical location in the web reaching the tensile strength. This is expressed as $V_{Rd,c}$, a product of geometric section property and a material tensile strength measure. The differences between the codes are not differences in principles but of implementation, especially in how each code handles the hollow-core geometry, the

location of the critical point in in the section, the definition of effective depth and the fourth fundamental assumption of inclusion of longitudinal reinforcement.

Table 2: Calculated results using design guidelines with b_w = 494 mm

Guideline	**Shear capacity**		
	$V_{Rd,c}$ (kN)	$V_{Rd,f}$ (kN)	
EN 1992:2004	425,61	-	f_{ctd} = 2,39 MPa, Min strength = 201,97 kN
MC 2010	340,5	201,9	$\phi = 0{,}8$; min. fibre contribution
RILEM TC 162-TDF	-	320,1	fibre contribution
EN 1168:2012	297,9	-	$\phi = 0{,}8$ for hollow-core slabs
NF P18-710 2016	476,0	1662,5	$V_{Rd,max}$ = 4875,9 kN
ACI 318-14	495,3	-	V_{ci} = 495,26 kN and V_{cw} = 844,86 kN
AS 3600-2009	425,61	-	f_{ctd} = 2,39 MPa
Brunesi and Nascimbene,2015	270	-	$c_s = 1{,}1$
Yang,1994	425,6	-	f_{ctd} = 2,39 MPa

4 Parameters influencing shear strength

The parameters that influence the shear strength in plain concrete and SFRC with $\rho = 0$ are detailed in Table 3. In a reinforced concrete member, shear capacity depends on a combination of the concrete matrix strength, dowel action of steel rebars, tension-stiffening between the cracks, and the presence of transverse rebars. With $\rho = 0$, all mechanisms related to the reinforcing bars are eliminated, and resistance mechanisms from concrete and fibres remain such as the strength of the compression zone above the critical diagonal crack, aggregate interlocking and fibre bridging in SFRC elements.

Concrete compressive strength has a significant influence on the web-shear strength of deep hollow-core slabs (Tawadrous and Marcous, 2018). It influences first, the tensile strength of concrete; second the depth of the compression zone block, with increase in f_{ck}, the block above neutral axis becomes shallower and more stress-intensive; third, the aggregate interlock efficiency, higher paste quality means stronger interlock contact where cracks propagate through aggregates rather than around them. At $\rho = 0$, the shear capacity before cracking depends on the tensile capacity of the concrete cross-section. For SFRC elements, fibres may not change the cracking load significantly but control the post-cracking response. Through aggregate interlocking mechanism, the shear is transferred in concrete matrix through friction and mechanical engagement between aggregate particles and the crack faces. Larger aggregates enable higher shear stress transfer at the same crack width opening due to rougher crack surface with deeper mechanical interlocking (Walraven, 1981). This mechanism is taken into consideration in Model Code 2010 by using $K_{dg} = 32/(16 + d_g)$, where d_g is the nominal size of the aggregates used in the concrete mix design, in PREFO brick it is taken as zero since the concrete strength exceeds 70 MPa. This shows that aggregate size is particularly important in smaller sized aggregate mixes, which are common in SFRC matrices because fine aggregates improve concrete mix workability and may improve fibre distribution.

In SFRC structures, the post-cracking response is defined by the residual flexural strengths f_{R1} and f_{R3}, corresponding to the cmod = 0,5 mm and 2,5 mm, obtained from a notched beam bending test. Vandewalle, 2000 provides the formulation for the increase in shear strength due to steel fibres, relating it to the post-cracking response of the SFRC (see Table 3, row 4).

Fibre volume fraction governs the number of fibres intersecting the area of the crack plane, which in turn controls the bridging force available to resist crack opening and sliding. Each fibre at the crack location contributes a pull-out force that depends on its bond characteristics, embedded length and fibre characteristics. For a fixed fibre content, fibre aspect ratio (l_f/d_f) is an important geometric fibre parameter governing a) the number of fibres crossing a unit crack area (longer fibres are more probable to span a crack), and b) the pull-out resistance per fibre (longer fibres have larger embedded length and therefore higher pull-out force depending on their full anchoring and tensile capacity). The hook at the fibre end provides mechanical anchorage that increase the effective bond by approximately 40-60 percent relative to straight fibres of the same dimensions. In shear, it is the energy absorbed during pull-out that provides post-cracking toughness and crack sliding resistance. The fibre orientation relative to the crack plane governs how efficiently the aspect ratio is utilized (Bayard, 2003, Vu et al, 2024). Fibres perpendicular to the crack are most efficient and fibres parallel to the crack contribute negligible to the shear resistance regardless of their aspect ratio. Fibre factor is defined as a product of fibre volume, aspect ratio and bond efficiency as the linearly governing SFRC shear parameter (Narayanan and Darwish, 1987). In practice, fibre orientation in cast concrete members is never isotropic and is modified by a) the wall effect, b) flow effect, c) vibration and settling. In the PREFO brick, there are multiple curved surfaces and voids, the thickness of web varies and that influences the orientation of the 30 mm length fibres. The orientation factor was reported to vary from approximately 0,4 (near formwork, 2D orientation) to 0,55 (interior, approaching isotropic) for self-compacting SFRC in flat elements (Švec et al, 2014).

Table 3. Summary of parameters influencing shear strength capacity (V) calculations

Parameters	**Influence on shear capacity**
Concrete compressive strength (f_c)	Governs cracking onset, and after that fibres take part. At $\rho = 0$, f_c is the sole matrix resistance parameter. $f_c \uparrow \Rightarrow V \uparrow$
Aggregate size (d_g)	Governs interlocking effectiveness at $\rho = 0$. Effect reverses in high strength concrete where cracks bisect aggregates. $d_g \uparrow \Rightarrow V \uparrow$
Residual flexural strength (f_{R1} & f_{R3})	Governs post-cracking strength at cmod = 0,5 mm and 2,5 mm in SFRC. $f_R \uparrow \Rightarrow V \uparrow$
Shear span to depth ratio (a/d)	Selects failure mode. $a/d \uparrow \Rightarrow V \downarrow$
Cross-section shape and void geometry	The ratio I/S governs the web-shear stress at the critical level. Shear strength reduced by $\varphi = 0{,}7$ for hollow core slabs with $h \geq 450$ mm. $void\ area \uparrow \Rightarrow V \downarrow$
Member depth (size effect)	EN1992 raises the depth factor to the power 1,5 for minimum shear strength. Steel fibres suppress this effect by arresting the cracks. $d \uparrow \Rightarrow V \downarrow$
Member width (b_w)	Varies linearly and is the sum of all web widths in an element. $b_w \uparrow \Rightarrow V \uparrow$
Fibre volume fraction (V_f)	Governs number of fibres crossing unit crack area. $V_f \uparrow \Rightarrow V \uparrow$

Fiber aspect ratio (l_f /d_f)	Combined $V_f \cdot l_f/d_f$ governs the bridging probability and pull-out resistance. $l_f/d_f \uparrow \Rightarrow V \uparrow$
Fiber orientation (η_0)	Governs the efficiency of fibres in bridging a crack and depends on fibre axis angle and crack plane normal. $\eta_0 \uparrow \Rightarrow V \uparrow$

The cross-sectional geometry of the structural element governs the shear capacity through two mechanisms: a) the shear stress distribution within the cross-section, (b) the net web area available to carry shear. For a solid rectangular section, shear stress at the neutral axis is $1{,}5\, V/b \cdot h$. For a hollow-core slab such as PREFO brick, the shear stress at any level depends on the first moment area *Q* above that level relative to the full web width *b* at that level, and it is maximum at the centre of the web with width 150 mm in the PREFO brick. The ratio of void area to the total cross-section directly reduces the effective shear resisting web area, and thus the shear capacity of the section

The quality of hardened SFRC is inherently sensitive to production variables. Beyond material composition, fabrication practices including compaction method, formwork geometry, surface finish, and material, exert a direct influence on fibre orientation and spatial distribution in the hardened matrix (Švec et al, 2014).

5 Experimental result from brick PREFO

The three bricks tested sustained an average applied load of 508 ± 25 kN before failing by a single flexural crack in the pure bending zone. The absence of any diagonal web-shear crack throughout the loading history indicates that the actual shear capacity of the brick exceeds 508 kN. Predictions based on *fib* Model Code 2010 and NF P 18-710 which includes the contribution of fibres overestimate the shear strength in the case of SFRC section with low content of fibres; whereas predictions based on only concrete contribution underestimate the shear strength which are based on the assumption that conventional reinforcement is present in the section. Additional experimental results especially achieved from shear failures are required to validate the predicted contributions.

6 Conclusions

This paper has presented a systematic review of eight literature references of codes and research studies for the evaluation of shear capacity in SFRC members without conventional longitudinal or transverse reinforcement, with direct application to a hollow-core SFRC brick system. The following conclusions are drawn:

1. All reviewed codes converge on the same physical principle: web-shear cracking is governed by the attainment of the principal concrete tensile strength at a critical section in the web.
2. The assumption that longitudinal reinforcement is present is embedded, explicitly or implicitly, in the expressions of EN 1992-1-1, RILEM TC 162-TDF and ACI 318. At $\rho = 0$, these formulations either collapse to a conservative minimum value or reduce to zero.
3. EN 1168:2012 is the most directly applicable code for the hollow-core SFRC brick reducing the shear strength by 30 percent. Its depth-dependent reduction factor for section height higher than 450 mm explicitly addresses the loss of net shear area on

hollow deep sections. The geometric shape coefficient $1/c_s$ provides a more detailed correction factor as a function of the shape of voids and the suddenness in the drop in the width of the section.

4. *fib* Model Code 2010 provides the most complete design framework for SFRC providing explicit formulations for $V_{Rd,c}$ and $V_{Rd,f}$ considering the post-cracking behaviour of SFRC.
5. NF P18-710 provides the most physically rigorous fibre contribution formulation integrating the full fibre bridging stress-crack width constitutive law.
6. The compression strut angle θ, relevant to the variable-angle truss formulations (AFGC, fib MC2010), ranges from 30° (AFGC minimum for UHPFRC) to 45° (fully plastic truss).

Acknowledgements

The authors gratefully acknowledge the financial support provided by Bpi France for the PREFO Project with the reference number DOS0199149 and the collaborative contributions of all project partners, including NGE Fondations and Université Gustave Eiffel. They also want to thank the support of MAST-EMGCU technical staff, especially Aurélie Chan Yong, Renaud-Pierre Martin, Benjamin Terrade and Laura Kerner.

References

Abdelhadi, N., Abdelhadi, M., and Gotoh, K., 1996. "Problems encountered in diaphragm wall excavation", *Nagasaki University Faculty of Engineering Research Reports*, 26(46), pp. 39–42.

ACI Committee 318, 2014. *Building Code Requirements for Structural Concrete (ACI 318-14) and Commentary (ACI 318R-14)*, American Concrete Institute, Farmington Hills, MI.

AFGC, 2013. *Ultra High Performance Fibre-Reinforced Concretes: Recommendations, Association Française de Génie Civil*, Paris, France.

Alberti, M. G., Enfedaque, A., and Gálvez, J. C., 2018. "A review on the assessment and prediction of the orientation and distribution of fibres for concrete", *Composites Part B: Engineering*, 151, pp. 274–290.

AS 3600, 2009. *Concrete Structures*, Standards Australia International Ltd., Sydney, Australia, 198 pp.

Bayard, O., 2003. "Approche multi-échelles du comportement mécanique des bétons à ultra hautes performances renforcés par des fibres courtes", PhD thesis, Cachan, Ecole normale supérieure.

Brunesi, E., and Nascimbene, R., 2015. "Numerical web-shear strength assessment of precast prestressed hollow core slab units", *Engineering Structures*, 102, pp. 13–30. doi: 10.1016/j.engstruct.2015.08.013

Casanova, P., 1996. "Bétons renforcés de fibres métalliques : du matériau à la structure. Études et recherches des Laboratoires des Ponts et Chaussées, Série Ouvrages d'art, Rapport OA 20. Paris, France : Laboratoire Central des Ponts et Chaussées (LCPC). ISBN : 2-7208-2490-3.

EN 1168, 2005. Precast Concrete Products — Hollow Core Slabs, European Committee for Standardization, Brussels, Belgium, 84 pp.

Eurocode 2, 2004. Design of Concrete Structures, EN 1992-1-1:2004, European Committee for Standardisation, Brussels, Belgium.

fib, 2012. *Model Code 2010*, Bulletins 65 and 66, Fédération Internationale du Béton, Lausanne, Switzerland.

fib, 2022. *Fibre Reinforced Concrete*, State-of-the-Art report. Fib bulletin No. 105. Lausanne, Switzerland. doi.org/10.35789/fib.BULL.0105

Frazão, C., Barros, J., Camões, A., and Ferreira, L., 2022. "Technical and environmental potentialities of recycled steel fibre reinforced concrete for structural applications", *Journal of Building Engineering*, 45, 103579. doi: 10.1016/j.jobe.2021.103579

Lei, M., Liu, Linghui., Lin, Yuexiang., Shi, Chenghua., Yang, Weichao., Cao, Chengyong., Liu, Yao., 2019. "Research progress on stability of slurry wall trench of underground diaphragm wall and design method of slurry unit weight", *Advances in Civil Engineering*, Article 3965374. doi: 10.1155/2019/3965374

Narayanan, R., and Darwish, I. Y. S., 1987. "Use of steel fibres as shear reinforcement", *ACI Structural Journal*, 84(3), pp. 216–227.

NF EN 12390-3, 2019. Testing Hardened Concrete — Part 3: Compressive Strength of Test Specimens, AFNOR, Paris, France.

NF EN 12390-13, 2021. Testing Hardened Concrete — Part 13: Determination of Secant Modulus of Elasticity in Compression, AFNOR, Paris, France.

NF EN 14651+A1, 2007. Test Method for Metallic Fibre Concrete — Measuring the Flexural Tensile Strength (Limit of Proportionality (LOP), Residual), AFNOR, Paris, France.

NF P18-710, 2016. National Addition to Eurocode 2 – Design of Concrete Structures: specific rules for Ultra-High Performance Fibre-reinforced Concrete (UHPFRC), AFNOR, Paris, France

Sadeghian, V., and Vecchio, F. J., 2018. "The modified compression field theory: then and now", *ACI Special Publication*, SP-328, *American Concrete Institute*, Farmington Hills, MI. doi: 10.14359/51711147

Švec, O., Žirgulis, G., Bolander, J. E., and Stang, H., 2014. "Influence of formwork surface on the orientation of steel fibres within self-compacting concrete and on the mechanical properties of cast structural elements", *Cement and Concrete Composites*, 50, pp. 60–72. doi: 10.1016/j.cemconcomp.2013.12.002

Tawadrous, R., and Morcous, G., 2018. "Shear strength of deep hollow-core slabs", *ACI Structural Journal*, 115(53), pp. 699–709.

Vandewalle, L., 2000. "RILEM TC 162-TDF: Test and design methods for steel fibre reinforced concrete," *Materials and Structures*, 33(195), pp. 75–81.

Vu, D. T., Terrade, B., Marchand, P., Bouteille, S., & Toutlemonde, F. (2024). "Constitutive model for steel fiber reinforced concrete under shear and tension accounting for fiber orientation effect", *European Journal of Environmental and Civil Engineering*,28(3), 547–572. https://doi.org/10.1080/19648189.2023.2219309

Walraven, J. C., 1981. "Fundamental analysis of aggregate interlock", *Journal of the Structural Division*, ASCE, 107(ST11), pp. 2245–2270.

Yang, L., 1994. "Design of prestressed hollow-core slabs with reference to web shear failure", *Journal of Structural Engineering*, ASCE, 120(9), pp. 2675–2696. doi: 10.1061/(ASCE)0733-9445(1994)120:9(2675)

Świnoujście, the largest Steel Fibre Reinforced Concrete diameter road tunnel in Europe

Bruno Rossi[1], Sébastien Wolf[1]

[1]: ArcelorMittal Fibres, Route de Finsterthal, L-7769 Bissen, G.D. of Luxembourg

Abstract

The Polish city of Świnoujście extends over the eastern part of the island of Uznam as well as over the islands of Wolin and Karsibór. A major new road tunnel was required beneath the Świna river to address the growing issue of traffic congestion between the islands. Prior to completion of the tunnel, traffic had relied on ferry connections. The design and construction of the two-way road tunnel at Świnoujście, beneath the Świna river, required high levels of flexibility and expertise to ensure the development and implementation of a workable solution for each section of the tunnel route. Geological conditions along the 1.48 km route were highly variable with the most demanding section below Świna Strait. In this section the blow-up pressure, that governs the upper threshold, was very low due to the low overburden (minimum 10m) while the stability pressure was high because this was the deepest section of the tunnel. Such conditions demanded greater attention during the Tunnel Boring Machine (TBM) operation and the design specification for the steel fibre reinforced concrete (SFRC) tunnel lining segments. The Świnoujście tunnel was constructed within the agreed contractual milestones using a large diameter Slurry TBM passing below the Świna Strait. The tunnel length is 1.48 km with an excavation diameter of 13.46 m with no major settlement issues or problems. 1,325 tons of HE++ 90/60 steel fibres were used in the reinforcement of the 500 mm thick tunnel lining segments that were manufactured for this key Polish infrastructure project. With an inner diameter of 12 m, the Świnoujście two-way road tunnel is the largest inner diameter tunnel in Europe to date that is reinforced with steel fibres only. This major infrastructure project provides a direct connection between Uznam and Wolin, beneath the Świna river, cutting the journey time to just a few minutes and significantly improving connections to and from homes, places of work and popular holiday destinations in West Pomerania.

Keywords

Steel Fibre Reinforced Concrete (SFRC), bending-hardening behavior, residual flexural strength, ultra-high tensile strength, ductility, tunnel lining segments.

1 Introduction

The Polish city of Świnoujście extends over the eastern part of the island of Uznam as well as over the islands of Wolin and Karsibór. A major new road tunnel was required beneath the Świna river to address the growing issue of traffic congestion between the islands. Prior to completion of the tunnel, traffic had relied on ferry connections. The two-way road tunnel at Świnoujście, beneath the Świna river, required high levels of flexibility and expertise to ensure the development and implementation of a workable solution for each section of the tunnel route. Geological conditions along the 1.48 km route were highly variable with the most demanding section below Świna Strait. In this section the blow-up pressure, that governs the upper threshold, was very low due to the low overburden (minimum 10 m) while the stability pressure was high because this was the deepest section of the tunnel. Such conditions demanded greater attention during TBM operation and the design specification for the SFRC tunnel lining segments. The Świnoujście tunnel was constructed within the agreed contractual milestones using a large diameter Slurry TBM passing below the Świna Strait. The 13.46 m diameter TBM has excavated the tunnel with no major settlement issues or problems (Figure 1). This major infrastructure cuts the journey time to just a few minutes and significantly improves connections to and from homes, places of work and popular holiday destinations in West Pomerania.



Figure 1: Internal view of the Tunnel during the TBM advancement.

2 Project overview

The total length of access roads is 3.4 km, while the tunnel itself is long 1.780 km. It was constructed using the TBM drilling disc technology - 1.484 km and the sub-ceiling method - 0.295 km (Table 1). The Client is the Swinoujście Municipality, located in the northern side of Poland. Porr & Gülermak were the two companies associated in a Joint Venture which has been awarded the construction of the tunnel. In charge of the design was SWS Engineering, while SFRC producer was Cemex.

Table 1: Tunnel lining data

Description	**Dimensions (meters)**
Tunnel Length	1500.00
Segment thickness	0.50
Inner diameter	12.00
Segment width	2.00
TBM diameter	13.46
Ring segmentation	8+0

A total of 784 rings (6272 segments) were installed in the tunnel. The average advance rate was 7 to 8 rings per day with a maximum of 9 rings per day (Figure 2).

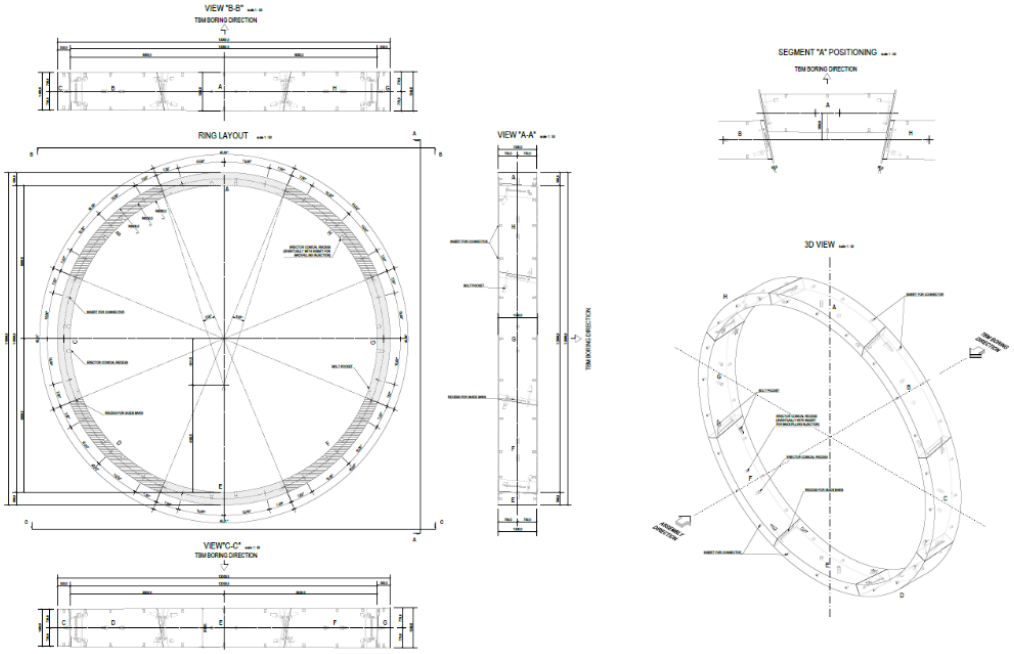


Figure 2: Segment geometry

3 Steel Fibre Reinforced Concrete recipe

After an initial phase of experimentation, a suitable recipe (Table 2) was defined to achieve the performance required by the designer (f_{R1k} > 5.0 MPa, f_{R3k} > 5.5 MPa) (Figure 3).

Table 2: Recipe

Description	**Kg / m^3**
Sand 0/2	685
Crushed gravel 2/8	325
Crushed gravel 8/16	720
Water	165
CEM III/A 42.5 R-NA	450
Steel Fibres HE++ 90/60, tensile strength 1900 MPa	43
Polypropylene length 6 mm, diameter 18 μm	2.0
Plasticizer	4.5



Figure 3: SFRC beams casting

Both types of fibres are dosed with feeders provided by the manufacturers onto the belt feeding the aggregate to the mixer. Overall, 29,000 m^3 of SFRC have been produced for the entire project, for a steel fibre consumption of 1,325 tons.

4 Mechanical properties

In accordance with the fib CEB-FIP Model Code 2010, the structural design of SFRC elements is based on the post-cracking residual tensile strength provided by the steel fibers.

Nominal values of the material properties can be determined by performing a flexural bending test: one of the most common refers to the EN 14651-2005: Test method for metallic fibered concrete - Measuring the flexural tensile strength (limit of proportionality (LOP), residual), which is based on a 3-point bending test on a notched beam (Figure 4).

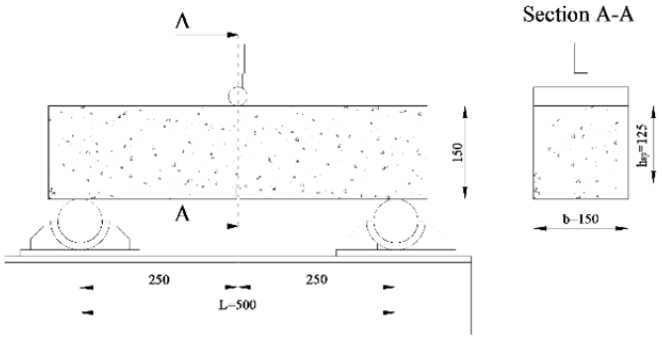


Figure 4: EN 14651 test setup

Beam specimens will be tested under three-point loading with a span length between supports of 50 cm at an age of 28 days. The specimens will be tested under displacement control at a rate of 0.05 mm/min based on the machine head until the CMOD reaches 0.1mm and a speed of 0.2 mm/min above this value. Beam mid-span deflections and CMOD will be measured using a non-contact infrared-based tracking system, which will track the position of markers attached to the surface of the specimens. Loads and marker positions will be recorded at 5Hz. The results can be expressed in terms of force (F) vs. Crack Mouth Opening Displacement (CMOD). To obtain reliable statistical results, a minimum number of beam tests is recommended (six specimens). A typical F-CMOD curve for FRC is shown in the picture below (Figure 5).

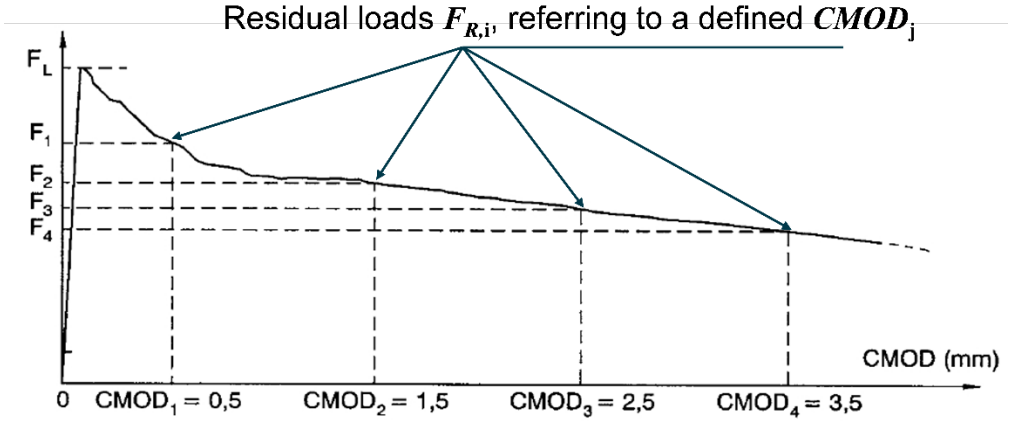


Figure 5: EN 14651 Load – Crack Opening diagram.

Parameters $f_{R,j}$ representing the residual flexural tensile strengths are evaluated from the F-CMOD relationship according to the below equation (fictitiously, a simplified linear-elastic behavior is assumed after the crack):

$$f_{R,j} = \frac{3F_{R,j}l}{2bh_{sp}^2}$$

Where:

$f_{R,j}$: residual flexural tensile strength corresponding to CMOD = $CMOD_j$

$F_{R,j}$: load measured during the test [kN]

l: span length (distance between the supports) = 500 mm

b: beam width = 150 mm

h_{sp}: is the distance between the tip of the notch and the top of the beam = 125 mm

The mechanical properties indicated in the design specifications for the SFRC are listed in the table below (Table 3).

Table 3: SFRC Mechanical properties.

Description	**Unit of measure**	
f_{ck}	MPa	50
Exposure class		XS3
Consistency class		S2
f_{R1k}	MPa	5.0
f_{R3k}	MPa	5.5
Early age compressive strength	MPa	25

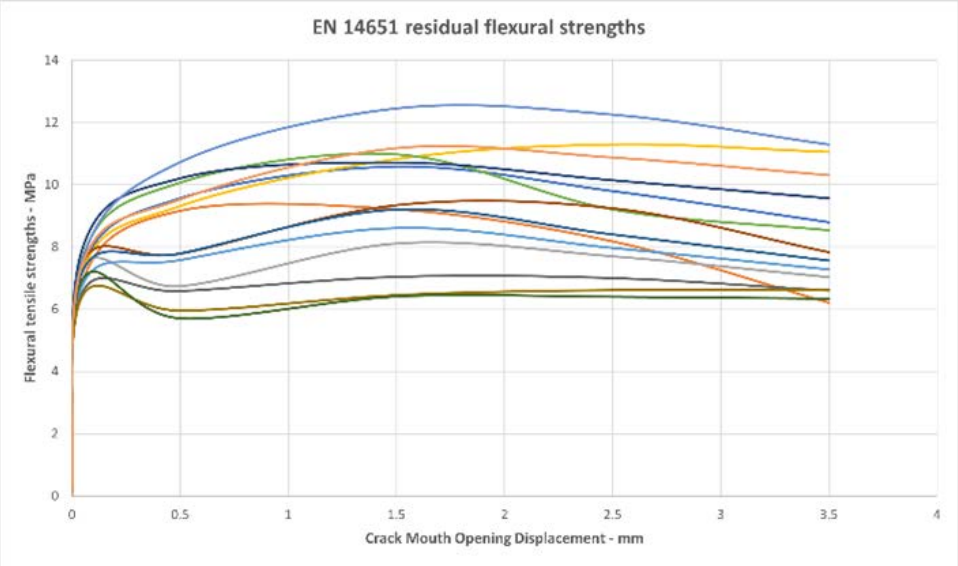


Figure 6: EN 14651 flexural strength - CMOD curves.

During the preliminary testing, 14 beams (150x150x600) have been casted, reinforcing the concrete reinforced with the HE++ 90/60, at a dosage rate of 43 kg/m^3; the targeted Model Code 5d class (f_{R1k} > 5.0 MPa; f_{R3k} > 5.5 MPa) has been fulfilled, achieving f_{R1k} = 5.49 MPa and f_{R3k} = 5.89 MPa (Figure 6); The k-values have been evaluated using a Student factor $k_{x,known}$ = 1.70 (RILEM TC 162-TDF). During production, to control the material mechanical properties, three beams per day have been cast; since the assessment criteria are much easier to meet, the performance achieved exceeded the 5d class.

5 Fire Resistance Tests

In addition to the mechanical properties, fire resistance tests were also carried out on small specimens as part of the project. The aim is to minimize the consequences of fire exposure. For this purpose, 2 kg of polypropylene micro fibres were added to the concrete, together with the steel fibres.

The reference standard is the PN-EN 1363-1: Fire resistance tests. This document establishes the general principles for determining the fire resistance of various elements of construction when subjected to standard fire exposure conditions. Alternative and additional procedures to meet special requirements are given in EN 1363-2.

A detailed description of the test procedure here below:

1. Duration of the test: 240 minutes.

2. Heating curve: Hydrocarbon, according to PN-EN 1363-2; temperature measurement in the oven directly from the thermocouple, without the use of plate thermometers.

3. Test load: None.

4. Test piece size: 2000x2000x250 mm (heated area: 1600x1600 mm) - prepared by the Client under the supervision of ITB (*Figure 7-8-9*).

5. Pre-test seasoning: At least 3 months; The conditions of the seasoning and the process itself are determined and supervised by the Customer.

6. Fastening structure (reinforced concrete slab with fire protection insulation) reducing the furnace light according to a separate design - prepared by ITB.

7. Disposal of test elements and clamping structures after testing - performed by ITB.

8. Measurements during and after the test:

    a. *Temperature in the furnace, pressure in the furnace, ambient temperature - in accordance with PN-EN 1363-1 and PN-EN 1363-2.*

    b. Temperature inside the test element at a distance of 20, 40, 60 and 100 mm from the bottom heated surface - arrangement according to the drawings of the Employer (Appendix No. 2); due to the lack of reinforcement, thermoelements are attached to supporting structures made of wire diameters from 4 to 6 mm; Thermocouples type K, 0.8 mm conductor thickness, made of thermocouple wire.

    c. Temperature on the surface of the cool test piece (at 250 mm from the heated surface) - 3 measurements.

    d. Moisture content of concrete before testing on core samples taken just before the start of the test - measurements are performed by the Customer.

    e. Chipping during and after testing - observation by means of a camera placed in the furnace and measurements made on the sample (measurement of the thickness of the chipping at least 40 points and measurement of the mass of the concrete chipped).

    f. Cracking, surface behavior, damage - accurate measurement is not possible due to the resolution of the camera in the furnace and the presence of the sample in the

furnace chamber after the test; images of all sample surfaces after the test and after the element has cooled down will be taken.

g. All other measurements not listed above, including, but not limited to, checking the strength of concrete before and after testing, including core extraction, shall be performed by the Customer.

h. The addiction of the polypropylene and steel fibres allowed the thickness of the spalling to be limited to less than 50 mm (Figure 10).



Figure 7-8-9. Preparation and casting of the fire resistance tests specimens.

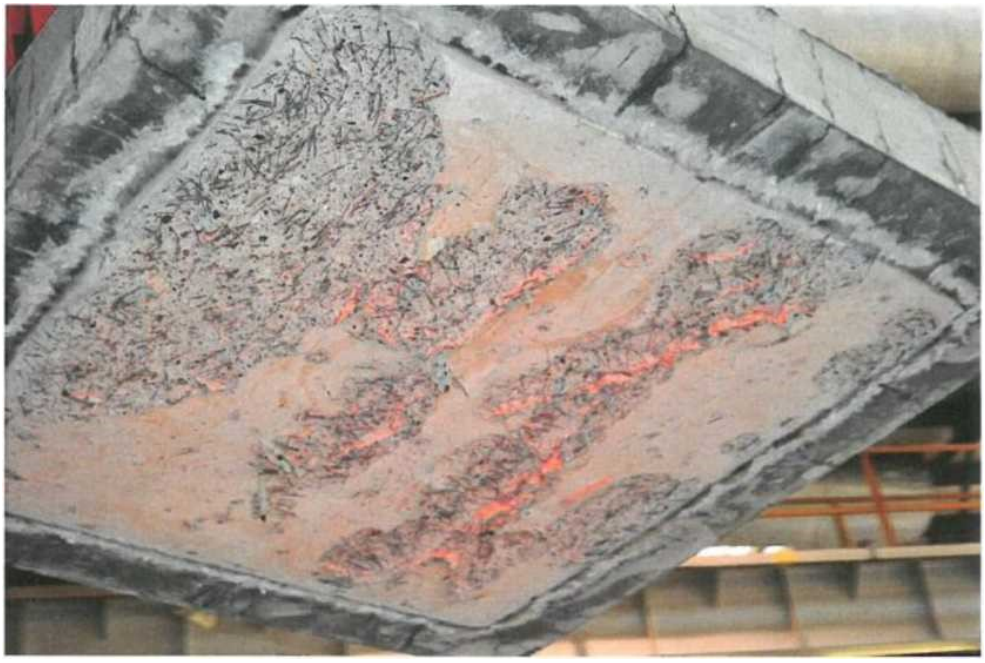


Figure 10. Test piece after t = 240 min, immediately after removal of the sample from the furnace - heated side view.

6 Concluding remarks

The Slurry TBM excavated the 1.48 km tunnel with an excavation diameter of 13.46 m with no major settlement issues or problems.

With an inner diameter of 12 m, the Świnoujście two-way road tunnel is the largest road tunnel in Europe to date, reinforced with steel fibres only.

1,325 tons of HE++ 90/60 steel fibres have been delivered to be used for the reinforcement of the 500 mm thick tunnel lining segments.

Mechanical and fire resistance tests have been carried out in accordance with the European standards.

During the preliminary testing, 14 beams (150x150x600) have been casted, reinforcing the concrete reinforced with the HE++ 90/60, at a dosage rate of 43 kg/m^3; the targeted Model Code 5d class (f_{R1k} > 5.0 MPa; f_{R3k} > 5.5 MPa) has been fulfilled, achieving f_{R1k} = 5.49 MPa and f_{R3k} = 5.89 MPa (Figure 6); The k-values have been evaluated using a Student factor $k_{x,known}$ = 1.70 (RILEM TC 162-TDF).

During production, to control the material mechanical properties, three beams per day have been cast; since the assessment criteria are much easier to meet, the performance achieved exceeded the 5d class.

The addiction of the polypropylene and steel fibres allowed the thickness of the spalling to be limited to less than 50 mm.

Despite a minimum overburden of about 8 m and a hydraulic head of about 24 m, a road tunnel lined with only fibers reinforced concrete segments has been successfully designed and built.

The construction of the tunnel took around four years, from 2019 to 2023.

7 Acknowledgements

The Authors acknowledge the support provided by the Consortium Gulermak-PORR in sharing with us information about this project, Mr Onur Erkus and Patricia Mak from Gulermak Poland.

8 References

Luciani, A. et all 2022. Swinoujscie-Tunnel-in-Poland-Design-and-Construction-aspects-of-a-big-diameter-slurry-TBM-excavation-under-Swina-Strait.

CEN, European Committee for Standardization “EN 1363-1: Fire resistance tests – Part. 1: General principles for determining the fire resistance of various elements of construction when subjected to standard fire exposure conditions”; “EN 1363-2: Fire resistance tests - Part 2: Alternative and additional procedures”.

CEN, European Committee for Standardization (2006) “EN 14721 - Test method for metallic fibre concrete - Measuring the fibre content in fresh and hardened concrete”.

CEN, European Committee for Standardization (2013) “EN 206 - Concrete - Specification, performance, production, and conformity”.

High Speed Two (HS2) Limited, Two Snowhill, Snow Hill Queensway, Birmingham B4 6GA, www.hs2.org.uk.

CEN, European Committee for Standardization (2019) "EN 12350 – Testing fresh concrete".
CEN, European Committee for Standardization (2019) "EN 12390 – Testing hardened concrete".
CEN, European Committee for Standardization (2006) "EN 14889-1 - Fibres for concrete - Part 1: Steel fibres - Definitions, specifications and conformity".
CEN, European Committee for Standardization (2005) "EN 14651 - Test method for metallic fibered concrete - Measuring the flexural tensile strength (limit of proportionality (LOP), residual)".
Federation International du Beton (2012) "fib CEP-FIP Model Code 2010 (fib Bulletin 65-66); Chap. 5.6 Fibres/Fibre Reinforced Concrete; Chap. 7.7 Verification of safety and serviceability of FRC structures ". Lausanne, Switzerland.
CEN, European Committee for Standardization (2002) "Eurocode 0: Basis of structural design".
CEN, European Committee for Standardization (2004) "Eurocode 2: Design of concrete structures — Part 1-1: General rules and rules for buildings".
PAS 8810-2016 – Tunnel design - Design of concrete segmental tunnel linings – Code of practice.
ACI Committee 544 (2016) "ACI 544.7R-16 - Report on Design and Construction of Fiber-Reinforced Precast Concrete Tunnel Segments". Farmington Hills, U.S.A.
The International Tunnelling and Underground Space Association (2016) "ITAtech Report nº 7 – Design Guidance for Precast Fibre Reinforced Concrete Segments – Vol. 1: Design Aspects".
The International Tunnelling and Underground Space Association (2018) "ITAtech Report nº 9 –Guideline for Good Practice of Fibre Reinforced Precast Segment – Vol. 2: Production Aspects".
Federation International du Beton (2017) "fib Bulletin 83 - Precast tunnel segments in fibre-reinforced concrete. State of the art report ". Lausanne, Switzerland.
Technical Data Sheet HE++ 90/60 steel fibres.

Case Study on the Application of ASTM F2322 to Precast FRC Panels in a Detention Facility

Eneas Dosantos[1], Victoria Olivera[1], Sofia Martínez[1], Luis Segura-Castillo[1]

[1]: Instituto de Estructuras y Transporte, Universidad de la República, Julio Herrera y Reissig 565, Montevideo 11300, Uruguay

Abstract

Incidents have been reported in penitentiary facilities built with conventional reinforced concrete where inmates extracted steel reinforcement bars and used them as weapons. To mitigate this risk, it exists a construction system based on precast panels of synthetic fibre-reinforced concrete that has been already used in Brazil. In this system each inmate's cell is formed by panels. This construction system was recently adopted in Uruguay for a new penitentiary facility. To establish appropriate safety criteria on panels, the project applied ASTM F2322-12. This standard reproduces impact attacks that an inmate could exert, imposing dynamic fatigue through series of 50 blows, alternating a blunt and sharp hammer tip. For the highest security level, it is required at least 600 blows to perforate the panel and allow the passage of a rigid prism of 127×203×203 mm³. The Uruguayan facility used concrete with a compressive strength of 50 MPa and 6 kg/m³ of synthetic macrofibres. During the construction, nine panels were tested (three plain, three with a window, and three with a door). This work presents the experimental campaign and describes, for a representative panel, the detailed crack pattern, including its evolution, as well as the fracture and material pull-out mechanisms in the impact zone. This provides experimental evidence on the performance of plastic fibre-reinforced concrete panels under successive impacts.

Keywords

Penitentiary, Synthetic, fibre-reinforced concrete, dynamic fatigue, impacts

1 Introduction

The design of structural systems for detention facilities involves not only conventional mechanical requirements but also specific security constraints associated with intentional actions. In this context, one of the recurrent issues observed in such facilities is the ability of detainees to manufacture weapons using elements available within the cells. Cases have been reported where steel reinforcement bars were extracted from reinforced concrete walls and subsequently used as sharp weapons (Dolovich, 2009). To reduce this risk, alternative construction solutions have been developed that limit the availability of extractable elements. One of these approaches consists of the use of precast panels made of synthetic fibre-reinforced concrete (FRC), where conventional reinforcement is notably reduced. These systems are based on modular panels that define each individual cell, providing both structural capacity and enhanced security performance (ACI Committee 544, 2002).

A relevant precedent can be found in Brazil, where many penitentiary facilities have been constructed using prefabricated FRC modules under proprietary systems such as Siscopen®. This approach removes one of the main sources of vulnerability associated with traditional reinforced concrete construction. More broadly, fibre-reinforced concrete has undergone significant development in recent decades, allowing its use as a partial or total substitute for conventional reinforcement (fib, 2012; di Prisco et al., 2009). While its application is well established in elements with moderate structural demand, its use in more demanding structural roles continues to expand (Vandewalle, 2000; Dupont and Vandewalle, 2003; Jansson et al., 2010; Deluce et al., 2014).

In Uruguay, the need to expand capacity in existing detention facilities has led to the adoption of this construction approach in a new complex. In this context, project-specific technical specifications were developed by the *Ministerio del Interior* in collaboration with the *Facultad de Ingeniería, Udelar*, incorporating additional performance requirements beyond those defined within the ASTM Committee F33, as part of a broader quality control and design framework for detention facilities (Ministerio del Interior de Uruguay, 2022; Segura and Dosantos, 2024; Olivera, 2025). For wall elements, ASTM F2322 was adopted as a performance-based test method to assess their resistance under repeated assault actions.

The objective of this study is to report the results of the application of ASTM F2322 as a performance-based test for precast synthetic FRC panels used in a detention facility in Uruguay. The structural response of these panels under repeated impacts is assessed, and the results and damage evolution are presented in detail for a representative panel. This work is part of a broader research project supporting subsequent numerical modelling to predict the structural response under impact loading.

2 Case study

Impacts were applied using a pendulum system in accordance with ASTM F2322, as shown in Figure 1. The device incorporates interchangeable impact tips, allowing the application of controlled energy impacts under repeatable conditions. Two types of impact tips are used: a blunt tip and a sharp tip, as illustrated in Figure 2. The corresponding impact energies are 271 J for the blunt tip and 136 J for the sharp tip. Impacts were applied in series of 50, alternating

between blunt and sharp tips in each series. The test was continued until either the required number of impacts was reached, or the failure condition was satisfied.

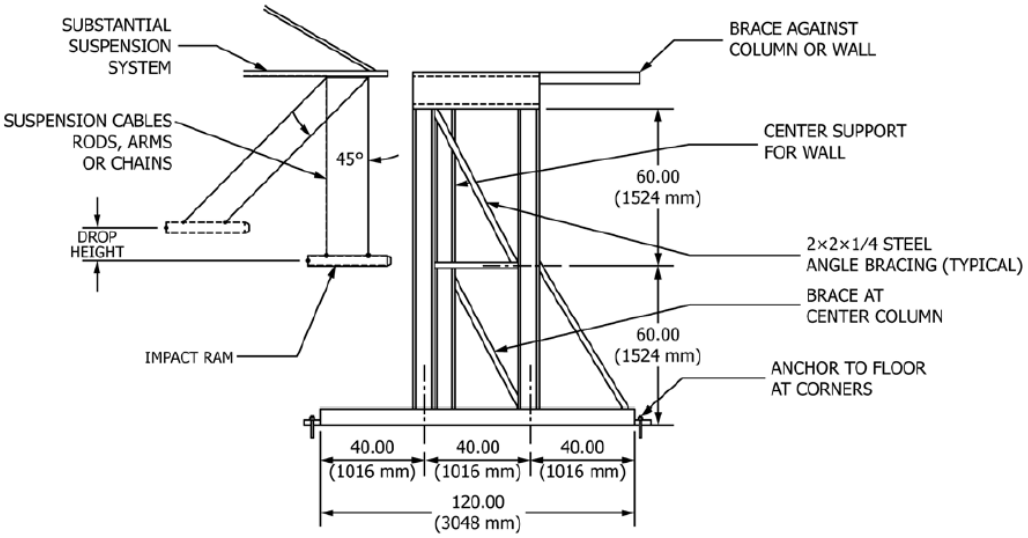


Figure 1. Pendulum impact system used in accordance with the standard test. (ASTM F2322, 2019).

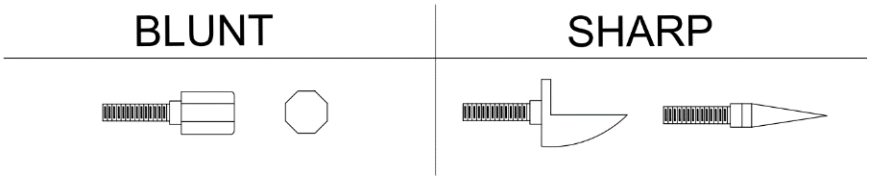
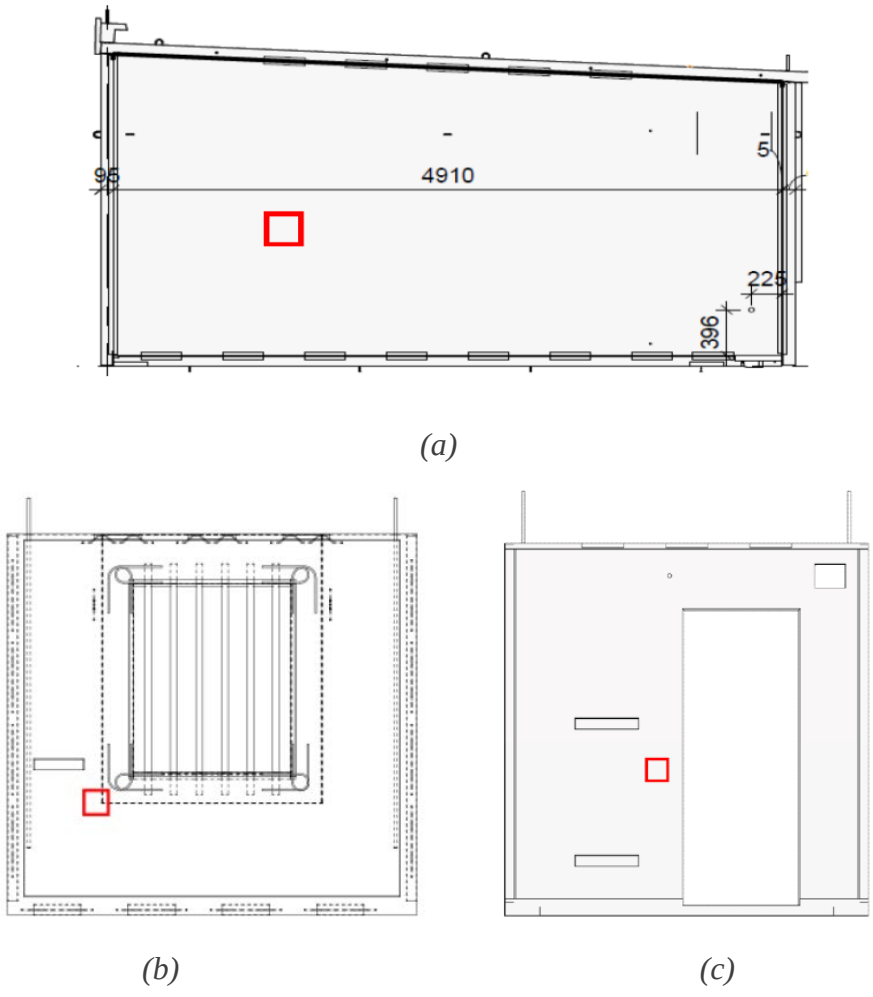


Figure 2 . Types of impact tips used for the test. (ASTM F2322, 2019)

The tested panel configurations and the selected impact locations are presented in Figure 3, where the red square indicates the target area for impact application. A total of nine panels were tested, distributed across three configurations—plain panels, panels with a window opening, and panels with a door opening—with three specimens tested for each configuration. In accordance with ASTM F2322, two types of specimens are considered: Type 1 panels, without openings, and Type 2 panels, including openings. For Type 1 panels, impacts were applied at the centre of the panel. For Type 2 panels, impacts were applied near the edges of the openings, where stress concentrations are expected to develop and more critical conditions may arise. The standard allows flexibility in the selection of the impact location, assigning this decision to the test agent, provided that the chosen position represents the most unfavourable condition for the element, considering aspects such as geometry, boundary conditions, and potential weak zones.



(a)

(b) *(c)*

Figure 3. Impact locations for different panel configurations: (a) plain panel, (b) panel with window, (c) panel with door.

Failure is defined in terms of “forcible egress”, corresponding to the formation of an opening that allows the passage of a rigid prism measuring 127 × 203 × 203 mm³. According to ASTM F2322, performance is classified into different security grades based on the number of impacts sustained without reaching this condition. In this study, compliance with Grade 1 classification is required, defined as the ability to withstand at least 600 impacts without satisfying the failure criterion. In addition, an increased performance criterion was defined in the project technical specifications, consisting of an additional 20% of impacts beyond the minimum requirement, corresponding to a total of 720 impacts (Ministerio del Interior de Uruguay, 2022). This overperformance requirement is part of the quality control framework adopted in the project, in which higher performance levels enable a reduction in testing frequency during production, provided that sufficient safety margins are achieved.

The test configuration is shown in Figure 4, where the panel, support conditions, and impact system arrangement are illustrated, defining the boundary conditions under which the response is evaluated.

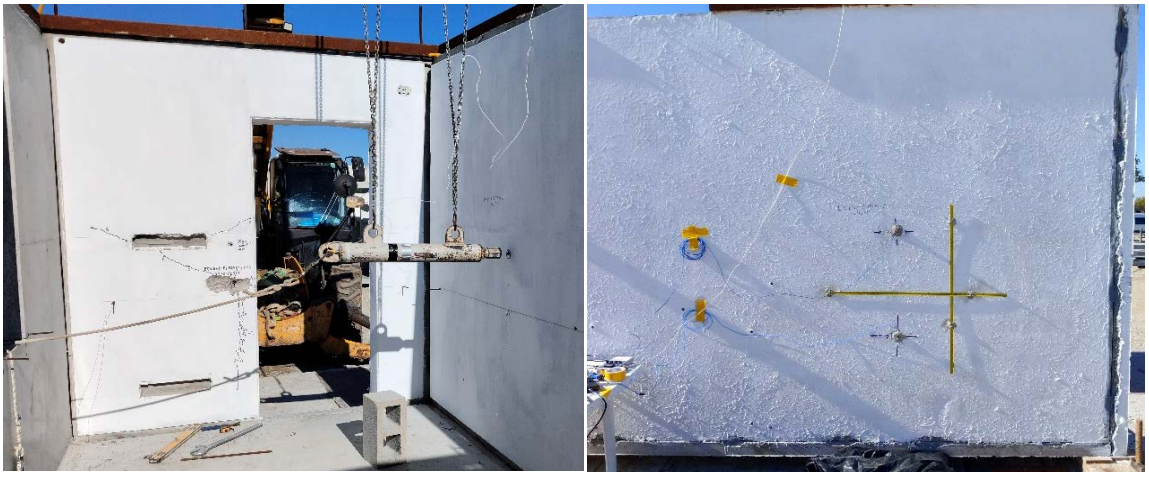


Figure 4. Test configuration.

The mix design used for the panels was established through experimental testing of different concrete mixtures subjected to the described assault test. Based on the results of that experimental campaign, the selected solution consisted of concrete with a compressive strength of 50 MPa and a fibre dosage of 6 kg/m³ of synthetic macrofibres. All specimens correspond to full-scale prefabricated elements representative of the actual construction system. The panels have a nominal thickness of 100 mm, while their overall dimensions vary depending on the panel configuration, particularly due to the presence and geometry of openings.

During testing, the evolution of damage was monitored through visual inspection and quantitative measurements. Although ASTM F2322 does not include requirements for monitoring damage evolution during the test, a complementary procedure was implemented to characterise damage progression and obtain additional information on the structural response. Cracks were marked directly on the panel surface as they appeared during the test, and each crack was labelled with a number corresponding to the impact series in which it was initiated, allowing the temporal evolution of the cracking pattern to be identified. These markings were subsequently digitalized and schematised to obtain the crack pattern representations presented. Based on this marked crack pattern, discrete control points P_i were selected as representative locations along relevant cracks and used as reference positions for measuring crack opening, assigning a unique label to each monitored location. Measurements were performed using a graduated magnifying lens at selected intervals during the test, allowing the evolution of crack opening to be related to the number of impacts. In addition, the depth of the impact crater was periodically recorded to characterise material removal at the impact face.

3 Results & Analysis

The failure process of the panel under repeated impacts can be divided into three stages. In the first stage (Figure 5a), localized damage and radial cracking develop. At the point of hammer impact, the concrete's crushing resistance is overcome, initiating the formation of a crater. On the back face, several radial cracks appear as a result of impact-induced flexure. With each successive blow, both the localized damage at the impact point and the radial cracks increase in extent, and the cracks propagate further in length and widen. In both mechanisms, the fibers play a crucial role by restraining and delaying crack propagation.

The second stage (Figure 5b) is characterized by the formation of a failure cone. Circumferential cracks develop and interconnect, forming a cone that extends from the impact zone to the back face. Once the cone surface is fully cracked, the fibers become the primary mechanism preventing immediate detachment. After the circumferential crack is fully formed, the hammer acts directly on the cone, which typically becomes dislodged in fewer than ten additional blows.

The third stage (Figure b) begins once a perforation has been achieved. The testing standard allows the hammer impact point to be relocated to an area adjacent to the opening. When this is done, a new semi-cone forms more rapidly and is subsequently dislodged. This process repeats until the opening becomes sufficiently large to meet the "forcible egress" condition, at which point the test concludes.

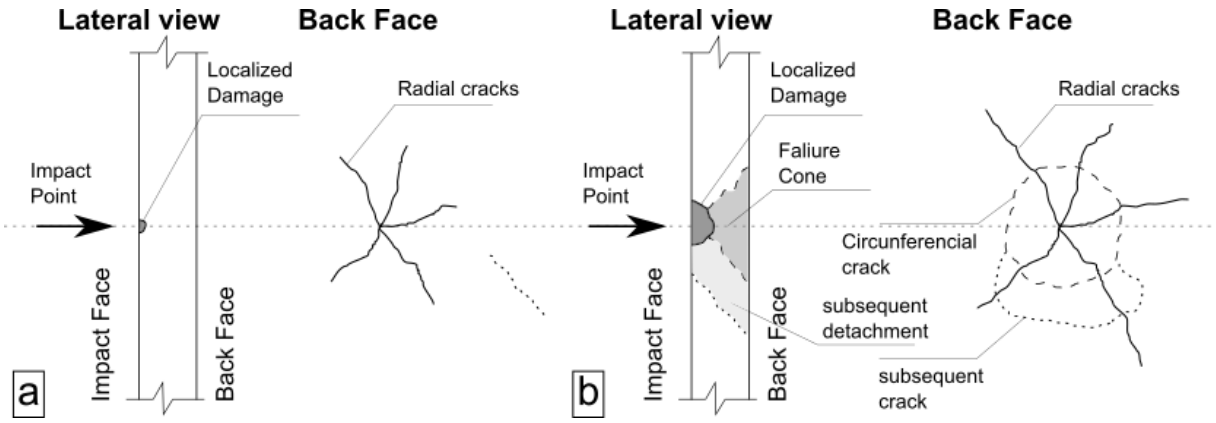


Figure 5. Schematic illustration of the progressive failure process in fiber-reinforced concrete panels under repeated impact. (a) First stage: localized damage and radial cracking. (b) Second and third stages: failure cone and "forcible egress".

Based on the previous description, this section presents a detailed analysis of the response of a representative plain panel subjected to ASTM F2322, capturing the governing response observed in the tests. Figure 6 illustrates the progressive development of damage in the impact zone, highlighting the transition from initial surface deterioration to the formation of a through-opening.

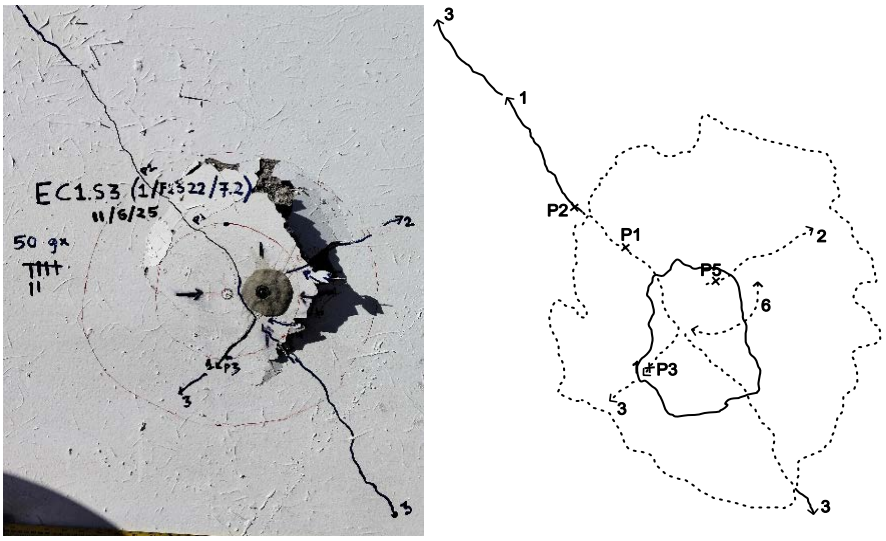
Damage initiates as localized crushing at the impact point, leading to the formation of a shallow crater. As the number of impacts increases, progressive material removal occurs in this region, accompanied by crack propagation towards the rear face of the panel. At 360 impacts, significant damage is observed across a large portion of the thickness, although no through-penetration is achieved. At 550 impacts, a full-depth penetration is observed, indicating that the damage has extended across the entire thickness of the element, but this condition does not yet satisfy the forcible egress criterion. With continued loading, the damaged area increases in size, leading to the formation of a larger opening. At 653 impacts, a through-opening allowing the passage of the standardized prism is achieved, corresponding to the "forcible egress" condition defined in Section 3. This indicates that the panel satisfies the requirement of sustaining at least 600 impacts without failure. However, the additional requirement defined in the project specifications, corresponding to a 20% increase in the number of impacts (720 impacts), is not achieved.



(a) *(b)* *(c)*

Figure 6. Evolution of damage in the impact zone at different stages of the test: (a) 360 impacts, (b) 550 impacts, (c) 653 impacts.

The cracking pattern observed on the rear face of the panel is presented in Figure 7. Figure 7 (a) shows the real image of the panel with the identified cracks, while Figure 7 (b) provides a schematic representation of the crack pattern, including the location of the monitored points P_i.



(a) *(b)*

Figure 7. Crack pattern on the rear face of the panel and location of monitored crack openings: (a) real image with cracks identified; (b) schematic representation of the crack pattern.

As shown in Figure 7, cracking develops from the impact point and propagates radially towards the boundaries of the affected zone, forming a dominant crack that governs the response, accompanied by secondary cracks as damage progresses. The pattern remains

localized, indicating that the response is governed by concentrated damage rather than distributed cracking, with a well-defined damage zone associated with progressive material removal, consistent with a truncated conical failure geometry through the thickness of the panel.

The evolution of crack opening at selected points is shown in Figure 8, where the crack width is plotted as a function of the number of impacts for each monitored point P_i. Each curve represents a different control point, identified by a distinct colour, allowing the comparison of crack opening evolution at different locations along the cracking pattern.

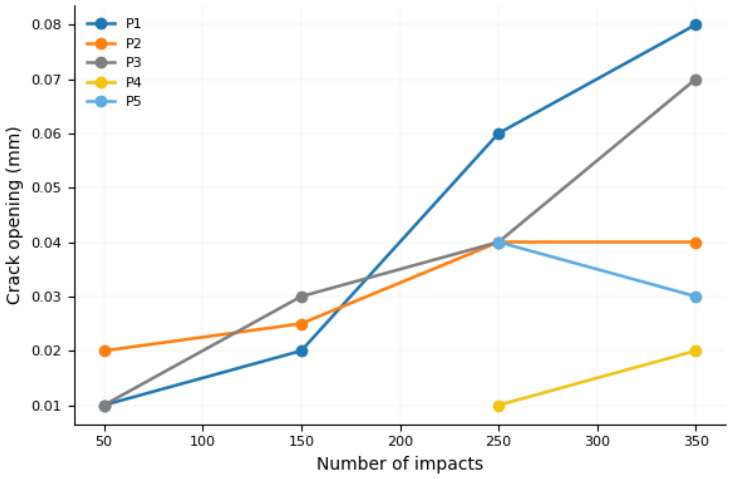


Figure 8. Crack opening evolution as a function of the number of impacts.

The results show a progressive increase in crack opening with the number of impacts. At early stages (up to approximately 150 impacts), crack openings remain limited across all monitored points. As the number of impacts increases, a more pronounced growth is observed, although with differences between locations. Point P_1 shows the largest increase, reaching values close to 0.08 mm at 350 impacts, while other points exhibit more moderate growth or stabilisation, such as P_5, which shows a slight reduction at later stages. The differences between points show that crack development is not uniform, with deformation concentrating in a dominant crack that controls the response of the panel.

Figure 9 shows the evolution of crater depth on the impact face, where the increase in penetration depth with the number of impacts is presented.

The depth of the damaged zone increases steadily, reaching values greater than 5 cm at advanced stages of the test, reflecting the progressive material crushing and removal at the impact location. The results show that the response is governed by localized damage in the impact zone, leading to the progressive formation of a through-opening.

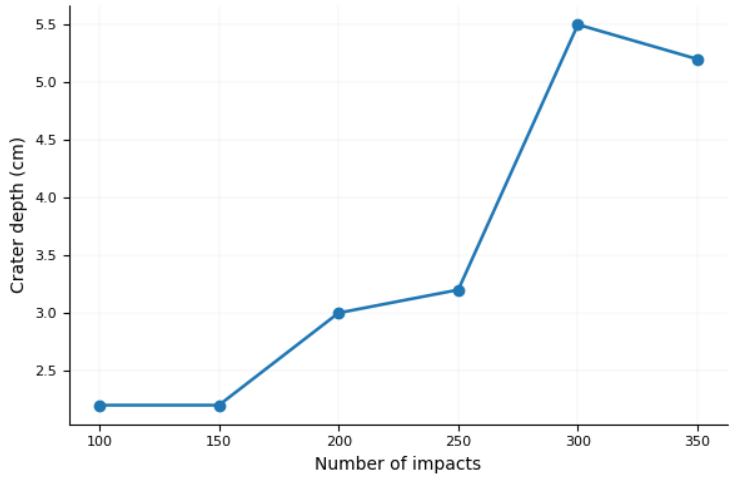


Figure 9. Crater depth evolution as a function of the number of impacts.

The damage evolution observed throughout the test is consistent with failure mechanisms previously reported for concrete elements subjected to impact loading. Sadraie et al. (2019) investigated plain and reinforced concrete slabs under low-velocity drop-weight impact and reported distinct failure mechanisms depending on the presence of reinforcement. Plain concrete specimens exhibited brittle localized perforation, whereas reinforced slabs developed a more progressive damage process characterized by localized crushing at the impact face, radial cracking on the rear face, and punching-type failure associated with gradual material removal. Despite the different loading configuration adopted in the present study, a comparable sequence of damage evolution was observed. This suggests that under repeated impact loading, structural response is governed by progressive local damage accumulation, while crack-bridging mechanisms provided by fibre reinforcement contribute to delaying complete perforation and controlling damage propagation.

4 Concluding remarks

The tested panels exhibited a damage process governed by localized degradation in the impact zone, with crack propagation concentrated in a dominant crack. The results show that crack development is not uniform, with deformation localised and controlled by this dominant crack as loading progresses.

The detailed analysis of a representative panel showed that damage evolves through progressive material crushing and removal at the impact face, leading to full-depth penetration and eventual formation of a through-opening. A clear distinction was observed between penetration and failure, with full-depth damage occurring prior to satisfying the forcible egress criterion.

The observed fracture surfaces indicate fibre pull-out as the governing mechanism, contributing to energy dissipation and delaying the formation of a through-opening. The panel reached the failure condition at 653 impacts, satisfying the Grade 1 requirement but not the additional project criterion of 720 impacts.

These results provide experimental evidence on the behaviour of synthetic fibre-reinforced concrete panels under repeated impacts, showing that their response is governed by progressive and localized damage mechanisms.

5 Acknowledgements

The authors thank the Ministerio del Interior of Uruguay and Consorcio Libertad (Teyma, Saceem and Ciemsa), for their collaboration and for allowing the use of the test results.

6 References

ACI Committee 544, 2002. *State-of-the-art report on fibre reinforced concrete*. ACI 544.1R. American Concrete Institute.

ASTM F33 *Committee on Detention and Correctional Facilities*, ASTM International.

ASTM F2322, 2019. *Standard test method for physical assault on vertical fixed barriers for detention and correctional facilities*. ASTM International.

Dolovich, S., 2009. *Cruelty, Prison Conditions, and the Eighth Amendment*. New York: New York University Press.

di Prisco, M., Plizzari, G., and Vandewalle, L., 2009. *Fibre reinforced concrete: new design perspectives.* Materials and Structures, 42, 1261–1281.

fib, 2012. Model Code 2010. Bulletin 65, Fédération Internationale du Béton, Lausanne.

Ministerio del Interior de Uruguay, 2022. *Licitación pública N.º 26/2022 – Anexo II D.* Available at: https://www.comprasestatales.gub.uy/consultas/detalle/mostrar-llamado/1/id/985182

Olivera, V., Novello, D., Segura-Castillo, L., 2025. *Quality control of fibre-reinforced concrete using the Montevideo test: A case study in real-world construction*. In: Proceedings of the fib Symposium 2025, Antibes, France, June 16–18.

Sadraie, H., Khaloo, A., & Soltani, H. (2019). Dynamic performance of concrete slabs reinforced with steel and GFRP bars under impact loading. Engineering Structures, 191, 62–81. https://doi.org/10.1016/j.engstruct.2019.04.038

Segura, L., Dosantos, E., 2024. *Ensayos de desempeño para unidad de rehabilitación.* In: 28° Jornadas Argentinas de Ingeniería Estructural (AIE 2024), Buenos Aires, Argentina.

Siscopen®, n.d. Prefabricated modular system for detention facilities. Verdi Construções S.A., Brazil. Available at: https://www.verdiconstrucoes.com.br

Behavior of Steel Fiber-Reinforced Concrete Structural Walls with Simplified Reinforcement Detailing under Reversed Cyclic Lateral Displacements

Gustavo J. Parra-Montesinos[1], Osman Carrillo[2], José A. Pincheira[3]

[1]: Professor, Dept. of Civil and Environ. Eng., Univ. of Wisconsin-Madison, USA

[2]: Doctoral Candidate, Dept. of Civil and Environ. Eng., Univ. of Wisconsin-Madison, USA

[3]: Associate Professor, Dept. of Civil and Environ. Eng., Univ. of Wisconsin-Madison, USA

Abstract

Reinforced concrete walls, due to their lateral stiffness and strength, are commonly used as the lateral-force-resisting system in mid- and high-rise structures in regions where large ground motions are expected. Given the inelastic displacement reversals that these walls may be subjected to, large amounts of closely-spaced transverse reinforcement are often necessary in the wall boundary regions to provide concrete confinement and delay buckling of longitudinal reinforcement. Further, through-thickness ties are often required to provide lateral support to the vertical web reinforcement. These reinforcement requirements are labor-intensive and time-consuming to implement and often translate into significant reinforcement congestion.

This paper discusses results from an ongoing experimental investigation aimed at simplifying reinforcement detailing in earthquake-resistant walls, particularly in boundary regions, through the use of high-strength hooked steel fibers. Two fiber-reinforced concrete walls with a shear span-to-length ratio equal to 2.6 were tested under horizontal lateral displacement reversals of increasing magnitude. For each wall, two simplified, less congested transverse steel layouts in the boundary regions were evaluated. The fibers used were 60 mm long and 0.75 mm in diameter, with a nominal tensile strength of 1800 MPa. Fiber volume fractions were 1.0% and 0.85% for the first and second wall, respectively. Both walls exhibited a flexural-dominated, hysteresis response with peak drift ratios in excess of 3.0%. Test results thus indicate that it is possible to reduce the amount and increase the spacing of transverse steel reinforcement in boundary regions of structural walls through the addition of high-strength hooked steel fibers.

Keywords

Structural walls; drift capacity, confinement, steel fibers, earthquakes, shear strength.

1 Introduction

Reinforced concrete structural walls are commonly used to provide lateral stiffness and strength to mid- and high-rise buildings located in regions of high seismicity. In the USA, these walls are typically used as the sole earthquake-resisting system with either reinforced concrete slab-column frames or steel frames designed to support gravity loads while undergoing earthquake-induced displacements.

For structures expected to undergo large inelastic displacement reversals (Seismic Design Category D, E, and F, as defined in ASCE 7-22), structural walls must comply with the requirements for *special structural walls* of ACI 318-25. Design provisions for these walls include transverse steel requirements in the wall boundary regions for concrete confinement and lateral bar support, minimum ratios for web vertical and horizontal distributed reinforcement, and requirements for through-thickness ties for web reinforcement support and overall wall stability. For walls with height-to-length ratio of at least 2.0, ACI 318-25 requires the use of *special boundary elements* where the following condition is satisfied,

$$\frac{1.5\delta_u}{h_{wcs}} \geq \frac{l_w}{600c} \tag{1}$$

where δ_u is the design displacement at the top of the wall for a design-level earthquake, h_{wcs} is the height of the wall above the critical section in bending, l_w is the length of the wall (horizontal dimension in direction of lateral displacement), and c is the neutral axis depth. In Eq. (1), $1.5\delta_u$ is meant to represent the displacement at the top of the wall associated with a Maximum Considered Earthquake-level ground motion. The right-hand side of Eq. (1), on the other hand, is an approximation of the wall drift ratio corresponding to a maximum compressive strain at the critical section of 0.003. Among the requirements for special boundary elements, the area of transverse reinforcement in each perpendicular horizontal direction must satisfy the following,

$$\frac{A_{sh}}{sb_c} \geq 0.3\left(\frac{A_g}{A_{ch}} - 1\right)\frac{f'_c}{f_{yt}} \geq 0.09\frac{f'_c}{f_{yt}} \tag{2}$$

where A_{sh} is the area of horizontal transverse steel in the direction evaluated, s is the vertical spacing of the transverse steel, b_c is the width of the wall core perpendicular to the steel for which A_{sh} is calculated, A_g is the gross cross-sectional area of the special boundary element, A_{ch} is the area of the core of the special boundary element, f'_c is the specified concrete compressive strength, and f_{yt} is the nominal yield strength of the transverse steel. For walls with Grade 414M primary longitudinal reinforcement (nominal yield strength = 414 MPa), spacing of transverse steel s cannot exceed 150 mm, 6 times the minimum diameter of the primary longitudinal steel, and 1/3 of the least dimension of the special boundary element. Although results from tests indicate that the ACI 318 provisions for special structural walls lead to adequate wall response under large displacement reversals (Huq et al., 2021), the requirements for amount and spacing of transverse reinforcement in special boundary elements are labor intensive and often lead to severe reinforcement congestion. An experimental program was thus undertaken to evaluate the feasibility of partially replacing transverse reinforcement in wall boundary regions without compromising deformation capacity.

2 Experimental program

The experimental program consists of the testing of four rectangular walls under combined axial compression and lateral displacement reversals. Two of the walls have been tested to date. Figure 1 shows the overall configuration of the specimens, while Fig. 2 shows the reinforcement detailing for the two specimens tested to date. Each wall specimen consisted of a base block anchored to the strong floor of the laboratory, a rectangular wall, and a cap beam used for displacement/load application. The wall cross-section was 1520 mm x 254 mm and the shear span-to-wall length ratio was 2.6. Specified concrete compressive strength was 55 MPa. Bekaert 4D 80/60 fibers were used over approximately 1830 mm from the bottom of the wall (1.2 times the wall length, l_w), where inelastic deformations were expected to occur. The fiber length and diameter were 60 mm and 0.75 mm, respectively, while the nominal wire tensile strength was 1800 MPa. The main differences between Specimens W1 and W2 lied in the spacing of transverse steel over the bottom $0.5l_w$ of the wall and the fiber dosage (80 kg/m^3 or 1.0% volume fraction for Wall 1 and 65 kg/m^3 or 0.84% volume fraction for Wall 2). Nominal yield strength for the steel reinforcement was 414 MPa.

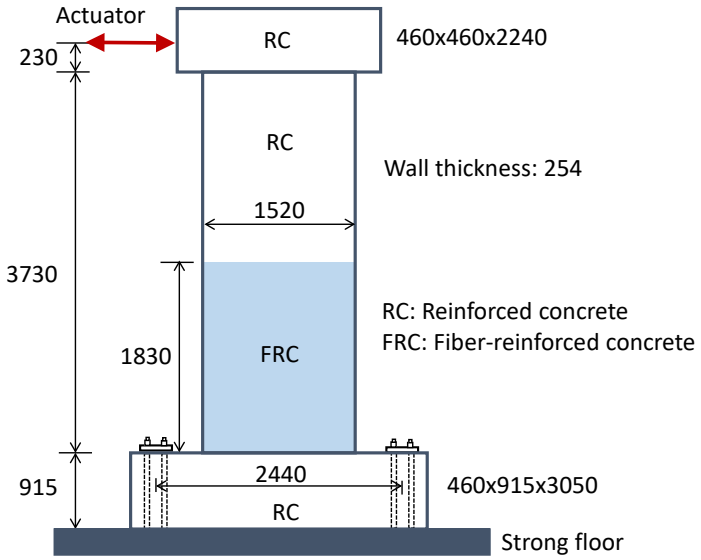
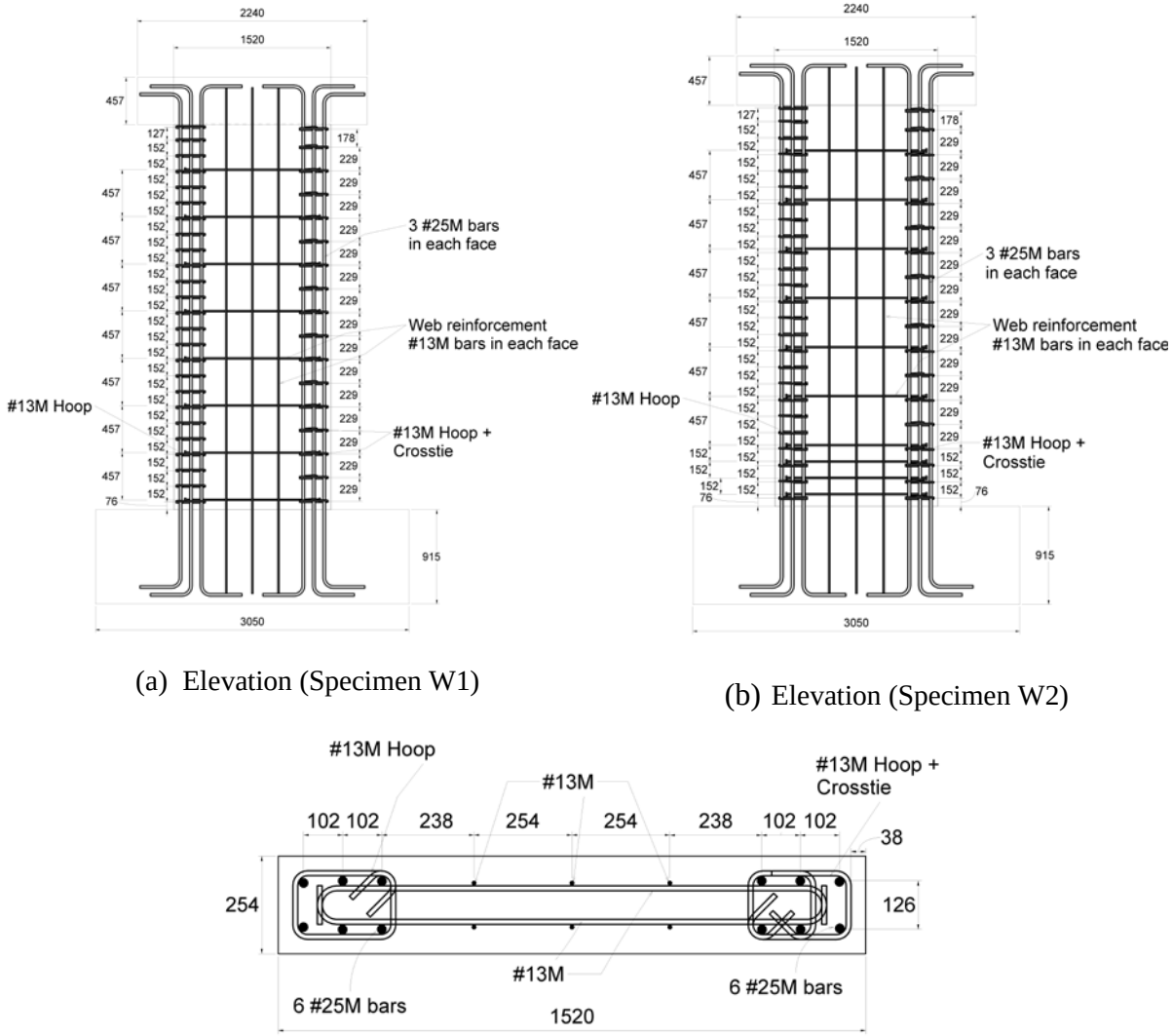


Figure 1: Test configuration (dimensions in mm)

The walls were designed to exhibit a flexure-dominated behavior, governed by yielding in the lower region of the wall. Six No. 25M (25 mm diameter) longitudinal bars were used in each boundary element, but the transverse steel layouts differed. One boundary element featured No. 13M (13 mm diameter) hoops with crossties at a spacing of either 229 mm (s = 9 bar diameters, d_b) or 152 mm (s = 6d_b) over $0.5l_w$ for Wall 1 and Wall 2, respectively, which corresponded to nine and six longitudinal bar diameters. This spacing was 229 mm above $0.5l_w$. The other boundary element featured No. 13M hoops without crossties at a 152 mm spacing (Fig. 2). For comparison purposes, an ACI 318-25 compliant special boundary element in the test walls would have required a maximum spacing of 29 mm (s = 1.2d_b) and 43 mm (s = 1.7 d_b) for single hoops and single hoops/crossties, respectively.

The SFRC portion of Specimen W1 was cast in one lift using ready-mix concrete. Upon removal of the formwork, the presence of several pockets both in the web and boundary regions of the wall required repairs, which were performed using either the same SFRC mixture or, for

smaller pockets, mortar with the same fiber dosage. For Specimen W2, the SFRC portion of the wall was constructed in three lifts, all mixed in the laboratory. No problems were encountered regarding the fiber-reinforced concrete in this specimen.



(a) Elevation (Specimen W1)

(b) Elevation (Specimen W2)

(c) Cross-section for Specimens W1 and W2

Figure 2: Reinforcement detailing for test specimens (dimensions in mm)

Lateral displacements were applied through a hydraulic actuator connected to the wall cap beam at one end and to a reaction wall at the other end. The specimens were laterally braced at the cap beam. Prior to application of lateral displacements, an axial compressive force equal to 670 kN (approximately $0.035A_g f'_c$, where A_g is the gross cross-sectional area of the wall) was applied at the top of the specimen. The target drift ratio history is shown in Fig. 3. Drift ratio is defined as the lateral displacement at the center of the cap beam relative to the top of the foundation divided by the vertical distance between these two locations. Two cycles were applied for each drift ratio level. Drift ratios were later corrected to account for foundation slip and rotation.

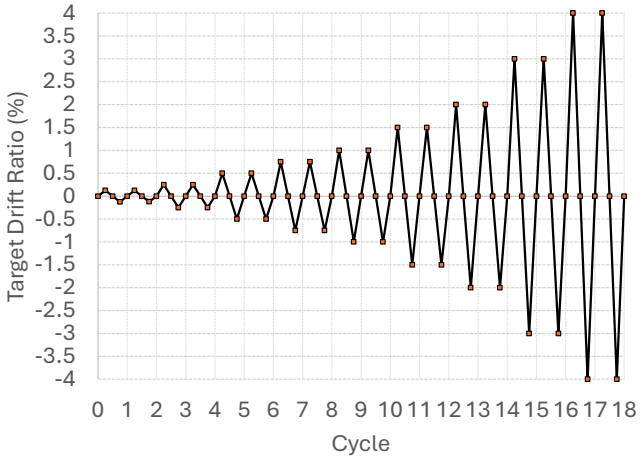


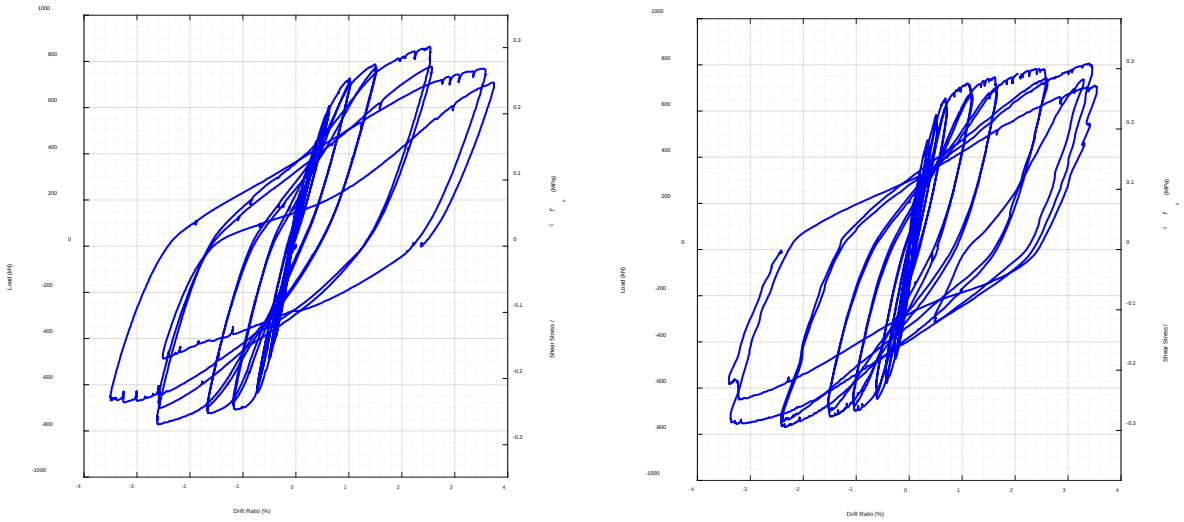
Figure 3: Target drift ratio protocol for wall specimens

Primary flexural reinforcement in the walls was A615 steel, while transverse and web reinforcement was A706 steel. In all cases, the reinforcement grade was 414M (nominal yield strength = 414 MPa). Average cylinder compressive strength for the fiber-reinforced concretes used in both walls ranged between 41.3 MPa and 53.1 MPa. Tests of 152 x 152 x 508 mm simply supported beams (span length of 457 mm) under four-point bending indicate an average first cracking strength between $0.9\sqrt{f'_c}$ and $1.0\sqrt{f'_c}$ (MPa). Average peak post-cracking stress was 1.1 times the average first cracking stress for the SFRC used in Specimen W1 and approximately equal to the average first cracking stress for the SFRC used in Specimen W2.

3 Test Results

3.1 Overall Behavior

The two wall specimens exhibited a flexure-dominated response with a drift ratio capacity exceeding 3.0%. This drift ratio is typically taken as an approximation of the peak drift for a Maximum Considered Earthquake-ground level shaking. Figure 4 shows the lateral force versus drift ratio response for the two walls. As can be seen, both specimens exhibited a stable behavior with relatively wide hysteresis loops. Peak average shear stress, calculated based on the gross cross-sectional area of the wall, corresponded to approximately $0.3\sqrt{f'_c}$ (MPa). Damage in the wall boundary regions remained minor to moderate for drift ratios up to approximately 2.5%. At larger drifts, concrete spalling/crushing and longitudinal bar buckling were observed in the wall boundary regions of both walls. Figure 5 shows the boundary region with single hoops of Specimen W2 at three drift ratios. Specimen W1 was able to sustain one full cycle to a drift ratio of approximately 3.6%, followed by significant strength loss when displaced in the negative direction due to failure of the compression zone confined by single hoops at 152 mm spacing. Specimen W2, on the other hand, sustained two cycles at a drift ratio of approximately 3.4%. The fact that both specimens were able to sustain drift ratios of up to approximately 3.5% with 1/3 or less of the amount of transverse reinforcement required for a special boundary element indicates that a significant reduction of transverse steel in special boundary elements can be achieved through the use of high-strength hooked steel fibers.



(a) Specimen W1 (b) Specimen W2

Figure 4: Lateral force versus drift ratio hysteresis

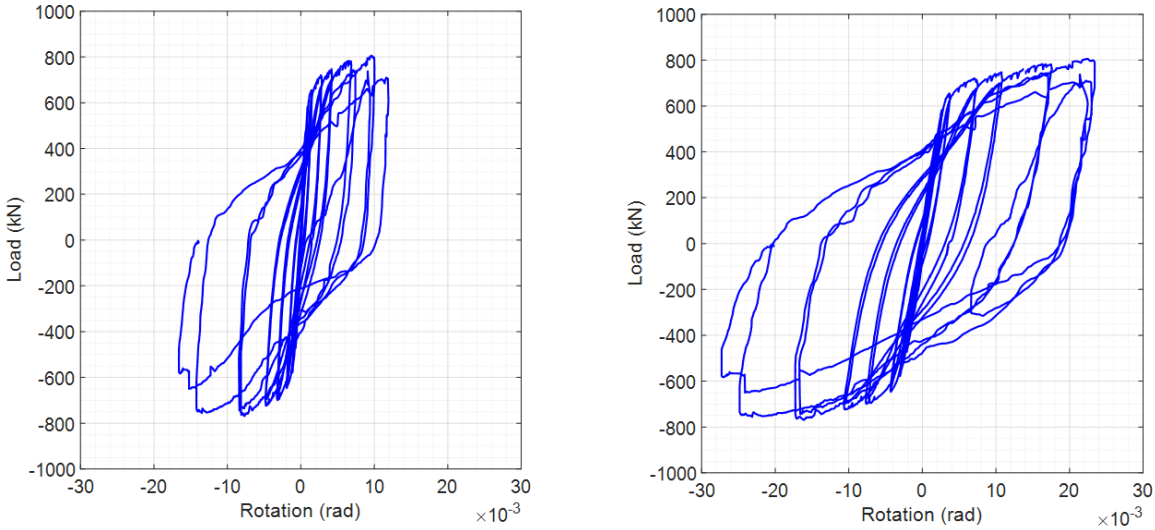


(a) 1.1% drift ratio 2.5% drift ratio 3.4% drift ratio

Figure 5: Damage in boundary region with single hoops of Specimen W2

3.2 Plastic Hinge Rotations

Most of the inelastic rotations in the wall specimens occurred over a height equal to $0.5l_w$. Figure 6 shows the load versus rotation response for the wall-foundation interface and from the bottom of the wall (including interface) to $0.5l_w$ for Specimen W2. As can be seen, the rotation responses were characterized by wide hysteresis loops. Prior to the last two cycles at a target drift ratio of 4.0%, rotations at the wall-foundation interface did not exceed 0.01 rad. During the last two cycles, the rotation response became unsymmetric, with a maximum rotation of 0.012 rad and 0.017 rad for the two loading directions. Total rotations at $0.5l_w$ reached a maximum of approximately 0.024 and 0.028 rad in the two directions of loading. Peak relative rotations between $0.5l_w$ and the interface were thus 0.012 rad and 0.011 rad for the two loading directions.



(a) Wall-foundation interface (b) At 0.5l_w

Figure 6: Lateral force versus rotation hysteresis for Specimen W2

3.3 Drift Contributions

Contributions from various mechanisms to applied drift for Specimen W2 at various drift ratio levels were calculated based on optical markers placed on the surface of the specimens and are shown in Fig. 7. The mechanisms considered were rotations at the wall-foundation interface, relative rotations between 0.8l_w and the interface, rotations above 0.8l_w, shear deformations, and horizontal sliding at the base of the wall with respect to the foundation.

Concentrated rotations at the wall-foundation interface and rotations over the bottom 80% of the wall length contributed approximately 30-35% and 40-50% of the total applied drift, respectively. Flexural rotations in the upper portion of the wall and shear deformations contributed approximately 10% of the total drift, shear deformations in the plastic hinge region contributing the most for drift ratios greater than 2.5%. Contribution from horizontal sliding at the wall-foundation interface to total drift was negligible until the cycles beyond 3.0% drift ratio, where horizontal slip contributed approximately 10% of the total drift.

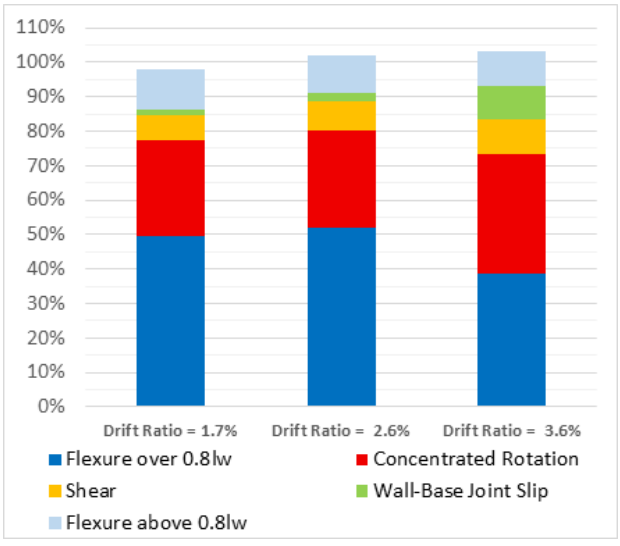


Figure 7: Drift contributions for Specimen W2

4 Conclusions

Results from the tests of two steel fiber-reinforced concrete walls under lateral displacement reversals indicate that steel fibers may be used as partial replacement of transverse reinforcement required in wall boundary regions for concrete confinement and lateral bar support. Both wall specimens sustained peak drift ratios of approximately 3.5% and exhibited a flexure-dominated behavior despite the fact that the amount of transverse reinforcement provided was 1/3 or less of that required for a special boundary element in accordance with ACI 318-25. Inelastic rotations concentrated mostly over 0.5 times the wall length from the base, reaching a maximum of nearly 0.03 rad. Failure of the specimens was due to excessive damage in the wall boundary regions that included significant concrete crushing/spalling and buckling of the primary flexural reinforcement.

5 Acknowledgements

Financial support for this investigation is provided by the ACI Foundation, NV Bekaert SA, Baker Concrete Construction, The Conco Companies, Largo Concrete, McClone Construction, and the Jun and Sandy Lee Structural Engineering Research Fund at the University of Wisconsin-Madison. The contributions from the laboratory manager, Jacob Zeuske, to the construction and testing of the wall specimens are greatly appreciated. The opinions expressed in this paper are those of the writers and do not necessarily represent the opinions of the sponsors.

6 References

ACI Committee 318, 2025. “Building Code for Structural Concrete-Code Requirements and Commentary,” American Concrete Institute, Farmington Hills, MI, USA.

ASCE, American Society of Civil Engineers, 2022. “Minimum Design Loads and Associated Criteria for Buildings and Other Structures (ASCE/SEI 7-22),” Reston, Virginia, USA.

Huq, M.S., Burgos, E.A., Lequesne, R.D., and Lepage, A., 2021. “High Strength Steel Bars in Earthquake-Resistant Reinforced Concrete T-Shaped Walls,” *ACI Structural Journal*, Vol. 118, No. 1, pp. 215-226.

Fibre reinforced concrete and UHPC; their application in structures

Jan L. Vitek[1]

[1]: Faculty of Civil Engineering, Czech Technical University in Prague, Prague, Czechia and Metrostav a.s. Prague, Czechia.

Abstract

Fibre reinforced concrete (FRC) is a cement composite, in which the fibres are used for transfer of tensile stresses. Concrete itself is a brittle material. To reduce the brittleness, the fibres are used. Preferably the number of fibres is a determining parameter for materials with strain hardening or strain softening. The steel fibres are stiff, their modulus of elasticity is high, and they significantly contribute to strain reduction after crack origin. Non-metallic fibres often exhibit small modulus of elasticity. Their activation after crack origin requires higher strain, provided their number is not extremely high. The fibres can fail due to their rupture or due to their pull out from the concrete matrix. Therefore, the quality of anchorage in concrete and their tensile strength are important parameters. Some producers developed steel fibres with hooked ends, so that their anchorage was stronger.

The paper illustrates some experience of the author with fibre reinforced concrete and its application in precast tunnel lining. It is an interesting application which allows for savings of steel reinforcement and for improved behaviour of tunnel segments. Careful experimental verification and numerical analysis are contributing for optimization of the concrete mix and fibre contents.

The paper also deals with UHPC (ultra-high-performance concrete), which is also a kind of fibre reinforced concrete. However, the mechanical properties of UHPC and also its durability are rather different from those of ordinary FRC. The steel fibres used in UHPC are shorter, thinner and they have bigger tensile strength. UHPC is a different material and the rules for production of the material, design and execution of structures are also different. It is recommended to use guidelines, which are developed especially for UHPC applications.

Keywords

Fibre reinforced concrete, crack, durability, failure, strain hardening, strain softening, structure, tensile strength, UHPC

1 Introduction

Fibre reinforced concrete (FRC) is developed for decades. The idea of dispersed reinforcement of concrete with the purpose to improve its properties under tension is rather good, however, there are some difficulties which makes the task more complex. The number of fibres must be sufficiently high, their distribution should be uniform, and it is not possible to place the fibres in those places where the tension is concentrated, which means that efficiency of fibres is rather limited. Additionally, the actual requirements on safety of structures require some robustness and ductility, which can be demanding on fibre contents in fibre reinforced concrete. The efficiency of fibres in FRC is highly dependent on concrete technology. A suitable composition of concrete is now significantly influenced by the development of chemical admixtures like superplasticizers, stabilizers, accelerators of hardening, etc. A suitable application of FRC requires a complex approach to the design of the structure together with a construction technology and a material technology. Different fibres can be applied for structural application. Steel fibres are very efficient in terms of the structural performance, synthetic fibres contribute to the mechanical properties without risk of corrosion, small PE or PP fibres help in the field of fire resistance and in elimination of cracks due to early shrinkage. The design of FRC may be a very complex task, which can result in a mix of different fibres in one concrete. In contrary of a classical FRC, UHPC (ultra-high-performance concrete) is relatively new. It is developed since about last 30 years. In structural applications, UHPC is always reinforced by fibres. High strength steel fibres are used most often, but sometimes other fibres can be used as well. The composition of UHPC is different in comparison with ordinary concrete which results in different behaviour of UHPC. The bond of fibres is much better and also the durability requirements can be satisfied with lower cover layer, the anchorage lengths of reinforcement are shorter as well as overlap lengths of reinforcing bars. The design rules for ordinary FRC and UHPC should not be therefore equal. The examples shown later will illustrate the differences between classical FRC and UHPC.

2 Structural behaviour of FRC

The role of fibres is primarily to improve the tensile properties of concrete which is generally brittle. A typical stress-strain diagram of FRC is shown in Fig. 1. In dependence on the fibre

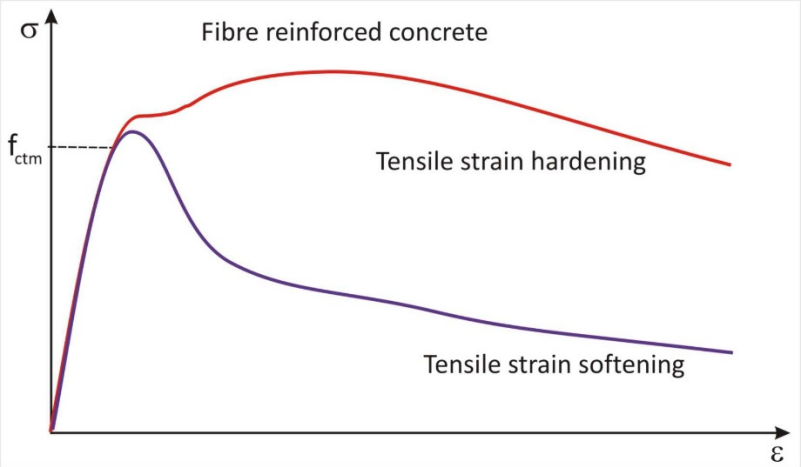
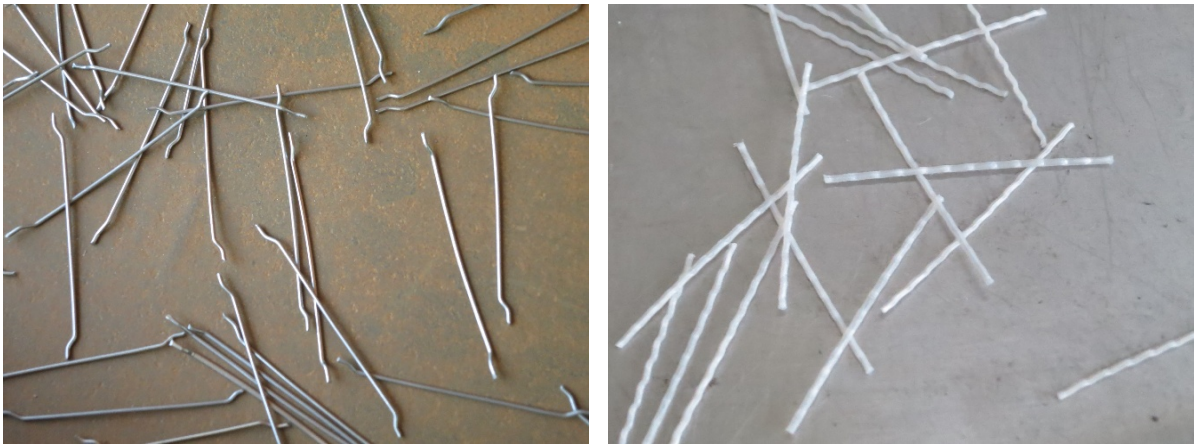


Figure 1: Typical stress-strain diagram of fibre reinforced concrete

contents and on the quality of fibres, FRC can exhibit either strain hardening or strain softening. The strain hardening is very welcome, because it contributes to the ductility and robustness, however, also some structures which are made of materials with strain softening can become robust enough if they provide sufficient redistribution of internal forces after local failure.

Fibres are generally activated after the concrete cracks. Because of a big difference in the modulus of elasticity of steel and concrete, before the crack origin the stress in steel fibres is small. In the crack, the tension is carried by fibres and if the crack width increases the stress in fibres grows. Then there are two possible modes of failure. Either the strength of the fibre is exceeded, then the fibre fails in tension, or the anchorage of fibres fails and the fibres are pulled off the concrete. To improve the anchorage of fibres, some fibres have hooks at their ends. Some producers use multiple hooks at the ends of steel fibres. Some synthetic fibres use an irregular cross-section along the fibres, which also improves their anchorage conditions. Fig. 2 shows examples of steel fibres with simple hooks and of synthetic fibres. According to our experience from experimental programs, the steel fibres tend to pull off concrete, while the synthetic fibres rather fail since their anchorage in concrete is quite good (Fig. 3).



a) b)

Figure 2: a) Steel fibres with simple hooks, b) Synthetic fibres



a) b)

Figure 3: a) Pull out of steel fibres, b) Tensile failure of synthetic fibres

The pull out of steel fibres (provided their strength is large enough) led to development of multiple hooks at the ends. Such fibres are delivered by some producers. The improved anchorage increases the efficiency of fibres and finally results in savings due to lower dosage of fibres.

The behaviour of steel and synthetic fibres was compared. The laboratory beams (150 x 150 x 700 mm) were subjected to 4 point bending test. In the first series, steel fibres 60 x 0.75 mm – 40 kg/m^3 were used. In the second series synthetic fibres 39 x 0.78 mm – 12 kg/m^3 were used. The number of synthetic fibres was about 2 times higher, but the response of beams did not achieve that of the beams steel fibres (Fig. 4). Significant drop of load after the crack origin is a result of slower activation of synthetic fibres because of their lower elastic modulus (3.6 GPa).

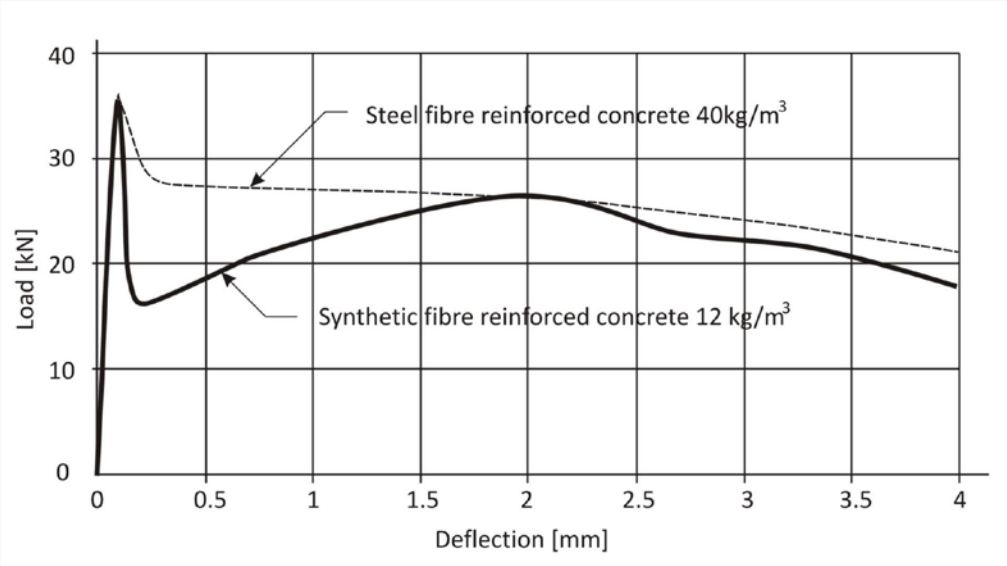


Figure 4: Comparison of the test results of steel and synthetic fibre reinforced concrete

Testing of fibre reinforced concrete

Two testing methods are used for verification of the load carrying capacity in bending. 1. Four point bending test (according to the Czech national code CSN P 732452 (CSN P, 2015) or similarly according to the German guide (Deutsche Ausschuss, 2010)) is made on the standard laboratory beam 150 x 150 x 700 mm which is subjected to four point bending test (Fig.5). The beam is without any notch, the crack originates in a general location. The crack appears at the weakest section, its position is not known in advance.

2. The second test is a 3-point bending test which follows the European code EN 14651 (EN 14651, 2007). A similar beam is tested, but there is a notch, which defines the location of the failure and the crack width is measured instead of the deflection. The scheme of the test is shown in Fig. 6.

The tested specimens in both methods are rather small. The fibres are often 60 mm long or sometimes even more, they are not distributed randomly, but they tend to follow the length of the mould. This effect is supported by the flow of FRC when the concrete is poured. The obtained results are sometimes more optimistic than an actual objective beam response. If the load carrying capacity of a structural element is dependent on fibre action (e.g. if additional bar

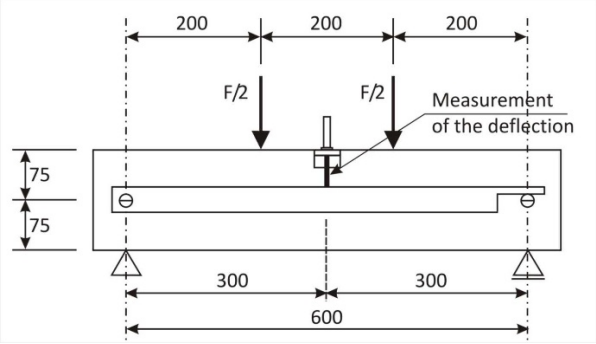


Figure 5: Three point bending test

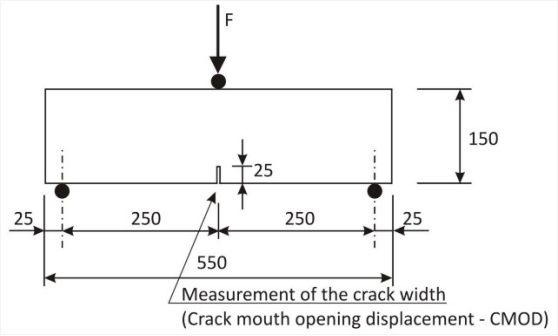


Figure 6: Three point bending test

reinforcement is missing), it is recommended to make a test of the actual element and not to rely only on the laboratory beam tests.

The test results often exhibit a significant statistical scatter (Vitek et al, 2015). Fig. 7 shows an example of tests of 36 beams which were cast during one day from identical concrete C45/55 in 2 batches. The steel fibre content was 35 kg/m3 (fibres 60 x 1mm, tensile strength 1500 MPa).

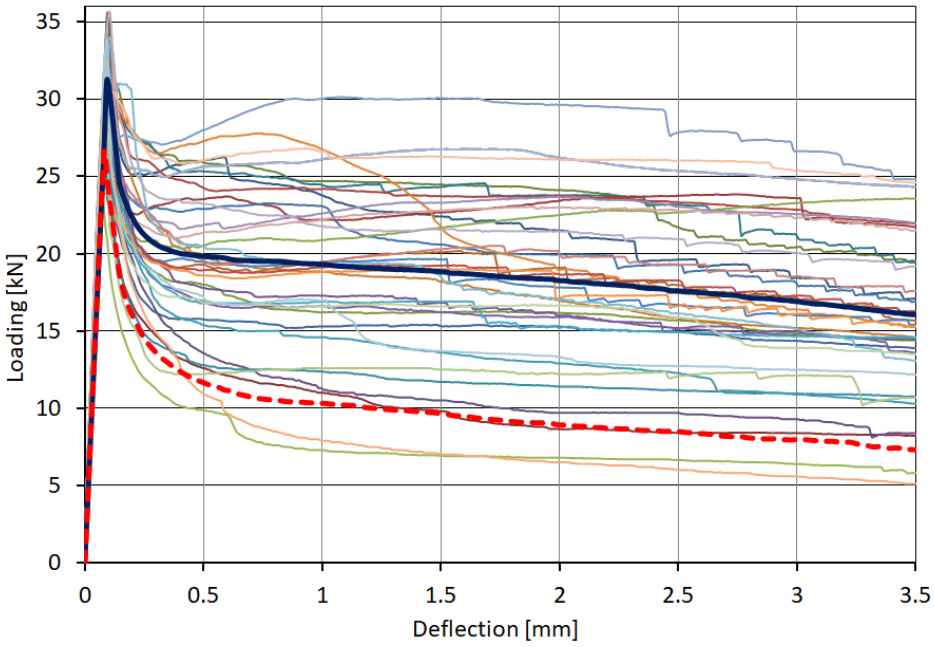


Figure 7: Results of the four-point bending test of 36 beams. Thick (blue) line = average values, dashed (red) line = characteristic values

3 Applications of FRC

Applications of pure FRC, i.e. FRC without additional bar reinforcement can be found in those structural elements where partial failure does not mean loss or reduction of safety. Such structural elements perform usually in interaction with soil, or they are parts of the structural system which allows for a significant redistribution of internal forces. Most typical applications are in industrial floors or in the tunnel linings. Industrial floors are concrete slabs supported by the soil base. The floor works similarly like a slab on elastic foundation; the load is partially

carried by a slab a partially by a subsoil. If slab failed, larger deflection activates the subsoil, but there is usually only very limited risk of larger damage.

In tunnel linings two typical applications can be found. Sprayed FRC can be used for primary linings in new Austrian tunnelling method. The lining is supported by the rock or soil massive and in case of a local cracking, the forces are redistributed.

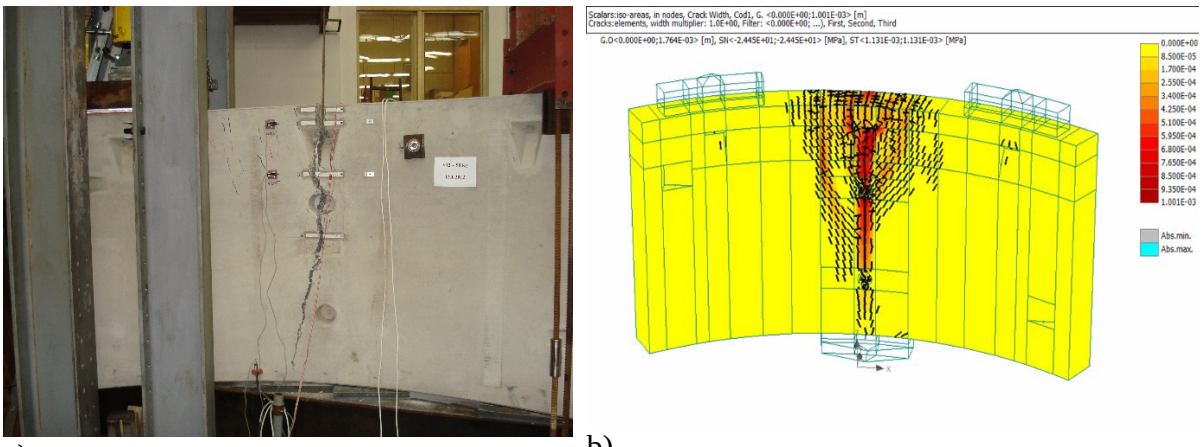
The other application of FRC can be in precast segments of final tunnel lining in TBM technology. The principle of function is also similar, the lining works in interaction with a rock/soil massive. There are two important loading situations. a) loading induced by a soil pressure in permanent loading combination. b) loading induced by hydraulic cylinders of the TBM during assembly of the tunnel lining. Long tunnels require a very large production of segments. Economical and reliable production can be optimized on the basis of experimental verification of structural performance of segments. Fig. 8a shows the bending test of the part cut off the actual segment. Finally, the segment failed in bending exhibiting one crack (Fig. 8b).



a) b)

Figure 8: a) Bending test of a tunnel segment, b) Wide crack before the failure

The effects of the loading by hydraulic cylinders during assembly of the lining were also experimentally tested (Fig. 9a). Beside that a nonlinear numerical analysis was carried out. The results are shown in Fig. 9b. Combination of experiments and numerical simulations contributed to optimization of fibre contents in FRC applied in a tunnel lining.



a) b)

Figure 9: a) Cracked segment under in plane loading, b) Results of a nonlinear numerical simulation

4 UHPC composition and material properties

UHPC is a cement composite, which is characterized by a very dense structure. The maximum aggregate size is limited usually to maximum 8 mm, but sometimes only to 1 mm. Water cement ratio is extremely low, cement content is high (600 to 1000 kg/m^3) and very fine materials like microsilica are used for filling of fine pores. Chemical admixtures (preferably excellent superplasticizers) make even the self-compacting UHPC with water-cement ratio lower than 0.25 possible. The very dense cement matrix does not allow water to penetrate into the material which results in excellent resistance against aggressive environment, including e.g. de-icing salts or sea water. The compression strength starts from 120 MPa and if a heat treatment is used during curing period, it can significantly exceed 200 MPa. The compression strength is dependent on the quality of constituents and on curing conditions. The experience from last decades shows that excellent durability can be achieved even at materials with rather low strength exceeding 120 MPa. The materials with higher strength are usually more expensive; it is suitable to find a reasonable compromise between the required properties and the costs. UHPC has high strength, but it is extremely brittle. When the compression strength is achieved, the specimen is immediately destroyed. Such property is unsuitable for structural applications. The fibres are added into the material to avoid its brittle behaviour. Most often high strength steel fibres are added. Their dimensions are different from those used in ordinary FRC. The fibres are usually short about 12-18 mm and rather thin 0.1-0.3 mm. The minimum fibre contents in UHPC for structural applications is 1.5% (vol.), in some applications the contents of 3% or more is required. UHPC is therefore sometimes called UHPFRC (ultra-high-performance fibre reinforced concrete). In structural applications UHPC is always reinforced by fibres, although sometimes non-metallic fibres are used.

Production of UHPC requires a good quality mixer and longer mixing time than ordinary concrete. Precast elements represent a main domain of new structures made of UHPC. But ready mixed UHPC can be produced too, and it can be transported even over long distances to the sites in truck mixers.

Tensile strength of UHPC is higher than that of ordinary FRC, but not so significantly as the compression strength. Materials with strain hardening and strain softening are distinguished similarly as ordinary FRC. For testing, the 3-point bending test according to EN 14651 is used most often. The classes defining the tensile properties are specified in guidelines for UHPC. Until now, no general guidelines were developed, but individual countries use their local recommendations e.g. SIA 2052 (2016), ÖBV (2023), TP267 (2024), etc.

Exceptional composition of UHPC exhibits also extraordinary properties which can be used appropriately in structural applications. Very low permeability allows for a reduction of concrete cover, which can lead to lower self-weight of structures with smaller dimensions. High density of UHPC and high cement contents results in very strong bond between UHPC and steel bars. The results of pullout tests are show in Fig. 10. The anchorage length was unified to 5 diameters of the steel bar. The tests of UHPC specimens finished by rupture of steel bars, while the bars from ordinary concrete were pulled off. Additional tests were executed, where the anchorage length was reduced. The results are shown in Fig. 11. The bars with anchorage length 5 and 4 diameters failed by steel rupture. The bars with anchorage length 3 and 2 diameters failed by pullout similarly as the bars with anchorage length 5 diameters anchored in ordinary concrete. Short anchorage lengths of bars in UHPC can be used also for a reduction of

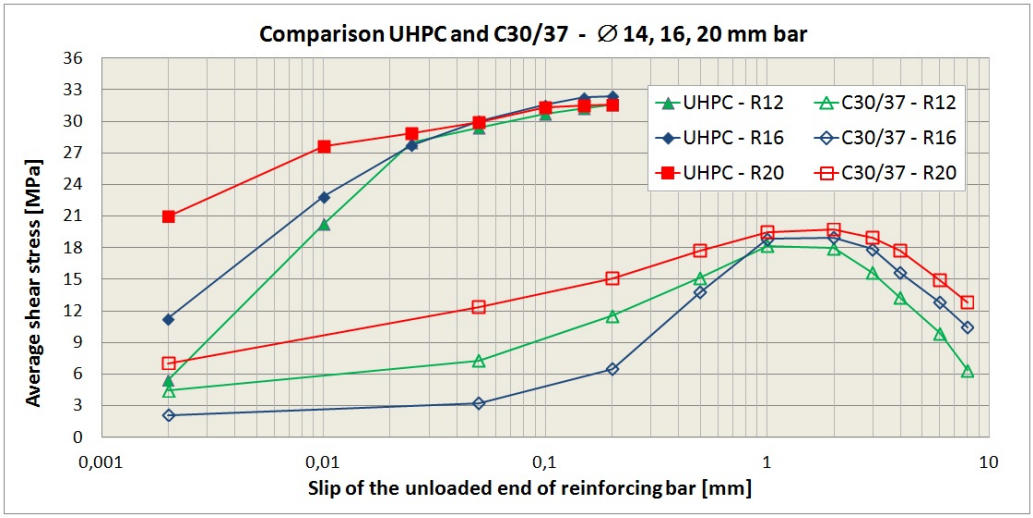


Figure 10: Comparison of the bond behaviour of UHPC and C30/37 with different bar diameters

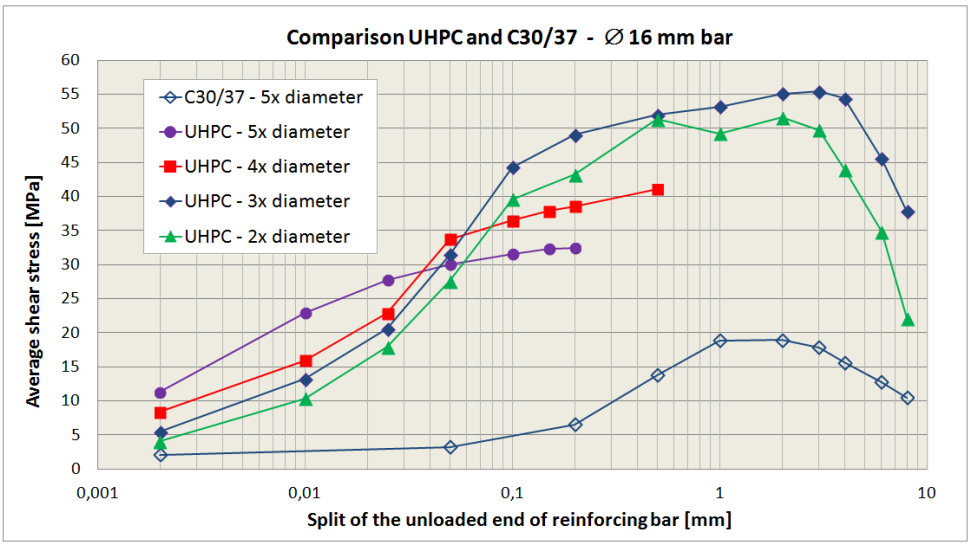


Figure 11: Comparison of the bond behaviour of UHPC and C30/37 with different anchorage length

overlaps of bars in working joints of structures. High strength of UHPC, if sufficient fibre contents is used, can be used for reduction or even avoidance of dense reinforcement under anchorages of prestressed tendons.

5 Application of UHPC in new structures

Advantages of UHPC, i.e. high mechanical parameters and its excellent durability can be applied in new structures. The self-weight of structures can be reduced, which brings additional savings in supporting structures and foundations. Lower weight is also good for transport and assembly of structural elements. Many applications were found in footbridges but also in precast bridge beams. UHPC became a domain for prestressed structures, where the high compression strength can be used. Pre-tensioned beams are very suitable because UHPC provides an excellent protection of strands against corrosion. The technology is very cheap. External prestressing is suitable for larger structures, since it allows for a design of thin and

light sections. Fig. 12 shows an example of a cable stayed footbridge with the main span 99 m long built in Czechia. The segments made of UHPC are directly exposed to the traffic without any surface layer or waterproofing. The bridge deck is prestressed by 2 external prestressing tendons located under the deck.



Figure 12: Cable stayed footbridge over Labe River in Luzec.

Fig. 13 shows an example of a beam footbridge with the span of 27 m. The footbridge is a single simply supported beam which is pretensioned. The strands are protected with UHPC which exhibits an excellent bond and complete elimination of cracks. The advantage of such bridge is a very low self-weight (3.6 kN/m^2), which made the assembly very simple. Two cranes installed the entire footbridge (31 t) in 2 hours, which reduced the closure of the street under the footbridge to about half a day including other associated works.



Figure 13: Simple beam footbridge in Tabor.

6 Application of UHPC in existing structures

High strength, excellent bond to ordinary concrete and high durability offer significant possibilities for strengthening of existing structures. Strengthening of existing bridges is a perspective area for UHPC applications. A thin layer of UHPC cast on the treated surface of

the bridge deck can play 3 roles: i) The levelling function makes the surface according to the required geometry, i.e. the unevenness in the surface of the deck can be levelled. ii) The strengthening function contributes to higher load carrying capacity of the bridge deck primarily in transversal direction (box girders) or to higher load carrying capacity of cantilevers. In the longitudinal direction the contribution to the load carrying capacity is usually smaller, but in combination with additional prestressing, it can become also significant. iii) The layer of UHPC can serve as a waterproofing. Then a high resistance against cracking is necessary, which requires a high fibre content (3% vol. or more). Last but not least the strengthening of the bridge deck with UHPC is rather fast. After removing of surface layers, the surface of the bridge deck must be treated and then the layer of UHPC is cast. It can be used directly for driving (usually grinding is necessary to achieve a good quality anti-slip surface) or the asphalt pavement is laid directly on the UHPC. The technology allows for shortening of closures of bridges. Large experience from difference countries can be found in special issue of Beton- und Stahlbetonbau Sonderheft, (2025). Fig. 14 shows an example of casting of UHPC layer using a finisher.



Figure 14: Casting of the UHPC using a finisher

7 Conclusions

Fibre reinforced concrete is a promising material. Dispersed reinforcement makes the casting process easier. The fibres are distributed in all parts of structural elements, also in the cover surface layer, which improves the resistance of structural elements against local damages. According to the number of fibres in FRC, behaviour with strain hardening or strain softening can be obtained. FRC without additional bar reinforcement or prestressing can be recommended for structures which allow for redistribution of internal forces in case of local damage which would guarantee sufficient ductility and robustness.

The paper presents two kinds of materials. Classical FRC has properties similar to ordinary concrete, the reinforcement is partly or fully replaced by fibres. UHPC is a special material made of high-quality materials. Its properties are different in comparison with ordinary concrete. The design of structural elements made of UHPC requires special attention. UHPC although it is a fibre reinforced composite has advanced properties which makes it possible to design structures lighter and more resistant against aggressive environment. Therefore, it can be recommended to use for the design preferably special guidelines developed for UHPC in different countries.

8 Acknowledgement

Partial results of the research project no. FV20472 supported by the Ministry of industry and trade were discussed. This support is gratefully acknowledged.

9 References

CSN P 73 2452. *Fibre-reinforced concrete – Testing of hardened fibre-reinforced concrete*. Institute for codification, metrology and state testing, 2015

Deutsche Ausschuss für Stahlbeton (DAfStb), *Richtlinie Stahlfaserbeton*. Beuth Verlag, Berlin, März 2010

EN 14651: 2005+A1:2007, *Test method for metallic fibered concrete – Measuring the flexural tensile strength (limit if proportionality (LOP), residual strength)*, CEN, 2007

Sonderheft, 2025. *Instandsetzung und Verstärkung von Brücken mit UHFB*, Beton- und Stahlbetonbau, Vol. 120, März 2025

ÖBV (Österreichische Bautechnik Vereinigung), 2023. *ÖBV Richtlinie UHPC*, Ausgabe März 2023, Wien

SIA 2052, 2016. *Ultra-Hochleistungs-Faserbeton (UHFB) – Baustoffe, Bemessung und Ausführung*. Schweizerische Ingenieur- und Architekturverein.

TP 267, 2024. *Ultra-high performance concrete (UHPC*), Technical specification of Ministry of transport of the Czech Republic, April 2024

Vitek, J.L., Smirinsky, S., Vesely, P., Kolisko, J., 2015. “Fibre distribution and efficiency in SFRC”. *Fibre concrete 2015*, CTU in Prague, Prague, Czechia, Sept. 2015

Material saving potential by using Steel Fibre Reinforced Concrete for Industrial Floors

Efim Griniov[1], Rewi Yolcu Sever[1], Dirk Schlicke[1]

[1]: Institute of Structural Concrete, Graz University of Technology, Graz, Austria.

Abstract

Concrete industrial floors are fundamental elements in production, storage, and logistics facilities. Conventional solutions are typically based on reinforced concrete slabs, where steel reinforcement is required to ensure both load-bearing capacity and crack control under serviceability conditions. In this context, Steel Fibre Reinforced Concrete (SFRC) represents a promising alternative, offering the potential to significantly reduce conventional reinforcement and overall material consumption.

This study investigates the material saving potential of SFRC industrial floors compared to conventionally reinforced concrete slabs. The analysis focuses on industrial floor systems with areas of up to 2500 m² and evaluates their structural performance under imposed deformations, soil-structure interaction, and mechanical loading from forklift traffic and storage rack systems. Both serviceability and ultimate limit state criteria are considered.

A comprehensive parametric study based on nonlinear finite element analyses is conducted to assess load-bearing behaviour, force redistribution, and crack development in SFRC slabs. The results demonstrate that the use of SFRC allows for a reduction in slab thickness and reinforcement demand while maintaining the required structural performance. Consequently, SFRC floor systems provide a more resource-efficient solution with reduced material consumption, simplified construction processes, and improved durability.

Keywords

Conventional reinforcement industrial floor, steel fibre reinforced industrial floor, material saving, nonlinear finite element analysis, crack width control, soil-structure interaction.

1 Introduction

Concrete industrial floors have been successfully designed and constructed for many decades. They serve as traffic surfaces, storage areas, and foundation elements, for example in high-rack warehouses, and must meet demanding performance requirements, including flatness, wear resistance, durability, and structural stability. Despite continuous advancements in concrete materials and well-established design approaches (DBV-Merkblatt SFRC 2013; DBV-Merkblatt 2017; Merkblatt ÖVBB 2021), recent years have seen an increasing number of damage cases in industrial floors, particularly under the combined effects of imposed and restrained deformations, as well as heavy forklift traffic and storage rack loads.

Industrial floors are typically constructed as large-scale slab systems. To accommodate imposed deformations, such systems are commonly subdivided by dilatation joints intended to reduce restraint stresses resulting from expected imposed deformations. However, these joints represent critical zones with respect to serviceability and durability. In practice, damage such as edge spalling and local deterioration frequently occurs at joints due to repeated dynamic loading from forklift traffic, leading to increased maintenance demands and higher life-cycle costs (Hohmann R. 2023; Wörner and Nordhues 2023).

This paper presents a comparative study of conventionally reinforced concrete floors and steel fibre reinforced concrete (SFRC) floors under defined design criteria. Both systems are designed to satisfy a crack width limit of 0.20 mm under serviceability conditions and to withstand loads from heavy forklift traffic and storage rack systems under ultimate limit state (ULS) conditions. The analysis is based on numerical finite element (FE) simulations, enabling a detailed assessment of structural behaviour under both serviceability (SLS) and ULS. Particular attention is given to the influence of restrained deformations, crack formation, and load-bearing capacity. For the reference case, a slab thickness of 25 cm is assumed. However, within a nonlinear analysis framework for SFRC floors, a reduction in slab thickness may be achieved, resulting in more resource-efficient solutions.

The results demonstrate the potential of SFRC floor systems to reduce joint-related damage, enhance durability, and optimize material usage compared to conventional reinforced concrete solutions. A holistic consideration of design, material behaviour, and soil-structure interaction is essential for achieving economically efficient and durable industrial floor systems.

2 Case Study for Concrete Industrial Floor

2.1 FE Modell of the concrete industrial floor

For this study, an industrial concrete floor geometry representative of practical applications was selected and modelled using a holistic finite element model. The numerical model represents an embedded industrial floor slab, discretized using 2D layer shell elements with a finite element size of 0.35 x 0.35 m. The FE analysis was performed using the software SOFiSTiK (SOFiSTiK AG).

The plan dimensions of the industrial floor were L_y=62.3 m in the y-direction and L_x=39.2 m in the x-direction, see Figure 1. Since the structure represents an industrial hall, column openings that were structurally decoupled from the slab and whose columns were supported on

footings were included in the model at regular spacings of 7.0 m in both directions. The openings for the footing supported columns have plan dimensions of 0.70 x 0.70 m.

For industrial floor with conventional steel bar reinforcement, concrete of strength class C30/37 was assumed, including an elastic modulus E_{cm} of 33000 MN/m². The slab was simulated using linear elastic material behaviour.

For the case of the steel fibre reinforced industrial floor, only the SFRC of strength class C30/37 with steel fibre strength class (SC) 2.0 and ductility class b was used, without any steel bar reinforcement. The characteristic residual flexural strengths were $f_{R,1k}$ of 2.0 MN/m² and $f_{R,3k}$ of 1.40 MN/m², in accordance with Annex L of the 2nd generation Eurocode 2 (prEN 1992-1-1:2023). The SFRC industrial floor was modelled using nonlinear material behaviour.

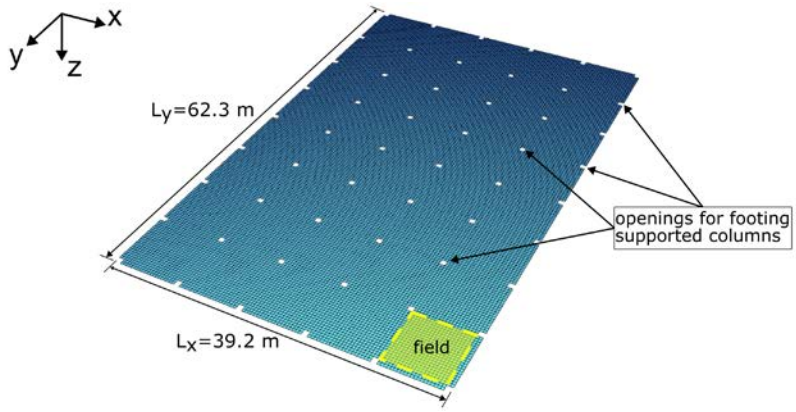


Figure 1: FE model of the concrete industrial floor

The interaction between the industrial floor and the soil was represented by a linear elastic half-space beneath the slab. The half-space was modelled with a depth of 50 m and consisted of two soil layers: a 0.20 m thick gravel base layer with a constrained modulus E_s of 100 MN/m², underlaid by a 49.8 m thick soil layer with a constrained modulus E_s of 40 MN/m². In the FE analysis, the horizontal stiffness of the half-space was assumed to be equal to 40% of the initial vertical stiffness in the z-direction.

2.2 Applied loads

2.2.1 Self-weight

The self-weight of the floor slab was automatically calculated within the FE software SOFiSTiK (SOFiSTiK AG) based on a concrete unit weight γ_c of 25.0 kN/m³ and included in the numerical model.

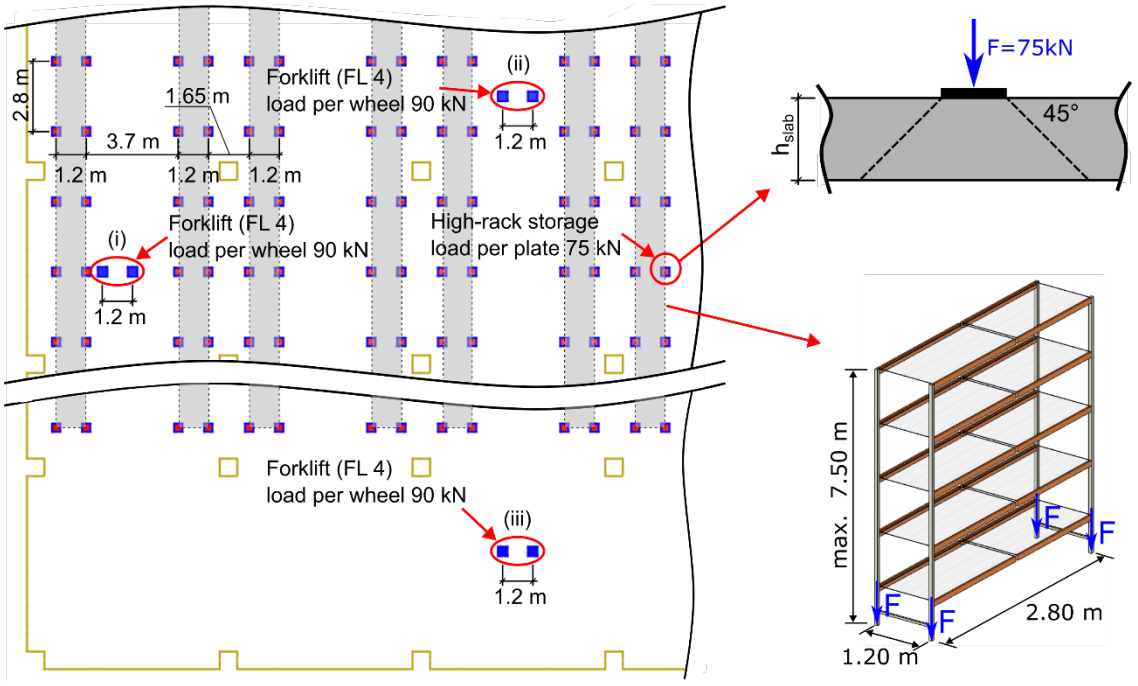
2.2.2 High-rack storage

To determine internal forces resulting from high-rack storage, double-row with spacings of 1.20 m between base plates in the transverse direction and 2.80 m in the longitudinal direction were considered. The maximum height of the racks is 7.50 m. The base plates measure 15 × 15 cm, with a maximum load of 75 kN per plate, see Figure 2. Load distribution through the floor slab thickness was assumed at an angle of 45°, in accordance with (EN 1991-2:2021).

The high-rack rows are oriented along the longitudinal axis of the floor slab. At the edges of the slab, a single row of racks is provided, whereas in the interior region, double-row racks are

arranged with an aisle width of approximately 3.70 m. The centre-to-centre distance between the double-row racks is 2.85 m.

To realistically capture the influence of forklift positioning, three representative load cases were modelled: (i) the forklift positioned at the centre of the aisle, laterally offset from a single high-rack row; (ii) the forklift positioned at the centre of the aisle, located between the base plates of the opposing high-rack rows and (iii) an isolated position without the influence of adjacent high-rack storage areas, see Figure 2.



(a) (b)

Figure 2:(a) Plan view single high-rack storage system and forklift loads, and (b) representation of the high-rack system

In the investigated warehouse, high-rack storage induces highly concentrated local point loads. These point loads result in elevated stress peaks in limited regions, necessitating careful modelling and appropriate evaluation of the simulation results. To avoid smearing of local loads due to the discretization of the FE mesh and resulting in unrealistic stress evaluation, a refined mesh with an element size of 0.35×0.35 m was adopted. This is consistent with the investigations presented in (Sever and Schlicke 2025), which indicate that such a mesh density is sufficiently fine for modelling local loads such as single rack base plates or forklift wheel loads.

2.2.3 Forklift load

To represent the dynamic loading induced by forklift traffic, a Class 4 (FL4) forklift with a wheelbase of 1.20 m was considered. In the finite element model, only the front wheels were taken into account, each carrying an axle load of 90 kN, in accordance with Eurocode 1 (EN 1991-1-1:2011). To account for dynamic effects associated with acceleration and deceleration, the axle load used for the internal force calculations was multiplied by a dynamic amplification factor of $\varphi = 2.0$, as specified in EN 1991-1-1:2011.

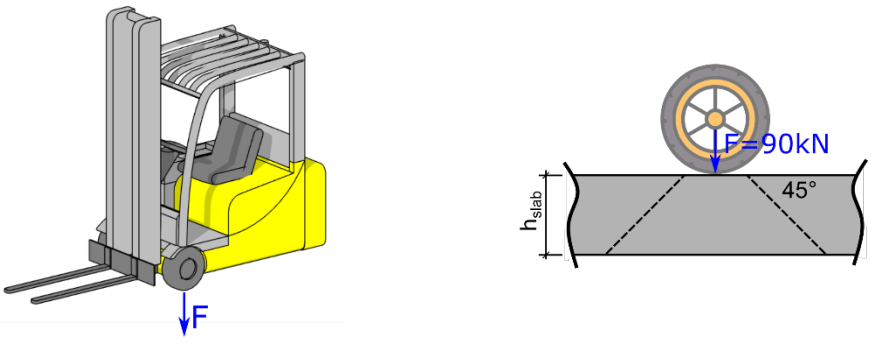


Figure 3: Representation of the forklift

The resulting wheel load corresponds to half of the axle load and was therefore equal to 90 kN per wheel, see Figure3. In the FE model, this load was applied as an equivalent distributed area load over the wheel contact area of 0.20 × 0.20 m, aligned along the slab centreline with a 45° distribution in accordance with (EN 1991-1-1:2011).

2.2.4 Imposed deformations

Imposed deformations were regarded with respect to drying shrinkage during the service life. With respect to rather sealed conditions at the bottom and free drying at the top surface the drying shrinkage was considered as a linear gradient ranging from 0.0 ‰ at the bottom surface to -0.10 ‰ at the top surface exposed to air. With regard to the constant part in the moist field of the 250 mm thick slab as well as parallel relaxation of the occurring restraint stresses due to creep it refers to a total shrinkage of 0.68 ‰.

3 Design of Conventionally Reinforced Industrial Floor

In this chapter, the numerical results are presented with a focus on the development of bending moments in the conventional reinforced concrete industrial floor. The assessment of the bending moments for the ULS and SLS were carried out using load combinations in accordance with Eurocode 0 (EN 1990:2013). According to (DBV-Merkblatt 2017), reduced partial safety factors for concrete and reinforcement steel bars may be applied for industrial floors with minor consequences of failure (low risk to life and health). The partial safety factors for concrete were set to $\gamma_c = 1.35$ and for steel to $\gamma_s = 1.15$.

3.1 Linear Elastic Analysis in the SLS and ULS

Figure 4 presents the bending moments m_{xx} and m_{yy} in the *x*- and *y*-directions of the concrete industrial floor for the ULS and SLS permanent load combinations.

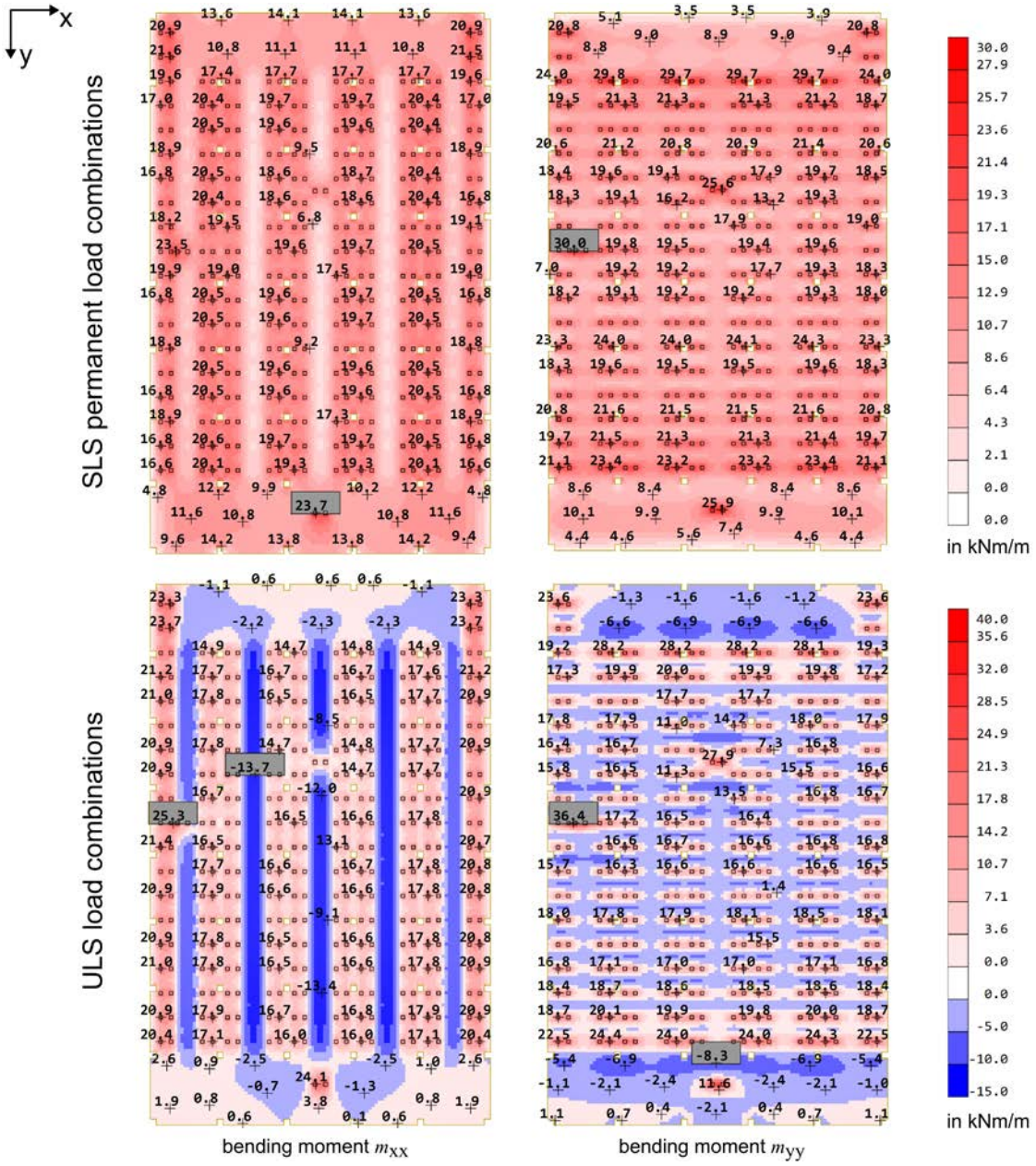


Figure 4: Distribution of bending moments m_{xx} and m_{yy} in conventional reinforced industrial floor

As shown in Figure 4, the ULS load case produces a maximum positive bending moment m_{yy} of 36.40 kNm/m at the position where the forklift is located at the centre of the aisle with an offset from a single high-rack row (i). The maximum positive bending moment m_{xx} of 25.30 kNm/m occurs at the centre of the aisle.

For the SLS permanent load combination, the maximum positive bending moment also occurs in the *y*-direction where the forklift is positioned at the centre of the aisle with offset from a single high-rack row (i) and amounts to 30.0 kNm/m. The corresponding maximum positive moment m_{xx} is 23.70 kNm/m.

3.1.1 Design in ULS and SLS

For the bending design of a conventional concrete industrial floor, a 1.0 m wide cross section of the concrete industrial floor is considered. A parabolic-rectangular stress distribution is assumed for the compression zone, see Figure 5. The bottom reinforcement is designed such that it can resist the applied bending moment m_{yy} of 36.40 kNm/m. The required reinforcement is calculated as 3.70 cm²/m, while the provided reinforcement (Ø10/15) corresponds as $a_{s,prov} = 5.24\ cm^2/m$. The resulting design bending resistance m_{Rd} is 51.1 kNm/m.

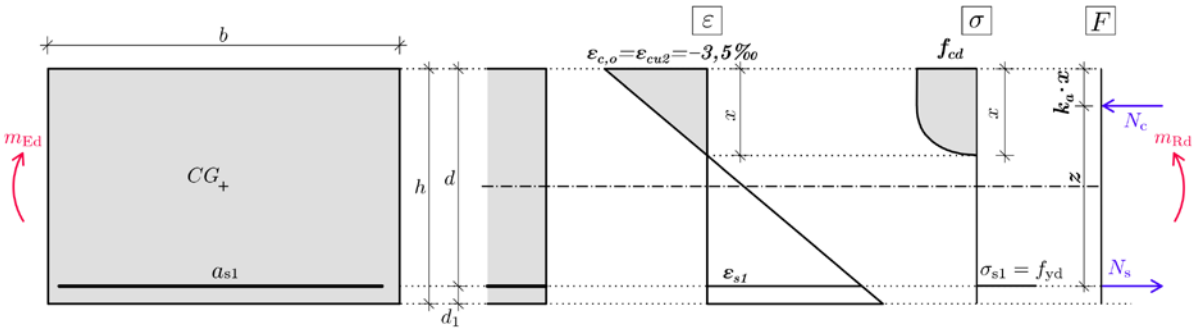


Figure 5: Bending design of the concrete industrial floor cross-section

The top reinforcement of the slab due to restraint stress induced by drying shrinkage is calculated according to Eq. 9.4 of (prEN 1992-1-1:2023), resulting in a required reinforcement area of 1.05 cm²/m The provided reinforcement (Ø8/25) corresponds to $a_{s,prov} = 2.01\ cm^2/m$ in both the *x*- and *y*-directions.

3.1.2 Calculation of Crack Width

The crack width calculation according to Eurocode 2 (EN 1992-1-1:2015) and Model Code 2010 (fib 2012) is based on an approach employing a mean bond stress, typically assumed as a constant value of $1.8 \cdot f_{ct,eff}$. However, studies reported in the literature indicate that a mechanically consistent approach allows for a more accurate prediction of crack widths. Accordingly, the recommended methodology is adopted in the present study.

For the verification of the crack width limit of 0.20 mm, the approach proposed by (Schlicke D. et al. 2021; 2022) and (Tue NV et al. 2021) is adopted. In contrast to the normative calculation models specified in EN 1992-1-1 and Model Code 2010, this approach does not assume a constant mean bond stress independent of the cracking state and crack width. The parameters required for the calculation of crack widths according to Eq. 1, representing the characteristic crack width in the single-crack stage, are taken from Table 1.

$$w_k = \frac{\sigma_{s1} \cdot \emptyset_s}{2 \cdot \tau_{sm} \cdot (1 + \alpha_e \cdot \rho_s)} \cdot \left[\frac{\sigma_{s1}}{E_s} \cdot (1 - k_t)\right] \quad (1)$$

The steel stress in the bottom reinforcement is determined under the SLS permanent load combination. For the applied bending moment $m_{yy} = 30.0\ kNm/m$, this results in steel stress of σ_{s1} 287.6 MN/m².

Table 1: Parameters for the crack width calculation

Parameter:	**Value:**
Tensile strength of concrete $f_{ct,eff}$ in MN/m²	2.90
Bond parameter α [-]	0.30
Bond parameter C [-]	0.35
Parameter λ [-]	2.86
Steel stress σ_{s1} in MN/m²	287.6
Modular ratio $\alpha_e = E_s/E_c$ [-]	6.06
Tensile reinforcement ratio ρ_s in %	0.73
Elastic modulus of steel E_s in MN/m²	200000
Diameter steel bar reinforcement $\emptyset_s$ in mm	10.0
Coefficient dependent on the duration of the load k_t [-]	0.60

Based on the calculated mean bond stress τ_{sm} von 3.56 MN/m² and the parameters given in Table 1, a maximum characteristic crack width of 0.195 mm is obtained, which is below the allowable limit of 0.20 mm.

4 Design of Steel Fibre Reinforced Industrial Floor

In this chapter, the numerical results are given with focus on the development of bending moments in the SFRC industrial floor. The assessment of the bending moments for the ULS and SLS were carried out using load combination in accordance with (EN 1990:2013). The nonlinear simulations were performed based on the γ_R-method and a global partial safety factor of 1.40 was applied to the entire FE model (DAfStb Stahlfaserbeton 2021).

4.1 Constitutive laws for nonlinear FE simulations

The stress-strain curve of SFRC was calculated according to the (prEN 1992-1-1:2023) Eq. L.7 to L.11 and implemented in the FE-program SOFiSTiK. The stress-strain relationships for the SFRC industrial floor are characterized by two parameters: the fibre orientation factor K_O and the component size factor K_G. For foundation slabs, K_O is 1.0 and K_G is 1.27. These factors account empirically for the fibre orientation developing during the concrete casting process and for the influence of member size on the coefficient of variation.

The value of $K_G = 1.27$ was calculated according to Annex L of (prEN 1992-1-1:2023) using the expression $K_G = 1.0 + 0.5 \cdot A_{ct} \leq 1.5$. The effective tensile area A_{ct} was calculated as $0.9 \cdot h \cdot b$ in accordance with (DAfStb Stahlfaserbeton 2021). To account for a flexural failure mechanism governed by three plastic hinges, this value was multiplied by a factor of three. This approach reflects the fact that the load-bearing system develops a three-hinge mechanism at ultimate load.

This study presents and discusses a design based on SC 2.0 b. This combination of strength and ductility corresponds to a fibre dosage of approximately 25-30 kg/m³. Figure 6 illustrates the stress-strain constitutive laws implemented in SOFiSTiK for concrete of strength class C30/37. The stress-strain relationship for SC 2.0 b is derived from experimental results (ArcelorMittal 2024).

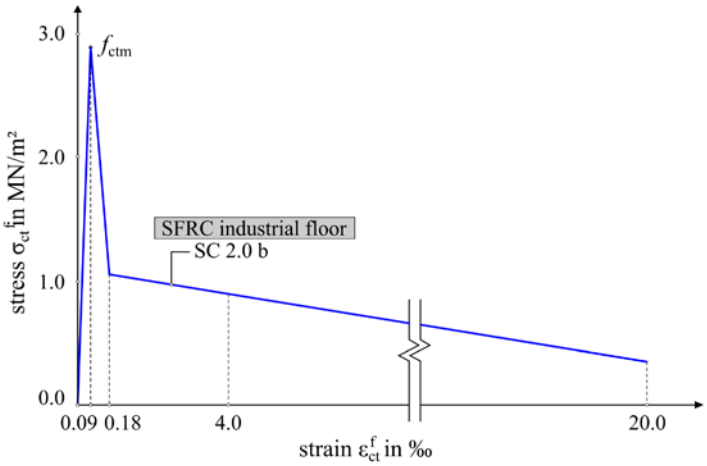


Figure 6: The tensile stress-strain behaviour of SFRC in SOFiSTiK

The stress-strain relationship of the SFRC under compressive loading was applied based on the work of (Zilch and Tecusan 2017) using the calculated mean value $f_{cR} = 0.85 \cdot \alpha_{cc} \cdot f_{ck}$ for concrete in SOFiSTiK.

4.2 Nonlinear analysis in the SLS and ULS

Figure 7 presents the principal tensile strains of the SFRC industrial floor model with a slab thickness h of 0.20 m. The thickness was iteratively reduced to this value until equilibrium of the FE model could still be achieved. The principal tensile strains are shown for both the bottom and top surfaces of the slab under the loading conditions described in Section 2.2.

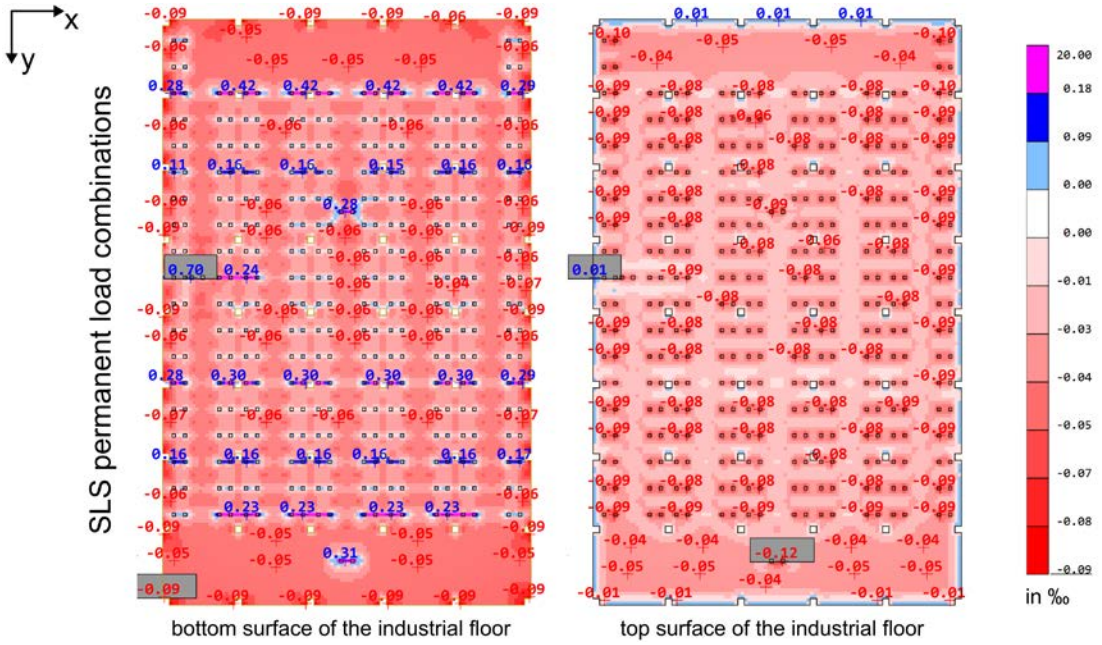


Figure 7: Principal tensile strain ε_I in SLS for SFRC industrial floor

In the nonlinear analysis, the tensile stresses are limited to the tensile strength of the concrete. Therefore, an evaluation of the tensile strains provides a more meaningful basis for interpreting

the structural response. In the present study, the cracking tensile strain, defined as $\varepsilon_{cr} = f_{ct}/E_c$ is 0.09 ‰. As shown in Figure 7, principal tensile strains at the bottom surface of the SFRC industrial floor exceed this value, while those at the top surface remain below it. This indicates that the tensile strength of the concrete is exceeded at the bottom surface and that cracking initiates in this region. The resulting crack formation under the applied loads is reflected in the crack width distribution shown in Figure 8, with a maximum crack width of 0.11 mm.

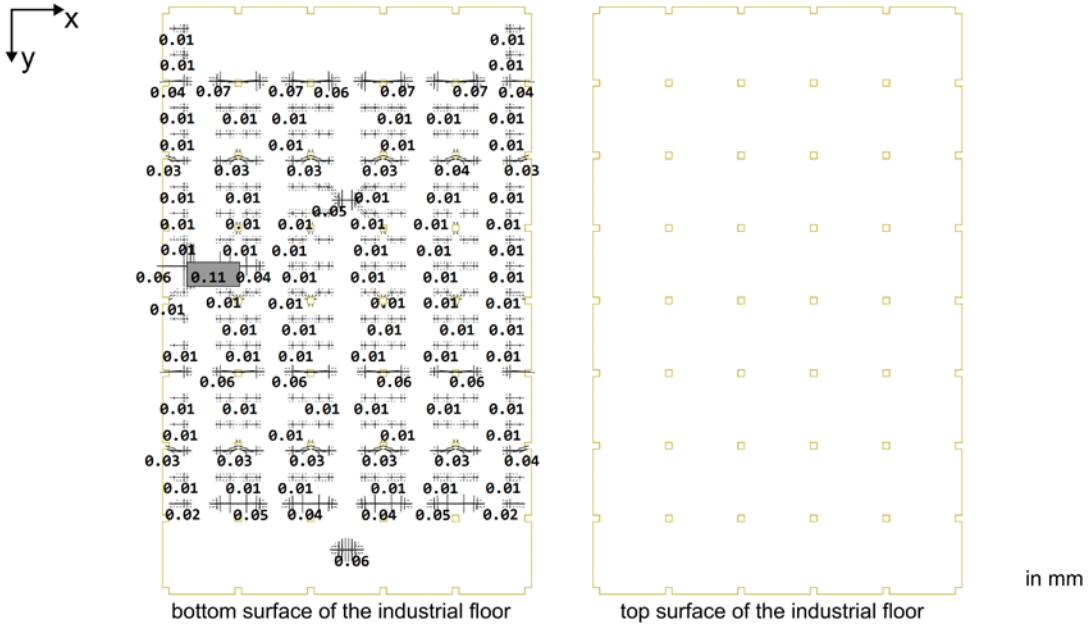


Figure 8: Crack width in SLS for SFRC industrial floor

For the evaluation of the structural behaviour of the SFRC industrial floor under ultimate limit state conditions, the convergence of the FE simulation is considered. In particular, the residual forces are monitored, and a convergence criterion of 2 % is applied. The FE analysis under ULS conditions demonstrates that the verification criterion is satisfied.

5 Material Saving Potential

In this chapter, the potential savings in steel and concrete are evaluated. For the conventionally reinforced industrial floor designed to satisfy both ultimate and serviceability limit state requirements, a total reinforcement area of 14.5 cm²/m in each direction at both surfaces is required for a slab thickness of 25 cm. Assuming a steel density of 7850 kg/m³, this corresponds to approximately 11.4 kg/m² of reinforcing steel. In contrast, the SFRC industrial floor requires approximately 30 kg/m³ of steel fibres, corresponding to about 6.0 kg/m² for a slab thickness of 20 cm. Accordingly, the investigated SFRC solution results in a reduction in total steel consumption of approximately 47 %.

In addition to the reduction in steel demand, the use of SFRC enables further savings in concrete due to the reduced or eliminated requirement for conventional reinforcement cover. In the present study, this leads to a reduction in slab thickness of 5 cm, corresponding to approximately 20 % less concrete volume. Consequently, the number of concrete deliveries is reduced, the required excavation depth is decreased, and the overall construction effort is lowered.

Furthermore, the use of SFRC eliminates the need for conventional reinforcement placement. As a result, processes such as delivery, storage, and installation of reinforcing bars are significantly reduced, leading to advantages in terms of construction time, cost efficiency, and logistical effort.

6 Conclusion

In the present study, an industrial floor slab reinforced with two different reinforcement concepts was investigated and compared: conventional reinforcement and steel fibre reinforcement. The conventionally reinforced slab was designed according to current engineering practice, with internal forces determined by linear elastic analysis, followed by a nonlinear cross-sectional design to verify the load-bearing capacity. For SFRC slab, both the determination of internal forces and the design verification were performed using a nonlinear analysis approach in accordance with the Annex L of Eurocode 2:2023, considering the post-cracking tensile resistance of SFRC. The results show that the SFRC floor system satisfies both serviceability and ultimate limit state requirements, including compliance with the crack width criterion under the applied loading conditions.

A major advantage of SFRC is its material-saving potential. In the investigated case, the SFRC solution reduced steel consumption by approximately 47 % and concrete volume by approximately 20 % compared with the conventionally reinforced reference floor system. In addition, the elimination of conventional reinforcement placement simplifies construction and reduces logistical effort. These material savings are expected to contribute to a lower environmental impact. The reduced consumption of steel and concrete, combined with simplified construction processes and reduced transportation effort, is likely to result in lower CO_2 emissions. In addition, the elimination of reinforcement placement reduces construction time and logistical complexity.

Furthermore, SFRC floor systems show improved performance with respect to durability and serviceability. The distributed fibre reinforcement enhances crack control particularly by avoiding macrocracks as the would typically occur in conventionally reinforced industrial floors. It also reduces the risk of joint-related damage, which is a common issue in conventionally reinforced industrial floors subjected to repetitive forklift loading. Overall, SFRC industrial floors represent a resource-efficient and durable solution with clear advantages in terms of material consumption, environmental impact, and structural performance, offering a promising approach for future industrial floor construction, particularly in projects where sustainability and cost efficiency are key considerations.

7 References

ArcelorMittal (2024): ArcelorMittal. Available online at https://barsandrods.arcelormittal.com/wiresolutions/steelfibres/products/hooked_end_fibres_he.

DBV-Merkblatt (2017): Industrieböden aus Beton / Industrial Concrete Floors. Fassung Februar 2017. Berlin: Deutscher Beton- und Bautechnik-Verein e.V (Merkblatt Industrieböden).

DBV-Merkblatt SFRC (2013): Industrieböden aus Stahlfaserbeton / Steel Fibre Reinforced Industrial Concrete Floors. Besonderheiten bei Bemessung und Konstruktion, Herstellung und Ausführung / Special Features of the Design and Detailing, Production and Conformity. Fassung Juli 2013. Berlin: Deutscher Beton- und Bautechnik-Verein e.V (Merkblatt Industrieböden).

DAfStb Stahlfaserbeton 2021, 2021: Stahlfaserbeton - Richtlinie des Deutschen Ausschusses für Stahlbeton (DAfStb).

EN 1991-1-1:2011, 2011: EN 1991-1-1:2011:Eurocode 1: Actions on structures - Part 1-1: General actions - Densities, self-weight, imposed loads for buildings.

EN 1992-1-1:2015, 2015: EN 1992-1-1:2015: Design of concrete structures.

EN 1990:2013: ÖNORM EN 1990:2013: Eurocode – Basis of structural design.

EN 1991-2:2021, 10/1/2021: ÖNORM EN 1991-2: Actions on structures - Part 2: Traffic loads on bridges.

fib (2012): Model Code for Concrete Structures 2010 (fib CEB-FIP).

Hohmann R. (2023): Fugen und Durchdringungen bei wasserundurchlässigen Bauwerken aus Beton. In K. Bergmeister, F. Fingerloos, J.-D. Wörner (Eds.): Betonkalender 2023 Teil 1. 2 volumes. Berlin: Ernst & Sohn, pp. 107–156.

Merkblatt ÖVBB 2021, August 2021: Herstellung von monolithischen Betonplatten.

prEN 1992-1-1:2023, 2023: prEN 1992-1-1 - Design of concrete structures.

Schlicke, D.; Krenn, C.; Mayer, M.; Betschoga, C. (2022): FE-basierteVerifikation der Rissbreitenberechnung nach DAfStb-Heft 466. In *Beton- und Stahlbetonbau* (9), pp. 666–679. Available online at https://doi.org/10.1002/best.202200055.

Schlicke D, Dorfmann EM, Fehling E,Tue NV. (2021): Calculation of maximum crack width for practicaldesign of reinforced concrete. In *Civil Engineering Design* (3), pp. 45–61. Available online at https://doi.org/10.1002/cend.202100004.

Sever, Y.; Schlicke, D. (2025): Modeling of local load applications in embedded slabs using finite element method. In *Beton- und Stahlbetonbau* 120 (6), pp. 426–433. DOI: 10.1002/best.202500013.

SOFiSTiK AG: SOFiSTiK. Version, 2024. Available online at https://www.sofistik.com.

Tue NV, Fehling E, Schlicke D,Krenn C. (2021): Crack width verification and minimum reinforcementaccording to EC 2: Current model with specifications in Germany and Austria vs proposal for revision. In *CivilEngineering Design* (3), pp. 210–218. Available online at https://doi.org/10.1002/cend.202100045.

Wörner, J.-D.; Nordhues, H.-W. (2023): Betonbau beim Umgang mit wassergefährdenden Stoffen. In K. Bergmeister, F. Fingerloos, J.-D. Wörner (Eds.): Betonkalender 2023 Teil 1. 2 volumes. Berlin: Ernst & Sohn, pp. 185–206.

Zilch, K.; Tecusan, R. (2017): Sicherheitsaspekte bei nicht-linearen FEM Berechnungen/Safety aspects in non-linear FEM calculations. In *Bauingenieur* 92 (12), pp. 518–527. DOI: 10.37544/0005-6650-2017-12-34.

Improving punching shear capacity in flat slabs using SIFCON with 3D steel reinforcing elements

Wisam K. Tuama[1], and György L. Balázs[1]

[1]: Department of Construction Materials and Technologies, Faculty of Civil Engineering, Budapest University of Technology and Economics, 1521 Budapest, Hungary.

Abstract

Flat slabs are particularly vulnerable to punching shear failure, which may happen in a brittle way. The objectives of the present extensive experimental study are to demonstrate reasonable use of Slurry Infiltrated Fiber Concrete (SIFCON). SIFCON is used in a quick and easy way, applying the fibers and then the mortar only where it is required as an addition to the conventional reinforcement. Present research is directed to the potential use of SIFCON in flat slabs using 3D steel fibers. Another type of fiber, hooked-end steel fiber, was used to provide the comparison. Six square flat slab specimens were cast; four of these were reinforced with flexural steel bars, whereas the others were not. The experimental results are presented, including first crack, peak load, deflection, ductility, and the crack pattern, as well as the rotation and the inclination of cracks of each specimen. According to the test results, the measurements demonstrate that SIFCON with 3D steel reinforcing elements is a highly effective material for increasing punching shear resistance, as well as for improving post-peak behavior and ductility.

Keywords

Flat slab, punching shear, Slurry Infiltrated Fiber CONcrete, 3D steel fibers, post-punching behavior.

1 Introduction

Flat reinforced concrete floor slabs are widely used in modern construction. The production technique relies on a flat, level formwork deck, which streamlines site operations and speeds up construction. In multi-story structures, the reduced structural depth enables more floors to be built within the same overall height. This efficiency reduces the amount of façade materials, partition walls, and mechanical, electrical, and plumbing runs, resulting in significant savings in both resources and costs (Weerasinghe et al. 2020; Tuama and Balázs 2025). The primary weakness of this roofing system is its susceptibility to punching shear failure, particularly when utilizing normal strength concrete (NSC) for flat slabs, which is brittle and vulnerable to such failures occurring around columns at designated intervals. To increase the punching shear strength of flat slabs made of normal-strength concrete, engineers have identified many strategies. These include adding drop panels, thickening the slab, adding column capitals, increasing shear reinforcement, and utilizing advanced materials such as fiber reinforced polymer (FRP) (Halvoník et al. 2019; Saleh et al. 2019; Tahmoorian et al. 2021)

For this purpose, prior studies have investigated the possibility of using fiber reinforced concrete (FRC) to enhance the punching shear capacity of reinforced slabs (Zamri et al. 2022). Slurry Infiltrated Fiber Concrete (SIFCON) is a specialized type of FRC with the fiber volume percentage remarkably high, ranging from 4% to 20%. (Tuama and Balazs 2025). SIFCON has a

different production method; a dense quantity of loose steel fibers is placed in the mold first, and a highly fluid mortar is then infiltrated to occupy the gaps between fibers. This manufacturing process creates a composite that is very tough and has significantly improved strength in compression, tension, shear, and impact resistance (Tauma and Balázs 2023).

While steel fibers are extensively used in SIFCON mixes, previous research has completely overlooked the use of three dimensional (3D) steel fibers. Most past studies have concentrated on regular steel fibers, such as hooked, crimped, straight, or micro-steel fibers, but there is little research on fiber shapes that can better interlock or fit together. The novel reinforcing element has a unique, three-dimensional shape. Csongor Czintos created and patented the technique of bending a single wire into four closed loops that are connected in the center. The novel reinforcing element can have varying diameters and loop lengths to satisfy the needs of diverse applications. The working system of STAREX elements is efficient when the loops overlap sufficiently. Without overlapping, there is no interaction. By compressing the concrete between each loop, force is transferred from one to the next (NA 2009).

Published studies on the use of SIFCON concrete to improve the punching shear capacity of flat slabs are still limited. In this study, specimens of reinforced concrete flat slabs and SIFCON flat slabs were cast and tested by subjecting them to concentrated loading. Two types of steel fibers were investigated: (1) 3D steel fibers, used for the first time in SIFCON flat slabs, and (2) hooked-end steel fibers. By comparing the findings, the study measures how the use of SIFCON concrete and the chosen fiber shape affect the punching shear capacity of flat slabs.

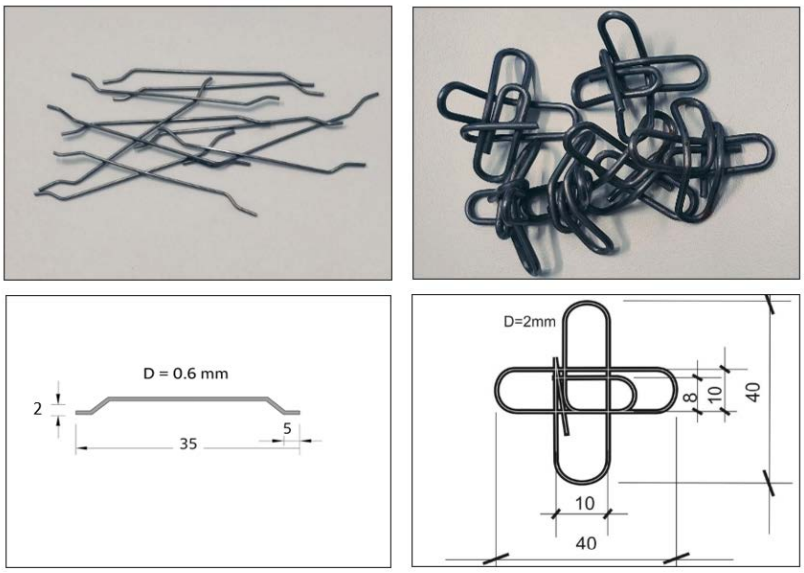
2 Experimental work

2.1 Constituent materials and mix proportions

This study details the material composition, which integrates SIFCON and NSC, in Table 1. For SIFCON, normal quartz sand with a maximum particle size of 1 mm and 4 mm is used as a fine aggregate. For NSC, 4/8 mm and 8/16 mm are used as coarse aggregates. The binding materials consist of Portland cement type CEM I (42.5) and silica fume. To guarantee optimal workability for the SIFCON mixture, the high range water reducing additive Master Builders Solutions was utilized. Flexural reinforcement was implemented in accordance with ACI 318-19 (ACI 318, 2019), utilizing Ø10 mm deformed bars placed on the tension side of the slabs to facilitate punching shear as the predominant failure mode. This study incorporated hooked-end and 3D geometry steel fibers at a volume fraction of 6 to 9%. Figure 1 illustrates the type of fiber utilized, while Table 2 delineates its technical specifications, as provided by the manufacturer.

Table 1 NSC and SIFCON optimal mixing proportions for 1 m^3

Cement (kg/m^3)	**Sand (0.4-1) mm (kg/m^3)**	**Sand (1-4) mm (kg/m^3)**	**Coarse agg. (kg/m^3)**		**Silica fume kg/m^3 10% rep.**	**Steel fiber %**	**w/b or w/c ratio**	**SP (by wt. of binder) %**
			(4-8) mm	**(8-16) mm**				
370	--	924	462	462	--	--	50%	--
873	970	--	--	--	97	6	30%	1.75%



(a) (b)

Figure 1 Steel fibers, the dimensions are millimeters (a-hooked-end and b- Starex 3D)

Table 2 Technical properties of the steel fibers

Fiber type	**Length** (mm)	**Diameter** (mm)	**Density** (kg/m^3)	**Tensile strength** (MPa)
Hooked-end	35 ±5%	0.6 ±5%	7,850	1350
Starex 3D	42 ±1%	1.5 ±5%	7,850	1250

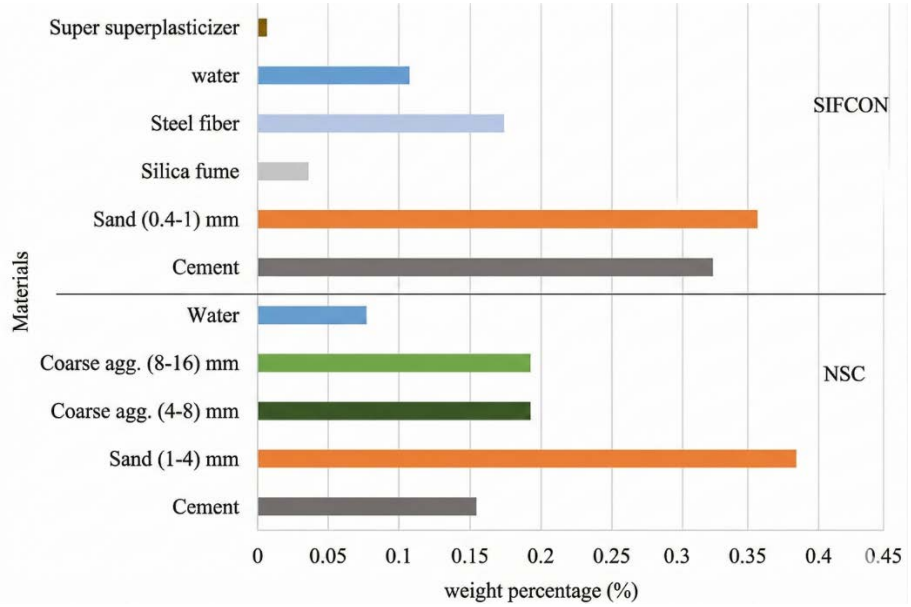


Figure 2 Materials proportion used in NSC and SIFCON mixture (% of total mix weight)

Figure 2 depicts the percentage of materials utilized in both NSC and SIFCON combinations, relative to the overall weight of the mix. This study selected a fiber volume content of 6% for the hooked-end fiber, as it was optimal for the mold dimensions; the same ratio was also applied

to the 3D fiber for subsequent comparison, alongside an additional fiber percentage of 9%, which the mold could accommodate. The mixing technique employed for the SIFCON slurry mixture was formulated based on prior research and initial experiments to guarantee excellent workability. The initial stage of the mixing process entailed integrating the dry components for three minutes. Thereafter, two-thirds of the water, pre combined with the superplasticizer, was incorporated and mixed for an additional 3 minutes. The final one third of the water, which also included superplasticizer, was subsequently added, and mixing persisted for an additional 2 minutes.

2.2 Specimen preparation and experimental testing

As part of this study, we test the flexural and compressive strengths of SIFCON and NSC concrete at 7 and 28 days for each substance and test type. The main objective of this research was to study the structural behavior of flat slabs under concentrated loading. The experimental program consisted of testing 6 slab specimens; one reference specimen was cast with NSC. 2 SIFCON flat slab specimens were cast using SIFCON with hooked-end steel fibers. 3 SIFCON flat slab specimens cast using SIFCON with 3D steel fibers. In this study, square concrete slabs were utilized as test specimens, each measuring 600 mm on each side with a constant thickness of 60 mm. The specimens were classified according to the type of concrete and fibers, as presented in Table 3 as well as Figure 3 show the specimen dimensions and layout of NSC and SIFCON flat slabs with reinforcement details.

Prior to the casting process, all constituent materials were carefully prepared and proportioned according to the mix volume. Steel molds were thoroughly cleaned, coated with release agent, and leveled on a flat surface. The sequence of casting for various concrete types is illustrated in Figure 4. For slabs made with NSC, reinforcement meshes were accurately placed inside the molds, ensuring proper bottom cover, as shown in Figure 4a. In SIFCON slabs, the steel fibers were introduced in a single batch into the mold before the slurry was poured, allowing the mix to penetrate and encapsulate the fibers, as shown in Figure 4b and 4c.

Table 3 The symbols of the flat slab specimens and their meanings.

No.	Symbol	Concrete type	Fiber type	Volume of fibers (%)	Conventional reinforcement
1	N	NSC	without	without	with
2	S	SIFCON	hooked-end	6	without
3	S+R	SIFCON	hooked-end	6	with
4	S3D	SIFCON	3D Starex	6	without
5	S3D+R	SIFCON	3D Starex	6	with
6	S3D9+R	SIFCON	3D Starex	9	with

Once mixing was complete, the fresh concrete was placed into the molds. The flat slab specimens were cured under wet coverings saturated with water, while additional samples were cured in a water tank maintained at a temperature of 23 ± 2 °C. Before testing, the flat slab specimens were coated with white emulsion to improve crack visibility. All specimens were tested at 28 days using a calibrated 600 kN electro-hydraulic testing machine under increasing concentric load until failure, as shown in Figure 5. The slabs were simply supported on four edges with a span of 500 mm using a square steel supporting frame.

Load was applied through a 60×60×15 mm steel plate connected to the actuator, at a constant rate of 0.5 mm/min. LVDTs were placed at the slab center and at two opposite quarter-span

points to measure deflection. During testing, the first crack load, peak load, ultimate load, central deflection, and average quarter-span deflection were recorded. Ultimate deflection was defined at 80% of the peak load (Chao et al. 2016). To assess the post-peak response of high ductility SIFCON, two ultimate deflection levels were considered: u_1 at 80% of the peak load after peak load and u_2 at 60% of the peak load after peak load.

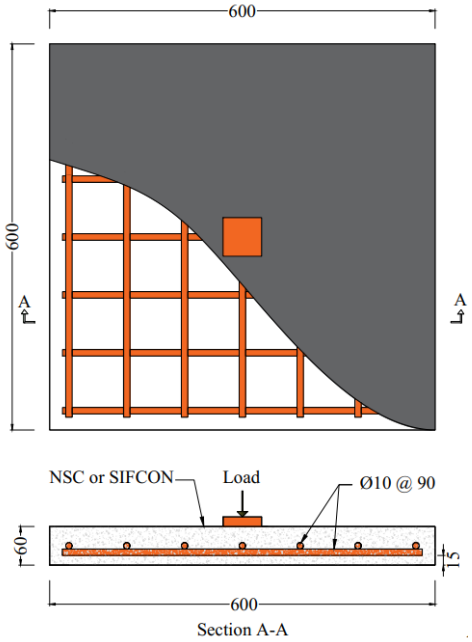


Figure 3 Specimen dimensions and layout of NSC and SIFCON flat slabs with reinforcement details

3 Results and discussion

3.1 Mechanical properties

The study of the mechanical properties of concrete is essential to understand the behavior of the concrete flat slab specimens. In this study, the mechanical properties of hardened SIFCON and NSC, consisting of compressive strength and flexural tensile strength, were tested at the ages of 7 and 28 days for the cubes prepared for this purpose. SIFCON concrete using hook-end steel fibers with a volume fraction of 6%, and 3D steel fibers with a volume fraction of 6% and 9%, was tested in this study. Table 4 shows the results of the compressive strength and flexural tensile strength, as well as the percentage increase of strength at 28 days compared to NSC.

The results show that the compressive strength of SIFCON with any fiber type is much higher than that of NSC. The SIFCON concrete containing hooked-end steel fibers showed the highest increase of 174% compared to the reference NSC. The result is consistent with the studies of many researchers (Soylu and Bingöl 2019; Sonone et al. 2020; Naji et al. 2021). The curved ends of the hooked-end steel fibers enhance the interaction between the two sides of the samples during failure.

As a result, the SIFCON reinforced with hooked-end steel fiber achieved the highest flexural strength value of 32 MPa. The increase in flexural strength is due to the ability of fibers with a higher volume fraction to expand, which enhances tensile strength and reduces both the number and width of cracks by acting as a bridge along the crack surfaces, resulting from the overall

increase in strength. The result is consistent with the studies of many researchers (Kchaitanya et al. 2018; Soylu and Bingöl 2019; Naji et al. 2021; Hamed and Abass 2022).

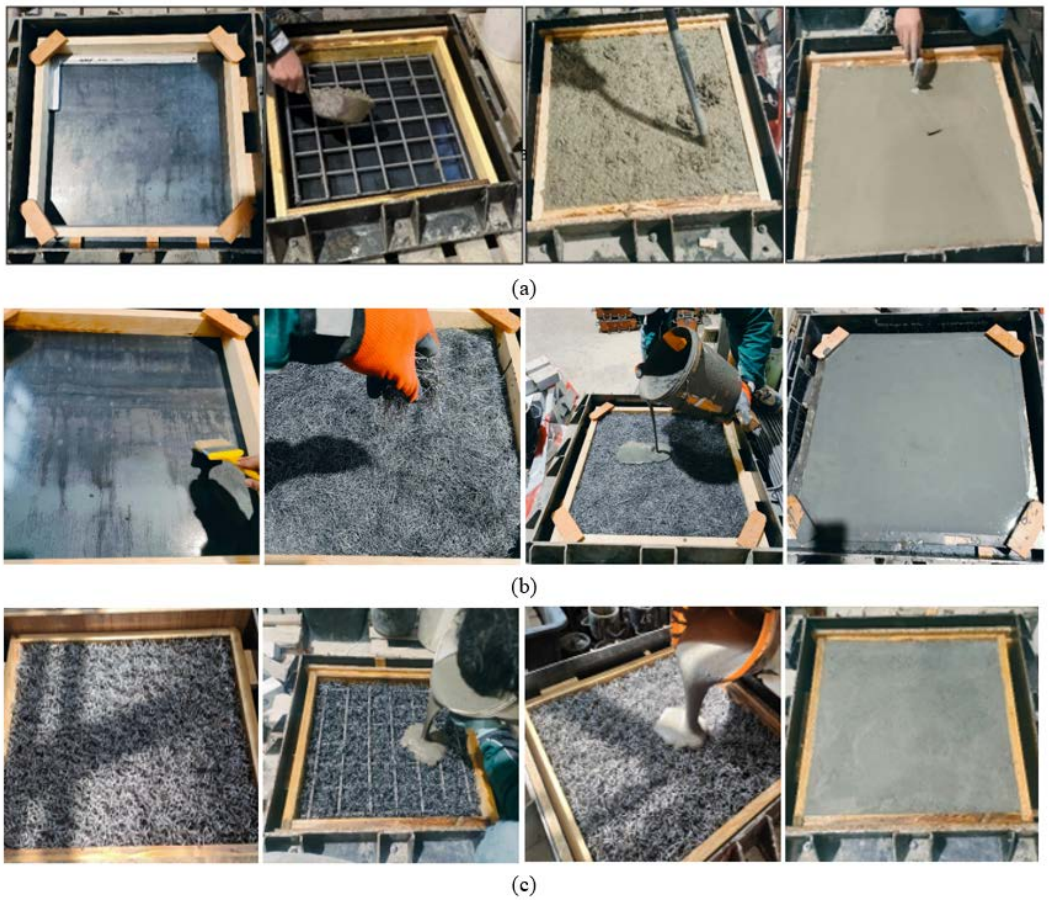


Figure 4 The steps of casting the different types of flat slab concrete (a- NSC slab, b- SIFCON slab with hooked-end steel fibers and c- SIFCON slab with 3D steel fibers)

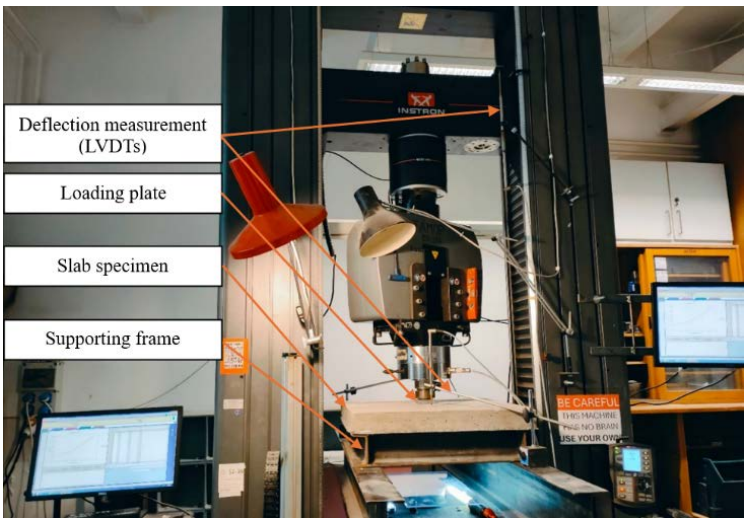


Figure 5 Punching shear test of flat slabs

Table 4 The mechanical properties results of the NSC and SIFCON

Type of concrete	Type of fiber	Volume fraction of fibers (%)	Compressive strength (MPa)		The percentage increase (%) in 28 days compared to NSC	Flexural tensile strength		The percentage increase (%) in 28 days compared to NSC
			7 days	28 days		7 days	28 days	
NSC	-	-	31.0	43.0	-	3.7	4.8	-
SIFCON	3D Starex	6	68.0	84.6	96.7	5.5	6.1	27.1
SIFCON	3D Starex	9	77.5	98.3	128.6	6.0	6.8	41.7
SIFCON	Hooked-end	6	89.0	118.0	174.4	23.5	32.0	566.7

3.2 Punching load and load-deflection response

The first cracking load and peak load of the tested flat slabs were evaluated. The results indicated that the use of SIFCON delayed the onset of first cracking, particularly when hooked-end steel fibers were incorporated. Although SIFCON reinforced with 3D fibers did not significantly delay the first-cracking load, it was observed that the interval between the first-cracking load and the ultimate load for flat slabs cast with SIFCON containing 3D steel fibers was considerably greater than that of slabs produced with SIFCON containing hooked-end steel fibers, as illustrated in Figure 6.

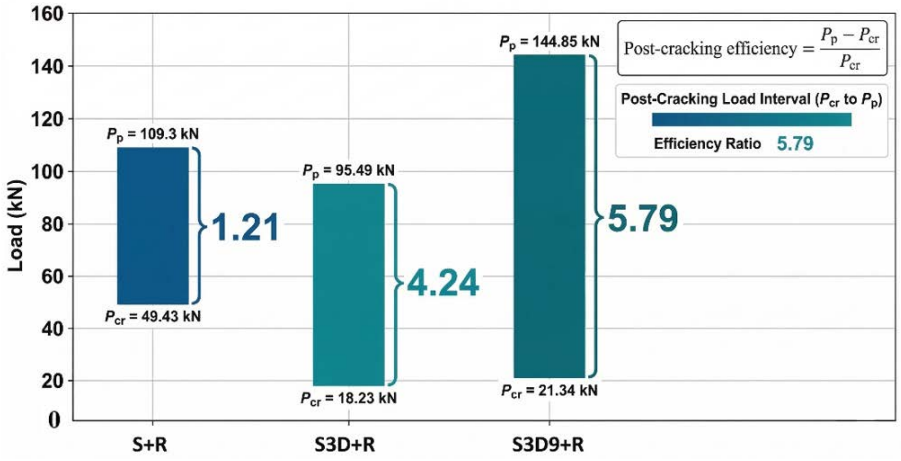


Figure 6 The interval between the first cracking load and the peak load of the flat slabs

Figure 6 show when the increase from first crack load P_{cr} to peak load P_p was expressed relative to the first cracking load indicates the post-cracking efficiency, the SIFCON flat slab with 3D steel fibers showed a value about four times higher than the comparable SIFCON flat slab with hooked-end steel fibers. This behavior indicates that the 3D steel fibers are particularly effective at maintaining stress transfer across cracked areas, which enhances the structural reliability of the flat slab after cracking begins.

It was found that 3D steel fibers can improve punching shear capacity, as shown in *Table 5*, especially when used together with reinforcing steel bars within the tested slab series. The shape of 3D steel fibers allows them to work in multiple directions and to interact with the expected surface of shear failure cracks in a way that is similar in concept to the shear studs strategy.

Table 5 The measured peak loads and deflections at peak load

No.	Specimen	P_p (kN)	Δ_{cp} (mm)	Δ_{qp} (mm)	η_p (%)

1	N	50.18	4.82	2.25	-
2	S	93.14	7.74	4.25	86
3	S+R	109.3	12.06	5.25	118
4	S3D	40.22	7.78	3.56	-20
5	S3D+R	95.49	9.48	3.86	90
6	S3D9+R	144.85	20.80	14.37	189

Note: P_p = Peak load (kN); Δ_{cp} and Δ_{qp} = Center and Quarters av. deflection by (mm) at peak load, respectively; η_p = The percentage of improved peak load compared to specimen N

The load-deflection behavior of the tested flat slabs provided a comprehensive representation of the structural response under concentrated loading, as shown in the Figure 7. The flat slabs cast entirely from SIFCON using hooked-end steel fibers show a maximum deflection of 24.8 mm in the S+R specimen. For the SIFCON flat slab with 3D steel fibers, the highest peak load and deflection were obtained in the S3D9+R flat slab, which is around 145 kN and 39 mm, respectively, and a large difference in deflection between u_1 and u_2 was also recorded.

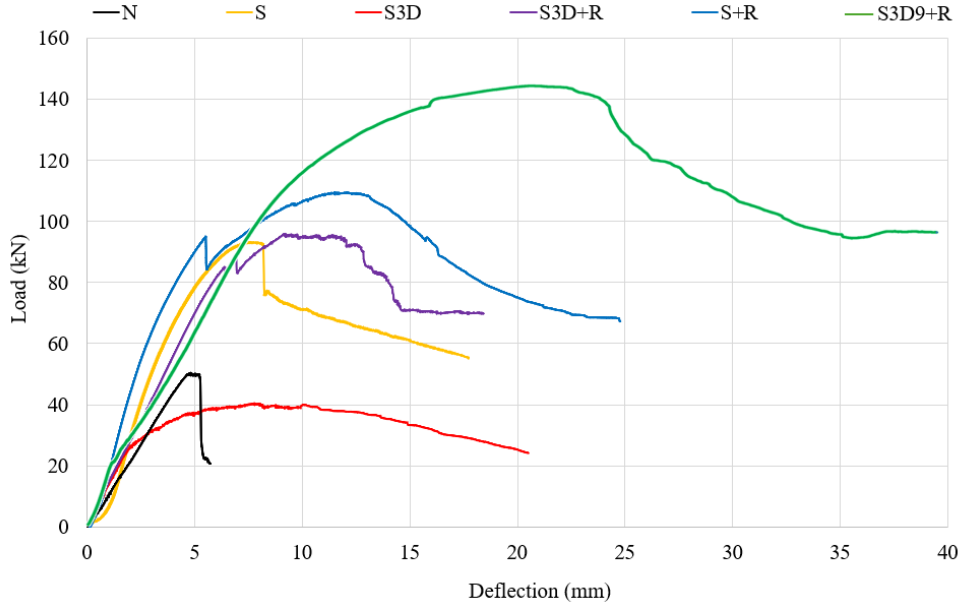


Figure 7 The load-deflection curves of all specimens

Notably, S3D still recorded substantial ductility, showing a 13 mm difference in deflection between the deflection at peak load and at the u_2 stage, illustrating that the 3D steel fibers alone can endow the slab with appreciable deformability. When fibers and conventional reinforcement are combined, both punching shear capacity and ductility improve markedly.

3.3 Failure mode and crack pattern

Three different failure modes were observed in the tested specimens: punching shear failure, flexural failure, and combined punching shear and flexural failure. Figure 8 shows the crack distribution at the tension side of the tested specimens. The reference specimen, N, exhibits a punching shear failure. The N slab initially cracked with a load of 11.18 kN; the cracks started from the area directly under the load until they formed a circular shape, where the deflection

was 4.82 mm. It is worth noting that for the N slab, some parts of the concrete collapsed and spalled.

For the specimens, which were cast entirely by SIFCON and with hooked-end steel fiber, the S and S+R specimens exhibit a flexural failure and combined punching shear-flexural failure, respectively. The load at the initial crack was 42.72 kN for the S slab and 49.43 kN for S+R. The cracks formed a diagonal crack in the S fat slab. However, although the S+R flat slab started with the same cracking pattern, it ended with a circular-shaped crack when reaching stage u_2. The S and S+R slabs reached their highest loads of 93.14 and 109.3 kN, respectively, with a deflection of 7.74 mm in the S slab and 12.06 mm in the S+R slab at maximum load.

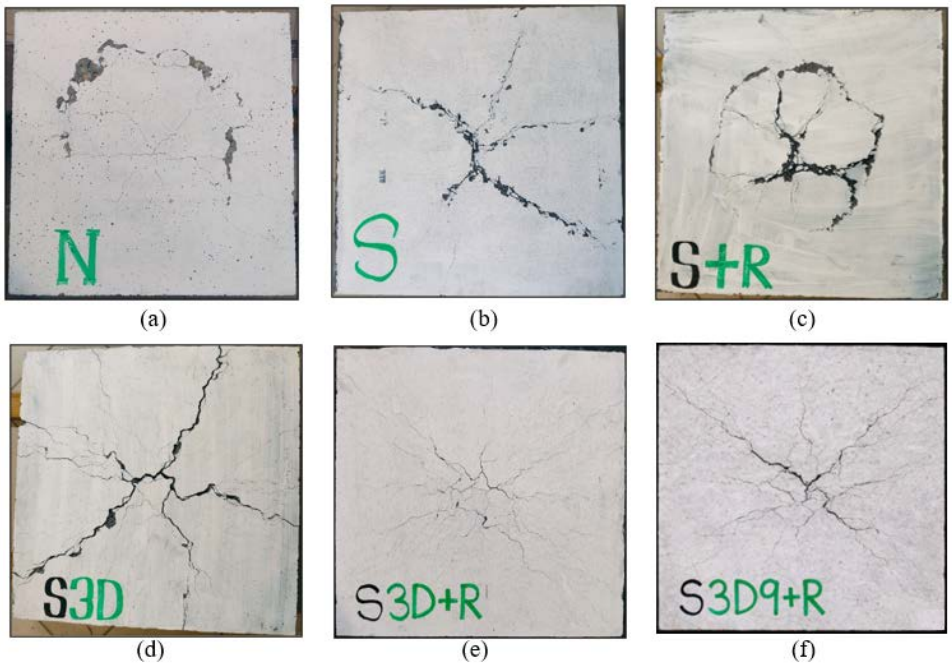


Figure 8 Crack pattern on the tension face of specimens: (a) N; (b) S; (c) S+R; (d) S3D; (e) S3D+R; (f) S3D9+R

In the flat slabs that were made wholly by SIFCON and used 3D steel fiber, the S3D specimen showed a simple bending response, where cracks originated at mid-span and propagated diagonally toward the supports. Specimens S3D+R and S3D9+R exhibited the mixed mode: load-induced longitudinal cracks first appeared parallel to the reinforcement, then evolved into diagonal and peripheral circular cracks. The mode of failure in the S3D slab was a flexural failure, as shown in Figure 8. For this type of flat slab, it was observed that the deflection is very large and the ductility is very high. When approaching the u_2 stage, the curve between the load and the deflection begins to take an almost horizontal path and does not descend, which forces us to stop the examination. The result is evidence that the 3D steel fibers, in addition to the excellent ease of their practical application in SIFCON, when used with reinforcement steel bars together, enhance the punching shear capacity to the maximum levels.

Finally, it can be said that the SIFCON, using any of the steel fibers that were used, led to improved punching shear and postponed failure, reaffirming that a higher fiber dosage markedly enhances both ductility and load-carrying capacity in the later stages of loading. What distinguishes 3D steel fibers is that they work best when used with reinforcing steel bars, perhaps because their arms interlock with the steel bars and provide more enhanced support.

3.4 Ductility

Ductility μ describes the capacity of a structural member to undergo substantial deformation after first yield. In this study, it is expressed as the ratio of the ultimate displacement, Δ_u, to the corresponding yield displacement, Δy, by Eq. (4.1) and the procedure proposed by Lim and Hong (Lim and Hong 2016). Because the slabs exhibited continuing deformation after peak load in this study, ductility ratios were evaluated at two ultimate stages, u_1 and u_2, to capture the influence of fiber reinforcement on post-peak behavior. The resulting indices, μ_1 and μ_2, are reported in Table 6 and provide a clearer picture of how SIFCON affects the later stages of the response.

$$\mu = \frac{\Delta u}{\Delta y} \tag{1}$$

Table 6 The ductility results

No.	Specimen	P_y (kN)	Δ_{cy} (mm)	Δ_{cu1} (mm)	Δ_{cu2} (mm)	μ_1	μ_2	$\eta\mu_1$ (%)	$\eta\mu_2$ (%)
1	N	48.90	4.65	5.22	5.30	1.12	1.14	-	-
2	S	83.44	5.56	8.85	17.54	1.59	3.15	42	176
3	S+R	93.94	5.40	16.71	24.78	3.09	4.59	176	303
4	S3D	31.98	3.23	15.84	20.51	4.90	6.35	338	457
5	S3D+R	86.78	6.83	14.22	20.7	2.08	3.03	86	166
6	S3D9+R	123.54	11.46	28.00	40.00	2.44	3.49	118	206

Note: P_y = yield load by (kN); Δ_{cy}= Center deflection by (mm) at yield load; $\Delta_{c(u1\ and\ u2)}$ = Center ultimate deflection by (mm) u_1 and u_2 respectively; μ_1 and μ_2 = the ductility 1 and 2; $\eta_{\mu1}$ and $\eta_{\mu2}$ = The percentage of improved ductility 1 and 2 compared to specimen N.

No significant readings were recorded for the u1 and u2 stages for the reference N slab, meaning that no high ductile behavior was observed for this slab. While for the flat slabs made entirely of SIFCON with hooked-end steel fiber, the maximum center deflection value, which was for the S+R specimen, was about 16.7 and 24.8 mm for u_1 and u_2, respectively. That is, the difference between the deflection at the highest load and point u_2 was 12.74 mm; this indicates the high ductility of this slab due to the amount of fibers present, which led to it being able to bear high loads in the later stages. A significant improvement was observed for the second stage, u_2, as shown in Figure 9.

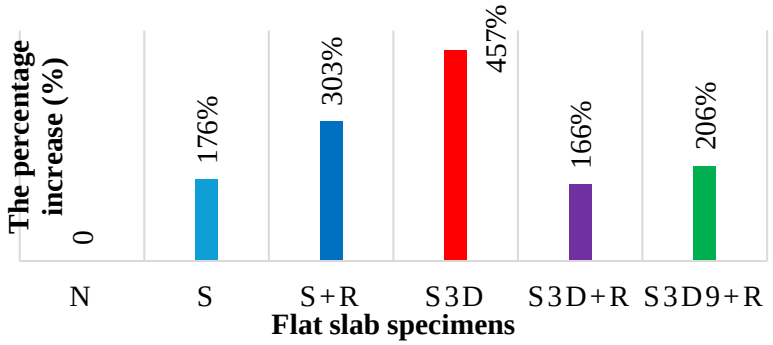


Figure 9 The percentage of improved ductility for SIFCON flat slabs at stage u2 compared to specimen N

For slabs cast entirely from SIFCON using 3D steel fibers, the best ductility was observed, especially in the final stage, u_2. The highest increase in ductility compared to the reference slab was recorded for the S3D flat slab, amounting to 457%. The flat slabs containing 3D steel fibers showed substantial displacement capacity beyond first cracking. The most pronounced increase occurred in the S3D9+R specimen, whose deflection rose from 20.85 mm at peak load to 40 mm at u_2.

4 Conclusion

This is a study about the potential structural application of steel fibers to improve the punching performance of flat slabs using SIFCON in the punching area. Hooked-end fibers and new 3-dimensional steel fibers were used. The experimental program provided measurements on load-deflection behaviors, crack pattern, and ductility in addition to compressive and flexural strengths of both SIFCON and NSC for comparison. The conclusions are the following:

1. The *mechanical properties* of the two varieties of concrete applied in this study, NSC and SIFCON, were evaluated. At 28 days, SIFCON with hooked-end steel fibers had higher compressive and flexural strengths of 118 and 32 MPa, respectively. Comparing SIFCON with the same volume fraction of hooked-end and 3D steel fibers to the reference NSC, the gains in compressive strength were 174% and 97%, respectively, and 129% for SIFCON with 9% of 3D steel fibers. In comparison to the reference NSC, the flexural strength gains for SIFCON with the same volume fraction of hooked-end and 3D steel fibers were 567% and 26%, respectively, and 42% for SIFCON with 9% of 3D steel fibers.
2. The SIFCON flat slabs with hooked-end steel fibers demonstrated a substantial improvement in the *first cracking* load, up 342% improvement above the control NSC slab. It also noted that the post-cracking efficiency of the SIFCON flat slab with 3D steel fibers showed a value about four times higher than the comparable SIFCON flat slab with hooked-end steel fibers.
3. When compared to the traditional NSC flat slab, the *maximum load* capacity of SIFCON flat slabs shows a significant improvement. Up to 118% increase in percentage for the SIFCON slab with hooked-end steel fiber, and significant improvements up to 189% were also achieved by SIFCON slabs with 3D steel fiber.
4. The *load-deflection* curves showed that all the SIFCON flat slabs had a high ductility and gradual post-peak decline, unlike the NSC slab, which failed sharply. The highest deflection was recorded in the SIFCON slab containing hooked-end steel fibers, which was 24.8 mm for the S+R slab, while in the SIFCON flat slabs with 3D steel fibers, the highest deflection was recorded as 39 mm for the S3D9+R slab.
5. The highest *ductility* index was observed by all SIFCON specimens, demonstrating their remarkable capacity to dissipate energy and withstand significant inelastic deformations before collapse. While the reference NSC slab, which was controlled by a brittle punching shear failure, had the lowest index. In order to shed light on fiber efficiency under the most recent loading, this study is also the first to investigate late-stage ductility at the deflection levels u_1 and u_2. The ductility amplification factor $\eta_{\mu 2}$ increased by around 457% in the S3D slab at the maximal deflection u_2.

6. SIFCON technology provided considerable practical advantages to create a high performance punching area around the columns of the flat slab by applying first the fibers and then the mortar, which resulted in a dense structure, especially in the case of 3D steel fibers.

5 References

Chao, S.-H., Kaka, V. and Kim, J. 2016. Formulating Constitutive Stress-Strain Relations for Flexural Design of Ultra-High-Performance Fiber-Reinforced Concrete. In: *International Interactive Symposium on Ultra-High Performance Concrete*. Iowa State University Digital Press.

Halvoník, J., Kalická, J., Majtánová, L. and Minárová, M. 2019. Reliability of models aimed at evaluating the punching resistance of flat slabs without transverse reinforcement. *Engineering Structures* 188, pp. 627–636. doi: https://doi.org/10.1016/j.engstruct.2019.03.055

Hamed, H.A. and Abass, Z.W. 2022. Effect of steel fiber proportion on SIFCON mechanical properties. *Journal of Engineering and Sustainable Development* 26(1), pp. 55–63.

Kchaitanya, D.V.S., Neeharika, P. and Nagakishore Bhavanam, D.S. 2018. An experimental studies of mechanical properties of conventional concrete with fiber reinforced concrete. *International Journal for Innovative Engineering & Management Research* 7(13).

Lim, W. and Hong, S. 2016. Shear Tests for Ultra-High Performance Fiber Reinforced Concrete (UHPFRC) Beams with Shear Reinforcement. *International Journal of Concrete Structures and Materials* 10(2), pp. 177–188. http://doi.org/10.1007/s40069-016-0145-8

NA. 2009. Conceptual Design of Concrete Buildings. *Buildings* (May), pp. 14–16.

Naji, H.F., Hussein, M.J. and Farsangi, E.N. 2021. Mechanical properties of SIFCON with variation steel fiber ratio and nano kaolin. *Journal of Mechanical Engineering Research and Developments* 44(2), pp. 363–370.

Saleh, H., Kalfat, R., Abdouka, K. and Al-Mahaidi, R. 2019. Punching shear strengthening of RC slabs using L-CFRP laminates. *Engineering Structures* 194, pp. 274–289. https://doi.org/10.1016/j.engstruct.2019.05.050

Sonone, R., Sharma, S. and Sharma, H. 2020. SIFCON-A high performance concrete-experimental investigations. *International Journal of Innovative Technology and Exploring Engineering (IJITEE)* 10(2), pp. 109–112.

Soylu, N. and Bingöl, A.F. 2019. Research on effect of the quantity and aspect ratio of steel fibers on compressive and flexural strength of SIFCON. *Challenge Journal of Structural Mechanics* 5(1), pp. 29–34.

Tahmoorian, F., Nemati, S., Sharafi, P., Samali, B. and Khakpour, S. 2021. Punching behaviour of foam filled modular sandwich panels with high-density polyethylene skins. *Journal of Building Engineering* 33, p. 101634. https://doi.org/10.1016/j.jobe.2020.101634

Tauma, W.K. and Balázs, L.G. 2023. Impact and blast resistance of slurry infiltrated fiber concrete (SIFCON): A comprehensive review. *Journal Concrete Structures* 24, pp. 129–136. https://doi.org/10.32970/CS.2023.1.18

Tuama, W.K. and Balázs, G.L. 2025. Behavior of Flat Slabs with Partial Use of SIFCON Subjected to Concentrated Loading. *Periodica Polytechnica Civil Engineering*. https://doi.org/10.3311/PPci.41452

Tuama, W.K. and Balazs, G.L. 2025. Review Paper Properties of Fibers and Mortar of Slurry Infiltrated Fiber Concrete (SIFCON). In: *Materials Science Forum*. pp. 67–76.

Weerasinghe, P., Nguyen, K., Mendis, P. and Guerrieri, M. 2020. Large-scale experiment on the behaviour of concrete flat slabs subjected to standard fire. *Journal of Building Engineering* 30, p. 101255.

Zamri, N.F., Mohamed, R.N., Awalluddin, D. and Abdullah, R. 2022. Experimental evaluation on punching shear resistance of steel fibre reinforced self-compacting concrete flat slabs. *Journal of Building Engineering* 52, p. 104441.

Evidence from slender beam tests on prestressed UHPC for lightweight, durable structures

Juan Navarro-Gregori[1], Yeiner A. Gómez-Velásquez[1], Juan A. Mateu-Sánchez[1], Pedro Serna[1], José R. Martí-Vargas[1]

[1]: Institute of Concrete Science and Technology (ICITECH), Universitat Politècnica de València, Valencia, Spain.

Abstract

This study reports preliminary findings from an experimental programme coupling prestressing with ultra-high-performance fibre-reinforced concrete (UHPC) to enable lightweight and durable members. Twelve slender prestressed UHPC beams, without passive reinforcement, were tested in four-point bending across two cross-sections (rectangular and I-shaped), three fibre dosages (130, 160 and 190 kg/m³), and two prestressing layouts (bottom-only and symmetric). Prestress losses were monitored from transfer to testing; material properties were obtained from compressive tests and unnotched four-point bending test; and global response was assessed in terms of serviceability and ultimate capacity. Rectangular beams exhibited the smallest prestress losses—particularly with symmetric layouts—whereas I-shaped sections experienced larger time-dependent reductions. All beams showed a consistent flexural sequence—uncracked linear branch, progressive post-cracking softening, peak load, and a residual branch driven by prestressing—without concrete crushing at peak. Rectangular beams reached higher peak loads, while I-shaped beams delivered comparable residual performance with lower sensitivity to fibre dosage, indicating a robust and lightweight solution. These results provide an experimental basis for design choices balancing strength and weight efficiency in prestressed UHPC members.

Keywords

effective prestress; flexural behaviour; prestressed beams; prestress losses; slender precast elements; UHPC.

1 Introduction

Ultra-high-performance concrete (UHPC), also referred to as UHPFRC, is a cementitious material that combines remarkably high compressive strength, post-cracking tensile resistance, and excellent durability. These properties make it attractive for structural applications requiring slender geometries, reduced self-weight, long service life, and efficient prefabrication. UHPC has progressed from local strengthening and rehabilitation applications to primary load-bearing members and bridge components (Graybeal et al., 2020; Hung et al., 2021).

UHPC is defined by dense particle packing, a low water-to-binder ratio, the absence of coarse aggregates, and the incorporation of steel fibres to provide post-cracking tensile capacity. Design-oriented documents consistently highlight its key advantages—high compressive strength, enhanced tensile behaviour, and exceptional durability (Association Française de Normalisation, 2016; JSCE, 2006; ACI 239, 2018). UHPC's superior mechanical performance enables the production of lightweight and durable structural members, which can reduce material use at the structural scale (Graybeal et al., 2020; Li et al., 2020).

Within this context, the combination of UHPC and prestressing offers a promising strategy for developing slender precast elements. Prestressing improves serviceability by limiting tensile stresses and deflections, whereas UHPC provides high compressive capacity, post-cracking resistance, and durability. This synergy may enable thinner and lighter members with enhanced structural efficiency and easier transport, handling, and erection (Sim et al., 2020; Graybeal & Helou, 2023). However, several issues remain insufficiently understood, including the quantification of prestress losses, the tensile contribution of UHPC at service and ultimate states, and the role of fibre distribution. These aspects are relevant because creep, shrinkage, and crack localization in prestressed UHPC members may differ from those in conventional concrete structures (Mohebbi & Graybeal, 2022; Tian et al., 2025).

The tensile and flexural performance of UHPC depends not only on fibre type and dosage but also on fibre orientation and distribution, which are governed by casting procedures, rheology, and member geometry. Consequently, tensile properties obtained from standard specimens may not represent those of real structural elements. Moreover, restrained shrinkage can modify the effective prestress level and influence cracking onset and long-term behaviour (Mezquida-Alcaraz et al., 2021; Zhao & Bo, 2022). Although bridge construction has led much of the UHPC development, substantial opportunities remain for optimized precast elements in building and industrialized construction, where reduced weight and improved durability offer notable advantages (López et al., 2014; Seyam & Balázs, 2023).

Against this background, the present study investigates the behaviour of slender prestressed UHPC beams without passive reinforcement, conceived as lightweight members for scalable precast production. Two cross-sectional typologies were studied—a rectangular reference section and an I-shaped section—together with three UHPC mixes and two prestressing layouts. The main objectives are to quantify prestress losses from transfer to testing, assess the flexural response as a function of section typology, UHPC mix, and prestressing layout, and identify the most efficient sectional concept in terms of load-carrying capacity and residual response.

2 Experimental programme

The experimental program comprised twelve prestressed UHPC beams arranged in two series of six specimens, with two cross-sectional typologies: a rectangular section (S0) taken as reference and an I-shaped section (S1), according to Figure 1 and Table 1. Within each series, the variables investigated were the UHPC type, defined by three steel fibre contents (C1, C2, and C3), and the prestressing layout, namely bottom-only prestressing (T-type), and symmetric prestressing (D-type). No longitudinal nor transverse passive reinforcement was provided, including end-zones, including in the end zones near the anchorages. Each beam was identified using the notation *X_YZ*, where *X* denotes the cross-section type (S0 or S1), *Y* the UHPC type (C1, C2, or C3), and *Z* the prestressing layout (T or D). All beams were 3800 mm long, allowing four-point bending tests with a clear span of 3500 mm and 1000 mm between loading points (Fig. 1). This configuration ensured a flexure-dominated response.

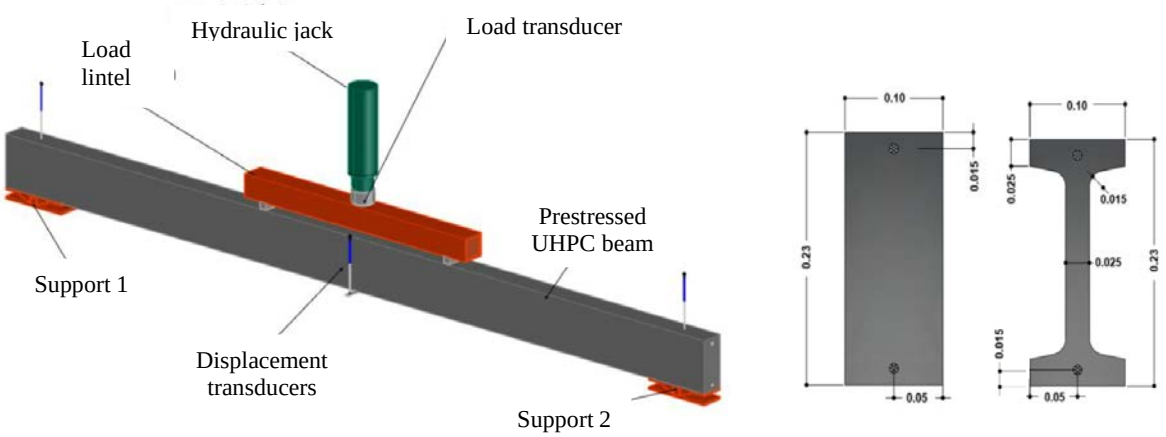


Figure 1:(a) Prestressed UHPC beam setup. (b) Cross-section geometries (Units in m)

Table 1: Cross-section details of the experimental program

Beam ID	**Cross-Section**	**Fibre Content** (kg/m^3)	**Prestressing**
S0_C1T	Rectangular	190	Bottom
S0_C2T	Rectangular	160	Bottom
S0_C3T	Rectangular	130	Bottom
S0_C1D	Rectangular	190	Symmetric
S0_C2D	Rectangular	160	Symmetric
S0_C3D	Rectangular	130	Symmetric
S1_C1T	I-shaped	190	Bottom
S1_C2T	I-shaped	160	Bottom
S1_C3T	I-shaped	130	Bottom
S1_C1D	I-shaped	190	Symmetric
S1_C2D	I-shaped	160	Symmetric
S1_C3D	I-shaped	130	Symmetric

The UHPC mixes were produced using Portland cement CEM I 42.5R SR5, silica fume, fine aggregates, water, and superplasticizer. Three concrete types were evaluated in this study. Mix

C1 incorporated a hybrid fibre reinforcement system consisting of 130 + 60 kg/m³ of steel fibres. Mix C2 employed a single steel-fibre dosage of 160 kg/m³, whereas Mix C3 contained 130 kg/m³ of steel fibres. The water-to-cement ratio was 0.21, and the mixes were designed to be self-compacting and to achieve a target compressive strength of 135 MPa on 100 mm cubes.

Two types of steel fibres were used in the program: straight fibres Dramix® OL 13/0.2 Fibers and, in the case of mix C1, an additional proportion of hooked-end fibres Dramix® 3D 80/30BGP fibres was used. All batches were produced at the ICITECH laboratory, and the fibres were incorporated gradually to ensure proper dispersion and adequate workability.

The compressive strength of the UHPC was determined on 100 mm cubes in accordance with UNE-EN 12390-3:2020, with tests conducted at different ages to evaluate strength development up to 28 days. The tensile behaviour of the material was assessed by means of unnotched four-point bending tests on 100 × 100 × 450 mm prismatic specimens, in accordance with UNE 83519:2023. The prestressing reinforcement consisted of 7-wire steel strands Y 1860 S7 9.3, with an ultimate tensile strength of 1860 MPa and a nominal diameter of 9.3 mm.

Before casting, the prestressing strands were positioned and instrumented with steel strain gauges to monitor stress variations during tensioning and transfer. In addition, vibrating-wire strain gauges were embedded at mid-span to monitor time-dependent concrete deformations. The prestressing system consisted of fixed and movable reaction frames, with the force applied by hydraulic jacks and measured using force transducers.

Strands were tensioned to ~75% of the ultimate tensile strength f_{pu} (≈1395 MPa; ≈75 kN/strand). Concrete was then cast in a continuous sequence to ensure proper filling and geometric consistency. Prestress transfer was conducted 48 hours after casting, once the UHPC had reached sufficient strength, and the beams were subsequently stored for approximately three months before mechanical testing.

The structural response of the beams was evaluated by means of four-point bending tests performed with a 200 kN servo-hydraulic jack connected to a universal testing machine. The applied load was measured using a force transducer placed between the loading beam and the specimen. Beam displacements were recorded using four potentiometric displacement transducers. Two were placed at mid-span to measure vertical deflection and detect any rotation of the specimen, while one additional transducer was installed at each support to account for unintended vertical movements and obtain the effective mid-span deflection. The tests were recorded using a high-resolution digital camera to document crack development and final failure.

3 Test results

Table 2 summarizes, for each beam, the total prestressing force measured immediately before transfer and immediately before the bending test. The difference represents the combined prestress losses due to elastic shortening at transfer and the time-dependent prestress losses accrued during the curing/storage period before testing. The table also reports the average concrete compressive strength for each beam and the ultimate load P_u attained in the test.

Table 2: Experimental beam results

Beam ID	f_{cm} (MPa)	**Pre-transfer force** (kN)	**Pre-test force** (kN)	**Prestress Losses %**	P_u (kN)
S0_C1T	129.0	80.85	70.74	12.5	55.26
S0_C2T	132.2	76.36	67.61	11.5	52.84
S0_C3T	131.9	76.85	66.72	13.2	44.78
S0_C1D	137.9	150.45	136.73	9.1	50.32
S0_C2D	141.9	151.77	139.18	8.3	43.90
S0_C3D	126.6	143.64	131.10	8.7	46.17
S1_C1T	129.0	76.58	59.79	21.9	38.71
S1_C2T	132.2	74.67	58.87	21.2	37.50
S1_C3T	131.9	73.26	60.47	17.5	38.93
S1_C1D	137.9	159.15	127.87	19.7	40.02
S1_C2D	141.9	148.57	127.00	14.5	37.74
S1_C3D	126.6	148.65	126.17	15.1	38.92

Figures 2 and 3 illustrate the load–mid-span deflection (P–δ) curves of the twelve tested beams, grouped according to the prestressing layout. For each prestressing layout, the influence of both the cross-sectional configuration (rectangular S0 section or I-shaped S1 section) and the UHPC type (C1, C2, or C3) can be identified.

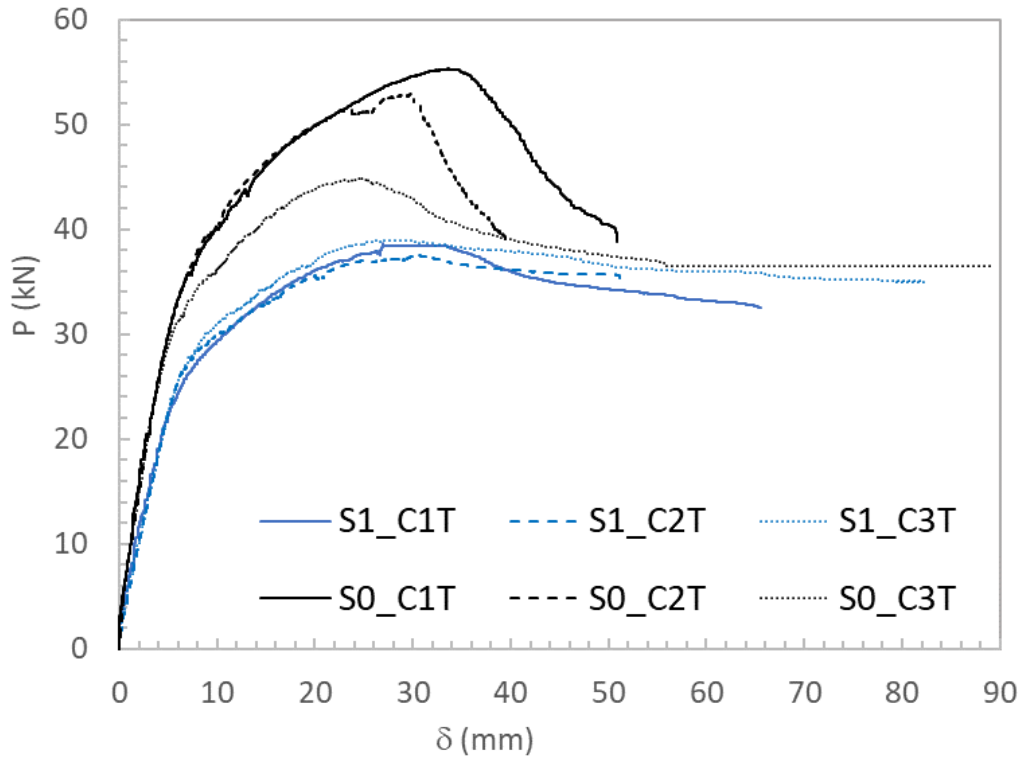


Figure 2: Load-mid-span deflection curves, bottom-only prestressed beams (T-type)

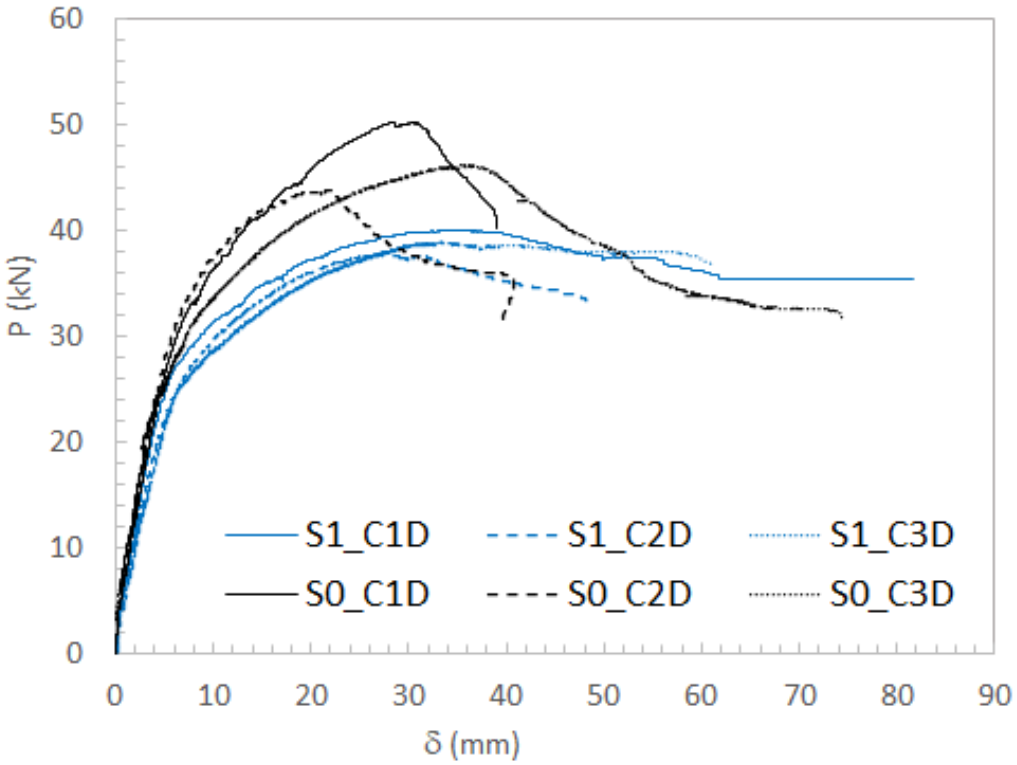


Figure 3: Load-mid-span deflection curves, symmetric prestressed beams (D-type)

4 Discussion

Prestress losses were consistently lower in the rectangular S0 sections. In this series, the D-type beams exhibited the smallest losses, with values around 8% and slightly below 10%, while the T-type beams showed higher losses, ranging from 11.5% to 13.2%, primarily because of the higher concrete stress at strand level in this configuration.

The same trend was observed in the S1 series, in which the T-type beams again presented greater losses (17.5–21.9%) than the D-type beams (14.5–19.7%). In general, the S1 sections exhibited higher prestress losses than the S0 sections, with an average difference of five percentage points.

The load–deflection response (Figures 2 and 3) of both the rectangular S0 and I-shaped S1 series showed similar behaviour in bending, with an initial uncracked linear branch followed by progressive stiffness degradation after cracking, a maximum peak load, and a post-peak residual branch associated with the contribution of the bottom prestressing strand.

In all tests, pronounced post-peak ductility was observed, with no crushing of the compression zone at peak load. Accordingly, flexural failure was governed by crack localization and progressive fibre pull-out rather than by compressive crushing of the UHPC. Beyond the peak, a residual branch associated with yielding of the bottom prestressing strand was evident. In several specimens, strand yielding—and, in some cases, subsequent fracture—occurred only at large deflections, confirming the high deformation capacity of the members.

The main differences between the two series were related to sectional efficiency and sensitivity to material variability. The rectangular S0 beams reached higher peak loads, with the T-type configuration tending to outperform the D-type one, although the results also revealed a marked influence of concrete type and, most likely, of fibre distribution and orientation induced by the casting process.

By contrast, the I-shaped S1 beams exhibited lower peak loads but similar residual strength, resulting in a highly ductile response with reduced sectional weight. In this series, the structural response was much less dependent on concrete type, suggesting a more stable flexural behaviour despite the lower load-carrying capacity.

Overall, the results highlight a trade-off between strength and lightweight efficiency, with rectangular S0 sections providing higher resistance and I-shaped S1 sections offering lighter but still remarkably ductile structural solutions, and in general, behaviour not significantly dependent on the type of UHPC used.

5 Concluding remarks

Slender prestressed UHPC beams without passive reinforcement can be successfully produced and evaluated under controlled laboratory conditions, and the adopted experimental methodology proved adequate for assessing their flexural behaviour.

Prestress losses were governed by cross-sectional geometry and prestressing layout rather than by concrete type, with the rectangular S0 beams showing lower losses than the I-shaped S1 beams.

All beams exhibited a similar flexural response, characterized by an initial uncracked stage, progressive stiffness degradation after cracking, a peak load, and a residual post-peak branch associated with fibre bridging and prestressing reinforcement.

No concrete crushing was observed at peak load, indicating that the compressive capacity of the UHPC was not fully mobilized under the tested conditions.

For the I-shaped S1 beams, the UHPC type had little influence on the overall bending response, as similar behaviour was observed for all mixes in terms of service deflection, peak load, and residual flexural performance.

The maximum bending load of the S1 beams was not significantly affected by the prestressing layout, since similar values were obtained for both bottom-only and symmetric prestressing, highlighting the potential of the latter for members subjected to moment reversal.

Overall, the results confirm the structural feasibility and robustness of slender prestressed UHPC beams, while also showing that cross-sectional design and prestressing arrangement play a key role in optimizing prestress retention and flexural performance.

Acknowledgements

This research was funded by Project PreULight “CIAICO/2022/045”, supported by the “Conselleria de Innovación, Universidades, Ciencia y Sociedad Digital, Generalitat Valenciana (ES)” and Project “PID2023-149364OB-I00/AEI/10.13039/501100011033” funded by the “Agencia Estatal de Investigación AEI (State Research Agency) of Spain.

6 References

ACI Committee 239. (2018). Ultra-high-performance concrete: An emerging technology report (ACI 239R-18). American Concrete Institute.

Association Française de Normalisation. (2016). Concrete—Ultra-high performance fibre-reinforced concrete—Specifications, performance, production and conformity (NF P 18-470). AFNOR.

Graybeal, B. A., Brühwiler, E., Kim, B.-S., Toutlemonde, F., Voo, Y. L., & Zaghi, A. (2020). International perspective on UHPC in bridge engineering. Journal of Bridge Engineering, 25, 04020094. https://doi.org/10.1061/(ASCE)BE.1943-5592.0001630

Graybeal, B. A., & Helou, R. G. (2023). Structural design with ultra-high performance concrete (FHWA-HRT-23-077). Federal Highway Administration.

Hung, C.-C., El-Tawil, S., & Chao, S.-H. (2021). A review of developments and challenges for UHPC in structural engineering: Behavior, analysis, and design. Journal of Structural Engineering, 147, 03121001. https://doi.org/10.1061/(ASCE)ST.1943-541X.0003073

Japan Society of Civil Engineers. (2006). Recommendations for design and construction of ultra high strength fiber reinforced concrete (JSCE Guidelines for Concrete No. 9). JSCE.

Li, J., Wu, Z., Shi, C., Yuan, Q., & Zhang, Z. (2020). Durability of ultra-high performance concrete—A review. Construction and Building Materials, 255, 119296. https://doi.org/10.1016/j.conbuildmat.2020.119296

López, J. A., Serna, P., Camacho, E., Coll, H., & Navarro-Gregori, J. (2014). First ultra-high-performance fibre-reinforced concrete footbridge in Spain: Design and construction. Structural Engineering International, 24, 101–104. https://doi.org/10.2749/101686614X13830788505793

Mezquida-Alcaraz, E. J., Navarro-Gregori, J., & Serna-Ros, P. (2021). Direct procedure to characterize the tensile constitutive behavior of strain-softening and strain-hardening UHPFRC. Cement and Concrete Composites, 115, 103854. https://doi.org/10.1016/j.cemconcomp.2020.103854

Mohebbi, A., & Graybeal, B. (2022). Prestress loss model for ultra-high performance concrete. Engineering Structures, 252, 113645. https://doi.org/10.1016/j.engstruct.2021.113645

Seyam, A. M., & Balázs, G. L. (2023). A review in technologies, definitions, properties and applications of ultra high-performance concrete (UHPC). Concrete Structures, 1, 15. https://doi.org/10.32970/CS.2023.1.15

Sim, C., Tadros, M., Gee, D., & Asaad, M. (2020). Flexural design of precast, prestressed ultra-high-performance concrete members. PCI Journal, 65, 35–61. https://doi.org/10.15554/pcij65.6-02

Tian, X., Fang, Z., & Shao, Y. (2025). Flexural behavior and design of prestressed ultra-high performance concrete (UHPC) beams: Failure mode and ductility. Journal of Structural Engineering, 151, 04025127. https://doi.org/10.1061/JSENDH.STENG-13830

Zhao, S., & Bo, Y. (2022). Effect of casting position on mechanical performance of ultra-high performance concrete. Materials, 15, 404. https://doi.org/10.3390/ma15020404

Fibre-Reinforced Concrete Pile-Supported Foundation Slab for a Building

Marco Antonio Carnio[1]; Viviane Visnardi Vaz[1], Isabela Oliveira Duarte[1]

[1]: Evolução Engenharia, Valinhos, Brazil.

Abstract

This paper presents a case of the structural design of a fibre-reinforced concrete (FRC) pile-supported foundation slab for a building. The slab was reinforced locally with conventional steel bars and was used for a 19-storey residential building. The 419 m² slab has a thickness of 60 cm and is supported by 123 piles, each measuring 40 cm in diameter. These piles were adopted as an alternative to meet the structural and construction requirements associated with multi-storey buildings. The study's primary objective is to evaluate the feasibility of using FRC in conjunction with conventional reinforcement as a design solution for pile-supported foundation slab for a building, taking into account ultimate limit state (ULS) verifications. The design was developed considering soil–structure interaction, with the foundation modeled as a combined slab–pile system. Flexural and shear verifications were carried out based on the criteria of ABNT NBR 16935 and on updates of the *fib* Model Code 2020, using an FRC 35-3.5c. The results indicate that the proposed solution meets the normative requirements, highlighting the contribution of fibres in combination with localized reinforcement in regions of higher demand. This study demonstrates that this approach provides a safe and rational foundation solution with reduced conventional reinforcement and constructive simplification.

Keywords

pile-supported foundation slab, fibre reinforced concrete, metallic fibres, polymer microfibres.

1 Introduction

The use of fibre-reinforced concrete (FRC) on pile-supported foundation slab for a building has emerged as an efficient structural solution for buildings, particularly due to the material's mechanical performance and ease of construction. Incorporating fibres into concrete significantly improves post-cracking behaviour, by promoting stress redistribution and increasing the load-bearing capacity at both ultimate and service limit states. Consequently, improved crack control and potential reductions in construction time can be achieved. Within the Brazilian regulatory framework, ABNT NBR 16935 addresses this solution by establishing guidelines for designing FRC structural elements.

This paper presents a case in which FRC was applied to the pile-supported foundation slab of a 19-storey residential building with cast-in-place concrete walls. The paper focuses on the adopted design criteria and the evaluation of the structural performance of the proposed solution.

2 Description of the construction project

The development consists of a 19-storey residential building, comprising a ground floor, 17 typical storeys, and a roof level. It is located in Recife, Pernambuco, Brazil. Each typical floor has an approximate area of 375 m² and contains six apartments. The total height of the building is approximately 53 m, measured from ground level to the roof.

The adopted structural system comprises cast-in-place solid concrete walls and slabs, forming a monolithic reinforced concrete structure. The walls perform both structural and enclosure functions, transferring vertical and horizontal loads to the foundation system, while the slabs act as diaphragms, ensuring load distribution among the vertical elements and overall structural stability.

3 Characteristics of the foundation

Geotechnical investigations identified near-surface soil layers with low bearing capacity and high compressibility, rendering shallow foundations unsuitable for the structure. At greater depths, soil strata with improved geomechanical properties were identified, capable of supporting the loads transmitted by the superstructure.

The adopted foundation solution consists of 123 continuous flight auger (CFA) piles, with a nominal diameter of 400 mm and an average length of approximately 23 m. The pile spacing ranges from 1.80 m to 2.50 m, with their layout defined according to the configuration of the structural walls, ensuring compatibility between the geotechnical arrangement and the structural system. For the soil–structure interaction analysis, a vertical subgrade reaction modulus of 471 tf/m³ was adopted to represent the stiffness of the foundation system.

4 Structural design of the pile-supported foundation slab

ABNT NBR 6118 establishes the minimum performance requirements for concrete structures, structured into three categories: structural safety, serviceability, and durability. To achieve a design that ensures both safety and economic efficiency, in compliance with these requirements, the structural development process should encompass the following stages: structural conception (definition of geometry and actions), structural analysis, specification, design (dimensioning), and quality control.

5 Structural conception

5.1 Geometry

The geometry of the pile-supported foundation slab was defined through the coordination of architectural and structural designs. In plan view, the slab's outline corresponds to the projection of the structural walls, extended by a 0.50 m-wide strip designed to form a structural edge and improve load transfer, as well as providing suitable construction conditions along the building's perimeter.

The slab has a total area of approximately 419 m², fully encompassing the walls layout and ensuring the integrated behaviour of the slab–pile system as a single foundation element.

Localized recesses with a depth of 25 cm were incorporated to accommodate plumbing and electrical services. These areas are integrated into the slab geometry through gradual transitions between the main slab plane and the recessed regions. The slab's structural thickness was kept constant at 60 cm to ensure global stiffness and uniform structural behaviour.

For construction purposes, the slab is executed in two stages. In the first stage, concreting is carried out up to the bottom level of the recesses, followed by a second stage up to the top surface of the slab. The bond between layers is ensured by the continuity of pile reinforcement, supplemented by the application of an epoxy-based bonding agent in the regions between piles, guaranteeing adequate adhesion and monolithic behaviour of the system, as illustrated in Figure 1.

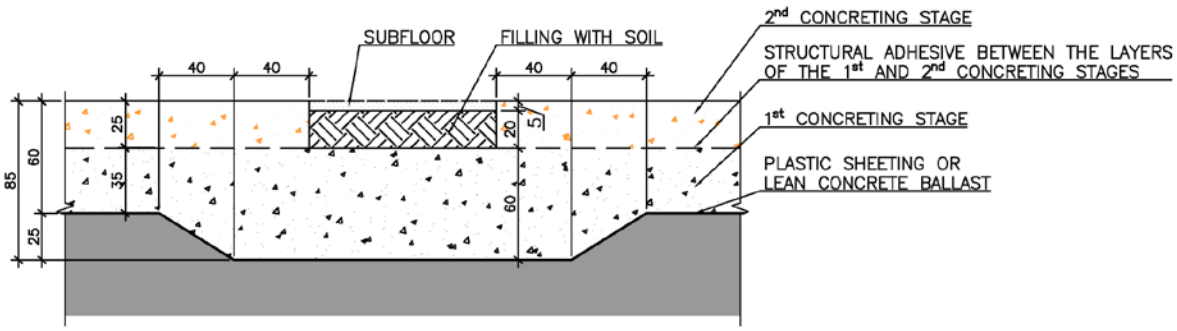


Figure 1: Foundation slab section in the recessed area.

Figure 2 presents the layout of the foundation slab, including the positioning of the recesses and piles.

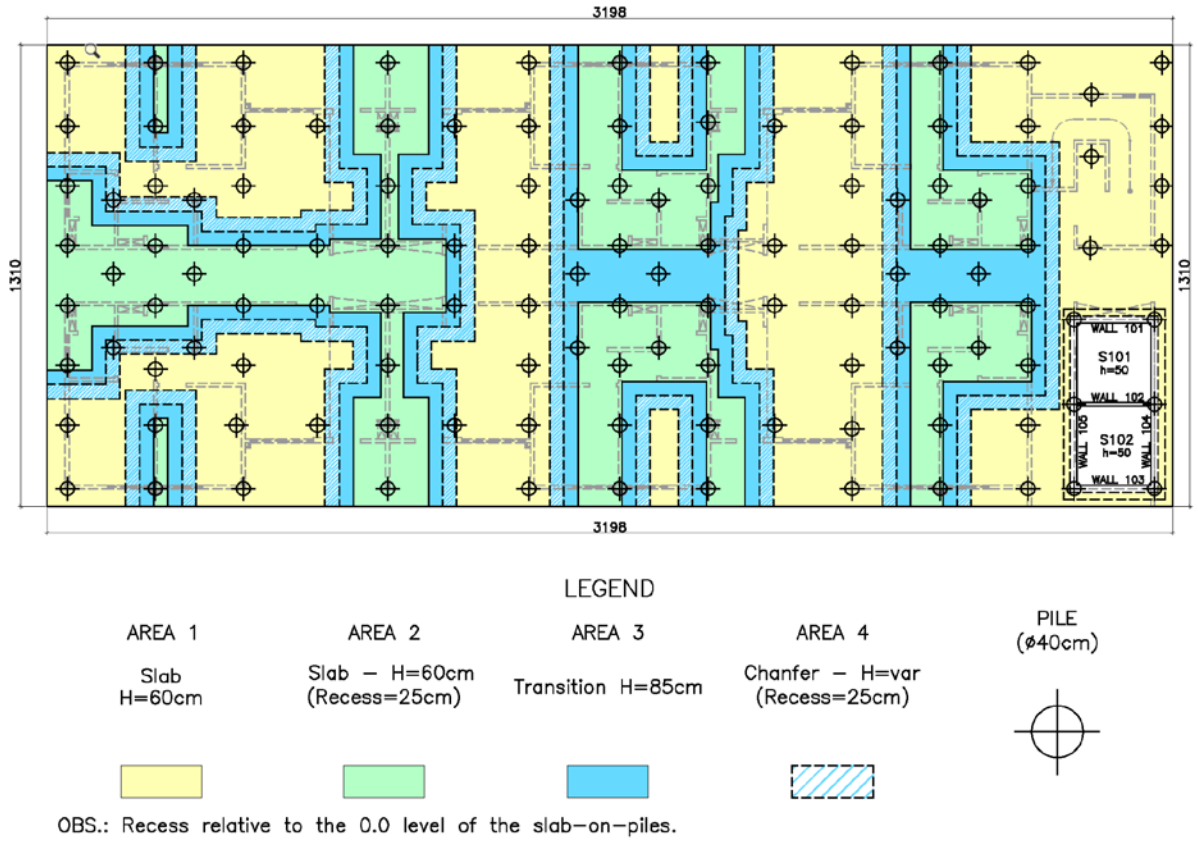


Figure 2: Foundation slab layout.

The piles extend 5 cm into the slab, with their reinforcement anchored up to the top surface of the slab (Figure 3), ensuring adequate bond and efficient force transfer between the deep foundation elements and the foundation slab.

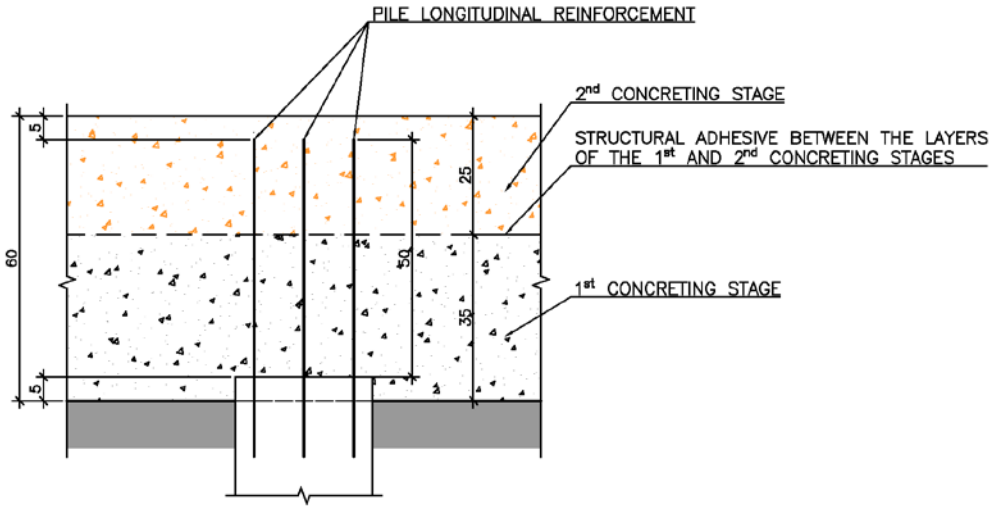


Figure 3: Pile-to-foundation slab positioning.

In addition, a recess corresponding to the elevator shaft, located in the lower-left region of the plan, was incorporated into the slab geometry. This geometric discontinuity was explicitly

considered in the structural model due to its influence on stiffness redistribution and stress flow in the affected region.

5.2 Loads

The design of the foundation slab considered both dead and live loads in accordance with the structural design of the building.

The actions from the superstructure, including the weight of the walls and slabs, non-structural elements, imposed floor loads, and wind-induced horizontal actions, were defined by the structural designer. These actions were obtained from the global structural model and applied to the foundation system through the structural walls.

The foundation model also included actions directly associated with the slab itself: its own weight, backfill loads in recessed areas required to accommodate building services and floor systems, floor finishing loads, and imposed loads at ground floor level.

Load combinations were established for structural analysis to verify both ultimate and serviceability limit states, enabling the assessment of the load-bearing capacity and global behaviour of the slab–pile system and associated deformations.

6 Structural analysis

The structural analysis of the FRC piles-supported foundation slab was performed using a grillage-type numerical model, with three degrees of freedom per node, corresponding to vertical translation and rotations about the in-plane orthogonal axes. This formulation enables an accurate representation of the slab's flexural behaviour, capturing force redistribution and the interaction between orthogonal strips.

The model was developed using TQS software, adopting a first-order linear elastic analysis under the assumptions of linear-elastic material behaviour and small deformations. Load combinations were defined in accordance with the applicable Brazilian standards, and design forces were obtained from the most unfavourable load envelopes.

These combinations were used to verify both ultimate and serviceability limit states, allowing the assessment of structural capacity, global behaviour, and associated deformations.

The pile supports were modelled as concentrated vertical restraints at nodes corresponding to their plan locations, allowing for the explicit representation of local stiffness and the resulting stress concentrations.

Soil–structure interaction was simulated using an elastic foundation model, with vertical springs discretised at the grillage nodes. The modulus of subgrade reaction adopted, which was defined from the geotechnical investigation, enabled the representation of soil deformability and the redistribution of contact stresses beneath the slab as a function of the relative soil-structure stiffness.

The internal forces obtained from the analysis – namely bending moments in both principal directions, shear forces, and vertical reactions – were used for the structural design of the foundation slab, including the verification of the FRC and the specification of localised reinforcement in regions of higher stress concentration.

7 Specifications

Table 1 presents the technical specifications of the FRC adopted for the design of the pile-supported foundation slab. According to the *fib* Model Code 2020, the material specification is defined by the compressive strength together with the residual strength f_{R1} and f_{R3}.

For f_{R3}, a range was specified, and the lower limit was adopted in the structural design.

In addition to the pile supports, the slab–subgrade interaction was considered in accordance with the geotechnical design. ABNT NBR 16935 permits the use of mean values for the flexural design of slabs supported on an elastic subgrade. Accordingly, mean values were adopted for the flexural design of the slab in this project.

For the punching shear verifications, however, characteristic residual strength values were adopted, using the relationship $f_{Rk}=0.7\ f_{Rm}$, in accordance with Annex L of EN 1992-1-1:2023.

The design values adopted in this project are summarized in Table 1.

Table 1: Properties of the concrete used in the project.

FRC *fib* Model Code 2020 classification	FRC 35–3.5c
Compression strength	C35
Young's Modulus of concrete (GPa)	Between 28 and 33
Residual strength f_{R1m} (MPa)	3.5
Residual strength f_{R3m} (MPa)	Between 3.15 and 3.85
Cement consumption	Between 280 kg/m³ and 350 kg/m³
Water/binder ratio	≤ 0.60
Maximum aggregate diameter (mm)	19
Dry mortar content (mass)	Between 55% and 60%

In this case study, steel fibres were employed as structural reinforcement, while polymer microfibres were used for shrinkage control. The technical specifications of the fibres are presented in Table 2.

Table 2: Specification of metallic fibres and polymer microfibres.

Shrinkage control	Type	Microfibres
	Material	Polypropylene
	Nominal length (mm)	12
	Maximum nominal diameter (µm)	18
	Minimum dosage (kg/m³)	0.90
Concrete reinforcement	Type	Hooked-end steel fibres
	Material	Steel
	Nominal length (mm)	60
	Maximum nominal diameter (µm)	0.80
	Dosage (kg/m³)	To be validated as per design residual resistances specification (minimum 25 kg/m³)

8 Design

The design of the FRC pile-supported foundation slab, combined with localized conventional reinforcement, was based on design forces obtained from the linear elastic analysis of the grillage model. Based on the load envelopes obtained from the structural model, both positive and negative bending moments in the two principal slab directions were considered, with the most unfavorable values adopted for cross-sectional verification.

Initially, the moment resistance associated with the FRC ($M_{Rd,FRC}$) was determined, accounting for the residual post-cracking contribution of the material based on the adopted mechanical parameters. In parallel, the elastic bending moment resistance of the section ($M_{Rd,e}$) was evaluated, corresponding to the limit of elastic behaviour prior to significant contribution from longitudinal reinforcement.

The moment resistance was calculated in accordance with the constitutive models prescribed by ABNT NBR 16935, which are based on the post-cracking behaviour of FRC under direct tension at the ultimate limit state (ULS). The standard defines two approaches – rigid-plastic and linear (with hardening or softening, see Figure 4) – established from flexural test results and characterized by the parameters f_{Fts} (service) and f_{Ftu} (ultimate).

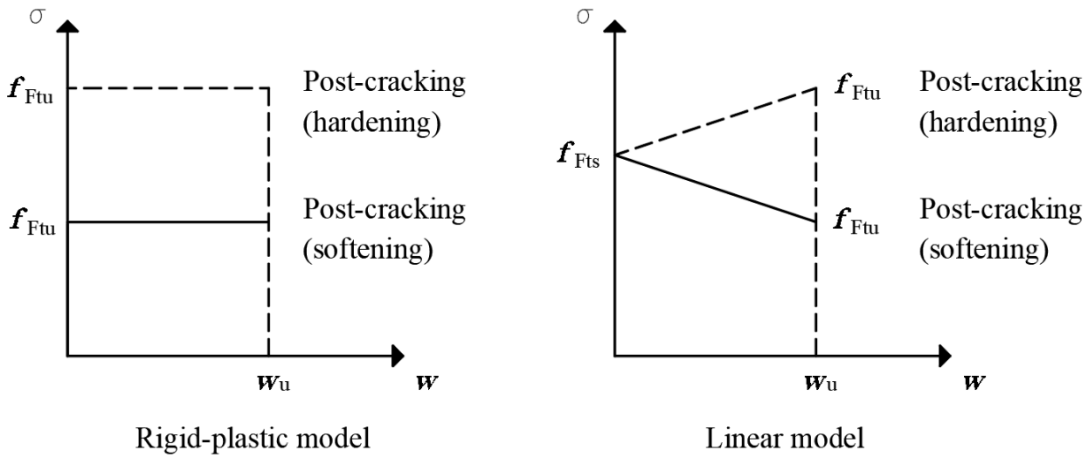


Figure 4: Constitutive laws post-cracking according to ABNT NBR 16935.

In the rigid-plastic model, a single reference parameter, f_{Ftu}, is adopted, as defined in Equation 1.

$$f_{Ftu} = \frac{f_{R3}}{3} \quad (1)$$

The moment resistance is determined in accordance with Equation 2.

$$M_{Rd,FRC} = \frac{f_{Ftud} \cdot b \cdot h^2}{2} \quad (2)$$

Where:

b is the width of the cross-section;

h is the height of the cross-section

The linear model uses two reference values, f_{Fts} and f_{Ftu}, obtained by means of Equations 3 and 4 (*fib* Model Code 2020).

$$f_{Fts} = 0{,}37 \cdot f_{R1} \quad (3)$$

$$f_{Ftu} = f_{Fts} - \frac{w_u}{CMOD_3} \cdot (f_{Fts} - 0{,}57 \cdot f_{R3} + 0{,}26 \cdot f_{R1}) \geq 0 \quad (4)$$

Where:

w_u is the ultimate crack opening for the CMOD value considered in the design, expressed in millimeters (mm).

Considering w_u equal to 2.5 mm (equivalent to $CMOD_3$), Equation 4 can be simplified and written according to Equation 5.

$$f_{Ftu} = 0{,}57 \cdot f_{R3} - 0{,}26 \cdot f_{R1} \quad (5)$$

The moment resistance is obtained by Equation 6.

$$M_{Rd,FRC} = \frac{f_{Ftsd} + f_{Ftud}}{2} \cdot \frac{b \cdot h^2}{2} \quad (6)$$

The values used to calculate the post-cracking strength parameters of the FRC in the ULS are obtained from Equations 7 and 8.

$$f_{Ftsd} = \frac{f_{Ftsk}}{\gamma_c} \quad (7)$$

$$f_{Ftud} = \frac{f_{Ftuk}}{\gamma_c} \quad (8)$$

Table 3 presents the values for the safety factor in accordance with ABNT NBR 16935.

Table 3: Safety factor for the materials in Ultimate Limit State (ULS)

Resistances	**Coefficients**
Compressive strength of FRC	$\gamma_c = 1{,}4$
Tensile strength of FRC	$\gamma_c = 1{,}5$
Residual strength of FRC	$\gamma_c = 1{,}5$

The elastic bending moment is calculated according to Equation 9.

$$M_{Rk,e} = \frac{\sigma_{ct} \cdot b \cdot h^2}{6} \quad (9)$$

Where:

$$\sigma_{ct} = f_{ctm} = 0{,}3 \cdot f_{ck}^{\frac{2}{3}} \quad (10)$$

Table 4 provides a summary of the design of the FRC pile-supported foundation slab.

Table 4: Summary of the dimensioning of the FRC pile-supported foundation slab

Rigid-plastic model		Linear model			Elastic bending moment	
f_{Ftum} (MPa)	$M_{Rd,FRC}$ (kN.m/m)	f_{Ftsm} (MPa)	f_{Ftum} (MPa)	$M_{Rd,FRC}$ (kN.m/m)	f_{ctm} (MPa)	$M_{Rd,e}$ (kN.m/m)
1,13	135,6	1,33	1,00	139,8	3,21	269,64

Based on the moment resistance values obtained for the FRC using the rigid-plastic and linear models, the higher value was adopted, namely $M_{Rd,FRC}$ = 139,8 kN.m/m. Since both constitutive models are permitted by the *fib* Model Code 2020 and ABNT NBR 16935 for the determination of the flexural resistance of FRC sections, the higher moment resistance was selected to make full use of the structural capacity of the section.

Figure 5 presents the grid model of the pile-supported foundation slab, while Table 5 summarises the average pile load, the maximum positive and negative bending moments, and the maximum design shear force obtained from the analysis.

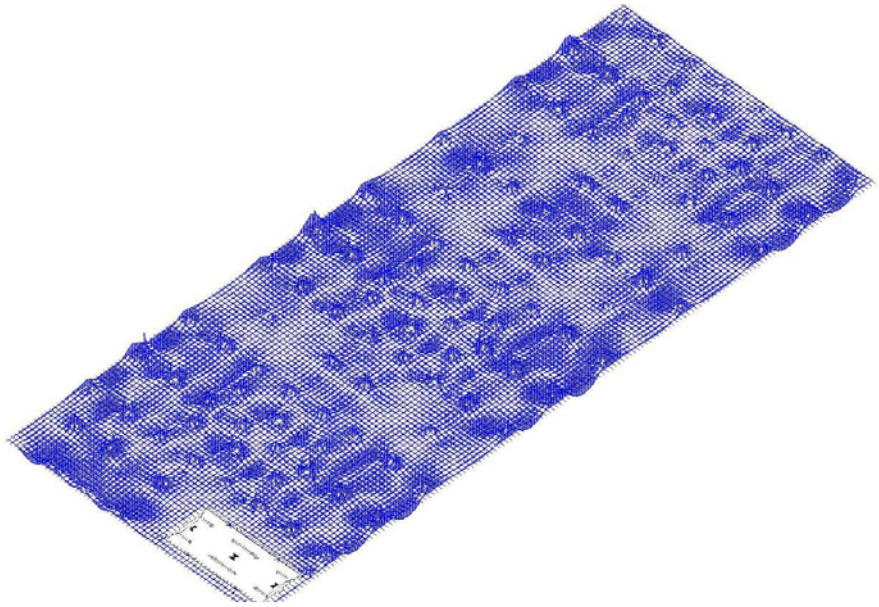


Figure 5: Grid diagram.

Table 5: Summary of the internal forces and average load in the pile-supported foundation slab.

Maximum positive design moment ($M_{p,Sd}$) (kN.m/m)	Maximum negative design moment ($M_{n,Sd}$) (kN.m/m)	Maximum design punching shear force (V_{Sd}) (kN)	Average load (kN/m²)
154	315	1722	207

As a general design assumption for the FRC pile-supported foundation slab, the presence of concentrated supports leads to stress concentrations in the support regions, typically resulting in negative bending moments exceeding the FRC resistance capacity.

Accordingly, the design procedure was established as follows.

Positive bending moments were limited to the FRC moment resistance ($M_{Rd,FRC}$). Where the values obtained from the linear elastic analysis exceeded this limit, plastic redistribution of moments was performed, with a maximum redistribution factor of 0.75. This value was selected considering the moment redistribution provisions of ABNT NBR 6118, which establishes a reference limit of 0.75 for reinforced concrete structures.

Subsequently, all sections were re-evaluated to identify regions where positive bending moments remained greater than $M_{Rd,FRC}$. In such cases, additional reinforcement was provided to supplement the positive bending capacity.

For negative bending moments, it was observed that, in regions directly above the piles, the design actions exceed the moment resistance of the FRC. Consequently, negative longitudinal reinforcement was provided in these areas to resist the excess tensile stresses.

The additional reinforcement required for both positive and negative bending moments was determined in accordance with the flexural design provisions of ABNT NBR 6118, considering the combined contribution of FRC and conventional reinforcement to the ultimate capacity of the sections.

Furthermore, punching shear verification was performed in the support regions, in accordance with the criteria established by ABNT NBR 16935 and the *fib* Model Code 2020. The slab was modelled as an FRC element with negative longitudinal reinforcement over the supports. The stresses along the critical perimeter around the supports were evaluated to assess the adequacy of the shear resistance and the potential need for additional reinforcement.

For slab elements incorporating FRC and punching shear reinforcement, Equation 11 was adopted.

$$V_{Rd} = V_{Rd,F} + V_{Rd,s} \geq V_{Sd} \quad (11)$$

In which:

$$V_{Rd,F} = V_{Rd,f} + V_{Rd,c} \quad (12)$$

The resistance provided by the fibres is calculated according to Equation 13.

$$V_{Rd,f} = \frac{f_{Ftuk}}{\gamma_f} \cdot b_0 \cdot d \quad (13)$$

Where:

$V_{Rd,f}$ represents the contribution of fibre reinforcement to shear strength;

f_{Ftuk} is the characteristic direct tensile strength of FRC, the final value, assuming wu = 1.5 mm;

b_0 is the shear-resisting control perimeter;

d is the shear-resisting effective depth of the slab.

The design shear resistance attributed to the concrete may be taken according to Equation 14.

$$V_{Rd,c} = k_\psi \cdot \frac{\sqrt{f_{ck}}}{\gamma_c} \cdot b_0 \cdot d \quad (14)$$

The parameter kΨ depends on the deformations of the slab and follows for the design value, as defined by Equation 15.

$$k_\psi = \frac{1}{1.5+0.9 \cdot k_{dg} \cdot \psi \cdot d} \leq 0.6 \quad (15)$$

$$k_{dg} = \frac{32}{16+d_g} \geq 0{,}75 \quad (16)$$

$$\psi = 1.5 \cdot \frac{r_s}{d} \cdot \frac{f_{yd}}{E_s} \quad (17)$$

Where:

d_g is the maximum size of the aggregate;

r_s denotes the position where the radial bending moment is zero with respect to the support axis.

When fibre reinforcement is mobilised to contribute to punching shear resistance, a minimum fibre content is required to ensure adequate deformation capacity, as defined by Equation 18.

$$V_{Rd,s} + V_{Rd,f} \geq 0{,}5 \cdot V_{sd} \qquad 18$$

Table 6 summarizes the punching shear verification of the pile-supported foundation slab.

Table 6: Summary of the punching shear verification of the pile-supported foundation slab.

Punching shear		Interior pile (kN)	Edge pile (kN)	Corner pile (kN)
Design Shear Strength	$V_{Rd,c}$	2341,5	1321,3	660,6
	$V_{Rd,f}$	864,5	432,3	216,1
	$V_{Rd,F}$	3206,0	1753,5	876,8
Design punching shear	V_{Sd}	1722,0	854,0	168,0
Utilization ratio	$V_{Sd}/V_{Rd,F}$	0,54	0,49	0,19

9 Quality control of FRC

Quality control of FRC shall be conducted in accordance with ABNT NBR 16938, encompassing both preliminary qualification and production control of the material. The qualification phase includes verifying the steel fibres, in accordance with ABNT NBR 15530 and characterising of the FRC composite.

For this purpose, flexural tensile tests shall be performed to determine the limit of proportionality (LOP) and the average residual strengths f_{R1m}, f_{R2m}, f_{R3m}, and f_{R4m}, in accordance with ABNT NBR 16940. Additionally, compressive strength tests shall be carried out in accordance with ABNT NBR 5739, alongside double punching tests to determine tensile strength and the average residual strengths $f_{R0.5m}$, $f_{R1.5m}$, $f_{R2.5m}$, and $f_{R3.5m}$, as specified in ABNT NBR 16939.

Following approval of the results obtained during the qualification phase, the FRC mix design is released for use in concrete production.

During construction of the foundation slab, quality control of the FRC shall be implemented, including consistency assessment by the slump test, in accordance with ABNT NBR 16889, and compressive strength test, in accordance with ABNT NBR 5739.

For monitoring tensile behaviour and residual strengths, the double punching test may be adopted, as specified in ABNT NBR 16939, in accordance with the provisions of ABNT NBR 16938. The application of this method in production control is enabled by establishing, during the material qualification phase, a correlation between the results obtained from flexural tensile tests (ABNT NBR 16940) and those derived from the double punching test.

Batch definition shall follow the criteria established in ABNT NBR 16938, adopting Type A control for applications subject to basic production control of FRC. Figure 6 presents a summary of the FRC quality control procedures, while Table 7 summarises the tests performed during production control and the corresponding batch formation criteria.

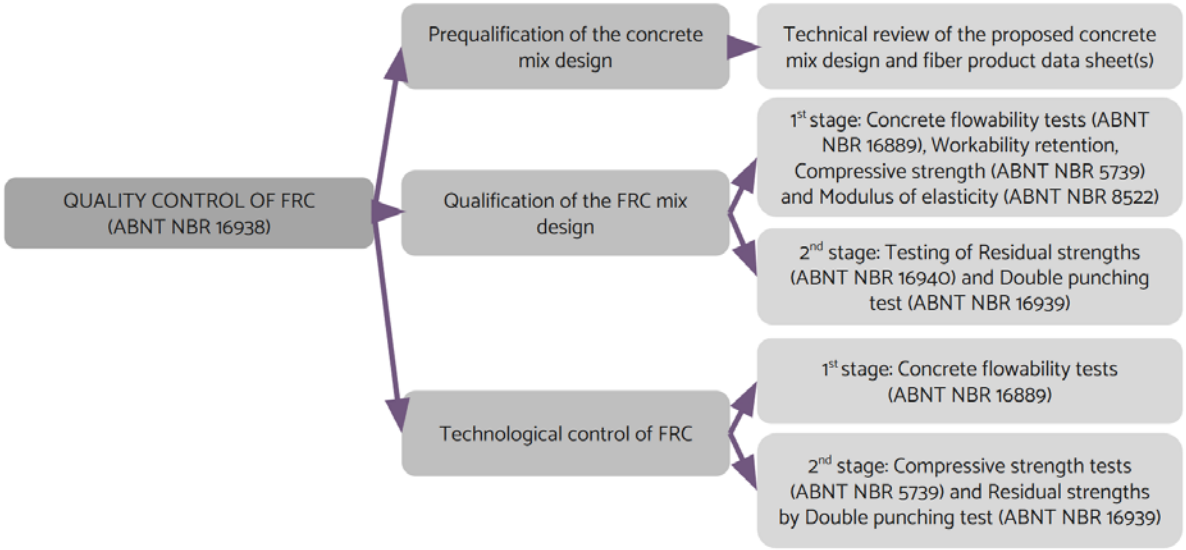


Figure 6: Summary of FRC quality control stages.

Table 7: Technological control of FRC.

Test	**Standard reference**	**Sampling**
Fluidity of concrete	ABNT NBR 16889	1 test for each truck
Compressive strength	ABNT NBR 5739	2 test specimens for each truck
Residual resistance by double punching test	ABNT NBR 16939	3 specimens with 2 samples for every 100 m³ or daily concreting time

10 Comparison of fibre-reinforced concrete and conventional reinforced concrete solutions

Following the detailed design of the reinforcement, the proposed solution resulted in a reinforcement ratio of around 40 kg/m³, taking into account the contributions of bar reinforcement, welded wire reinforcement, and discontinuous fibres. For comparison, the reinforcement ratio of conventional reinforced concrete is approximately 120 kg/m³.

Compared with the conventional reinforced concrete solution, the fibre-reinforced concrete solution resulted in a 66% reduction in the reinforcement ratio. This demonstrates its potential to significantly reduce the amount of steel used in the structure.

11Concluding remarks

This case study demonstrates the feasibility of using FRC in slabs on pile foundations. In such structural elements, loads are transferred through concentrated reactions, leading to high local stress levels, primarily associated with punching shear and negative bending moments. Using a combination of FRC and conventional reinforcement in regions of concentrated loading enhances stress redistribution and improves the system's overall structural efficiency.

Design and structural verifications, performed in accordance with the fib Model Code for Concrete Structures 2020, ABNT NBR 16935, and ABNT NBR 6118, satisfy the required safety and performance criteria, thereby validating the proposed solution. Additionally, quality control procedures in accordance with ABNT NBR 16938 are essential to ensure material conformity and the reliability of the construction process.

In this context, using FRC for slabs on pile foundations represents a technically and economically efficient solution, consistent with applicable standards and capable of ensuring adequate structural performance and safety.

12 References

EN 1992-1-1:2023, Eurocode 2: Design of Concrete Structures – Part 1-1: General Rules and Rules for Buildings, Bridges and Civil Engineering Structures. British Standards Institution (BSI), London, UK, 2023.

fib, 2023. *Model Code 2020*, Fèdération Internationale du Béton, Lausanne.

NBR 16935-2021; Design of fibre reinforced concrete structures – Procedure. Brazilian Association of Technical Standards (ABNT): Rio de Janeiro, Brazil, 2021.

NBR 6118-2023; Design of concrete structures. Brazilian Association of Technical Standards (ABNT): Rio de Janeiro, Brazil, 2023.

NBR 16938-2021; Fibre reinforced concrete – Quality control. Brazilian Association of Technical Standards (ABNT): Rio de Janeiro, Brazil, 2021.

NBR 15530-2019; Concrete steel fibres – Requirements and test methods. Brazilian Association of Technical Standards (ABNT): Rio de Janeiro, Brazil, 2019.

NBR 16940-2021; Fibre reinforced concrete – Determination of the flexural tensile strengths (limit of proportionality and residual strengths) – Test Method. Brazilian Association of Technical Standards (ABNT): Rio de Janeiro, Brazil, 2021.

NBR 5739-2018; Concrete – Compressive test of cylindrical specimens. Brazilian Association of Technical Standards (ABNT): Rio de Janeiro, Brazil, 2018.

NBR 16939-2021; Fibre reinforced concrete – Determination of tensile strength using double punching test (cracking and residual strength) – Test method. Brazilian Association of Technical Standards (ABNT): Rio de Janeiro, Brazil, 2021.

NBR 16889-2020; Fresh concrete – Slump test. Brazilian Association of Technical Standards (ABNT): Rio de Janeiro, Brazil, 2020.

Behaviour of fibre reinforced concrete in industrial floors: Comparison between the Montevideo test and EN 14651 bending test for an on-site application

Carlos Aire[1], Eneas Dosantos[2] and Luis Segura[3]

[1]: Instituto de Ingeniería, UNAM, Mexico, aire@pumas.iingen.unam.mx.

[2]: Universidad de la República, Uruguay, edosantos@fing.edu.uy.

[3]: Universidad de la República, Uruguay, lsegura@fing.edu.uy.

Abstract

The tensile characterisation of fibre reinforced concrete (FRC) in industrial floors is commonly based on flexural tests such as EN 14651. The Montevideo test (MVD) has been increasingly used for quality control due to its good correlation with flexural test results and its growing application in large-scale projects. The objective of this study is to evaluate the mechanical response of FRC using the MVD and to compare it with the EN 14651 flexural test within a full-scale application. An experimental campaign was carried out on concrete sampled during the casting of an industrial floor incorporating synthetic macrofibres. Two independent sampling series were considered, including both notched beams and cubic specimens tested using the respective methods. The results show that both approaches capture a consistent post-cracking softening response. The load–CMOD curves present similar trends, with comparable dispersion between methods. Comparison against available conversion expressions shows that a linear conversion derived specifically for synthetic fibre-reinforced concrete with softening behaviour provides a better fit (RMSE = 0.87 MPa) than a general-purpose proportional conversion (RMSE = 0.97 MPa). The limit of proportionality shows good agreement between methods, with a mean ratio of 1.10 consistent with previously reported values. Variations between sampling series are observed despite identical mix design. The smaller specimens, lower material demand and simpler testing procedure make the MVD a practical option for routine characterisation and quality control of FRC in industrial applications.

Keywords

FRC, EN 14651 flexural test, Montevideo test MVD, full-scale application, industrial floor, fibre distribution, residual strength

1 Introduction

The use of Fibre Reinforced Concrete (FRC) in structural applications has grown substantially over the past three decades. Fibres improve toughness, control cracking, and enhance durability (Naaman and Reinhardt, 2006; di Prisco et al., 2009). Industrial floors are one of the most common applications, where post-cracking residual strength directly resists shrinkage cracking, flexural cracking, and long-term deformation (Figueiredo, 2011; Barros et al., 2005). Compared to plain concrete reinforced with welded wire mesh, FRC offers clear advantages in crack width control, joint spacing, and serviceability (di Prisco et al., 2013).

Accurate characterisation of post-cracking residual strength is the foundation of FRC structural design, yet its reliable measurement in the field remains a practical challenge (RILEM TC 162-TDF, 2003; fib, 2012). The EN 14651 (2007) bending test is the most widely used standard for this purpose. Result variability at low-to-moderate fibre dosages is well documented, with coefficients of variation between 15% and 25%, attributable to the stochastic nature of fibre distribution within the fracture plane (Parmentier et al., 2008; Zerbino et al., 2012; Torrijos et al., 2010).

The Montevideo test (MVD), proposed by Segura et al. (2018; 2024) as a practical alternative for FRC characterisation, is an indirect tensile test derived from the wedge splitting test (Brühwiler and Wittmann, 1990), adapted to a standardised cubic geometry with notch dimensions equivalent to those of the EN 14651 beam. Smaller specimens, lower material demand, and simpler handling make it particularly well suited for on-site testing and quality control programmes in large-scale projects. Good correlation with EN 14651 results has been reported and refined conversion equations proposed (Segura et al., 2018; 2024; Aire et al., 2026 [Submitted]), and its adoption has been growing in recent years (Olivera et al., 2025).

The full-scale application considered in this study consisted of an industrial floor for a pharmaceutical storage warehouse in Tlajomulco de Zúñiga, Jalisco, Mexico, covering 36,000 m² with a slab thickness of 200 mm, cast in panels of 480 m². The pavement incorporated synthetic macro-fibre reinforcement. Specimens were collected from two batches during casting and tested with both methods to evaluate their correlation at full scale.

The **objective** of this paper is to evaluate the mechanical response of FRC using the MVD and to compare it with the EN 14651 flexural test within a full-scale application.

The main contribution of this study is not the development of a new correlation equation, but the validation of previously proposed laboratory-based correlations under industrial-scale production conditions. These correlations are not empirical: they were derived from the mechanical behaviour of the material, and their mechanical basis and full derivation are presented in a companion study (Aire et al., 2026). A deeper mechanical analysis is therefore beyond the scope of the present paper.

2 Experimental programme

The mix design was identical across all batches, with a cement content of 340 kg/m³ and a water-to-cement ratio of 0.70. Fibre reinforcement consisted of synthetic macrofibres of PE/PP blend, 58 mm long, with a tensile strength of 600 MPa and an elastic modulus of 6.5 GPa, dosed at 5.3 kg/m³. Figure 1 shows a general view of the industrial floor during casting.

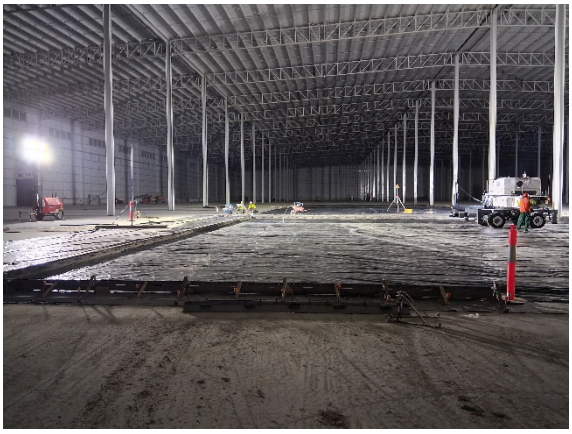


Figure 1. General view of the slab during casting.

Fresh concrete was sampled on site during the casting of a single panel. Two independent series were collected from separate batches: batch #6 (Series S1) and batch #9 (Series S2), out of 14 batches supplied for that panel. Each series comprised three notched beams and three cubes, identified as SxVj and SxCj respectively, where x denotes the series number and j the specimen number within the series. Specimens were cast in two layers compacted on a vibrating table and demoulded at 24 hours. Figure 2 shows the beam and cube specimens after screeding according to the standard requirements. Specimens were then cured under water for 28 days and transported to the laboratory for testing.



Figure 2. Beam and cube specimens from the same batch after screeding.

Notched beams were tested in three-point bending under closed-loop CMOD control in accordance with EN 14651 (2007). The limit of proportionality f_{LOP} and residual flexural tensile strengths f_{R1} to f_{R4} were determined from the load–CMOD curve using the standard expression from Equation 1.

$$f_{R,j} = \frac{3 \cdot F \cdot l}{2 \cdot b \cdot h_{sp}^2} \tag{1}$$

where F is the load at the corresponding CMOD, $l = 500$ mm is the span, $b = 150$ mm is the specimen width, and $h_{sp} = 125$ mm is the effective depth. A typical failure mode is shown in Figure 3, where cracking initiates at the notch tip and propagates vertically through the mid-span section.

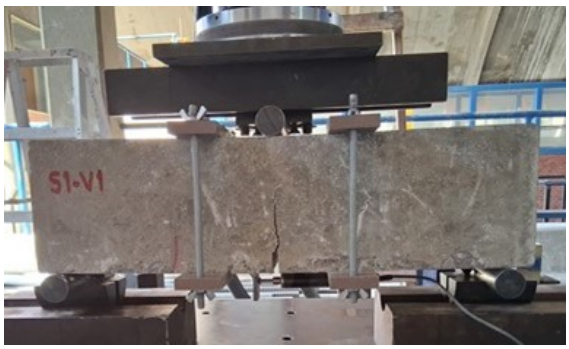


Figure 3. EN 14651 beam specimen during testing.

Cubic specimens were tested using the MVD method (Segura et al., 2018; 2024), in which a metal wedge applies indirect tension through a notch at mid-height of the cube. Tests were carried out under closed-loop displacement control. Residual strengths are obtained from the MVD load–CMOD curves using Equation (2), where F_{Ri}^{MVD} is the load at the corresponding $CMODi$, while the span l, width b and effective depth h_{sp} retain the values defined for Equation 1.

$$f_{Ri,MVD} = \frac{3F_{Ri}^{MVD} l}{2bh_{sp}^2} \tag{2}$$

Figure 4 shows a typical MVD specimen after testing. The failure mode is analogous to that of EN 14651, with a single vertical crack propagating from the notch tip driven directly by the wedge acting against the notch faces.



Figure 4. MVD cube specimen after testing.

Values obtained from MVD tests are converted to EN 14651 equivalent values following the expressions proposed by Segura-Castillo et al. (2018; 2024) (SC24) and Aire et al. (2026) (A26).

For the LOP, only SC24 is used (Equation 3), as no improved expression has been proposed for this parameter.

$$f_{LOP,EN} = 1.1\, f_{LOP,MVD}\ [MPa] \tag{3}$$

For residual strengths, both SC24 (Equation 4) and A26 (Equation 5) are applied and compared.

$$f_{Ri,EN} = 1.4\, f_{Ri,MVD}\ [MPa] \tag{4}$$

$$f_{Ri,EN} = 1.34 \cdot f_{Ri,MVD} + 0.37\ [MPa] \tag{5}$$

3 Test Results & Analysis

Figure 5 shows the load–CMOD curves for all EN 14651 beams, including the mean response plotted in green. All specimens exhibit a softening post-cracking response, with residual load increasing from fR1 to fR4 and peak loads occurring at similar CMOD values. Series S1 curves are closely grouped and show a consistent parallel trend, while Series S2 presents greater spread, with one specimen displaying an atypical hardening-type response. Series S2 is generally above S1, indicating batch-to-batch variability despite identical mix design and fibre dosage.

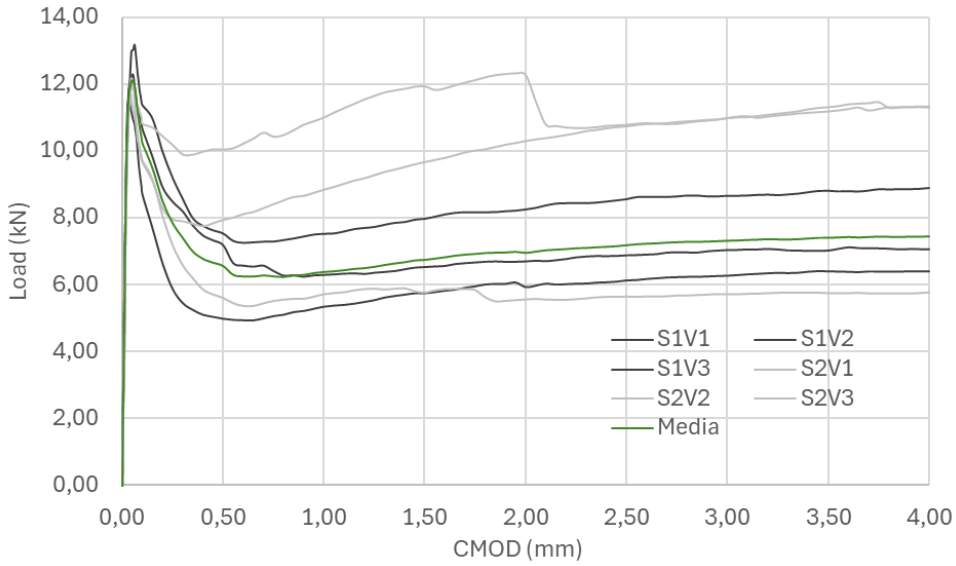


Figure 5. Load–CMOD curves for all EN 14651 specimens.

Figure 6 shows the load–CMOD curves for all MVD specimens, including the overall mean values plotted in green. All curves exhibit a softening post-cracking response with a consistent parallel trend, more uniform than observed in EN 14651. Series S2 is again above S1, consistent with the trend observed in the beam tests. The load levels are notably lower than in EN 14651, with MVD curves peaking below 6 kN compared to values exceeding 10 kN in the beam tests, reflecting the geometric and mechanical differences between both configurations.

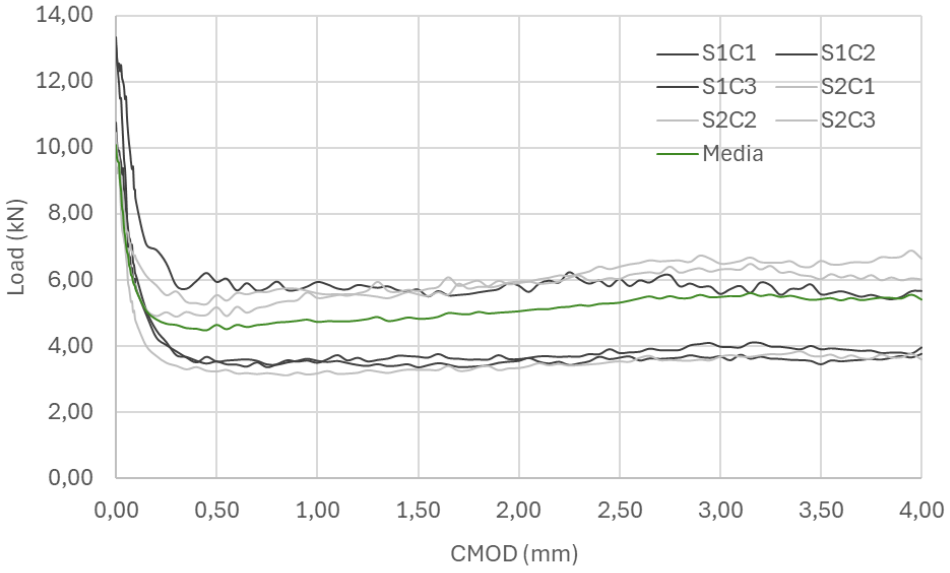


Figure 6. Load–CMOD curves for all MVD specimens.

Table 1 presents the residual strengths for EN 14651 and MVD, pooling both series (n = 6 per method), including mean values, standard deviations (STD DEV) and coefficients of variation (CV). Combining the two series reflects the natural batch-to-batch variability expected in a real production context.

Table 1. Mean residual strengths fRi for EN 14651 and MVD.

f_{Ri}	EN 14651			MVD		
	MEAN (MPa)	**STD DEV (MPa)**	**CV (%)**	**MEAN (MPa)**	**STD DEV (MPa)**	**CV (%)**
f_{R1}	2,31	0,58	25%	1,44	0,38	26%
f_{R2}	2,54	0,79	31%	1,46	0,39	27%
f_{R3}	2,60	0,73	28%	1,57	0,44	28%
f_{R4}	2,69	0,77	29%	1,56	0,43	28%

Coefficients of variation range from 25% to 31% for EN 14651 and from 26% to 28% for the MVD. These values exceed the range of 10–20% typically considered acceptable for FRC quality control (Parmentier et al., 2008; Zerbino et al., 2012). The relatively high CVs may be explained by two factors. First, FRC performance is sensitive to fibre dispersion homogeneity and non-uniform distribution was observed on some fracture surfaces, directly affecting fibre efficiency and test results. Second, the overall CV is based on only 6 specimens across two series of 3, which limits its statistical robustness.

The root mean squared error (RMSE) was computed for both expressions against the individual f_{Ri} measurements. Since all residual strengths fall within a similar range, a relative error metric is not required, and the RMSE is sufficient for this comparison. A26 shows lower RMSE values than SC24 at all residual strength levels (Table 2), with an overall RMSE of 0.87 MPa vs 0.97 MPa. This is consistent with the fact that A26 was derived exclusively from synthetic fibre-reinforced concrete with softening behaviour, while SC24 was based on a wider dataset covering different fibre types, matrices and dosage ranges.

Table 2. RMSE of conversion expressions SC24 and A26 for residual strengths.

Residual Strength	**RMSE (MPa)**	
	SC24	**A26**
f_{R1}	0.81	0.75
f_{R2}	1.05	0.93
f_{R3}	0.96	0.87
f_{R4}	1.04	0.92
f_{mean}	**0.97**	**0.87**

Figure 7 shows the dataset from Aire et al. (2026) with the corresponding linear regression, fit equation and R^2, alongside the mean f_{Ri} values from the six specimens tested in this study (Series S1 and S2).

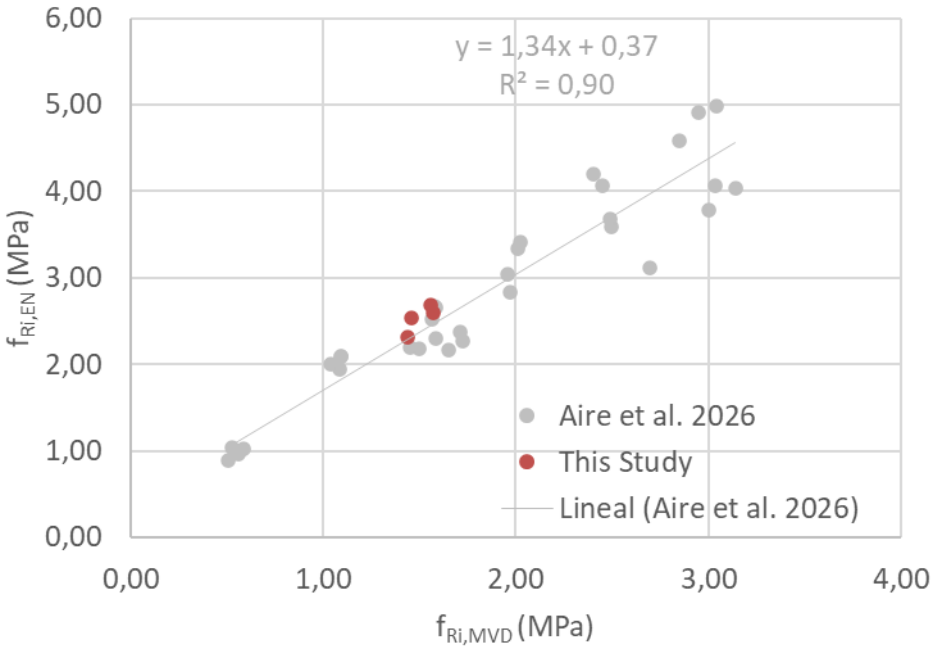


Figure 7. Mean fRi values (EN 14651 vs MVD) for all dataset with A26 values.

Table 3 presents the individual f_{LOP} values for each specimen, together with the mean, standard deviation and coefficient of variation for each test method.

Table 3. Limit of proportionality f_{LOP} for EN 14651 and MVD in MPa.

SERIES	EN	MVD
S1V1/C1	4,22	4,20
S1V2/C2	3,93	4,27
S1V3/C3	3,74	3,44
S2V1/C1	3,85	3,11
S2V2/C2	3,76	3,08
S2V3/C3	3,90	3,20
MEAN (MPa)	**3,90**	**3,55**
STD DEV (MPa)	**0,17**	**0,54**
CV (%)	**4%**	**15%**

The LOP shows notably different variability between methods: EN 14651 presents a CV of 4%, within the expected range for this parameter, while the MVD shows a CV of 15%. This higher scatter in the MVD could be partly explained by the indirect tensile mechanism of the test, which may be more sensitive to local heterogeneity in fibre distribution near the notch, compared to the bending-dominated response of EN 14651. The mean LOP values are 3.90 MPa for EN 14651 and 3.55 MPa for the MVD, giving a mean ratio of $k_{LOP} = \frac{f_{LOP}^{EN}}{f_{LOP}^{MVD}} = 1.10$, in close agreement with the value proposed in Equation 2.

4 Concluding remarks

The results suggest that the MVD test is a suitable practical tool for routine FRC characterisation and quality control in large-scale industrial floor applications. These findings are based on a single project; further validation across different mix designs and fibre types is recommended.

Both the EN 14651 flexural test and the MVD test captured a consistent post-cracking softening response in synthetic macro-fibre reinforced concrete, with comparable trends between methods and across sampling series.

Residual strength variability was observed between Series S1 and S2 despite identical mix design and fibre dosage, with CVs ranging from 25% to 31% for EN 14651 and from 26% to 28% for the MVD. This highlights the inherent sensitivity of FRC response within different batches and the importance of achieving homogeneous mixes.

Comparison of two available conversion expressions for residual strengths shows that A26 (Aire et al., 2026) consistently gives lower RMSE than SC24 (Segura-Castillo et al., 2024) across all fRi levels, with overall values of 0.87 MPa and 0.97 MPa respectively. A26 is recommended for synthetic FRC with softening behaviour in the dosage range of this study.

The LOP shows good agreement between methods, with a mean ratio of 1.10, consistent with the value proposed by Segura-Castillo et al. (2024). The higher variability observed for the MVD (CV = 15% vs 4% for EN 14651) could be partly explained by the indirect tensile mechanism of the test, which may be more sensitive to local heterogeneity near the notch.

5 Acknowledgements

This study was conducted at the Institute of Engineering, UNAM as part of research project for BARCHIP. The authors gratefully acknowledge BARCHIP's funding for this research.

6 References

Aire, C., Dosantos, E., and Segura-Castillo, L. (2026). Residual Strength Evaluation of Synthetic Fibre Reinforced Concrete via the MVD Test: An Expanded Correlation with EN 14651. Construction and Building Materials (Submitted).

Barros, J.A.O., Cunha, V.M.C.F., Ribeiro, A.F., and Antunes, J.A.B. (2005). Post-cracking behaviour of steel fibre reinforced concrete. Materials and Structures, 38(1), 47–56.

Brühwiler, E., and Wittmann, F.H. (1990). The wedge splitting test, a new method of performing stable fracture mechanics tests. Engineering Fracture Mechanics, 35(1–3), 117–125.

di Prisco, M., Plizzari, G., and Vandewalle, L. (2009). Fibre reinforced concrete: new design perspectives. Materials and Structures, 42(9), 1261–1281.

di Prisco, M., Colombo, M., and Dozio, D. (2013). Fibre-reinforced concrete in fib Model Code 2010: principles, models and test validation. Structural Concrete, 14(4), 342–361.

EN 14651 (2007). Test method for metallic fibered concrete – Measuring the flexural tensile strength (limit of proportionality (LOP), residual). European Committee for Standardisation (CEN).

fib (2012). Model Code 2010. Bulletin 65. Fèdération Internationale du Béton, Lausanne.

Figueiredo, A.D. (2011). Concreto reforçado com fibras. Tese de Livre Docência, Escola Politécnica, Universidade de São Paulo, São Paulo.

Parmentier, B., De Grove, E., Vandewalle, L., and Van Rickstal, F. (2008). Dispersion of the mechanical properties of FRC investigated by different bending tests. In: Tailor Made Concrete Structures. Walvaren and Stoelhorst (eds).

Naaman, A.E., and Reinhardt, H.W. (2006). Proposed classification of HPFRC composites based on their tensile response. Materials and Structures, 39(5), 547–555.

Olivera, V., Novello, D., and Segura-Castillo, L. (2025). Quality Control of Fibre-Reinforced Concrete Using the Montevideo Test: A Case Study in Real-World Construction. Proceedings of the fib Symposium 2025, Antibes, France.

RILEM TC 162-TDF (2003). Test and design methods for steel fibre reinforced concrete: σ–ε design method. Materials and Structures, 36(8), 560–567.

Segura, L., Monte, R., and Figueiredo, A. (2018). Characterisation of the tensile constitutive behaviour of fibre-reinforced concrete: A new configuration for the Wedge Splitting Test. Construction and Building Materials, 192, 731–741. https://doi.org/10.1016/j.conbuildmat.2018.10.101

Segura-Castillo, L., Monte, R., Galobardes, I., and de Figueiredo, A.D. (2024). Determination of tensile residual strength of fibre reinforced concrete by a robust and simple test. Materials and Structures, 57, 112. https://doi.org/10.1617/s11527-024-02321-1.

Torrijos, M.C., Barragán, B.E., and Zerbino, R.L. (2010). Placing conditions, mesostructural characteristics and post-cracking response of fibre reinforced self-compacting concretes. Construction and Building Materials, 24(6), 1078–1085.

Zerbino, R., Tobes, J.M., Bossio, M.E., and Giaccio, G. (2012). On the orientation of fibres in structural members fabricated with self compacting fibre reinforced concrete. Cement and Concrete Composites, 34(2), 191–200.

Experimental characterization and FEA-supported design of a jointless macro synthetic fibre reinforced industrial floor in Latin-America

Luis Leonardo[1], Abraham Hidalgo[2], Claudio Parada[2], Jesús Munoz[2], Péter Károly Juhász[3,4]

[1] : Monofloor México

[2] : BarChip LATAM

[3] : Chief engineer in JKP STATIC Ltd, Budapest, Hungary.

[4] : Adjunct lecturer in Budapest University of Technology and Economics, Budapest, Hungary.

Abstract

Jointless industrial floors in warehouse buildings are increasingly becoming a standard solution rather than a special design approach. Nevertheless, a standardized design method for determining the maximum joint spacing of such floors is currently unavailable; existing guidelines provide only general recommendations. This paper reviews the European TR34 and the American ACI 360R design guidelines with a focus on joint spacing criteria.

To complement existing design approaches, a finite element model was developed and applied to assess the behaviour of a jointless industrial floor subjected to shrinkage and environmental effects. Material parameters were determined through laboratory testing, and time-dependent shrinkage relationships were derived from the experimental results. The numerical analyses were performed using the ATENA software and were used to support the interpretation of field measurements and observed floor performance.

The designed jointless floor, reinforced with an optimized dosage of synthetic macro fibers, was constructed and continuously monitored. Residual strength values, shrinkage behavior of the fiber-reinforced concrete, and longitudinal floor movements were measured on site and compared with numerical predictions. The presented case study illustrates the potential of combining experimental characterization and finite element modelling to support the design and assessment of jointless industrial floors.

Keywords

Industrial floor, FEA design, Reinforced concrete, Synthetic fibers.

1 Introduction

In recent decades, industrial floors have undergone significant evolution in response to the increasing operational demands of logistics and manufacturing facilities. Traditionally, concrete floors have been designed with control joints, whose primary function is to induce and control crack formation resulting from concrete shrinkage. These conventional systems have proven to be functional and widely implemented; however, they present important limitations related to maintenance, long-term durability, and performance under intensive traffic conditions. Joints, in particular, often become critical points of deterioration, leading to issues such as spalling, loss of load transfer, increased repair costs, and disruptions to logistics operations.

In this context, jointless industrial floors have emerged as an innovative alternative aimed at eliminating or significantly reducing the number of control joints, allowing the construction of large continuous concrete slabs. This approach not only enhances the structural integrity of the system but also improves operational performance by minimizing surface discontinuities. To achieve this behavior, various design and construction systems have been developed, including the use of high fiber contents—particularly synthetic macrofibers or steel fibers—post-tensioned slabs, and shrinkage-compensating concretes. Each of these systems addresses shrinkage and crack control through different mechanisms, such as increasing stress redistribution capacity, introducing internal compressive stresses, or compensating for volumetric changes in the material.

At the same time, the digital transformation and automation of logistics processes have imposed new requirements on industrial floors. The implementation of technologies such as Automated Guided Vehicles (AGVs), Very Narrow Aisle (VNA) systems, Warehouse Management Systems (WMS), Automated Storage and Retrieval Systems (AS/RS), and Autonomous Mobile Robots (AMRs) demands surfaces with stricter geometric tolerances, greater flatness and levelness, reduced vibration, and enhanced durability. In this context, the presence of traditional joints can negatively affect the precision, speed, and reliability of these automated systems, making jointless floors particularly attractive.

Despite their advantages, the design of jointless floors still presents significant challenges, particularly in determining the maximum spacing between construction joints and controlling shrinkage effects under varying environmental conditions. Existing design guidelines, such as TR34 (The Concrete Society, 2013) and ACI 360R (ACI, 2010), provide general recommendations; however, they lack detailed methodologies that explicitly incorporate the time-dependent behavior of concrete and its interaction with environmental conditions.

Within this framework, the present work focuses on a case study of a jointless industrial floor design supported by experimental testing and finite element assessment for the design of jointless industrial floors reinforced with synthetic macrofibers in Latin America. As a case study, this proposed assessment approach was applied to the CDN4 project for PiSA Farmacéutica in Guadalajara, Mexico, designed to operate with automated equipment (AGVs) under demanding performance requirements.

The project included a restriction on the use of steel fibers; therefore, synthetic macrofibers were adopted as a viable alternative, taking advantage of their benefits in crack control, durability, and compatibility with electrical conductivity requirements. The system consists of a fiber-reinforced concrete floor designed to achieve high flatness and levelness standards, incorporating a hardened surface layer (slurry) to improve wear resistance and electrostatic dissipation.

Prior to construction, testing and technical validations were conducted, including material characterization, evaluation of the workability of fiber-reinforced concrete, and implementation of a quality control plan during construction. Additionally, sampling campaigns were carried out to assess mechanical performance and shrinkage behavior. These results were used to calibrate the numerical model and to support the interpretation of field measurements obtained during the project, providing an initial assessment of the applicability of the modelling approach under real construction conditions.

1.1 Limitations, standards, and the real nature of concrete shrinkage in Latin America

In Mexico, considered as a case study, the control of concrete shrinkage is generally defined within a regulatory framework that, although it establishes criteria for the classification, production, and evaluation of materials, presents significant limitations when attempting to predict the real behavior of concrete under field conditions.

Mexican regulations, primarily associated with NMX standards (Normas Mexicanas) and their partial alignment with international references such as ASTM, establish guidelines for materials and testing procedures, among which the following stand out:

– NMX-C-414-ONNCCE (2017) for hydraulic cements;
– NMX-C-255 for aggregates;
– NMX-C-159 for specimen preparation and curing;
– NMX-C-173 (2010) for measuring the drying shrinkage of concrete.

Although these standards provide an adequate technical basis for material characterization, their approach is predominantly descriptive and focused on quality control rather than on predicting structural behavior.

In particular, Mexican regulations tend to classify concrete into categories such as Class 1 and Class 2, depending on application and required levels of control. However, this classification primarily follows a prescriptive approach, defining how concrete should be produced rather than how it should behave in terms of volumetric deformation.

Furthermore, there are no clear and uniform shrinkage limits (expressed, for example, as microstrain at specific ages), which results in high variability in acceptance criteria among projects. This lack of standardization is further intensified by the limited integration of shrinkage considerations into structural design, particularly regarding cracking behavior, joint design, and long-term durability.

Consequently, although the Mexican regulatory framework enables consistent material characterization, it presents important challenges when attempting to extrapolate these results to the actual performance of concrete under service conditions.

1.2 Influence of materials on shrinkage

Concrete behavior with respect to shrinkage is strongly influenced by its constituent materials.

In the case of cements commonly used in Mexico (Cement Portland Ordinary – CPO, Combined Performance Category – CPC, Cement Portland Pozzolana – CPP, Cement-Polymer Systems – CPS), their chemical composition and heat of hydration directly affect shrinkage evolution, particularly at early ages. However, current standards do not explicitly link cement type to expected performance in terms of deformation behavior.

Aggregates, on the other hand, play a fundamental role by acting as the rigid skeleton of concrete, controlling shrinkage magnitude through their elastic modulus, mineralogical type, maximum size, and gradation. Despite this, in practice their selection is often driven more by cost and availability criteria than by their contribution to the volumetric performance of the system.

As a result, even when advanced mix design methodologies such as the Shilstone approach (Shilstone, 1990) are applied, the final behavior of concrete can become highly variable if the interaction between aggregates, cement, and admixtures is not considered in an integrated manner.

1.3 Shrinkage as a time-, humidity-, and environment-dependent phenomenon

Although concrete shrinkage is commonly expressed as a laboratory-measured value, its real manifestation in the field responds to a far more complex system involving environmental, geometric, and construction-related variables that are not fully captured by traditional testing methods.

From a theoretical perspective, moisture loss in concrete can be described through diffusion mechanisms, such as those established by Fick’s laws. However, this process is not static; rather, it evolves according to environmental conditions, resulting in a shrinkage trajectory dependent on both time and ambient relative humidity.

Concrete shrinkage should not be understood as a single intrinsic material property, but rather as the outcome of a dynamic system in which moisture governs evolution, time defines the trajectory, restraint transforms deformations into stresses, and the environment amplifies or mitigates the phenomenon.

Within this context, attempting to predict the real behavior of concrete – particularly joint opening or cracking – based solely on values obtained under controlled laboratory conditions implies assuming a scenario that rarely exists in practice.

1.4 Reinforcement systems for jointless floors

Jointless floors offer significant benefits for the operational performance of industrial flooring; however, they also present major challenges in design, planning, and on-site execution.

Some of the main aspects to consider in the construction of jointless floors include the control of concrete shrinkage, due to the inherent tendency of the material to contract (generating tensile stresses in larger slab panels), the long-term prediction of cracking caused

by service loads, and slab edge curling resulting from moisture and temperature differentials between the top and bottom surfaces of the slabs (Juhász and Schaul, 2023).

Therefore, given the particular characteristics associated with these flooring systems, it is necessary to implement structural reinforcement systems capable of counteracting these phenomena, which otherwise lead to different types of distress and pathologies.

The primary reinforcement systems used for jointless floors in Latin America include heavily reinforced steel slabs, post-tensioned steel tendons, as well as steel and synthetic macrofibers.

Among the advantages of using BarChip MQ58 synthetic macrofibers as structural reinforcement in jointless floors are their contribution to compensating concrete shrinkage in the plastic state, control of crack propagation and crack width in the hardened state (maintaining crack widths below 0.5 mm), provision of residual strength, and reduction in labor costs due to shorter placement times for reinforced concrete.

1.5 Fiber-reinforced concrete testing under EN 14651

To evaluate fiber performance in concrete, a beam testing methodology defined under EN 14651 is commonly used (with specimen dimensions of 150×150×550 mm). This test measures the flexural tensile behavior of fiber-reinforced concrete through the application of a central load on the specimen. The standardized methodology provides a procedure for evaluating properties such as post-cracking strength, residual load-bearing capacity, and the deflection behavior of fiber-reinforced concrete beams under controlled crack opening at the lower central section of the beam (EN 14651, 2007).

The determination of flexural tensile strength under this standard is performed using a closed-loop servo-controlled hydraulic testing machine, applying a three-point bending load to the specimen at an average deflection rate within the range of 0.05 to 0.2 mm/min, until a crack mouth opening displacement (CMOD) of 4 mm is reached at the bottom notch, as illustrated in Fig. 1.



Figure 1: The beam test setup was performed according to EN 14651

1.6 Experimental testing of fiber-reinforced concrete – Montevideo test

Another methodology used to evaluate fiber performance in concrete is the cube test governed by the Montevideo experimental procedure (with specimen dimensions of 150×150×150 mm), which measures the behavior of the composite material under indirect tensile loading generated through compression. This is achieved by applying a wedge load in

the upper notch while providing partial support through a slender steel plate at the bottom of the specimen. This standardized methodology provides a procedure for evaluating properties such as post-cracking strength, residual load-bearing capacity, and the indirect tensile behavior of fiber-reinforced concrete under the opening of an induced crack at the top surface of the cube (Segura, et al., 2024).

The determination of compressive-induced tensile strength under this experimental procedure is carried out using compression testing machines commonly available in concrete quality control laboratories. A compressive load is applied through the slender support and wedge onto the specimen at an average displacement rate of 0.5 mm/min, until a crack mouth opening displacement (CMOD) of 4 mm is reached at the upper notch, as illustrated in Fig. 2.



Figure 2: Cube test setup according to the Montevideo method

2 Designing methods of industrial floors

2.1 TR34

Current design methodologies, such as TR34 (The Concrete Society, 2013), provide solid foundations for the dimensioning of industrial floors by considering loads, service conditions, durability, and shrinkage control, allowing both traditional jointed systems and large-panel or jointless floor solutions to be addressed.

However, they present relevant limitations. Concrete shrinkage is an unavoidable phenomenon; therefore, it is not possible to completely eliminate the risk of cracking nor entirely dispense with joints. In traditional systems, deterioration tends to concentrate at the joints, affecting load transfer and increasing maintenance requirements; whereas in jointless floors, although these critical points are reduced, uncertainty associated with restraint-induced cracking increases.

Additionally, factors such as environmental conditions, interaction with the subbase, and the time-dependent behavior of concrete cannot always be predicted accurately within current design approaches. This, together with the limited coverage of some advanced systems, highlights the need for more comprehensive methodologies, particularly in response to the higher performance demands arising from automation in modern industrial facilities.

2.2 ACI 360R

Another widely used methodology for the design of industrial floors is the ACI 360R (ACI, 2010) design guide, which provides technical recommendations for the analysis and design of concrete slabs supported on ground.

This methodology is based on Westergaard's theory and considers as a fundamental design principle that the concrete slab and the supporting soil act as a global integrated system, in which the soil behaves as an elastic support that generally distributes the applied loads.

The design objective under this methodology is to determine slab thickness, slab dimensions, load transfer capacity, crack control strategies, and the type of global reinforcement that enables the concrete to withstand the structural demands imposed on the floor.

Among the capabilities of this methodology is the design of slab thickness for different loading typologies, the analysis of load applications at various locations (such as interior, edge, and corner positions), the provision of recommendations for joint spacing, and guidance on the use of different types of structural reinforcement.

However, several limitations are associated with this methodology. It does not establish a specific design procedure for jointless floors (with joint spacing greater than 7.5 m), does not explicitly consider loads generated by automated equipment (such as Automated Guided Vehicles, AGVs), and generally adopts higher safety factors compared to other industrial floor design methodologies (such as TR34). Finally, it relies on equations derived from the Westergaard model, which simplifies the actual behavior of the soil–slab interaction.

For this reason, given the limitations of the industrial floor design methods currently used in Latin America, the adoption of viable alternatives, such as numerical analysis, becomes essential to achieve a more accurate approximation of the actual behavior of the floor structure and, consequently, to optimize resource utilization

2.3 Numerical analysis

The ultimate limit state (ULS), as defined by design standards, corresponds to the condition in which the structure is no longer capable of carrying additional loads. In the case of industrial floors, this condition is difficult to define, as failure cannot be identified as clearly as for structural elements such as slabs. Design standards addressing the ULS are typically based on the flexural and shear resistance of the floor; however, these do not necessarily coincide with the actual load-bearing capacity of the system. Consequently, compliance with the prescribed limit values given in the relevant guidelines is required when assessing the ULS.

In contrast, the serviceability limit state (SLS) represents a more relevant criterion for industrial floors. Failure in this context is more reasonably associated with deformations and crack widths that impair functionality. However, current guidelines provide limited guidance for the evaluation of these parameters, particularly in the case of jointless industrial floors. Therefore, the structural assessment was carried out at the SLS using finite element analysis, considering characteristic values for loads and mean values for material properties.

The finite element analysis was performed using the ATENA software (Cervenka Consulting, 2026). The material model is based on the Willam–Menétrey failure criterion (Menétrey and Willam, 1995), while the effect of fiber reinforcement was incorporated using the modified fracture energy method, as described in detail in *fib* Bulletin 117 (*fib*, 2025). The subbase beneath the slab was also modeled using three-dimensional finite elements, connected to the slab with an interface element. The subbase was modeled using a Drucker–Prager material model. The subgrade was represented by nonlinear springs calibrated based on the determined bedding parameters (Fig. 3).

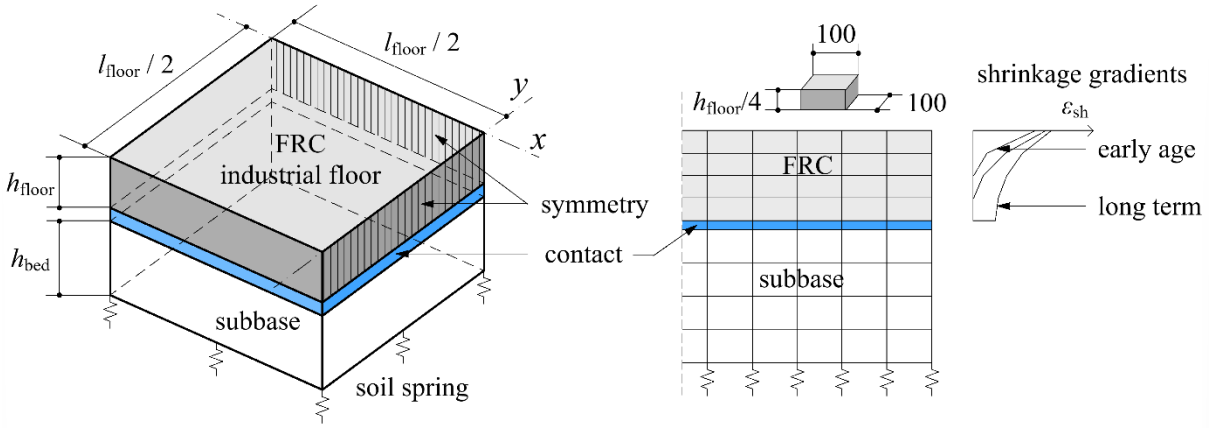


Figure 3: Finite element model of the floor

Time-dependent loading and shrinkage of the slab were introduced through sequential analysis intervals: in the first interval, self-weight was applied; in the second interval, initial shrinkage was introduced, accounting for an assumed cross-sectional gradient; in the third interval, the full service load was applied; and in the fourth interval, the remaining shrinkage was considered. These intervals represent actual time-dependent processes. The ultimate shrinkage value was obtained from experimental testing, while the evolution of the shrinkage gradient over time was determined based on environmental conditions – primarily relative humidity – and an estimated diffusion coefficient.

By applying both loads (self-weight and imposed loads) together with shrinkage effects, the crack pattern, crack widths, and deformation response of the slab were obtained. The resulting crack widths and deformations were found to be within acceptable limits, with a maximum crack width of 0.275 mm and a maximum deformation of 2.86 mm (Fig. 4).

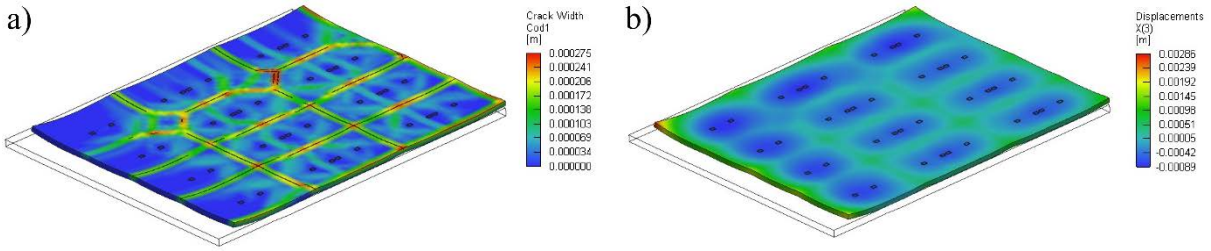


Figure 4: Results of FEA a) crack width and b) displacements

3 Design challenges of jointless industrial floors

3.1 Nonlinear hygrometric path

Ambient relative humidity is not constant; it varies with daily and seasonal cycles, continuously modifying the moisture gradient within the concrete.

This implies that shrinkage evolves nonlinearly over time and that concrete does not necessarily follow the theoretical curve originally predicted.

3.2 Difference between theoretical, measured, and observed shrinkage

There is a fundamental disconnect among three levels of analysis:

– Theoretical value, based on idealized diffusion and hydration models, represented as a continuous curve over time.
– Laboratory testing (prisms/bars), performed under controlled conditions, with simplified geometry and minimal restraint.
– Field behavior (joint opening / cracking), resulting from real conditions that include movement restraint, thermal and moisture gradients, subbase interaction, and construction sequencing.

Joint opening measured in the field does not represent shrinkage alone, but rather the integrated response of a complex system in which multiple phenomena act simultaneously.

3.3 Phenomena not replicable in laboratory conditions

Conventional shrinkage tests do not capture critical conditions present in real construction environments, such as:

– moisture gradients through the slab thickness;
– differences between top and bottom surfaces (curling/warping);
– friction with the subbase (with or without polyethylene layers);
– partial or total restraint to movement;
– thermal history of the element;
– variability in curing processes.

Therefore, laboratory testing represents an idealized behavior, whereas field conditions reflect a restrained, heterogeneous system that continuously evolves over time.

3.4 Advanced variables and limitations in current modeling approaches

Beyond the differences between theoretical values, laboratory testing, and field behavior, there exists a set of fundamental variables that govern the actual evolution of shrinkage and that are not yet fully defined or standardized within current regulatory frameworks or conventional design methodologies.

Among these variables are:
– the concrete diffusion coefficient, which governs the evolution of moisture content over time and its distribution within the section;
– the viscoelastic behavior of the material, including creep and relaxation phenomena in both cracked and uncracked states;
– the time–shrinkage relationship, particularly in scenarios where the rate of moisture loss is not constant;
– real loading conditions over time, which are often not clearly defined during the design stage;
– environmental conditions, including relative humidity and temperature;
– convection and evaporation mechanisms that determine the rate of surface moisture loss.

Additionally, in fiber-reinforced systems, an additional question arises regarding the long-term behavior of the composite material, particularly concerning creep and relaxation within cracked sections.

3.5 Implications for design and prediction

Even when an optimized mix design and laboratory-measured shrinkage values are available, direct extrapolation to field behavior introduces a significant degree of uncertainty.

This occurs because theoretical values lose predictive capability when the interaction among material properties, environmental conditions, and boundary conditions is not incorporated.

The inclusion of these variables within predictive models requires not only advanced formulations but also simulation tools capable of representing system evolution over time, such as approaches based on finite element analysis (FEA), which must be calibrated using real-scale data.

3.6 Conceptual framework and need for advanced modeling

The analysis presented in Sections 3.1 and 3.3 highlights a fundamental gap between current industrial floor design methodologies and the physical mechanisms governing concrete behavior in real service conditions.

Design guides such as TR34 (The Concrete Society, 2013) and ACI 360R (ACI, 2010) provide robust engineering frameworks for slab dimensioning, load analysis, and serviceability considerations. However, these methodologies rely primarily on simplified assumptions regarding shrinkage behavior, soil–structure interaction, and environmental effects. As a result, shrinkage is typically incorporated through empirical factors or prescriptive joint spacing recommendations rather than through explicit simulation of the governing physical processes.

Conversely, the behavior described in Chapter 3 demonstrates that concrete shrinkage is not a single material property but a coupled, time-dependent phenomenon influenced by moisture diffusion, environmental variability, structural restraint, and viscoelastic material response. The discrepancy between theoretical predictions, laboratory measurements, and field observations indicates that conventional analytical approaches cannot fully capture system evolution over time.

This mismatch becomes particularly critical in jointless floor systems, where the reduction of joints transfers uncertainty from discrete locations (joints) to distributed mechanisms such as restrained deformation and cracking development.

Therefore, a design methodology capable of integrating material behavior, environmental boundary conditions, and structural response within a unified framework is required. Numerical approaches based on advanced finite element analysis (FEA) provide a suitable platform for this integration, allowing simulation of moisture-driven deformation, stress redistribution, and long-term performance under realistic conditions.

The present study provides an initial investigation into the application of finite element modelling techniques for incorporating these coupled mechanisms and assessing the behaviour of jointless industrial floors under Latin American environmental conditions.

4 A Mexican case study

4.1 CDN4 Project – PiSA Farmacéutica

The industrial floor of the CDN4 project for PiSA Farmacéutica in Guadalajara, Mexico, was designed considering the specific Floor Requirements for operation with automated equipment (AGV) and constructed in accordance with a design developed by JKP STATIC and Monofloor, as a high-performance system intended for demanding industrial conditions.

Within these Floor Requirements, the recommendation to avoid the use of steel fibers in the flooring system was also included. Therefore, the use of macrosynthetic fibers was analyzed as a viable alternative to this restriction, due to their advantages in terms of crack control, durability, residual strength, and compatibility with conductivity requirements and automated system operations, as they do not generate magnetic interference or corrosion-related risks.

The design provides high structural capacity to withstand concentrated and repetitive loads, as well as strict control of flatness and levelness, which is essential for the proper operation of automated equipment. Additionally, the design aims to minimize the impact of joints, maintain nearly zero slopes, and ensure adequate friction conditions, supporting continuous, precise, and safe operation.

The constructed system corresponds to a fiber-reinforced concrete floor, placed with laser-guided leveling control and finished with high-precision surface treatments. As a key element, a hydrated layer (slurry coat) of mineral hardener was incorporated, applied fresh-on-fresh with an approximate thickness of 3.7 mm, improving wear resistance and surface quality.

The placement process of this layer consists of preparing the hardener as a fluid mortar, applying it continuously over the fresh concrete, integrating it through mechanical troweling, and ensuring controlled curing. Additionally, this layer is connected to the grounding system, enabling compliance with the electrical conductivity requirement of the floor ($RE < 10^6$ ohm).

Overall, the floor is characterized by high flatness, durability, surface strength, and electrostatic dissipation capacity, meeting the operational requirements of the project (DS Automotion GmbH, 2021; DS Automotion GmbH, 2023).

Prior to construction, testing and technical validations were carried out to ensure system performance from the design stage. These included determining the physical properties of aggregates used for concrete production, as well as evaluating the workability of fiber-reinforced concrete both at laboratory scale and through on-site industrial trials, with the objective of verifying its behavior during placement and finishing.

Additionally, a quality control plan was established to ensure proper system execution, incorporating best practices throughout all stages of the construction process, including fiber dosing and addition, mixing, transport, placement, leveling, surface finishing, and curing of the concrete slab. This control was key to ensuring material uniformity, proper integration of components, and compliance with the floor performance requirements.

As part of this comprehensive quality assurance approach, criteria were also defined for specimen sampling and testing procedures for fiber-reinforced concrete, which are presented and developed in the following section.

4.2 Specimen sampling and results

For the present Jointless Floor project in Mexico, three beam sampling campaigns were conducted for control testing (in accordance with EN 14651), two sampling campaigns of cubes and beams were carried out for a research project in collaboration with Universidad Nacional Autónoma de México (UNAM), and finally two sampling campaigns were performed to evaluate the shrinkage of concrete placed on site (in accordance with NMX C173).

The results obtained from the control samples tested at the Mexican Institute of Cement and Concrete (IMCYC) for the macrofiber-reinforced concrete used in this project are shown in Table 1. These results ensure average values exceeding the residual strength parameters used in the model iterations for the ATENA software applied to the structural design of the jointless floor in Mexico, with f_{R1}, f_{R2}, f_{R3}, and f_{R4} values of 1.65, 2.00, 2.35, and 2.50 MPa, respectively.

Table 1: Residual strength values from control tests performed at IMCYC for beams

Sampling	Campaign number	LOP (MPa)	f_{R1} - CMOD 0.5 mm (MPa)	f_{R2} - CMOD 1.5 mm (MPa)	f_{R3} - CMOD 2.5 mm (MPa)	f_{R4} - CMOD 3.5 mm (MPa)
Control (IMCYC)	1	4.50	2.10	2.60	2.90	3.10
	2	4.20	1.90	2.40	2.60	2.80
	3	4.80	1.90	2.30	2.80	3.00
	CV	6.7%	5.9%	6.3%	5.5%	5.1%
	Mean	**4.50**	**1.97**	**2.43**	**2.77**	**2.97**

For their part, Tables 2 and 3 present results from the two experimental campaigns conducted in collaboration with UNAM for beams and cubes, respectively. These results likewise show average values that exceed the residual strength parameters used in the model iterations within the ATENA software applied to the structural design of the present project.

Table 2: Residual strength values from research tests performed at UNAM for beams

Sampling	Campaign number	LOP (MPa)	f_{R1} - CMOD 0.5 mm (MPa)	f_{R2} - CMOD 1.5 mm (MPa)	f_{R3} - CMOD 2.5 mm (MPa)	f_{R4} - CMOD 3.5 mm (MPa)
Research (UNAM)	1	3.81	2.05	2.13	2.26	2.34
	2	3.74	2.46	2.89	2.85	2.98
	CV	1.3%	12.9%	21.4%	16.3%	17.0%
	Mean	**3.78**	**2.26**	**2.51**	**2.56**	**2.66**

Table 3: Residual strength values from research tests performed at UNAM for cubes

Sampling	Campaign number	LOP (MPa)	f_{R1} - CMOD 0.5 mm (MPa)	f_{R2} - CMOD 1.5 mm (MPa)	f_{R3} - CMOD 2.5 mm (MPa)	f_{R4} - CMOD 3.5 mm (MPa)
Research (UNAM)	1	3.81	2.30	2.25	2.38	2.28
	2	3.01	2.46	2.56	2.81	2.87
	CV	16.6%	4.8%	9.1%	11.7%	16.2%
	Mean	**3.41**	**2.38**	**2.41**	**2.60**	**2.58**

Considering the aforementioned results, the research study conducted in collaboration with UNAM concludes with the following correlation equations for the proportional limit and residual strengths, expressed as a function of the loads obtained from the Montevideo test.

$$f_{LOP} = \frac{3f_{LOP}l}{2bh_{sp}^2} = 1.44\frac{f_{LOP}^{MVD}l}{bh_{sp}^2} \qquad (1)$$

$$f_{Ri} = \frac{3f_{i}l}{2bh_{sp}^2} = 2.47\frac{f_{Ri}^{MVD}l}{bh_{sp}^2} \qquad (2)$$

On the other hand, the average results of the evaluation of concrete shrinkage under laboratory conditions for both campaigns are presented in Fig. 5, where it is evident that the shrinkage of the concrete placed in the project at 92 days (with 480 με and 500 με respectively) is less than 600 με in the model iterations for the ATENA software applied to the design of the jointless floor.

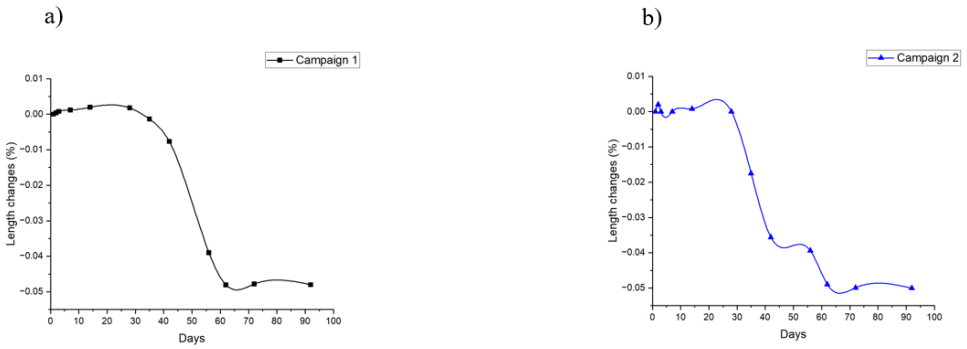


Figure 5: a) shrinkage campaign 1 and b) shrinkage campaign 2

Finally, in situ physical measurements were conducted at three months to determine the opening length of the construction joints (Fig. 6). By comparing these shrinkage measurements (as a function of both the long and short slab dimensions, with values of 250 με) with the concrete shrinkage values determined under laboratory conditions, it was verified that the shrinkage values are evidently lower due to the restraints present at the slab joints and the friction generated between the slab and its base.

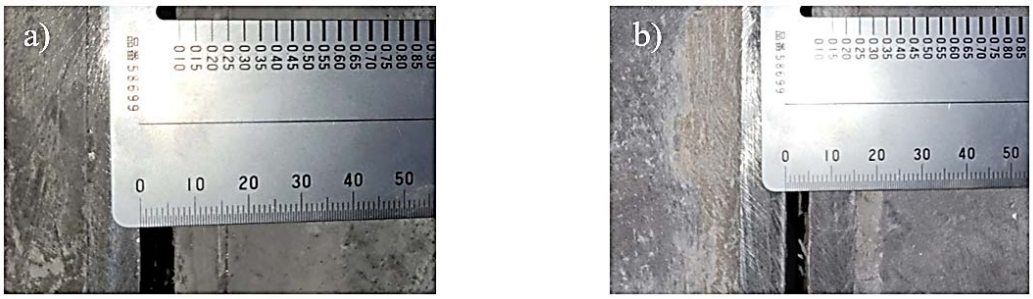


Figure 6: a) joint opening long side and b) joint opening short side

5 Concluding remarks

The design of jointless industrial floors cannot be considered a straightforward extension of conventional slab design, as it involves a significantly higher level of complexity due to the interaction of material behavior, environmental conditions, and boundary constraints. Unlike traditional structural elements, failure mechanisms in industrial floors are not always clearly defined, and serviceability criteria often govern performance.

The results presented in this study confirm that concrete shrinkage is not a single deterministic parameter but a time-dependent, environment-driven phenomenon that must be evaluated as part of a coupled system. The observed discrepancies between theoretical predictions, laboratory measurements, and field performance highlight the limitations of simplified design approaches.

In this context, a comprehensive understanding of concrete material parameters – including diffusion properties, viscoelastic response, and fiber-reinforced post-cracking behavior – is essential for reliable prediction. The study demonstrates that advanced finite element analysis (FEA) provides a suitable framework to integrate these variables and to simulate the evolution of stresses, deformations, and cracking over time.

A case study from Mexico was presented to illustrate the challenges associated with current regulatory frameworks and to evaluate the applicability of the modelling approach under real construction and environmental conditions. Furthermore, specific experimental procedures and material characterization approaches were developed to support the numerical modeling process and improve prediction accuracy.

The presented results indicate that the integration of experimental characterization and FEA-based modelling can support the assessment of jointless floor behaviour and help reduce uncertainty in design decisions. This is particularly relevant for modern industrial applications requiring high precision, such as automated logistics systems.

Further research and additional case studies are needed to establish more robust performance-based design methodologies for jointless industrial floors.

6 References

ACI 360R-10, 2010. *Guide to Design of Slab on Ground*, Farmington Hills, USA.

ASTM C157/C157M-24, 2024. *Standard Test Method for Length Change of Hardened Hydraulic-Cement Mortar and Concrete*, ASTM International.

Cervenka Consulting (2026), www.cervenka.cz/products/atena last accessed 2026/03/28.

DS Automotion GmbH, 2021. *Floor Requirements Specification (Revision 1.3)*, Linz, Austria.

DS Automotion GmbH, 2023. *Floor Requirements Specification – Supplement for Magnetic Navigation (Revision 2.0)*, Linz, Austria.

EN 14651:2007+A1:2008, 2007. *Test method for metallic fibre concrete. Measuring the flexural tensile strength (limit of proportionality (LOP) residual)*, Brussels, Belgium: European Committee for Standardization.

Fédération internationale du béton (*fib*), 2025. *FEM-based approaches for the design of FRC Structures*. fib Bulletin No. 117. Lausanne, Switzerland: Fédération internationale du béton (*fib*). DOI: https://doi.org/10.35789/fib.BULL.0117

Juhász, P.K., Schaul, P., 2023. "Parametric numerical study on jointless macro synthetic fiber reinforced concrete industrial floors", in: *ACI-fib-RILEM International Workshop 2023*, Tempe, Arizona, USA, 18-20 September 2023.

Menétrey, P., Willam, K. J., 1995. Triaxial Failure Criterion for Concrete and Its Generalization, ACI Structural Journal 92 (3) pp 311–318. DOI: https://doi.org/10.14359/1132

NMX-C-173-ONNCCE-2010, 2010. Industria de la Construcción – Concreto Hidráulico – Determinación de la variación en longitud de especímenes de mortero de cemento y de concreto endurecidos, ONNCCE, México.

NMX-C-414-ONNCCE-2017, 2017. Industria de la Construcción – Cementantes Hidráulicos – Especificaciones y Métodos de Ensayo, ONNCCE, México.

Segura, L., Monte, R., Galobardes, I., Figueiredo, A., 2024. "Determination of tensile residual strength of fibre reinforced concrete by a robust and simple test", *Materials and Structures* 57. DOI: https://doi.org/10.1617/s11527-024-02321-1

Shilstone, J.S.M., 1990. Concrete Mixture Optimization, ACI Concrete International 12(6) pp 33-39.

The Concrete Society, 2013. *Concrete Industrial Ground Floors. Technical Report No. 34 (4th Edition)*. Camberley, UK: The Concrete Society.

Hybrid Fibre-Reinforced Concrete Shear Walls for Seismic-Resilient Structures

Alexandru Trandafir[1]

[1]: Technical University of Civil Engineering Bucharest, Bucharest, Romania.

Abstract

Concrete shear walls are used as the primary lateral force-resisting system in multi-story buildings. Their seismic response is governed by the behaviour of the plastic region at the wall base, where high shear demands and large inelastic deformations concentrate. This paper investigates a hybrid structural solution aimed at enhancing the seismic response and resilience of shear walls. The proposed concept uses fibre-reinforced concrete combined with conventional reinforcement in the critical base region of the wall, while the remaining height is built using conventional concrete. This approach exploits the superior post-cracking behaviour, enhanced shear resistance, and improved deformability of fibre-reinforced concrete in critical regions. Existing test data on shear walls with steel fibres indicate a stable hysteretic response under reversed cyclic loading, increased normalized shear strength, and enhanced displacement capacity compared to conventional walls. The research focuses on the shear and deformation capacity of plastic regions, addressing the interaction between steel fibres and reinforcement under combined flexure and shear. Numerical simulations are used to evaluate the seismic behaviour of hybrid shear walls and contribute to the development of novel, repairable, and seismic-resilient wall structures. Compared to conventional walls, fibre-reinforced specimens exhibited at least a 50% increase in deformation capacity and a substantial increase in maximum shear resistance.

Keywords

Fibre reinforced concrete, hybrid shear walls, shear resistance, seismic response, resilience

1 Introduction

Reinforced concrete (RC) shear walls are widely used as primary lateral force-resisting systems in buildings located in seismic regions. Their seismic performance is largely governed by the behaviour of the plastic hinge region that forms at the wall base during strong earthquakes. This plastic region is subjected to high shear forces, large flexural demands, and significant inelastic deformations. It therefore governs the failure mechanism and displacement capacity of the structure (Paulay and Priestley, 1992). Under reversed cyclic loading, structural degradation concentrates in the plastic hinge region, leading to diagonal cracking, stiffness deterioration, and progressive shear strength degradation. Concrete spalling and crushing can occur at moderate drift levels, exposing the longitudinal reinforcement and requiring adequate transverse confinement to prevent bar buckling. To prevent these failure modes, dense transverse reinforcement is required to provide confinement and resistance. However, such detailing often leads to reinforcement congestion and becomes increasingly impractical for high-strength concrete. The post-earthquake condition of conventional RC shear walls also raises concerns regarding resilience. Large residual deformations, wide cracks, and localized crushing can compromise repairability, and lead to extended downtime or demolition in severe cases (Kam et al, 2011). These outcomes are inconsistent with resilience-oriented design objectives, which emphasize controlled damage and rapid recovery.

Fibre-reinforced concrete (FRC) offers a potential solution to these limitations. Steel fibres modify the post-cracking response of concrete through a crack-bridging mechanism that resists tensile stresses across cracks and provide improved residual tensile strength (Di Prisco et al, 2009; and Amin and Foster, 2016). In addition, fibres contribute to shear resistance and provide distributed confinement at the material level (Dazio et al 2008). The higher material cost of FRC, however, limits its use in entire structural members. A more efficient approach is to use FRC locally in the plastic region at the wall base, where inelastic demands are largest, while the remaining wall height is constructed with conventional RC. This hybrid solution aims to enhance seismic performance while maintaining practical and economic efficiency.

This paper examines the concept of hybrid FRC shear walls and evaluates its potential to improve seismic performance and resilience. Experimental results from previous studies performed by different authors are collected to assess the effect of fibres on strength, deformation capacity, and failure mechanism. Selected results are further discussed based on existing modelling approaches to evaluate the role of fibres in the cyclic response of shear walls.

2 Concept of hybrid fibre-reinforced concrete shear walls

The concept of hybrid fibre-reinforced shear walls, first introduced by Parra-Montesinos (2005), is based on strategic zoning of materials along the wall height to optimize structural performance and construction efficiency. As shown in Fig. 1, steel FRC is applied in the critical region at the wall base, where inelastic demands and shear stresses are largest, while conventional RC is used in the remaining height. The FRC zone extends from the base to about 1-2 times the wall length or up to about two stories. Above this region, structural demands decrease significantly, and the use of conventional RC ensures material efficiency without compromising global behaviour. The transition between FRC and RC can be made through a construction joint, as commonly used in practice, or through a properly detailed interface ensuring stress transfer and deformation compatibility.

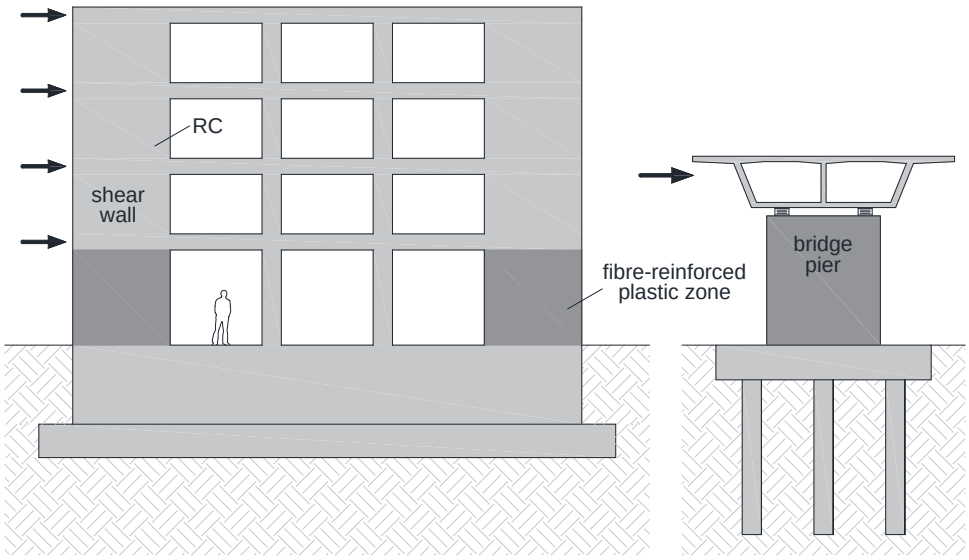


Figure 1: Concept of hybrid fibre-reinforced concrete shear wall with localized FRC plastic zone.

The localization of FRC at the wall base follows the characteristic response of cantilever shear walls under seismic loading, where plastic deformations concentrate near the base due to bending moment distribution. Within this region, multiple mechanisms develop, including flexural cracking, high shear stresses, reinforcement yielding, concrete spalling and crushing in boundaries, and potential buckling of flexural reinforcement (Paulay and Priestley, 1992).

The use of FRC modifies these mechanisms through fibre crack-bridging, which transmits tensile stresses across cracks, limits crack widths, and promotes a more distributed cracking pattern when sufficient fibres are used in the concrete mix (Di Prisco et al, 2009). Fibres also enhance shear resistance through crack bridging, with measured increases in post-cracking shear capacity of 40% (Amin and Foster, 2016), while reducing shear strength degradation under increasing deformations. In boundary zones, the three-dimensional fibre distribution improves compression behaviour by delaying cover spalling and concrete crushing, and thus restraining bar buckling (Dazio et al 2008). Under reversed cyclic loading, progressive fibre pull-out contributes to energy dissipation and stabilizes the hysteretic response (Hung et al, 2017). The resulting behaviour is characterized by improved shear resistance, crack control, deformation capacity, and damage tolerance. Therefore, the hybrid wall configuration concentrates steel FRC only in the plastic region, combining enhanced seismic performance with practical and economic feasibility.

3 Overview of existing steel FRC shear wall tests

Experimental research over the past two decades has shown that fibre reinforcement improves shear strength, deformation capacity, and damage control in structural walls. Early tests by Dazio et al (2008) demonstrated that shear walls with high fibre contents (3-6% by volume) can achieve stable hysteretic response and high ductility without transverse reinforcement, indicating effective crack control and material-level confinement. System-level tests by Lequesne et al (2013) confirmed that walls with steel FRC in the first storey exhibit a ductile, flexure-dominated response at the base, reaching drifts of about 2.5% at failure while sustaining high shear stress demands. In contrast, tests by Athanasopoulou and Parra-Montesinos (2013) showed that FRC walls can still fail in sliding shear as fibres do not prevent such failure.

Table 1 summarizes the main geometric and material properties of the shear wall specimens considered in this study (Athanasopoulou and Parra-Montesinos, 2013; Hung et al, 2017, 2020; Li et al, 2023; and Ni et al 2024). The specimens were tested as cantilevers with a shear span-to-depth ratio a/h=1.08-2.25. Section depth varies between h=1000-1500 mm, while web thickness is b=102-160 mm. Flexural web reinforcement ratio is ρ_l=0.21-0.71%, while shear reinforcement ratio is ρ_w=0.13-0.83%, with yield strength f_{yw}=422-849 MPa. Concrete compressive strength ranges between f_c=40-166 MPa, with an axial load ratio (ALR) up to 0.30. Fibre volumetric ratio is ρ_f=0-2.5%, with the FRC walls incorporating steel fibres with an aspect ratio between l_f/d_f=55-79. The measured peak shear force, V_{exp}, ranges from 278 to 2814 kN.

Table 1: Summary of properties of test specimens.

Specimen name	**b (mm)**	**h (mm)**	**a/h (-)**	**ρ_l (%)**	**ρ_w (%)**	**ρ_f (%)**	**l_f/d_f (-)**	**f_{yw} (MPa)**	**f_c (MPa)**	**ALR (%)**	**V_{exp} (kN)**
S1	102	1016	1.20	0.71	0.71	0	-	660	46.2	0	363
S2	102	1016	1.20	0.31	0.31	2.0	55	660	48.3	0	278
S5	102	1016	1.20	0.63	0.63	1.5	55	633	39.3	0	354
S7	102	1016	1.50	0.21	0.13	2.0	55	660	46.9	0	365
U-H-0.5	160	1700	1.13	0.33	0.44	0	-	849	166	0	1330
UF-N-0.5	160	1700	1.13	0.47	0.63	2.0	79	455	125	0	1637
U-H-0.8	160	1700	1.13	0.71	0.83	0	-	825	158	0	2082
UF-H-0.8	160	1700	1.13	0.71	0.83	2.0	79	825	115	0	2599
HF/75-H	160	1700	1.13	0.50	0.50	0.75	79	785	82	0	2152
U/0-H	160	1700	1.13	0.50	0.50	0	-	785	114	0	1922
UF/150-N	160	1700	1.13	0.50	0.50	1.5	79	420	93	0	2291
UF/150-H	160	1700	1.13	0.50	0.50	1.5	79	785	93	0	2291
UF1.5/150	150	1000	2.25	0.45	0.45	1.5	65	719	92[a)]	0.29	1071
UF2.5/150	150	1000	2.25	0.45	0.45	2.5	65	719	105[a)]	0.29	1303
UF2.5/300	150	1000	2.25	0.45	0.23	2.5	65	719	105[a)]	0.29	1303
HC50	120	1200	1.08	0.56	0.56	0	-	400	59.2	0.30	1501
UC50-1	120	1200	1.08	0.56	0.56	2.3	65	400	150[b)]	0.24	2720
UC60-1	120	1200	1.08	0.56	0.56	2.3	65	400	150[b)]	0.28	2757
UC50-2	120	1200	1.08	0.38	0.38	2.3	65	422	150[b)]	0.24	2639
UC60-2	120	1200	1.08	0.38	0.38	2.3	65	422	150[b)]	0.28	2814
UC50-3	120	1200	1.08	0.38	0.19	2.3	65	422	150[b)]	0.24	2602

Notes: [a)] values from cube tests multiplied by 0.8; [b)] measured values not reported.

Two geometrically-similar test series were performed by Hung et al (2017, 2020). These tests provide a direct comparison between walls with and without steel fibres that feature similar reinforcement layouts. The specimens were subjected to reversed cyclic loading without axial compression. These short members (a/h=1.13) show that fibre reinforcement increases both strength and deformation capacity. Non-fibre specimens exhibited rapid crack localization and strength degradation, while FRC walls maintained stable response and sustained larger drifts. Tests by Li et al (2023) on squat walls (a/h=*1.08*) with ρ_f=2.3% and ALR≈0.26 failed by web crushing after yielding of flexural reinforcement. In contrast, the slender walls (a/h=2.25) tested by Ni et al (2024) failed in flexure and exhibited significant displacement ductility.

4 Comparative assessment of seismic response

Table 2 summarizes the measured resistance and deformation parameters of the specimens, including peak shear resistance v_{exp}, normalized shear resistance $v_{exp}/\sqrt{f_c}$, net concrete strength contribution v_{net} and its normalized value, and drift capacity. The parameter $\rho_w f_{yw}$ represents the clamping stress provided by transverse reinforcement, while σ_f denotes the effective fibre stress evaluated according to Pfyl (2003). These walls resisted peak shear stresses up to $1.6\sqrt{f_c}$ (MPa) and sustained ultimate drifts larger than 1.5%, highlighting the combined increase in strength and deformation capacity. The experimental data provide a consistent basis for comparing the effect of fibres on shear response and deformation behaviour across different test programs. The results show clear differences between conventional RC and FRC specimens. RC walls typically exhibit $v_{exp}/\sqrt{f_c}$ in the range of 0.4-0.7 and limited drift capacity with θ_u≈1-1.5%. In contrast, steel FRC specimens reach normalized shear stresses approaching or exceeding unity, which correspond to significantly larger drifts up to 3%.

The influence of steel fibres is particularly evident in the tests by Athanasopoulou and Parra-Montesinos (2020), where the RC specimen (S1) exhibited early crack localization and limited drift capacity, while FRC specimens developed finer, more distributed cracking and sustained larger deformations despite comparable peak shear stress. However, sliding shear was the governing failure mechanism, highlighting the importance of proper interface detailing.

Consistent trends are observed in the tests by Hung et al (2017, 2020), which provide direct comparisons between non-fibre UHPC and UHPFRC specimens. Non-fibre specimens showed rapid strength degradation following crack localization, while fibre-reinforced walls maintained stable hysteretic response and sustained larger drifts. For fibre volumetric ratios larger than 1%, fibres reduced transverse reinforcement strain demand by about 30% and enhanced energy dissipation, resulting in wider hysteretic loops and more gradual strength degradation. Results by Li et al (2023), together with findings from Hung et al (2017, 2020) and Ni et al (2024), show that squat walls with ρ_f=2.3% and ALR≈0.26 can achieve peak shear resistance significantly larger than empirical code-based limits such as $0.83\sqrt{f_c}$ in ACI 318-25. Overall, the comparative analysis indicates that adding a moderate amount of fibres enhances shear resistance, deformation capacity, and damage tolerance while promoting a transition from brittle shear-dominated failure towards more stable flexural-shear or diagonal tension behaviour. Sliding shear failure at the wall base remains largely unaffected by fibres and requires appropriate interface detailing to mitigate premature failure.

Table 2: Summary of measured deformations and shear resistance.

Specimen name	a/h	$\rho_w f_{yw}$ (MPa)	σ_f (MPa)	v_{exp} (MPa)	v_{net} (MPa)	$v_{exp}/\sqrt{f_c}$ (-)	$v_{net}/\sqrt{f_c}$ (-)	θ_u (%)	θ_u/θ_y (-)	Failure mode
S1	1.20	4.69	0	3.51	N/A	0.52	N/A	2.40	1.14	S
S2	1.20	2.05	3.3	2.69	0.64	0.39	0.09	3.00	1.88	S
S5	1.20	3.99	2.1	3.43	N/A	0.55	N/A	1.50	1.76	S
S7	1.50	0.86	3.2	3.53	2.68	0.52	0.39	2.10	1.40	DT
U-H-0.5	1.13	3.70	0	5.54	1.84	0.43	0.14	1.50	3.00	F+DT
UF-N-0.5	1.13	2.86	8.9	6.82	3.96	0.61	0.35	3.00	6.00	F+S
U-H-0.8	1.13	6.85	0	8.67	1.82	0.69	0.14	1.00	2.00	F+DC
UF-H-0.8	1.13	6.85	8.4	10.83	3.98	1.01	0.37	3.00	6.00	F+DT
HF/75-H	1.13	4.16	2.5	8.96	4.80	0.99	0.53	1.50	2.00	F+DT
U/0-H	1.13	4.16	0	8.01	3.85	0.75	0.36	1.00	1.33	DC
UF/150-N	1.13	2.47	5.5	9.55	7.08	0.99	0.73	1.50	2.00	F+DT
UF/150-H	1.13	4.16	5.5	9.55	5.39	0.99	0.56	1.50	2.00	F+DT
UF1.5/150	2.25	3.24	4.5	7.14	3.90	0.74	0.41	3.56	5.09	F
UF2.5/150	2.25	3.24	8.1	8.68	5.45	0.85	0.53	3.56	3.56	F
UF2.5/300	2.25	1.65	8.1	8.68	7.03	0.85	0.69	3.56	3.96	F
HC50	1.08	2.24	0	10.42	8.18	1.35	1.06	0.85	1.93	F+DC
UC50-1	1.08	2.24	9.5	18.89	16.65	1.54	1.36	0.98	2.31	F+DC
UC60-1	1.08	2.24	9.5	19.14	16.90	1.56	1.38	1.32	1.98	F+DC
UC50-2	1.08	1.60	9.5	18.33	16.72	1.50	1.37	1.23	2.05	F+DC
UC60-2	1.08	1.60	9.5	19.54	17.93	1.60	1.46	1.40	2.68	F+DC
UC50-3	1.08	0.80	9.5	18.07	17.27	1.48	1.41	1.65	2.64	F+DC

Notations: $v_{exp}=V_{exp}/bh$=measured peak resistance; $v_{net}=v_{exp}-\rho_w f_{yw}$=measured peak stress resisted by concrete; σ_f=effective fibre stress (Pfyl, 2003); θ_y=measured yield drift; θ_u=measured ultimate drift; S=sliding shear; F=flexure; DT=diagonal tension; DC=diagonal compression. For brevity, the name of specimens used by Hung et al. (2017, 2020) is abbreviated as follows: U=UHPC (ultra-high performance concrete), UF=UHPFRC (ultra-high performance fibre-reinforced concrete), H=HS (high-strength steel), and N=NS (normal-strength steel).

5 Effect of steel fibres on seismic response of FRC walls

5.1 Modelling approaches for evaluation of shear response in FRC walls

While the preceding sections summarized the experimental evidence on the influence of steel fibres on shear resistance and ductility, this section focuses on analytical and numerical approaches for interpreting and predicting the measured behaviour of FRC shear walls. Experimental results can be evaluated using mechanics-based approaches for shear response of RC and FRC members (Mihaylov, 2019; and Gehri et al, 2025). In conventional walls subjected to cyclic loading, web crushing typically develops after longitudinal reinforcement yielding, as crack opening increases, strain localizes, and the diagonal compression field progressively deteriorates. This failure mechanism limits both shear strength and deformation capacity and is reflected in design provisions through empirical strength limits as in ACI 318-25.

Fibre contributions can be described using the limit-analysis framework proposed by Gehri et al (2025), based on plasticity theory. In this approach, fibres are idealized as a homogeneous, isotropic, perfectly plastic material that resists tensile stresses across cracks, acting perpendicular to the concrete compression field while providing negligible compressive strength. For a given stress field orientation, equilibrium results in a lower-bound solution for web crushing failure, which coincides with the upper-bound solution under specific conditions. This represents the actual failure state under monotonic loading as expressed in Eq. 1:

$$v_{max} = \frac{f_c}{2} + \frac{\sigma_f}{2} \tag{1}$$

where v_{max} is the maximum shear resistance (in MPa), f_c is the concrete compressive strength, and σ_f is the effective fibre stress that can be determined according to Eq. 2:

$$\sigma_f = \frac{3}{8}\rho_f\left(0.6 f_c^{2/3}\right)\frac{l_f}{d_f} \tag{2}$$

where the first term is a fibre orientation factor proposed by Pfyl (2003), the parenthesis is the average bond stress of fibres in the concrete matrix, and l_f/d_f is the fibre aspect ratio. Note that the first term in Eq. (1) is typically taken as $0.83\sqrt{f_c}$ (MPa) under reversed cyclic loading conditions. Therefore, the relative contribution of steel fibres becomes even more significant.

In terms of stresses transmitted across cracks, the relative effectiveness of fibres compared with transverse reinforcement can be quantified using the stirrup-to-fibre efficiency ratio proposed by Mihaylov (2019), with a value of unity indicating equal effectiveness in resisting tension across cracks. The stirrup-to-fibre efficiency ratio is expressed according to Eq. 3:

$$\frac{\rho_w}{\rho_f} = \frac{\sigma_f}{0.9 f_{yw}\cos\alpha} \tag{3}$$

where ρ_w is the transverse (shear) reinforcement ratio, ρ_f is the fibre volumetric ratio, f_{yw} is the yield strength of the transverse reinforcement, and α is the critical diagonal crack angle.

Application of Eq. 3 to the specimens of Hung et al (2017, 2020) produces values on the order of 0.01, indicating that fibres provide negligible contribution to diagonal tension resistance when high-strength transverse reinforcement (f_{yw}≈800 MPa) is used. Instead, their primary role is to control cracking, prevent concrete spalling, and stabilize the diagonal compression field, thereby enhancing the global shear response under reversed cyclic loading.

5.2 Assessment of fibre effects on resistance using modelling approaches

The effect of fibres on shear resistance and post-yield response is highlighted by comparing specimens HF/75-H and U/0-H tested by Hung et al (2020). Shear wall HF/75-H, made with high-strength concrete f_c=82 MPa and 0.75% steel fibres exhibiting strain-softening behaviour, reached a normalized shear resistance of $0.99\sqrt{f_c}$, 20% above the ACI 318-25 limit. Failure occurred after flexural yielding, indicating that fibres delayed degradation of the compression field. In contrast, U/0-H, without fibres, failed immediately after yielding due to rapid compression field deterioration. Despite the low fibre content, the fibres in HF/75-H are predicted to develop an effective stress $\sigma_f \approx$2.5 MPa, similar to the tensile strength of U/0-H (3.1 MPa). The corresponding shear resistance difference of 0.95 MPa between the fibre and non-fibre specimens is consistent with the contribution of fibres predicted by Eq. (1): 1.25 MPa.

Figure 2 shows the measured and numerically predicted load-drift response of HF/75-H. The numerical simulation, performed under monotonic loading, accurately captures the global response up to failure, including post-cracking stiffness and the transition to shear failure after flexural yielding. The peak resistance is V_{pred}=2124 kN, resulting in an experimental-to-predicted strength ratio V_{exp}/V_{pred}=1.01. The displacement capacity is also well reproduced, although ductility is slightly overestimated due to the absence of load reversal effects in the analysis. The response was simulated in VecTor2 (Vecchio, 2000), with fibre effects considered through existing constitutive models accounting for crack-bridging stresses and their influence on compression softening and post-peak ductility (Lee et al, 2011; and Lee et al, 2015).

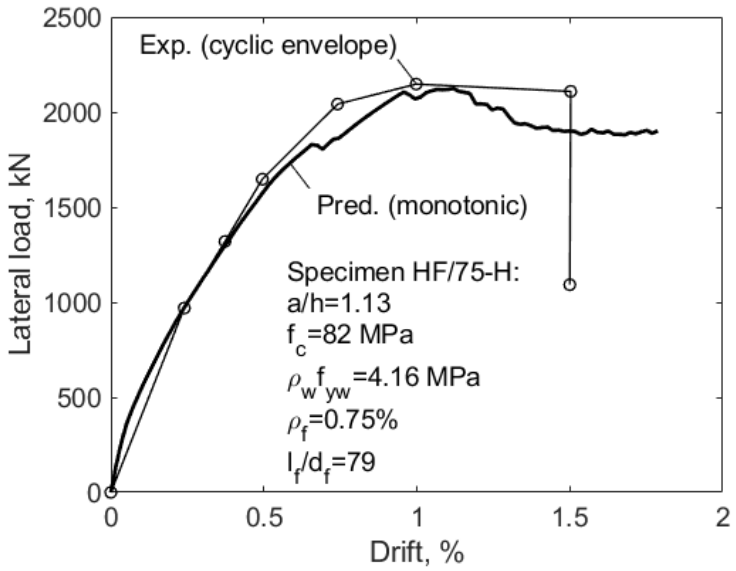


Figure 2: Measured and predicted load-drift response envelope of specimen HF/75-H.

Increasing fibre content to ρ_f=1.5%, resulted in a strain-hardening tensile response with σ_f=5.5 MPa. The corresponding increase in shear resistance was about 0.6 MPa, consistent with the predicted relative contribution of the fibre component of 1.5 MPa. Note that this difference suggests that the fibre strength contribution was not fully mobilized, as the specimens reached their flexural capacity prior to complete development of the fibre strength enhancement. Similar behaviour was measured when comparing non-fibre U/0-H and UF/150-N(H) with 1.5% fibres and strain hardening response.

Figure 3 shows the predicted variation of normalized shear resistance with fibre volumetric ratio for a reference wall according to the properties of HF/75-H. The results show a progressive increase in normalized shear strength as the fibre content increases from 0 to 3%. Notably, even at low fibre content (ρ_f=0.75%, l_f/d_f=79), the normalized shear resistance of the high-strength concrete specimen exceeds the ACI 318-25 limit by 20%. Importantly, the addition of low-to-moderate fibre contents shifts the failure mode from brittle shear to ductile flexural behaviour.

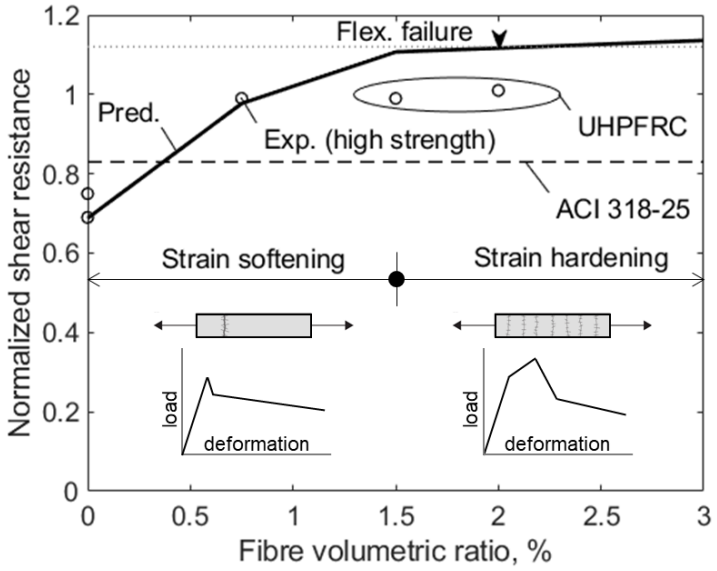


Figure 3: Effect of fibre volumetric ratio on normalized shear resistance.

For fibre volumetric ratios exceeding 1.5%, the response approaches a plateau governed by full development of flexural yielding followed by concrete crushing at the base section (flexural failure). The predicted curve is in good agreement with test results from Hung et al (2017, 2020), shown as circles in Fig. 3. The lower normalized shear resistance of the UHPFRC specimens can reflect differences in shear transfer mechanisms under cyclic loading and the limited number of available tests. Overall, the results confirm that steel fibre reinforcement is an effective approach to increase shear strength and promote ductile response in shear walls.

6 Concluding remarks

This paper presented a comparative assessment of RC and FRC shear walls based on test data and supporting modelling. The results show that steel fibres enhance seismic response primarily through improved crack control and reduced degradation of the diagonal compression field under reversed cyclic loading. Notably, normalized shear resistance exceeds the ACI 318-25 limit by about 20%, highlighting the efficiency of fibres even at moderate dosages. Low-to-moderate fibre contents promote a transition from brittle shear failure to more ductile flexural or flexural-shear behaviour, resulting in increased deformation capacity and more stable post-yield response. Numerical simulations accurately reproduce the response up to failure, including post-cracking stiffness and the transition from flexural yielding to shear failure. Overall, the results confirm that steel fibres are an effective complement to conventional reinforcement, particularly for improving damage tolerance and achieving more ductile and stable seismic performance in hybrid shear walls, supporting their practical application and consideration in future seismic design provisions.

7 Acknowledgements

This work was supported by a National Research Grant of the Technical University of Civil Engineering Bucharest (UTCB), Romania, project number 13807/2025.

8 References

ACI 318, 2025. *Building Code for Structural Concrete*, American Concrete Institute, US.

Amin, A., Foster, S.J., 2016, "Shear strength of steel fibre reinforced concrete beams with stirrups," *Engineering Structures*, 111, 323-332.

Athanasopoulou, A., and Parra-Montesinos, G., 2013, "Experimental Study on the Seismic Behavior of HPFRC Low-Rise Walls," *ACI Structural Journal*, 110(5).

Dazio, A., Buzzini, D. and Trüb, M., 2008, "Nonlinear cyclic behaviour of hybrid fibre concrete structural walls," *Engineering Structures*, 30(11), pp.3141-3150.

Di Prisco, M., Plizzari, G. and Vandewalle, L., 2009, "Fibre reinforced concrete: new design perspectives," *Materials and Structures*, 42(9), pp.1261-1281.

Gehri, N., Amin, A., Kraus, M.A. and Kaufmann, W., 2025, "Limit analysis and design recommendations for fiber-reinforced concrete subjected to shear," *Structural Concrete*, 26(1), pp.293-318.

Hung, C.C., Li, H. and Chen, H.C., 2017, "High-strength steel reinforced squat UHPFRC shear walls: Cyclic behavior and design implications," *Engineering Structures*, 141, pp.59-74.

Hung, C.C., and Hsieh, P.L., 2020, "Comparative study on shear failure behavior of squat high-strength steel reinforced concrete shear walls with various high-strength concrete materials," *Structures*, 23, pp.56-68.

Kam, W.Y., Pampanin, S., and Elwood, K., 2011, "Seismic performance of reinforced concrete buildings in the 22 February Christchurch (Lyttelton) earthquake," *Bulletin of the New Zealand Society for Earthquake Engineering*, 44(4), pp.239-278.

Lee, S.C., Cho, J.Y. and Vecchio, F.J., 2011, "Diverse embedment model for steel fiber-reinforced concrete in tension: Model development," *ACI Materials Journal*, 108(5).

Lee, S.C., Oh, J.H. and Cho, J.Y., 2015, "Compressive behavior of fiber-reinforced concrete with end-hooked steel fibers," *Materials*, 8(4), pp.1442-1458.

Lequesne, R.D., Parra-Montesinos, G.J. and Wight, J.K., 2013, "Seismic behavior and detailing of high-performance fiber-reinforced concrete coupling beams and coupled wall systems," *Journal of Structural Engineering*, 139(8), pp.1362-1370.

Li, Y.Y., Nie, J.G., Ding, R. and Fan, J.S., 2023, "Seismic performance of squat UHPC shear walls subjected to high-compression shear combined cyclic load," *Engineering Structures*, 276, p.115369.

Mihaylov, B., 2019, "A kinematics-based approach for the shear strength of short fibre-reinforced concrete coupling beams," *Engineering Structures*, 182, pp.501-509.

Ni, X., Zhao, B., Zhang, Q. and Lu, X., 2024, "Seismic performance and flexural strength prediction of high-strength bar reinforced UHPFRC walls under high axial load ratio," *Journal of Building Engineering*, 87, pp.109053.

Parra-Montesinos, G.J., 2005, "High-performance fiber-reinforced cement composites: an alternative for seismic design of structures," *ACI Structural Journal*, 102(5).

Paulay, T., Priestley, N., 1992, Seismic Design of Reinforced Concrete and Masonry Buildings.

Pfyl, T., 2003, Structural behavior of steel fibre-reinforced concrete, PhD, Zurich, Switzerland.

Vecchio, F., 2000, "Disturbed stress field model for reinforced concrete: formulation," *Journal of Structural Engineering*, 126(9), pp.1070-1077.

Mechanical Performance and Redundancy of Direct Fastenings in Fibre-Reinforced Concrete: An Experimental Evaluation

Alhussain Yousef[1], Panagiotis Spyridis[1]

[1] : Chair of Concrete Structures and Infrastructures Engineering, University of Rostock, Rostock, Germany.

Abstract

Power-actuated fasteners (PAFs) are widely used for the rapid attachment of non-structural elements to concrete, but their load-bearing performance is strongly affected by substrate heterogeneity and installation variability. With the increasing use of steel- and synthetic-fibre-reinforced concretes (FRCs), a systematic assessment of fibre influence on installation quality and pull-out behaviour is required. This study presents an experimental and probabilistic investigation of PAF behaviour in fibre-reinforced concrete. Eight concrete mixtures with different fibre types and dosages were examined through a large series of pull-out tests. Installation damage, pull-out resistance, and displacement behaviour were evaluated using statistical measures to characterise variability and failure behaviour. In addition, the redundancy behaviour of PAF groups was analysed using a data-driven probabilistic approach based on Monte Carlo simulations, where group resistance was evaluated using two mechanical models. The results indicate that fibre reinforcement influences installation quality and deformation behaviour, while its effect on mean resistance is not consistent. The system behaviour is shown to be strongly governed by variability and the occurrence of low-capacity events, which significantly affect the characteristic resistance of PAF groups.

.

Keywords

Power-actuated fasteners (PAFs), Fibre-reinforced concrete (FRC), Pull-out behaviour, Redundancy, Probabilistic modelling

1 Introduction

The construction industry is increasingly shifting towards more sustainable concrete solutions, including the use of alternative binders, recycled aggregates, and fibre reinforcement, in order to reduce environmental impact and improve durability. Fibre-reinforced concrete (FRC), incorporating steel or synthetic fibres, is widely used to enhance crack resistance, tensile strength, ductility, and overall structural performance (ACI, 2009; Altun et al., 2007). At the same time, power-actuated fasteners (PAFs) have become an efficient solution for the rapid attachment of non-structural elements to concrete. Unlike conventional anchors, which require pre-drilling and mechanical or bonded installation, PAFs are installed through a high-speed, energy-driven process, significantly reducing installation time, noise, and dust emissions (Eligehausen et al., 2006; Hilti, 2019). During installation, the fastener penetrates the concrete at velocities of up to 100 m/s, and its anchorage is achieved through a combination of interlocking, friction, and localized material modification mechanisms (Hilti, 2019; Fang and Wu, 2017). However, due to the dynamic installation process and the inherent heterogeneity of concrete, PAF systems exhibit a relatively high variability in both installation quality and load-bearing capacity compared to conventional fastening systems (Bergmeister, 1988; Gerber, 1987). For this reason, their design is often based on redundancy concepts, where multiple fasteners are used to ensure load redistribution and prevent sudden system failure (Patzak, 1979; EOTA, 2018; DIN, 2019). Such systems are commonly applied in safety-relevant applications, including suspended ceilings, pipelines, and partition walls (Gould and Lichti, 2013; Shan et al., 2020; Su and Shan, 2019; Michels et al., 2018; Lamanna et al., 2004). The mechanical performance of fastening systems is strongly influenced by the properties of the concrete substrate. Previous studies have shown that fibre reinforcement can enhance the load-bearing behaviour of anchors and fasteners, primarily through crack-bridging effects and improved post-cracking behaviour (Langenbeck et al., 2023; Scholz et al., 2023; Spyridis and Mellios, 2022; Spyridis et al., 2022; Mellios et al., 2024). In addition, experimental investigations indicate that both fibre type and aggregate characteristics may affect the penetration process and pull-out resistance of PAFs (Yousef and Spyridis, 2025a.; Yousef et al., 2022; Mellios et al., 2022). A probabilistic assessment of redundant PAFs in fibre-reinforced concrete, including the introduction of two redundancy models based on superposition and cascade approaches, has been investigated in detail in (Yousef and Spyridis, 2025b). Moreover, data-driven approaches indicate that concrete surface damage can serve as an indicator for the pull-out capacity of PAFs (Yousef and Spyridis, 2026). Despite these findings, the influence of fibre reinforcement on the combined behaviour of installation quality, load-bearing capacity, and statistical variability of PAFs remains insufficiently understood. In particular, limited research exists on how fibre-induced changes in variability affect system behaviour and failure mechanisms of fastening systems. This aspect becomes especially relevant in the context of redundancy and robustness, which are recognized as key design principles for fastening systems under uncertain conditions (Spyridis and Strauss, 2020; Spyridis et al., 2021). However, the interaction between material-induced variability—such as that introduced by fibre reinforcement—and the effectiveness of redundancy has not yet been fully clarified.

2 Scope and Objectives of the Study

The present study aims to investigate the behaviour of power-actuated fasteners in fibre-reinforced concrete through a combined experimental and probabilistic approach. A

comprehensive test program involving different fibre types and dosages is evaluated in terms of installation damage, pull-out resistance, and displacement behaviour. The experimental results are analysed using statistical measures to characterize variability and failure behaviour. In addition, the redundancy behaviour of PAF groups is assessed using a data-driven probabilistic approach based on Monte Carlo simulations, where random samples are directly drawn from the experimental dataset. The group resistance is evaluated using different mechanical models, considering the influence of deformation behaviour and sequential failure. The main objective is to provide a deeper understanding of how fibre reinforcement influences not only the mechanical performance of individual fasteners, but also the reliability and load-bearing capacity of fastening systems under realistic conditions.

3 Experimental Programme

An experimental campaign was conducted to investigate the behaviour of power-actuated fasteners (PAFs) in different fibre-reinforced concrete (FRC) substrates. A total of eight concrete slabs with dimensions of 1500 × 2000 × 160 mm were produced, including one reference slab without fibres and seven slabs with varying fibre types and dosages. The investigated fibre types included four steel fibre configurations (Dramix 3D and 4D, with lengths of 60 mm and 35 mm) and synthetic fibres (BarChip48). Steel fibres were used with dosages of 40 and 80 kg/m³, while synthetic fibres were added at 6 and 8 kg/m³. All concrete mixtures were based on a C20/25 composition with a water–cement ratio of 0.65. In addition, standard specimens (cubes and cores) were prepared to determine compressive and tensile strengths (Table 1). For each test series, 40 PAFs (Hilti X-X 27 MX) were installed using a DX 5 MX tool, resulting in a total of 320 tests. A minimum edge distance of 250 mm was maintained to avoid boundary effects. The fasteners were installed through pre-fabricated steel plates with a central hole to ensure consistent installation conditions and to minimize additional resistance during penetration. Following installation, axial pull-out tests were performed using a hydraulic testing system. The applied load was measured with a load cell, while the displacement at the fastener head was recorded using a displacement transducer. The tests provided load–displacement curves, from which the maximum pull-out resistance and corresponding displacement were determined. In addition to the mechanical response, the installation quality was assessed immediately after setting. The surface condition of the concrete was classified into four damage categories, ranging from no visible damage to complete installation failure. This classification was used to evaluate the influence of fibre reinforcement on installation behaviour and to support the subsequent statistical analysis.

Table 1: Details of test series and fibre and concrete properties.

Slab	**Fibre type**	**Fibre lenght**	**Fibre dosage**	**Fibre Diameter**	**Test series**	**$f_{cm,cube,28}$**	**$f_{ct,\ cyl.28}$**
		[mm]	**[Kg/m³]**	**[mm]**		**[MPa]**	**[MPa]**
1	Steel 3D-65/60BG	60	80	0.9	Series 1	25.8	3.44
2	Steel 3D-65/60BG	60	40	0.9	Series 2	26.9	2.66
3	Steel 4D-65/60BG	60	40	0.9	Series 3	24.1	2.65
4	Steel 3D-65/35BG	35	40	0.55	Series 4	29.4	4.10
5	Steel 4D-65/35BG	35	40	0.55	Series 5	30.5	3.54
6	Syn.-BarChip48	48	6	0.8	Series 6	29	2.70
7	Syn.-BarChip48	48	8	0.8	Series 7	25.1	2.80
8		-	-		Series 8	26.8	2.9

4 Evaluation of Installation Behaviour (Pre-Test)

4.1 Penetration Performance

The penetration performance of the power-actuated fasteners (PAFs) was assessed based on the successful installation of the fasteners into the concrete substrate. A successful installation was defined as a stable and properly embedded fastener without immediate failure after the setting process. Across all test series, a high installation success rate was observed, indicating that PAFs can be reliably installed in both conventional and fibre-reinforced concretes. Minor variations between the series suggest that fibre reinforcement may influence the penetration process; however, no systematic dependency on fibre type was identified. Instead, the results indicate that penetration behaviour is governed by a combination of concrete properties, such as tensile strength, heterogeneity, and local fibre distribution

4.2 Damage of Concrete Surface

The surface condition of the concrete after installation was evaluated using a classification system consisting of four damage classes (OFBS 0–3). These range from no visible damage (class 0) to severe damage or immediate installation failure (class 3). The results show that fibre-reinforced concretes generally exhibit improved surface performance compared to the reference concrete (Figure 1), reflected by a higher proportion of installations with no visible damage. This behaviour can be attributed to the crack-bridging effect of fibres, which limits the propagation of microcracks during the high-speed penetration process. However, the influence of fibre type on surface damage remains limited, and variations between test series indicate that additional factors, such as concrete strength and material heterogeneity, also play a significant role. Overall, the majority of test series achieved high installation quality, with a large proportion of fasteners falling within the lower damage classes.

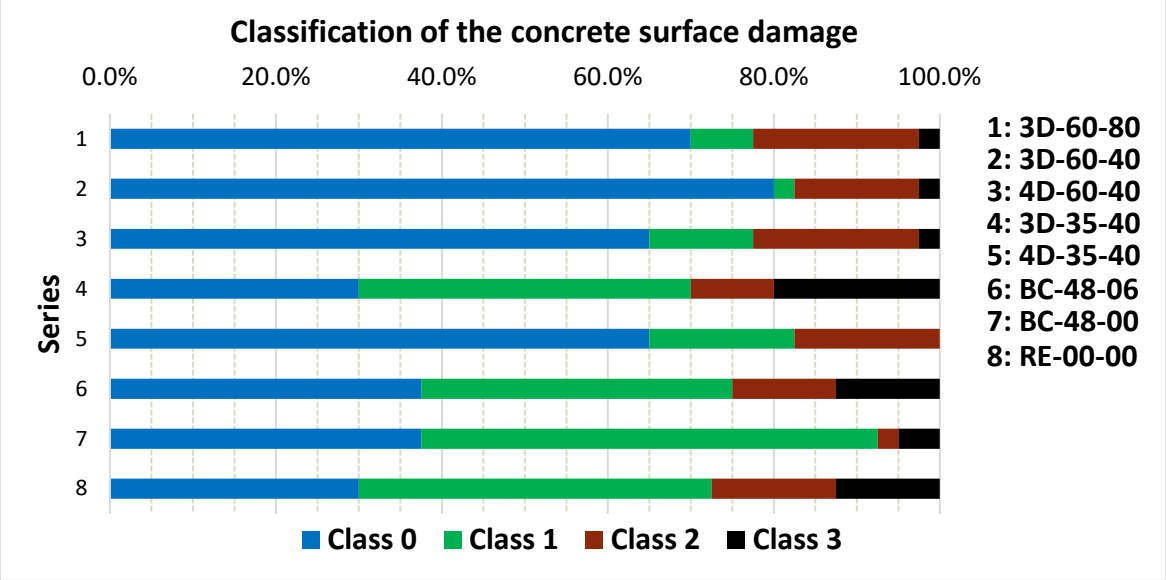


Figure 1: Statistical classification of concrete surface damage in each test series

5 Post-Test Evaluation

5.1 Pull-Out Resistance

The pull-out resistance of the tested PAFs shows a wide distribution across all series, with measured values ranging from approximately 0.1 kN to 7.1 kN**,** while the mean values are generally between 2 kN and 4 kN (Figure 2). This significant spread reflects the inherent variability of the installation process and the heterogeneous nature of the concrete substrate. The variability is further illustrated by the coefficients of variation (COV), which range from approximately 0.36 to 0.73**,** indicating considerable differences in scatter between the series. A comparison between the test series shows that fibre reinforcement influences the mechanical performance, although no uniform trend can be identified. Series with long steel fibres (60 mm) (Series 2 and 3) exhibit relatively higher mean values and, more importantly, lower variability (COV ≈ 0.36–0.38)**,** indicating a more stable and predictable behaviour.

Series with short steel fibres (35 mm) (Series 4 and 5) show differing behaviour despite similar configurations: while Series 5 exhibits moderate variability (COV ≈ 0.41) and more stable results, Series 4 is characterized by significantly higher scatter (COV ≈ 0.73), accompanied by lower mean and minimum values, suggesting that increased scatter and local material effects may govern the performance more strongly than the fibre type itself.

The series with synthetic fibres (Series 6 and 7) show mean resistance levels comparable to steel fibre series but are associated with moderate to high variability (COV ≈ 0.62 and 0.36), suggesting that their contribution to load transfer is less consistent. The reference concrete (Series 8) also exhibits relatively high variability (COV ≈ 0.52), further emphasizing that the presence of fibres does not automatically reduce scatter.

Overall, the results indicate that fibre reinforcement may influence the pull-out behaviour, particularly in terms of stability and variability, rather than leading to a systematic increase in mean resistance. The observed differences suggest that variability and local effects play a dominant role**,** and that fibre properties such as length and dosage primarily affect the consistency of the response rather than the absolute strength.

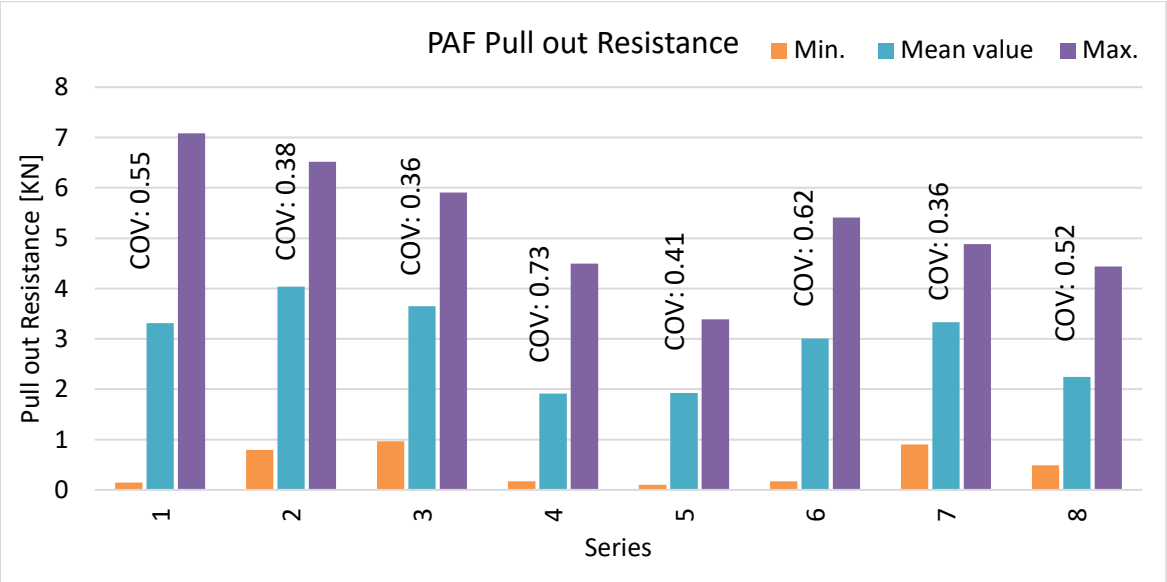


Figure 2: Statistical investigation of PAF pull out resistance in each test series

5.2 Displacement Behaviour

The displacement at maximum load was evaluated to characterise the deformation behaviour of the fastening system. The results show clear differences between fibre-reinforced and non-reinforced concrete. The reference concrete exhibits a brittle response with limited deformation, while series with long steel fibres and higher dosages show significantly larger displacements. For example, Series 1 reaches normalized displacement values of approximately 0.018 mm/kN, indicating a more ductile behaviour due to effective crack-bridging. In contrast, series with synthetic fibres and short steel fibres show much lower deformation levels, with values around 0.0007–0.0009 mm/kN, corresponding to a stiffer and more brittle response. Although these normalized displacement values are not directly relevant for practical engineering design, they provide valuable insight into the influence of fibre reinforcement on ductility and deformation capacity of the fastening system.

6 Redundancy and Group Behaviour of PAFs

To evaluate the load-bearing behaviour of power-actuated fasteners (PAFs) used in groups, two complementary redundancy models are considered: a linear addition method and a superposition method. Both approaches represent idealized failure mechanisms of PAF groups under tensile loading and allow a simplified assessment of system behaviour based on single-fastener results.

6.1 Linear Addition Method

In the linear addition approach, the resistance of a PAF group is determined by summing the individual capacities of all fasteners. For a system consisting of *n* fasteners, the total group resistance F can be written as:

$$F = \sum_{k=1}^{n} F_k \quad (1)$$

Where F_k denotes the pull-out resistance of the k-th PAF.

This formulation assumes that all fasteners act concurrently and are able to share the applied load evenly, which requires sufficient deformation capacity within the system. The model does not account for progressive failure or redistribution of forces following the failure of individual fasteners. Consequently, the linear addition approach can be interpreted as an idealised upper-limit estimation of the group resistance, providing a reference for the maximum achievable benefit from redundancy.

6.2 Superposition Method

In contrast to the linear addition approach, the superposition method accounts for differences in deformation capacity between individual fasteners and the resulting load redistribution within the group. The method is based on the assumption that fasteners exhibit elastic behaviour up to their maximum resistance, characterized by their individual stiffness.

For a group of n PAFs, each fastener is defined by its pull-out resistance F_i and the corresponding displacement at maximum load d_i The stiffness of each fastener is expressed as:

$K_i = F_i / d_i$ (2)

The fasteners are ordered according to increasing displacement capacity (d1<d2<⋯<dn). As loading progresses, fasteners with lower deformation capacity reach their maximum resistance first and fail, while the remaining fasteners continue to carry additional load. The group resistance is determined by evaluating the load level at each failure stage. For each step, the total load is calculated by combining the resistance of the failed fastener with the elastic contributions of the remaining fasteners. The maximum value obtained from all stages is taken as the load-bearing capacity of the PAF group (Figure 3).

This method captures the influence of deformation compatibility and sequential failure, providing a more realistic estimation of group behaviour compared to the linear addition approach, particularly for systems with limited ductility.

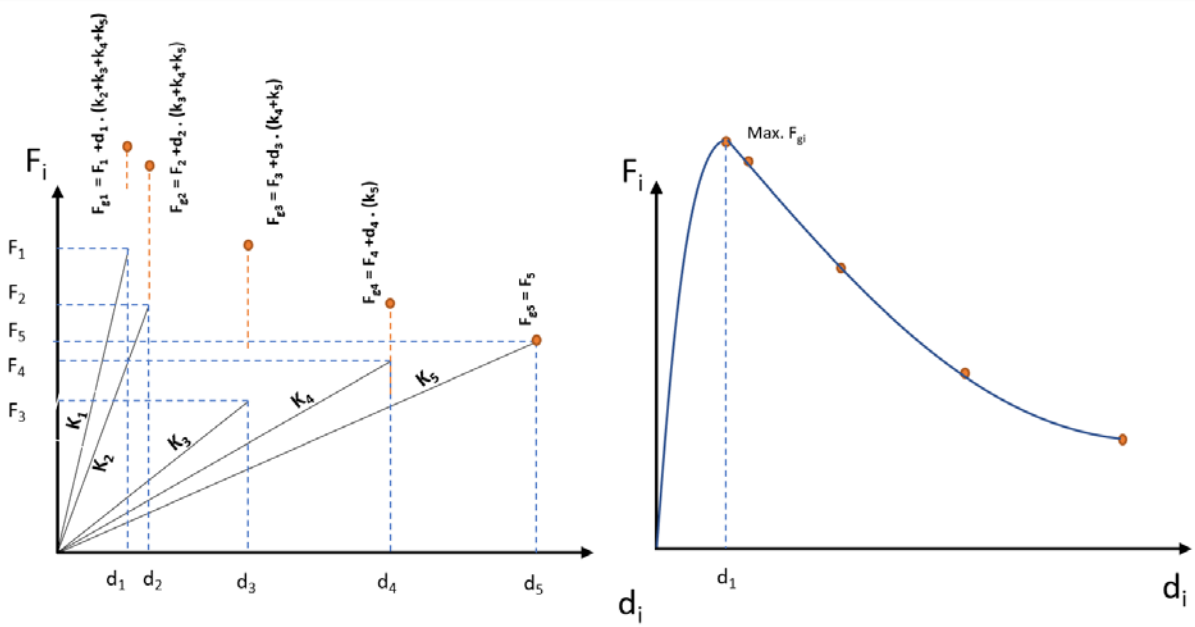


Figure 3: Superposition Method

7 Probabilistic Redundancy Assessment of PAF Groups

The probabilistic evaluation of PAF groups was carried out using a Monte Carlo simulation implemented in MATLAB. The analysis was based directly on the experimental dataset, where each data point consists of a pair of pull-out resistance and the corresponding displacement.

In contrast to a filtered evaluation, data points associated with setting failures (near-zero resistance values) were explicitly included in the analysis. This decision reflects practical application conditions, where installation failures may not always be detectable due to the presence of fixtures or limited visual access. Therefore, these cases were considered on the safe side to ensure a realistic and conservative assessment of system behaviour. For each simulation, PAF groups of different sizes were generated by randomly sampling from the dataset. Two mechanical models were applied to evaluate the group resistance: the **Linear Addition Method (LAM)** and the **Superposition Method (SPM)**, as indicated in the Figure 4.

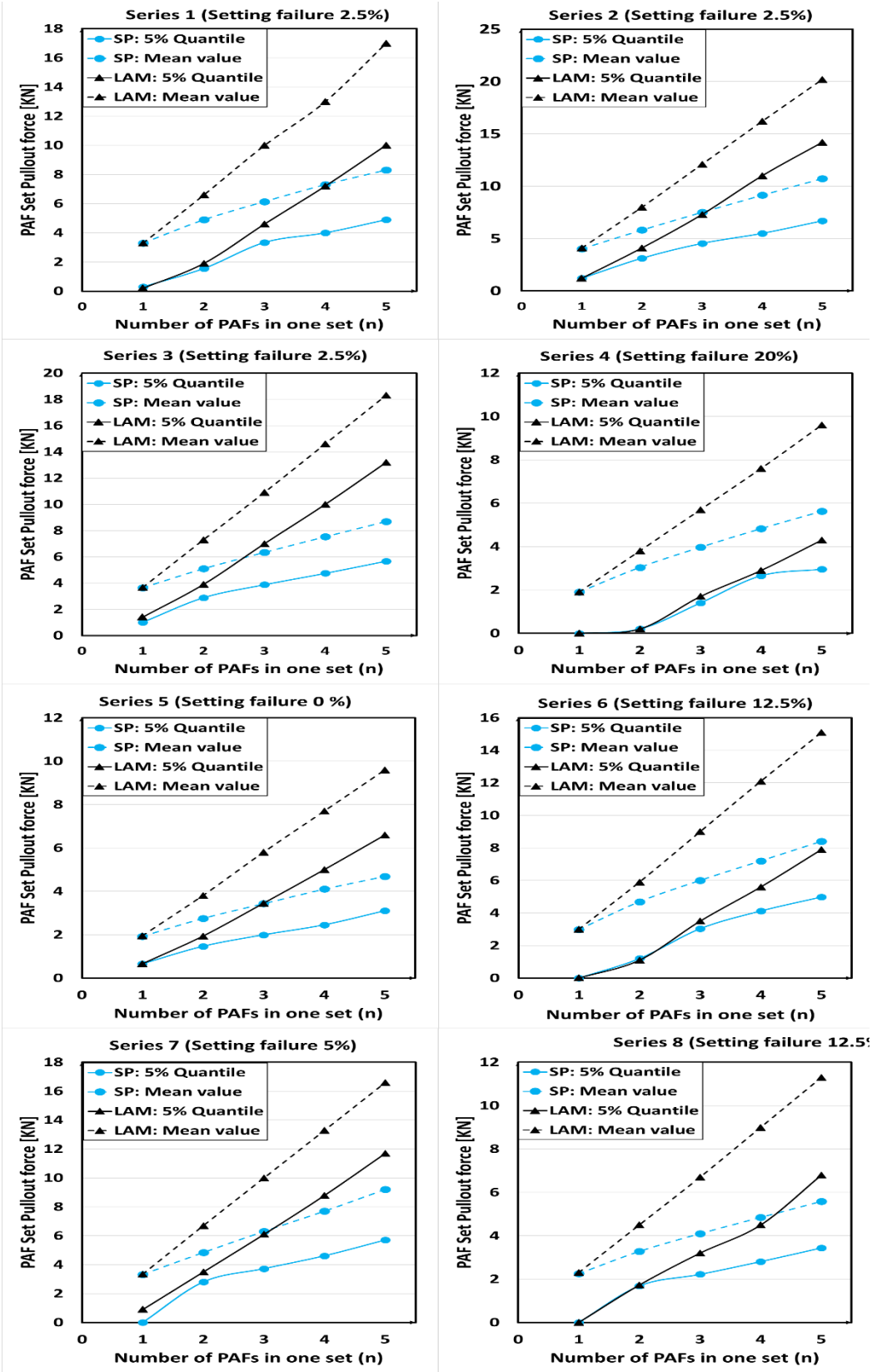


Figure 4:Probabilistic Redundancy Assessment: Linear addition method vs. Superposition method

The results in Figure 4 show consistent differences between the Addition Method (LAM) and the Superposition Method (SPM) across all series. The LAM generally yields higher group resistances for both mean values and 5% quantiles, as it assumes simultaneous load sharing without considering deformation compatibility or progressive failure. In contrast, the SPM provides lower values, particularly for the 5% quantile, reflecting stiffness differences and sequential failure. The divergence between both methods increases with the number of fasteners, indicating that idealised load redistribution may overestimate system capacity. A clear tendency is observed between the proportion of setting failures and the 5% quantile. Series with low failure rates (0–2.5%) show a continuous increase in lower-bound resistance with group size, whereas higher failure rates (e.g. Series 4: 20%, Series 6 and 8: ≈12.5%) lead to reduced 5% quantiles, especially for small groups. This highlights the strong influence of low-capacity values on the characteristic system behaviour, even when mean values are similar. No consistent trend in mean resistance can be directly attributed to fibre type. Series with long steel fibres (Series 2 and 3) show relatively stable behaviour, while short steel fibre series (Series 4 and 5) differ significantly, mainly due to the presence of setting failures. In particular, Series 5 (no failures) performs more consistently than Series 4 despite similar fibre properties. Synthetic fibre series (Series 6 and 7) exhibit moderate mean values but lower 5% quantiles, indicating higher variability. The reference series (Series 8) shows a comparable trend, suggesting that fibre addition does not necessarily improve system performance. Overall, the results indicate that PAF group behaviour is governed primarily by variability and the occurrence of low-capacity events, while the influence of fibre reinforcement appears indirect, mainly affecting installation quality and scatter rather than mean resistance.

8 Conclusion

This study investigated the behaviour of power-actuated fasteners in fibre-reinforced concrete through a combined experimental and probabilistic approach. The results show that fibre reinforcement influences both installation quality and mechanical response; however, no consistent increase in mean pull-out resistance can be observed across all series. Instead, the effect of fibres appears to be more pronounced in terms of variability and deformation behaviour.

The experimental results indicate that the pull-out behaviour of PAFs is characterized by significant scatter, with coefficients of variation ranging from approximately 0.36 to 0.73. Series with long steel fibres tend to exhibit more stable behaviour, while other configurations show increased variability, highlighting the importance of local material effects and installation conditions.

The probabilistic group analysis demonstrates clear differences between the Linear Addition Method (LAM) and the Superposition Method (SPM). While the LAM provides an upper-bound estimation of group resistance, the SPM yields lower and more conservative values due to the consideration of deformation compatibility and sequential failure. The influence of setting failures is particularly evident in the 5% quantile, where even moderate failure rates lead to a noticeable reduction in system capacity.

Overall, the results suggest that the behaviour of PAF groups is governed primarily by variability and the occurrence of low-capacity events. Fibre reinforcement appears to influence system performance mainly through its effect on installation quality and scatter, rather than through a systematic increase in resistance. These findings highlight the importance of

considering variability and redundancy effects in the assessment and design of fastening systems under realistic conditions.

9 References

ACI PRC-544.1R-96, Report on Fibre Reinforced Concrete (Reapproved 2009), American Concrete Institute, Farmington Hills, MI, USA., (2009)

Altun, F., Haktanir, T., K. Ari, Effects of steel fibre addition on mechanical properties of concrete and RC beams, Constr. Build. Mater. 21 (2007)

Bergmeister, K.: Stochastik in der Befestigungstechnik mit realistischen Einflussgrößen. Dissertation, University of Innsbruck, Faculty of Civil Engineering and Architecture, Innsbruck (1988).

DIN CEN/TR 17079. Design of anchorage of fastening systems in concrete - Redundant non-load-bearing systems. Berlin: Beuth Verlag (2019).

Eligehausen, R., Mallée, R., Silva, J. F.: Anchorage in Concrete Construction. Berlin: Ernst & Sohn Verlag (2006).

EAD 330083-02-0601. Power-actuated fastener for multiple use in concrete for non-structural applications. Brussels: EOTA. (2018).

Fang, Q. and Wu, H., 2017. Concrete structures under projectile impact. In Concrete Structures Under Projectile Impact (pp. 497-558). Springer, Singapore

Gerber, W.: Theorie zum Eintreiben und Verankern von Bolzen in Beton. Bauingenieur, 62, 213-218 (1987).

Gould, W., Lichti, D.: Power Forward: Diving Power-Actuated Fastener (PAF) Code Provisions. STRUCTURE magazine, Ilinois: Structure (2013).

Hilti Corporation: Direct Fastening Technology Manual 2019. Online manual of fastening technology, Schaan: Hilti Deutschland AG (2019).

Lamanna AJ, Bank LC, Scott DW. Flexural strengthening of reinforced concrete beams by mechanically attaching fibre-reinforced polymer strips. Journal of composites for construction, 8(3):203-10 (2004).

Langenbeck, A. D., Spyridis, P., Beßling, M., & Orlowsky, J. (2023). Experimental investigations of power-actuated fastenings in TRC. Developments in the Built Environment, 14, 100158.

Mellios, N., Losse, J., & Spyridis, P. (2024). Hybrid assessment of fibre orientation influence on the load resistance of anchors in SFRC. Civil Engineering Design, 5(5-6), 107-117

Mellios, N., Yousef, A., Spyridis, P.: Probabilistic finite elements of direct fixings in concrete with discrete aggregates. In: (eds. Di Prisco, M., Meda, A., Balázs, G.L.) Proceedings of the 14th fib PhD Symposium, Rome, Italy, 5-7 September 2022.

Michels, J., Shahverdi, M., Czaderski, C.: Flexural strengthening of structural concrete with iron-based shape memory alloy strips. Structural Concrete, Volume 19, Issue 3, fib, Berlin: Ernst & Sohn Verlag (2018).

Patzak, M.: Zur Frage der Sicherheit von Setzbolzenbefestigungen in Betonbauteilen. Beton + Fertigteil-Technik, Issue 5/1979, Wiesbaden: Bauverlag (1979).

Scholz, R., Franck, P., Yousef, A., Spyridis, P., & Walther, F. (2023). Validating the performance of direct fastening (PAF) into concrete with high-speed measuring technology. ce/papers, 6(5), 213-220.

Shan, Z. W., Looi, D. T. W., Su, R. K. L.: A novel seismic strengthening method of RC columns confined by direct fastening steel plates. Engineering Structures, 218, 110838. (2020).

Spyridis, P., & Mellios, N. (2022). Tensile performance of headed anchors in steel fibre reinforced and conventional concrete in uncracked and cracked state. Materials, 15(5), 1886.

Spyridis, P., Hufelschulte, F., & Mellios, N. (2022). Einfluss der Stahlfaserbewehrungsarten auf den Betonversagenswiderstand von Befestigungen. Beton-und Stahlbetonbau, 117(3), 176-185.

Spyridis, P., Strauss, A. (2020).: Robustness assessment of redundant structural systems based on design provisions and probabilistic damage analyses. Buildings 10.12.

Spyridis. P., Strauss. A., Di-Sario. M. (2021). Principles For the Evaluation of Redundancy in Fastening Systems. Life-Cycle Civil Engineering: Innovation, Theory and Practice, 1st Edition, 9780429343292

Su, R. K. L., Shan, Z. W.: Axial strengthening of RC columns by steel encasement with direct fastening connection. IOP Conference, Material Science and Engineering (2019).

Yousef, A., Mellios, N. Spyridis, P.: Probabilistic finite elements of direct fixings in concrete with discrete steel-fibres. In: (eds. Di Prisco, M., Meda, A., Balázs, G.L.) Proceedings of the 14th fib PhD Symposium, Rome, Italy, 5-7 September 2022.

Yousef, A., Spyridis, P (2025a), Structural and Redundancy Performance of Power Actuated Fasteners as Direct Fastenings in Fibre Reinforced Concrete, structural concrete, SUCO_70071

Yousef, A.,Spyridis, P. (2025b), Probabilistische Bewertung redundanter Befestigungen in faserbewehrtem Beton. Bauingenieur, 00(11), 306–317. https://doi.org/10.37544/0005-6650-2025-11-36

Yousef, A.; Spyridis, P. (2026), Data-Driven Calibration of Analytical and Probabilistic Models for Power-Actuated Fasteners in Concrete Buildings, 16, 1152.https://doi.org/10.3390/buildings16061152

Fibres in new types of concrete

Optimization of Fiber Orientation in Steel Fiber Reinforced Concrete by Robotic Extrusion

Filippo Medeghini[1,2], Ivan Trabucchi[2], Giulia Brentana[2], Giuseppe Tiberti[2], Giovanni A. Plizzari[2], Peter Mark[1]

[1]: Institute of Concrete Structures, Ruhr University Bochum, Bochum, Germany.

[2]: Department of Civil, Environmental, Architectural Engineering and Mathematics, University of Brescia, Brescia, Italy.

Abstract

Steel Fiber Reinforced Concrete (SFRC) derives its mechanical performance largely from the orientation and distribution of its fibers. In most of the conventional casting processes, fiber orientation is generally random, leading to quasi-isotropic material behavior. This approach fails to exploit the full structural potential of fibers and results in inefficient material use, particularly in regions subjected to well-defined tensile stress states.

The key goal of this work is to optimize SFRC structural elements by actively steering fiber orientation along tensile stress trajectories and by enabling localized placement of material with tailored performance, using a fully mechanized process.

To this end, a robotic extrusion-based casting procedure is being developed, allowing SFRC to be placed along arbitrary, predefined paths. An ad-hoc casting strategy exploits controlled border and flow effects during extrusion to preferentially orient fibers in the direction of material deposition. The process further enables the combination of different concrete mixes within a single element, matching the local structural demands.

Initial results obtained from full-scale slab specimens, produced using a semi-mechanized implementation of the casting strategy, demonstrate that around 60% of the fibers can be oriented along the prescribed curved casting path. These findings provide the basis for the ongoing transfer of the process into a fully mechanized production setup, which is currently being realized in a newly developed plant at the Ruhr University Bochum.

Keywords

Steel fiber reinforced concrete, fiber orientation, fiber alignment, structural optimization, electromagnetic induction, automation

1 Introduction

Steel Fiber Reinforced Concrete (SFRC) is increasingly used as a structural material due to its enhanced post-cracking behavior and its ability to transfer tensile stresses across cracks (di Prisco et al., 2009). The mechanical performance of SFRC is strongly governed by the orientation and spatial distribution of the fibers within the cementitious matrix (Ferrara and Meda, 2006). In conventional casting processes, however, fibers are dispersed in a largely random manner, resulting in quasi-isotropic material behavior. While this may be sufficient for elements subjected to diffuse or multi-axial stress states, it represents a significant limitation in regions where tensile stresses follow well-defined trajectories. In such cases, the structural potential of the fibers is not fully exploited, leading to inefficient material use (Boulekbache et al., 2010).

From a structural perspective, the load-bearing capacity of SFRC can be significantly enhanced if fibers are preferentially aligned along principal tensile stress directions (Laranjeira et al., 2012). This concept is analogous to the targeted placement of conventional reinforcement, but current SFRC production methods do not provide sufficient control over fiber orientation at the structural scale. Existing approaches to influence fiber alignment are either limited to small-scale laboratory conditions (Look et al., 2021; Mu et al., 2024) or rely on indirect effects during casting, such as flow-induced orientation in narrow sections (Leporace-Guimil et al., 2025), which cannot be systematically controlled for arbitrary geometries.

To address this limitation, this work investigates a casting strategy that enables the active control of fiber orientation through a path-controlled material placement process. The underlying idea is to align fibers along predefined trajectories by guiding the flow of fresh concrete during placement. In contrast to conventional casting, where the material is poured into a formwork and flows freely, the proposed approach is based on an extrusion-like deposition of SFRC along prescribed paths. This allows the direction of material flow—and thus the dominant fiber orientation—to be directly linked to the structural requirements.

The long-term objective is the realization of a fully mechanized production process capable of placing SFRC along arbitrary trajectories with high precision and repeatability. Such a process would not only enable tailored fiber orientation but also allow for the localized use of different concrete mixes within a single structural element, matching material properties to local demand. However, the implementation of a fully automated system requires a prior understanding of the governing mechanisms and the achievable degree of fiber alignment.

Within this context, the present contribution focuses on the experimental validation of the proposed casting concept. Full-scale slab specimens are produced using a semi-mechanized implementation of the extrusion-based process, allowing the influence of controlled material deposition on fiber orientation to be assessed. The results provide quantitative insight into the achievable alignment and form the basis for the ongoing development and transfer of the process into a fully mechanized production environment.

2 Casting concept and fiber orientation mechanism

The proposed casting approach is based on the placement of SFRC using an extrusion-like deposition process. In contrast to conventional casting, where fresh concrete is poured into the formwork and flows freely under gravity, the material is here placed continuously along predefined trajectories. These trajectories can be defined arbitrarily and are intended to follow the principal tensile stress paths within the structural element.

The process relies on an orienting device that directs the fresh SFRC during placement. This device consists of a series of vibrating narrow channels through which the concrete is forced prior to deposition. After exiting the orienting device, the material is deposited along the prescribed path, forming a continuous strip, with subsequent layers placed adjacent or on top of each other to build up the desired geometry, as can be seen in Figure 1 (top). The concrete consistency is specifically calibrated to ensure that the material remains stable after placement, without significant spreading or loss of shape. This allows the deposited strips to retain their geometry, independent from the formwork borders. A detailed description of the orienting device's parameters and functioning is given in (Medeghini et al., 2025).

The alignment of fibers in the proposed process is induced within the orienting device. As the SFRC flows through the vibrating narrow channels, strong boundary effects act on the fibers, orienting them along the direction of material flow (Stähli et al., 2008; Boulekbache et al., 2010). This orientation occurs before deposition and is preserved due to the calibrated concrete consistency, which prevents uncontrolled flow after exiting the device. The result is a targeted alignment of fibers along the casting trajectory, directly linking the manufacturing process to the intended structural load paths.

Beyond controlling fiber orientation, the process enables the placement of different SFRC mixes within a single structural element. By varying the material during the extrusion process, it becomes possible to locally adapt the mechanical properties of the concrete to the structural demand.

In the context of this study, this capability is considered by concentrating High-Performance SFRC (HP-SFRC) in regions of increased tensile demand, while using a Normal-Performance mix (NP-SFRC), cast in a traditional manner, in the regions under compression or moderate tension. This approach has the potential to further increase material efficiency, although its systematic implementation requires a fully controlled and automated production process.

3 Experimental program

The aim of this study is to verify the feasibility of the proposed casting method and orienting device at the structural scale, and to quantify its influence on fiber orientation and resulting material performance in comparison to conventional casting methods.

A key reference for this comparison is provided by standard beam tests according to EN 14651 (CEN, 2007), which define the residual tensile performance of SFRC for structural design. Therefore, the experimental program is designed to compare: specimens produced with the orienting device, specimens cast using traditional methods, and standard EN 14651 beams representing the reference material behavior.

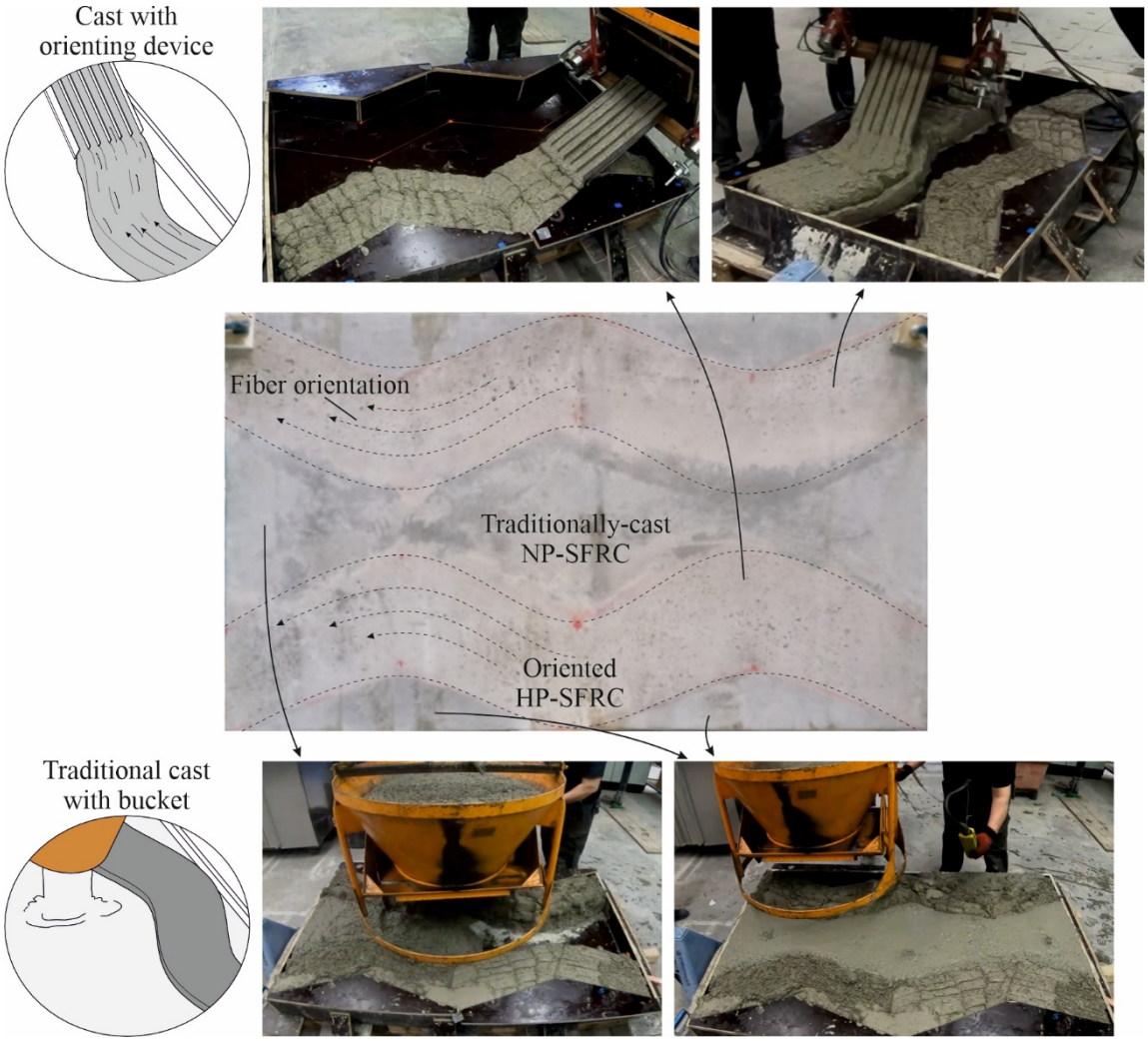


Figure 1: Production of the optimized slab Op30C: casting of the oriented HP-SFRC strips (top), traditional casting of the NP-SFRC (bottom), modified from (Medeghini, 2026)

To this end, four full-scale slab elements are produced (see Figure 2), representing successive stages in the development of the casting strategy. A first reference slab (named SFRC) is cast entirely using a conventional method, with the NP-SFRC material cast from a bucket and compacted by internal vibration.

The remaining three slabs combine conventionally cast regions with zones produced using the orienting device and the HP-SFRC. In specimen Op15S, two straight longitudinal strips of 150 mm width are cast along the slab edges using the orienting device, while the central region is cast conventionally with the NP-SFRC. In specimen Op30S, the width of the oriented strips is increased to 300 mm while maintaining straight casting paths. Finally, specimen Op30C represents the final optimization configuration, in which 300 mm wide strips are arranged along curved trajectories, fully exploiting the potential of path-controlled placement.

The casting sequences of specimen Op30C are illustrated in Figure 1. All slabs are subsequently tested under partial area loading, and specifically in a double splitting configuration. The resulting structural response and crack patterns (see Figure 2) form the basis

for the progressive optimization of the casting strategy but are not the focus of the present contribution. They are reported in (Medeghini et al., 2025).

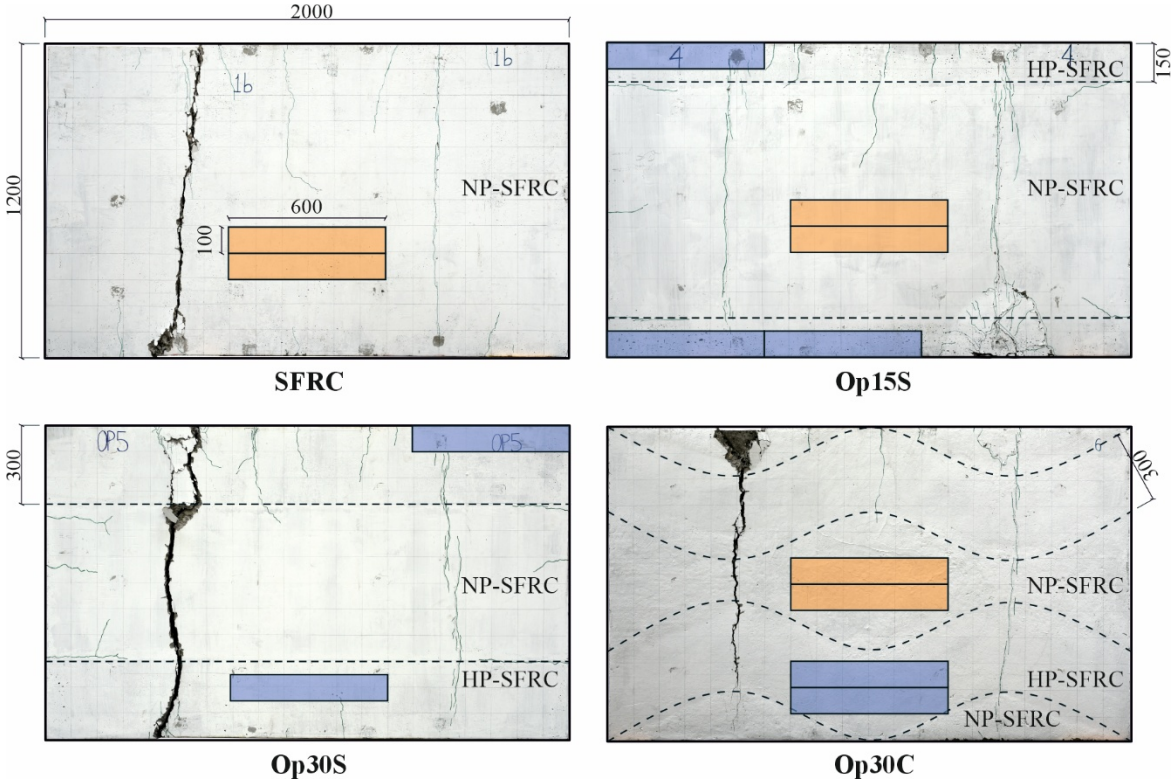


Figure 2: Dimensions of the slabs and position of the extracted small beams

Two SFRC mixes are used. The HP-SFRC contains 120 kg/m³ of steel fibers, equally divided into macro- and micro-fibers (M and m, respectively). The NP-SFRC contains 40 kg/m³ of macro-fibers of the same type (M). The main properties of the fibers are reported in Table 1. The maximum aggregate size of the HP-SFRC and NP-SFRC is 8 and 16 mm, respectively.

Table 1: Properties of the steel fibers

Fiber properties	**Macro (M)**	**Micro (m)**
Shape	Hooked end	Straight
Length (mm)	35	13
Diameter (mm)	0.55	0.20
Tensile strength (MPa)	1345	2750

After structural testing of the slabs, additional specimens are extracted for material characterization. Small beams are cut from predefined regions of the slabs (see Figure 2), selecting areas without visible cracking, both from the HP-SFRC and NP-SFRC materials.

Both the standard beams and the beams extracted from the slabs are tested in three-point bending according to EN 14651. Due to geometric constraints during extraction, the cut specimens have a width of 100 mm instead of the standard 150 mm. Apart from this modification, the testing procedure follows the standard configuration, allowing a direct comparison of residual tensile behavior.

Finally, to quantify fiber orientation, cubic specimens with edge lengths of 100 mm or 150 mm are extracted from the slabs and analyzed using an electromagnetic induction method, as shown in Figure 3.

This method is based on the interaction between an externally generated electromagnetic field and the steel fibers embedded in the SFRC sample. When exposed to the magnetic field produced by the electromagnetic induction device, the fibers modify the field depending on their orientation. This influence is detected by a coil surrounding the cubic specimen.

By measuring the response of a specimen in the three main spatial directions, it is possible to determine the mean orientation of the fibers within the volume. The method provides a non-destructive, volumetric assessment of fiber orientation, in contrast to traditional image-based techniques, which are limited to surface or sectional analysis (Medeghini et al., 2024).

The measured signals can be evaluated using different approaches to derive orientation coefficients. Semi-empirical formulations have been proposed by Cavalaro (Cavalaro et al., 2015), while Wichmann established a direct correlation between the measured response and the percentage of fibers aligned in a given direction (Wichmann et al., 2013). In this study, the simplified approach proposed by Wichmann is adopted.

The evaluation yields orientation coefficients in three orthogonal directions, allowing then the proportion of fibers aligned with the casting path to be quantified. This enables a direct comparison between oriented and non-oriented regions, as well as with the reference orientation state of standard beams.

A detailed description of the measurement principle and evaluation procedure is provided in (Wichmann et al., 2013; Medeghini et al., 2024).

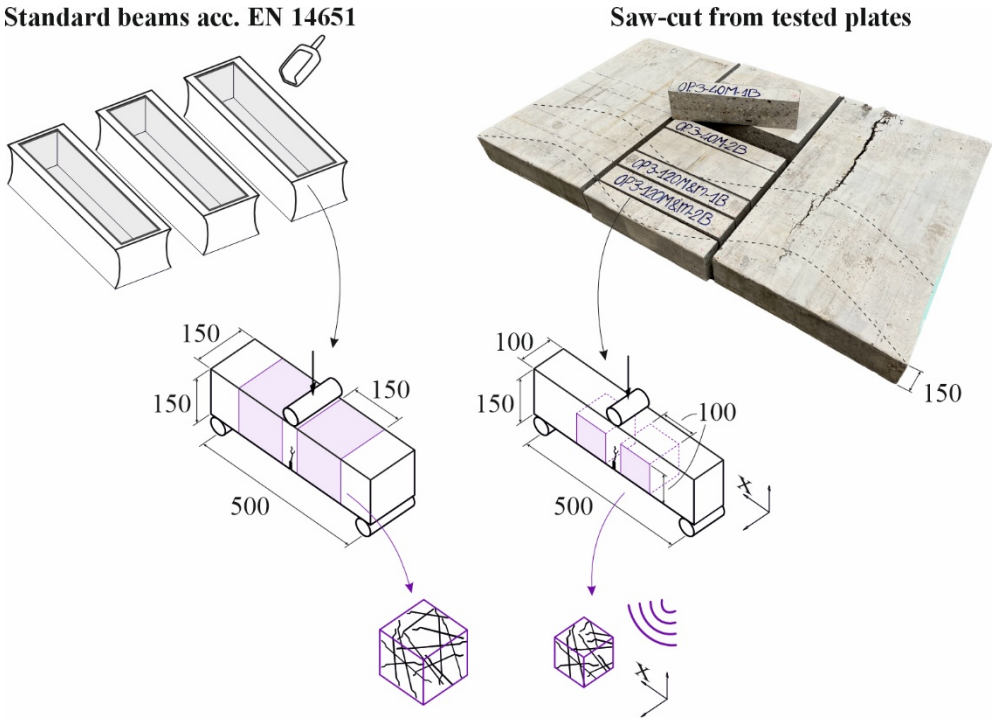


Figure 3: Specimen preparation and evaluation workflow: extraction, three-point testing (EN 14651) and electromagnetic induction-based fiber orientation measurement

4 Test Results

The residual tensile behavior obtained from the three-point bending tests is shown in Figure 4 and summarized in Table 2. The parameters $f_{R,1m}$ to $f_{R,4m}$ represent the residual flexural tensile strengths at increasing crack mouth opening displacements (CMOD), as defined in *fib* Model Code (fib, 2023), and characterize the post-cracking behavior of SFRC.

With respect to the reference performance obtained from standard beams, the specimens produced with the orienting device exhibit an average increase in residual strength of approximately 9%. In contrast, specimens obtained from traditionally-cast regions show a reduction in performance of about 32%. This difference highlights the strong influence of the casting process on the mechanical response.

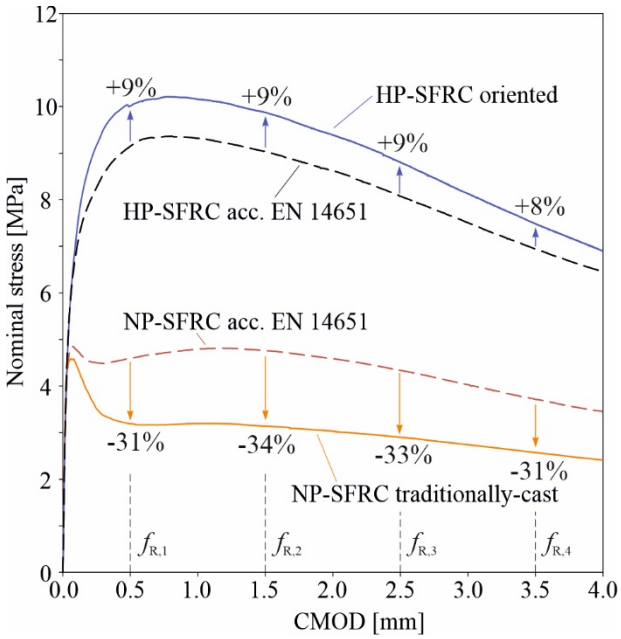


Figure 4: Nominal stress vs. CMOD mean curves of standard beams and beams cut from slabs

The scatter of the results, expressed through the Coefficient of Variation (CV) of $f_{R,1m}$ to $f_{R,4m}$, is around 20% for the standard beams, which is consistent with values reported in the literature and in current design recommendations. The oriented specimens extracted from the slabs show a slightly lower variability, with a CV of approximately 17%, whereas the traditionally cast specimens exhibit the highest scatter, with a CV of about 30%. The relatively high variability observed overall can be attributed to the fact that the specimens originate from different concrete batches, despite having identical mix designs.

The fiber orientation results are also reported in Table 2. Specimens produced with the orienting device show a preferential alignment along the longitudinal axis of the beams (X direction, see Figure 3), with values exceeding 58%. This corresponds to an increase of approximately 13% compared to the standard beams cast according to EN 14651. The remaining fibers are distributed in the transverse directions (Y and Z, with Z always defining the vertical direction during casting), each accounting for roughly 20% of the total orientation.

In contrast, specimens obtained from traditionally cast regions exhibit a significantly reduced orientation along the X axis, approximately 26% lower than in the standard beams.

Their fiber distribution is roughly isotropic, close to two-dimensional, with similar proportions in the X and Y directions and slightly lower values along Z.

The measured Fiber Content (FC) is generally consistent between cast and extracted specimens. However, for the HP-SFRC with hybrid fiber reinforcement, the electromagnetic induction method does not allow a reliable quantification of the total fiber content. This is due to the different magnetic responses of macro- and micro-fibers, which prevent an exact calibration of the measurement system and do not allow the individual contributions of each fiber type to be distinguished.

Despite this limitation, the coefficient of variation of the measured fiber content can be accurately calculated for all specimens, and is generally low. The HP-SFRC shows a lower variability compared to the NP-SFRC. Furthermore, specimens produced with the orienting device exhibit a variability comparable to that of the standard beams, whereas traditionally cast specimens show a higher scatter, with coefficients of variation of approximately 15% compared to 11% for the reference specimens.

Table 2: Mechanical properties, fiber orientation and fiber content of standard beams acc. EN 14651 and beams cut from slabs

	HP-SFRC			**NP-SFRC**		
	cast EN 14651	**cut (oriented)**	**cut / cast**	**cast EN 14651**	**cut (traditional)**	**cut / cast**
$f_{R,1m}$ [MPa]	9.17 (21%)	10.01 (16%)	1.09	4.60 (22%)	3.19 (28%)	0.69
$f_{R,2m}$ [MPa]	9.02 (21%)	9.86 (19%)	1.09	4.76 (21%)	3.13 (33%)	0.66
$f_{R,3m}$ [MPa]	8.06 (22%)	8.80 (18%)	1.09	4.33 (20%)	2.90 (34%)	0.67
$f_{R,4m}$ [MPa]	6.93 (22%)	7.47 (16%)	1.08	3.71 (19%)	2.57 (30%)	0.69
Or. X [%]	51.6 (12%)	58.3 (20%)	1.13	54.2 (8%)	39.9 (18%)	0.74
Or. Y [%]	32.3 (10%)	22.6 (22%)	0.70	29.2 (12%)	38.5 (16%)	1.32
Or. Z [%]	16.1 (26%)	19.1 (30%)	1.19	16.7 (24%)	21.6 (21%)	1.29
FC [kg/m^3]	118.7* (5.5%)	115.6* (5.6%)	0.97	40.7 (11%)	39.1 (15%)	0.96

*Fiber content for hybrid fiber mix cannot be defined exactly

5 Discussion

The results demonstrate that the casting process directly governs fiber orientation and, consequently, the mechanical response of SFRC. The preferential alignment achieved with the orienting device leads to an increase in the proportion of fibers oriented along the load-bearing direction, which translates into an improved residual tensile performance. Conversely, conventional casting results in a roughly isotropic fiber distribution and reduced mechanical efficiency.

The relationship between fiber orientation and mechanical performance is consistent with findings reported in the literature under comparable testing conditions (Medeghini et al., 2022). The typical ranges of fiber orientation for different casting states are summarized in Table 3. In particular, the ratio between the amount of fibers directed along the longitudinal axis (X direction) in oriented (60%) and traditionally cast specimens (35-40%) ranges between 1.5 and 1.7.

Table 3: Typical percentage of fibers along the longitudinal axis with different casting methods

Orientation state	**Fibers along X**
Favorably oriented Cast acc. EN 14651 Roughly isotropic	60 % 45 – 55 % 35 – 40 %

This increase in favorable orientation is directly reflected in the mechanical response shown in Figure 4. When referenced to the standard EN 14651 beams, the traditionally cast specimens reach an average relative performance of 0.68, while the oriented specimens reach 1.09. Hence, the transition from traditional casting to directed fiber orientation leads to an increase in performance of around 60%, indicating a direct correlation between fiber alignment and residual tensile strength.

In addition, the reduced scatter observed in the oriented specimens suggests that the controlled casting process not only enhances performance but also improves the reliability of the material behavior. In contrast, the higher variability in traditionally cast specimens reflects the inherent randomness of fiber distribution in conventional placement methods.

Overall, the results confirm that targeted fiber orientation is a key parameter for improving both the efficiency and predictability of SFRC, and that the proposed casting approach provides a viable means to achieve this at the structural scale.

6 Outlook

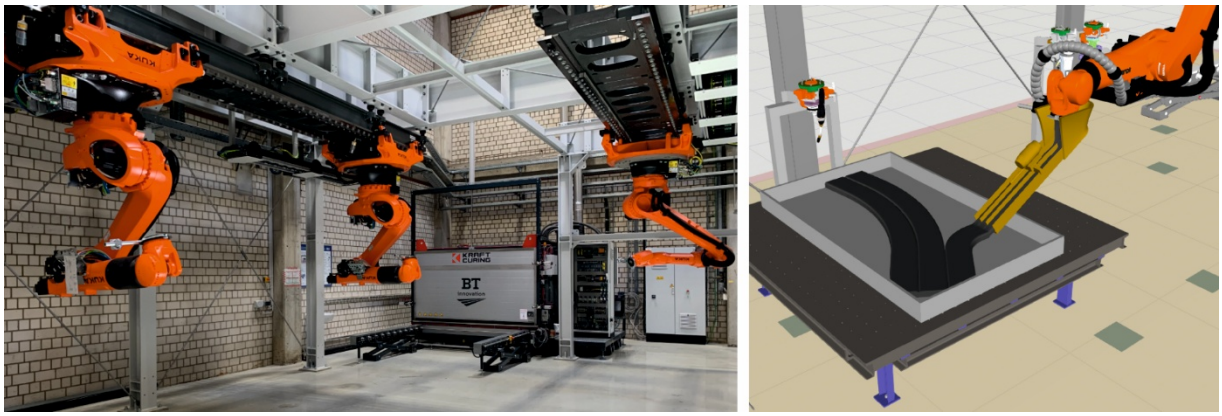
The results presented in this study demonstrate the feasibility of controlling fiber orientation through a path-controlled casting process and its direct impact on the mechanical performance of SFRC. However, the experimental investigations are based on a semi-mechanized implementation, in which key process steps—such as material feeding, positioning, and path control—are only partially automated. This limits both the precision and the reproducibility of the process.

To fully exploit the potential of directed fiber orientation, a transition towards a fully mechanized and integrated production system is required. Such a system must ensure precise control of all relevant process parameters, including material consistency, flow through the guiding device, and accurate positioning along predefined trajectories. In addition, continuous quality control and process monitoring are necessary to guarantee consistent material behavior.

A mechanized facility has been recently developed at the Ruhr University Bochum and is able to address these requirements (Hoppe et al., 2025). The plant integrates multiple industrial robots (see Figure 5a) to perform key production steps, including concrete casting, reinforcement handling, and quality assessment, within a coordinated and automated workflow. The process chain is organized as a sequence of stations, enabling a controlled and repeatable production of concrete elements with high geometric and material precision.

The integration of such a system enables path-controlled material placement with robotic precision and high process reliability, allowing casting trajectories to be executed accurately and repeatably (see Figure 5b). In this context, the trajectories can be directly derived from structural optimization methods, enabling fiber orientation to follow principal stress paths and establishing a direct link between design and manufacturing.

In the next step, the proposed casting method will be implemented within this mechanized environment. This will allow the investigation of process stability, scalability, and reproducibility under controlled conditions, and will provide the basis for transferring the approach from experimental validation to practical application.



(a) (b)

Figure 5: (a) high-precision production plant at the Ruhr University Bochum (taken from (Hoppe et al., 2025)) and (b) vision of the fully mechanized extrusion method for oriented SFRC

7 Concluding remarks

This study demonstrates the feasibility of actively controlling fiber orientation in steel fiber reinforced concrete through a path-controlled casting process. By guiding the material flow using a dedicated device, a preferential alignment of fibers along predefined trajectories is achieved at the structural scale.

The experimental results show that this controlled orientation leads to a measurable improvement in mechanical performance. Compared to standard beams according to EN 14651, the oriented samples exhibit an average increase in residual tensile strength of about 9%, while traditionally cast specimens show a reduction of approximately 32%. These differences are directly linked to the achieved fiber orientation, with a higher proportion of fibers aligned along the load-bearing direction in the oriented specimens.

In addition to improving performance, the proposed process reduces the variability of the material response, indicating a more reliable and predictable behavior compared to conventional casting methods.

Overall, the results confirm that targeted fiber orientation is a key parameter for enhancing the structural efficiency of SFRC. The proposed approach provides a viable basis for integrating material placement and structural design, enabling the development of optimized concrete elements with tailored properties.

8 References

Boulekbache, B., Hamrat, M., Chemrouk, M., Amziane, S., 2010. “Flowability of fibre-reinforced concrete and its effect on the mechanical properties of the material”

Construction and Building Materials 24 (9), pp1664–1671. https://doi.org/10.1016/j.conbuildmat.2010.02.025.

Cavalaro, S.H.P., López, R., Torrents, J.M., Aguado, A., 2015. "Improved assessment of fibre content and orientation with inductive method in SFRC" *Materials and Structures* 48 (6), pp1859–1873. https://doi.org/10.1617/s11527-014-0279-6.

CEN, 2007. EN 14651: Test method for metallic fibre concrete-Measuring the flexural tensile strength (limit of proportionally (LOP), residual), Belgium, Brussels. https://doi.org/10.31030/1386060

di Prisco, M., Plizzari, G., Vandewalle, L., 2009. "Fibre reinforced concrete: new design perspectives" *Materials and Structures* 42 (9), pp1261–1281. https://doi.org/10.1617/s11527-009-9529-4.

Ferrara, L., Meda, A., 2006. "Relationships between fibre distribution, workability and the mechanical properties of SFRC applied to precast roof elements" *Materials and Structures* 39, pp411–420. https://doi.org/10.1617/14247.

fib, 2023. Model Code for Concrete Structures 2020, Final draft, Lausanne.

Hoppe, J., Forman, P., Wolf, M., Mark, P., Gerhard, D., 2025. „Automated, quality-assured processes for the rapid production of adaptive, reinforced concrete modules - implementation in a research facility" (in German) *Beton- und Stahlbetonbau* 120 (7), pp504–516. https://doi.org/10.1002/best.202500016.

Laranjeira, F., Aguado, A., Molins, C., Grünewald, S., Walraven, J., Cavalaro, S., 2012. "Framework to predict the orientation of fibers in FRC: A novel philosophy" *Cement and concrete Research* 42 (6), pp752–768. https://doi.org/10.1016/j.cemconres.2012.02.013.

Leporace-Guimil, B., Conforti, A., Plizzari, G.A., 2025. "Evaluation of orientation factors influencing the shear and flexural behavior of elements in steel fiber reinforced concrete" *Construction and Building Materials* 474, 141054. https://doi.org/10.1016/j.conbuildmat.2025.141054.

Look, K., Heek, P., Mark, P., 2021. "Towards Rebar Substitution by Fibres – Tailored Supercritical Fibre Contents" In: Serna, P., Llano-Torre, A., Martí-Vargas, J.R., Navarro-Gregori, J. (Eds.), BEFIB 2020. Improvements and innovations : RILEM-fib International Symposium on FRC, vol. 30. Springer, Cham, Switzerland, pp908–919.

Medeghini, F., 2026. "Steered Fiber Orientation and Targeted Material Placement: Optimizing the Mechanical Response of Steel Fiber Reinforced Concrete" PhD thesis, Bochum, Germany.

Medeghini, F., Guhathakurta, J., Tiberti, G., Simon, S., Plizzari, G.A., Mark, P., 2022. "Steered fiber orientation: correlating orientation and residual tensile strength parameters of SFRC" *Materials and Structures* 55 (10). https://doi.org/10.1617/s11527-022-02082-9.

Medeghini, F., Tiberti, G., Guhathakurta, J., Simon, S., Plizzari, G.A., Mark, P., 2024. "Fiber orientation and orientation factors in steel fiber-reinforced concrete beams with hybrid fibers: A critical review" *Structural Concrete* 26(1), pp481-500. https://doi.org/10.1002/suco.202400461.

Medeghini, F., Trabucchi, I., Brentana, G., Tiberti, G., Plizzari, G.A., Mark, P., 2025. "Tailoring SFRC to mechanical needs: Full-scale experiments with optimized hybrid SFRC composition and fiber alignment to stress path" *Engineering Structures* 343, 121231. https://doi.org/10.1016/j.engstruct.2025.121231.

Mu, R., Chen, J., Qing, L., Fan, C., Wang, X., Liu, Y., Mei, S., Liu, H., Cao, C., 2024. "Properties of a steel fiber reinforced cementitious composite stool with digitally distributed steel fibers" *Construction and Building Materials* 430, 136454. https://doi.org/10.1016/j.conbuildmat.2024.136454.

Stähli, P., Custer, R., van Mier, J.G.M., 2008. “On flow properties, fibre distribution, fibre orientation and flexural behaviour of FRC” *Materials and Structures* 41 (1), pp189–196. https://doi.org/10.1617/s11527-007-9229-x.

Wichmann, H.-J., Holst, A., Budelmann, H., 2013. “A practice-conform measurement method for determination of fiber dosage and orientation in steel fiber reinforced concrete” (in German) *Beton- und Stahlbetonbau* 108 (12), pp822–834. https://doi.org/10.1002/best.201300060.

Textile waste as reinforcement fiber for construction panels

Diego Carro-López[1], Belén González-Fonteboa[1] and Carolina Martínez-García[1]

[1] : CITEEC, Universidade da Coruña, Campus de Elviña s/n, 15071 A Coruña, Spain.

Abstract

The fashion industry, driven by the "fast fashion" phenomenon, is at a critical crossroads. It is responsible for approximately 10% of the global carbon footprint and generates over 100 million tons of textile waste annually, of which only 11% is effectively reused or recycled. The typology of waste from textiles is heterogeneous and some of the fractions have potential for direct recycling, i.e. 100% cotton. This works analyses mixes of an unrecyclable and very common mix of cotton and synthetic fibers. This waste material was incorporated in mortars using gypsum and cement as binders with a 100 % of replacement. Some mixes with low binder content resulted in flexural strength below 1 MPa and compressive strength under 3 MPa. Other mixes present more interesting properties for construction applications, flexural strength at 28 days reached 5-7 MPa and compressive strength in the range of 10 MPa. The textile waste presented high water absorption, strongly reducing the workability of the mixes. For this reason, a mechanical compaction procedure was developed to produce panels with the mixes resulting in panel prototypes of 400x300x40 mm. showing a the thermal conductivity of λ=0.06 W/m·K in the range of many insulation materials.

Keywords

Textile waste; cement; gypsum; recycle;

1 Introduction

The textile industry is a global giant, representing 4.2% of the global economy, and continues to grow at a consistent rate of 3.4% (Abbate, Centobelli, Cerchione, Nadeem, & Riccio, 2023). This industry is ranked the fourth most environmentally damaging sector in the world and responsible for approximately 10% of the world's total greenhouse gas (GHG) emissions (Abbate et al., 2023). From 2000 to 2015, for example, clothing production doubled from 50 billion units to over 100 billion units, not solely due to a growing world population and gross domestic product, but disproportionately due to the concept of "fast fashion". This consumerist trend entails clothing collections changing much more frequently and people wearing each garment fewer times before discarding it. The sustainability of the textile sector is still far from optimal and the majority of textile waste has been dealt with through landfill disposal and incineration (Siliņa, Dāboliņa, & Lapkovska, 2024).

The recycling options fall into several categories with decreasing degree of desirability (Seifali Abbas-Abadi et al., 2025). Firstly, reuse, that implies the recovery the functionality of the clothes: fashion update, repair or new dying if needed. In the European Union 22% of clothing waste is collected for reuse or recycling, of which only 7-10% is suitable for direct reuse and the rest goes for recycling. The next strategy would be mechanical recycling that implies the recovery of the fibres by force application and the weaving of new yarn to produce new fibre. Even though this seems the ideal solution, it presents substantial limitations due to the shortening of the fibres and the presence of additives and dyes. For instance, white cotton can only be transformed into new cotton including at least 50% of virgin cotton to ensure adequate quality (Lindström, Sjöblom, Persson, & Kadi, 2020); there are more difficulties in the path, if the cotton of the original piece of cloth is coloured, the fabric needs to be chemically washed white, and depending on the dyes, the result might not even be white, resulting in low value fabrics.

The next option is the chemical recycling that could be materialized in form of different formats: solvolysis, pyrolysis and gasification (Choudhury, Tsianou, & Alexandridis, 2024), these processes could lead to obtain new fibre with equivalent quality to the original. However, they have crucial limitations: even though there are promising laboratory processes that, -in theory-, produce a full recovery of materials, the diversity of textile fibres, dyes and additives has made it impossible to make any of these treatments viable at industrial scale and with the real variability of the waste stream (Seifali Abbas-Abadi et al., 2025).



Figure 1. Textile waste hierarchy in the Waste Framework Directive (Directive 2008/98/EC)

The next step down on the desirable waste treatment is energy recovery, this implies the calcination of the textile waste recovering energy, this obviously contributes to the GHG emissions significantly. Lastly, the worse scenario, is one where the textile waste is derived to landfill, sadly this is the most common situation nowadays (Siliņa et al., 2024).

The actual market of textile is changing towards synthetic materials accounting for 70% of the total and with a distribution as follows: Polyester 54%, cotton 22%, viscose 6% and polyamide 5% ("Global textile fiber market share by type 2023| Statista," n.d.). There are multiple challenges to recycle the clothes that are being produced in the actual market. There is a growing tendency for blended fabrics that include fibres of several origins that combine interesting properties from both materials. One of the most common mixtures is cotton and polyester that is more wrinkle-resistant, and it is widely used in shirts and sport wear (Rittfors, 2020).

There are multiple studies that analyse the use of textile wastes as alternatives to steel and polypropylene fibres for fibre-reinforced concrete with a maximum substitution value of 2% in volume (Tran et al., 2022). This approach follows the usual practices and mix proportions of fibre-reinforced concrete. The maximum level of substitution found in literature is from the work of Aspiras & Manalo (Aspiras & Manalo, 1995). These authors prepared mixes up to 22% of unsorted textile waste cuttings from cotton, polyester, silk and rayon. As other authors, they refer for the difficulties in the compaction, and they specify just handpressing as compacting procedure. They refer to a density of 0.93-1.15 g/cm3, and a flexural strength of 7.6-16.2 MPa.

2 Experimental program

The mortar mixtures used in this study were formulated using CEM II/C-M (V-L) 42.5 R cement, complemented with E-35 gypsum as an additional binder. To enhance mechanical performance, a textile reinforcement was incorporated into the matrix. The textile was a mixture of cotton and polyester, the most common unrecyclable textile waste.

The mixtures were prepared in dry form (water/cement ratio not applied at this stage) and designed to achieve a low-density composite, with a target bulk density ranging from 0.7 to 0.9 kg/l. Due to the porous nature of the textile aggregate, the resulting material exhibited a high water absorption capacity, reaching up to 550%, which was characterized according to standard procedures for porous building materials EN 1097-6 (AENOR, 2025). The dry characteristics of the mixtures made it impossible to measure the workability with conventional tests. The mechanical characterization was limited to 3 specimens tested for flexural and compressive strength at 28 days according to EN 196-1 (AENOR, 2005). The curing conditions were under climatic chamber at 20 ºC and 95% of RH until the test time of the samples. The compaction process was performed manually due to the dryness of the mixtures, as the reference method of EN 196-1, compaction by hits, was totally ineffective.

3 Test Results

The mixtures analysed included cement or gypsum as binder, obtaining higher performance with the cement. In both cases, the very high absorption of the textile waste produced very dry mixtures that prevented the measurement of the consistency of the mortar. None of the usual methods allowed to determine the differences between the mixtures in the workability aspect.



Figure 2. Example of excessively dry mixture with textile waste

The variables for the mix design were –all in weight– the textile to binder ratio, the water to binder ratio and the superplasticizer content. After some intial tests, the efforts were centered on mixtures without natural aggregates, using only the textile waste. The results of the viable mixtures are presented in Table 1 and there are some results with cement that surpass 10 MPa at compressive strength, however the mixtures with higher textile content can reach 3 MPa even with gypsum as binder.

Table 1: Test series and fibre characteristics for all the sets of specimens tested.

Code	Binder	Water/Binder [Weight]	Binder/Textile [Weight]	Density [kg/l]	Flexural strength [MPa]	Compressive strength [MPa]
C001	Cement	0.8	4:1	1.24	7.4	13.4
C021	Cement	1.5	3:1	1.37	1.6	2.8
G001	Gypsum	2.0	1:1	0.91	0.06	3.3

With these mixtures, prototypes of panels with textile waste were prepared, focusing on the scalability of the process and the method of pressure application to obtain a good finishing for the panel surface. The mixtures analyzed were promising, however there was a limitation due to the excessive dryness. Aspiras & Manalao (Aspiras & Manalo, 1995), suggested to mechanically compact the mixture. This was a success, producing multi-purpose panels with both cement and gypsum compacted under 5 MPa of pressure (Figure 3).

Two prototypes of panel were developed based on the previous mixes, resulting in a thermal conductivity measurements of λ=0.06 W/m·K independently of the binder. This shows potential as insulation material that could serve as recycling path for the textile waste.



Figure 3. Example of textile panel mixing and panel formation through pressure compaction

4 Concluding remarks

This work analyses the use of unrecyclable textile waste as the main aggregate to produce lightweight cement- and gypsum-based mortars. The experimental results demonstrate that feasible mixtures can be obtained despite the extremely high water absorption and the associated workability limitations. Compressive strengths ranging from approximately 3 MPa to over 10 MPa were achieved, depending on the binder type and mix proportions. Mechanical compaction proved to be an effective manufacturing method, enabling the production of prototype panels with good surface quality. These panels exhibited a thermal conductivity of $\lambda = 0.06$ W/m·K, highlighting their potential as non-structural insulating construction materials while providing a promising recycling route for textile waste that is otherwise difficult to valorise.

Acknowledgements

This work stems from an ongoing project, a Neotec CDTi project awarded to the company RUDI 1944: “Second Textile Life: Circular Innovation in Furniture and Construction Materials”, which focuses on transforming textile waste into aesthetically striking furniture. Our gratitude to the company RUDI 1944 and to the CDTi *Centro para el Desarrollo Tecnológico y la Innovación*.

5 References

Abbate, S., Centobelli, P., Cerchione, R., Nadeem, S. P., & Riccio, E. (2023). Sustainability trends and gaps in the textile, apparel and fashion industries. *Environment, Development and Sustainability*, *26*(2), 1. https://doi.org/10.1007/S10668-022-02887-2

AENOR. EN 196-1 Methods of essay of cement. Part1: Mechanical properties (2005). Spain.

AENOR. UNE-EN 1097-6:2025 Tests for mechanical and physical properties of aggregates - Part 6: Determination of particle density and water absorption (2025).

Aspiras, F. F., & Manalo, J. R. I. (1995). Materials Processing Technology Utilization of Textile Waste Cuttings as Building Material. *Journal of Materials Processing Technology*, *48*, 379–384.

Choudhury, K., Tsianou, M., & Alexandridis, P. (2024). Recycling of Blended Fabrics for a Circular Economy of Textiles: Separation of Cotton, Polyester, and Elastane Fibers. *Sustainability (Switzerland)*, *16*(14). https://doi.org/10.3390/su16146206

Global textile fiber market share by type 2023| Statista. (n.d.). Retrieved December 4, 2025, from https://www.statista.com/statistics/1250812/global-fiber-production-share-type/

Lindström, K., Sjöblom, T., Persson, A., & Kadi, N. (2020). Improving Mechanical Textile Recycling by Lubricant Pre-Treatment to Mitigate Length Loss of Fibers. *Sustainability 2020, Vol. 12, Page 8706*, *12*(20), 8706. https://doi.org/10.3390/SU12208706

Rittfors, J. (2020). *Thermochemical textile recycling Investigation of pyrolysis and gasification of cotton and polyester Master's thesis in Innovative and Sustainable Chemical Engineering*. Chalmers.

Seifali Abbas-Abadi, M., Tomme, B., Goshayeshi, B., Mynko, O., Wang, Y., Roy, S., … Van Geem, K. M. (2025). Advancing Textile Waste Recycling: Challenges and Opportunities Across Polymer and Non-Polymer Fiber Types. *Polymers*, *17*(5). https://doi.org/10.3390/polym17050628

Siliņa, L., Dāboliņa, I., & Lapkovska, E. (2024). Sustainable textile industry – wishful thinking or the new norm: A review. *Journal of Engineered Fibers and Fabrics*, *19*. https://doi.org/10.1177/15589250231220359;SUBPAGE:STRING:FULL

Tran, N. P., Gunasekara, C., Law, D. W., Houshyar, S., Setunge, S., & Cwirzen, A. (2022). Comprehensive review on sustainable fiber reinforced concrete incorporating recycled textile waste. *Journal of Sustainable Cement-Based Materials*, *11*(1), 41–61. https://doi.org/10.1080/21650373.2021.1875273

Reducing Cost and Environmental Footprint of 3D-Printed UHPC Using Recycled Tire Steel Fibers

Shunyang Yao[1], Min Zhou[1], Doo-Yeo Yoo[2], Behzad Nematollahi[1]

[1]: School of Mechanical, Aerospace and Civil Engineering, University of Sheffield, UK.

[2]: Department of Architecture and Architectural Engineering, Yonsei University, Seoul, South Korea

Abstract

Ultra-high performance concrete (UHPC) is ideal for 3D concrete printing due to its extraordinary mechanical properties and durability performance. However, the high environmental footprint and cost associated with using manufactured steel fibers (MSFs) in UHPC compromise the material's sustainability performance and the commercial viability of UHPC. To tackle this challenge, this study investigated the effects of replacing MSFs with recycled tire steel fibers (RSFs) on the flowability, compressive strength, and flexural performance of 3D-printed UHPC (3DP-UHPC). Five mixtures were prepared with RSF replacement levels of 0%, 0.5%, 1.0%, 1.5%, and 2% by volume. The results showed that, compared with the mixture containing 2 vol.% MSF, the compressive strength of 3DP-UHPC incorporating 2 vol.% RSF was 12% lower in the Z-direction but 8% and 5% higher in the Y- and X-directions, respectively. Meanwhile, the corresponding flexural strength was 17%, 15%, and 8% lower in the Z-, Y-, and X-directions, respectively. On the other hand, the cost, carbon emissions, and embodied energy were reduced by 32%, 22%, and 18%, respectively. Overall, the results confirmed that the complete replacement of MSF with RSF was feasible, with no substantial deterioration in the compressive and flexural strengths of 3DP-UHPC, while significantly reducing its cost and environmental footprint.

Keywords

3D concrete printing, Ultra-high performance concrete, Recycled tire steel fibers, Manufactured steel fibers, Sustainability.

1 Introduction

The continuous layer-wise extrusion process inherent in 3D concrete printing (3DCP) poses considerable challenges to integrating conventional steel reinforcement (Mechtcherine et al, 2021). Therefore, any reinforcing strategy must avoid significant pauses or manual intervention in the extrusion process. To address this, the authors previously developed a 3D-printed ultra-high performance concrete (3DP-UHPC), which reduces dependence on conventional steel rebars because of its superior tensile and flexural strength, high toughness, and deflection-hardening behavior (Arunothayan et al, 2021 and 2022).

However, UHPC utilizes a high amount of manufactured steel fibers (MSFs, 160 kg/m³). Both the cost and environmental impacts of MSFs are very high, causing a high cost and environmental footprint for UHPC compared to normal-strength concrete (NSC), limiting the wide application and commercial viability of UHPC. According to Isa et al (2020), UHPC containing 1.5 vol.% MSFs costs approximately \$950/m^3 against \$150–200/m^3 for NSC. Furthermore, according to Voo and Foster (2010), the carbon emission associated with UHPC production is around 1065 kg/m^3, which is more than three times higher than that of NSC (including 15% fly ash with compressive strength of 40 MPa) (297.5 kg/m^3). Previous studies have investigated the effects of recycled tire steel fibers (RSFs) as a low-cost, sustainable alternative to MSFs in cast UHPC production (Isa et al, 2020). However, no study has yet investigated the effects of replacing MSFs with RSFs on the fresh and hardened properties of 3DP-UHPC. This study aims to fill this knowledge gap. Environmental and cost analyses were also conducted to investigate the overall reduction of the material cost and environmental footprint of 3DP-UHPC made of RSFs.

2 Mixture Proportions and Materials

The binder was composed of OPC (CEM I 52.5N) and silica fume. Two silica sand sizes were used, referred to as “coarser” and “finer” sands, with a mass ratio of 1:1. Polycarboxylate ether-based superplasticizer (SP) and nano clay (NC) were used to control workability and rheology, respectively. The MSFs used in this study were copper-coated straight fibers with a nominal diameter, length, and tensile strength of 0.2 mm, 6 mm, and 2850 MPa, respectively. The RSFs used in this study were the same as those labeled as “RTSF 3” in Isa et al (2020), which had a nominal diameter and tensile strength of 0.22 mm and 2500 MPa, respectively. The length distribution and statistical analysis of the RSFs are shown in Fig. 1 and Table 1, respectively (Isa et al, 2020). Table 2 presents the mixture proportions of the 3DP-UHPC mixtures. Five mixtures were prepared with RSF replacement levels of 0%, 0.5%, 1.0%, 1.5%, and 2% by volume. The proportions of the R0 mixture are adopted from the authors’ previous study (Yao et al, 2026). The NC content in R75 and R100 mixtures was reduced to maintain good printability at higher RSF contents.

Table 1: Statistical analysis of RSF distribution after the refinement process (Isa et al, 2020).

Fiber length			**Mean (mm)**	**Standard deviation (mm)**	**Variance (mm^2)**	**Kurtosis**	**Skewness**
< 9 mm	**9-15 mm**	**> 15 mm**					
35.7%	47%	17.3%	11.6	5.1	25.8	2.5	1.1

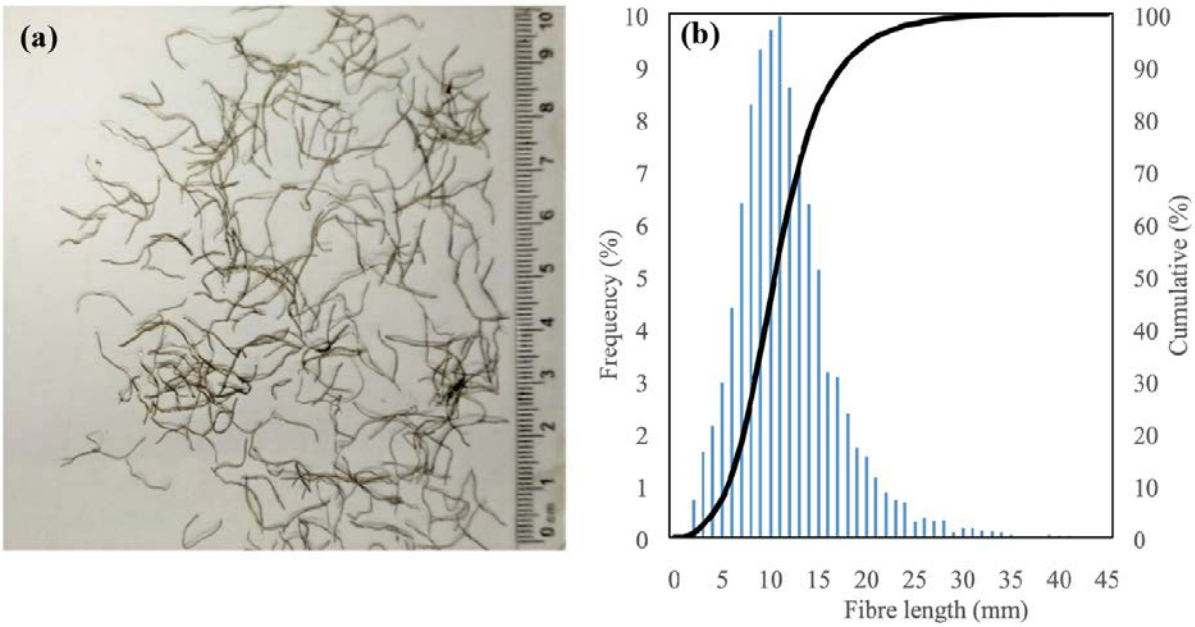


Figure 1: (a) Sample and (b) length distribution of RSFs after the refinement process (Isa et al, 2020).

Table 2: Mixture proportions of 3DP-UHPCs.

Mix ID	Binder		Sand	Water	SP	NC	Steel fiber	
	OPC	Silica fume					MSF	RSF
R0	0.75	0.25	1.0	0.17	3%	0.25%	2%	0
R25	0.75	0.25	1.0	0.17	3%	0.25%	1.5%	0.5%
R50	0.75	0.25	1.0	0.17	3%	0.25%	1%	1%
R75	0.75	0.25	1.0	0.17	3%	0.20%	0.5%	1.5%
R100	0.75	0.25	1.0	0.17	3%	0.15%	0	2%

Note: All values are mass ratios of the binder mass except for fibers (volume fraction). The proportions of the R0 mixture are reproduced from the authors' previous study (Yao et al, 2026).

3 Experimental Methods

3.1 Mixing process

A consistent mixing procedure was adopted for all mixtures. Binder components and sands were first dry blended in a 20-liter planetary mixer for 1 min. Subsequently, about 95% of the mixing water was introduced and mixed at low speed for 2 min. The remaining water premixed with the SP was then added, and mixing continued for 7 min at low speed, followed by 4 min at medium speed to obtain a homogeneous and flowable matrix. Steel fibers were then gradually incorporated and mixed for 3 min at low speed and 1 min at medium speed to promote uniform dispersion. Finally, NC was introduced and mixed for 1 min at low speed and 2 min at medium speed.

3.2 Printing and curing procedures

A custom-built gantry-type 3D concrete printer fitted with an auger extruder with a 30 mm diameter nozzle was used. The width and height of each printed filament were 30 mm and 10 mm, respectively. Two solid slabs with dimensions of 270 × 245 × 50 mm^3 and 240 × 245 × 60 mm^3 were printed. The printed slabs were then covered with plastic sheets and stored at room temperature (23 ± 3 °C) for 24 h. Subsequently, they were cut into 40 × 40 × 160 mm^3 prisms and 50 mm cubes. The printed cubes and prisms were then immersed in water inside sealed containers for 24 h, followed by heat curing in an oven at 90 °C for 48 h. After that, the specimens were stored at room temperature for an additional 72 h, resulting in a total curing period of 7 days before mechanical testing. According to the literature, further curing of up to 28 days does not change the compressive strength significantly (Arunothayan et al, 2021; AFGC, 2002).

3.3 Testing methods

Flowability of the fresh mixtures was evaluated using the flow table test in accordance with ASTM C1437. Two perpendicular spread diameters were measured before and after 25 drops of the flow table. Compressive strength tests were conducted on 50 mm cubes under a loading rate of 0.6 MPa/s. Printed cubes were tested along three directions, namely X, Y, and Z (see Fig. 2). Flexural performance was assessed using 40 × 40 × 160 mm^3 prisms subjected to three-point bending over a 120 mm span at a displacement rate of 0.5 mm/min. Printed prisms were also tested in three directions, namely X, Y, and Z (see Fig. 2).

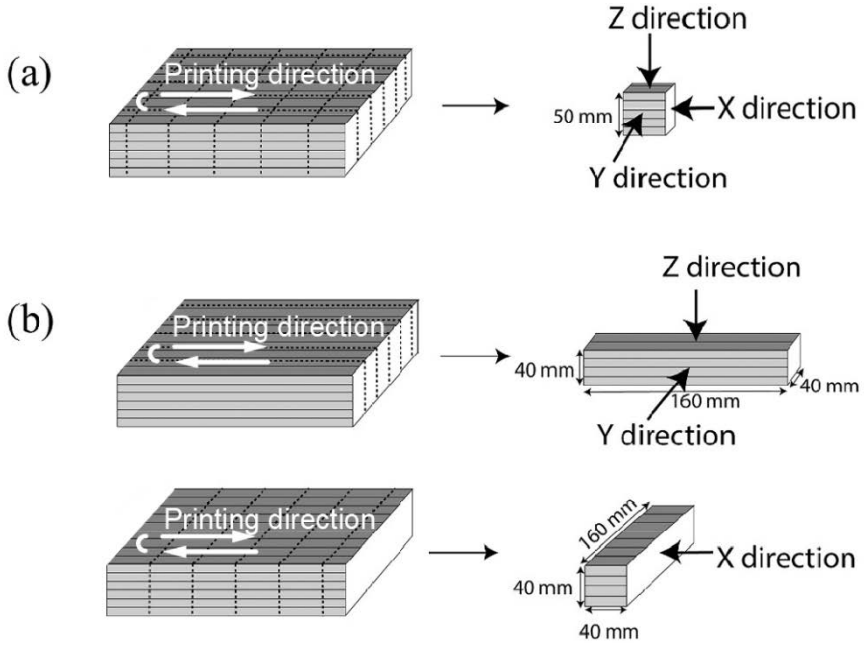


Figure 2: Loading directions for printed specimens in (a) compression and (b) flexure. (adopted from Arunothayan et al (2022)).

4 Results and Discussion

4.1 Flowability

As shown in Table 3, the spread diameters of R0, R25, and R50 mixtures were similar. As the NC content in these mixtures was the same (see Table 2), it can be said that replacing up to 50% of MSF with RSF did not have a significant effect on the flowability. However, initial trials showed that higher RSF content in R75 and R100 reduced the flowability considerably, which made these mixtures not suitable for printing. Therefore, the NC dosage was reduced in the R75 and R100 mixtures (see Table 2). Following this adjustment, the after-drop spread diameter of the R75 and R100 mixtures was up to 14% higher than that of the R0 mixture, while the before-drop spread diameter remained below 115 mm, which was suitable for printing using the printing setup used in this study.

Table 3: Spread diameter results (mm).

R0		**R25**		**R50**		**R75**		**R100**	
Before	After	Before	After	Before	After	Before	After	Before	After
101	135	100	140	105	138	114	152	107	154

Note: The results of the R0 mixture are reproduced from Yao et al (2026).

4.2 Compressive strength

Fig. 3 shows the compressive strength results, ranging from 130.2 to 205.3 MPa across testing directions and RSF content. This confirms that all printed specimens satisfied the minimum compressive strength requirement of UHPC (>120 MPa) as per ASTM C1856 (2024). The variation in compressive strength across testing directions reflects the inherent anisotropy of 3DPC. In all mixtures (except R50), the highest and lowest compressive strengths were recorded in the Z- and X-directions, respectively. However, an anomaly was observed in R50, where the lowest strength was recorded in the Z-direction (137.2 MPa), while its strengths in the X- and Y-directions remained relatively high at 167.3 and 176.0 MPa, respectively. The anomaly observed in R50 requires further investigation.

Excluding R50, replacing MSF with RSF reduced or increased compressive strength in the range of 3-13%, depending on the testing direction and RSF content. Considering the results of R100, the compressive strength was 12% lower, but 8% and 5% higher, respectively, in the Z-, Y-, and X-directions, compared to R0. Thus, it can be concluded that the complete replacement of MSF with RSF was possible without a significant change in compressive strength.

4.3 Flexural performance

As shown in Fig. 4, anisotropic behavior was also observed in flexural strength. In fiber-reinforced 3DPC, fibers tend to align along the printing path during extrusion (Arunothayan et al, 2021). As a result, the specimens loaded in the Y- and Z-directions (perpendicular to the fiber orientation) exhibited higher flexural strength than those loaded in the X-direction (parallel to the fiber orientation). The same pattern has been reported in the literature (Arunothayan et al, 2021).

As shown in Fig. 4, replacing MSF with RSF reduced the maximum flexural strength. The extent of reduction depended on the testing direction and RSF content. The reductions in the Z-, Y-, and X-directions were 9-15%, 3-14%, and 6-18%, respectively, depending on the RSF content. The reduction is likely due to the irregular geometry (length and shape) of RSFs, affecting orientation of fibers during printing. Considering the results of R100, where the strength reduction compared to R0 was 17%, 15%, and 8%, respectively, in the Z-, Y-, and X-directions, it can be concluded that the complete replacement of MSF with RSF was possible without a significant change in the maximum flexural strength.

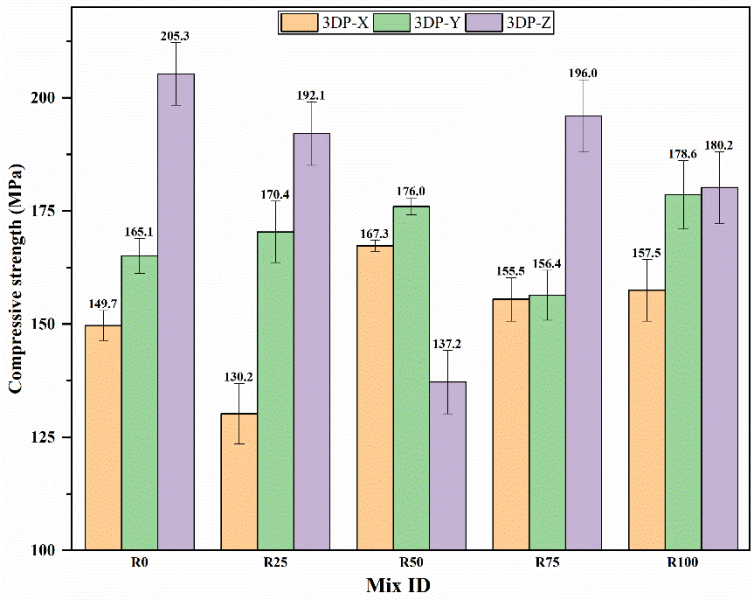


Figure 3: Compressive strength results.
Note: The results of the R0 mixture are reproduced from Yao et al (2026).

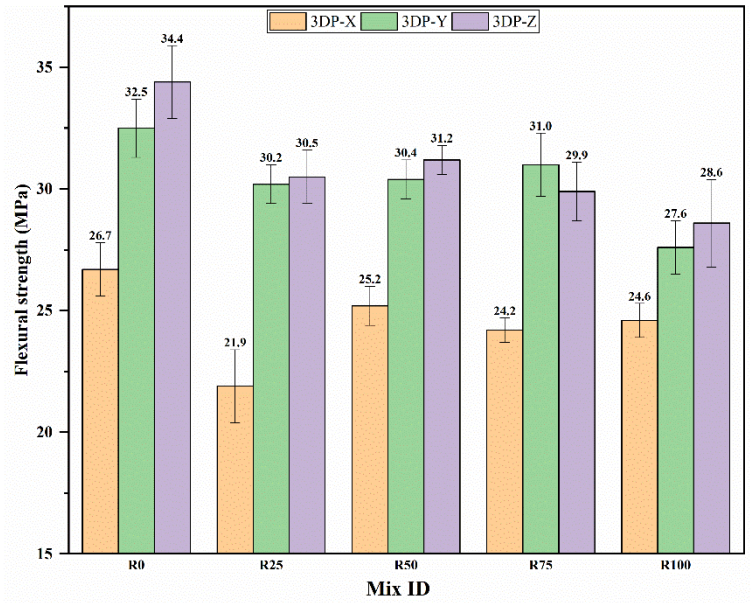
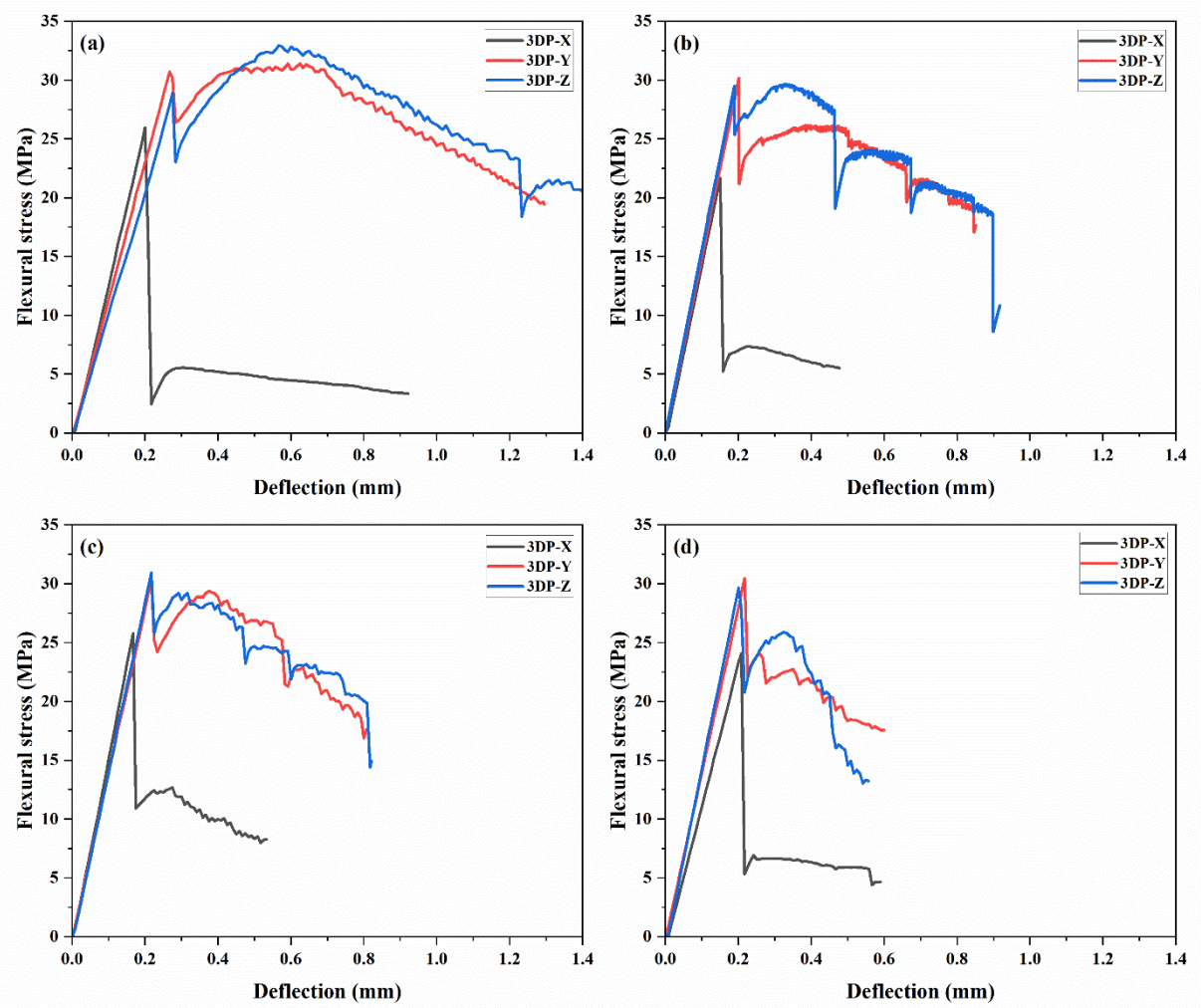


Figure 4: Flexural strength results.

Fig. 5 shows representative flexural stress vs. mid-span deflection curves for all mixtures. The post-crack flexural performance of the specimens significantly depended on the testing direction and RSF content. Replacing MSF with RSF did not significantly affect the post-peak flexural performance of the specimens in the X-direction, but it noticeably influenced their post-peak behavior in the Y- and Z-directions. In all mixtures, the specimens in the X-direction showed deflection-softening behavior with a significant drop in flexural stress after the first crack. This is because, in the X-direction, the load was parallel to the interlayer (see Fig. 2) and fiber orientation (Arunothayan et al, 2021). In R0 (see Fig. 5a), the specimens in the Y- and Z-directions generally showed deflection-hardening behavior. However, in R25, R50, and R75 (see Figs. 5b, 5c, and 5d), the specimens in the Y- and Z-directions generally showed deflection-softening behavior. Nevertheless, they still showed a more gradual post-peak softening response and retained a greater post-peak residual strength, compared with those tested in the X-direction. In R100 (see Fig. 5e), the specimens in the Y- and Z-directions generally showed deflection-hardening behavior but with lower deflection capacity compared to R0. The effect of RSF on post-peak response in the Y- and Z-directions can be attributed to the irregular geometry (length and shape) of RSF, affecting the crack-resistance capacity during crack propagation.



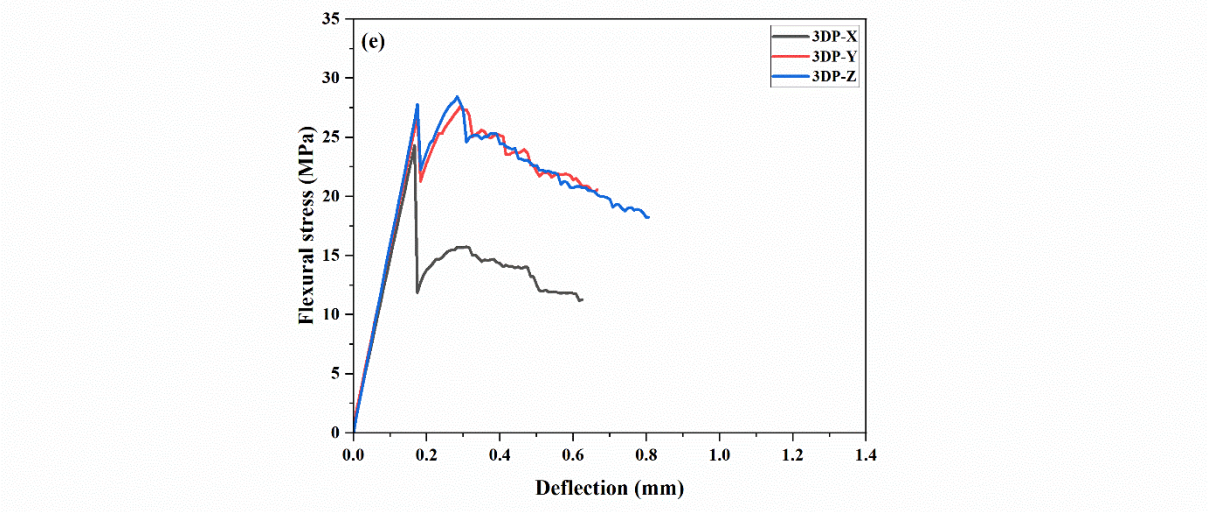


Figure 5: Representative flexural stress vs deflection curves: (a) R0, (b) R25, (c) R50, (d) R75, and (e) R100.

The flexural toughness of the mixtures was determined from the area under the flexural stress-deflection curves (Fig. 5) up to 0.8 mm deflection, equal to 1/150 of the span length. As shown in Table 4, flexural toughness showed clear anisotropic behavior, with the X-direction consistently presenting the lowest flexural toughness in all mixtures. R0 exhibited the highest flexural toughness in both Y- and Z- directions. Compared to R0, the incorporation of RSFs led to a reduction in flexural toughness in both Y- and Z- directions. However, the flexural toughness in the X-direction did not exhibit a consistent trend with increasing RSF content. Compared with R0, the incorporation of RSF reduced the flexural toughness in the X-direction by 8% and 11% in R25 and R75, respectively. In contrast, the flexural toughness in the X-direction increased by 22% and 65% in R50 and R100, respectively. These increases can be attributed to the higher residual post-peak strengths observed in R50 and R100 (see Figs. 5c and 5e), compared with R0 (see Fig. 5a).

Table 4: Flexural toughness results (kJ/m^2).

Mix ID	**R0**	**R25**	**R50**	**R75**	**R100**
X-direction	1.19 ± 0.40	1.09 ± 0.52	1.45 ± 0.28	1.06 ± 0.11	1.97 ± 0.39
Y-direction	4.57 ± 0.13	3.31 ± 0.46	3.78 ± 0.21	3.08 ± 0.72	3.22 ± 0.23
Z-direction	4.72 ± 0.29	3.54 ± 0.29	3.52 ± 0.57	2.86 ± 0.53	3.44 ± 0.21

4.4 Environmental impact and cost analyses

Table 5 presents the costs and environmental impacts associated with MSF and RSF production. According to this table, replacing 2 vol% MSF with 2 vol% RSF reduces the carbon emissions and embodied energy of 3DP-UHPC by about 22% and 18%, respectively. In addition, the costs of MSFs and RSFs at 2 vol% (157 kg/m^3) are about $643 and $184 per cubic meter of UHPC, respectively. Therefore, replacing 2 vol% MSF with 2 vol% RSF reduces the cost of 3DP-UHPC by approximately $460 per cubic meter, corresponding to an overall cost reduction of about 32%.

Table 5: Costs and environmental impacts associated with MSF and RSF production.

Material	Carbon emissions (kg/kg)	Embodied energy (MJ/kg)	Cost ($/t)
MSF	1.50[a]	22.2[a]	4095[c]
RSF	0.083[b]	12.0[b]	1174[b]

[a] Estimated from the data of Suer et al (2022). [b] Estimated from the data of Isa et al (2020). [c] Adopted from Habert et al (2013).

5 Concluding remarks

This study investigated the fresh and hardened properties of 3DP-UHPC mixtures incorporating RSF in place of MSF. Based on the experimental results and comparative analysis, the following conclusions can be drawn:

- Regardless of the RSF content and testing directions, all mixtures satisfied the minimum compressive strength requirement of UHPC (i.e., >120 MPa as per ASTM C1856 (2024)).
- Excluding R50, replacing MSF with RSF reduced or increased compressive strength in the range of 3-13%, depending on the testing direction and RSF content.
- Replacing MSF with RSF reduced the maximum flexural strength in the Z-, Y-, and X-directions by 9-15%, 3-14%, and 6-18%, respectively, depending on the RSF content.
- The post-crack flexural performance of the specimens significantly depended on the testing direction and RSF content. Replacing MSF with RSF did not significantly affect the post-peak flexural performance of the specimens in the X-direction, but it noticeably influenced their post-peak behavior in the Y- and Z-directions.
- In all mixtures, the specimens in the X-direction showed deflection-softening behavior with a significant drop in flexural stress after the first crack.
- The specimens in the Y- and Z-directions generally exhibited deflection-hardening behavior in R0 (with 2 vol.% MSF) and R100 (with 2 vol.% RSF), whereas deflection-softening behavior was generally observed in R25, R50, and R75 (with combined MSF and RSF).
- The flexural toughness showed clear anisotropic behavior, with the X-direction consistently presenting the lowest flexural toughness in all mixtures. R0 exhibited the highest flexural toughness in both Y- and Z- directions. Compared to R0, the incorporation of RSFs led to a reduction in flexural toughness in both Y- and Z- directions.
- Replacing up to 50% of MSF with RSF did not have a significant effect on the flowability. However, at higher RSF content, the NC dosage was reduced to maintain good printability.
- Complete replacement of MSFs with RSFs reduced carbon emissions, embodied energy, and costs of the 3DP-UHPC by approximately 22%, 18%, and 32%, respectively.

6 Acknowledgements

The authors greatly acknowledge the support provided by the Royal Society International Exchanges Award 2023 (IES\R3\233378).

7 References

Arunothayan, A. R., Nematollahi, B., Ranade, R., Bong, S. H., Sanjayan, J. G., & Khayat, K. H., 2021. "Fiber orientation effects on ultra-high performance concrete formed by 3D printing", *Cement and Concrete Research*, 143, 106384. doi: 10.1016/j.cemconres.2021.106384.

Arunothayan, A. R., Nematollahi, B., Ranade, R., Khayat, K. H., & Sanjayan, J. G., 2022. "Digital fabrication of eco-friendly ultra-high performance fiber-reinforced concrete," *Cement & Concrete Composites*, 125, 104281. doi: 10.1016/j.cemconcomp.2021.104281.

Association Francaise de Génie Civil (AFGC), 2002. "Ultra High Performance Fiber-Reinforced Concretes: Interim Recommendations", *AFGC Scientific and Technical Documents*.

ASTM C1437, 2007. "Standard Test Method for Flow of Hydraulic Cement Mortar", ASTM International, West Conshohocken.

ASTM C1856, 2024. "Standard Practice for Fabricating and Testing Specimens of Ultra-High Performance Concrete", ASTM International, West Conshohocken.

Voo, Y. L. and Foster, S. J., 2010. "Characteristics of ultra-high performance "ductile" concrete and its impact on sustainable construction", *The IES Journal. Part A, Civil and Structural Engineering*, *3*(3), pp. 168–187. doi: 10.1080/19373260.2010.492588.

Habert, G., Denarié, E., Šajna, A., & Rossi, P., 2013. "Lowering the global warming impact of bridge rehabilitations by using Ultra High Performance Fibre Reinforced Concretes", *Cement & Concrete Composites*, 38, pp. 1–11. doi: 10.1016/j.cemconcomp.2012.11.008.

Isa, M. N., Pilakoutas, K., Guadagnini, M., & Angelakopoulos, H., 2020. "Mechanical performance of affordable and eco-efficient ultra-high performance concrete (UHPC) containing recycled tyre steel fibres", *Construction & Building Materials*, 255, 119272. doi: 10.1016/j.conbuildmat.2020.119272.

Mechtcherine, V., Buswell, R., Kloft, H., Bos, F. P., Hack, N., Wolfs, R., Sanjayan, J., Nematollahi, B., Ivaniuk, E., and Neef, T., 2021. "Integrating reinforcement in digital fabrication with concrete: A review and classification framework", *Cement & Concrete Composites*, 119, 103964. doi: 10.1016/j.cemconcomp.2021.103964.

Suer, J., Traverso, M., and Jäger, N., 2022. "Review of Life Cycle Assessments for Steel and Environmental Analysis of Future Steel Production Scenarios", *Sustainability*, 14(21), 14131. doi: 10.3390/su142114131.

Yao, S.Y., Nematollahi, B., Chougan, M., and Yoo, D., 2026. "3D-printed low-carbon UHPC using limestone calcined clay cement (LC3)", doi: 10.20944/preprints202604.1951.v1.

Fibres with no orientation

György L. Balázs[1], Wisam K. Tuama[1], Oscar Pfeffermann[2], Gábor Kardos[3], Salem Nehme[1], Sándor Sólyom[1]

[1] : Department of Construction Materials and Technologies, Faculty of Civil Eng., Budapest University, of Technology and Economics, Műegyetem rkp. 3, 1111 Budapest, Hungary

[2] : Glob Invest 2000 Ltd., Kossuth square 18, H-1055 Budapest, Hungary

[3] : *FUNDAMENT 4 Ltd., Hungary*

Abstract

Fibres in concrete offer several advantages in terms of material characteristics, technological aspects, and construction procedures. However, ensuring a uniform random distribution of fibres in practice is often challenging and difficult to verify.

A major step has been achieved in improving the efficiency of fibres by introducing a novel 3-dimensional fibre geometry. It effectively addresses orientation and balling problems, as its inherently 3-dimensional shape eliminates preferential alignment. It also provides spatial confinement throughout the concrete matrix, enhancing interaction among aggregates. Mixing of these new fibres – even in large quantities – is straightforward due to their geometry.

The new fibre has a special 3-dimensional geometry consisting of four closed loops connected at a common centre. The material of the fibre can be steel, or any other material suited to the specific application. This fibre provides a general improvement to the concrete matrix in terms of tensile, compressive, shear, and torsional strength, as well as deformation behaviour.

The paper discusses the mixing process, material characteristics, and potential future applications. Applications may include both structural and non-structural elements, strengthening solutions, nuclear reactors, and 3D concrete printing, among others.

This 3-dimensional fibre offers an exceptional opportunity to enable fully automated production of reinforced concrete elements, covering the entire process from reinforcement production (fibre manufacturing) to the mixing and placement of concrete in arbitrary forms.

Keywords

3-dimensional fibre, no-orientation, no-balling, automation, digitalization, structural and non-structural applications

1 Introduction

Development of concrete and reinforced concrete included several important steps from early applications: develop reinforcement for flexure and shear, development of prestressing

(pre-tensioning and post-tensioning), development of admixtures (already five generations) to improved workability and various other properties in order to improve characteristics of fresh as well as hardened concrete characteristics (Müller, Haist, 2009; Di Prisco, Plizzari, Vandewalle, 2009; Tiberti, Germano, Mudadu, Plizzari, 2018).

Development of fibre reinforced concretes in last decades – especially with steel fibres – intended to improve fibre properties, toughness, energy absorption, crack propagation, serviceability, durability, ultimate, shear, fatigue, creep etc. (Romualdi, Mandel, 1964; Balaguru, Shah, 1992; Niyogi, Dwarakanathan, 1995; Kovács, Balázs,2003; Balázs, 2006; Mobasher, Peled, Pahilajani, 2006.De Montaignac, Massicotte, Charron, Nour, 2012; *fib* (2014) Serna, Llano-Torre, Carvalho, 2017; Tiberti, Trabucchi Al Hamaydeh, Minelli, Plizzari, 2019. This was followed by MC2010 and MC2020 development for design. Details if measuring technique is discussed and compared (Valdez, Juárez-Alvarado, Mendoza-Rangel, Terán Torres, 2021).

Ultra high performance concrete (Reinhardt, Naaman, 1999; Toutlemonde, Resplendino, 2013; Reggia, Morbi, Plizzari, 2020) and strain hardening behaviour received special emphases owing to the quantitative change in behaviour (Mechtcherine, Slowik, Kabele, 201817).

All these contributed to improve concrete properties and technology. Concrete became the most successful structural material during the last one and a half centuries for a wide range of applications owing to its simplicity (Meda, Minelli, Plizzari, 2012).

The new reinforcing element in form of a 3-dimensional form may open a new view and possible solutions simply because further improvements may be still welcome in concrete properties as well as concrete technology.

Automation of concrete constructions requires new solutions almost in any sector of the industry. **Figure 1** intended to summarize the potentials in using the new reinforcing element for everyday applications for elements of buildings, bridges, roads, railways, hydraulic structures as well as for special applications like reinforcement in UHPC, SIFCON, nuclear, impact resistance-and 3D printing, respectively.

The scope of this paper is to introduce the *new type of reinforcement* in general which can be easily applied and provides potentially solutions for everyday cases substituting conventional reinforcement as well as for special cases ECC type materials, UHPC or SIFCON.

The objective of this paper is to discuss advantages of basic behaviour and show preliminary test results presented in Figure 1 in Sections 2 to 7 in details.

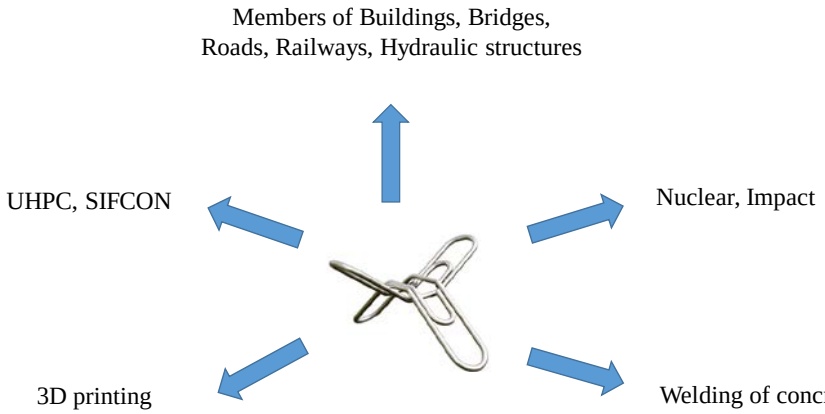


Figure 1: Potentials in application of the new reinforcing element (schematic diagram).

2 The new reinforcing element

The new reinforcing element – like a special fibre – but has a 3-dimensional form. It is produced from a single wire in successive steps of bending and creating finally four closed loops that are connected in the same centre (Figure 1). Fibre name is: Starex; and the name of the concrete which includes Starex in an appropriate composition of concrete is called as: Perfycon. Data for a typical Starex fibre are (other geometries and strengths are also possible): diameter of the wire: 0.89 mm, overall width/length of fibre: 30 mm, width of hook: 6 mm, characteristic value of yield strength: 1280 MPa (value provided by patent holder Csongor Czintos).

The fibre can have different diameters and different lengths of loops depending on the type of application, i.e. depending on the sizes of the element and type of execution (placing, pumping, shotcreating, self-compacting, etc.). The fibre material is steel currently, but different materials are supposed for the future: like carbon, basalt, etc.).

3 Four criteria are fulfilled simultaneously

The *following 4* criterions indicate the extraordinary characteristics of the *new reinforcing element* that are fulfilled simultaneously (1) no balling of fibres, (2) homogeneity and (3) isotropy as well as (4) hundred percent anchorages with special transfer mechanism. These 4 criterions provide a unique situation for the behaviour.

3.1 Mixing with no balling, homogeneous distribution and isotropic behaviour

Balling of fibres often creates a critical point of fibre applications both for steel and for other types of fibres depending on the form and type of anchorage of fibres.

In general, if balling starts by a fibre application, it is not possible to stop by further mixing. The ball is increasing in size by involving more and more fibres. Even if the strength of the ball is almost negligible, the fibres create a rather dense structure by including high amount of air excluding the ingress of cement paste

Past decades resulted different solutions how to reduce probability of balling of fibres. These solutions include simple measures in order to keep the fibres loose before applying, or little instruments to make the fire loose just before placing into the fresh concrete or to join the fibres into a group of fibres that have larger size for reducing the probability of balling by gluing the fibres together.

Balling of 3-dimensional fibres presented herein in Figure 1 have unique characteristics to avoid balling. The fibre loops have parallel sides. If the fibre loops slip into each other, they easily move away again without any tendency for balling. Avoidance of balling is a major step forward in any fibre application. In case of fibre in Figure 1 *balling is excluded both theoretically and practically*.

Intention of fibre application is to provide an evenly distributed influence by the addition of fibres. Random orientation is often endangered whenever physical constraints are provided, like boundaries (walls) of the element, flow of the fresh concrete (self-compacting concrete), vibration if orientation is forced, etc. All these are very difficult to check within the hardened

concrete. Technological measures are often given to avoid orientation, but these are not always efficient enough.

Another important feature of the new fibre is its central symmetric form which *does not allow orientation* produced during mixing.

The 3D symmetry of fibres in addition to homogeneity of fibre distribution and minimum overlapping of fibres isotropy is also fulfilled.
The closed form of fibre loops enables to use even high fibre dosages without having difficulties during mixing. This is valid even if fibres are placed in large quantities on the top of the fresh concrete mix. We have already mixed 280 kg/m^3 fibres without difficulties. It implies that the fibres should not create difficulties during transportation. Fibre distribution is easily checked by CT (Figure 2).

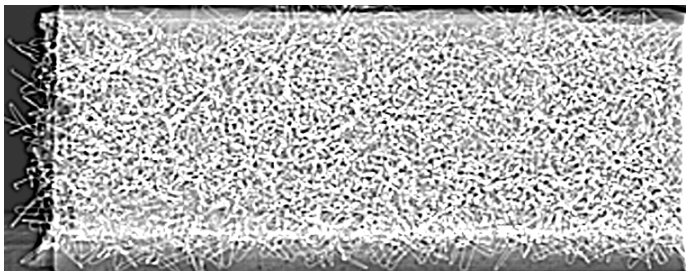


Figure 2: CT image of Starex concrete = Perfycon

Concrete compositions for experiments presented in the following Sections were specifically developed for the applications. Tests were carried out at the Laboratory of Department of Construction Materials and Technologies at the Budapest University of Technology, Hungary.



Figure 3: Tests to measure the efficiency of overlapping fibre loops

Efficiency of fibre mixes with the new 3-dimensional fibres depends on the overlapping of fibre loops.

I order to develop the advantageous effect of force transfers among the fibres in 3 dimensions a minimum overlapping of fibre loops is needed. Beyond a minimum overlapping of fibre loops the performance of fibre interaction increases considerably.

Figure 3 indicates the efficiency of the anchorages of loops by increasing the size of the overlapping. The transfer overlapping of loops were tested with gradual increase of the size of the overlapping.

3.2 Hundred percent anchorages - force transfer mechanism from fibre to fibre

One of the major advantages of the new fibre that fibre loops can be perfectly anchored at their all ends. The local equilibrium of loops is given by the two fibre legs of any loop can be stressed to yield, on one hand and the bearing stresses of concrete within the loop on the other hand. Local bearing stresses of concrete can be considerably higher than the uniaxial compressive strength of concrete.

The load bearing capacity of a loops depends on the geometrical and the mechanical properties of both the steel fibre as well as the embedding matrix of concrete. The closed loops are connected in the centre of the 3-dimensional fibre. Therefore, the efficiency of anchorage of loops can be assumed to be 100% in general whenever the concrete strength is enough to develop the yield strength of fibre.

The 3-dimensional form of fibres provides a complex force transfer mechanism from fibre to fibre through the contribution of concrete in three dimensions.

If adjacent fibre loops are stressed in tension the intermediate concrete strut acts to transfer the force by compression (Figure 4).



Figure 4: Force transfer mechanism in tension through compression in concrete

The fibre loops together with the concrete give successive steps of the force transfer mechanism in all 3 directions of the concrete element.

The details of force transfer mechanism depend on the maximum size of the aggregate, consistency of cement past for workability as well as compressive and tensile strength of the matrix for load transfer and for load bearing.

To define the maximum aggregate size of the matrix it is interacting to following parameters: the bend diameter of loops, yield strength of fibre and the cross section of loop, cement content, consistency.

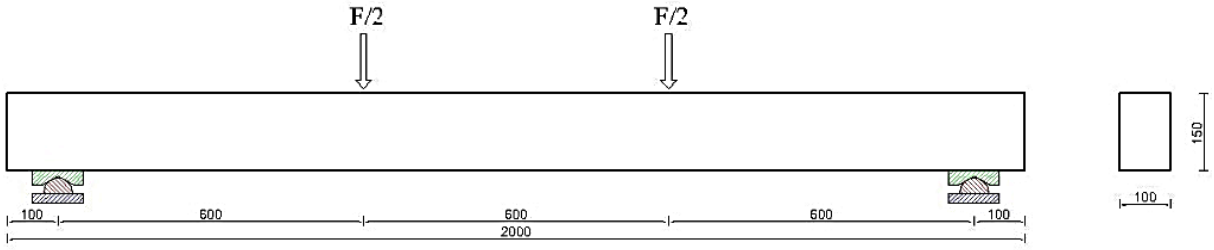
The initial intention is with the new 3-dimensional fibre reinforcement to define concrete mixes suitable to prepare with conventional concrete mixers.

This new type of reinforcing material may open new ways of modelling too.

4 Beam test

A 2 m long beam over a span of 1.8 m with cross-section of 100 x 150 mm cross-section has been tested in 4-point bending. Schematic representation of the loading system is presented in Figure 5.a (Balázs, Nehme, Sólyom, Stocker, 2019).

a)



b)

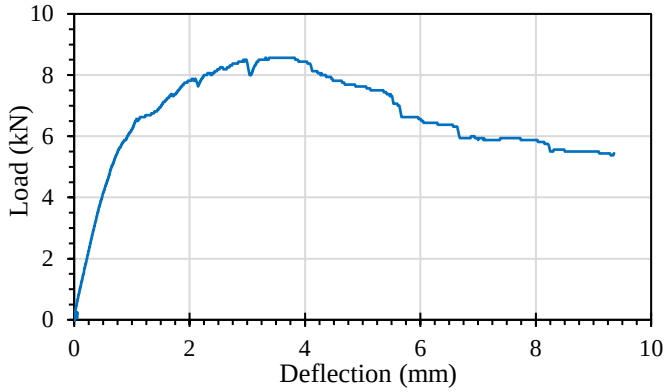


Figure 5: Test setup and load vs. deflection diagram of 2 m beam; span: 1.8 m; cross section: 100x150 mm. 4-pont bending. Un-notched specimen. Average compressive strength of the concrete mix with the fibres: 152 N/mm^2. Fibre content: 240 kg/m^3 Starex steel fibres.

Following the initial linear elastic ascending branch until first cracking, non-linear increase has been observed before reaching the maximum. It was followed by a gradual descending branch. A single crack has been formed in the vicinity of one of the loads. A good fibre distribution was observed after failure.

Average compressive strength at the time of testing of beam, measured on 6 cubes of 100 sides was 152 N/mm^2.

5 Internal confinement in compression

In this Section we intend to demonstrate the extraordinary confining effect by the newly developed fibre in compression.

A major characteristic of the fibre concrete including the 3-dimensional fibres is *the internal confinement provided by the fibres*. The complex 3-dimensional system enables of fibres to

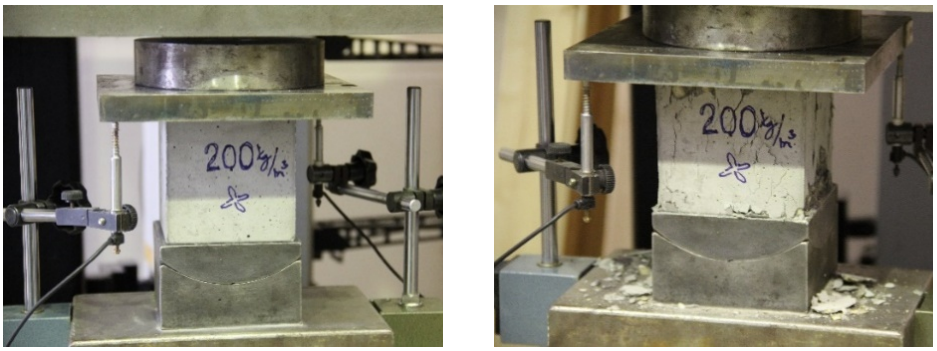
keep control of deformations in all 3-dimensional. By speaking about uniaxial compression, the lateral extensions in the other two directions are controlled by the fibre hooks within the volume of the specimen. Owing to the 3-dimensional form of the fibre every loop interacts with the neighbouring loops.

Advantage of the presented system is that the confinement is evenly distributed within the concrete volume and not only provided at the boundaries of the elements.

The internal confinement is effective especially for compression as well as for tension whenever the necessary amount of fibres is provided.

The internal confinement enables to keep the concrete together through the whole loading process. Even distribution of deformations and vertical cracks are indicated in Figure 6 during a compressive test.

This high deformation capacity can be important e.g. for the column of a high rise building.

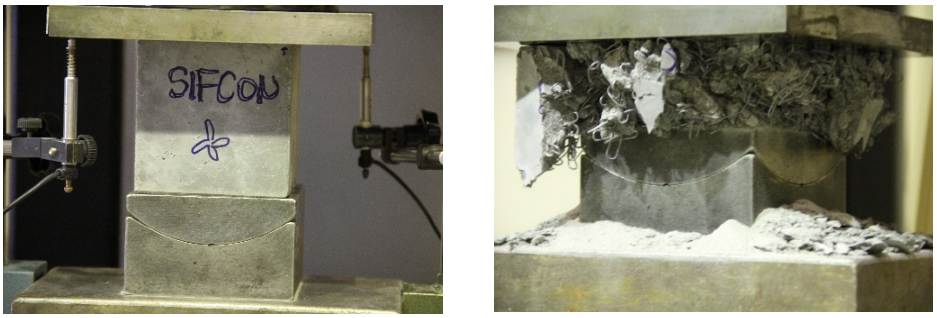


a) Starting the test b) Close to failure

Figure 6: Compressive test. Even distribution of deformations in compressive tests of a cube of 100 mm sides before (a) and during failure (b). Compressive strength 83 N/mm^2

6 SIFCON in compression

SIFCON application of the newly developed fibre is very promising. The space structure of the fibre may provide a definition of the amount of fibres within a unit volume is a unique situation for SIFCON concretes.



a) Starting the test b) Exercising large deformations

Figure 7: SIFCON specimen of 100 mm sides in compression. Compressive strength 110 N/mm^2

The SIFCON specimen of 100 mm cube tested in compression is shown in Figure 7.a before and after testing. The strength of this SIFCON specimen was 110 N/mm^2.The deformations in transverse direction are clearly visible from Figure 7.b.

During loading the specimen exercised extremely large compressive deformations in longitudinal direction without external confinement. The deformations in transverse direction are clearly visible from Figure 7.

The specimen survived finally more than 50% of compressive strain. This extremely high compressive deformation was only possible by the internal fibre interaction system provided by the new 3-dimensional fibres. This extraordinary internal confinement has not yet been seen with other fibres. The SIFCON made by the new 3-dimensional fibre gives a well-defined skeleton of fibres.

7 Concluding remarks

A new reinforcing element in the form of a 3-dimensional steel fibre has been developed. It is produced from a single wire through successive bending operations, ultimately forming four closed loops connected at a common centre. The new steel fibre can be easily mixed into concrete even up to high dosages using conventional mixing equipment. Preliminary studies with the new fibre indicate considerable improvements in both technological performance and structural behaviour, such as:

(1) No balling, no preferential orientation of fibres, and no boundary effects,
(2) Homogeneous distribution of fibres
(3) Isotropic behaviour of the material
(4) Complete anchorage of every fibre loops with special transfer mechanism. No pull-out of fibres
(5) Extraordinary internal confinement in compression by the complex system of fibres,

The first four criteria provide a unique basis for material behaviour.

Test results are presented on flexural behaviour demonstrated by testing a 2 m long beam (in Section 5); on SIFCON indicating very high longitudinal as well as transverse deformations without failure owing to the extraordinary internal confinement provided by the new fibre (in Section 7); and a surprising result on "*welding of concrete"* (Section 8),

The exceptional 3-dimensional characteristics of the fibre offer a wide range of potential applications as fibre reinforced concrete as well as potentially substitute for reinforced concrete in a wide range demonstrated in Figure 1,

New solutions based on the new fibre may support sustainability,

Further research is needed to verify its mechanical performance under various conditions, including creep, shrinkage, modulus of elasticity, local concentrated loads, fatigue, blast, impact and long term behaviour, etc.

8 Acknowledgements

The Author acknowledges the support by the inventor Csongor Czintos (patent Perfycomp Co., P1600552) supporting the experiments discussed in this paper.

9 References

Balázs, L.G. (2006), 'Increase of shear and flexural capacities in steel fibre reinforced concrete', Proceedings of 2nd Int. Conf. of Asian Concrete Federation, 20-21 Nov. 2006, Bali, Indonesia, 104-112.

Balázs, L.G, Nehme, S.G., Sólyom, S. Stocker, G. (2019), 'Beam tests by Starex steel fibres, Technical report on tests with 2 m and 0,6 m long beams by Starex steel fibres', BME Report 47787-573/2018, Budapest, 10. Jan. 2019

De Montaignac, R., Massicotte, B., Charron, J. P., & Nour, A. (2012), 'Design of SFRC structural elements: post-cracking tensile strength measurement', *Materials and structures*, *45*(4), 609-622.

Di Prisco, M., Plizzari, G., & Vandewalle, L. (2009), 'Fibre reinforced concrete: new design perspectives'. *Materials and structures*, *42*(9), 1261-1281.

Kovács, I., Balázs, G. L. (2003), 'Structural behaviour of steel fibre reinforced concrete', *J. Structural Concrete*, 57-63.

fib (2013), 'Model Code 2010 for Concrete Structures', Wiley, Fèdération Internationale du Béton, Lausanne

fib (2014), 'Fibre-reinforced concrete: From design to structural applications', ACI-*fib* Workshop Proceedings (Eds. Massicotte, B., Charon, J.Ph., Plizzari, G., Mobasher, B., Joint publication by *fib* Bull 79 and ACI SP-310, *fib* Lausanne, DDC Print

fib (2023) Model Code 2020, Fèdération Internationale du Béton, Lausanne

Mechtcherine, V., Slowik, V., Kabele, P. (Eds.) (2018), 'Strain-Hardening Cement-Based Composites – SCH4', RILEM Bookseries Vol 15, Springer

Meda, A., Minelli, F., & Plizzari, G. A. (2012), 'Flexural behaviour of RC beams in fibre reinforced concrete', *Composites Part B: Engineering*, *43*(8), 2930-2937.Müller, S.H., Haist, M., (2029), 'Chapter 3.1 Concrete', *fib* Textbook on behaviour, design and performance, *fib* Bull 51, *fib* Lausanne DDC Print, 35-149.

Mobasher, B., Peled, A., & Pahilajani, J. (2006), 'Distributed cracking and stiffness degradation in fabric-cement composites'. *Materials and structures*, *39*(3), 317-331.

Niyogi, S. K. and Dwarakanathan, G. I. (1995), 'Fiber reinforcement beams under moment and shear', ASCE Journal of Structural Engineering, 1995, 111, No. 3, 516–527.

Reggia, A., Morbi, A., Plizzari, G.A. (2020), 'Experimental study of a reinforced concrete bridge pier strengthened with HPFRC jacketin', Engineering StructuresVolume 210, 1 May 2020, Article number 110355

Reinhardt, H. W. and Naaman, A. E. (1999), 'High performance fiber reinforced cement composites'. Proceedings of the 3rd International RILEM/ACI Workshop, Mainz, Germany, 17–19 May 1999.

Romualdi, J. P. and Mandel, J. (1964), 'Tensile strength of concrete affected by uniformly distributed and closely spaced short lengths of wire reinforcement', *ACI Journal*, 1964, 61, No. 6, 657–671.

Serna, P., Llano-Torre, A. and Carvalho, S.H.P. (Eds.) (2017), 'Creep Behaviour in Cracked Sections of Fibre Reinforced Concrete', Proceedings of the Int. RILEM Workshop FRC-CREEP 2016, RILEM Bookseries, Springer

Tiberti, G., Germano, F., Mudadu, A., & Plizzari, G. A. (2018), 'An overview of the flexural post-cracking behavior of steel fiber reinforced concrete', *Structural Concrete*, *19*(3), 695-718.

Tiberti, G., Trabucchi, I., Al Hamaydeh, M., Minelli, F., Plizzari, G.A. (2019), 'Crack development in steel-fibre-reinforced concrete members with conventional rebars', Magazine of Concrete ResearchVolume 71, Issue 11, 1 June 2019, Pages 599-610Balaguru, P. N. and Shah, S. P. (1992), 'Fiber-Reinforced Cement Composites', McGraw-Hill, New York

Toutlemonde, F, Resplendino, J. (Eds.) (2013), 'UHPFRC 2013, Design and Building with UHPFRC: from innovation to large-scale realizations', RILEM-fib-AFGC Int. Symp. on Ultra-High Performance Fibre-Reinforced Concrete, 1-3 October 2013 Marseille, France, RILEM Proceedings PRO 87, RILEM Publications S.A.R.L.

Valdez Aguilar, J.; Juárez-Alvarado, C.A.; Mendoza-Rangel, J.M.; Terán Torres, B.T. Effect of the Notch-to-Depth Ratio on the Post-Cracking Behavior of Steel-Fiber-Reinforced Concrete. Materials **2021**,14, 445. https://doi.org/10.3390/ma14020445, pp. 3-17.

Vandewalle, L. (2000), "Cracking behaviour of concrete beams reinforced with a combination of ordinary reinforcement and steel fibres", *Materials and Structures*, 33, pp164-170. doi: 10.1007/BF02479410

Additively manufactured carbon short-fiber reinforced concrete – non-destructive testing to investigate deteriorations under fatigue

Christian U. Grosse[1], Oliver Fischer[2], Malte A. Peter[3], Dirk Volkmer[4]

[1]: Chair of Non-Destructive Testing, Technical University of Munich, Lichtenbergstr. 2, D-85748 Garching near Muenchen, Germany,

[2]: Chair of Concrete and Masonry Structures, Technical University of Munich, Theresienstr. 90, D-80333 Muenchen, Germany

[3]: Research Unit Applied Analysis, University of Augsburg, Universitätsstr. 12, D-86159 Augsburg, Germany

[4]: Chair of Solid State Chemistry, University of Augsburg, Universitätsstr. 1, D-86159 Augsburg, Germany

Abstract

In a project within the DFG priority program SPP2020 "Cyclic damage processes in high-performance concretes in the Experimental-Virtual-Lab", the damage progression in additively manufactured carbon short-fiber-reinforced high-performance concrete under highly cyclic tensile and flexural loading was investigated. For multi-scale investigations, various Non-Destructive Testing (NDT) techniques were deployed to localize and identify fracture processes, as well as to document damage evolution as a function of variations in material and manufacturing parameters. This led to an improved understanding of the properties and provides the basis for optimizing this innovative hybrid construction material.
In addition to acoustic emission analysis, ultrasonic technology, coda wave interferometry, digital image correlation, and X-ray computed tomography were used as NDT techniques. These experimental investigations were supplemented by cross-scale material modeling of damage development and wave propagation. The project, funded by the German Research Foundation (DFG), was carried out in close cooperation between the Chairs of Concrete and Masonry Structures and Non-Destructive Testing at the Technical University of Munich, as well as the Chair of Solid State Chemistry and the Research Unit Applied Analysis at the University of Augsburg. The focus of the presentation is on non-destructive testing techniques.

Keywords

Virtual lab, carbon short-fiber-reinforced concrete, X-ray, acoustic emission techniques, ultrasound,

1 Introduction and Experimental Program

Carbon short-fiber reinforced high-performance concrete (CSFRC) represents a new class of cementitious composites designed to overcome the inherent brittleness and limited fatigue resistance of conventional concrete (Hambach et al. 2016; Hambach & Volkmer 2017). By incorporating short, high-strength carbon fibers into the cement matrix and aligning them preferentially along the principal tensile stress directions, the material exhibits a unique combination of high tensile strength, pronounced strain-hardening behavior, and enhanced damage tolerance.

A key characteristic of CSFRC is the controlled fiber orientation achieved through extrusion-based and additive manufacturing processes. This anisotropic microstructure allows the fibers to be activated effectively at relatively low strain levels, resulting in multiple cracking with narrow crack spacing instead of early crack localization. From a structural engineering perspective, this behavior is highly advantageous, as it increases energy dissipation capacity, reduces crack widths, and improves durability under service and fatigue loading.

The investigated specimens covered a wide range of length scales, from micro-scale samples suitable for high-resolution imaging and in-situ analyses to macro-scale specimens representative of structural elements (Fig. 1). This multiscale testing concept provided an ideal framework for systematically applying and evaluating non-destructive testing techniques, enabling consistent study of damage phenomena across scales. While the material-related concepts and findings were addressed in numerous papers (Engelhardt et al. 2022; Lauff et al. 2019; Lauff et al. 2021; Rutzen et al. 2019; Rutzen et al. 2021), a summary of this project, as well as of SPP2020, will be published in a book (Oneschkow & Lohaus 2026).

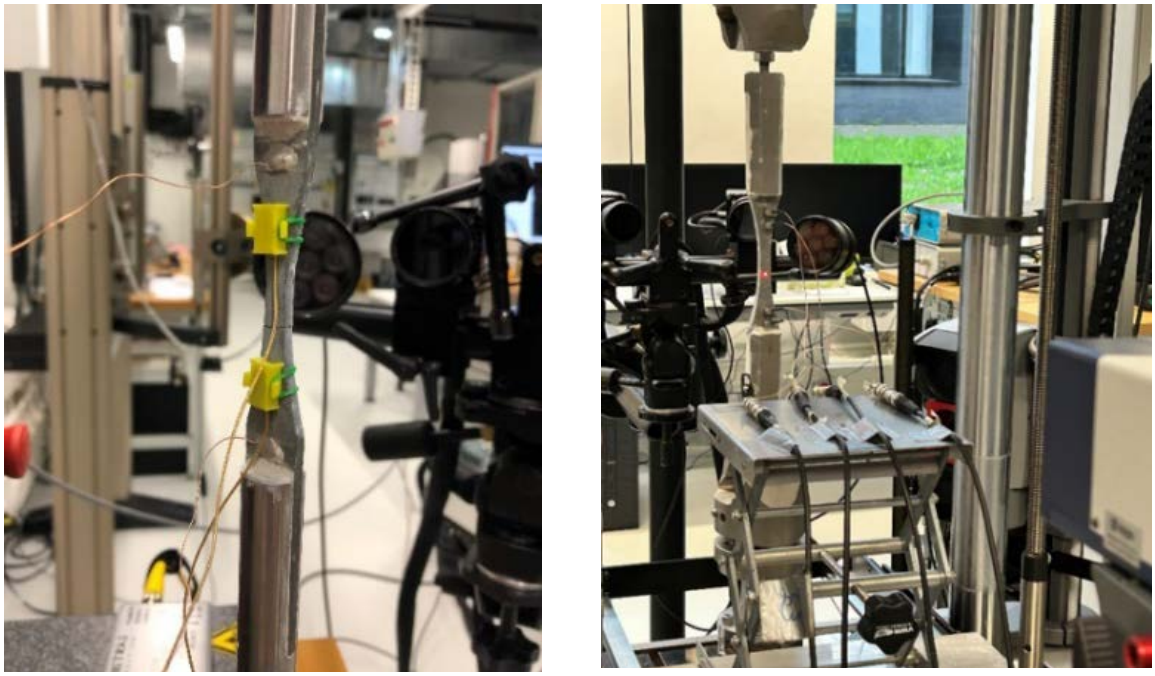


***Figure 1**: Static tensile test setups for microscopic, mesoscopic, and macroscopic scale CSFRC specimens, illustrating the multiscale experimental concept and the integration of non-destructive measurement techniques such as strain gauges, acoustic emission sensors, and laser vibrometry (Oneschkow & Lohaus 2026).*

A typical stress–strain behavior of CSFRC is characterized by a transition from linear-elastic response to strain-hardening with multiple cracking before final localization. This behavior is exemplarily shown for micro-scale specimens in Figure 2 (Rutzen et al. 2021).

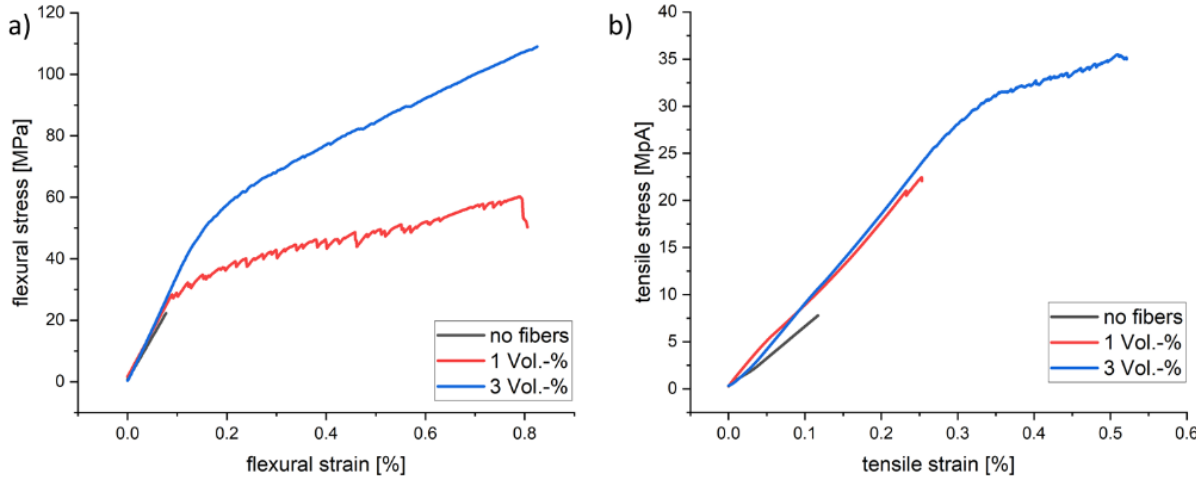


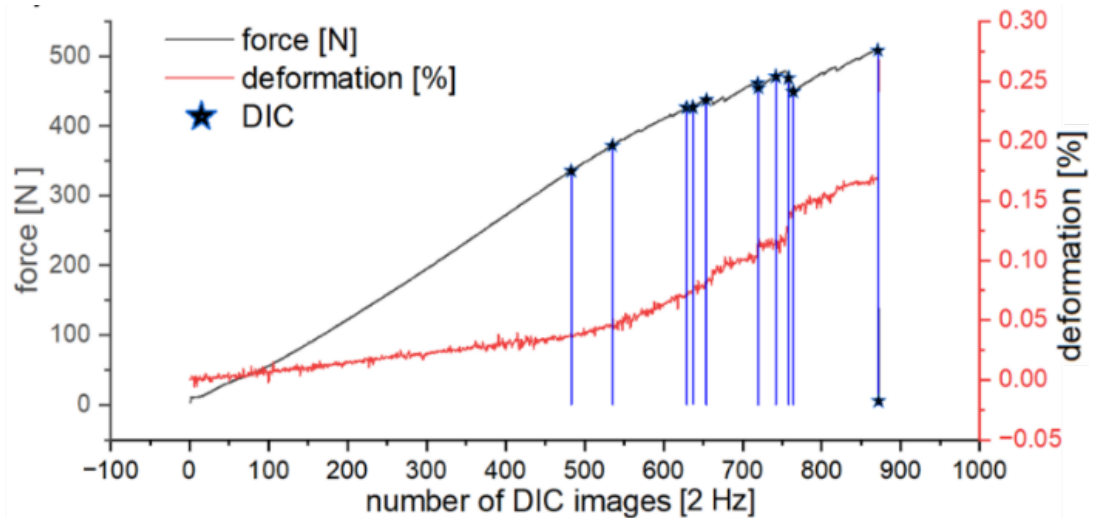
***Figure 2**: Exemplary stress–strain behavior of micro-scale CSFRC specimens under static loading, demonstrating strain-hardening and multiple cracking enabled by carbon short-fiber reinforcement (Oneschkow & Lohaus 2026).*

2 Implementation of Non-Destructive Testing Techniques

2.1 Digital Image Correlation

Digital Image Correlation (DIC) was employed as a surface-based, full-field optical measurement technique to capture strain localization, crack initiation, and crack propagation in CSFRC specimens. For micro-scale tensile tests, DIC enables detailed analysis of the transition from linear-elastic deformation to multiple microcracking and final crack localization, as shown in Figure 3.

a)



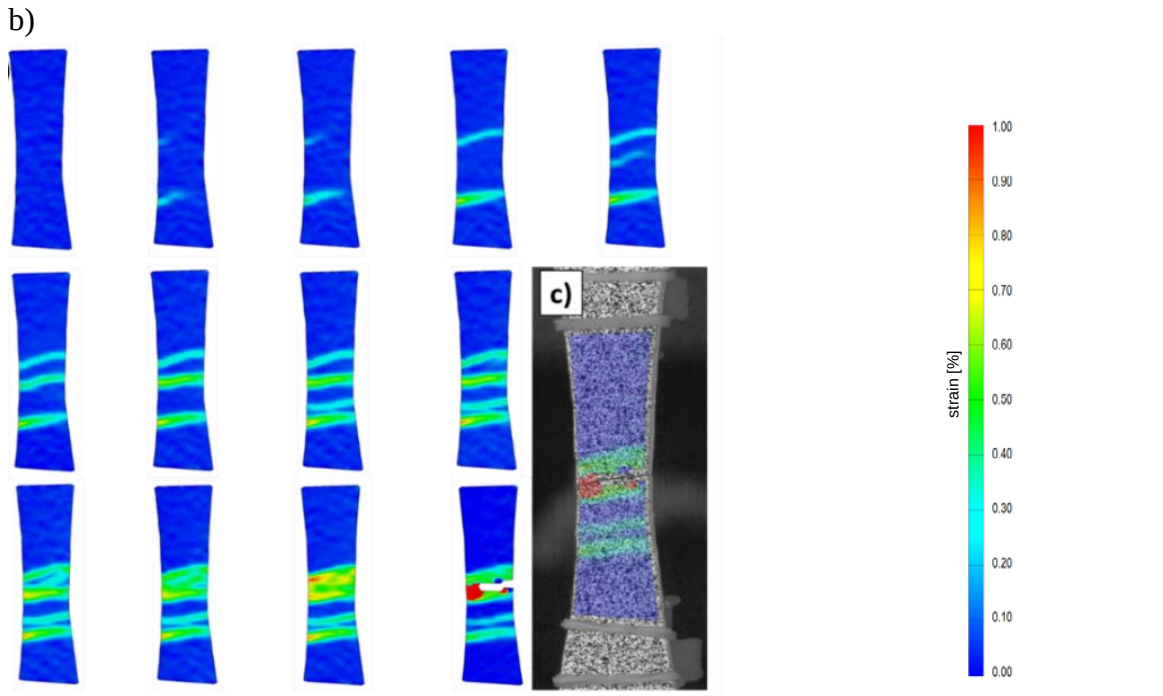


Figure 3: *DIC results for a micro tensile CSFRC specimen, showing the evolution from linear elastic deformation to distributed microcracking and final localization (Oneschkow & Lohaus 2026).*

For macro-scale specimens subjected to variable-amplitude fatigue loading, DIC reveals pronounced crack opening, partial crack closure, and redistribution of the strain field depending on the applied loading sequence. These effects, illustrated in Figure 4, highlight the influence of load history on damage evolution and crack activity in CSFRC, showing crack opening, partial crack closure, and damage redistribution.

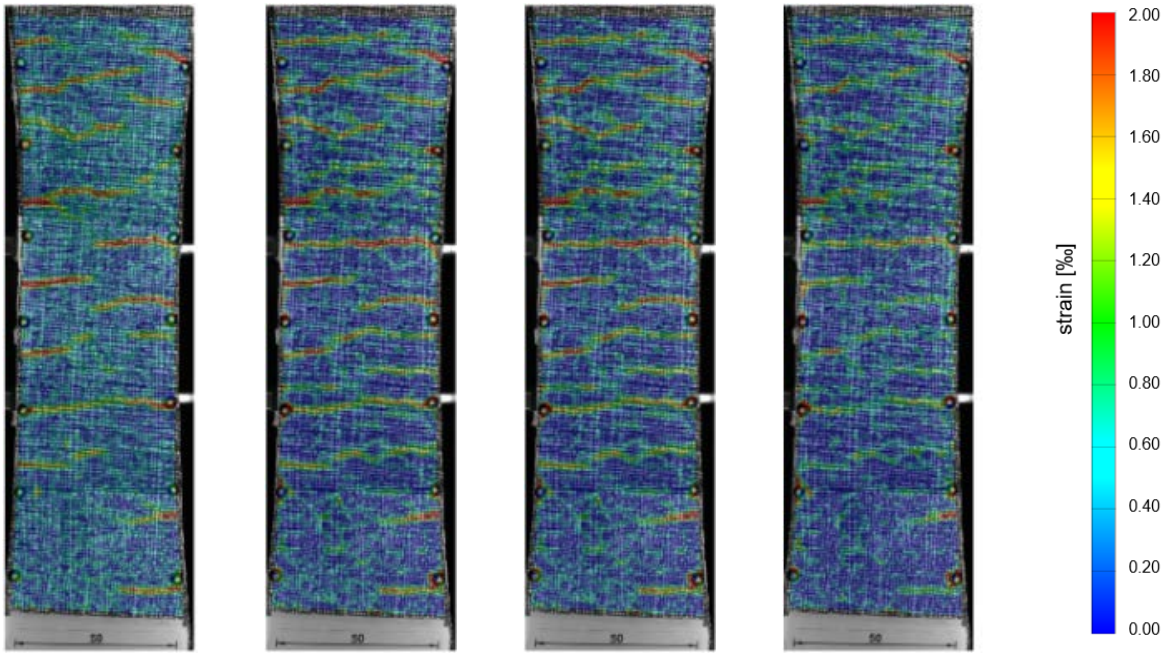


Figure 4: *DIC-based strain fields of a macro-scale dog-bone-shaped CSFRC specimen subjected to variable cyclic tensile loading immediately before the start of the harmonic load, after 3 million cycles, after 5 million cycles, and after 6 million cycles (i.e., immediately before failure) from left to right.*

2.2 Cyclic Loading and Acoustic Emission

To investigate sequence effects on fatigue damage, four different cyclic loading schemes (increasing/decreasing upper load as well as increasing/decreasing load amplitude with constant medium load) were applied in tensile and flexural fatigue tests. A schematic overview of the applied load histories is provided in Figure 5.

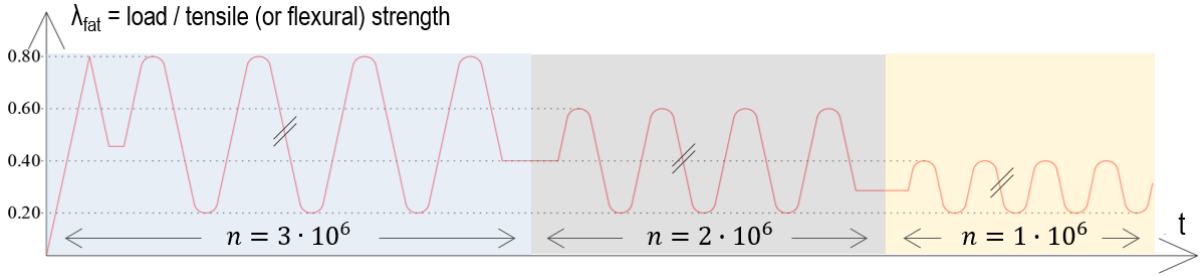


Figure 5: *Schematic overview of harmonic cyclic loading schemes applied in tensile and flexural fatigue tests, exemplarily shown for load type 1 (decreasing upper load).*

Acoustic Emission (AE) monitoring (Grosse et al. 2021) was used to detect internal damage mechanisms such as matrix microcracking and fiber-related fracture processes (Aggelis et al. 2013). The temporal evolution of AE activity correlates strongly with the mechanical response during fatigue loading, as illustrated in Figure 6. Low-energy AE signals are associated with matrix cracking, while high-energy events occur shortly before final failure.

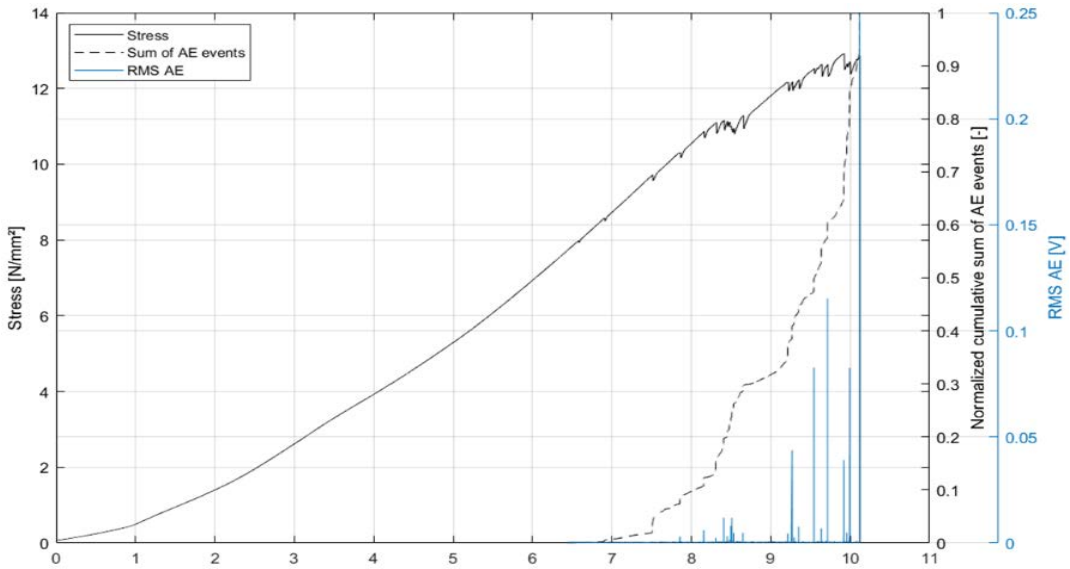


Figure 6: *AE response during a tensile fatigue test on a meso-scale CSFRC specimen, showing cumulative AE events, RMS AE signal, and applied stress (Oneschkow & Lohaus 2026).*

Spatial localization of AE events demonstrates that damage remains distributed over large specimen regions for most of the fatigue life and localizes only shortly before failure. The correlation between AE event localization and surface crack patterns obtained from DIC is shown in Figure 7.

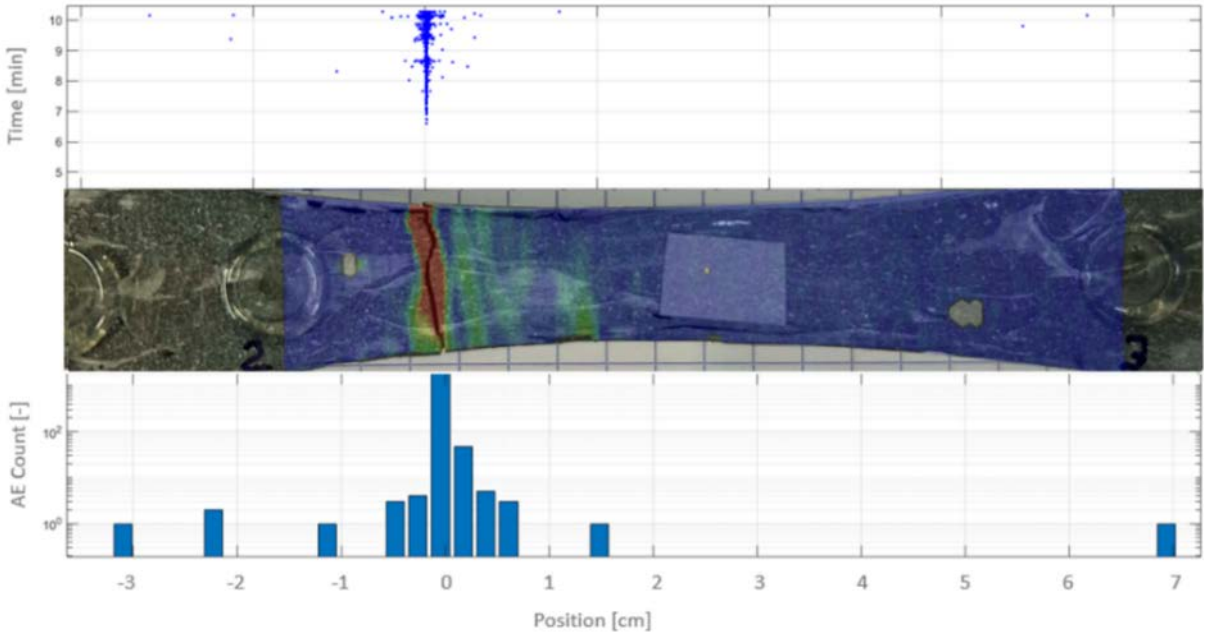


Figure 7: *Temporal and spatial distribution of localized AE events in a CSFRC specimen, correlated with crack patterns obtained from DIC (Oneschkow & Lohaus 2026).*

2.3 X-ray Computed Tomography

X-ray computed tomography (CT) was employed to obtain three-dimensional insight into the internal microstructure of CSFRC specimens. CT analysis reveals the degree of fiber alignment achieved through extrusion-based processing, which is a key factor governing the mechanical performance of CSFRC. An example of the in-plane fiber orientation distribution is shown in Figure 8.

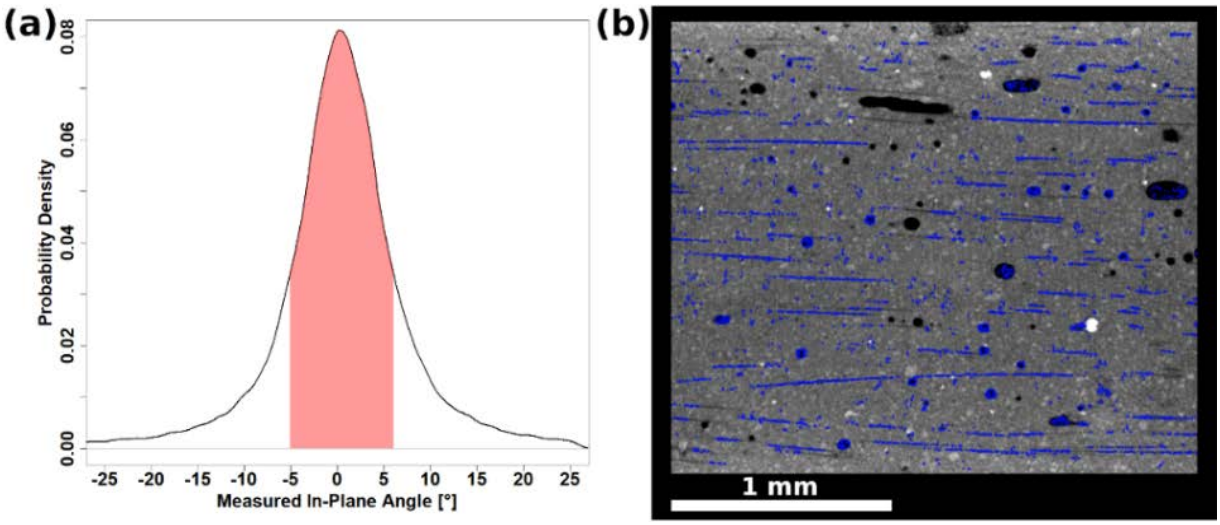


Figure 8: *Fiber alignment in extruded CSFRC specimens obtained from X-ray computed tomography (b), showing the distribution of in-plane fiber orientation angles (a) (Oneschkow & Lohaus 2026).*

Segmented CT data further reveal the development of crack patterns during fatigue loading. With increasing fatigue damage, crack density increases while crack spacing decreases, confirming the effectiveness of fiber bridging mechanisms in controlling crack growth. Representative segmented crack patterns are shown in Figure 9.

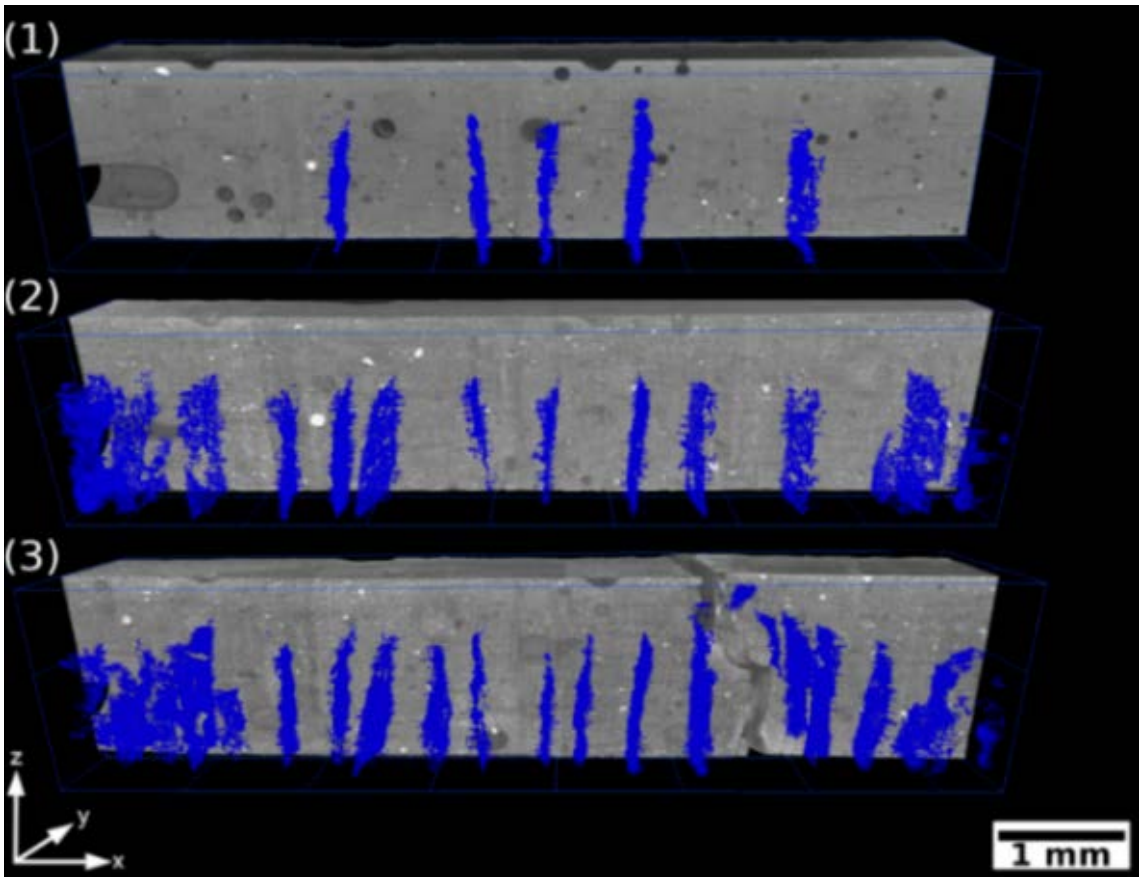


Figure 9: *Segmented crack patterns of a micro-scale CSFRC beam specimen loaded under bending at different stages of fatigue loading, derived from X-ray tomography (Oneschkow & Lohaus 2026).*

3 Conclusions

The combined application of Digital Image Correlation, Acoustic Emission monitoring, and X-ray computed tomography enables a comprehensive multiscale characterization of damage and fatigue mechanisms in carbon short-fiber reinforced concrete. Other NDT techniques (e.g., coda wave interferometry) have been applied, but data are not reported here. The results demonstrate that CSFRC exhibits pronounced strain-hardening behavior and delayed crack localization due to effective fiber bridging. A comprehensive report about all findings is compiled to be published as part of a book (Oneschkow & Lohaus 2026).

The integration of complementary non-destructive testing techniques is essential for understanding distributed cracking, damage accumulation, and localization under cyclic loading. The presented approach provides a sound experimental basis for future fatigue

modeling and supports the development of structural health monitoring concepts for advanced fiber-reinforced concrete structures.

4 Acknowledgements

This research was funded by the German Research Foundation (DFG) as part of the Priority Program SPP2020: 'Cyclic deterioration of High-Performance Concrete in an experimental-virtual lab' (Project Number 354003768, Grant Numbers FI1720/7-1, GR1664/13-1, PE1464/6-1, VO829/13-1). The Authors are grateful to everyone involved in the priority program SPP 2020, as the working atmosphere among the groups was characterized by fruitful collaboration. Special appreciation goes to Michael Engelhardt, Philipp Lauff, Tanja Lochner, Polina Pugacheva, Manuel Raith, Lisa Reischmann, Matthias Rutzen, and Ursula Weiß.

5 References

Aggelis, D.G., Dassios, K.G., Kordatos, E.Z., Matikas, T.E.: Damage accumulation in cyclically-loaded glass-ceramic matrix composites monitored by acoustic emission. The Scientific World Journal, 2013(12):869467, https://doi.org/10.1155/2013/869467

Engelhard, M., Kalytta-Mewes, A., Volkmer, D.: Testing methods for deformation characterization on 3D printed carbon fiber reinforced cementitious composites (2022). Proc. 14th fib PhD Symposium, Rome/Italy (2022)

Grosse, C.U., Ohtsu, M., Aggelis, D.G., Shiotani, T. (eds): Acoustic Emission Testing: Basics for Research – Appl. in Eng., Springer Publ. (2021), https://doi.org/10.1007/978-3-030-67936-1

Hambach, M., Möller, H., Neumann, T., Volkmer, D.: Portland cement paste with aligned carbon fibers exhibiting exceptionally high flexural strength (> 100 MPa). Cement and Concrete Research (2016). https://doi.org/10.1016/j.cemconres.2016.08.011

Hambach, M., Volkmer, D.: Properties of 3D-printed fiber-reinforced Portland cement paste. Cement & Conc. Composites (2017). https://doi.org/10.1016/j.cemconcomp.2017.02.001

Lauff, P., Pugacheva, P., Rutzen, M., Weiß, U., Fischer, O., Volkmer, D., Peter, M.A., Grosse, C.U.: Evaluation of the behavior of Carbon Short Fiber Reinforced Concrete (CSFRC) based on a multi-sensory experimental investigation and a numerical multiscale approach. Materials 2021, 14(22), 7005, https://doi.org/10.3390/ma14227005

Lauff, P., Raith, M., Große, C., Rutzen, M., Volkmer, D., Reischmann, L., Weiß, U., Peter, M., Fischer, O.: Investigation of localised damage indicators of a carbon short-fibre reinforced high performance concrete under dynamic and flexural load. Proc. fib Symposium Krakow/Poland, 1952-1959 (2019)

Oneschkow N., Lohaus, L. (Eds.). Cyclic Deterioration of High-Performance Concrete – Reports of the SPP 2020 Experimental-Virtual-Lab. Springer Nature, (2026), 397 p, doi.org/10.1007/978-3-032-19394-0

Rutzen, M., Lauff, P., Niedermeier, R., Fischer, O., Raith, M., Grosse, C.U., Weiss, U., Peter, M.A., Volkmer, D.: Influence of fiber alignment on pseudoductility and microcracking in a cementitious carbon fiber composite material. Materials and Structures (2021) 54:58. https://doi.org/10.1617/s11527-021-01649-2

Rutzen, M., Volkmer, D., Weiß, U., Reischmann, L., Peter, M.A., Lauff, P., Fischer, O., Raith, M. and Grosse, C.U.: Microstructural analysis of crack growth caused by static and dynamic loads in a carbon fiber reinforced cement paste. Proc. Adv. in Eng. Mat., Structures and Systems: Innovations, Mechanics and Applications. Zingoni, A. (ed.), CRC Press (2019)

Design framework for alkali-activated slag-based concrete incorporating single (3D) and multiple (4D, 5D) hooked-end steel fibres

Laura Rossi[1], Maria Paula Zappitelli[2], Ravi A. Patel[1], Frank Dehn[1]

[1] : Institute of Building Materials and Concrete Structures (IMB) & Materials Testing and Research Institute (MPA), Karlsruhe Institute of Technology (KIT), Karlsruhe, Germany

[2] : Department of Civil Engineering, Engineering College, National University of La Plata (UNLP), La Plata, Argentina

Abstract

Recent advancements in steel fiber technology and the development of alkali-activated slag-based concrete (AASC) have opened new opportunities for producing sustainable, high-performance fiber-reinforced composites. Steel fiber-reinforced AASC (SFRAASC) can combine the enhanced mechanical anchorage provided by the additional bends of double (4D) and triple (5D) hooked-end steel fibers with the superior tensile strength and fiber-matrix bond strength of the AASC matrix. However, the lack of design standards accounting for the distinctive mechanical behavior of AASC limits the use of SFRAASC in structural applications. This study presents an integrated experimental, analytical, and numerical study aimed at establishing a predictive design framework for estimating the compressive and tensile behavior of SFRAASC. The proposed framework requires only a limited set of input parameters: the compressive response of the unreinforced matrix (cubic and cylindrical compressive strength and stress-strain behavior under uniaxial compression) and the fiber characteristics (geometry, volume fraction and reinforcing index). By minimizing experimental investigations and enabling numerical implementation, the framework provides a practical and efficient tool to support the broader structural application of SFRAASC as a sustainable alternative to conventional steel fiber-reinforced Portland-cement based concrete (SFRPCC).

Keywords

Alkali-activated slag-based concrete, fiber-reinforced concrete, mechanical properties, empirical models, finite element modelling, design framework

1 Introduction

Steel fiber-reinforced alkali-activated slag-based concrete (SFRAASC) has attracted increasing interest as a sustainable and high-performance alternative to conventional steel fiber-reinforced Portland cement-based concrete (SFRPCC). Recent studies (Adesina, 2020; Rossi et al., 2023; Rossi et al., 2024a) have demonstrated that SFRAASC can outperform SFRPCC of comparable strength grade, incorporating the same fiber type and dosage, under both compressive and tensile loading conditions. Although alkali-activated slag-based concrete exhibits an inherently brittle tensile behavior (Adesina, 2020, Lim et al., 2022), its microstructural characteristics, including the nature of its reaction products, pore structure, and micro-cracking induced by drying shrinkage (Beglarigale et al., 2016), promote enhanced bond strength at the fiber-matrix interface. This improved interfacial behavior results in greater resistance to fiber pullout and, consequently, superior tensile performance compared with traditional SFRPCC.

Despite its promising mechanical performance, the use of SFRAASC in structural applications remains limited, primarily due to the lack of dedicated design standards and constitutive models (Ye and Dehn, 2026). Currently available design codes developed for traditional SFRPCC, such as Eurocode 2 and the *fib* Model Code 2020, cannot be directly applied to cement-free composites, as they do not account for fundamental differences in mechanical behavior. While the experimental data in Fig. 1 exhibit considerable scatter, the comparison with the *fib* Model Code 2020 correlations for PCC (dashed lines) indicates systematic deviations, namely a lower modulus of elasticity and a higher tensile strength for SFRAASC at comparable compressive strength levels. These deviations, evident in the overall trends rather than individual data points, support the assertion of distinct mechanical behavior. Therefore, a combined experimental and analytical approach is required to adapt existing provisions and develop new design frameworks capable of reliably predicting the mechanical performance of SFRAASC.

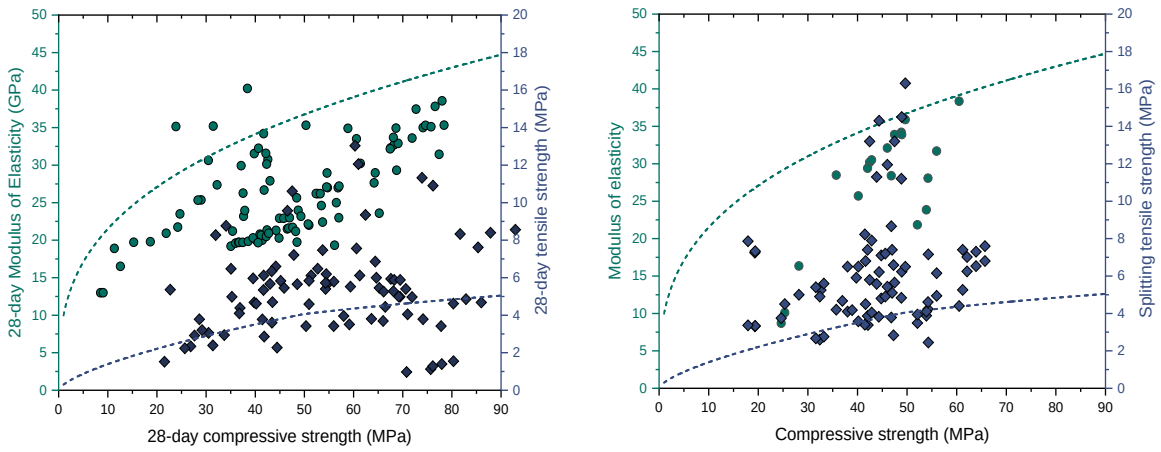


Figure 1: Correlation between compressive strength and modulus of elasticity (green points) and indirect tensile strength (blue points) for (a) AASC and (b) SFRAASC. Dashed lines indicate correlations prescribed by the fib Model Code 2020 for PCC.

As part of the DuRSAAM project, an extensive experimental campaign was conducted at the KIT IMB/MPA/CMM laboratories to fully characterize the mechanical performance of

alkali-activated slag-based concrete (AASC) incorporating single (3D) and multiple (4D, 5D) hooked-end steel fibers under both compressive and tensile loading. The campaign evaluated the compressive response, flexural behavior under three-point bending, and the fiber-matrix interaction, with results reported in previous publications (Rossi et al. 2023; Rossi et al., 2024a; Rossi et al., 2024b; Rossi, 2025).

These experimental data, together with literature data, were used as input parameters for analytical modelling to develop a predictive design framework for SFRAASC. This framework enables prediction of the mechanical behavior of SFRAASC based on a limited set of input parameters: the compressive behavior of the unreinforced concrete matrix and the fiber characteristics (geometry, volume fraction, and reinforcing index). By relying on minimal experimental input, the framework provides an efficient and reliable tool for estimating SFRAASC performance, thereby supporting its broader adoption as a sustainable alternative to conventional SFRPCC in structural applications.

Section 2 of this paper summarizes the key analytical relationships derived for alkali-activated slag-based concrete incorporating hooked-end steel fibres, based on both experimental data and results reported in the literature (Rossi et al. 2023; Rossi et al., 2024a; Rossi et al., 2024b; Rossi, 2025). Section 3 presents a practical use case of the framework, while Section 4 illustrates an alternative finite element modelling (FEM) approach for SFRAASC mix design.

2 Design framework

Based on the authors 'experimental results and literature data on alkali-activated slag-based concrete incorporating various hooked-end steel fibers at different volume fractions, existing empirical models originally developed for traditional cement-based composites were critically assessed, adapted, and recalibrated for application to SFRAASC.

2.1 Uniaxial compressive stress-strain behavior

As published by Rossi et al. (Rossi et al., 2023), existing empirical models developed to predict the stress-strain response of SFRPCC under uniaxial compression are material-specific and cannot be reliably applied to SFRAASC. To address this limitation, a new analytical model was proposed for SFRAASC (Rossi et al., 2023), which expresses the normalized compressive stress ($\sigma_c/\sigma_{c,max(FRC)}$) as a function of the normalized strain ($\varepsilon_c/\varepsilon_{c,max(FRC)}$), and two material parameters, β and γ, governing the pre-peak and post-peak response, respectively:

$$\frac{\sigma_c}{\sigma_{c,max(FRC)}} = \begin{cases} \frac{\beta(\varepsilon_c/\varepsilon_{c,max(FRC)})}{\beta-1+(\varepsilon_c/\varepsilon_{c,max(FRC)})^{\beta}}, & \varepsilon_c/\varepsilon_{c,max(FRC)} \leq 1 \\ e^{\gamma(1-\varepsilon_c/\varepsilon_{c,max(FRC)})}, & \varepsilon_c/\varepsilon_{c,max(FRC)} > 1 \end{cases} \quad (1)$$

The parameters β and γ depend on the elastic moduli of the composite, i.e. secant ($E_{sec(FRC)}$) and initial secant ($E_{it(FRC)}$), the fiber reinforcing index RI_v ($RI_v = (l_f/d_f) \cdot v_f$), the peak compressive stress ($\sigma_{c,max(FRC)}$), and the stress corresponding to an ultimate strain of 0.0035. These parameters are defined as follows:

$$\beta = 0.457 \cdot e^{2.874 \cdot (E_{sec(FRC)}/E_{it(FRC)})} \quad (2)$$

$$\gamma = 0.697 \cdot e^{-1.432 \cdot (RI_v \cdot \sigma_{c,u(FRC)}/\sigma_{c,max(FRC)})} \quad (3)$$

2.2 Correlation between mechanical performance

As reported by Rossi et al. (Rossi et al., 2024b), existing analytical models for SFRPCC correlate its main compressive and tensile mechanical performance with the compressive strength of the plain concrete matrix and the fiber reinforcing index (RI_v). However, these models require further calibration to accurately predict the performance of SFRAASC, reflecting its lower modulus of elasticity and a higher tensile strength compared with traditional cement-based concrete of the same strength grade. Full details are reported in Rossi et al. (Rossi et al., 2024b), while the resulting newly calibrated correlations are summarized in Table 1.

Table 1: Empirical correlations to predict the performance of SFRAASC

Mechanical properties	**Empirical model for SFRAASC**
Compressive strength	$f'_{cuf} = 1.04f'_{cu} + 2.12RI_v$
Modulus of elasticity	$E_{cyf} = 3.68(f'_{cu})^{0.5} + 9.07RI_v$
Splitting tensile strength	$f'_{sptf} = 0.07f'_{cu} + 1.85RI_v$
Flexural tensile strength	$f'_{flf} = 0.10f'_{cu} + 4.17v_f$

f'_{cuf} and f'_{cu} denote the cube compressive strength of the concrete with and without fibres, respectively. E_{cyf}, f'_{sptf}, and f'_{flf} represent the modulus of elasticity, splitting tensile strength, and flexural tensile strength of the fiber-reinforced concrete, while RI_v and v_f denote the fibre reinforcing index and fibre volume fraction, respectively.

2.3 Residual tensile flexural strengths f_{R1} and f_{R3}

The *fib* Model Code 2020 provides a bilinear post-cracking tensile constitutive model for SFRPCC (Fig. 2), defined based on the characteristic residual flexural strengths f_{R1k} and f_{R3k}. These values can be calculated from experimental residual flexural strengths f_{R1} and f_{R3}, obtained from load-CMOD curves measured in three-point bending tests on notched beams.

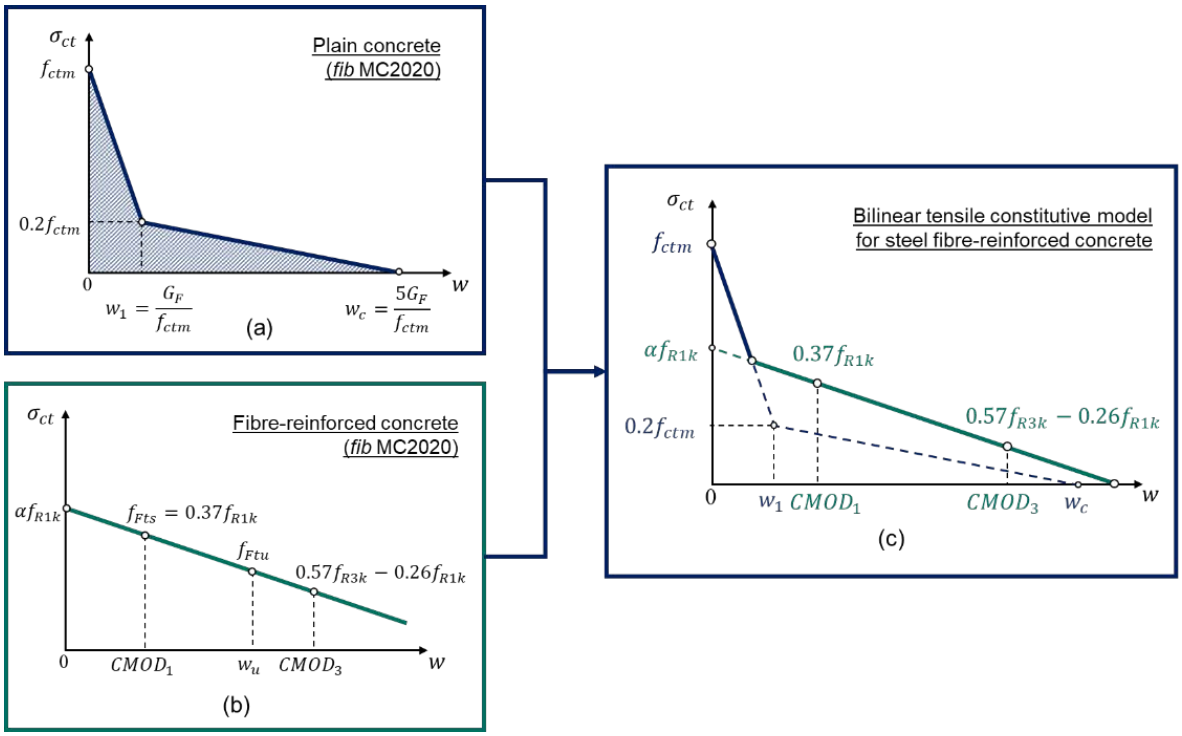


Figure 2: Tensile constitutive model for (a) PCC and (b) SFRPCC according to the fib Model Code 2020. The post-cracking tensile stress-crack opening for SFRPCC is described by (c)

As demonstrated by Rossi et al. (Rossi et al., 2024a), among the currently available empirical equations to predict the residual flexural strengths of SFRPCC, the correlations proposed by Venkateshwaran et al. (Venkateshwaran et al., 2018) provide the highest prediction accuracy when applied to SFRAASC to derive the residual flexural strengths f_{R1} and f_{R3} and their characteristic values f_{R1k} and f_{R3k}. Therefore, the coefficients of these empirical models were recalibrated for SFRAASC (Rossi et al., 2024a). The newly proposed equations are summarized in Table 2.

Table 2: Empirical correlations to predict f_{R1} and f_{R3} and f_{R1k} and f_{R3k} of SFRAASC

SFRAASC	
$f_{R1} = \Psi\left(0.063(f_{cm})^{\frac{1}{2}} + 10.991RI_v + 0.064N^2\right)$	$f_{R1k} = \Psi\left(-0.103(f_{cm})^{\frac{1}{2}} + 10.466RI_v + 0.053N^2\right)$
$f_{R3} = \Psi\left(0.169(f_{cm})^{\frac{1}{2}} + 11.037RI_v + 0.059N^2\right)$	$f_{R3k} = \Psi\left(-0.029 \cdot (f_{cm})^{\frac{1}{2}} + 11.115RI_v + 0.069N^2\right)$

$\Psi = \left(1 + l_f/100\right)^{1/2}$ = factor accounting for the fibre geometry (l_f = fibre length), f_{cm} = cylindrical compressive strength of the composite, RI_v = fibre reinforcing index, and N = number of bends at the fibre ends (N = 1 for 3D fibres, N = 1.5 for 4D fibres, N = 2 for 5D fibres)

From the values of f_{R1k} and f_{R3k}, the residual flexural strengths f_{Fts} and f_{Ftu}, corresponding to the serviceability limit state (SLS) and ultimate limit state (ULS), respectively, can be calculated according to the *fib* Model Code 2020 as follows:

$$f_{Fts} = 0.37 \cdot f_{R1k} \tag{4}$$

$$f_{Ftu} = \begin{cases} f_{Fts} - \frac{w_u}{CMOD_3}(f_{Fts} - 0.57f_{R3k} + 0.26f_{R1k}), & w_u \neq 2.5\ mm \\ 0.57f_{R3k} - 0.26f_{R1k}, & w_u = 2.5\ mm \end{cases} \tag{5}$$

where w_u denotes the maximum crack opening accepted in structural design.

2.4 Single-fiber pull-out behavior

From experimental data, a correlation between the single-fiber pullout behavior and the residual flexural strengths f_{R1} and f_{R3} can also be established for SFRAASC. The residual strengths can be estimated by combining the number of fibers (N_f) at the cracked cross-section of the notched beam, determined experimentally or analytically according to Eq. (6) (Dupont and Vandewalle, 2005), with the average fiber-matrix bond strength (τ_{avg}) obtained from the pull-out load-displacement curves.

$$N_f = \frac{G \cdot \alpha}{\left(\frac{\pi}{4} d_f^2\right) \cdot \rho_s} \cdot b \cdot h_{sp} \tag{6}$$

where G is the fibre dosage [kg/m^3], α is the fibre orientation coefficient (generally assumed as α = 0.58) (Dupont and Vandewalle, 2005), b is the beam width, h_{sp} is distance between the notch tip and the top of the beam, d_f is the fibre diameter, and ρ_s is the steel fibre density. Based on the assumed linear relationship $y = A \cdot x$, where y represents the residual flexural strength and $x = \tau_{avg} \cdot N_f$, the coefficient A was calibrated using the experimental data published in Rossi (Rossi, 2025). The resulting empirical correlations are given in Table 3. Using these correlations, the average fiber-matrix bond strength (τ_{avg}) can also be calculated, as also shown in Table 3.

Table 3: Correlation between the single-fiber pullout behavior and f_{R1} and f_{R3}

	3D fibers	4D fibers	5D fibers
f_{R1}	$f_{R1} = 0.0039 \cdot \tau_{avg} \cdot N_f$	$f_{R1} = 0.0024 \cdot \tau_{avg} \cdot N_f$	$f_{R1} = 0.0022 \cdot \tau_{avg} \cdot N_f$
f_{R3}	$f_{R3} = 0.0045 \cdot \tau_{avg} \cdot N_f$	$f_{R3} = 0.0026 \cdot \tau_{avg} \cdot N_f$	$f_{R3} = 0.0025 \cdot \tau_{avg} \cdot N_f$
τ_{avg}	$\tau_{avg} = \begin{cases} f_{R1}/0.0039 \cdot N_f \\ f_{R3}/0.0045 \cdot N_f \end{cases}$	$\tau_{avg} = \begin{cases} f_{R1}/0.0024 \cdot N_f \\ f_{R3}/0.0026 \cdot N_f \end{cases}$	$\tau_{avg} = \begin{cases} f_{R1}/0.0022 \cdot N_f \\ f_{R3}/0.0025 \cdot N_f \end{cases}$

The design framework is given in Figure 3.

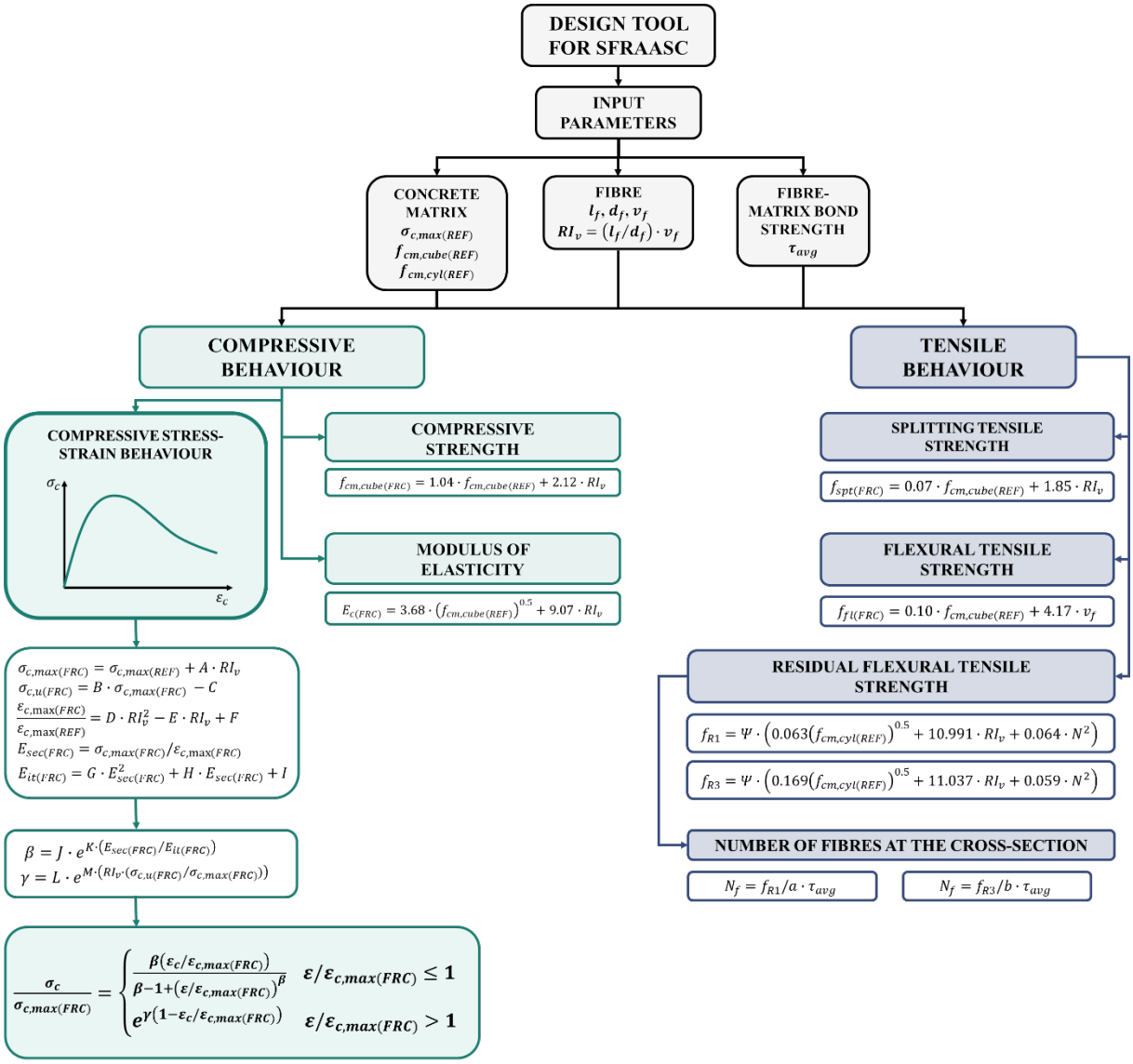


Figure 3: Design framework including the analytical correlations derived to predict the compressive and tensile behavior of SFRAASC

2.5 Practical application

The predictive empirical models summarized in the previous sections can be applied as design tools following two complementary approaches:

1. Predict the mechanical performance of SFRAASC from the properties of the plain concrete matrix and the fiber characteristics, assuming a prescribed fiber content.
2. Determine the minimum fiber dosage required to achieve a target post-cracking performance (e.g., a specific residual flexural tensile strength f_{R1}).

In this study, the second approach is adopted, and its practical use is illustrated through a simple example, summarized in Table 4 (Rossi, 2025).

The procedure follows a design-oriented sequence:

1. The cubic compressive strength of the reference concrete matrix ($f_{cm,cube(REF)}$) is evaluated experimentally.
2. The fiber properties are prescribed, as typically provided by the manufacturer, including fiber length (l_f), diameter (d_f), aspect ratio (l_f /d_f) and geometry (N, defined as the number of bends at the fiber ends).
3. The analytical equations proposed in the previous sections are used to solve for the required fiber volume fraction (v_f [vol.-%]), assuming as target value the residual flexural strength f_{R1} evaluated experimentally. The fiber volume fraction is treated as the only unknown variable.
4. The corresponding fiber dosage (m_f [kg/m^3]) is calculated.

This procedure aligns with a performance-based design approach, demonstrating how the proposed framework can be used as a practical design tool not only for post-processing experimental results.

Table 4: Prediction of the fiber minimum volume fraction to achieve the target f_{R1}

	$f_{cm,cube(REF)}$ [MPa]	l_f [mm]	l_f/d_f	N	Ψ	$f_{R1,target}$ [MPa]	$v_{f,exp}$ [MPa]	$v_{f,pred}$ [MPa]	m_f [kg/m^3]
3D	47.4	60	65	1	1.26	2.93	0.25	0.26	20
	47.4	60	65	1	1.26	5.66	0.50	0.56	44
	47.4	60	65	1	1.26	6.88	0.75	0.69	54
4D	47.4	60	65	1.5	1.26	3.15	0.25	0.27	21
	47.4	60	65	1.5	1.26	5.55	0.50	0.53	42
	47.4	60	65	1.5	1.26	7.86	0.75	0.79	62
5D	47.4	60	65	2	1.26	2.44	0.25	0.18	14
	47.4	60	65	2	1.26	6.23	0.50	0.59	47
	47.4	60	65	2	1.26	7.66	0.75	0.75	59

2.6 Numerical modelling and FEM implementation

The experimental data obtained by performing three-point bending tests on notched beams and single-fiber pullout test, or alternatively the corresponding values derived using the analytical correlations of the design framework presented in Figure 2, form the basis for a numerical modelling of the composite, in which the concrete matrix and the steel fibers are modelled separately.

The concrete matrix is described using a Concrete Damage Plasticity (CDP) model, with input parameters derived from the compressive stress-strain response and the tensile behavior obtained experimentally or predicted by the analytical framework. The fiber-matrix interaction is represented through the Cohesive Zone model (CZM), calibrated using the average bond strength and pullout behaviour obtained from single-fiber pullout tests. This approach allows the progressive debonding and pullout of fibers to be explicitly captured within the numerical model, as shown in Figure 4. Therefore, the flexural response of SFRAASC can be simulated numerically, reproducing the load-CMOD behavior observed in the experimental three-point bending tests.

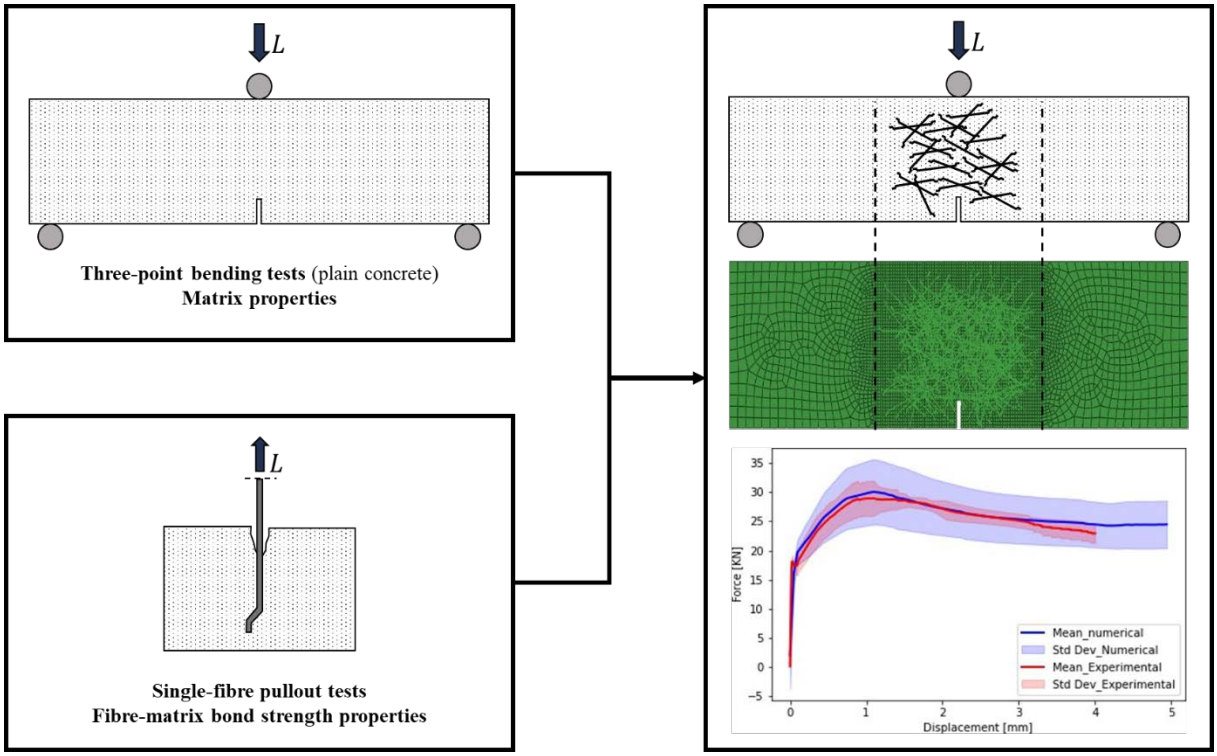


Figure 4: Implementation of the numerical framework for the finite element modelling with discrete fiber representation of SFRAASC and mix design optimization

This finite element modelling with discrete fiber representation links macroscopic flexural performance to matrix properties, fibers characteristic and interfacial behavior. When used in conjunction with the proposed analytical framework, the numerical model provides a powerful tool for mix design optimization of SFRAASC. By systematically varying matrix properties and fiber parameters (type, geometry, and dosage), the composite response can be tailored to achieve specific performance targets, such as a prescribed residual flexural strength, promoting a performance-based design approach for SFRAASC.

3 Concluding remarks

This paper presented a combined experimental, analytical, and numerical investigation aimed at developing a predictive design framework for alkali-activated slag-based concrete (AASC) incorporating single (3D) and multiple (4D, 5D) hooked-end steel fibers. The framework was built on an extensive experimental campaign conducted within the DuRSAAM project at the KIT IMB/MPA/CMM laboratories, which provided detailed characterization of the compressive response, flexural behavior under three-point bending, and fiber-matrix interaction. These results, collected from previous publications of the authors (Rossi et al. 2023; Rossi et al., 2024a; Rossi et al., 2024b; Rossi, 2025), were combined with additional data available in the literature to support analytical modelling and numerical implementation.

Using this comprehensive dataset, the empirical relationships originally developed for SFRPCC were recalibrated and new analytical expressions were derived. On this basis, the following conclusions can be drawn:

- Existing empirical models developed for SFRPCC are not directly applicable to SFRAASC, as they do not capture the distinctive mechanical behavior of these cement-free composites, particularly with respect to stiffness and tensile response;
- Newly calibrated analytical models were proposed to predict the compressive behavior, elastic properties, and post-cracking residual flexural strengths of SFRAASC relying on a limited set of input parameters related to the concrete matrix and fiber characteristics;
- A direct correlation between single-fiber pullout behavior and post-cracking flexural tensile behavior was established, enabling estimation of residual tensile properties from fiber-matrix bond characteristics;
- The proposed analytical framework can be integrated into a discrete numerical modelling strategy, in which the concrete matrix and steel fibers are modelled separately and their properties defined through the concrete damage plasticity (CDP) model and the cohesive zone model (CZM), allowing reliable simulation of the flexural response of SFRAASC elements;
- The combined analytical-numerical approach enables structural-scale simulations for SFRAASC element using a limited number of experimentally accessible parameters, providing a consistent link between laboratory testing, analytical modelling, and finite element implementation.

Overall, the proposed framework offers a practical, efficient, and performance-based pathway for predicting the mechanical and structural performance of SFRAASC. By integrating experimental characterization, analytical correlations, and numerical modelling, this approach supports reliable design and broader structural application of SFRAASC as a sustainable alternative to conventional steel fiber-reinforced Portland cement-based concrete.

4 Acknowledgements

This project has received funding from the European Union's Horizon 2020 research and innovation program under Grant Agreement No 813596 DuRSAAM. The opinions expressed in this document reflect only the author's view and reflect in no way the European Commission's opinions. The European Commission is not responsible for any use that may be made of the information it contains.

5 References

Adesina, A., 2020. “Performance of fibre reinforced alkali-activated composites – A review”, Materialia, 12, doi: 10.1016/j.mtla.2020.100782

Beglarigale, A., Aydin, S. Kızılırmak, C., 2016. “Fiber-matrix bond characteristics of alkali-activated slag cement-based composites”, Journal of Materials in Civil Engineering, 28(11), doi: 10.1061/(ASCE)MT.1943-5533.0001642

Dupont, D. and Vandewalle, L., 2005. “Distribution of steel fibres in rectangular sections”, Cement and Concrete Composites, 27(3), pp. 391-398, doi: 10.1016/j.cemconcomp.2004.03.005

Lim, H.-J., Cho, C.-G., You, J.-Y., Jeon, J.-J., 2022. “Mechanical properties of alkali-activated slag fiber composites varying with fiber volume fractions”, Materials, 15(18):6444, doi: doi.org/10.3390/ma15186444

Rossi, L., Patel, R.A., Dehn, F., 2023. “Compressive behaviour of alkali-activated slag-based concrete and Portland cement concrete incorporating novel multiple hooked-end steel fibres”, Materials and Structures, 56(5), doi: 10.1617/s11527-023-02180-2

Rossi, L., Zappitelli, M. P., Patel, R.A., Dehn, F., 2024. “Flexural tensile behaviour of alkali-activated slag-based concrete and Portland cement-based concrete incorporating single and multiple hooked-end steel fibres”, Journal of Building Engineering, 98, doi: 10.1016/j.jobe.2024.111090

Rossi, L., Patel, R.A., Dehn, F., 2024. “New analytical models to predict the mechanical performance of steel fiber-reinforced alkali-activated concrete”, Structural Concrete, doi: 10.1002/suco.202301104

Rossi, L., 2025. “Alkali-activated slag-based concrete incorporating single and multiple hooked-end steel fibres: New developments and challenges”, Doctoral Dissertation, Karlsruhe Institute of Technology (KIT), doi: 10.5445/IR/1000181222

Venkateshwaran, A., Tan, K. H., Li, Y., 2018. “Residual flexural strengths of steel fiber reinforced concrete with multiple hooked-end fibers”, Structural Concrete, 19(2), pp. 352-365, doi: 10.1002/suco.201700030

Ye, G. and Dehn, F. (Eds.), 2026. “Mechanical properties of alkali-activated Materials: State-of-the-Art Report of the RILEM Technical Committee 294-MPA”, RILEM State-of-the-Art Reports, Springer, doi: 10.1007/978-3-032-07116-3

Experimental Investigation of Hemp Fiber-Reinforced Recycled Aggregate Mortar

Bojan Poletanovic[1], Farshad Ameri[1], Lukas Hausner[1], Ildiko Merta[1]

[1]: Institute of Material Technology, Building Physics, and Building Ecology, Faculty of Civil and Environmental Engineering, TU Wien, Vienna, Austria

Corresponding author: bojan.poletanovic@tuwien.ac.at

Abstract

The growing demand for sustainable construction materials has promoted the use of construction and demolition waste as recycled aggregates (RAs) in cementitious composites. In this study, the effect of hemp fiber reinforcement on the mechanical properties of the mortars made with 100% recycled fine aggregates was analyzed. The mortars were produced using RAs and blast furnace slag cement, with hemp fibers of 5 mm and 10 mm lengths added at 0.5 vol% and 1.0 vol% dosage. Mechanical properties were evaluated through flexural and compressive strength tests, along with energy absorption capacity, all conducted at the mortars' age of 28 days. Results show that fiber addition reduces compressive strength (up to 38%) due to increased porosity, while flexural strength remains largely unchanged. In contrast, energy absorption capacity significantly improves, with increases of up to 105%, and enhanced post-peak behavior due to crack-bridging effects. Overall, hemp fibers effectively improve the toughness and ductility of RA mortars, supporting their potential for more sustainable construction applications.

Keywords

Recycled aggregates, mortar, mechanical properties, natural fibers, hemp fibers

1 Introduction

The construction sector is increasingly shifting toward sustainable materials to reduce the depletion of natural resources and mitigate environmental impacts [1]. Construction and demolition waste (CDW) is generated when structures reach the end of their service life or are damaged by extreme events such as earthquakes or explosions. The accumulation of such waste poses significant landfill challenges, particularly in densely populated urban areas. Reusing these materials as RAs in concrete production offers an effective strategy to minimize waste disposal while conserving natural resources [2].

However, the presence of adhered mortar on recycled concrete aggregates (RCA) reduces the mechanical performance of recycled aggregate concrete (RAC) compared to natural aggregate concrete (NAC) [3]. The formation of multiple interfacial transition zones (ITZs) within RAC weakens its strength and durability. As a result, RAC typically exhibits lower strength, greater shrinkage, and increased cracking potential [4]. Therefore, improving the properties of RCA and enhancing the ITZ in RAC is essential for its effective and practical application [5].

The addition of fibers to mortars and concrete can markedly enhance their toughness, crack resistance, and, in some cases, their strength [6–11]. The incorporation of fibers in RAC can significantly improve ductility while also enhancing the sustainability of conventional cement-based materials [12]. Natural fibers have become a preferred alternative to synthetic fibers for reinforcing concrete in recent decades [13]. Hemp fibers have been shown to improve the bending strain capacity and deflection performance of cementitious composites [14].

In this study, mortar mixtures incorporating 100% recycled fine aggregates and hemp fibers were developed and experimentally investigated. The research focuses on evaluating the hardened properties, including flexural strength, compressive strength, and energy absorption capacity. Different fiber lengths (5 and 10 mm) and volumetric dosages (0.5 vol% and 1.0 vol%) were considered to assess their effects on the composite's overall performance. The outcomes of this study aim to contribute to understanding bio-based fiber reinforcement in RA composites and to support the development of sustainable construction materials suitable for practical applications.

2 Experimental program

2.1 Mixture design

The mixture design adopted in this study was based on the technical standard ÖNORM EN 196-1 [15], following the formulation of a standard mortar specimen. The exact mixture design is shown in Table 1. In all mixtures, 1350 g of 100% recycled fine aggregate was used as a full replacement for standard sand. For this purpose, a 0/16 RB-A1 recycled mixed aggregate sand containing a minimum of 90% recycled concrete was sieved to below 2 mm. Since all mixtures contained the same amount of 100% recycled fine aggregate, including the reference mixture, no additional water compensation or pre-saturation based on aggregate water absorption was applied. Nevertheless, a two-stage mixing procedure was adopted, where half of the mixing water was initially mixed with the RA before the addition of cement and fibers (Table 2). Electron microscopic and photographic images of the Hemp fibers and the RAs are shown in

Fig. 1. The resulting sieve line of the RA is shown in Fig. 2. To further reduce the CO_2 footprint of the mix, low-global-warming-potential blast-furnace slag cement (CEM III/B) was used.

Table 1: Overview of the used mix design

Mix Name	Mix code	Water	CEM III/B	RB-A1[1]	Hemp fiber 5 mm	Hemp fiber 10 mm	SP[2]
		(g)					
REF	0	225.0	450	1350	-	-	5
Hemp_5 mm_0.5 vol%	5_0.5	240.6	450	1350	6.23	-	5
Hemp_5 mm_1.0 vol%	5_1.0	256.2	450	1350	12.46	-	5
Hemp_10 mm_0.5 vol%	10_0.5	240.6	450	1350	-	6.23	5
Hemp_10 mm_1.0 vol%	10_1.0	256.2	450	1350	-	12.46	5

1) RA consisting of a minimum 90% recycled concrete

2) A superplasticizer with a specific gravity of 1.05 was used as an admixture.

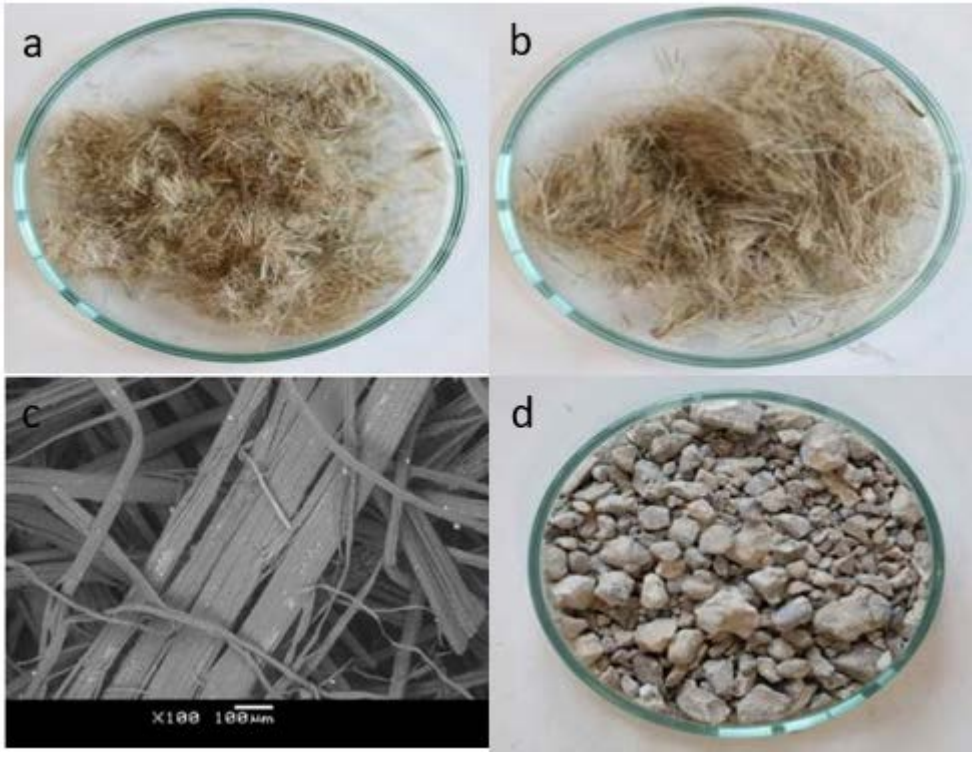


Figure 1. (a) 5 mm long hemp fibers, (b) 10 mm long hemp fibers, (c) Electron microscopy image of a hemp fiber, (d) RB-A1 (0/16 mm)

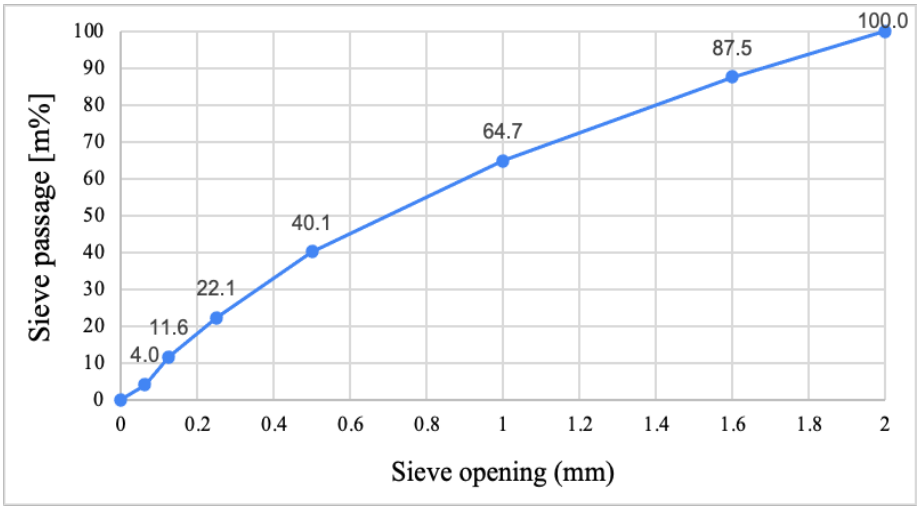


Figure 2. Sieve analysis of the RA

The mixing procedure was adapted to address the usage of RAs and hemp fibers and is shown in Table 2. The mixing was performed using a standard mortar mixer (Fig. 3), and prismatic specimens with dimensions of 40 × 40 × 160 mm³ were cast (Fig. 4).

Table 2: Mixing procedure and storage conditions

2min	Dry mixing of RAs
Pause	Add ½ of Water
1min	Wet mixing of aggregates
Pause	Add CEM III/B, Hemp fibers, and the rest of the water
5min	The additives were incorporated during mixing
Finish	Measure the Slump Hägermann-Trichter spread with 15 shocks for each batch
24h – 48h	Demolding
	Stored in a 20 °C underwater environment until testing

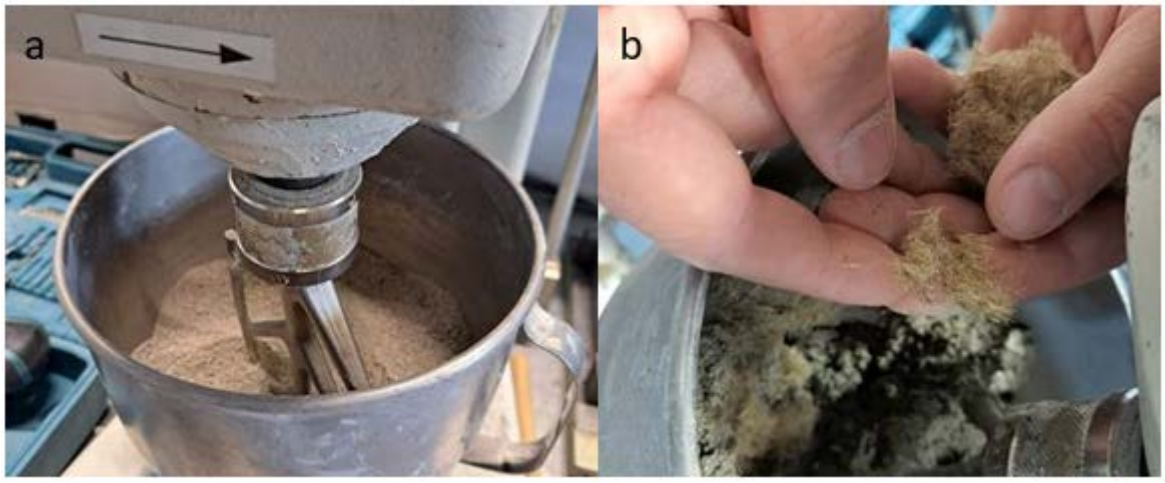


Figure 3. Photographs of (a) the dry mixing stage and (b) the addition of hemp fibers.



Figure 4. Produced mortar prisms (40 × 40 × 160 mm³)

2.2 Experimental method

A three-point bending test (3PBT) was performed on six mortar prism specimens measuring 40 × 40 × 160 mm³, in accordance with EN 1015-11 [16], for each specimen group at 28 days of age. The flexural strength was determined from the 3PBT results. Testing was carried out using a Zwick/Roell Z250 mechanical testing machine (Germany) with a load capacity of 200 kN and a stiffness of 8×10^{-3} mm/kN. The deflection rate was set to 400 µm/min under ambient conditions of 21 °C and 50% relative humidity. The load was applied at the midpoint of the specimens with a span length of 100 mm. The specific energy absorption capacity (toughness) was calculated from the force–midspan deflection curve obtained during the 3PBT, as the area under the curve, divided by the specimen cross-sectional area. The compressive strength tests were conducted in accordance with EN 1015-11 [16] after the 3PBT. These tests were performed on one half of the fractured specimens by applying compressive load over a 40 × 40 mm² area, using three identical specimens.

3 Results and discussion

The plain mortar exhibited a compressive strength of 52.9 MPa (Fig. 5). The addition of short hemp fibers reduced the compressive strength, mainly due to increased entrapped air and fiber agglomeration, which raised the porosity of the mortar. At a fiber dosage of 0.5 vol%, the compressive strength decreased by about 11%, regardless of fiber length (Fig. 5). When the dosage was increased to 1 vol%, the reduction became more pronounced, reaching 19% and 38% for fiber lengths of 10 mm and 5 mm, respectively. Interestingly, a smaller decrease in compressive strength was observed with the longer fibers (10 mm) than with the shorter ones (5 mm), which is somewhat counterintuitive. Higher porosity would typically be expected in mixtures with longer fibers, resulting in greater strength reduction. However, considering that the primary contribution of short fiber reinforcement in mortars is to delay crack initiation in the pre-cracking stage and to slow crack propagation in the post-peak regime through stress transfer mechanisms such as crack bridging, it can be hypothesized that longer fibers enhance these mechanisms more effectively, partially compensating for the adverse effects of increased porosity.

Similar reductions in compressive strength have also been reported for hemp-fiber-reinforced cementitious materials containing natural aggregates [9,17].

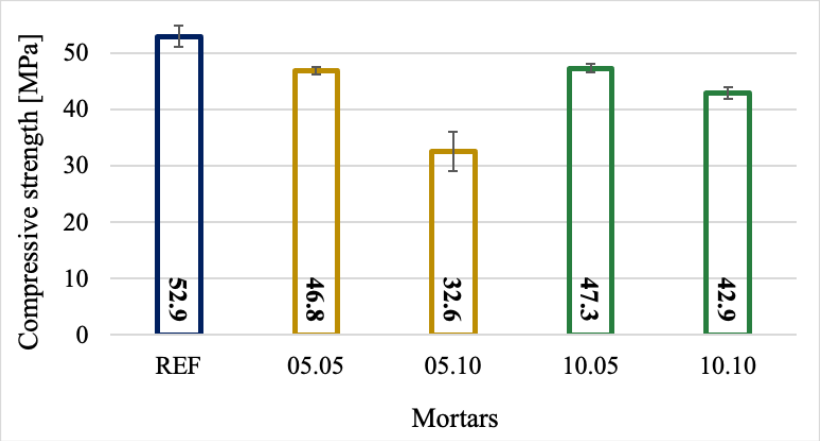


Figure 5. Compressive strengths of the mortars

A trend similar to that observed for compressive strength was also noted in flexural strength (Fig. 6). The flexural strength of the plain, non-fiber-reinforced mortar was 8.1 MPa. The addition of short hemp fibers resulted in a 19% reduction only in the mixture containing 0.5 vol % 5 mm-long fibers, compared to the reference mortar. In all other fiber-reinforced mixtures, no significant changes in flexural strength were observed.

In a study on cementitious mortars reinforced with hemp fibers and containing only natural aggregates, a similarly small, almost negligible, reduction in flexural strength was reported after adding 1 vol% hemp fibers with a length of 10 mm [9] . In a study on cementitious materials incorporating silica sand, the use of 6 mm long hemp fibers at a dosage of 1 vol% resulted even in an increase in flexural strength of up to 9% [17].

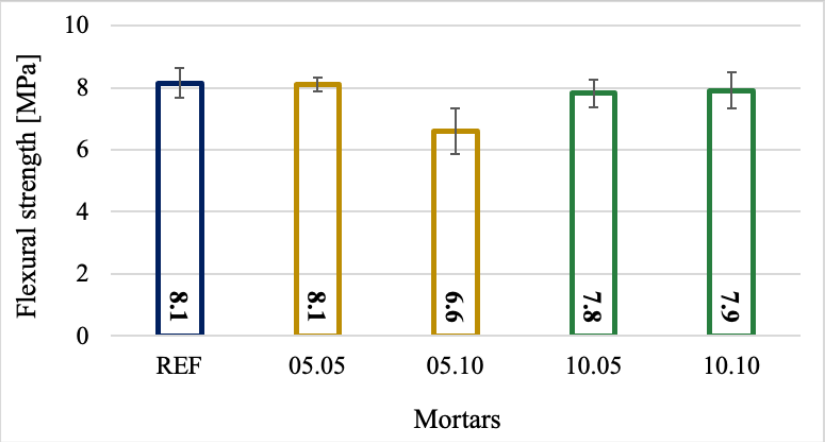


Figure 6. Flexural strengths of the mortars

Regarding the energy absorption capacity, the reference mortar achieved 280 N/m. The addition of hemp fibers also enhanced the total energy absorption capacity in mortars containing recycled fines (Figs. 7 and 8). It was observed that adding hemp fibers at 0.5 vol% increased the total energy absorption capacity by an average of 43%. At a fiber content of 1.0 vol%, the increase reached 105%, irrespective of fiber length.

In a study on cementitious mortars reinforced with hemp fibers (dosage 1 vol% and 10 mm fiber length) and containing only natural aggregates [9] It was found that incorporating hemp fibers increased energy absorption capacity by up to 348% compared to plain mortar. This enhancement was significantly greater than the improvement observed with recycled fines in the present study.

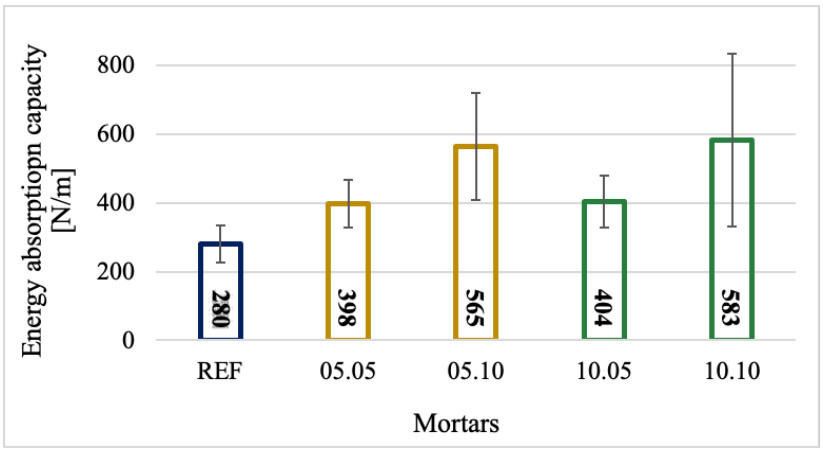


Figure 7. Energy absorption capacity of the mortars

The improvement in energy absorption capacity is mainly attributed to the enhanced post-peak behavior provided by crack-bridging mechanisms. As shown in Fig. 8, the hemp fibers enable stress transfer across cracks and delay crack propagation after peak load, resulting in increased deformation capacity and toughness. As shown in Fig. 8, once the peak load is reached, the non-reinforced mortar exhibits almost no further deformation capacity. In contrast, mortars reinforced with 1.0 vol% fibers show a considerably smaller drop in load after the peak compared to those with 0.5 vol%, resulting in a higher post-peak plateau and, consequently, superior post-peak energy absorption.

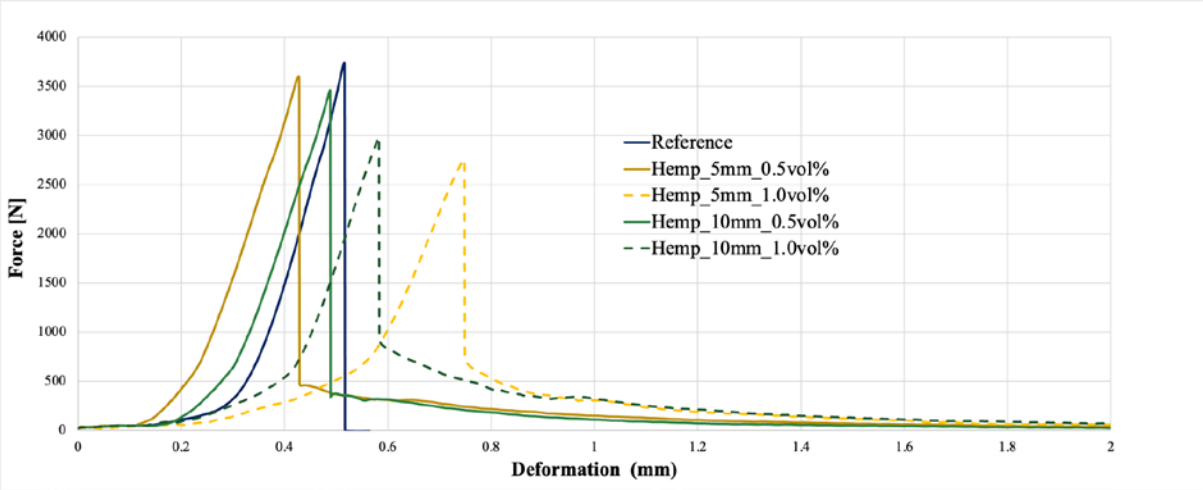


Figure 8. Force-displacement curves of the mortars obtained from 3PBT

4 Concluding remarks

The growing demand for sustainable construction materials has increased interest in using construction and demolition waste as RAs in cementitious composites. The fiber-reinforced mortar mixtures prepared in this study used RAs as a full replacement for natural sand and low-carbon blast-furnace slag cement (CEM III/B). Hemp fibers with lengths of 5 mm and 10 mm were added at dosages of 0.5 vol% and 1.0 vol%. The mechanical performance was evaluated through flexural and compressive strength tests, as well as energy absorption capacity derived from three-point bending tests conducted at 28 days. The results indicate that incorporating hemp fibers reduces compressive strength, primarily due to increased porosity and fiber agglomeration. At 0.5 vol% fiber content, compressive strength decreased by approximately 11%, while at 1.0 vol%, reductions of up to 38% were observed. Flexural strength remained largely unaffected, with only minor reductions in specific mixtures. In contrast, the addition of hemp fibers significantly improved the energy absorption capacity, with increases of up to 105% at higher fiber dosages (1 vol%). Overall, the findings demonstrate that while hemp fiber reinforcement may reduce strength, it substantially enhances the energy absorption and deformation capacities of RA mortars. This highlights the potential of combining RAs with natural fibers to develop more sustainable and ductile cementitious materials for practical construction applications.

Future research should include measurements of density and porosity to better quantify the influence of hemp fibers on the internal structure and mechanical performance of recycled aggregate mortars.

5 Acknowledgements

This research was supported by the Interreg CENTRAL EUROPE Programme 2021–2027 within the framework of Project CE0100390 – ReBuilt: Circular and Digital Renewal of Central Europe Construction and Building Sector. The authors would also like to thank Arpad Kis, our colleague from Institute of Material Technology, Building Physics, and Building Ecology,

Faculty of Civil and Environmental Engineering, TU Wien (Vienna, Austria), who participated in the preparation of the specimens, for his valuable support.

6 References

[1] A. Almusaed, I. Yitmen, J.A. Myhren, A. Almssad, Assessing the Impact of Recycled Building Materials on Environmental Sustainability and Energy Efficiency: A Comprehensive Framework for Reducing Greenhouse Gas Emissions, Buildings 14 (2024). https://doi.org/10.3390/buildings14061566.

[2] S. Ghosn, B. Hamad, E. Awwad, Structural and life cycle assessments of recycled aggregate concrete beams incorporating industrial hemp fibers, Structural Concrete 24 (2023). https://doi.org/10.1002/suco.202201219.

[3] G. Bai, C. Zhu, C. Liu, B. Liu, An evaluation of the recycled aggregate characteristics and the recycled aggregate concrete mechanical properties, Constr. Build. Mater. 240 (2020). https://doi.org/10.1016/j.conbuildmat.2019.117978.

[4] C. Bu, L. Liu, X. Lu, D. Zhu, Y. Sun, L. Yu, Y. Ouyang, X. Cao, Q. Wei, The Durability of Recycled Fine Aggregate Concrete: A Review, Materials 15 (2022). https://doi.org/10.3390/ma15031110.

[5] B. Ali, S.S. Raza, R. Kurda, R. Alyousef, Synergistic effects of fly ash and hooked steel fibers on strength and durability properties of high strength recycled aggregate concrete, Resour. Conserv. Recycl. 168 (2021). https://doi.org/10.1016/j.resconrec.2021.105444.

[6] R.P. Borg, E. Cuenca, R. Garofalo, F. Schillani, M.L. Nasner, L. Ferrara, Performance Assessment of Ultra-High Durability Concrete Produced From Recycled Ultra-High Durability Concrete, Front. Built Environ. 7 (2021). https://doi.org/10.3389/fbuil.2021.648220.

[7] Y. Yu, J. Xu, W. Chen, B. Wu, Mesoscale modeling of flexural fracture behavior in steel fiber reinforced concrete, Advances in Structural Engineering 27 (2024). https://doi.org/10.1177/13694332241226921.

[8] B. Poletanovic, J. Dragas, I. Ignjatovic, M. Komljenovic, I. Merta, Physical and mechanical properties of hemp fibre reinforced alkali-activated fly ash and fly ash/slag mortars, Constr. Build. Mater. 259 (2020). https://doi.org/10.1016/j.conbuildmat.2020.119677.

[9] I. Merta, V.Z. Serjun, A.M. Pranjić, A. Šajna, M. Štefančič, B. Poletanović, F. Ameri, A. Mladenović, Investigating the synergistic impact of freeze-thaw cycles and deicing salts on the properties of cementitious composites incorporating natural fibers and fly ash, Clean. Eng. Technol. 24 (2025). https://doi.org/10.1016/j.clet.2024.100853.

[10] B. Poletanovic, I. Janotka, M. Janek, M. Bacuvcik, I. Merta, Influence of the NaOH-treated hemp fibres on the properties of fly-ash based alkali-activated mortars prior and after wet/dry cycles, Constr. Build. Mater. 309 (2021). https://doi.org/10.1016/j.conbuildmat.2021.125072.

[11] I. Merta, E.K. Tschegg, Fracture energy of natural fibre reinforced concrete, Constr. Build. Mater. 40 (2013). https://doi.org/10.1016/j.conbuildmat.2012.11.060.

[12] B. Ali, L.A. Qureshi, A. Raza, M.A. Nawaz, S.U. Rehman, M.U. Rashid, Influence of Glass Fibers on Mechanical Properties of Concrete with Recycled Coarse Aggregates, Civil Engineering Journal (Iran) 5 (2019). https://doi.org/10.28991/cej-2019-03091307.

[13] A. Geremew, A. Outtier, P. De Winne, T.A. Demissie, H. De Backer, An Experimental Investigation on the Effect of Incorporating Natural Fibers on the Mechanical and Durability Properties of Concrete by Using Treated Hybrid Fiber-Reinforced Concrete Application, Fibers 13 (2025). https://doi.org/10.3390/fib13030026.

[14] R. Fragoudakis, J.A. Gallagher, V. Kim, A Computational Analysis of the Energy Harvested by Gfrp and Nfrp Laminated Beams under Cyclic Loading, in: Procedia Eng., 2017. https://doi.org/10.1016/j.proeng.2017.07.032.

[15] E.N. ÖNORM, 196-1: 2016-10-15: Prüfverfahren für Zement–Teil 1: Bestimmung der Festigkeit, (2016).

[16] E.N. 1015-11, Methods of test for mortar for masonry–Part 11: Determination of flexural and compressive strength of hardened mortar, CEN (1999).

[17] B. Çomak, A. Bideci, Ö.S. Bideci, Effects of hemp fibers on characteristics of cement based mortar, Constr. Build. Mater. 169 (2018) 794–799.

Mechanical Performance of Concrete Reinforced with Recycled Tyre-Cord Steel Fibres

Peter Czirak[1], Jaroslav Prokop[1]

[1]: Slovak Academy of Sciences, Dubravska cesta 9, 845 03 Bratislava, Slovakia.

Abstract

The environmental consequences of steel fibres produced through industrial methods have led to a growing interest in sustainable alternatives for fibre-reinforced concrete. This research examines the mechanical properties of concrete reinforced with recycled fibres sourced from end-of-life tyre steel cords, both independently and in a hybrid mix with traditional steel fibres. Four distinct concrete mixtures were analysed: a control mix devoid of fibres, concrete incorporating recycled fibres at a rate of 20 kg/m³, concrete containing industrial steel fibres at 20 kg/m³, and a hybrid fibre-reinforced concrete with a total fibre content of 20 kg/m³, consisting of 70% recycled fibres and 30% industrial fibres. The compressive strength after 28 days and the flexural characteristics were assessed. The flexural tensile strength (f_{ctfl}) and the residual flexural tensile strengths were measured at crack mouth opening displacements of 0.5 mm (f_{R1}), 1.5 mm (f_{R2}), 2.5 mm (f_{R3}), and 3.5 mm (f_{R4}). The findings indicate that recycled tyre-cord steel fibres do not negatively impact compressive strength and significantly enhance post-cracking performance when compared to plain concrete. Industrial steel fibres yield greater residual strength at minor crack openings, whereas hybrid fibre systems demonstrate a well-balanced flexural response throughout the entire CMOD range. The incorporation of recycled tyre-cord steel fibres promotes waste valorisations, diminishes dependence on virgin steel fibres, and offers a technically feasible and sustainable reinforcement option for fibre-reinforced concrete.

Keywords

Crack width, fibre reinforced concrete, post-crack performance, flexure, tension stiffening, hybrid fibres.

1 Introduction

Fiber-reinforced concrete (FRC) has developed into a quasi-ductile cementitious composite that can address the natural brittleness found in traditional concrete. The addition of discrete fibres, whether steel, synthetic, or hybrid, facilitates stress transfer across cracks via bridging mechanisms, thereby greatly enhancing post-cracking performance. A key aspect of characterizing this behaviour is the Crack Mouth Opening Displacement (CMOD), which has emerged as the primary fracture parameter in both experimental and analytical studies (Zhang et al. 2001).

Unlike global deformation metrics such as mid-span deflection, CMOD provides a localized measure of crack evolution, making it particularly suitable for fracture mechanics-based analysis (Abdallah et al. 2023) .

CMOD originates from linear elastic fracture mechanics (LEFM) and cohesive crack theory, where it represents the relative displacement between crack faces at the mouth of a notch. In quasi-brittle materials such as concrete, CMOD is particularly useful because, it correlates directly with crack propagation, enables stable post-peak testing, and serves as a proxy for crack opening displacement (COD) in cohesive models (Kumar et al. 2014; Xu and Reinhardt 1998).

In FRC, the presence of fibres modifies the classical fracture response. Instead of abrupt crack propagation, fibres induce a strain-softening or strain-hardening response, depending on fibre dosage and distribution. CMOD thus becomes a state variable governing the transition from elastic behaviour to post-cracking ductility(Pokorska et al. 2023).

The implementation of hybrid fibre systems, which integrate two or more types of fibres with unique mechanical and geometrical characteristics, significantly improves this behaviour by triggering various crack-bridging mechanisms across multiple length scales.

Generally, macrofibres (such as steel fibres) enhance load-carrying capacity and manage macrocrack propagation at higher CMOD values, whereas microfibres (like polypropylene or PVA fibres) are more proficient in inhibiting microcrack initiation and early crack growth at lower CMOD levels (Banthia and Gupta 2004).This collaborative interaction results in a more stable and gradual crack development process, which is evident in a smoother and more prolonged load CMOD response (Afroughsabet and Ozbakkaloglu 2015).

Various forms of fibre possess distinct characteristics that can enhance one another, balancing the advantages and disadvantages inherent in each type. A singular fibre type enhances the mechanical attributes and longevity of the material; however, it is inadequate in inhibiting the development of significant cracks. The combination of different fibres facilitates the achievement of multilevel fracture mechanisms. For instance, low-modulus fibres augment ductility, whereas high-modulus fibres enhance strength and rigidity, resulting in optimized material properties when used together (Lawler et al. 2003).

2 Experimental program

2.1 Materials

Binders: Cement CEM II/A-LL 42.5 R, Danucem Slovakia.

Aggregate: Ordinary round aggregates from riverbed deposits, Velke Ulany, Slovakia

Fibres

R- Recycled fibres – corrugated fibres from used tire cords, various properties, 54795 pcs/kg

A- Arcelor Mittal HE 1/60 – fibres with hooked end. 60 mm long, 1 mm diameter, 2600 pcs/kg

Additives: Plasticiser, STACHEMENT 2014, Stachema a.s., Slovakia

Table 1: design mixes for tested specimens.

Nomination	Cement kg/m^3	Water kg/m^3	Agg. 0-4 kg/m^3	Agg. 4-8 kg/m^3	Agg. 8-16 kg/m^3	Plasticiser kg/m^3	Fibres kg/m^3
S0	350	165	1010	320	540	1.75	0
2R	350	165	1010	320	540	1.75	20
2A	350	165	1010	320	540	1.75	20
2H3A	350	165	1010	320	540	1.75	20*

* 30% type A, 70 % type R

Based on the aspect ratio (l_f/d_f) of recycled steel fibres (RSF), which has an average value of 61, three types of industrially-produced steel fibres (ISF) were selected for comparative analysis. These ISF variants were chosen due to their slenderness ratios that closely resemble those of the RSF, allowing for a significant evaluation of their performance in concrete mixtures. The chosen ISFs consist of A (ArcelorMittal HE 1/60 fibbers). To assess the impact of these fibres on concrete performance, four distinct concrete mixtures were formulated, namely: S0 – plain concrete without fibres, which acted as the reference mix, 2R containing 20 kg/m³ of recycled steel fibres (RSF), 2A containing 20 kg/m³ of Type A ISF, and type 2H3A containing 20 kg/m³ (30% type A, and 70 % type R).

Riverbed aggregates were screened into size fractions of 0-4 mm, 4-8 mm, and 8-16 mm, constituted the primary mineral fillers utilized in the mixture. These aggregates were selected due to their consistent quality and grading, which are essential for attaining the desired mechanical properties and workability of the final composite. The binding material employed was Portland composite cement CEM II/A-LL 42.5 R, recognized for its reliable strength development and compatibility with various admixtures while improving sustainability of the product. To ensure proper hydration of the cement, tap water that meets the relevant standards for concrete production was utilized. In order to enhance the workability of the fresh mixture while reducing the water-to-cement ratio, superplasticizer Stachement 2014 was added. This high-range water-reducing admixture improved the flow characteristics without compromising strength or durability. The mix design applied in this study is detailed in Table 1, with a water-cement ratio of 0.47 maintained across all mixes.

The experimental component of the investigation consisted of a series of experiments in which 550 mm long beams of 150×150 mm cross-section as shown in Figure 1 were cast using either plain concrete (as the control) or the same mixture reinforced with various types of fibres. Three samples for each mixture were cast and cured for 28 days fulfilling the conditions of (“EN

12390-2:2019" 2019). Density of each sample was checked according to ("EN 12390-7:2019" 2019). The mix design for the concrete was the same for all the trials, and is listed in Table 1.

Bending tests were conducted on beams featuring a stress-notch concentrator, and the relationship between the applied force and the crack mouth opening displacement (CMOD) was documented throughout the testing process. The configuration for the experimental assessment of tensile strength in bending and fracture characteristics is illustrated in Fig.1. Both the sample and the experimental arrangement complied with the standards set forth in ("EN 14651+A1:2008" 2008).

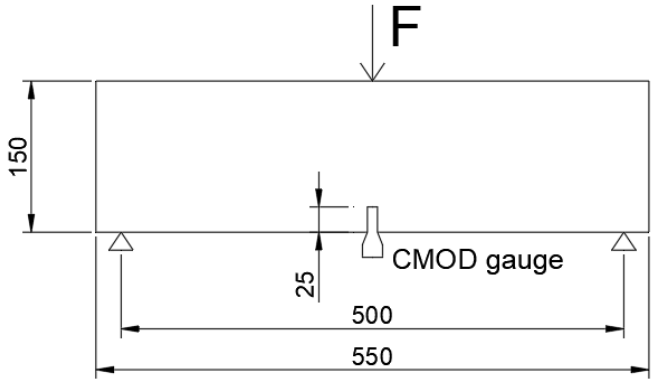


Figure 1 – Loading scheme

Load CMOD diagram are shown in the figures below:

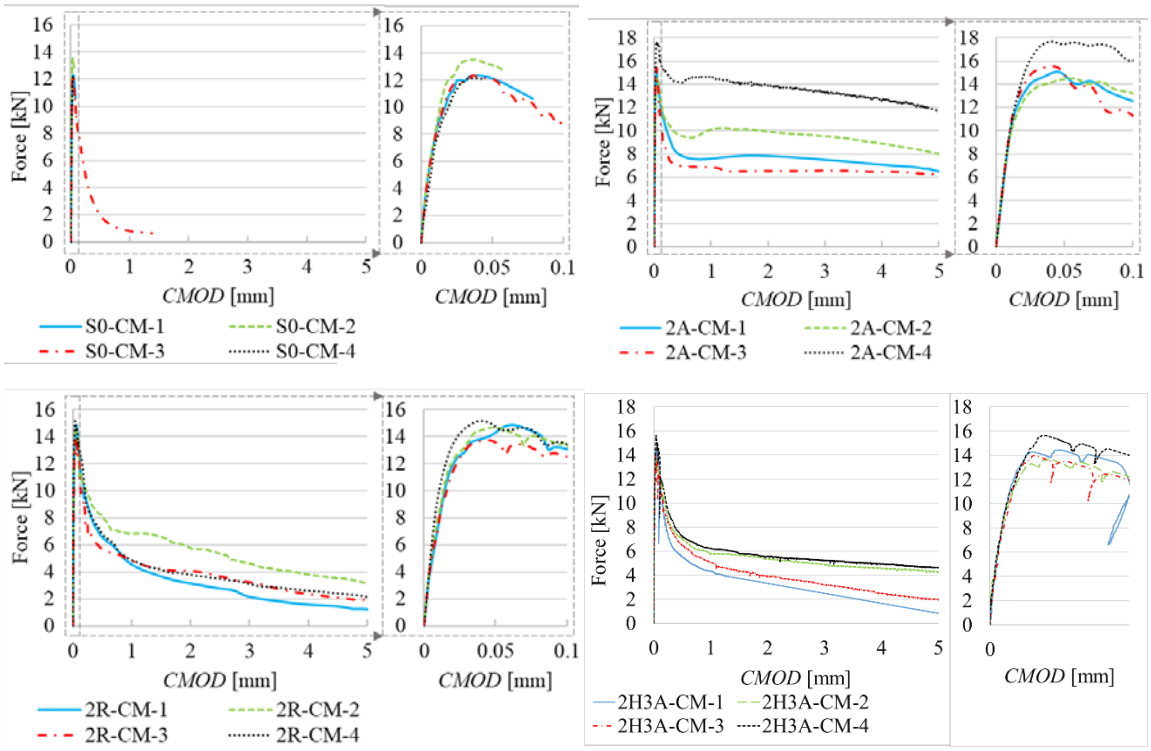


Figure 2 CMOD diagrams (S0, 2A, 2R, 2H3A)

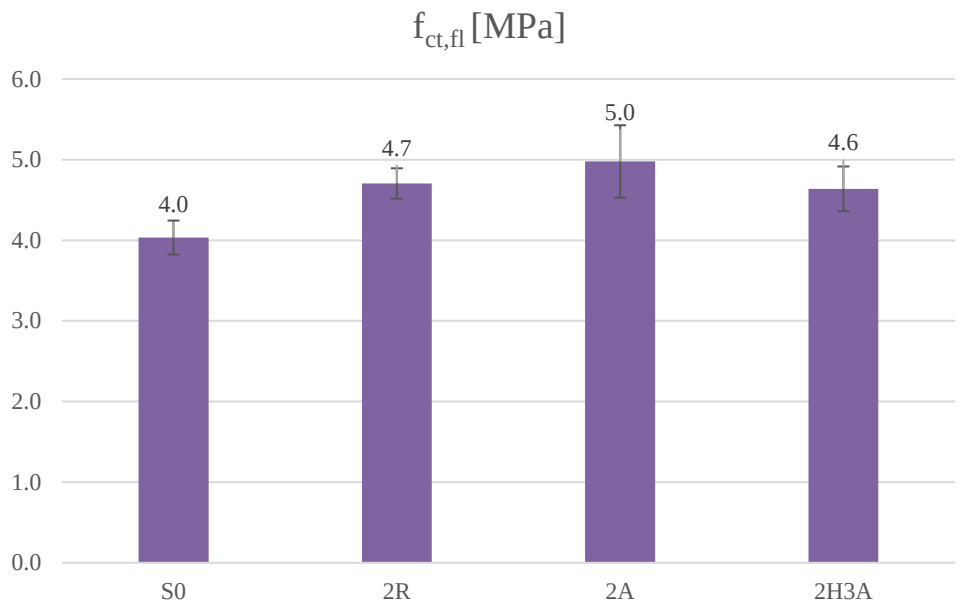


Figure 3 Flexural tensile strength capacity

Figure 3 illustrates the flexural tensile strength at the limit of proportionality ($f_{ct,fl}$) for all tested mixtures. The reference concrete S0 exhibited the lowest flexural strength due to the absence of crack-bridging reinforcement. The incorporation of recycled tyre-cord steel fibres in mixture 2R increased the flexural strength compared to the control mixture, confirming that recycled fibres are capable of delaying crack initiation and redistributing tensile stresses in the cementitious matrix. The mixture reinforced with industrial hooked-end steel fibres (2A) achieved the highest flexural strength 5.0 MPa because of the superior anchorage and pull-out resistance of the industrial fibres. The hybrid mixture (2H3A) exhibited a flexural strength 4.6MPa which is close to 4.7 MPa achieved by samples with 2R.

The observed trend agrees with previous studies demonstrating that steel fibres with improved geometry and anchorage mechanisms are more effective in enhancing tensile and flexural strength, while recycled fibres provide moderate strengthening but superior sustainability benefits. (Tiberti et al. 2014) reported that higher fibre efficiency is generally associated with better bond conditions and crack-bridging ability, particularly in the pre-peak regime. Likewise, (Banthia and Gupta 2004) observed that hybrid fibre systems can preserve flexural performance while reducing the volume of industrial fibres required.

Figure 4 presents the load corresponding to the limit of proportionality (LOP), which represents the transition from elastic behaviour to the onset of macrocracking. The plain concrete mixture S0 showed the lowest f_{LOP} = 3.8 MPa value, reflecting the brittle response of unreinforced concrete. The recycled fibre mixture 2R demonstrated a noticeable increase in LOP, indicating that randomly distributed recycled steel fibres are able to restrain microcrack growth before unstable crack propagation occurs.

The hybrid mixture 2H3A achieved the highest f_{LOP} = 5.6 MPa among all tested mixtures. This result suggests that the combined action of recycled tyre-cord steel fibres and industrial hooked-end fibres is particularly effective in delaying the formation of the first macrocrack. The recycled fibres likely contributed to controlling microcracks at early loading stages, while the industrial fibres improved stress redistribution and anchorage.

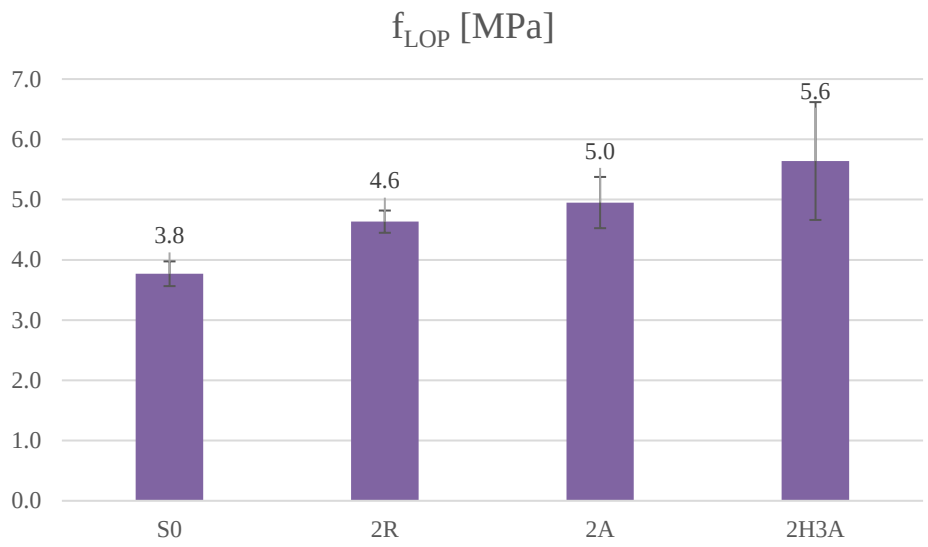


Figure 4 Load at Limit of Proportionality

The industrial fibre mixture 2A also exhibited higher f_{LOP} = 5.0 MPa than the reference concrete f_{LOP} = 3.8 MPa, but its performance remained slightly lower than that of the hybrid system with f_{LOP} = 5.6 MPa. This indicates that the interaction between different fibre types can generate a synergistic effect that is more beneficial than the use of a single fibre type alone.

From a structural perspective, a higher LOP is advantageous because it increases the serviceability range of the material before visible cracking develops. Previous research has shown that hybrid fibre systems can improve the stress level at crack initiation and enhance the transition from elastic to post-cracking behaviour. According to (Pereira et al. 2012), the use of multiple fibre types activates different crack-bridging mechanisms across multiple scales, resulting in improved crack control and higher resistance to crack initiation.

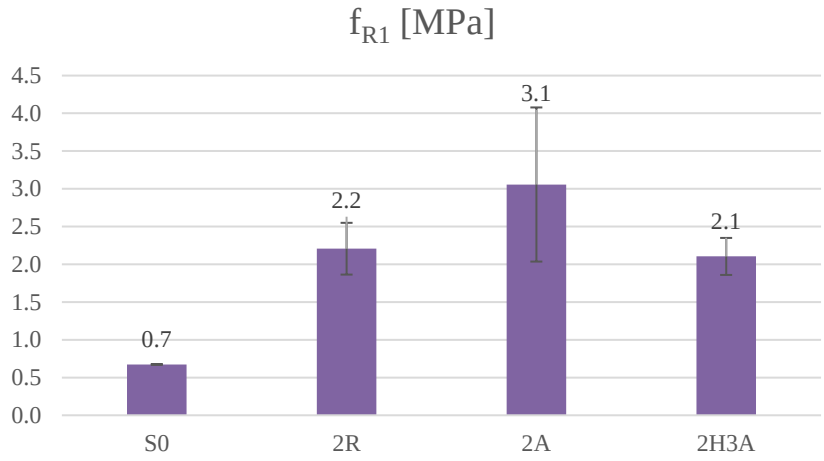


Figure 5 CMOD for 0.5 mm

Figure 5 shows the residual flexural strength at a crack mouth opening displacement (CMOD) of 0.5 mm, corresponding to the f_{R1} residual strength parameter defined in EN 14651. At this early stage of crack opening, industrial steel fibres in mixture 2A provided the highest residual strength f_{R1} = 3.1 MPa due to their effective bond and crack-bridging action. The recycled fibre

mixture 2R also exhibited significant residual load-bearing capacity f_{R1} = 2.2 MPa, demonstrating that tyre-cord steel fibres can effectively bridge cracks immediately after crack initiation.

The hybrid mixture 2H3A showed a residual strength f_{R1}= 2.1 MPa that is close to that 2.2 MPa of 2A, suggesting that the inclusion of a smaller amount of industrial fibres is sufficient to improve the early post-cracking response of recycled-fibre concrete. This behaviour is important because f_{R1} is directly related to crack control under serviceability conditions.

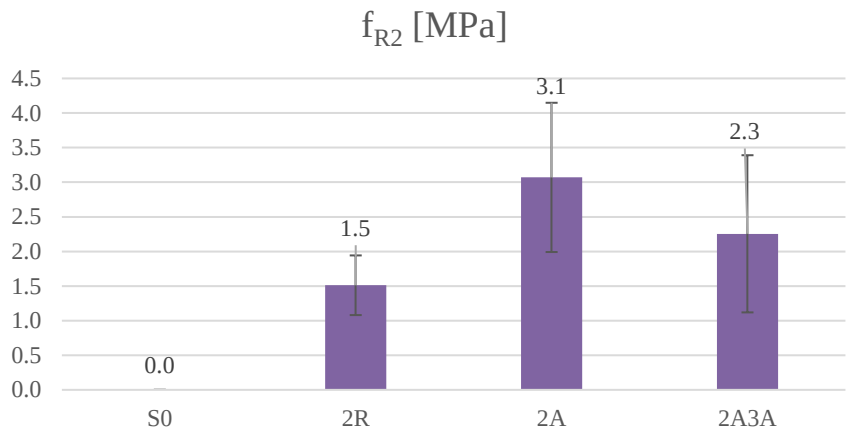


Figure 6 CMOD for 1.5 mm

Figure 6 indicates f_{R2} values at crack mouth opening displacement (CMOD) of 1.5 mm. All fibre-reinforced mixtures maintained substantial post-cracking resistance, while the reference mixture S0 experienced a pronounced drop in load-carrying capacity. The industrial fibre mixture 2A remained dominant with f_{R2} = 3.1 MPa because the hooked-end fibres provided strong mechanical anchorage and resisted fibre pull-out. Compared to f_{R1}, the difference between the industrial fibre mixture 2A and the hybrid mixture 2H3A became slightly different in a favour of hybrid system. This indicates that the industrial hooked-end fibres retained their bridging efficiency effectively as crack opening increased. The hybrid mixture maintained high residual strength f_{R2} = 2.3 MPa, confirming that the recycled fibres continued to contribute significantly to crack-bridging during intermediate crack openings.

The recycled fibre mixture 2R continued to exhibit meaningful residual strength f_{R2} = 1.5 MPa despite the irregular shape and varying dimensions of the tyre-cord steel fibres. This confirms that recycled fibres are particularly effective in sustaining load transfer during intermediate crack openings.

Figure 7 represents the f_{R3} residual flexural strength at crack mouth opening displacement (CMOD) of 2.5 mm. At this crack opening level, the role of fibre pull-out resistance becomes more pronounced than the initial bond strength. The industrial fibre mixture 2A still exhibited the highest residual capacity f_{R3} = 3.0 MPa, but the hybrid mixture 2H3A continued to show a slightly better performance with f_{R3} = 1.4 MPa , than recycled fibres with f_{R3} = 1.3 MPa. The hybrid mixture 2H3A exhibited a more gradual decrease in residual strength comparing to f_{R2}, which indicates a stable post-cracking response and improved ductility.

The recycled fibre mixture 2R demonstrated better retention of residual strength than plain concrete, indicating that recycled fibres remain active even after substantial crack opening. This

result is particularly important because the ratio between f_{R1} and f_{R3} or f_{R4} is commonly used in design codes to assess whether a fibre-reinforced concrete can replace conventional reinforcement in certain structural applications (di Prisco et al. 2013; Jin et al. 2025).

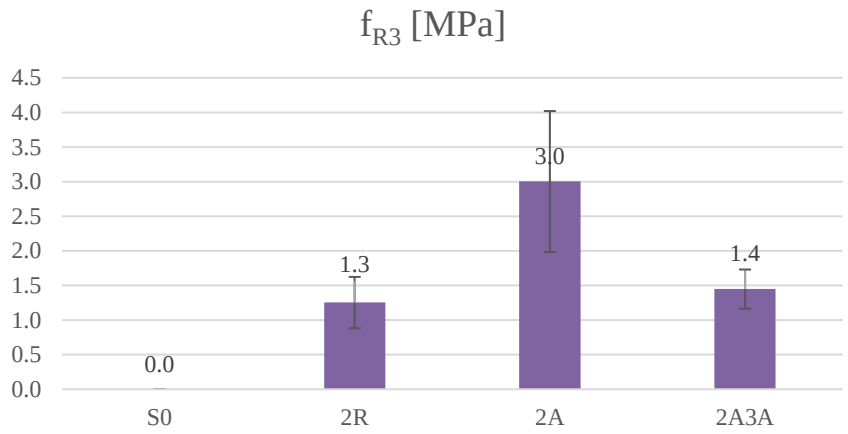


Figure 7 CMOD for 2.5 mm

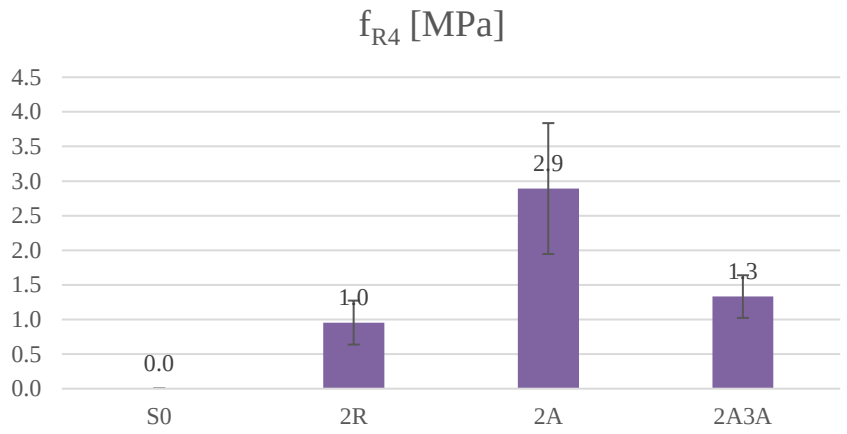


Figure 8 CMOD for 3.5 mm

Figure 8 presents the residual flexural strength f_{R4} at crack mouth opening displacement (CMOD) of 3.5 mm, corresponding to an advanced stage of crack propagation. At this level, the performance of the mixtures depends primarily on fibre pull-out resistance, fibre orientation, and the ability of the fibres to remain anchored in the concrete matrix.

The industrial fibre mixture 2A retained the highest residual strength f_{R4} = 2.9 MPa, confirming the effectiveness of hooked-end fibres in resisting pull-out at larger crack openings. The recycled fibre mixture 2R showed lower residual strength f_{R4} = 1.0 MPa, than the industrial fibre mixture but still maintained considerable load-carrying capacity compared to the control mixture. Hybrid system with f_{R4} = 1.3 MPa performed better than 2R system.

The ability of recycled fibres to sustain residual stresses at large CMOD values is highly relevant for structural applications where energy absorption, toughness, and crack width control are critical (*fib MC (2020)* 2024). Previous studies by (Lawler et al. 2003; Pokorska et al. 2023) demonstrated that hybrid and recycled fibre systems can enhance fracture energy dissipation and produce more stable crack propagation mechanisms.

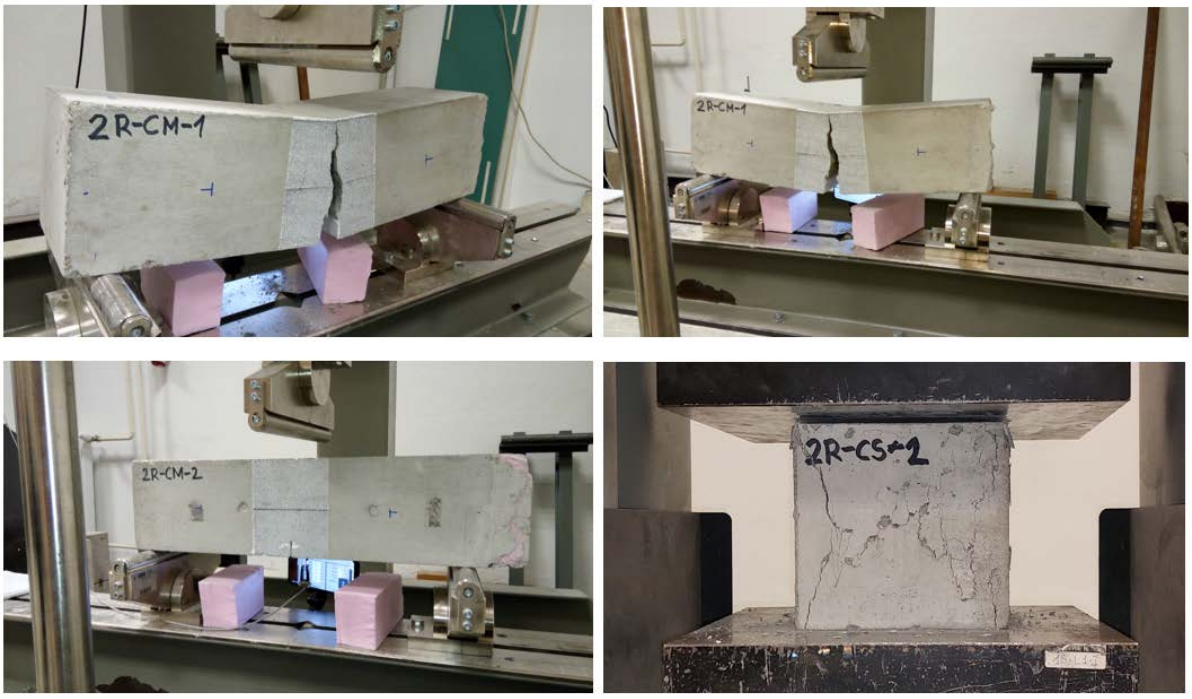


Figure 9 Laboratory testing

Testing specimen and equipment are shown in figure 9.

3 Analysis

The experimental results confirm that fibre reinforcement significantly improves the post-cracking behaviour of concrete. While the addition of fibres has usually only a limited effect on compressive strength, it substantially enhanced flexural behaviour, crack resistance, and residual load-bearing capacity.

The plain concrete mixture S0 behaved in a brittle manner, with sudden load loss immediately after crack initiation. In contrast, all fibre-reinforced mixtures demonstrated gradual crack development and increased residual strength. This improvement can be attributed to the fibre-bridging mechanism, in which fibres transfer stresses across cracks and delay crack propagation.

The industrial fibre mixture 2A achieved the best overall mechanical performance. It provided the highest flexural strength, the highest LOP, and the highest residual strengths across all CMOD levels. This behaviour is mainly related to the regular geometry and hooked-end anchorage of the industrial fibres, which increase pull-out resistance and allow the fibres to remain effective even at large crack openings.

The recycled tyre-cord steel fibre mixture 2R demonstrated lower performance than 2A but still showed substantial improvement compared to plain concrete. Recycled fibres increased the tensile strength, improved the LOP, and maintained significant residual strength after cracking. Despite the irregular geometry and variability in size and mechanical properties potentially diminishing the crack-bridging efficiency of individual fibres in comparison to industrial fibres, these traits can enhance fibre dispersion within the matrix and encourage the development of

numerous microcracks. This resultant distributed cracking behaviour improves toughness and increases energy absorption capacity following matrix cracking.

The hybrid mixture 2H3A provided the most balanced behaviour. It combined the strong anchorage of industrial fibres with the dense crack-bridging network formed by recycled fibres. As a result, the hybrid mixture achieved good residual strength across the entire CMOD range and exhibited the most stable post-cracking response. This balanced behaviour is particularly beneficial for structural elements subjected to repeated loading, impact, or large deformations (Wei et al. 2023).

The findings are consistent with the literature on hybrid fibre systems, which indicates that combining different fibre types can optimize mechanical performance by activating multiple reinforcement mechanisms at different stages of cracking. (Banthia and Gupta 2004) demonstrated that hybrid fibres can simultaneously improve crack initiation resistance and post-cracking ductility. Similarly, (Afroughsabet and Ozbakkaloglu 2015) found that hybrid fibre systems produce superior toughness and energy absorption compared to single-fibre systems.

4 Concluding remarks

The experimental results confirm that fibre reinforcement significantly improves the post-cracking behaviour of concrete. While the addition of fibres has usually only a limited effect on compressive strength, it substantially enhanced flexural behaviour, crack resistance, and residual load-bearing capacity.

The plain concrete mixture S0 behaved in a brittle manner, with sudden load loss immediately after crack initiation. In contrast, all fibre-reinforced mixtures demonstrated gradual crack development and increased residual strength. This improvement can be attributed to the fibre-bridging mechanism, in which fibres transfer stresses across cracks and delay crack propagation.

The industrial fibre mixture 2A achieved the best overall mechanical performance. It provided the highest flexural strength, the highest LOP, and the highest residual strengths across all CMOD levels. This behaviour is mainly related to the regular geometry and hooked-end anchorage of the industrial fibres, which increase pull-out resistance and allow the fibres to remain effective even at large crack openings.

The recycled tyre-cord steel fibre mixture 2R demonstrated lower performance than 2A but still showed substantial improvement compared to plain concrete. Recycled fibres increased the tensile strength, improved the LOP, and maintained significant residual strength after cracking. Their irregular shape and heterogeneous geometry may reduce their efficiency compared to industrial fibres, but they also contribute to better fibre dispersion and multiple crack formation.

The hybrid mixture 2H3A provided the most balanced behaviour. It combined the strong anchorage of industrial fibres with the dense crack-bridging network formed by recycled fibres. As a result, the hybrid mixture achieved good residual strength across the entire CMOD range and exhibited the most stable post-cracking response. This balanced behaviour is particularly beneficial for structural elements subjected to repeated loading, impact, or large deformations (Wei et al. 2023).

The findings are consistent with the literature on hybrid fibre systems, which indicates that combining different fibre types can optimize mechanical performance by activating multiple

reinforcement mechanisms at different stages of cracking. (Banthia and Gupta 2004) demonstrated that hybrid fibres can simultaneously improve crack initiation resistance and post-cracking ductility. Similarly, (Afroughsabet and Ozbakkaloglu 2015) found that hybrid fibre systems produce superior toughness and energy absorption compared to single-fibre systems.

5 Acknowledgements

This study was financially supported by the Slovak Research, and Development Agency under the contracts APVV-23-0383, and APVV-19-0490, the Slovak Grant Agency VEGA under the contract N 2/0080/24, the European project Interreg CENTRAL EUROPE 2021-2027 under the contract CE0100390, and Post doc program APD 0222.

6 References

Abdallah, M. A., Elakhras, A. A., Reda, R. M., Sallam, H. E.-D. M., & Moawad, M. (2023). Applicability of CMOD to Obtain the Actual Fracture Toughness of Rightly-Cracked Fibrous Concrete Beams. *Buildings*, *13*(8), 2010. https://doi.org/10.3390/buildings13082010

Afroughsabet, V., & Ozbakkaloglu, T. (2015). Mechanical and durability properties of high-strength concrete containing steel and polypropylene fibers. *Construction and Building Materials*, *94*, 73–82. https://doi.org/10.1016/j.conbuildmat.2015.06.051

Banthia, N., & Gupta, R. (2004). Hybrid fiber reinforced concrete (HyFRC): fiber synergy in high strength matrices. *Materials and Structures*, *37*(10), 707–716. https://doi.org/10.1007/BF02480516

di Prisco, M., Colombo, M., & Dozio, D. (2013). Fibre-reinforced concrete in fib Model Code 2010: principles, models and test validation. *Structural Concrete*, *14*(4), 342–361. https://doi.org/10.1002/suco.201300021

EN 12390-2 Testing hardened concrete - Part 2: Making and curing specimens for strength tests. (2019). Accessed 7 July 2025

EN 12390-7 Testing hardened concrete - Part 7: Density of hardened concrete. (2019). Accessed 7 July 2025

fib Model Code for Concrete Structures (2020). (2024) (1.2.). Lausanne, Switzerland: fib.

Jin, A.-H., Woo, J.-S., Yun, H.-D., Kim, S.-W., Park, W.-S., & Choi, W.-C. (2025). Influence of concrete strength and fiber properties on residual flexural strength of steel fiber-reinforced concrete. *Construction and Building Materials*, *489*, 142366. https://doi.org/10.1016/j.conbuildmat.2025.142366

Kumar, S., Pandey, S. R., & Srivastava, A. K. L. (2014). Determination of double-*K* fracture parameters of concrete using peak load method. *Engineering Fracture Mechanics*, *131*, 471–484. https://doi.org/10.1016/j.engfracmech.2014.09.004

Lawler, J. S., Wilhelm, T., Zampini, D., & Shah, S. P. (2003). Fracture processes of hybrid fiber-reinforced mortar. *Materials and Structures*, *36*(3), 197–208. https://doi.org/10.1007/BF02479558

Pereira, E. B., Fischer, G., & Barros, J. A. O. (2012). Effect of hybrid fiber reinforcement on the cracking process in fiber reinforced cementitious composites. *Cement and Concrete Composites*, *34*(10), 1114–1123. https://doi.org/10.1016/j.cemconcomp.2012.08.004

Pokorska, I., Poński, M., Kubissa, W., Libura, T., Brodecki, A., & Kowalewski, Z. (2023). Computational Fracture Evolution Analysis of Steel-Fiber-Reinforced Concrete Using Concrete Continuous Damage and Fiber Progressive Models. *Materials*, *16*(16), 5635. https://doi.org/10.3390/ma16165635

Test method for metallic fibre concrete - Measuring the flexural tensile strength (limit of proportionality (LOP), residual). (2008).

Tiberti, G., Minelli, F., Plizzari, G. A., & Vecchio, F. J. (2014). Influence of concrete strength on crack development in SFRC members. *Cement and Concrete Composites*, *45*, 176–185. https://doi.org/10.1016/j.cemconcomp.2013.10.004

Wei, J., Li, J., Liu, Z., Wu, C., & Liu, J. (2023). Behaviour of hybrid polypropylene and steel fibre reinforced ultra-high performance concrete beams against single and repeated impact loading. *Structures*, *55*, 324–337. https://doi.org/10.1016/j.istruc.2023.06.036

Xu, S., & Reinhardt, H. W. (1998). Crack Extension Resistance and Fracture Properties of Quasi-Brittle Softening Materials like Concrete Based on the Complete Process of Fracture. *International Journal of Fracture*, *92*(1), 71–99. https://doi.org/10.1023/A:1007553012684

Zhang, J., Stang, H., & Li, V. C. (2001). Crack bridging model for fibre reinforced concrete under fatigue tension. *International Journal of Fatigue*, *23*(8), 655–670. https://doi.org/10.1016/S0142-1123(01)00041-X

Elevated Temperature Performance of 3D-Printed Low-Carbon Alkali-Activated UHPC

Xiao (Arling) Zhao[1], Mehdi Chougan[1], Ravi Ranade[2], Behzad Nematollahi[1]

[1]: School of Mechanical, Aerospace and Civil Engineering, Faculty of Engineering, The University of Sheffield, S1 3JD, United Kingdom.

[2]: Department of Civil, Structural, and Environmental Engineering, University at Buffalo, State University of New York, USA.

Abstract

While ultra-high performance concrete (UHPC) is highly suitable for 3D concrete printing (3DCP), its high cement content compromises the material sustainability credentials of 3DCP. To address this, the authors recently developed a 3D-printed alkali-activated UHPC (A-UHPC) as a low-carbon alternative. The dense microstructures of UHPC and A-UHPC make them vulnerable to explosive spalling at elevated temperatures. While the elevated temperature performance of cast/printed UHPCs has been investigated in the literature, the effect of elevated temperatures on cast/printed A-UHPCs remains unknown. To fill this knowledge gap, this paper reports the elevated temperature performance of the cast and printed A-UHPC developed by the authors. The residual compressive strength, appearance change, mass loss, and microstructure of the specimens exposed to target temperatures of 200, 400, 600, and 800°C were evaluated. Both cast and printed A-UHPC showed increased compressive strength at 200°C and 400°C compared to the control specimens. However, the strength dropped sharply at 600°C and deteriorated severely at 800°C, particularly in the printed specimens. The findings are in good agreement with macroscopic and microstructural analyses.

Keywords

3D concrete printing, Ultra-high performance concrete, Alkali-activated UHPC, Elevated temperature.

1 Introduction

Ultra-high-performance concrete (UHPC) is an ideal printing material for 3D concrete printing (3DCP) because its high tensile strength and toughness reduce the need for conventional steel rebars, its excellent durability ensures long-term performance of printed structures, and its ultra-high compressive strength enables the manufacture of slender structural elements and efficient material utilisation (Arunothayan et al, 2021, 2022). However, the high cement content of UHPC may compromise the sustainability credentials of 3DCP. To tackle this, the authors have recently developed an alkali-activated UHPC (A-UHPC) as a low-carbon alternative. Although the elevated-temperature behaviour of cast and 3D-printed UHPC has been studied extensively (Arunothayan and Sanjayan, 2023; Li et al, 2019), experimental data on the performance of printed A-UHPC at elevated temperatures and its comparison with conventionally cast A-UHPC are limited.

Therefore, this study examines the elevated temperature performance of the recently developed cast and 3D-printed A-UHPC. Specimens were exposed to temperatures up to 800°C. Then, compressive strength testing, macroscopic damage observations, mass loss measurements, and microstructural analyses were conducted to elucidate fabrication-related differences in thermal degradation and structural integrity of specimens.

2 Experimental program

2.1 Materials and specimen preparation

Table 1 shows the mix design of the A-UHPC, which was adopted from the authors' previous study (Zhao et al, 2025). Ground granulated blast-furnace slag (GGBS) and silica fume (SF) were used as precursors. Wollastonite was used as a rheology modifier and micro-reinforcement. Silica sand was used as fine aggregate. The alkali activator consisted of 8 M potassium hydroxide (KOH) solution and potassium silicate (K-Sil) solution (SiO_2 = 23.4 wt% and K_2O = 11.4 wt%). A superplasticiser (SP) and borax decahydrate were incorporated as chemical admixtures to regulate workability and setting behaviour. Copper-coated straight steel fibres (6 mm in length, 0.2 mm in diameter, and 2850 MPa in tensile strength) were used.

Table 1: Mixture design of A-UHPC.

Precursors		**Alkali solutions**		**Sand**	**Water**	**SP**	**Borax**	**Wollastonite**	**Fibre**
GGBS	**SF**	**K-Sil**	**KOH**						
0.80	0.20	0.141	0.095	0.70	0.02	0.01	0.03	0.02	0.02

Note: All values are mass ratios of the total precursors, except fibre content (volume fraction).

The dry ingredients (GGBS, SF, sand, borax, and wollastonite) were first blended in a 20-litre planetary mixer at low speed for 2 min. The activator solution and water were then added gradually, followed by the SP, and mixed at low speed for 3 min and then at medium speed for 1 min. Fibres were gradually added and mixed at low speed for 3 min, then at medium speed for 1 min.

Printing was carried out using a custom-built gantry concrete printer equipped with an auger extruder. Solid slabs with a cross-section of 232 mm × 220 mm were printed in six layers, each 10 mm thick. The printed slabs were covered with plastic sheets and cured for 24 h at ambient

temperature (20 ± 1°C). They were then cut into 50 mm cubes. Heat curing was used in this study, for which the printed and cast cubes were placed in sealed containers and transferred to an oven at 60 °C for 24 h. A cup of water was placed inside the sealed containers, beside the specimens, to generate high humidity and prevent excessive moisture loss from the specimens. At the end of heat-curing, the specimens, still in sealed containers, were removed from the oven and stored at ambient temperature for a further 120 h. The specimens were exposed to elevated temperatures after a total curing period of 7 days from casting/printing. Preliminary trials conducted by the authors showed that further curing of specimens up to 28 days does not increase the compressive strength significantly. This is because the applied heat-curing substantially accelerates early-age reactions in alkali-activated systems (Chen et al, 2023).

An electric furnace was used to expose the specimens to target temperatures of 200, 400, 600, and 800°C at a heating rate of 4°C/min. The same linear heating rate has been adopted in A-UHPC and UHPC studies investigating residual mechanical properties after exposure to elevated temperatures (Huang et al, 2025; Liang et al, 2019). During heating, all specimens were placed in a covered steel container to prevent damage to the furnace if spalling occurred. It should be noted that there was sufficient space between specimens to promote uniform heat distribution. Once the target temperature was reached, it was maintained for 2 h to ensure uniform temperature distribution within the specimens, after which the specimens were left inside the furnace to cool down naturally to room temperature.

2.2 Compressive strength

Compressive strength testing was conducted after the specimens had cooled down to room temperature, with loading applied under displacement control at a rate of 0.6 mm/min. Control specimens (20°C) without thermal exposure were tested at 7 days of age. For printed specimens, compressive tests were performed in three directions: Z, Y, and X (see Figure 1).

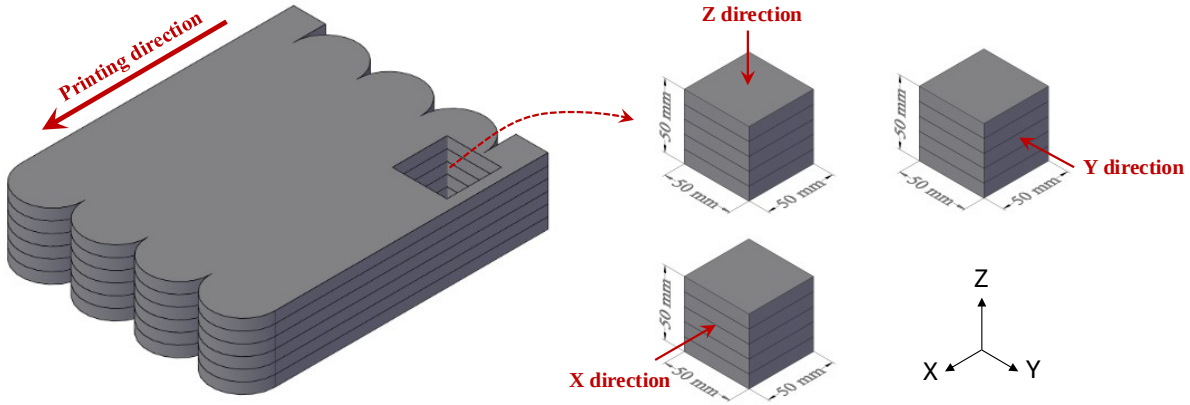


Figure 1: Schematic illustration of the loading directions and specimen extraction from the printed slabs (reproduced from Zhao et al, 2025).

2.3 Microstructural analysis

Fourier transform infrared spectroscopy with attenuated total reflectance (FTIR-ATR) (PerkinElmer Frontier) was employed to characterise the molecular bonding of the reacted phases. The spectra were collected in the range 4000–600 cm^{-1} at a resolution of 4 cm^{-1} with 32 scans. After exposure to the target temperatures, the mortar from each specimen was ground into powder and used for FTIR analysis.

Thermogravimetric analysis (TGA, SDT Discovery 650) was performed to assess dehydration and thermal decomposition of hardened specimens. Around 20 mg of ground mortar material was heated from 30 to 900°C at 10°C/min under an argon atmosphere.

3 Test results and analysis

3.1 Macroscopic response to elevated temperature

3.1.1 Appearance change

Figure 2 shows the macroscopic appearance of cast and 3D-printed specimens after exposure to elevated temperatures. Up to 400°C, both cast and printed specimens retained their original geometry, with no visible damage, including surface cracking, spalling, or interlayer delamination. However, a clear fabrication-dependent damage pattern was observed at higher temperatures. At 600°C, the cast specimens showed a distinct horizontal crack. At 800°C, excessive cracking was observed, but each specimen largely remained intact (i.e., did not split into multiple pieces). By contrast, the printed specimens exhibited pronounced layer separation at both 600°C and 800°C, with partial detachment between adjacent printed layers. This suggests that the printed interfaces were more susceptible to thermal damage, resulting in a greater loss of structural integrity than in the cast specimens.

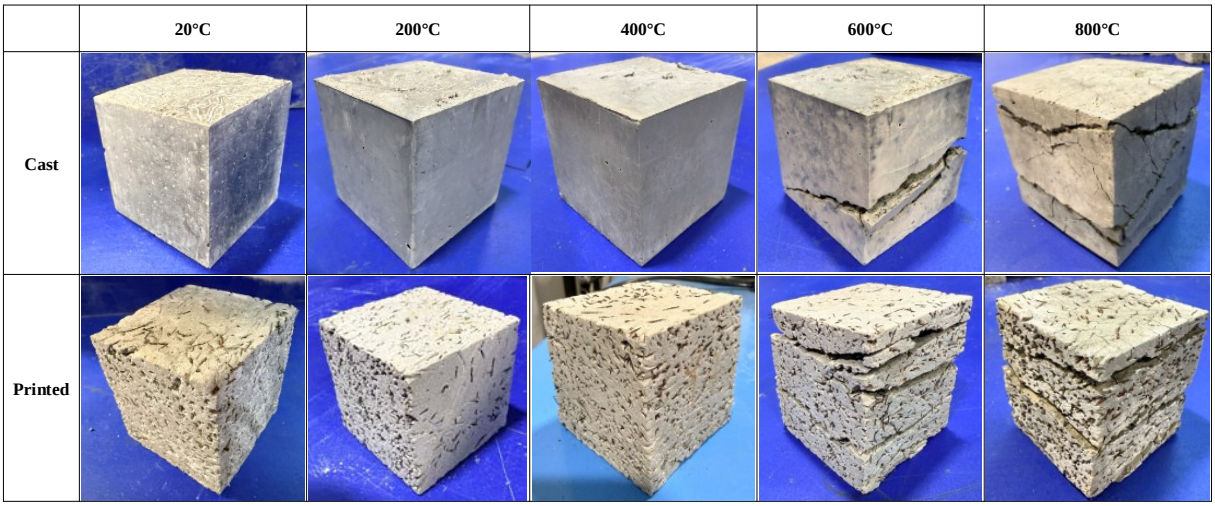


Figure 2: Appearance of specimens subjected to different elevated temperatures.

3.1.2 Mass loss

Figure 3 presents the mass loss of cast and 3D-printed specimens after exposure to elevated temperatures. For the cast specimens, mass loss increased from 3.9% at 200°C to 8.8% at 400°C, with the highest value of 10.3% observed at 600°C. The printed specimens exhibited a similar evolution, increasing from 4.1–4.6% at 200°C to 9.5% at 400°C and reaching maximum values of 11.2–11.5% at 600°C, depending on the testing direction. This temperature-dependent increase is consistent with the progressive evaporation of bound water and dehydration of reaction products commonly reported in geopolymer systems under elevated temperatures (Zhang et al, 2019). At 800°C, the measured mass loss decreased slightly to 9.5% for the cast specimens and 10.2–10.8% for the printed specimens. This reduction suggests that a substantial proportion of thermally removable components had already been released at 600°C, leaving

relatively limited additional mass change during further heating. Notably, across all temperatures, the printed specimens exhibited slightly higher mass loss than the cast specimens, with differences becoming more pronounced at 600°C and 800°C.

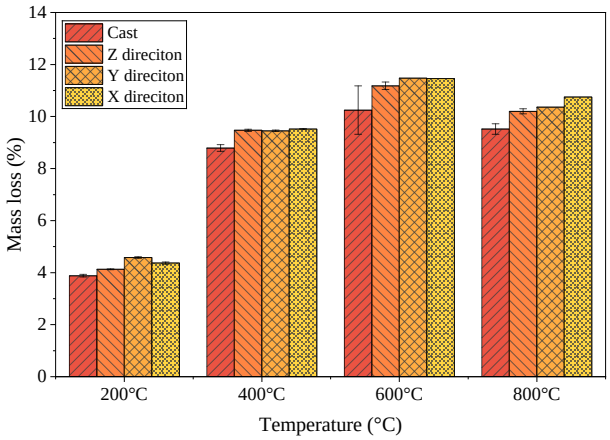


Figure 3: Mass loss in specimens subjected to different elevated temperatures. Note: for Y- and X- directions at 600°C and 800°C exposures, only one sample survived, so no error bar was shown.

3.2 Compressive strength and residual performance

Table 2 presents the residual compressive strengths of the cast and printed specimens after exposure to elevated temperatures, with the control specimens at 20°C as the reference. For both fabrication methods, the residual strength increased at 200°C and 400°C. In the cast specimens, the strength increased by approximately 35% and 61% at 200°C and 400°C, respectively. A similar enhancement was observed in the printed specimens, although the magnitude varied with testing direction. The increase at 200°C was about 26%, 31%, and 31% in Z-, Y-, and X-directions, respectively, while at 400°C they reached approximately 53%, 92%, and 62%. Such strength enhancement is consistent with previous observations in conventional UHPC and alkali-activated materials, where moderate thermal exposure promotes moisture removal and continued polycondensation of reaction products, thereby contributing to matrix densification and strength development (Dong et al, 2024; Tu and Zhang, 2023).

Table 2: Residual compressive strength of specimens exposed to elevated temperature.

Temperature (°C)	**Cast (MPa)**	**Z-direction (MPa)**	**Y-direction (MPa)**	**X-direction (MPa)**
20	129.6 ± 4.6	139.3 ± 1.8	92.0 ± 6.6	116.2 ± 1.5
200	174.9 ± 6.1	176.1 ± 0.8	120.2 ± 9	152.1 ± 0.9
400	208.2 ± 3.5	213.7 ± 5.9	177 ± 3.4	188.8 ± 0.8
600	103.0 ± 7.5	53.0 ± 3.2	N/A	N/A
800	24.3 ± 1.3	15.2 ± 0.4	N/A	N/A

Note: “N/A” denotes that the residual strength of the printed specimens in the Y- and X-directions was not measured as the specimens experienced severe thermal damage at 600°C and 800°C (see Figure 2).

Beyond 400°C, the residual strength decreased in both cast and printed specimens. At 600°C, the residual strength decreased by about 21% in the cast specimens and by about 62% in the printed specimens in the Z-direction, compared to the control specimen at 20°C. The

significantly larger reduction in the Z-direction at 600°C may be due to noticeable interlayer deterioration of the printed specimens (see Figure 2). Similar behaviour was reported for 3D-printed UHPC, where exposure beyond 400°C was reported to deteriorate interlayer bonding, fibre effectiveness, and fibre-matrix interaction (Dong et al, 2024, 2022). At 800°C, the residual strength further decreased by around 81% in the cast specimens and 89% in the printed specimens in the Z-direction, compared to the control specimen at 20°C. It should be noted that the residual strengths of the printed specimens in the Y- and X-directions could not be measured as the printed specimens experienced severe thermal damage at 600°C and 800°C (see Figure 2).

It should be noted that the 3D-printed A-UHPC used in this study showed superior elevated-temperature performance compared to the conventional 3D-printed UHPC. Arunothayan and Sanjayan (2023) reported spalling, visible cracking, and interlayer delamination in 3D-printed UHPC at temperatures above 200°C. In contrast, as shown in Figure 2, the printed A-UHPC specimens retained their integrity with no obvious spalling or interlayer separation at 200°C and 400°C. In addition, as mentioned above, the residual strength of the printed A-UHPC specimens at 200°C and 400°C was higher than that of the control specimens at 20°C. The superior elevated temperature performance of the 3D-printed A-UHPC compared to 3D-printed UHPC is mainly because of the high-temperature resistance of alkali-activated binder compared to conventional cement-based binder, which has been reported in several studies (Liu et al, 2024).

3.3 Microstructural analysis

Figure 4 presents the FTIR spectra of the cast and printed specimens after elevated temperature exposure. Both specimen types displayed a dominant absorption band at approximately 950–1000 cm^{-1}, associated with Si–O–T (T = Si or Al) vibrations in calcium-aluminosilicate hydrate gels (Revathi and Jeyalakshmi, 2021). No additional characteristic peaks appeared after exposure to elevated temperatures, indicating that neither the printing process nor thermal exposure up to 800°C resulted in the formation of new distinct phases.

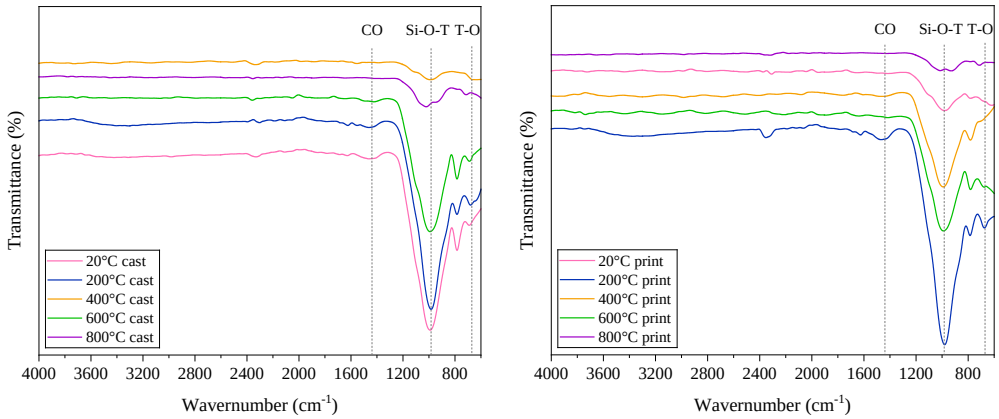


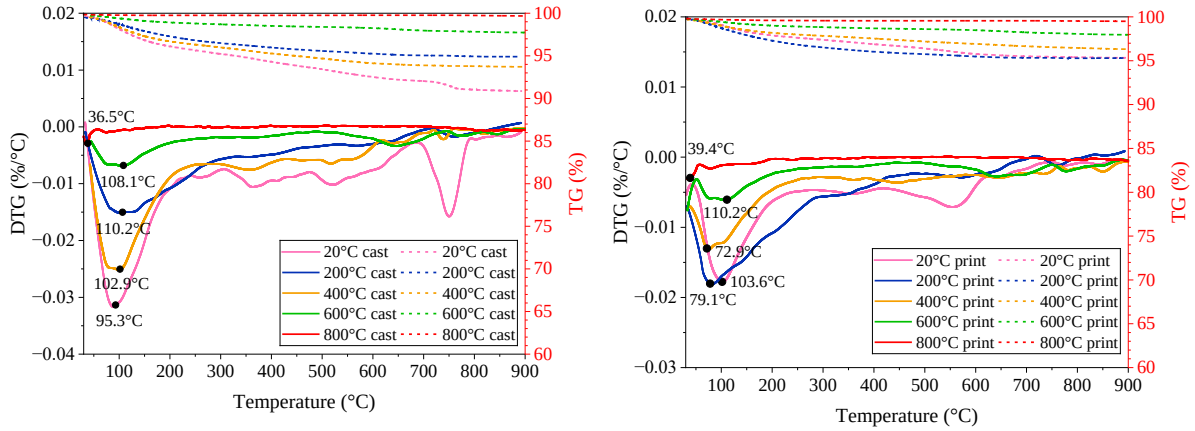
Figure 4: FTIR results of (a) cast and (b) printed specimens under elevated temperatures.

Figure 5 shows the thermogravimetric (TG) mass loss of cast and printed specimens after exposure to different elevated temperatures. A pronounced weight loss below approximately 110°C is observed for all specimens, corresponding to the release of physically bound water

(Duxson et al, 2006). Beyond this low-temperature region, systematic differences emerged among specimens exposed to different elevated temperatures. The total TG mass loss, calculated from the difference between the initial and final weight percentages during TG heating, decreased with increasing prior exposure temperature, from 9.1% at 20°C to 0.4% at 800°C for the cast specimens, and from 5.5% to 0.6% for the printed specimens. This indicates that specimens previously exposed to higher temperatures, particularly 600°C and 800°C, contained fewer thermally removable components during subsequent TG heating.

More noticeable differences between cast and printed specimens occurred at lower exposure temperatures (20–400°C), where the printed specimens showed lower TG mass loss associated with the derivative thermogravimetry (DTG) peaks than the cast specimens. This trend is consistent with the macroscopic mass loss results reported in Section 3.1.2, where the printed specimens had already experienced greater mass reduction during elevated temperature exposure. At higher exposure temperatures (600–800°C), the TG responses of cast and printed specimens become comparable, with only minor differences in total mass loss.

A secondary mass-loss feature is observed only for the control specimens at 20°C. During the subsequent TG heating, this feature appears at 500–600°C for the printed specimen, whereas it shifts to a higher temperature range of 700–800°C for the cast specimen. According to previous classifications of thermal behaviour of alkali-activated materials, mass loss during TG heating between 300 and 700°C has been associated with continued condensation of T-OH groups and related structural reorganisation, while changes between 700–950°C may involve viscous sintering and related decomposition process (Wang et al, 2020). These thermally induced transformations correspond to the temperature range where pronounced mechanical degradation was observed in Section 3.2, particularly for the specimens exposed to 600°C and above. The temperature shift of the secondary feature between the cast and printed specimens at 20°C suggests that the thermal evolution of the remaining mass loss process differs between the two fabrication methods, although the underlying mechanism cannot be uniquely identified from the present data.



(a) (b)

Figure 5: DTG and TG results of (a) cast and (b) printed specimens under elevated temperatures.

4 Concluding remarks

The elevated temperature resistance of cast and 3D-printed A-UHPC was evaluated in this study. The following conclusions are drawn:

- Both cast and printed specimens remained visually intact up to 400°C. At 600°C and 800°C, severe thermal damage developed, with printed specimens showing pronounced interlayer separation and loss of structural integrity.
- Mass loss increased from 200°C to 600°C and decreased slightly at 800°C for both cast and printed specimens. Printed specimens showed slightly higher mass loss than cast specimens, suggesting greater moisture release during heating.
- Up to 400°C, the residual compressive strength of both cast and printed specimens was higher than the strength of the control specimens at 20°C. The maximum residual strength was observed at 400°C, with an increase of 61% in the cast specimens and 53–92% in the printed specimens, depending on the testing direction, compared to the control specimens.
- Severe strength degradation occurred at 600°C and 800°C. At 600°C, the compressive strength decreased by around 21% for cast specimens and 62% for printed specimens in the Z-direction relative to the control specimens. Exposure to 800°C resulted in an 81–89% loss of strength in cast and printed specimens.
- At 600°C and 800°C, fabrication- and testing direction-dependent thermal damage was observed. The cast specimens and the printed specimens in the Z-direction did not split into multiple pieces. However, the printed specimens in the X- and Y-directions exhibited significant spalling, interlayer separation, and loss of structural integrity, consistent with the observed deterioration in strength.
- FTIR and TGA results indicated no formation of new distinct phases after elevated temperature exposure up to 800°C. Increasing exposure temperature progressively reduced the amount of thermally removable components, while differences between cast and printed specimens became less pronounced after exposure to 600–800°C.

5 Acknowledgements

The authors greatly acknowledge the support provided by the Royal Society International Exchanges 2023 award (IES\R3 \233378), as well as the Royal Society International Science Partnerships Fund - International Collaboration Award 2023 (ICAO\R1\231045). The authors are also grateful to Master Builders Solutions for providing the superplasticiser and to Sibelco for supplying the wollastonite used in this study.

6 References

Arunothayan, Arun R., Behzad Nematollahi, Ravi Ranade, Shin Hau Bong, Jay G. Sanjayan, and Kamal H. Khayat. 2021. ‘Fiber Orientation Effects on Ultra-High Performance Concrete Formed by 3D Printing’. *Cement and Concrete Research*, 143: 106384. doi:10.1016/j.cemconres.2021.106384

Arunothayan, Arun R., Behzad Nematollahi, Ravi Ranade, Kamal H. Khayat, and Jay G. Sanjayan. 2022. ‘Digital Fabrication of Eco-Friendly Ultra-High Performance Fiber-

Reinforced Concrete'. *Cement and Concrete Composites*, 125: 104281. doi:10.1016/j.cemconcomp.2021.104281

Arunothayan, Arun R., and Jay G. Sanjayan. 2023. 'Elevated Temperature Effects on 3D Printed Ultra-High Performance Concrete'. *Construction and Building Materials*, 367: 130241. doi:10.1016/j.conbuildmat.2022.130241

Chen, Weiwei, Bo Li, Ming-Zhi Guo, Juan Wang, and Yung-Tsang Chen. 2023. 'Impact of Heat Curing Regime on the Compressive Strength and Drying Shrinkage of Alkali-Activated Slag Mortar'. *Developments in the Built Environment*, 14: 100123. doi:10.1016/j.dibe.2023.100123

Dong, Liang, Yekai Yang, Zhongxian Liu, Quanchang Ren, Jun Li, Yan Zhang, and Chengqing Wu. 2022. 'Microstructure and Mechanical Behaviour of 3D Printed Ultra-High Performance Concrete after Elevated Temperatures'. *Additive Manufacturing*, 58: 103032. doi:10.1016/j.addma.2022.103032

Dong, Liang, Yekai Yang, Zhongxian Liu, Yan Zhang, and Chengqing Wu. 2024. 'Interface Bonding Characteristics of 3D Printed Ultra-High Performance Concrete after Elevated Temperatures'. *Journal of Building Engineering*, 93: 109801. doi:10.1016/j.jobe.2024.109801

Duxson, Peter, Grant C. Lukey, and Jannie S.J. Van Deventer. 2006. 'Thermal Evolution of Metakaolin Geopolymers: Part 1 – Physical Evolution'. *Journal of Non-Crystalline Solids*, 352(52–54): 5541–55. doi:10.1016/j.jnoncrysol.2006.09.019

Huang, Junjie, Jun Li, Ruizhe Shao, and Chengqing Wu. 2025. 'Effect of High Temperature and Cooling Method on Compression and Fracture Properties of Ultra-High Performance Geopolymer Concrete'. *Journal of Building Engineering*: 112433. doi:10.1016/j.jobe.2025.112433

Li, Ye, Kang Hai Tan, and En-Hua Yang. 2019. 'Synergistic Effects of Hybrid Polypropylene and Steel Fibers on Explosive Spalling Prevention of Ultra-High Performance Concrete at Elevated Temperature'. *Cement and Concrete Composites*, 96: 174–81. doi:10.1016/j.cemconcomp.2018.11.009

Liang, Xiangwei, Chengqing Wu, Yekai Yang, and Zhongxian Li. 2019. 'Experimental Study on Ultra-High Performance Concrete with High Fire Resistance under Simultaneous Effect of Elevated Temperature and Impact Loading'. *Cement and Concrete Composites*. doi:10.1016/j.cemconcomp.2019.01.017

Liu, Yuzhong, Xiang Hu, Yunxing Du, Behzad Nematollahi, and Caijun Shi. 2024. 'A Review on High-Temperature Resistance of Geopolymer Concrete'. *Journal of Building Engineering*, 98: 111241. doi:10.1016/j.jobe.2024.111241

Revathi, T., and R. Jeyalakshmi. 2021. 'Fly Ash–GGBS Geopolymer in Boron Environment: A Study on Rheology and Microstructure by ATR FT-IR and MAS NMR'. *Construction and Building Materials*, 267: 120965. doi:10.1016/j.conbuildmat.2020.120965

Tu, Wenlin, and Mingzhong Zhang. 2023. 'Behaviour of Alkali-Activated Concrete at Elevated Temperatures: A Critical Review'. *Cement and Concrete Composites*, 138: 104961. doi:10.1016/j.cemconcomp.2023.104961

Wang, Yaguang, Xiaoming Liu, Wei Zhang, Zepeng Li, Yuliang Zhang, Yong Li, and Yongyu Ren. 2020. 'Effects of Si/Al Ratio on the Efflorescence and Properties of Fly Ash Based Geopolymer'. *Journal of Cleaner Production*, 244: 118852. doi:10.1016/j.jclepro.2019.118852

Zhang, Hongen, Lang Li, Tao Long, Prabir Kumar Sarker, Xiaoshuang Shi, Gaochuang Cai, and Qingyuan Wang. 2019. 'The Effect of Ordinary Portland Cement Substitution on the

Thermal Stability of Geopolymer Concrete'. *Materials*, 12(16): 2501. doi:10.3390/ma12162501

Zhao, Xiao (Arling), Behzad Nematollahi, Mehdi Chougan, Doo-Yeol Yoo, and Hong Wong. 2025. 'Development of 3D-Printable Alkali-Activated UHPC for Additive Construction'. doi:10.2139/ssrn.5538120

Curing effect on compressive strength of UHPC incorporation Copper Slag

Mohammad Mohsin Khan[1], Subhan Ahmad[2], Faisal Mukhtar3, Mohammed A. Al-Osta[3]

[1]IRC for Construction and Building Materials, King Fahd University of Petroleum & Minerals, Dhahran-31261, Saudi Arabia

[2]Faculty of Civil Engineering, Universiti Teknologi Malaysia, Johor Bahru- 81310, Malaysia

[3]Department of Civil and Environmental Engineering, King Fahd University of Petroleum & Minerals, Dhahran-31261, Saudi Arabia

Abstract

Present experimental study evaluates the compressive strength performance of UHPC incorporating varying percentages of copper slag (10%, 20%, and 30%) compared with a control mix under different curing regimes: steam curing for 48 hours, heat curing for 48 hours, water curing for 7 days, and water curing for 28 days. The objective was to assess the influence of copper slag (CS) content and curing method on compressive strength development. The results indicate that curing regime significantly affects compressive strength across all UHPC mixes. The control mix achieved the highest overall strength, recording 146.54 MPa under steam curing, 125.97 MPa under heat curing, 107.38 MPa after 7 days of water curing, and 135.73 MPa after 28 days of water curing. Incorporation of CS reduced strength relative to the control; however, performance varied with replacement level and curing method. Under steam curing, compressive strengths of 101.93 MPa, 115.76 MPa, and 121.4 MPa were obtained for CS-10%, CS-20%, and CS-30%, respectively, indicating improved performance at higher replacement levels. Conversely, heat curing resulted in a marked reduction in strength as CS content increased, with values decreasing to 67.82 MPa, 59.66 MPa, and 48.25 MPa for CS-10%, CS-20%, and CS-30%, respectively. Water curing for 28 days significantly enhanced strength development compared to 7-day curing for all mixes. The CS-20% mix achieved 119.31 MPa at 28 days, closely approaching the control mix, while CS-30% reached 107.35 MPa. Overall, steam curing and extended water curing proved more effective than heat curing in promoting strength gain in CS-modified UHPC. The findings suggest that CS replacement levels between 20% and 30%, when combined with appropriate curing methods, can yield satisfactory compressive strength performance suitable for structural applications.

Keywords

Ultra-high-performance concrete, Copper slag content effect, Compressive strength, curing effect

1 Introduction

Ultra-high-performance concrete (UHPC) is an advanced cementitious material characterized by exceptional compressive strength, superior durability, and a highly dense microstructure achieved through optimized particle packing and low water-to-binder ratios. Despite these advantages, UHPC typically contains a high cement content, leading to increased cost and significant carbon emissions. Consequently, recent research has focused on incorporating industrial by-products such as copper slag (CS) to enhance sustainability without compromising performance. Copper slag, a by-product of copper smelting, is rich in silica, iron oxide, and alumina, and exhibits a glassy structure, making it a promising candidate as a supplementary cementitious material or filler in UHPC systems (Gu et al., 2023; Tahwia et al., 2022).

The incorporation of copper slag in UHPC has been widely studied in recent years, primarily focusing on its influence on mechanical and durability properties. Finely ground copper slag particles can act as micro-fillers, improving particle packing density and reducing pore volume, which contributes to enhanced matrix densification. Several studies have reported that moderate replacement levels (typically 10–20%) can maintain or slightly improve compressive strength due to improved packing and reduced porosity (Edwin et al., 2022; Moura et al., 2007). However, higher replacement levels often lead to a reduction in compressive strength due to the dilution effect, where the reduction in cement content decreases the formation of calcium silicate hydrate (C–S–H) gel, the primary strength-contributing phase (Bahmani et al., 2024; Al-Jabri et al., 2011).

In addition to material composition, the curing regime plays a crucial role in governing the mechanical performance of UHPC. Conventional water curing allows gradual hydration and development of a homogeneous microstructure, resulting in high long-term strength. In contrast, thermal curing methods, such as heat curing and steam curing at elevated temperatures (60–90 °C), are commonly employed to accelerate hydration reactions and enhance early-age strength development. Studies have shown that elevated curing temperatures significantly increase the degree of hydration and promote the formation of dense C–S–H gel, leading to improved compressive strength at early ages (Arora et al., 2019; Yoo & Banthia, 2016). However, excessive temperature exposure may cause rapid moisture loss, internal thermal stresses, and microcracking, which can negatively affect long-term mechanical properties (Kang et al., 2020; Xu et al., 2023).

The interaction between copper slag incorporation and curing conditions is particularly important in UHPC systems. Copper slag exhibits relatively low early-age pozzolanic reactivity, which limits its contribution to strength development under normal curing conditions. However, elevated temperature curing can partially activate its latent hydraulic and pozzolanic properties, enhancing its reactivity and contribution to the formation of secondary hydration products such as C–A–S–H gel (Wang et al., 2025; He et al., 2026). Steam curing, in particular, has been reported to improve hydration kinetics and refine pore structure, leading to improved compressive strength compared to standard curing (Xu et al., 2022). Conversely, dry heat curing may result in non-uniform microstructures and reduced mechanical performance due to accelerated but incomplete hydration (He et al., 2026).

Recent studies have further highlighted the importance of optimizing both copper slag content and curing regime to achieve balanced performance. For instance, Gu et al. (2023) demonstrated that copper slag incorporation improved packing density and microstructural compactness in UHPC, while maintaining acceptable compressive strength at moderate replacement levels.

Similarly, Arunachelam (2022) reported that copper slag significantly enhanced the performance of ultra-high-performance geopolymer systems through improved densification and reduced porosity. Other studies have emphasized that optimal curing conditions can mitigate the adverse effects of cement dilution by enhancing hydration and activating supplementary materials (Lin et al., 2009; Mohaisen et al., 2023).

Overall, the current literature suggests that both copper slag content and curing regime are interdependent factors influencing the compressive strength of UHPC. While copper slag contributes to sustainability and improved particle packing, its effectiveness depends strongly on curing conditions and replacement levels. Therefore, a systematic investigation of curing effects on copper slag-incorporated UHPC is essential to develop optimized, high-performance, and sustainable concrete systems.

2 Experimental program

2.1 Raw material and mix design

The materials used in the UHPC mixtures included Ordinary Portland Cement (OPC Type I), silica fume, dune sand, fibers, and a high-range water-reducing admixture. The OPC complied with ASTM C150 specifications and exhibited 7- and 28-day compressive strengths of 29.97 and 37.76 MPa, respectively. Silica fume was incorporated to enhance particle packing and pozzolanic reactivity. Locally available dune sand from Saudi Arabia was used as fine aggregate, characterized by a specific gravity of 2.53, low water absorption (0.4%), and smooth, rounded particles that improve workability. A polycarboxylate-based, chloride-free superplasticizer with 65% water content and specific gravity of 1.095 was used to achieve the desired flowability. Additionally, 2% of steel fiber were incorporated to improve mechanical, see Fig. 1(a). The UHPC mix design was optimized with a binder content of 850 kg/m³, consisting of 680 kg/m³ OPC and 170 kg/m³ silica fume, with a water content of 195.5 kg/m³, corresponding to a water-to-binder ratio of 0.23. The superplasticizer dosage was maintained at 2.5% of the binder content. The copper slag replaced with cement in the UHPC mixes by 10%, 20% and 30% by volume, see Fig. 1(b). The mixing process of all dry constituents and casting process of fresh UHPC containing the copper slag followed as described in the khan et al., (2025). The 50 × 50 × 50 mm cube specimen were casted and demold after 24 hrs. for various type of curing.



Figure 1. (a) Steel fibers (b) Copper slag

2.2 Testing Procedure

After casting, all 50 × 50 × 50 mm cube specimens were covered with plastic sheets to minimize moisture loss and stored at room temperature for 24 hours prior to demoulding. Following

demoulding, three different curing regimes were adopted. For water curing, the specimens were immediately immersed in a curing tank containing clean potable water maintained at 25 ± 2 °C. The cubes were fully submerged to ensure uniform hydration, and the water level was regularly monitored to prevent exposure of specimen surfaces. The specimens were cured for the designated periods of 7 and 28 days before testing. For high-temperature (heat) curing, the demoulded specimens were placed in an electric furnace preheated to 80 °C, see Fig. 2(a). The temperature was maintained constant throughout the curing duration of 48 hours. After completion, the specimens were removed and allowed to cool gradually to ambient laboratory conditions to avoid thermal shock prior to testing. For steam curing, the demoulded specimens were transferred to a steam curing chamber. The temperature was gradually increased to 80 °C to prevent thermal cracking and maintained for 48 hours under controlled humidity conditions, see Fig. 2(b). Continuous steam was supplied to ensure a saturated environment during curing. After steam curing, the specimens were allowed to cool slowly to room temperature to prevent microcracking caused by sudden temperature variations before testing. The compressive strength test was performed using a 1000 kN digital compression testing machine in accordance with ASTM C39, see Fig. 2(c). Load was applied at a constant rate of 0.2 MPa/s. Three specimens per mix were tested, and average strength with standard deviation was reported.



Figure 2. (a) High temperature curing (b) Steam curing (c) Compression testing

3 Test Results

3.1 Copper slag content effect

The effect of copper slag (CS) powder as a partial cement replacement on the compressive strength of UHPC at 28 days water curing is presented in Fig. 3. The control mixture without copper slag achieved a compressive strength of 135.73 MPa, representing the highest strength among all mixtures. When cement was replaced with copper slag powder (passing 90 μm sieve), the compressive strength decreased to 110.92 MPa, 119.31 MPa, and 107.35 MPa for CS-10%, CS-20%, and CS-30%, respectively. Compared with the control mix, the compressive strength reductions were approximately 18.27%, 12.10%, and 20.91% for 10%, 20%, and 30% copper slag replacement, respectively. Although all copper slag mixtures exhibited lower compressive strength than the control UHPC, the CS-20% mixture demonstrated relatively improved performance compared with CS-10%, indicating that moderate incorporation of copper slag may partially compensate for the loss of cement through microstructural densification effects.

The reduction in compressive strength with increasing copper slag content can primarily be attributed to the dilution effect associated with cement replacement. Cement hydration produces calcium silicate hydrate (C–S–H) gel, which is the primary phase responsible for strength development in UHPC matrices. When cement is partially replaced with copper slag, the quantity of reactive clinker minerals available for hydration decreases, thereby reducing the formation of hydration products and leading to a decline in compressive strength. In addition,

copper slag generally exhibits limited pozzolanic reactivity compared with highly reactive supplementary cementitious materials such as silica fume or metakaolin, particularly at early ages, which further contributes to the reduction in compressive strength when it replaces cement in the binder system. Previous studies performed by Abdalla et al., (2023) and Eqwin et al., (2022) have similarly reported that replacing cement with copper slag tends to reduce mechanical strength due to the lower reactivity and slower hydration characteristics of the slag particles.

Despite this dilution effect, the relatively higher compressive strength observed for the CS-20% mixture compared to CS-10% can be attributed to the micro-filler and particle packing effect of finely ground copper slag particles. Copper slag particles passing the 90 μm sieve can act as fine fillers within the UHPC matrix, improving particle packing density and reducing micro-voids in the cement paste. This improved packing leads to a denser microstructure and enhanced interfacial bonding between hydration products and fine particles, which partially compensates for the reduction in cement content. Similar observations have been reported by Silva et al., (2024) and Eqwin et al., (2022) in recent studies where copper slag used as a supplementary cementitious material contributed to improved matrix densification and pore structure refinement at moderate replacement levels.

However, when the replacement level increased to 30%, the compressive strength showed the most significant reduction (≈21%) compared with the control mixture. At higher replacement levels, the dilution effect becomes dominant, as the amount of cement available for hydration becomes insufficient to generate an adequate quantity of C–S–H gel. Consequently, the matrix becomes relatively weaker and the overall microstructure becomes more porous, leading to reduced compressive strength. Similar trends have been reported in previous investigations (Eqwin et al., 2022; Wang et al., 2021) where excessive incorporation of copper slag resulted in a reduction in mechanical strength due to decreased binder reactivity and increased porosity.

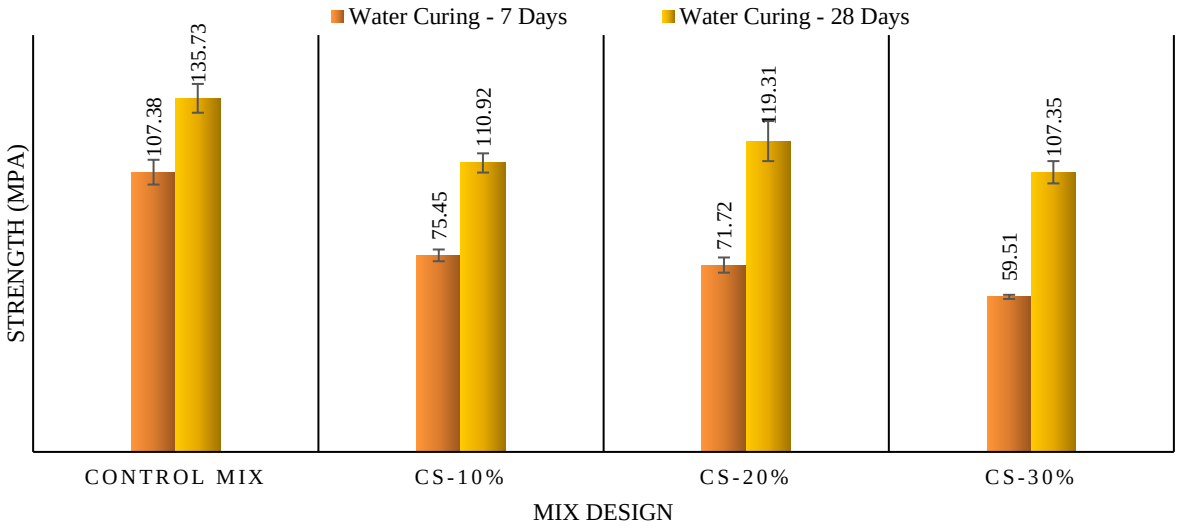


Figure 3. Compressive strength of UHPC with copper slag after 28 days water curing

3.2 Heat curing effect

Fig. 4 illustrates the effect of high-temperature heat curing (80 °C for 48 h) on the compressive strength of UHPC mixtures containing copper slag (CS) as a partial cement replacement, compared with the control UHPC subjected to 28-day water curing. The control mixture under

water curing achieved a compressive strength of 135.73 MPa, while the same mixture subjected to heat curing exhibited a compressive strength of 125.97 MPa, representing a 7.19 % reduction relative to the water-cured control specimen. This slight decrease suggests that although elevated temperature accelerates hydration reactions and promotes early strength development, excessive temperature may cause rapid moisture evaporation and non-uniform hydration, which can lead to microstructural heterogeneity and minor microcracking within the UHPC matrix.

When cement was partially replaced by 90 µm copper slag powder, the compressive strength of the heat-cured UHPC mixtures decreased significantly compared with the water-cured control mix. The compressive strengths recorded for CS-10%, CS-20%, and CS-30% mixtures under heat curing were 67.82 MPa, 59.66 MPa, and 48.25 MPa, respectively. Compared with the 28-day water-cured control mixture (135.73 MPa), the compressive strength reductions were approximately 50.03 %, 56.05 %, and 64.45 % for 10 %, 20 %, and 30 % copper slag replacement levels, respectively. These results clearly indicate that the combined influence of cement dilution and elevated curing temperature significantly affects the strength development of UHPC containing copper slag (Eqwin et al., 2022). Furthermore, the compressive strength progressively decreases with increasing copper slag content, demonstrating that higher replacement levels negatively influence the mechanical performance of UHPC under heat curing conditions.

The effect of heat curing at elevated temperature further amplifies this behavior. High-temperature curing accelerates the hydration reactions of cement and promotes early strength development, but excessive temperature can produce a less uniform microstructure due to rapid hydration and internal thermal stresses. Such conditions may result in micro-cracks or increased porosity within the cement matrix, thereby reducing compressive strength compared with specimens cured under standard water curing conditions (Mohaisen et al., 2023).

Furthermore, the reduced compressive strength of copper slag mixtures under heat curing can also be associated with the limited secondary hydration of copper slag particles. While finely ground copper slag can act as a micro-filler that improves particle packing density, the reduced cement content limits the formation of sufficient hydration products to develop a dense matrix. Similar observations have been reported in UHPC studies where copper slag was used as a cementitious replacement material, indicating that excessive replacement levels may reduce mechanical strength due to the dilution effect and limited binder reactivity (Eqwin et al., 2022).

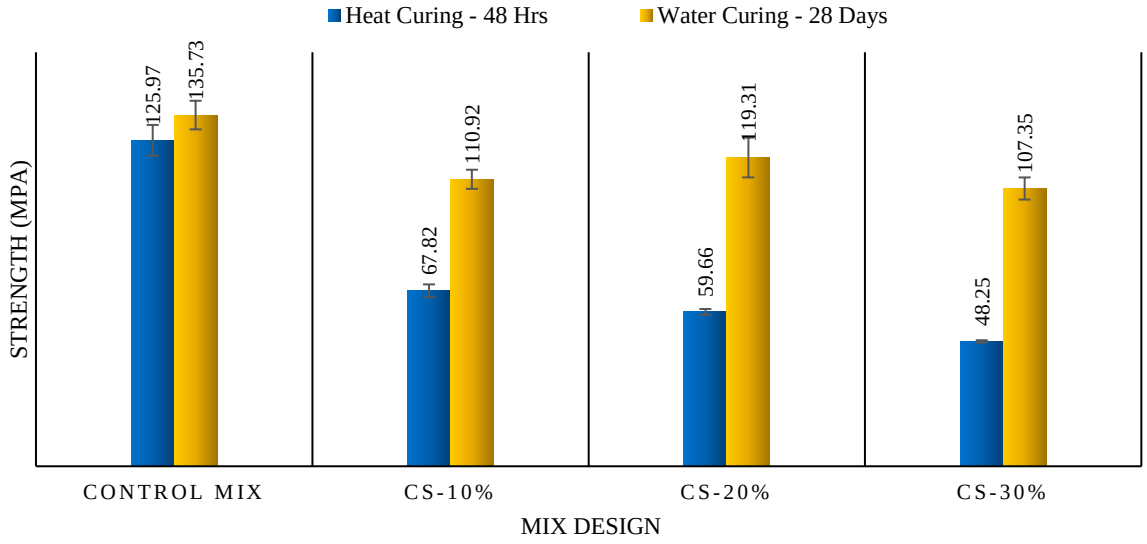


Figure 4. Compressive strength of UHPC with copper slag after 48 hrs of heat curing

3.3 Steam curing effect

The effect of steam curing (80 °C for 48 h) on the compressive strength of UHPC mixtures incorporating copper slag (CS) as partial cement replacement is illustrated in Fig. 5. For comparison, the control UHPC under conventional 28-day water curing achieved a compressive strength of 135.73 MPa, whereas the same mixture subjected to steam curing reached 146.54 MPa, representing an increase of approximately 7.97 %. This improvement indicates that steam curing promotes rapid hydration and enhances early-age strength development in UHPC. High-temperature curing accelerates the hydration of cement and supplementary materials, leading to increased formation of calcium silicate hydrate (C–S–H) gel and improved microstructural densification. Previous studies have reported that elevated-temperature steam curing can significantly enhance the hydration degree of UHPC and reduce porosity, thereby improving compressive strength compared with standard curing conditions (Xu et al., 2022 & Mohaisen et al., 2023).

When cement was partially replaced with copper slag powder (90 µm passing), the compressive strength values under steam curing were 101.93 MPa, 115.76 MPa, and 121.40 MPa for CS-10%, CS-20%, and CS-30%, respectively. Compared with the 28-day water-cured control mixture (135.73 MPa), the compressive strength decreased by approximately 24.90 %, 14.71 %, and 10.56 % for CS-10%, CS-20%, and CS-30%, respectively. Although the compressive strength values are lower than the water-cured control mixture, the results demonstrate that steam curing significantly improves the performance of copper slag mixtures compared with typical early-age curing conditions. Among the copper slag mixtures, the CS-30% mixture exhibited the highest compressive strength under steam curing, suggesting that elevated temperature promotes the activation of copper slag particles and enhances their filler and secondary reaction effects.

The observed trend can be explained by two main mechanisms: accelerated hydration and micro-filler effects. Steam curing at elevated temperature accelerates cement hydration and increases the rate of formation of hydration products such as C–S–H and calcium hydroxide, which contribute to the early densification of the UHPC matrix. At the same time, finely ground copper slag particles act as micro-fillers, improving particle packing density and reducing pore volume within the matrix. These mechanisms collectively enhance the compactness of the microstructure and partially compensate for the reduction in cement content. Xu et al., (2022) has shown that steam curing reduces pore size distribution and improves the hydration degree in UHPC, leading to higher compressive strength and improved matrix integrity.

However, the reduction in compressive strength compared with the water-cured control mixture is primarily associated with the dilution effect caused by cement replacement. Copper slag has relatively lower pozzolanic reactivity than cement, and therefore the replacement of cement reduces the amount of reactive binder available for hydration. Consequently, the formation of C–S–H gel decreases with increasing copper slag content. Nevertheless, under steam curing conditions, the elevated temperature partially activates the latent hydraulic or pozzolanic potential of copper slag particles, which explains why the strength reduction decreases as the replacement level increases from 10 % to 30 %.

These findings are consistent with previous studies (Qian et al., 2025 & Hamada et al., 2022) that have reported improved early-age strength development in UHPC subjected to steam

curing due to accelerated hydration kinetics and reduced porosity. At the same time, excessive replacement of cement with less reactive materials may still lead to a reduction in ultimate compressive strength due to the dilution of the cementitious matrix.

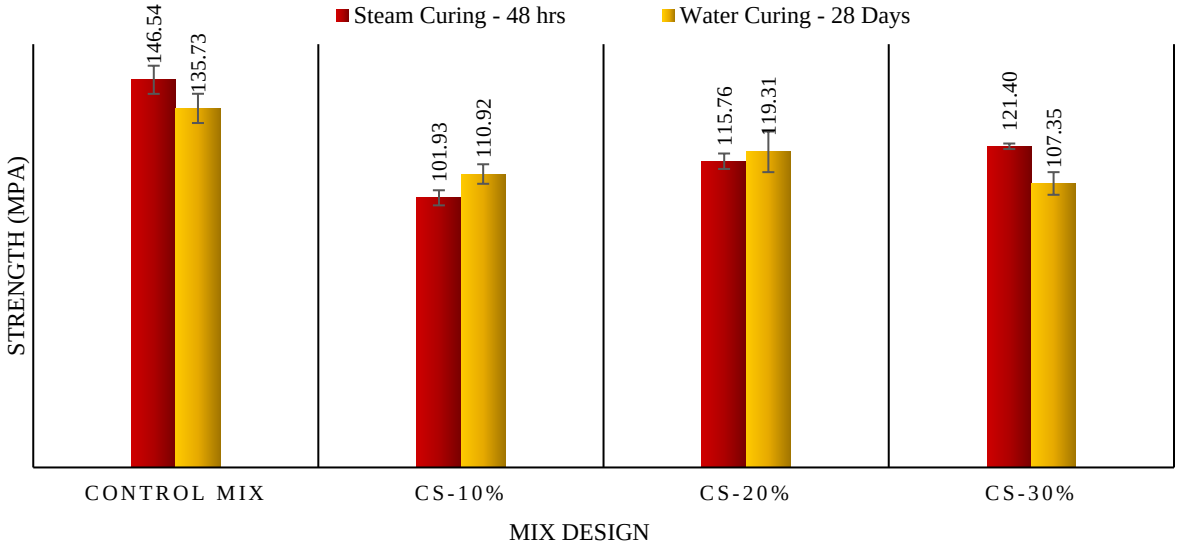


Figure 5. Compressive strength of UHPC with copper slag after 48 hrs of steam curing

4 Concluding remarks

- Copper slag incorporation slightly reduces UHPC compressive strength subjected to water curing; however, moderate replacement (≈20%) maintains relatively high strength due to improved particle packing and matrix densification, indicating an optimal balance between mechanical performance and sustainability through reduced cement consumption.

- Heat curing at 80 °C for 48 h reduces compressive strength of copper slag UHPC, especially at higher replacements, as limited pozzolanic reactivity and cement dilution hinder microstructural development; lower replacement levels (≈10%) are more suitable under elevated temperature curing conditions.

- Steam curing at 80 °C for 48 h enhances compressive strength of UHPC, including copper slag mixtures, by accelerating hydration and densifying the matrix, indicating that moderate to high replacement levels can still achieve high strength under accelerated curing regimes.

Acknowledgements

Authors gratefully acknowledge the financial support provided by Interdisciplinary Research Centre for Construction and Building Materials (IRC-CBM) for carrying out the present study..

5 References

Abdalla, T. A., Omer, E. I., Khalifa, N. M., Albasheir, M. A., Abdulrahman, H. M., & Abdown, A. G. (2023). Effect of copper slag on workability and compressive strength of concrete. *Seybold Rep*, 18, 2657-2669.

Al-Jabri, K. S., Al-Saidy, A. H., & Taha, R. (2011). Effect of copper slag as a fine aggregate on the properties of cement mortars and concrete. *Construction and Building Materials*, 25(2), 933-938.

Arora, A., Almujaddidi, A., Kianmofrad, F., Mobasher, B., & Neithalath, N. (2019). Material design of economical ultra-high performance concrete (UHPC) and evaluation of their properties. *Cement and Concrete Composites*, 104, 103346.

Arunachelam, N., Maheswaran, J., Chellapandian, M., Murali, G., & Vatin, N. I. (2022). Development of high-strength geopolymer concrete incorporating high-volume copper slag and micro silica. *Sustainability*, 14(13), 7601.

Bahmani, H., Mostafaei, H., Santos, P., & Fallah Chamasemani, N. (2024). Enhancing the mechanical properties of Ultra-High-Performance Concrete (UHPC) through silica sand replacement with steel slag. *Buildings*, 14(11), 3520.

Edwin, R. S., Gruyaert, E., & De Belie, N. (2022). Valorization of secondary copper slag as aggregate and cement replacement in ultra-high performance concrete. *Journal of Building Engineering*, 54, 104567.

Gu, X., Sun, W., & Ai, Y. (2023). Application of Copper Slag in Ultra-high Performance Concrete: Gu, Sun, and Ai. Jom, 75(4), 1059-1067.

Hamada, H., Alattar, A., Tayeh, B., Yahaya, F., & Almeshal, I. (2022). Influence of different curing methods on the compressive strength of ultra-high-performance concrete: A comprehensive review. *Case Studies in Construction Materials*, 17, e01390.

He, K., Liu, C., Zhong, L., Tang, J., & Hui, D. (2026). Microstructural regulation and multiscale performance evolution of ultra-high performance concrete incorporating copper slag. *Construction and Building Materials*, 506, 144861.

Kang, H., & Moon, J. (2021). Secondary curing effect on the hydration of ultra-high-performance concrete. *Construction and Building Materials*, 298, 123874.

Khan, M. M., Ahmad, S., Al-Huri, M., Mukhtar, F., & Al-Osta, M. A. (2026). Mechanical behaviour and impact response of ultra-high-performance concrete incorporating steel and polypropylene fibers. *Next Materials*, 10, 101436.

Li, X., Zhang, Y., & Wang, Z. (2023). Influence of curing regimes on UHPC strength. *Case Studies in Construction Materials*, 18, e01921.

Lin, F., & Meyer, C. (2009). Hydration kinetics modeling of Portland cement considering the effects of curing temperature and applied pressure. *Cement and Concrete Research*, 39(4), 255-265.

Mohaisen, K. O., Ahmad, S., Adekunle, S. K., Maslehuddin, M., & Al-Dulaijan, S. U. (2023). Effect of Curing Methods on the Performance of UHPC. *Arabian Journal for Science and Engineering*, 48(10), 13791-13805.

Moura, W. A., Gonçalves, J. P., & Lima, M. B. L. (2007). Copper slag waste as a supplementary cementing material to concrete. *Journal of materials science*, 42(7), 2226-2230.

Qian, Y., Yang, D., Zhao, J., Mao, X., Ren, G., & Cao, Z. (2025). Development of cementless alkali-activated ultra-high performance concrete under various steam curing regimes: Mechanical properties, permeability, and microstructure. *Journal of Building Engineering*, 101, 111857.

Silva, Y. F., Burbano-Garcia, C., Araya-Letelier, G., & Gonzalez, M. (2024). Short-and long-term experimental performance of concrete with copper slag: Mechanical and physical properties assessment. *Case Studies in Construction Materials*, 20, e03302.

Tahwia, A. M., Essam, A., Tayeh, B. A., & Abd Elrahman, M. (2022). Enhancing sustainability of ultra-high performance concrete utilizing high-volume waste glass powder. *Case Studies in Construction Materials*, 17, e01648.

Turkane, S. D., Chouksey, S. K., Nawale, A. V., Sahu, R. T., Gayake, S. B., & Gunjal, S. M. (2024). Utilization of copper slag as fine sand replacement in concrete: a response surface methodology approach. *Discover Civil Engineering*, 1(1), 129.

Wang, R., Shi, Q., Li, Y., Cao, Z., & Si, Z. (2021). A critical review on the use of copper slag (CS) as a substitute constituent in concrete. *Construction and Building Materials*, 292, 123371.

Wang, Y., Li, X., Miao, W., Su, Y., He, X., & Strnadel, B. (2025). The carbon mineralization behavior of copper slag and its impact on pozzolanic reactivity. *Cement and Concrete Composites*, 157, 105899.

Xu, D., Tang, J., Hu, X., Zhou, Y., Yu, C., Han, F., & Liu, J. (2023). Influence of silica fume and thermal curing on long-term hydration, microstructure and compressive strength of ultra-high-performance concrete (UHPC). *Construction and Building Materials*, 395, 132370.

Xu, X., Jin, Z., Yu, Y., & Li, N. (2022). Impact properties of Ultra High Performance Concrete (UHPC) cured by steam curing and standard curing. *Case Studies in Construction Materials*, 17, e01321.

Yoo, D. Y., & Banthia, N. (2016). Mechanical properties of ultra-high-performance fiber-reinforced concrete: A review. *Cement and Concrete Composites*, 73, 267-280.

Effect of steel fiber geometry and dosage on the mechanical and post-cracking behavior of UHPFRC

Sándor Sólyom[1], Anna Szijártó[1], György L. Balázs[1]

[1]: Department of Construction Materials and Technologies, Faculty of Civil Engineering Budapest University of Technology and Economics, Műegyetem rkpt 3, 1111 Budapest, Hungary.

Abstract

One of the fundamental limitations of conventional concrete is its low tensile – compared to that of compressive – strength and brittle behavior, which leads to a sudden loss of load-bearing capacity after crack initiation. To mitigate this drawback, fiber reinforced concrete (FRC) has been developed and increasingly applied, with substantial research achieved over recent decades, particularly following the introduction of high-performance fibers. The literature clearly demonstrates that fiber type, geometry, and volume play a decisive role in governing the post-cracking behavior, toughness, and energy absorption capacity of concrete, especially in structural applications subjected to high mechanical demands.

The objective of the present study was to investigate the influence of steel fiber geometry on the behavior of UHPFRC mixtures. Straight (DUCTIL MS 65/13 UHS) and hooked-end (DUCTIL MHE 70/14 UHS) fibers were used. Mixtures with different fiber volume contents (0, 1, 2 and 4 V%) were produced and subjected to experimental testing, including fresh concrete, compressive and splitting-tensile strength, as well as modulus of elasticity and crack mouth opening displacement (CMOD) tests.

Based on the results, hooked-end fibers provided favorable post-cracking behavior, with higher residual load-bearing capacity and a more gradual post-peak response compared to straight fibers. The effect of fibers on compressive strength was moderate, while splitting tensile strength showed a significant increase with fiber content, with consistently higher values for hooked-end fibers. Overall, hooked-end fibers proved more effective in enhancing tensile performance and crack resistance of UHPFRC.

Keywords

UHPFRC, steel fiber, hooked-end, compressive strength, splitting tensile strength, CMOD

1 Introduction

Global average cement consumption is estimated at approximately 500-550 kg per person per year, while concrete consumption reaches around 2-3 tons per capita annually. These values exhibit significant regional variation, with consumption levels exceeding 1500 kg per person per year in countries such as China (Gabelli Funds, 2025; World Cement Association, 2024; industry statistics). Concrete is widely used owing to its favorable properties such as high compressive strength, durability, and cost-effective production, which make it indispensable in modern construction. Nevertheless, one of its inherent limitations is its relatively low tensile strength and brittle fracture behavior. Under tensile loading, concrete is prone to crack initiation, and once cracks develop, the load-bearing capacity of the structure may decrease rapidly. Therefore, crack control is of paramount importance for ensuring the durability, reliability, and service life of concrete structures (Neville, 2011; Mindess et al., 2003; Bentur & Mindess, 2006).

To mitigate brittle fracture behavior, increasing attention has been devoted to recent decades to fiber reinforced concretes (FRC). Discrete, randomly distributed fibers within the cementitious matrix can bridge cracks, thereby enhancing ductility, energy absorption capacity, and crack resistance. The foundations of fiber reinforcement were established by the pioneering work of Romualdi and Batson, who demonstrated that steel fibers can significantly improve the flexural strength and crack resistance of concrete (Romualdi & Batson, 1963). Since then, research efforts have primarily focused on optimizing fiber type, dosage, and geometry, which collectively govern the mechanical performance of FRC (Naaman, 2003; di Prisco et al., 2009).

In recent decades, the development of cement-based composites has led to the emergence of a new generation of materials, among which Ultra-High Performance Fiber Reinforced Concrete (UHPFRC) stands out. UHPFRC is a cementitious composite characterized by a dense microstructure, a low water-to-binder ratio, high-strength fibers, with compressive strength values often exceeding 150 MPa (Richard & Cheyrezy, 1995; Graybeal, 2014; Fehling et al., 2014). The presence of fibers enables stress transfer across cracks and promotes quasi-ductile, and strain-hardening behavior, in which the material is capable to sustain increasing loads even after the formation of initial cracks (Naaman et al., 2006; Yoo et al., 2016). As a result, UHPFRC allows the design of slender, high load-bearing, and durable structural elements, which in many cases can partially or even fully replace conventional reinforcement (Russell et al., 2013; Toutlemonde et al., 2013).

Of particular importance is the interaction between the fibers and the cementitious matrix, which governs the efficiency of crack bridging and the pull-out resistance of the fibers (Naaman, 2003; Wille & Naaman, 2011). In the case of straight fibers, load transfer is primarily governed by adhesion and frictional mechanisms, whereas deformed fibers, such as hooked-end fibers, additionally provide mechanical anchorage. Consequently, hooked-end fibers generally exhibit higher pull-out load and more favorable post-cracking behavior (Kang & Kim, 2011; Abdallah et al., 2017; Yoo et al., 2016), thereby significantly enhancing the toughness and energy absorption capacity of the composite.

Although numerous studies have investigated the influence of fiber content and fiber material on the behavior of FRC (Wu et al., 2016; Kim et al., 2019), comparative analyses of different fiber geometries under identical matrix compositions are less frequently reported for UHPFRC systems. This is partly because deformed fibers are less commonly used in UHPFRC due to their relatively short length and the associated limitations in developing effective

mechanical anchorage within the dense matrix. As a result, straight steel fibers are typically preferred, even though fiber anchorage and distribution remain critical factors governing post-cracking load-bearing capacity and strain-hardening behavior (Yoo et al., 2016; Wille et al., 2011).

The investigation of mechanical properties and in particular the post-cracking behavior, is of paramount importance in the case of ultra-high performance fiber-reinforced concrete (UHPFRC), as these characteristics directly govern its structural performance. While the tensile strength defines the onset of cracking, the load-carrying capacity after cracking and the residual tensile strength primarily control the stiffness, deformation capacity, crack width development, energy absorption, and ultimate load-bearing capacity of structural elements. The fib Model Code 2010 emphasizes that the structural applicability of fiber-reinforced concrete is fundamentally determined by their residual strength parameters, since these are essential for both serviceability and ultimate limit state design. In the case of UHPFRC, particular attention must be paid to crack localization, crack width, and stress transfer mechanisms across cracks, as these factors govern not only the ductility of the material but also the overall safety, durability, and in-service performance of the structure.

Accordingly, this study aims to evaluate the effects of steel-fiber geometry and dosage on the mechanical and post-cracking behavior of UHPFRC using an identical matrix composition. Straight and hooked steel fibers were incorporated at volume fractions of 1%, 2%, and 4%, and their effects on compressive strength, modulus of elasticity, splitting tensile strength, and flexural behavior were systematically compared. The influence of specimen size on compressive strength was also examined. The study was conducted to determine whether increases in fiber content result in proportional improvements in the investigated properties and to identify the influence of fiber geometry on reinforcement efficiency.

2 Materials and methods

The selected fiber volume contents (0, 1, 2, and 4 V%) were chosen to cover the full transition from a fiber-free UHPC matrix to low-, conventional-, and high-fiber UHPFRC compositions. The 0 V% mixture served as a reference, while 2 V% represents the most commonly adopted baseline in UHPFRC practice (Graybeal, 2014). The lower and higher fiber dosages allow the evaluation of threshold effects at reduced fiber contents and potential diminishing returns at increased fiber volumes (Yoo and Banthia, 2016).

A fiber volume fraction of approximately 2 V% is widely regarded as the conventional benchmark in UHPFRC applications; field-cast FHWA mixtures typically contain around this dosage, and the broader literature identifies 1.5-3 V% as the characteristic range for achieving high tensile strength and ductility (Graybeal, 2014). At the same time, reduced fiber contents around 1 V% have been investigated to improve workability and economic efficiency (Yoo et al., 2016), while higher dosages up to 4 V% are frequently studied in research studies to assess whether the mechanical benefits observed at conventional fiber contents persist at substantially increased reinforcement levels.

Two types of steel fibers (Table 1) were applied in the experimental program: straight DUCTIL MS 65/13 UHS and hooked-end DUCTIL MHE 70/14 UHS fibers. Six concrete mixtures with varying compositions were prepared using CEM I 52.5 N cement, in combination with one fraction of quartz sand (0/4 mm). The water-to-cement ratio (w/c) was set to 0.29, and the cement content was 750 kg/m^3. Each mixture contained a constant amount (75 kg/m^3) of

FL30 quartz powder, while the dosage of superplasticizer was adjusted to achieve the required workability. Table 2 presents the composition of each mixture and the corresponding amount of superplasticizer (MasterBuilders Glenium 300) used.

The symbols of the mixtures were defined to reflect both fiber content and fiber type. The reference mixture without any fibers was denoted as M0. The numerical value following the letter "M" indicates the fiber content expressed in volumetric percentage (0, 1, 2 and 4 V%). The character following the digit specifies the type of fiber used, straight (S) or hooked-end (H).

Table 1: Properties of the applied fibers

Type	**DUCTIL MS 65/13 UHS straight (S)**	**DUCTIL MHE 70/14 UHS hooked-end (H)**
Material	steel	steel
Shape	straight	hooked-end
Density	7850	7850
Length	13	14
Tensile	2800	2800
Diameter	0.20	0.20

Table 2: Concrete mix designs for 1 m^3

Material [kg]	**M0**	**M1H**	**M2S / M2H**	**M4S / M4H**
CEM I 52.5 N	750	750	750	750
FL30 quartz powder	75	75	75	75
0/4 sand	1314	1288	1261	1208
Steel fiber	-	78.5	157	314
MasterBuilders Glenium 300	6	6	6	6
Water	217.5	217.5	217.5	217.5

Compressive strength

The compressive strength was determined at age 28 days using specimens of different sizes. Cubes of 100 × 100 × 100 mm were prepared in molds, while 40 mm and 70 mm cubes were cut from the residual halves of 40 × 40 × 160 mm and 70 × 70 × 250 mm prisms, respectively, after flexural testing. During testing, the specimens were loaded in a universal testing machine under monotonically increasing load until failure with a loading rate of 0.5 MPa/s. The test was carried out based on the requirements of EN 12390-3:2019.

Modulus of elasticity

The modulus of elasticity was determined at age 28 days using 70 × 70 × 250 mm prismatic specimens and a universal testing machine. The specimens were loaded up to approximately one-third of the expected ultimate load, ensuring that the measurements remained within the elastic range of the material. During the test, the stress calculated from the applied load and the measured strain were used to construct the stress-strain diagram. The modulus of elasticity can be conceptually related to the slope of the linear portion of the stress–strain curve in accordance with Hooke's law. However, as defined in the standard, it is not determined directly from this slope, but rather calculated as the ratio of the difference between the stress levels corresponding to specified plateau values and the associated strain increment. The test was carried out in accordance with the requirements specified in EN 12390-13:2021.

Crack Mouth Opening Displacement

The crack mouth opening displacement (CMOD) test was performed at 28 days on 70 × 70 × 250 mm notched prisms under displacement control, ensuring stable crack propagation in accordance with EN 14651:2005+A1:2008. The test is conducted under crack mouth opening displacement control, meaning that the applied load is adjusted to ensure a prescribed rate of crack opening at the notch. The test was carried out in accordance with the requirements specified in EN 14651:2005+A1:2008.

Splitting tensile strength

The splitting tensile strength was determined at age 28 days on 150 × 150 × 150 mm cube specimens. During the test, a line load with a loading rate of 0.5 MPa/s was applied to the specimens, generating tensile stresses within the cross-section, which ultimately led to cracking. The splitting tensile strength of the concrete was calculated based on the measured splitting load, providing a reliable characterization of the material's tensile behavior and the crack-bridging effect of fiber reinforcement. The test was carried out in accordance with the requirements specified in EN 12390-6:2024.

Figure 1 presents schematic illustrations and representative photographs of the four experimental tests.

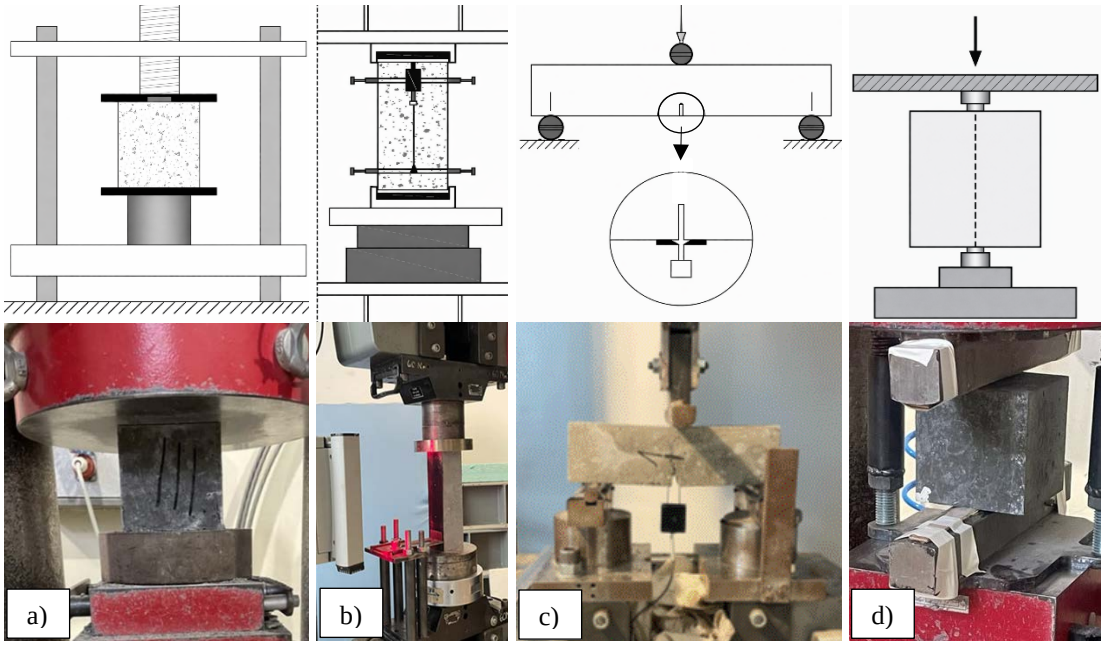


Figure 1: Pictures and schematic diagrams of test setups, a) compressive; b) modulus of elasticity; c) CMOD; d) splitting

3 Test Results

The compressive strength, density, splitting tensile strength, and modulus of elasticity results at 28 days are summarized in Figure 2 and 3. Figure 2 presents density (left) and compressive strength (right), while Figure 3 shows splitting tensile strength (left) and modulus of elasticity (right). All values on the diagrams represent the average of three specimens, the error bars indicate the minimum and maximum measured values. Figure 4 summarizes the CMOD results.

In this case as well, three specimens were tested for each mixture; however, Figure 4 presents the most representative curves for each mixture.

The right diagram in Figure 2 presents the 28-day compressive strength results of concrete mixtures with different fiber contents and fiber types, for three different specimen sizes. Compared with the reference mixture (M0), the effect of fiber addition on compressive strength was more evident for the 100 mm cubes, whereas no consistent improvement was observed for the smaller specimens. Fiber incorporation, particularly at higher dosages, may reduce the workability and compactability of UHPFRC, thereby increasing the amount of entrapped air and the likelihood of local fiber agglomeration and other heterogeneities. In smaller specimens, an individual void, fiber cluster, or locally weakened zone occupies a larger proportion of the loaded cross-section and can therefore exert a stronger influence on the measured compressive strength. In larger specimens, the effects of such local heterogeneities may be averaged over a greater loaded area and material volume. This may explain why the influence of fiber addition appears less consistent for the smaller cubes and more apparent for the 100 mm specimens.

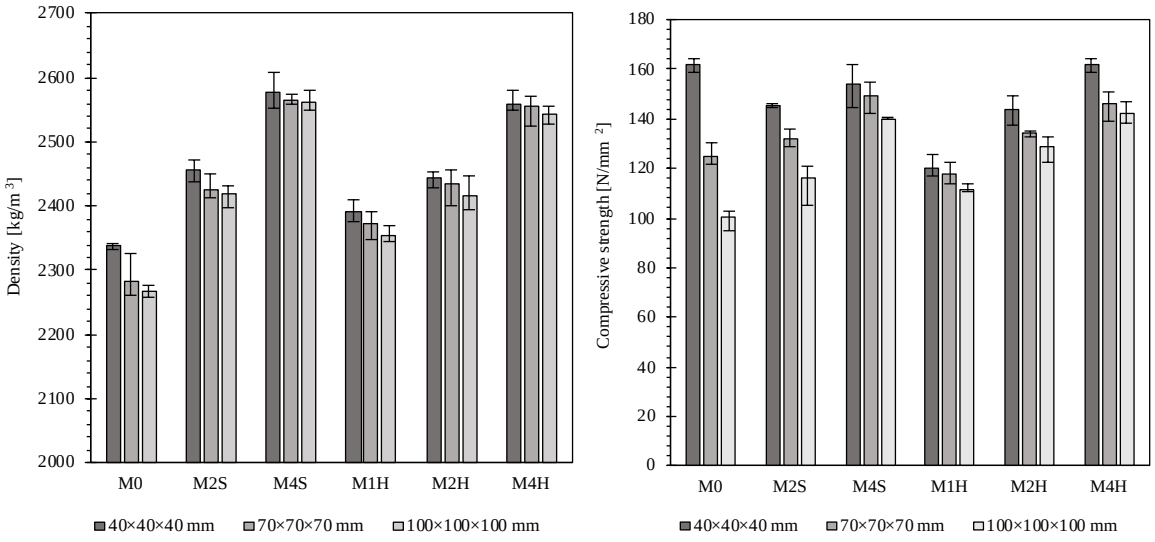


Figure 2: left: Density results at age 28 days obtained from specimens of different sizes; right: Compressive strength results at age 28 days obtained from specimens of different sizes

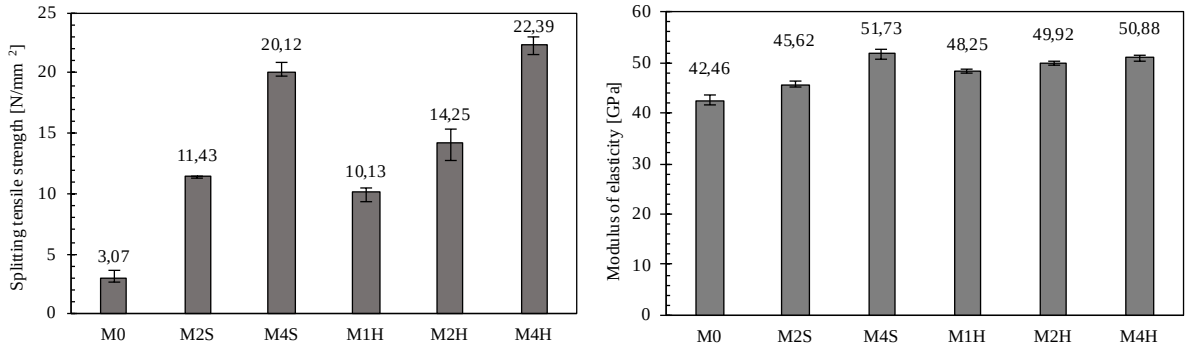


Figure 3: left: Splitting tensile strength results at 28 days; right: Modulus of elasticity results at 28 days

In the case of mixtures containing straight steel fibers (M2S and M4S), a consistent but moderate increase can be identified: increasing the fiber content leads to higher compressive strength, particularly for smaller specimens.

Among the mixtures reinforced with hooked steel fibers (M1H, M2H, and M4H), compressive strength generally increases with increasing fiber content, although the trend is nonlinear. While M2H and especially M4H achieve high strength values – with M4H providing the highest compressive strength among the fiber-reinforced mixtures for the smallest specimens – the improvement is more moderate at the lowest fiber content (M1H).

The effect of specimen size is clearly visible: smaller cubes (40 mm) consistently exhibit higher compressive strength, whereas larger specimens (100 mm) result in lower values. This can be attributed to the well-known size effect (Bažant, 1998; Yi et al., 2006), according to which larger volumes have a higher probability of containing defects and weaker zones. Therefore, the specimen size adopted in practice should be selected in accordance with the relevant testing standard and the specific experimental conditions, while comparisons between different studies should be based on specimens of equivalent geometry and dimensions.

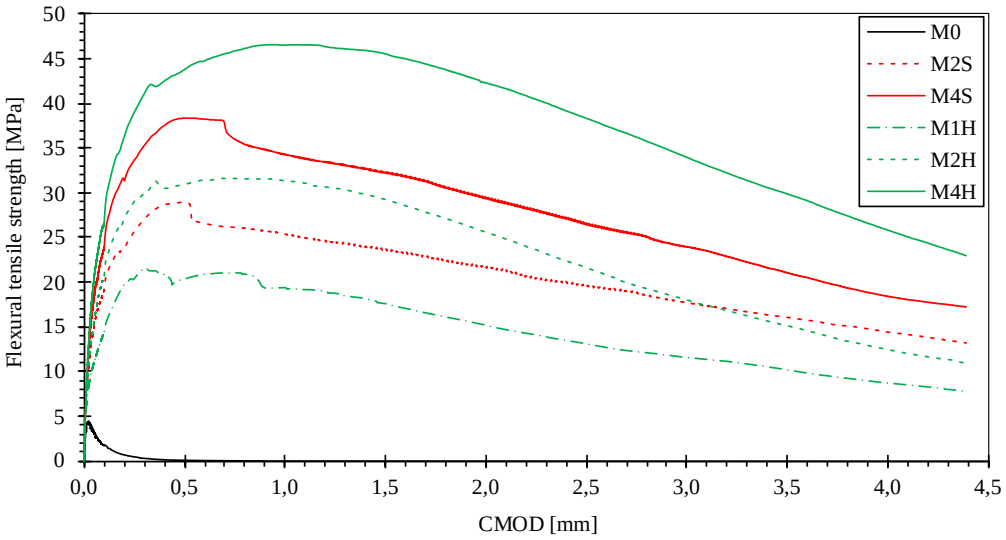


Figure 4: CMOD test results at 28 days

The left diagram in Figure 3 presents the 28-day splitting tensile strength of UHPFRC mixtures with varying fiber contents and fiber types, visibly demonstrating the significant effect of fibers. The reference mixture without fibers (M0) exhibits a splitting tensile strength of 3.07 N/mm^2. In comparison, the addition of a relatively low dosage of fibers (1 V%) results in a multiple increase (approx. 3.3 times) in strength. For mixtures containing straight fibers, a fiber content of 2 V% (M2S) increases the strength to 11.43 N/mm^2, while 4 V% (M4S) leads to a value of 20.12 N/mm^2, representing nearly a sixfold increase relative to the reference. This indicates that the increase in splitting tensile strength with fiber content is not linear but rather accelerates with higher fiber volumes.

From a practical perspective, the observed increase in splitting tensile strength is particularly important because tensile cracking is often the governing performance criterion in UHPFRC structural elements. Higher tensile strength can delay crack initiation, improve crack

distribution, and contribute to enhanced durability by reducing crack widths and limiting the ingress of aggressive substances. The results also indicate that increasing the fiber content may allow designers to achieve improved tensile performance without modifying the matrix composition, which can be advantageous for applications where crack control and serviceability requirements govern the design.

Mixtures incorporating hooked-end, high-strength fibers exhibit even more favorable results. At a fiber content of 1 V% (M1H), a splitting tensile strength of 10.13 N/mm^2 is already achieved, which is comparable to that of the mixture containing 2 V% straight fibers. With increasing fiber content, the strength continues to rise: 14.25 N/mm^2 at 2 V% (M2H) and 22.39 N/mm^2 at 4 V% (M4H), the latter being the highest value among all investigated mixtures. This clearly indicates that hooked-end fibers contribute more effectively to crack bridging and load transfer than straight fibers, likely due to their superior mechanical anchorage. The hooked ends increase the pull-out resistance of the fibers and enable more efficient stress transfer across developing cracks. While straight fibers rely primarily on adhesion and friction at the fiber-matrix interface, hooked-end fibers require additional deformation and energy to be extracted from the matrix. Consequently, higher loads can be carried after crack initiation, resulting in enhanced crack-bridging efficiency and higher splitting tensile strength. The fact that the 1 V% hooked-end mixture achieved a splitting tensile strength comparable to that of the 2 V% straight-fiber mixture further highlights the importance of fiber geometry and suggests that optimizing fiber shape may be a more efficient strategy for improving tensile performance than merely increasing fiber dosage.

The right diagram of Figure 3 presents the 28-day modulus of elasticity of UHPFRC mixtures with different fiber contents and fiber types. It can be observed that the presence of fibers generally increases the stiffness of the composite; however, the magnitude of this effect is more moderate compared to strength-related properties. The reference mixture without fibers (M0) exhibits a modulus of elasticity of 42.46 GPa, while all fiber-reinforced mixtures show higher values.

For mixtures containing straight fibers, an increase in fiber content results in an increase in the elastic modulus. The mixture with 2 V% fibers (M2S) reaches a modulus of 45.62 GPa, while at 4 V% (M4S) the value increases to 51.73 GPa, which is the highest among all investigated mixtures. This indicates that straight fibers contribute effectively to enhancing the stiffness of the matrix, particularly at higher fiber contents. Mixtures containing hooked-end fibers also show an increase compared to the reference; however, the effect of fiber content is more gradual and balanced. Even at 1 V% (M1H), a notable increase is observed (48.25 GPa), which further rises to 49.92 GPa at 2 V% (M2H) and 50.88 GPa at 4 V% (M4H). In this case, the increase is more gradual and less pronounced than for straight fibers.

Figure 4 illustrates the effect of fibers on the behavior of concrete in the crack mouth opening displacement (CMOD) test. The reference specimen without fibers (M0) exhibits a distinctly brittle behavior, as the load drops sharply after reaching the peak value, with practically no residual load-bearing capacity. In contrast, even 1 V% dosage of steel fibers significantly improves the response: both the peak load and, more importantly, the post-cracking load-bearing capacity (i.e., ductility) increase. With increasing fiber content (from 1% to 2% and 4%), a clear trend can be observed, showing higher maximum loads and enhanced residual strength at larger crack openings, indicating an improved crack-bridging capability.

Comparing straight and hooked fibers, hooked steel fibers provide better performance at the same dosage, especially at larger crack opening values. The best performance is achieved by the mixture containing 4% hooked fibers (M4H), which exhibits both the highest peak load and the greatest residual load-bearing capacity throughout the entire loading range. Overall, the results demonstrate that fiber reinforcement significantly enhances the post-cracking behavior and energy absorption capacity of concrete, particularly when higher fiber contents and hooked fiber geometries are applied. Such enhancements in post-cracking response indicate a more favorable structural behavior, allowing increased deformation capacity and more stable crack development under service and ultimate load conditions.

Overall, splitting tensile strength is strongly governed by both fiber content and geometry, with hooked-end fibers providing consistently superior results. The modulus of elasticity is also enhanced by fiber incorporation, with straight fibers showing a more pronounced, content-dependent increase, whereas hooked-end fibers result in a more gradual improvement. However, fibers have a moderate effect on compressive strength, with higher fiber contents yielding the best performance, while specimen size significantly influences the measured values. The relatively low scatter of the results indicates good reliability of the measurements.

Overall, the quantitative results confirm that fibers primarily improved the tensile and post-cracking performance of UHPFRC. Splitting tensile strength increased from 3.07 MPa for the reference mixture to 20.12 MPa with 4 V% straight fibers and 22.39 MPa with 4 V% hooked-end fibers, corresponding to increases of approximately 555% and 629%, respectively. Even 1 V% hooked-end fibers increased the splitting tensile strength to 10.13 MPa, more than three times the reference value. The modulus of elasticity increased more moderately, from 42.46 GPa for M0 to a maximum of 51.73 GPa for M4S, representing an improvement of approximately 22%. The CMOD results similarly showed a progressive increase in peak and residual load-bearing capacity with fiber dosage, with M4H providing the most favorable post-cracking response. By contrast, the effect on compressive strength was comparatively moderate and depended strongly on specimen size, fiber geometry, and dosage.

4 Conclusions

This study investigated the influence of steel fiber geometry and fiber volume content on the mechanical and post-cracking behavior of ultra-high performance fiber-reinforced concrete (UHPFRC). Straight and hooked-end high-strength steel fibers were applied at volume contents of 1, 2 and 4%, while a fiber-free mixture served as reference.

Fiber geometry: the experimental results demonstrate that fiber geometry plays a critical role in post-cracking behavior. At identical fiber contents, mixtures with hooked-end fibers exhibited higher residual load-bearing capacity, improved crack-bridging capability and a more gradual post-cracking response compared to mixtures with straight fibers. This behavior is attributed to the enhanced mechanical anchorage of hooked-end fibers, leading to increased pull-out resistance.

Splitting tensile strength showed a non-linear increase with fiber content and was highly sensitive to fiber geometry. Hooked-end fibers proved considerably more efficient, achieving at 1 V% tensile strength levels comparable to those of mixtures containing 2 V% straight fibers. The highest splitting tensile performance was obtained with 4 V% hooked-end fibers.

Compressive strength: in contrast, the influence of fibers on compressive strength was moderate. Although fiber addition generally increased compressive strength relative to the reference mixture, this effect was limited and dependent on specimen size, fiber content and fiber type, confirming that fibers primarily enhance tensile and post-cracking properties rather than compressive strength.

Fiber content: fibers also led to an increase in stiffness for all UHPFRC mixtures. Straight fibers resulted in a more pronounced, nearly linear increase in the modulus of elasticity with fiber content, whereas hooked-end fibers provided a more uniform but less dosage-sensitive stiffening effect. CMOD tests further confirmed that increasing fiber content markedly improves post-cracking performance, leading to higher peak load, enhanced residual strength and superior energy absorption capacity, with the most favorable response observed for the mixture containing 4 V% hooked-end fibers.

Overall and structural aspects: the results highlight that fiber geometry is an important governing parameter in determining the structural performance of UHPFRC. Hooked-end steel fibers enable a more efficient utilization of fibers, particularly in structural applications where residual tensile capacity, crack width control, ductility and serviceability behavior govern the design.

5 Acknowledgements

Support from the Central Europe Leuven Strategic Alliance (grant number: CELSA/25/10) is highly valued. The authors also acknowledge the support of the NKFIH Hungarian Research Grant No. 2020-1.1.2-PIACI-KFI-2021-00252, entitled “Development of innovative and aesthetic prefabricated cementitious carbon fiber composite concrete façade and cover elements at MOLNARBETON Ltd.”. The authors further gratefully acknowledge Dr. Ralf Winterberg and Ductil GmbH for generously supplying the fibers used in this study.

6 References

Abdallah, S., Fan, M., and Zhou, X., 2017. Pull-Out Behaviour of Hooked End Steel Fibres Embedded in Ultra-High Performance Mortar with Various W/B Ratios, International J. of Concrete Structures and Materials, 11(2), pp.301–313. doi: 10.1007/s40069-017-0193-8

Bažant, Z. P., and Planas, J., 1998. Fracture and Size Effect in Concrete and Other Quasibrittle Materials, CRC Press. doi: 10.1201/9780203756799

Bentur, A., and Mindess, S., 2006. FiberReinforced Cementitious Composites, 2nd ed., Taylor & Francis / CRC Press

di Prisco, M., Plizzari, G., and Vandewalle, L., 2009. Fiber reinforced concrete: new design perspectives, Materials and Structures, 42(9), pp.1261-1294. doi: 10.1617/s11527-009-9529-4

European Standard, EN 12390-3:2019, Testing hardened concrete. Part 3: Compressive strength of test specimens

European Standard, EN 12390-6:2024, Testing hardened concrete. Part 6: Tensile splitting strength of test specimens

European Standard, EN 12390-13:2021, Testing hardened concrete. Part 13: Determination of secant modulus of elasticity in compression

European Standard, EN 14651:2005+A1:2008, Test method for metallic fibered concrete. Measuring the flexural tensile strength (limit of proportionality (LOP), residual)

Fehling, E., Schmidt, M., Walraven, J., Leutbecher, T., and Fröhlich, S., 2014. Ultra-High Performance Concrete UHPC: Fundamentals, Design, Examples, Ernst & Sohn, Berlin

fib, 2013. Model Code 2010 for Concrete Structures, Erst and Sohn, Wiley

Gabelli Funds. (2025). Global cement industry overview. gabelli.com/research/global-cement-industry

Graybeal, B., 2014. Material Property Characterization of Ultra-High Performance Concrete, Federal Highway Administration (FHWA), Washington D.C. https://www.fhwa.dot.gov/publications/research/infrastructure/structures/bridge/14090/14090.pdf

Industry statistics. (2024–2025). Cement and concrete consumption data.

Kang, S.-T., and Kim, J.-K., 2011. The relation between fiber orientation and tensile behavior in ultra high performance fiber reinforced cementitious composites, Cement and Concrete Research, 41(10), pp.1001-1014. doi: 10.1016/j.cemconres.2011.05.009

Kim, J.J.; Yoo, D.Y. Effects of fiber shape and distance on the pullout behavior of steel fibers embedded in ultra-high-performance concrete. Cem. Concr. Compos. 2019, 103, 213–223. https://doi.org/10.1016/j.cemconcomp.2019.05.006.

Mindess, S., Young, J. F., and Darwin, D., 2003. Concrete, 2nd ed., Prentice Hall, Upper Saddle River, NJ.

Naaman, A. E., 2003. Engineered Steel Fibers with Optimal Properties for Reinforcement of Cement Composites, J. of Advanced Concrete Tech 1(3), pp.241-252. doi: 10.3151/jact.1.241

Naaman, A. E., and Reinhardt, H. W., 2006. Proposed Classification of HPFRC Composites Based on Their Tensile Response, Materials and Structures, 39(5), pp.547-555. doi: 10.1617/s11527-006-9103-2

Neville, A. M., 2011. Properties of Concrete, 5th ed., Pearson Education Limited, Harlow.

Richard, P., and Cheyrezy, M., 1995. Composition of Reactive Powder Concretes, Cement and Concrete Research, 25(7), pp.1501-1511. doi: 10.1016/0008-8846(95)00144-2

Romualdi, J. P., and Batson, G. B., 1963. Mechanics of Crack Arrest in Concrete, J. of the Eng. Mechanics Division, ASCE, 89(EM3), pp.147-168. doi: 10.1061/JMCEA3.0000381

Russell, H. G., and Graybeal, B. A., 2013. Ultra-High Performance Concrete: A State-of-the-Art Report for the Bridge Community, Federal Highway Administration (FHWA-HRT-13-060), Washington D.C.

Toutlemonde, F., and Resplendino, J., 2013. Design and Applications of Ultra-High Performance Fibre-Reinforced Concrete, Wiley

Wille, K., Naaman, A. E., and Parra-Montesinos, G. J., 2011. Ultra-High Performance Concrete with Compressive Strength Exceeding 150 MPa (22 ksi): A Simpler Way, ACI Materials Journal, 108(1), pp.46-54. doi: 10.14359/51664215

World Cement Association, 2024. WCA Long Term Forecast for Cement and Clinker Demand. www.worldcementassociation.org/images/

Wu, Z.; Shi, C.; He, W.; Wu, L. Effects of steel fiber content and shape on mechanical properties of ultra high performance concrete. Constr. Build. Mater. 2016, 103, 8–14. https://doi.org/10.1016/j.conbuildmat.2015.11.028.

Yi, S.-T., Yang, E. I., and Choi, J.-C., 2006. Effect of specimen sizes, specimen shapes, and placement directions on compressive strength of concrete, Nuclear Engineering and Design, 236(2), pp.115–127. doi: 10.1016/j.nucengdes.2005.08.004

Yoo, D.-Y., and Banthia, N., 2016. Mechanical properties of ultra-high-performance fiber-reinforced concrete: A review, Cement and Concrete Composites, 73, pp.267-280. doi: 10.1016/j.cemconcomp.2016.08.001

Performance of Date Palm Pedicel and Coir Fibre in Natural Fibre Reinforce Concrete for Sustainable Construction

Abdallah Al Abri[1]; Kazi Md Abu Sohel[1]; Sherif El-Gamal[1]; Khalifa Al-Jabri[1]

[1]: Department of Civil and Architectural Engineering, Sultan Qaboos University, Muscat, Oman.

Abstract

The development of high-performance materials made from natural resources is increasing globally due to environmental and sustainability concerns. Palm fibre is one of the natural smart materials that can be used to produce fibre-reinforced concrete, eliminating synthetic, glass and metal fibre. A significant amount of agricultural waste is produced and dumped in landfills, including palm date parts such as leaves, trunks, fruit bunches and surface fibres. However, these fibres are a great source of natural fibre for the concrete. Several studies show that the natural fibres in concrete enhance the mechanical properties of concrete. In this study, two types of natural fibre namely date palm pedicel fibre and coconut shell (coir) fibre are considered to compare their performance in concrete. Date palm pedicel fibre (DPPF) and coconut shell fibre *i.e.* coir fibre (CF) were prepared in four conditions: raw, alkaline treatment, boiled, and boiled with alkaline treatment. The tensile behaviour of each fibre type was examined using a universal testing machine, following ASTM D3822 guidelines. Measurements included tensile strength, Young's modulus, breaking distance, and elongation at failure. Once the fibres were characterized, they were incorporated into concrete mixes to produce natural fibre reinforced concrete (NFRC) and tested for mechanical performances. Compressive strength, splitting tensile strength, and flexural strength for the NFRC were evaluated after 7 and 28 days of curing for both coir- and pedicel-reinforced concrete. It was found that alkaline treatment, especially when boiling followed by alkaline treatment, substantially improved the strength and stiffness of the fibres. Generally, coir fibres experienced higher elongation under tensile force compared to that of date palm pedicel fibre. Similarly, the tensile strength of date palm pedicel fibre showed higher tensile strength than coir fibre for both treated and untreated cases. However, both fibres achieved sufficient strength after statement making them very much appropriate be used for reinforcing brittle cement-based materials. The NFRC test results showed noticeable improvements in tensile and flexural performance, confirming the crack-bridging ability and energy absorption characteristics imparted by the natural fibres.

Keywords

Fibre reinforced concrete, Natural fibre, Date palm fibre, Coir fibre, Natural fibre treatment

1 Introduction

Metallic, synthetic, and glass fibre have been used in concrete and cement mortar mixes for many years to improve tensile and other mechanical properties. However, the production of these fibres was costly, resulted in CO_2 emissions, and required the use of non-renewable materials (Tonoli et al. 2010). Therefore, over the past few years, efforts have been made to replace the manufactured fibres with natural fibres. The use of natural fibres in cementitious matrix is gaining attraction among the researchers around the world because of its affordability and sustainability (Bendahane et al., 2023).

Natural fibres are typically categorized into two main types: primary and secondary fibres. Primary fibres refer to fibres that are cultivated for their fibre content, and this category includes jute, sisal, kenaf, palm, and hemp fibres. On the other hand, secondary fibres are fibres that are obtained from byproducts of plant cultivation, and this category includes agroresidues, coir fibres, and pineapple fibres. There are six main types of natural fibres, which can be further classified based on the part of the plant from which they are derived. The six types are bast fibres (such as flax and jute), leaf fibres (such as sisal and pineapple leaf fibres), seed fibres (such as cotton and coconut), kernel fibres (such as hemp and kenaf), grass and reed fibres (such as wheat, maize, and rice), and all other types (such as wood and roots) (Karthi et al. 2020, Aravindh et al., 2022, Bendahane et al., 2023). Table 1 summarizes common plant fibres and their common mechanical properties, as described in the literature. Tensile strength and elongation at break are crucial for determining the mechanical properties of plant fibre-reinforced concrete. However, previous research works highlighted that the variations in plant fibre extraction and processing methods can lead to significant differences in experimental results. Therefore, it is critical to consider the relevant characteristics and composition of plant fibres, along with local climatic conditions, when developing standards or guidelines for their extraction processes and testing methodologies.

Table 1: Characterization of typical plant fibres

Type of Fibre	Density (g/ cm^3)	Fibre Length (mm)	Diameter (µm)	Tensile Strength (MPa)	Young's Modulus (GPa)	Elongation at breakage (%)	References
Alfa	1.40	0.2-30	6.0-22.0	18–25	18-58	1.4-2.4	Ajouguim et al. 2023; Al Abri and Sohel 2024
Bamboo	0.6-1.1	0.8	19.8	540–630	11-17	4.3-9.7	Correia et al. 2014; Zhang et al. 2021, Abri and Sohel 2024
Bagasse	1.25	10.1-16.09	180-390	197.8-290	17-27	1.1	Nazir et al. 2021; Abri and Sohel 2024
Banana	1-1.5	12	45	550	5-20	4.5-6.5	Palanisamy and Ramasamy 2022; Abri and Sohel 2024
Coconut/ coir	0.88-1.36	200-300	12 - 35	170-275	3-26	18.0-36.7	Hasan et al. 2021; Abri and Sohel 2024
Cotton	1.5-1.6	25-37	12-35	5.5-12.6	287-597	7.0-8.0	Mahdi and Dean 2020; Abri and Sohel 2024
Flax	1.4-1.5	6-80	12.4-23.9	800-1500	60-80	2.0-3.0	Olivito et al. 2014; Abri and Sohel 2024
Hemp	1.4-1.6	5-55	10.9-42	550-900	70	1.0-6.0	Liu et al. 2017; Abri and Sohel 2024

Jute	1.46	1-6	5-25	393-770	10-30	1.5-1.8	Ramakrishna and Sundararajan 2005; Abri and Sohel 2024
Kenaf	1.2-1.4	40-300	55-60	230-1000	14.5-73	9.1-12.3	Fiore et al. 2015; Abri and Sohel 2024
Oil palm	0.7-1.55	25	19.4	65-220	0.44-1.9	3.2	Raut and Gomez 2016; Abri and Sohel 2024
Pineapple leaf	1.32	10-90	50-150	159	11.84	2.0-2.8	Sivasubramanian et al. 2022; Abri and Sohel 2024
Sisal	1.45	0.5-8	10-20	600-700	9.4-22.0	2.0-2.5	Sahu and Gupta 2017
Date palm turn surface fibre	0.917 ± 0.127	71-290	100-1000	58–203	2–7.5	5–15.5	Alawar et al. 2009; Al-Khanbashi et al. 2005; Kriker et al. 2005; Adamu et al. 2022

Adamu et al. (2022) studied the possibility of adding date palm surface fibres (DPF) to the concrete matrix. Date palm fibre (DPF) offers several benefits when considered as a natural reinforcement material: it is abundant, inexpensive, environmentally friendly, and sourced directly as a by-product of palm date trees. Despite these benefits, its incorporation into cement composites poses challenges, most notably a slight decrease in mechanical strength and an increase in porosity. To effectively use DPF in concrete applications, it needs to be combined with an additive that can mitigate these drawbacks of the NFRC-based cement composites. Consequently, it is proposed to use Silica fume to partially replace the cement and accordingly reduce the porosity and minimize the undesirable effect of the DPF on the strength of the composite. Numerous studies were conducted on the use of different parts of the date palm tree (*e.g.*, palm trunk fibre and leaf sheath fibre or turn surface fibre) in the concrete mixture to produce fibre-reinforced concrete (Dhakal et al., 2018, Benaimeche et al., 2018). Similar to the date palm fibre, many studies have investigated extensively the precise mix proportions to achieve the optimal mix of coir-fibre reinforced concrete. Varghese and Unnikrishnan (2023) explained the production process of coir fibre reinforced concrete. All of these studies described the improvement of mechanical properties of the concrete or mortar reinforced with date palm fibres. However, none of the studies considered different treatment options of the fibres.

In the present work, the effect of different chemical and treatment processes on the strength and morphological properties of the date palm pedicel fibre and coir fibre was carried out. The strength properties of the concrete with the treated fibre were determined experimentally.

2 Experimental program

2.1 Fibre Extraction and Preparation

The extraction of natural fibres both date palm pedicel fibre (DPPF) and coir fibre (CF) was successfully carried out using fibre extraction machine. Coir fibres were obtained from coconut husk waste collected from local market, while date palm pedicel fibres were extracted from locally sourced Omani date palm residues after collecting the ripped dates. The fibre extraction process included mechanical separation, cleaning, and controlled drying in an oven for 24 hours. These processes ensure that the fibres are uniform and reproducible. Because standardized methods for processing pedicel fibres are largely absent in the literature, several extraction trials were carried out. Through repeated refinement, an optimized procedure was

developed that produced fibres with consistent length, clean surfaces, and uniform physical appearance. This optimization is an important outcome of this study because it provides a practical methodology for utilizing locally available agricultural waste fibres in cementitious applications while also improving the reproducibility of experimental results. Figure 1 illustrates the date palm pedicel branches and mechanically extracted forms date palm pedicel fibres. Finally, both pedicels and coir were then cut into uniform length of 50 mm using a band saw machine.



Figure 1: Raw and extracted pedicel fibre

2.2 Fibre Treatment Procedures

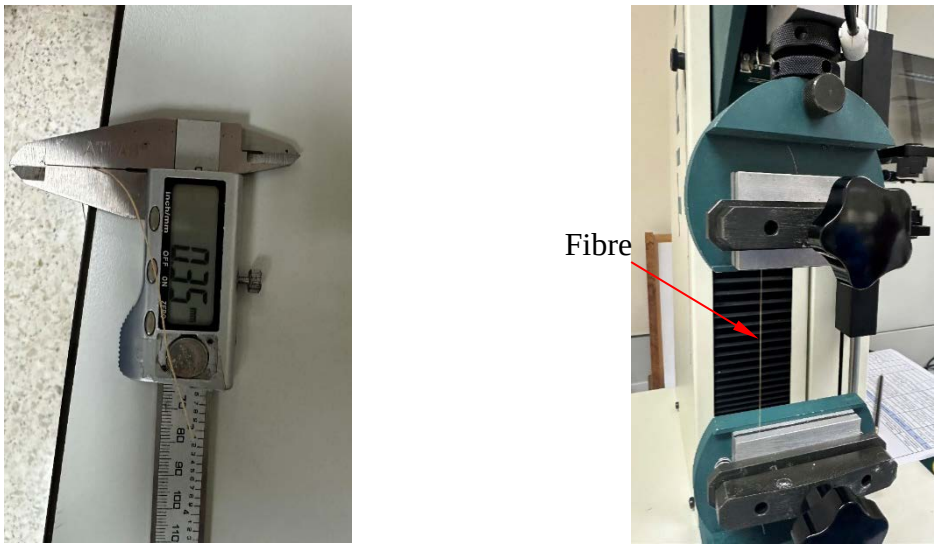
Three types of treatment processes were conducted to purify and improve their compatibility with the concrete matrix and their long-term durability. The first process was direct chemical treatment, where both coir and pedicel fibres were treated with 5% sodium hydroxide (NaOH) for an hour to remove surface impurities, lignin, and hemicellulose, increasing surface roughness and improving interfacial bonding with the cement matrix. Following that, a 30-minute secondary treatment with 2% acetic acid was used to neutralize residual alkalinity and stabilize the fibre surface. In the second type of treatment process was boiling the fibres for 3 hours. This process makes it easy to sperate the raw fibre with less impurities on the surface. The third process is the combination of boiling and alkaline treatment with 5% NaOH followed by washed with 2% acetic acid. This approach was chosen to increase fibre durability while reducing degradation in the alkaline concrete environment. Figure 2 depicts the chemical treatment of pedicel fibre in sodium hydroxide (NaOH) solution. The colour change observed in the NaOH solution during chemical treatment is due to the extraction of lignin, hemicellulose, waxes, and phenolic compounds from the fibres, confirming the alkaline treatment process's effectiveness.

2.3 Characterization of Natural Fibres

A comprehensive characterisation program was carried out to determine the suitability of extracted date palm pedicel fibre and coir fibre as concrete reinforcement materials in terms of physical and strength properties. The physical and mechanical properties of the fibres were investigated through tensile strength testing and water absorption measurement. Tensile tests were performed using Universal Testing Machine (UTM) to determine ultimate tensile strength, elastic modulus, elongation at break, and failure modes of the fibres. Figure 3 shows the diameter measurement and the setup for tensile test.



Figure 2: Colour change of the NaOH solution during alkaline treatment of date palm pedicel fibres



(a) (b)

Figure 3: (a) diameter measurement (b) tensile test using UTM

2.4 Natural fibre reinforced concrete design

The mix design of the concrete was followed by the ratio of 1:1.6:2.5 (cement : fine aggregate : coarse aggregate). The water cement ratio was 0.485 and superplasticizer was used to increase the workability of concrete, and the dosage was 0.45% of cement. The target design compressive strength was 35 MPa. To produce natural FRC, 0.5% and 1.0% fibres by weight of cement were added to the concrete mixture. Length of the fibre was 50 mm. The selected fibre length and dosage were based on preliminary experimental investigations conducted by the authors to optimize the use of coir and date palm pedicel fibres in concrete. In those trials, fibre lengths of 25, 50, and 75 mm were evaluated, and the 50 mm length showed the most effective balance between crack-bridging capacity, strength enhancement, and fibre dispersion.

Similarly, fibre contents ranging from 0.5% to 1.0% by weight of cement provided the most favourable mechanical response without causing excessive reduction in workability or compaction quality. Therefore, the present study adopted 50 mm fibre length with 0.5% and 1.0% fibre contents to further evaluate the comparative performance of coir and date palm pedicel fibres in concrete. Various concrete specimens were prepared at different coir and pedicel fibres content (0.5% and 1% by weight of cement). Based on the fibre characterization results, the concrete mixtures were prepared using coir and date palm pedicel fibres that had been alkaline-treated and subsequently washed with acetic acid. This treatment condition was selected because it enhanced the tensile strength and stiffness of both fibres while improving surface roughness, which is beneficial for fibre-matrix interaction in cementitious composites. Therefore, the mechanical performance reported in the following sections corresponds to concrete reinforced with alkaline-treated treated coir and date palm pedicel fibres at 0.5% and 1.0% by weight of the cement. In addition, a standard specimen without fibre reinforcement was prepared to serve as a benchmark. Cylinders with dimensions of 200 mm by 100 mm diameter and prism with dimensions of 500×100×100 mm were prepared in accordance to ASTM C78.

Table 1: Mix design for 35 MPa cast concrete mix used in all trials.

Ingredient	**Quantity (kg/m^3)**
Cement	442
Fine aggregate	711
Coarse aggregate	1067
Water	214.4 kg/m^3
Super plasticizer	2 liter/ m^3
Target slump	80 to 120 mm

The concrete cylinders were tested after 28 days of water curing under compressive load using an automatic concrete compression testing machine. The split tensile test on cylinder specimens was conducted using the same machine. Four point bending test was conducted on prism specimen to determine the flexural strength of the FRC concrete cast 28 days before.

3 Test Results

3.1 Fresh-state behaviour of concrete mixtures

The fresh-state behaviour of the concrete mixtures was evaluated using the slump test. The control mixture achieved a slump of 118 mm, which is considered medium to high range workable concrete. The incorporation of natural fibres reduced the slump, indicating a decrease in workability. The slump decreased to 107 mm and 103 mm for PED-0.5% and PED-1.0%, respectively, and to 105 mm and 101 mm for CF-0.5% and CF-1.0%, respectively. Although all fibre-reinforced mixtures remained within the target slump range of 80 to 120mm (medium to high workability), the reduction became more evident as the fibre content increased from 0.5% to 1.0%. This behaviour can be attributed to the hydrophilic nature and high surface area of the natural fibres, which increase water demand and internal friction during mixing. In addition, the presence of discrete fibres may restrict aggregate movement and reduce compactability. The slightly lower slump observed in the coir fibre mixtures may be related to their higher aspect ratio, which can increase fibre interaction and resistance to flow.

3.2 Physical and mechanical properties of coir and date palm pedicel fibre

Tensile strength testing was performed on pedicel and coir fibres subjected to four different treatment conditions, namely raw, only chemical treatment, boiled, and boiled with subsequent chemical treatment. The tensile test results are shown in Figure 4. The tensile strength of raw date palm pedicel fibre (DPPF) and coir fibre (CF) are 302 and 98 MPa, respectively. It can be seen that chemical (alkaline) treatment significantly enhances the mechanical performance of both type of fibres. When coir fibre was treated with alkaline, its tensile strength and Young's modulus increased by 17% and 56%, respectively, compared to the raw condition. This increase in strength and stiffness can be attributed to the removal of surface impurities, waxes, and lignin by alkaline media, which results in improved fibre integrity and load transfer mechanism. However, this strength improvement was accompanied by a reduction in elongation at break from 4.13% to 3.76%. This indicate that the chemical treatment makes the fibre stiffer and less ductile compared to that of the raw fibre.

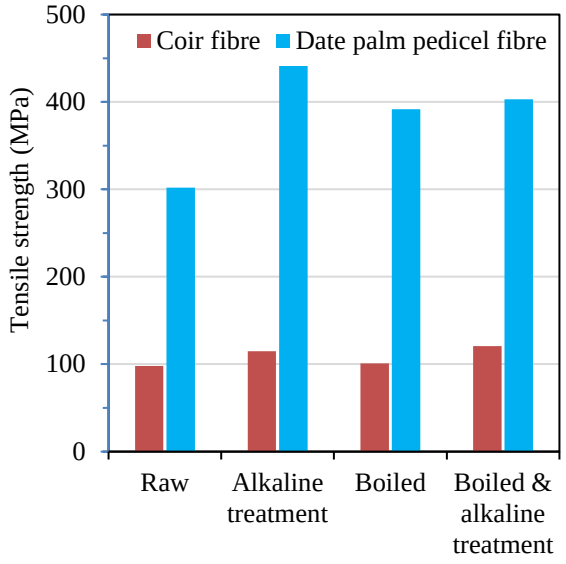
Boiling treatment alone had a slight effect on the tensile strength of coir fibres, though it did in a noticeable reduction in stiffness. This is likely because some of the amorphous regions underwent partial thermal breakdown. However, when the fibres were boiled and then treated with an alkaline solution, their tensile strength increased by 6% over that of only chemically treated fibre. This suggests a synergistic effect of thermal cleaning and chemical modification in increasing fibre strength while maintaining moderate ductility.

Date palm pedicel fibres (DPPF) had significantly higher tensile strength and stiffness than coir fibres across all treatment conditions, demonstrating their superior reinforcing potential. When subjected to alkaline treatment, both tensile strength and Young’s modulus increase remarkably, as can be seen in Figures 4(a) and 4(b). This strength enhancement demonstrates how chemical processing improves cellulose exposure and fibre crystallinity. Similar to coir fibres, alkaline treated pedicel fibres showed lower elongation at break from 39.15% to 30.57% compared to the raw state, indicating that alkaline treatment increases stiffness and reduces ductility of natural fibres.

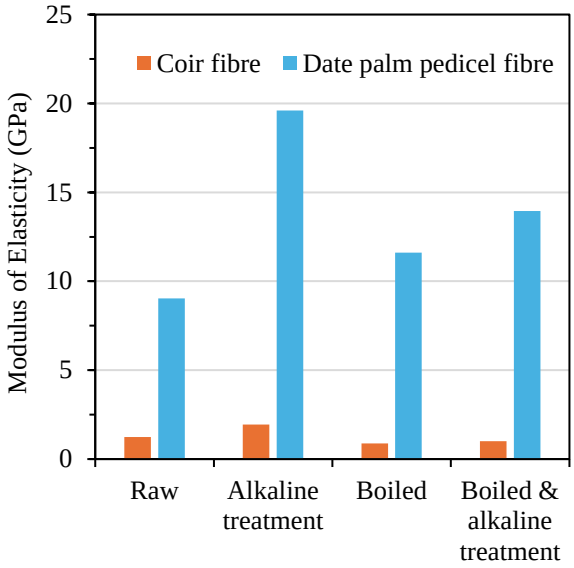
Overall, the findings show that alkaline treatment is the primary factor influencing fibre mechanical performance, while boiling serving as a secondary modification step. The treated fibres' increased strength and stiffness indicate their suitability for crack-bridging and load-transfer mechanisms in fibre-reinforced concrete applications.

Water absorption tests were carried out to determine the hydrophilic characteristics of both types of fibres and their potential impact on concrete workability. Figure 5 depicts the results of a water absorption test on DPPF and CF fibres before and after different treatment conditions, such as raw, raw with chemical treatment, boiled, and boiled with subsequent chemical treatment.

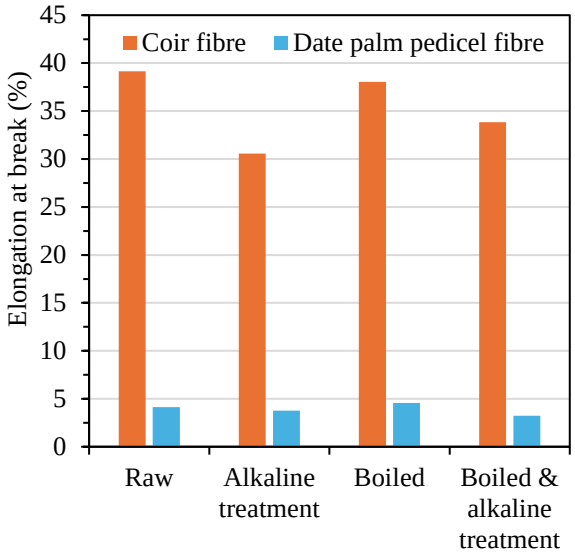
The water absorption test results for both DPPF and CF fibres show that all applied treatment methods have a significant impact on their hydrophilic characteristics. For DPPF fibres, the raw fibres absorbed water approximately 97% of their dry state weight. After chemical treatment, this water absorption slightly increased to 107%, while in case of only boiling treatment, the absorption increased to 111%. However, in case of the combined application of boiling and chemical treatment, the absorption rate increased significantly to 156%. This sharp increase indicates that removing surface waxes and impurities, as well as loosening the fibre's internal structure, significantly improved its ability to absorb water.



(a): Tensile strength



(b): Young's modulus



(c): Elongation at breakage

Figure 4: results of tensile test.

Coir fibres (CF) followed a similar trend of DPPF fibre, as can be seen in Figure 5. However, the raw fibres absorbed less water (~54%) than DPPF fibre (97%). The only chemical and boiling treatments increased absorption by 99% and 109%, respectively. Furthermore, the combined boiling and chemical treatment resulted in the highest water absorption of 128% for CF fibre. Overall, both fibres demonstrate that treatment processes make them more hydrophilic. The DPPF fibres typically absorbed more water than CF fibres. These findings are significant for the application of natural fibres to produce fibre reinforced concrete, because increased water absorption may affect fibre-matrix bonding and overall water demand of the concrete mix.

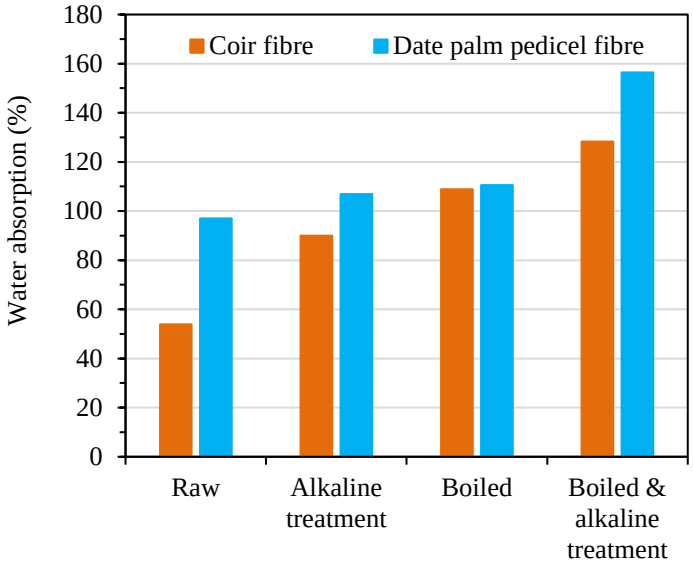


Figure 5: results of water absorption test.

3.3 Performance of Coir and Pedicels Fibre Reinforced Concrete

This section describes the experimental study on concrete reinforced with coir and date palm pedicel fibres at concentrations of 0.5% and 1.0% of the cement weight. The results are compared to a standard control mix (conventional concrete), with emphasis on compressive strength, splitting tensile strength, and flexural strength. For each mix variation, three specimens were tested, and the reported values are the average of the three test results. The variability of the test results is presented using error bars corresponding to the standard deviation of the three tested specimens for each mixture

3.3.1 Compressive Strength

The compressive strength results at 7 and 28 days are presented in Figure 6. After 7 days, the control mix achieved 37.53 MPa. Introducing 0.5% and 1.0% dosages of coir fibre (CF) led to a slight decrease in the compressive strength, with values of 36.71 MPa and 34.38 MPa, respectively, which are 2.2% and 8.4% lower than the control mix strength. The mixes containing pedicel fibres showed more pronounced decreases, measuring 32.27 MPa at 0.5% dosage and 28.73 MPa at 1.0% dosage, respectively, which are 14% and 23.5% lower than the control mix strength.

After 28 days of curing, the compressive strength of the control mix reached 40.92 MPa. The strength of the coir fibre blended mix was similar to that of the control mix, with 40.39 MPa at 0.5% dosage and 39.51 MPa at 1.0% dosage, which were 1.3% and 3.4% lower than the control mix strengths, respectively. The strength of the DPPF fibre blended mix also improved significantly after 28 days of curing. The strength of DPPF bladed mixes was 38.67 MPa at 0.5% dosage and 37.40 MPa at 1.0% dosage, which were 5.5% and 8.6% less than the control mix strengths, respectively.

The findings are consistent with the general expectation that incorporating natural fibres causes a slight drop in concrete compressive strength, particularly when higher fibre amounts are used. This reduction is most likely caused by fibre agglomeration (fibre balling effect), the

formation of additional voids, and continuity interruption in the cement matrix. The effect was more noticeable in mixes with DPPF than in those with CF, demonstrating how fibre type and shape influence performance. Generally, the diameter of DPPF is higher than that of CF. Despite these reductions, the compressive strength remains within acceptable limits for structural use, especially at 0.5% fibre dosage. Overall, the findings highlight a trade-off: a minor decrease in strength is compensated for by increases in ductility and crack resistance, both of which are highly important in real-world applications.

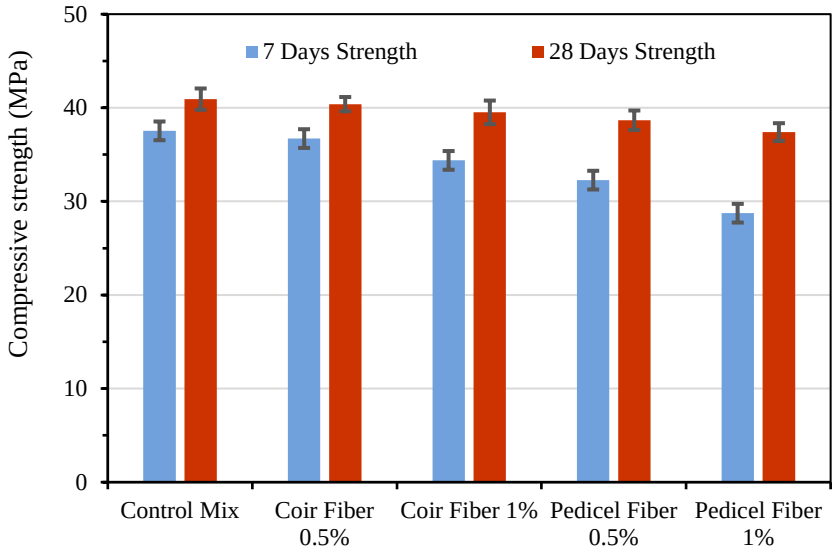


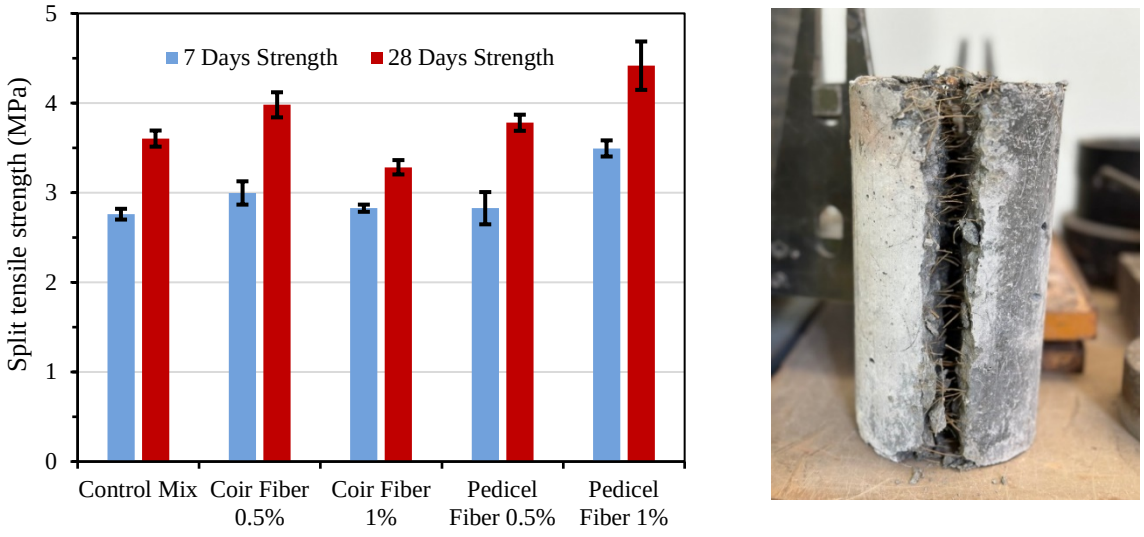
Figure 6: Compressive strength of 3 mix types at 7 and 28 days.

The reduction in compressive strength due to fibre addition was more evident at 7 days than at 28 days, particularly at the higher fibre dosage. This behaviour can be attributed to the early-age condition of the cementitious matrix, where hydration is still progressing and the fibre–matrix interfacial transition zone has not fully developed. The hydrophilic nature of natural fibres also absorbed part of the mixing water and disturbed local compaction, leading to additional voids and weaker interfacial regions at early age. With continued curing, further hydration improves matrix densification and fibre–matrix bonding, thereby reducing the strength difference between the control and fibre-reinforced mixtures at 28 days. The larger early-age reduction observed in the pedicel fibre mixtures may be related to their higher water absorption and larger diameter compared with coir fibres.

3.3.2 Split Tensile Strength

Figure 7(a) shows results of splitting tensile strength tests at 7 and 28 days of curing. At the age of 7 days, the control mix achieved a split tensile strength of 2.76 MPa. The addition of 0.5% and 1% dosages of coir fibres resulted in a slight increase in split tensile strength of 2.997 MPa and 2.83 MPa, respectively, which were 8.6% and 2.4% higher than the control mix strength. The pedicel fibre mixes performed similarly or better than the coir fibre mixes. At the age of 7days, the concrete mixes with 0.5% and 1% degases of DPPF achieved split tensile strength of 2.83 MPa and 3.49 MPa, respectively, which were 2.4% and 26.5% higher than the control mix strength, respectively. At 28 days, the control mix achieved split tensile strength of 3.60 MPa. The coir fibre mixes produced 3.98 MPa (0.5% coir, 10.5% higher than control mix) and 3.28 MPa (1.0% coir, 9.0% lower than the control). The poor performance of the 1.0% coir mix at 28 days is most likely due to poor fibre dispersion within the concrete matrix, which can

result in fibre balling and weak zones that impair tensile strength development. The pedicel mixes demonstrated significant enhancement: 3.78 MPa (0.5% pedicel, 4.9% higher than control) and 4.42 MPa (1.0% pedicel, 22.6% higher than the control mix strength).



(a) (b)

Figure 7: (a) Split tensile strength of 3 mix types at 7 and 28 days (b) Crack-bridging effect of date palm pedicel fibres during splitting tensile testing.

These findings show that incorporating natural fibres, particularly pedicel fibres, at a 1.0% dosage significantly increases the splitting tensile strength of concrete. The fibres' bridging effect improves crack prevention property under tensile loading, as shown in Figure 7(b) especially, while coir fibres increased tensile strength at lower dosages, challenges such as fibre clumping and poor dispersion at higher dosages may limit their effectiveness, as demonstrated by the 1.0% coir mix performance. The pedicel fibres, on the other hand, showed consistent and significant improvements over both curing periods, indicating their potential role in improving the tensile performance of fibre-reinforced concrete.

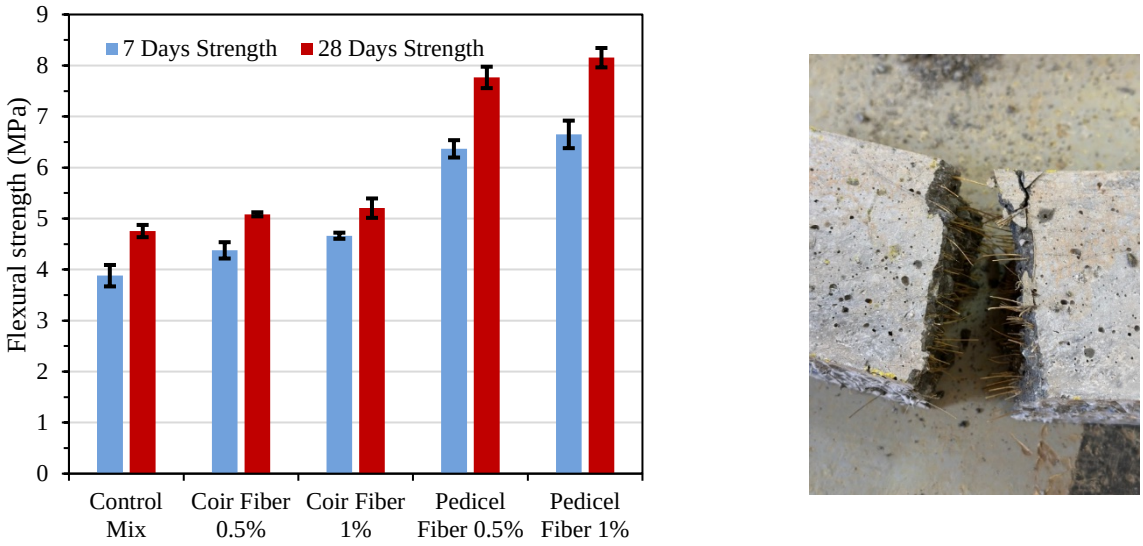
3.3.3 Flexural Strength

The flexural strength of the concrete mixes was evaluated using prism specimens measuring 500 × 100 × 100 mm and tested under a four-point loading setup in accordance with ASTM C78/C78M - Standard Test Method for Flexural Strength of Concrete (using simple beam with third-point loading). Figure 8(a) shows the results for the 7- and 28-day curing periods. Figure 8(b) shows the fibre pull out at flexural crack in the beam. The close inspection showed that some of the fibres were fractures along with the pull-out fibres.

After 28 days of curing, the control mix had attained 4.76 MPa, as flexural strength. The coir fibre mixes performed slightly better than the control, with 5.08 MPa (0.5% coir, 6.7% improvement) and 5.20 MPa (1.0% coir, 9.2% improvement). The pedicel fibre mixes demonstrated significant gains, reaching 7.77 MPa (0.5% pedicel, 63% higher than control) and 8.15 MPa (1.0% pedicel, 71% higher than the control mix strength).

The results clearly show that adding natural fibres, particularly pedicel fibres, significantly increases the flexural strength of FRC concrete. This improvement is due to high tensile strength of the fibres and ability to bridge cracks effectively (see Figure 8(b)), which improves

both crack resistance and energy absorption under bending loads. Coir fibres also helped to increase flexural strength, but not as much as the DPPF. This is most likely due to their lower tensile strength and stiffness than the pedicel fibres.



(a) (b)

Figure 8: (a) Flexural strength of 3 mix types at 7 and 28 days, and (b) Crack bridging by pedicel fibres under flexural loading.

In addition to fibre tensile properties, fibre geometry should also be considered when interpreting the flexural response. Based on the measured diameter ranges and a fibre length of 50 mm, the aspect ratio was approximately 556-625 for coir fibre and 357-417 for date palm pedicel fibre. Although coir fibre had a higher aspect ratio, the superior flexural performance of the pedicel fibre mixtures cannot be attributed to aspect ratio alone. In fibre-reinforced concrete, crack-bridging efficiency depends on the combined effect of fibre aspect ratio, tensile strength, elastic modulus, interfacial bond, and dispersion quality. The higher tensile strength and elastic modulus of pedicel fibre enabled more effective stress transfer across flexural cracks. In contrast, the exceptionally high aspect ratio of coir fibre may have promoted greater fibre interaction and less uniform dispersion, especially at higher fibre contents. As a result, the lower aspect ratio of pedicel fibre did not reduce its reinforcing effectiveness, since its superior mechanical properties played the dominant role in governing the flexural behaviour.

4 Concluding remarks

This study presents a thorough approach to evaluating the properties of DPPF and CF fibres under different treatment conditions, as well as their performance when used in a concrete mix to produce NFRC. From the experimental works following conclusions can be drawn:

- Both fibres benefit from alkaline treatment, which enhances surface bonding and mechanical properties. Boiling with alkaline treatment resulted in cleaner surfaces with increased fibrillation and cellulose content of coir and pedicel fibres.

- Date pedicel fibre achieved the highest tensile strength when subjected to boiling and alkaline treatment. Its higher tensile strength and stiffness make it suitable for load-bearing and structural rigidity applications, which can be more effective at improving cementitious composites for structural purposes. In contrast, coir fibre demonstrated a higher ductility in tensile testing, making it ideal for applications that require flexibility and crack-bridging.
- Mechanical testing of pedicel and coir fibre reinforced concrete revealed significant improvements in splitting tensile and flexural strength at a 1.0% dosage, resulting in consistent strength gains that are ideal for structural performance. Similarly, adding coir fibres improves flexural strength and splitting tensile strength but in lower extent than date palm pedicel fibre.

Overall, both coir and date palm pedicel fibres show promise in terms of concrete tensile and flexural strength, as well as a balance of strength and increased ductility, crack resistance, and energy absorption capability.

5 Acknowledgements

The author gratefully acknowledges the support received through IG funding from Sultan Qaboos University for this work, under grant number IG/ENG/CAED/24/01.

6 References

Adamu, M., Marouf, M.L., Ibrahim, Y.E., Ahmed, O.S., Alanazi, H. and Marouf, A.L., 2022. "Modeling and optimization of the mechanical properties of date fiber reinforced concrete containing silica fume using response surface methodology," *Case Studies in Construction Materials*, *17*, p.e01633.

Al Abri, A. and Sohel, K.M.A., 2024. "Sustainable Fiber Reinforced Concrete: Coir and Date Palm Fiber in Concrete – A Review," *Proceedings of the 5th International Conference on Advanced Engineering Technologies 2024*, Bayburt University, Turkey, September 25-27.

Alawar, A., Hamed, A.M. and Al-Kaabi, K., 2009. "Characterization of treated date palm tree fiber as composite reinforcement," *Composites Part B: Engineering*, *40*(7), pp.601-606.

Ajouguim, S., Page, J., Djelal, C. and Saadi, L., 2023. "Effect of treated Alfa fibers on hydration kinetics, mechanical, and adhesion properties of fiber cement composite," *Journal of Building Engineering*, *71*, p.106558.

Aravindh, M., Sathish, S., Ranga Raj, R., Karthick, A., Mohanavel, V., Patil, P.P., Muhibbullah, M. and Osman, S.M., 2022. "A Review on the Effect of Various Chemical Treatments on the Mechanical Properties of Renewable Fiber-Reinforced Composites," *Advances in Materials Science and Engineering*, *2022*(1), p.2009691.

Benaimeche, O., Carpinteri, A., Mellas, M., Ronchei, C., Scorza, D. and Vantadori, S., 2018. "The influence of date palm mesh fibre reinforcement on flexural and fracture behaviour of a cement-based mortar," *Composites Part B: Engineering*, *152*, pp292-299.

Bendahane, K., Belkheir, M., Mokaddem, A., Doumi, B. and Boutaous, A., 2023. "Date and doum palm natural fibers as renewable resource for improving interface damage of cement composites materials," *Beni-Suef University Journal of Basic and Applied Sciences, 12:37.*

Correia, V. da C, Santos, S.F., Mármol, G., Curvelo, A.A. da S. and Savastano, H., 2014. "Potential of bamboo organosolv pulp as a reinforcing element in fiber–cement materials," *Construction and Building Materials*, *72*, pp.65-71.

Dhakal, H., Bourmaud, A., Berzin, F., Almansour, F., Zhang, Z., Shah, D.U. and Beaugrand, J., 2018. "Mechanical properties of leaf sheath date palm fibre waste biomass reinforced polycaprolactone (PCL) biocomposites," *Industrial crops and products*, *126*, pp394-402.

Fiore, V., Di Bella, G. and Valenza, A.J.C.P.B.E., 2015. "The effect of alkaline treatment on mechanical properties of kenaf fibers and their epoxy composites," *Composites Part B: Engineering*, *68*, pp14-21.

Hasan, K.F., Horváth, P.G., Kóczán, Z. and Alpár, T., 2021. "Thermo-mechanical properties of pretreated coir fiber and fibrous chips reinforced multilayered composites," *Scientific Reports*, *11*(1), p.3618.

Al-Khanbashi, A., Al-Kaabi, K. and Hammami, A., 2005. "Date palm fibers as polymeric matrix reinforcement: fiber characterization," *Polymer composites*, *26*(4), pp.486-497.

Karthi, N., Kumaresan, K., Sathish, S., Gokulkumar, S., Prabhu, L. and Vigneshkumar, N., 2020. "An overview: Natural fiber reinforced hybrid composites, chemical treatments and application areas," *Materials today: proceedings*, *27*, pp2828-2834.

Kriker, A., Debicki, G., Bali, A., Khenfer, M.M. and Chabannet, M., 2005. "Mechanical properties of date palm fibres and concrete reinforced with date palm fibres in hot-dry climate," *Cement and Concrete Composites*, *27*(5), pp554-564.

Mahdi, E. and Dean, A., 2020. "The effect of filler content on the tensile behavior of polypropylene/cotton fiber and poly (vinyl chloride)/cotton fiber composites," *Materials*, *13*(3), p.753.

Nazir, M.H., Ayoub, M., Zahid, I., Shamsuddin, R.B., Yusup, S., Ameen, M. and Qadeer, M.U., 2021. "Development of lignin based heterogeneous solid acid catalyst derived from sugarcane bagasse for microwave assisted-transesterification of waste cooking oil," *Biomass and Bioenergy*, *146*, p.105978.

Olivito, R.S., Cevallos, O.A. and Carrozzini, A., 2014. "Development of durable cementitious composites using sisal and flax fabrics for reinforcement of masonry structures," *Materials & Design*, *57*, pp258-268.

Palanisamy, E. and Ramasamy, M., 2022. "Dependency of sisal and banana fiber on mechanical and durability properties of polypropylene hybrid fiber reinforced concrete," *Journal of Natural Fibers*, *19*(8), pp3147-3157.

Ramakrishna, G. and Sundararajan, T., 2005. "Impact strength of a few natural fibre reinforced cement mortar slabs: a comparative study," *Cement and concrete composites*, *27*(5), pp547-553.

Raut, A.N. and Gomez, C.P., 2016. "Thermal and mechanical performance of oil palm fiber reinforced mortar utilizing palm oil fly ash as a complementary binder," *Construction and Building Materials*, *126*, pp476-483.

Sahu, P. and Gupta, M.K., 2017. "Sisal (Agave sisalana) fibre and its polymer-based composites: a review on current developments," *Journal of Reinforced Plastics and Composites*, *36*(24), pp1759-1780.

Sivasubramanian, P., Mayandi, K., Santulli, C., Alavudeen, A. and Rajini, N., 2022. "Effect of fiber length on curing and mechanical behavior of pineapple leaf fiber (PALF) reinforced natural rubber composites," *Journal of Natural Fibers*, *19*(11), pp.4326-4337.

Tonoli, D., Henrique, G. and de Souza Almeida, A.E.F., 2010. "Surface properties of eucalyptus pulp fibres as reinforcement of cement-based composites," *Holzforschung*, *64*(5), pp595-601.

Zhang, W., Wang, C., Gu, S., Yu, H., Cheng, H. and Wang, G., 2021. "Physical-mechanical properties of bamboo fiber composites using filament winding," *Polymers*, *13*(17), p.2913.

Design specifications

Beyond Superposition: Rethinking Fiber Bridging in Concrete Elements with Bar Reinforcement

Viktor Gribniak and Aleksandr Sokolov

Laboratory of Innovative Building Structures, Vilnius Gediminas Technical University, Saulėtekio Av. 11, LT-10223 Vilnius, Lithuania

Abstract

Nowadays, design aims to reduce the CO_2 footprint by improving concrete performance without increasing cement content, notably through optimized reinforcement strategies. Steel fiber-reinforced concrete (SFRC) is promising; however, in bar-reinforced elements, the limited crack openings suppress the activation of fiber-bridging observed in standard RILEM/EN-14651 tests. At the same time, using the residual strength values obtained in the standard tests to model SFRC with bar reinforcement (SFRC-RC) double-counts the tension-softening effect, which emerges in both the SFRC and tension-stiffening models, and thus overestimates post-cracking stiffness. This contribution offers a modeling approach that separates tensile resistance into tension-softening (concrete fracture), tension-stiffening (bar interaction), and fiber-bridging resistance mechanisms. It employs a slab-shaped RC beam test that induces multiple cracks, along with an accompanying closed-form inverse analysis. The fiber-bridging model is obtained by subtracting the RC response from the combined SFRC-RC response determined for the same geometry and loading configurations, thereby defining a constitutive term consistent with smeared-crack FE analysis and avoiding the double-counting of tension-softening inherent in models calibrated from single-crack residual tests. Verification of beams made from the same concrete with different steel fiber volumes (0, 0.5%, and 1.0%) shows that the theoretical bridging model matches the experimental assessments at larger cracking deformations (smeared-concrete strains exceeding 12 times the cracking strain). However, at early cracking, the fiber content has a negligible influence because the deformation range is governed primarily by matrix microcracking, which is controlled by synthetic microfibers. The experimental results also confirm the limited efficiency of fibers under the crack-width restraint imposed by reinforcement bars, which suppresses fiber activation in the multi-crack regime.

Keywords

Reinforced concrete, fibers, residual stiffness, flexure, tension-stiffening, tension-softening

1 Introduction

The structural efficiency of fiber-reinforced concrete (FRC) is increasingly examined in the context of reducing the environmental footprint of cementitious materials (Mohamed et al., 2023). Contemporary design practice aims to enhance crack resistance, stiffness retention, and serviceability without increasing cement content, thereby supporting the shift toward more sustainable concrete composites (Hafez et al, 2024). Steel fibers are among the most effective mechanical admixtures for improving the post-cracking behavior of concrete, as numerous experimental and theoretical investigations, e.g., Barros et al. (2005), Di Prisco et al. (2009), Gribniak et al. (2013), Deifalla et al. (2021), Li et al. (2022), have shown that fibers can sustain tensile stresses after matrix cracking and significantly increase energy-dissipation capacity. These advantages have motivated the development of standardized testing procedures for quantifying the post-cracking residual strength of steel fiber-reinforced concrete (SFRC), most notably RILEM-based three-point bending tests on pre-notched prisms (RILEM, 2003) and related methodologies adopted in European standards (CEN, 2007).

Despite their widespread use, these standardized tests have a fundamental limitation: they are designed to characterize SFRC as a standalone material, in which a single dominant crack governs the specimen's mechanical resistance. The residual strengths derived from these tests reflect the combined contribution of tension-softening and fiber-bridging mechanisms, implicitly assuming that the crack width is sufficiently large (exceeding 0.5 mm) for fiber pullout to dominate. However, this assumption does not hold when SFRC is used in combination with conventional reinforcement bars. In reinforced concrete (RC) elements, the development of multiple cracks, driven by bond interaction between steel bars and concrete, substantially reduces the crack opening at each crack. As a result, the ability of fibers to mobilize bridging stresses is diminished, while the matrix softening component remains intrinsically present. Figure 1 schematically depicts the post-cracking resistance components of SFRC that are not distinguishable by standardized prism tests, because the test configuration forces a single, wide crack whose response inherently couples the tension-softening and fiber-bridging effects. Consequently, the resulting constitutive laws embed mechanisms that are not representative of the distributed cracking typical of RC members.

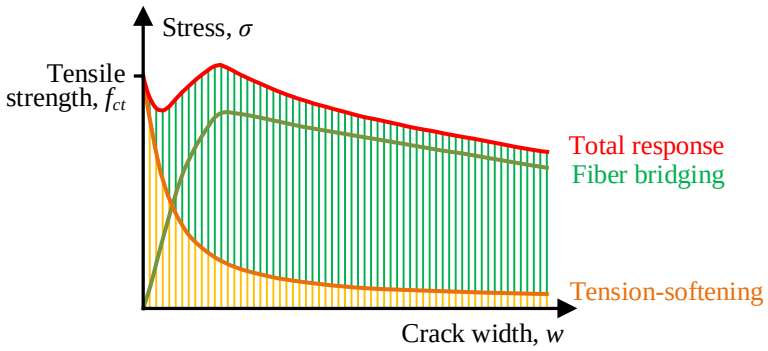


Figure 1: Post-cracking tension resistance components of SFRC. Note: The sum of the green and orange vertical lines (that are the ordinates of the fiber-bridging and tension softening diagrams) forms the SFRC resistance (red diagram)

Stang and Aarre (1991), Gribniak et al. (2012), Bernardi et al. (2016), Mazaheripour et al. (2016), and Meskenas et al. (2021) have demonstrated that directly applying residual strengths obtained from notched-prism bending tests to bar-reinforced members leads to an

overestimation of stiffness and a misrepresentation of structural behavior. This discrepancy arises because tension-softening is double-counted: once through the residual strength parameters calibrated on single-crack tests and again through the tension-stiffening model.

Gribniak et al. (2012, 2017) demonstrated that the mechanical response of SFRC in RC elements is governed by the superposition of three resistance components, namely, tension-softening, associated with fracture of the concrete matrix, tension-stiffening, induced by bond-controlled strain distribution between steel bars and concrete, and fiber bridging, which contributes to residual stress only when crack openings exceed the threshold necessary for fiber activation.

Instead of relying on material tests that enforce a predefined crack pattern (a single crack), Gribniak and Sokolov (2023) offered utilizing slab-shaped RC beam specimens designed to form multiple cracks under a four-point bending setup. The corresponding moment-curvature response is inverted to derive the equivalent tensile stress-strain relationship of the concrete. By testing both plain concrete and SFRC specimens with identical bar reinforcement, the proposed theoretical model can isolate the tension-softening and tension-stiffening components, thereby extracting the fiber-bridging contribution as an independent mechanical effect. This simplified analytical formulation, based on a rectangular approximation of tensile stress in the cracked zone, enables the solution of the inverse problem in closed form, avoiding the iterative instability typical of inverse analysis, as exemplified by Gribniak et al. (2017). Gribniak and Sokolov (2023) also demonstrated that the resulting fiber-bridging model is compatible with smeared-crack simulations, thereby eliminating unintended duplication of the tension-softening effect.

This study builds on these developments and extends them in two directions, using the same hooked-end 35 mm steel fibers as in prior work. First, it provides experimental verification of the fiber-bridging model (Gribniak & Sokolov, 2023) using a series of slab-shaped RC beams made from identical concrete but incorporating different fiber volumetric contents (0, 0.45%, and 0.92%). Second, the study evaluates the extent to which fiber-bridging is influenced by the crack-restraining action of reinforcement bars, an effect that is largely ignored in conventional SFRC constitutive models. The experimental program includes test results for eight beams designed to isolate the fiber-bridging contribution without duplicating the tension-softening effect inherent in bar-reinforced members.

2 Testing concept and analytical framework

This study employs the so-called “standardized” testing protocol, the reliability of which has been demonstrated by Gribniak et al. (2021, 2024, 2025) for various loading conditions. It uses slab-shaped (200×100×1000 mm) beams reinforced with three 8-mm steel bars, whose geometry and loading arrangement were designed to maximize the number of cracks in the bending moment zone while maintaining a test procedure simple enough to be implemented under laboratory conditions. The relatively low depth and extended moment region promote the formation of 10–12 cracks along the tensile face. Figure 2 shows the beam geometry and the load configuration. Vertical displacements are captured through linear variable displacement transducers (LVDT, L_1–L_9), and a digital image correlation (DIC) system controls the side surface deformations, enabling consistent estimation of the moment-curvature relationship. The repeatability of the moment-curvature response across nominally identical specimens demonstrates the robustness of the experimental layout (Gribniak et al., 2021, 2024, 2025).

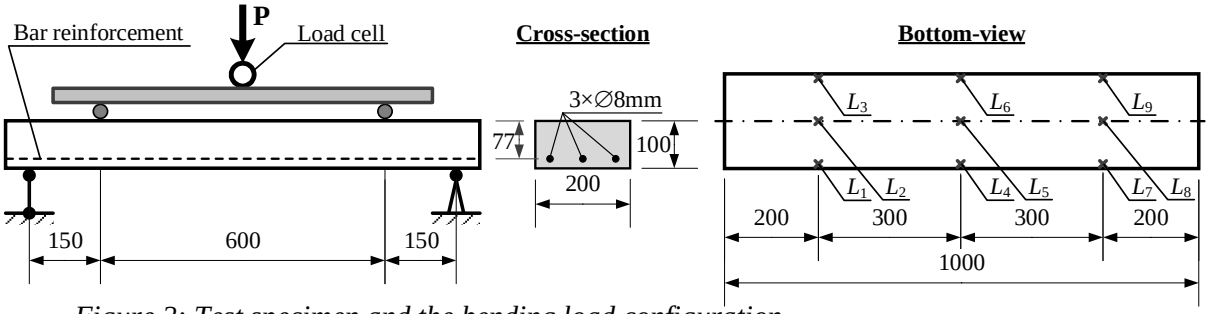


Figure 2: Test specimen and the bending load configuration

The test configuration (Fig. 2) enables estimation of the average curvature of the 600 mm pure bending zone in two alternative ways: using vertical displacement measurements and deformations captured by the DIC systems on the side surfaces. The following equations define the average curvature values:

$$\kappa = \frac{8\cdot\Delta}{l^2+4\cdot\Delta^2}, \quad \Delta = \frac{1}{3}\left(\sum_{i=4}^{6}\delta_i - \sum_{i=1}^{3}\delta_i - \sum_{i=7}^{9}\delta_i\right); \tag{1}$$

$$\kappa = \frac{\sum \upsilon}{d_u}, \quad \sum \upsilon = \frac{1}{n\cdot l_u}\left(\sum_{i=1}^{n} u_i^t + \sum_{i=1}^{n} u_i^b\right). \tag{2}$$

In the above equations, Δ determines the deflection over the pure bending zone; δ_i is the vertical displacement captured by the LVDT device L_i, i = 1, 2, …, 9 (Fig. 2); $\sum\upsilon$ defines the total strain of the side surface; u_i^t and u_i^b are the relative displacements over the "top" and "bottom" DIC measurement bases; the number and location of the DIC monitoring points can be set arbitrarily, which defines the length l_u and the distance d_u between the monitoring lines and the number of the measurement segments n. The symmetrical placement of digital cameras on both sides of the beam sample generates two comparable sets of surface deformation data.

The derived moment-curvature values form the basis for the subsequent inverse analysis, which aims to define the equivalent tensile stress-strain law of the tensile concrete. This study adopts the analytical model of SFRC proposed by Gribniak and Sokolov (2023). It employs the smeared crack and Euler-Bernoulli plane-section models. It also assumes elastic material models of bar reinforcement and compressive concrete, and a rectangular stress distribution in the tensile concrete. The latter simplification resulted from both experimental observations and the typical use of simplified tensile stress models for SFRC (Amin & Gilbert, 2018). Figure 3 shows the assumed theoretical modeling concept.

The force equilibrium and strain compatibility conditions determine the expressions of the equivalent tensile stress σ_t^* and corresponding strain ε_t^* as explicit functions of curvature κ and external bending moment $\mathbf{M}_{ext}$. This presentation skips the intermediate expressions, available in references (Gribniak et al., 2021, 2024, 2025), providing only the formulas necessary to determine the equivalent stress-strain relationship for further analysis:

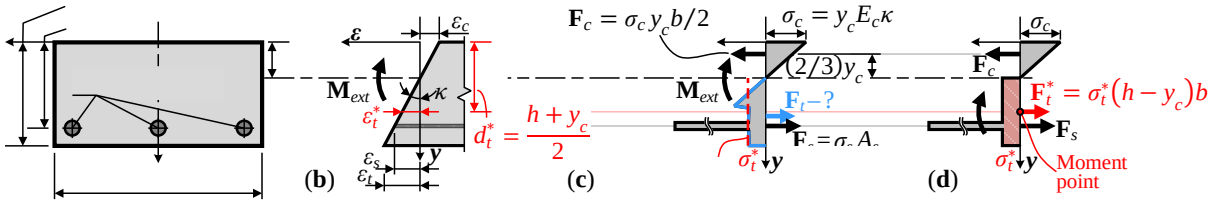


Figure 3: Theoretical modeling approach: (a) cross-section of the RC beam sample; (b) strain distribution; (c) and (d) the actual and simplified distribution of stresses

$$\sigma_t^* = \kappa \frac{y_c^2 b E_c - 2(d-y_c) E_s A_s}{2(h-y_c)b}; \quad (3)$$

$$\varepsilon_t^* = \kappa(h-y_c)/2. \quad (4)$$

In the above equations, b, h, and d are the width, height, and effective depth of the cross-section (Fig. 3a); A_s and E_s are the cross-section area and modulus of elasticity of steel bars; E_c is the modulus of elasticity of SFRC (it is assumed the same as for plane concrete); y_c determines the position of the neutral axis unknown during the analysis. The simplified material model assumptions ensure the explicit solution for y_c, which can be calculated as follows:

$$y_c = \frac{1}{3C_3}\left\{2\sqrt{C_2^2 - 3C_3C_1}\cos\left(\frac{1}{3}\cos^{-1}\left\{-\frac{27C_3^2C_0 - 9C_3C_2C_1 + 2C_2^3}{2\left[C_2^2 - 3C_3C_1\right]^{1.5}}\right\}\right) - C_2\right\}, \quad (5)$$

with coefficients

$$C_0 = \kappa d^2 E_s A_s\left(1 - \frac{h}{2d}\right) - \mathbf{M}_{ext}, \quad C_1 = \frac{\kappa E_s A_s (h-3d)}{4}, \quad C_2 = \frac{2C_1}{h-3d} + 3C_3 h, \quad C_3 = \frac{\kappa E_c b}{12}. \quad (6)$$

This formulation avoids iterative calculations and enables consistent reconstruction of the constitutive SFRC model directly from the measured moment-curvature response.

A key aspect of this framework is that tests are conducted on both RC beams and SFRC RC beams fabricated from the same concrete mixture and having the same bar reinforcement layout and geometry. This pairing allows the analytical model to reconstruct two separate stress-strain diagrams: one representing the combined tension-softening and tension-stiffening response of the RC beam, and another representing the combined tension-softening, tension-stiffening, and fiber-bridging response of the SFRC RC beam. By subtracting these two diagrams, the fiber-bridging component is isolated as an independent contribution to the tensile resistance.

Gribniak and Sokolov (2023) verified this concept, proved its adequacy for modeling full-scale SFRC RC beams, and developed the fiber-bridging model compatible with the smeared-crack approach widely used in finite element (FE) software. Moreover, because the rectangular stress approximation closely matches the shape of the tensile stress distribution observed in the multi-crack regime, the analytical solution achieves an accuracy comparable to the resolution of the monitoring devices used during testing. The following expression determines the fiber-bridging stresses σ_f related to the tensile strength of the concrete f_{ct}:

$$\frac{\sigma_f}{f_{ct}} = 0.1878 \cdot \ln\frac{\varepsilon_{ct}}{\varepsilon_{cr}} + 0.0022. \quad (7)$$

In this equation, ε_{ct} and ε_{cr} denote the tensile and cracking strains of the concrete. Remarkably, the model does not distinguish between ordinary concrete and SFRC, treating SFRC as concrete with enhanced mechanical performance, as reflected in the additional fiber-bridging stresses. Consequently, the model assumes that the modulus of elasticity (E_c) and the tensile strength (f_{ct}) determine the pseudo-elastic stage, which is identical for both ordinary concrete and SFRC. Equation 7 provides a verified representation of the fiber-bridging response for a 1.0 vol.% content of 35-mm hooked-end fibers. In the following section, this expression serves as the basis for constructing a simplified analytical representation to interpret the experimentally observed behavior of specimens with different fiber contents.

3 Analytical interpretation of fiber-bridging response

This section introduces a simplified analytical model to serve as a baseline for comparing and interpreting the fiber-bridging response of beam specimens with varying fiber volumetric contents. The formulation builds upon the logarithmic relationship established in Equation 7. It adopts the simplifying assumption that this relationship can represent the bridging effect in a generalized manner, while allowing its slope (i.e., the coefficient of the logarithmic term) to vary linearly with the fiber volumetric content. Gribniak and Sokolov (2023) demonstrated that Equation 7 is applicable for both small-scale beam samples (Fig. 2) and 3000-mm-long beams tested by Gribniak et al. (2012). Therefore, the residual fiber-bridging stress values obtained for the 3000-mm SFRC beams were used to calibrate the simplified analytical model. Gribniak et al. (2012) identified that the tension-stiffening effect practically disappears when a concrete strain of approximately 2.0-2.5 micro-strain is reached. Table 1 presents the calibration values of the fiber-bridging response corresponding to deformation exceeding the tension-stiffening boundary. These values were obtained by Gribniak et al. (2012) using superposition principles (consistent with those adopted in this study) and an iterative inverse analysis procedure to derive the fiber-bridging stresses from test data on full-scale RC beams. In this context, the analytical model is not intended for predictive application, but rather to provide a reference framework for evaluating deformation-dependent trends and identifying deviations between the experimentally observed and idealized fiber-bridging behavior.

Table 1: Calibration values of Equation 7 adopted from the reference (Gribniak et al., 2012).

Fiber volumetric content (%)	**Normalized strain (ε_{ct} / ε_{cr})**	**Normalized stress (σ_f / f_{ct})**
0.5	22.2	0.3476
1.0	22.2	0.6128
1.5	25.2	1.080

Let a denote the coefficient of the logarithmic term in Equation 7. Based on the adopted simplifying assumption and the calibration values described above, the following expression defines its dependence on the fiber volumetric content V_f:

$$a = 0.2191 \cdot V_f - 0.0113; \tag{8}$$

To investigate the fiber-bridging response using the proposed simplified analytical representation as a baseline, this study employs test data from eight small-scale beam elements (Fig. 2). To ensure consistency with previous results, these specimens were fabricated using the same mix proportions as in Gribniak and Sokolov (2023). In this study, the samples were fabricated in two series, each in two batches. The first series was dedicated to estimating the fiber-bridging effect at 0.45% fiber content; the second series investigated the effect of fiber on the residual stiffness of beam samples reinforced with 0.92% fiber volume. The maximum fiber content was chosen to match that used in the previous study (Gribniak & Sokolov, 2023), to verify the robustness of the analysis results. The second fiber content was selected near half of this value to assess the adequacy of the theoretical model (Eqn. 8) and to compare the bridging effect across different fiber volumes. Each fabrication series employed two reference RC beams and two beams additionally reinforced with fibers. The reference specimens in each series were fabricated using the same concrete proportions per cubic meter: 845.3 kg of 0-4 mm sand, 860.7 kg of 4-11 mm crushed granite aggregates, 465.8 kg of CEM II/A-LL 42.5 N cement, 197.6 liters of water, and 0.6% (by cement weight) of a superplasticizer. The SFRC beams employed

the same concrete proportions, including 35 kg (V_f = 0.45%) and 71.8 kg (V_f = 0.92%) of hooked-end DRAMIX 35/0.55 mm steel fibers. Following the recommendations of Gribniak and Sokolov (2023), the SFRC beams additionally included 0.9 kg of synthetic ADFIL 13 mm microfibers to stabilize cracking and reduce scatter in the results.

Along with the beam samples, four 100 mm cubes were fabricated for each batch to estimate the concrete's compressive strength. The compression tests resulted in the 54.2±0.9 MPa and 53.6±1.7 MPa strength of the reference and SFRC samples in the first series (V_f = 0.45%), and 54.6±1.0 MPa and 55.4±1.3 MPa strength values of the reference and SFRC specimens in the second test series (V_f = 0.92%). These results revealed compatibility among the strength values across all batches.

This test program employs the same equipment and testing procedure as the previous study (Gribniak & Sokolov, 2023). A 5 MN servohydraulic WALTER+BAI testing machine with load control and data-collection software DION 7 (Löhningen, Switzerland) was used for the bending tests. The tests were conducted under displacement control at a loading speed of 0.4 mm/min. Figure 2 shows the loading setup and the LVDT arrangement. The data logger ALMEMO 5690–2 recorded the measurements from the load cell and LVDTs every second. In addition, two EOS 77D SLR cameras with an 18–135 mm EF-S lens (Canon Inc., Tokyo, Japan) and a remote controller were positioned 0.5 m apart on opposite sides of the beams; the settings were as follows: ISO 100, f/4.5 aperture, 1/200 s exposure, and 24 mm focal length. These DIC systems monitored surface deformations within the pure-bending zone. The GOM CORRELATE software (GOM METROLOGY, Germany) was used to capture the pixel movements. To facilitate software tracking of the displacement field, the monitored surfaces were painted white and sprayed with fine black droplets before testing.

Figure 4 shows the curvature monitoring results of two selected beams, employing the alternative measurement techniques described in Section 2. This figure demonstrates excellent agreement among the alternative diagrams, thereby demonstrating the reliability of the proposed measurement procedure. However, previous studies (Gribniak et al., 2021, 2024, 2025) have shown that vertical displacement is a more robust indicator of average curvature than DIC measurements. Therefore, this study also prioritizes vertical displacement (Eqn. 1) to calculate the average curvature; DIC measurements (Eqn. 2) are used to verify the curvature evaluation.

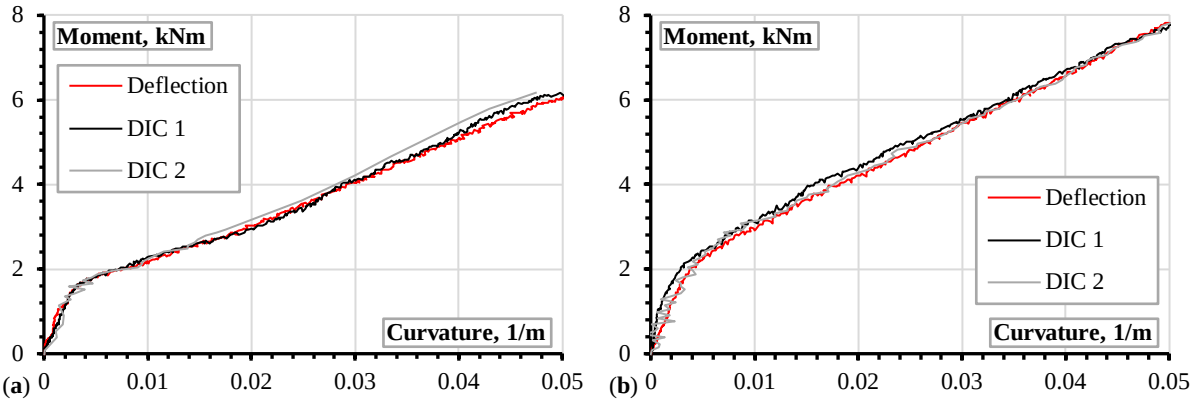


Figure 4: Moment-curvature relationships of selected beams obtained by using alternative measurement techniques: (a) a reference beam and (b) an SFRC beam (V_f = 0.92%).

Figure 5 shows the moment-curvature relationships of all the beam samples in the program. Remarkably, the relatively low amount of fibers (35 kg/m³, Fig. 5a) does not induce a visually detectable effect in the moment-curvature diagrams. The doubled fiber content (71.8 kg/m³, Fig. 5b) apparently stiffens the flexural resistance. Still, a quantification of the effect is barely possible from Figure 5. To quantify the fiber effect, this study employs the analytical approach described in Section 2. Figure 6 shows the corresponding normalized equivalent stress-strain diagrams, including the averaged response of the nominally identical beams in the series. The theoretical values of the concrete's tensile strength and modulus of elasticity were used to normalize these diagrams. These values were calculated using the experimental (compression) test results and Eurocode 2 (CEN, 2004) equations.

The difference in the residual stiffness of SFRC and reference beams became apparent in Figure 6. Following the superposition principle (Fig. 1), Figure 7 shows the differences in the mean normalized equivalent stresses between SFRC and ordinary RC beams that are presented in Figure 6. Alongside the experimentally estimated dotted diagrams (denoted "Test 0.45%" and "Test 0.92%"), Figure 7 shows the predicted fiber-bridging effect, using the updated model (Eqn. 7) with the coefficient near the natural logarithm expressed by Equation 8. The black crosses in Figure 7 correspond to the residual stress values of the large-scale beams in Table 1, which were used for the calibration of the simplified theoretical model (Eqn. 8). The dashed lines in Figure 7 show the corresponding modeling results. The calibration errors range from 3% to 9%, which is considered acceptable for such a simplistic modeling concept.

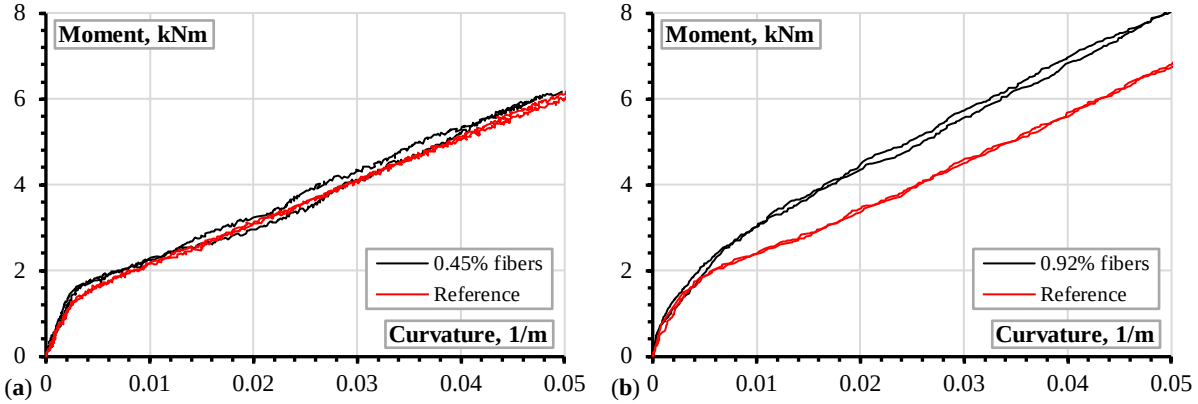


Figure 5: Moment-curvature relationships of the test beams: (a) the first (V_f = 0.45%) and (b) the second (V_f = 0.92%) series.

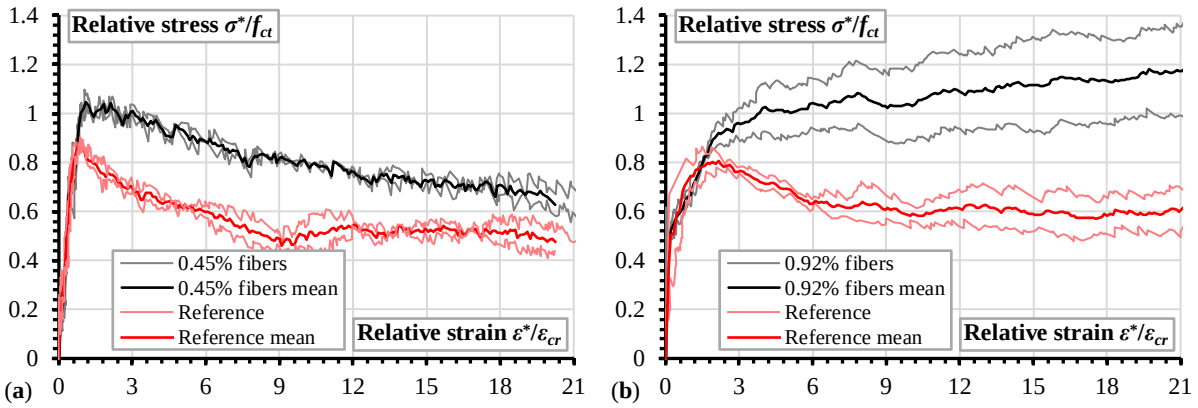


Figure 6: Normalized equivalent stress-equivalent strain diagrams: (a) the first (V_f = 0.45%) and (b) the second (V_f = 0.92%) beam series.

The solid lines in Figure 7 correspond to the fiber percentages used in the small-beam samples used as baselines to interpret the fiber-bridging response in this study. The results of the second series (green dots, V_f = 0.92%) follow the trend indicated by the analytical baseline. This trend is consistent with the modeling results reported by Gribniak and Sokolov (2023). However, the shape of the residual stress diagram for the first sample series (red dots, V_f = 0.45%) deviates from the analytical baseline. At the same time, the initial portions of the experimental diagrams for different fiber contents are nearly coincident, indicating similar behavior during the early cracking stage. This disagreement may be attributed to the microfiber effect, bridging the microcracks (Gribniak et al., 2021). For strains up to approximately 9×ε_{cr}, the responses of beams with different fiber volumes are nearly identical, indicating that fiber content has a negligible influence in this early cracking regime. This observation supports the previous results (Gribniak et al., 2021), suggesting that this deformation range is primarily governed by microcrack formation, controlled by the synthetic microfibers. Beyond 12×ε_{cr}, the theoretical fiber-bridging curve (solid red line) diverges from the response of the SFRC beams, exhibiting higher residual stresses. This behavior suggests that the simplified assumptions embedded in the analytical representation become more applicable at moderate cracking deformations, while remaining limited in the early cracking regime.

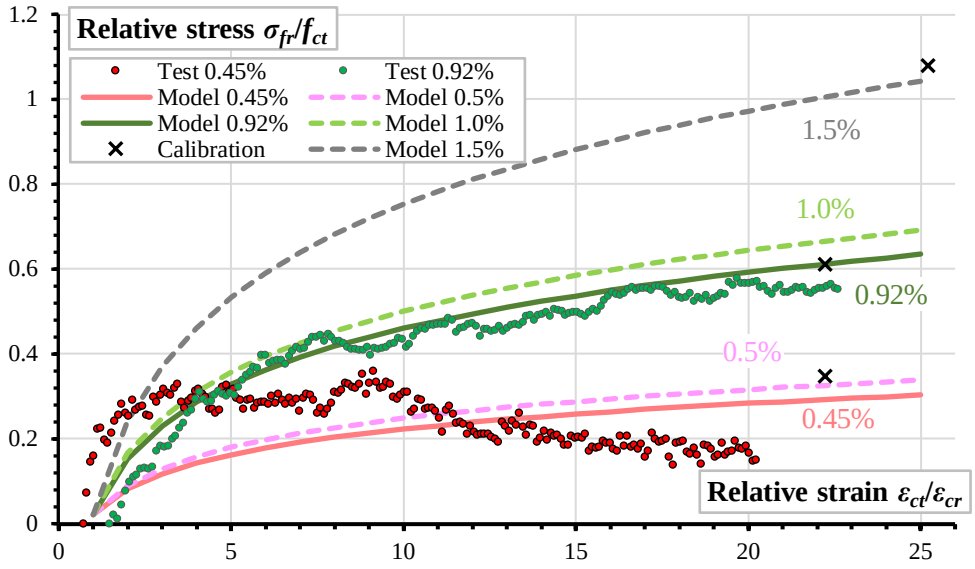


Figure 7: Modeling the fiber-bridging effect. Note: the percentages describe the fiber volumetric content.

This threshold behavior supports the conceptual separation embedded in the analytical model. In the early deformation stage, the response is governed primarily by matrix cracking and bond-controlled strain redistribution, both of which are common to plain and fiber-reinforced RC members. Once the crack openings exceed the activation range required for fiber pullout, the contribution of fibers becomes more pronounced, and the analytical bridging law captures the increasing residual stresses in this deformation range. This behavior is consistent with micromechanical observations that hooked-end steel fibers become effective only at crack openings on the order of tenths of a millimeter (Li et al., 1993). At the same time, the discrepancy between the shapes of the experimentally obtained and theoretical diagrams (Fig. 7) underscores limitations of the simplified analytical representation when applied to different fiber types, combinations, and volumetric contents. Still, the separation of the fiber-

bridging effect (Figs. 1 and 7) provides a consistent and physically grounded framework for interpreting the behavior of SFRC RC members without inadvertently amplifying softening effects. The dotted diagrams in Figure 7 also reveal that the mechanical efficiency of fibers develops progressively from zero, which contrasts with the interpretation derived from standardized notched prism tests (CEN, 2007) when applied to bar-reinforced members, primarily due to the crack-restraining actions of reinforcement bars.

The proposed experimental and analytical framework (Fig. 3) is consistent with the constitutive concepts embedded in Eurocode 2 (CEN, 2004); rather, it clarifies the limitations of interpreting residual strengths from standardized notched prism tests when applied to SFRC elements incorporating bar reinforcement. In this sense, the proposed approach complements existing design provisions by enabling a more consistent mechanical representation of fiber-bridging behavior in multi-crack structural elements.

4 Conclusions and outlook

The study introduced a testing and analytical framework that isolates the fiber-bridging contribution in reinforced concrete members by combining slab-shaped RC beam tests with a closed-form inverse procedure. This approach separates the tensile resistance into tension-softening, tension-stiffening, and fiber-bridging components, thereby avoiding the stiffness overestimation that arises when standardized residual strengths are applied directly to RC elements.

The reported experimental results confirmed that the proposed method adequately identifies the deformation range in which fibers become mechanically effective and provides a bridging-only constitutive law compatible with strain-based modeling of RC members. However, the analytical representation was established based on a limited experimental dataset, corresponding to a single concrete grade and a single hooked-end steel fiber type. Because early-stage cracking behavior depends on matrix strength and fiber-matrix bond characteristics, the strain threshold at which fiber-bridging becomes noticeable may change for different concretes or fiber geometries. Broader experimental coverage is needed to generalize the activation threshold and refine the fiber-bridging law.

This experimental and analytical study draws the following outcomes:

- The closed-form inverse formulation adequately reconstructed the tensile response, producing stable stress-strain curves without iterative sensitivity. The absence of the iterative approximation makes the accuracy of the inverse analysis procedure comparable to that of the measurement devices employed in the test program.
- The considered fiber content had a negligible influence on early cracking, up to approximately nine times the cracking strain, suggesting that this deformation range is governed primarily by the formation of microcracks governed by the action of synthetic microfibers.
- The simplified analytical representation provides a consistent baseline for interpreting deformation-dependent fiber-bridging behavior, rather than a predictive constitutive model applicable to all fiber types and volumetric contents.
- Beyond the early-cracking threshold, the analytical bridging law followed the experimentally observed residual stress trends, suggesting that the method captures the strain-dependent activation of fiber pullout within this deformation range.

- Bridging effectiveness is lower than implied by standardized notched-prism tests, indicating that bar-induced crack restraint suppresses fiber engagement by limiting crack openings below the activation threshold.
- The methodology is scalable, with the bridging law extracted from small specimens showing compatibility with full-scale beam behavior.

5 Acknowledgements

This research work has received funding from the project “Civil Engineering Research Centre” (agreement No S-A-UEI-23-5, ŠMSM).

6 References

Amin, A. and Gilbert, R. I., 2018, “Instantaneous Crack Width Calculation for Steel Fiber-Reinforced Concrete Flexural Members,” *ACI Structural Journal*, 115(2), pp. 535-543. doi: 10.14359/51701116

Barros, J. A. O., Cunha, V. M., Ribeiro, A. F., and Antunes, J. A. B., 2005, “Post-Cracking Behaviour of Steel Fibre Reinforced Concrete,” *Materials and Structures*, 38(1), pp. 47-56. doi: 10.1007/BF02480574

Bernardi, P., Michelini, E., Minelli, F., and Tiberti, G., 2016, “Experimental and Numerical Study on Cracking Process in RC and R/FRC Ties,” *Materials and Structures*, 49(1), pp. 261-277. doi: 10.1617/s11527-014-0494-1

CEN (European Committee for Standardization), 2004, *Eurocode 2: Design of Concrete Structures - Part 1-1: General Rules and Rules for Buildings* EN 1992-1-1:2004, CEN, Brussels, 225 p.

CEN (European Committee for Standardization), 2007, *Test Method for Metallic Fibre Concrete — Measuring the Flexural Tensile Strength (Limit of Proportionality (LOP), Residual)* EN 14651:2005+A1:2007, CEN, Brussels, 17 p.

Deifalla, A. F., Zapris, A. G., and Chalioris, C. E., 2021, “Multivariable Regression Strength Model for Steel Fiber-Reinforced Concrete Beams under Torsion,” *Materials*, 14(14), 3889. doi: 10.3390/ma14143889

Di Prisco, M., Plizzari, G., Vandewalle, L., 2009, “Fibre Reinforced Concrete: New Design Perspectives,” *Materials and Structures*, 42, pp. 1261-1281. doi: 10.1617/s11527-009-9529-4

Gribniak, V., Kaklauskas, G., Hung Kwan, A. K., Bacinskas, D., and Ulbinas, D., 2012, “Deriving Stress–Strain Relationships for Steel Fibre Concrete in Tension from Tests of Beams with Ordinary Reinforcement,” *Engineering Structures*, 42, pp. 387-395. doi: 10.1016/j.engstruct.2012.04.032

Gribniak, V., Kaklauskas, G., Torres, L., Daniunas, A., Timinskas, E., and Gudonis, E., 2013, “Comparative Analysis of Deformations and Tension-Stiffening in Concrete Beams Reinforced with GFRP or Steel Bars and Fibers,” *Composites Part B: Engineering*, 50, pp. 158-170. doi: 10.1016/j.compositesb.2013.02.003

Gribniak, V., Kaklauskas, G., Juozapaitis, A., Kliukas, R., and Meskenas, A., 2017, “Efficient Technique for Constitutive Analysis of Reinforced Concrete Flexural Members,” *Inverse Problems in Science and Engineering*, 25(1), pp. 27-40. doi: 10.1080/17415977.2015.1135139

Gribniak, V., Sultani, H. A., Rimkus, A., Sokolov, A., and Torres, L., 2021, "Standardised Quantification of Structural Efficiency of Hybrid Reinforcement Systems for Developing Concrete Composites," *Composite Structures*, 274, 114357. doi: 10.1016/j.compstruct.2021.114357

Gribniak, V., Sultani, H. A., Rimkus, A., Boris, R., Sokolov, A., and Torres, L., 2024, "Quantifying the Flexural Stiffness Changes in the Concrete Beams with Externally Bonded Carbon Fiber Sheets under Elevated Environment Temperature," *Alexandria Engineering Journal*, 104, 688-700. doi: 10.1016/j.aej.2024.08.044

Gribniak, V., Plioplys, L., Antonovič, V., Sokolov, A., and Kudžma, A., 2025, "Systematic Investigation of the Bond Performance of Steel Reinforcement in Refractory Castables after High-Temperature Treatment," *Construction and Building Materials*, 491, 142715. doi: 10.1016/j.conbuildmat.2025.142715

Gribniak, V. and Sokolov, A., 2023, "Standardized RC Beam Tests for Modeling the Fiber Bridging Effect in SFRC," *Construction and Building Materials*, 370, 130652. doi: 10.1016/j.conbuildmat.2023.130652

Hafez, H., Malchiodi, B., Tošić, N., Drewniok, M., Purnell, P., and De la Fuente, A., 2024, "Decarbonization Potential of Steel Fibre-Reinforced Limestone Calcined Clay Cement Concrete One-Way Slabs," *Construction and Building Materials*, 435, 136847. doi: 10.1016/j.conbuildmat.2024.136847

Li, V. C., Stang, H., and Krenchel, H., 1993, "Micromechanics of Crack Bridging in Fibre-Reinforced Concrete," *Materials and Structures*, 26(8), pp. 486-494. doi: 10.1007/BF02472808

Li, C., Zhu, H., Niu, G., Cheng, S., Gu, Z., and Yang, L., 2022, "Flexural Behavior and a New Model for Flexural Design of Concrete Beams Hybridly Reinforced by Continuous FRP Bars and Discrete Steel Fibers," *Structures*, 38, pp. 949-960. doi: 10.1016/j.istruc.2022.02.037

Mazaheripour, H., Barros, J. A. O., and Sena-Cruz, J., 2016, "Tension-Stiffening Model for FRC Reinforced by Hybrid FRP and Steel Bars," *Composites Part B: Engineering*, 88, pp. 162-181. doi: 10.1016/j.compositesb.2015.10.042

Meskenas, A., Ramanauskas, R., Sokolov, A., Bacinskas, D., and Kaklauskas, G., 2021, "Residual Stress – Strain Relations Inversely Derived from Experimental Moment – Curvature Response of RC Beams with Fibres Compared to the Recommendations of Design Codes," *Structures*, 34, pp. 3363-3375. doi: 10.1016/j.istruc.2021.09.070

Mohamed, A. M., Tayeh, B. A., Abu Aisheh, Y. I., and Salih, M. N. A., 2023, "Exploring the Performance of Steel Fiber Reinforced Lightweight Concrete: A Case Study Review," *Case Studies in Construction Materials*, 18, e01968. doi: 10.1016/j.cscm.2023.e01968

RILEM TC 162-TDF, 2003, "Test and Design Methods for Steel Fibre Reinforced Concrete: σ-ε-Design Method. Final Recommendations," *Materials and Structures*, 36, pp. 560-567. doi: 10.1007/BF02480834

Stang, H., and Aarre, T., 1991, "Evaluation of Crack Width in FRC with Conventional Reinforcement," *Cement and Concrete Composites*, 14(2), pp. 143-154. doi: 10.1016/0958-9465(92)90007-I

Quality Control of Steel Fibre-Reinforced Concrete: Traditional Method versus Innovative Approach

Simone Spagnuolo[1], Alberto Meda[1], Benoit De Rivaz[2]

[1]: Tunnelling Engineering Research Centre - University of Rome Tor Vergata, Rome, Italy
[2]: Bekaert, Zwevegem, Belgium.

Abstract
The increasing use of Fibre Reinforced Concrete (FRC) in structural and precast applications has intensified the need for robust quality control procedures, as its mechanical performance depends not only on the cementitious matrix but also on the content, distribution, and orientation of steel fibres, parameters that current destructive methods can assess only partially, with high costs and no information on fibre orientation. This study investigates a newly developed non-destructive inductive method based on electromagnetic principles, comparing it with conventional destructive techniques on specimens extracted from segments adopted for an Italian railway tunnel project and on laboratory-produced samples with controlled fibre orientation, with the dual objective of evaluating its reliability under real operating conditions and defining an optimised procedure for its calibration and practical implementation. The experimental results show that the inductive approach provides good sensitivity and can serve as an effective screening tool. Its accuracy being strongly dependent on the adopted acceptance threshold, while also offering significant economic and time-related benefits by enabling quality control checks without specimen crushing, thus reducing verification time and overall testing costs.

Keywords
Inductive method, fibre-reinforced concrete, quality control methods, fibre content, fibre orientation

1 Introduction

In recent decades, the construction industry has increasingly adopted advanced structural materials to improve mechanical performance, durability, and sustainability. Among these, Fibre-Reinforced Concrete (FRC) has gained widespread attention because it combines the high compressive strength of conventional concrete with enhanced ductility, toughness, and crack control provided by dispersed fibres. In particular, Steel Fibre-Reinforced Concrete (SFRC) has demonstrated excellent tensile and post-cracking behaviour, making it an effective alternative to conventional reinforcement in structural and infrastructural applications (Naaman, 2003; di Prisco et al., 2009; fib Bulletin 83, 2019).

The mechanical performance of SFRC depends not only on the cementitious matrix but also on fibre content, distribution, and orientation. These characteristics are strongly influenced by production processes such as mixing, pumping, transportation, and casting, which may cause fibre clustering, segregation, or preferential alignment along the concrete flow (Kooiman, 2000; Grünewald, 2004). Consequently, the actual material properties may differ from design assumptions, highlighting the need for reliable quality control procedures.

Current quality control is mainly based on destructive techniques involving core extraction or dedicated specimens, followed by matrix disintegration and magnetic separation of the fibres. Although standardized procedures (e.g., UNI-EN 14721:2005+A1:2007; fib Bulletin 83) provide accurate estimates of fibre content, they are laborious, expensive, and environmentally demanding. Moreover, they do not provide information on fibre orientation, despite its significant influence on the anisotropic mechanical behaviour of SFRC (Laranjeira et al., 2012).

To address these limitations, several non-destructive testing (NDT) techniques have been investigated, including eddy current methods, ultrasonic testing, electromechanical impedance (EMI), impact-based techniques supported by machine learning, and X-ray computed tomography (CT). While these approaches provide useful qualitative or localized information, they often remain limited by penetration depth, quantification capability, cost, or applicability to full-scale structures (Ozyurt et al., 2006; Robins et al., 2001; Barnett et al., 2010).

This study investigates an electromagnetic induction-based methodology for the non-destructive characterization of SFRC. The method exploits the variation in coil inductance induced by the presence of ferromagnetic steel fibres, allowing an indirect estimation of both fibre content and average orientation. A newly developed testing device measures the inductance variation with respect to a reference (empty coil), and, following appropriate calibration, correlates these measurements with the volumetric fibre content (C_f) and fibre orientation.

The proposed methodology is validated through a comparison with the conventional destructive technique for fibre content assessment, while also providing information on fibre orientation, which cannot be obtained using traditional methods. The experimental campaign was conducted at the Tunnelling Engineering Research Centre (TERC) of the University of Rome Tor Vergata and focused on precast SFRC tunnel lining segments used in a real railway project in Italy. Testing included both cores extracted from full-scale segments and specimens manufactured with controlled fibre content and orientation using the same mix design and production facility as the actual tunnel segments.

The objective is to assess the reliability and applicability of the inductive technique under realistic production conditions. By providing a rapid, repeatable, and non-destructive alternative to conventional quality control methods, the proposed approach contributes to improving SFRC characterization and supports its wider adoption in structural engineering practice.

2 Inductive method

The inductive method is based on classical electromagnetism and enables the indirect estimation of both the volumetric content and the average orientation of steel fibres in FRC. The technique relies on the interaction between the alternating magnetic field generated by a coil and the ferromagnetic steel fibres embedded in the concrete matrix. When a specimen is placed inside the coil, the high magnetic permeability of the fibres modifies the magnetic field distribution, increasing the magnetic flux linked to the coil and, consequently, its inductance (Fig.1).

According to the Faraday–Neumann–Lenz law, this change in magnetic flux produces a measurable variation in inductance. Its magnitude depends not only on the amount of steel fibres but also on their orientation with respect to the magnetic field. Fibres aligned with the field generate a greater increase in inductance, whereas fibres oriented perpendicular to the field produce a weaker response. Consequently, the measured inductance variation reflects the combined effect of fibre content and average orientation.

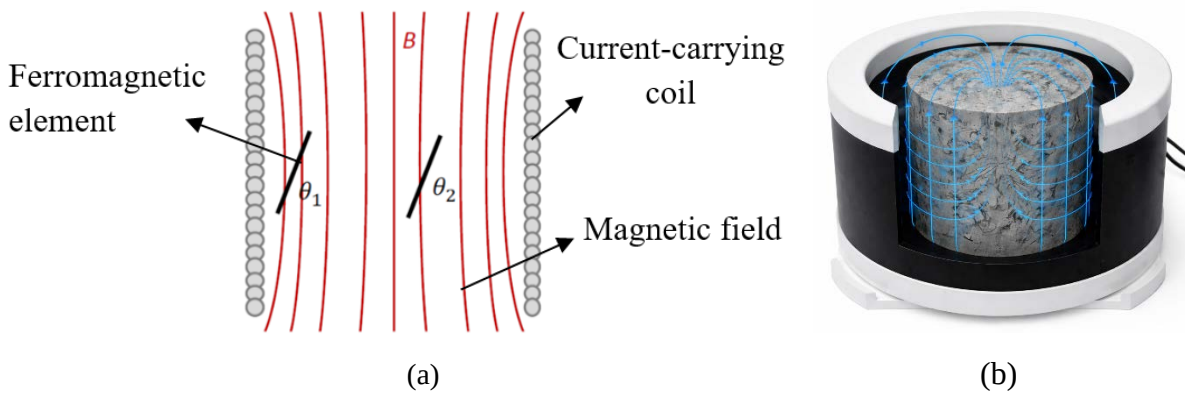
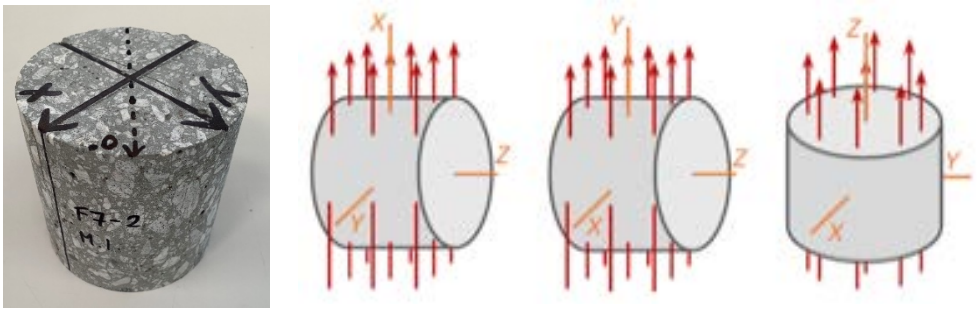


Figure 1: (a) Schematic of a current-carrying coil generating a magnetic field in which ferromagnetic fibres are embedded, and (b)Testing device.

Inductance measurements provide the experimental data required to estimate both the fibre content and the average fibre orientation in FRC. Before testing, a three-dimensional Cartesian reference system (x, y, z) is defined on each specimen to ensure consistent measurements (Fig.2a). For cylindrical specimens, the z-axis coincides with the specimen height, whereas the x and y axes lie in the transverse plane.

Following the reference measurement of the empty coil (L_0), the specimen is positioned inside the coil and tested sequentially along the three orthogonal directions by rotating it accordingly (Fig.2b). For each direction (i=x, y, z), the inductance L_i is measured and the corresponding inductance variation is calculated as $\Delta L_i = L_i - L_0$, where ΔL_i , expressed in millihenry (mH), represents the specimen's magnetic response in the considered direction.

Owing to the ferromagnetic nature of the steel fibres, the inductance variation is expected to be positive.



(a) (b)

Figure 2: (a) Three-dimensional Cartesian reference system (x, y, z) on specimen, and (b) The magnetic field generated by the device passes through the specimen along the different directions.

The measured inductance cannot be directly converted into fibre content and therefore requires calibration to determine the coefficient β, which relates the electromagnetic response to the actual fibre dosage. The fibre content is calculated as:

$$C_f = \beta \cdot \sum_i \frac{\Delta L_i}{B_{v,i}} = \beta \cdot \left(\frac{\Delta L_x}{B_{v,x}} + \frac{\Delta L_y}{B_{v,y}} + \frac{\Delta L_z}{B_{v,z}}\right) = \beta \cdot L_e \quad (1)$$

where ΔL_i is the inductance variation measured along direction i, $B_{v,i}$ is a geometric correction factor accounting for the effective specimen volume interacting with the magnetic field, and L_e is the equivalent inductance obtained by summing the normalized directional contributions.

The correction factor $B_{v,i}$ depends exclusively on specimen geometry. For cubic specimens, the analysed volume is identical in all directions and a single value of B_v can be adopted. Consequently, when specimens have identical dimensions, this factor is implicitly included in the calibration coefficient β and no additional correction is required. If different cube sizes are considered, the inductance values must be normalized to account for the different analysed volumes before applying the same calibration relationship. For cylindrical specimens, however, the effective analysed volume varies with the measurement direction because of the geometric asymmetry. Therefore, different values of $B_{v,i}$ are required, although the differences remain limited. For cylinders with a diameter and height of 100 mm, $B_{v,i}$ equals 536 for the x–y plane and 538 for the z-direction.

The calibration coefficient β is determined experimentally using specimens with known fibre content. Each specimen is first tested inductively to obtain L_e and subsequently analysed destructively by extracting, drying, and weighing the fibres to determine the actual fibre content ($C_f = m_f/V$). A linear regression through the origin between C_f and L_e provides the calibration coefficient β, which depends only on the electromagnetic and geometric characteristics of the adopted fibre type. Once calibrated, the fibre content of unknown specimens is simply obtained from $C_f = \beta \cdot L_e$.

The same measurements also provide an estimate of the average fibre orientation through the normalized directional contribution (Eq.2) where ω_i represents the relative magnetic

contribution along direction i. Higher values indicate a preferential fibre alignment parallel to the corresponding measurement axis. Although the method does not reconstruct the complete three-dimensional fibre network, it provides a reliable non-destructive assessment of both fibre content and preferential orientation, making it well suited for quality control of FRC elements.

$$\omega_i = \frac{\Delta L_i / B_{v,i}}{L_e} \tag{2}$$

3 Experimental program

The experimental program was carried out on precast SFRC tunnel lining segments manufactured with C45/55 concrete reinforced with hooked-end steel fibres (length 60 mm, diameter 0.75 mm, aspect ratio l/d=80, tensile strength up to 1800 MPa). The design fibre dosage was 40 kg/m³, a typical value for structural tunnel applications, providing sufficient residual strength to replace conventional passive reinforcement according to the adopted performance-based design approach.

Following full-scale testing, cylindrical cores were extracted from undisturbed regions of the segments and processed into specimens with a diameter of 100 mm and a height-to-diameter ratio of 1. These specimens were used for compressive strength, Brazilian splitting tensile strength, inductive measurements, and subsequent destructive determination of fibre content. The average compressive and tensile strengths were 92.4 MPa (Std. dev. 1.3 MPa) and 7.7 MPa (Std. dev. 2.5 MPa), respectively.

The experimental investigation focused on quality control of SFRC through the evaluation of fibre content and orientation. While the reference fibre content was determined by conventional destructive procedures involving crushing, fibre extraction, and weighing, the proposed inductive method required calibration of the coefficient β (Eq. (1)), relating inductance variation to the actual fibre content (C_f). For this purpose, fifteen cylindrical specimens with known fibre dosages of 30, 40, and 50 kg/m³ (five specimens per dosage) were produced and tested (Fig.3a). It should be noted that the calibration procedure is not intrinsically limited by the maximum fibre dosage; the practical upper limit is determined by the hardware capabilities of the measuring system rather than by the inductive method itself.

The calibration results established a linear relationship between equivalent inductance and fibre content, whose reliability was assessed through the coefficient of determination (R^2). In addition, specimens with controlled fibre orientations (x–y plane and z-direction) were manufactured to identify the direction of maximum inductance response and provide a reference for interpreting specimens with unknown fibre orientation (Fig.3b).



(a) (b)

Figure 3: Reference samples. (a) Known fibre dosage and orientation, and (b) Samples to be use as reference for the comparison and the calibration of the coefficient β.

Cylindrical cores (F1–F7) were extracted from two SFRC tunnel lining segments (Fig.4a). Each core, originally 400 mm high, was subdivided into four 100 mm specimens from intrados to extrados (Fi-j, with i=1–7 and j=1–4; e.g., F1-4 denotes the extrados specimen from core F1), yielding a total of 28 specimens for inductive testing (Fig.4b). A Cartesian reference system was defined for each specimen, with the x-axis aligned with the TBM thrust direction, the y-axis in the transverse plane, and the z-axis normal to the segment surface (Fig.4c). Inductive measurements were performed sequentially along the three orthogonal directions by rotating the specimen inside the coil. For each specimen, five measurement sets were acquired, each comprising one empty-coil reference measurement and three measurements along the x-, y-, and z-axes. This procedure ensured the repeatability of the estimated fibre content (C_f), resulting in a total of 560 inductance measurements. After the inductive tests, all specimens were subjected to destructive analysis to determine the actual fibre content, which was used to validate the proposed methodology (Fig.4d).

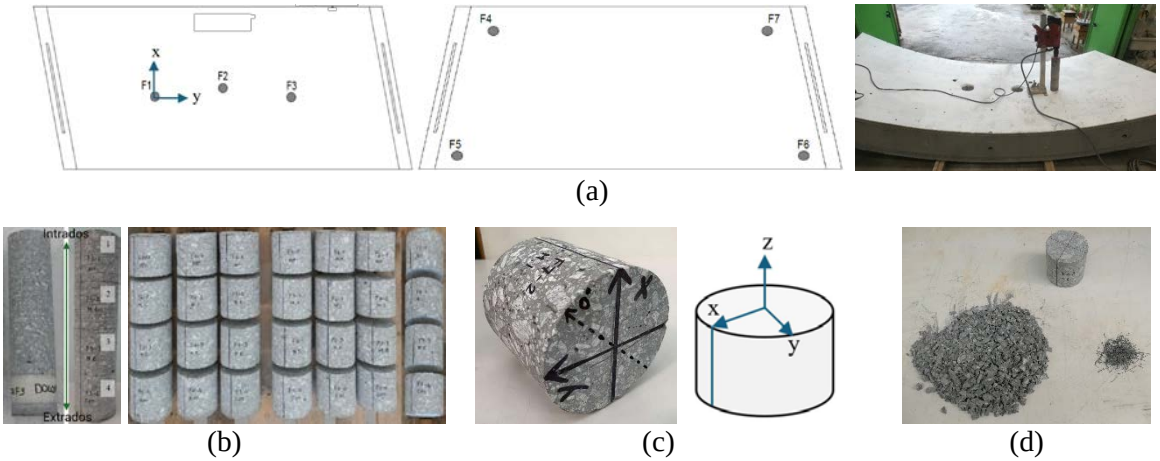


Figure 4: (a) Position of the extracted cored specimens, (b) Prepared samples, and (c) Cartesian coordinate system.

4 Fibre content results

The calibration procedure produced a linear relationship between equivalent inductance and fibre content, resulting in a calibration coefficient β=8277.6 and a coefficient of determination of R^2=0.9502. The high R^2 value confirms the reliability of the proposed calibration for estimating fibre content from inductive measurements.

Fig.5 compares the fibre contents obtained using the destructive reference method and the proposed inductive technique, together with the design value of 40 kg/m³. Overall, the two methods show good agreement: 96% of the specimens (27/28) exhibit deviations within ±20%, while 75% (21/28) fall within ±10%, confirming the reliability of the inductive approach for fibre content estimation.

Excluding specimen F3-4, whose fibre content (12.45 kg/m³) is below the instrument detection limit (20 kg/m³), the inductive method overestimates fibre content in 12 of 27 specimens (44%), with an average deviation of +5.9% (≈2.2 kg/m³), and underestimates it in the remaining 15 specimens (56%), with an average deviation of −4.9% (≈2.1 kg/m³). The error distribution is therefore balanced, indicating the absence of systematic bias. Larger discrepancies are mainly associated with specimens exhibiting low fibre contents or

unfavourable fibre distributions and orientations, which reduce the magnetic response and consequently the measurement sensitivity.

The comparison also highlights the potential of the inductive method as a quality-control screening tool. Using the acceptance criterion defined in fib Bulletin 83 (±20% of the design dosage, i.e. 32–48 kg/m³), both methods identify six non-compliant specimens. Four are consistently classified by both techniques, whereas two false positives (F7-1 and F7-4) and two false negatives (F2-4 and F4-4) are observed. Since all misclassifications occur close to the acceptance limits, a more conservative threshold was investigated for the inductive method.

Adopting a ±15% acceptance range (34–46 kg/m³) for the inductive measurements, while retaining the ±20% criterion for the destructive method, increases the number of specimens flagged for further investigation to 11 (39% of the total). Under this approach, all six truly non-compliant specimens are correctly identified, eliminating false positives, while the remaining five false negatives are limited to specimens lying close to the acceptance boundaries. This strategy considerably improves inspection reliability while restricting destructive testing to less than 40% of the specimens, thereby reducing testing time and costs. The proposed ±15% threshold therefore represents an effective compromise for the quality control of SFRC structural elements.

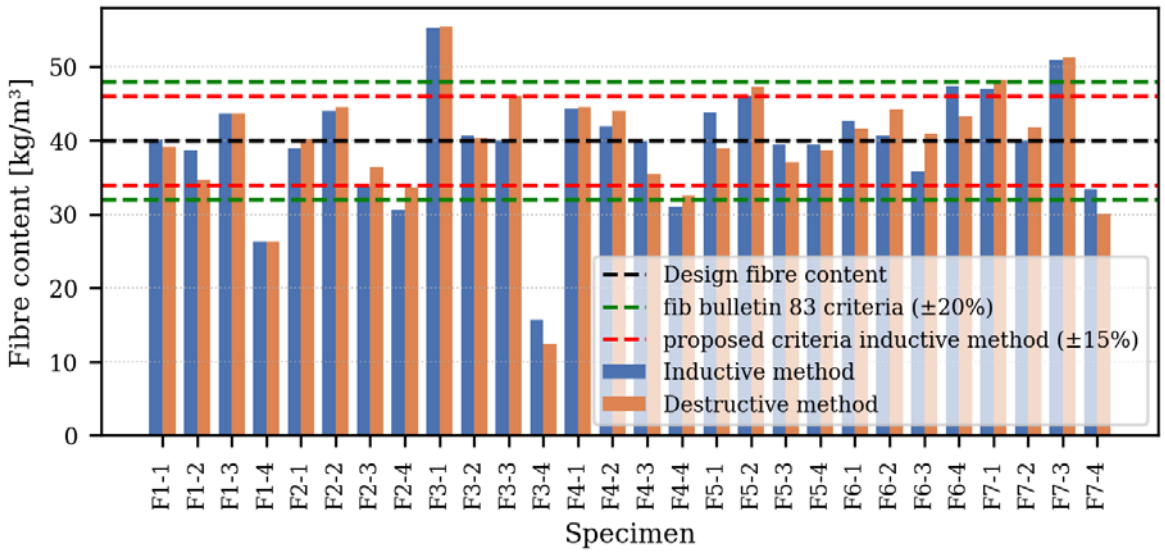


Figure 5: Fibre content (C_f): comparison between the inductive and traditional methods

5 Fibre orientation results

Table 1 summarizes the inductive measurements performed on the reference specimens with controlled fibre orientation, while Fig.6 reports the fibre orientation obtained for the specimens extracted from the tunnel segments. Individual specimen results are shown in Fig.6a, whereas Fig.6b presents the average orientation for each core, providing a synthetic representation of the fibre distribution.

The reference specimens confirm the capability of the inductive method to identify the dominant fibre orientation. Specimens produced with fibres intentionally aligned in the x–y plane exhibit in-plane orientation values between approximately 98 and 99.8%, with only a limited out-of-plane contribution ($\omega_z \approx 0$–2%).

Table 1: Fibre orientation on the reference specimens (C1-C3).

Specimen	ω_z (%)	ω_{x-y} (%)	**Total** (%)
1	1.99	98.01	100
2	0.21	99.79	100
3	1.51	98.49	100

Conversely, specimens produced with fibres oriented along the z-axis still show an in-plane contribution ranging from approximately 18% to 38%.

These results demonstrate that perfectly controlled fibre alignment cannot be achieved, even under laboratory conditions, owing to concrete flow during casting, compaction effects, and the geometry of hooked-end fibres, which also affects the electromagnetic response. Consequently, the measured orientation should be interpreted as an indicator of the dominant orientation trend rather than an exact directional distribution.

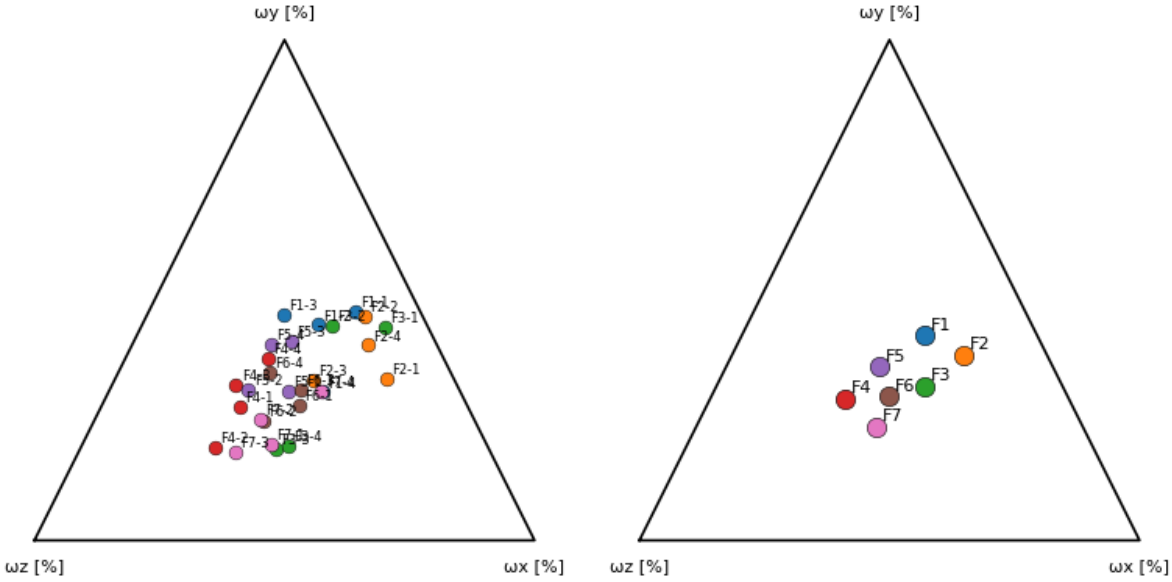
The fibre orientation of the specimens extracted from the tunnel segments reveals a moderately anisotropic distribution throughout the segments. None of the analysed specimens approaches either a fully isotropic or a fully unidirectional configuration, indicating that all three principal directions contribute to the fibre network.

A clear spatial trend is observed between the central cores (F1–F3) and the edge cores (F4–F7). The central region is characterized by a predominantly planar orientation, with fibres preferentially aligned within the x–y plane and a relatively limited contribution along the z-direction. Local differences are nevertheless observed: F1 exhibits a greater contribution along the y-axis, F2 shows a preferential alignment along x, whereas F3 presents the largest internal variability, including a moderate increase in the z-component in some specimens. Overall, these cores remain representative of a mainly planar anisotropy.

The edge cores display a different orientation pattern, characterized by a systematic increase in the z-component. This trend is particularly evident in F4 and F7, where the specimens are consistently shifted toward the z vertex of the ternary diagram, while F5 and F6 exhibit a more balanced distribution among the three directions. The increased out-of-plane contribution is likely associated with the confinement imposed by the formwork during casting, which restricts fibre rotation within the segment plane and promotes partial reorientation through the thickness.

The averaged core values (Fig.6b) further reduce the specimen-to-specimen variability and clearly highlight these spatial trends. The central cores remain clustered in the region associated with dominant x–y orientation, whereas the edge cores consistently exhibit higher z-components, with F4 showing the strongest through-thickness orientation, followed by F7. Cores F5 and F6 occupy intermediate positions, indicating a more balanced fibre distribution.

Overall, the results demonstrate that fibre orientation varies systematically within the tunnel segment. The central region is characterized by a predominantly planar anisotropy, whereas the edge region exhibits a more pronounced three-dimensional orientation due to the increased contribution of the z-direction, likely induced by boundary effects during casting. The consistency between individual specimens and averaged core values confirms that the inductive method is capable of capturing these spatial orientation patterns, providing a reliable non-destructive tool for assessing fibre orientation in SFRC elements.



(a) (b)

Figure 6: Fibre orientation: (a) Individual specimens; and (b) Averaged cores.

6 Concluding remarks

This study experimentally validated an inductive, non-destructive technique for assessing both the steel fibre content and the average fibre orientation in Steel Fibre-Reinforced Concrete (SFRC), through comparison with conventional destructive quality control methods.

The experimental programme included calibration specimens with controlled fibre contents and orientations, used to determine the calibration coefficient β and establish the relationship between inductance, fibre content, and preferential fibre orientation, together with cores extracted from full-scale precast tunnel lining segments to evaluate the method under realistic production conditions.

The results demonstrate that the inductive technique provides reliable fibre content estimations. Using the acceptance criterion defined in fib Bulletin 83 (±20% of the design dosage), most specimens were correctly classified, while adopting a more conservative ±15% threshold further improved the identification of potentially non-compliant elements, reducing classification uncertainty with only a limited increase in the number of specimens requiring destructive verification.

Beyond fibre content estimation, the proposed method offers the unique capability of evaluating the average fibre orientation, a parameter that cannot be obtained using conventional destructive procedures. Although the orientation assessment should currently be interpreted as qualitative rather than strictly quantitative, the method successfully identified the spatial orientation patterns within the tunnel segments, distinguishing the predominantly planar fibre distribution in the central region from the greater through-thickness orientation observed near the segment edges.

The proposed methodology combines rapid execution, repeatability, and non-destructive operation, allowing repeated measurements on the same element and providing spatially resolved information without altering the specimen. Its only significant limitation is the reduced

sensitivity for fibre contents below approximately 20 kg/m³, although this threshold is generally lower than the fibre dosages adopted in structural SFRC applications and therefore has limited practical impact.

Overall, the proposed inductive methodology represents a reliable and efficient quality control tool that complements conventional destructive testing. By significantly reducing the number of destructive tests while simultaneously providing information on fibre orientation, it enables a more comprehensive characterization of SFRC elements. These features make the technique particularly attractive for industrial quality control of precast components and support its future implementation in routine production, contributing to safer, faster, and more sustainable quality assurance procedures for steel fibre-reinforced concrete.

7 Acknowledgements

The Authors acknowledges the support provided by Bekaert for providing the inductive devise, and the technical staff of the Tunnelling Engineering Research Centre (TERC), University of Rome Tor Vergata, for their valuable contribution to the research project.
The statements made herein are solely the responsibility of the authors.

8 References

Barnett, S.J., Lataste, J.F., Parry, T., Millard, S.G., and Soutsos, M.N., 2010. “Assessment of fibre orientation in ultra high performance fibre reinforced concrete”. *Cement and Concrete Research.*

di Prisco, M., Plizzari, G., and Vandewalle, L., 2009. “Fibre reinforced concrete: new design perspectives”. *Materials and Structures*.

fib, 2019. *fib Bulletin No. 83 – Precast tunnel segments in fibre-reinforced concrete*. Fédération Internationale du Béton.

Grünewald, S., 2004. “Performance-based design of self-compacting fibre reinforced concrete”. Delft University of Technology.

Kooiman, A.G., 2000. “Modelling Steel Fibre Reinforced Concrete for Structural Design”. Delft University of Technology.

Laranjeira, F., Grünewald, S., Walraven, J., and Blom, C., 2012. “Assessment of steel fibre distribution in concrete using image analysis”. *Materials and Structures*.

Naaman, A.E., 2003. “Engineered Steel Fibers with Optimal Properties for Reinforcement of Cement Composites”. *Journal of Advanced Concrete Technology*.

Ozyurt, N., Mason, T.O., and Shah, S.P., 2006. “Monitoring fiber dispersion in fiber-reinforced cementitious materials using AC impedance spectroscopy”. *Cement and Concrete Composites.*

Robins, P., Austin, S., and Jones, P., 2001. “Non-destructive testing of concrete structures”. *Construction and Building Materials*.

Fiber distribution in concrete beams with rebars and steel fibers

Mohammad Abu-Ahmad[1], Yuri S. Karinski[2] and Avraham N. Dancygier[3]

[1] Faculty of Civil and Environmental Engineering, Technion – Israel Institute of Technology, Technion City, Haifa 3200003, Israel.

[2] National Building Research Institute, Technion – Israel Institute of Technology, Technion City, Haifa 3200003, Israel.

[3] Engineering Faculty, Kinneret Academic College on the Sea of Galilee, Zemach, Israel & Faculty of Civil and Environmental Engineering, National Building Research Institute, Technion – Israel Institute of Technology, Haifa, Israel.

Abstract

The work presented in this paper aims to study experimentally the fiber distribution in R/SFRC beams using a destructive method, with a further aim of quantifying the effect of the rebars volume and location in the cross-section. The experimental program is based on sawing of R/SFRC beams with various reinforcement ratios. Nine equal rectangular sub-areas were marked on the cut faces to enable image analysis of the different parts of the cross-section. A preliminary study included determination of a proper threshold level for the image analysis and evaluation of calibration correction factors to calculate the number of fibers within particular sub-areas of the cross-section, taking into account the presence and diameter of the rebars. Initial results presented here from beams with very low (0.15%) and very high (3.3%) reinforcement ratios, indicate the effects on the actual fiber contents within different parts of the beam, caused by the casting direction and the rebars volume and location. They show that casting from the top leads to more fibers in the bottom layer of the beam than in its top layer, and that a larger reinforcement ratio in the beam's tensile zone leads to larger actual fiber volumetric ratio in this zone. The presented study will allow further required calibration of a theoretical model to quantify the phenomenon of 'cracking localization' in flexural elements.

Keywords

Fiber distribution, image analysis, rebars effect, steel fiber reinforced concrete

1 Introduction

The phenomenon of 'cracking localization' (CL) has been observed in concrete elements with rebars and steel fibers (R/SFRC elements), when the reinforcement ratio of the rebars is relatively small (e.g., Jordon et al, 2014; Gebreyesus et al, 2023). In these cases, it has been shown that CL is caused by the non-uniform distribution of the fibers along the element's length (Karinski et al, 2017) and a theoretical model was developed to explain and quantify this phenomenon (Dancygier et al, 2014; Karinski et al, 2024). To calibrate the model, several key parameters are required. Since the model is based on the statistical distribution of the fibers, one of these parameters is the standard deviation of the fiber distribution. It is also required to know how this distribution is affected by the presence of the rebars and their location in the cross-section (Gebreyesus et al, 2025). Because this phenomenon corresponds to cracking, it occurs in members under tensile stress, whether in axially loaded elements (Jordon et al, 2014; Redaelli et al, 2007; Dancygier et al, 2017) or in the tensile zone of beam cross-sections (Yang et al, 2010; Dancygier and Savir, 2006; Yoo et al, 2018). While in axially loaded elements the rebars are located symmetrically in the cross-section, the tension bars in beams have a different arrangement.

The fiber distribution in SFRC elements has been studied in different ways, both non-destructive methods (e.g., Li et al, 2021; Ponikiewski, 2015) and destructive methods (e.g., Yoo et al, 2016; Karinski et al, 2017, 2018). Commonly, these methods use image analysis techniques to process their results.

The advantage of the destructive methods is their relatively low cost. In these methods the specimen is sawed into slices. Then the sawed surfaces are prepared to enable high resolution photography that will be suitable for a further image analysis, which requires determining a "gray-level threshold" (e.g., Otsu, 1979) to distinguish between the fibers and the other concrete ingredients, especially, the coarse aggregates. This threshold makes it possible to extract the visible fibers' area from the image. When the aim of the analysis is to count the number of the fibers, this count must be derived from their measured area. But because the fibers have random spatial orientations, their cross-sections do not appear in the image as perfect circles. Instead, they take on irregular shapes depending on their orientation relative to the cutting plane. Therefore, to obtain a correct number of the fibers in the analyzed area, a correction factor should be applied, such that the actual number of fibers is obtained (Lee et al, 2009; Yoo et al, 2016).

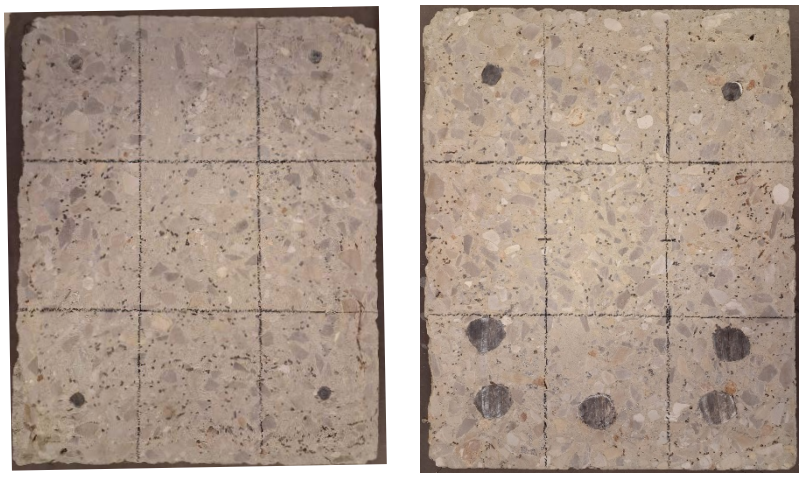
The current work aims to study experimentally the fiber distribution in R/SFRC beams using a destructive method, with a further aim of quantifying the effect of the rebars volume (reinforcement ratio) and arrangement (location in the cross-section).

2 Methodology

The experimental program is based on sawing R/SFRC beams having a cross-section of 240 mm width and 300 mm height and a length of 3.6 m, with various reinforcement ratios and with 60 kg/m^3 of fibers (fiber volumetric ratio, V_f = 0.76%). Dramix RC-65/35-BN 3D hooked end steel fibers (Bekaert, 2005) were used. These fibers are 35-mm long, 0.55 mm in diameter, and they have an aspect ratio of 64. This paper includes initial results obtained from beams with two reinforcement ratios ρ:

- ρ = 0.15%: two top 8-mm rebars and two 8-mm rebars at the bottom, arranged as shown in Fig. 1a
- ρ = 3.3%: two top 12-mm rebars and five 22-mm rebars at the bottom, arranged as shown in Fig. 1b

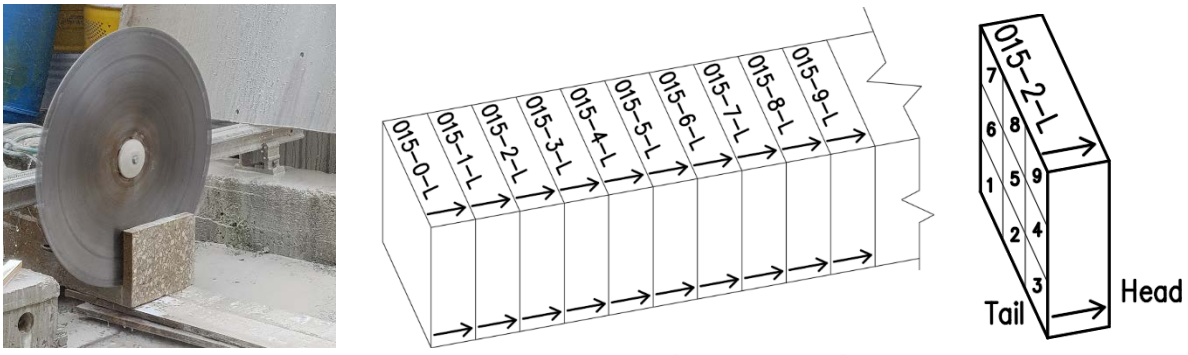
Construction of the specimens was done in laboratory conditions with a moving casting point, where the casting direction was from the top of the cross-section. Fig. 1 shows the rebars location in the cross-sections of these beams.



(a) ρ = 0.15% (b) ρ = 3.3%

Figure 1: Rebars location in the beam cross-sections (pictures taken before surface preparation)

The current methodology comprises sawing cross-sectional specimens along parts of R/SFRC beams, as illustrated in Fig. 2, to enable studying of the fiber distribution, both within the cross-section and along the beam length. All specimens (slices) had a thickness of 35 mm, which is equal to the fiber length.



(a) sawing (b) cutting order

Figure 2: Preparation of the slices

The sawed cross-sections were polished to better distinguish in the following photographs between the fibers and the matrix and aggregate background. As further preparation of the slices, nine sub-areas of 80X100 mm rectangles were marked on their faces to enable analysis

of the different parts of the cross-section (see Fig. 1 and Fig. 2b). The fiber count on the two opposing faces of the cross-section was done by photographing each face and analyzing the images using a calibrated correction factor (CF). The analysis was performed for each of the rectangular sub-areas marked on the cross-section's face. The larger number of the two adjacent faces was taken into account in the statistical analysis. This is because it is possible that a tip of a fiber would show on one face but not on the opposing one (for example, because of the sawing process).

3 Photography and image analysis

After performing preliminary checks to develop optimal conditions for photographing, the following setup was chosen:

- 500-mm diameter lamp
- Low light intensity with mixed white balance.
- F13 aperture
- Shutter speed of 2.5 seconds,

All images were taken in a completely dark lab, using long exposure to achieve uniform illumination and clear contrast. Before taking the pictures, the rebars cross-sections were darkened to eliminate their presence from the further image analysis. The photographing setup is shown in Fig. 3.

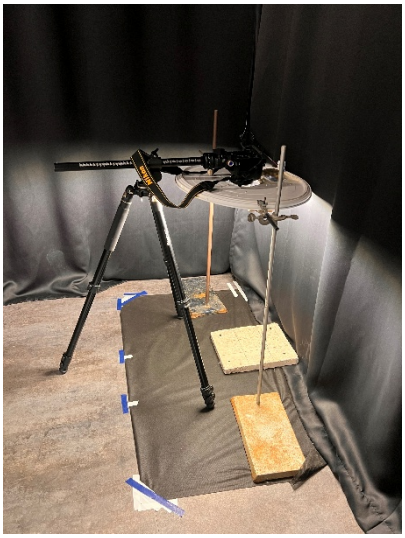
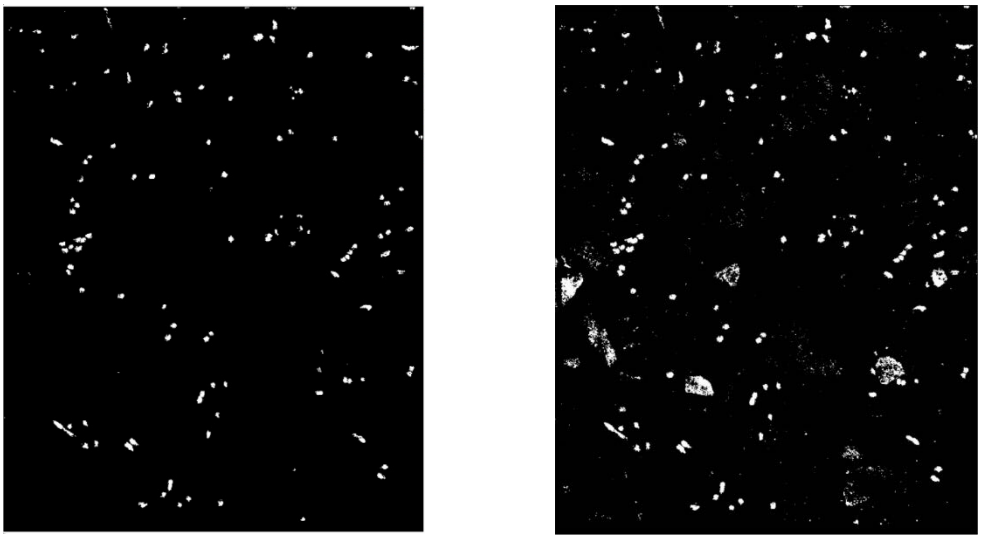


Figure 3: Photographing setup

The image analysis was performed with MATLAB software (The MathWorks, 2024) applying a black-and-white format using a predefined gray-level threshold (ranging from 0 to 255). Due to the fibers' metallic nature and high reflectivity after the surface polish, their pixels appear brighter, and consequently for a high threshold level (TL), only the fibers are shown as white areas in the image (as illustrated in Fig. 4a). A too-high level results in an image that does not show all the fibers, whereas a too-low level may lead to an image with white areas that include parts of the aggregates (see Fig. 4b).



(a) high TL (no aggregates are visible) (b) low TL (aggregates are visible)

Figure 4: Example of black and white images of the sliced surfaces

Fig. 4 shows an example of a slice for two TL levels. When the TL was set to 68 (Fig. 4b) the average fiber content measured in **all** the slices (after applying a correction factor, as explained in the following text) is apparently ~2.0%, which is much larger than V_f = 0.76% that was used in the SFRC mixture. This means that for this low TL the average white area in all images includes both fibers and some of the aggregates, an example of which can be clearly observed in the figure. When TL is increased to 78 the measured V_f (average of all slices) decreases to 0.61%, which is less than 0.76% (a further decrease of the TL below 78 yield V_f > 0.76%). The discrepancy between this result (0.61%) and the known V_f of 0.76% is caused by the scatter of fibers orientation, where some fibers are oriented sufficiently perpendicular to the specimen longitudinal axis, such that they do not appear at both faces of the (vertical) slice (Karinski et al, 2017).

The following analysis was performed for each beam type (ρ=0.15% and ρ=3.3%) as follows:

- 80X100-mm rectangular sub-areas were chosen (see Fig 2b) from different cross-sections. It is expected that because the rebars affect the fiber orientation, the CF values should be different for parts of the cross-section that include rebars and those that do not. Furthermore, for a similar reason, a specific CF is expected for each rebar diameter. Therefore, five different types of sub-areas were analyzed: sub-areas without rebars (Fig. 1), with a single 8-mm rebar (Fig. 1a), with a single 12-mm rebar, with a single 22-mm rebar and with two 22-mm rebars (Fig. 1b). Six specimens were analyzed of each type of these sub-areas.
- The fibers at each rectangle were counted manually (this number is denoted $N_{f,man}$)
- Each rectangle was then photographed, and the images were transformed into binary black-and-white as explained above, using a selected threshold level.
- The total white area $A_{f,total}$ at each rectangle was obtained by the image analysis software.
- The correction factor, CF, was calculated for the selected TL (see following text) as follows:

$$CF = \frac{1}{6}\sum_{i=1}^{6}\left(\frac{N_{f,man}\cdot A_f}{A_{f,total}}\right)_i \quad (1)$$

where A_f is the cross-sectional area of each fiber.

- Each of the CF values was then validated against six other corresponding rectangular sub-areas. For this purpose, the manually counted number of fibers in these additional sub-areas were compared with the number N_f obtained by applying the calibrated CF, which is given by:

$$N_f = CF \cdot \frac{A_{f,total}}{A_f} \quad (2)$$

The validation shows a reasonable agreement with root mean square errors that ranged from 5% to 13%.

The final CF values were evaluated by an iterative procedure that included these stages: 1) Manual count of the fibers ($N_{f,man}$); 2) Transformation of the photographs into binary B&W images using an initial TL, selected according to an intensity grayscale histogram; 3) Obtain $A_{f,total}$; 4) Calculate CF values (Eq. (1); 5) Calculate the average of the measured fiber volumetric ratios, $V_{f,act}$, along a whole set of cross-sections (refer to Fig. 2b and see Chapter 4); 5) Check whether (a) $V_{f,act} \geq V_f$ and (b) there are no visible aggregates; 6) If both (a) and (b) are true then decrease TL and repeat from stage 2 and if either of them is false then set previous TL & CF values for the further analysis.

The following CF values are summarized in Table 1 for rectangles without rebars (e.g., central part of the section in Fig. 1), with a single 8-mm rebar (corner rectangles in Fig. 1a), with a single 12-mm rebar (corner top rectangles in Fig. 1b), with a single 22-mm rebar (central bottom rectangle in Fig. 1b), and with two 22-mm rebars (bottom corner rectangles in Fig. 1b).

Table 1: CF values for the different types of rectangular areas within the cross-section.

ρ = 0.15% TL = 78	**Without rebars**	**With a single 8-mm rebar**
CF	0.36	0.45

ρ = 3.3% TL = 76	**Without rebars**	**With a single 12-mm rebar**	**With a single 22-mm rebar**	**With two 22-mm rebars**
CF	0.33	0.32	0.39	0.50

4 Results and discussion

The analysis was performed for 11 and 12 cross-sections (Fig. 2b) of the beams with ρ = 0.15% (Fig. 1a) and 3.3% (Fig. 1b), respectively. The measured number of fibers in each sub-area (see Fig. 5) at each cross-section, N'_f, was obtained by using their corresponding CF values (Table 1). The actual fiber volumetric ratio V'_f in each sub-area was then obtained (for each cross-section) as follows:

$$V_f' = \frac{N_f' \cdot A_f}{A_c}, \quad (3)$$

where A_c is the net area of the concrete at a particular sub-area (i.e., after subtracting the rebars' area). These results, of each sub-area, are then used to study the fiber distribution along the beam, both for the entire cross-section (C.S.) or different parts of it.

Table 2 shows the distribution of V'_f, as well as its average (measured volumetric ratio, $V_{f,act}$) and standard deviation that were obtained for the entire cross-section.

The table shows that there is a discrepancy between the average value of V'_f and the known V_f of 0.76%, which, as explained above, is caused by the scatter of fibers orientation. Note that these results conform to those of the 80x80-mm specimens with a centrally located rebar reported in (Karinski et al, 2017), in which the average value was 0.5%~0.6% (compared with the same V_f = 0.76%).

Table 2: Distribution of V'_f (%) for the entire cross-section.

C.S. / Beam	1	2	3	4	5	6	7	8	9	10	11	12	$V_{f,act}$	Stdev
ρ = 0.15%	0.84	0.53	0.62	0.54	0.76	0.61	0.59	0.45	0.53	0.65	0.58	--	**0.61**	**0.11**
ρ = 3.3%	0.49	0.64	0.43	0.60	0.50	0.45	0.58	0.77	0.93	0.58	0.69	0.66	**0.61**	**0.14**

Consider the sub-areas that do not include rebars (refer to Fig. 1 and see in Fig. 5: No. 4, 5, 6 and 8 for both specimen types with the addition of No. 2 for ρ = 0.15%).

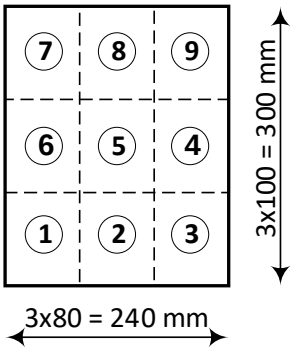


Figure 5: Division into sub-areas

Table 3 shows $V_{f,act}$, measured in different combinations of sub-areas without fibers according to Fig. 5.

Table 3: Measured volumetric ratios, $V_{f,act}$ (%) in sub-areas without rebars.

	ρ = 0.15%			ρ = 3.3%	
Sub-areas{1}	**4, 5, 6**	**2, 4, 5, 6, 8**	**2, 5, 8**	**4, 5, 6**	**4, 5, 6, 8**
$V_{f,act}$	0.63	0.63	0.64	0.58	0.55
Stdev	0.11	0.12	0.15	0.18	0.16

{1} Combinations of sub-areas shown in Fig. 5.

The results shown in the table indicate that $V_{f,act}$ is about the same for all sub-area combinations with ~10% smaller values at the cross-section with the larger reinforcement ratio (ρ=3.3%).

Unlike axially loaded elements (Karinski et al, 2017, 2018), in bending the CL phenomenon is caused by the non-uniform fiber distribution along the beam tensile zone (Karinski et al, 2024). Hence, the effect of the longitudinal rebars on the fiber distribution is examined along the beam within layers of the cross-sections that include the rebars, and it is shown in Table 4. For ρ = 3.3% the lower half of the cross-section (Fig. 5) is considered because it is evident that the tensile zone is at the bottom of the cross-section (Fig. 1b). For ρ = 0.15% the distribution is given for both top (7,8,9) and bottom (1,2,3) layers (refer to Fig. 1a).

Table 4: Distribution of V'_f (%) for top and bottom layers of the cross-section.

C.S. / Beam	1	2	3	4	5	6	7	8	9	10	11	12	$V_{f,act}$	Stdev
ρ = 0.15% Top layer	0.82	0.40	0.44	0.57	0.74	0.64	0.46	0.32	0.52	0.67	0.61	--	**0.56**	**0.15**
ρ = 0.15% Bottom layer	0.94	0.65	0.75	0.46	0.68	0.60	0.68	0.52	0.55	0.65	0.59	--	**0.64**	**0.13**
ρ = 3.3% Top layer	0.31	0.39	0.29	0.61	0.31	0.24	0.46	0.41	0.81	0.36	0.46	0.34	**0.42**	**0.16**
ρ = 3.3% Bottom layer	0.64	0.92	0.59	0.70	0.76	0.75	0.89	1.11	1.13	0.88	0.96	0.75	**0.84**	**0.17**

The two rows in Table 4 that correspond to the top layers show a considerable difference of $V_{f,act}$, where the bottom layer includes ~14% more fibers than the top layer for ρ = 0.15% and they are even twice larger for ρ = 3.3%. This difference may correspond to the effect of the casting direction (from top to bottom) on the fiber distribution along the height of the cross-section, which conforms also to findings of other researchers (e.g. Ferrara et al, 2011). This effect of the casting direction is also supported by comparing $V_{f,act}$ within corresponding top and bottom sub-areas, 7 vs. 1, 8 vs. 2 and 9 vs. 3 in Fig. 5 (e.g., for ρ = 0.15% they are: 0.55% vs. 0.67%, 0.61% vs. 0.65% and 0.52% vs. 0.60%, respectively).

The effect of the rebars volume (diameter and number of the rebars) is demonstrated by comparing $V_{f,act}$ at the bottom layer of ρ = 0.15% and 3.3%. It shows that a larger reinforcement ratio leads to larger actual fiber volumetric ratio (here – by ~30%, compare 0.84% with 0.64% in Table 4). This result suggests that a greater number of fibers were measured at the bottom layer of the cross-section with ρ = 3.3%, and their volume is even larger than the known V_f of 0.76%. This may be due to the reduced concrete volume around the rebars, which occupy a larger fraction of the sub-area, as well as the increased alignment of fibers parallel to the beam's longitudinal axis (as pointed out in Chapter 3).

5 Concluding remarks

The current work aims to study experimentally the fiber distribution in R/SFRC beams using a destructive method, with a further aim of quantifying the effect of the rebars volume (reinforcement ratio) and arrangement (location in the cross-section). The experimental program is based on sawing of R/SFRC beams with various reinforcement ratios and a fiber volumetric ratio V_f = 0.76%. All sawed specimens (slices) had a thickness equal to the length of the fibers. The work refers to the fibers' distribution along the beam. Nine equal rectangular

sub-areas were marked on the cut faces to enable image analysis of the different parts of the cross-section. The larger number of the two adjacent faces was taken into account in the statistical analysis to obtain the actual fiber volumetric contents. A preliminary study included determination of a proper threshold level for the image analysis and evaluation of the calibrating correction factors to calculate the fiber numbers within particular sub-areas of the cross-section, taking into account the presence and diameter of the rebars.

The analysis of the entire cross-section shows a discrepancy between the average and known fiber volumetric contents. This difference is caused by the scatter of fibers orientation, where some fibers are oriented sufficiently perpendicular to the specimen longitudinal axis, such that they are not visible at both faces of the (vertical) slice. The effect of the reinforcement was studied by examination of the fiber contents within the tensile zone of the beam's cross-section. The results indicate that there is an effect of the casting direction, where in the current measurements, the bottom layer includes ~14% more fibers than the top layer. The effect of the rebars volume was also studied, and it shows that a larger reinforcement ratio in the beam's tensile zone leads to larger actual fiber volumetric ratio in this zone (here – by ~30%). This result also indicates that the larger diameter rebars led to more fibers that are oriented in a direction parallel to the longitudinal axis of the beam.

The presented study will allow further required calibration of a theoretical model to quantify the phenomenon of 'cracking localization' in flexural elements.

6 Acknowledgements

This work was partly supported by a joint grant from the Centre for Absorption in Science of the Ministry of Immigrant Absorption and the Committee for Planning and Budgeting of the Council for Higher Education under the framework of the KAMEA Program.

7 References

Bekaert. Product data sheet Dramix RC-65/35-BN, 2005.

Dancygier, A. N. and Savir, Z., 2006. "Flexural behavior of HSFRC with low reinforcement ratios", *Engineering Structures*, 28(11) pp1503–12.

Dancygier, A. N. and Karinski, Y. S., 2014. "Probabilistic model of the crack localization in axially loaded fibrous reinforced concrete bars", *Engineering Structures*, 79 pp 417–26.

Dancygier, A. N., Karinski, Y. S. and Navon Z., 2017. "Cracking localization in tensile conventionally reinforced fibrous concrete bars", *Construction and Building Materials*, 149 pp 53–61.

Ferrara, L., Ozyurt, N. and di Prisco, M., 2011 High mechanical performance of fibre reinforced cementitious composites: the role of "casting-flow induced" fibre orientation. *Mater Struct* **44**, 109–128 (2011). https://doi.org/10.1617/s11527-010-9613-9

Gebreyesus, Y. Y., Karinski, Y. S., Dancygier, A. N. and di Prisco, M., 2023. "Experimental investigation of cracking localization in RC beams with steel fibers", *Structural Concrete*, 24 pp 1386–1401.

Gebreyesus, Y. Y., Karinski, Y. S. and Dancygier, A. N., 2025. "An enhanced approach to assess the reduction of flexural ductility of R/SFRC beams and slabs", *International Journal of Protective Structures*, 16(4) pp 933-946.

Jordon, R. D., Seong-Cheol, L., Vecchio, F. J., 2014. "Cracking behavior of steel fiber-reinforced concrete members containing conventional reinforcement", *ACI Structural Journal*, 111(1) pp 93–102.

Karinski, Y. S., Dancygier, A. N. and Gebreyesus, Y. Y., 2024. "Probabilistic model for cracking localization in reinforced fibrous concrete beams", *Journal of Engineering Mathematics*, 144(1) pp 23.

Karinski, Y. S., Dancygier, A. N. and Navon, Z., 2017. "Experimental verification for a probabilistic model of fibers distribution along a reinforced concrete bar", *Materials and Structures*, 50(2) pp 119.

Karinski, Y. S. and Dancygier, A. N., 2018. "Effects of fibers and conventional reinforcement contents on fibers scattering in prismatic bars," *Cement and Concrete Composites*, 86 pp 171–177.

Lee, B. Y., Kim, J. K., Kim, J. S. and Kim, Y.Y., 2009. "Quantitative evaluation technique of Polyvinyl Alcohol (PVA) fiber dispersion in engineered cementitious composites", *Cement and Concrete Composites* 31 pp 408-417.

Li, Y., Ruan, X., Akiyama, M., Zhang, M., Xin, J. and Lim, S., 2021. "Modelling method of fibre distribution in steel fibre reinforced concrete based on X-ray image recognition", *Composites Part B: Engineering*, 223 pp 109124.

Otsu, N., 1979. "A Threshold Selection Method from Gray-Level Histograms", *IEEE Transactions on Systems, Man, and Cybernetics*, 9(1) pp. 62–66.

Ponikiewski, T., Gołaszewski, J., Rudzki. M. and Bugdol, M, 2015. "Determination of steel fibres distribution in self-compacting concrete beams using X-ray computed tomography", *Archives of Civil and Mechanical Engineering*, 15(2) pp. 558–568.

Redaelli, D., Muttoni, A.,2007. "Tensile behaviour of reinforced ultrahigh performance fiber reinforced concrete elements", Proceedings of *fib* Symposium, Dubrovnik pp 267–274.

The MathWorks, Inc., 2024. "MATLAB R2024a." The MathWorks Inc., Natick, MA, USA.

Yang, I. H., Joh, C. and Kim, B. S., 2010. "Structural behavior of ultra-high performance concrete beams subjected to bending", *Engineering Structures*, 32(11) pp 3478–3487.

Yoo, D. Y., Banthia, N., Kang, S. T. and Yoon, Y. S., 2016. "Effect of fiber orientation on the rate-dependent flexural behavior of ultra-high-performance fiber-reinforced concrete", *Composite Structures*, 157 pp 62–70.

Yoo, D. Y. and Moon, D. Y., 2018. "Effect of steel fibers on the flexural behavior of RC beams with very low reinforcement ratios", *Construction and Building Materials*, 188 pp 237–254.

Experiences from using Montevideo test for quality control of fiber-reinforced concrete

Ingrid Lande[1], Guillem Rojas[2], Terje Kanstad[3]

[1]: University of Agder (UiA), Grimstad, Norway

[2]: University of Stavanger (UiS), Stavanger, Norway

[3]: Norwegian University of Science and Technology (NTNU), Trondheim, Norway

Abstract

For fiber-reinforced concrete (FRC), flexural properties must be determined for both quality control and for design. The standard test method for characterizing the residual tensile properties of concrete in Europe is the three-point bending test of notched beams (*EN 14651*). However, this test can be resource-demanding for concrete producers and fiber suppliers. As part of an industrial R&D project involving participants from across the Norwegian concrete industry, a new test method, known as the Montevideo test (MVD), has been applied and further developed. The MVD test involves applying a compressive force through a wedge into a notched prismatic specimen, while recording the vertical force and the crack mouth opening displacement (CMOD) of the notch, similarly to *EN 14651*.

This paper presents a collection of results gathered from the R&D project, including tests on multiple concrete mixes with different steel fiber contents, fiber types, and concrete consistencies, from conventional concrete to self-compacting concrete and ultra-high-performance concrete, tested in two different laboratories. The results of the MVD test are compared with those obtained using *EN 14651*. A strong correlation was obtained with R^2 of 0.96 and CoV similar to that of 3PBT, ranging from 6% to 33%. The findings indicate that the MVD method provides parameters describing the flexural strength of FRC with comparable accuracy to *EN 14651*, representing a potential alternative to EN *14651*. This is consistent with previous research. Furthermore, the MVD method can be easier to use for on-site quality control and potentially be used for the determination of fiber orientation factors, facilitating a future broader use of FRC in construction of structural elements. However, further research is required to fully validate these findings.

Keywords

Fiber reinforced concrete, residual flexural tensile strength, Montevideo test, Three-point bending test

1 Introduction

For several decades, there has been an interest in using fiber reinforcement in concrete structures to fully or partly replace ordinary rebars. The motivation includes more efficient construction, health, safety, and environment (HSE) issues for the workers, cost, and environmental considerations as well as structural benefits such as improved crack control. Significant international initiatives have been established, leading to the inclusion of fiber reinforced concrete (FRC) in the *fib Model Code* and the upcoming Eurocode 2 (*FprEN 1992*). In Norway, the Norwegian Concrete Association has published a national guideline on FRC in load-carrying structures (*NB38*) (The Norwegian Concrete Association, 2024). The characterization of FRC relies on accurate experimental methods to determine post-cracking behavior. All these standards apply the three-point bending test (3PBT) of notched beams, performed in accordance with *EN 14651* (European Committee for Standardization, 2005), to quantify the tensile properties of the FRC for structural design. Although the 3PBT method is considerably simpler to execute compared to direct tension tests, it is still resource-demanding and time-consuming to carry out for the concrete producers.

One important initiative in Norway aiming to increase the use and knowledge of FRC is the industrial R&D project *FiberCon* (2022–2025), partly funded by the Norwegian Research Council. The project comprised six work packages from mix design, production, structural solutions, applications, quality control, and environmental impact. One focus was to investigate alternative methods to conduct quality control of FRC, and to identify efficient test procedures for evaluating residual flexural strength, both for new and existing structures. In the R&D project, the Montevideo test (MVD) proposed by (Segura-Castillo et al., 2024) has been investigated as an alternative to 3PBT. The MVD is a simple wedge-splitting test for evaluating the residual flexural tensile strength of FRC.

This paper presents a collection of results from the *FiberCon* project focusing on experiences from using the MVD test for evaluating the residual flexural tensile strength of various FRC. The MVD results are compared with those obtained using the standard 3PBT following *EN 14651* to determine their comparative performance and practical viability. A quantitative evaluation of a transformation parameter between *EN 14651* and the MVD test is obtained, i.e., a linear relationship between the post-cracking loads (F_{R1}-F_{R4}) measured for 3PBT and for the MVD test. The findings are further compared with the results of previous experimental campaigns. This comprehensive analysis aims to assess and validate the MVD test as a robust tool for the structural characterization of FRC.

2 Experimental program

2.1 Overview of experimental campaigns and batches

This study provides an overview of five different experimental campaigns to evaluate the feasibility of the Montevideo test for the characterization and quality control of fiber-reinforced concrete. The experimental campaigns include vibrated concrete (VC), self-compacting concrete (SCC), and ultra-high-performance concrete (UHPC). While the data has been previously published in other papers, it is here consolidated to provide a comprehensive overview of the findings from the industrial research project *FiberCon*. All batches were produced at different ready-mix concrete plants in Norway.

Table 1 provides an overview of the different experimental programs. The table gives location and year of execution, the number of batches and the production method.

Table 1: Overview of the experimental campaigns

Program name	**Location / Year**	**Nr. Batches / Consistency**	**Production method** (1)	**Reference**
G23	Gjøvik 2023	3 batches, VC and SCC	Manually placed	(Abedi et al., 2025; Rojas et al., 2025)
R24	Rudshøgda 2024	5 batches, VC and SCC	Manually placed	(Orizio et al., 2026)
K24	Kristiansand 2024	1 batch, SCC	Manually placed	(Lande et al., 2026)
L24	Larvik 2024	1 batch, UHPC	Pumped concrete	(Lande et al., 2025)
K25	Kristiansand 2025	2 batches, SCC	Manually placed	(Lande et al., 2026)

(1) *All concretes have been fabricated in a ready-mix concrete plant.*

Table 2 presents an overview of the different concrete batches, including the specified concrete type, fiber type and content, as well as the slump values (measured according to *NS-EN 12350-7* or *NS-EN 12350-2*) and average compressive strength of a minimum three 100 mm cubes (*NS-EN 12390-3*). Additional tests were also done for the various batches; however, they are not included in the present paper.

For the SCC and VC concretes, the applied steel fiber type was either 4D hooked-end steel (*HE steel*) or a composite macro fiber based on basalt (*Mini bars*). The HE steel fiber had a length (l_f) of 60 mm and diameter (d_f) of 0.9 mm, and a tensile strength of 1550 MPa. The composite macro fiber had a l_f of 43 mm, a d_f of 0.6 mm, and a tensile strength of 1000 MPa. For the UHPC batch, a typical micro steel fiber (*MS steel*) suitable for UHPC was used, with a fiber length of 12.5 mm, a diameter of 0.2 mm, and a tensile strength of 2800 MPa.

Table 2: Overview of batches

Batch ID	**Concrete type**	**Fiber type**	**Fiber content [kg/m^3]**	**Slump/slump flow [mm]**	**Compressive strength [MPa]**
G23 – B1	C35 SCC	HE steel	35	Slump flow: 610	53
G23 – B2	C35 SCC	Mini bars	10	Slump flow: 610	47
G23 – B3	C35 VC	HE steel	35	Slump: 220	57
R24 – B1	C45 SCC	HE steel	33	Slump flow: 575	66
R24 – B2	C45 SCC	HE steel	30	Slump flow: 630	69
R24 – B3	C45 SCC	Mini bars	9	Slump flow: 750	65
R24 – B4	C45 VC	HE steel	31	Slump:170	68
R24 – B5	C45 VC	Mini bars	8	Slump: 210	64
K24 – B1	C35 SCC	HE steel	35	Slump flow: 726	67
L24 – B1	C150 UHPC	MS steel	225	Slump flow: 550	170
K25 – B1	C35 SCC	HE steel	35	Slump flow: 540	72
K25 – B2	C35 SCC	HE steel	55	Separation	73

2.2 Residual flexural tensile strength

Two test methods were applied for residual flexural tensile strength: the standardized three-point bending test (3PBT) and the Montevideo splitting test (MVD). The 3PBT was executed at two labs in Norway, at the University of Agder (UiA) and at SINTEF. The MVD was carried out at UiA and at the Norwegian University of Science and Technology (NTNU).

The residual flexural tensile strength was first evaluated using the 3PBT, carried out in accordance with *EN 14651* (European Committee for Standardization, 2005). Figure 1 shows the test setup. Prismatic beams measuring 150 mm × 150 mm × 600 mm were cast using different casting procedures depending on the concrete type. For vibrated concrete (VC), the casting method in *EN 14651* was followed, including external vibration. For self-compacting concrete (SCC), the "Danish method" was applied, where the concrete is poured from one end of the mold and allowed to flow and fill the form. For some SCC batches, a modified version of this ("Mod. Danish method") was applied, where the concrete is first poured at one end and then gradually distributed along the mold by moving the casting point. Both methods for SCC are described in NB 38 (The Norwegian Concrete Association, 2024). The applied casting method for the various batches is given in Table 3. After curing, a central notch with a depth of 25 mm and width of 5 mm was cut into each beam. The beams are rotated 90° about the longitudinal axis before sawing the notch. The notched beams were tested in three-point bending, loaded with a centric point load (F_j). During testing, crack mouth opening displacement (CMOD) and load were recorded. CMOD was determined either indirectly using the relation between mid-span deflection and CMOD given in the standard, or directly. Direct CMOD measurement was performed either using Linear Variable Differential Transformers (LVDT) or a Digital Image Correlation (DIC) system. An analysis of the use of LVDTs and DIC shows similar results for CMOD. Residual flexural tensile strengths (f_{R1}, f_{R2}, f_{R3} and f_{R4}) were calculated for CMOD values of 0.5, 1.5, 2.5 and 3.5 mm, using Eq. (1):

$$f_{R,j} = \frac{3 \cdot F_j \cdot l}{2 \cdot b \cdot h_{sp}^2} \tag{1}$$

where F_j (F_{R1}-F_{R4}) is the load at the relevant CMODs (j = 1, 2, 3 and 4) (N), l is the span length (mm), b is the width of the beam and h_{sp} is the depth of the notched beam (mm).

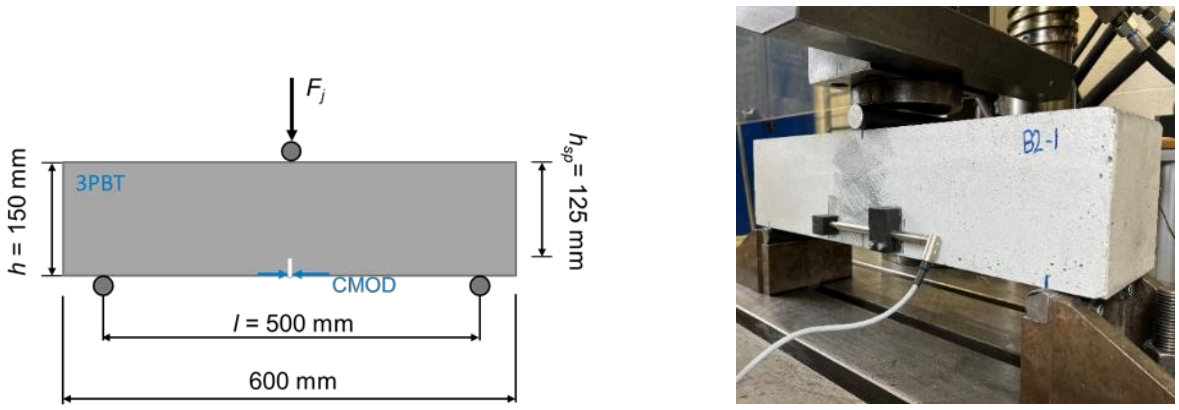


Figure 1: Three-point bending test setup. Picture from test at University of Agder.

From each tested beam, two 150 mm × 150 mm cubes were cut and subjected to the MVD test as shown in Figure 2. The MVD test was conducted in accordance with the procedure described by (Segura-Castillo et al., 2024).

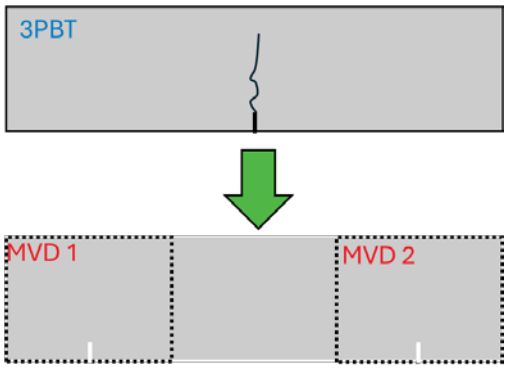


Figure 2: Test specimens for 3PBT and MVD.

Figure 3 shows the MVD test setup. The notch was cut on the same side as the central cut for the 3PBT. As for 3PBT, load and CMOD are to be registered during testing. The load was applied through a steel wedge with an angle of 30° positioned in the notch. No rotation of the wedge was allowed by the test setup ("fixed wedge rotation"). Two metal L profiles were added in the notch, as well as multi-purpose lubrication, to minimize friction. The material of the L profiles was either steel or tin. For the test at the NTNU lab (batches *G23* and *R24*), tin was used while for the batches tested at UiA (*K24*, *L24* and *K25*) steel was used. The effect of the type of material for the steel profiles has not been studied in detail and requires further investigation. CMOD was measured either by LVDTs at the notch tip or using DIC. The same loading rate was applied in all cases, i.e., 0.5–0.6 mm/min.

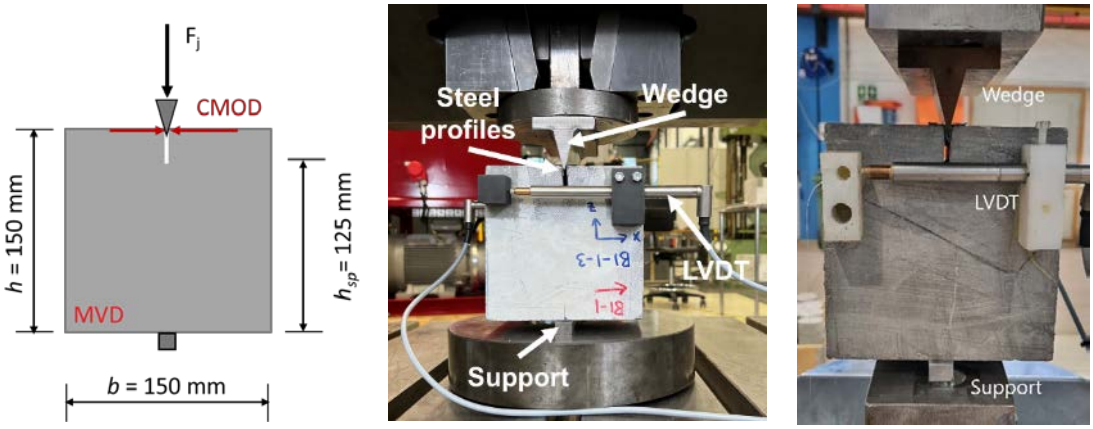


Figure 3: Montevideo test setup. Pictures from tests at UiA (left) and NTNU (right).

For the MVD test, the residual strengths were calculated using the procedure proposed by (Rojas et al., 2025; Segura-Castillo et al., 2024) (Eq. 2):

$$f_{R,j} = k_{MVD} \cdot \frac{3 \cdot F_{Ri}^{MVD} \cdot l}{2 \cdot b \cdot h_{sp}^2} \tag{2}$$

where F_{Ri}^{MVD} is the MVD load for the relevant CMODs (j = 1, 2, 3 and 4) (N), l is the span length (mm), b is the width of the beam and h_{sp} is the depth of the notched beam (mm). k_{MVD} is the transformation parameter, determined by establishing a linear relationship between the post-cracking loads (F_{R1}-F_{R4}) measured for 3PBT and for MVD test (Segura-Castillo et al., 2024).

Table 3 shows an overview of the casting method, number of test specimens, CMOD detection, and test age of all batches.

Table 3: Residual flexural strength testing

Batch ID	Type	Casting	Test	Nr. specimens	CMOD detection	Test age
G23 – B1	SCC	Danish method	3PBT	7	Vertical displacement	36
			MVD	14	2 LVDT	88-188
G23 – B2	SCC	Danish method	3PBT	6	Vertical displacement	36
			MVD	12	2 LVDT	88-188
G23 – B3	VC	EN14651	3PBT	7	Vertical displacement	36
			MVD	14	2 LVDT	88-188
R24 – B1	SCC	Danish method	3PBT	6	Vertical displacement	28
			MVD	12	2 LVDT	63
R24 – B2	SCC	Danish method	3PBT	6	Vertical displacement	28
			MVD	12	2 LVDT	63
R24 – B3	SCC	Danish method	3PBT	6	Vertical displacement	28
			MVD	12	2 LVDT	63
R24 – B4	SCC	Danish method	3PBT	6	Vertical displacement	28
			MVD	12	2 LVDT	63
R24 – B5	VC	EN14651	3PBT	6	Vertical displacement	28
			MVD	12	2 LVDT	63
K24 – B1	SCC	Danish method	3PBT	4*	DIC	35
			MVD	8	DIC+2 LVDTs	180
L24 – B1	UHPC	Place by pumping	3PBT	6	DIC	43
			MVD	12	DIC+2 LVDTs	233
K25 – B1	SCC	Mod. Danish method	3PBT	6	DIC+2 LVDTs	30
			MVD	12	DIC+2 LVDTs	37
K25 – B2	SCC	Mod. Danish method	3PBT	6	DIC+2 LVDTs	29
			MVD	12	DIC+2 LVDTs	37

* Primary test of MVD based on a sample of beams tested in 3PBT to achieve low variations.

3 Results and discussion

Figure 4 shows the correlation between the residual loads for all CMOD values (0.5 mm, 1.5 mm, 2.5 mm, and 3.5 mm) for both 3PBT and MVD with error bars representing the standard deviation. The figure also includes data from (Segura-Castillo et al., 2024). Each point on the figure represents the average value of a residual load for each batch. Hence, there are four points

for each batch. Considering only previous results from (Segura-Castillo et al., 2024), the transformation parameter (k_{MVD}) between the test methods was 1.4. The study by (Segura-Castillo et al., 2024), included various concrete types, steel fiber type and content, specimen size, and CMOD detection. The k_{MVD} was obtained by finding the slope of the linear regression between the 3PBT and the MVD. However, including the results from *FiberCon*, the k_{MVD} was found to be 1.51 (Figure 4). A high coefficient of determination (R^2) was obtained as 0.96 using *Python*. A linear regression model with a zero intercept was initially used (Figure 4). A model with a free intercept yielded y = 1.514x + 0.573, which indicates that the assumption of a zero intercept is reasonable.

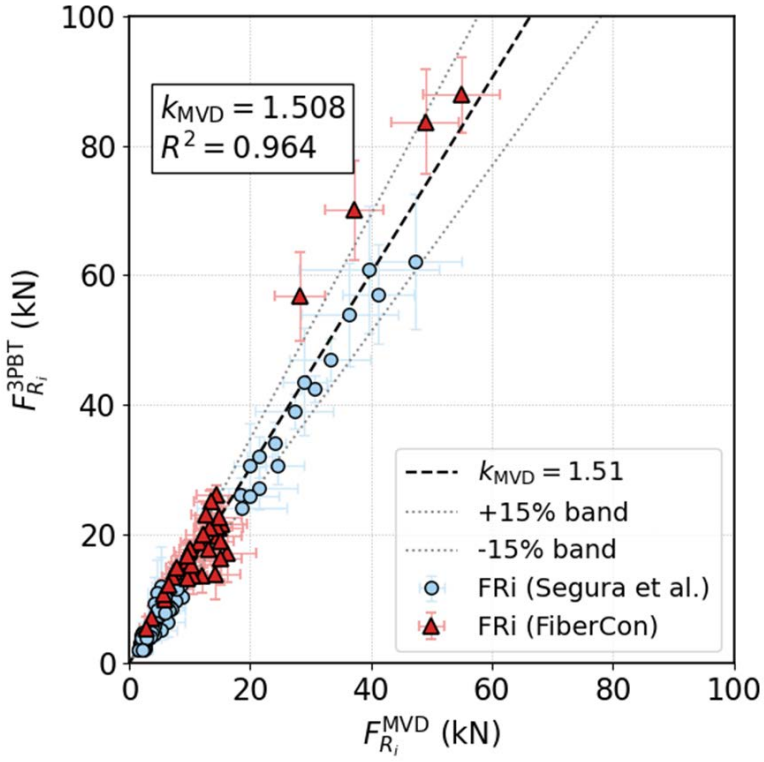
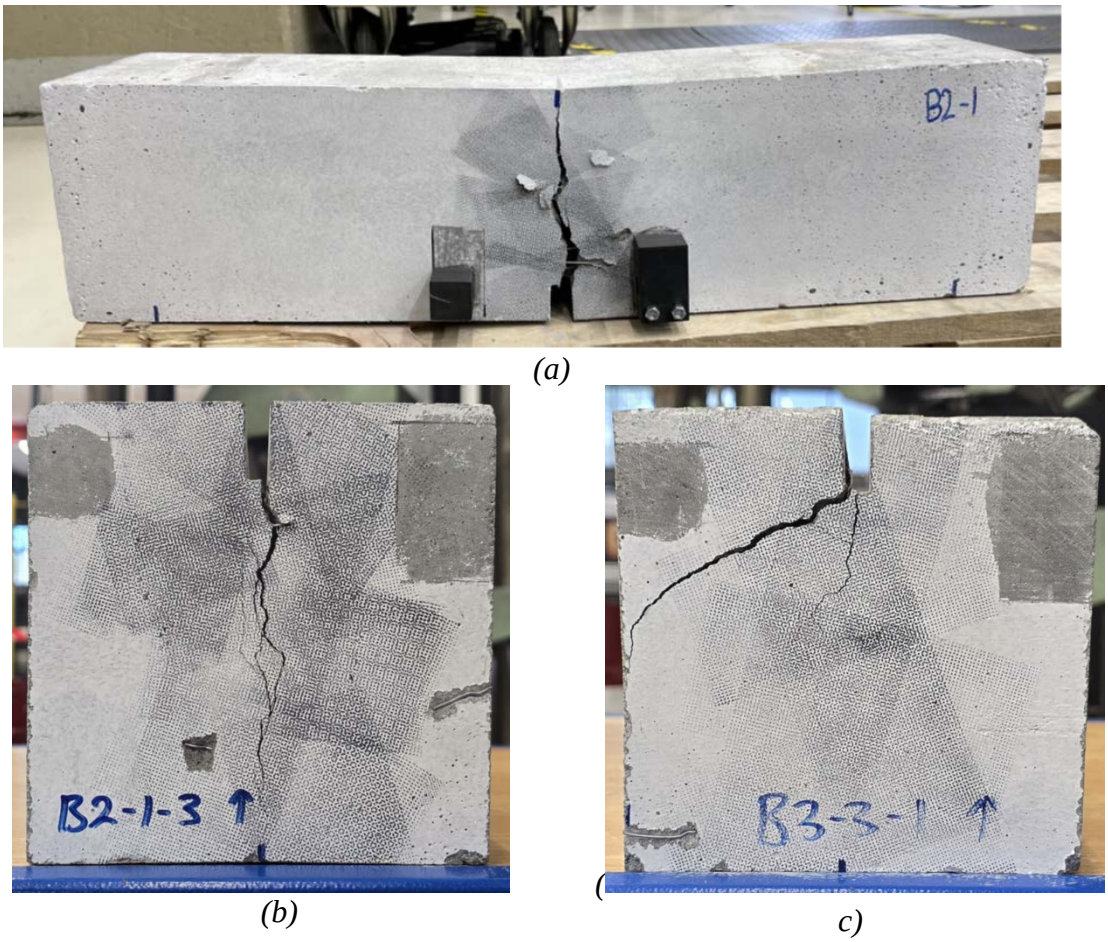


Figure 4: Correlation of average load (R_i) from 3PBT and MVD tests, both from this study (FiberCon) and (Segura-Castillo et al., 2024), analyzed using Python.

Usually, the crack pattern of the test methods is similar, with vertical cracks developing from the notch (Figure 5 (a) and (b)). For the batches *K24*, *K25*, and *L24*, all tested specimens were photographed after testing (Figure 5). The images showed that some cubes tested in the MVD were more prone to developing non-vertical cracks (spurious cracks) (Figure 5(c)). Several *K25* specimens exhibited cracks propagating toward the lateral edge. Such lateral cracking often propagates toward regions with fewer fibers. Consequently, if a cube has high fiber concentration under the notch, the cracks may propagate laterally, preventing the specimen from mobilizing its full post-cracking strength. Batches with these cracks were excluded from the analysis (Figure 4). One possible solution to avoid this issue is to use wider test specimens, widths above 150 mm. Later tests have shown promising results. In addition, batch *R24–B2* was excluded because the testing machine crashed during testing.

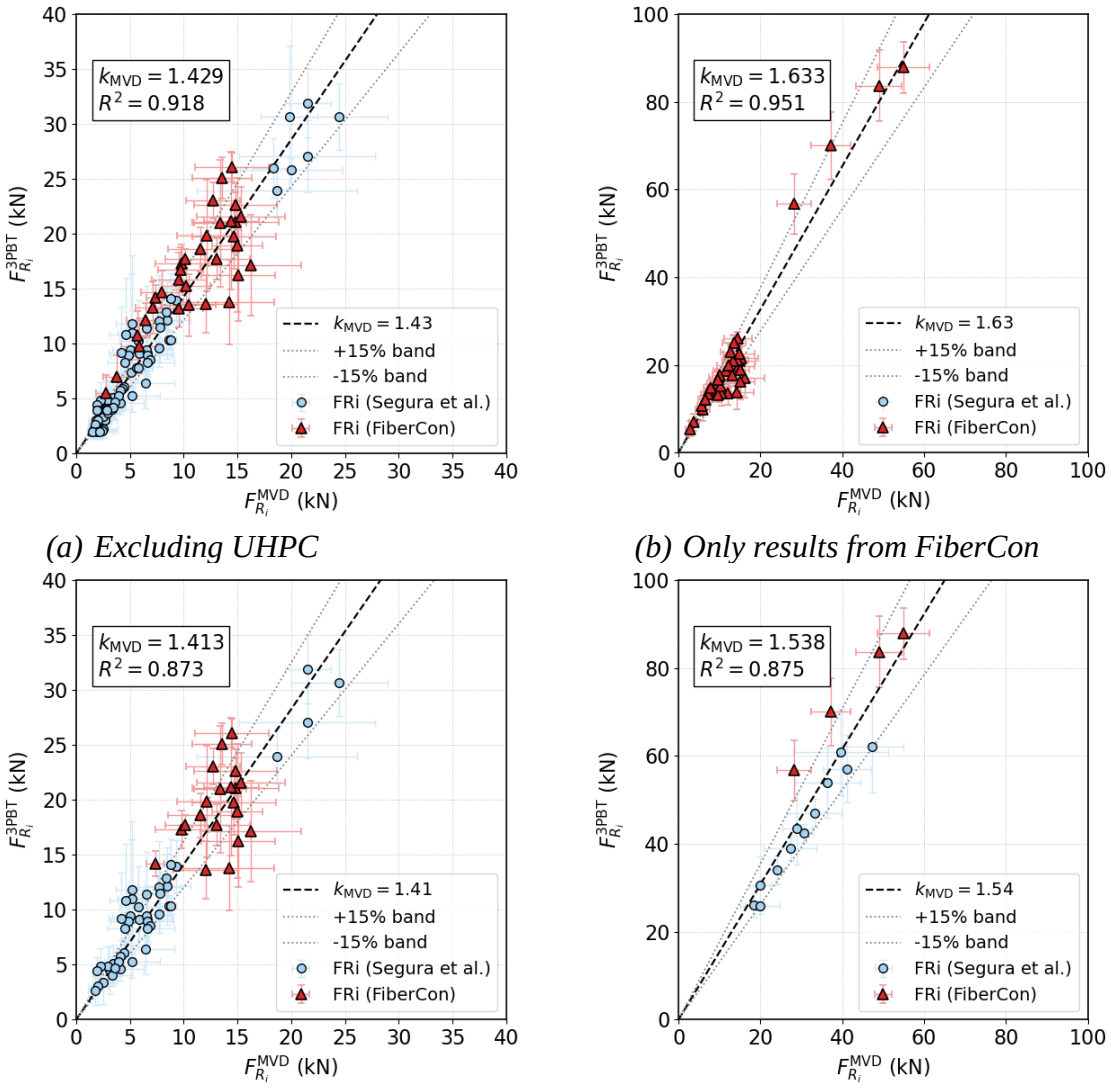


(a) *(b)* *(c)*

Figure 5: Typical and acceptable crack propagation for (a) 3PBT and (b) MVD and (c) shows unacceptable crack propagation in a MVD cube.

Figure 6 provides a sensitivity analysis of the experimental datasets. The results indicate that the transformation parameter varies between 1.4 and 1.6. When UHPC data are excluded, a transformation parameter of 1.43 (Figure 6(a)) is obtained. It is debated whether using notched beams is suitable for UHPFRC due to the strain-hardening and multiple micro cracking behavior of this material (López et al., 2016). Hence, it is reasonable to analyze the results without these values. The R^2 value remains high (0.92). Figure 6(b) provides only *FiberCon* results, giving a higher transformation parameter of 1.63. When considering the entire test series and limiting the dataset to batches containing steel fibers, a transformation parameter of 1.41 is obtained. Restricting the dataset to only include UHPC from the present study and (Segura-Castillo et al., 2024) gives a value of 1.54. Overall, relatively small variations are observed, ranging from 1.4 to 1.6.

Additional research is required to establish the transformation parameter. Furthermore, both in the present study and in comparison with (Segura-Castillo et al., 2024), there are differences between test setup, concrete compositions and types, steel fiber type and content, casting methods, etc., which may affect the results. However, the findings indicate that the test method remains robust across these differences.



(a) Excluding UHPC

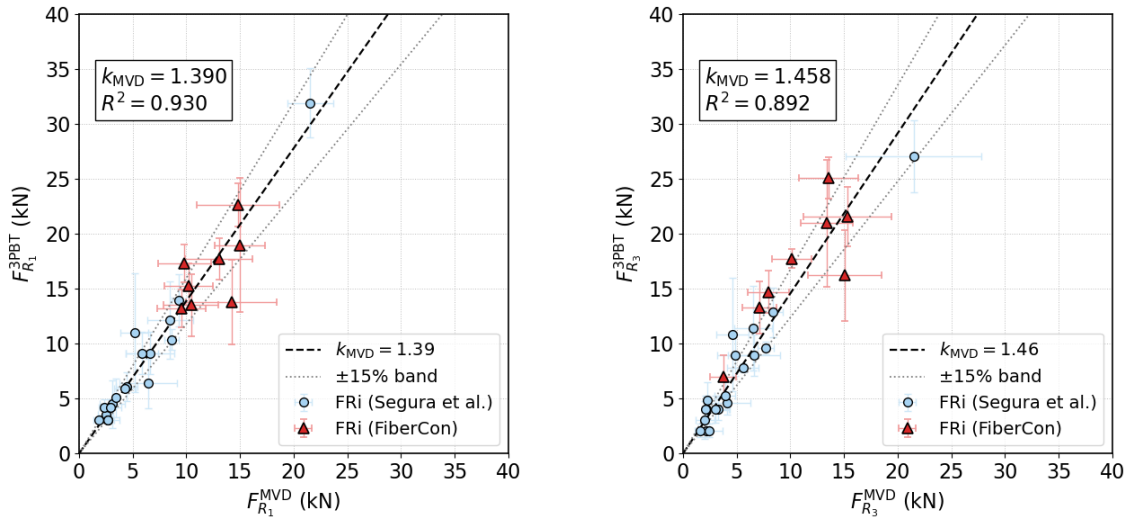
(b) Only results from FiberCon

(c) Excluding UHPC and only steel fibers

(d) Only UHPC

Figure 6: Sensitivity analysis of the correlation of average load (R_i) from 3PBT and MVD tests, analyzed using Python.

Figure 7 shows the correlation including (a) only R1 values and (b) only R3 values. For design calculations in the *fib Model Code* (International Federation for Structural Concrete, 2024), f_{R1} values are used for service limit state calculations, while f_{R3} is used for ultimate limit state calculations. The results indicate that there are slight differences in the k_{MVD} between the different residual strength levels, with R1 giving a lower value (1.39) compared to 1.46 for R3. These aspects should be further investigated, along with further sensitivity analysis.



(a) *(b)*

Figure 7: The correlation of average load from 3PBT and MVD tests excluding UHPC for (a) R1 and (b) R3.

By inserting the obtained k_{MVD} = 1.51 from Figure 4 into Eq. 2, the residual flexural strength of the 3PBT and the MVD can be calculated using Eq. 1 and Eq. 2, respectively. The results show that the MVD test can provide residual flexural strengths similar to those derived from the 3PBT. However, some batches show more pronounced deviations between MVD and 3PBT, indicating that more research is needed to validate and refine the transformation parameter.

For batches from *K25*, the MVD underestimated the residual flexural strength compared to the 3PBT. Analyzing the load–CMOD curves revealed that the beams tested in the 3PBT exhibited hardening behavior, whereas the corresponding specimens tested in the MVD showed softening behavior or limited hardening (Lande et al., 2026). These beams were also cast using a moving casting point (“Mod. Danish method”), which may have influenced the fiber distribution. Batch *K25-B2* also showed fiber separation due to the high fiber content (55 kg/m^3), leading to uneven fiber distribution. These two batches were excluded in the analysis in Figure 4 due to the propagation of horizontal cracks in several test specimens during the MVD test.

Another finding is that it is possible to apply MVD also to UHPC. It was found that using the same transformation parameter for UHPFRC gave similar residual tensile strength values. As mentioned earlier, it has been discussed whether notched beams are suitable for testing UHPC due to the strain-hardening and multiple cracking behavior. For notched beams, several micro-cracks can appear at the notch and not as a single crack (López et al., 2016). Using a four-point bending test would give a more realistic behavior of UHPFRC, making its multiple cracking more pronounced.

An analysis of the scatter in results showed that the coefficient of variation (CoV) ranged from 5 to 32% for the 3PBT prisms and 6 to 33% for the MVD cubes. Thus, the overall variability of the two test methods is similar.

From experiences gained from *FiberCon*, the MVD appears to be a promising method for quality control of FRC. The test is easier to perform and potentially faster to execute than the 3PBT. In our experience, the method can be further simplified by only considering the vertical

displacement because the relationship between the CMOD and the stroke displacement is consistent.

In addition, drilled cores of existing structures can be tested with MVD to evaluate the residual strength because the test can also be performed on cylindrical specimens. However, further development of the test method is required before broader implementation can be recommended. Clear guidelines on execution of MVD tests are needed, including specimen size, details of test setup, and definition of acceptable and non-acceptable cracks. Such standardization will contribute to more consistent and reliable results.

Another important step is to extend the research on the MVD method into larger experimental programs, including a wider range of concrete types and different laboratory facilities. Comparative studies in which clear requirements for the test setup are followed, and where both 3PBT and MVD are performed at 28 days, will be essential for verifying the robustness and applicability of the method.

4 Conclusions

This paper presents a collection of results from the Norwegian industrial R&D project *FiberCon.* The work presented focuses on experiences with applying the Montevideo (MVD) wedge-splitting test to evaluate the residual flexural tensile strength of various fiber-reinforced concrete types (FRC). The MVD results were compared with those obtained using the standardized three-point bending test EN *14651* (3PBT) to assess their comparative performance and practical applicability.

Based on the results from 12 batches produced at different ready-mix concrete plants, the MVD test appears to be a promising method for simpler quality control of FRC. A strong correlation was found between the residual strength from 3PBT and the MVD, with a transformation parameter between the two test methods of 1.51 and an R^2 of 0.96. A sensitivity analysis shows that the transformation parameter remains stable (1.4–1.6) with R^2 between 0.87 and 0.95. This indicates that the method is robust across various experimental campaigns, with variations in test setup, concrete types and compositions, fiber types and fiber content. The scatter observed in the MVD and 3PBT results was of similar magnitude with CoV values ranging from 6% to 33%.

However, some batches exhibited deviations in residual strength between the test methods, indicating that additional research is needed to validate and refine the transformation parameter. Future studies should be conducted under clearly defined requirements for test setups.

5 Acknowledgements

This work is part of the industrial research project *FiberCon*, led by Dr.techn. Olav Olsen AS and granted by the Norwegian Research Council, Project number 327710-IPNÆRINGSLIV21. During the preparation of this work the author(s) applied CoPilot for grammar, and overall language quality.

6 References

Abedi, M., Rojas, G., Domingo, M., Martius-Hammer, T. A., Kanstad, T., & Ji, G. (2025). Steel fiber distribution and orientation in full-scale walls cast from FRC with various

consistencies and casting procedures: evaluation by the inductive method. *Materials and Structures*, *58*(3), 81. https://doi.org/10.1617/s11527-025-02608-x

European Committee for Standardization. (2005). *NS-EN 14651:2005+A1:2007 Test method for metallic fibre concrete - Measuring the flexural tensile strength (limit of proportionality (LOP), residual)*. https://online.standard.no/nb/ns-en-14651-2005a1-2007

International Federation for Structural Concrete. (2024). *fib Model Code for Concrete Structures 2020 (MC2020)*. https://www.fib-international.org/publications/fib-bulletins/fib-model-code-2020.html

Lande, I., Knudegaard, E. B., Thomassen, M., & Rojas, G. (2026). Preliminary findings using the Montevideo test for evaluation of flexural strength in fibre-reinforced concrete unpublished, submitted to 7th fib Congress 2026, Lisbon, Portugal.

Lande, I., Thorstensen, R. T., Petersen, B. G., & Kanstad, T. (2025). Full-scale Production and Material Properties of Ultra-High-Performance Fiber-Reinforced Concrete (UHPFRC) for Rehabilitation of Bridge Decks in Norway. *Frontiers in Built Environment*, *11*, 1570920.

López, J. Á., Serna, P., Navarro-Gregori, J., & Coll, H. (2016). A simplified five-point inverse analysis method to determine the tensile properties of UHPFRC from unnotched four-point bending tests. *Composites Part B: Engineering*, *91*, 189-204. https://doi.org/https://doi.org/10.1016/j.compositesb.2016.01.026

Orizio, E., Rojas, G., Kanstad, T., & Plizzari, G. (2026). Structural application of fiber reinforced concrete. Fibre distribution and orientation in full-scale walls. *unpublished, submitted for publication in fib Structural Concrete*.

Rojas, G., Domingo, M., & Kanstad, T. (2025). Fiber distribution and orientation in full scale walls investigated from drilled cores using the inductive method and the Montevideo splitting test. *Construction and Building Materials*, *489*, 142347. https://doi.org/https://doi.org/10.1016/j.conbuildmat.2025.142347

Segura-Castillo, L., Monte, R., Galobardes, I., & de Figueiredo, A. D. (2024). Determination of tensile residual strength of fibre reinforced concrete by a robust and simple test. *Materials and Structures*, *57*(5), 112.

The Norwegian Concrete Association. (2024). *NB 38 Fibre reinforced concrete in load-carrying structures (In Norwegian: "NB 38 Fiberarmert betong i bærende konstruksjoner"*. https://betong.net/nettbutikk/nb-publikasjoner/38-pdf-fiberarmert-betong-i-baerende-konstruksjoner-2020/

Three-Point Bending Test of UHPFRC with Increased Aggregate Size and Variable Fibre Content

Malena Thomassen[1], Ingrid Lande[2]

1. PhD Research fellow, Department of Engineering Sciences, University of Agder, Grimstad, Norway
2. Associate professor, Department of Engineering Sciences, University of Agder, Grimstad, Norway

*Corresponding author email: malena.thomassen@uia.no

Abstract

Ultra-High-Performance Fibre-Reinforced Concrete (UHPFRC) has been used to rehabilitate over 400 bridges in Switzerland, typically with maximum aggregate size below 1 mm and 3 vol-% micro steel fibres. The approach is to add a thin UHPFRC layer to bridge decks to increase capacity, restore integrity, and prevent water ingress. Fibre-Reinforced Concrete (FRC) is tested per *NS-EN 14651* using three-point bending to measure flexural tensile strength, usually with larger aggregates and lower fibre content. In Norway, UHPFRC is rare, and research is exploring the use of larger aggregates and varying fibre contents for local, large-scale production. This study presents preliminary three-point bending results on 24 beams. A commercial Premix with D_{max} = 0.6 mm and a locally produced UHPFRC (*Silo UHPFRC*) with D_{max} = 8 mm were tested, both with fibre contents of 2 vol-% and 3 vol-%. Results show that the Silo UHPFRC exhibited higher flexural strength and residual flexural tensile strength than the commercial *Premix* for all CMOD values. Increasing fibre content from 2 vol-% to 3 vol-% improved the results of all CMOD levels for the fine *Premix*, and increased f_L, f_{R1} and f_{R2} for the Silo UHPFRC. For larger cracks (f_{R3} and f_{R4}), residual strength in the *Silo UHPFRC* decreased slightly, likely due to fibre clustering and local misalignment caused by coarse aggregates. Variability in residual strength was higher for the *Silo UHPFRC*, indicating heterogeneous post-cracking behaviour. These findings demonstrate that locally produced *Silo UHPFRC* can achieve comparable material properties to the commercial *Premix*, but with a significantly higher standard deviation.

Keywords

3-Point Bending Test, UHPFRC, Fibre content, Maximum Aggregate Size, post-crack performance, flexure

1 Introduction

Ultra-High Performance Fibre-Reinforced Concrete (UHPFRC) is an advanced material with high durability, compressive strength above 120 MPa, high resistance to water and chloride ingress, low water-to-binder ratio and a high particle packing density [1-3]. A high content of micro steel fibre, usually 2-3 vol-%, provides UHPFRC with a tensile strength above 7 MPa

with strain hardening behaviour [4]. Internationally, the maximum aggregate size is often set to less than 1 mm to provide a sufficient fibre distribution and the high particle packing [3, 4]. UHPFRC is often used to rehabilitate bridges and building new structures using prefabricated elements [5]. In Switzerland, UHPFRC has been used to rehabilitate more than 400 bridges since 2004, with the majority of the structures built after the publication of the technical UHPFRC standard SIA2052 [6].

Standard test methods for fibre-reinforced concrete (FRC) to assess flexural behaviour typically rely on the three-point bending test (3PBT), described in EN 14651. However, for UHPFRC, the 3PBT should only be applied when the material exhibits strain-softening behaviour, as defined in NF P18-470 [7, 8]. According to the Norwegian Concrete Association Publication 38 (National Guidelines for FRC) [9], the maximum aggregate size should be greater than 16 mm, which contradicts the use of UHPFRC. The Norwegian Concrete Association is currently developing a national guideline for the use of UHPFRC, which requires an evaluation of suitable testing methods for locally produced materials with varying maximum aggregate sizes (D_{max}). Norwegian concrete producers aim to utilise materials already available in their silos, typically with a 0/8 mm aggregate grading, in combination with micro steel fibres.

This paper presents preliminary findings from a comparison of 3PBT results obtained using commercially available UHPFRC with a D_{max} of 0.6 mm and a locally produced UHPFRC with a D_{max} of 8 mm, both tested with fibre contents of 2 and 3 vol-%.

2 Experimental program

The specimens were cast in two batches due to the capacity of the mixer. The mixes are named using the following system, *Premix* refers to the commercial product, see Table 1, and *Silo* (Table 2) refers to locally produced UHPFRC. The fibres used are micro steel fibres with length of 12.5 mm and fibre diameter of 0.175 mm. Slump flow was measured in accordance with *NS EN 459-2*. However, due to a non-thixotropic UHPFRC mix design, slump flow was not measured with joints as specified in *NS EN 459-2*.

Table 1: Mix design for Premix 2 vol-% and 3 vol-% given in kg/m^3

Material	**Premix 2vol-%**	**Premix 3vol-%**
Pre-bagged powder	1155.0	1143.2
Aggregates (0.6 mm)	1020.9	1010.5
Set-accelerating admixture	5.77	5.71
Shrinkage-reducing admixture	2.5	2.48
Superplasticizer	36.0	35.64
Surface enhancer	2.0	1.98
Water	123.9	122.67
Steel fibres	157.0	235.5

Table 2: Mix design for Silo 2 vol-% and 3 vol-% given in kg/m^3

Material	Silo 2vol-%	Silo 3vol-%
Cement	776.6	770.0
Silica fume	152.0	152.0
Limestone filler	163.7	162.0
Aggregates (0/8 mm)	1010.5	998.8
Shrinkage-reducing admixture	3.9	-
Superplasticizer	12.7	12.7
Viscosity-modifying admixture	7.76	-
Water	176.8	187.1
Steel fibres	157.0	235.5

All specimens were cast without vibration. Directly after casting, the beams were covered in plastic and cured for 24 hours. After curing, the specimens were marked and stored in water before they were tested after 28 days. The compressive strength of both materials was determined in accordance with *NS-EN 12390-3* [10] and the average value may be found in the Table 3. A total of 24 beams, 150 mm × 150 mm × 600 mm, were prepared in accordance with *NS-EN 14651* [11]. Six beams of each combination of fibre and aggregate size were rotated 90° from the cast surface, and tested as illustrated in Figure 1. The loading rate was set to the minimum load of the available equipment, using a rate of 0.6 mm displacement per minute. The distance between the supports was 500 mm, and a notch was cut in the middle of the beam measuring 5 mm width and 25 mm height. Crack Mount Opening Displacement (CMOD) was measured. One deviation from *NS-EN 12390-3* [10] is the lack of LVDT sensors. Instead of using LVDT, a Digital Image Correlation program (DIC) was used to gather more information regarding crack pattern, that will be used in a follow-up article, comparing the result from three-point bending test with four-point bending test according to *SIA2052*. The CMOD value was measured using a virtual extensometer in the post-processing software (Vic-3D) as displacement at the original placing of the LVDT sensor in accordance with *NS-EN 14651* [11]. As shown in Table 3, the slump flow diameter differed between the two mixes. The premix slump flow was within the manufacturer's requirements. The silo UHPFRC exhibited a significantly lower slump flow due to the larger aggregates in combination with the high fibre content.

Table 3: Compressive strength and slump flow

Material	Fibre content	D_{max}	Slump flow diameter	Average compressive strength
Premix	2%	0.6 mm	260 mm	157 MPa
Premix	3%	0.6 mm	265 mm	170 MPa
Silo	2%	8 mm	180 mm	144 MPa
Silo	3%	8 mm	172 mm	163 MPa

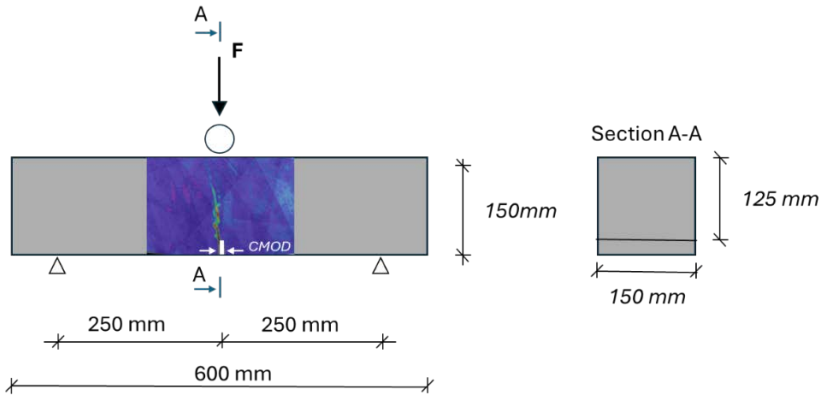


Figure 1: The arrangement and test set-up of 3 point bending test, with DIC

For each beam specimen, the residual flexural tensile strength was evaluated at CMOD values of 0.5 mm, 1.5 mm, 2.5 mm, and 3.5 mm, in accordance *NS-EN 14651* [11]. The corresponding strengths are referred to as f_{R1}, f_{R2}, f_{R3}, and f_{R4}, respectively. The residual flexural strengths (f_{Rj}) associated with these CMOD levels were determined using the equation specified in EN 14651:

$$f_{R,j} = \frac{3F_j l}{2bh_{sp}^2}$$

where Fj represents the applied load at the specified CMOD level *(j = 1, 2, 3, or 4)* expressed in Newtons, l is the span length (mm), b is the width of the beam (mm), and h_{sp} denotes the effective depth of the notched beam (mm). The flexural tensile strength at limit of elasticity, LOP, were measured at CMOD 0.05 mm, using the same formula (j=L).

The characteristic load for UHPFRC was calculated assuming a normal distribution of the test results and applying Student's t-distribution in accordance with *NF P 18-470* [12]. For 6 specimens, a student coefficient of 2.015 was used, and the characteristic value (corresponding to a non-exceedance probability of less than 5%) was determined as:

$$f_k = \bar{x} - t \cdot \frac{s}{\sqrt{n}}$$

Where $\bar{x}$ is the mean value of the samples, t is the Student's t coefficient, s is the sample standard deviation, and n is the number of test specimens.

3 Results and Discussion

Average flexural tensile strength and residual flexural tensile strength for each material are given in Table 4. The standard deviation is given in parentheses. For all series, Load-CMOD values were plotted, and may be found in Figure 2. Figure (a) represents *Premix 2 vol-%*, (b) *Premix 3 vol-%*, (c) *Silo 2 vol-%*, (d) *Silo 3 vol-%*.

Table 4: Average flexural tensile strength and residual flexural tensile strength for all configurations

	Premix 2 vol-%	**Premix 3 vol-%**	**Silo 2 vol-%**	**Silo 3 vol-%**
f_L[MPa]	10.29 *(0.85)*	11.83 *(1.17)*	12.79 *(0.64)*	13.42 *(0.88)*
f_{Max}[MPa]	15.06 *(2.03)*	18.31 *(1.66)*	25.42 *(3.04)*	26.38 *(3.09)*

$f_{R,1}$[MPa]	14.87 *(2.01)*	17.46 *(1.44)*	24.51 *(2.56)*	25.52 *(2.59)*
$f_{R,2}$[MPa]	12.44 *(1.62)*	14.31 *(1.85)*	24.13 *(3.27)*	25.11 *(3.17)*
$f_{R,3}$[MPa]	9.81 *(1.00)*	11.45 *(1.92)*	20.60 *(2.48)*	20.50 *(3.16)*
$f_{R,4}$[MPa]	7.67 *(0.64)*	8.84 *(1.57)*	17.37 *(2.51)*	16.0 *(3.09)*

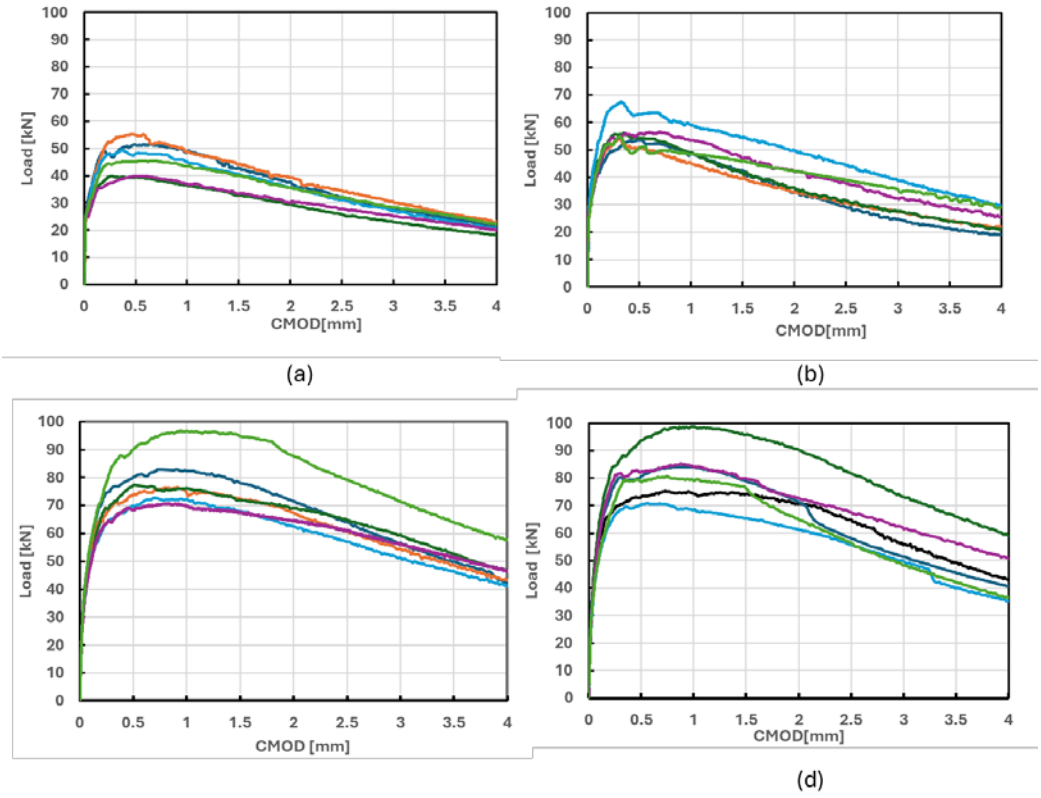


Figure 2: Load- CMOD curves of the three-point bending test for (a) Premix 2 vol-%, (b) Premix 3 vol-%, (c) Silo 2 vol-%, and (d) Silo 3 vol-%.

The maximum flexural tensile strength results demonstrate a clear influence of both fibre content and mix design, as shown in Figure 3. For the *Premix UHPFRC*, increasing the fibre volume fraction from 2 vol-% to 3 vol-% leads to an increase in strength from 15.06 MPa (±2.03) to 18.31 MPa (±1.66), confirming the positive contribution of higher fibre content to the load-carrying capacity. In comparison, the *Silo UHPFRC* exhibits significantly higher strength values overall, increasing from 25.42 MPa (±3.04) at 2 vol-% to 26.38 MPa (±3.09) at 3 vol-%. This indicates that, unlike the premix material, the effect of increasing fibre content in the silo mixes is relatively limited in terms of maximum capacity.

In terms of variability, the *Premix UHPFRC* shows lower standard deviations compared to the *Silo UHPFRC*, indicating more consistent and predictable behaviour, possibly due to more uniform fibre distribution. Although the *Silo mixtures* achieve higher peak strengths, they also exhibit greater scatter, which may be attributed to less uniform fibre distribution or variations introduced by the larger aggregates. The marginal increase in strength between 2 vol-% and 3 vol-% for the *Silo UHPFRC* suggests diminishing returns at higher fibre contents, possibly due to fibre interaction effects such as clustering or reduced efficiency in stress transfer. Consequently, while *Silo UHPFRC* provides superior maximum capacity, *Premix UHPFRC*

offers enhanced reliability, which may be advantageous in applications where consistency is critical.

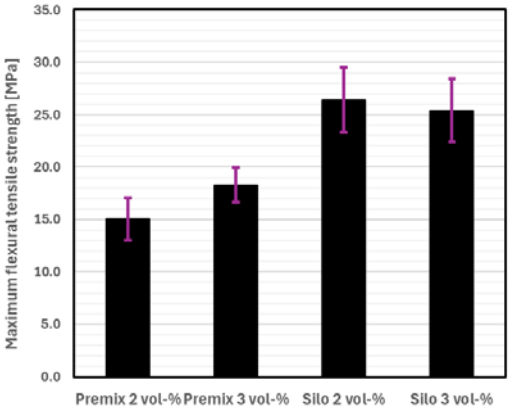


Figure 3: Average flexural tensile strength at maximum load for all 4 mixes

3.1 Limit of Proportionality

The results show that the commercial UHPFRC product (*Premix UHPFRC*) with an ultra-fine aggregate system (D_{max} = 0.6 mm) generally exhibited lower flexural tensile strength at the limit of proportionality compared to the UHPFRC with D_{max} = 8 mm (*Silo UHPFRC*), for both fibre volume fractions. The flexural tensile strength was evaluated at CMOD = 0.05 mm in accordance with *NS-EN 14651*. For the *Silo UHPFRC*, the average flexural tensile strength at limit of proportionality was 12.79 MPa and 13.42 MPa for 2.0 vol-% and 3.0 vol-% fibre content, respectively. In comparison, the commercial product (*Premix UHPFRC*) exhibited average flexural tensile strengths of 9.16 MPa and 11.83 MPa for 2.0 vol-% and 3.0 vol-% fibres, respectively. Increasing the fibre volume fraction from 2.0% to 3.0% resulted in a clear increase in f_L for both materials. A study conducted by Lande et al. [13] on the similar *Silo UHPFRC* mixture shows a clear increase in flexural strength when increasing the fibre content, similar to the findings in this research. However, in this research, the relative gain was more pronounced for the commercial *Premix* with D_{max} = 0.6 mm. This may be due to improved fibre efficiency at higher fibre contents, where a larger number of fibres actively contribute to resisting tensile stresses. At lower fibre contents, the finer matrix may provide a more uniform fibre distribution, while the addition of fibres up to 3.0 vol-% increases the number of load-carrying fibres bridging microcracks. In contrast, the presence of larger aggregates in the *Silo UHPFRC* may locally disturb fibre orientation and distribution, as coarse aggregate particles can push fibres aside during casting. Wang et al. [14] observed that increasing the steel fibre content in UHPFRC led to a less uniform fibre dispersion, particularly in mixes with a low water-to-binder ratio. In such cases, steel fibres showed a greater tendency to agglomerate, as the limited amount of cement paste was insufficient to adequately coat the fibre surfaces, restricting their mobility and hindering proper dispersion.

The standard deviation of f_L was higher for specimens with 3.0 vol-% fibres compared to those with 2.0 vol-% fibres for both materials, see Figure 4. This observation is consistent with findings reported in the literature [14-16], where fibre contents around 3.0 vol-% are associated with an increased risk of fibre clustering and agglomeration. Such effects may lead to local variations in fibre density, resulting in weaker zones with fewer fibres and, consequently, lower the limit of proportionality values in some specimens. This may be of particularly significance

if these weak zones occur at the notch, since this is where fracture is initiated due to a smaller cross-section.

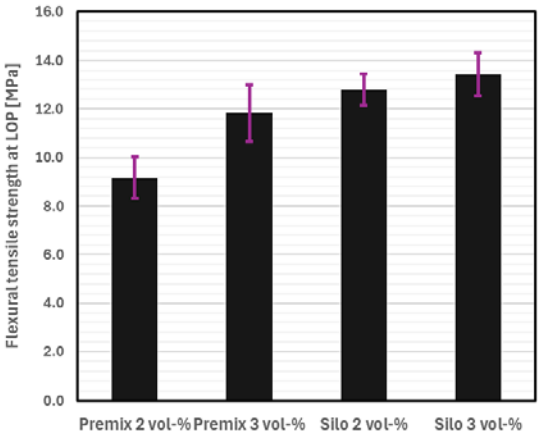


Figure 4: Average flexural tensile strength at limit of proportionality, for all 4 mixes.

Despite this, the standard deviation was generally lower for the Silo UHPFRC compared to the commercial product. This may appear contradictory to the findings of Shen et al. [15] of uneven fibre distribution caused by coarse aggregates and suggests that factors other than fibre distribution may play a dominant role in governing the variability of the flexural tensile strength at the limit of proportionality for the investigated materials. The limit of proportionality may be affected by the concrete matrix and is relatively insensitive to both fibre volume and aggregate size. Because the UHPFRC matrix is highly optimized with very fine additions that almost eliminate weak zones in the interfacial transition zone, the initial cracking strength remains stable and may be less affected by the "ball-bearing" effects or flow-induced orientation that impact residual strength [17]. Additionally, the higher modulus of elasticity found in mixtures with stiffer coarse aggregates can help reduce autogenous shrinkage, further minimizing the risk of early-age micro-cracking that might otherwise increase statistical scatter at the limit of proportionality [18]. Since a commercial product is used, the exact binder volume is unknown, the premix contains both fillers and binders, and one reason for the Silo UHPFRC to have a higher limit of proportionality may be caused by a higher binder content, and a different w/b ratio causing the matrix to be stronger and indicating a higher limit of proportionality. Future research will involve using a similar UHPFRC mix design and only changing the D_{max} and fibre content.

3.2 Residual Flexural Tensile Strength

3.1.1 Characteristic values

The characteristic values of the residual flexural tensile strengths $f_{R,1k}$ and $f_{R,3k}$ are summarized in Table 4, together with their ratios, which are used to determine the ductility class (*a*–*e*) in accordance with NB38 [9]. The premix exhibits ratios of 0.68 and 0.61, corresponding to ductility class *a*, whereas the silo-mixed material shows higher ratios of 0.83 and 0.76, corresponding to ductility class *b*. At lower ductility classes, the failure mode is more brittle, characterized by a pronounced reduction in post-cracking strength and limited deformation capacity. Consequently, the premix demonstrates a more abrupt loss of load-

carrying capacity compared to the silo-mixed material, which exhibits a more gradual softening response.

All batches present ratios below 1.0, indicating a strain-softening behaviour in bending. Although the residual strength values are relatively high, the material cannot be classified as strain-hardening in tension unless the ratio significantly exceeds unity, as outlined in [19]. However, when evaluating the Load-CMOD curves in Figure 2, all graphs show a deflection-hardening behaviour, where the strength of the specimen increases when the fibres are activated. Using the ratio between $f_{R,1k}$ and $f_{R,3k}$ might not yield representative results for UHPFFRC materials. Due to the stiffness of the UHPFRC, it seems that most of the strength development is captured prior to CMOD = 0.5 mm ($f_{R,1k}$), and the strength development is already descending when reaching this point. Since $f_{R,1k}$ are to represent the material when cracks start to develop and thus the deflection hardening phase begins, it may be questioned that this value should be lower for UHPFRC. Based on the 4 mix designs used in this research, all values for $f_{R,1}$ are found near the point of maximum load. For the *Premix*, the beam has already entered the softening phase and thus started to decrease rapidly in strength. Similarly, the *Silo* mixes reach CMOD = 0.5 mm at the end of the hardening phase. In both cases, the most significant part of the Load-CMOD curve is excluded, as the hardening phase happened prior to the values for CMOD = 0.5mm and CMOD = 1.5 mm.

Table 4: Residual flexural tensile strengths $f_{R,1c}$ and $f_{R,3c}$ and the ratio between them for all 4 mixes

Batch	Fibre content	$f_{R,1k}$	$f_{R,3k}$	$f_{R,3c}$/ $f_{R,1c}$
Premix	2%	13.2	9.0	0.68
Premix	3%	16.3	9.9	0.61
Silo	2%	22.4	18.6	0.83
Silo	3%	23.4	17.9	0.76

The influence of increasing the fibre content from 2% to 3% appears to be limited. For the *Premix*, this increase results in a moderate improvement in $f_{R,1k}$, while the gain in $f_{R,3k}$ is negligible, suggesting that a critical fibre volume fraction is being approached where the matrix can no longer effectively disperse the fibres. For the silo material, the increase to 3% fibre content provides virtually no benefit and even indicates a slight reduction in performance. This behaviour is consistent with fibre “balling” or reduced fibre efficiency at high dosages. No fibre “balling” was observed in the used batches; however, the material was difficult to cast due to reduced flowability after adding the 3 vol-% of fibres. Beyond a certain threshold, increased fibre content may significantly reduce workability, leading to poor fibre orientation and, consequently, diminished mechanical performance. Furthermore, the ratio between $f_{R,3c}$ and $f_{R,1k}$ is reduced with increasing fibre content, indicating a shift towards more brittle behaviour despite the higher fibre dosage.

3.1.2 Average values

The residual flexural tensile strengths derived from the 3PBT indicate marked differences in post-cracking behaviour. For all CMOD levels, the Silo UHPFRC (D_{max} = 8 mm) exhibited significantly higher residual flexural tensile strengths compared to the commercial premix with D_{max} = 0.6 mm, regardless of fibre volume fraction. At $f_{R,1}$ the Silo UHPFRC reached average residual strengths of 24.51 MPa and 25.52 MPa for 2.0 vol-% and 3.0 vol-% fibres, respectively, compared to 14.87 MPa and 17.46 MPa for the premix material. This trend remained consistent

for $f_{R,2}$, $f_{R,3}$ and $f_{R,4}$, demonstrating a superior post-cracking load-carrying capacity for the *Silo UHPFRC*, see Figure 5. According to research conducted by Leutbecher et al. [7] the flow behaviour of concrete during casting is crucial for fibre orientation. UHPFRC has high viscosity, which causes the mix to adhere to the formwork walls when poured, creating turbulence in the central part of the cross-section that disrupts fibre alignment. The use of larger aggregates modifies these flow dynamics and can help counteract this effect, resulting in a more favourable fibre orientation and distribution, thereby improving the overall strength.

As illustrated in Figure 5, $f_{R,1}$, $f_{R,2}$, $f_{R,3}$ and $f_{R,4}$ exhibit a decreasing trend when plotted, indicating softening behaviour. In this figure, the question of whether the CMOD values accurately represent the material behaviour becomes more pronounced. The *Premix UHPFRC* shows an almost linearly decreasing trend, as these values are extracted after deflection hardening has occurred and the maximum load has been surpassed. For the silo UHPFRC, this behaviour is less pronounced, likely because the deflection hardening phase shown in Figure 2 extends over a larger range. Despite uncertainties regarding the representativeness of the CMOD values, the *Premix UHPFRC* demonstrates a significantly lower standard deviation compared to the *Silo UHPFRC*, indicating more predictable behaviour.

Increasing the fibre volume fraction from 2.0% to 3.0% resulted in increased residual flexural tensile strengths for the *Premix UHPFRC* at all CMOD levels. The relative increase was particularly pronounced at higher CMOD levels ($f_{R,3}$ and $f_{R,4}$) indicating an enhanced contribution of additional fibres to crack bridging and post-cracking resistance in the ultra-fine matrix. For the *Silo UHPFRC*, increasing the fibre content led to a slight increase in residual strength at lower CMOD levels (f_{R1} and f_{R2}) whereas a reduction in average residual flexural tensile strength was observed at higher CMOD levels (f_{R3} and f_{R4}). This suggests that, beyond a certain fibre volume fraction, the efficiency of additional fibres in the coarser aggregate system may decrease, potentially due to fibre interaction, clustering, or less favourable fibre orientation, which can reduce the effectiveness of crack bridging at larger crack openings. The fibres used in this study are 12.5 mm long, while the maximum aggregate size is 8 mm. According to recommendations, the fibre length should be at least twice the size of the largest aggregate, which in this case would correspond to a fibre length exceeding 16 mm [9]. Although previous research on the *Silo UHPFRC* material by Lande et al. [13] indicates a generally uniform fibre distribution even when using a D_{max} of 8 mm, the relatively small ratio between fibre length and aggregate size may still influence crack-bridging performance at larger crack openings. At increased CMOD, the presence of coarse aggregates may promote aggregate interlocking within the crack, causing fibres to become misaligned or locally disturbed, which can increase the likelihood of fibre pull-out. This effect may be more pronounced at a fibre volume fraction of 3 vol-% compared to 2 vol-%, as the higher fibre content can reduce the amount of surrounding cementitious matrix available per fibre, potentially leading to weaker fibre–matrix bonding and less effective anchorage. Similar observations have been reported by Zhong et al. [20] who found that while coarse aggregates contributed to a more uniform global fibre distribution, they also adversely affected local fibre dispersion due to disturbances caused by larger aggregate particles. Consequently, the combination of relatively short fibres, larger aggregates, and higher fibre volume fractions may increase the vulnerability of the material at larger crack openings.

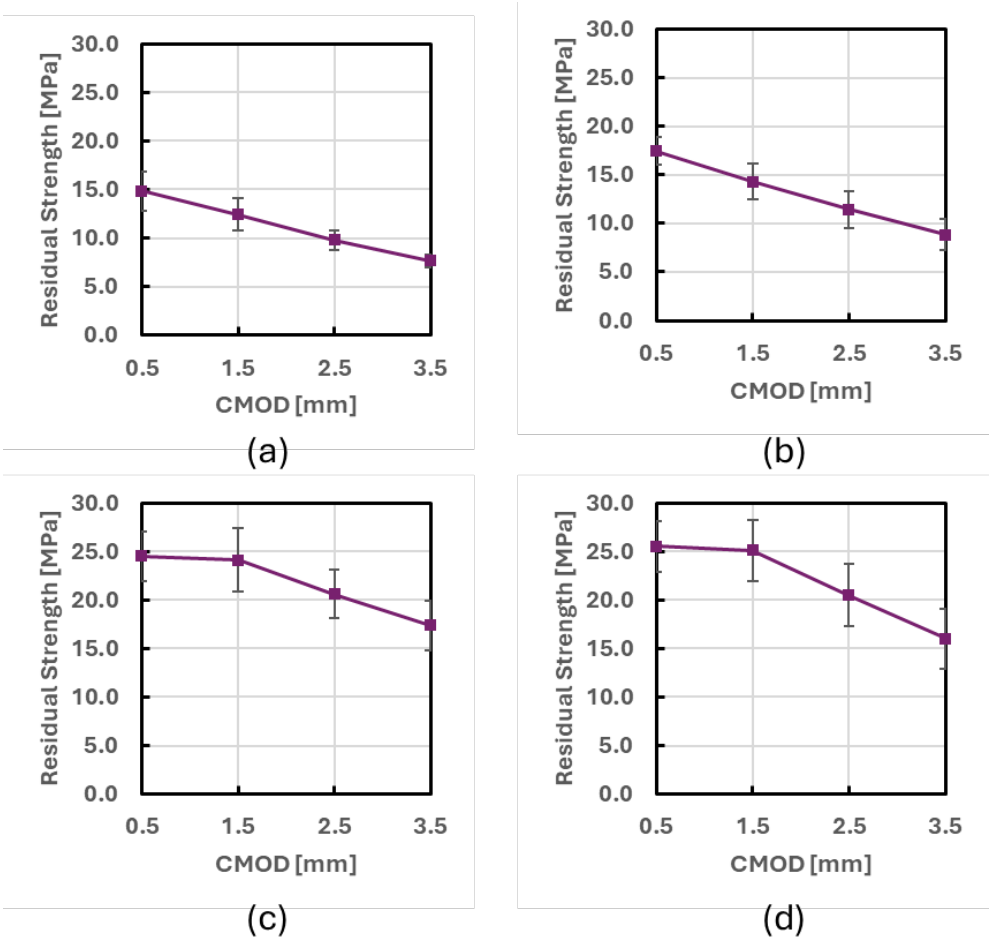


Figure 5: Average residual flexural tensile strength for (a) Premix 2 vol-%, (b) Premix 3 vol-%, (c) Silo 2 vol-%, and (d) Silo 3 vol-%. Error bars show standard deviation

In contrast to the strength level, the standard deviation of the residual flexural tensile strengths was consistently higher for the Silo UHPFRC than for the premix material at all CMOD levels, regardless of fibre content. This higher scatter is particularly evident for f_{R2}–f_{R4}, where standard deviations exceeding 3 MPa were observed for the *Silo UHPFRC*. The increased variability suggests a more heterogeneous post-cracking response, likely influenced by local variations in fibre orientation and crack path induced by the presence of coarse aggregates. Zhong et al. [20] observed more locally irregularities were more frequent for larger aggregate sizes than for smaller ones and may explain the larger standard deviation if the notch intersects one of these weak zones. This contradicts the research done by Leutbecher et al. [7] showing that coarse-grained mixtures (such as those with D_{max}=8 mm) can actually result in a more homogeneous distribution of strength across a beam's cross-section than fine-grained mixtures. In fine-grained UHPFRC, local post-cracking strength has been shown to be systematically heterogeneous, varying from 28% to 135% of the cross-sectional mean, whereas the inclusion of larger aggregates helps stabilize this distribution. However, this research was conducted using 1 vol-% of fibres, and the result may differ when the amount of fibre triples.

4 Concluding remarks

This study investigated the flexural behaviour of commercially available UHPFRC with D_{max} = 0.6 mm (*Premix UHPFRC*) and locally produced UHPFRC with D_{max} = 8 mm (*Silo UHPFRC*) at fibre contents of 2.0 and 3.0 vol-% using three-point bending test.

Limit of Proportionality: The Silo UHPFRC with larger aggregates generally exhibited higher flexural tensile strength at the limit of proportionality compared to the commercial Premix. Increasing fibre content from 2.0% to 3.0% improved f_L for both materials, with a more pronounced relative gain for the fine Premix likely due to improved fibre efficiency. The variability in f_L was relatively low, suggesting that initial cracking is mainly governed by the concrete matrix rather than fibre distribution or aggregate size.

Residual Flexural Strength: The Silo UHPFRC demonstrated significantly higher residual strengths at all CMOD levels, indicating superior post-cracking performance. Increasing fibre content improved residual strength in the fine Premix, for all CMOD values, while for the Silo UHPFRC, residual strength at larger crack openings (f_{R3} and f_{R4}) was slightly reduced, likely due to fibre clustering and local misalignment. The standard deviation of residual strengths was higher for the Silo UHPFRC, reflecting increased heterogeneity in post-cracking behaviour caused by larger aggregates and fibre interactions.

5 Acknowledgements

The efforts of students at University of Agder: Eirik Benjamin Knudegaard, Mikael Vermeulen, Aram Akhte, and Johan Seljehaug Johansson in conducting some of the laboratory experiments are greatly appreciated. The authors also gratefully acknowledge the contribution of Senior Engineer Anette Heimdal and Cecilie Ødegård for contributing to conducting the flexural strength tests. As an alternative to language editing services, CoPilot was used during the preparation of the draft of this manuscript to improve readability and for spell-check, for some parts of the text.

6 References

[1] E. Brühwiler, "UHPFRC technology for the extension of the service duration of bridges," 2024, pp. 158–166.

[2] B. Graybeal, E. Brühwiler, B.-S. Kim, F. o. Toutlemonde, Y. Voo, and A. E. Zaghi, "International Perspective on UHPC in Bridge Engineering," *Journal of Bridge Engineering*, vol. 25, 09/01 2020, doi: 10.1061/(ASCE)BE.1943-5592.0001630.

[3] F. H. Administration, "Design and Construction of UHPC-Based Bridge Preservation and Repair Solutions," 2022.

[4] *Swiss UHPFRC Model Standard: Ultra-High Performance Fibre Reinforced Cementitous composite (UHPFRC) - Materials, dimensioning and execution (adapted from SIA 2052)*, E. Brühwiler, 2024 2024.

[5] N. Bertola, P. Schiltz, E. Denarié, and E. Brühwiler. (2021) A Review of the Use of UHPFRC in Bridge Rehabilitation and New Construction in Switzerland. *Frontiers in Built Environment*.

[6] E. Brühwiler, "UHPFRC technology for the extension of the service duration of bridges," in *Bridge Maintanence, Safety, Managment, Digitalization and Sustainability*, 2024, pp. 158–166.
[7] T. Leutbecher and J. Rebling, "Predicting the postcracking strength of ultra-high performance fiber reinforced concrete by means of three-point bending tests according to EN 14651," *Structural Concrete*, vol. 20, pp. 2081–2095, 07/16 2019, doi: 10.1002/suco.201900070.
[8] *CONCRETE - ULTRA-HIGH PERFORMANCE FIBRE-REINFORCED CONCRETE - SPECIFICATIONS, PERFORMANCE, PRODUCTION AND CONFORMITY*, A. F. d. Normalisation, France, 2016.
[9] *NB 38 - Fiber-reinforced concrete in structural applications (Fiberarmert betong i bærende konstruksjoner)*, The Norwegian Concrete Association, 2025.
[10] *NS-EN 12390-3:2019 Testing hardened concrete - Part 3: Compressive strength of test specimens*, European Committee for Standardization, Brussels, 2019.
[11] European Committee for Standardization, "NS-EN 14651:2005+A1:2007 Test method for metallic fibre concrete - Measuring the flexural tensile strength (limit of proportionality (LOP), residual)," Brussels, 2005. [Online]. Available: https://online.standard.no/nb/ns-en-14651-2005a1-2007
[12] *NFP 18 710 : 2016*, Association Francaise de Normalisation, 2016.
[13] I. Lande, R. T. Thorstensen, B. G. Petersen, and T. Kanstad, "Full-scale Production and Material Properties of Ultra-High-Performance Fiber-Reinforced Concrete (UHPFRC) for Rehabilitation of Bridge Decks in Norway," *Frontiers in Built Environment*, vol. 11, p. 1570920, 2025.
[14] R. Wang, X. Gao, H. Huang, and G. Han, "Influence of rheological properties of cement mortar on steel fiber distribution in UHPC," *Construction and Building Materials*, vol. 144, pp. 65–73, 2017/07/30/ 2017, doi: https://doi.org/10.1016/j.conbuildmat.2017.03.173.
[15] C. Shen *et al.*, "Investigating the influence of coarse aggregate characteristics and fiber dispersion on the flexural performance of ultra-high performance concrete (UHPC)," *Journal of Building Engineering*, vol. 97, p. 110738, 2024/11/15/ 2024, doi: https://doi.org/10.1016/j.jobe.2024.110738.
[16] D. Ravichandran, P. R. Prem, S. K. Kaliyavaradhan, and P. S. Ambily, "Influence of fibers on fresh and hardened properties of Ultra High Performance Concrete (UHPC)—A review," *Journal of Building Engineering*, vol. 57, p. 104922, 2022/10/01/ 2022, doi: https://doi.org/10.1016/j.jobe.2022.104922.
[17] K. Droll, "Influence of additions on ultra high performance concretes – grain size optimisation " *International Symposium on Ultra High Performance Concrete*, vol. 3, pp. 285–301, 2004.
[18] J. Ma, M. Orgass, F. Dehn, D. Schmidt, and N. Tue, *Comparative Investigations on UltraHigh Performance Concrete with and without Coarse Aggregates*. 2004.
[19] M. di Prisco, G. Plizzari, and L. Vandewalle, "Fibre reinforced concrete: new design perspectives," *Materials and Structures*, vol. 42, no. 9, pp. 1261–1281, 2009/11/01 2009, doi: 10.1617/s11527-009-9529-4.
[20] R. Zhong *et al.*, "Effect of coarse aggregate on the stability and mechanical performance of ultra-high performance concrete (UHPC)," *Composites Part B: Engineering*, vol. 297, p. 112210, 2025/05/15/ 2025, doi: https://doi.org/10.1016/j.compositesb.2025.112210.

Exploring the potential of explicit steel fiber – lattice matrix coupling in high-fidelity simulation of steel-fiber-reinforced composites

Saeid Mehrpay[1], Jelle Billiet[1], Jan Vorel[2], Daniele Pelessone[3], Eskinder Desta Shumuye[4], Tamon Ueda[5], and Roman Wan-Wendner[1]

[1] : Department of Structural Engineering and Building Materials, Faculty of Engineering and Architecture, Ghent University, 9052 Gent, Belgium.

[2] : Department of Mechanics, Faculty of Civil Engineering, Czech Technical University in Prague, Prague 16629, Czech Republic.

[3] : Engineering and Software System Solutions, Inc. (ES3), San Diego, CA 92101, US.

[4] : Institute for Advanced Study & Institute for Carbon Neutrality, Shenzhen University, Shenzhen 518060, China.

[5] : Guangdong Provincial Key Laboratory of Durability for Marine Civil Engineering, College of Civil and Transportation Engineering, Shenzhen University, Shenzhen 518060, China.

Abstract

Macroscopic models that derive the behavior of fibrous composites by parameter fitting are quite popular and effective. They extend the constitutive models or revise the yield surface of plain concrete to represent the favorable effects based on fiber type and content. Nonetheless, to resolve and predict the influence of low-scale phenomena at the material level, such as the influence of biased distributions and orientations of fibers with arbitrary shapes on failure mechanisms, mesoscopic models are usually preferred over smearing the fiber contents. Such models implement various levels of simplification to incorporate the fiber-matrix interaction. Possible methods range from the implementation of full bond or simple adhesive/frictional contact models, depending on the available options in the simulation framework, or incorporating an abstract fiber with bond parameters that are fitted for the target product. A low-level, explicit mesoscopic model fully resolving the geometrical details of individual fibers in the matrix, alongside tailored bond-friction behavior, has so far been missing due to various technical and computational constraints. Enabling such a high-fidelity model to act as a testbed can be beneficial in myriad ways. This study takes the initiative in upscaling a low-level explicit fiber-lattice coupling based on the slideline contact model. Following that, the fiber orientation bias in such a model is observed, and the tensile failure of the composite is examined.

Keywords

Fiber-reinforced concrete, high-fidelity model, fiber-lattice coupling, explicit fiber simulation, hooked-end steel fiber

1 Introduction

From a broad perspective, computational techniques for simulating fibrous concrete take two general approaches: the implicit and explicit approaches. The former method is effective and affordable, especially when used with continuum constitutive models. In such cases, the failure mechanism of the fibrous material is revised by parameter fitting to derive a new failure surface that represents the behavior of the composite. A good example of such a method is demonstrated by Yin et al. (2023). An explicit approach may be used if the derivation of the fibrous composite is from a lower-scale distribution of entities representing the fiber orientation and distribution. Nonetheless, some form of simplification is usually applied with such approaches, which is compensated for by calibration parameters to represent the targeted fiber. This form of explicit modeling is employed in numerous cases to simulate fibrous composites of various types. LDPM-F, the Lattice-Discrete Particle Model with fiber coupling, is an instance of such an application (Schauffert and Cusatis, 2012). Such simplifications will allow studying scaled problems with an affordable computational cost. Nevertheless, to have a model that serves the purpose of geometrical resolution of fiber, high-fidelity models need to be developed. High-fidelity models can incorporate the accurate shape of fiber to analyze its behavior by examining how changes in shape and interactions with the matrix influence performance, rather than relying on pre-established behavioral assumptions.

High-fidelity models of fibers are rare and usually limited to small scales due to their computational cost and the limitation of computational power. Technical limitations of the computational framework or used approach, such as available contact models, the simplification of the model to reduce cost (e.g., a 2D representation of the matrix overlooking 3D effects such as hoop force), and solver instability due to nonlinear interlayers (fiber plasticity, the matrix nonlinearity, and the nonlinear contact algorithm resembling the bond behavior), are some of the bottlenecks influencing the accuracy and applicability. Relying on fully 3D elements that discretize the fiber and force the matrix to conform to the fiber dimensions (mesh-conforming approach) presents another challenge, as the computational costs increase prohibitively with the number of fibers and the model's dimensions.

This work presents a high-fidelity version of LDPM-F by incorporating the LDPM discrete-mesoscopic model for the concrete matrix with a generalized contact algorithm for scaled fiber-lattice explicit coupling (Slideline contact model (Pelessone, 1986) as cited in (1989)). LDPM can capture the nonlinear behavior of the concrete matrix with discontinuities, while the Slideline contact provides a realistic nonlinear bond constitutive model and eliminates the need for a mesh-conforming strategy. In the absence of experimental results, this study serves as proof of concept, with experimental studies currently in progress.

2 Methodology

A case of uniaxial tension on a cylindrical steel fiber-reinforced specimen is considered from an early study that investigated the packing strategies of such a model (Saeid Mehrpay *et al.*, 2026). The Lattice-Discrete Particle Model represents the concrete matrix, which is coupled to the hooked-end fibers via the Slideline contact model (Pelessone, 2001; Li *et al.*, 2022). The fiber dispersion follows the conceptualization used in LDPM-F model (Schauffert and Cusatis, 2012). The reference input parameters of the material models and fiber-lattice coupling

algorithm are presented in Table 1 and Table 2. The specimens are assumed to be reinforced with 1% VF (volume fraction) of 3D-80/60-BG Dramix fibers. The fibers' geometries are modeled based on realistic dimensions measured using a 3D surface-scanning microscope.

Table 1: Material models reference input parameters

Set	Part	Parameter	Value
1	LDPM Concrete Matrix	Material Model Preset	Standard Concrete
		Strength	40. MPa
		Young's Modulus	30. GPa
		Aggregate Size Range	4.0 to 10.0 mm
		Fuller's Coefficient	0.5
2	Steel Fiber	Density	7.8 g/cm^3 × mass-scaling coef.*
		Young's Modulus	210. GPa
		Poisson's Ratio	0.3
		Yield Stress	1225. MPa
		Hardening Modulus	0. GPa
		Plastic Behavior	Isotropic Hardening
		Failure Stretch	0.15
		Decay Parameter	0.8
		Joint Stiffening	Within 100 neighboring joints

* The reference mass-scaling for fiber is $\times 10^4$

Table 2: Fiber-lattice explicit coupling reference parameters (also see Mehrpay et al.*, 2026)*

Set	Model	Parameter	Value
1	Bond Material	Hardening Parameter	2.0
		Initial Strength	1.50 MPa
		Decayed Strength	1.40 MPa
		Residual Strength	1.30 MPa
		Bond Decay Coefficient	1.0
		Initial Friction Coefficient	0.40
		Ultimate Decayed Friction	0.12
		Friction Decay Standard Dev.	1.0 mm
		Decay Onset	0.5 mm
		Decay Reference	1.5 mm
2	Slideline Contact Algorithm	Spallation Opening Limit	0.1 mm
		No. of Circumferential Divisions	8 or 32*
		Penalty Stiffness	1. e +9 N/m

* The reference value is 32

The model's geometry is depicted in Figure 1. The ends of the cylinder are clamped, with the lower end prescribed with downward displacement to induce tensile failure in the cylinder. The reference rate of loading is 5 mm/s.

The response is first verified for sensitivity to the analysis's maximum time step. After ensuring stability, the following aspects are investigated: loading rate; fibers' cross-sectional mesh dimensions (circumferential divisions); fibers' longitudinal element dimensions; the

influence of the cylinder ends prescription (clamping depth) on the failure plane due to affecting fiber orientation (boundary zones); and the possible adverse effect of mass-scaling (mass-scaling is increasing the mass of material by an algorithm or manually to prevent small elements or badly formed mesh enforce a very small time-step to the explicit-dynamic solver).

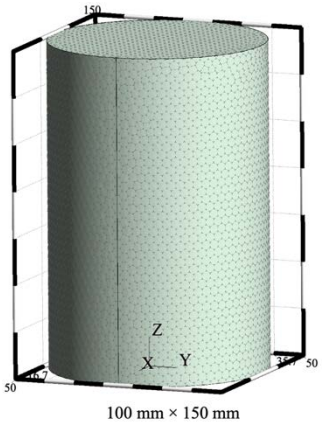


Figure 1: The modeled specimen geometry

Table 3: Summary of the influential factors investigated

Set	Factor	Studied Values or Range
1	Analysis Time Step	0.05 µs and 0.10 µs
2	Loading Rate	1 mm/s to 1000 mm/s
3	Fibers' Cross-section Mesh Size	8 and 32 Circumferential Divisions
4	Fibers' Longitudinal Mesh Size	Fixed and Variable Discretization
5	Clamped Depth at the Boundaries	10 mm and 30 mm
6	Fibers' Mass-scaling Factor	100 times to 10000 times

3 Results and Discussion

3.1 Time-step verification

Explicit solvers do not rely on iterative methods; instead, they advance the solution using the equations of motion, which is unconditionally stable if a small enough time step is used. Numerical efficiency can be increased by mass-scaling, which may change the results if applied excessively. A time-step sensitivity verification is needed to verify the stability and reliability of the explicit results. The highest loading rate (1000 mm/s) and the smallest meshing dimension used in this study (0.1 mm longitudinal with 32 circumferential divisions) are used in this verification.

The outcome demonstrates a minute difference between the maximum time steps of 5.0 µs and 10.0 µs (Figure 2), suggesting that the latter is sufficiently small. The maximum time-step of 10.0 µs will be used for follow-up simulations.

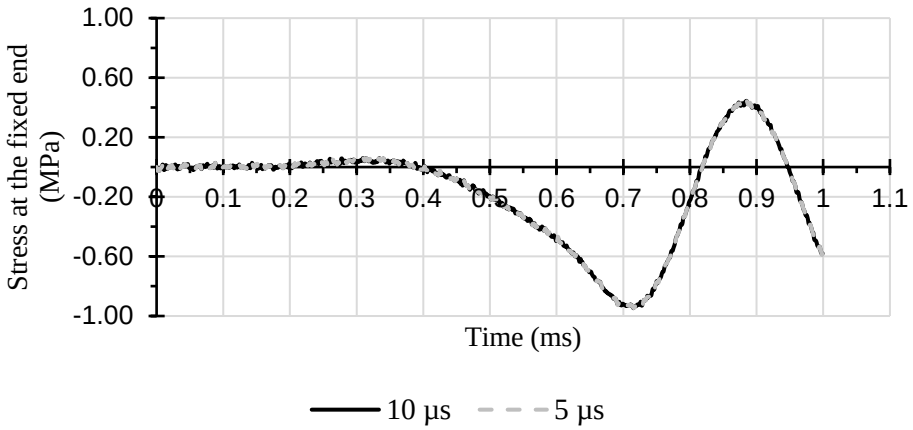


Figure 2: Time-step size sensitivity verification

3.2 Loading rate sensitivity

Investigating the effect of the loading rate helps select a computationally justified dynamic loading rate that approximates pseudo-static behavior. Accordingly, simulations are executed using loading rates from 1000 to 1 mm/s (Figure 3). The loading ramp duration (the initial portion of loading from zero to the target rate) is 0.1 ms in all cases.

For the high strain-rate with a loading speed of 1000 mm/s, the delay between the induced load and support reaction on the other end is quite evident. The aggressive mass scaling used in the fibers could exacerbate this adverse effect. As the loading rate decreases, this effect diminishes, and harmonious reactions are observed at a loading rate of 1 mm/s. While 5 mm/s still shows some level of agitation, it is selected as the reference loading rate to manage the computational cost.

3.3 The influence of the boundary zones

The distribution of fibers near the cylinder walls is biased due to the wall effect. The influence depth by the ends of the cylinder can be considered to be about half the length of the fibers (Dupont and Vandewalle, 2005; Alberti *et al.*, 2017; Saeid Mehrpay *et al.*, 2026). This effect is clearly demonstrated in Figure 4a by showing the average orientation state (η_{avg}) of the fibers over the height of the cylinder. It is determined by $\eta = \frac{1}{n}\sum_i \cos\theta_i$ where θ_i is the angle between the axis of fiber *i* and the longitudinal axis of the cylinder (Schönlin, 1988).

The boundary zones may not represent the typical fiber behavior in the bulk material, as inclined fibers exhibit reduced bridging effect and a pronounced dowelling effect. Alongside the limited anchorage length, the favorable effect of the fibers can be less called upon. Figure 4b shows that clamping the ends of the cylinder within a depth of 10 mm coincidentally resulted in the formation of a failure region within the upper boundary zone. To investigate the failure mode of the cylinder outside these boundary regions, the clamped depth is increased to 30 mm on each side for the results that follow.

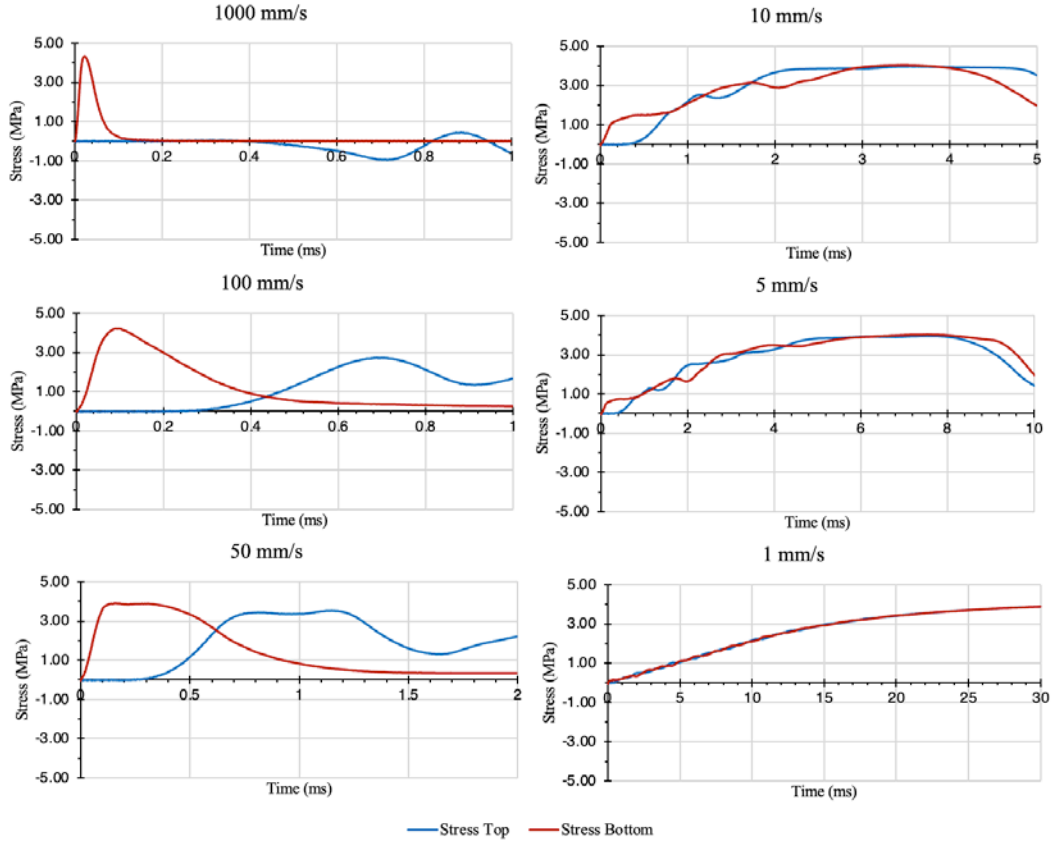
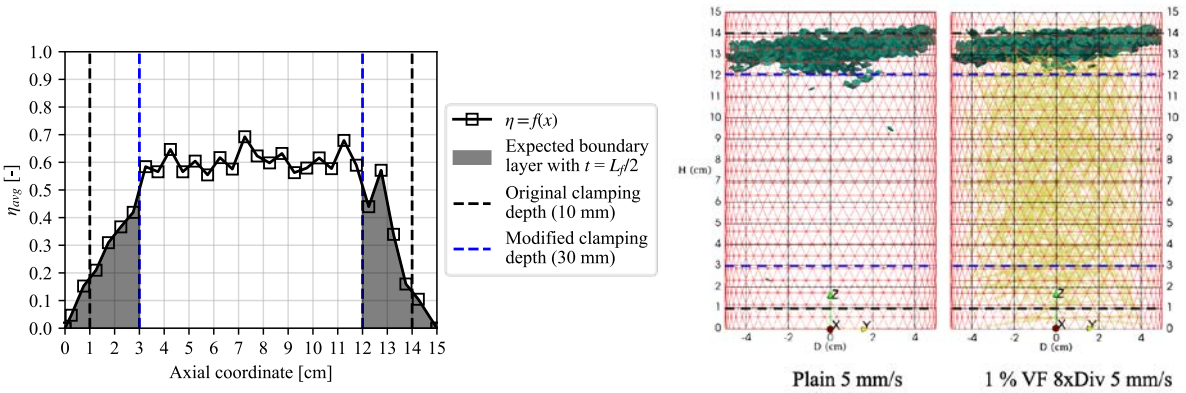


Figure 3: Loading rate sensitivity: stress at the top versus the bottom of the specimen



(a) (b)

Figure 4: (a) Fiber orientation factor (η) in the boundary zones of the cylinder, and (b) the failure plane for clamping within boundary zones (dashed black lines)

3.4 Mesh-size and discretization sensitivity

The fiber discretization includes a cross-sectional meshing (circumferential divisions) and longitudinal meshing dimension of the fiber and the tunnel parts of the slideline model. These dimensions need to be adequately small (Li *et al.*, 2022). The former study on single fiber pullout demonstrates that the meshing dimension of 0.1 mm for the fiber and 0.05 mm for the

tunnel geometry with 32 circumferential divisions was sufficient to replicate single fiber pullout behavior (Mehrpay *et al.*, 2026). In full matrix simulations, fibers are not fully pulled out. Furthermore, the computational resources need to be managed more efficiently. Accordingly, a variable element size strategy in fibers is investigated. Figure 5 demonstrates how a variable mesh allows fiber element dimensions to gradually increase away from the hooked ends. The range of the element size in the variable mesh is set from 0.1 to 1 mm for the fiber and 0.05 to 0.5 mm for the tunnel segments. These values are tested along with reduced circumferential divisions from 32 to 8 (Figure 6).

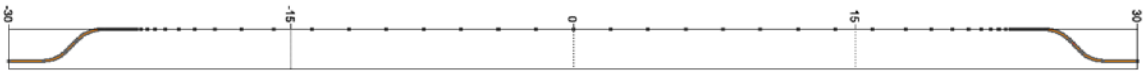


Figure 5: Variable meshing dimension with coarser segments far from the curved sections

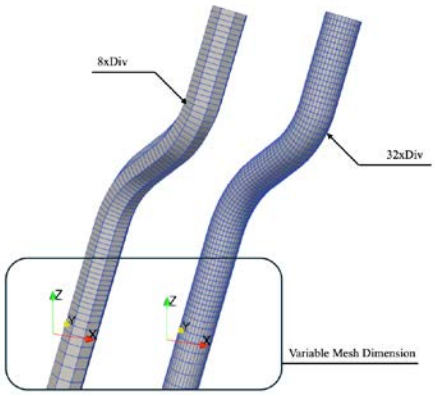


Figure 6: Circumferential division of fiber cross-section

The stress-strain responses of some of the models are depicted in Figure 7 along with a plain concrete cylinder as a reference. A delayed post-peak drop, along with fluctuations in the response, can be observed. As will be shown in the next section, this is the induced influence of mass-scaling in the fiber elements. Comparing the failure pattern and stress distribution does not seem to depict an outstanding difference between these models, as shown in Figure 8.

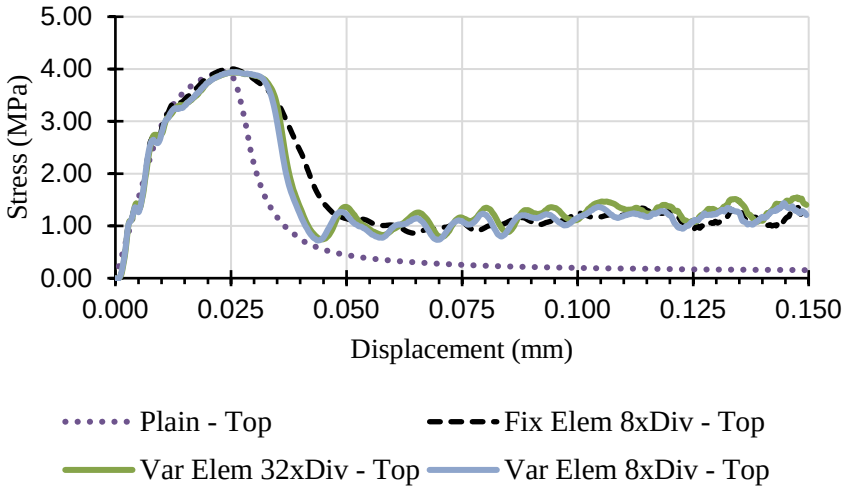


Figure 7: Influence of variable meshing dimension and cross-sectional divisions

3.5 Mass-scaling sensitivity

As stated before, an aggressive mass-scaling ($\times 10^4$) is induced to prevent excessively small analysis time-steps. This scaling factor is directly applied to all fiber elements, potentially introducing inertia effects. The sensitivity of the model is verified with respect to mass-scaling, and the responses are depicted in Figure 9, where the reference mass-scaling of 10,000 times is compared with reduced mass-scaling values of ×1,000 and ×100 along with a case of plain concrete as reference (all stresses calculated from reactions at the top). It can be observed that as the mass scaling is reduced from ×10,000 to ×100, the early post-peak response converges to that of the plain model, with a more stable residual strength that continues to distinguish the fiber-reinforced models.

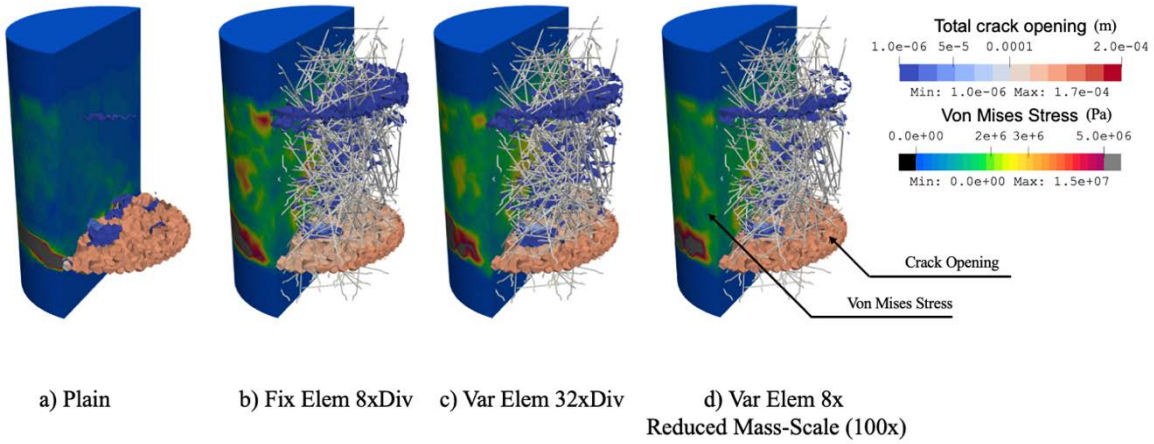


Figure 8: The effect of element size and mass-scaling model on the failure pattern

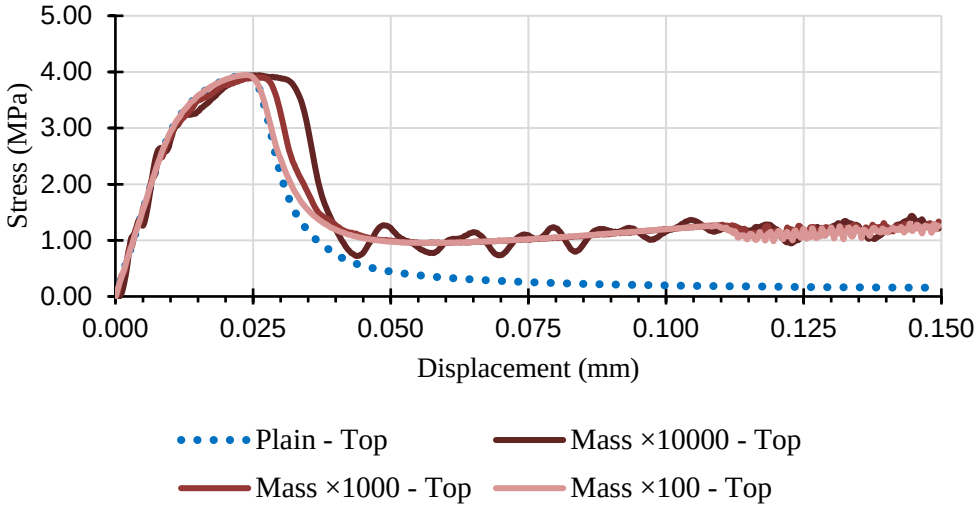


Figure 9. Influence of the mass-scaling factor applied to the fiber

3.6 Calculation costs

The calculation costs of several models are compared in Table 4. In this comparison, all models use a loading rate of 5 mm/s, and the analyses are conducted using 6 threads on a dual-socket machine with Intel Xeon® Gold 6442Y processors. The analysis time can also be reduced by increasing the loading rate, allowing the targeted ultimate displacement to be reached in fewer analysis steps. This, however, will pronounce the inertial effects which determine the influence of mass-scaling on the results. This basically demonstrates that aggressive mass-scaling could be a trade-off for a slower loading rate to reduce side effects. From the table, it can be observed that by using a variable mesh size, the calculation cost can significantly decrease.

Table 4: Calculation cost comparison (5 mm/s loading rate, 30 mm prescription depth)

Case	Condition (VF, element size*, circumferential divisions)	Wall time**
1	1 % VF, fixed elements: 0.1 mm @ 0.05 mm, 8x	36 hrs, 29 min, 43 sec
2	1 % VF, variable 0.1 – 1.0 mm @ 0.05 – 0.5 mm, 8x	12 hrs, 13 min, 28 sec
3	1 % VF, variable 0.1 – 1.0 mm @ 0.05 – 0.5 mm, 32x	40 hrs, 8 min, 31 sec

* fiber elements dimension @ tunnel segment dimension

** to reach 0.149 mm displacement at 5 mm/s

4 Concluding Remarks

A series of models was investigated to produce a scalable, high-fidelity SFRC composite model. It was demonstrated that the Slideline contact model coupled with LDPM has the potential to be upscaled from a single embedded fiber to model SFRC composites at the material level, incorporating the directional and geometrical effects of every single fiber. Possible analysis parameters were verified under a case study of a direct tensile failure test. Based on the obtained results, excessive mass-scaling on fibers may influence the computational outcome by exaggerated inertia effect. Thus, the combined effect of mass scaling and loading rate needs to be verified. An algorithm that applies mass-scaling based on fiber element size may reduce this effect. A variable meshing strategy for embedded fibers and tunnels can be considered to reduce the computational time. As the results obtained lack experimental evidence, future studies will focus on validating the method against experimental results.

5 Acknowledgements

This study was supported by VLAIO (Flanders Innovation & Entrepreneurship) funding in collaboration with NV Bekaert SA under grant number HBC.2024.0196. Computational studies were conducted using the Mars solver, and the authors acknowledge Engineering and Software System Solutions, Inc. (ES3) for providing the software license. The third author would like to acknowledge the financial support by GACR 26-23871S.

6 References

Alberti, M. G., Enfedaque, A. and Gálvez, J. C., 2017. "On the prediction of the orientation factor and fibre distribution of steel and macro-synthetic fibres for fibre-reinforced concrete", *Cement and Concrete Composites*, 77, pp. 29–48. doi:https://doi.org/10.1016/j.cemconcomp.2016.11.008.

Dupont, D. and Vandewalle, L., 2005. "Distribution of steel fibres in rectangular sections", *Cement and Concrete Composites*, 27(3), pp. 391–398. doi:https://doi.org/10.1016/j.cemconcomp.2004.03.005.

Hallquist, J. O. and Whirley, R. G., 1989. *Dyna3D User's Manual, Revision 5*. Lawrence Livermore National Laboratory (LLNL). Available at: https://www.osti.gov/servlets/purl/5920559.

Li, C., Zhou, X. and Cusatis, G., 2022. "Micromechanics of Fiber–Concrete Interaction: Numerical Modeling and Experimental Validation", *Journal of Engineering Mechanics*. American Society of Civil Engineers, 148(5), p. 04022020. doi:10.1061/(ASCE)EM.1943-7889.0002097.

Mehrpay, S., Wan-Wendner, R. W.-W., Wang, L., Ueda, T., Pelessone, D., Vorel, J. and Adel, M., 2026. "Fiber's key characteristics in aligned pullout: insights from computations", in *Computational Modelling of Concrete and Concrete Structures*. *Euro-C*, CRC Press.

Pelessone, D., 1986. "Private communication". P.O. Box 85608, San Diego, CA.: GA Technologies.

Pelessone, D., 2001. *MARS User's Manual*.

Saeid Mehrpay, Daniele Pelessone, Jan Vorel, Jelle Billiet, and Roman Wan-Wendner, 2026. "A NOVEL STRATEGY FOR PACKING OF ARBITRARILY SHAPED FIBERS AND AGGREGATES", in. *fib Congress 2026*, Lisbon.

Schauffert, E. A. and Cusatis, G., 2012. "Lattice Discrete Particle Model for Fiber-Reinforced Concrete. I: Theory", *Journal of Engineering Mechanics*, 138(7), pp. 826–833. doi:10.1061/(ASCE)EM.1943-7889.0000387.

Schönlin, K., 1988. "Ermittlung der Orientierung, Menge und Verteilung der Fasern in faserbewehrtem Beton.", *Beton- und Stahlbetonbau*, 83(6), pp. 168–171. doi:10.1002/best.198800280.

Yin, X., Li, Q., Chen, B. and Xu, S., 2023. "An improved calibration of Karagozian & Case concrete/cementitious model for strain-hardening fibre-reinforced cementitious composites under explosion and penetration loadings", *Cement and Concrete Composites*, 137, p. 104911. doi:10.1016/j.cemconcomp.2022.104911.

Characterization of fiber-reinforced concretes activated at very early ages

Benoit de Rivaz[1]

Nicolas Leclere[2]

[1] : NV Bekaert, Zwevegem, Belgium.

[2] : Sigma Béton, Isle d'Abeau, France.

Abstract

Tunnels can be excavated using traditional explosives. A temporary fiber-reinforced shotcrete lining could be used to ensure wall stability. These fibers absorb post-cracking forces and limit crack propagation. This study focuses on the early-age mechanical behavior of chemically activated wet-mix shotcretes. A new preparation and characterization protocol was developed based on NF EN 14488-5 and NF EN 14488-3 method B standards. The influence of fiber spacing on the granular skeleton was considered. For the studied formulations, performance was evaluated at 7.5 hours, 24 hours, and 28 days at ambient temperatures between 20°C and 25°C. Prospect includes optimizing the granular-fiber skeleton ratio, assessing the impact of admixture concentration and concrete consistency on mechanical properties, and studying the effect of ambient temperature on strength development.

Keywords

Fiber-reinforced concrete, steel-fibers, early-age mechanical performance, wet-mix shotcrete, residual flexural, energy absorption behavior, granular-fiber skeleton interaction.

1 Introduction

In France and Europe, the use of wet-sprayed fiber-reinforced concrete for the support of tunnel walls during excavation work is governed by the NF EN 14487-1 standard. This standard specifies compliance requirements to ensure the safety of people working in tunnels, particularly by preventing the fall of rock elements. Sprayed concrete also ensures the stability of the walls after excavation, pending the implementation of the final lining. The vaulted geometry of tunnels requires rapid strength development to guarantee the integrity of the structure from the very first moments, whether by the concrete's own weight or by the stress of the surrounding terrain.

Short-term performance, defined as the period less than 24 hours after spraying, is evaluated according to the NF EN 14488-2 standard. During suitability tests, companies define their requirements in terms of early-age strength class (J1, J2, J3) based on the required performance, to ensure safety. Evaluating the evolution of ductility at the early age of fiber-reinforced sprayed concrete, according to the NF EN 14488-3 method B or by measuring energy absorption capacity according to the NF EN 14488-5 standard, is particularly complex. The fragility of test specimens makes their transport from the site to the laboratory delicate, risking com-promising their integrity. However, it is crucial to understand the evolution of concrete behavior and the contribution of fibers to its structural reinforcement from the very first moments.

These pre-qualification tests aim to provide insights into the performance of activated concretes, allowing rapid optimization of fiber-formulation parameters and adapting the recipe without systematically requiring on-site spraying tests. A new methodology for the laboratory fabrication and characterization of activated concrete samples to approximate correct implementation by spraying. The ductility of a typical fiber-reinforced sprayed concrete formula was evaluated at an early age and at a normative curing duration. The characterized concrete formulas consider the impact of fibers on the loosening of the granular skeleton.

2 Experimental program

The formulation, machine settings, and spraying techniques influence the performance of sprayed fiber-reinforced concrete. However, due to the logistics required for these very early age tests, the effect of spraying has not been studied. All test specimens were made in the laboratory.

The experimental program is based on:

- Compressive strength measurements (NF EN 12390-3 standard) at 7.5 hours, 24 hours, and 28 days on activated fiber-reinforced concrete cylinders (11x22 cm);
- Residual flexural strength measurements (NF EN 14488-3 method B standard) at 7.5 hours, 24 hours, and 28 days on activated fiber-reinforced concrete notched panels (60x60x10 cm);
- Residual energy absorption measurements by punching (NF EN 14488-5 standard) at 7.5 hours, 24 hours, and 28 days on activated fiber-reinforced concrete panels (60x60x10 cm). The performance of the concrete was evaluated according to the classification specified in the fib Model Code 2010;
- Continuous temperature evolution measurements for 24 hours on activated fiber-reinforced concrete for 24 hours.

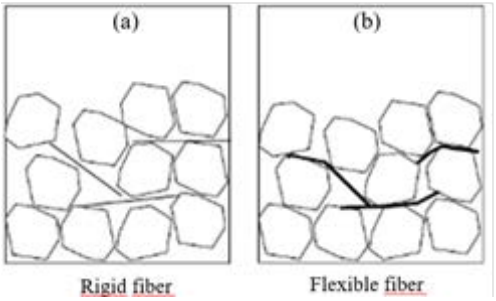
3 Materials and mix designs

The concrete was formulated based on materials used in experimental sprayed fiber-reinforced concrete projects in France. Two fibers were characterized. The first is metallic (Dramix® 4D 65/35 BG) with dosages of 25 kg/m³ and 40 kg/m³. The second is synthetic (Synmix® HP 55) with dosages of 5 kg/m³ and 8 kg/m³. These fibers differ in their composition, morphology, and mechanical properties. Table 1 summarizes the characteristics of fibers.

Table 1: Characteristics of the fibers.

Designation	**Dramix® 4D 65/35 BG**	**Synmix® HP 55**
Length (mm)	35	55
Diameter (mm)	0,55	0,64
Aspect ratio (mm)	65	86
Tensile strength (MPa)	1850	510

A compactness analysis was conducted following a protocol inspired by ([1] De Larrard, 2000). This method relies on experimental compactness measurements of the granular cuts, completed with the proportion of fibers in the concrete to recreate the loosening effect of the larger elements, as shown in Figure 1.



(a) (b)

Figure 1: Diagrams illustrating the loosening effect of gravel in the presence of rigid fibers (case a), or in the presence of flexible fibers such as synthetic fibers (case b); excerpt from (De Larrard, 2000).

The cement matrix was adapted to increase compressive strength and reduce porosity. A water-to-cement ratio (W/C) of 0.40 was applied. Silica fume was also added to improve the pumpability of the concrete. The granular curve was adjusted with a sand-to-gravel ratio (S/G) of 0.5. The goal is to increase the sand content in anticipation of potential spraying tests, to improve pumpability, following these initial pre-characterization tests in the laboratory.

Figure 2 shows the granular packing curve of the formula compared to the granulometric range for a Dmax 10mm cut according to the NF P 95-102-1 standard (2023), based on ASQUAPRO recommendations.

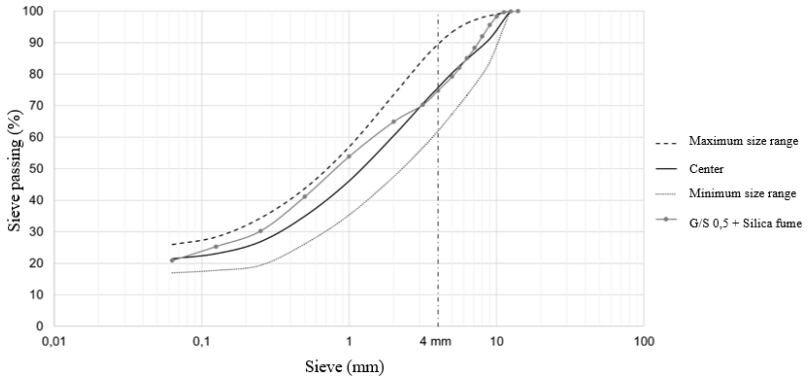


Figure 2: Granular skeleton envelopes (aggregates – hydraulic binders – additions) of the study concrete with a G/S ratio of 0.5 (NF P95-102-1 (2023) Annex E).

The concrete mix designs used in the experimental program are given in Table 2 below.

Table 2: Composition of the four mix designs.

Materials	**Formula Dramix® 4D 65/35 BG**	**Formula Synmix® HP 55**
Gravel / Sand	0,5	0,5
CEM I 52,5 N SR3 CE PM-CP2 NF (kg/m^3)	450	450
Silica fume (kg/m^3)	25	25
Dramix® 4D 65/35 BG (Bekaert) (kg/m^3)	25 40	0
Synmix® HP 55 (Bekaert) (kg/m^3)	0	5 8
Admixture 1 (%weight of powder)	0,3	0,3
Admixture 2 (%weight of powder)	1,2	1,2
Activator (%weight of cement)	4	4
Efficient water (kg/m^3)	178	178
Efficient water / Cement	0,40	0,40
Efficient water / Powder (< 63 µm)	0,37	0,37

Regarding the consistency of wet-sprayed concrete, the recommendations of Asquapro's fascicle 4 indicate that to achieve optimal pumpability, the concrete consistency should follow a class S3 to S4 [3].

To facilitate the preparation of test specimens and achieve an optimal matrix, the activator dosage was set at 4% of the cement mass. The dosages typically encountered on-site range between 6% and 8%. A lower concentration avoids concrete setting prematurely in the mixer

and gives enough time to manufacture test specimens. This value strikes a balance to achieve the minimum performance necessary for the press detection thresholds.

The nature and dosage of fibers influence the workability of concrete by impacting the granular arrangement and stiffening the cement matrix, known as the tightening effect. The workability of fiber-reinforced concretes can usually be improved by adding superplasticizer and rheology extender admixtures. In this study, the admixtures dosage parameter had been fixed.

For better readability of the results, the formula coding is annotated as follows: Fiber type Dosage / Test deadline in hours or days, such as:

- Dramix® 4D 65/35 BG : M25/7,5 hours - M25/24 hours - M25/28 days;
- Dramix® 4D 65/35 BG : M40/7,5 hours – M40/24 hours – M40/28 days;
- Synmix® HP 55: S5/7,5 hours - S5/24 hours - S5/28 days;
- Synmix® HP 55: S8/7,5 hours – S8/24 hours – S8/28 days.

4 Materials and methods for producing test specimens

The testing press used for flexural and punching tests is a universal testing machine (UTM). Its measurement range varies from 1 kN to 100 kN, compliant with class 0.5 over this range. The method for preparing and activating the concrete is summarized in Figure 3.

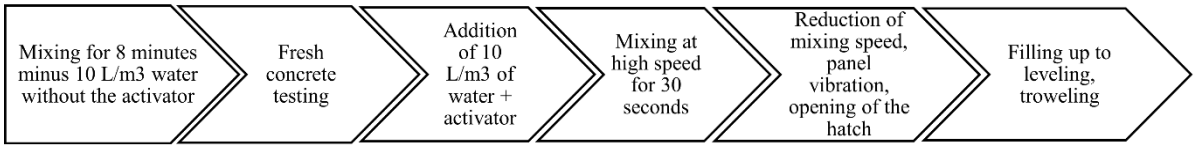


Figure 3: Steps for preparing test specimens.

Each panel was produced individually by 50 L batches. Activator was first pre-mixed with an equivalent of 10 L/m³ of water before being introduced into the concrete. All tests were carried out at ambient temperatures between 20°C and 25°C. Up to 24 hours, the specimens were also kept in their molds under polyethylene sheeting at a temperature between 20°C and 25°C. For the 28-day curing period, the specimens were stored in humid conditions (relative humidity > 95%) at a temperature between 20°C and 25°C.

5 Results

5.1 Visual aspects of test specimens

Slumps have been measured before adding the premixed activator and additional water. The average slump values are between 30 – 50 mm. Despite the firm consistency obtained, the method used to prepare the 60 × 60 × 10 cm panels on a vibrating table proved suitable for producing sound specimens with no surface defects. The observation of the rupture faces of the panels did not show defects such as fiber nests or compaction issues, regarding cylinders for

compressive strength, compaction defects were observed (Fig. 4). The fabrication methodology should be adapted for further tests.

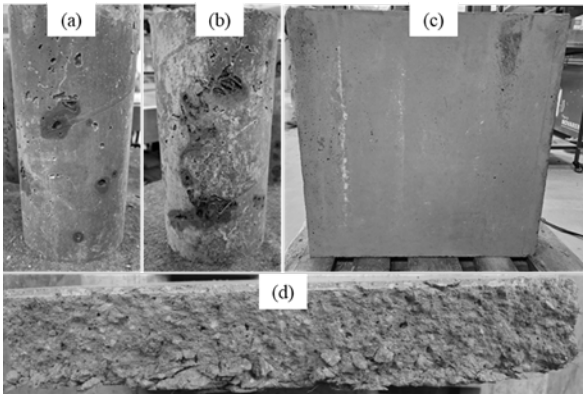


Figure 4:Example of test specimens: cylinder type (a), (b), panel (c), and observation of a rupture face on one panel (d).

5.2 Compressive strength according to NF EN 12390-3

The average compressive strengths of the active fiber-reinforced concretes were measured at different intervals on 9 cylinders of 11x22 cm (Fig. 5).

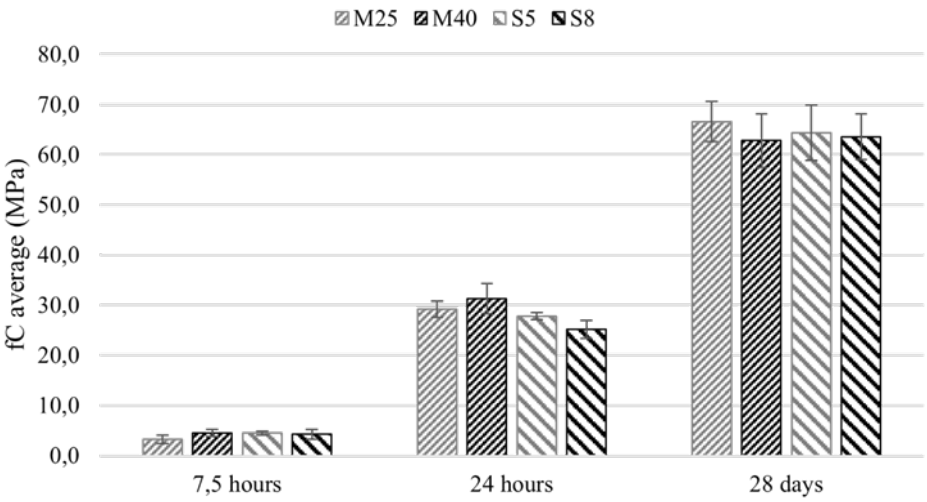


Figure 5: Compressive average and characteristic strengths at 7.5 hours, 24 hours, 28 days.

The modification of the dosage and the nature of the fibers has little impact on the compressive strengths. The tests at 7.5 hours required sulfur capping, with average strengths ranging from 3.2 MPa to 4.5 MPa. The four tested formulas show equivalent strength developments. At 28 days, the average strengths vary between 62.8 MPa and 66.6 MPa. At 24 hours and 28 days, the standard deviations range from 1 MPa to 5 MPa. The compaction defects of the specimens could explain this variability. The characteristic strengths allow the concrete to be classified as at least C50/55.

5.3 Absorption energy according to NF EN 14488-5

The average absorption energies measured at a deflection of 25 mm are presented for each formula in Figure 6.

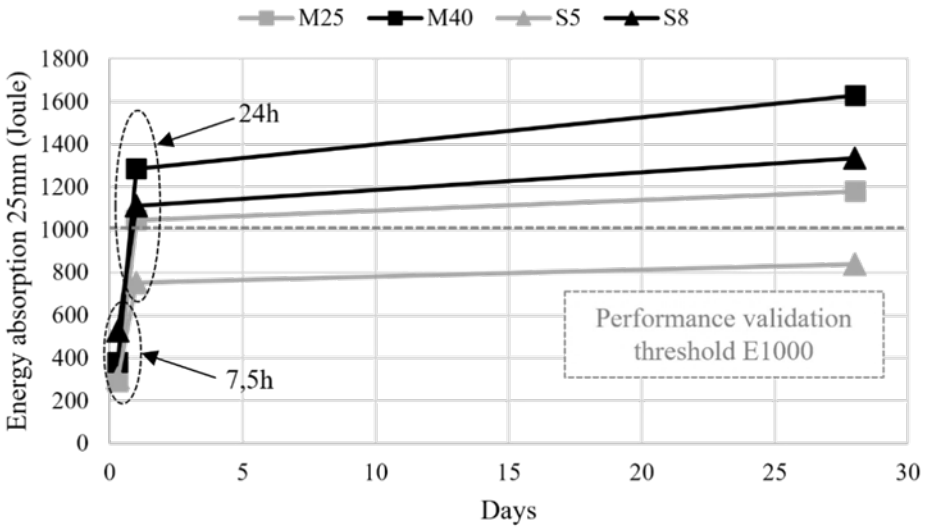


Figure 6: Energy absorption at 25 mm according to NF EN 14488-5 at 7.5 hours, 24 hours, 28 days

For this experimental campaign, the reference threshold at 28 days is 1000 Joules (E1000). This threshold may be required for terrains needing support materials with high absorption capacity to compensate for lack of cohesion or to withstand high stress.

At 7.5 hours, none of the concretes provide a fiber reinforcement combined with sufficient hardening to reach a performance threshold of E600. At 24 hours, the formulas show a similar trend in performance gain. The formulas M25, M40, and S8 already reach the E1000 threshold targeted at 28 days. Only the concrete S5 does not have a sufficient fiber-matrix combination to allow optimal grip during the punching duration, significant enough to achieve the performance.

At 24 hours after activation, the desired performances of the concretes at 28 days are achieved for three concrete configurations. The performances of the concretes continue to increase. It is noted that for this test, the performances of the synthetic solution dosed at 8 kg/m³ are almost equivalent to those of the metallic fiber formula dosed at 25 kg/m³. Only the concrete S5 does not reach the threshold of 1000 Joules.

5.4 Residual strength according to NF EN 14488.3 method b

5.4.1 Dramix® 4D 65/35BG

The performance of concretes reinforced with 25 kg/m³ and 40 kg/m³ of steel fibers is summarized in the Table 3. The performances are classified according to the 2010 model code of the fib [2].

Table 3: Dramix® 4D 65/35 BG– Flexural tensile strength classes.

Formula	Testing age	Fr1s	Fr3s	Model Code 2010 classification
M25	7.5 hours	0.18 MPa	0.27 MPa	0 e
	24 hours	1.42 MPa	1.68 MPa	1 d
	28 days	2.81 MPa	2.93 MPa	2.5 c
M40	7.5 hours	1.34 MPa	1.44 MPa	1 c
	24 hours	2.56 MPa	2.80 MPa	2.5 c
	28 days	3.87 MPa	3.82 MPa	3 c

The average and characteristic flexural strengths of each formula are given in Figure 7.

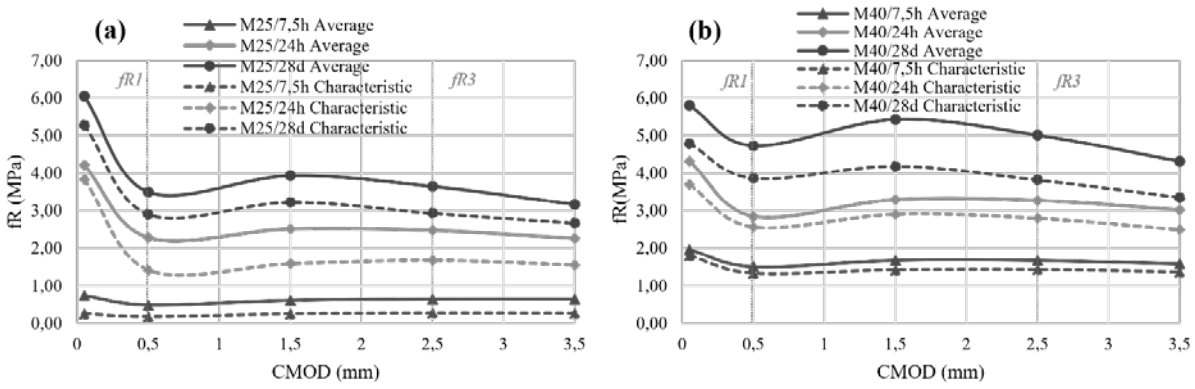


Figure 7: Dramix® 4D 65/35 BG - Average and characteristic residual flexural strengths for mixes through time – (a) 25 kg/m³ and (b) 40 kg/m³.

5.4.2 Synmix® HP 55

The performance of concrete reinforced with 5 kg/m³ and 8 kg/m³ of steel fibers is summarized in the table 4. The performances are classified according to the 2010 model code of the *fib* [2].

Table 4: Synmix® HP 55 – flexural tensile strength classes.

Formula	Testing age	Fr1s	Fr3s	Model Code 2010 classification
S5	7.5 hours	0.58 MPa	0.57 MPa	0 c
	24 hours	1.03 MPa	1.11MPa	1 c

	28 days	1.29 MPa	1.29 MPa	1 d
S8	7.5 hours	0.66 Mpa	0.65 Mpa	0 c
	24 hours	1.75 Mpa	2.04 Mpa	1.5 c
	28 days	1.86 MPa	2.46 MPa	1.5 e

The average and characteristic flexural strengths of each formula are given in Figure 8.

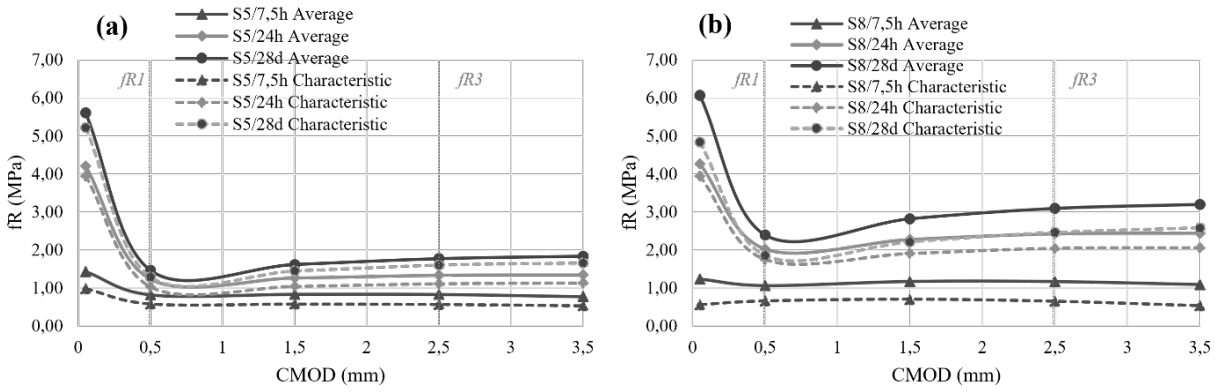


Figure 8: Synmix® HP 55 - Average and characteristic residual flexural strengths for mixes through time - (a) 5 kg/m³ and (b) 8 kg/m³.

6 Conclusion and prospects

A new method for characterizing early-age performances of wet spray activated concrete at a laboratory level has been developed. It enables a pre-selection of fiber types and content and more globally of concrete formulations as an upstream phase of shotcrete test.

The concrete mix was adapted to consider the spacing of the granular skeleton generated by the synthetic or metallic fibers. In general, it would be relevant for study phases to consider this approach to correct paste defects. Adjusting the compactness would also improve fiber grip in the matrix and concrete pumpability. The rheological and tribological behavior of these concretes could be studied additionally.

The experimental campaign was conducted using a single activator incorporated at a dosage of 4% by cement mass. This value was chosen as a compromise between workability and setting time to make the test specimens. For future studies, higher levels of activator as well as other types could provide a more representative basis for prequalifying concrete regarding the need of the structure.

Concrete consistency should be more fluid and closer to those on-site, at least 160 mm according to the formulation. The effect of activation on rheology should also be considered. Despite the firm consistency, no fiber defects were observed in the test panels.

The performance of activated concrete at a very early age is influenced by the external temperature, the material temperature, and the concrete temperature after activation. To compare the performances of concrete at a very early age, it is essential to control the initial temperature of the concrete and the ambient environment. The specimens can be instrumented to verify that the tests were conducted under the same conditions.

Compressive strength was measured. The type and dosage of fibers did not influence the results: all the concretes exhibited the same strength development over time. The required mechanical class C50/55 is reached.

Flexural and punching performances of activated concretes were measured at an early age, i.e., less than 24 hours. Only two very early age intervals were studied. Other measurement intervals could be conducted for a finer analysis of activated concrete behavior. The method assesses the influence of different fiber types on the targeted performance characteristics. At 28 days, metallic fibers continue to improve tensile strength. Performances of 2c and 3c are obtained respectively for dosages of 25 kg/m³ and 40 kg/m³. The improvement of post-cracking strength behavior at 28 days is more significant with the metallic fiber than the synthetic fiber.

Due to the current state of the art, EN 14 488-3 method b would be the reference standard for spray concrete material characterization [4] [5] [6] [7] [8] [9] [10] [11].

Absorption energies were measured. For synthetic fibers, only the formulation containing 8 kg/m³ met the threshold of 1000 J.

7 Acknowledgements

This research project received financial support from Bekaert, who also supplied the steel fibers used in the experimental campaign.

8 References

De Larrard, F., 1999. “Concrete Mixture-Proportionning – A Scientific Approach”, *Modern Concrete Technology Serie, N°9, E & FN SPON*, London.

fib, 2013, *fib Model Code for Concrete Structures 2010*, Weinheim, Germany: Wiley-VCH Verlag GmbH & Co. KGaA. DOI: 10.1002/9783433604090.

ASQUAPRO 2010. *Fascicule 4 – Formulation des bétons projetés*, France

Carlesso, D.M., Leporace-Guimil, B., Aguado, A., de la Fuente, A. & de Rivaz, B., 2025. “Sprayed steel fiber reinforced concrete: strength classes obtained through EN 14488-3 Method B”, *Tunnelling into a Sustainable Future – Methods and Technologies*, CRC Press. doi: https://doi.org/10.1201/9781003559047-37 .

Larive, C., Chalencon, F., Leclere, N., De Rivaz, B., Tolka, N., Bonjour, T., Mestari, A., Zghondi, J. & Bouteille, S. 2025. “New experiments to improve sprayed concrete performances for final support and lining”, *Tunnelling into a Sustainable Future – Methods and Technologies.* CRC Press. doi: https://doi.org/10.1201/9781003559047-287 .

Peaston, C., and De Rivaz, B., 2024. “EN 14488-3 notched panel versus EN 14651 notched beam testing for pre-construction trial conformance testing of Sprayed Concrete Linings (SCL),” *Tunnelling for a Better Life* (Yan, Celestino, Thewes & Eberhardt (Eds), ISBN 978-1-032-80042-4.

Peaston, C., and De Rivaz, B., 2024. “Notched beam and panel test alternatives for conformance testing of sprayed concrete linings consistent with limit state design,” *9th International Symposium on Sprayed Concrete*, 17–20 June 2024, Sandefjord, Norway.

Zenebe Gezahegn, M., Tiberti, G., Trabucchi, I., and Plizzari, G.A., 2024. “Post-cracking performance criteria for fibre-reinforced sprayed concrete in permanent tunnel linings,” *Sprayed Concrete Symposium*.

Laval University, 2021. *Three point bending test on square panel with notch on sprayed specimens (3PBT on square panel) – Dramix 4D 65/35 BG*, Laval University Report, Mat 2021.

Meda, A., 2018. *Comparison between EN14651 EFNARC three point bending test*, University Tor Vergata Roma, Report, April 2018.

AFTES, 2023. *Wet-Mix Sprayed Concrete for Permanent Application in Underground Structures: Principles and Specification*, Guide 2023.

Lattice Discrete Particle Modeling of Steel Reinforced UHPFRC Members under Eccentric Loading

Jiahui Feng[1], Wenyong Cai[1], Lin Wan–Wendner[1]

[1]: Department of Civil Engineering, KU Leuven, Sint-Katelijne-Waver, Belgium.

Abstract

The Lattice Discrete Particle Model (LDPM) simulates the meso-structure of concrete using a system of discrete particles randomly distributed in three-dimensional space, with the capability of incorporating steel reinforcement and fibers. It can effectively characterize the mechanical response of materials under various loads and provide qualitative and quantitative predictions of the load-bearing capacity, deformation characteristics, and crack development of concrete components. In this study, with calibration and validation based on experimental data, LDPM is employed to simulate the entire damage evolution process of steel reinforced ultra-high performance fiber reinforced concrete (UHPFRC) members under eccentric compression load. It focuses on investigating the influence of steel fibers on eccentric compression mechanism, specifically the inhibitory effect of steel fibers on the initiation and propagation of micro-cracks. The simulation results can be used to quantify the crack-bridging effect of steel fibers and reveal how their interaction with steel reinforcement collectively governs the failure mode and ductility of UHPFRC members.

Keywords

Ultra-high performance fiber reinforced concrete (UHPFRC), Lattice Discrete Particle Model (LDPM), eccentric compression, damage evolution, crack-bridging effect

1 Introduction

Ultra-high performance fiber reinforced concrete (UHPFRC) has emerged as one of the most representative advanced construction materials in civil engineering in recent years. UHPFRC exhibits mechanical and durability characteristics that far surpass those of ordinary concrete and high-performance concrete. These material properties include compressive strengths typically exceeding 150 MPa (Graybeal, 2006; Richard and Cheyrezy, 1995), superior tensile ductility (Yoo and Yoon, 2016), outstanding durability (Russell and Graybeal, 2013), and remarkable energy dissipation capacity. Consequently, UHPFRC has gradually become a focal point of research in the international engineering community (Yoo and Banthia, 2017).

As a critical vertical structural component subjected to combined compression and bending, columns in practical structural systems rarely experience idealized concentric axial loading. Instead, they typically undergo eccentric compression. The failure mechanism of eccentrically loaded columns under combined compression-bending is substantially more complex. It involves not only the nonlinear damage evolution inherent to the material but also the dynamic migration of the neutral axis across the cross-section, the spatial distribution of fiber crack-bridging forces, and the coupling of second-order effects at the member scale (Yousef and Askar, 2025; Singh et al, 2015). Therefore, accurately predicting the full-range load-deformation response and failure mode of UHPFRC eccentrically loaded columns constitutes an essential prerequisite for the safe and efficient application of this material in structural engineering.

In recent years, the Lattice Discrete Particle Model (LDPM), first systematically proposed by Cusatis et al. (2011a, 2011b), has attracted considerable attention from the international research community owing to its distinctive mesoscale modeling philosophy. By discretizing the material into a set of randomly distributed particle nodes connected by lattice elements to transmit forces and moments, LDPM enables realistic description of aggregate-level mechanical interactions in heterogeneous materials and beyond (Wan-Wendner and Di Luzio, 2022; Wan et al, 2016). The model can naturally reproduce the stochastic, bifurcating, and coalescing characteristics of crack patterns, and has demonstrated good predictive accuracy and physical consistency in simulating concrete behavior under uniaxial, biaxial, and triaxial loading conditions (Cusatis et al, 2010). An extended formulation, LDPM-F, further incorporates the explicit representation of discrete fibers within the mesoscale framework, enabling mechanical simulation of fiber-reinforced cementitious composites (Schauffert and Cusatis, 2012; Rezakhani et al, 2025).

Nevertheless, applying LDPM to UHPFRC still presents several key challenges, and numerical simulation of UHPFRC eccentrically loaded columns using LDPM remains at an early stage. Therefore, this study focuses on UHPFRC eccentrically loaded columns and systematically employs the LDPM to investigate their mesoscale damage mechanisms and macroscopic mechanical responses.

2 LDPM Simulation

2.1 Material properties

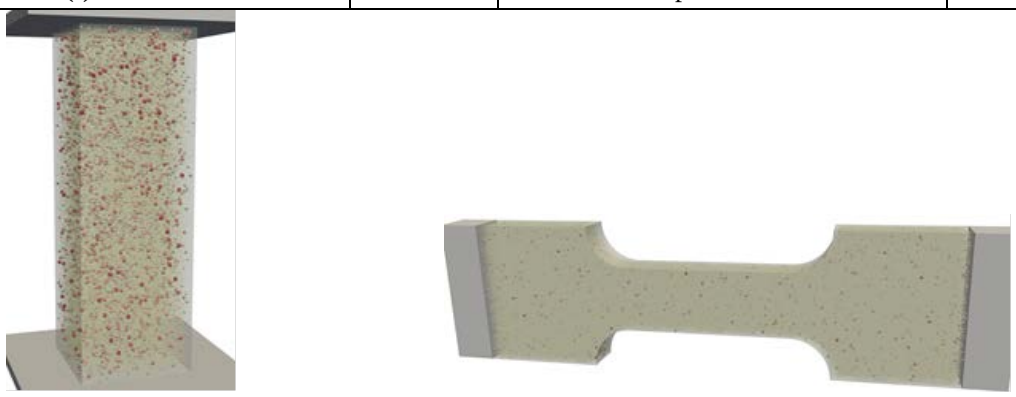
When modeling UHPFRC, a multiscale material parameter system is adopted: the matrix material parameters at the mesoscale and the steel fiber material parameters at the macroscale

are listed in Table 1. It should be noted that the mesoscale parameters are equivalent values calibrated inversely from macroscopic test results, rather than directly measured values. Within the LDPM framework, fiber-concrete interaction is explicitly simulated through fiber-interface contact surfaces at the mesoscale, with their mechanical effects directly reflected in the contact constitutive relationships. All material parameters must be systematically calibrated by comparing LDPM numerical simulations with experimentally measured compressive/tensile performance curves.

The prism with dimensions of 100mm × 100mm × 300mm and the dumbbell-shaped specimen with a special geometry featuring a key middle cross-section of 80mm × 50mm were constructed using code commands, and randomly distributed particles were generated within them, as shown in Figure 1. The numerical simulation results of the UHPFRC prism are presented in Figure 2a, while the uniaxial tensile stress-strain curves of UHPFRC are shown in Figure 2b. The research results demonstrate that the LDPM model established in this study can be used to effectively simulate the compressive and tensile mechanical properties of UHPFRC.

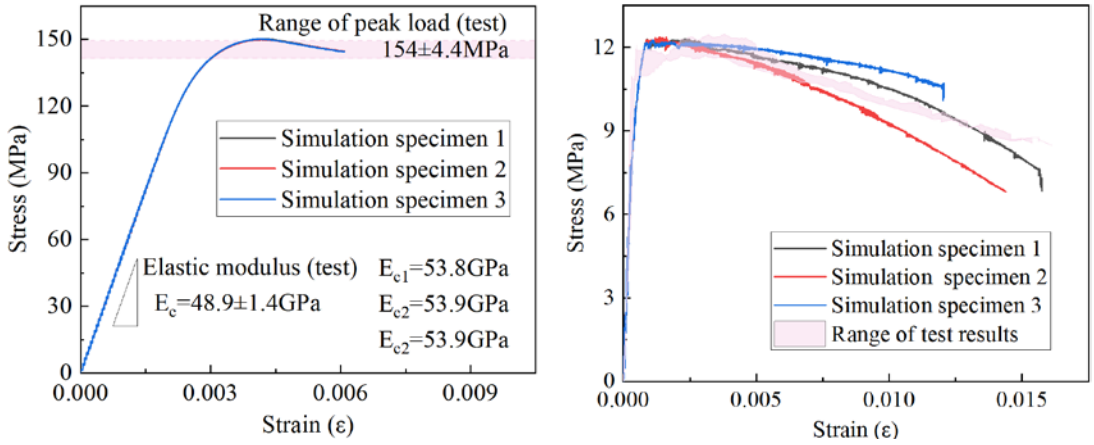
Table 1: Matrix material at the mesoscale and steel fiber material at the macroscale.

Concrete		**Steel fiber**	
Mesoscale LDPM parameters	**values**	**Macroscale material properties**	**values**
Effective normal modulus (MPa)	70000	Elastic modulus (GPa)	210
Tensile strength (MPa)	7	Spalling parameter (MPa)	150
Tensile characteristic length (mm)	90	Fiber strength (MPa)	2000
Softening exponent (-)	0.2	Fiber strength degradation	0.3
Dilatancy coupling parameter (-)	0.584	Support parameter	0.04
Compressive strength (MPa)	500	Bond strength (MPa)	13
Shear strength ratio (-)	5.5	Debonding fracture energy (N/m)	10
Initial hardening modulus ratio (-)	0.36	Pull-out hardening	0.04
Transfer strain ratio (-)	2.0	Plasticity parameter	0.7
Initial friction (-)	0.5	Cook-Gordon parameter	2



(a) (b)

Figure 1: (a) prism under axial compression, (b) dumbbell-shaped specimen under axial tension

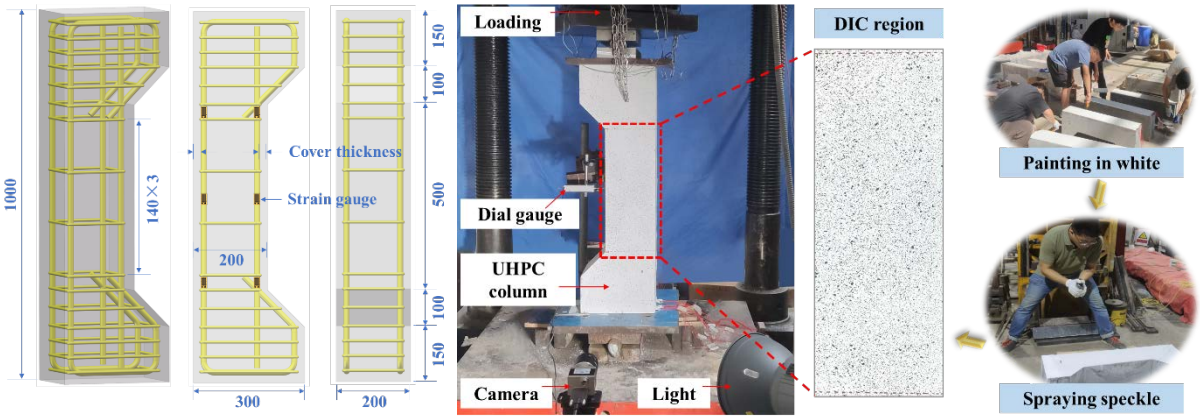


(a) (b)

Figure 2:Simulation results: (a) prism under axial compression, (b) dumbbell-shaped specimen under axial tension

2.2 Experimental program

As shown in Figure 3, the slenderness ratio of the UHPFRC short columns in this test is 5, and the columns have a height of 1000 mm and both cross-sectional width and thickness measuring 200 mm. To broaden the application positions for eccentric loading, the UHPFRC columns are designed with a corbel-shaped configuration. In this study, the data of specimen R5-E110-2.0vol%-L1.0%-C20 is obtained by comparsion with the LDPM simulation. This specimen refers to a short column subjected to a compressive load with an eccentricity distance of 110 mm, containing steel fibers at 2.0 % by volume, a longitudinal reinforcement ratio of 1.0 %, and a concrete cover thickness of 20 mm.



(a) (b)

Figure 3:(a) 3D design drawing of UHPFRC columns (unit: mm), (b) Loading and measurement

The load-deflection curve is depicted in Figure 4. The curve undergoes four distinct stages: elastic stage, elastic-plastic stage, yielding stage, and failure stage. (a) Elastic stage A: The specimen exhibits excellent linear response prior to cracking. (b) Elastic-plastic stage B: The flexural rigidity decreases due to the development of flexural cracks. (c) Yielding stage C: As

crack width continues to expand, the synergistic effect between fibers and matrix diminishes, and the stress transfer effect of UHPFRC in the tensile zone significantly weakens. (d) Failure stage D: As UHPFRC in the tensile zone progressively exits service due to crack propagation, its load-bearing contribution weakens compared to both the elastic-plastic and yielding stages. When UHPFRC experiences progressive crushing, both tensile and compressive reinforcements yield, and the cross-section enters a fully plastic state. The curve ultimately manifests as a pronounced load-bearing capacity reduction following the peak load.

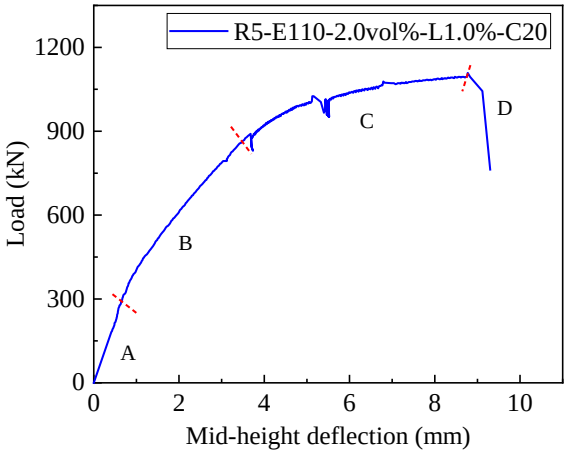
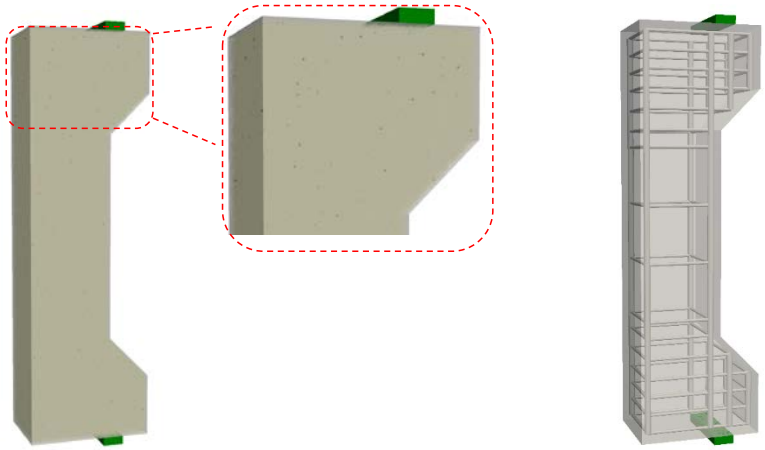


Figure 4: Load-deflection curve

2.3 Simulation model

The Multiphysics Analyses of the Response of Structures (MARS) solver has the capability to extract mesh data from ABAQUS input files and supports reading parts and instances defined in ABAQUS CAE. In the ABAQUS modeling workflow, parts are first created through geometric definition, followed by meshing to obtain node coordinates and element connectivity matrices. Columns and steel reinforcement can be created through translation and rotation operations and precisely positioned. The mesh size for ABAQUS columns modeling is 1.5 times the minimum aggregate particle size. The same material parameter system as the prism model in Section 2.1 is adopted, and random aggregate distribution and fiber distribution are generated within the specimen.

A loading steel plate part is created, assigned rigid body properties, and moved to the corresponding position based on the eccentric distance. Selected particles at the beam ends of the column are defined with frictional contact with the steel plate. The bottom loading plate is constrained in all directions, and the load is applied to the upper steel plate. The translational displacement along the loading direction and the in-plane rotational displacement of the upper steel plate are released. The load is vertically applied to the upper loading plate at a displacement-controlled rate of 15 cm/s. The LDPM model of the eccentrically compressed column is shown in Figure 5.

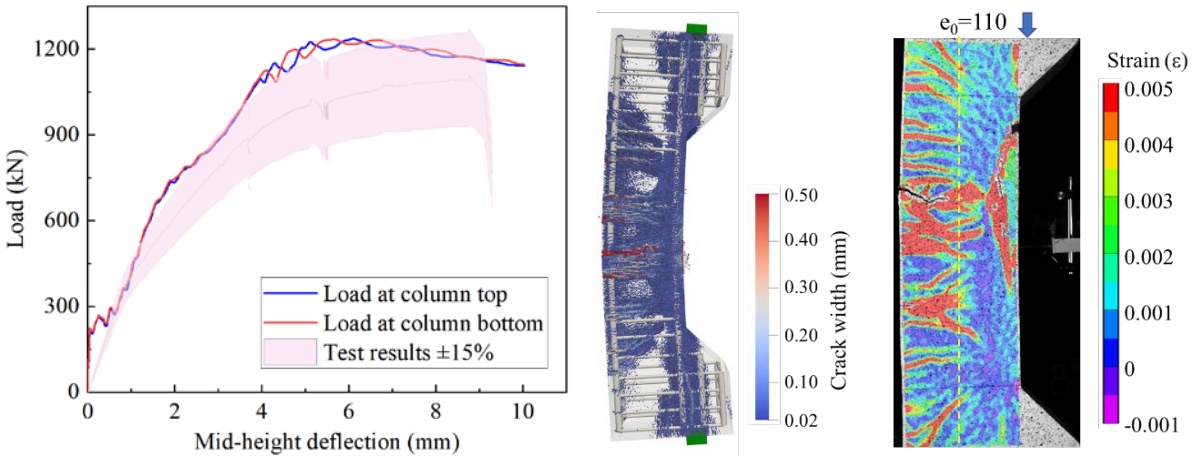


(a) (b)

Figure 5:LDPM model of column under eccentric compression (a) Aggregate and fiber, (b) Steel reinforcement

2.4 Model validation

LDPM mesoscopic numerical model was established. The comparison between the simulated and experimental load-mid-height deflection curves is shown in Figure 6a. The black dashed line represents the experimental results, while the red and blue solid lines represent the simulated load results obtained from the bottom and top, respectively. The ultimate bearing capacity of the specimen measured in the experiment was 1108.6 kN, while the LDPM simulation result was 1226.8 kN, with a ratio of 1.11 between them. Meanwhile, the curve shapes show good consistency during the elastic stage and the early stage of yielding. The LDPM simulation also accurately reproduced the failure mode characteristics of the specimen, as shown in Figure 6b, where dense flexural cracks formed in the tension zone, while the compression zone exhibited typical UHPFRC crushing phenomena. These results fully validate the reliability of the LDPM model in predicting the mechanical behavior of UHPFRC members under eccentric compression.



(a) (b)

Figure 6:Results validation: (a) load-mid-height deflection curves, (b) failure mode characteristics

3 Results and discussions

To investigate the influence of steel reinforcement and steel fibers on the mechanical properties of UHPFRC members under eccentric compression load, this chapter established two working cases for LDPM simulation analysis, including Case 1 (with reinforcement + fibers) and Case 2 (with reinforcement + without fibers). The load-midspan deflection curves are shown in Figure 7. The simulation results indicate that the inclusion of steel fibers has a significant impact on the load-bearing capacity and initial stiffness of the members.

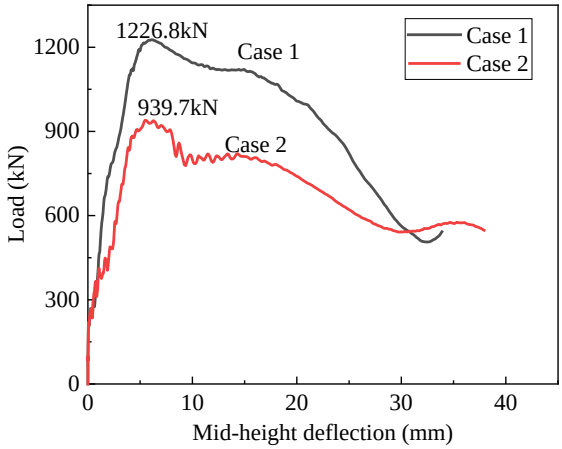


Figure 7:Load-mid-height deflection curves from parameter-extended LDPM simulations

By comparing Case 1 with Case 2, the reinforcing effect of steel fibers can be clearly revealed. The incorporation of steel fibers increased the peak load from 939.7 kN to 1226.8 kN, representing an increase of 23.4%.

Figure 8 intuitively presents the evolution process of cracks in UHPFRC columns through LDPM simulation. The color bar in the figure represents the crack width range of 0.02 to 0.50 mm. When cracks exceed 0.50 mm, the color of their particle failure surfaces is the same as that of 0.50 mm cracks.

Steel reinforcement and steel fibers play different but complementary roles in suppressing crack development: steel reinforcement, as macro-scale reinforcement, promote crack uniformity and increase crack distribution density through stress redistribution; steel fibers, as micro-scale reinforcement, inhibit crack width expansion through the crack-bridging effect and promote the formation of micro-crack clusters. When working synergistically (Case 1), they form a "macro-micro" dual crack control mechanism that not only ensures uniform crack distribution but also effectively limits crack width development, enabling the structural member to maintain good integrity and ductility prior to failure.

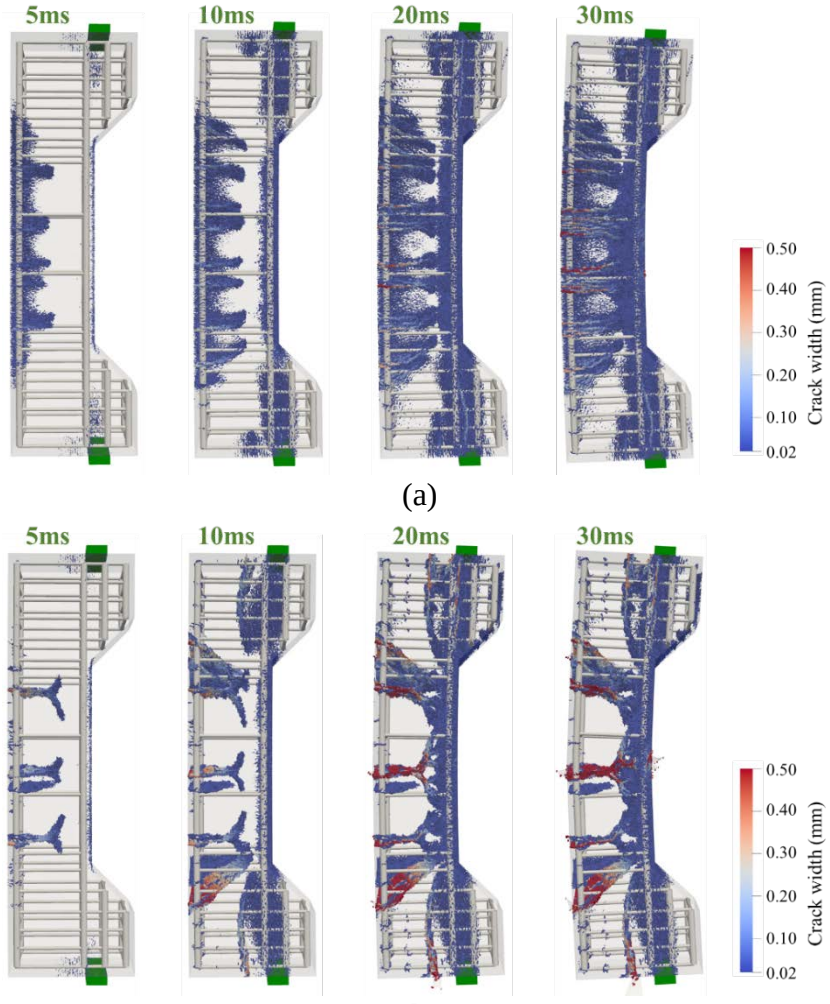


Figure 8: Crack evolution process in LDPM simulation: (a) Case 1, (b) Case 2

4 Concluding remarks

A mesoscale numerical model of UHPFRC columns was established based on LDPM, revealing the influence of steel fibers on the damage evolution process. Steel fibers, as microscopic reinforcement, significantly improve crack control capability through effective bridging of microcracks, transforming the failure process from brittle to stable propagation.

The ratio of ultimate bearing capacity from LDPM simulation to experimental results is 1.11, and the load-mid-height deflection curve shows good consistency during the elastic stage and early yielding stage. The LDPM simulation also accurately reproduces the failure mode characteristics of the specimen, fully validating the reliability of the LDPM model in predicting the eccentric compression mechanical behavior of UHPFRC members.

5 Acknowledgements

The numerical modeling work was supported by the VSC (Flemish Supercomputer Center) allocated at KU Leuven, funded by the Research Foundation - Flanders (FWO) and the Flemish Government.

6 References

Graybeal, B. A. (2006). Material property characterization of ultra-high performance concrete. FHWA-HRT-06-103, Federal Highway Administration, Washington, D.C.

Richard, P., & Cheyrezy, M. (1995). Composition of reactive powder concretes. Cement and Concrete Research, 25(7), 1501–1511. https://doi.org/10.1016/0008-8846(95)00144-2

Yoo, D.-Y., & Yoon, Y.-S. (2016). A review on structural behavior, design, and application of ultra-high-performance fiber-reinforced concrete. International Journal of Concrete Structures and Materials, 10(2), 125–142. https://doi.org/10.1007/s40069-016-0143-x

Russell, H. G., & Graybeal, B. A. (2013). Ultra-high performance concrete: A state-of-the-art report for the bridge community. FHWA-HRT-13-060, Federal Highway Administration, Washington, D.C.

Yoo, D.-Y., & Banthia, N. (2017). Mechanical and structural behaviors of ultra-high-performance fiber-reinforced concrete subjected to impact and blast. Construction and Building Materials, 149, 416–431. https://doi.org/10.1016/j.conbuildmat.2017.05.136

Yousef, A. M., & Askar, H. S. (2025). Experimental and numerical study of eccentrically loaded UHPFRC slender columns. Results in Engineering. https://doi.org/10.1016/j.rineng.2025.105025

Singh, M., Ali, M., & Sheikh, A. H. (2015). Structural behaviour of ultra-high performance fibre reinforced concrete columns subjected to eccentric loading. In IABSE Symposium Report, Vol. 105. International Association for Bridge and Structural Engineering, Zurich.

Cusatis, G., Pelessone, D., & Mencarelli, A. (2011a). Lattice discrete particle model (LDPM) for failure behavior of concrete. I: Theory. Cement and Concrete Composites, 33(9), 881–890. https://doi.org/10.1016/j.cemconcomp.2011.02.011

Cusatis, G., Pelessone, D., Mencarelli, A., & Baylot, J. (2011b). Lattice discrete particle model (LDPM) for failure behavior of concrete. II: Calibration and validation. Cement and Concrete Composites, 33(9), 891–905. https://doi.org/10.1016/j.cemconcomp.2011.02.010

Wan-Wendner, L., & Di Luzio, G. (2022). Discrete modeling of deterministic size effect of normal-strength and ultra-high performance concrete under compression. Construction and Building Materials, 342, Art.No. ARTN 127791. doi: 10.1016/j.conbuildmat.2022.127791

Wan, L., Wendner, R., & Cusatis, G. (2016). A novel material for in situ construction on Mars: experiments and numerical simulations. Construction and Building Materials, 120, 222-231. doi: 10.1016/j.conbuildmat.2016.05.046

Cusatis, G., Mencarelli, A., Pelessone, D., & Baylot, J. (2010). The lattice discrete particle model (LDPM) for the simulation of uniaxial and multiaxial behavior of concrete: Recent results. Fracture Mechanics of concrete and concrete structures—Recent advances in fracture mechanics of concrete, 509-515.

Schauffert, E. A., & Cusatis, G. (2012). Lattice discrete particle model for fiber-reinforced concrete. I: Theory. Journal of Engineering Mechanics, 138(7), 826–833. https://doi.org/10.1061/(ASCE)EM.1943-7889.0000387

Rezakhani, R., Bousikhane, F., & Cusatis, G. (2025). Insights on lattice discrete particle model calibration and validation procedure to simulate polypropylene and steel fibre-reinforced concrete. Fibers, 13(2), 16. https://doi.org/10.3390/fib13020016

Predictive performance of Eurocode 2 design recommendations for steel-fibre-reinforced concrete structures

Joaquim Barros[1,2], Marcílio Filho[1]

[1]:ARISE, Department of Civil Engineering, University of Minho, Guimarães (4800-058), Portugal.

[2]:barros@civil.uminho.pt l.

Abstract

Annex L of Eurocode 2 (EC2) provides recommendations for serviceability and ultimate limit state (SLS and ULS, respectively) design verifications of steel-fibre-reinforced concrete (SFRC) structures. The predictive performance of the EC2 design formulations is assessed using experimental results from blind simulation competitions (BSCs) on SFRC structural elements designed to exhibit different failure modes.

The BSC programme includes structural elements reinforced with both steel-fibres and conventional steel bars, where fibres contribute to shear, flexural, and punching resistance, as well as to improved behaviour under SLS conditions. The first BSC comprises SFRC beams designed to fail in shear; the second involves statically indeterminate shallow SFRC beams intended to fail in bending; and the third includes SFRC slab–specimens designed to fail in punching. The relevant material properties of the SFRC and the conventional reinforcement were determined experimentally.

During testing, the applied load, strains in critical regions of both SFRC and conventional reinforcements, and crack-widths were recorded. These experimental results are used to evaluate the predictive performance of the EC2 formulations with respect to flexural, shear, and punching resistance. Additionally, experimentally measured crack-widths are analysed to provide a critical assessment of the EC2 predictions for SLS design verifications.

Keywords

Eurocode 2, steel-fibre-reinforced concrete, flexural capacity, shear capacity and punching capacity, crack-width.

1 Introduction

The guidelines introduced in the fib Model Code 2010 (MC2010) for the analysis and design of fibre-reinforced concrete (FRC) structures made a major contribution to the adoption of FRC as an alternative construction material in several structural applications by the structural engineering community. These developments were also supported by dedicated software (Valente et al, 2018) that allowed to assess the technical and economic advantages of fibre reinforcement over traditional metallic reinforcements in current and new construction systems. Critical appraisal of the MC2010 design recommendations over more than a decade has shown the need to improve some formulations and to incorporate new knowledge generated by the extensive research carried out during this period. The fib Model Code 2020 (MC2020) reflects this strategy and vision with more consolidated design formulations covering tensile strain softening and tensile strain hardening FRC. The effects of fibre orientation and the size of the cracked fracture surface are explicitly considered in the variables that define the tensile behaviour of FRC, resulting in constitutive laws that can better represent the geometry of the structural element being designed and the adopted construction technology. Based on the MC2020 design recommendations, the most recent Eurocode 2 (EC2) includes an annex (L) dedicated to the design of steel-fibre-reinforced concrete (SFRC) structures.

Taking advantage of a series of blind simulation competitions (BSC) organized by the *fib* WG 2.4.1, the formulations proposed in EC2 are applied to SFRC elements failing in bending (Barros et al, 2023), shear (Barros et al, 2021) and punching (Barros et al, 2025) in order to have a critical assessment of their predictive performance in the context of structural design. In the case of the elements failing in bending, the design verifications cover both serviceability and ultimate limit states (SLS and ULS, respectively). The analyses are based on design and average values of the material properties of the involved materials, allowing the assessment of the global safety factor for the design scenario (design values) and the accuracy of the adopted formulations (average values).

2 Assessment of the predictive performance of EC2 formulations

2.1 R/SFRC elements failing in bending

2.1.1 EC2 formulation for reinforced SFRC (R/SFRC) elements failing in bending

Figure 1 is a schematic representation of the cross-section of the hogging region of the R/SFRC beams tested in the 2nd BSC (Barros et al, 2023). It is used to support the description of the EC2 formulations for the SLS and ULS design verifications. In cases where the SFRC is designed to be uncracked at SLS, the tensile strength of the SFRC at the furthest fibre from the neutral axis shall be disregarded for ULS design within a layer of $c_{f.dur}$=10 mm from the exposure surface. According to the diagram in Figure 1b, the neutral axis depth ($x = x_{ULS}$) is determined from the following axial force equilibrium equation:

$$0 = k_1 f_{cd} b_w k_2 x_{ULS} - A_{st}\sigma_{st} - A_{sc}\sigma_{sc} - f_{Ftu,ef.d}(h_{cr} - x_{ULS})b_w \quad (1)$$

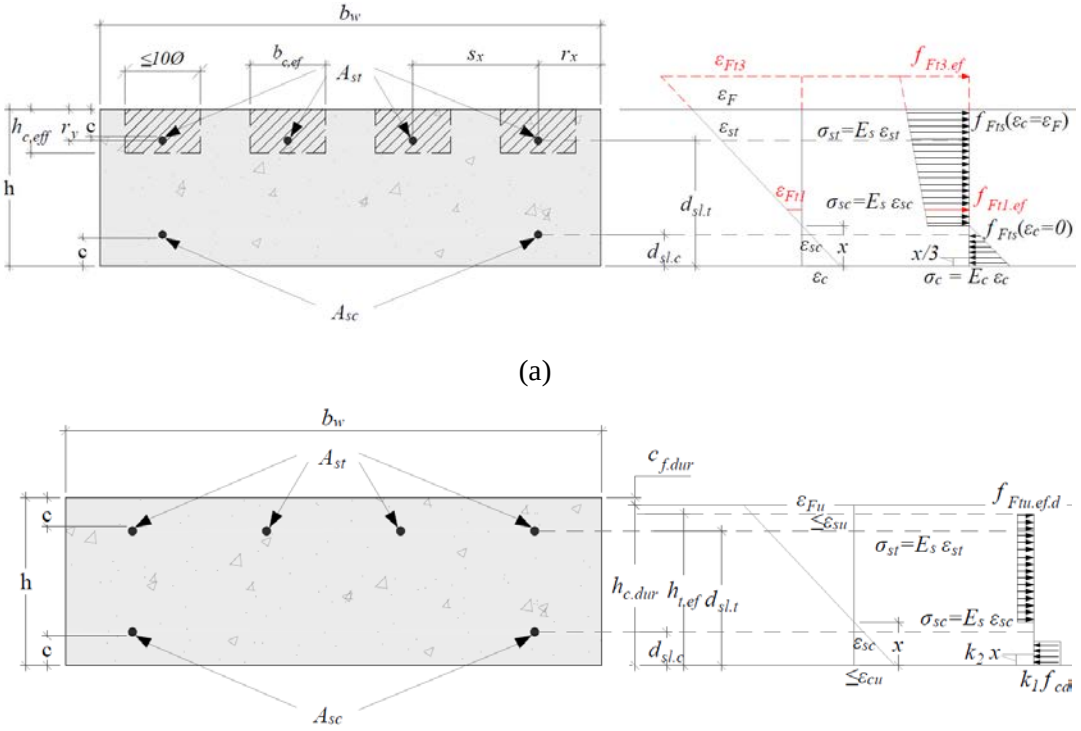


Figure 1: Diagrams of strains and stresses in a SFRC's cross-section for the design verifications at: (a) SLS; and (b) ULS.

where k_1 and k_2 are parameters that define the rectangular compressive stress block and are obtained from:

$$k_1 = \begin{cases} \left[1 - \left(1 - \frac{\varepsilon_c}{\varepsilon_{c2}}\right)^2\right] & for\ 0 \le \varepsilon_c \le \varepsilon_{c2} \\ 1 & for\ \varepsilon_{c2} \le \varepsilon_c \le \varepsilon_{cu} \end{cases}$$

$$k_2 = 0.4 \tag{2}$$

In this equation ε_{c2}=0.0025 is the SFRC compressive strain at the peak compressive stress, f_{cd}, and ε_{cu}=0.006 the ultimate compressive strain of SFRC. In Eq. (1) A_{st} and A_{sc} are the cross-sectional area of the conventional flexural reinforcement in tension and compression, respectively, and σ_{st} and σ_{sc} their corresponding stresses. In this equation $f_{Ftu,ef.d}$ is the design value of the effective resisting tensile stress supported by SFRC, obtained from:

$$f_{Ftuk} = 0.33 f_{R3k} \tag{3}$$

$$f_{Ftud} = f_{Ftuk}/\gamma_{SF} \tag{4}$$

$$f_{Ftu,ef.d} = k_0 k_G f_{Ftud} \tag{5}$$

where f_{R3k} is the characteristic value of the residual flexural tensile stress at a crack mouth opening displacement (CMOD) of 2.5 mm obtained in three-point notched beam bending tests (3PNBBT) executed according to the recommendation of EN 14651. In Eq. (4) γ_{SF} is the partial safety factor for SFRC taken as 1.5 for persistent and transient design situations. The k_0 is a

parameter to take into consideration the fibre orientation in the cross-section (Dupont and Vandewalle, 2005), which can, for simplicity, be taken as unity, or obtained from:

$$k_0 = n_{\varphi,e}/n_{\varphi,p} \tag{6}$$

where $n_{\varphi,e}$ is the fibre orientation on the cross-section of the structural element to be designed, while $n_{\varphi,p} = 0.60$ is the fibre orientation factor on the cross-section of the prismatic specimen considered to determine f_{R1} (residual flexural tensile stress at CMOD=0.5 mm) and f_{R3}. The parameter k_G is a factor that accounts for the size of the cracked area of the member relative to the cross-section of the 3PNB, determined from:

$$k_G = 1 + A_{ct}0.5 \leq 1.5 \tag{7}$$

where A_{ct} is the area of the tension zone (in m^2) of the member's cross-section, calculated as follows:

$$A_{ct} = (h - x_{ULS})b_w \tag{8}$$

In Eq. (1) the h_{cr} is the depth of the cross-section resisting to tensile stresses provided by fibre reinforcement:

$$h_{cr} = \min(h_{c.dur}, h_{t,ef}) \tag{9}$$

where $h_{c.dur}$=h-$c_{f,dur}$, while $h_{t,ef}$ is the distance from the most compressed fibre to the fibre subjected to the tensile strain ε_{Fu}=0.02 (strain level above which it is assumed null tensile capacity for the SFRC). After the depth of the neutral axis has been obtained, the design value of the resisting bending moment of the cross-section (M_{Rd}) is determined from:

$$\begin{aligned} M_{Rd} = {} & A_{st}\sigma_{st}\left(d_{sl,t} - k_2 x_{ULS}\right) + A_{sc}\sigma_{sc}\left(d_{sl,c} - k_2 x_{ULS}\right) \\ & + f_{Ftu,ef.d}(h_{cr} - x_{ULS})b_w((h_{cr} + x_{ULS})/2 - k_2 x_{ULS}) \end{aligned} \tag{10}$$

where $d_{sl,t}$ and $d_{sl,c}$ are the internal arms of the flexural reinforcement in tension and in compression, respectively. Regarding SLS design verifications, the average crack-width is obtained from:

$$\bar{w} = k_{1/r}s_{rm}(\varepsilon_{sm} - \varepsilon_{cm}) \tag{11}$$

where:

$$k_{1/r} = [h - x_{SLS}]/[d_{sl} - x_{SLS}] \tag{12}$$

$$s_{rm} = \begin{cases} 1.5c + k_{fl}k_b\emptyset/\left(7.2\rho_{sl,ef}\right)(1 - \alpha_f) & for\ s_x \leq 10\emptyset \\ h - x_{SLS} & for\ s_x > 10\emptyset \end{cases} \tag{13}$$

being x_{SLS} the neutral axis obtained according to Figure 1a for the most unfavourable SLS load combination, d_{sl} is the internal arm of the flexural reinforcement in tension, and:

$$\alpha_f = 0.37k_0k_Gf_{R1k}/f_{ctm} \leq 1 \tag{14}$$

where f_{ctm} is the average tensile strength of SFRC. The post-cracking tensile capacity of SFRC at SLS is defined by a linear diagram based on the following two stress-strain points (Figure 1a):

$$f_{Ft1,ef} = 0.37 k_0 k_G f_{R1k} \quad (15)$$

$$\varepsilon_{Ft1} = 0.5mm/l_{cs} \quad (16)$$

and

$$f_{Ft3,ef} = k_0 k_G (0.57 f_{R3k} - 0.26 f_{R1k}) \quad (17)$$

$$\varepsilon_{Ft3} = \min(2.5mm/l_{cs}, \varepsilon_{Ftu} = 0.02) \quad (18)$$

This linear relationship allows the tensile capacity to be evaluated at zero concrete strain $f_{Fts}(\varepsilon_c = 0)$, and at the maximum tensile strain within the cross-section, above which the tensile stress is assumed to be zero (Figure 1a). In Eqs. (16) and (18) l_{cs} is the characteristic length, in mm, taken as 125 mm as recommended by EC2. In Eq. (13), the parameters k_{fl} and $\rho_{sl,ef}$ are determined by the following equations:

$$k_{fl} = 1/2\left(1 + \left[h - x_{cri} - h_{c,ef}\right]/\left[h - x_{cri}\right]\right) \quad (19)$$

$$\rho_{sl,ef} = A_{st,bar}/A_{c,ef,bar} \quad (20)$$

where x_{cri} is the depth of the neutral axis at cracking initiation, taken as h/2 by simplification, and $h_{c,ef}$ is the effective height of the cross-section:

$$h_{c,ef} = \min\left(r_y + 5\phi_{sl}; h - x_{SLS}; 10\phi_{sl}; 3.5r_y\right) \quad (21)$$

being ϕ_{sl} (=6mm) the diameter of the longitudinal steel reinforcement and r_y (=28mm) its distance to the most tensioned fibre of the cross-section (Figure 1a). In Eq. (20), $A_{c,ef,bar}$ represents the effective area of concrete in tension surrounding the reinforcement, calculated according to

$$A_{c,ef,bar} = b_{c,ef} h_{c,ef} \quad (22)$$

$$b_{c,ef} = \min(r_x + 5\phi_{sl}; 10\phi; 3.5r_x; b_w/2) \quad (23)$$

where r_x (=50mm) is the distance of the steel bar closest to the lateral face of the cross-section to this face (Figure 1a). Finally, the difference between the average strains on the reinforcement and surrounding concrete is obtained from:

$$\varepsilon_{sm} - \varepsilon_{cm} = \frac{\left[\sigma_s - \frac{k_t f_{ct,ef}\left(1+\alpha_e \rho_{sl,ef}\right)}{\rho_{sl,ef}}\right]}{E_s} \geq (1 - k_t)\sigma_s/E_s \quad (24)$$

where σ_s is the steel stress in cracked section for the SLS load combination, $f_{ct,ef}$ is taken equal to f_{ctm}, α_e is the ratio between the modulus of elasticity of steel and SFRC (E_s/E_c), and k_t is an empirical coefficient dependent on the load duration and nature, taken as 0.6 for short-term or instantaneous loading.

2.1.2 2nd Blind Simulation Competition

The 2nd BSC comprised twin statically indeterminate shallow beams with rectangular cross-sections (Barros et al, 2023). These beams, made of SFRC, also included conventional longitudinal steel bars in their bottom zone and in a specific length over the intermediate support (hogging region). Figure 2 illustrates the geometry, the reinforcement configuration, and the support and loading conditions.

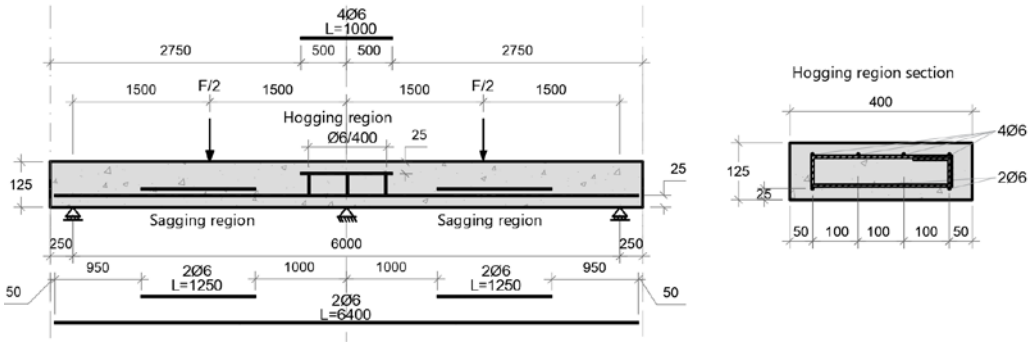


Figure 2: Geometry of the continuous shallow beam of the 2nd BSC (Barros et al, 2023) (dimensions in mm).

The composition of the SFRC corresponds to a concrete C50/60 XD3 (P) CL 0.20 D_{max} 12.5 S4 with 60 kg/m^3 of hooked-end steel-fibres of 60 mm length (l_f), 0.9 mm diameter (d_f) (aspect ratio l_f/d_f of 67), and tensile strength (f_{fu}) of 1900 MPa. The average mechanical properties at age at which the beams were tested, and the number of tested specimens, are presented in Table 1. The properties of the steel reinforcements are indicated in Table 2

Table 1: Properties of SFRC for the continuous shallow beams failing in bending – average, standard deviation () and characteristic [] values of: secant modulus of elasticity in compression (E_{cm}), compressive strength (f_{cm}), limit of proportionality (f_{Lm}) and residual flexural strengths (f_{Rim}, i=1 to 4).

Concrete designation	Compression		Bending (3PNBBT)					Number of 3PNBBT specimens
	E_{cm} [GPa]	f_{cm} [MPa]	f_{Lm} [MPa]	f_{R1m} [MPa]	f_{R2m} [MPa]	f_{R3m} [MPa]	f_{R4m} [MPa]	
SFRC	33.9 (1.9)	61.85 (1.3) [59.47]	5.4 (0.9) [3.7]	6.2 (1.5) [3.4]	7.9 (1.9) [4.4]	8.5 (2.2) [4.5]	8.6 (2.2) [4.6]	4

Table 2: Average, standard deviation () and characteristic [] values of the properties of the steel reinforcements for the continuous shallow beams failing in bending: yield stress (f_{sy}), yield strain determined by the "0.01% Offset Method" ($\varepsilon_{y0.01}$), ultimate tensile strength (f_{su}).

Steel bar	Average diameter [mm]	f_{sy}* [MPa]	$\varepsilon_{y0.01}$ [‰]	f_{su} [MPa]
Ø6	5.7	627.25 (15.4) [599.03]	2.56 (0.2)	769.57 (13.3) [745.20]

*Yield stress determined by the "0.2% Offset Method", according to ASTM 370 (2002)

2.1.3 Comparison of EC2 predictions and experimental-based results

Table 3 and Table 4 indicate the values of the variables making part of the formulation for SLS and ULS verifications, respectively (k_G=1.02, A_{st}=113mm^2 and h_{cr}=0.115m). Table 5 presents the experimental beam's peak load ($F_{t,max}$) and the F_{Rd} according to EC2 recommendations adopting k_0=1. It also includes the average load carrying capacity (F_{Rm}) predicted with EC2 formulation using average values for the material properties and unit values

for the partial safety factors of the materials, as well as the design load carrying capacity according to the ECoV method (Cervenka, 2008), $F_{Rd,ECoV}$.

Table 3: Values of the variables for SLS crack-width calculation (2nd BSC).

		x_{SLS} [mm]	k_{1r} [mm]	α_F [mm]	s_{rm} [mm]	f_{ctm} [MPa]	f_{R1} [MPa]	σ_s [MPa]
Design	Sagging	26.26	1.40	0.30	98.7	4.29	3.45	222.7
	Hogging	23.41	1.38		101.6			370.1
Average	Sagging	42.70	1.51	0.54	82.3	4.29	6.20	67.7
	Hogging	32.42	1.43		92.6			178.6

Table 4: Values of the variables for ULS design resistance (2nd BSC).

		A_{sc} [mm^2]	σ_{st} [MPa]	σ_{sc} [MPa]	f_c [MPa]	$f_{Ftu,ef}$ [MPa]	x_{ULS} [mm]	M_R [kNm]
Design	Sagging	0	520.9	0.0	34.74	1.00	9.13	7.99
	Hogging	57		520.9			11.69	8.56
Characteristic	Sagging	0	599.0	0.0	59.47	1.51	7.94	10.12
	Hogging	57		599.0			9.90	10.83
Average	Sagging	0	627.2	0.0	61.85	2.87	9.69	13.67
	Hogging	57		627.2			11.38	14.36

Table 5: Experimental and EC2 predictions in terms of crack-width at SLS conditions of the 2nd BSC's beams.

Shallow beam	Experimental					EC2							
	$F_{t,SLS}$ [kN]	δ_{SLS} [mm]	$w_{H,SLS}$ [mm]	$w_{S,SLS}$ [mm]	$F_{t,max}$ [kN]	$w_{H.d}$ [mm]	$w_{H.m}$ [mm]	$w_{S.d}$ [mm]	$w_{S.m}$ [mm]	F_{Rd} [kN]	F_{Rk} [kN]	F_{Rm} [kN]	$F_{Rd.ECoV}$ [kN]
Beam 1	19.1	2.3	-	0.004	40.5	0.10	0.05	0.07	0.02	29.0	37.7	51.9	27.2
Beam 2	28.1	5.6	0.07	0.027	44.1								

F_{Rd} is 31% lower than the observed experimental resistance. When k_0 was determined accounting for the $n_{\varphi,e}$ (k_0=0.94), the calculated F_{Rd} was 2% lower than the one obtained assuming k_0 =1. F_{Rm} exceeds the average $F_{t,max}$ by 23%, while the design value obtained with the ECoV method ($F_{Rd,ECoV} = F_{Rm}/[\gamma_R\ \gamma_{Rd}]$) was the smallest one due to the significant difference between average and characteristic values of f_{Ri} (Table 1), which contributed to a relatively large $\gamma_R = 1.80$ (γ_{Rd}=1.06 was considered, assuming models with low uncertainties).

Table 3 a lso includes the SLS load ($F_{t,SLS}$), assumed as 85% of the yield initiation load (when top reinforcement in the hogging region yields) and the corresponding deflection at the mid-span (δ_{SLS}), and the experimental and analytical average crack-width at δ_{SLS} (w_{SLS}). The subscripts "H" and "S" are used to refer to the hogging and sagging regions, respectively. It should be noted that markedly different crack-width values were measured experimentally in the sagging region in the two beams. EC2 [1] limits the crack-width for durability purposes to values between 0.2 and 0.45 mm, depending on the exposure class and the concrete cover thickness. Both experimental and analytical crack-widths meet the minimum value specified by the standard (0.2 mm). However, the analytical crack-widths are up to 61% and 75% higher

than the experimental values in the hogging and sagging regions, respectively. When considering average values for the material properties, the crack-width becomes closer to the values registered experimentally, mainly in the hogging region.

2.2 R/SFRC elements failing in shear

2.2.1 EC2 formulation for R/FRC elements failing in shear

According to EC2 [1], the design shear resistance of an R/SFRC beam is determined using the following equation:

$$\tau_{Rd,cF} = \eta_{cF}\tau_{Rd,c} + \eta_F f_{Ftu.ef.d} \tag{25}$$

where $f_{Ftu.ef.d}$ is calculated through Eq. (5), η_F is a fibre factor assumed equal to 1, η_{cF} is a concrete factor determined from:

$$\eta_{cF} = \max[1.2 - 0.5 f_{Ftuk}; 0.4] \leq 1 \tag{26}$$

with f_{Ftuk} being determined from Eq. (3). In Eq. (25) $\tau_{Rd.c}$ is the design shear strength of the concrete, obtained from:

$$\tau_{Rd,c} = max[0.66/\gamma_v \left(100\rho_{sl} f_{ck} d_{dg}/d_{sl}\right)^{1/3}; \tau_{Rd,c.min}] \tag{27}$$

$$\tau_{Rd,c.min} = 11/\gamma_v \left(f_{ck} d_{dg}/(f_{syd} d_{sl})\right)^{1/2} \tag{28}$$

where γ_v is the partial safety factor for shear and punching resistance for members without shear reinforcement, whose recommended values are given in Table 4.3 of EC2, herein taken as 1.4 (persistent and transient design situation) for both shear and punching. The ρ_{sl} is the reinforcement ratio of the flexural tensile reinforcement:

$$\rho_{sl} = A_{sl}/(b_w d_{sl}) \tag{29}$$

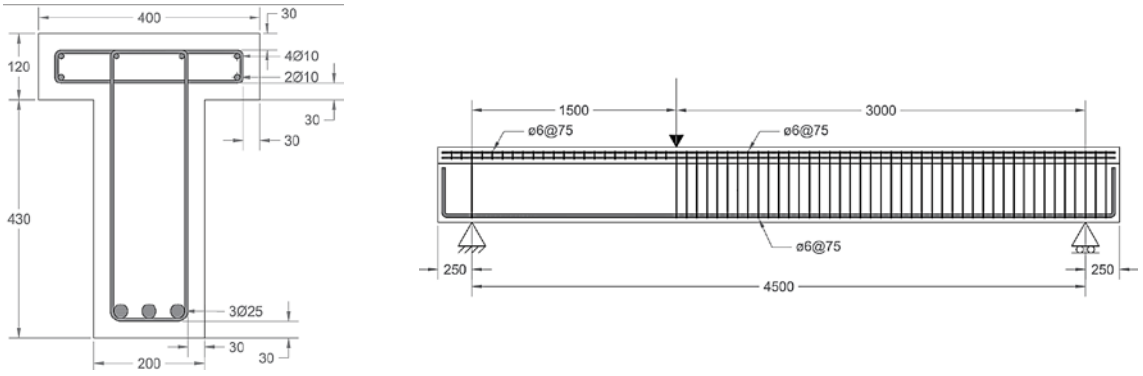
where A_{sl} is the cross-sectional area of longitudinal tensile reinforcement. In Eqs. (27) and (28), d_g is a size parameter characterizing the failure zone roughness, determined from:

$$d_{dg} = 16\ mm + D_{lower} \leq 40\ mm, for\ f_{ck} \leq 60\ MPa$$
$$d_{dg} = 16\ mm + D_{lower}(60/f_{ck})^2 \leq 40\ mm, for\ f_{ck} > 60\ MPa \tag{30}$$

where D_{lower} is the smallest value of the upper sieve size D of the aggregates. If the maximum dimension of the aggregates to be used in a SFRC, D_{max}, is known, D_{lower} can be replaced by D_{max}.

2.2.2 1st Blind Simulation Competition

In the 1st BSC, two full-scale T-section SFRC beams flexurally reinforced with conventional steel bars (R/SFRC) and without steel stirrups in the critical shear span were tested. The beams were subjected to a three-point loading configuration up to failure. Figure 3 shows the geometry, the configuration of the conventional steel reinforcements, and support and loading conditions. A concrete cover thickness (c) of 30 mm and a reinforcement ratio (ρ_{sl}) of 0.147 was adopted.



(a) (b)

Figure 3: Geometry of the beam: (a) cross-section and (b) longitudinal view (Barros et al, 2021) (dimensions in mm).

The SFRC composition was similar to the adopted in the 2nd BSC, except the consistency class, which was S5, and the geometry and tensile strength of the hooked-end steel-fibres (l_f=33 mm, d_f=0.55 mm, f_{fu}=1100 MPa). The mechanical properties of the SFRC determined at 14 days of age, and the number of tested specimens are presented in Table 6. The properties of the conventional steel reinforcements used in the beams are indicated in Table 7.

Table 6: Properties of SFRC for the beam failing in shear – average, standard deviation () and characteristic [] values of: secant modulus of elasticity in compression (E_{cm}), compressive strength (f_{cm}), limit of proportionality (f_{Lm}) and residual flexural strengths (f_{Rim}, i=1 to 4).

Concrete designation	Compression		Bending (3PNBBT)					Number of 3PNBBT specimens
	E_{cm} [GPa]	f_{cm} [MPa]	f_{Lm} [MPa]	f_{R1m} [MPa]	f_{R2m} [MPa]	f_{R3m} [MPa]	f_{R4m} [MPa]	
SFRC	32.9 (0.4)	64.2 (1.5) [61.45]	5.6 (0.2) [3.4]	4.8 (0.7) [2.9]	4.2 (0.6) [2.5]	3.2 (0.5) [1.9]	2.5 (0.4) [1.5]	4

Table 7: Average, standard deviation () and characteristic [] values of the properties of the steel reinforcements for the beam failing in shear: yield stress (f_{ym}) and ultimate tensile strength (f_{tum}).

Steel bar	f_{ym} [MPa]	f_{tum} [MPa]
Ø6	527 (11) [507]	700 (16) [671]
Ø10	538 (7) [525]	696 (6) [685]
Ø25	557 (2) [553]	678 (1) [676]

2.2.3 Comparison of EC2 predictions and experimental-based results

The design and average values of the variables and parameters employed in the EC2 formulation are indicated in Table 8. γ_v=1.0 is used when using average and characteristic values for the materials properties.

Table 8: Adopted variables for ULS resistance design (1st BSC).

	k_G	$f_{Ftu.ef}$ [MPa]	η_{cF}	d_{dg} [mm]	f_c [MPa]	f_{sy} [MPa]	$\tau_{R,c.min}$ [MPa]	$\tau_{R,c}$ [MPa]	$\tau_{R,cF}$ [MPa]
Design		0.44	0.88	27.92	61.45	479.8	0.66	0.81	1.16
Characteristic	1.05	0.66	0.88	27.92	61.45	551.7	0.87	1.13	1.67
Average		1.11	0.67	26.92	64.20	557.0	0.86	1.13	1.87

Table 9 presents the experimental T-section beam's peak load ($F_{t,max}$) and the design and average value of the beam's shear capacity according to EC2 formulation (F_{Rd}, F_{Rm}). The ratio F_{Rd}/ $F_{t,max}$ is about 0.46, which is much lower than the corresponding ratio obtained in the 2nd BSC (0.69), s expectable because shear failure is more brittle than flexural failure. When k_0 is determined considering $n_{\varphi,e}$ (k_0=0.90), the obtained F_{Rd} is 3.9% smaller than the one obtained with k_0 =1. Considering average values and unit values for the safety factor of the materials, $F_{Rm}/F_{t,max}$=0.76 was obtained, which is still conservative. By using the ECoV method, a $F_{Rd,ECoV}/F_{t,max}$=0.58, an intermediate level between using design and average values. In the ECoV method a $\gamma_R = 1.24$ was obtained and a γ_{Rd}=1.06 was assumed.

Table 9: Adopted variables for ULS resistance design (1st BSC).

T-section beam	Experimental	EC2			
	$F_{t,max}$ [kN]	F_{Rd} [kN]	F_{Rk} [kN]	F_{Rm} [kN]	$F_{Rd.ECoV}$ [kN]
Beam 1	355.4				
Beam 2	317.7	156.9	225.7	254.0	192.8
Average	336.0				

2.3 R/SFRC elements failing in punching

2.3.1 EC2 formulation for R/FRC elements failing in punching

According to EC2 [1], the design punching resistance of an R/SFRC slab is determined from the following equation:

$$\tau_{Rd,cF} = \max[\eta_c \tau_{Rd,c} + \eta_F f_{Ftu.ef.d}; \eta_c \tau_{Rd,c.min} + \eta_F f_{Ftu.ef.d}] \quad (31)$$

where η_F=0.4, and η_c is determined from:

$$\eta_c = \min[\tau_{Rd,c}/\tau_{Ed}; 1] \quad (32)$$

$$\tau_{Rd,c} = min[0.6 k_{pb}/\gamma_v \left(\frac{100\rho_{sl} f_{ck} d_{dg}}{d_{sl}}\right)^{\frac{1}{3}}; 0.5/\gamma_v (f_{ck})^{1/2}] \quad (33)$$

with,

$$k_{pb} = 1 \leq 3.6\sqrt{1 - b_0/b_{0.5}} \leq 2.5 \quad (34)$$

representing the punching shear gradient enhancement. In this equation, b_0 is the length of the perimeter at the face of the supporting area and $b_{0.5}$ is the length of the control perimeter located at $0.5d_V$ from the column face, where:

$$d_V = (d_{sl,x} + d_{sl,y})/2 \quad (35)$$

being $d_{sl,x}$ and $d_{sl,y}$ the internal arm of the flexural tensile reinforcements in *x* and *y* directions, with a ratio $\rho_{sl,x}$ and $\rho_{sl,y}$, respectively, and:

$$\rho_{sl} = \sqrt{\rho_{sl,x}\rho_{sl,y}} \tag{36}$$

In Eq. (32), τ_{Ed} is the design value of the average punching shear stress actuating in the surface d_V $b_{0.5}$,

$$\tau_{Ed} = \beta_e \frac{V_{Ed}}{b_{0.5} d_V} \tag{37}$$

with $\beta_e = 1.15$ for internal columns, as in the 3rd BSC. The meaning of the remaining considered variables was already introduced. For the design value of the actuating punching load, V_{Ed}, it was considered equal to 70% of the experimental punching resistance.

2.3.2 3rd Blind Simulation Competition

In the 3rd BSC two slabs with conventional longitudinal reinforcement (R/SFRC) and without conventional shear reinforcement were subjected to a punching loading configuration up to failure (Barros et al, 2025). Figure 4 shows the geometry, the configuration of the conventional steel reinforcements, and the support (coinciding with the holes in the slab) and loading (applied upward in a steel plate of 200×200 mm^2 in the centre of the slab) conditions. A concrete cover thickness of 20 mm was adopted. The SFRC composition was the same as that used in the 2nd BSC. The mechanical properties of SFRC at the age the slabs were tested, and the number of tested specimens, are presented in Table 10. The properties of the conventional steel reinforcements used in the slabs are presented in Table 11.

Table 10: Properties of SFRC for the slabs subjected to punching – average, standard deviation () and characteristic [] values of: secant modulus of elasticity in compression (E_{cm}), compressive strength (f_{cm}), limit of proportionality (f_{Lm}) and residual flexural strengths (f_{Rim}, i=1 to 4).

Concrete designation	Compression	Bending (3PNBBT)						Number of 3PNBBT specimens
	E_{cm} [GPa]	f_c [MPa]	f_L [MPa]	f_{R1} [MPa]	f_{R2} [MPa]	f_{R3} [MPa]	f_{R4} [MPa]	
SFRC	28.1 (0.7)	52.77 (0.9) [51.12]	5.5 (0.4) [3.3]	7.3 (2.1) [3.6]	8.7 (2.5) [4.3]	8.6 (2.1) [4.9]	7.9 (1.6) [4.7]	8

Table 11: Average, standard deviation () and characteristic [] values of the properties of the steel reinforcements for the slabs subjected to punching: yield stress (f_{ym}), yield strain determined by the "0.01% Offset Method" ($\varepsilon_{y0.01}$), ultimate tensile strength (f_{tum}).

Steel bar	Average diameter [mm]	f_{ym}* [MPa]	$\varepsilon_{y0.01}$ [‰]	f_{tum} [MPa]
Ø8	7.7	597.2 (3.4) [591.0]	2.37 (0.1)	720.5 (6.6) [707.9]
Ø12	11.5	619.0 (5.9) [608.2]	2.47 (0.2)	731.0 (7.7) [716.9]

*Yield stress determined by the "0.2% Offset Method", according to ASTM 370 (2002)

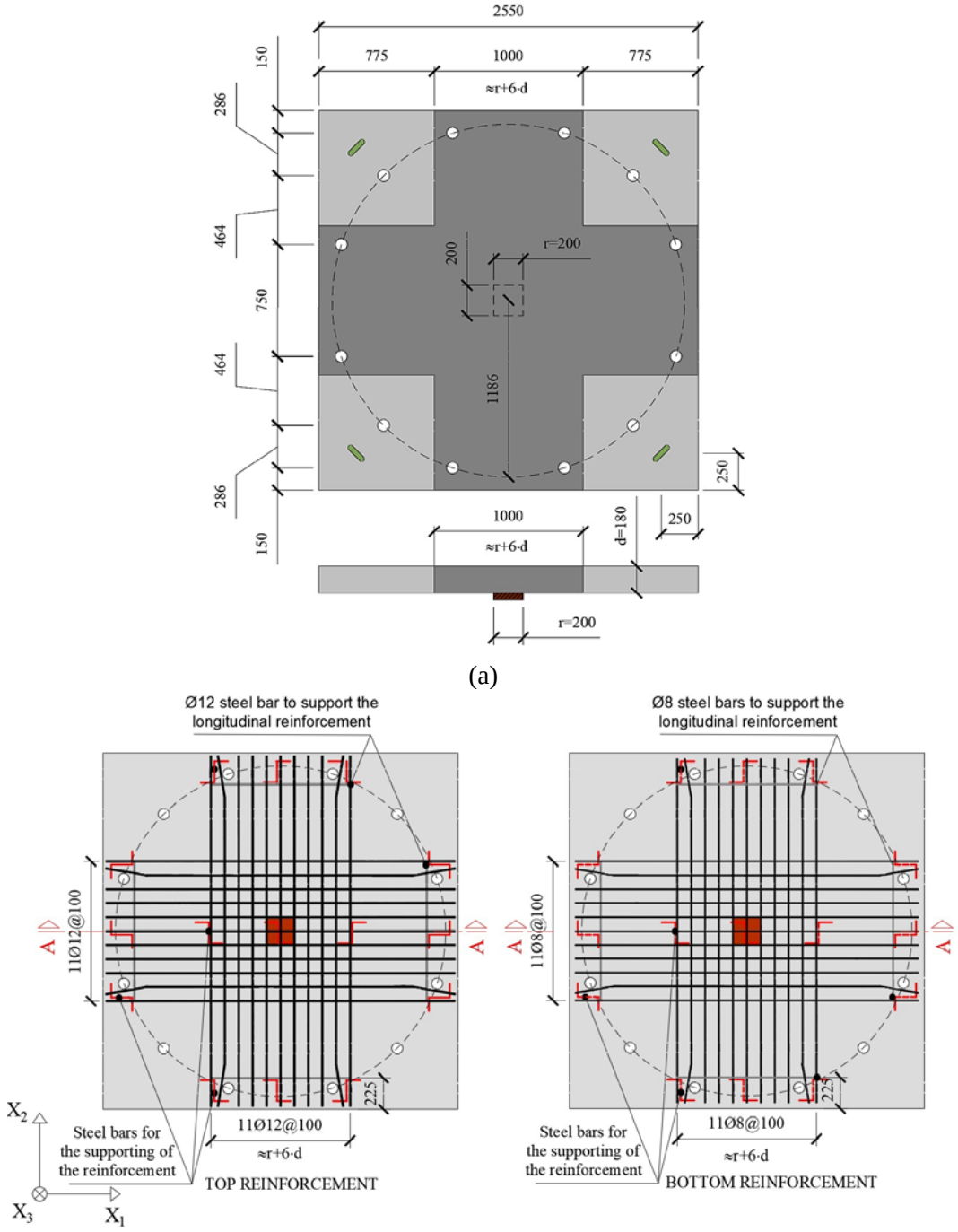


Figure 4: 3rd BSC: (a) geometry of the slab; (b) arrangements of the reinforcements (Barros et al, 2025) (dimensions in mm).

2.3.3 Comparison of design- and experimental-based results

The design and average values of the variables and parameters employed in the EC2 formulation are indicated in Table 12, and k_{pb}=2.18, d_{dg}=28.5mm, d_V=148mm and τ_E=2.18MPa. γ_v=1.0 is used when using average and characteristic values for the materials properties. According to Figure 4, b_0 and $b_{0.5}$ are 0.8 and 1.26m respectively.

Table 13 presents the experimental peak load (F_{max}) and the design and average value of the punching capacity obtained with the EC2 formulation (F_{Rd}, F_{Rm}). It is verified that $F_{Rd}/F_{t,max}$=0.47, $F_{Rm}/F_{t,max}$=0.76 and $F_{Rd,ECoV}/F_{t,max}$=0.57, which are values quite close to the ones obtained for the R/SFRC beams failing in shear. When k_0 was determined considering the $n_{\varphi,e}$ of the slab's cross-section (k_0=0.90), the F_{Rd} is 5.6% lower than the one obtained with k_0=1. In the ECoV method a $\gamma_R = 1.89$ was obtained (γ_{Rd}=1.06 was considered).

Table 12: Adopted variables for ULS resistance design (3rd BSC).

	f_c [MPa]	$\tau_{R,c}$ [MPa]	η_c	$f_{Ftu.ef}$ [MPa]	$\tau_{R,cF}$ [MPa]
Design	51.12	1.84	0.84	1.26	2.16
Characteristic	51.12	2.57	1.00	1.89	3.33
Average	52.77	2.60	1.00	3.29	4.70

Table 13: Experimental and analytical load punching capacity of the 3rd BSC's slabs.

Slabs	Experimental	EC2			
	F_{max} [kN]	F_{Rd} [kN]	F_{Rk} [kN]	F_{Rm} [kN]	$F_{Rd.ECoV}$ [kN]
Slab 1	565.88				
Slab 2	507.96	352.63	542.69	765.83	383.03
Average	508.27				

3 Concluding remarks

Using the comprehensive material- and structural-level results available from three blind simulation competitions on R/SFRC structures, this work assessed the predictive performance of the Eurocode 2 (EC2) formulations for elements failing in shear, bending, and punching. The use of average values for the material properties with unit values for the partial safety factors on the formulations (*m* subscript for identification), as well as the Estimation of the Coefficient of Variation (ECoV) method (*d,ECoV* subscript for identification) were also explored for the predictions. Subscripts d, m, and d,ECoV denote design values, average material properties with unit partial factors, and the ECoV-based design prediction, respectively. The following remarks can be extracted from the obtained results:

- For the shallow R/SFRC beams failing in bending, $F_{Rd}/F_{t,max}$=0.69, $F_{Rm}/F_{t,max}$=1.23 and $F_{Rd,ECoV}/F_{t,max}$=0.64, where $F_{t,max}$ is the maximum load carrying capacity registered experimentally. The EC2 formulation predicted much larger crack-width than the values registered experimentally, mainly in the bottom surface of the beams. Closer agreement was obtained when average material properties were used.
- For the R/SFRC beams failing in shear, $F_{Rd}/F_{t,max}$=0.46, $F_{Rm}/F_{t,max}$=0.76 and $F_{Rd,ECoV}/F_{t,max}$=0.58.
- For the R/SFRC beams failing in punching, $F_{Rd}/F_{t,max}$=0.47, $F_{Rm}/F_{t,max}$=0.76 and $F_{Rd,ECoV}/F_{t,max}$=0.57, therefore very close to the values registered in R/SFRC beams failed in shear.
- When k_0 was determined considering the $n_{\varphi,e}$ of the member's cross-section, F_{Rd} decreased by up to 5.6% relative to the value obtained with k_0=1.0.

4 Acknowledgements

This work was financed by national funds through FCT – Foundation for Science and Technology, through the project TuRUpAI Multiscale modelling for optimum retrofitting of tunnels with fibre reinforced shotcrete designed by machine learning (https://doi.org/10.54499/2022.06602.PTDC). It was also supported by FCT/MCTES under the R&D Unit Institute for Sustainability and Innovation in Structural Engineering (ISISE), under the references UID/4029/2025 (https://doi.org/10.54499/UID/04029/2025) and UID/PRR/04029/2025 (https://doi.org/10.54499/UID/PRR/04029/2025), and under the Associate Laboratory Advanced Production and Intelligent Systems ARISE, under reference LA/P/0112/2020.

5 References

Barros, J.A.O., Sanz, B.; Filho, M.; Figueiredo, F.; Kabele, P.; Yu, R.C.; Meschke, G.; Planas, J.; Cunha, V.; Caggiano, A.; Ozyurt, N.; Ventura-Gouveia, A.; Bos, A.V.D.; Poveda, E.; Gal, E.; Cervenka, J.; Ney, G.E.; Rossi, P.; Dias-da-Costa, D.; Juhasz, P.K.; Cendon, D.; Ruiz, G.; Valente, T., 2023, "Blind competition on the numerical simulation of continuous shallow steel-fibre reinforced concrete beams failing in bending", *fib Structural Concrete Journal*, 24(3), pp. 3877-3907 doi: 10.1002/suco.202200754.

Barros, J.A.O., Sanz, B.; Filho, M.; Figueiredo, F.; Kabele, P.; Yu, R.C.; Meschke, G.; Planas, J.; Cunha, V.; Caggiano, A.; Ozyurt, N.; Ventura-Gouveia, A.; Bos, A.V.D.; Poveda, E.; Gal, E.; Cervenka, J.; Ney, G.E.; Rossi, P.; Dias-da-Costa, D.; Juhasz, P.K.; Cendon, D.; Ruiz, G.; Valente, T., 2025, "Blind competition on the numerical simulation of slabs reinforced with conventional flexural reinforcement and fibres subjected to punching loading configuration", *fib Structural Concrete Journal*, 26(1), 385-424 doi: 10.1002/suco.202400061

Barros, J.A.O., Sanz, B.; Kabele, P.; Yu, R.C.; Meschke, G.; Planas, J.; Cunha, V.; Caggiano, A.; Ozyurt, N.; Ventura-Gouveia, A.; Bos, A.V.D.; Poveda, E.; Gal, E.; Cervenka, J.; Neu, G.E.; Rossi, P.; Dias-da-Costa, D.; Juhasz, P.K.; Cendon, D.; Ruiz, G.; Valente, T., 2021, "Blind competition on the numerical simulation of steel fibre reinforced concrete beams failing in shear", *fib Structural Concrete Journal*, 22(2), pp. 939-967 doi: 10.1002/suco.202000345.

Cervenka, V., 2008, "Global Safety Format for Nonlinear Calculation of Reinforced Concrete.", *Beton- Und Stahlbetonbau*, 103(S1), pp. 37-42. doi: 10.1002/best.200810117.

Dupont, D., Vandewalle, L., 2005, "Distribution of steel fibres in rectangular sections." *Cement and Concrete Composites*; 27(3) , pp. 391–398 doi: 10.1016/j.cemconcomp.2004.03.005.

EN 14651, 2005. Test method for metallic fibre concrete – measuring the flexural tensile strength (limit of proportionally (LOP), residual), European Committee for Standardisation (CEN).

Eurocode 2, 2023. Design of Concrete Structures, EN 1992-1-1:2023, European Committee for Standardisation (CEN).

fib, 2012. *Model Code 2010*, Bulletin 65, Fèdération Internationale du Béton, Lausanne

fib, 2023. *Model Code 2020*, Bulletin 2020, Fèdération Internationale du Béton, Lausanne

Valente, T.D.S., Barros, J.A.O., Lourenço, L.A.P., 2018, "FRCcalc – Software for design of fiber reinforced concrete elements according to MC2010 recommendations", FRC2018: Fibre Reinforced Concrete: from Design to Structural Application, Joint ACI-fib-RILEM International Workshop, Brescia, *Published in the fib Bulletin 95*, ACI-SP343, doi:10.35789/fib.BULL.0095

Assessing Fibre Orientation and Mechanical Performance in UHPFRC: A Data-Driven Review and Machine Learning Study

Bedirhan Enes Kelek[1], Olcay Gürabi Aydoğan[1], Duçem Medya Gündoğmuş[1], Nilüfer Özyurt[1]

[1]: Civil Engineering Department, Boğaziçi University, Istanbul, Turkiye.

Abstract

Ultra-High Performance Fibre-Reinforced Concrete (UHPFRC) has progressed significantly beyond laboratory research and is now applied across a wide range of structural, and architectural domains, primarily driven by its superior mechanical properties, durability, and design flexibility. With the increasing use of structural applications, the design of UHPFRC components has become more important, and fibre orientation has become a key parameter. The number of studies initiated in the 2000s, focusing on the effects of fibre orientation density on UHPFRC performance, has increased exponentially since the 2020s. Scientific papers on fibre orientation in UHPFRC were reviewed, and ~350 data rows were analyzed. A database (UHPFRC-OriD) relating UHPC mix designs, processing parameters, fibre orientation, and mechanical performance was established to better understand the complex relationships among these parameters and the resulting UHPFRC performance, leveraging machine learning tools to interpret complex data. The compiled data were further evaluated using frequency histograms to analyze the distribution of key parameters across a wide variety of UHPFRC systems. The relative importance of the relevant parameters for compressive and flexural strengths was studied using interpretable machine learning methods, particularly SHAP analyses.

Keywords

UHPFRC database, fibre orientation, data-driven investigation, machine learning

1 Introduction

Cement-based construction materials have evolved significantly over the last few decades to meet the demands of modern engineering for higher load-bearing capacity, lightweight, slender structures, and extended service life for buildings. Researchers have increasingly focused on developing cement-based materials with such superior properties. The most prominent outcome of this extensive research is Ultra-High Performance Fibre-reinforced Concrete (UHPFRC), an advanced cementitious composite engineered to exhibit superior performance. To attain ultra-high performance, the researchers optimized the size of granular materials using packing density theory and completely eliminated coarse aggregates from the mixture (de Larrard and Sedran, 1994). The matrix was further enhanced through heat treatments and pressure, and its ductility and toughness were considerably improved by incorporating 1.5% to 3% by volume of short steel fibres (Amran *et al.*, 2023). This methodology, combining micro-scale optimization of significantly fine particles, a low water-to-cement ratio, and high-strength steel fibres, established the fundamental principles of present-day UHPFRC (Gong *et al.*, 2022).

Today, UHPFRC's superior mechanical and durability properties have propelled its widespread use across diverse applications in the construction industry. In bridge engineering, UHPFRC is employed to construct pedestrian and highway bridges and to fabricate lightweight structural elements, such as bridge joints, and durable deck pavements. The first UHPFRC bridge was built at the Sherbrooke pedestrian bridge in Canada in 1997, which paved the way for the application of UHPFRC in bridge engineering (Zhou *et al.*, 2018). Additionally, UHPFRC has emerged as a prominent material for structural retrofitting and repair. Furthermore, UHPFRC's capacity to be molded into very slender and complex shapes without traditional steel reinforcement has enabled enhanced architectural design. This is demonstrated in building facades, roof lattices, and decorative panels with highly intricate geometries (Azmee and Shafiq, 2018).

However, designing and constructing UHPFRC components to meet required mechanical and durability performance, as well as economic and environmental constraints, remains difficult due to high variability in materials, mix designs, component geometries, processing conditions, and testing techniques. The vast amount of data reported in the scientific literature also shows high variability, making it difficult to evaluate relationships among the effective parameters. The use of conventional techniques to understand the effects of different parameters on performance remains ineffective, failing to yield new insights into the phenomena. Recent developments in machine learning (ML) tools open new paths for analyzing such complex data, potentially revealing new insights into the hidden aspects of the phenomena.

This paper presents a part of a study aimed at establishing a database on UHPFRC for understanding the distribution of relevant data, with a focus on fibre orientation. To correctly interpret the data and understand the relationships among the effective parameters, all relevant data were gathered, covering material/mix design characteristics, fibre parameters (volume, geometry), formwork geometry, processing conditions, specimen geometry, orientation quantification approach, and reported mechanical performance indicators. Subsequently, the dataset was systematically analyzed using histogram-based visualizations to illustrate the distributions of key features influencing performance. This allowed for a clear assessment of the spread and dispersion of the variables, revealing a pronounced variability across the reported values and highlighting the inherent heterogeneity of the data. Such high variability and complex, non-linear parameter interactions further underscore the need for advanced

techniques, such as machine learning, to reliably capture and interpret the underlying relationships. Subsequently, machine learning techniques were employed to capture and interpret the complex, interdependent relationships among the parameters governing mechanical performance.

2 Methodology

2.1 Database Development (UHPFRC-OriD)

A structured and transparent study selection process for the development of the UHPFRC-OriD database was established using an adapted PRISMA-inspired workflow. The robustness and reproducibility of the final dataset were ensured through the consistent application of predefined inclusion and exclusion criteria during data extraction, alongside the systematic implementation of the key stages of identification, screening, eligibility, and inclusion. The database compilation began with a systematic search phase, during which relevant publications were retrieved from major scientific databases, including Scopus, Web of Science, and Google Scholar, using carefully selected keyword combinations. Subsequently, the identified records underwent an eligibility assessment against predefined inclusion criteria. These criteria focused on several key aspects, including the relevance of the material type, the completeness of the mix composition data, and the presence of quantifiable fibre orientation information obtained through image analysis. Additional requirements included the reporting of orientation descriptors, details of the casting procedure, and specimen geometry. To maintain a consistent, comparable dataset, only studies investigating UHPFRC composites were included. Given the central role of fibre orientation in the scope of this database, priority was given to studies that not only reported orientation data but also provided sufficient contextual information on casting parameters—such as casting direction—and associated mechanical performance indicators, particularly tensile behavior. Information extracted from each publication was systematically entered into a standardized Excel template, covering material and mixture properties, processing procedures, specimen geometries, orientation descriptors, and mechanical performance data.

The UHPFRC-OriD database synthesizes experimental data reported in scientific studies published between 2008 and 2026. The database timeframe starts in 2008, marking the earliest study (to our knowledge) to report fibre orientation in UHPFRC using image-analysis-based descriptors aligned with the methodology adopted in this work. To enable consistent interpretation, the dataset integrates key variables describing both composition and processing. Material-related inputs include matrix design parameters (binder types, aggregate proportions, water-to-binder ratio) and steel fibre characteristics (volume fraction, geometry, and mechanical properties). In parallel, processing and geometric descriptors—such as casting direction, flow distance, and specimen and mold dimensions—are incorporated, with mold constraints expressed relative to fibre length (w/f_L and t/f_L) due to their known influence on fibre orientation. Casting direction is defined with respect to the principal tensile stress (parallel, perpendicular, or random), and is treated as a primary parameter; when not reported, a random distribution is assumed. To capture both internal structure and performance, the database further combines fresh-state rheological properties when reported (e.g., slump flow, yield stress, viscosity) with hardened-state mechanical responses (e.g., compressive and tensile strengths), alongside quantified fibre orientation metrics. The diversity of analytical approaches used to quantify fibre orientation in the UHPFRC literature poses a significant challenge for the

consistent interpretation of material performance. While many structural and design-oriented studies estimate orientation indirectly through mechanical orientation factors derived from inverse analyses of flexural or tensile responses, others use simplified indicators, such as alignment indices or fibre efficiency factors, to capture their role in crack-bridging mechanisms. In contrast, image-based methods—including image analysis and X-ray computed tomography—provide geometrical descriptions, such as angle probability distributions. In light of this variability, the present database compiles the mathematical expressions of fibre orientation derived from image-based approaches (currently limited to studies reporting fibre orientation on cut sections), as used by different research studies, to enable a more consistent and comparable framework.

It is observed that the four orientation descriptors presented below have been predominantly preferred by researchers, as is given in Table 1. Here, the angle (θ) represents the orientation angle of the fibre relative to the principal load direction. Analysis of descriptor usage revealed that Descriptors A and D were rarely adopted, appearing in only 7 and 3 of the 41 studies, respectively. This limited use can be attributed to their relatively simplistic nature and their inability to fully capture the complexity of fibre orientation distributions. In contrast, Descriptors B and C were more widely employed due to their stronger theoretical grounding and improved capability to represent orientation in a statistically meaningful manner. As evident from their mathematical formulations, Descriptors B and C can be expressed in terms of statistical moments ($\alpha_1 = \langle\cos\theta\rangle$, $\alpha_2 = \langle\cos^2\theta\rangle$) of the orientation distribution, allowing them to capture not only the mean alignment but also the dispersion characteristics of fibres.

Table 1. Fibre orientation descriptors used in the reviewed papers

Descriptor A defines the orientation factor as the ratio of fibres intersecting a section (Dupont and Vandewalle, 2005)	$\alpha_0 = n_f \frac{A_f}{V_f}$
Descriptor B represents the average directional orientation providing a first-order measure of fibre alignment relative to a reference direction (Huang, Gao and Teng, 2021)	$\alpha_1 = \frac{1}{N_f}\sum_{i=1}^{N_f} \cos\theta_i$
Descriptor C accounts for the probabilistic nature of orientation by integrating the weighted cosine-squared distribution, thereby incorporating the full orientation distribution function and offering a more comprehensive statistical representation (Huang, Gao and Khayat, 2021)	$\alpha_2 = \int_{\theta_{min}}^{\theta_{max}} p(\theta)\ \cos\theta^2\ \mathrm{d}\theta$
Descriptor D provides the mean fibre orientation angle, which gives an intuitive but less structurally representative measure of orientation.(Li *et al.*, 2025)	$\theta_{avg} = \frac{1}{N_f}\sum_{i=1}^{N_f} \theta_i$

2.2 Machine Learning

To analyze the database, a tree-based machine learning algorithm, "Gradient Boosted Decision Trees (GBDT)" was implemented. Tree-based models are particularly well-suited because they can capture non-linear relationships in high-dimensional data. Prior to model training, the dimension of the dataset was reduced to the most relevant physical parameters. Selection of the independent variables was guided by their documented significance in governing the compressive and tensile strengths in the literature. This feature selection strategy

is critical to mitigate the overfitting caused by excessive dimensionality (Chan, Yio and Wong, 2026). The data was split into 8:2 for training and test sets, and the machine learning model was trained and tuned using a 5-fold cross-validation technique. The evaluation metrics, the Normalized Root Mean Square Error (NRMSE) and the R^2 score, were used to assess the model's performance.

To better understand the predictive behavior of the implemented tree-based model and obtain meaningful physical insights into UHPFRC materials, SHAP (SHapley Additive exPlanations) values were computed (Lundberg and Lee, 2017). As a post-hoc interpretability method based on coalitional game theory, SHAP quantifies the contribution of each feature to the model output by considering both individual effects and interactions among features. Unlike conventional feature importance methods, the tree-based SHAP algorithm evaluates feature contributions across all possible combinations, providing a more complete interpretation. This makes it particularly suitable for explaining the complex behavior of UHPFRC materials.

3 Results and Discussions

3.1 Overview of Database

Currently, the database covers 345 data points from 41 papers. In this paper, the data were limited to papers that provided the most preferred orientation descriptors (Descriptors B and C). The majority of the studies investigated the relationship between fibre orientation and tensile behavior using flexural test results, while a relatively smaller number of data points were reported for direct tensile strength. Additionally, flexural test specimens that did not exhibit strain hardening beyond the limit of proportionality (LOP) were excluded from the data, as observed for specimens with a low fibre volume ratio (0.5%). Finally, a data-driven analysis was conducted using 182 data points. To mitigate the risk of overfitting of the machine learning model, which is a common challenge with relatively small datasets in scientific and engineering problems (Pakzad *et al.* 2023; Ullah *et al.*, 2025), we split the data into training and test sets and also employed cross-validation during hyperparameter tuning.

The statistics of the critical features in the dataset are shown in Fig. 1. The evaluation of the extracted data indicates that the water-to-binder ratio varies from 0.13 to 0.24, while the fine aggregate-to-binder ratio spans from 0.59 to 1.45. For steel fibres, lengths range from 6 mm to 30 mm. However, 13 mm is the most frequently used in the dataset, with around 60% of the datapoints using it. The fibre volume fractions (V_f) range from 0.5% to 4.0%, with 2.0% volume fraction being the most common in the database, comprising about 40% of the datapoints. The utilized fibre geometries are predominantly straight; however, hooked and twisted fibres were reported in five and one references, respectively. The compressive strength of the UHPFRC mix ranges from 98 to 232.1 MPa, with a mean of 149.6 MPa. The flexural strength values range from 6.14 to 48.6 MPa, with a mean of 25.4 MPa.

The water-to-binder ratio shows a narrow distribution, clustered around ~0.20 (50%), indicating mix designs with similar water-to-binder ratios. In contrast, the fine aggregate-to-binder ratio shows a wider spread, with a concentration around 0.8 (~55%), reflecting moderate variability. Fibre length is strongly concentrated around 13 mm (>65%), while the fibre aspect ratio is centered around ~60–70 but displays a broader range, indicating higher variability. Compressive strength and flexural strength span a wide range, suggesting significantly different UHPFRC materials.

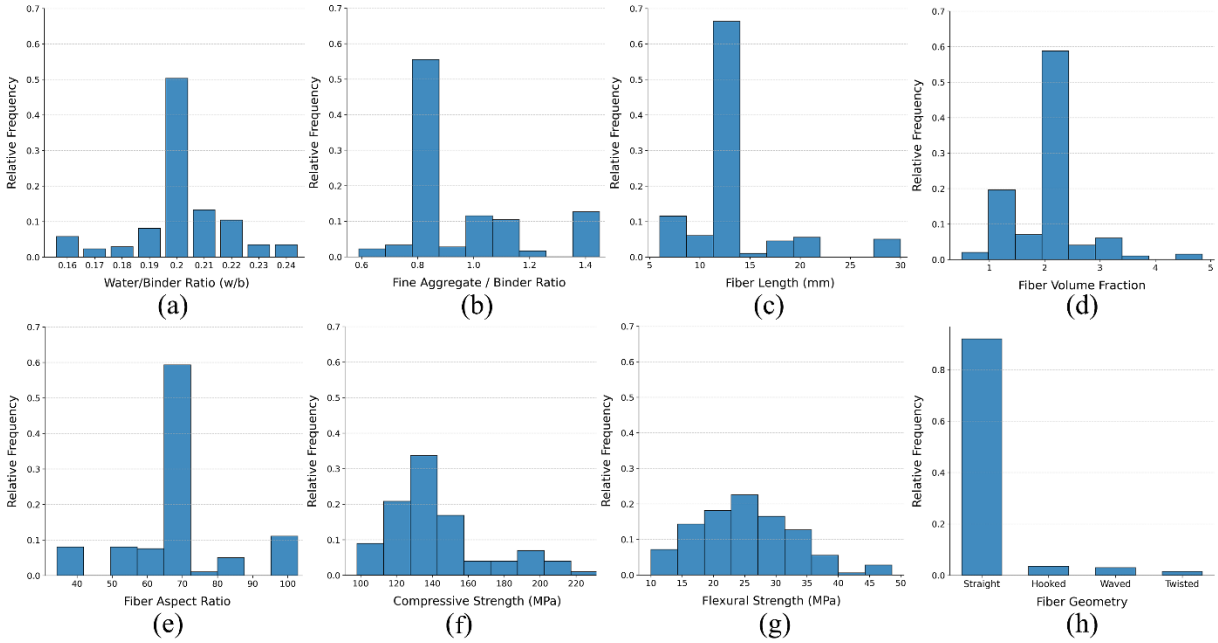
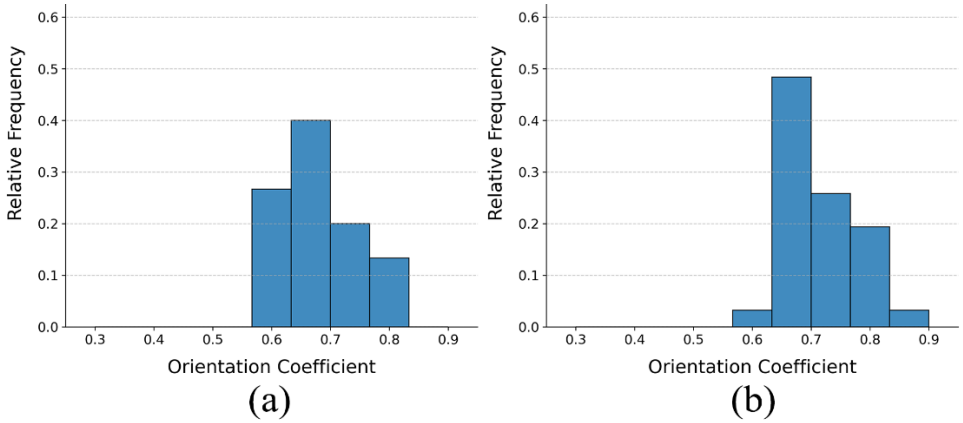


Figure 1: Data distribution histograms for the datapoints utilized in this study; (a) water-to-binder ratio, (b) fine aggregate-to-binder ratio, (c) fibre length, (d) fibre volume fraction, (e) fibre aspect ratio, (f) compressive strength, (g) flexural strength, (h) fibre geometry.

Fig. 2 presents the orientation coefficient as reported for random and parallel-cast specimens using two different descriptors (B and C). As seen in the figure, Descriptor C (the second-order moment $\alpha_2 = \langle \cos^2\theta \rangle$) consistently yields lower values than Descriptor B (the first-order moment $\alpha_1 = \langle \cos\theta \rangle$) because the orientation angles are effectively treated within a positive range where the angle between the fibre and loading stress is calculated using the geometry of the ellipse and the values between $0^\circ < \theta < 90^\circ$ are considered, for which $\cos^2\theta \leq \cos\theta$. As a result, no cancellation occurs, and the first-order moment behaves as a larger average projection descriptor. Overall, the input parameters show mixed variability, while the outputs—particularly strength—cover a broad range, making the dataset suitable for machine learning applications with appropriate handling.



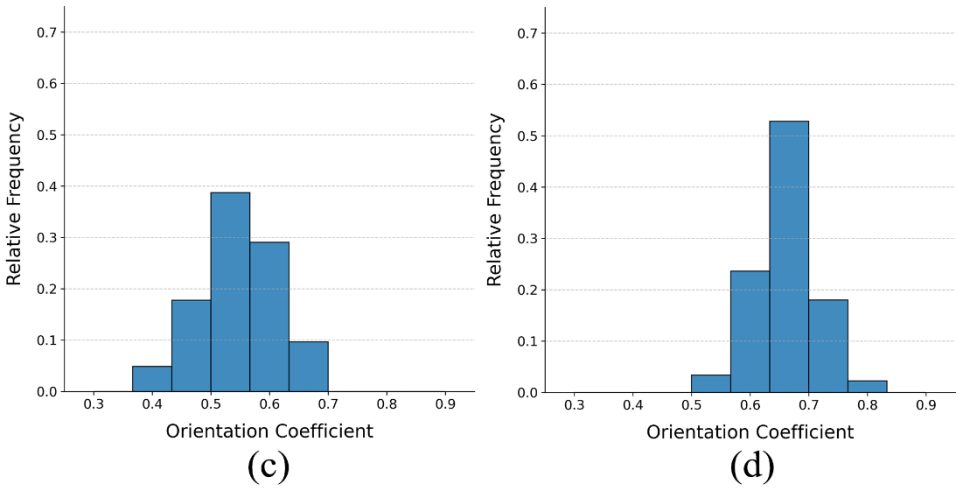


Figure 2: Orientation coefficient histograms (Descriptor B); (a) random cast (15 datapoints), (b) parallel cast (31 datapoints), (Descriptor C); (c) random cast (62 datapoints), (d) parallel cast (89 datapoints).

3.2 Data-driven Investigation

By consolidating data from a wide range of studies, the database enables a holistic evaluation of how material properties, processing conditions, and formwork characteristics influence fibre orientation and, ultimately, the mechanical performance of UHPFRC. However, the relationships among these parameters are inherently complex, multi-parametric, and often non-linear, further complicated by variability in experimental setups and inconsistencies in reported orientation descriptors across the literature. In such a heterogeneous data landscape, conventional deterministic or regression-based approaches remain limited in their ability to capture governing mechanisms. In contrast, machine learning techniques provide a powerful framework to analyze complex, multi-source datasets by simultaneously accounting for interacting variables and uncovering non-linear dependencies. When combined with explainable AI methods such as SHAP, these approaches not only enhance predictive capability but also enable transparent identification of the most influential parameters, offering physically meaningful insights into process–orientation–performance relationships in UHPFRC.

The comprehensive dataset compiled within the database has been systematically summarized in structured Excel tables and reported in a separate publication (Amran *et al.*, 2023). In the same study**,** various fibre orientation descriptors were thoroughly reviewed and discussed in detail to ensure clarity and comparability across different approaches. Additionally, within that work**,** advanced machine learning techniques were employed to evaluate the relative importance of key parameters influencing fibre orientation, enabling a deeper, data-driven understanding of the governing factors. In this study, available data were used to evaluate feature importance for the following mechanical performance indicators: compressive and flexural strengths.

3.2.1 Compressive Strength Analysis

The GBDT model was trained and tested using the relevant parameters as inputs of the model. In this dataset, the GBDT model achieved an R^2 score of 0.85 and an NRMSE of 0.104, indicating that the ML model captures the underlying mechanism. Fig. 3 demonstrates the SHAP values of the features. Portland cement (PC)-to-binder ratio was ranked as the most

influential parameter for the compressive strength of UHPFRC material. Following the PC-to-binder feature, the fine aggregate-to-binder ratio and water-to-binder ratio are found to be the next important features for compressive strength.

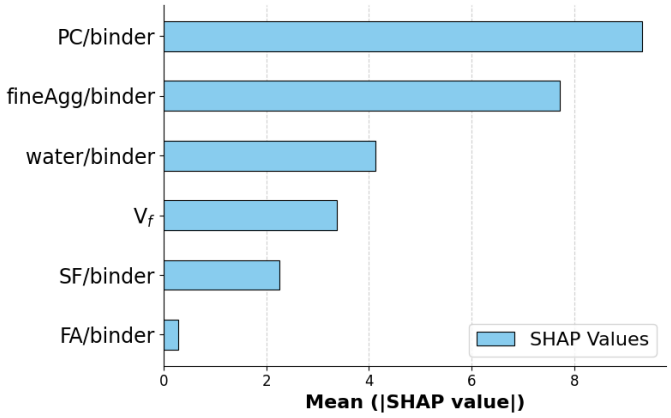


Figure 3: Importance of the features for the compressive strength analysis.

The SHAP summary plot (Fig. 4) highlights the relative importance and directional influence of key input parameters on compressive strength. In this plot, positive SHAP values indicate that a feature's contribution to the predicted fibre orientation parameter increases, while negative values indicate a decrease. Each colored dot represents a distinct data point, with its specific feature value represented by a blue-to-pink color gradient corresponding to low-to-high values. Among the variables, PC/binder and water/binder ratios appear to exert the most pronounced influence, as indicated by the wider spread of their SHAP values. While PC/binder generally exerts a moderate influence, a limited number of cases (with high PC/binder values) exhibit exceptionally high SHAP values, indicating strong localized effects that expand the overall scale of the plot.

In contrast, parameters such as FA/binder and SF/binder show a more limited, concentrated effect near zero, suggesting a comparatively lower contribution to the model output. The color gradient further reveals that higher PC/binder ratios are generally associated with increased compressive strength, whereas higher water/binder ratios tend to reduce it, consistent with established material behavior (Fig. 4). Overall, the distribution and spread of SHAP values indicate a complex, non-linear interaction among the variables, in which the influence of each parameter depends strongly on its combination with others.

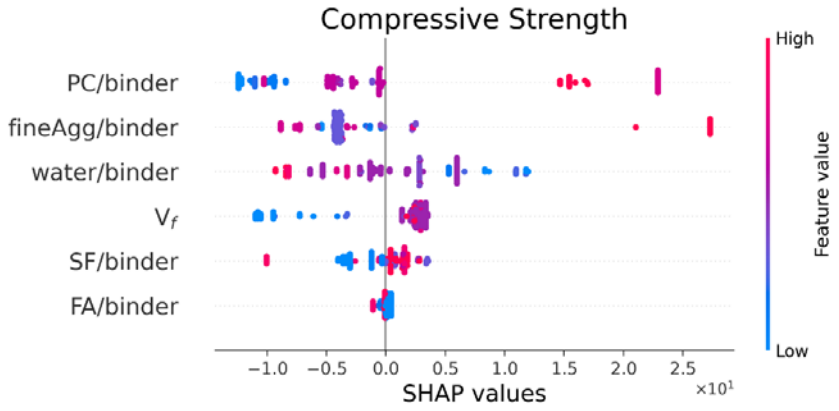


Figure 4: Summary plot of the features for the compressive strength analysis.

3.2.2 Flexural Tensile Strength Analysis

As mentioned before, the datapoints using the fibre orientation coefficients α_1 and α_2 (Descriptors B and C, respectively) were included in the analysis. However, their underlying mathematical formulations differ significantly, leading to diverse orientation measurements for the same specimen. Utilizing data from (Huang *et al.*, 2018; Li and Zhou, 2023), which reported both orientation coefficient values for identical specimens, a linear regression analysis was conducted to derive a relationship between the two models and unify these metrics in a single dataset. The fitted regression line achieved an R^2 score of 0.73, which is an adequate level of conversion accuracy given the complex mechanism underlying the problem. Using the fitted line, Descriptor B was converted to Descriptor C prior to the model training.

The features illustrated in Fig. 5 are accounted for in the analysis of the flexural strength target. The trained GBDT model achieved an R^2 score of 0.72 and an NRMSE of 0.135, which could be considered adequate given the complexity and variability of the experimental results. The feature importance analysis, as illustrated in Fig. 5, shows that the orientation coefficient is the most significant parameter for the flexural strength target. After the orientation coefficient, the PC/binder parameter ranks as the most important feature, with a similar SHAP value. This indicates that these two features have similar effects on the flexural tensile strength. The next most influential features are the fibre volume (V_f) and fibre length (f_L). Because of the limited and low-variance data for the aspect ratio, the model may not capture the physical effect of this parameter on the flexural strength.

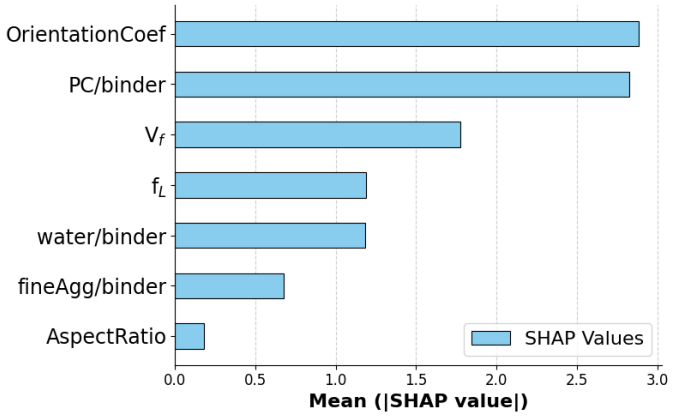


Figure 5: Importance of the features for the flexural strength analysis.

Fig. 6 presents the orientation coefficient of the datapoints and their corresponding SHAP values. The plot demonstrates that parallel-cast specimens (red dots) generally exhibit higher orientation coefficients than random-cast specimens (blue dots). Here, a positive SHAP value implies that the orientation coefficient increases the prediction of the target variable (flexural tensile strength), whereas a negative SHAP value indicates a decrease in the model's prediction. Furthermore, the results reveal a nonlinear relationship between fibre orientation and flexural strength (Fig. 6). Orientation coefficients below 0.52 have a relatively uniform, minor impact, whereas those above 0.52 have a more pronounced effect on strength. Also, the plot suggests that fibre orientation contributes significantly more to flexural strength when the coefficient exceeds a threshold of approximately 0.60.

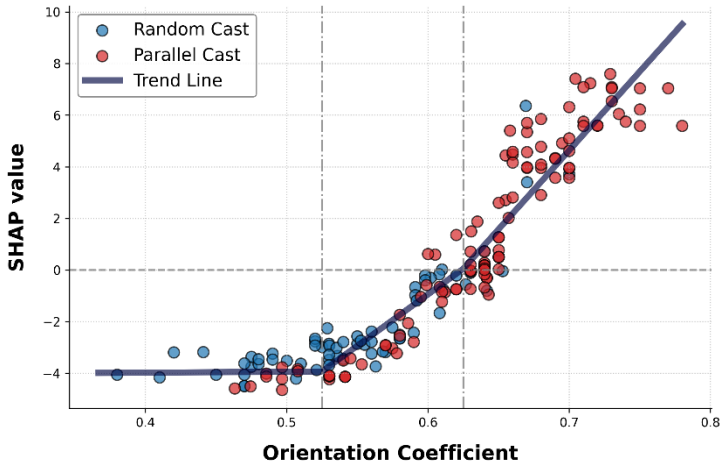


Figure 6: SHAP values of orientation coefficients for random and parallel casting directions.

Although orientation coefficients in the range of 0.60–0.65 are typically considered favorable, the SHAP analysis indicates that their contribution to flexural tensile strength remains below the dataset average. This suggests that, within the compiled dataset, higher levels of fibre alignment (above ~0.65) are required to achieve above-average mechanical performance. This observation highlights a transition zone where fibres are not yet fully effective at crack bridging, underscoring that conventionally "good" orientation levels may not correspond to optimal structural performance.

4 Concluding Remarks

This study was conducted to gain a better understanding of the relationships among the parameters that affect the mechanical performance of UHPFRC materials, based on a newly established database (UHPFRC-OriD). The objective of this database is to identify the effective physical factors governing fibre orientation and mechanical performance across a broad spectrum of UHPFRC systems, encompassing diverse material compositions, mixture designs, and casting/processing conditions. Studies published between 2008 and 2026 were systematically screened and evaluated following a PRISMA-like structured workflow, in accordance with predefined selection criteria, focusing specifically on UHPFRC studies reporting fibre orientation based on image analysis of cut sections.

In this study, the database was examined through frequency histograms to characterize the distributions of key features. The fibre orientation descriptors most frequently adopted by researchers were identified, and these predominant descriptors were subsequently utilized in machine learning analyses to assess feature importance and elucidate their influence on mechanical performance. The results retrieved from the database and ML-based analyses can be summarized as follows:

- The statistical evaluation reveals a clear clustering of key parameters, with the majority of studies adopting a water-to-binder ratio of around 0.2, fibre lengths of approximately 13 mm, and aspect ratios near 65.
- Analysis of orientation descriptor usage indicates that researchers predominantly preferred Descriptors B and C (as given in Table 1), reflecting their stronger capability to capture fibre orientation in a statistically meaningful and physically representative manner compared to alternative descriptors.

- Descriptor B, representing the first-order moment ($\langle\cos\theta\rangle$), typically produces higher values than the second-order moment Descriptor C ($\langle\cos^2\theta\rangle$), because the orientation angles are effectively treated within a non-signed range, for which $\cos^2\theta \leq \cos\theta$.
- Frequency histograms of Descriptors B and C clearly reveal the distribution ranges of fibre orientation coefficients under both random and parallel casting conditions, providing a systematic comparison across casting scenarios and offering a valuable contribution to the literature by consolidating dispersed experimental evidence.
- Rather than simply identifying which parameters are most influential (e.g., the effect of PC/binder ratio, fine agg./binder ratio, and water/binder ratio on compressive strength), SHAP analysis enables a more detailed interpretation by revealing how variations in each feature—across increasing or decreasing ranges—nonlinearly influence the output response. This allows for a deeper understanding of complex, non-monotonic relationships that cannot be captured through conventional correlation or importance metrics alone. This is clearly seen in Fig. 6, which shows the level of fibre orientation coefficient required to yield an above-average contribution to flexural tensile strength.
- Although the current database comprises 345 entries from 41 scientific papers, it will be further expanded to incorporate alternative fibre orientation characterization methods. The integration and collective evaluation of an increasingly large and diverse dataset is expected to enable a deeper understanding of previously unresolved behavior, ultimately leading to significant advancements in both material design and structural applications of UHPFRC.

Data Availability Statement

If you would like to access or contribute to the database, please direct all correspondence to the following e-mail address “bedirhan.kelek@bogazici.edu.tr”.

5 References

Amran, M., Murali, G., Makul, N., Tang, W.C., Alluqmani, A.E. (2023) “Sustainable development of eco-friendly ultra-high performance concrete (UHPC): Cost, carbon emission, and structural ductility,” *Construction Building Materials*, 398, p. 132477. doi: /https://doi.org/10.1016/j.conbuildmat.2023.132477.

Azmee, N.M. and Shafiq, N. (2018) “Ultra-high performance concrete: From fundamental to applications,” *Case Studies in Construction Materials*, 9, p. e00197. doi: /https://doi.org/10.1016/j.cscm.2018.e00197.

Chan, T.C., Yio, M.H.N. and Wong, H.S. (2026) “Natural carbonation of concrete: a data-driven analysis,” *Cement and Concrete Composites*, 167, p. 106436. doi: /https://doi.org/10.1016/j.cemconcomp.2025.106436.

Dupont, D. and Vandewalle, L. (2005) “Distribution of steel fibres in rectangular sections,” *Cement and Concrete Composites*, 27(3), pp. 391–398. doi: /https://doi.org/10.1016/j.cemconcomp.2004.03.005.

Gong, J., Ma, Y., Fu, J., Hu, J., Ouyang, X., Zhang, Z., Wang, H. (2022) "Utilization of fibers in ultra-high performance concrete: A review," *Composite Part B Engineering*, 241, p. 109995 doi: https://doi.org/10.1016/j.compositesb.2022.109995.

Huang, H., Gao, X., Li, L., Wang, H. (2018) "Improvement effect of steel fiber orientation control on mechanical performance of UHPC," *Construction and Building Materials*, 188, pp. 709–721. doi: https://doi.org/https://doi.org/10.1016/j.conbuildmat.2018.08.146.

Huang, H., Gao, X. and Khayat, K.H. (2021) "Contribution of fiber alignment on flexural properties of UHPC and prediction using the Composite Theory," *Cement and Concrete Composite*, 118, p. 103971. doi: /https://doi.org/10.1016/j.cemconcomp.2021.103971.

Huang, H., Gao, X. and Teng, L. (2021) "Fiber alignment and its effect on mechanical properties of UHPC: An overview," *Construction and Building Materials*, 296, p. 123741. doi: /https://doi.org/10.1016/j.conbuildmat.2021.123741.

de Larrard, F. and Sedran, T. (1994) "Optimization of ultra-high-performance concrete by the use of a packing model," *Cement and Concrete Research*, 24(6), pp. 997–1009. doi: https://doi.org/10.1016/0008-8846(94)90022-1.

Li, P., Zhang, X., Xiong, G., Ji, G., Han, X. (2025) "Relationship between fiber dispersion, workability, and mechanical performance in Self-Compacting Ultra-High Performance Concrete (SC-UHPC): An experimental and modeling study," *Construction and Building Materials*, 491, p. 142790. doi: https://doi.org/https://doi.org/10.1016/j.conbuildmat.2025.142790.

Li, Z. and Zhou, W. (2023) "Tensile behavior of UHPFRC made by a fiber orientation device with adjustable vibrational frequency," *Construction and Building Materials*, 401, p. 132914. doi: /https://doi.org/10.1016/j.conbuildmat.2023.132914.

Pakzad, S.S., Roshan, N. and Ghalehnovi, M. (2023) "Comparison of various machine learning algorithms used for compressive strength prediction of steel fiber-reinforced concrete," *Scientific Reports*, 13(1), p. 3646. doi: https://doi.org/10.1038/s41598-023-30606-y.

Ullah, I., Javed, M.F., Alabduljabbar, H., Ullah, H. (2025) "Estimating the compressive and tensile strength of basalt fibre reinforced concrete using advanced hybrid machine learning models," *Structures*, 71, p. 108138. doi: https://doi.org/10.1016/j.istruc.2024.108138.

Zhou, M., Lu, W., Song, J., Lee, G.C. (2018) "Application of Ultra-High Performance Concrete in bridge engineering," *Construction and Building Materials*, 186, pp. 1256–1267. doi: https://doi.org/10.1016/j.conbuildmat.2018.08.036.

Validity Check of Punching Shear Design for Steel Fibre Reinforced Flat Slabs with Shear Reinforcement Based on New Test Results

Sören Faustmann[1,2] and Oliver Fischer[1]

[1]: Technical University of Munich, Chair of Concrete and Masonry Structures, Munich, Germany.

[2]: Büchting + Streit AG, Munich, Germany

Abstract

Punching shear is a well-known and widely studied failure mode for flat slabs and is often critical to their design. If the punching capacity of the flat slab is insufficient, it can be strengthened with punching shear reinforcing elements such as stirrups or headed studs. An alternative is the use of steel fibre reinforced concrete (SFRC), which can provide similar increases in load-capacity as stirrups. There are only a few studies on the load-bearing behaviour of slabs combining shear reinforcement with SFRC, with specimens mostly showing flexural failure, having very small dimensions or using unconventional shear reinforcement. Validation of a design approach, provided by the next generation of Eurocode 2 (FprEC2) or the Model Code 2020 (MC20), was not possible for such slabs due to the lack of suitable data. To enable sufficient validation, a series of tests was carried out at the Technical University of Munich (Germany) with a total of 23 flat slabs combining stirrups or headed studs with SFRC. This paper presents the main attributes of the test specimens, as well as the achieved punching shear capacities. Additionally, we provide a brief overview of the punching shear design according to EC2 and MC20. For the first time a validation of the design approaches is carried out for shear-reinforced SFRC slabs based on a comparison between experimental ultimate loads and calculated punching shear capacities. Furthermore, trend dependencies of the design approaches for the investigated parameters such as the punching shear reinforcement ratio and the residual flexural tensile strength (as the most an essential mechanical parameter for SFRC) are presented and discussed.

Keywords

punching shear design; flat slab; fib Model Code 2020, next generation of Eurocode 2

1 Introduction

Flat slabs have been very popular for over 100 years and are still frequently used in construction today. The most critical issue in design is usually punching shear – a local failure at the junction between the slab and the column (Ungermann et al. 2022; Welsch ad Held 2012). Shear reinforcement elements are typically used to reinforce flat slabs against punching shear. An alternative is the use of steel fibre reinforced concrete (SFRC), which can also significantly increase the punching shear capacity. A combination of both strengthening methods (shear reinforcement and SFRC) was largely unexplored until recently. In Germany, the use of SFRC and shear reinforcement is therefore explicitly excluded in design and application due to a lack of experimental data (German Guideline SFRC, 2021; DAfStb-Heft 614, 2015). A literature review confirms that only 11 punching shear tests involving punching shear reinforcement and SFRC are known worldwide (see, Faustmann, 2025). These all exhibited either flexural failure or unusual slab dimensions, punching shear reinforcement types or concrete types.

The *fib* Model Code 2020 (MC20) and the next generation of Eurocode 2 (FprEC2) already provide for the combined consideration of SFRC and shear reinforcement through the addition of load-bearing contributions. However, based on the experimental data described, these design approaches can only have been validated using flat slabs with shear reinforcement or SFRC. It remains doubtful whether the interaction effects between steel fibres and punching shear, such as those that may result from stiffness-dependent effects, can be accurately predicted. In response to this research gap, 23 punching shear tests on SFRC slabs with shear reinforcement have been carried out at the Technical University of Munich (TUM) in recent years (see also Faustmann et al., 2024; Faustmann and Fischer, 2023; All results summarised in (Faustmann, 2025). These tests demonstrated that through the combination of SFRC and shear reinforcement a significant increase in load-bearing capacity can be achieved, both for failure within the shear reinforcement and for failure at the level of maximum punching strength. Furthermore, the tests enable, for the first time, a systematic validation of the design approaches mentioned before.

This paper begins by explaining the fundamental design concepts according to MC20 and FprEC2. As both are based on the Critical Shear Crack Theory (CSCT) by Muttoni et al. (Muttoni, 2008), the basics of CSCT are first briefly outlined. Then, the TUM punching shear tests are briefly presented; further details can be found in the appendix. Section 4 compares the design results with the experimental failure loads.

2 Design Approaches

2.1 Background: The Critical Shear Crack Theory (CSCT)

Both design approaches considered, MC20 and FprEC2, are based on the CSCT by Muttoni et al (Muttoni, 2008). The basic assumption of the CSCT is an idealised critical shear crack (CSC) with an inclination of 45°, which opens in direct proportion to the global slab rotation ψ (see Fig. 1a). The slab rotation can be predicted using the expected applied vertical force V and the resulting flexural moments, e.g. via integration of the moment-curvature relationship, and is illustrated in Fig. 1b. This is opposed with a failure criterion, here exemplified by a reinforced concrete slab without shear reinforcement and without steel fibres. The predicted punching failure occurs at the intersection between the load-rotation curve and the failure criterion.

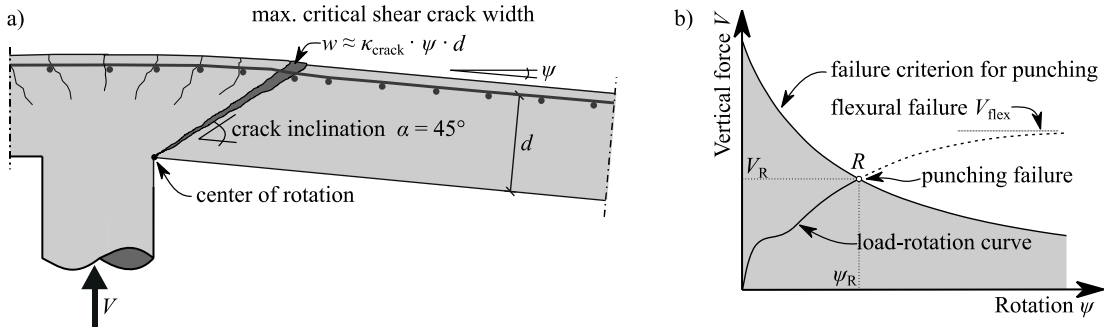


Figure 1: Basic assumptions of CSCT. (a) Shear crack geometry and slab rotation, (b) failure criterion and load-rotation relationship (reproduced from Muttoni, 2008 and Muttoni and Fernández Ruiz, 2010).

The CSCT has been extended to cover a wide range of applications, for a compilation see (Muttoni and Simões, 2023). However, the basic principles shown in Fig. 1 remain unchanged. Fig. 2a illustrates the application of the CSCT to shear-reinforced SFRC slabs, featuring a CSC inside the shear-reinforced area. As the slab rotation ψ and thus the CSC width increases, the concrete contribution V_c decreases, which is mainly attributed to a reduction in aggregate interlock. At the same time, the crack growth increasingly activates the shear reinforcement, and the contribution V_s increases until the yield strength of the shear reinforcement is reached. Similarly, the fibre contribution V_f is activated by the shear crack opening and eventually stagnates at larger crack openings (Maya et al., 2012; Moraes Neto et al., 2013; Muttoni and Fernández Ruiz, 2010).

The punching shear capacity is limited by a potential failure of the concrete compression strut, which typically manifests as a steep shear crack between the shear reinforcement and the column (see Fig. 2b). In this case, adding more shear reinforcement does not result in higher load-bearing capacities, which is why this is referred to as failure on the level of maximum punching strength. As this is manly a concrete failure, the ultimate load of tis failure mode is expressed as a multiple of the concrete contribution V_c.

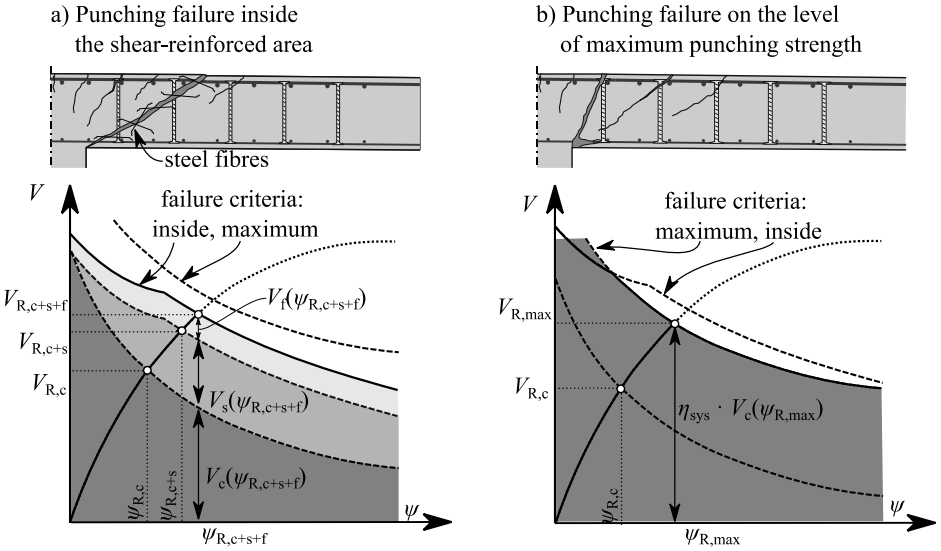


Figure 2: Application of the CSCT to steel fibre and shear-reinforced slabs (inspired by (Einpaul et al., 2016; Schmidt, 2010).

Punching may also occur outside the shear-reinforced area. As this was not the case in all experimental tests, and no interaction between steel fibres and the punching shear reinforcement is expected in this failure mode, this is not considered further.

2.2 *fib* Model Code 2020 (MC20)

Eq. 1 shows the general formulation of the design equation for punching shear, expressed as a sum of load-bearing contributions from concrete $V_{Rd,c}$, shear reinforcement $V_{Rd,s}$ and steel fibres $V_{Rd,f}$. In accordance with the CSCT described above, $V_{Rd,c}$ and $V_{Rd,s}$ are determined as a function of global slab rotation ψ. The steel fibre contribution $V_{Rd,f}$ is described in simplified terms and does not take ψ into account.

$$V_{Rd} = V_{\mathrm{Rd,c+s+f}} = V_{\mathrm{Rd,c}}(\psi) + V_{\mathrm{Rd,s}}(\psi) + V_{\mathrm{Rd,f}} \leq V_{\mathrm{Rd,max}}(\psi) \tag{1}$$

The global slab ψ rotation can be calculated at various levels of approximation (LoA). For structural design of new structural elements, LoA II and LoA III are specified; the latter is considered in Eq. 2.

$$\psi_{\mathrm{LOA,III}} = 1.2 \cdot \frac{r_s}{d} \frac{f_{yd}}{E_s} \left(\frac{m_{Ed}}{m_{Rd}}\right)^{1.5} \tag{2}$$

In addition to empirical factors and exponents, the equation includes the geometric parameters r_s (distance between the column axis and the radial bending moment being zero) and d (effective depth), as well as the material properties of the flexural reinforcement f_{yd} (yield strength) and E_s (Young's modulus). The ratio of the applied bending moment m_{Ed} (for internal columns without load eccentricity, m_{Ed} is approximately $V_{Ed}/8$) to the flexural resistance m_{Rd} is shown in brackets. Once the slab rotation ψ has been determined, the $V_{Rd,c}$ can be calculated according to Eq. 3.

$$V_{\mathrm{Rd,c}}(\psi) = k_\psi \cdot \frac{\sqrt{f_{ck}}}{\gamma_c} \cdot b_{05} \cdot d_v \tag{3}$$

Here, b_{05} is the perimeter at a distance of $0.5d_v$ while d_v is the effective static height for shear. The parameter k_ψ (Eq. 4) takes into account the slab rotation ψ, the influence of the maximum aggregate size d_g via the factor $k_{dg} = 32/(16+d_g)$ (with d_g in [mm]), as well as size effects via the effective depth d.

$$k_\psi = \frac{1}{1{,}5 + 0.9 \cdot k_{dg} \cdot \psi \cdot d} \leq 0.6 \tag{4}$$

The shear reinforcement contribution $V_{Rd,s}$ is calculated using Eq. 5 based on ΣA_{sw} (the sum of the cross-sectional areas of all shear reinforcement elements between $0.35d$ and $1.0d$), the eccentricity parameter k_e (for internal columns without load eccentricity $k_e = 1.0$) and the effective steel stress σ_{swd}.

$$V_{\mathrm{Rd,s}} = \sum A_{sw} \cdot k_e \cdot \sigma_{swd} \tag{5}$$

The latter is calculated as a function of the slab rotation ψ, see Eq. 6.

$$\sigma_{swd} = \frac{E_s \cdot \psi}{6}\left(1 + \frac{f_{bd}}{f_{ywd}} \cdot \frac{d}{\emptyset_w}\right) \leq f_{ywd} \tag{6}$$

The properties of the shear reinforcement E_s (Young's modulus), f_{ywd} (yield strength), and $Ø_w$ (diameter), as well as the calculated bond stress f_{bd} (simplified to 5 N/mm² for ribbed bars) and the effective depth d are taken into account. The steel stress is limited to the yield strength f_{ywd}.

The steel fibre contribution is determined in Eq. 7 by integrating a stress block along the perimeter b_{05} over the effective depth d_v.

$$V_{Rd,f} = f_{Ftud} \cdot b_{05} \cdot d_v \tag{7}$$

The design stress f_{Ftud} is calculated as:

$$f_{Ftud} = 0.33 \cdot \kappa_0 \cdot \kappa_G \cdot f_{R3,k}/\gamma_{sf} \tag{8}$$

The basis is $f_{R3,k}$ (characteristic residual flexural tensile stress at *CMOD* = 2.5 mm in the three-point flexural test according to EN 14651), which is converted into an equivalent stress block using a factor of 0.33. The parameter κ_G takes into account the size of the tensile area. The factor κ_0 accounts for the steel fibre orientation, with MC20 giving the user some freedom to select a suitable κ_0. For isotropic distribution, κ_0 = 1.0 is recommended; for unfavourable fibre orientation, κ_0 = 0.5. As recent research results indicate a predominantly horizontal fibre orientation (Hernández Fraile et al., 2024), which has an unfavourable effect on shear force dissipation, the fibre orientation coefficient is set to κ_0 = 0.5.

The punching shear capacity is limited in Eq. 1 to $V_{Rd,max}$ (see. Eq. 9).

$$V_{Rd,max} = \eta_{sys} \cdot V_{Rd,c}(\psi) \tag{9}$$

Here, the factor η_{sys} depends on the detailing of the shear reinforcement. For stirrups: η_{sys} = 2.4. For headed studs: η_{sys} = 2.8.

2.3 FprEC2

Also in FprEC2, three load contributions are calculated and summed up, using Eq. 10.

$$V_{Rd,c+s+f} = V_{Rd,c} + V_{Rd,s} + V_{Rd,f}$$
$$V_{Rd,c+s+f} = \left(\eta_c \cdot \tau_{Rd,c} + \eta_s \cdot \rho_w \cdot f_{ywd} + \eta_f \cdot f_{ftud}\right) \cdot b_{05} \cdot d_v \leq V_{Rd,max} \tag{10}$$

No explicit slab rotation ψ is included in the design equations. However, the change in load-bearing contributions resulting from increasing slab rotation and the associated shear crack width – such as a decreasing concrete load-bearing contribution V_c or an increasing load-bearing contribution of the shear reinforcement V_s due to activation – is implicitly accounted for via the interaction coefficients η_i. All load-bearing contributions are first calculated as stresses. They are then multiplied by the perimeter b_{05} and the effective depth d_v to give the respective load-bearing contribution $V_{Rd,i}$. The design value of the stress for concrete contribution is given by Eq. 11.

$$\tau_{Rd,c} = \frac{0{,}6}{\gamma_v} \cdot k_{pb} \left(100 \cdot \rho_l \cdot f_{ck} \cdot \frac{d_{dg}}{d_v}\right)^{\frac{1}{3}} \tag{11}$$

In addition to general and known parameters such as ρ_l (flexural reinforcement ratio), f_{ck} (characteristic concrete strength) and d_{dg} (aggregate size factor analogous to MC20), a punching shear coefficient $k_{pb} = 1 \leq 3.6(1\text{-}b_0/b_{05})^{0.5} \leq 2.5$ is included This coefficient takes into account the increased load-bearing capacity resulting from the multi-axial stress state during punching. The interaction coefficient η_c is calculated according to Eq. 12.

$$\eta_c = \frac{\tau_{Rd,c}}{\tau_{Ed}} = \frac{\tau_{Rd,c}}{V_{Ed}/(b_{05} \cdot d_v)} \tag{12}$$

For the shear reinforcement contribution (see Eq. 10), the shear reinforcement ratio ρ_{sw} is calculated from the cross-sectional area of one shear reinforcement element divided by the tangential and radial spacing. The interaction coefficient η_s to account for the activation of the shear reinforcement and detailing of the shear reinforcement is given in Eq. 13.

$$\eta_s = \frac{d_v}{150 \cdot \emptyset_w} + \left(15 \cdot \frac{d_{dg}}{d_v}\right)^{0,5} \cdot \left(\frac{1}{\eta_c \cdot k_{pb}}\right)^{1,5} \leq 0{,}8 \tag{13}$$

Here the applied force V_{Ed}, and thus the expected global slab rotation ψ, is also indirectly taken into account via η_c. For the steel fibre contribution V_f, the design stress f_{Ftud} is calculated in the same way as in MC20 (see Eq. 8). However, in FprEC2, the steel fibre orientation coefficient κ_0 is defined for shear and punching shear to $\kappa_0 = 1.0$. In addition, there is the interaction coefficient η_f, which is a constant 0.40. The upper limit, the maximum punching strength, is given in Eq. 14. It is calculated as a multiple of the fundamental value of the concrete contribution (see Eq. 11).

$$V_{Rd,max} = \eta_{sys} \cdot \tau_{Rd,c} \cdot b_{05} \cdot d_v \tag{14}$$

For headed studs the factor η_{sys} is defined to $\eta_{sys} = 0.70 + 0.63 \cdot (b_0/d_v)^{0.25} \geq 1.0$, for stirrups $\eta_{sys} = 0.50 + 0.63 \cdot (b_0/d_v)^{0.25} \geq 1.0$, where b_0 is the column perimeter.

3 Experimental program

Over the past few years, a total of 23 full-scale punching shear tests have been carried out at the Technical University of Munich (TUM) on shear-reinforced SFRC slabs. Initial test results have been published in German language (Faustmann and Fischer, 2023; Landler and Fischer, 2021); a full English description can be found in (Faustmann, 2025). In this section, the experiments will be described briefly to provide an overview of the data used.

Fig. 3 shows the test setup, which was also used in other studies such as (Faustmann et al., 2024; Landler and Fischer, 2019). The test specimens at the top are octagonal in shape, with maximum dimensions of 2800 × 2800 mm and a slab thickness of 250 mm. All test specimens were provided with either stirrups (see no. 2a in Fig. 3) or studs (see no. 2b in Fig. 3) as shear reinforcement, as well as strong flexural reinforcement made of high-strength reinforcing steel. A cubic column stub with an edge length of 300 mm was monolithically connected. A central hydraulic cylinder applied the load. The test specimens were held in place by 12 tie rods at a radial distance of 1200 mm, with a hydraulic ring line ensuring that the forces exerted by all 12 tie rods were always equal. These where held by a reaction block, so the laboratory floor was not subjected to any forces from the hydraulic cylinder.

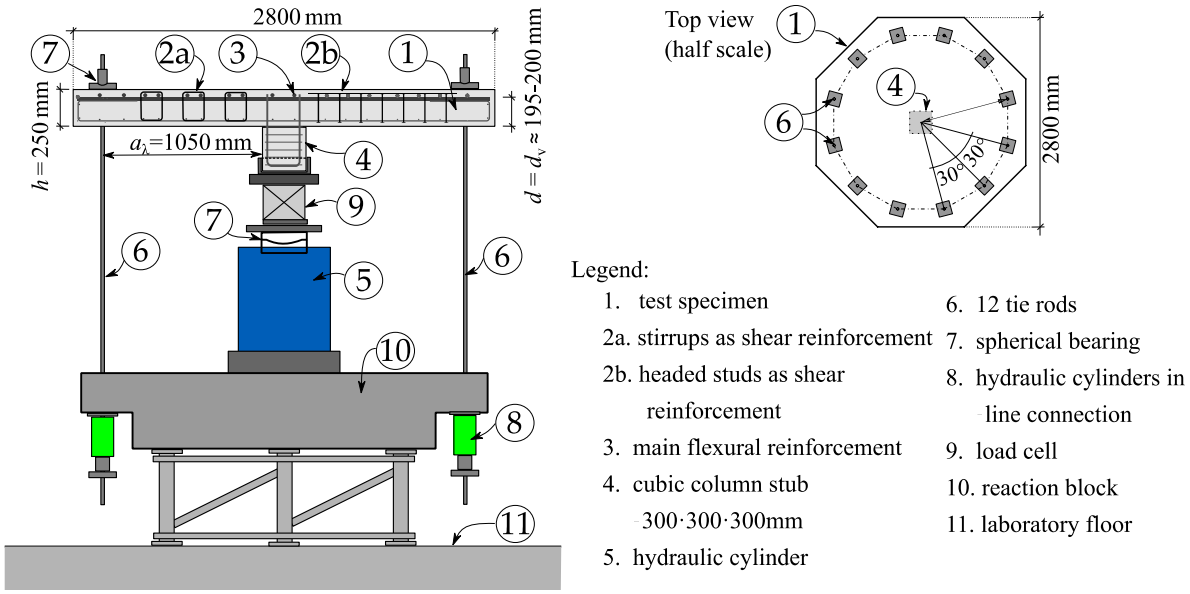


Figure 3: Schematic illustration of test specimens and test setup.

Due to the uniform external geometry, all 23 test specimens show an effective depth $d = d_v$ of 195 to 200 mm and a shear slenderness a_λ/d of approximately 1050/200 = 5.25, which is typical for flat slabs. 13 tests were carried out with closed stirrups, 10 tests with headed studs. The variation in the remaining parameters and the resulting range is shown in Fig. 4 in a set of four histograms.

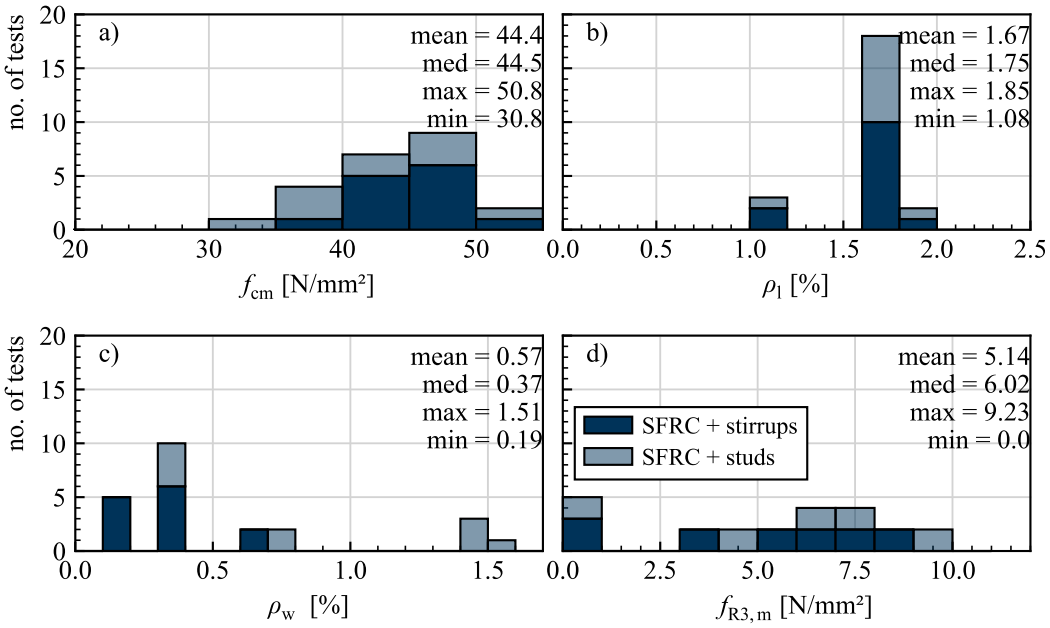


Figure 4: Histograms of key parameters of the 23 experimental tests.

The compressive strength of the concrete varied between 30 and 50 N/mm², which corresponds to typical SFRC (Look et al., 2021). Most tests were carried out with a high flexural reinforcement ratio ρ_l of approximately 1.75% to avoid flexural failure. In three tests, the flexural reinforcement ratio was reduced as far as possible to 1.08%. The punching

reinforcement ratio ρ_w varied considerably between 0.19% and 1.51%. Bekaert steel fibres of type Dramix 4D 65/35BG (Bekaert 4D) or Dramix 65/60BG (Bekaert 5D) were used in dosages ranging from 0 (fibre-free benchmark test) to 80 kg/m³. This resulted in average residual flexural tensile strengths $f_{R3,m}$ according to DIN EN 14651 (DIN EN 14651) of between 0 and 9.23 N/mm². A complete tabular description of all test specimens and their respective configurations can be found in Table A1 in the Appendix.

All tests showed either punching failure within the shear-reinforced area or at the level of maximum punching strength. For both failure modes, increasing the SFRC performance results in a higher ultimate load and increased deformation capacity. Fig. 5 visualises essential results on chosen examples for the two prevailing failure modes. Fig. 5a shows the recorded load-rotation relationships for three tests conducted with stirrups and ρ_w = 0.35% and varying steel fibre content from 0, through 40, up to 80 kg/m³, resulting in $f_{R3,m}$ values of 0, 5.76 and 8.48 N/mm². These tests showed punching failure within the shear-reinforced area. It is evident that as $f_{R3,m}$ increases, both the maximum load V and the maximum slab rotation ψ increase. Similarly, Fig. 5b shows three tests with $V_{Rd,max}$ failure. Here too, the maximum load and slab rotation at failure increase with $f_{R3,m}$. A full description can be found in (Faustmann, 2025).

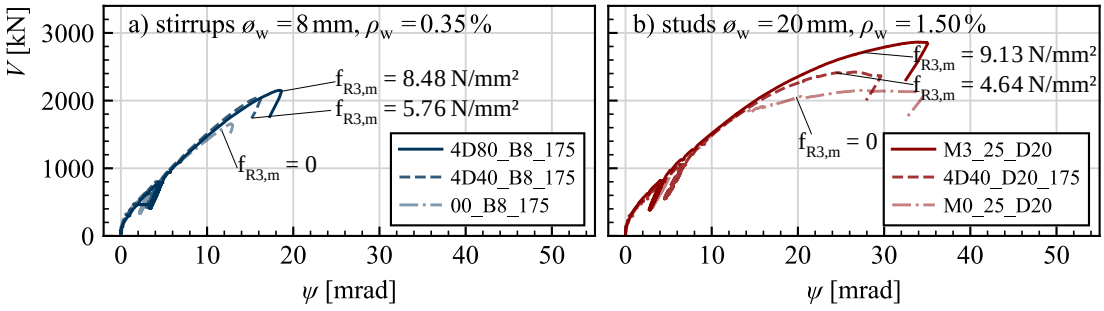


Figure 5: Representative examples of experimentally determined load-rotation relationships under varied SFRC performance: (a) specimens with punching inside the shear-reinforced area, and (b) specimens with failure at the level of maximum punching strength.

4 Comparing experimental to calculated ultimate loads

To compare the experimental results with the design approaches, the calculated load capacities for all test configurations are determined using the equations in Section 2. All partial safety factors were set to 1.0 ($\gamma_c = \gamma_s = \gamma_f = 1.0$). The characteristic material properties concrete compressive strength f_{ck} and residual flexural tensile strength $f_{R3,k}$ are replaced by average values from associated small-scale tests series f_{cm} and $f_{R3,m}$. The flexural capacity per unit length m_{Rd} is included in the calculation according to MC20. It is calculated using stress blocks, taking into account the fibre contribution. In both design approaches considered, the applied force V_{Ed} is included. This takes into account the rotational state of the slab and therefore the associated shear crack width. To obtain a calculation result independent of the experimental ultimate load, the calculation is iterated until the assumed applied force V_{Ed} corresponded to the calculated punching resistance V_{Rd}. A compilation of all calculated ultimate loads according to design approaches V_{cal} can be found in Table A2 in the Appendix.

Once the design load V_{cal} is determined, the ratio V_{Test}/V_{cal} can be computed. A value higher than 1.0 indicates that the design predicts a lower load than that measured in the test – i.e. a safe

design. Values lower than 1.0 indicate an unsafe design. The mean values and coefficients of variation for the ratio V_{Test}/V_{cal} are summarised in Table 1.

Table 1: Statistical evaluation of the ratios V_{Test}/V_{cal}.

	MC20		FprEC2	
no. of tests	*mean*(V_{Test}/V_{cal})	*COV*(V_{Test}/V_{cal})	*mean*(V_{Test}/V_{cal})	*COV*(V_{Test}/V_{cal})
23	1.287	0.081	1.39	0.10

Fig. 6 shows the V_{Test}/V_{cal} ratio as data points plotted against the four key variable parameters. All data points for both design approaches always are in the range $V_{Test}/V_{cal} > 1.0$. In addition, a regression line or trend line is plotted in red for the analysis according to MC20, and in blue for the analysis according to FprEC2. In Fig. 6a, the average concrete compressive strength f_{cm} is plotted on the x-axis. For both MC20 and FprEC2 analyses, data points are scattered without any discernible pattern. However, it can be seen that the red data points for MC20 tend to lie closer to the ideal match $V_{Test}/V_{cal} = 1.0$ than the blue points for FprEC2.

Fig. 6b shows the influence of the flexural reinforcement ratio. Here, a slightly rising regression line is evident, with the values according to MC20 again being lower than those according to FprEC2. Trends relating to the punching reinforcement ratio are shown in Fig. 6c. According to MC20, a slightly downward trend is evident. For the tests with a punching reinforcement ratio of 1.5%, which clearly failed at the level of maximum punching strength, V_{Test}/V_{cal} values of approximately 1.2 are obtained. According to FprEC2, however, an upward trend is visible. In particular, for high punching reinforcement ratios, values of up to $V_{Test}/V_{cal} = 1.69$ are observed, which is very conservative.

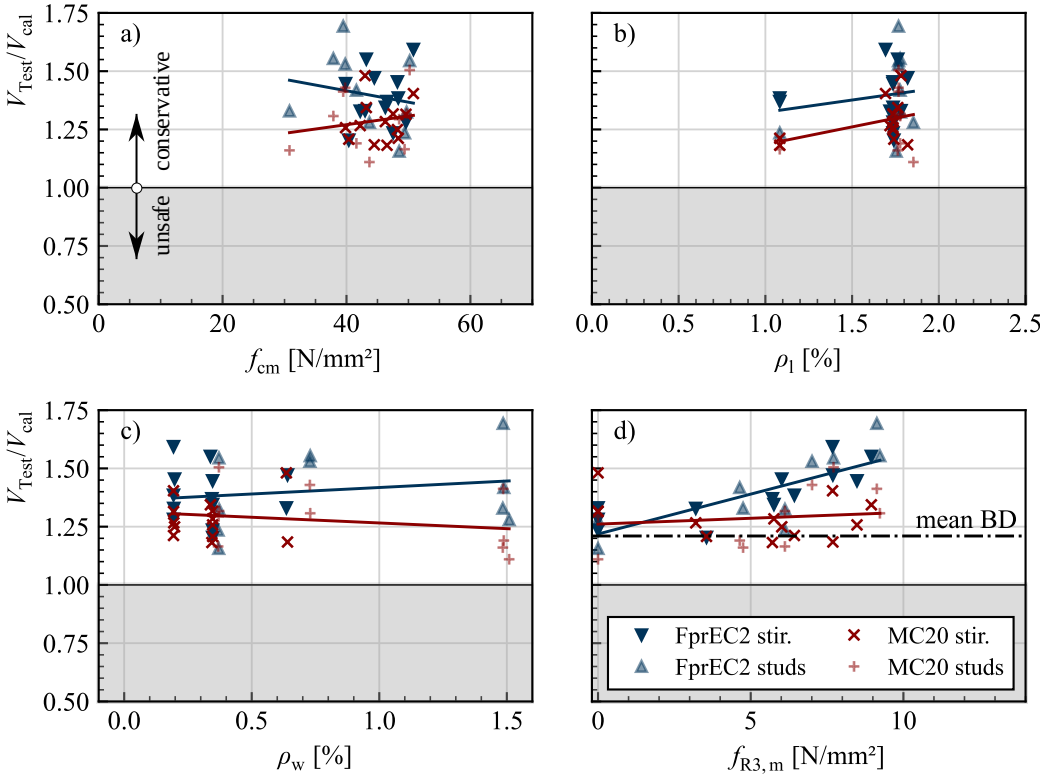


Figure 6: Ratios V_{Test}/V_{cal} of the experimental (V_{Test}) and calculated ultimate loads (V_{cal}) according to MC20 and FprEC2, plotted versus key parameters.

Fig. 6d illustrates the influence of the mean residual flexural strength $f_{R3,m}$. The red regression line for MC20 runs horizontally at a level of approximately 1.27. The influence of $f_{R3,m}$ therefore appears to be represented in MC20 without any apparent trend. According to FprEC2, however, a clearly rising trend is evident. The benchmark tests without steel fibres ($f_{R3} = 0$) show a value of approximately $V_{Test}/V_{cal} = 1.2$, which corresponds to the mean value from a comparable analysis of the background document to FprEC2 concerning flat shear reinforced slabs without steel fibres. The aforementioned mean value (precise value 1.21) is additionally plotted as a horizontal line in Fig. 6d. The agreement between the mean value from the background document and the available data points from the reference tests without steel fibres is confirmed by both the evaluated data in this paper and in the background document. As SFRC performance (f_{R3} value) increases, the V_{Test}/V_{cal} values continue to rise. For high f_{R3} values, the load capacity prediction is ultimately highly conservative, with a maximum V_{Test}/V_{cal} of 1.69.

5 Discussion

The comparison in Section 4 shows that the 23 experimental ultimate loads V_{Test} are always greater than the calculated ultimate loads V_{cal} according to MC20 and FprEC2. The mean value of V_{Test}/V_{cal} according to MC20, at 1.287, is within a typical range, including some model safety. However, for FprEC2, the mean value of 1.394 is very conservative and significantly higher than its Background Document counterpart of 1.21. The coefficients of variation for both design approaches are rather small at 8% and 10%. One reason for this is that all tests considered share the same external geometry and were also tested on the same test rig. Within the examined framework, both design approaches appear safe, although MC20 yields more realistic results. We identified two main reasons for this. Firstly, the fibre contribution according to MC20 is higher than according to FprEC2. Whilst the formulation of the fibre contributions according to Eq. 7 and Eq. 10 is essentially the same, the fibre orientation coefficient differs significantly (MC20 $\kappa_0 = 0.5$; FprEC2 $\kappa_0 = 1.0$). In FprEC2, an interaction coefficient $\eta_f = 0.40$ is additionally multiplied. This results in a ratio of the fibre contributions according to MC20/FprEC2 of $(0.5)/(1.00 \cdot 0.40) = 1.25$. The higher fibre contribution of MC20 provides an accurate representation of the experimentally observed influence of f_{R3}, which is shown by an approximately horizontal trend line for MC20 in Fig. 6d. To improve FprEC2 in future, a higher—and therefore more realistic—fibre contribution could easily be achieved by increasing the interaction coefficient η_f by the difference compared to MC20, i.e. by +25%.

Secondly, the calculated value for $V_{Rd,max}$ is decisive. Neither of the used design approaches explicitly takes into account any positive effect of the steel fibres on the maximum load-bearing capacity $V_{Rd,max}$ and the associated increased rotation capacity (see Fig. 5). According to MC20, the concrete contribution in the rotational state $\psi_{R,max}$ is calculated and multiplied by a factor (2.4 or 2.8). Eq. 2 for calculating slab rotation also incorporates the flexural capacity, which in turn depends on the SFRC performance (f_{R3}). According to MC20, the predicted rotation at failure $V_{Rd,max}$ decreases as the f_{R3} value increases. For example, for test M0_25_D20 (plain concrete, $f_{R3} = 0$), a slab rotation of $\psi_{R,max} = 9.96$ mrad is calculated; for the corresponding test M3_25_D20 with f_{R3}=9.13 N/mm², $\psi_{R,max} = 8.91$ mrad (ψ_{cal} -11%) is obtained. Due to the lower predicted rotation and the associated smaller calculated shear crack width, the concrete contribution to load-bearing capacity and its multiple $V_{Rd,max}$ increase (see Fig. 2). MC20 therefore predicts increasing $V_{Rd,max}$ load-bearing capacities with SFRC, which corresponds to the observations from the experiments and explains the relatively good agreement between V_{Test}

and V_{cal}. However, the experiments reveal increased rotations in the failure state at $V_{Rd,max}$ failure with increasing SFRC performance (cf. M0_25_D20/M3_25_D20: ψ_{Test} +25%). This represents a fundamental difference that should be addressed in future revisions of MC20.

According to FprEC2, $V_{Rd,max}$ is defined as a multiple (of the magnitude 1.5) of the load-bearing capacity of a reinforced concrete slab without steel fibres and without shear reinforcement (and, implicitly, the corresponding rotational state $\psi_{R,c}$ as shown in Fig. 2). The calculated load-bearing capacity $V_{Rd,max}$ is completely independent of f_{R3}. For slabs with high SFRC performance, in which $V_{Rd,c+s+f}$ increases significantly due to the fibre contribution, $V_{Rd,max}$ often becomes the determining factor in design. Taking into account the experimentally observed increase in load-bearing capacity of $V_{Rd,max}$ is crucial here in order to achieve improved predictive capability. Both design approaches could be improved with regard to $V_{Rd,max}$ by extending the factor η_{sys} in Eq. 9 and Eq. 14, by adding a fibre contribution to give η^{f}_{sys}. One possible formulation is as follows: $\eta^{f}_{sys} = \eta_{sys} + x \cdot f_{ftud}$, where x represents a calibration factor based on the experimental results. First positive results for such a formulation can be found in (Faustmann, 2025).

6 Conclusions

In this paper, the design approaches according to MC20 and FprEC2 for shear-reinforced SFRC slabs were systematically validated by comparing the calculated results with 23 new test results. Design calculations using both approaches yield safe results. It is evident that the steel fibre contribution according to MC20 realistically reflects the effect observed in the experiments. In FprEC2, the calculated fibre contribution is 25% lower than in MC20 and is highly conservative when compared with the experimental results.

In particular, neither of the two design approaches currently takes into account the positive effect of steel fibres on failure at the level of maximum punching strength, which is associated with increased load-bearing capacities and rotational capabilities. This should be incorporated in future to bring the design closer to the experimental results observed.

7 References

Bekaert 4D. *Data sheet for steel fibers Dramix 4D 65/35BG. Online available:* https://www.bekaert.com/content/dam/corporate/dop/Datasheet_Dramix%204D%206535BG_en-US_20250424_6535BG_Dramix%204D.pdf, last access March 2026

Bekaert 5D. Data sheet for steel fibers Dramix 5D 65/60BG. Online available: https://www.bekaert.com/content/dam/corporate/dop/Datasheet_Dramix%205D%206560BG_en-US_20250424_6560BG_Dramix%205D.pdf, last access March 2026

DAfStb-Heft 614, 6. 2015. *Erläuterungen zur DAfStb-Richtlinie Stahlfaserbeton.* DAfStb Heft 614. Beuth, Berlin.

DIN EN 14651, 2007. “Test method for metallic fibre concrete - Measuring the flexural tensile strength (limit of proportionality (LOP), residual; German version EN 14651:2005+A1:2007. Beuth Verlag GmbH. doi: 10.31030/1386060.

Einpaul, J., F. Brantschen, M. Ruiz, and A. Muttoni. 2016. "Performance of Punching Shear Reinforcement under Gravity Loading: Influence of Type and Detailing." *ACI Structural Journal*, 113: pp. 827–838. doi: 10.14359/51688630

Faustmann, S.,2025. “Steel fibers and punching shear reinforcement – a combination for higher slab performance”, Dissertation, Technical University of Munich, Munich. https://nbn-resolving.org/urn:nbn:de:bvb:91-diss-20251117-1780717-0-4

Faustmann, S., and O. Fischer. 2023. "Durchstanztragverhalten von stahlfaserverstärkten Flachdecken mit Bügeln." *Beton- und Stahlbetonbau*, 119(1): pp. 2–11. doi: 10.1002/best.202300067

Faustmann, S., J. Landler, O. Fischer, U. Bauermeister, and J. Furche. 2024. "Punching shear behavior of steel fiber-reinforced slabs with Filigran® punching shear reinforcement." *Structural Concrete*: pp. 1–20. doi: 10.1002/suco.202400689

fib 2024. *fib Model Code for Concrete Structures (2020) (MC20). Ernst W. + Sohn Verlag.*

FprEC2 Final Draft FprEN 1992, 1-1. 2023. Eurocode 2 - Design of concrete structures - Part 1-1: General rules and rules for buildings, bridges and civil engineering structures.

FprEC2 BD. 2023. Background document to FprEN 1992-1-1:2023-04 (Formal-Vote-Draft).

German Guideline SFRC 2021. Deutscher Ausschuss für Stahlbeton, Richtlinie Stahlfaser Beton. Beuth, Berlin.

Hernández Fraile, D., E. Faccin, F. Minelli, G. Plizzari, and A. Muttoni. 2024. "Fibre orientation in SFRC slabs and consequences for punching shear and flexural resistance." *Engineering Structures*, 302(117364): pp. 1–19. doi: 10.1016/j.engstruct.2023.117364

Landler, J., and O. Fischer. 2019. "Steigerung der Durchstanztragfähigkeit und Duktilität durch die Zugabe moderner Hochleistungsstahlfasern." *Beton- und Stahlbetonbau*, 114(9): pp. 663–673. doi: 10.1002/best.201900025

Landler, J., and O. Fischer. 2021. "Durchstanztragverhalten stahlfaserverstärkter Flachdecken mit Durchstanzbewehrung." *Beton- und Stahlbetonbau*, 116(5): pp. 348–359. doi: 10.1002/best.202000102

Look, K., J. Landler, P. Mark, and O. Fischer. 2021. "Fasermengen und Leistungsklassen." *Beton- und Stahlbetonbau*, 116(S1): pp. 13–23. doi: 10.1002/best.202100004

Maya, L. F., M. Fernández Ruiz, A. Muttoni, and S. J. Foster. 2012. "Punching shear strength of steel fibre reinforced concrete slabs." *Engineering Structures*, 40: pp. 83–94. doi: 10.1016/j.engstruct.2012.02.009

Moraes Neto, B. N., J. A. O. Barros, and Melo, Guilherme S. S. A. 2013. "A model for the prediction of the punching resistance of steel fibre reinforced concrete slabs centrically loaded." *Construction and Building Materials*, 46: pp. 211–223. doi: 10.1016/j.conbuildmat.2013.04.034

Muttoni, A. 2008. "Punching Shear Strength of Reinforced Concrete Slabs without Transverse Reinforcement." *ACI Structural Journal*, 105: pp. 440–450. doi: 10.14359/19858.

Muttoni, A., and M. Fernández Ruiz. 2010. *MC2010: The Critical Shear Crack Theory as a mechanical model for punching shear design and its application to code provisions*: fib. The International Federation for Structural Concrete. doi: 10.35789/fib.bull.0057.ch03

Muttoni, A., and J. T. Simões. 2023. "Shear and punching shear according to the Critical Shear Crack Theory: background, recent developments and integration in codes." *Revista IBRACON de Estruturas e Materiais*, 16(3). doi: 10.1590/s1983-41952023000300002

Schmidt, P. 2020. *Punching in Shear-reinforced Flat Slabs and Column Bases*, Dissertation, RWTH Aachen University, Aachen. doi: 10.18154/RWTH-2021-01568

Ungermann, J., M. Kalus, M. Claßen, and J. Hegger. 2022. "100 Jahre Durchstanzen im Massivbau – Alles erforscht?" *Beton- und Stahlbetonbau*, 117(8): pp. 613–624. doi: 10.1002/best.202200039

Welsch, T., and M. Held. 2012. "Zur Geschichte der Stahlbetonflachdecke." *Beton-Stahlbetonbau*, 107(2): pp. 106–116. doi: 10.1002/best.201100075

8 Appendix

Table A1: Overview of the characteristics of all test specimens.

Test	h [mm]	d_v [mm]	$f_{cm,cyl}$ [N/mm²]	$f_{cm,cube}$ [N/mm²]	*Type* [-]	V_f [kg/m³]	$f_{R1,m}$ [N/mm²] | (%)	$f_{R3,m}$ [N/mm²] | (%)	ρ_l [%]	f_{yl} [N/mm²]	ρ_w [%]	$Ø_w$ [mm]	f_{ysw} [N/mm²]
SFRC slabs with <u>stirrups</u> as punching shear reinforcement													
M3_25_B10	250	186	44.5	51.5	5D	80	8.41|(12)	7.69|(13)	1.82	764	0.64	10	530
M0_25_B10	250	190	43.0	50.1	-	-	-	-	1.78	764	0.64	10	530
M3_25_B8	250	192	43.2	47.6	5D	80	9.87|(14)	8.95|(6)	1.76	764	0.34	8	566
4D80_B8_175	250	195	39.9	48.3	4D	80	9.95|(6)	8.48|(6)	1.74	735	0.35	8	504
4D40_B8_175	250	195	46.3	49.2	4D	40	5.70|(15)	5.76|(9)	1.74	735	0.35	8	504
4D40_B8_108	250	200	46.5	53.7	4D	40	5.92|(12)	5.71|(14)	1.08	988	0.34	8	542
4D20_B8_175	250	195	40.4	46.0	4D	20	2.98|(12)	3.55|(15)	1.74	735	0.35	8	504
00_B8_175	250	196	47.5	53.2	-	-	-	-	1.74	748	0.35	8	512
4D80_B6_175	250	200	50.8	60.4	4D	80	9.50(9)	7.68|(7)	1.69	735	0.19	6	493
4D40_B6_175	250	195	48.2	52.2	4D	40	6.18(12)	6.02|(8)	1.74	735	0.20	6	493
4D40_B6_108	250	200	48.4	55.1	4D	40	6.15(9)	6.43|(7)	1.08	988	0.19	6	561
4D20_B6_175	250	197	42.2	45.6	4D	20	2.75(7)	3.20|(9)	1.72	735	0.19	6	493
00_B6_175	250	199	49.6	53.1	-	-	-	-	1.74	748	0.19	6	585
SFRC slabs with <u>studs</u> as punching shear reinforcement													
M3_25_D20	250	195	39.5	43.6	5D	80	10.08|(18)	9.13|(12)	1.77	968	1.49	20	586
4D40_D20_175	250	194	41.6	47.8	4D	40	3.98|(29)	4.64|(25)	1.78	923	1.49	20	550
4D40_D20_175_red	250	196	30.8	32.6	4D	40	3.84|(21)	4.75|(21)	1.76	923	1.48	20	550
M0_25_D20	250	186	43.7	50.2	-	-	-	-	1.85	968	1.51	20	589
M3_25_D14	250	194	37.9	42.8	5D	80	10.16|(12)	9.23|(10)	1.78	968	0.73	20	537
4D80_D14_175	250	195	39.8	44.6	4D	80	8.16|(7)	7.01|(13)	1.77	900	0.73	14	552
4D80_D10_175	250	195	50.2	59.4	4D	80	9.47|(10)	7.71|(9)	1.77	900	0.37	14	551
4D40_D10_175	250	194	49.7	53.1	4D	40	6.06|(8)	6.12|(8)	1.78	900	0.37	10	546
4D40_D10_108	250	200	49.4	55.1	4D	40	5.79|(19)	6.12|(21)	1.08	988	0.37	10	546
00_D10_175	250	197	48.5	53.9	-	-	-	-	1.75	923	0.37	10	562

h:slab thickness; d_v: effective depth for punching and bending; $f_{cm,cyl}$: mean cylinder compressive strength; $f_{cm,cube}$: mean cube compressive strength; ***Type***: steel fibre type ; V_f: steel fibre content; $f_{R1,m}$: mean residual flexural tensile strength at CMOD = 0.50 mm according to EN 14651, determined from six specimens. Coefficient of Variation (COV[%]) is shown in brackets; $f_{R3,m}$: mean residual flexural tensile strength at CMOD = 2.50 mm according to EN 14651, determined from six specimens. Coefficient of Variation (COV[%]) is shown in brackets; ρ_l: flexural reinforcement ratio; f_{yl}: yield strength of flexural reinforcement; ρ_w: punching shear reinforcement ratio according to FprEC2; $Ø_w$: diameter of the punching shear reinforcement; f_{ysw}: yield strength of the punching shear reinforcement

Table A2: Ultimate loads and rotations, as well as calculated values according to design approaches for all specimens.

	Experiment			MC 2020				FprEC2		
Test	V_{Test} [kN]	ψ_{Test} [mrad]	V^{f}_{flex} [kN]	$V_{Rd,c+s+f}$ [kN]	$V_{Rd,max}$ [kN]	V_{Test}/V_{cal} [-]	ψ_{cal} [mrad]	$V_{Rd,c+s+f}$ [kN]	$V_{Rd,max}$ [kN]	V_{Test}/V_{cal} [-]
SFRC slabs with <u>stirrups</u> as punching shear reinforcement										
M3_25_B10	2186	16.9	3345	1898	1846	1.18	8.23	1950	1485	1.47
M0_25_B10	1989	16.6	3096	1343	2184	1.48	5.62	1585	1494	1.33
M3_25_B8	2343	16.3	3485	1744	2030	1.34	6.89	1684	1510	1.55
4D80_B8_175	2154	18.5	3364	1713	2001	1.26	6.70	1628	1489	1.45
4D40_B8_175	2058	16.2	3408	1603	2269	1.28	5.95	1529	1565	1.35
4D40_B8_108	1891	19.9	3162	1600	1954	1.18	8.69	1496	1380	1.37
4D20_B8_175	1687	13.8	3190	1396	2204	1.21	5.35	1400	1492	1.20
00_B8_175	1659	12.8	3232	1260	2445	1.32	4.55	1343	1583	1.24
4D80_B6_175	2430	16.9	3672	1731	2456	1.40	5.82	1525	1649	1.59
4D40_B6_175	1942	14.7	3454	1555	2379	1.25	5.56	1335	1515	1.45
4D40_B6_108	1861	17.9	3222	1535	2083	1.21	7.94	1343	1398	1.39
4D20_B6_175	1699	13.0	3264	1342	2328	1.27	4.81	1279	1531	1.33
00_B6_175	1643	11.4	3387	1249	2562	1.32	4.11	1281	1642	1.28
SFRC slabs with <u>studs</u> as punching shear reinforcement										
M3_25_D20	2866	33.9	3957	2611	2029	1.41	8.91	3578	1693	1.69
4D40_D20_175	2432	26.6	3797	2346	2043	1.19	9.18	3149	1715	1.42
4D40_D20_175_red	2076	23.1	3357	2240	1789	1.16	8.98	3157	1562	1.33
M0_25_D20	2153	27.2	3624	2087	1939	1.11	9.96	2950	1682	1.28
M3_25_D14	2584	26.5	3859	1985	1976	1.31	8.94	2182	1663	1.55
4D80_D14_175	2597	23.4	3769	1818	2209	1.43	7.56	2114	1697	1.53
4D80_D10_175	2619	20.4	4108	1740	2504	1.50	6.22	1695	1834	1.54
4D40_D10_175	2140	16.1	4007	1625	2470	1.32	5.87	1616	1818	1.32
4D40_D10_108	1884	19.0	3221	1617	2362	1.17	8.59	1525	1597	1.24
00_D10_175	1639	13.7	3886	1267	2487	1.29	4.27	1417	1825	1.16

V_{Test}: peak load in experimental test; ψ_{Test}: rotation at peak load in experimental test; V^{f}_{flex}: flexural strength according to yield line theory with consideration of the steel fibres; $V_{Rd,c+s+f}$: punching shear resistance inside the shear-reinforced area according to design code; $V_{Rd,max}$: punching shear resistance on the level of maximum punching strength according to design code; V_{Test}/V_{cal}: ratio V_{Test} over the minimum of $V_{Rd,c+s+f}$ and $V_{Rd,max}$

Fibre-Reinforced Shotcrete Test Methods: Impact of the Application Process and Analytical–Numerical Correlations

Todd Clarke[1,2], Peter Schaul[3], Des Vlietstra[4]

[1] : BarChip Inc. Kurashiki, Japan

[2] : Victoria University, Werribee, Australia

[3] : BarChip EMEA Ltd. Dublin, Ireland

[4] : BarChip Australia Pty Ltd. Queensland, Australia

Abstract

Reliable characterization of fibre reinforced concrete (FRC), and particularly fibre reinforced sprayed concrete (FRS - shotcrete), depends on selecting appropriate test methods capable of capturing post-cracking performance and in-situ behaviour. This paper reviews and evaluates key standardised testing approaches, including beam tests, square panel tests and the round determinate panel (RDP) test. Each method provides different insights into toughness, residual strength and crack propagation, and their suitability varies according to whether the specimens are cast or sprayed.

The application process plays a decisive role in the mechanical response. FRS typically exhibits fibre orientation and compaction effects that result in greater strength reductions in flexural beam tests than in cast specimens. In contrast, RDP testing exhibits generally lower reductions in residual capacity for sprayed materials, reflecting its more representative radial cracking pattern and its closer alignment with in-situ behaviour of shotcrete linings. This makes RDP testing particularly relevant for tunnelling and ground-support applications, in which sprayed materials dominate.

A further contribution of this work is to adopt previously developed methodologies that convert RDP load–deflection data into equivalent stress–crack-width (σ–w) behaviour, allowing direct analytical comparison with constitutive curves derived from beam tests. Field test data are used to demonstrate the correlation and highlight the robustness of RDP results for characterising FRS. The findings underscore the importance of test selection and support the effectiveness of RDP testing for realistic assessment of FRS performance and can support numerical modelling using field panel test data. In the paper, an advanced numerical model was prepared for further verification.

Keywords

Synthetic fibre reinforced concrete, FRC, RDP, test methods, verification, FEA

1 Introduction

Fibre reinforced concrete (FRC) is widely used as a structural material because fibres bridge cracks, improve post-cracking behaviour, and increase energy absorption. Depending on fibre type and dosage, this changes the brittle response of plain concrete into strain-softening or strain-hardening behaviour. Accordingly, the fib Model Code 2020 (2024) classifies structural FRC using experimentally determined residual strengths rather than fibre dosage alone.

Fibre reinforced sprayed concrete (FRS) is commonly used for primary ground support in tunnelling and underground construction. Its post-cracking response governs load redistribution, crack control, and serviceability. However, measured performance depends strongly on specimen geometry and test configuration (Parmentier et al., 2008).

FRC is commonly tested using notched beams according to EN 14651 (2005), with residual flexural strengths determined at specified crack mouth opening displacements. Similar procedures are given in ASTM C1609 (2019). Although simple and standardized, beam tests involve a small fracture area and only a limited number of fibres. This can cause significant scatter, particularly at fibre contents below 0.5% by volume (Minelli and Plizzari, 2015). Reported coefficients of variation range from 10% to 30% (Parmentier et al., 2008). This variability may reduce characteristic residual strengths and produce conservative stress-crack width relationships. The single crack plane also does not fully represent the multidirectional stresses in sprayed tunnel linings.

Panel tests better reproduce the structural behaviour of fibre reinforced linings. The Round Determinate Panel (RDP) test, standardized in ASTM C1550 (2020), uses a centrally loaded circular slab supported at three points. Three radial cracks develop, creating a larger fracture area and mobilizing more fibres than beam tests. Consequently, panel tests typically show lower scatter, with coefficients of variation of about 6–9% (Parmentier et al., 2008). Minelli and Plizzari (2015) also found round panels to provide more repeatable post-cracking results.

The RDP test better represents the biaxial stress field and distributed cracking of tunnel linings. Bernard (2002) identified strong correlations between beam and panel results at equivalent crack openings. Minelli and Plizzari (2015) further proposed a method for deriving stress-crack width relationships from panel load-deflection data. This allows panel results to be converted into residual strengths compatible with EN 14651 and the *fib* Model Code 2020 framework.

The distinction between cast FRC and sprayed FRS is also important. Spraying affects fibre orientation and compaction, while beam tests are highly sensitive to the fibres crossing a single crack plane. Preferential alignment parallel to the sprayed surface may therefore reduce measured beam strengths. The radial cracking pattern of the RDP test is less sensitive to fibre orientation, making it particularly suitable for sprayed concrete.

This study compares EN 14651 beam testing with the RDP method for cast and sprayed FRC. Field data are used to evaluate correlation, variability, and robustness. The derived constitutive relationships are then applied in analytical and numerical models. The study highlights the importance of test selection and supports RDP testing as a representative and statistically robust method for sprayed concrete in tunnelling and ground-support applications.

2 Experimental program

The experimental program was designed to evaluate the mechanical performance of two macro synthetic fibre types under both cast and wet mix sprayed conditions, using procedures representative of tunnelling and underground construction practice. The fibres assessed were BarChip 56 which is a fibre 56mm in length and BarChip 48, which is 48 mm in length and served as a benchmark for comparative purposes. Both fibres were tested at dosage rates of 4 kg/m³ and 7 kg/m³.

All sprayed specimens were produced under conditions consistent with site practice. The alkali free accelerator dosage was maintained within the typical project range of 6–8 % by weight of cement. Although it is common in laboratory panel production to reduce accelerator dosage to improve finish and reduce rebound, the program intentionally retained the full in situ dosage. This allowed the study to examine the influence of accelerator content on fibre distribution, early age behaviour, and the comparability between cast and sprayed specimens.

A single concrete mix was developed using locally available aggregates and cementitious materials. The target was to achieve at least 40 MPa compressive strength under sprayed conditions, accounting for the strength reduction typically associated with accelerator use. To ensure this performance margin, a 60 MPa design mix presented below in Table 1 was adopted for all testing.

Table 1: Mix Design of the experimental program for 1 m^3 concrete

Constituent	**Amount**		**Constituent**	**Amount**	
Cement	380	kg	Total Batch Water	195	litres
Fly Ash	50	kg	Superplasticiser	~ 4	litres
Silica Fume	20	kg	Retarder	1	litres
Coarse Aggregate 10/7mm	275	kg	Total Weight	2422	kg
Manufactured Sand	1159	kg	Fibre reinforcement	4 and 7	kg
Fine Sand	341	kg			
Slump 200 +/- 20mm,					

Flexural performance was assessed in accordance with EN 14651. Two moulding approaches were used to distinguish between individual-beam effects and bulk cast behaviour. In case of *Individual cast or sprayed beams* the beams were produced directly in single moulds measuring 150 mm × 150 mm × 550 mm. These specimens reflect the influence of mould boundaries, including potential fibre alignment along the walls. While in case of *Cast and cut or sprayed and cut beams* larger beam boxes measuring approximately 1000 mm × 550 mm were used to produce blocks from which six beams were sawn. This configuration reduces the "wall effect", providing a more representative assessment of fibre orientation and distribution in bulk concrete. Test results refer to these categories explicitly to distinguish between boundary affected and boundary free specimens. As part of the test programme, five sprayed RDP specimens, five cast RDP specimens, one cast and one sprayed beam box, and three cast and three sprayed individual beams were prepared for each test series and were cured underwater.

To characterise the influence of accelerator on early age strength, a dedicated core box was sprayed with accelerated concrete. Cores extracted from this box were tested in compression.

In parallel, standard cylinders were cast from the unaccelerated concrete to determine baseline compressive strength for the mix used in casting.

Both cast and sprayed ASTM C1550 round determinate panels were produced to evaluate energy absorption capacity under centrally applied loading, providing an additional performance metric complementary to EN 14651 beam testing.

3 Test results and analytical models

3.1 Standard results

Compressive strength was measured using both cast cylinders (i.e. unaffected by accelerator) and cores extracted from sprayed specimens. Table 2 depicts the 28-day results and illustrates the impact of accelerator on the compressive strength of the 4 mixes.

Table 2: Compressive strength results

Mix	**Dosage [kg/m^3]**	**Cast compressive strength** [MPa] **(CoV)**	**Sprayed compressive strength** [MPa] **(CoV)**	**Reduction due to accelerator** [%]
BC48	4	33.7 (0.9%)	32.2 (27.2%)	4.5
BC48	7	59.5 (2.9%)	46.2 (0.6%)	22.4
BC56	4	59.2 (2.1%)	40.7 (2.8%)	31.3
BC56	7	52.7 (1.1%)	33.8 (1.7%)	35.9

Except for the BC48-4kg sprayed samples (which exhibited low compressive strength in both cast and sprayed specimens), the accelerator significantly reduced the mixes 'compressive strength. This was expected, as highlighted by Galobardes et al (2014), hence why the mix design was developed to produce a 60 MPa shotcrete. As is becoming more common practice in civil shotcrete projects, EN 14651 beam specimens were sprayed and cast as described in section 2.

The results clearly depict a critical difference between sprayed and cast specimens. Through the spraying process, both the impact of accelerator (as seen from the compressive strength results) and fibre alignment can be seen. Second to this, the choice of moulding method also plays a critical role in the outcome. Table 3 shows that spraying or casting individual beams give significantly higher results than spraying or casting larger panels and subsequently sawing beam specimens from these. The walls in the individual moulds create a preferential alignment of the fibres (which would be even more significant for very stiff fibres), and care should be taken if assessing in-situ performance from individual beam results, as the “wall effect” (Juhasz 2020) does not exist in a sprayed tunnel lining, for example. Table 3 highlights the average f_R values and the CoV for each set of beams.

The ASTM C1550 (2020) RDP was used to assess the toughness behaviour of each fibre-reinforced concrete. Engaging a much larger cracked area than the EN 14651 beams, the RDP generally produces sets of results with a significantly lower CoV than that observed from the notched beam test. The impact of spraying on the results can be clearly seen, with significantly lower results observed for sprayed panels compared to cast panels. Table 4 displays the average toughness values for each mix along with the associated CoV for each set of panels.

Table 3: Key results from EN 14651 tests at 28 days age

Set	Mould configuration	Strength LOP f_L [MPa] (CoV)	Strength CMOD1 $f_{R,1}$ [MPa] (CoV)	Strength CMOD2 $f_{R,2}$ [MPa] (CoV)	Strength CMOD3 $f_{R,3}$ [MPa] (CoV)	Strength CMOD4 $f_{R,4}$ [MPa] (CoV)
BC48 4 kg/m^3	Sprayed	4.7 (4.3%)	1.93 (11%)	2.73 (5.6%)	3.03 (11%)	2.73 (11%)
	Cast	7.53 (4.1%)	2.67 (5.7%)	4.1 (2.8%)	4.87 (6.6%)	4.07 (3.8%)
	Sprayed & Cut	3.67 (13%)	1.1 (26%)	1.22 (28%)	1.27 (29%)	1.15 (32%)
	Cast & Cut	5.5 (9.3%)	1.43 (35%)	2.12 (37%)	2.43 (36%)	2.35 (38%)
BC48 7 kg/m^3	Sprayed	4.13 (11%)	2.33 (18%)	3.2 (11%)	3.2 (10%)	3.37 (17%)
	Cast	6.47 (3.6%)	3.5 (10%)	5.53 (9.3%)	6.13 (5.7%)	6.23 (12%)
	Sprayed & Cut	4.2 (15%)	1.68 (57%)	2.42 (56%)	2.55 (53%)	2.45 (53%)
	Cast & Cut	6.65 (5%)	2.72 (19%)	4.45 (18%)	5.28 (14%)	5.2 (16%)
BC56 4 kg/m^3	Sprayed	4.53 (8.4%)	1.77 (32%)	2.57 (29%)	2.8 (27%)	2.8 (23%)
	Cast	6.4 (4.7%)	1.67 (18%)	2.43 (21%)	2.6 (24%)	2.43 (21%)
	Sprayed & Cut	4.5 (7%)	1.3 (11%)	1.77 (18%)	1.93 (17%)	1.83 (21%)
	Cast & Cut	5.1 (4.4%	1.28 (21%)	2.08 (20%)	2.7 (26%)	2.72 (27%)
BC56 7 kg/m^3	Sprayed	4.4 (0 %)	2.1 (8.2%)	3.23 (13%)	3.57 (13%)	3.57 (13%)
	Cast	6.27 (6.6%)	2.83 (7.3%)	4.9 (2%)	5.07 (4.1%)	4.6 (3.8%)
	Sprayed & Cut	3.55 (25%)	1.1 (49%)	1.67 (64%)	1.8 (61%)	1.65 (57%)
	Cast & Cut	5.32 (38%)	2.7 (12%)	3.65 (10%)	3.67 (12%)	3.5 (20%)

Table 4: Key results from ASTM C1550 tests at 28 days age

Set	Mould configuration	Peak Load [kN]	Toughness [J]			
			5 mm	10 mm	20 mm	40 mm
		(CoV)	(CoV)	(CoV)	(CoV)	(CoV)
BC48 4 kg/m^3	Sprayed	23.2 (8.5%)	47.1 (19%)	87 (21%)	145 (19%)	200 (17%)
	Cast	32.9 (4.6%)	73 (6.8%)	145 (9.8%)	254 (11%)	366 (13%)
BC48 7 kg/m^3	Sprayed	25.5 (7.7%)	64 (12%)	135 (13%)	245 (14%)	363 (13%)
	Cast	31.6 (9.5%)	95 (1.6%)	215 (4.4%)	404 (6.2%)	600 (9.7%)
BC56 4 kg/m^3	Sprayed	24.4 (6.1%)	48.9 (3.2%)	96 (5.4%)	170 (6.5%)	257 (6.8%)
	Cast	30.8 (4.7%)	67 (10%)	136 (10%)	237 (10%)	350 (10%)
BC56 7 kg/m^3	Sprayed	24.2 (5.7%)	62 (11%)	134 (8.2%)	241 (2.8%)	356 (5.6%)
	Cast	30.2 (3.9%)	94 (2.4%)	213 (2.9%)	398 (3.5%)	600 (4.4%)

3.2 Derivation of Stress vs. Crack width from RDP's

As the ASTM C1550 test does not include any direct crack width measurement, the derivation of the stress vs. crack width curve requires the estimation of crack width through other means. An alternative to measuring crack width directly is the virtual energy-based yield line method, which derives a simplified crack width relationship from the point load displacement. In this approach, the uniaxial flexural capacity of the material at the point of cracking is combined with an assumed failure pattern to estimate the point load capacity, from which crack width can then be inferred kinematically — without any direct crack measurement (Minelli & Plizzari, 2015).

While the yield line method was originally formulated for nominally plastic materials, meaning its suitability for FRC exhibiting post-crack softening behaviour warrants careful

scrutiny, the experimental validation presented by Minelli & Plizzari (2015) justifies its use fo r this further analysis of RDP results. Equation 1 presents the formula used to convert central deflection to crack width:

$$w = \frac{\sqrt{3}\delta t}{r} \quad (1)$$

where w is the maximum crack width at the bottom of the panel (a function of the crack rotation angle multiplied by the thickness), δ is the post-crack deflection at the centre of the panel (slightly less than the total central deflection at the centre due to elastic deformation of the panel prior to cracking) (Bernard, 2020), t is the average panel thickness, and r is the distance from the centre of the panel to the supports (in this case, 375 mm).

It is suggested by Bernard (2020) that the post-crack flexural strength derived from the RDP is sensitive to panel thickness due to the softening behaviour of FRC, particularly at the larger crack widths. Thinner panels will exhibit a higher flexural strength at a given central deflection than a thicker panel for numerous reasons; however, a modification to the thickness correction factor was proposed by Bernard (2020), to enable a simplified method to be adopted for deriving stress values from the RDP that are independent of thickness. ATSM C1550 includes the following formula for determining the corrected load, P, based on panel thickness and diameter:

$$P = P'\left(\frac{t_o}{t}\right)^{\alpha}\left(\frac{d_o}{d}\right) \quad (3)$$

where P' is the measured load resistance, t_o is the nominal panel thickness (75 mm), t is the measured panel thickness, d_o is the nominal panel diameter (800 mm), d is the measured panel diameter and $\alpha = 2.0 - \delta_C/40$. Bernard proposed a modification to the α factor, which has subsequently been adopted in this work to revise the corrected load for implementation in the derivation of the residual flexural strength from the RDP's. The adopted α factor is:

$$\alpha = 2.0 + \frac{24 - {\delta_c}^2}{30\delta_c} \leq 2 \quad (4)$$

where δ_C is the panel's central deflection as measured by the test method. Based on this, the force value is corrected to account for thickness variations and subsequently, the residual strength values (f_{Ri}) are derived according to Equation (5) (Bernard 2020).

$$f_{Ri} = \frac{2rP}{\sqrt{3}t_o^2 R} \quad (5)$$

where R is the radius of the panel.

3.3 Comparison EN14651 vs ASTM C1550 residual strengths

Residual strengths from both the ASTM C1550 RDP's and the EN 14651 beams have been derived, and the average values are plotted in Figure 1 (a) to (d) for each mix, respectively, as a function of crack width. Using specimens that most closely replicate in situ behaviour, the stress-crack width results derived from the RDP's are compared with the results from the specimens that were sprayed into the large box and sawn into EN 14651 beams. Note that the beam results are plotted as a function of crack width, rather than CMOD, as nominated by the standard, to allow direct comparison with the RDP stress-crack width curves. CMOD is converted to crack width at the tip of the notch using equal triangles (with the assumption that plane sections remain plane). A simplified formula for this conversion is provided in Equation 6 (Minelli & Plizzari, 2015).

$$w_{CTOD} = 0.786 \times CMOD \quad (6)$$

These results show good alignment between the residual strengths derived from the RDP's and those from the EN 14651 beams. The drop after cracking in the RDP is slightly less significant than that observed in the beams, however in majority of cases the two show very similar trends, particularly at ULS (i.e., f_{R3}).

3.4 Constitutive Law

Finally, the ultimate goal of these tests is to extract a constitutive law for the FRC material that can be adopted and applied in design calculations. Based on the test data and the inherent COV in the two test methods, the f_{Ftsd} and f_{Ftud} values have been derived according to *fib* Model Code 2020 (2020) for the BC56 4kg set and compared in Table 5.

Table 5: f_{Ftsd} and f_{Ftud} values

Set	Mould configuration	f_{Ftsd} [MPa]	f_{Ftud} [MPa]
BC56 4 kg/m^3	Sprayed RDP	0.40	0.35
	Cast RDP	0.50	0.47
	Sprayed & Cut Beam	0.31	0.30
	Cast & Cut Beam	0.24	0.32

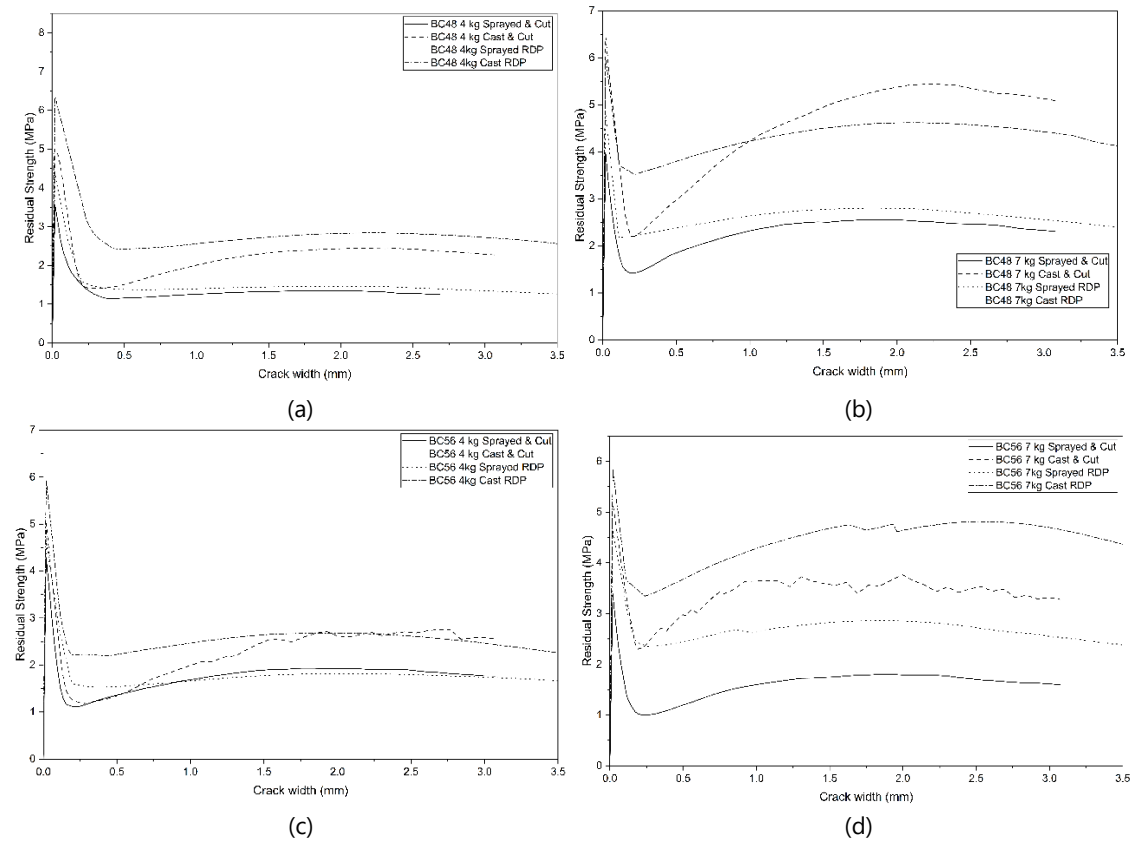


Figure 1: Stress vs crack width derived from both RDP's and sawn beams for (a) BC48 4kg, (b) BC48 7kg, (c) BC56 4kg and (d) BC56 7kg

With the lower scatter of the RDP test and the more representative failure mechanism, the final design values that can be adopted range from 15% to 75% higher than if derived from the beam tests. This difference is significant for design. Because the fib Model Code 2020 derives

characteristic and design values by penalising the mean strength in proportion to its coefficient of variation (CoV), the far greater scatter of the sawn beams (CoV of the residual strengths exceeding 50% for several sprayed-and-cut sets (Table 3)), against markedly lower values for the RDP (Table 4) drives the beam-based design values disproportionately downward. This behaviour is consistent with the wider literature, which reports that the high within-batch variability of beam tests has burdened fibre-reinforced shotcrete design with excessive and uneconomic conservatism (Bernard, 2013; Parmentier et al., 2008), and that characteristic values obtained from small-scale specimens are unrepresentative of, and unduly penalising for, full-scale structures (Cavalaro et al., 2015). Importantly, the higher RDP-derived values are not the result of a relaxed safety format; they follow from reduced test-induced scatter and a failure mechanism that more closely reproduces the in-situ lining. Therefore, they constitute a more reliable, not a less safe, basis for design, provided the adopted partial safety factors continue to reflect the residual tensile strength variability of FRC (Cugat et al., 2020). Adopting the RDP as the reference test thus removes conservatism embedded in the test method rather than in the material, enabling more economical fibre dosages without a corresponding reduction in structural reliability.

While the weight of an RDP can be quite large relative to a beam, the beam box required to produce representative results from sprayed concrete weighs twice as much, at 195 kg. Hence, using RDPs to derive stress crack width results can be a simpler, more efficient method than the currently adopted EN 14651 beams.

4 Numerical inverse analysis

4.1 Material model of concrete and FRC

The concrete was simulated using an advanced constitutive law based on combined failure surfaces. This class of material models enables the representation of the distinct mechanical responses of concrete under tensile and compressive loading, including elastic–plastic and brittle behaviour, compressive and tensile strength limits, and fracture energy dissipation. Various constitutive frameworks have been proposed in the literature for this purpose. The most widely adopted combinations include Von Mises–Rankine, Drucker–Prager–Rankine, and Menétrey–Willam–Rankine criteria, with the Rankine surface typically governing the tensile domain.

It is important to emphasize that these formulations primarily define the peak strength envelope of the material and do not inherently capture the post-cracking softening response. To account for the residual load-carrying capacity after cracking, additional constitutive relationships must be introduced. In the present study, the post-cracking behaviour of fibre-reinforced concrete (FRC) was modelled in accordance with the ITAtech guidelines (ITAtech Activity Group Support, 2015). Crack initiation is assumed to occur when the principal tensile stress exceeds the tensile strength of the concrete. Following crack formation, a residual stress is transmitted across the crack surfaces as a function of crack opening displacement. The stress transfer mechanism is associated with an energy dissipation parameter known as the fracture energy (G_f). This parameter is influenced by aggregate characteristics, including shape (rounded or angular), size distribution, and the quality of the bond between aggregate particles and the cementitious matrix.

The incorporation of fibres increases the fracture energy (G_{Ff}), thereby improving ductility and post-cracking performance. This modelling concept is commonly referred to as the

modified fracture energy approach (Juhász, 2013). In the present numerical models, the enhanced fracture energy was represented by a constant residual tensile strength parameter, f_{Ftu}, calibrated to the specific FRC mix.

Concrete was modelled using three-dimensional solid brick elements and a combined fracture–plasticity constitutive law (Cervenka and Papanikolaou, 2008). Tensile behaviour was represented by a smeared crack and crack band approach with crack initiation governed by the Rankine criterion, while compressive behaviour followed the Menétrey–Willam (1995) failure surface. The uniaxial compressive stress–strain relationship was defined according to Eurocode 2 (Eurocode, 2004), and crack width evolution was derived from the inverse-analysis-based stress–crack opening relationship using the characteristic length concept. This framework enables objective energy dissipation and realistic simulation of crack initiation and propagation in quasi-brittle materials.

4.2 Numerical modelling of the Round Determinate Panel (RDP) test

The numerical validation for BC48 specimens was performed using the finite element software ATENA, a specialized platform for the nonlinear analysis of concrete and reinforced concrete structures developed by Cervenka Consulting (Cervenka et al., 2026). This software enables the implementation of advanced constitutive models suitable for fibre-reinforced concrete, including the combined fracture–plasticity formulation described previously. To ensure accurate replication of the experimental conditions, the complete test configuration was explicitly modelled. This included the loading apparatus and the support conditions.

The analysis was conducted under displacement-controlled loading in order to accurately simulate both the pre-peak and post-peak structural response. Throughout the simulation, midpoint deflection and reaction forces were monitored to obtain the load–displacement relationship.

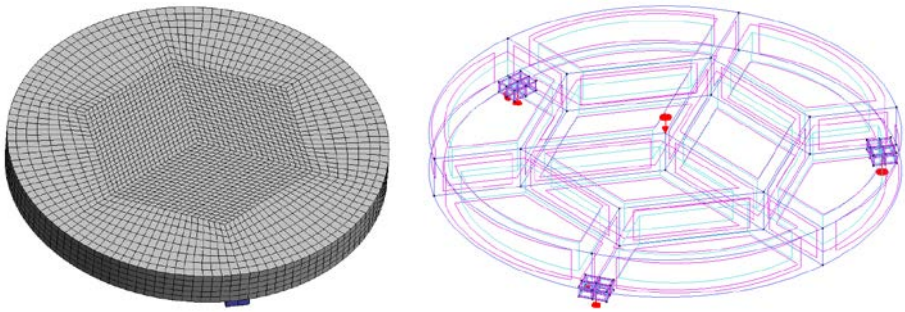


Figure 1: Structural hexahedra mesh of the RDP panel (left), and support - loading conditions (right)

A structured hexahedral mesh (Figure 2) was used to ensure accurate crack localization and propagation. The model was discretized with brick elements of 2.0 cm edge length, with five layers through the thickness to capture stress distribution and damage evolution. The mesh orientation was aligned with the expected crack paths to improve the representation of bending-induced cracking. Support and loading conditions were modelled according to ASTM (2010), with the displacement load applied directly at the centre of the element and without an additional steel distribution plate, enabling close reproduction of the local stress concentrations and boundary conditions of the physical test.

The material parameters were calibrated using the measured mechanical properties obtained from site tests at the age of 28 days. The compressive and tensile strengths were therefore defined on the basis of the real test results. The direct tensile strength was derived from beam test data: first, the flexural tensile strength was determined experimentally, and then the corresponding direct tensile strength was calculated back using the relationship proposed in TR34 (The Concrete Society, 2016). In this way, the input parameters of the constitutive model were linked directly to the measured material response.

The principal objective of the numerical calibration was to adjust the added fracture energy parameter so that the finite element model reproduced the same energy absorption values as those obtained experimentally at deflections of 5, 10, 20, and 40 mm. This criterion was selected because energy absorption is a key performance indicator for fibre-reinforced concrete under flexural loading and provides a robust basis for assessing the adequacy of the post-cracking response predicted by the model. The results of the finite element analysis are presented in Table 6.

Table 6: Mean results of the RDP test and FEA model

Casting method	Dosage (kg/m^3)	Energy absorption of the test [J]				Energy absorption of the FEA [J]			
		5 mm	10mm	20mm	40mm	5 mm	10mm	20mm	40mm
Sprayed	4 kg/m^3	47	87	145	200	52	97	152	224
Cast	4 kg/m^3	73	145	254	366	84	165	262	364
Sprayed	7 kg/m^3	64	135	245	363	82	161	255	356
Cast	7 kg/m^3	95	215	404	600	130	264	462	654

Based on the results, it can be observed that the finite element analysis showed very good agreement with the experimental results at all measured displacement levels for both the sprayed and the cast specimens. This indicates that the calibrated material model was able to capture the structural response with sufficient accuracy not only in the initial loading stage, but also in the post-cracking range characterized by increasing deflection and energy dissipation. The close correspondence between the numerical and experimental energy absorption values confirms that the selected modelling approach, together with the adopted fracture energy calibration procedure, is suitable for reproducing the flexural behaviour of both production technologies.

4.3. The inverse analysis

Inverse analysis is commonly used in the modelling of fibre-reinforced concrete to identify constitutive parameters that cannot be determined directly from standard mechanical tests and must instead be derived by fitting the numerical response to experimental results (Jepsen et al., 2018; Baby et al., 2013). This approach is particularly important for the characterization of the post-cracking tensile behaviour of fibre-reinforced concrete, since flexural tests provide only indirect information on the intrinsic tensile response of the material (Baby et al., 2013).

In the present study, the material parameters previously defined on the basis of the RDP test were used to develop a numerical model of a three-point bending beam test following the standard EN 14651 test arrangement. The EN 14651 method evaluates the behaviour of fibre-reinforced concrete by means of the load–CMOD relationship obtained from a simply supported notched beam subjected to a central point load (EN 14651, 2005).

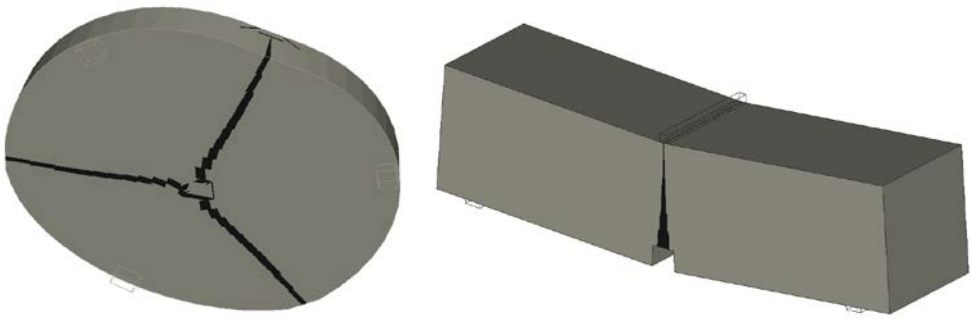


Figure 2: Crack propagation of RDP (left) and EN 14651 beam test (right) models

The aim of the inverse analysis was to determine the material parameter required for further analytical design. For this purpose, the beam test was simulated using the same material parameters that had previously been calibrated from the RDP test. Although the fibre orientation was not modelled explicitly, the material model was derived from tested panels whose performance inherently depends on the actual fibre orientation; therefore, the effect of fibre orientation was included implicitly. The main output parameter of the analysis was the f_{Ftu} value, which can serve as a basis for subsequent analytical design. The f_{Ftu} parameter was determined according to the rigid-plastic material idealization adopted in the fib Model Code 2020 framework, in which the post-cracking tensile behaviour of fibre-reinforced concrete is related to residual strength parameters obtained from bending tests (di Prisco et al., 2013). Figure 2 shows the crack propagation of RDP and beam models.

Accordingly, the load–CMOD curve obtained from the numerical analysis was first used to determine the f_{R3} parameter, and the f_{Ftu} value was then calculated from this result following the *fib* Model Code approach (di Prisco et al., 2013). Finally, the f_{Ftu} values obtained from the inverse analysis were compared with those derived from the experimental beam test results. The results and the corresponding differences are presented in Table 7. This comparison provides an assessment of how accurately the material model calibrated on the basis of the RDP test can reproduce the residual design parameters obtained from the EN 14651 beam test.

Table 7: Mean results of the inverse analysis

Casting method	**Dosage (kg/m^3)**	**Residual flexural strength of the test**	**Residual flexural strength of the FEA**	**Difference**
		$f_{Ftu.test}$ [MPa]	$f_{Ftu.FEA}$ [MPa]	[-]
Sprayed	4 kg/m^3	0.42	0.41	3%
Cast	4 kg/m^3	0.81	0.80	1%
Sprayed	7 kg/m^3	0.85	0.76	10%
Cast	7 kg/m^3	1.76	1.59	9%

For this comparison, the results of those beam tests were used in which the specimens had been cut from large cast or sprayed panels. In this way, it could be ensured that the wall effect did not have a significant influence on the measured response, and that the structural behaviour observed in the panel tests remained consistent with that obtained from the beam specimens. This approach was particularly important for the assessment of sprayed and cast materials, since the specimen preparation method may influence fibre orientation and distribution.

Based on the results summarized in Table 7, it can be concluded that the inverse analysis provided a good estimation of the residual flexural strength in all investigated cases. The

difference between the values derived from the experimental tests and those obtained from the finite element analysis remained limited for all specimen types and fibre dosages. The maximum deviation was 10%, which can be regarded as acceptable, particularly when considering the inherent scatter of fibre-reinforced concrete test results.

A generally good agreement can be observed for both casting methods. At the lower fibre dosage of 4 kg/m^3, the correspondence between the experimental and numerical results was especially close, with deviations of only 3% for the sprayed specimens and 1% for the cast specimens. At the higher dosage of 7 kg/m^3, the differences increased to 10% for the sprayed specimens and 9% for the cast specimens. Although these deviations are still within an acceptable range, they indicate that the accuracy of the inverse analysis slightly decreases with increasing fibre content.

It can also be seen that, in the case of sprayed panels, the differences were slightly higher than those observed for the cast specimens. This tendency may be related to the more pronounced variability in fibre orientation and distribution resulting from the spraying process, which can influence the post-cracking behaviour and, consequently, the residual strength parameters derived from the tests. A similar trend can be identified for the higher fibre dosage, where the discrepancy between test and numerical results became larger for both production methods. Nevertheless, the overall agreement confirms that the inverse analysis procedure is capable of providing a reliable estimate of the f_{Ftu} parameter and can therefore be considered suitable for deriving input values for further analytical design.

A comparison of the numerical and analytical approaches indicates that both methods are capable of providing a satisfactory estimation of the mean f_{Ftu} value. Based on the comparison with the experimental results, the numerical procedure showed the higher overall accuracy, with an average deviation of approximately 6%, whereas the analytical method resulted in an average difference of about 12%. It can further be observed that the closest agreement between the numerical and analytical predictions was obtained for the sprayed specimens with a fibre dosage of 7 kg/m^3. At the same time, the numerical model generally provided more accurate estimates at the lower fibre dosage level, indicating that the predictive capability of the numerical approach was strongest in the less heavily fibre-reinforced mixes. In addition, while the numerical model consistently underestimated the f_{Ftu} value, the analytical method overestimated it in almost all cases, indicating that the numerical inverse analysis provides results on the safe side.

In conclusion, deriving the f_{Ftu} value from panel test results can be particularly useful in the design of shotcrete linings. In many cases, structural verification requires not only the assessment of energy absorption, but also the preparation of normal force–moment interaction diagrams, for which the f_{Ftu} parameter is essential. In this respect, sprayed panel test results may provide a more representative basis for design than traditional beam tests, especially when the beams are cast. Since fibre orientation and distribution in shotcrete are strongly influenced by the spraying process, panel tests produced under realistic application conditions can better reflect the actual structural behaviour. Therefore, the presented methods can provide a more accurate basis for further analytical design.

5 Concluding remarks

The study shows that the selection of the test method has a major influence on the measured post-cracking behaviour of fibre-reinforced concrete, especially for sprayed applications, where fibre orientation and accelerator effects strongly affect the results. The experimental results indicate that round determinate panel testing provides lower scatter and a more representative assessment of sprayed concrete performance than conventional beam testing, particularly when compared with beams affected by wall-induced fibre alignment. The analytical conversion of panel test results into equivalent stress–crack width relationships demonstrated good agreement with beam-based residual strengths, supporting the use of RDP testing as a basis for constitutive characterization and design. The numerical modelling and inverse analysis further confirmed that material parameters calibrated from panel tests can reproduce both panel energy absorption and beam-derived f_{Ftu} values with acceptable accuracy. In conclusion it can be stated that deriving design parameters directly from sprayed panel tests can provide a more reliable and realistic basis for the analytical design of shotcrete linings than relying solely on traditional beam testing.

6 Acknowledgements

The Authors acknowledge the support provided by BarChip Inc. in funding this work, Cooma Sand & Concrete for preparation of the shotcrete mix, Endacom for providing equipment and personnel for spraying of the samples and K&H Geotechnical Services for conducting the tests described in this paper.

7 References

ASTM C1609/C1609M-19, 2019. *Standard Test Method for Flexural Performance of Fiber-Reinforced Concrete (Using Beam With Third-Point Loading)*, ASTM International, West Conshohocken, PA.

ASTM C1550, 2020. *Standard Test Method for Flexural Toughness of Fiber Reinforced Concrete (Using Centrally Loaded Round Panel)*, ASTM International, West Conshohocken, PA.

Baby, F., Graybeal, B., Marchand, P., and Toutlemonde, F., 2013. "UHPFRC tensile behavior characterization: inverse analysis of four-point bending test results," *Materials and Structures*, 46, pp. 1337-1354.

Bernard, E.S., 2002. "Correlations in the behaviour of fibre reinforced shotcrete beam and panel specimens," *Materials and Structures/Matériaux et Constructions*, 35, pp. 156-164.

Bernard, E.S., 2013. "Development of a 1200-mm-Diameter Round Panel Test for Post-Crack Assessment of Fiber-Reinforced Concrete," *Advances in Civil Engineering Materials*, 2(1), ASTM International.

Bernard. E. S., 2020. "Correlations in Performance of Fiber-Reinforced Concrete Assessed Using EN 14651 and Modified ASTM C1609/C1609M-19 Beam Tests". *Advances in Civil Engineering Materials.* 64–80, pp. https://doi.org/10.1520/ACEM20210127

Cavalaro, S.H.P., and Aguado, A., 2015. "Intrinsic scatter of FRC: an alternative philosophy to estimate characteristic values," *Materials and Structures*, 48, pp. 3537–3555.

CEN, 2004. “EN 1992-1-1:2004+A1:2014 Eurocode 2: Design of concrete structures - Part 1-1: General rules and rules for buildings,” *European Committee for Standardization*, Brussels, Belgium

Červenka, J., and Papanikolaou, V.K., 2008. “Three dimensional combined fracture-plastic material model for concrete,” *International Journal of Plasticity*, 24(12), pp. 2192-2220.

Červenka, V., Jendele, L., and Červenka, J., 2026. “ATENA Program Documentation Part 1.” *Cervenka Consulting*, Prague, Czech Republic.

Cugat, V., Cavalaro, S.H.P., Bairán, J.M., and de la Fuente, A., 2020. “Safety format for the flexural design of tunnel fibre reinforced concrete precast segmental linings,” *Tunnelling and Underground Space Technology*, 103, 103500.

di Prisco, M., Colombo, M., and Dozio, D., 2013. “Fibre-reinforced concrete in fib Model Code 2010: principles, models and test validation,” *Structural Concrete*, 14(4), pp. 342-361.

EN 14651, 2005. *Test method for metallic fibre concrete — Measuring the flexural tensile strength (limit of proportionality (LOP), residual)*, European Committee for Standardization (CEN), Brussels.

fib, 2024. *fib Model Code for Concrete Structures 2020*. fédération internationale du béton (fib), Lausanne.

Galobardes, I.,Salvador, R., Figueiredo, A., Cavalaro, S. & Rueda, A., 2014. “Wet mix sprayed concrete set accelerating admixtures: Comparison between traditional aluminate based accelerators and new formulations of alkali free accelerators.” 10.13140/2.1.3097.3447.

ITAtech Activity Group Support, 2015. *ITAtech Design Guidance for Precast Fibre Reinforced Concrete Segments - Draft Report*, ITAtech Report No. 7 / Draft, July 2015.

Jepsen, M.S., Damkilde, L., Löfgren, I., and Berrocal, C., 2018. “Adaptive inverse analysis (AIA) applied and verified on various fiber reinforced concrete composites,” *Materials and Structures*, 51, Article 79.

Juhász, K.P., 2013. “Modified fracture energy method for fibre reinforced concrete,” in *Fibre Concrete 2013: Technology, Design, Application*, Prague, Czech Republic, 12-13 September 2013, pp. 89-90, Paper p07.

Juhász, K.P., 2020. “Effects of pouring technique on orientation of steel and synthetic macrofibres in fibre-reinforced concrete.” *Concrete Structures, 21*, pp.2-10.

Menétrey, P., Willam, K.J., 1995. “Triaxial Failure Criterion for Concrete and its Generalization,” ACI Structural Journal, 92(3), pp. 311-318

Minelli, F., and Plizzari, G.A., 2015. “Derivation of a simplified stress–crack width law for Fiber Reinforced Concrete through round panel tests,” *Cement and Concrete Composites*, 58, pp. 33-43

Parmentier, B., Vandewalle, L., Van Rickstal, F., 2008. “Evaluation of the scatter of the postpeak behaviour of fibre reinforced concrete in bending: a step towards reliability,” in 7th RILEM International Symposium on Fibre Reinforced Concrete: Design and Applications (BEFIB 2008), Chennai, India, 17-19 September 2008, pp. 133-143

The Concrete Society, 2016. *TR34: Concrete industrial ground floors — a guide to design and construction*, 4th ed., Camberley: The Concrete Society

Theoretical and Experimental Correlation Between ASTM C1609 and MVD Tests

Victoria Olivera[1], Carlos Aire[2] and Luis Segura-Castillo[1*]

[1]: Instituto de Estructuras y Transporte, Universidad de la República, Uruguay

lsegura@fing.edu.uy

[2]: Instituto de Ingeniería, Universidad Nacional Autónoma de México, Mexico.

Abstract

ASTM C1609 is one of the most widely used standards for quality control of fibre-reinforced concrete pavement overlays such as whitetopping; however, it requires large beams and often exhibits instabilities. As an alternative, the MVD test uses cubic specimens, provides stable measurements, and can be performed in conventional laboratory testing machines. This study aims to evaluate its correlation with the four-point bending test in order to establish a transformation parameter that enables the use of the MVD as an equivalent quality control method. To obtain this parameter, both theoretical and experimental analyses were conducted. For the experimental campaign, specimens from three FRC mixtures were tested, including two types of synthetic fibres. Analytically, it is assumed that after cracking the behaviour of the specimen resembles two rigid bodies and that the crack opening tensile law is inherent to the material and, consequently, identical for both specimen types. The analysis yielded a theoretical transformation parameter of 4.32, while the experimental value is 4.27. These results show consistent agreement between both methods and support the feasibility of the MVD as a practical alternative for quality control in fibre reinforced concrete pavements. Additionally, the MVD test was carried out at a higher displacement rate as a preliminary assessment of test stability and potential reduction of testing time; these results were not used to determine the transformation parameter.

Keywords

Crack width, fibre-reinforced concrete, post-crack performance, flexure, pavement, whitetopping, quality control.

1 Introduction

Fibre-reinforced concrete (FRC) integrates discrete macrofibres (e.g., steel or polymers) into the concrete matrix, boosting residual tensile strength, ductility, and crack control. This makes FRC ideal for pavements and whitetopping rehabilitations, where fibres mitigate cracking, enhance flexural performance, abrasion resistance, and joint load transfer (ACI Committee 544, 2018; Fédération Internationale du Béton (fib), 2024; Zerbino et al., 2022).

Currently, one of the most widely used tests for the design and quality control of FRC pavements (ASTM, 2019) is the four-point bending test (4PB) specified in ASTM C1609 (ACI Committee 544, 2018). In this test, a beam measuring 150 × 150 × 500 mm^3 is subjected to four-point bending under a controlled loading rate specified by the standard, while the applied load is recorded as a function of deflection. From these data, key parameters such as the limit of proportionality, residual strengths, and toughness are obtained, which are commonly used for FRC characterization and structural design. However, its implementation involves relatively large specimens, specialized instrumentation, and requires a closed-loop servo-controlled testing system to ensure stable capture of the post-cracking response (ASTM, 2019) (Banthia & Islam, 2013).

As an alternative, the Montevideo test (MVD) is an indirect tensile test that uses a notched cubic specimen (150 × 150 × 150 mm^3). Under the standard procedure, the specimen is loaded at a displacement rate of 0.5 mm/min. A wedge is driven into the notch to induce a single crack, while steel angles provide steel-to-steel contact during loading (Segura-Castillo et al., 2024). Figure 1 shows the test in progress. The method can be performed using conventional testing machines and offers practical advantages due to the smaller specimen size, which simplifies casting, transport, handling and reduces testing time, thus reducing costs.



(a) (b)

Figure 1: MVD test: a) Testing Machine, b) detail of test sample (Olivera et al., 2026)

To define a linear transformation between 4PB and MVD tests, a transformation parameter k^{4PB} is defined as the factor that allows the results obtained from the MVD test (F^{MVD}) to approximate those from the four-point bending test (F^{4PB}), i.e. $F^{4PB} = k^{4PB} F^{MVD}$.

Limited data exist on correlation between MVD and 4PB results. (Cornelius et al., 2019) tested three mixes (plain, 20 kg/m^3 steel fibres, 30 kg/m^3 steel fibres): three 4PB beams and four MVD cubes each. The experimental transformation parameter obtained for the force corresponding to a displacement at midspan equal to L/150 (F_{150}) was 3.33 and 3.88, for the mixture with 20 kg/m^3 and 30 kg/m^3, respectively.

Although the MVD test offers practical advantages compared to the 4PB test—such as smaller specimens and simpler instrumentation—the overall test duration remains of the same order of magnitude, mainly due to the prescribed displacement rate. Increasing the loading rate could therefore represent an additional improvement to further reduce testing time.

However, previous studies have shown that the loading rate may influence the mechanical response of fibre-reinforced concrete. (Stephen & Gettu, 2019) evaluated the flexural behavior of polypropylene fibre-reinforced concrete (PFRC) using three-point bending tests (EN 14651) at CMOD rates ranging from 0.01 to 100 µm/s. The results showed that the tensile strength decreased by about 40% between the highest and lowest loading rates, highlighting the need to assess the effect of rate when modifying testing procedures.

In this context, the present study investigates the correlation between the MVD and four-point bending (4PB) tests through both a theoretical and an experimental approach. The experimental program includes two independent campaigns conducted in Uruguay and Mexico, evaluating three FRC mixtures with different fibre type and dosage, plus one without fibres for control. In parallel, an analytical study of the cracked sections in both tests is performed to derive a theoretical value of the transformation parameter k^{4PB} . This paper presents preliminary results of a companion article currently submitted for publication (Olivera et al., 2026). In addition, this work experimentally evaluates a modified version of the MVD test in which the loading rate is increased.

1.1 Previous experience – Validation of rigid-body rotation on MVD test

A preliminary experimental campaign was carried out to investigate whether the post-cracking behaviour observed in the MVD test corresponds to a rigid-body rotation mechanism (Palacios, 2024). It is presented here to provide support for one of the hypotheses adopted in the analytical model developed in this work.

The experimental campaign included six specimens produced with the same mixture ($f_{c,m,28d}$ = 65 MPa, $E_{c,m,28d}$ = 33 GPa; double hooked-end steel fibres, 30 kg/m³, 60 mm length). Using a Digital Image Correlation (DIC) analysis, the crack opening as a function of height, *w(y)*, was determined. Figure 2 presents the experimentally measured *w(y)* curves together with the theoretical prediction.

It can be observed that all experimental curves exhibit an approximately linear trend. Furthermore, as the Crack Mouth Opening Displacement (CMOD) increases, the experimental curves become increasingly linear and progressively closer to the theoretical curve predicted by rigid-body behaviour.

Table 1 presents the range of determination coefficients obtained for the experimental curves. Since all R^2 values are higher than 0.90, it can be concluded that a linear approximation provides a good representation of the crack opening profile, and the error of this approximation reduces when increasing CMOD.

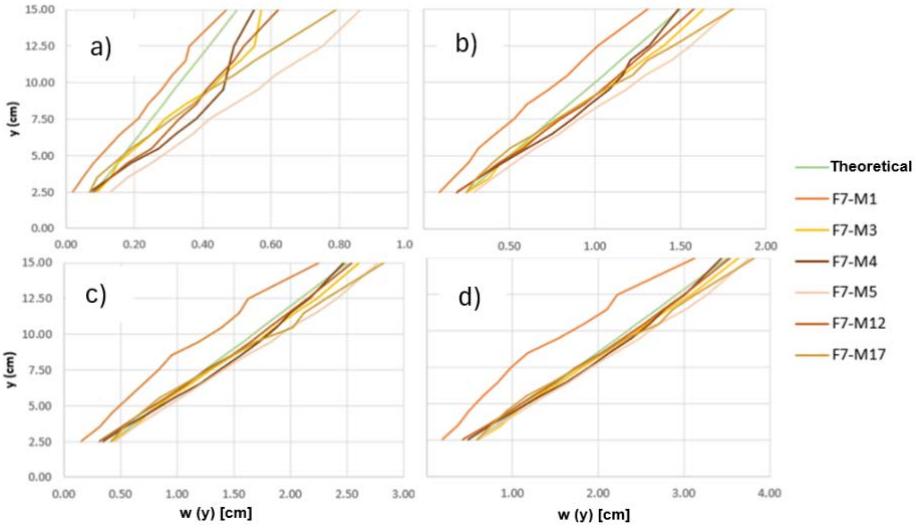


Figure 2: Crack opening as a function of height (*y*) measured through DIC, and theoretical curve. For a) CMOD=0.5 mm b) CMOD= 1.5 mm c) CMOD= 2.5 mm d) CMOD=3.5 mm

Table 1: Envelope of determinator factors for experimental curves.

CMOD (mm)	R^2_{min}	R^2_{max}
0.5	0.916	0.998
1.5	0.979	0.998
2.5	0.988	0.998
3.5	0.976	0.999

Although these results are not conclusive, given the limited number of specimens and the differences in fibre content and mechanical properties with respect to the mixtures studied in this work, they indicate that the rigid-body rotation assumption after cracking is plausible. Further experimental investigation is required to assess the general validity of this assumption.

2 Analytical model

This section analytically derives the relationship between the force applied in the 4PB, F^{4PB}, and the force applied in the MVD, F^{MVD}, for equivalent crack openings in both specimens.

Consider a beam (height h_{4PB}, width b_{4PB}) subjected to the 4PB test and a notched cube (ligament height h_{sp}, width b_{MVD}) subjected to MVD test. The analytical model is based on the following assumptions:

H1 – *Rigid-body rotation*: After cracking, deformation localizes at a single section, and the two parts of the specimen rotate as rigid bodies about a point located at the compression edge. Consequently, the crack opening varies linearly along the height of the section.

H2 – *Equal crack opening range*: In both tests, the crack opening varies from zero at the compression edge to a maximum value $w_{\max}$ at the tension edge.

H3 – *Compression localization*: Compressive stresses are assumed to be concentrated at the extreme fibre opposite to the crack mouth.

H4 – *Material law*: The stress-crack opening relationship $\sigma(w)$ is intrinsic to the material and therefore identical in both tests.

H5 – *Regularity of the constitutive law*: The function $\sigma(w)$ is continuous and integrable.

Figure 3 schematically shows the crack-opening distribution and stress profiles at the fracture section for both tests. The derivation proceeds by considering the tensile resultant T and its lever arm Z for each test and deriving moment equilibrium on both tests. This allows the relationship between F^{4PB} and F^{MVD} to be established.

Moment equilibrium about the compression edge equates internal tensile resultant T and lever arm Z:

$$4PB) \qquad T_{4PB}Z_{4PB} = \frac{F_{4PB}L}{6}$$

$$MVD) \qquad T_{MVD}Z_{MVD} = P_{eff}h_{sp} = k_{\mu}F_{MVD}h_{sp}$$

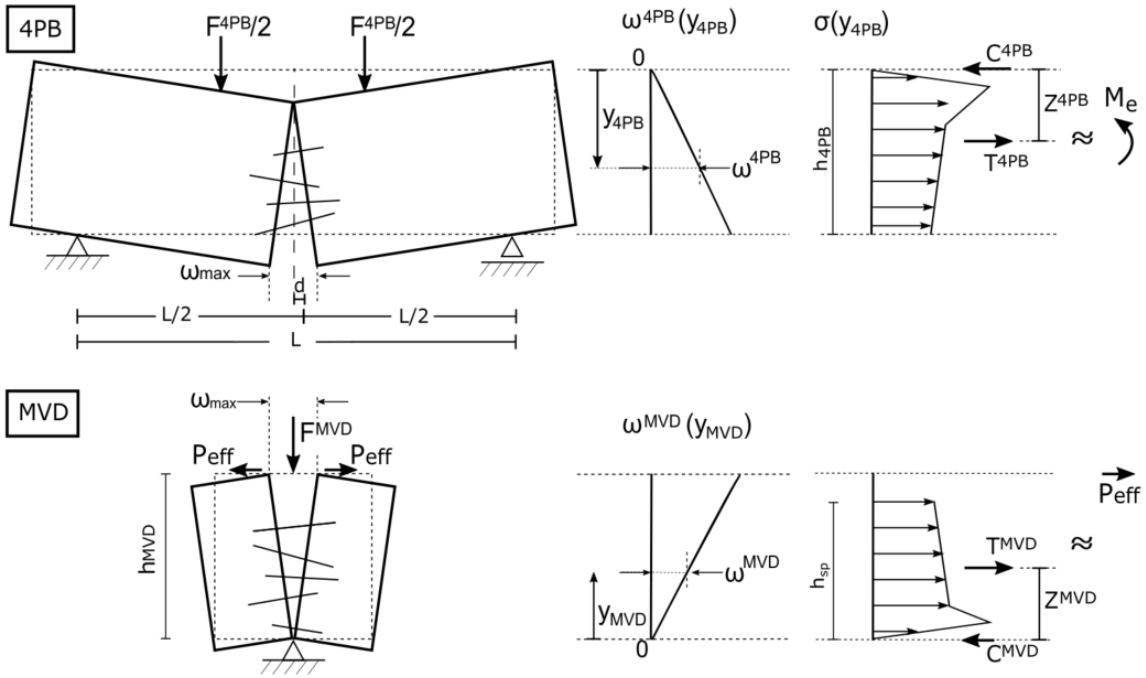


Figure 3: Fracture section during each test.

Introducing the change of variables $y_{MVD} = (h_{sp}/h_{4PB})y_{4PB}$, and definitions of the tensile resultant and its lever arm, the relationship (1) can be obtained, where the transformation parameter is defined (2)

$$F^{4PB} = 6k_{\mu}\frac{b_{4PB}}{b_{MVD}}\frac{h_{4PB}^2 h_{MVD}}{h_{sp}^2 L}F^{MVD} \qquad (1)$$

$$k^{4PB} = 6k_{\mu}\frac{b_{4PB}}{b_{MVD}}\frac{h_{4PB}^2 h_{MVD}}{h_{sp}^2 L} \quad (2)$$

The detailed calculations are presented in the companion article (Olivera et al., 2026). Using the friction parameter obtained from literature (Segura-Castillo et al., 2018) $k_{\mu} = 1.5$, standard dimensions ($h_{4PB} = h_{MVD} = 150$ mm, $h_{sp} = 125$ mm, $L = 450$ mm, $b_{4PB} = b_{MVD} = 150$ mm), Eq. 2 simplifies to a theoretical k^{4PB} value

$$k_{teo}^{4PB} = 4.32 \quad .$$

This result directly depend on k_{μ}, which is influenced by the loading rate as well as by the geometry and material properties of both the wedge and the contact plate. To date, no experimental studies have been carried out to evaluate the effect of varying these parameters on the friction parameter. Further research is required to assess how these variables influence this parameter.

3 Experimental program

Three different FRC mixtures were studied, incorporating two types of synthetic fibres at different dosages. For each mixture, at least six beams and 12 cubes were tested under the 4PB and MVD tests, respectively. Results were compared to obtain the transformation parameter. In addition, at least three cylinders per mix were tested to monitor compressive strength.

3.1 Casting and materials

Two different base mix designs were used: one named “MX” and the other one named “UY”, the first one made on México, and the second one on Uruguay. Different types and amounts of fibres were added to these base mixtures, resulting in three different compositions. These mixes are identified using the following code: **XX-YY-Z**, where **XX** indicates the base mixture, **YY** corresponds to the fibre type used (F4 and F5), and **Z** denotes the fibre dosage (in kg/m³). An exception to this nomenclature is the mixture without fibres, which is designated as “MX-C”.

The fibres used were synthetic, with lengths of 48 mm and 54 mm. Their properties are presented in Table 2. Table 3 summarizes the average compressive strength and coefficient of variation (CV) of each mix design. All coefficients of variation are below 5%, which falls within the expected range for this property.

Table 2: Fibres´ properties

Property	Unit	F4	F5
Base resin	-	Polyolefin	Modified Olefin
Length	mm	48	54
Tensile strength	MPa	465	640
Specific gravity	-	0.90	0.90-0.92
Elastic modulus	GPa	7.5	10

Table 3: Average compressive strength for each mix design.

Mix	Average compressive strength [MPa] (CV [%])
UY-F5-2.6	34.9 (2.4)
MX-C	48.0 (3.8)
MX-F4-4	44.6 (0.5)
MX-F4-6	42.3 (3.1)

All cubes from MX mixtures were obtained by sawing previously tested beams into two halves. From each mixture, 6 cubes were tested under standard MVD (displacement rate of 0.5 mm/min) and 6 under modified MVD. Modified test is explained in section 3.2.

3.2 Testing

Age. All prisms tested in accordance with ASTM C1609 were tested at 28 days old. Cubes from UY-F5-2.6 mixture were tested at 28 days, whereas all cubes corresponding to MX-YY-Z mixtures were tested at 98 days. For this study, any variation in concrete strength beyond 28 days is neglected as a simplifying assumption. This assumption should be recognized as a limitation of the present work.

Curing. Specimens from UY-F5-2.6 were cured in a water tank and removed from it on the day of testing, no more than 3 hours in advance. Specimens from MX mixtures were cured in a moist curing chamber and removed one day prior to testing.

MVD test. The testing machine records load as function of actuator displacement (δ), thus it is necessary to convert displacement to Crack Mouth Opening Displacement (CMOD). The transformation function is given by Eq (3), and is derived from a geometry analysis of the wedge, as detailed in (Segura-Castillo et al., 2018).

$$CMOD = (\delta \quad - \delta_L) 2tan(15°) \tag{3}$$

Where δ_L is the displacement at the peak corresponding to the limit of proportionality.

Standard and modified MVD test. The standard test was performed under an actuator displacement rate of 0.5 mm/min. A modified procedure was also evaluated: testing under a constant displacement rate of 2.0 mm/min.

3.3 Equivalence between displacement and CMOD in 4PB test

To compare results between both tests, all results were expressed as function of the CMOD. To do so, after testing each beam from UY-F5-2.6 mix under ASTM C1609, the average position of the crack was measured. The distance between the middle of the beam and the crack, d_i, was measured. This value was obtained by measuring d_1 and d_2, defined as the distances between the crack and the midspan section on each side of the beam, and computing their average. The mean vale, d_m, was then calculated from all beams, resulting in d_m=23.55 mm.

Once d_m is known, it is possible to estimate the CMOD as function of displacement (δ) for each beam. Figure 4 shows the post-cracking geometry of the beam, from which the relationship between the parameters of interest can be obtained through a kinematic analysis (Eq. (4)).

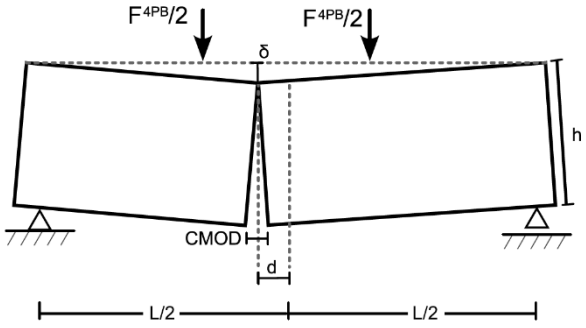


Figure 4: Representation of beam geometry after crack (Olivera et al., 2026).

$$CMOD = \frac{hL}{(L/2 - d)(L/2 + d)}\delta \quad (4)$$

Finally, the CMOD equivalent for a displacement of 0.75 mm (L/600) is 1.03 mm, and for 3.00 mm (L/150) is 4.11 mm, corresponding to F_{600} and F_{150}, respectively.

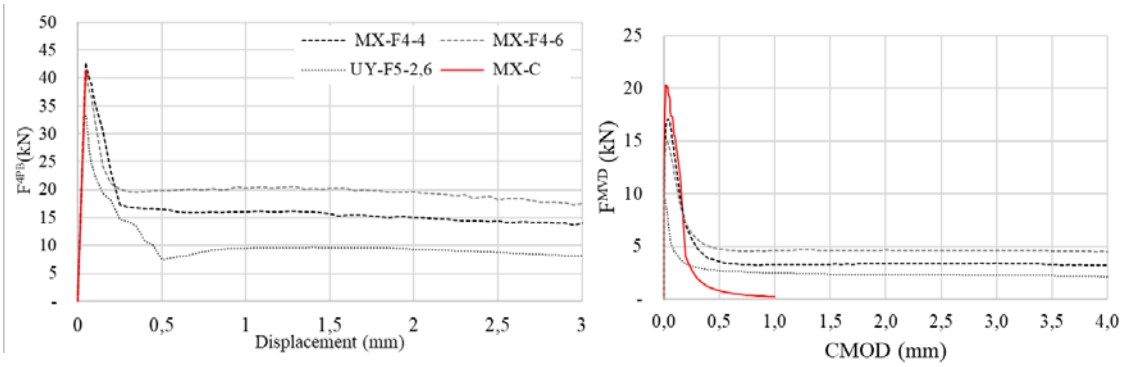
4 Test results and analysis

4.1 ASTM C1609 and standard MVD test

Figure 5a shows the mean load–displacement curves obtained from the ASTM C1609 test for each series, and Figure 5b shows mean load-CMOD curves obtained from the standard MVD test. All curves exhibit softening behavior, consistent with the use of synthetic macrofibres at these dosage levels. On both tests it can be observed that with higher dosages, higher residual strength is obtained.

The MX mixtures presented higher limit of proportionality (LOP) loads than the UY mixture, in agreement with their higher compressive strength. This trend is consistent with the empirical relationship proposed by ACI 318, which states that tensile strength scales with the square root of compressive strength. The 29% higher compressive strength measured for MX-F4-4 relative to UY-F5-2.6 suggests that its LOP should increase by a factor of approximately $\sqrt{1.29}$. This leads to an estimated LOP value of 5.54 MPa, whereas the experimental value obtained was 5.72 MPa. The resulting discrepancy of only 3% suggests that the observed differences in LOP can be largely explained by the variation in compressive strength.

During ASTM C1609 test from UY mixture, some beams experience post-peak instability. However, after instability the tests continued. No instability was observed during the MVD tests.



(a) (b)

Figure 5: Load–actuator displacement/CMOD curves a) ASTM C1609 test b) standard MVD test.

Coefficients of variation (CV) were calculated for each mixture and are presented on Table 4. Most CV values remain below 30%, which aligns with ranges commonly reported for post-cracking flexural tests on FRC. Both test results exhibit higher dispersion (≈14–30% for 4PB and 16-28% for MVD test) in residual strength compared to load at limit of proportionality (F_{LOP}) values (≈5–7% for 4PB and 7-9% for MVD test). This reflects the more homogeneous response of the cementitious matrix relative to the variability associated with fibre distribution and orientation.

Table 4: Coefficient of Variation for each mix on each load of interest.

	F_{LOP}		F_{600}		F_{150}	
	MVD	4PB	MVD	4PB	MVD	4PB
UY-F5-2.6	7%	5%	28%	30%	26%	28%
MX-F4-4	9%	5%	16%	14%	24%	15%
MX-F4-6	9%	7%	15%	21%	15%	23%

4.2 Standard vs. Modified MVD test

The modified test was applied only to mixtures MX-F4-4 and MX-F4-6. Results show that the load-CMOD response obtained with the modified setup follows the same general trend as that of the standard test (Figure 6). In addition, no instabilities were observed through the tests.

ANOVA tests were performed to assess the effect of the modified test procedure. At a significance level of 10%, no significant differences were found for mixture MX-F4-4 ($p = 0.74\ and\ p = 0.44$), while results for MX-F4-6 ($p = 0.09\ for\ both$) suggest that the increased loading rate may have affected the measured response.

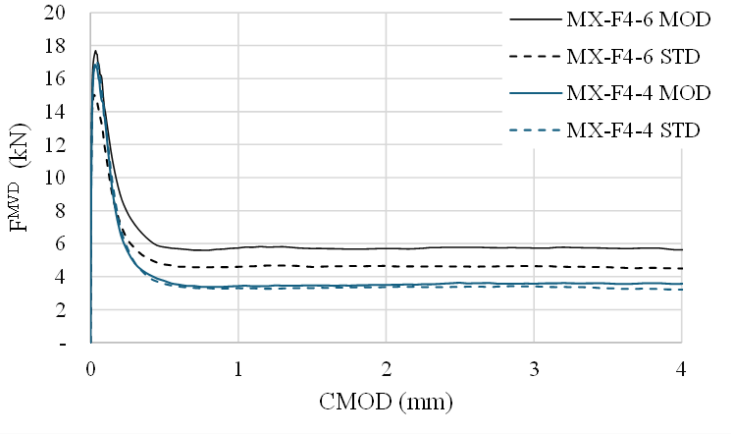


Figure 6: Load–CMOD curves for standard MVD (STD) and modified (MOD) test. Average results for each mixture.

Figure 7 shows average results obtained from standard against modified MVD test (F^{MVD}_{Std} and F^{MVD}_{Mod}, respectively) for each mix studied, for limit of proportionality results and residual strengths. This study, although preliminary, suggests that there can be an increase on resistance of up to 24% (CV 27%) when increasing velocity for a dosage of 6 kg/m^3. Further investigation is needed in this field. Additionally, it should be investigated whether the observed increase in strength is inherent to the material itself or results from the testing procedure (for example, due to changes in the interaction between the wedge and the steel plate when the loading rate is modified).

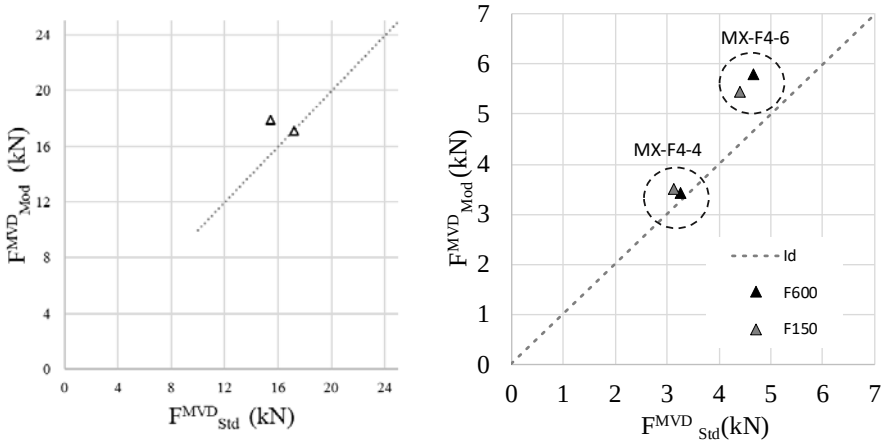


Figure 7: Average results of MVD test per mixture under Standard MVD vs. Modified MVD. a) Limit of proportionality b) residual strength

4.3 Transformation parameter

The experimental transformation parameter (k) was calculated as the slope of the best-fit line relating (F_{4PB}) and (F_{MVD}). In order to account for the variability within each experimental series, a Monte Carlo simulation was performed. For each of the six experimental series (considering three mixtures and two residual forces levels – F_{600} and F_{150}), force samples obtained from both the MVD and 4PB tests were used to calculate the sample mean and variance, which were taken as estimators of the corresponding population parameters.

Post-cracking strength was assumed to follow a normal distribution (Bernard & Xu, 2019). Since only a limited number of experimental replicates were available for each series, a Student's *t*-distribution was adopted to account for the uncertainty associated with small sample estimation during the Monte Carlo simulation.

From the resulting distribution, a 95% confidence interval was then obtained from the simulated results resulting in (CI=[3.57,5.03]), with a mean value of k_{exp}^{4PB}=4.27. Figure 8 show the mean result for each individual series, mean k_{exp}^{4PB} and confidence interval (CI).

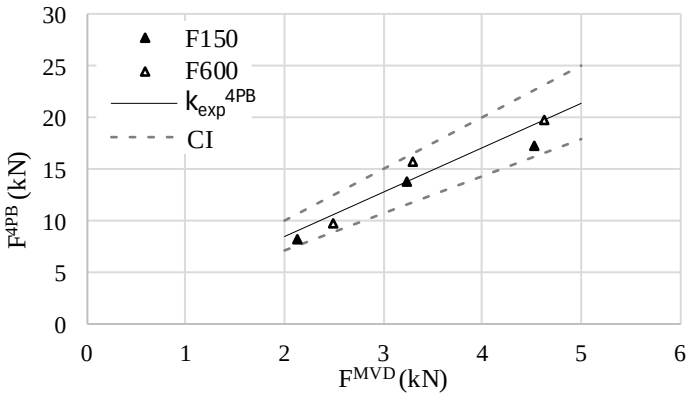


Figure 8: Mean results for each series of 4PB test against average results of MVD test, for each strength of interest, mean experimental transformation parameter, and confidence interval.

5 Conclusions

The transformation parameter between the four-point bending test (4PB) and the Montevideo (MVD) test was determined both experimentally and theoretically, yielding values of 4.27 and 4.32, respectively. The relative error of theoretical value with respect to experimental value is 1.17%.

Experimentally, three fibre-reinforced concrete mixtures were evaluated, using two types of fibres and two concrete matrices. Both tests exhibited similar load–displacement responses. However, the MVD test showed greater testing stability, as no specimen experienced unstable failure. Theoretically, the cracked sections were analyzed, assuming rigid-body rotation of the specimens. Obtained results show great agreement and suggest that MVD test could be a reliable alternative for 4PB test.

In addition, the effect of increasing the displacement rate in the MVD test was investigated as a preliminary assessment of test stability and the potential for reducing testing time. Since this evaluation was exploratory, these results were not considered in the determination of the transformation parameter. Six cubes per mixture were tested at a displacement rate four times higher than the standard rate. The results indicate that the test remains stable under this increased loading rate, while yielding slightly higher values compared to those obtained under standard conditions. This suggests that the MVD test could potentially be performed in a shorter time, further improving its advantages in terms of efficiency and cost. However, additional research is required to confirm these findings.

6 Acknowledgements

The authors gratefully acknowledge Barchip for providing materials, Rafael Leites, Diego Novello, and José Alexis Escobedo for their assistance with the experimental part.

7 References

ACI Committee 544. 544.4R-18: Guide to design with fiber-reinforced concrete. 2018.

ASTM. C 1609: Test Method for Flexural Performance of Fiber-Reinforced Concrete (Using Beam With Third-Point Loading). Epub ahead of print 1 May 2019. DOI: 10.1520/C1609_C1609M-19.

Banthia, N., & Islam, S. T. (2013). Loading Rate Concerns in ASTM C1609. Journal of Testing and Evaluation, 41(6), 1032–1036. https://doi.org/10.1520/JTE20120192

Bernard, E. S., & Xu, G. G. (2019). Normality of Post-Crack Performance Data for Fiber-Reinforced Concrete. Advances in Civil Engineering Materials, 8(1), 145–157. https://doi.org/10.1520/ACEM20180054

Cornelius V, Hasard D, Neme M, et al. Correlation between 4-point bending test and Montevideo test for the characterization of FRC. Krakow, Polonia: Proceedings of the Fib Symposium 2019: Concrete - Innovations in Materials, Design and Structures., 2019.

Fédération Internationale du Béton (fib). fib Model Code for Concrete Structures 2020. Lausanne, Switzerland, 2024.

Olivera V, Aire C, Segura-Castillo L. Correlation Between the Montevideo Test and ASTM C1609 for Fiber-Reinforced Concrete. ACI Structural and Materials Journals; Submitted.

Palacios, F. (2024). Análisis de losetas biempotradas de hormigón reforzado con fibras. Universidad de la República.

Segura-Castillo L, Monte R, de Figueiredo AD. Characterisation of the tensile constitutive behaviour of fibre-reinforced concrete: A new configuration for the Wedge Splitting Test. Constr Build Mater 2018; 192: 731–741.

Segura-Castillo L, Monte R, Galobardes I, et al. Determination of tensile residual strength of fibre reinforced concrete by a robust and simple test. Materials and Structures/Materiaux et Constructions; Vol. 57. Epub ahead of print 1 June 2024. DOI: 10.1617/s11527-024-02321-1.

Stephen SJ, Gettu R. Rate-dependence of the tensile behaviour of fibre reinforced concrete in the quasi-static regime. Materials and Structures/Materiaux et Constructions; 52. Epub ahead of print 1 October 2019. DOI: 10.1617/s11527-019-1405-2.

Zerbino R, Barragán B, Conforti A, et al. Hormigón Reforzado con Fibras. 2nd ed. Buenos Aires: Asociación Argentina de Tecnología del hormigón, 2022.

A stochastic mixing model for fibre distribution in fibre-reinforced concrete and its implications

Péter Károly Juhász[1,2]

[1] : Chief engineer in JKP STATIC Ltd, Budapest, Hungary.

[2] : Adjunct lecturer in Budapest University of Technology and Economics, Budapest, Hungary.

Abstract

In fibre-reinforced concrete, the distribution of fibres is generally assumed to be uniform, while their orientation is considered random. The spatial distribution of fibres can be effectively described using stochastic models. Under normal-consistency concrete conditions, fibre orientation may be assumed to be random; however, in the vicinity of the formwork, a certain degree of preferential alignment can be observed.

The most widely used method for determining material parameters is the three-point bending beam test. Owing to the small reference cross-sectional area, this test exhibits considerable scatter in the measured results. This variability is predominantly governed by the number and spatial position of fibres intersecting the fracture section. From a probabilistic viewpoint, this scatter is largely a statistical consequence of the limited fracture surface and the stochastic nature of fibre dispersion, rather than solely a material inconsistency. During evaluation, incorporating the fibre moment contribution leads to material parameters that are more representative of actual structural behaviour.

In real structural elements, the flexural load-bearing capacity of a cross-section is mainly governed by the same two factors, namely the number and position of fibres within the section. As the cross-sectional area increases, the relative statistical variability decreases, and the behaviour approaches the deterministic limit defined by the mean fibre distribution. Moreover, on-site fibre dosage control can be performed by evaluating measured fibre counts against a confidence interval derived from a stochastic mixing model at a prescribed confidence level.

To address these aspects, this paper introduces a novel stochastic mixing model for fibre distribution and demonstrates its applicability to material parameter evaluation, structural capacity assessment, and on-site quality control.

Keywords

Mixing model, stochastic modelling, fibre distribution, fibre-moment, quality control

1 Introduction

One of the main limitations in the application of fibre-reinforced concretes is the large scatter observed in the experimentally determined material parameters (Bernard, 2002; Parmentier, 2008; di Prisco et al, 2009; Sanal, I., Zihnioglu, 2013). This pronounced variability arises partly from the small reference volume of the test specimens (Juhász, 2025), and partly from the intrinsic scatter caused by the random spatial distribution of fibres (Cavalaro and Aguado, 2015). To obtain results with sufficient accuracy, a significantly larger number of specimens than those typically used in conventional concrete testing is required; accordingly, the relevant EN 14651 (2005) standard prescribes a minimum of 12 test specimens. Owing to the large scatter, the statistically derived characteristic values of the material parameters are often very low and, in some cases, may even become negative, rendering them unusable from an engineering perspective (Juhász, 2020).

Several approaches exist to mitigate the effect of large scatter. One option is to modify the specimen size in order to increase the reference volume or fracture surface. A representative example is the ASTM RDP test, in which the fracture surface area is significantly larger than that of standard beam tests. Consequently, the scatter of the test results is considerably reduced; moreover, further increasing the specimen size leads to an additional and substantial reduction in scatter (Bernard, 2013). Another approach involves the statistical evaluation of test results (Cavalaro and Aguado, 2015), as well as modified evaluation methods that explicitly account for the actual fibre positions within the specimen (Juhász, 2020).

It should be noted, however, that the pronounced scatter and the resulting low characteristic values are primarily associated with small-scale specimens. For larger reference volumes or cross-sectional areas, the scatter is significantly reduced. To account for this effect, certain guidelines recommend the use of mean test values (TR34, 2016) or allow for reduced partial safety factors when considering larger structural elements (*fib* Model Code, 2010; Richtlinie Faserbeton, 2008). The present paper aims to contribute recommendations for the further development of such approaches.

2 Intrinsic scatter due to fibre dispersion

In FRC, the distribution of fibres is characterized by the position of the centroid of fibres (O_f). The orientation of the fibres within a specified coordinate system is defined by their polar coordinates: α and γ (Fig. 1a). The proposed mixing model assumes a uniform dispersion of fibres, while the orientation of fibres remains uniform and stochastic. Local boundary effects (e.g. wall-effects) are neglected for standard beam dimensions, as their influence on global fibre statistics has been shown to be minor (Juhász, 2025). This model enables the determination of the number of intersection points of fibres across the cross-sectional area.

2.1 Distribution of fibres in the matrix

The number of fibres in a given volume V_0 is N_0 (Fig. 1b). Let us introduce N_d [1/m^3] as the dosage value, then $N_0 = N_d V_0$. The probability of a single fibre being in a volume V ($V \in V_0$) is:

$$P_1 = \frac{V}{V_0} \tag{1}$$

The probability that n fibres are located within a volume V can be described using a hypergeometric distribution. However, for large populations, where the sample size is small compared to the total population, the hypergeometric distribution can be approximated by a binomial distribution as follows:

$$P_{1,n} = \binom{N_0}{n} P_1^n \left(1-P_1\right)^{N_0-n} \tag{2}$$

with mean value (m_1), standard deviation (σ_1) and coefficient of variation (CV) given by:

$$m_1 = N_1 = P_1 N_0 = N_d V \tag{3}$$

$$\sigma_1 = \sqrt{N_0 P_1 \left(1-P_1\right)} \tag{4}$$

$$CV = \frac{\sigma_1}{N_1} = \frac{1}{\sqrt{N_0}} \sqrt{\frac{V_0}{V} - 1} \tag{5}$$

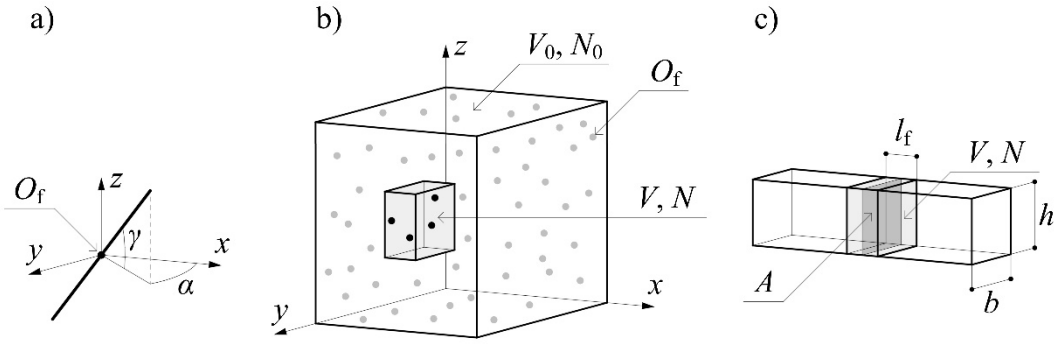


Figure 1: Distribution of fibres in the initial and reference volume (a) fibre local coordinate system, (b) V_0 and V, (c) interpretation of V in a beam specimen.

Let the fracture cross-section be A, which is assigned to volume V as shown in Fig. 1c, where l_f denotes the fibre length. The fibres within volume V can intersect cross-section A. Consider a standard-sized beam with $b = h = 150$ mm and l_f=50 mm. In Fig. 2a, the relative variability is shown as a function of the V/V_0 ratio for different dosages. When V_0=V, the relative variability becomes zero, as the number of fibres in V is equal to the total number of fibres in V_0. The volume of a standard beam is V_{beam} = 150×150×600 mm, and the corresponding relative variability is plotted in the diagram. It is clear that even for a beam volume, the relative variability approaches the maximum value. In practical terms, during the production of concrete beams, the maximum relative variation can be considered, which depends solely on the amount of fibres added and not on the total volume of mixed concrete. The values of maximum coefficient of variation (CV_{max}) as a function of the dosage in case of V_{beam} are plotted in Fig. 2b. If V_0 tends towards infinity, CV_{max} and the corresponding standard deviation can be determined as follows:

$$CV_{max} = \lim_{V_0 \to \infty} \frac{1}{\sqrt{N_d V_0}} \sqrt{\frac{V_0}{V} - 1} = \frac{1}{\sqrt{N_d V}} \tag{6}$$

$$\sigma_{1,max} = CV_{max} N_1 = \sqrt{N_d V} \tag{7}$$

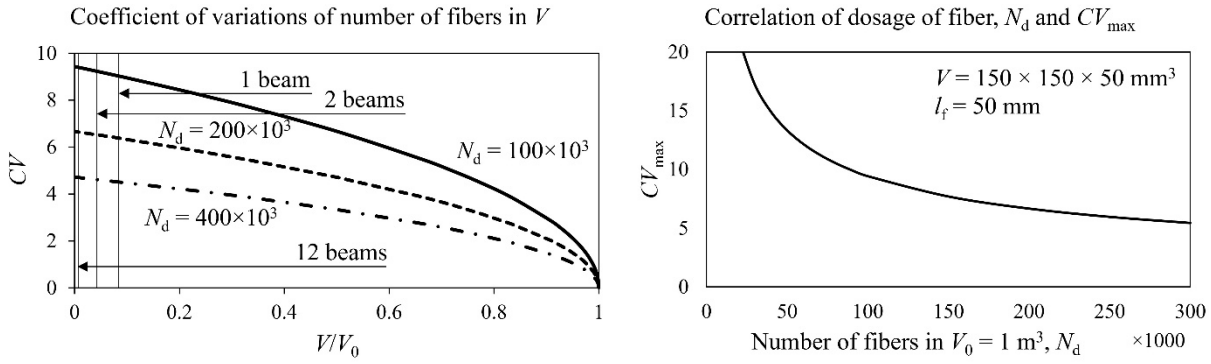


Figure 2: Coefficients of variation
(a) CV as a function of V/V₀ (b) CV$_{max}$ as a function of fibre dosage

The coverage interval (90% probability interval) of fibre quantity can thus be determined as follows:

$$N \in \left[N_1 - 1.645\sigma_{1,\max}; N_1 + 1.645\sigma_{1,\max} \right] \tag{8}$$

Furthermore, when the expected number of fibres is sufficiently large, the binomial distribution may be approximated by a normal distribution in accordance with the central limit theorem. Accordingly, the random variable N is assumed to follow a normal distribution with parameters m_1 and σ_1. In practical applications, σ_1 may be conservatively replaced by its maximum value, $\sigma_{1,\max}$.

2.2 Cross-sectional intersection of fibres

The probability of fibre intersection within volume V is 0.5, as reported in several studies in the literature (Naaman, 1972; Krenchel, 1975; Stroeven, 1978). The influence of the wall effect is already negligible for specimens of standard beam dimensions (Juhász, 2020b) and is therefore disregarded in the present analysis. The probability of fibre intersection follows a binomial distribution; therefore, the expected number of fibres intersecting the cross-section is:

$$m_2 = N_2 = P_2 N_1 = 0.5 N_1 = 0.5 N_d V \tag{9}$$

and the standard deviation of this is:

$$\sigma_2 = \sqrt{N_2 P_2 \left(1 - P_2\right)} = \sqrt{0.25 N_2} = \sqrt{0.125 N_d V} \tag{10}$$

2.3 Model formulation

The number of fibres intersecting the cross-section, given the fibre length and dosage, can also be determined in a single step by combining the distribution parameters into a single expression. In this case, the expected number of fibres intersecting the cross-section is:

$$N_3 = m_3 = P_1 P_2 N_0 = 0.5 N_d V \tag{11}$$

and its standard deviation and coefficient of variation are:

$$\sigma_3 = \sqrt{\sigma_1^2 + P_2^2 \sigma_1^2 + \sigma_2^2} = \sqrt{1.25\sigma_1^2 + \sigma_2^2} = \sqrt{1.25 N_d V + 0.125 N_d V} = \sqrt{1.375 N_d V} \tag{12}$$

$$CV_3 = \sqrt{5.5}\frac{1}{\sqrt{N_d V}} \tag{13}$$

The coverage interval (90% percentile interval) is:

$$N_i \in \left[N_3 - 1.645\sigma_3 ; N_3 + 1.645\sigma_3\right] \tag{14}$$

Eqs. (11)–(13) directly describe the statistical distribution of the number of fibres intersecting a given cross-section as a function of fibre dosage and fibre length. This formulation therefore links the stochastic mixing process at the volumetric level to the mechanical behaviour observed at the fracture section. It follows directly from Eq. (13) that the coefficient of variation decreases with increasing fibre dosage and increasing cross-sectional area, which explains the experimentally observed size effect in the scatter of bending tests.

The model demonstrates that the large scatter observed in standard beam tests is not primarily a material inconsistency, but a statistical consequence of limited fracture surface area and stochastic fibre dispersion.

3 Cross-section-dependent scatter due to fibre moment

In bending beam tests, not only the number of fibres intersecting the cracked section, but also their distance from the compressed zone of the cross-section is relevant (Bernard and Xu, 2017; Enfedaque et al, 2019). Even with the same number of fibres intersecting the cracked cross-section, the load–CMOD curves derived from FRC bending beam tests can exhibit a significant difference if the location of the fibres is different – for instance, if one sample has more intersecting fibres closer to the compressed zone than the other sample. In particular, the cross-section having more fibres closer to the compressed zone has a smaller moment capacity than that having more fibres farther from the cross-section, as shown in Fig. 3.

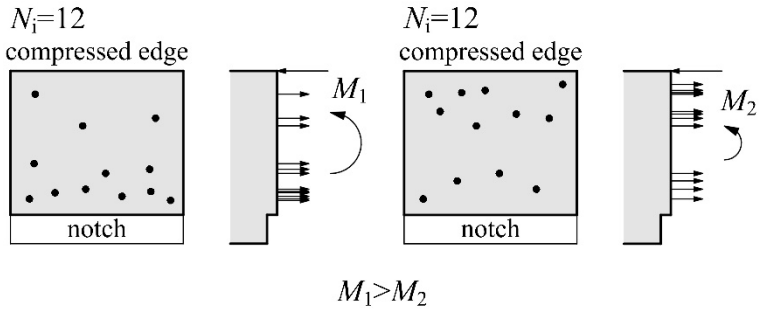


Figure 3: The effect of fibre position on the moment capacity of beams

After completing the beam test, the number and position of fibres on the fracture surface can be easily identified; however, determining the anchorage length and orientation of the fibres requires more advanced analysis. To parameterize the spatial distribution of fibres, Juhász introduced the concept of the fibre-moment (Juhász, 2015, 2020), which can be determined relatively easily and provides significant information about the tested beam. While the relationship between the number of fibres and the residual strength has been widely discussed in the literature (Barros et al, 2005; Lappa, 2007; Zerbino et al, 2012), only a few studies have considered the distance of fibres from the compressed zone (Bernard and Xu, 2017).

Based on this method, both the number of fibres in the cross-section and their distance from the compressed extreme fibre are analysed. Although the fibre orientation angle and anchorage length are not explicitly considered, previous research has demonstrated that the fibre-moment maintains a strong linear correlation with the residual strength (Juhász, 2018, 2020). The total fibre force distributed across the section is treated as a smeared tensile stress, consistent with established design recommendations, where this stress is assumed to remain approximately constant (RILEM, 2003; ACI, 1998; *fib* Model Code, 2012). As a result, it is reasonable to assume uniform fibre force within the cracked section, allowing the fibre-moment to be interpreted as a first-order moment. This parameter is unique to each tested beam and captures the spatial distribution of fibres across the section. The number of fibres is determined through visual inspection, which inherently introduces a degree of measurement uncertainty. However, in similar investigations, the discrepancy between fibre counts obtained via image analysis and manual counting was found to be negligible (Medeghini et al, 2025).

For precise determination, the fibre-moment can be expressed as follows:

$$S_{\mathrm{f,test}} = \sum_{s=1}^{N_i} z_s N_{\mathrm{i,s}} \tag{15}$$

where z_i is the distance associated with the fibre *i* from the compressed extreme fibre of the beam, with the thickness of the compressed concrete zone being neglected (see Fig. 4a).

The fibre-moment can also be calculated using a simplified approach by dividing the cross-section into horizontal bands (see Fig. 4b). Sensitivity analysis has shown that using five bands provides sufficient accuracy for practical purposes (Juhász, 2023). In this case, the fibre-moment can be determined as follows:

$$S_{\mathrm{f,test}} = \sum_{j=1}^{5} t_j N_{\mathrm{i,j}} \tag{16}$$

where t_j and $N_{\mathrm{i,j}}$ is according to Fig. 4b.

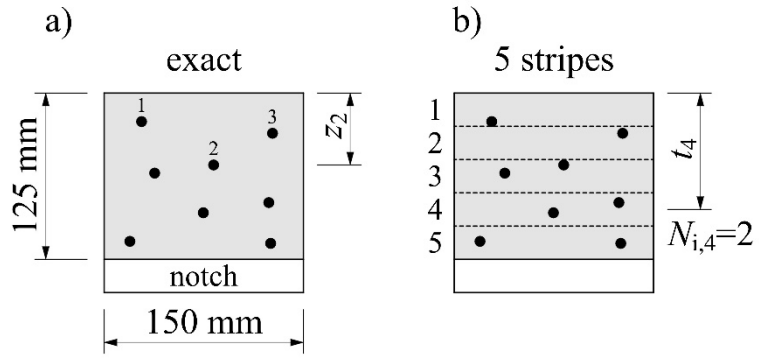


Figure 4: Determination of fibre-moment
(a) accurate calculation of fibre-moment (b) determination of fibre-moment using the band method.

The fibre-moment and residual strength values for individual beams are closely aligned along a straight line with a correlation coefficient $\delta > 0.9$, which allows for the elimination of variability due to the distribution of fibres during the evaluation of material parameters (Fig. 5). This strong correlation was observed for both steel and synthetic macrofibers, at both lower

and higher dosage levels, and across all residual strength parameters (Juhász, 2015, 2018; Tóth et al, 2017). A detailed description of the evaluation method can be found in (Juhász, 2020).

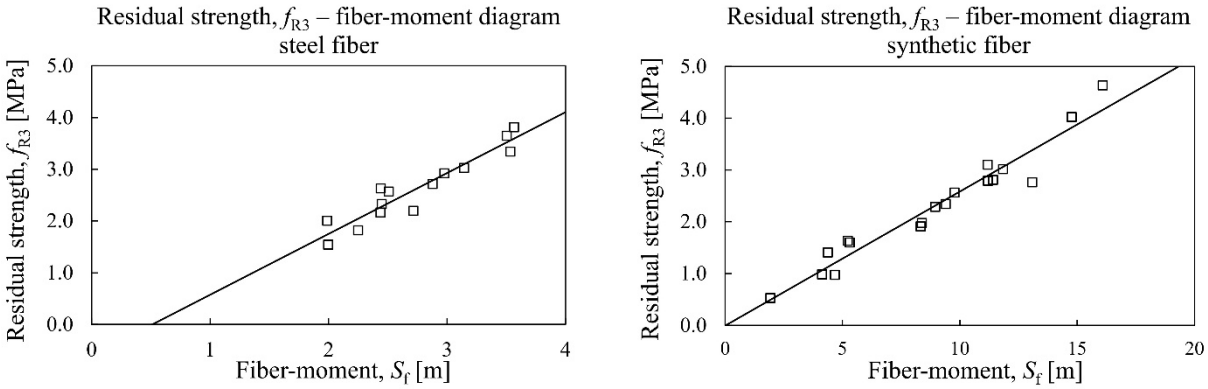


Figure 5: Residual strength ($f_{R,3}$) and fibre-moment (S_f) correlation diagram in case of (a) steel and (b) synthetic macrofibre

Assuming a perfectly homogeneous distribution, the centroid of the intersecting fibres coincides with the centroid of the cross-section. Under these conditions, an ideal fibre-moment can be defined:

$$S_{\mathrm{f,ideal}} = N_{\mathrm{i}} \frac{h}{2} \tag{17}$$

4 Improvement of beam test evaluation

The fibre-moments of the test specimens ($S_{\mathrm{f,j}}$) and the corresponding residual strength ($f_{\mathrm{R,i,j}}$) are approximately directly proportional, in other words, a larger fibre-moment corresponds to a larger residual strength. Consequently, a linear function can be fitted to the data of the complete set with linear regression, which is known as the reference function:

$$r\left(S_{\mathrm{f}}\right) = a\, S_{\mathrm{f}} + b \tag{18}$$

where:

$$a = \frac{\sum_{\mathrm{j=1}}^{\mathrm{n}} \left(S_{\mathrm{f,j}} - S_{\mathrm{f,m,t}}\right)\left(f_{\mathrm{R,i,j}} - f_{\mathrm{R,i,m}}\right)}{\sum_{\mathrm{j=1}}^{\mathrm{n}} \left(S_{\mathrm{f,j}} - S_{\mathrm{f,m,t}}\right)^2} \tag{19}$$

$$b = f_{\mathrm{R,i,m}} - S_{\mathrm{f,m,t}} a \tag{20}$$

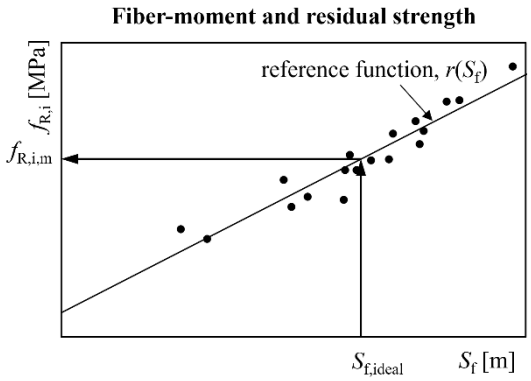


Figure 6: Mean residual strength evaluated from the reference function and ideal fibre-moment

If the effect of concrete is not considered, the values of the linear functions are expected to be approximately zero at the origin, which physically translates to the residual strength being zero at a fibre moment of zero.

If the expected number of fibres within the volume V is known, the mean value of the fibre moment can be inferred with the help of the ideal fibre-moment, Eq. (17). Subsequently, the mean residual strength ($f_{R,i,m}$) may be approximated by evaluating the reference function at this fibre moment (Fig. 6).

If the scatter of the results is interpreted as the distance from the reference curve, a characteristic reference curve may be defined by shifting the original reference curve. The value of the characteristic function evaluated at the mean fibre moment then represents the characteristic residual strength. A detailed description of this procedure is provided in (Juhász, 2020).

5 On-site verification of fibre content considering intrinsic scatter

The on-site verification of fibre quantity and mixing quality is of particular importance; therefore, based on the stochastic methods derived above, a testing procedure is presented that allows their assessment at a selected probability level. If the observed fibre count in a sample falls within this interval, the fibre dosage and mixing can be considered statistically acceptable.

The recommended procedure is as follows. From a given concrete mixer batch, three samples of volume V_t are taken, preferably from the beginning, middle, and end of the discharged concrete. In each sample, the number of fibres is counted, yielding $N_{t,1}$, $N_{t,2}$ and $N_{t,3}$. Two types of coverage intervals are then defined: one for the verification of fibre quantity and another for the assessment of mixing homogeneity.

For the verification of fibre quantity, the expected value and the standard deviation are calculated based on Eqs. (3) and (7):

$$N_t = N_d 3V_t \tag{21}$$

$$\sigma_t = \sqrt{N_d 3V_t} \tag{22}$$

Based on these values, the 90% probability interval is subsequently defined as:

$$\left(N_{t,1}+N_{t,2}+N_{t,3}\right)\in\left[N_t-1.645\sigma_t;N_t+1.645\sigma_t\right] \tag{23}$$

If this condition is satisfied, the fibre dosage and mixing can be considered compliant at the selected 90% reliability level.

To assess the quality of mixing, the counted values are evaluated separately in a similar manner:

$$N_{t,m}=N_d V_t \tag{24}$$

$$\sigma_{t,m}=\sqrt{N_d V_t} \tag{25}$$

$$N_{t,i}\in\left[N_{t,m}-1.645\sigma_{t.m};N_{t,m}+1.645\sigma_{t,m}\right]\quad i=1,2,3 \tag{26}$$

For the volume, the use of a standard 150 mm cube mould, or a formwork element of comparable dimensions, is recommended.

6 Concluding remarks

This paper investigates the scatter observed in fibre-reinforced concrete, which can be decomposed into intrinsic scatter and cross-section-dependent scatter. In both cases, the coefficient of variation decreases with increasing cross-sectional size and fibre dosage. This explains why the scatter of the standard small-scale three-point bending beam test (3PBBT) is particularly high and why it often results in unfavourable characteristic values. For fibre-reinforced concrete, the consideration of size effects therefore becomes an even more critical factor in the definition of material parameters.

The present study introduces the mechanisms responsible for the observed scatter and their theoretical derivation, and introduces novel evaluation approaches for the standard 3PBBT, as well as methods for defining acceptable intervals for on-site verification of fibre dosage. The paper further proposes a procedure, based on the derived statistical methods, for assessing on-site mixing quality and the quantity of dispersed fibres at a given reliability level.

It is evident that, from both an evaluation and a testing perspective, fibre-reinforced concrete must be conceptually decomposed into the concrete matrix and the fibres. In the case of fibre-reinforced concrete, the number of fibres is a key governing parameter, alongside the residual strength value.

7 References

ACI Committee 544, 1998. Design considerations for steel fiber reinforced concrete, *ACI Structural Journal* 85 (5) pp 563–579, https://doi.org/10.14359/3144

Barros, J.A.O., Cunha, V.M.C.F., Ribeiro, A.F., Antunes, J.A.B., 2005. “Post-cracking behaviour of steel fibre reinforced concrete,” *Materials and Structures* 38(275) pp 47–56, https://doi.org/10.1007/BF02480574

Bernard, E.S., 2002. “Correlations in the behaviour of fibre reinforced shotcrete beam and panel specimens,” *Materials and Structures*, 35 pp 156–164, https://doi.org/10.1007/BF02533584

Bernard, E. S., 2013. "Development of a 1200-mm-Diameter Round Panel Test for Post-Crack Assessment of Fiber-Reinforced Concrete," *Advances in Civil Engineering Materials* 2, no. 1 pp 457–471, https://doi.org/10.1520/ACEM20120021

Bernard, E.S., Xu, G.G., 2017. "Influence of fibre count on variability in post-crack performance of fibre reinforced concrete," *Materials and Structures* 50(169), https://doi.org/10.1617/s11527-017-1035-5

Cavalaro, S.H.P., Aguado, A. 2015. "Intrinsic scatter of FRC: an alternative philosophy to estimate characteristic values," *Materials and Structures*, 48(11) pp 3537–3555, https://doi.org/10.1617/s11527-014-0420-6

di Prisco, M., Plizzari, G. and Vandewalle, L. 2009. "Fibre reinforced concrete: new design perspectives," *Materials and Structures*, 42 pp 1261–1281, https://doi.org/10.1617/s11527-009-9529-4

EN 14651 "Test Method for Metallic Fibre Concrete, Measuring the Flexural Tensile Strength (Limit of Proportionality (LOP), Residual)," EN 14651+A1:2007, European Committee for Standardization, Brussels, Belgium, 2005, https://doi.org/10.3403/30092475

Enfedaque, A., Alberti, M.G., Galvez, J.C., 2019. "Influence of fiber distribution and orientation in the fracture behavior of polyolefin fiber-reinforced concrete," *Materials* 12 (2) 220, https://doi.org/10.3390/ma12020220

fib, International Federation for Structural Concrete (2012). *Model code 2010, Final Complete Draft, Bulletins 65 and 66*, March 2012-ISBN 978-2-88394-105-2 and April 2012-ISBN 978-2-88394-106-9.

Juhász, P.K., 2015. "Evaluation of fibre reinforced concrete beam test results based on the examination of the real fibre distribution," in: *Fibre Concrete 2015, Technology, Design, Application*, Czech Republic, Prague, 2015.

Juhász, P.K., 2018. *The Effect of Synthetic Fibre Reinforcement on the Fracture Energy of the Concrete*, PhD thesis, Budapest University of Technology and Economics.

Juhász, P.K., 2020. "A proposed evaluation method for three-point beam tests of fiber-reinforced concrete," *Journal of Testing and Evaluation* 49 (5) pp 3838–3858, https://doi.org/10.1520/JTE20190782

Juhász, P.K., 2020b. "Effects of pouring technique on orientation of steel and synthetic macrofibers in fibre-reinforced concrete," *Concrete Structures*, pp 40-48. https://doi.org/10.32970/CS.2020.1.1

Juhász, P.K., 2023. "Proposed evaluation method for three-point bending beam tests of fiber reinforced concrete," in: *FRC2023: Fiber Reinforced Concrete: from Design to Structural Applications Joint ACI-fib-, RILEM International Workshop*, Tempe, AZ, USA.

Juhász, P.K. 2025. "Improved evaluation of fiber reinforced concrete beam tests using an analytical model of fiber distribution and fracture cross-section location," *Journal of Building Engineering* 111, https://doi.org/10.1016/j.jobe.2025.113544

Krenchel, H., 1975. "Fibre spacing and specific fibre surface," in A. Neville (ed) *Fibre reinforced cement and concrete*, London: The Construction Press, pp 67-75.

Lappa, E.S., 2007. *High Strength Fibre Reinforced Concrete Static and Fatigue Behaviour in Bending*, PhD thesis, Technische Universiteit Darmstadt.

Medeghini, F., Tiberti, G., Guhathakurta, J., Simon, S., Plizzari, G.A., Mark, P., 2025. "Fiber orientation and orientation factors in steel fiber-reinforced concrete beams with hybrid fibers: a critical review," *Structural Concrete* 26 (1) pp 481–500, https://doi.org/10.1002/suco.202400461

Naaman, A.E., 1972. *A Statistical Theory of Strength for Fiber Reinforced Concrete*, PhD Thesis, Massachusetts Institute of Technology.

Österreichische Vereinigung für Beton- und Bautechnik (ÖVBB), 2008. *Richtlinie Faserbeton.* Wien.

Parmentier, B., Vandewalle, L., and Van Rickstal, F., "Evaluation of the scatter in post-peak behaviour of fibre reinforced concrete in bending: a step towards reliability," in: R. Gettu (Ed.), BEFIB 2008: *7th RILEM International Symposium on Fibre Reinforced Concrete*, RILEM Publications SARL, 2008, pp 133–143.

RILEM Technical Committee 162 TDF, 2003. RILEM TC 162-TDF: test and design methods for steel fibre reinforced concrete – σ-ε design method – final recommendation, *Materials and Structures* 36 (262) pp 560–567, https://doi.org/10.1007/BF02480834

Sanal, I., Zihnioglu, N.Ö., 2013. "To what extent does the fiber orientation affect mechanical performance?" *Construction and Building Materials*, 44 pp 671–681, https://doi.org/10.1016/j.conbuildmat.2013.03.079

Stroeven, P., 1978. "Morphometry of fiber reinforced cementitious materials," *Materials and Structures* 11(61), pp 31–37, https://doi.org/10.1007/BF02478701

The Concrete Society, 2016. *TR34 Concrete Industrial Ground Floors*, The Concrete Society. ISBN 978-1-904482-77-2

Tóth, M., Juhász, P.K., Pluzsik, A., 2017. "Effect of mixed fibers on the ductility of concrete," *Journal of Materials in Civil Engineering* 29(9), https://doi.org/10.1061/(ASCE)MT.1943-5533.0001927

Zerbino, R., Tobes, J.M., Bossio, M.E., Giaccio, G., 2012. "On the orientation of fibres in structural members fabricated with self compacting fibre reinforced concrete," *Cement and Concrete Composites* 34(2) pp 191–200, https://doi.org/10.1016/j.cemconcomp.2011.09.005.

Direct Tensile Tests on Drilled Cores with Different Fiber Orientation: Test Setup and σ-w-Relationships

Maximilian Kronau[1], Roman Wan-Wendner[2], Oliver Fischer[1]

[1] : Chair of Concrete and Masonry Structures, School of Engineering and Design, Technical University of Munich, Germany

[2] : Department of Structural Engineering and Building Materials, Faculty of Engineering and Architecture, Ghent University, Belgium

Abstract

Based on ongoing research and the implementation in codes and standards, steel fiber reinforced concrete (SFRC) is increasingly used in structural concrete, e.g. elevated slabs and tunnels. Determining the material properties, particularly the post-cracking tensile strength, is crucial for safe and cost-effective design. In addition to the approach in Model Code 2020 (MC20), which refers to three-point bending tests (3PBT) according to EN 14651, the required material properties and σ-w-relationships can also be determined using direct tensile tests (DTT). While these tests often provide relatively easy to use results, they are significantly more complex and vulnerable during execution. Another influencing factor besides the test type is fiber orientation, which often differs in the structural element from that of the test specimens in the laboratory. To evaluate the influence of both factors, this paper compares the results of DTTs and 3PBTs. The results of the series reveal significant discrepancies in the determined σ-w-relationships. The concluding discussion highlights the necessity of selecting an appropriate constitutive model in accordance with MC20 in dependance of the application and purpose, as well as the importance of carefully accounting for fiber orientation.

Keywords

Steel Fiber Reinforced Concrete (SFRC), Material Characterization, Direct Tensile Tests, Fiber Orientation, Model Code 2020

1 Introduction

The application range of steel fiber reinforced concrete (SFRC) has expanded significantly in recent years. While its initial use was primarily limited to ground slabs and industrial floors, SFRC is now employed in almost all areas of concrete construction (Vijayan et al. 2022). This development is driven, on the one hand, by the introduction and continuous improvement of design standards, which facilitate its use for designers and engineers, and, on the other hand, by the enhanced mechanical properties of modern SFRC materials. As a result, this alternative reinforcement technique is increasingly used not merely as a supplement to conventional reinforcing steel but is progressively replacing traditional reinforcement either partially or entirely. Consequently, in contrast to conventional concrete, it is essential to characterize SFRC not only by its compressive properties, but also by its tensile behavior, in particular its post-cracking tensile strength, and to provide suitable data for structural design.

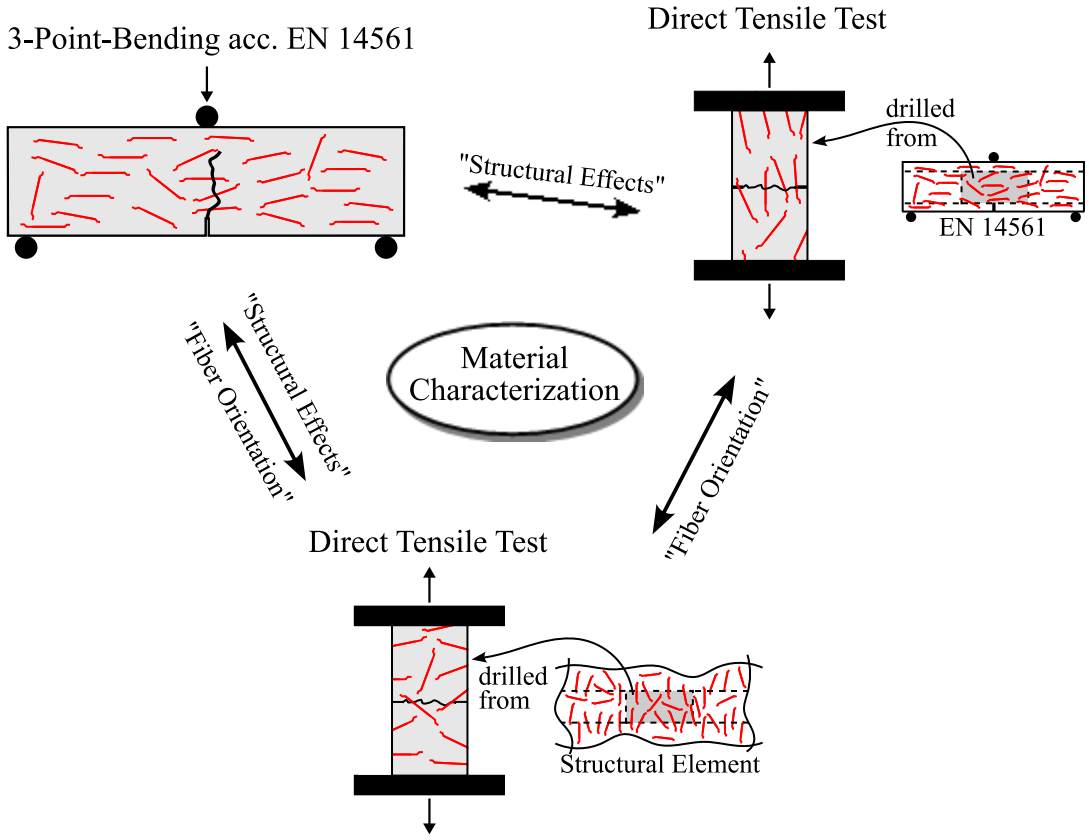


Figure 1: Material characterization of SFRC: Influencing factors between different approaches.

According to the Model Code 2020 (MC20) (fib 2024), the material characterization of SFRC is based on 3-point bending tests (3PBT) in accordance with EN 14651 (CEN 2007). Using the residual flexural tensile strengths determined at predefined CMOD values of 0.50 mm and 2.50 mm, the corresponding uniaxial tensile strengths of the material are subsequently derived, depending on the specific design requirements. Although the determination of tensile properties from uniaxial tensile tests (UTTs) provides a direct assessment of the material behavior due to reduced structural effects, such tests are time-consuming and costly to perform. A further key aspect is the influence of fiber orientation on the resulting material resistance. In

general, fibers aligned parallel to the considered stress direction are more effective than fibers with a certain inclination angle. If the fiber orientation in specimens manufactured in accordance with EN 14651 differs from that in the actual structural member, different material resistances may result despite identical concrete composition (aggregate, fiber type, and fiber content). This discrepancy must therefore be carefully considered in structural design. However, quantifying these deviations is not trivial. On the one hand, it is rarely possible to extract bending specimens of sufficient number and required dimensions directly from structural elements. On the other hand, the pronounced structural effects inherent to bending tests limit the ability to isolate the influence of fiber orientation. Drilled core specimens represent a suitable alternative for such investigations, as they can be extracted both from bending beams and from actual structural members. This approach enables, on the one hand, the identification of test-related uncertainties and, on the other hand, a direct comparison with the material properties present in the real structure. However, uniaxial tensile tests on extracted core specimens pose additional challenges compared to tests on specimens prepared under controlled laboratory conditions. An overview of the described issues and relationships is displayed in Figure 1.

In this contribution, a test setup for uniaxial tensile testing of drilled core specimens is therefore presented first, which minimizes structural effects despite the use of glued specimens and significantly reduces test-related failures (e.g. joint failure). Subsequently, three different tensile test series are presented, all based on the same material but exhibiting different fiber orientations. In addition, a series 3PBT according to EN 14651 was conducted in order to establish a link to the Model Code 2020 in the final discussion of the results.

2 Experimental program

2.1 Specimens and Material

The influences of fiber orientation and structural effects are investigated using four different test series, all produced from the same material. The following series were examined:

- 3PBT according to EN 14651 (7 specimens)
- UTT “Beam EN 14651” - cores drilled from EN 14651 beams (7 specimens)
- UTT “Concreting A” - cores drilled from structural element 1 (7 specimens)
- UTT “Concreting B” - cores drilled from structural element 2 (7 specimens)

Table 1: Mechanical properties of the regarded SFRC

SFRC mechanical properties	Value [MPa]
$f_{cm,cube}$	85.70
E_{cm}	40 226
$f_{ctm,sp}$	6.72
f_{R1m} (COV)	10.29 (0.21)
$_{fR3m}$ (COV)	11.03 (0.17)

The SFRC used corresponds to a compressive strength class of C60/75 and a performance class according to Model Code 2020 of “5.0d”. Within the scope of this study, all test series are evaluated on a mean value basis. Table 1 summarizes the mechanical properties of the material.

The investigated SFRC was designed for segment production. The concrete mix composition is presented in Table 2.

Table 2: Mix design of the regarded SFRC.

SFRC mix design	Value [kg/m³]
Reactive additions*	430.0
Sand 0-4mm	689.0
Gravel 4-8mm	406.0
Gravel 8-16mm	767.0
Water	150.0
Superplasticiser	4.9
Steel fibers (DE 60/0.90 H, Krampe Harex)	45.0
PP-fibers (PM 6/18, Krampe Harex)	1.5

* Not further specified here due to project constraints.

The specimens of the test series “Beam EN 14651” were extracted from the undamaged end regions of the tested bending beams. The positions of the drilled cores were selected such that no formwork effects the fiber orientation. The cores of the series “Concreting A” were taken from a prism cast in an inclined position, whereas the prism for the series “Concreting B” was produced horizontally. The detailed casting procedure is not further discussed here. The focus of this study is not on the causes of the different fiber orientations within the specimens, but rather on their resulting influence on the mechanical behavior of the material. The drilled cores have a length of 20.0 cm and a diameter of 10.3 cm (series “Concreting A” and “Concreting B”) and 11.2 cm (series “Beam EN 14651”). The notch depth was selected such that the diameter of the cracked cross-section is approximately 8.5 cm. Due to the manual notching process, slight variations in notch depth occur. Therefore, all results are evaluated in terms of stresses acting on the cracked cross-sections.

The fiber orientation was determined using an opto-analytical method, see e.g. (Medeghini et al. 2025; Kronau et al. 2024). For each drilled core, a cross-sectional surface located as close as possible to the crack in the notch was analyzed. The corresponding fiber inclinations were derived and documented based on the elliptical cross-sections observed. The fiber orientation in the bending beams was not explicitly investigated. Instead, reference is made to orientation values reported in the literature.

2.2 Test Setup of Direct Tensile Tests

The execution of uniaxial tensile tests involves a variety of challenges, which are discussed e.g. in (Faustmann, Kronau & Fischer 2024; Felicetti & Yarmohammadian 2026; Mészöly & Randl 2024). In summary, the following key boundary conditions and issues can be identified:

- Structural effects: uncertainties in the measured values caused by the test setup
- Glued specimens: avoiding premature failure of the bonded joints
- Final assembly: minimizing restrained forces

At the Chair of Concrete and Masonry Structures at TUM, a test setup was developed and designed based on these conditions for reliable and robust tensile testing. The objective of the setup is to enable simple and practical test execution while significantly reducing negative

influences on the quality. A complete elimination of all crucial aspects is not aim of the test setup.

To minimize structural effects during testing, all components of the test setup were designed to be as robust and stiff as possible. In principle, the specimen should be approximately clamped on both sides within the testing machine to avoid adverse influences of anisotropy and material inhomogeneities on crack localization and failure mechanisms. The connection system to the testing machine is shown in Figure 2-(1). Another crucial aspect for successful testing is the load transfer into the specimen across the glued interface between the loading plates and the specimen. This is particularly an issue for high-strength concretes, where failure often occurs at the joint rather than at the intended location within the specimen, resulting in an invalid test. To minimize the risk of joint failure, the load-transfer plate was reinforced with a bolted flange, as shown in Figure 2-(2). This significantly increases the glued area and reduces local stresses. The flange was secured with four screws so that the preparation of plates after testing (e.g. removing the glue) is easier.

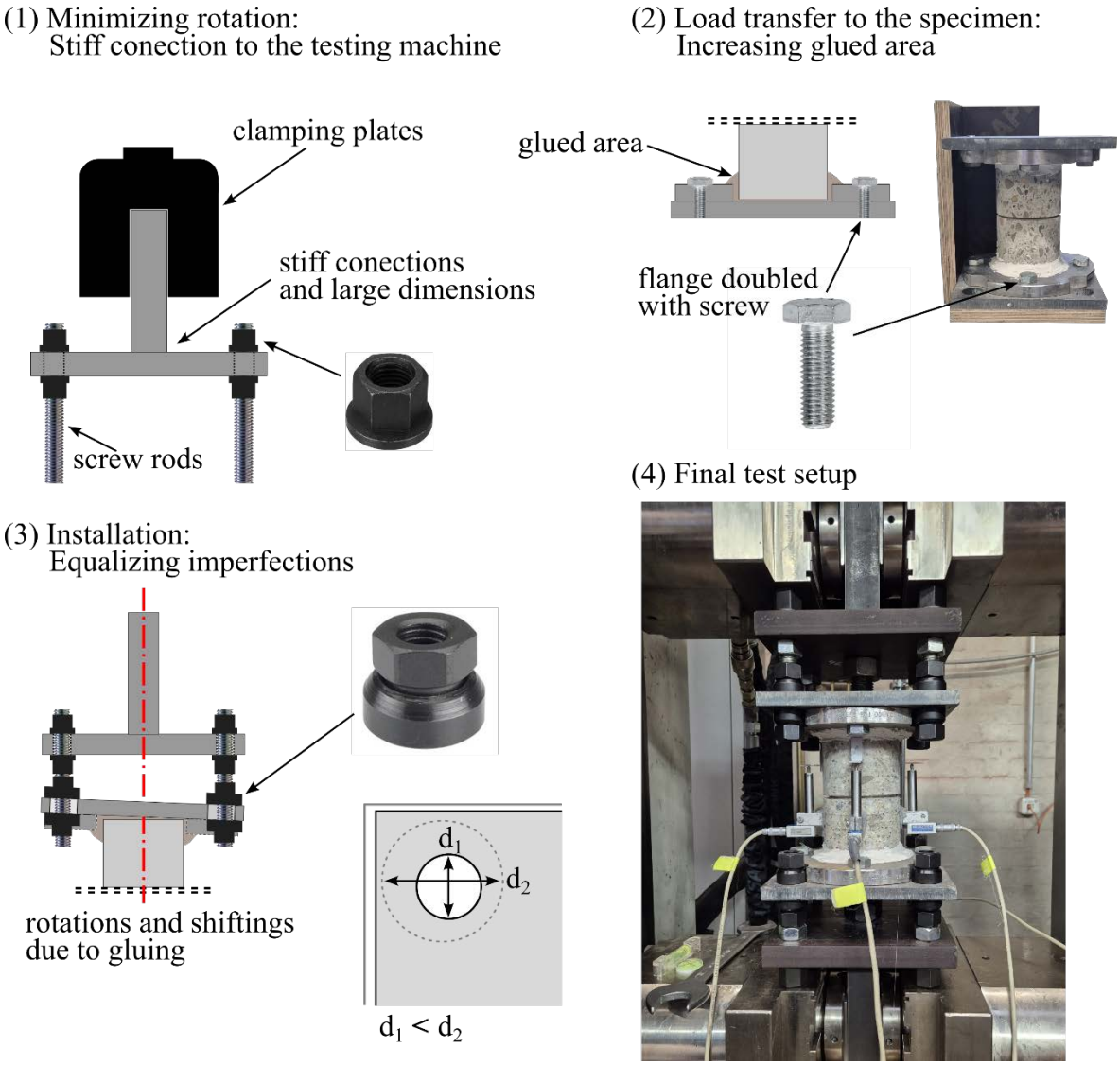


Figure 2: Concept and test setup of the direct tensile tests.

The test specimen is glued in place using precisely aligned supplementary fixtures, ensuring that the upper and lower plate can be installed with minimal misalignment and rotation (see Figure 2-(2)). Despite this setup and careful preparation, it is not possible to entirely avoid geometric imperfections. However, due to the rigidity of the test setup, these imperfections do not cause any further problems, provided they do not induce constraint forces during installation in the testing machine.

The connection of the loading plates to the connecting structure was designed accordingly. The four screwed rods located at the corners are passed through four holes in the loading plates first. These holes are larger than the diameter of the rods to ensure that no horizontal constraint forces arise as long as the offset is smaller than the difference between the two radii, see Figure 2-(3). Other geometric imperfections include the unavoidable relative rotation of the loading plates in relation to the connecting structure. These rotations generate restrained moments that can lead to premature cracking in the notched cross-section, for example. For this reason, the joint is secured using tapered nuts, which adapt to the sloped surface. Screwing the threaded rods on both sides and tightening the tapered nuts in a crosswise pattern under constant compressive load minimises these restrained stresses. The final assembly is shown in Figure 2-(4). The crack opening is measured using four LDVTs with a measurement distance of 10.0 cm. Elastic strains in the concrete are neglected.

2.3 Results

Figure 3 plots the results of the uniaxial tensile test series. For each series, the left column presents the mechanical test results, the right column displays the corresponding fiber orientation. The results are grouped according to their respective manufacturing processes. The mechanical test results are reported as a stress-crack (σ-w) relationship. The single shapes of the specimens are displayed in gray, the mean is displayed in color. The fiber orientations are shown in separate histograms. All fibers detected from the individual specimens within a series were combined. The average inclination angle θ, representing the angle of the fibers relative to the direction of tensile stresses, is also shown.

None of the specimens tested resulted in premature termination of the test due to bond failure or other test-related reasons. The Coefficients of Variation (COV) are also relatively low, considering the small cracking cross-sections (see also Figure 3). In the “Beam EN 14651” and “Concreting B” series, however, there are individual test specimens whose values deviate significantly from the mean. This is due to local conditions regarding fiber orientation or quantity (see Chapter 3.2). The differences in the mean values between the series reflect the differences in their mean fiber inclination angles θ. The step-like progression of the curves after the stress maximum can be assigned to individual fiber ruptures, which were also acoustically noticed during testing. Overall, the test results can be assessed as plausible and thus reliable for further analysis.

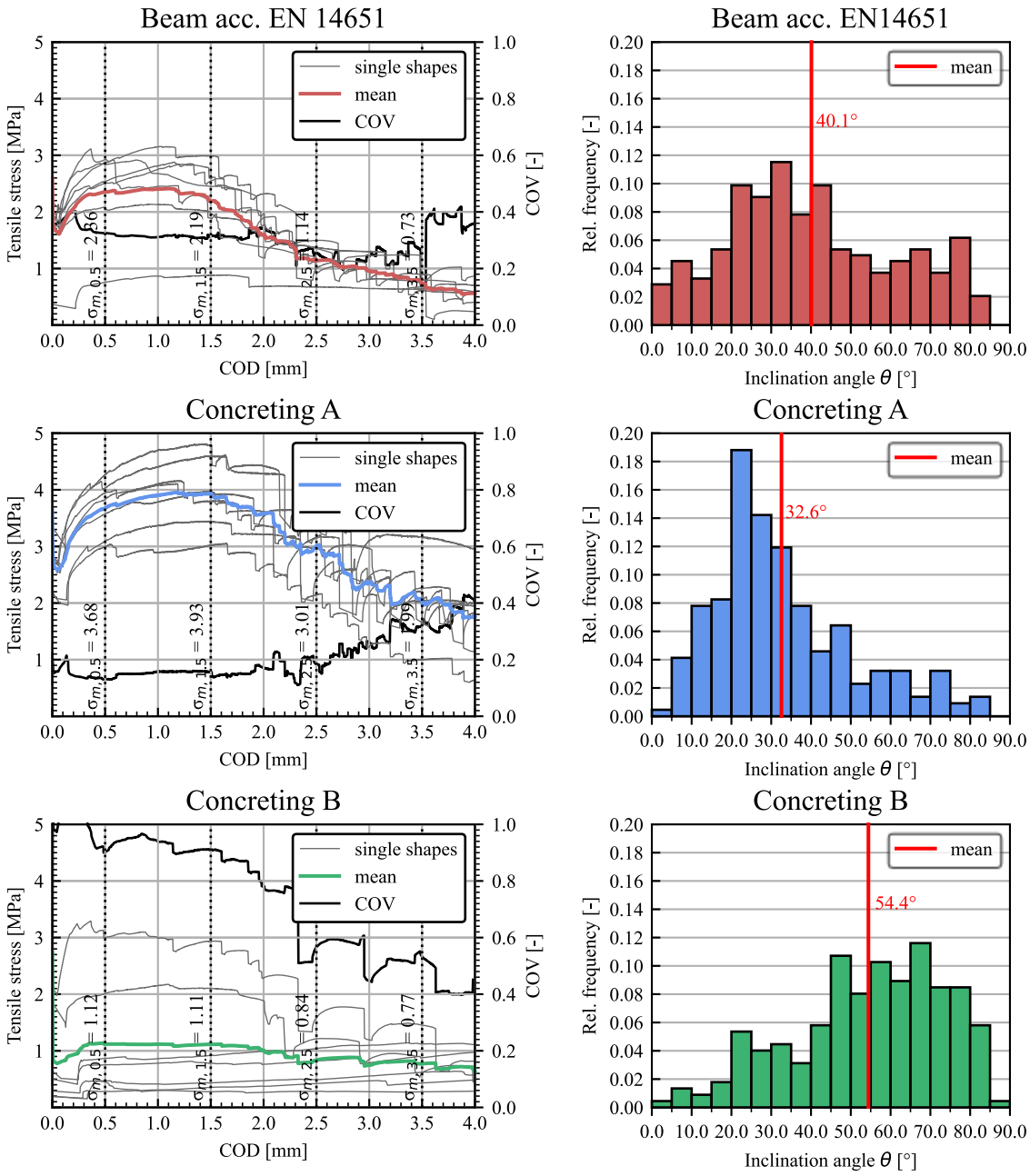


Figure 3: Results of the UTTs and analysis of fiber orientation; left: mechanical results, right: histograms of inclination angles θ.

3 Evaluation of Selected Aspects

3.1 σ-w-relationships

To contextualize the results with respect to the Model Code 2020, the mean curves of all three UTT series are presented together on the right side of Figure 4. In addition, a σ-w-relationship according to “LoA II” of MC20 was derived from the accompanying 3PBT (see Figure 4, left).

Table 3: Residual tensile strength at crucial CODs and orientation parameters.

	MC20 - LoA II [MPa]	"Beam EN 14651" [MPa]	"Concreting A" [MPa]	"Concreting B" [MPa]
Crack width = 0,50 [mm]	3.81 (+61%)	2.36	3.68	1.12
Crack width = 1,50 [mm]	3.71 (+69%)	2.19	3.93	1.11
Crack width = 2,50 [mm]	3.61 (+217%)	1.61	3.01	0.84
Fiber orientation α [-]	0.58	0.55	0.71	0.43
Orientation factor k_0 [-]	1.00	0.95	1.22	0.74

A comparison of the σ-w-relationship derived from the Model Code 2020 with the results of the UTTs conducted on specimens extracted from the same beams ("Beam EN 14651") reveals a significant overestimation of the post-cracking tensile strength. In contrast, the "Concreting B" test series shows a better agreement. To assess the influence of fiber orientation on these deviations, the fiber orientation α according to (Dupont & Vandewalle 2005) and the orientation factor k_0 according to MC20 (eq.18.5-1) were determined for each series. No sectional fiber analysis was conducted for the beams of the 3PBTs. Instead, values from the literature were adopted, which can be considered approximately transferable due to the standardized production conditions according to EN 14651. As reported in (Dupont & Vandewalle 2005), an average fiber orientation of α = 0.58 can be assumed. Data of another wide experimental campaign verifies this value (Tiberti et al. 2018). Since the UTT series "Beam EN 14651" exhibits a fiber orientation of α = 0.55, the value from literature can be considered plausible also for the investigated bending beams in this study and is assumed for further analysis.

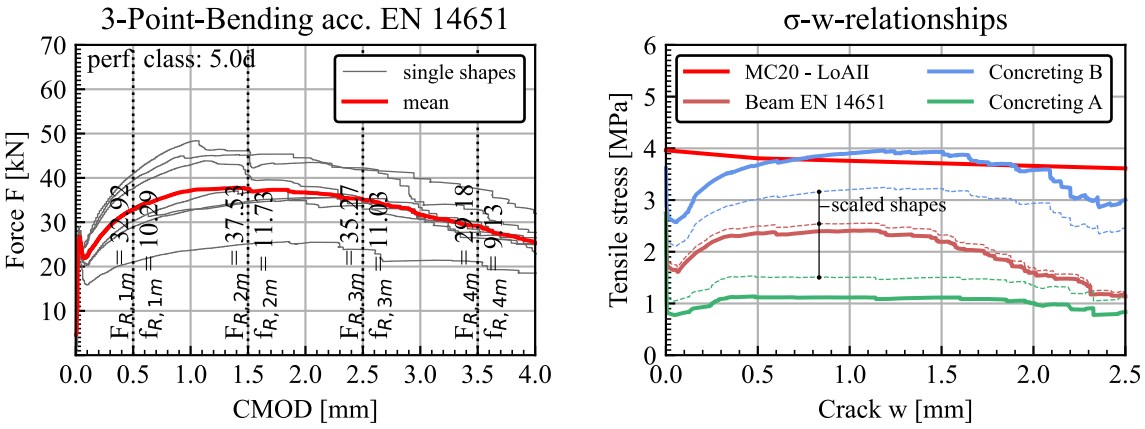


Figure 4: Left: Results of the 3PBT series; Right: σ-w-relationships.

All fiber orientations α of the series and the corresponding orientation factors k_0 are listed in Table 1. In addition, the stress values at crack opening displacements (COD) of 0.5 mm, 1.5 mm, and 2.5 mm are provided. If the σ-w-curves are scaled to a uniform orientation factor k_0 = 1.0 according to MC20, the dashed curves shown in Figure 4 (right side) are obtained. It becomes evident that correcting the influence of fiber orientation leads only to a limited agreement of the curves. In this context, not only the magnitude of the curves is relevant, but also the change in their qualitative shape. While the "Concreting B" series exhibits an

approximately horizontal post-cracking response, the mean curves become increasingly convex with better aligned fibres.

3.2 Fiber orientation

To investigate the influence of fiber orientation k_0 on the post-cracking stresses, the fiber orientation in the vicinity of the crack surface was determined for each individual specimen. The corresponding orientation factor k_0 was then calculated according to MC20. The results are presented in Figure 5 for COD of 0.50 mm and COD of 2.50 mm. Coloring the test specimens allow each data pair to be assigned to a specific series. The determined fiber orientations k_0 also explain the outliers described in chapter 2.3. For instance, the highest value in the "Concreting B" series has the highest fiber orientation coefficient k_0 of the series, and the negative outlier in the "Beam EN 14651" series has the most unfavorable local fiber orientation in the series (see Figure 5). Additionally, linear regression lines were determined based on the available experimental data. To compare this trend with the curve of eq. 18.5-1 from MC20, that slopes were also plotted. In doing so, the tensile stress σ at a fiber orientation of $k_0 = 1.0$ was set to the corresponding value of the linear approximations.

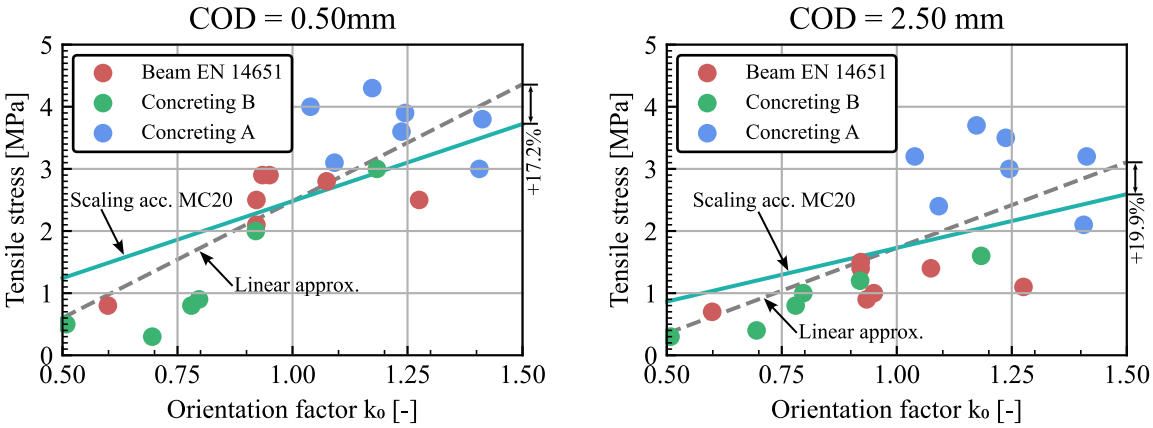


Figure 5: σ-k_0 data pairs of all individual test specimens at COD = 0.50 mm and COD = 2.5 mm.

A comparison of the trends reveals deviations in the slope for both COD values of 0.50 mm and 2.50 mm. As a result, the post-crack tensile strengths tend to be overestimated when fiber orientation is low, and the beneficial effect of favorably oriented fibers cannot be fully exploited. The percentage deviations at the limits of the permissible range according to MC20 ($k_{0,min} = 0.50$ and $k_{0,max} = 1.50$) are 17.2% for COD = 0.50 mm and 19.9% for COD = 2.50 mm. This suggests that, at least for the SFRC considered in this study, the influence of fiber orientation may be greater than that reflected by eq. 18.5-1 in the MC20. Nevertheless, additional experimental data is required to generalise and confirm this finding.

3.3 Discussion

The σ-w-relationships derived from UTTs differ significantly in terms of stress level from those obtained according to the MC20 (LoA II) based on 3PBT. In general, the stress levels derived on the basis of MC20 are considerably higher. Similar discrepancies have also been reported by (Amin, Foster & Muttoni 2015), who compared uniaxial tensile test data with constitutive laws on the Basis of Model Code 2010 (MC10) (fib 2013) and observed a systematic overestimation of the stress level. Based on inverse analysis, it is demonstrated that σ-w-relationships derived from bending tests do not directly correspond to those obtained from

uniaxial tensile testing. Comparable findings can be obtained when evaluating the data reported by (Faustmann, Kronau & Fischer 2024). However, these differences must be interpreted considering the underlying model formulation. The stress levels of the σ-w relationships in MC10 and MC20 are calibrated in a design-oriented manner and are based on moment equivalence between experimental results and the corresponding model, see e.g. (Di Prisco, Colombo & Dozio 2013). Consequently, the objective of these constitutive relationships is not to reproduce the actual material response in the post-cracking regime in a quantitative or qualitative sense, but to consistently predict the flexural load-bearing capacity of a cross-section.

For applications in which local load transfer is decisive, such as nonlinear finite element analyses, the constitutive relationships defined by MC20 - LoA II and further processed in MC20 - LoA III are therefore only conditionally suitable. Studies such as in (Zani, Martinelli & Di Prisco 2023; Aidarov et al. 2024), which primarily investigate bending problems, demonstrate that the choice of material parameters has a significant influence on the calculations, even when simplified, design-oriented constitutive models are employed. In many cases, the assumption of a linear fiber pull-out response leads to a qualitatively similar curve shape in uniaxial tension. However, the suitability of such approaches for nonlinear analyses that account for stress redistribution and crack width evolution remains uncertain.

The flexural capacity of a cross-section exhibits an approximately linear relationship with fiber orientation (Medeghini et al. 2022). However, the extent to which this relationship is adequately represented by the linear scaling approach using k_0 proposed in the MC20, has so far only been investigated to a limited extent. Suitable data basis is not consistently available, as evaluations are based on alternative parameters, e.g. (Tiberti et al. 2018; Faustmann et al. 2025).

Furthermore, it can be observed that favourably aligned fibers affect not only the stress level but also the qualitative shape of the σ-w-relationship. A simple linear scaling of existing constitutive relationships is therefore to be viewed critically, particularly when aiming to represent the real material response. This becomes especially relevant in applications where local effects and redistributions govern structural behavior. For instance, in simulations of local load introduction from prestressing systems or the structural behavior of longitudinal joints of segmental linings, load redistribution and crack width development are strongly influenced by the qualitative shape of the adopted constitutive relationship. Whether simplified approaches according to MC20 - LoA III provide consistently conservative results in such cases remains unclear. The MC20 takes this conceptional differences, in contrast to MC10, into account by the introduction of the LoA IV. Nevertheless, the importance of deriving consistent constitutive relationships with the ambition of material identity for accurate nonlinear simulations is often not conscious in engineering practice. The experimental investigations presented here highlight the importance of maintaining this conceptual distinction and explicitly accounting for effects of local fiber orientation in the modeling approach. This is especially important when considering SFRC with overcritical material behavior.

4 Concluding remarks

This study presented an experimental investigation on the tensile behavior of steel fiber reinforced concrete (SFRC) based on three different UTT series with varying fiber orientations, complemented by one 3PBT series according to EN 14651. A test setup for uniaxial tensile

testing of drilled core specimens was developed, enabling a reliable and relatively easy testing procedure with reduced structural effects. The results demonstrate that fiber orientation has a significant influence on the resulting σ-w-relationships, affecting both the stress level and the qualitative shape of the post-cracking response. The comparison with the σ-w-relationship derived from the MC20 based on 3PBTs shows clear discrepancies in both magnitude and curve shape. These differences can be attributed to the design-oriented calibration of the models in the MC20, which are intended to reproduce flexural capacity rather than the actual material behavior.

Furthermore, the evaluation of fiber orientation indicates that its influence may be more pronounced than currently accounted for in the MC20. For nonlinear analyses, it is therefore essential to adopt constitutive relationships that adequately represent both the quantitative and qualitative aspects of the tensile response to correctly capture load redistribution and crack evolution. This requirement is addressed in the MC20 through the introduction of LoA IV. Ongoing experimental studies aim to further expand the available database. In addition, future research will include the application of discrete modeling approaches and material models, such as LDPM-F (Schauffert & Cusatis 2012; Poudel et al. 2025), to further investigate the highlighted aspects and their influence.

5 References

Aidarov, S, Nogales, A, Tošić, N & La Fuente, A de 2024, 'Influence of fiber orientation on flexural-based design of steel fiber-reinforced concrete slabs: Experimental and numerical program', *Structural Concrete*, vol. 25, no. 2, pp. 956–972.

Amin, A, Foster, SJ & Muttoni, A 2015, 'Derivation of the σ- w relationship for SFRC from prism bending tests', *Structural Concrete*, vol. 16, no. 1, pp. 93–105.

CEN 2007, *EN 14651. Test method for metallic fibered concrete - Measuring the flexural tensile strength (limit of proportionality (LOP), residual)*, European Commitee for Standardization.

Di Prisco, M, Colombo, M & Dozio, D 2013, 'Fibre-reinforced concrete in fib Model Code 2010: principles, models and test validation', *Structural Concrete*, vol. 14, no. 4, pp. 342–361.

Dupont, D & Vandewalle, L 2005, 'Distribution of steel fibres in rectangular sections', *Cement and Concrete Composites*, vol. 27, no. 3, pp. 391–398.

Faustmann, S, Kronau, M & Fischer, O 2024, 'Direct tensile tests on steel fiber reinforced concrete with focus on wall effect and fiber orientation', *Materials and Structures*, vol. 57, no. 8.

Faustmann, S, Weber, S, Kalytta, C, Degen, S, Neunzig, C & Fischer, O 2025, 'Steel fiber reinforced concrete with different recycled aggregates—In-depth experimental investigation of fresh and hardened properties', *Structural Concrete*, vol. 26, no. 5, pp. 6164–6179.

Felicetti, R & Yarmohammadian, R 2026, '3action: Advances in direct-tensile testing of concrete', *Materials and Structures*, vol. 59, no. 2.

fib 2013, *fib Model Code for Concrete Structures 2010*, International Federation for Structural Concrete (fib), Lausanne, Switzerland.

fib 2024, *fib Model Code for Concrete Structures (2020)*, International Federation for Structural Concrete (fib), Lausanne, Switzerland.

Kronau, M, Strotmann, A, Faustmann, S, Fischer, O & Jungwirth, J 2024, 'Evaluation of fibre orientation of Ultra-High Performance Fibre Reinforced Shotcrete with an opto-analythical approach'. *Proceedings of the 15th fib International PhD Symposium in Civil Engineering. Budapest, Hungary, 28-30 August 2024*, ed G Balázs, Fédération international du béton (fib), Lausanne, pp. 1193–1200.

Medeghini, F, Guhathakurta, J, Tiberti, G, Simon, S, Plizzari, GA & Mark, P 2022, 'Steered fiber orientation: correlating orientation and residual tensile strength parameters of SFRC', *Materials and Structures*, vol. 55, no. 10.

Medeghini, F, Tiberti, G, Guhathakurta, J, Simon, S, Plizzari, GA & Mark, P 2025, 'Fiber orientation and orientation factors in steel fiber-reinforced concrete beams with hybrid fibers: A critical review', *Structural Concrete*, vol. 26, no. 1, pp. 481–500.

Mészöly, T & Randl, N 2024, 'Assessment of Methods to Derive Tensile Properties of Ultra-High-Performance Fiber-Reinforced Cementitious Composites', *Materials (Basel, Switzerland)*, vol. 17, no. 13.

Poudel, S, Cibelli, A, Del Prete, C, Wan-Wendner, R, Mazzotti, C & Buratti, N 2025, 'Insights on Lattice Discrete Particle Model Calibration and Validation Procedure to Simulate Polypropylene and Steel Fibre-Reinforced Concrete', *Fibers*, vol. 13, no. 2.

Schauffert, E & Cusatis, G 2012, 'Lattice Discrete Particle Model for Fiber-Reinforced Concrete. I: Theory', *Journal of Engineering Mechanics*, Vol. 138, No. 7, pp. 826–833.

Tiberti, G, Germano, F, Mudadu, A & Plizzari, GA 2018, 'An overview of the flexural post-cracking behavior of steel fiber reinforced concrete', *Structural Concrete*, vol. 19, no. 3, pp. 695–718.

Vijayan, DS, Sivasuriyan, A, Parthiban, D, Jakimiuk, A, Bayat, H, Podlasek, A, Vaverková, MD & Koda, E 2022, 'A Comprehensive Analysis of the Use of SFRC in Structures and Its Current State of Development in the Construction Industry', *Materials (Basel, Switzerland)*, vol. 15, no. 19.

Zani, G, Martinelli, P & Di Prisco, M 2023, 'Role of the tensile constitutive modeling on the structural response of fiber reinforced concrete flat slabs: A numerical study', *Structural Concrete*, vol. 24, no. 1, pp. 1313–1327.

Blind prediction of steel fiber-reinforced slab punching resistance based on lessons learned from previous contests

Jiří Kovář[1,2], Jan Červenka[1]

[1]: Cervenka Consulting s. r. o., Prague, Czech Republic.

[2]: CTU, Faculty of Civil Engineering, Prague, Czech Republic.

Abstract

Blind prediction contests provide a transparent, well-documented benchmark for nonlinear modelling of fiber-reinforced concrete (FRC) structures and expose the consequences of material uncertainty and model representativeness. Building on lessons from the fib 2020 shear-beam competition - where many models overestimated capacity due to overly optimistic post-cracking tensile behavior and inconsistent cracked-shear assumptions - the present study focuses on the fib 2023 SFRC slab punching test prediction.

The fib 2023 contest involved predicting the punching resistance of a slab reinforced by steel fibers and conventional reinforcing bars. Notched-beam and round-panel test data and results were provided for inverse identification of the model parameters.

Based on the experience from the 2020 fib contest, the tensile softening diagram was calibrated to the lower-bound round-panel response with inverse analysis. A three-dimensional nonlinear FE model developed in ATENA software, with the calibrated material law, reproduced a punching-governed failure mode and delivered very close agreement with the experimental results.

This study highlights that conservative, mechanism-aware calibration, rather than mean-curve fitting, can substantially improve predictive reliability for shear/punching exposed FRC members.

Keywords

Blind prediction, fiber reinforced concrete, punching resistance, nonlinear FE simulation

1 Introduction

Nonlinear analysis (NLA) becomes much more demanded tool in the structural analysis of concrete structures as the structures become more complex (as for shape, material or the overall structural solution). Numerous software for NLA is used worldwide and nowadays, the results of traditional structures (such as reinforced concrete elements subjected to regular loading) are usually very accurate and reliable. However, wider range of modified concrete types are used to provide advantages in different loading types of structures, e.g. fiber-reinforced concrete (FRC).

FRC is known for its improvement of tensile behavior of concrete, which provides higher resistance, for example in tension caused by shrinking or in tensile parts of bending element. The improvement of fiber reinforcement in case of shear-dominant loading was also observed in numerous studies (Batson, et al., 1972; Swamy, et al., 1985; Narayanan, et al., 1987). Mainly in the post-crack or failure behavior, providing structure with more ductility and preventing sudden brittle collapse. In NLA, this behavior can be represented through the tensile strength and, more importantly, the tensile softening law. However, defining a generally applicable softening function for concrete with randomly distributed fibers is not straightforward. Therefore, this part of the material model must usually be calibrated using experimental data.

This contribution presents a nonlinear finite elements analysis (NLFEA) of an FRC slab subjected to punching carried out in ATENA software (Červenka, et al., 2022), using fracture-plastic material model (Červenka, et al., 1998; Červenka, et al., 2008), which proved to be able to predict reliable results of FRC elements subjected to bending. In recent publication (Skadins, et al., 2024), it was discussed and clarified why the shear (and therefore punching) simulation is not a trivial task and proposed assumptions to make in such analysis. These guidelines were adopted and used in the presented simulation. The results indicate that it is an appropriate approach and should be adopted in nonlinear simulations of FRC members subjected to shear-dominant loading.

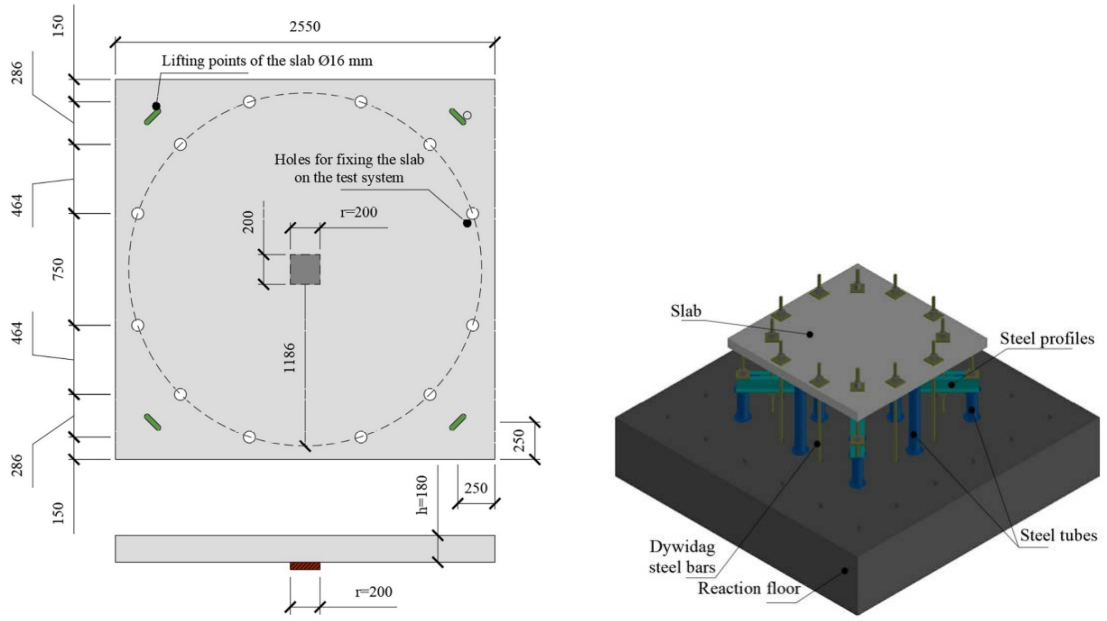
2 Benchmark setup overview

Benchmarks are a valuable tool to calibrate the material models and provide analysts with crucial information to improve the models in a way of blind prediction and comparison to real-life, experimentally verified load-displacement response.

The analyzed benchmark specimen was a slab reinforced by conventional flexural reinforcement and steel fibers and tested under a centrally applied punching load. The benchmark specification provided specimen geometry, reinforcement layout, and the locations of the monitored quantities, together with the required material characteristics. In the present contribution, the geometry of the slab, the arrangement of the flexural reinforcement, and the loading configuration are illustrated by the figures adopted from the benchmark documentation (Barros, et al., 2025).

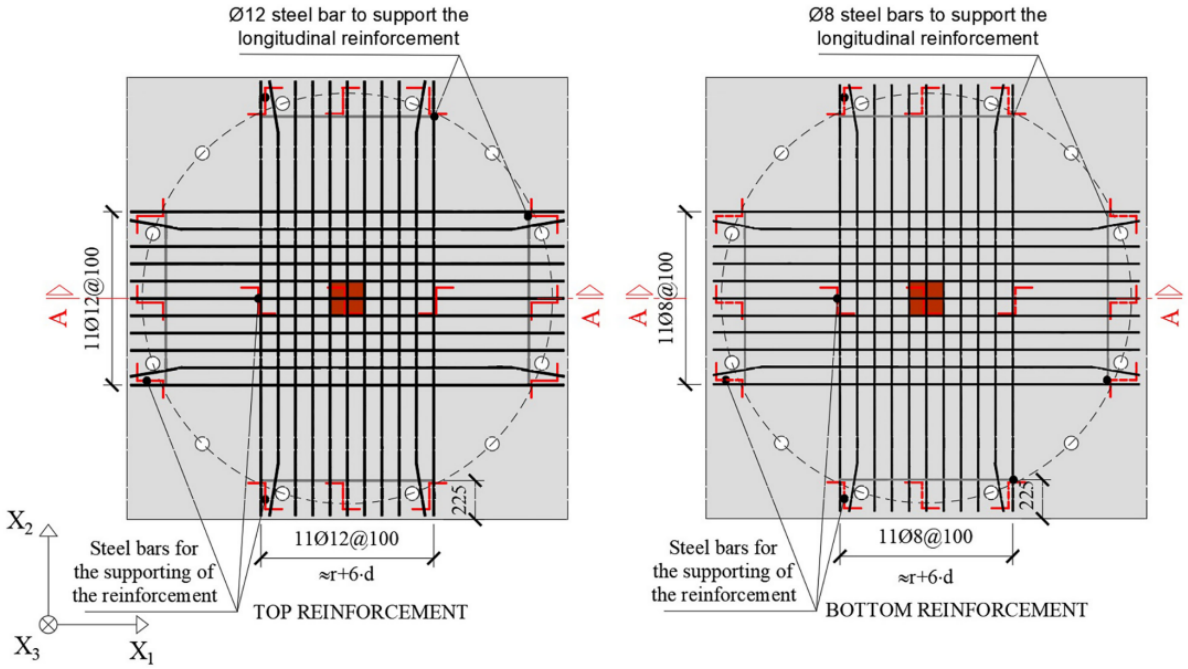
The slab geometry and test setup can be seen in Figure 1. The discrete reinforcement bars are distributed in the mid bands of the slab symmetrically in both directions, spaced by 100 mm – reinforcement near the top surface is of diameter 12 mm, near the bottom surface of diameter 8 mm with cover of 20 mm (see Figure 2). Additionally, hooked-end steel fibers were used with

diameter of 0.9 mm, length 60 mm and tensile strength of 1900 MPa. The content of fiber reinforcement in concrete mixture is 60 kg/m^3. (Barros, et al., 2025)



(a) (b)

Figure 1: Experiment setup: (a) plan view with dimension, (b) 3D setup view, (Barros, et al., 2025)



(a) (b)

Figure 2: Layout of the flexural reinforcement of the slab specimen (a) top layer, (b) bottom layer, (Barros, et al., 2025)

The input material parameters for concrete and reinforcement were taken from the benchmark specification. Selected quantities are summarized in the Table 1-2 below, all specifications were used as described in the benchmark documentation (Barros, et al., 2025). Parameters that were not prescribed directly, but had to be identified through inverse analysis and calibration, are discussed separately in the following chapter dealing with the fitting procedure and constitutive assumptions.

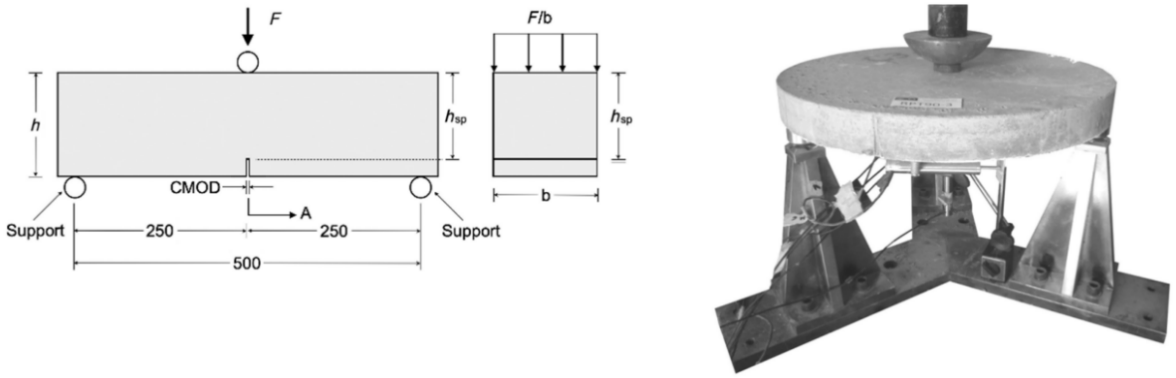
Table 1: Material parameters - concrete (adopted from benchmark doc.).

Parameter	**Value**	**Units**
Modulus of elasticity	26.35	GPa
Poisson ratio	0.2	-
Compressive strength	50.15	MPa
Tensile strength	4.49	MPa

Table 2: Material parameters – reinforcement (adopted from benchmark doc.).

Parameter	**Values for R12**	**Values for R8**	**Units**
Modulus of elasticity	228.25	237.83	GPa
Yield strength	619.00	597.25	MPa
Strength	730.97	720.50	MPa
Limit strain	0.20625	0.3555	-

Besides the main slab test, the benchmark also included supporting material-test information intended for calibration of the post-crack tensile response (mainly the tension softening law) of the FRC. In particular, round-panel tests (according to ASTM C1550-05) and notched-beam tests (acc. to EN 14651:2005) were available as a basis for fine-tuning the post-cracking tensile law. The setup of these standardized tests can be seen in the following Figure 3 and described in more detail in the original publication (Barros, et al., 2025).



(a) (b)

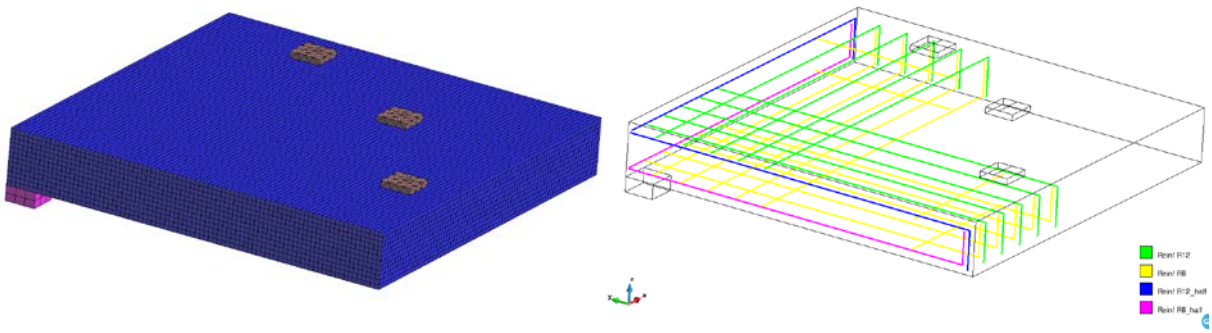
Figure 3:Supporting calibration tests schematic setup (a) 3 point bending test notched beam, (b) round-panel test, (Barros, et al., 2025)

3 Analysis

The nonlinear analysis of the slab benchmark was carried out in ATENA using a three-dimensional nonlinear finite element model with the fracture-plastic constitutive formulation for concrete (Červenka, et al., 1998; Červenka, et al., 2008). The smeared crack method with fixed crack is used.

Due to the geometrical, loading and reinforcement symmetry, only one quarter of the slab was modeled (see Figure 4), and symmetric boundary conditions were prescribed on the corresponding planes of symmetry (i.e. fixed displacement in perpendicular direction). The concrete part of the model was discretized by regular hexahedral elements with linear approximation and a side length of 15 mm (Figure 5). This mesh density was selected as a reasonable compromise between computational cost and the accuracy of the structural response. The mesh sensitivity study was not performed, the size was selected mainly based on the maximum nominal size of the coarse aggregate, which is 14 mm. Also, the aggregate interlock is activated with size corresponding to the maximum nominal size.

The conventional flexural reinforcement was modeled discretely according to the benchmark reinforcement layout (see Figure 6). Separate reinforcement groups were defined for the top and bottom bars in accordance with the provided material properties. The reinforcement bars are modelled as embedded reinforcement with perfect bond. The steel loading and support plates were assumed as elastic material mainly to provide realistic stiffness and geometry of the experimental loading/support setup. The concrete parameters were set as specified in the benchmark documentation and the post-cracking tensile law obtained from the inverse analysis was subsequently adjusted.



(a) (b)

Figure 4: (a) FE mesh of the numerical model, (b) discrete reinforcement bars

As discussed above, the key issue of the FRC simulations is the adoption of a realistic tensile softening law. The benchmark documentation provided results of standardized supporting tests, both test types are useful for calibration of the post-cracking response of FRC, however, they provide different kinds of information. The notched-beam test is a commonly used standardized material test suitable for classification of residual flexural tensile response, while the round-panel test is considered more representative for plate-like structural behavior and was therefore regarded as more relevant for the present slab punching benchmark.

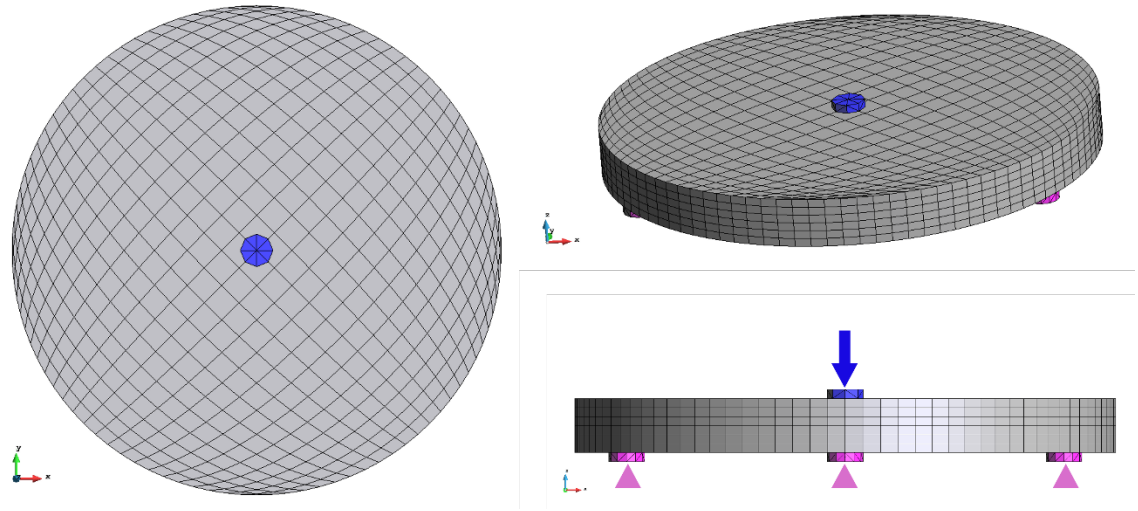


Figure 5: Numerical FE model of the round-panel calibration test.

For this reason, the final tensile diagram adopted in the nonlinear analysis was determined mainly by inverse analysis of the round-panel tests (see FE model in Figure 7). Following the experience from previous benchmark studies focused on shear-dominant behavior of FRC members (discussed thoroughly in (Skadins, et al., 2024)), the parameters were not fitted to the average experimental response as usual, but approximately to the lower bound of the measured panels response. The reason for this assumption is that after casting and compaction of the FRC mixture, the fibers tend to follow horizontal direction favorable for bending load, which is not as favorable in case of shear loading and failure.

In particular, the adopted fit corresponded to the conservative experimental curve represented by specimen No. 5. This approach was chosen intentionally, since previous work showed that calibration to an average flexural response may lead to an overly optimistic estimate of the shear or punching resistance. Consequently, the shear stiffness softening is applied (even though (Skadins, et al., 2024) proves that it has little influence) following the tensile softening law and is calculated as follows:

$$G/G_c = \frac{s_f \sigma_n/\varepsilon_f}{s_f \sigma_n/\varepsilon_f + G} \quad (1)$$

where s_f is shear factor (constant with value of 20), σ_n is normal stress and ε_f is tensile strain from tensile softening diagram and G is shear modulus.

The final response of the round panel simulation is shown in Figure 8 along with comparison to all the tested panels responses. Tensile softening function used in this analysis was adopted and used in the blind prediction. The function is illustrated in Figure 9.

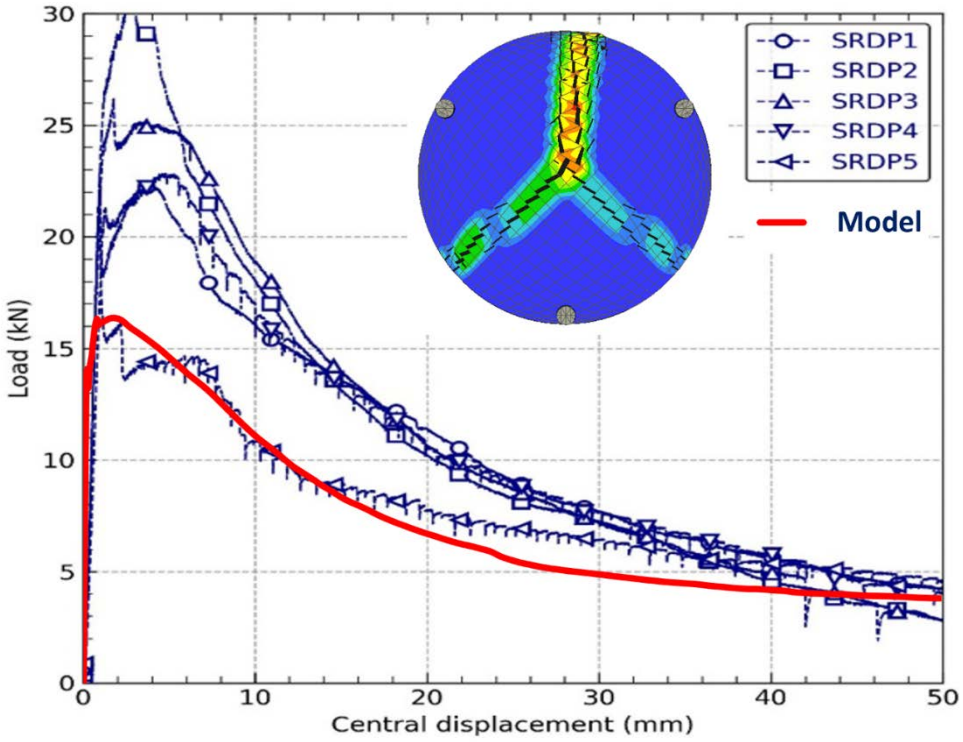


Figure 6: LD diagram from the calibration of post-tension response along with comparison of the experimental test results.

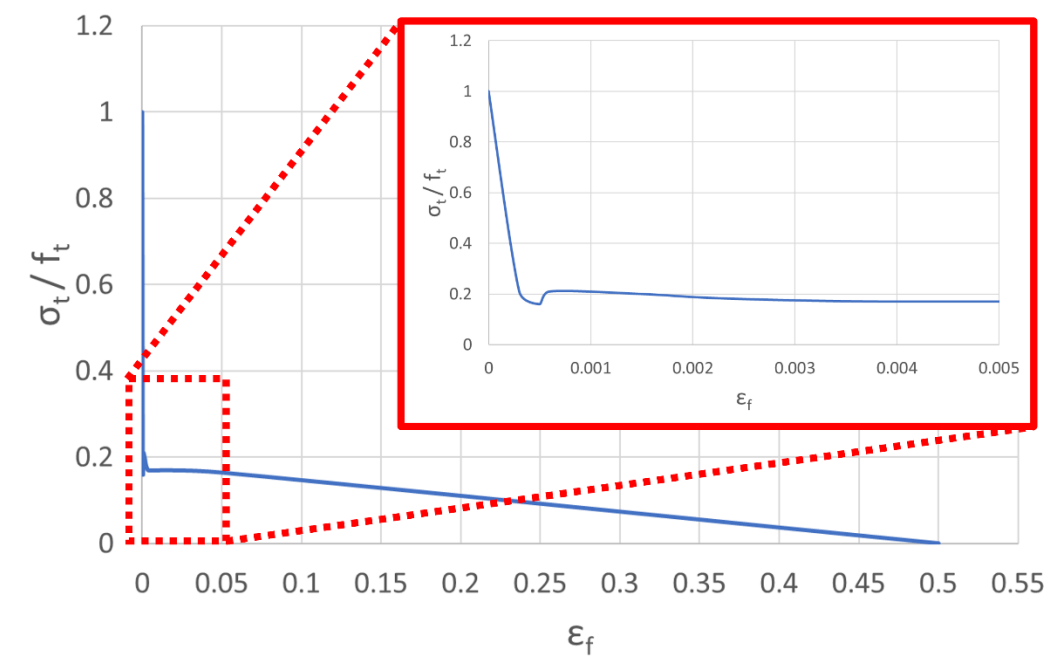


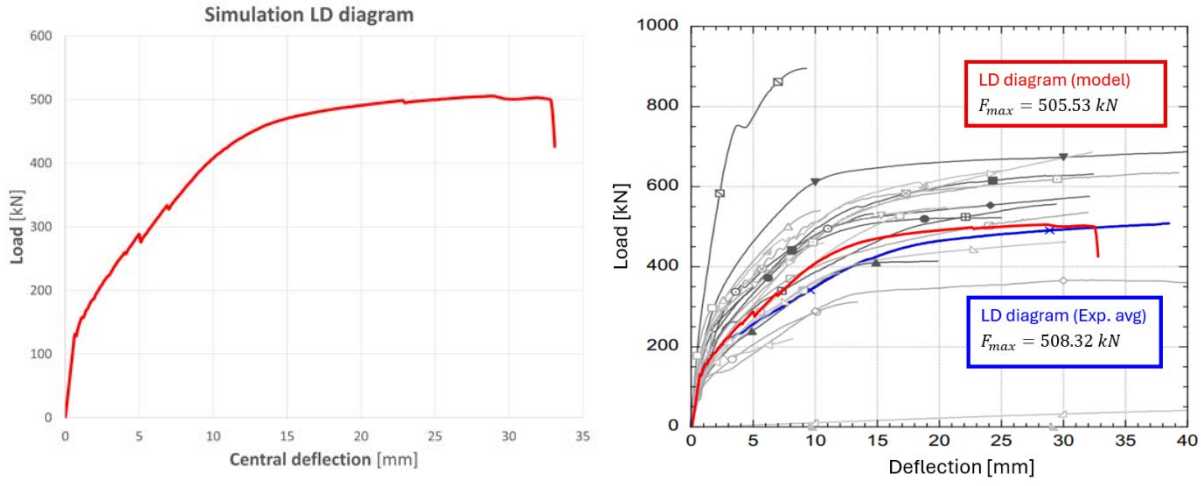
Figure 7: Tensile softening function determined by the inverse analysis, localization scaling used when applying this diagram in finite element model, i.e. $\varepsilon_f = L_t/L_{ch}$ *, where* L_t *is crack band size, and* L_{ch} *is characteristic size, for which the above tensile diagram is valid.*

4 Results and comparison

Several response quantities were monitored within the benchmark program, including the global load–displacement (LD) response and selected local measurements. In the present paper, the discussion is centered mainly on the global load–displacement diagram and the observed failure character, which are the most relevant quantities for assessing the predicted structural response and eventually the governing criteria in the structural design. Other monitored quantities are presented along with the experiment and other participants' results and are briefly commented. Overall, the comparison is very good for the global response and satisfactory for most monitored quantities.

The obtained LD diagram (Figure 10) shows a very good agreement with the experimentally observed global response, especially with respect to the ultimate load level and the overall shape of the response curve. Since the ultimate load is one of the most important quantities from the engineering point of view, this agreement can be considered the main indicator that the adopted modelling strategy was appropriate for the analyzed structure. The numerical simulation predicted failure at a maximum load of approximately 505.5 kN against peak load in the experiment which was 508.32 kN (see comparison in Figure 10b).

Comparison of the rest of the monitored quantities are shown in Figure 11. Horizontal axis always shows the central deflection of the slab, the vertical differs in every diagram and depicts the monitored quantity: *(a-c)* displacement at point 2, 3 and 4, *(d)* maximal crack width in the measured DIC region, *(e)* average compressive strain at the specified point on the bottom surface, *(f)* average tensile strain at the specified points in reinforcement bars.



(a) *(b)*

Figure 8: Simulation response – LD diagram of the slab response prediction on its own (a) and with comparison of the experimentally obtained curve and predictions of other participants (b)

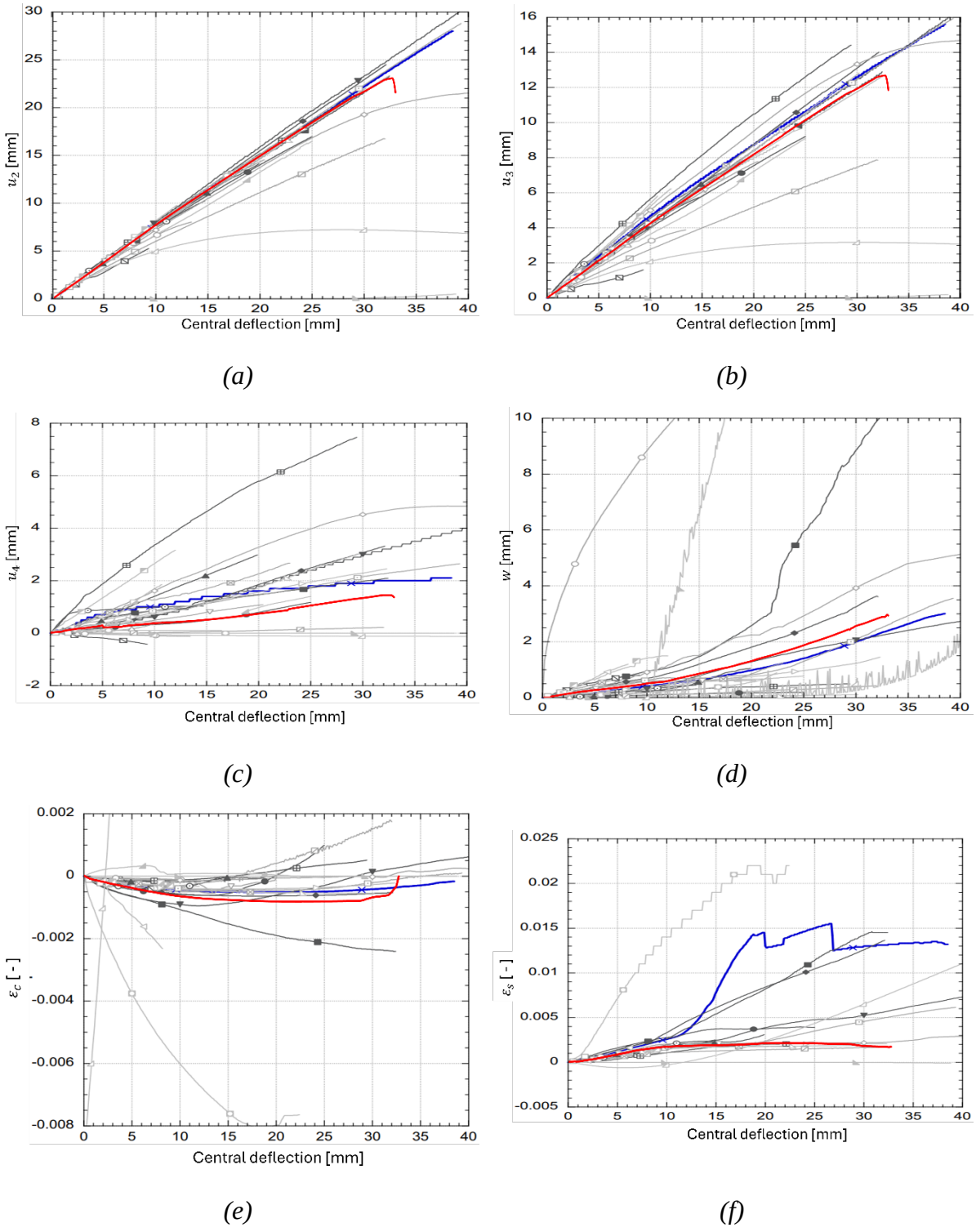
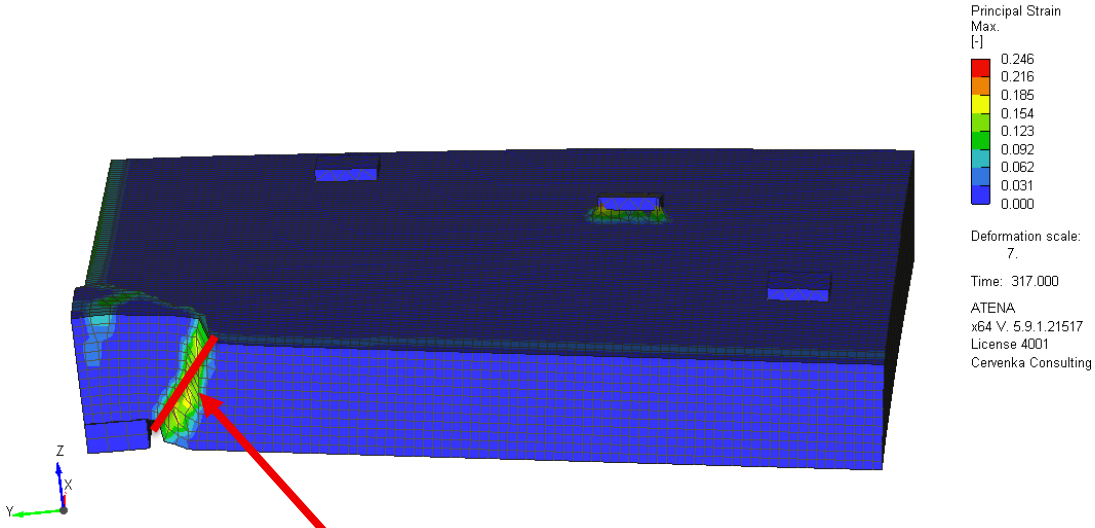


Figure 9: Results of monitored criteria. Horizontal axis is always Central deflection measured at Point 1 [mm] compared against: (a) deflection at Point 2, (b) deflection at Point 3, (c) deflection at Point 4, (d) maximum crack width at the DIC region, (e) average compressive strain at measured points, (f) average tensile strain in the bars at measured points (red curve is presented model result, blue is the average experiment result, grey are other participants' results)

The character of failure corresponded to punching, which is consistent with the expected governing mechanism of the tested slab. Figure 12 shows the comparison of the simulation failure criteria along with the picture of the section of the specimen (slab 2) after the experiment (Barros, et al., 2025). Visually assessed and compared (Figure 12, Figure 13), punching failure character and crack pattern obtained in the analysis is in close agreement with the experiment result.



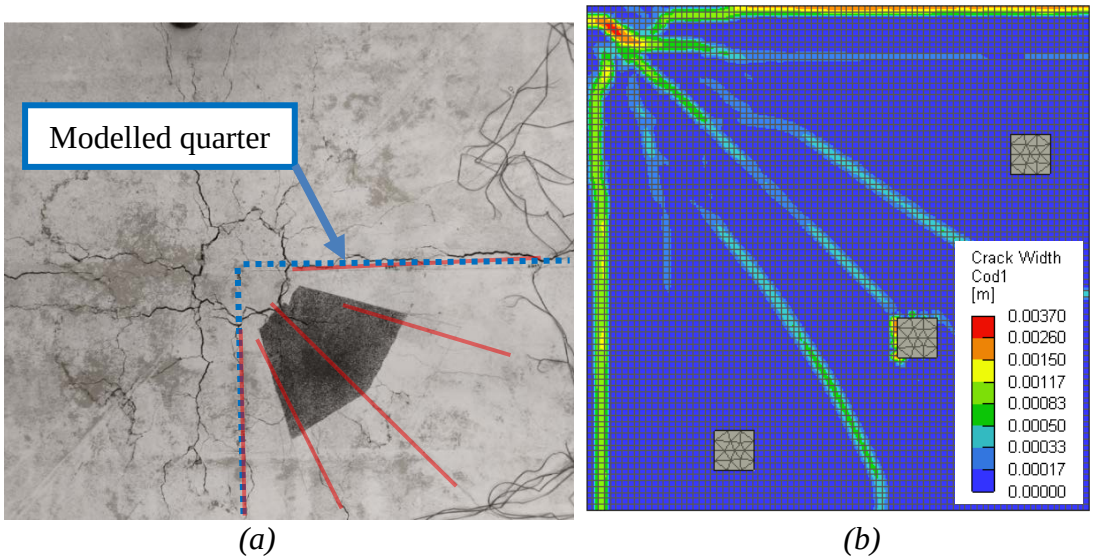
(a)



(b)

Figure 10: Failure comparison to experiment results; (a) shows the failure character in the simulation, (b) shows photo of the specimen (slab 2) after the experiment (Barros, et al., 2025), red lines on photo and model picture are of same inclination and illustrate the similarity of crack pattern

Figure 13a and 13b show the crack pattern comparison. The 90° cracks developing from center outwards are quite severe and agree with the experiment as well as the 45° cracks developing from center to the corner of the slab. Slight differences can be observed in the central area where the photo shows a square-like or circular cracks open whereas in simulation, the cracks localize differently.



(a) *(b)*

Figure 11: Crack pattern width of the slab at peak load (top view); (a) photo from experiment (Barros, et al., 2025), (b) ATENA simulation results (crack width)

5 Discussion

Comparison of the presented prediction with the available experimental load-displacement response and other observed quantities show that the conservative fitting strategy adopted for the tensile softening law did not lead to an unnecessarily low estimate of the slab capacity. On the contrary, it provided a realistic prediction of global resistance while preserving the expected punching-type failure mechanism. This observation supports the assumption that, for members governed by shear or punching, calibration based on mean material-test response may be too optimistic, whereas a lower-bound fit can lead to a more robust structural prediction.

The model LD response is slightly stiffer in the range of approx. 5 ~ 12 mm of central deflection. This part is driven mostly by bending and the difference might be explained by omitting the initial shrinkage of the structure.

In the Figure 11, quite a satisfactory comparison of simulation and experimental results can be observed with exception of tensile strain in the top reinforcement bars (Figure 11f). This fact can be explained by the different localization of the cracks in the middle area where in the experiment, it can be seen that the crack is perpendicular to the flexural reinforcement which explains the jump in reinforcement strain in the experiment diagram. This jump did not happen in the simulation most likely because the central crack did not localize perfectly in perpendicular direction of the bar but is rather inclined and is about 45° from the bar (as was shown Figure 13).

It is also noticeable that most of the predictions follow the underestimation of the strains which proves that an exact localization prediction is an extremely difficult task and the prediction of local strains is highly sensitive to the exact crack path and its localization.

6 Conclusion

Blind prediction benchmarks are a valuable way to verify nonlinear FE models and modelling assumptions for FRC structures. In the present study, the punching resistance of a steel fiber-reinforced slab was predicted in ATENA using a tensile softening law calibrated approximately to the lower-bound round-panel response, following experience from previous shear-dominant benchmark studies. This strategy proved appropriate, since the obtained load–displacement response showed very close agreement with the experiment, including nearly identical load-carrying capacity. Most monitored quantities also showed satisfactory agreement, with the exception of the tensile strain in the reinforcement bars, where local crack localization likely played an important role. The predicted punching failure mode and crack pattern were also in good qualitative agreement with the experimental observations. Overall, the results confirm that conservative, mechanism-aware calibration can improve the reliability of nonlinear simulations of FRC members subjected to shear- or punching-dominant loading.

7 Acknowledgements

This research was funded by Grant Agency of the Czech Republic, grant number 24-10892S under the project “Machine Learning for Multiscale Modelling of Spatial Variability and Fracture for Sustainable Concrete Structures”.

8 References

Barros, J. A. O., Sanz, B., Filho, M., Kabele, P., Yu, R. C., Meschke, G., Planas, J., Cunha, V., Neu, G. E., Caggiano, A., Gouveia, V., Ozyurt, N., Poveda, E., van den Bos, A., Cervenka, J., Gal, E., Rossi, P., Dias-da-Costa, D., Juhasz, P. K., Cendon, D., and Ruiz, G., 2025, “Blind competition on the numerical simulation of slabs reinforced with conventional flexural reinforcement and fibers subjected to punching loading configuration” *Structural Concrete*. Wiley Online Library, Vol. 26. - pp. 385--424.

Batson, G., Jenkins, E., and Spatney, R., 1972, “Steel fibers as shear reinforcement in beams” *Journal of American Concrete Institute*. Vol. 69.

Červenka, J., and Papanikolaou, V. K., 2008, “Three dimensional combined fracture--plastic material model for concrete”, *International journal of plasticity*. Elsevier Vol. 24. - pp. 2192 - 2220.

Červenka, J., Červenka, V., and Eligenhausen, R., 1998, “Fracture-plastic material model for concrete, application to analysis of powder actuated anchors”, *FraMCoS proceedings 1998*. Vol. 3. - pp. 1107 - 1116.

Červenka, V., Červenka J., and Jendele L., 2022, “*ATENA program documentation – Theory*”. - Prague : Cervenka Consulting s.r.o.

Narayanan, R. and Darwish, I.Y.S., 1987, “Use of steel fibers as shear reinforcement” *Structural Journal*. 3 : Vol. 84. - pp. 216 - 227.

Skadins, U. and Cervenka J., 2024, “Lessons learnt from blind competition of shear behavior of fiber-reinforced concrete T-beam”, *Structural Concrete*. Wiley Online Library. 1 : Vol. 25. - pp. 506 - 525.

Swamy, R.N., and Bahia, H.M., 1985, “The effectiveness of steel fibers as shear reinforcement”, *Concrete International*. 3 : Vol. 7. - pp. 35 - 40.

Statistical approach to quality control of steel fibre reinforced concrete using inductive measurements during production

Nadia Quijano[1], Natividad García-Troncoso[2], Samantha Hidalgo Astudillo[1], Stanislav Aidarov[3] and Albert de la Fuente[1].

[1]: Civil and Environmental Engineering Department, Universitat Politècnica de Catalunya (BarcelonaTECH), Barcelona, Spain, nadia.quijano@upc.edu, samantha.elizabeth.hidalgo@upc.edu, and albert.de.la.fuente@upc.edu.

[2]: Facultad de Ingeniería en Ciencias de la Tierra (FICT), Escuela Superior Politécnica del Litoral, ESPOL, Campus Gustavo Galindo, Km 30.5 Vía Perimetral, Guayaquil,090902, Ecuador, nlgarcia@espol.edu.ec

[3]: Department of Project and Construction Engineering, Universitat Politècnica de Catalunya (BarcelonaTECH), Barcelona, Spain, stanislav.aidarov@upc.edu

Abstract

Quality control of steel fibre reinforced concrete (SFRC) is strongly influenced by the distribution of fibres within the material and by the uncertainty associated with its measurement. The inductive method is a rapid and non-destructive approach of estimating fibre content; however, its application in decision-making remains limited due to the lack of clearly defined conformity criteria. This study presents a statistical approach based on experimental data for quality control based on inductive measurements. An experimental programme was conducted on mixtures with fibre contents of 20, 40 and 60 kg/m³. An experimental Δ_L–C_f regression model was fitted to relate total inductance variation to fibre content, and its associated prediction uncertainty was quantified through residual analysis, showing an approximately normal distribution. The experimental results were reinterpreted as production batches, enabling the definition of acceptance criteria based on tolerance intervals. In addition, Monte Carlo simulations were implemented to propagate the prediction uncertainty associated with the fitted regression model and quantify the probability of acceptance of each batch. The results show that fibre dosage variability has a significant impact on quality control outcomes. Within the investigated mixtures, more stable behaviour was observed at intermediate dosages, while increased dispersion was observed at low dosages and in mixtures where non-uniform fibre distribution was intentionally induced to assess the robustness of the method. The main contribution of this work is to present an approach to fit simple linear regressions between the inductance and fibre content and conformity criteria oriented to a preliminary quality control. The proposed methodology enables inductive measurements to be used as a practical decision-making tool and represents a preliminary step towards establishing a rational basis for acceptance and rejection in quality control applications, pending further validation under broader production conditions.

Keywords

Steel fibre reinforced concrete, inductive method, quality control, probabilistic analysis, fibre content

1 Introduction

Steel fibre reinforced concrete (SFRC) has gained increasing relevance in structural applications due to its enhanced mechanical performance, particularly in terms of crack control, ductility and post-cracking behaviour. This has enabled their use as a partial or total replacement of conventional reinforcement in a range of structural applications. [1], [2], [3]

The structural performance of SFRC is strongly dependent on the actual fibre content and its distribution within the concrete matrix. Variations in fibre dosage may lead to significant differences in residual strength, toughness and crack control capacity, directly affecting both serviceability and ultimate limit states [4], [5]. Therefore, ensuring the correct fibre content during production is a key aspect of quality control.

Traditional quality control methods for fibre reinforced concrete are typically based on destructive procedures, such as fibre extraction and weighing, or on indirect mechanical tests (EN 14721, [6]). Although these methods provide reliable results, they are time-consuming, labour-intensive and difficult to implement under real construction conditions, where rapid decision-making is required (ACI 544.3R, [7]).

In this context, non-destructive techniques based on magnetic induction have been developed as an alternative for estimating fibre content in concrete. These methods rely on the interaction between steel fibres and an applied magnetic field, allowing a reliable estimation of fibre content [5]. Previous research has shown that the inductive method can provide accurate estimations of fibre content when properly calibrated, with relatively low prediction errors [8].

In practice, quality control requires not only estimating fibre content but also determining whether a given batch complies with predefined acceptance criteria. This involves explicitly accounting for both material variability and measurement uncertainty, which are recognised as key factors influencing the mechanical performance and reliability of SFRC [4], [5]

Even when the average fibre content is close to the target value, local variability may significantly affect structural behaviour, particularly in terms of residual strength and crack control capacity [9], [10]. From a statistical perspective, this highlights the need to incorporate uncertainty into engineering decision-making, using tools such as confidence intervals, hypothesis testing and probabilistic analysis.

In this context, the present study proposes a statistical and probabilistic framework for the quality control of SFRC based on inductive measurements. The approach combines the fitting of a regression curve based on experimental results including the associated uncertainty. The experimental results produced in this research are reinterpreted to represent simplified production scenarios, enabling the evaluation of acceptance and rejection criteria as a function of sampling size and variability. Both deterministic and probabilistic approaches are considered in order to assess the reliability of the inductive method as a decision-making tool in quality control of SFRC.

2 Experimental programme

2.1 Materials and mix design

The mixtures were prepared with CEM II/A-L 42.5 R cement, well-graded aggregates, and suitable plasticisers to achieve low water-to-cement ratios and ensure adequate workability, including self-compacting behaviour.

High-strength hooked-end steel fibres (60 mm in length and 0.9 mm in diameter, with a tensile strength of 1,550 N/mm²) were incorporated at nominal fibre content ($C_{f,nom}$) of 20, 40 and 60 kg/m³, hereafter referred to as M20, M40, and M60 respectively. For each fibre dosage, a total of 35 cubic specimens with dimensions of 150 mm were cast. The mix proportions are summarised in Table 1, while the specimen preparation procedure is illustrated in Figure 1.

Table 1. Concrete mixture (in kg/m³)

Component	M20	M40	M60
Cement	470	470	470
Sand 0/4 mm	1186	1186	1186
Fine gravel 4/10 mm	169	169	169
Coarse gravel 10/20 mm	339	339	339
Water	188	188	188
Additives	7.0	7.7	8.9
Fibre	20	40	60

The specimens were cast under controlled laboratory conditions to minimise external sources of variability. After casting, the specimens were cured under standard conditions until testing. The number of specimens was selected to allow a robust estimation of variability within each mixture. The dataset provides sufficient statistical representation to analyse variability and support the proposed quality control approach.

It should be noted that, in addition to representing different fibre dosages, the M60 mixture was intentionally produced under less controlled mixing conditions to induce a higher level of variability in fibre distribution. This experimental choice was made to evaluate the robustness of the inductive method under non-uniform conditions that might occur in real production conditions. In contrast, the M20 and M40 mixtures were produced under controlled conditions without intentionally introducing additional variability.

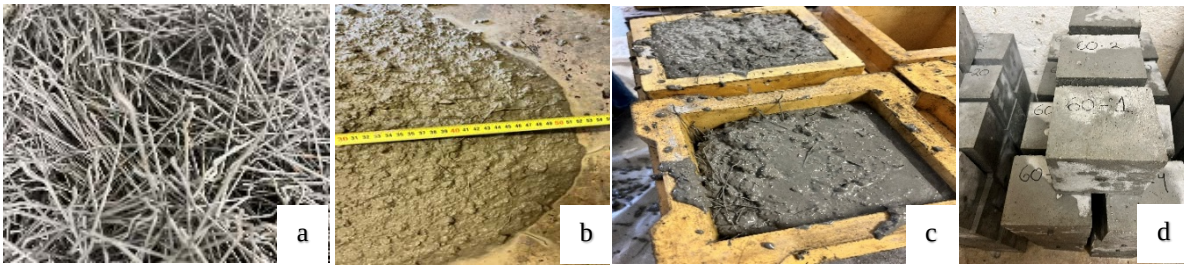


Figure 1. **SFRC** *mixes. a) Steel fibres, b) Slump test, c) and d) Production process of cubic specimens.*

2.2 Inductive measurements

Fibre content was evaluated using a non-destructive inductive method based on the variation of magnetic inductance caused by the presence of steel fibres within the concrete matrix. This technique requires the fitting of a regression line between fibre content and inductance variation

measured in a reference sample set of specimens produced with the targeted steel fibre (this fitting process has to be repeated for each fibre). This approach has been widely used for the estimation of fibre content in steel fibre reinforced concrete, showing good accuracy when the relationship between the inductive response and the actual fibre content is properly calibrated.[4], [5]

For each specimen, inductance measurements were carried out along three orthogonal directions, denoted as ΔL_x, ΔL_y and ΔL_z. These measurements account for the influence of fibre orientation on the inductive response, which has been identified as a key factor affecting inductive-based estimations [4], [5]. The measurements were performed using the SmartFibreC® device. The total inductance variation was obtained as the sum of the three components, according to Equation (1).

$$\Delta L = \Delta_{L_x} + \Delta_{L_y} + \Delta_{L_z} \quad (1)$$

The relationship between inductance and fibre content can be expressed through Equation (2).

$$C_f = \omega \cdot \sum_{i=x,y,z} \Delta L_i = \omega \cdot \Delta L \quad (2)$$

where C_f is the fibre content, ω is a calibration parameter, and ΔL is the total inductance variation. In practice, scatter around this ideal relationship may arise from the uncertainty associated with the inductive response, including the sensitivity of the magnetic field, the position of the specimen within the device and other measurement-related conditions. To determine the actual fibre content, a destructive procedure was carried out on selected specimens. The specimens were crushed, and the fibres were extracted and weighed. The real fibre content was computed using Equation (3).

$$C_{f,real} = \frac{m_f}{V} \quad (3)$$

where m_f is the mass of extracted fibres and V is the volume of the specimen. The measurements were performed on hardened concrete specimens, ensuring stable conditions and minimising the influence of fresh-state variability. The inductive method enables accurate and precise measurement without damaging the specimens, making it particularly suitable for quality control applications [4].

However, the estimation of fibre content from inductive measurements is subject to uncertainty associated with the measurement process and with the calibrated relationship between ΔL and C_f. This uncertainty must be quantified and considered in the subsequent statistical and probabilistic analyses.

2.3 Dataset used for fitting the ΔL–Cf regression and data reinterpretation for quality control

A subset of specimens was selected to fit the experimental relationship between the total inductance variation, ΔL, and the actual fibre content, $C_{f,real}$. The inductive device was not calibrated in this study; instead, a simple linear regression model was fitted using specimens for which both the inductive response and the actual fibre content obtained by destructive fibre extraction were available. The dataset used for fitting the regression model is reported in Table 2, while Figure 2a provides its graphical representation together with the fitted regression line and the physical zero-fibre reference point. This zero-fibre point was included only to illustrate

the physical consistency of the relationship and was not used to fit the regression model or to calculate the prediction error metrics. For the selected specimens, the actual fibre content was determined by crushing the specimens, recovering and weighing the steel fibres, and dividing the recovered fibre mass by the specimen volume. The fitted model expresses fibre content as a function of the measured total inductance variation, and the residuals were subsequently used to quantify the prediction uncertainty associated with the fitted regression model.

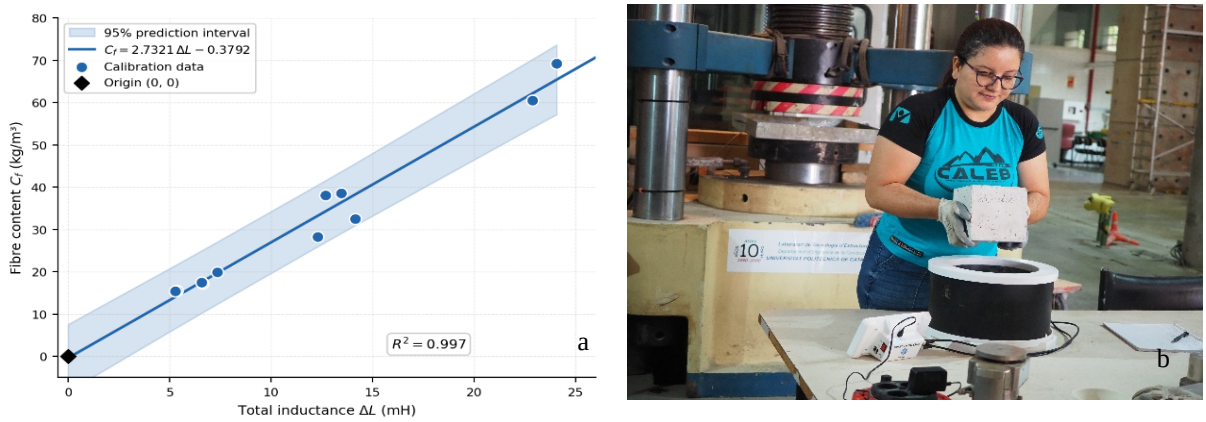


Figure 2. a) Relation between inductance change and fibre content and b) Inductive method.

Table 2 Dataset used for fitting the Δ_L–C_f regression model: total inductance variation, recovered fibre mass, actual fibre content obtained by destructive extraction, predicted fibre content and relative error.

Specimen	**ΔL (mH)**	***Recovered fibre mass (g)***	**$C_{f,real}$ (kg/m³)**	**$C_{f,pred}$ (kg/m³)**	**$\varepsilon_{rel,i}$ (%)**
20-03	7.33	67.0	19.85	19.66	-1.0
20-07	5.37	52.5	15.56	14.28	-8.2
20-12	6.63	58.0	17.19	17.74	3.3
20-19	6.57	59.0	17.48	17.56	0.5
20-29	5.27	52.0	15.41	14.01	-9.1
20-33	12.30	95.5	28.30	33.23	17.4
40-31	14.13	109.5	32.44	38.23	17.8
40-34	12.67	128.5	38.07	34.23	-10.1
40-35	22.87	204.0	60.44	62.09	2.7
60-07	24.07	233.5	69.19	65.37	-5.5
60-16	13.47	130.0	38.52	36.41	-5.5

Although the experimental program was conducted under controlled laboratory conditions, the dataset was reinterpreted to simulate real production scenarios and bridge the gap between laboratory measurements and practical quality control. Specimens were grouped into batches of three samples, representing typical sampling procedures in concrete production. This approach enables the evaluation of within-batch variability and provides a more realistic basis for assessing compliance with the target fibre content. It also supports decision-making based on representative samples and forms the basis for defining acceptance and rejection criteria at the batch level, as developed in the following sections.

The total uncertainty associated with the inductive estimation can be conceptually decomposed into three main contributions: (i) intrinsic material variability, (ii) measurement uncertainty associated with the inductive device, and (iii) fitting uncertainty associated with the Δ_L–C_f regression model.

2.4 Fitting an experimental linear regression C_f – ΔL for quality control

The relationship between inductance and fibre content was obtained by fitting a simple linear regression model to the dataset reported in Table 2 and graphically represented in Figure 2a. A linear regression model was adopted (Equation 4).

$$C_{f,pred} = 2.732\Delta L - 0.379 \quad (4)$$

where $C_{f,pred}$ is the predicted fibre content (kg/m³) for the ΔL measured. The statistical significance of the model was assessed through the standard error of the slope coefficient (SE_β), the relative uncertainty of the slope expressed as $CoV_\beta = SE_\beta/\beta$, its associated *p*-value and the coefficient of determination. The value of CoVβ was approximately 5.7%, indicating a relatively low uncertainty in the fitted slope coefficient. The linear regression model showed a high goodness of fit, with $R^2 = 0.977$, and the slope was statistically significant, confirming the strong relationship between inductance variation and fibre content. The fitted intercept was slightly negative (−0.379 kg/m³); however, it was not statistically different from zero (p = 0.83), and the prediction interval at $\Delta L = 0$ included zero. Therefore, this value only reflects the uncertainty of the regression close to the origin and has no practical implication within the investigated range. Although the variability increased with fibre content, a simple linear regression was retained as a first operational approximation for quality control purposes. A weighted regression could provide a more rigorous estimation in future work; however, the high coefficient of determination, the absence of systematic trends in the residuals and the exploratory nature of the proposed quality-control framework support the use of a simple linear regression in this study.

The prediction uncertainty was quantified through the standard deviation of the residuals of the fitted regression model, defining intervals associated with individual estimates of fibre content rather than with the mean response. This is consistent with quality control applications, where decisions are based on individual measurements.

The residuals (res_i) were computed according to Equation (5).

$$\varepsilon_i = C_{f,pred,i} - C_{f,real} \quad (5)$$

where $C_{f,real}$ is the fibre content obtained through destructive testing (kg/m³). The residuals provide a direct measure of the estimation error and allow the uncertainty associated with the inductive method to be quantified.

These residuals exhibited a mean value close to zero, indicating that the model is essentially unbiased. The standard deviation of the residuals was approximately 3.14 kg/m³, which represents the uncertainty associated with the inductive measurement method and corresponds to the fitting error. The distribution of residuals showed a symmetric pattern around zero, suggesting normality. This indicates that the variability observed is predominantly random with no drift or systematic error embedded. To further assess the predictive performance of the model, the relative error was calculated using the same sign convention according to Equation (6).

$$\varepsilon_{rel,i}(\%) = \frac{C_{f,pred} - C_{f,real}}{C_{f,real}} \quad (6)$$

The comparison between measured and predicted fibre contents, together with the corresponding ε_i is presented in Table 2. Additional validation data are not available within the

scope of the present study; however, the fitting dataset reported in Table 2 and the residual analysis shown in Figure 3 provide the experimental basis for assessing the reliability of the method.

Global error metrics were also evaluated. The mean absolute error (MAE) was approximately 2.33 kg/m³, while the root mean square error (RMSE) reached 2.99 kg/m³. The mean absolute percentage error (MAPE) was approximately 7.48%. Based on these results and considering previous studies on the inductive assessment of fibre content in SFRC [3], [4], a preliminary operational tolerance of ±10% around the nominal fibre content was adopted. This threshold was selected on the safe side as an illustrative acceptance criterion for the proposed quality-control framework and should not be interpreted as a structurally calibrated limit. The adopted tolerance is slightly higher than the MAPE obtained for the fitted regression model, providing an additional margin to account for prediction uncertainty and practical variability in quality-control applications.

This level of accuracy is consistent with the requirements of quality control applications, where the objective is to support decision making, although further validation under varied production conditions is required.

Based on the residual analysis, the estimated fibre content can be expressed in probabilistic terms as $C_{f,pred} = \widehat{C_f} + \varepsilon$, where $\varepsilon \sim N(0,\sigma^2)$ with $\sigma \approx 3.14$ kg/m³. The normality assumption of the residuals was assessed using both the Q–Q plot shown in Figure 3a and the Shapiro-Wilk test. Considering the 11 specimens used for the curve fitting and excluding the physical zero-fibre reference point, the Shapiro–Wilk test yielded W = 0.922 and p = 0.336; therefore, the normality assumption could not be rejected at the 5% significance level. In addition, the relationship between inductance and residual error was examined, as shown in Figure 3b, confirming the absence of systematic trends or curvature and supporting the validity of the linear model and the independence of residuals.

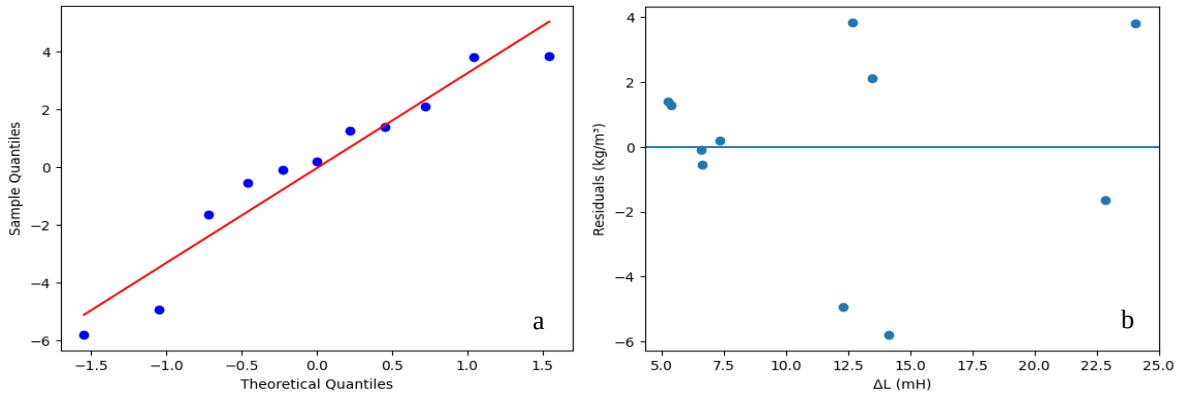


Figure 4. (a) Q–Q plot of residuals and (b) residuals as a function of total inductance variation.

3 Experimental results and discussion

3.1 Fibre content variability

The estimated fibre content obtained by using the linear regression model is presented in Figure 4. A statistical summary is provided in Table 3. Although the mean values remain close to the

nominal dosages for M20 and M40, the key aspect is the dispersion of the data, which governs the reliability of quality control decisions.

The coefficient of variation (CoV) confirms that variability (intra-batch dispersion) is present in all mixtures, with M20 showing slightly higher relative dispersion than M40. In contrast, the M60 mixture exhibits the highest variability, both in absolute and relative terms. This behaviour is not solely the result of random variability, but is partly associated with intentionally induced heterogeneity during specimen production. As described in Section 2.1, the M60 mixture was produced under less controlled mixing conditions to assess the robustness of the proposed method under unfavourable conditions.

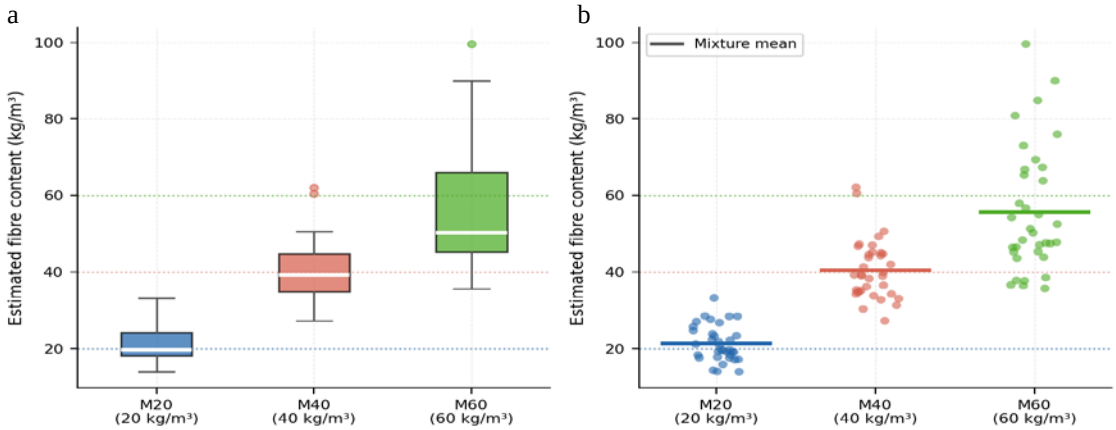


Figure 5. (a) Distribution of estimated fibre content and (b) fibre content per specimen

Table 3. Statistical summary of estimated fibre content

Statistic	M20	M40	M60
Number of specimens, (n)	35.0	35.0	34.0
Mean (kg/m³)	21.3	40.5	54.3
Median (kg/m³)	19.7	39.2	52.9
Standard deviation (kg/m³)	4.7	7.8	14.7
Coefficient of variation (CoV, %)	22.1	19.2	27.1
Minimum (kg/m³)	13.9	27.2	35.7
Maximum (kg/m³)	33.2	62.1	90.0
Interquartile range (kg/m³)	6.2	10.0	22.0

Since the full set of specimens corresponding to each mixture was analysed, the observed differences cannot be attributed solely to sampling variability. In particular, the lower mean value obtained for the M60 mixture reflects a systematic deviation (drift) is attributed to deviations in the actual fibre dosage and the intentional non-uniform fibre distribution imposed in this batch. These observations highlight the importance of explicitly considering variability when interpreting fibre content measurements and assessing compliance with target values.

3.2 Influence of sample size on acceptance results

The acceptance criterion was evaluated as a function of sample size. Starting from three specimens, the sample size was increased up to the total number of specimens for each mixture

(n = 35). For each sample size, 10,000 random subsets without replacement were generated to eliminate the dependency on a specific grouping. The mean fibre content of each subset was evaluated against the acceptance criterion defined by a preliminary operational tolerance interval of ±10% around the nominal value, adopted in this study as an illustrative criterion for assessing the proposed framework. This value corresponds to the theoretical target fibre dosage and should not be interpreted as a general acceptance limit for all SFRC applications. The use of the sample mean as an estimator is consistent with standard quality control practices; however, for small sample sizes, the mean may be affected by high dispersion and may not be fully representative of the batch. In such cases, the statistical power of the acceptance criterion is reduced, increasing the likelihood of accepting non-compliant batches (Type II error). The proportion of subsets satisfying this condition represents the probability of acceptance. Figure 5 shows the evolution of the acceptance probability as a function of sample size for each mixture.

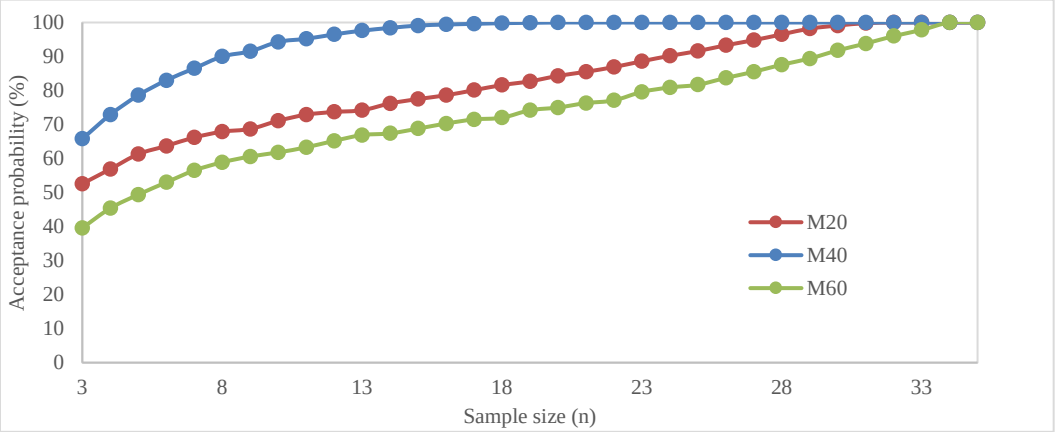


Figure 6 Probability of acceptance versus sample size for different fibre dosages.

The results indicate that the acceptance outcome is strongly influenced by the number of specimens considered. For small sample sizes, the probability of acceptance shows significant variability, reflecting the influence of sampling uncertainty; in this context, it is important to remark that the standard error of the sample mean is inversely proportional to the root sample size ($\sqrt{n}$). Thus, as the sample size increases, the acceptance probability tends to stabilise and the statistical power of the assessment increases, reducing the likelihood of Type II errors, while the probability of Type I error remains governed only by the selected significance level, α.

Among the analysed mixtures, the 40 kg/m³ dosage exhibits the highest probability of acceptance over most of the investigated range, indicating relatively stable behaviour. In contrast, the M20 mixture and the M60 -batch produced under intentionally non-uniform conditions- showed lower acceptance probabilities, reflecting higher variability in fibre distribution. Therefore, the results obtained for M60 should not be interpreted as a general effect of the 60 kg/m³ fibre dosage alone, but as the combined effect of high fibre content and intentionally induced heterogeneity during production.

3.3 Statistical interpretation of acceptance criteria

A statistical framework was adopted to evaluate the reliability of quality control decisions based on inductive measurements. The limitations associated with small sample sizes were evaluated through hypothesis testing and probabilistic interpretation, in connection with the results presented in Section 3.2.

A Student's t-test was performed considering a significance level of 5%. However, due to the limited number of specimens (e.g. n = 3), the statistical power of the test is low and may fail to detect significant deviations from the nominal value. For instance, a batch with an average fibre content of 16.1 kg/m³ for a nominal value of 20 kg/m³ yielded a p-value of 0.053, which does not lead to rejection at the 5% significance level despite the evident deviation. This behaviour agrees with the results presented in Section 3.2 and indicates that decisions based on small samples may not be statistically reliable. In this context, tolerance-based criteria provide a more robust and operational approach for quality control.

For each sample size, 10,000 realizations were generated by randomly sampling specimens from the experimental dataset and propagating the prediction uncertainty of the fitted regression model through a normally distributed error term, $\varepsilon \sim N(0,\sigma^2)$, where $\sigma = 3.14$ kg/m³ corresponds to the standard deviation of the residuals of the fitted regression model. The probability of acceptance was computed as the proportion of simulated batches satisfying the ±10% acceptance. The acceptance probability was obtained as the percentage of simulated subsets satisfying this criterion, as summarised in Table 4

Table 4. Probability of acceptance as a function of sample size (Monte Carlo simulation)

Number of specimens (n)	M20 (%)	M40 (%)	M60 (%)
3	54.0	65.8	40.4
5	61.7	78.7	49.3
10	70.7	93.8	60.5
15	77.7	98.9	69.1
20	83.4	100.0	74.4
25	91.8	100.0	82.8
30	99.2	100.0	91.6
35	100.0	100.0	100.0

The results show that the probability of acceptance increases with the number of specimens considered, reflecting the reduction of sampling uncertainty. For small sample sizes, the acceptance outcome is highly variable and depends strongly on the specific specimens selected. As the sample size increases, the results stabilise and converge towards a consistent assessment of compliance.

The differences between mixtures are also evident. The M40 mixture exhibits a rapid stabilisation and reaches full acceptance for relatively small sample sizes, indicating low variability. The M20 mixture shows a progressive increase in acceptance probability, while the M60 mixture presents lower acceptance levels and a slower convergence, reflecting its higher variability and the intentionally induced heterogeneity.

This probabilistic interpretation complements the deterministic analysis by providing a quantitative measure of the likelihood of compliance. It also reinforces the limitations of hypothesis testing in small samples and highlights the importance of considering both sampling size and measurement uncertainty in quality control applications.

3.4 Discussion and decision-making framework

The results indicate that variability is the governing factor in the quality control of steel fibre reinforced concrete. Mean values alone are not sufficient to describe material performance, as the dispersion of fibre content directly affects both deterministic and probabilistic acceptance.

The results presented in Sections 3.2 and 3.3 show that both sampling size and measurement uncertainty must be considered jointly to ensure reliable decision-making.

Incorporating uncertainty provides a more robust basis for decision making, as it accounts for both central tendency and measurement uncertainty. In this study, this is achieved through the combined use of tolerance-based criteria and probabilistic analysis, which allows the limitations of purely statistical tests to be addressed.

As stated in Section 3.2, the acceptance threshold of ±10% of the nominal fibre content was adopted as a preliminary operational tolerance to evaluate the proposed quality control framework. This threshold should not be interpreted as a calibrated acceptance limit accounting for structural reliability, since its direct relationship with residual mechanical performance has not yet been established. Future work should link this tolerance to structural performance indicators and operational control curves. At the same time, the experimental results exhibit coefficients of variation between 19% and 29%, indicating significant intrinsic variability. This highlights that material variability is of a higher order than measurement uncertainty, and therefore must be explicitly considered in acceptance decisions.

The limitations of hypothesis testing for small sample sizes further support this approach. The *t*-tests showed low statistical power and may fail to detect non-compliant batches, whereas tolerance-based criteria provide a more robust and practical procedure. The probabilistic approach complements this by quantifying the likelihood of acceptance. The Monte Carlo simulation combines the variability observed in the experimental dataset with the uncertainty associated with the regression model, providing a probabilistic interpretation of acceptance decisions within the scope of the available experimental observations.

The results also show that increased variability may significantly affect quality control outcomes, particularly under highly non-uniform fibre distribution conditions, such as those intentionally induced in the M60 mixture to assess the robustness of the proposed approach.

4 Concluding remarks

This study proposes a statistical and probabilistic framework for the quality control of SFRC based on inductive measurements. The results confirm that the inductive method provides reliable estimations when properly calibrated. The proposed acceptance criterion is based on fibre content control and should be linked to residual mechanical performance before being used as a structurally calibrated limit.

- The experimental analysis demonstrates that variability in fibre content governs quality control outcomes. While mean values remain close to nominal dosages, dispersion significantly affects batch acceptance, highlighting that compliance cannot be assessed solely on average values.
- Within the investigated mixtures, the results show that more stable behaviour is obtained at intermediate fibre dosages, whereas lower acceptance levels are associated with both low dosages and conditions of increased variability. In particular, the behaviour observed in the M60 mixture reflects the response of the proposed framework under intentionally induced non-uniform fibre distribution, confirming its sensitivity to unfavourable conditions.
- The incorporation of probabilistic methods allows measurement uncertainty to be explicitly considered and provides a more robust basis for decision making compared to

traditional deterministic or hypothesis-testing approaches, particularly when limited sample sizes are involved.

- The proposed methodology enables the transformation of inductive measurements into a practical decision-making tool for acceptance and rejection, supporting the definition of rational and transparent acceptance criteria in quality control applications.

Future work should focus on linking fibre content variability with structural performance indicators, enabling the definition of acceptance criteria directly based on mechanical behaviour. The applicability of the proposed framework is currently limited to the tested fibre type and dosage range, and further studies are required to assess its generalisation to other materials, fibre types, and production conditions.

5 Acknowledgements

The authors acknowledge to Bekaert, partner in the development of the inductive method and Licensee, and to KrampeHarex for providing the steel fibres through BIU Internacional that were used in this experimental program. The assistance of Khadija Oufli Ouhdach and Kristýna Carrera during the experimental campaign is also gratefully acknowledged.

6 References

[1] P. Pujadas, A. Blanco, S. H. P. Cavalaro, A. De La Fuente, and A. Aguado, “Multidirectional double punch test to assess the post-cracking behaviour and fibre orientation of FRC,” *Constr. Build. Mater.*, vol. 58, pp. 214–224, May 2014, doi: 10.1016/j.conbuildmat.2014.02.023.

[2] G. Tiberti, F. Minelli, G. A. Plizzari, and F. J. Vecchio, “Influence of concrete strength on crack development in SFRC members,” *Cem. Concr. Compos.*, vol. 45, pp. 176–185, Jan. 2014, doi: 10.1016/J.CEMCONCOMP.2013.10.004.

[3] S. H. P. Cavalaro, R. López, J. M. Torrents, and A. Aguado, “Improved assessment of fibre content and orientation with inductive method in SFRC,” *Materials and Structures/Materiaux et Constructions*, vol. 48, no. 6, pp. 1859–1873, Jun. 2015, doi: 10.1617/s11527-014-0279-6.

[4] J. M. Torrents, A. Blanco, P. Pujadas, A. Aguado, P. Juan-García, and M. Á. Sánchez-Moragues, “Inductive method for assessing the amount and orientation of steel fibers in concrete,” *Materials and Structures/Materiaux et Constructions*, vol. 45, no. 10, pp. 1577–1592, Oct. 2012, doi: 10.1617/s11527-012-9858-6.

[5] UNE, “UNE-EN 14721:2006+A1 Test method for metallic fibre concrete. Measuring the fibre content in fresh and hardened concrete.,” Madrid, 2008. [Online]. Available: www.aenor.es

[6] ACI Comite 544.3R, “Guide for specifying , proportioning , and production of fiber-reinforced concrete,” *American Concrete Institute*, 2008.

[7] J. hang Shi, J. Xia, R. jie Wu, K. yu Chen, J. Wang, and Y. yi Hoo, “Non-destructive testing method of fiber content in steel fiber reinforced concrete based on magnetization loss,” *J. Magn. Magn. Mater.*, vol. 586, Nov. 2023, doi: 10.1016/j.jmmm.2023.171205.

Effect of fibre orientation and hook type on the tensile response of FRC

Ahmed Hamed[1], Mário Pimentel [1]

[1]: *CONSTRUCT, University of Porto, Faculty of Engineering, R. Dr. Roberto Frias, s/n 4200-465 Porto, Portugal.*

Abstract

The tensile behaviour of fibre-reinforced concrete (FRC) is strongly influenced by fibre orientation, fibre properties, and fibre–matrix interaction. This work presents a predictive model based on detailed pull-out mechanics, incorporating the geometry of fibre end hooks and their inclination relative to the crack plane. To simulate the response in three-point bending (3PBT) and direct tensile tests, representative 3D fibre distributions are generated using probability density functions that define spatial position and orientation. The overall tensile response is obtained by summing individual fibre contributions under equilibrium and kinematic assumptions for crack development.

Model predictions are validated against experimental data for concretes with compressive strengths ranging from 50 to 100 MPa, considering fibres with varying hook-end shapes and orientation factors. After validation, the model is applied to quantify the benefits of complex hook geometries and the influence of fibre orientation on tensile performance. Finally, a practical scaling factor is proposed to account for fibre orientation in post-cracking stress design.

Keywords

Steel fibres reinforced concrete; double hooked end fibres; tensile behaviour; pull-out behaviour, analytical modelling; numerical simulation.

1 Introduction

The structural performance of fibre-reinforced concrete (FRC) is governed by its post-cracking tensile response, which arises from stress transfer through fibres bridging cracked sections (Tiberti *et al.*, 2018; Chen *et al.*, 2022). Accurately predicting this behaviour remains challenging due to the complex interaction between fibre geometry, pull-out mechanisms, orientation and matrix properties, particularly for concretes reinforced with advanced hooked-end steel fibres (Abdallah, Fan and Rees, 2018). Over recent decades, advances in fibre technology and concrete mix design have led to the development of high-performance (Blazy *et al.*, 2021; Nunes, Pimentel and Sousa, 2021) and ultra-high-performance fibre-reinforced concretes (Pimentel, Sine and Nunes, 2024), enabling structural applications with reduced fibre contents and higher matrix strengths. These developments have been supported by extensive experimental (Tiberti *et al.*, 2018; Gao *et al.*, 2021; Chen *et al.*, 2022) and analytical research (Laranjeira, Aguado and Molins, 2010; Laranjeira, Molins and Aguado, 2010; Breitenbücher *et al.*, 2014; Zhan and Meschke, 2014; Abdallah, Fan and Rees, 2018) and are reflected in modern design provisions. Despite this progress, the accurate prediction of post-cracking tensile behaviour particularly for concretes reinforced with double hooked-end steel (5D) or 1.5X hooked end (4D) fibres remains challenging, largely due to the complexity of fibre pull-out mechanisms and the strong influence of fibre orientation.

This paper aims to assess whether the tensile behaviour of FRC can be predicted with sufficient accuracy based on steel fibre properties and concrete compressive strength, thus enabling optimization of mix designs targeting the desired tensile performance classes. To this end, an integrated analytical and numerical framework is developed to predict both the direct and indirect tensile responses of FRC. The simulation of fibre distribution and orientation were implemented to represent the randomness of fibres within a concrete element. The composite tensile behaviour at cracked sections is obtained from the individual contributions of the fibres, for which detailed pullout models were developed considering the detailed hook-end geometry.

2 Description of fibre orientation

The mechanical performance of FRC composites is strongly influenced by the spatial orientation and distribution of the reinforcing fibres (Guenet, 2016; Sine, 2021; Pimentel, Sine and Nunes, 2024). In the three-dimensional space, a fibre can freely rotate according to the angles θ (polar) and ∅ (azimuthal), and all possible orientations describe the surface of a sphere. The fibre orientation in three dimensions can be described using a probability density function, assuming fibres are rigid cylinders represented by unit vectors (Sine, 2021). Guenet (Guenet, 2016; Guénet *et al.*, 2016) proposed a bell-shaped probability density function capable of representing preferential fibre alignment while satisfying the required periodicity conditions. In this work, this approach is adopted, being the probability density function of the fibre orientation in the 3D space given in Eq. (1):

$$\Psi(\theta,\emptyset) = \frac{k_g}{2\pi \sinh k_g} \cosh\left[k_g(\cos\theta\cos\beta_0 + \sin\theta\cos\emptyset\sin\beta_0)\right] \quad (1)$$

The parameter k_g characterizes the sharpness of the function: k_g=0 defines a uniform distribution, and when $k_g \to \infty$, Ψ tends to Dirac Delta function, i.e., the orientation becomes

unidirectional (1D). The angle β_0 defines the direction of preferential fibre orientation. For details, refer to (Sine, 2021).

The fibre orientation given in eq. (2) is a useful scalar descriptor of the fibre orientation with direct application on the estimation of the post-cracking tensile strength of FRC:

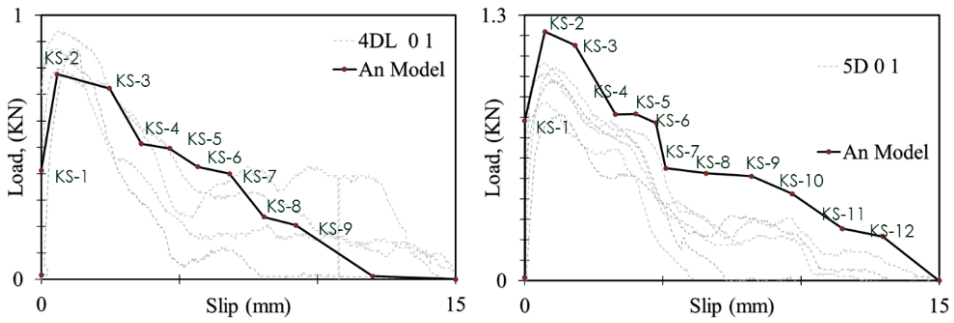
$$\alpha_{0,i} = n_{f,i} \frac{A_f}{V_f} \tag{2}$$

where $n_{f,i}$ is the number of fibres per unit area crossing the plane normal to the i-axis, A_f is the cross-section area of a single fibre and V_f is the volumetric fibre fraction.

3 Analytical pull-out model of double hooked end fibres

Previous studies have shown that fibre orientation significantly influences anchorage performance (Laranjeira, Aguado and Molins, 2010; Laranjeira, Molins and Aguado, 2010), while more complex hook geometries (e.g., 4D and 5D fibres) generally enhance pull-out resistance compared with conventional hooks (Abdallah, Fan and Rees, 2018).

The analytical model proposed by Zhan (Zhan and Meschke, 2014; Zhan, 2016) provides a direct method for calculating the anchorage force provided by aligned single hooked-end fibres (3D) during the pull-out process. In this analytical model, the anchorage effect of the hooked end is simulated through a multilinear load–displacement relationship, which represents a sequence of discrete key states (KS) during the pull-out process. By using the equilibrium of forces and moments in the segments of the hooked end, the resulting anchorage force is calculated for every key state, considering the yielding of steel and the damage of concrete (Zhan and Meschke, 2014; Zhan, 2016).



(a) (b)

Figure 1: key states (KS) during the pull-out for hooked-end fibres.: a) 4D (d_f=0.9, l_f=60, f_y=1600), b)5D (d_f=0.9, l_f=60, f_y=2300).

An analytical model is developed in (Hamed, 2026) for double hooked-end fibres (4D and 5D) by extending the original model proposed by Zhan (Zhan and Meschke, 2014; Zhan, 2016) incorporating additional stages to account for variations in hook geometry among the different fibre types. The pull-out response is described through a sequence of key states representing progressive hook deformation, straightening, and sliding during extraction. For each key state, equilibrium and yield or slip conditions are applied to determine internal forces and evaluate the anchorage contribution of the hook. The frictional behaviour of the straight fibre segments is incorporated using the straight-fibre pull-out model also proposed by Zhan (Zhan and

Meschke, 2014; Zhan, 2016), resulting in a unified analytical description of the pull-out behaviour. A full description of the model formulation is provided in Hamed (Hamed, 2026). Examples of the predicted pull-out responses for 4D and 5D fibres compared with experimental results are shown in Figure 1a and Figure 1b, respectively.

The influence of fibre inclination is accounted for using the model proposed by Laranjeira et al. (Laranjeira, Molins and Aguado, 2010), which modifies the pull-out response based on the fibre orientation relative to the crack plane.

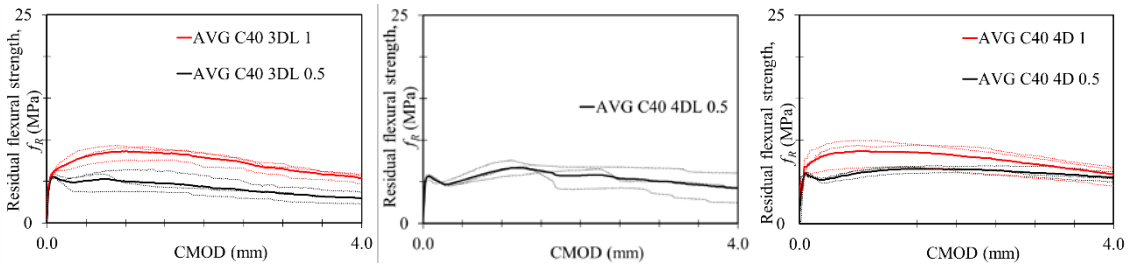
4 Experimental program

The flexural performance is investigated using three-point bending test (3PBT), focusing on hooked-end steel fibres with different hook-shapes (3D, 4D, 5D), varying length, strength, and volume fractions (0.5% and 1.0%) across different concrete grades (C40, C70 and C100). For the C40 and C70 concrete mixes, the following materials were used: Type I Portland cement (CEM I 42.5R); limestone powder Betocarb® HP-OU (LP); silica fume Elkem 940-U (SF, C70 only); standard sand; granite coarse aggregate (CA); superplasticizer Sika® ViscoCrete® 20HE (Sp) and tap water. Concerning the study for the high-performance concrete mix (C100), the same type of cement, LP, SF, Sp and tap water were used. However, a different type of natural sand is employed, and the CA was replaced by a crushed coarse aggregate (dmax=8mm; amphibolite rock). Three types of hooks shapes were investigated which included single hook (3DL), 1.5X hook (4D, 4DL), and double hook (5D). The 3DL Fibre is 60 mm long with a diameter of 0.9 mm, and a tensile strength of 1160 N/mm²; 4D is 35 mm in length with a diameter of 0.55 mm, and a tensile strength of 1850 N/mm²; 4DL is 60 mm long with a diameter of 0.9 mm, and a tensile strength of 1600 N/mm²; and 5D, is 60 mm long with a diameter of 0.9 mm and tensile strength of 2300 N/mm².

The slump flow test was carried out according to EN 12350-8. The compressive strength after 28 days (f_c, 28d) was taken as the average of the cube compressive strength evaluated in three samples. The compressive strength test was conducted according to EN 12390-3. The 3PBT was carried out according to EN 14651:2005 + A1:2007.

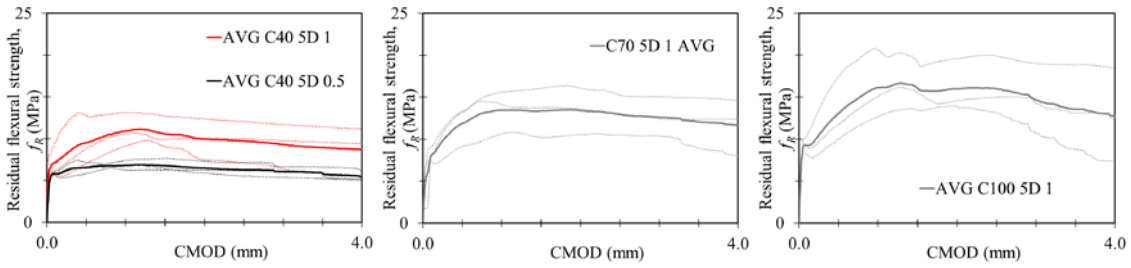
5 Test Results

The concrete grades C40, C70, and C100 had slump flows of 742.5 mm, 837.5 mm, and 705 mm, respectively, with corresponding 28-day compressive strengths of 57.8/61.9 MPa, 83/98.2 MPa, and 107.2/122 MPa (cylinders/cubes). Figure 2 and Figure 3 illustrate the post-cracking behaviour of the various mixes in the 3PBT, represented as the f_R -CMOD relationship.



(a) (b) (c)

Figure 2: C40 flexural results with: a) 3DL (0.5, 1%), b) 4DL (0.5%), c) 4D (0.5, 1%).

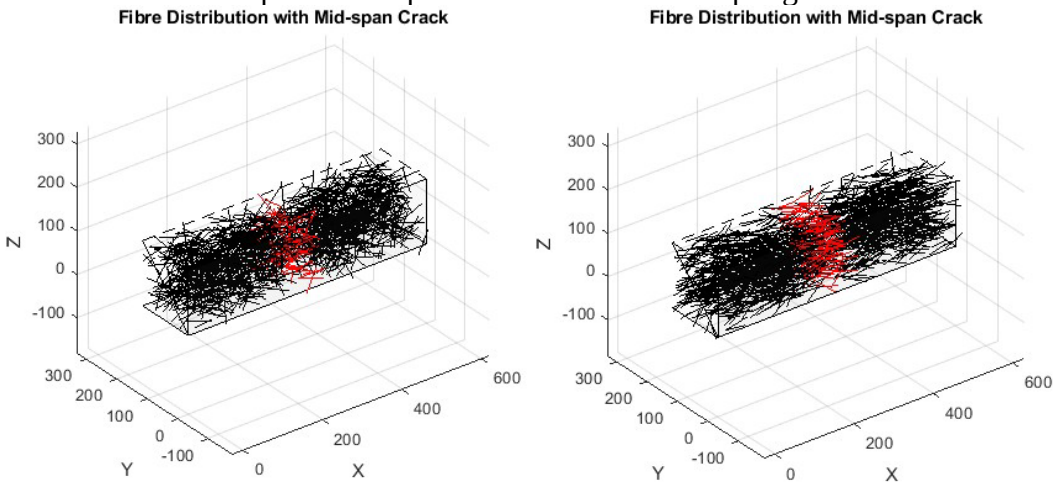


(a) (b) (c)

Figure 3: 5D fibres flexural results with: a) C40 (0.5, 1%), b) C70 (1%), c) C100 (1%).

6 Model for the tensile behaviour of FRCs

In this study, both direct tensile test (DTT) and three-point bending test (3PBT) responses are simulated. The simulation models steel fibres randomly distributed within a 3D concrete beam of dimensions L×W×H, with positions generated using a uniform random distribution within the specimen volume. Fibre orientation is defined by a unit vector and generated using a Guenet distribution (Guenet, 2016; Guénet *et al.*, 2016), allowing control of anisotropy through the sharpeness parameter k_g (see Figure 1). Boundary effects are considered by identifying and adjusting the orientation of the fibres located near the specimen walls. This adjustment is achieved by constraining the allowable orientation angles relative to the normal of the nearest wall. A single planar crack is assumed and the fibres intersecting this crack plane are identified. For each crossing fibre, the fibre is divided into two embedded lengths, L_1 and L_2, corresponding to the portions on either side of the crack, while the fibre orientation angle (θ) relative to the crack plane is also determined. Each intersecting fibre undergoes a pull-out analysis, which returns the force–slip relationship for both embedded segments. The shorter embedded length generally governs the pull-out behaviour, as it reaches debonding and pull-out first. Using the pull-out model previously described, the fibre bridging effect is obtained via the summation of the pull-out response of all fibres intercepting the crack.



(a) (b)

Figure 4: Representation of fibre Distribution in 3D, numerical simulation output showing influence of variation in k_g on the fibre orientation inside an element: a) k_g=0, b) k_g=10.

To evaluate the post-cracking behaviour of FRC in a direct tensile test, the cracks are assumed to open without any rotation, corresponding to the kinematics that is expected when fixed-fixed boundary conditions are employed at both ends.

The total fibre bridging force, $F_f(w)$, is obtained by summing the interpolated responses of all fibres, $F_{f,i}(w)$, resulting from the fibre pull-out simulations assuming that they act independently:

$$F_f(w) = \sum_{i=1}^{Nf} F_{f,i}(w) \tag{3}$$

The resulting bridging stress is calculated by dividing the summed fibre force by the cross-sectional area of the specimen:

$$\sigma_f(w) = \frac{F_f(w)}{A} \tag{4}$$

where A=W×H is the specimen cross-sectional area.

The stress contribution of the cementitious matrix $\sigma_m(w)$ is modelled using an exponential tension-softening law adapted from Voo and Foster (Voo and Foster, 2003) and used by Ali Amin (Amin, Ali ,Stephen J. Foster, 2015). The total stress across the cracked section iss then obtained by superimposing the matrix and fibre stresses:

$$\sigma_{total}(w) = \sigma_m(w) + \sigma_f(w) \tag{5}$$

In structural simulations of bending tests, a sectional analysis is performed considering that plane sections remain plane. The member cross-section is defined by its width (W) and depth (D). The characteristic length is taken as the section depth (l_{cs}=D), over which strains develop and longitudinal displacements are derived from the local longitudinal strains at the crack section. The section is discretized into n = 200 horizontal layers of thickness Δy. The vertical coordinate y is defined from the section centroid. The pull-out simulations provide the local bridging response for each fibre (i) crossing the crack plane, defined by the centroid coordinate z_i and the pull-out curve $[w_i, F_i]$ (crack width–force).

For each curvature increment κ, the algorithm determines the neutral axis depth **(y_n)** that satisfies the axial equilibrium condition:

$$N_{axial} = N_{Conc} + N_{fibres} \tag{6}$$

where N_{axial} is the applied axial force, N_{Conc} is the resultant concrete axial force obtained by integrating the stress distribution, and N_{fibres} is the sum of the tensile forces in all active fibres.

For each layer, the concrete strain is computed as:

$$\varepsilon(y) = (y - y_n)\kappa \tag{7}$$

and the corresponding stress $\sigma_c(\varepsilon)$ is obtained through a nonlinear constitutive model, which accounts for both compression and tension softening. For compressive strains, the stress–strain relationship follows the structural analysis model proposed in Eurocode 2 (EN1992-1-1).

A fibre is considered active if its depth lies within the tension zone (z_i>y_n). For each such fibre, the local crack width is estimated from the curvature-induced opening:

$$w_i = |(z_i - y_n)kl_{cs}| \quad (8)$$

The corresponding fibre force is then interpolated from the pull-out curve:

$$F_i = f_{pullout}(w_i) \quad (9)$$

The total fibre tensile force N_{fibres} is obtained by summing all F_i values. The neutral axis depth y_n is found iteratively by the bisection method until the difference between N_{axial} and the computed total force is below a specified tolerance.

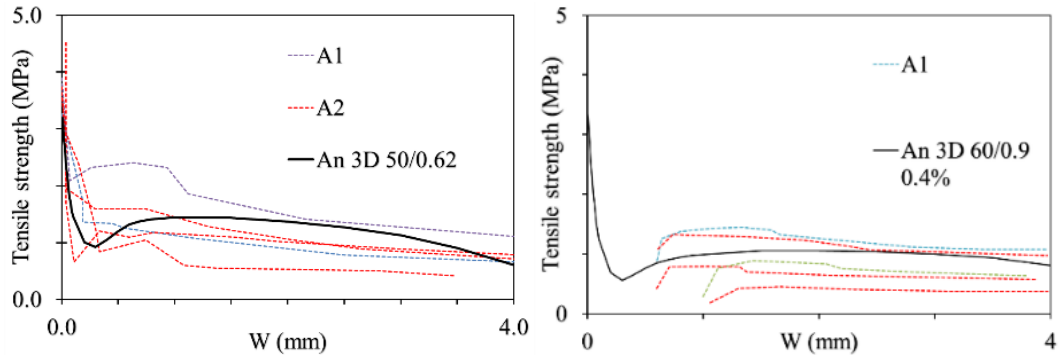
After axial equilibrium is achieved, the section moment is obtained as the sum of the concrete (M_{Conc}) and fibre (M_{fibres}) contributions:

$$M_{total} = M_{Conc} + M_{fibres} \quad (10)$$

7 Comparison with experimental results

The proposed numerical model was validated against experimental results from both direct tensile tests (DTT) and three-point bending tests (3PBT). In all simulations, the specimen geometry, boundary conditions, and material parameters were adopted from the corresponding experimental studies. To reduce variability associated with random fibre orientation and spatial distribution, the numerical response was obtained as the average of multiple simulation runs, ranging from a minimum of ten to a maximum of one hundred runs. An isotropic fibre orientation was assumed (k_g = 0), unless experimental fibre orientation parameters or fibre counts were reproduced numerically.

Good agreement is obtained with experimental DTT results reported by Susetyo (Susetyo, 2009) and Amin (Amin, 2015) for unnotched specimens reinforced with 3D fibres as illustrated in Figure 5.



(a) (b)

Figure 5: DTT results of 3D fibres in concrete C1 (f_c=59 MPa): a) 0.5% of (50/0.62), b) 3D (60/ 0.9) 0.4% (63.6 MPa).

Additional validation was performed using experimental 3PBT results. For C40 concrete with 0.5% fibre content, the model slightly underestimates the experimental response but captures the overall trend of the flexural behaviour, as shown in Figure 6. The mean numerical and experimental orientation factors are 0.55 and 0.42 for 3DL fibres, 0.51 and 0.47 for 4DL fibres.

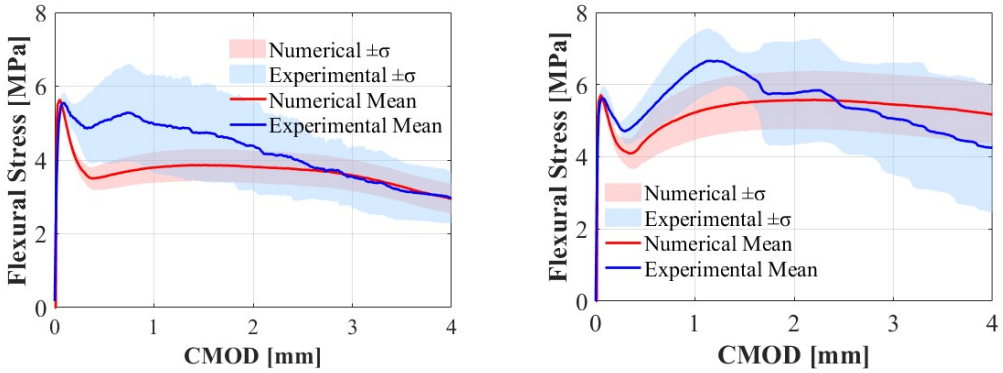


Figure 6: C40 flexural results with (0.5% fibre content): a) 3DL, b) 4DL.

For a 1% fibre dosage, very good agreement is obtained for 5D fibres, accurately capturing both the initial stiffness and post-cracking behaviour. The experimental orientation factors for 5D fibres are 0.68 and 0.59 for C40 and C100 concretes, respectively, compared with a numerical value of 0.52, as illustrated in Figure 7.

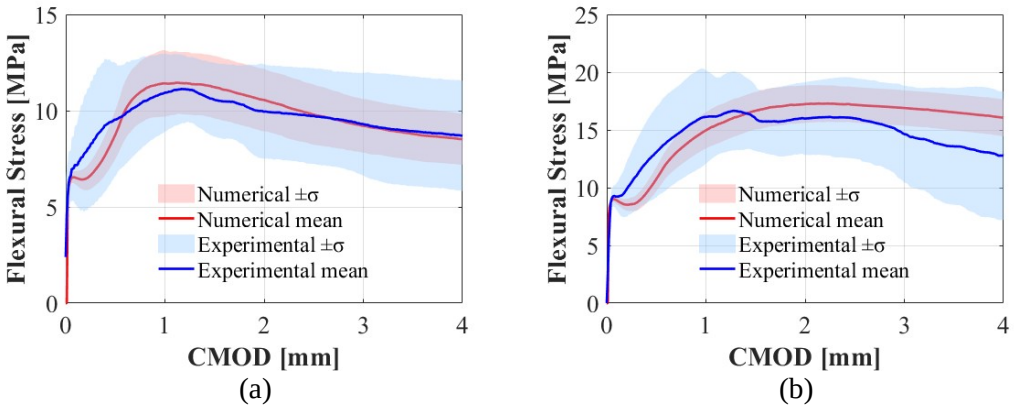


Figure 7: 5D flexural results with (1% fibre content) of: a) C40, b) C100.

8 Parametric investigation for the tensile behaviour of FRCs

The influence of hook type on the model predictions was also investigated for three types of hooked-end fibre. Fibres with a higher number of hooks exhibit greater pull-out resistance and higher residual strengths, highlighting the important role of mechanical anchorage in improving the post-cracking behaviour of FRC as shown in Figure 8. The results correspond to 3PBT simulations using a concrete with a compressive strength of 58MPa and a fibre volumetric fraction of 0.5%. All the fibres have 60mm length and 0.9mm diameter. The average fibre orientation factors are 0.56, 0.50 and 0.51 for the 3DL, 4DL and 5D virtual test specimens, respectively.

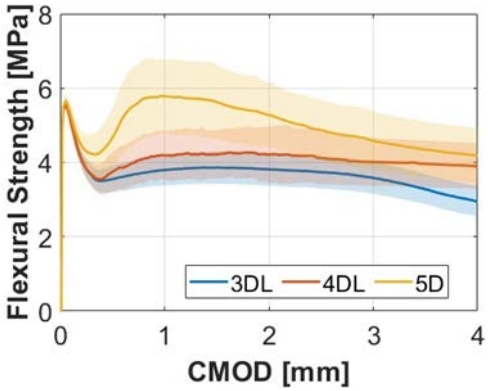
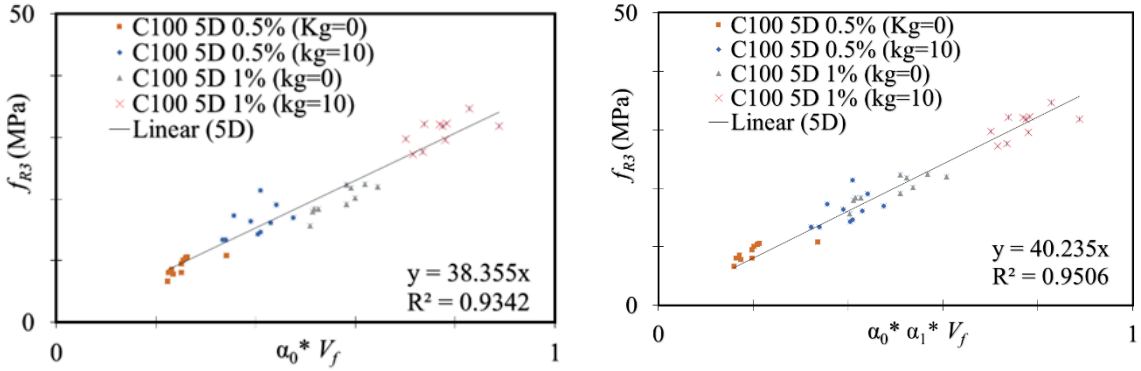


Figure 8: The effect of hook type variation of fibres using 0.5% of fibre content on 3PBT results, 3DL vs 4DL vs 5D.

To account for differences in fibre orientation, the fibre orientation factor α_0 and the fibre efficiency factor α_1 were considered. The product of the fibre orientation factor α_0 defined in Eq. (2), by the volumetric fibre fraction V_f, represents the total fibre cross-sectional area crossing the crack plane per unit area. However, not all fibres engage simultaneously and the efficiency factor α_1 accounts for the loss of crack-bridging efficiency associated with fibre inclination. The fibre efficiency factor α_1 proposed by Abrishambaf et al. (Abrishambaf, Pimentel and Nunes, 2017) is given by Eq. (11):

$$\alpha_{1,i} = 1.686.\sqrt{\alpha_{0,i}} - 0.406 \quad ,0 \le \alpha_{1,i} \le 1 \tag{11}$$

This factor links fibre orientation to the effective number of load-carrying fibres and allows the effective fibre reinforcement ratio to be expressed as $\alpha_0\alpha_1 V_f$. Incorporating α_1 significantly improves the linear correlation between the number of fibres crossing the crack plane and the predicted mechanical response as shown in Figure 9. This figure shows the results of numerical simulations considering fibre volumetric fractions V_f= 0.5% and 1% and uniform (k_g=0) and strongly oriented (k_g=10) fibre orientation distributions.



(a) (b)

Figure 9: C100 f_{R3} flexural response as a function of: a) fibre reinforcement ratio ($\alpha_0 V_f$), b) effective fibre reinforcement ratio ($\alpha_1\alpha_0 V_f$).

Finally, the ability of the model to reproduce anisotropic tensile behaviour was assessed by considering different fibre orientation distributions as illustrated in Figure 10. Increasing the orientation parameter k_g leads to stronger preferential alignment and pronounced directional

variation in the post-cracking tensile response. While k_g = 0 represents isotropic fibre distribution, higher values correspond to increasingly anisotropic orientations. The results show that fibre alignment enhances tensile capacity for the cracks normal to the direction of preferential fibre orientation, here defined by the angle 0º, while reducing effectiveness as the crack rotates, as presented in Figure 11a. Figure 11b further demonstrates that the product of the fibre orientation and efficiency factors, $\alpha_0\alpha_1$, accurately reproduces the anisotropic tensile response even in very extreme scenarios with strong fiber orientation, showing good agreement with the numerical simulations across different crack angles. For each value of k_g, the solid lines represent the ratio of the post-cracking tensile strength at a given crack angle to that at zero crack angle ($\sigma_{Cf}(\theta) / \sigma_{Cf}(\theta=0)$), as obtained directly from the numerical simulations. The dotted lines represent the corresponding ratio of the combined orientation parameters, calculated as $(\alpha_0 \cdot \alpha_1)_\theta / (\alpha_0 \cdot \alpha_1)_{\theta=0}$.

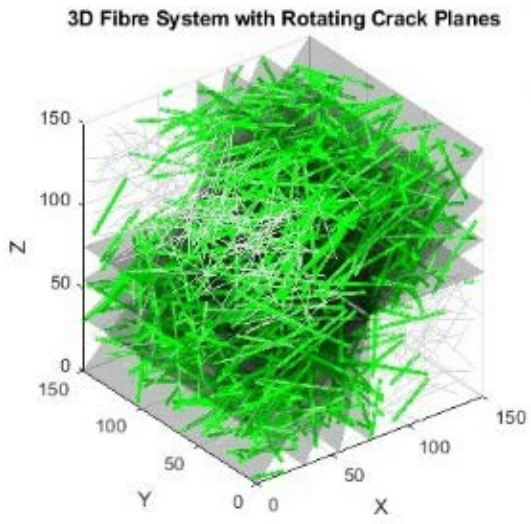
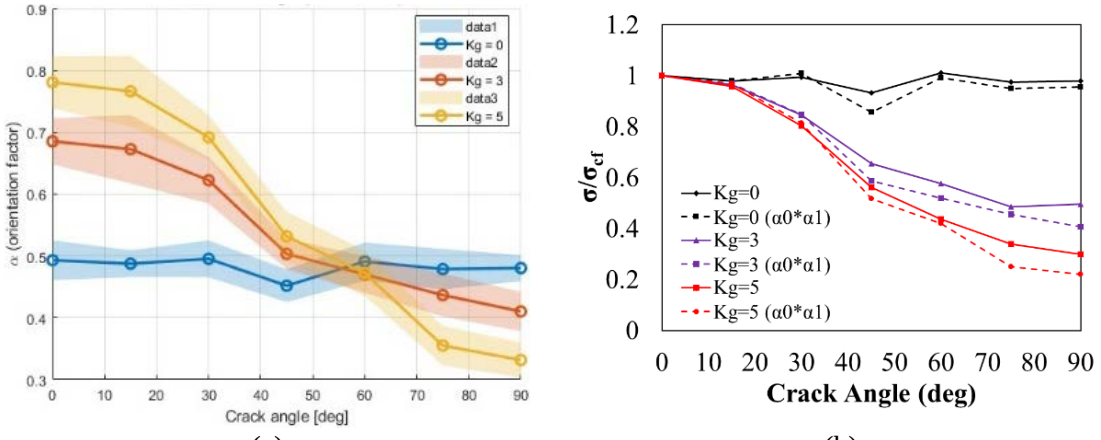


Figure 10: Fibre distribution within cracked section with various cracks inclination using fibre content of V_f=1% for k_g=3.



(a) (b)

Figure 11: Results for same specimen with 1% of 5D hooked end fibres using different k_g with respect to different angle for the crack plane: a) Orientation factor, b) Post-cracking stress normalized the post-cracking stress of the crack oriented at 0º.

9 Concluding remarks

This study developed a numerical framework for predicting the tensile behaviour of fibre-reinforced concrete (FRC) based on the analytical pull-out response of single hooked-end steel fibres. The model explicitly simulates fibre distribution and orientation within a representative concrete element and evaluates the composite response by superimposing the pull-out contributions of fibres intersecting a crack plane, enabling prediction of both direct tensile and flexural behaviour.

Validation against experimental direct tensile test (DTT) results from the literature and three-point bending test (3PBT) results showed good agreement across different fibre geometries and concrete strength classes. The variations in hook geometry demonstrated that fibres with a higher number of end-hooks (e.g., 5D) achieved superior pull-out performance and residual flexural strength due to enhanced mechanical anchorage. An engineering approach for scaling the constitutive law was investigated by explicitly incorporating fibre orientation through the product $\alpha_0\alpha_1 V_f$, which can be defined as the effective fibre reinforcement ratio. This allows capturing the effects of preferential alignment and anisotropy at the meso-scale, and proved essential for linking fibre orientation to the effective number of load-carrying fibres at the crack plane. The application of the efficiency factor α_1 significantly improved correlations between fibre count and mechanical response, particularly when orientation distributions varied markedly. This demonstrates that the constitutive law can be rationally scaled across different specimen geometries and fibre arrangements.

10 Acknowledgements

Support from the Portuguese Foundation for Science and Technology (FCT) through the Ph.D. grant (2021. 06674.BD) is gratefully acknowledged. Materials supply by Secil, Chryso Portugal, Sika is also gratefully acknowledged. This work was also supported by: UID/04708/2025 (https://doi.org/10.54499/UID/04708/2025), of the CONSTRUCT - Instituto de I&D em Estruturas e Construções - funded by FCT, I.P./ MECI, through the national funds.

11 References

Abdallah, S., Fan, M. and Rees, D. W. A. (2018) 'Predicting pull-out behaviour of 4D/5D hooked end fibres embedded in normal-high strength concrete', Engineering Structures. Elsevier, 172(October 2017), pp. 967–980. doi: 10.1016/j.engstruct.2018.06.066.

Abrishambaf, A., Pimentel, M. and Nunes, S. (2017) 'Influence of fibre orientation on the tensile behaviour of ultra-high performance fibre reinforced cementitious composites', Cement and Concrete Research, 97, pp. 28–40. doi: 10.1016/j.cemconres.2017.03.007.

Amin, Ali ,Stephen J. Foster, A. M. (2015) 'Derivation of the σ-wrelationship for SFRC from prism bending tests', Structural Concrete, 16(1), pp. 93–105. doi: 10.1002/suco.201400018.

Amin, A. (2015) Post cracking behaviour of steel fibre reinforced concrete : from material to structure. School of Civil and Environmental Engineering The University of New South Wales Sydney, Australia.

Aurélio Guilherme Sine (2021) Strengthening of reinforced concrete elements with uhpfrc, the Faculty of Engineering of the University of Porto for the degree of Doctor in Civil Engineering - Structures. Faculty of Engineering of University of Porto.

Blazy, J. et al. (2021) 'Development of an HPFRC for Use in Flat Slabs', in RILEM Bookseries. Springer Science and Business Media B.V., pp. 209–220. doi: 10.1007/978-3-030-58482-5_19.

Breitenbücher, R. et al. (2014) 'Experimental, analytical and numerical analysis of the pullout behaviour of steel fibres considering different fibre types, inclinations and concrete strengths', Structural Concrete, 15(2), pp. 126–135. doi: 10.1002/suco.201300058.

Chen, G. et al. (2022) 'Flexural Tensile Behavior of Single and Novel Multiple Hooked-End Steel Fiber–Reinforced Notched Concrete Beams', Journal of Materials in Civil Engineering, 34(6), pp. 1–15. doi: 10.1061/(asce)mt.1943-5533.0004214.

Gao, D. et al. (2021) 'Diverse angle-length-width model for 3D/4D/5D steel fiber reinforced concrete under tension', Construction and Building Materials. Elsevier Ltd, 266(97), p. 121149. doi: 10.1016/j.conbuildmat.2020.121149.

Guenet, T. (2016) Modélisation du comportement des bétons fibrés à ultra-hautes performances par la micromécanique : effet de l'orientation des fibres à l'échelle de la structure. Université Paris-Est et Université Laval.

Guénet, T. et al. (2016) 'Numerical Modeling of UHPFRC Tensile Behavior by a Micromechanics FEM Model Taking into Account Fiber Orientation', in 9th International Conference on Fracture Mechanics of Concrete and Concrete Structures FraMCoS-9. doi: 10.21012/fc9.010.

Hamed, A. T. F. (2026) Multi-level approach to the tensile response of fibre-reinforced concrete. Faculty of Engineering of University of Porto, (Submitted).

Laranjeira, F., Aguado, A. and Molins, C. (2010) 'Predicting the pullout response of inclined straight steel fibers', Materials and Structures/Materiaux et Constructions, 43(6), pp. 875–895. doi: 10.1617/s11527-009-9553-4.

Laranjeira, F., Molins, C. and Aguado, A. (2010) 'Predicting the pullout response of inclined hooked steel fibers', Cement and Concrete Research. Elsevier Ltd, 40(10), pp. 1471–1487. doi: 10.1016/j.cemconres.2010.05.005.

Nunes, S., Pimentel, M. and Sousa, C. (2021) 'Mechanical and Fracture Behaviour of an HPFRC', in Fibre Reinforced Concrete : Improvements and Innovations II, pp. 174–185. doi: 10.1007/978-3-030-83719-8_16.

Pimentel, M., Sine, A. and Nunes, S. (2024) 'Non-destructive evaluation of the steel fibre content and anisometry in thin UHPFRC elements', NDT and E International, 145(February). doi: 10.1016/j.ndteint.2024.103128.

Susetyo, J. (2009) Fibre reinforcement for shrinkage crack control in prestressed, precast segmental bridges, PhD Thesis. University of Toronto.

Tiberti, G. et al. (2018) 'An overview of the flexural post-cracking behavior of steel fiber reinforced concrete', Structural Concrete, 19(3), pp. 695–718. doi: 10.1002/suco.201700068.

Voo, Y. L. and Foster, S. (2003) 'Variable Engagement Model for the Design of Fibre Reinforced Concrete Structures', Advanced Materials for Construction of Bridges, Buildings, and Other Structures III.

Zhan, Y. (2016) Multilevel Modeling of Fiber-Reinforced Concrete and Application to Numerical Simulations of Tunnel Lining Segments. Ruhr University Bochum, Germany.

Zhan, Y. and Meschke, G. (2014) 'Analytical Model for the Pullout Behavior of Straight and Hooked-End Steel Fibers', Journal of Engineering Mechanics, 140(12), pp. 1–13. doi: 10.1061/(asce)em.1943-7889.0000800.

Performance optimisation of Hybrid Fiber Reinforced Concrete with macro-synthetic and steel fibers for concrete industrial floors

Luca Facconi[1], Giovanni Plizzari[1], Marco Paparella[2], Matteo Draconte[2], Francesco Surico[2], Luca Torelli[2]

[1]: Department DICATAM, University of Brescia, Brescia, Italy.

[2]: Mapei SpA, Milan, Italy.

Abstract

In traditional Fiber Reinforced Concrete (FRC), fibers are often added to improve the concrete's resistance to cracking and to enhance its post-crack tensile strength. However, despite these improvements, there are challenges related to the achievement optimal crack control and maintaining high performance under various loading conditions. These challenges become even more pronounced in environments subject to cyclic loading, extreme temperatures, or aggressive chemicals, where the concrete may experience rapid deterioration.

To address these issues, hybrid FRC, which combines different types of fibers, has emerged as a promising solution. The combination of macro-synthetic fibers and steel fibers may produce synergies and advantages to each material; in fact, steel fibers are particularly efficient for improving the initial post-cracking resistance (especially shorter fibers), while macro-synthetic fibers are highly effective for bridging cracks for larger crack openings.

The present study aims to investigate the performance of hybrid FRC, incorporating both macro-synthetic and steel fibers, focusing on its post-crack tensile and flexural resistance. The idea behind the experimentation is the combination of different fiber materials to obtain synergies in terms of residual strength and ductility of FRC.

Some case studies of industrial floors having different thickness were numerically analyzed some selected FRCs for better comparing the role of the different material behavior on the global response of the slab on grade.

Keywords

Hybrid fiber reinforcement, Steel fibers, macro-synthetic fibers, fiber reinforced concrete, post-crack strength, concrete industrial floors.

1 Introduction

Fiber Reinforced Concrete (FRC) is a composite material that has gained significant attention in the construction industry due to its enhanced mechanical properties as compared to conventional concrete. In fact, the addition of fibers into concrete mixes aims to improve the material's post-cracking behavior, limiting crack propagation (fibers create multiple crack-bridging mechanisms) and increasing the overall durability and toughness [1]. As a consequence, FRC is widely used in several applications, including industrial floors, tunnel linings and bridge decks.

However, despite these improvements, there are still challenges for achieving optimal crack control and maintaining high performance under various loading conditions. These challenges become even more pronounced in structures subject to cyclic loading, extreme temperatures, or aggressive chemicals, where the concrete may experience rapid deterioration.

To address these issues, hybrid FRC, which combines different types of fibers, has emerged as a promising solution [2,3,4,5]. Specifically, the combination of synthetic and steel macro-fibers, is considered herein for investigating the behavior of hybrid FRC focusing on its post-cracking tensile and flexural strength [6,7].

Furthermore, some insights into the potential advantages of hybrid FRC in improving the performance of industrial floors is discussed and some case studies of industrial floors having different thickness were numerically analyzed for better comparing the role of the material behavior on the global response of the slab on grade.

2 Hybrid systems of fibers

Fiber efficiency for smaller or larger cracks depends on fiber geometry and material as well as on the concrete matrix. Material optimization may consider the combination of different (for material and/or geometry) types of fibers for enhancing structural requirements at both Service (SLS) and ultimate (ULS) Limit States, including post cracking strength at small and large crack opening, shrinkage cracking, fire resistance, etc. [2,3].

In particular, the combination of synthetic and steel fibers in FRC aims to take advantage of the complementary properties of each type of fiber since:

- synthetic fibers enhance early-age crack control and resistance to corrosion; in fact, these fibers are particularly effective in controlling plastic shrinkage cracks which often occur at early age [8];

- steel fibers provide an enhanced post-crack strength and are less influenced by creep phenomena under long-term loading. Therefore, the combination of synthetic and steel fibers in a hybrid FRC mix activates synergies for enhancing structural behavior, making it well-suited for applications requiring durability beside the structural capacity.

3 Materials

The main properties of the fibers adopted are summarized in Table 1 while Figure 1 shows the macro synthetic and the steel fibers used in the experimental campaign.

Table 1: Geometrical properties of the fibers.

Fiber Type	Length	Diameter	Elastic modulus	Tensile strength
Macro synthetic fibers /twisted	50 mm	0,4 mm	5.000 MPa	660 MPa
Steel fibers/ Hooked	60 mm	1,00 mm	190.000 MPa	1.230 MPa



(a) (b)

Figure 1:Macro synthetic fibers (a) and steel fibers (b) used in the experimental campaign.

A standard concrete class C30/37 with a consistency class S4 was adopted.Experimental results.

4 Nonlinear structural analysis of an industrial floor

This section investigates the structural performance of some of the FRC materials introduced above when used in slab-on-grade construction, where fibers were considered as the only reinforcement of concrete. A typical industrial pavement, designed to carry storage racks, was analyzed through nonlinear finite element simulations, focusing attention on the influence of some key parameters (such as FRC performance and slab thickness) on the overall bearing capacity of the pavement. To reflect a realistic scenario, multiple rows of storage racks were arranged in a typical rack configuration, commonly adopted in warehouses to facilitate the movement of personnel, equipment, and goods. The shelving system was placed on a continuum jointless slab on grade having dimensions of 25x25 m^2. The following sections describe in detail the properties of the finite element model and report an exhaustive discussion of the analysis results.

4.1 Pavement geometry

The plan view of the pavement geometry is reported in Fig. 1. The slab is laid on a continuous subgrade characterized by a Winkler coefficient of 0.1 N/mm^3. The racking system consists of four rows placed symmetrically with respect to the center of the slab. Each row consists of seven racks, each supported by four base plates measuring 120×120 mm^2. According to the support layout, the base plates are spaced 2.7 m in the longitudinal direction and 1.0 m in the transverse direction. It was assumed that the load acting on each rack is evenly distributed among its four supports. Consequently, the two base supports located at the ends of the rows

carry half the load applied to the intermediate supports. The aisle width is equal to 3 m whereas the distance of the rows from the borders of the pavement ranges from 3 m to 6 m. The pavement shown in Fig. 1 represents a single floor area without construction joints. Therefore, as discussed in the following section, no constraints were applied along the perimeter of the numerical model, allowing the edges to move freely in the vertical direction, similarly to the free borders of a real industrial floor. The parametric study considered three different slab thicknesses, i.e. 150 mm, 200 mm and 250 mm, representative of practical applications. No conventional reinforcement was included in the slab as fibers were considered the only reinforcement for concrete. A concrete class C30/37 (Eurocode 2, 2023) was considered.

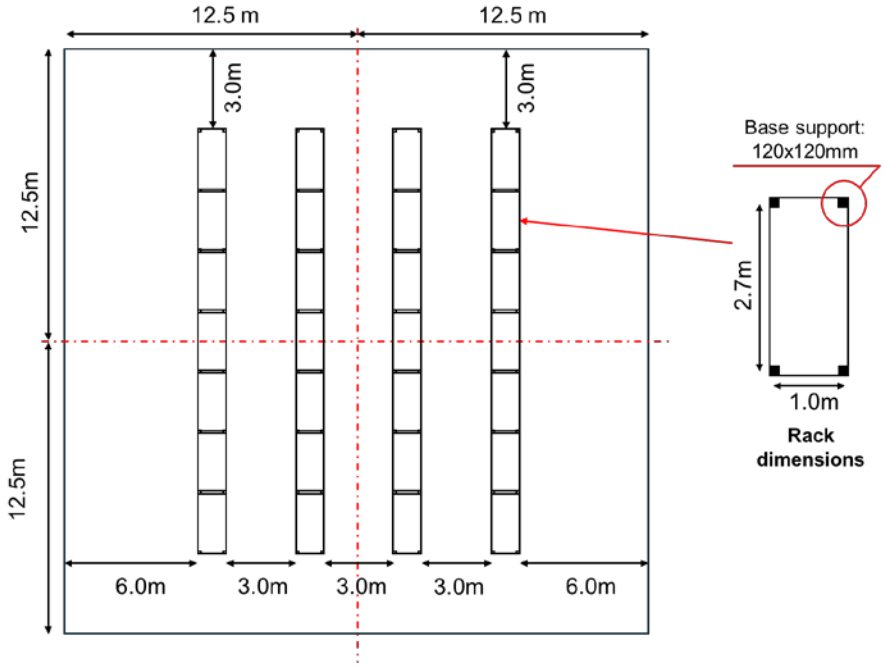


Figure 1: Pavement geometry and racking layout.

4.2 Description of the numerical model

A three-dimensional finite element (FE) model was performed using the commercial software Diana 10.6 (2022). By considering the double geometrical and loading symmetry, only one quarter of the slab was modeled, resulting in a reduced slab area with dimensions of 12.5 × 12.5 m²; the FE mesh representing the considered slab portion is depicted in Fig. 2.

A total of 10800 4-nodes isoparametric shell elements, having dimensions of about 120x120 mm^2, were used to discretize the model. As shown in Fig. 2, symmetry boundary conditions were applied along two of the four slab edges to appropriately restrain horizontal translations and rotations, ensuring that the reduced model replicates the behavior of the full slab. In order to simulate the behavior of the subgrade, uniaxial no-tension elastic springs were connected to the mesh nodes perpendicularly to the slab plane. An axial stiffness of 1400 N/mm was assigned to the springs in order to reproduce the Winkler coefficient (i.e., 0.1 N/mm^3) of the ground.

In order to assess the design resistance of the floor through non-linear simulation, the partial safety factor method adopted by the Eurocode 2 (2023) (ANNEX F, clause 7.11.3.4) was adopted for determining the structural response. According to this approach, the design

resistance (R_d) is determined by adopting the design material strengths (f_{cd}) as input parameters in the analysis. The concrete constitutive laws implemented in the simulations were all based on the design strength of concrete, calculated by dividing the characteristic strength (f_{ck}) by the partial safety factor for FRC (γ_F=1.5).

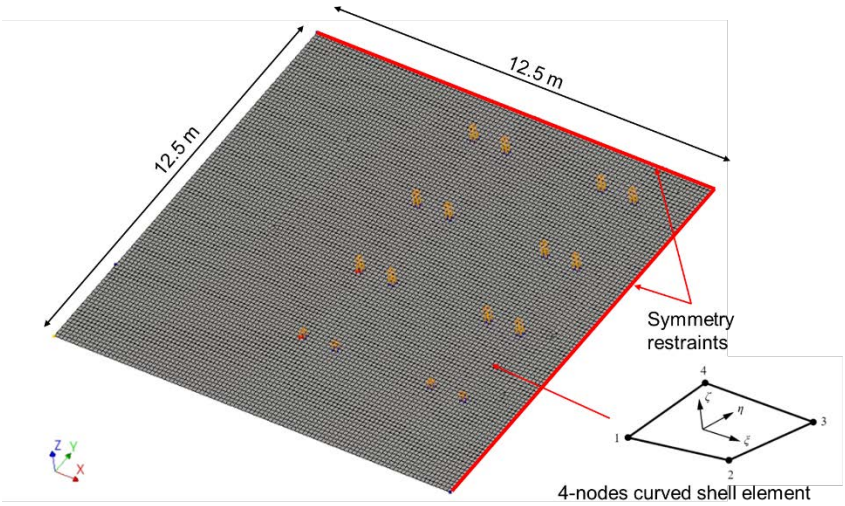


Figure 2: Finite element model of the slab.

The mechanical behavior of concrete was simulated using the "Total strain rotating" model, based on the concept of distributed cracking ("smeared crack model"), which allows the tensile and compressive behavior of the material to be represented in terms of principal stress-strain laws derived from material characterization tests. A Poisson's ratio equal to 0.2 and an initial elastic modulus (E_{cm}) of 33 GPa were assumed for FRC. The nonlinear compressive behavior of FRC was represented by means of the stress (f_c) – strain (ε) parabolic relationship proposed by the Eurocode 2 (2023) for plain concrete (clause 5.1.6), which is defined by the following relation:

$$f_c = f_{cd} \cdot \left[\frac{k\eta - \eta^2}{1+\eta(k-2)}\right] \quad for \;\; \varepsilon_c \leq 0.35\% \;\; ; \;\; f_c = 0 \quad for \;\; \varepsilon_c > 0.35\% \tag{1}$$

where: $k=1.05 \cdot E_{cm} \cdot \varepsilon_{c1}/f_{cd}$;

$\eta = \varepsilon_c/\varepsilon_{c1}$;

$f_{cd} = \alpha \cdot f_{ck}/\gamma_F = 0.85 \cdot 30/1.5 = 17$ MPa is the long-term design strength of concrete C30/37;

$\varepsilon_{c1} = 0.22\%$ is the strain at peak compressive strength.

According to the Annex L of the Eurocode 2 (2023), the tensile behavior of FRC can be represented by a multilinear uniaxial tensile (f_t)-strain (ε_t) law (Fig. 3). Before cracking, material behavior is governed by a linear law that is fully defined by the design tensile strength $f_{ctd}=f_{ctk}/\gamma_F=1.33$ MPa, which is derived from the characteristic tensile strength $f_{ctk}=2.00$ MPa, and the corresponding strain $\varepsilon_{ctd}=f_{ctd}/E_{cm}=4x10^{-3}$ %. The bi-linear constitutive law governing the tensile behavior after cracking is defined by the parameters summarized in Table 4, including the design residual strengths $f_{Ft1,ef,d}$ and $f_{Ft3,ef,d}$ obtained from the following relations:

$$f_{Ft1,ef,d} = k_0 \cdot k_G \cdot 0.37 \cdot f_{R,1d} \tag{2}$$

$$f_{Ft3,ef,d} = k_0 \cdot k_G \cdot \left(0.57 \cdot f_{R,3d} - 0.26 \cdot f_{R,1d}\right) \tag{3}$$

where $f_{R,1d}= f_{R,1k}/\gamma_F$ and $f_{R,3k}/\gamma_F$ are the design residual strengths corresponding to the characteristic residual strengths of the different FRC materials (Table 4); k_0 and k_G are the parameters accounting respectively for the fiber orientation and the of member size, which are herein assumed equal to 1. The tensile strains ε_{Fts} and ε_{Ftud} result from the following equations:

$$\varepsilon_{Fts} = 0.5\, mm/h_{cr} \quad (4)$$

$$\varepsilon_{Ftud} = 2.5\, mm/h_{cr} \leq 2\% \quad (5)$$

where the parameter h_{cr}=120 mm is referred to as the "characteristic length" and is automatically calculated by the finite element program (Diana, 2022) as $(A_{el})^{0.5}$, where A_{el} is the area of the individual shell element forming the finite element mesh.

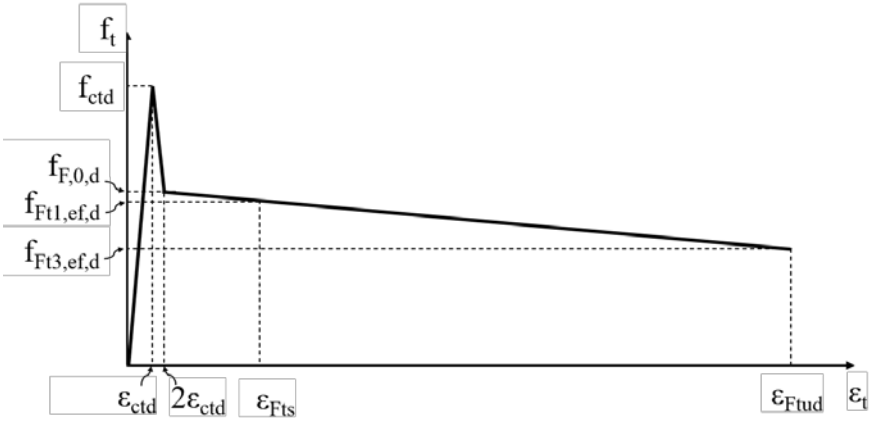


Figure 3: Typical design stress-strain law for FRC in tension.

Table 4: Parameters defining the design tensile stress-strain relationships of FRC.

MIX	f_{ctd}	ε_{ctd}	$f_{R1,d}$	$f_{R3,d}$	$f_{F,0,d}$	$f_{Ft1,ef,d}$	ε_{Fts}	$f_{Ft3,ef,d}$	ε_{Ftud}
	(MPa)	(%)	(MPa)	(MPa)	(MPa)	(MPa)	(%)	(MPa)	(%)
FRC-2.5-9-0	1.33	$4x10^{-3}$	0.80	0.95	0.29	0.30	0.42	0.33	2.00
FRC-2.5-8-2	1.33	$4x10^{-3}$	0.93	0.88	0.37	0.35	0.42	0.26	2.00
FRC-2.5-10-0	1.33	$4x10^{-3}$	0.88	0.90	0.34	0.33	0.42	0.28	2.00
FRC-5-0-0	1.33	$4x10^{-3}$	0.90	1.12	0.31	0.33	0.42	0.41	2.00
FRC-0-0-22	1.33	$4x10^{-3}$	1.17	1.17	0.45	0.43	0.42	0.36	2.00

The parametric study was carried out by considering the five FRC materials reported Table 4 and three different slab thicknesses, namely 150 mm, 200 mm, and 250 mm, resulting in a total of 15 simulations. The analyses were performed by monotonically increasing the loads applied to the floor up to the attainment of the maximum resistance. The following section reports and discusses the results of the numerical study.

4.3 Numerical results

The diagram in Fig. 4 exhibits the response of the different floors analyzed in this study in terms of the total load acting at the base of each rack support (P) versus the corresponding maximum vertical deflection in the Z-direction (TDtZ). The curves exhibit an initial linear response, with stiffness increasing as the slab thickness increases. This linear behavior persists until the onset

of cracking beneath the rack supports, occurring at load levels of approximately 110 kN, 170 kN, and 250 kN for the 150 mm, 200 mm, and 250 mm thick slabs, respectively. With regard to the mechanisms governing the global response, all slabs presented similar behavior regardless of slab thickness and of the material adopted in the simulations. As an example, Fig. 5 presents the contours of vertical deflection obtained at different loading stages for the 250 mm thick slab made with FRC-5-0-0; the same figure also shows the contours of principal post-cracking tensile strains (Eknn) detected on the bottom and top surfaces of the floor, providing insight into crack initiation and propagation as the applied load increases. Specifically, the segment-like symbols included in the strain contours represent the magnitude and direction of the principal strains, which are respectively associated with the crack width and orientation detected on the bottom surface of the slab. Note that in order to get an estimate of the average crack width, the strain values depicted in these contours must be multiplied by the characteristic length h_{cr}=120 mm defined in the previous section. The results showed that cracks with a width ranging between 0.1 mm and 0.2 mm appeared beneath the rack supports at a load of about 190 kN, whereas no crack were detected on the top surface. The cracks on the bottom surface were all mainly oriented in the X-direction, which corresponds to the shorter side of the single rack (Fig. 5a). As the load increased, these cracks progressively propagated along the X-direction and, at a load of approximately 330 kN, a crack with an average width of about 0.5 mm was present at the bottom surface across the two rows of the racking system (Fig. 5b). At the same time, a crack width of approximately 0.25 mm formed at the top surface at an intermediate position between the supports of the same rack. The attainment of the maximum load-carrying capacity (i.e., 350 kN for a floor having a thickness of 250 mm) was associated with the development of an extensive crack pattern (Fig. 5c), characterized by cracks with a maximum width of 0.7 mm and 0.5 mm at the bottom and top surfaces, respectively.

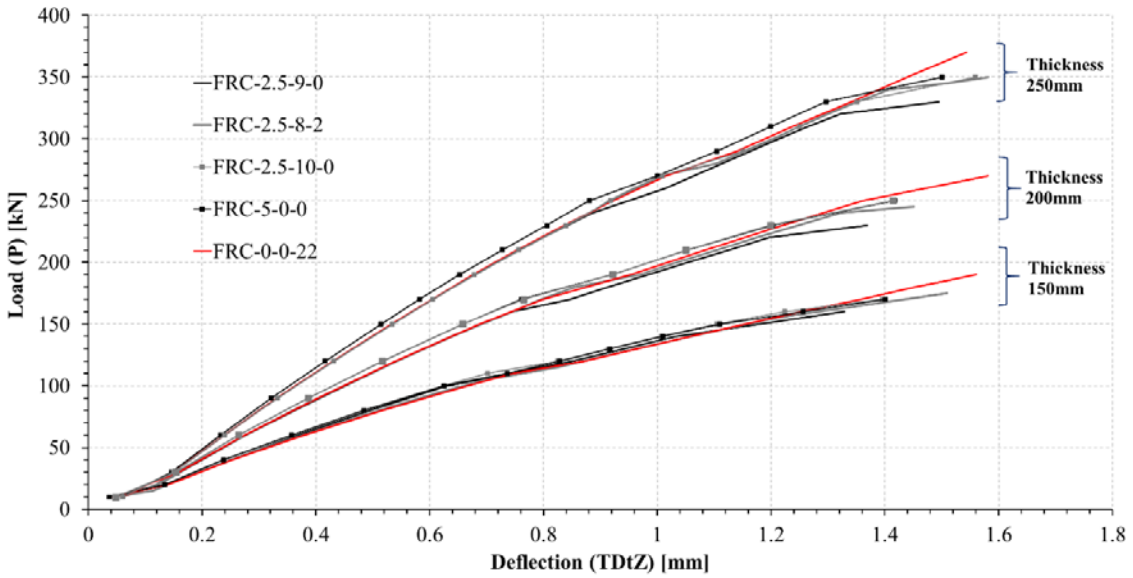
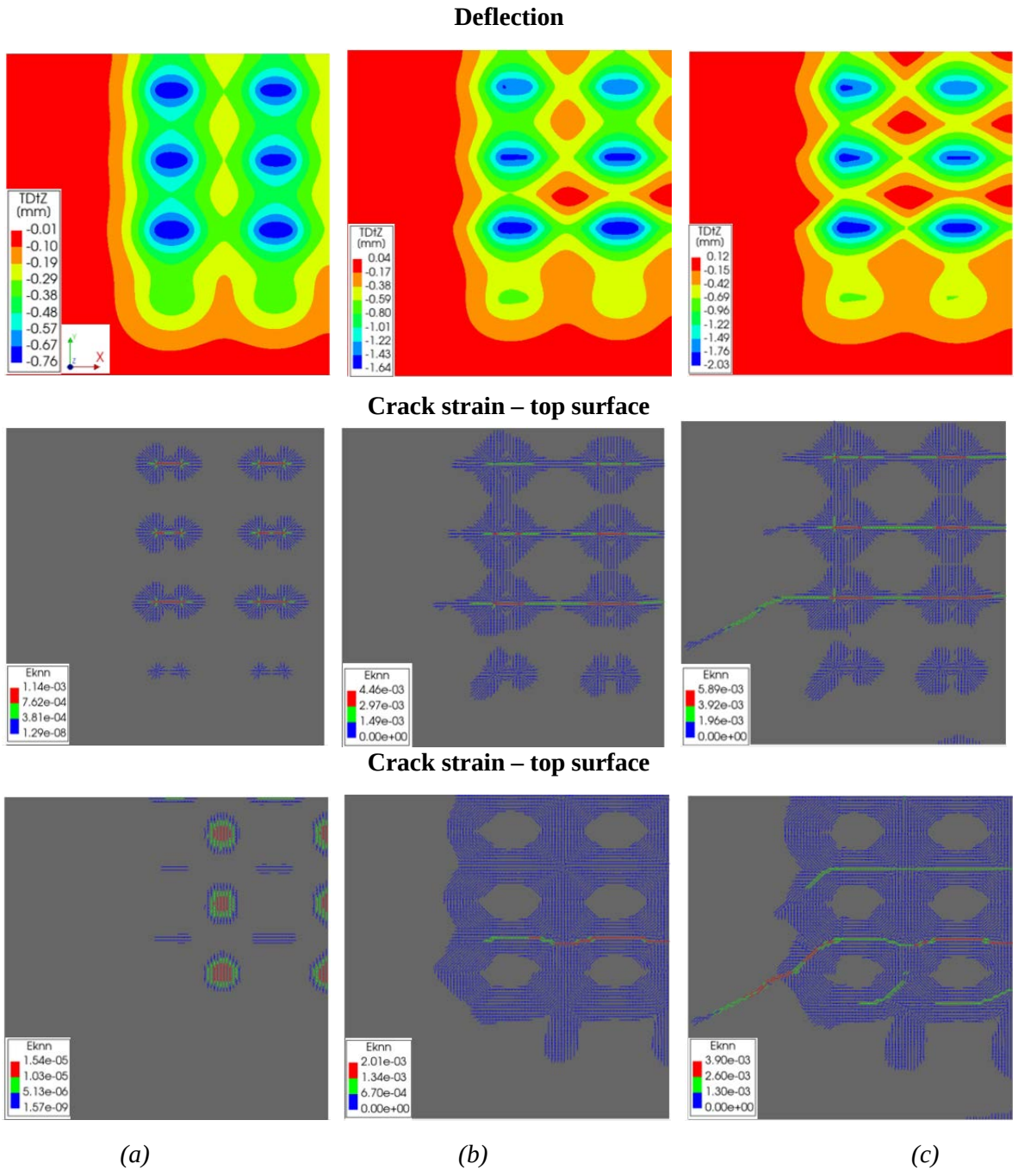


Figure 4: Load (P) vs. vertical deflection (TDtZ) response of the floors.

Fig. 6 shows a bar chart summarizing the maximum capacities against slab thickness. The variation between the maximum and minimum resistance observed for the same thickness was relatively small. In particular, compared with the floor made with 22 kg/m³ of steel fibers only (i.e., FRC-0-0-22), which consistently exhibited the highest resistance, the other floors showed a reduction in capacity ranging from 5% to 15%. A comparison among the four materials containing either only macro-synthetic fibers or hybrid fibers indicates that FRC-2.5-9-0

exhibited the lowest capacity, whereas the other materials achieved approximately the same maximum resistance. Overall, however, the performance of these slabs was very similar, as the differences in maximum capacity were very limited.



(a) *(b)* *(c)*

Figure 5: Contours of vertical displacements (TDtZ) and principal post-cracking tensile strains (Eknn) of the 250 mm thick floor made with FRC-5-0-0: (a) P=190 kN; (b) P=330 kN; (c) P=350 kN.

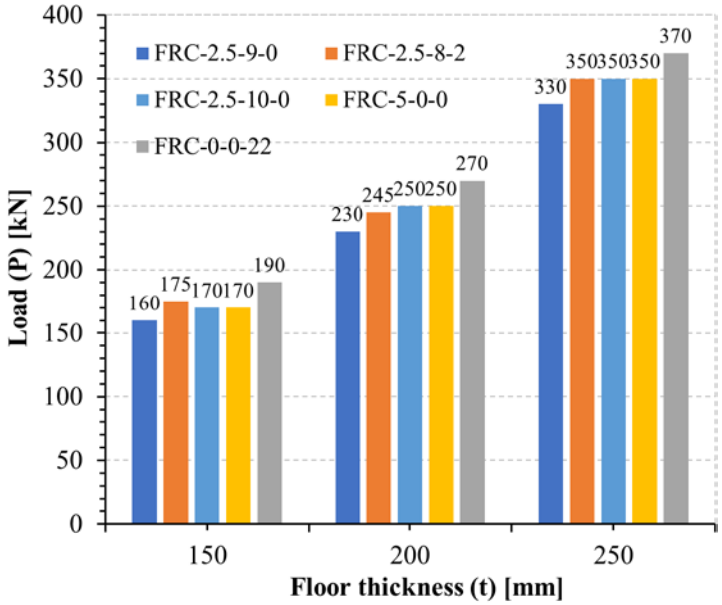


Figure 6: (a) Maximum floor capacity vs. floor thickness (t).

5 Concluding remarks

Experimental results from tests carried out on hybrid FRCs with steel and macro-synthetic fibers are presented in this paper. Flexural tests were carried out on standard beams with the aim of better understanding possible synergies between synthetic and steel fibers.

The adopted hybrid FRCs, characterized by a low fiber content, may represent a significant opportunity for concrete industrial floors that require low mechanical properties due to the high degree of redundancy.

A nonlinear numerical study was carried out on industrial floors made of different types of FRC, including hybrid FRCs, without conventional rebars (or welded mesh). Numerical results show that, due to the similar post-cracking performance of the different FRCs and due to the high degree of redundancy of the slab on grade, the global response (and thus the global bearing capacity) of the slab on grade is very similar. Furthermore, the crack opening at the bottom side of the slab under the rack feet is very small since it reaches a few tenths of a millimeter at service conditions.

6 Acknowledgements

The Author acknowledges the support provided by.

7 References

[1] di Prisco M., Plizzari G., Vandewalle L. 2009. “Fibre reinforced concrete: New design perspectives”, *Materials and Structures* 42(9):1261-1281, https://doi.org/10.1617/s11527-009-9529-4.

[2] Sorelli, L.G., Meda, A. and Plizzari, G.A. 2005. "Bending and uniaxial tensile tests on concrete reinforced with hybrid steel fibers." *Journal of Materials in Civil Engineering* 17(5):519-527.
[3] Banthia, N. and Sappakittipakorn, M. 2007. "Toughness enhancement in steel fiber reinforced concrete through fiber hybridization." *Cement and Concrete Research* 37(9):1366-1372 https://doi.org/10.1016/j.cemconres.2007.05.005.
[4] Li, Y., Bao, X., Chen, X., Zhang, R. and Cui, H. 2024. "Fracture behaviour of hybrid fibre reinforced concrete with a low fibre content considering the form of layered beams." *Construction and Building Materials* 443:137632. https://doi.org/10.1016/j.conbuildmat.2024.137632.
[5] Deng, F., Chi, Y., Xu, L., Huang, L. and Hu, X. 2021. "Constitutive behavior of hybrid fiber reinforced concrete subjected to uniaxial cyclic tension: Experimental study and analytical modeling." *Construction and Building Materials* 205:123650. https://doi.org/10.1016/j.conbuildmat.2021.123650.
[6] Oh, B.H., Park, D.G., Kim, J.C. and Choi, Y.C. 2005. "Experimental and theoretical investigation on the post-cracking inelastic behavior of synthetic fiber reinforced concrete beams." *Cement and Concrete Research* 35: 384 – 392.
[7] Li, B., Chi, Y., Xu, L., Shi, Y. and Li, C. 2018. "Experimental investigation on the flexural behavior of steel-polypropylene hybrid fiber reinforced concrete." *Construction and Building Materials* 191: 80-94. https://doi.org/10.1016/j.conbuildmat.2018.09.202.
[8] Li, K.F., Yang, C.Q., Huang, W, Zhao, Y.B., Wang, Y, Pan, Y and Xu, F. 2021 "Effects of hybrid fibers on workability, mechanical, and time-dependent properties of high strength fiber-reinforced self-consolidating concrete." *Construction and Building Materials* 277:122325. https://doi.org/10.1016/j.conbuildmat.2021.122325.
[9] European Committee for Standardization. 2005. "EN 14651 Test method for metallic fibered concrete – Measuring the flexural tensile strength (limit of proportionality (LOP)",. Brussels, Belgium.
[10] Sorelli L., Meda A. and Plizzari G. 2006. "Steel Fiber Reinforced Concrete slabs on grade: a structural matter". *ACI Structural Journal* 153(4), p. 551-558, ISSN: 0889-3241.

Abrishami, H. H., and Mitchell, D., 1997. "Influence of Steel Fibres on Tension Stiffening," *ACI Structural Journal*, 94(6) pp769-776.
AS/NZS 4671: 2001 *Steel Reinforcing Materials*, Standards Australia, Sydney.
Australian Standard AS3600, 2014. *Concrete Structures*, Standards Australia, Sydney.
Australian Standard AS3600, 2014 *Concrete Structures*, Commentary, Standards Australia, Sydney
Bernard, E.S., 2016. "Investigation of Crack Width Control Using Barchip Macro-synthetic Fibres in Reinforced Concrete Beams", *World Tunneling Congress 2016*, San Francisco, April 22-28.
Bischoff, P. H., 2003. "Tension Stiffening and Cracking of Steel Fibre-Reinforced Concrete," *Journal of Materials in Civil Engineering*, ASCE, 15(2), pp. 174-182 doi: 10.1061/(ASCE)0899-1561(2003)15:2(174)
Conforti, A., Zerbino, R., and Plizzari, G.A., 2018. "Influence of steel, glass and polymer fibers on the cracking behavior of reinforced concrete beams under flexure", Structural Concrete, 1-11. doi: 10.1002/suco.201800079

Deluce, J.R., Lee, S-C., and Vecchio, F.J. 2014, "Crack Model for Steel Fibre-Reinforced Concrete Members Containing Conventional Reinforcement", *ACI Structural Journal*, 111(1) pp93-102. doi: 10.14359/51686433

DIANA FEA BV, DIANA User's Manual – Release 10.6. Delft, The Netherlands: DIANA FEA BV, 2022.

Dupont, D., and Vandewalle, L., 2003, "Calculation of Crack Widths with the σ-ε Method," Test and Design Methods for Steel Fibre Reinforced Concrete: Background and Experiences, *Proceedings of the RILEM TC162-TDF Workshop*, RILEM Technical Committee 162-TDF, Bochum, Germany, pp119-144.

Eurocode 2: 2023. Design of Concrete Structures – Part 1-1: General rules and rules for buildings, bridges and civil engineering structures. British Standard BS EN 1992-1-1:2023, European Committee for Standardisation (CEN).

fib, 2012. *Model Code 2010*, Bulletin 65, Fèdération Internationale du Béton, Lausanne

Gilbert R.I. and Bernard, E.S., 2015. "Time-dependent Analysis of Macro-synthetic FRC Sections with Bar Reinforcement", *World Tunneling Congress 2015*, Dubrovnik, May 22-28.

Gilbert R.I., Mickleborough, N.C. and Ranzi, G., 2017. *Design of prestressed concrete to Eurocode 2*, Second Edition, CRC Press (Spon Press), Florida.

Jansson, A., Gylltoft, K., and Löfgren, I, 2010. "Flexural behaviour of members with a combination of steel fibres and conventional reinforcement", *Nordic Concrete Research*, (42) pp155–171.

Tiberti, G., Minelli, F., Plizzari, G.A., and Vecchio, F.J., 2014. "Influence of concrete strength on crack development in SFRC members", *Cement & Concrete Composites*, 45, pp176-185. doi: 10.1016/j.cemconcomp.2013.10.004

Vandewalle, L., 2000. "Cracking behaviour of concrete beams reinforced with a combination of ordinary reinforcement and steel fibres", *Materials and Structures*, 33, pp164-170. doi: 10.1007/BF02479410

Performance-Based Design approach for anchorages in Steel Fibre Reinforced Concrete considering concrete related failure modes

Dr. Norbert Vita[1], Prof. Akanshu Sharma[2]

[1] fischerwerke GmbH & Co. KG, Waldachtal, Germany

[2] Lyles School of Civil Engineering, Purdue University, West Lafayette, USA

Abstract

Steel fibre reinforced concrete (SFRC) is increasingly used as a construction material due to its enhanced post-cracking behaviour and optimized load-transfer mechanisms, with major applications remaining in industrial floor slabs and tunnel linings. Consequently, the use of mechanical fasteners in SFRC has grown significantly in recent decades.

With the introduction of the new generation of European Assessment Documents (EADs), anchors can now be formally qualified for use in SFRC. However, current assessments are limited to verifying equivalence with normal concrete, preventing the exploitation of improved mechanical properties - such as increased residual tensile strength - in design. This stands in contrast to numerous experimental studies that demonstrate superior anchorage performance in SFRC.

To bridge this gap between experimental findings and design practice, this paper proposes a performance-based design model for the concrete breakout resistance of anchors in SFRC. The model links the pull-out capacity directly to the residual flexural strength defined in current material standards and extends the Concrete Capacity Design (CCD) method by introducing SFRC-specific parameters. In contrast to existing design provisions, the proposed approach enables a material-dependent anchorage design that explicitly reflects the advantageous behaviour of SFRC.

The validation is based on an extensive data set comprising own experimental investigations and published test results. The comparison of predicted values with literature data for both tensile and shear loading - considering single as well as grouped anchors - shows a strong correlation. This confirms the predictive accuracy and robustness of the proposed model for estimating concrete breakout capacity in SFRC.

Keywords

Performance-based model, steel-fibre reinforced concrete, concrete breakout failure, residual flexural strength

1 Introduction

Steel fibre reinforced concrete (SFRC) is increasingly used in structural and non-structural applications due to its improved post-cracking behaviour and residual tensile strength (Maidl 1995). The crack-bridging action of steel fibres enhances the load-transfer capacity across cracks and can improve the resistance of structural components governed by concrete fracture (Mechtcherine 2010, Holschemacher et al. 2017).

Applications such as industrial floors, tunnel linings, and foundation slabs frequently require the use of post-installed anchors. Although several investigations have demonstrated improved anchorage performance in SFRC, the influence of key parameters such as embedment depth, fibre content, concrete strength, and edge distance has not yet been systematically investigated. Consequently, current assessment and design approaches generally treat SFRC as equivalent to conventional concrete and do not explicitly account for its enhanced post-cracking behaviour (Eligehausen et al. 2006).

To address this gap, the present study combines experimental investigations with literature data to develop a performance-based design approach for the concrete breakout resistance of anchors in SFRC. The proposed model explicitly considers SFRC material properties and their contribution to concrete-related failure modes.

2 State of the Art

Steel fibre-reinforced concrete (SFRC) is produced by adding discrete steel fibres to the fresh concrete mixture, where they are randomly distributed within the concrete matrix. After cracking, sufficiently embedded fibres bridge the crack faces and transfer tensile stresses across the crack, thereby improving the residual tensile strength, ductility, and post-cracking behaviour of concrete (Maidl 1995; Holschemacher et al. 2017). The influence of steel fibres on the load-bearing capacity of uncracked concrete (State I) is generally limited. Their primary contribution becomes significant after cracking (State II), where fibres bridge the crack faces, transfer tensile stresses across the fracture zone, and hinder crack propagation and crack opening (Holschemacher et al. 2017; Reinhardt 2010; Schnütgen 2005).

Commercial steel fibres are available in various geometries, including straight, wavy, and hooked-end fibres. Typical fibre lengths range from 25 to 60 mm, with aspect ratios between approximately 45 and 80. The effectiveness of the fibres generally increases with fibre content and fibre aspect ratio, although higher values may reduce workability (Holschemacher et al. 2017; Wietek 2017). Hooked-end fibres are the most commonly used type because their mechanical anchorage provides improved bond behaviour and pull-out resistance (Abdallah 2017; Spyridis et al. 2022).

Steel fibre dosage is usually expressed in kg/m³ or as a volume fraction. Typical amounts range from 15-60 kg/m³ for conventional concrete and 30-80 kg/m³ for shotcrete applications. At higher fibre contents, measures such as the use of superplasticizers may be required to ensure adequate workability and homogeneous fibre distribution. To reduce the risk of fibre balling, the maximum aggregate size should generally not exceed one third of the fibre length (Holschemacher et al. 2017).

The design of SFRC members may be carried out according to the DAfStB Guideline "Steel Fibre Reinforced Concrete" (DAfStB 2021), while industrial floors can be designed in accordance with the DBV Guideline for Steel Fibre Reinforced Industrial Floors (DBV 2013).

Anchorage in SFRC

The increasing use of steel fibre reinforced concrete (SFRC) in industrial floors, tunnel linings, precast elements, and foundation slabs has led to a growing demand for reliable fastening systems. The behaviour of cast-in and post-installed anchors in normal-strength concrete (C20-C50) has been extensively studied over the past decades. These investigations have led to the development of analytical approaches, most notably the semi-empirical Concrete Capacity Design (CCD) method, which is widely used to predict the concrete breakout capacity of fasteners (Fuchs et al. 1995). The CCD method has been adopted by major design standards for fastening systems (fib Bulletin 58 2011, EN 1992-4 2018, ACI 318-11 2008). However, the incorporation of steel fibres modifies the fracture behaviour and mechanical response of concrete, which may influence the failure mechanisms and load-bearing capacity of anchored connections. Therefore, the applicability of the CCD method to SFRC and its potential extension for predicting concrete breakout resistance require further investigation.

The cracking process of anchorages in SFRC undergoing concrete cone failure under tension loading is depicted schematically in Figure 1 (Eligehausen et al. 2006 and Tóth et al. 2019). For anchors in plain (unreinforced) concrete (left), the transfer of stresses across the crack (caused at the end of the anchor by the introduction of load from the anchor) is generally dependent on the crack width and only possible at the crack tip by cohesion. Meanwhile, in the case of steel fibre reinforced concrete (right), the stresses can be transferred across the crack by the steel fibres and their crack-bridging effect, even at larger crack widths.

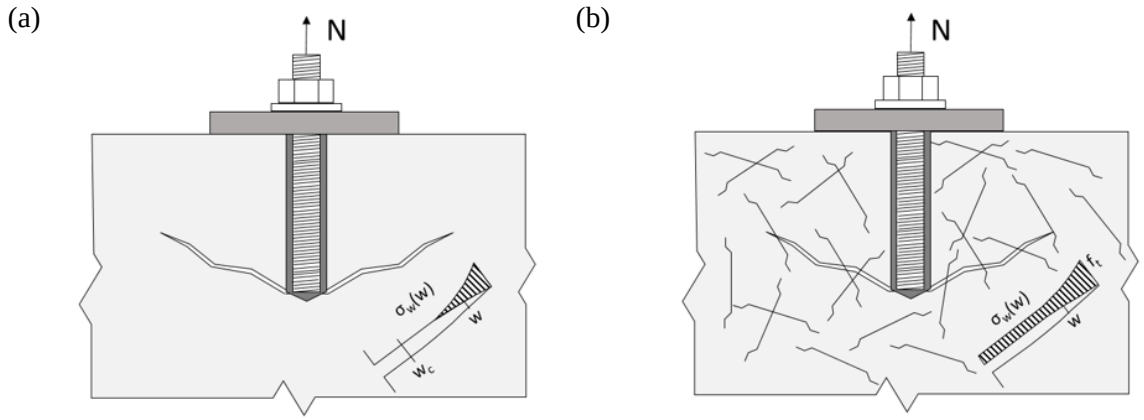


Figure 1:Anchorage (bonded) crack propagation under tension loading depending on concrete type, (a) plain concrete (Eligehausen et al. 2006), (b) steel fibre reinforced concrete (Vita 2024)

Numeros studies have investigated the load-bearing behaviour of anchors installed in SFRC. Early research on post-installed and bonded anchors generally reported little or no statistically significant increase in load capacity compared with plain concrete, often attributing this to the non-uniform distribution and orientation of steel fibres (Walter and Amman 1992, Klug et al. 2002, Gesoglu et al. 2005). Nevertheless, some investigations observed moderate improvements in concrete breakout resistance and ductility, particularly when concrete failure governed the response (Kurz et al. 2012, Coventry et al. 2011, Cattaneo and Muciaccia, 2015),

while studies on cast-in anchors, anchor channels, and headed fasteners reported capacity increases of up to 40-80 % and enhanced post-peak behaviour due to the crack-bridging effect of the fibres (Nilforoush et al. 2017, Vidyaranya 2019, Mahrenholtz et al. 2019). More recent work has also confirmed that bonded anchors in SFRC exhibit installation performance, resistance, and crack sensitivity comparable to those in conventional concrete (Tóth et al. 2019, Spyridis et al. 2022, Vita and Sharma 2021, 2023). In addition, Tóth et al. (2019) performed a comprehensive evaluation of existing test data and identified key parameters governing the beneficial effect of steel fibres on anchor performance. Their analysis demonstrated that significant increases in ultimate load can be achieved when specific geometric criteria are satisfied and anchors failing by concrete cone breakout. Based on these findings, a design approach incorporating an increase factor for SFRC, given in Equation (1), was proposed and validated in Tóth et al. (2019). However, the proposed formulation remains conservative, as several influencing parameters, such as embedment depth, concrete strength, and edge distance, are not explicitly considered.

$$\gamma_{fibre} = \frac{k_{fibre}}{300} + 1 < 1.25 \quad (1)$$

where k_{fibre} is the amount of steel fibre in kg/m^3 with a minimum allowable value of 30 kg/m^3.

Consequently, although the available results indicate that steel fibres can positively influence anchorage performance under certain conditions, additional research is needed to improve the understanding of fastening behaviour in SFRC and to support the development of performance based design methods.

Although a considerable amount of experimental research on anchors in SFRC has been conducted, the influence of key parameters such as fibre content, embedment depth, concrete strength, and edge distance has not yet been systematically investigated. As a result, the underlying mechanisms that enhance concrete breakout resistance in SFRC are not fully understood, which restricts the efficacy of existing design methodologies. To bridge this gap, this study introduces a performance-based design framework for anchors in SFRC under tensile or shear loads, specifically focusing on concrete-related failure modes. This methodology is derived from a comprehensive experimental campaign involving tension and shear testing of bonded anchors, where geometric and material factors were systematically adjusted to evaluate their effect on anchorage resistance. Comprehensive findings from single-anchor tests are documented in Vita and Sharma (2023), with anchor group test results detailed in Vita (2024). Based on the assessment of the experimental results together with available literature data, a performance-based design concept is proposed that explicitly accounts for the mechanical behaviour of SFRC and its influence on the concrete breakout resistance of anchorages

3 Experimental investigations

In order to investigate the influence of various parameters on the performance of anchorages in SFRC in the event of concrete failure, tension and shear tests were carried out on single anchors while varying different test parameters as well as anchor groups. The test parameters were anchor embedment depth (h_{ef}) and size, edge distance, amount of steel fibres, concrete compressive strength, and concrete condition (cracked or uncracked). In case of the anchor group tests, two different anchor group geometries were investigated (1x3 and 2x2) while varying various test parameters. The test parameters varied were anchor group geometry, edge distance, amount of steel fibres, concrete compressive strength, and load eccentricity. For

reasons of flexibility, bonded anchors were chosen for the test. Bonded anchors consist of a threaded rod and a vinylester or epoxy-based adhesive. The bonding properties of the adhesives depend on several factors: the properties of the adhesive material, the cleaning of the drill hole and the moisture content of the concrete. Bonded anchors transfer the loads introduced by a chemical bond. The installation and test parameters, such as anchor diameter, embedment depth and edge distances, were defined in such a way that the concrete cone failure mode determines the resistance. The experimental investigations were carried out in two different concrete mixtures (with low and high compressive strength) and two different fibre dosages (low and high amount) to be able to compare the test results directly.

The detailed test parameters and test results of single anchor tests are described in details in Vita and Sharma (2023). In general, the test results on single anchor under tension or shear loading shows that bonded anchors installed in SFRC have a significantly higher load-bearing capacity than those in plain concrete when failure occurs through concrete cone or concrete edge breakout failure. Depending on the test results, the mean ultimate load in SFRC was 11% to 78% higher than in plain concrete. The variability of the test results was low, with coefficients of variation below 15% for all series and below 10% for the SFRC specimens, indicating reliable and consistent performance. Anchors installed in SFRC also exhibited substantially larger displacements at ultimate load, demonstrating a more ductile behaviour due to the activation of steel fibres after crack initiation

Anchor group tests consistently demonstrated enhanced load-bearing capacity and improved displacement behaviour in steel fibre reinforced concrete (SFRC) compared with plain concrete, as describe in detailed in Vita (2024). Depending on anchor group geometry, edge distance, fibre content, and load application, the increase in ultimate load ranged from 12% to 80%. The highest enhancement was observed for the 1×3 anchor group configuration without edge influence under eccentric loading (see Figure 2 b). In general, eccentric loading conditions resulted in greater capacity increases than centric loading, which can be attributed to the improved ductility and load redistribution provided by the steel fibres, particularly when fibres are present between adjacent anchors.

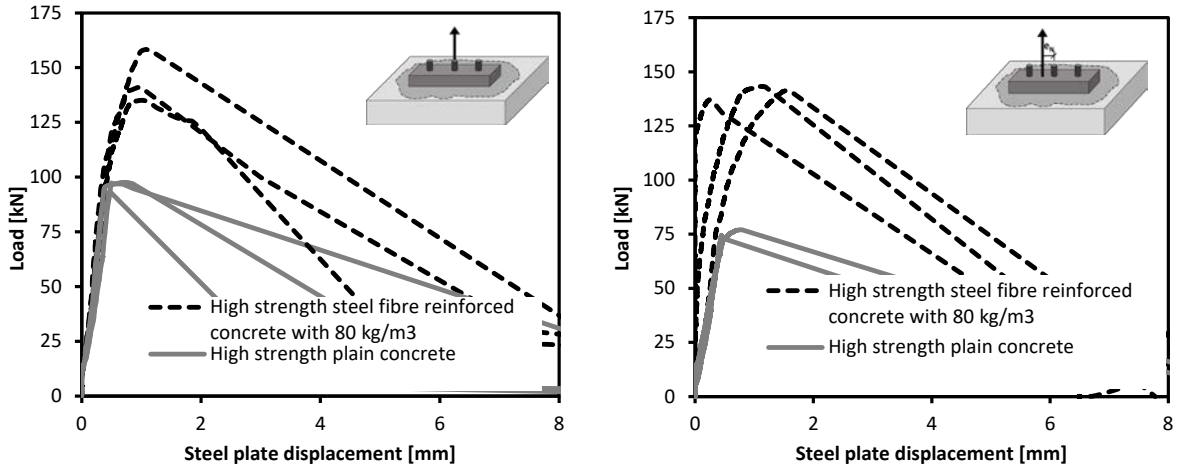
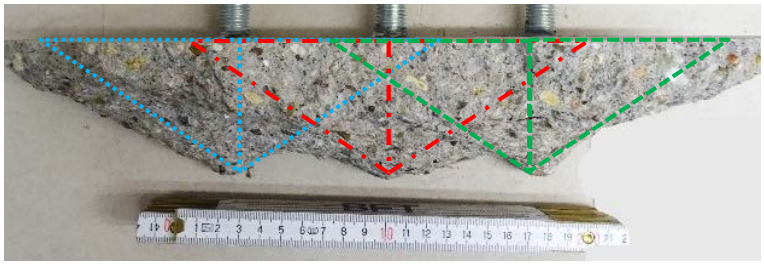


Figure 2: Comparison of the load-displacement curves obtained from tension tests on 1x3 anchor groups observed in high-strength plain (solid grey) and in high-strength steel fibre reinforced concrete with 80 kg/m3 amount (dashed grey) under centric loading (a) and eccentric loading (b) (Vita, 2024)

Furthermore, a comparison of the failure surfaces revealed no significant differences in the shape of the concrete breakout cones between plain concrete and SFRC specimens, indicating that the concrete cone geometry and, consequently, the crack propagation area remain essentially unchanged by the presence of steel fibres, see and compare Figure 3 (a) and (b). The scatter of the ultimate loads remained low (CoV < 15%) and comparable to that observed in plain concrete, with the highest scatter of 12.6% recorded in the anchor group test series under eccentric loading near a free edge in high-strength SFRC

(a)



(b)

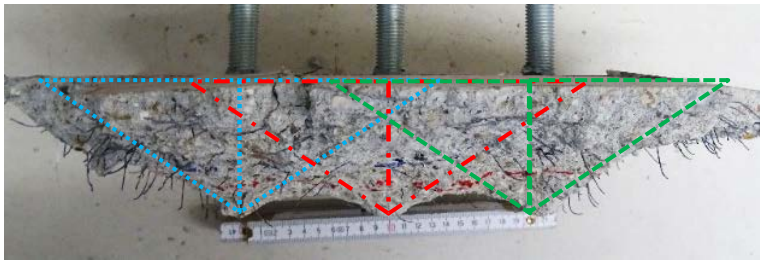


Figure 3: Side views of failed anchor groups, 1x3 tested far away from the edge under centric tensile loading (see also Figure 2 a) in plain (a) and in SFRC (b) (Vita,2024)

4 Comparison with existing models

Figure 4 (a) compares the failure loads predicted according to EN 1992-4 with the peak loads measured in tension tests on single anchors and anchor groups installed in plain concrete and steel fibre reinforced concrete (Vita 2024). The results indicate that the CCD method (Fuchs et al. 1995) specified in EN 1992-4 significantly underestimates the concrete breakout resistance of both single anchors and anchor groups installed in SFRC. Similar observations have been reported in previous studies by Nilforoush (2017) and Tóth et al. (2019).

A comparison between the experimentally measured failure loads in tension and shear and the values predicted by the current design provisions demonstrates that the equations in EN 1992-4 provide reliable estimates for concrete cone and concrete edge failure in normal concrete. However, because the beneficial contribution of steel fibres is not considered in the current design model, the predicted resistances for SFRC remain overly conservative, particularly for certain test series. The experimental results clearly demonstrate the positive influence of steel fibres on anchor performance. Therefore, this beneficial effect should be incorporated into future calculation approaches to enable a more accurate prediction of the load-bearing capacity of anchors installed in SFRC.

In general, the beneficial effect of steel fibres on the load-bearing behaviour of anchorages can be incorporated into the design procedure by applying an enhancement factor, ψ_{SFRC}, to the failure loads calculated according to EN 1992-4. As stated in Tóth et al. (2019), the factor was

derived from a lower-bound evaluation of an extensive experimental database and accounts for the increased resistance provided by steel fibre reinforcement. The corresponding formulation is given by Eq. 1 and depends solely on the steel fibre content. However, the application of this increase factor is limited to anchorages that fulfil specific requirements regarding both the material properties of the SFRC and the anchor installation parameters.

Figure 4 (b) compares the failure loads predicted using EN 1992-4 in combination with the increase factor ψ_{SFRC} with the peak loads measured in tension tests on single anchors and anchor groups installed in SFRC according to Vita (2024). The results demonstrate that the approach proposed by Tóth et al. (2019) provides a substantially improved correlation with the experimental data, particularly for anchors with relatively shallow embedment depths and relatively small loads. Nevertheless, for anchors with larger embedment depths with higher resistance, Eq. 1 still tends to slightly underestimate the experimentally observed failure loads.

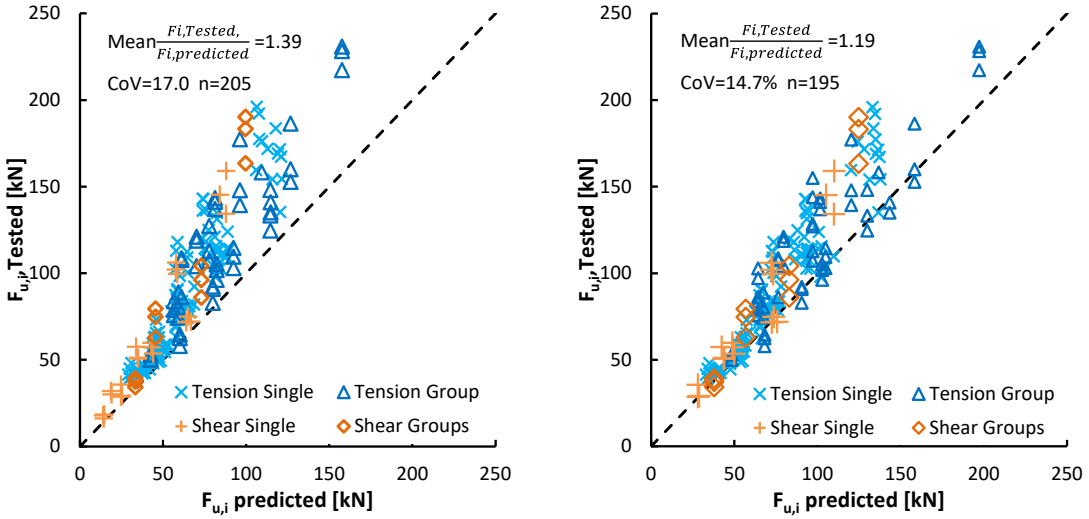


Figure 4: Comparing of measured and predicted tension failure loads for single and anchor groups according to(a) EN 1992-4:2018 (b) model approach acc. to Tóth et al. 2019.

5 Performance based model approach

To support the development of an improved calculation approach, the relationship between the concrete breakout resistance of post-installed bonded anchors and selected SFRC material parameters was investigated in detail in Vita (2024). As part of that work, a comprehensive regression analysis was performed using the experimental results obtained from anchor tests and the corresponding material properties of the concrete (plain concrete and SFRC) batches. The material properties $f_{fct,L}$, representing the flexural strength at the limit of proportionality, and $f_{eq,2}$, representing the equivalent flexural strength, were determined from three-point bending tests on notched beams in accordance with RILEM TC 162-TDF (Rilem, 2002). These parameters are given by Equation (2) and Equation (3), respectively.

$$f_{fct,L} = \frac{3F_L l}{2b(h-a_0)^2} \tag{2}$$

in which F_L is the load at the limit of proportionality, defined as the highest load value recorded up to a deflection of 0.05 mm; b (150 mm), h (150 mm), l (500 mm) are the width, height and span of the test specimen, respectively; a_0 (25 mm) is the notch depth; and ($h-a_0$) is the distance between the notch tip and the top surface of the cross section.

The parameter $f_{eq,2}$ was evaluated up to a deflection of δ_2, where $\delta_2 = \delta_L + 0.65$ mm and δ_L is the deflection corresponding to F_L. For the evaluation of the equivalent flexural strength, only the energy associated with fibre fracture ($D^f_{BZ,II}$ - defined as the area under the load-deflection curve) was considered, while the energy required for the fracture of plain concrete (D^b_{BZ}) was excluded. Consequently, the equivalent flexural strength can be calculated using the following equation:

$$f_{eq,2} = \frac{3}{2}\frac{l}{b(h-a_0)^2}\frac{D^f_{BZ,II}}{0.5} \quad (3)$$

Figure 4 summarizes the identified correlations between the increase in anchor failure load and the material parameters: (a) $f_{fct,L}$ - flexural strength corresponding to the limit of proportionality and (b) $f_{eq,2}$ - equivalent flexural strength, for different embedment depths (h_{ef}=65 mm and h_{ef}=100 mm) in case of single anchors. The analysis revealed that the flexural strength ($f_{fct,Lf}$) exhibited only a weak correlation with the load increase in tensile test, with a coefficients of determination (R^2) below 0.511. In contrast, the equivalent flexural strength ($f_{eq,2}$) showed a significantly stronger correlation with the relative ultimate tension load (increase of the SFRC). Since both parameters directly reflect the contribution of steel fibres to the post-cracking behaviour of the concrete, this observation is physically plausible. Particularly strong correlations were obtained for the equivalent flexural strength, for which R^2 values between 0.729 and 0.923 were reported for tension tests conducted in SFRC without edge effects (Vita and Sharma 2023).

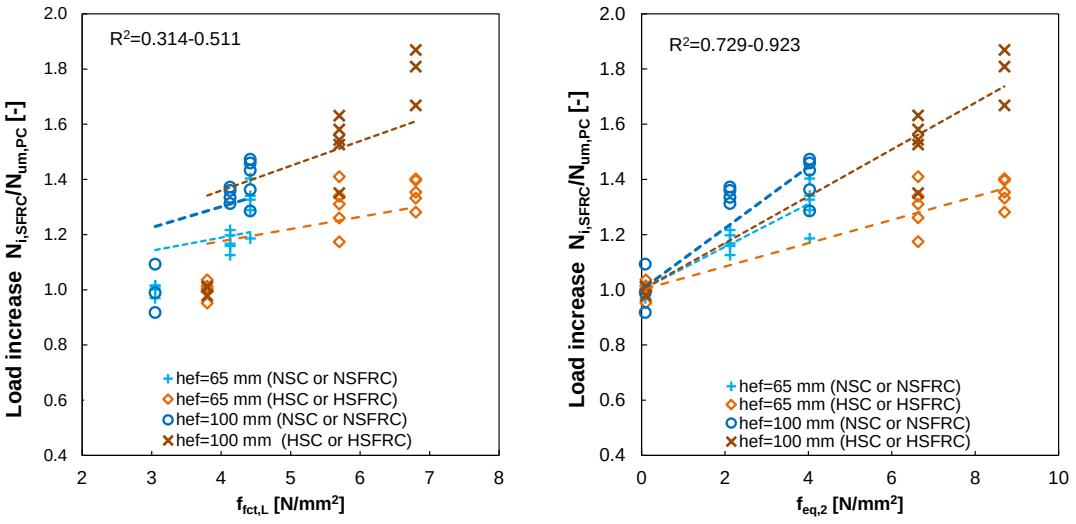


Figure 5: Relationship between the failure load increase ($N_{u,i,SFRC}/N_{u,PC}$) and a) the flexural strength corresponding to the limit of proportionality $f_{fct,L}$; or b) the equivalent flexural strength $f_{eq,2}$ (Vita 2024).

As can be seen in Figure 5, the increase in concrete breakout resistance of anchorages installed in SFRC exhibits an approximately linear relationship with the equivalent flexural strength. This observation indicates that the equivalent flexural strength is an appropriate mechanical parameter for quantifying the beneficial contribution of steel fibres to the load-carrying capacity of anchorages subjected to concrete failure modes, such as concrete cone breakout and concrete edge breakout. Accordingly, the following equation is proposed to account for the beneficial effect of steel fibres on the concrete failure resistance of single anchorages (Vita 2024):

$$\psi_{SFRC} = (1 + 0.04 \cdot f_{eq,2}) \cdot \left(\frac{h_{ef}}{1.7 \cdot L_f}\right)^{0.04 \cdot f_{eq,2}} \geq 1.0 \tag{4}$$

where $f_{eq,2}$ is the equivalent flexural strength in [N/mm^2] calculated from three-point bending tests acc. to Eq.(3); h_{ef} the effective embedment depth of the anchor in [mm]; and L_f the steel fibre length in [mm]. The embedment-depth term in Eq. (4) accounts for the geometric relationship between anchor embedment depth and fibre length. With increasing embedment depth relative to fibre length, more fibres are likely to intersect the crack surface and become activated, resulting in an increased contribution to the anchor breakout resistance. However, Equation (4) is only valid if the embedment depth of the anchor h_{ef} or in case of shear load the edge distance c_1 is greater than 1.7-times the fibre length ($h_{ef} \geq 1.7 \cdot L_f$ or $c_1 \geq 1.7 \cdot L_f$). This boundary condition corresponds to the limit proposed by Tóth et al (2021). To calculate the mean ultimate breakout load of bonded anchors ($N_{u,c}$) under tension load, the general equation in the EN 1992-4 should be multiplied with the increase factor ψ_{SFRC} according to Equation (4):

$$N_{u,c}^{SFRC} = 1.33 \cdot 11.0 \cdot f_{cm}^{0.5} \cdot h_{ef}^{1.5} \cdot \frac{A_{c,N}}{A_{c,N}^{0}} \cdot \psi_{s,N} \cdot \psi_{SFRC} \tag{5}$$

where f_{cm} is the mean compressive strength of the concrete, and $A_{c,N}$, $A^0_{c,N}$ as well as the $\psi_{s,N}$ -factor can be calculated acc. to EN 1992-4.

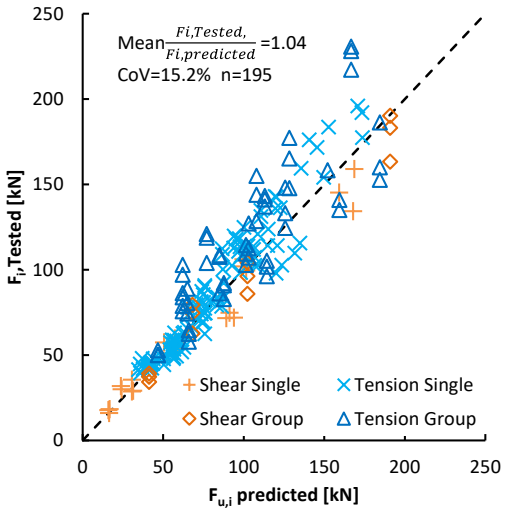


Figure 6: Comparison of measured and predicted failure loads for single anchors and anchor groups under tension and shear loading, calculated using the new model approach (Vita and Sharma 2022, Vita 2024).

Figure 6 compares the failure loads predicted using the proposed model approach with the experimental results obtained from tension and shear tests on single bonded anchors and anchor groups reported by Vita and Sharma (2022) and Vita (2024). The predicted ultimate failure loads ($F_{i,predicted}$) were determined by applying the design equations of EN 1992-4 for concrete cone failure and concrete edge failure, respectively, and multiplying the resulting values by 1.33 to convert them from design to ultimate load level. Subsequently, the increase factor ψ_{SFRC} defined in Eq. (4) was applied while using the measured concrete compressive strengths. In addition, in case of anchors installed in cracked SFRC, the calculated ultimate loads were multiplied by 0.7 to take into account the negative influence of the crack as proposed by Vita and Sharma (2022).

As shown in Figure 6, the proposed calculation approach results in an overall mean measured-to-predicted failure load ratio of 1.04 with a CoV of 15.2%. Separately, mean measured-to-predicted ratios of 1.058 (CoV = 14.8%) and 0.956 (CoV = 21.7%) were obtained for tension and shear loading, respectively. The close agreement between the experimental and predicted results demonstrates that Eq. (4), which incorporates the equivalent flexural strength $f_{eq,2}$, provides a reliable prediction of concrete breakout capacities for post-installed anchors in SFRC. Consequently, the proposed approach can be considered suitable for estimating the concrete cone and concrete edge breakout failure loads for post-installed anchorages in SFRC.

It should be noted that the proposed model approach according to Eq. (5) is currently applicable only within the range of boundary conditions covered by the experimental database. These conditions can be summarized as follows:

- Hooked-end steel fibres: lengths $30mm \leq L_f \leq 60$mm and diameters $0.5mm \leq d_f \leq 0.8$mm;
- Steel fibre content ranging from 20 to 80 kg/m³;
- Concrete compressive strength f_{cc}between 35 and 80 N/mm²;
- Maximum aggregate size $D_{max} \leq \frac{1}{3}L_f$;
- Failure governed by concrete cone breakout under tension loading and by concrete edge breakout or pry-out failure under shear loading;
- Effective embedment depth $h_{ef} \geq 1.7L_f$;
- For tension-loaded anchors located close to a free edge, the minimum edge distance $c_1$should be selected as a function of the embedment depth h_{ef}. For example, $c_1 = 2L_f$ for $h_{ef} = 3L_f$, and $c_1 = 3L_f$for $h_{ef} = 2L_f$.

In this study, only bonded anchors were tested to enable a systematic variation of parameters and to obtain concrete cone and concrete edge failures under tension and shear loading, respectively. Since the observed enhancement is related to the concrete failure mode rather than the anchor type, similar benefits are expected for other anchor types, such as undercut and expansion anchors, provided that failure is governed by concrete fracture. However, non-concrete failure modes (e.g., pull-out or pull-through of expansion anchors) may behave differently in SFRC than in plain concrete, as reported by Vita (2024). Therefore, the suitability of anchor types in SFRC should be verified within the approval process according to the relevant EAD and ETA assessment.

6 Concluding remarks

This research focused on the development of a performance-based design method for estimating the resistance of anchors in steel fibre reinforced concrete (SFRC). For this purpose, a comprehensive database of tension and shear tests on bonded anchors was evaluated and used

to developed the proposed model. The assessment of the experimental data enabled the quantification of the contribution of steel fibres to anchorage resistance and the extension of the Concrete Capacity Design (CCD) concept to SFRC structures. The proposed model takes into account the beneficial effect of the steel fibres through an increase factor, ψ_{SFRC}, related to the equivalent flexural strength ($f_{eq,2}$) obtained from three-point bending tests.

The experimental results obtained for bonded anchors in SFRC, together with the failure loads predicted by the proposed equations for tension and shear loading, demonstrate good agreement. However, unless further evidence is obtained, the applicability of the proposed model is restricted to the boundary conditions (e.g. fibre type, geometry, content, concrete strength class). Therefore, although the results are promising, the model cannot yet be considered a generally applicable design method for anchorages in SFRC and requires further validation.

Future research should focus on extending the applicability of the model to different fibre geometries, such as double- or triple-hooked steel fibres, as well as other fibre types, including wavy fibres. In addition, the behaviour of anchorages under combined tension and shear loading should be investigated. Since steel fibres improve the tensile behaviour of concrete, beneficial effects on other concrete-related failure modes, including splitting failure, can also be expected. Experimental studies are therefore required to quantify the contribution of steel fibres to the splitting resistance of anchorages.

Finally, the experimental programme considered only static and quasi-static loading conditions. Further investigations are needed to assess the influence of steel fibres on anchorage performance under seismic and fatigue loading and to expand the range of practical applications of anchorages in SFRC

7 Acknowledgements

The authors acknowledge the financial support provided by fischerwerke GmbH & Co. KG. Furthermore, the experimental investigations presented in this paper and the research work were carried out at the Institute of Construction Materials, University of Stuttgart.

8 References

Abdallah S., Fan M., Zhou X (2017). Anchorage effect of various hooked-end steel fibres on pull-out behaviour of ultra-high performance mortar, 9th RILEM International Symposium on Fibre Reinforced Concrete (BEFIB 2016), Vancouver

ACI Committee 318 (2008). Building Code Requirements for Structural Concrete (ACI 318-11) and Commentary. Farmington Hills, MI: American Concrete Institute

Cattaneo S., Muciaccia G.(2015) Adhesive anchors in high performance concrete. Materials and Structures. 2015;49. https://doi.org/10.1617/s11527-015-0677-4

Coventry K., Richardson A., Intyre C., Aresh B. (2011) Pullout Performance of Chemical Anchor Bolts in Fibre Concrete. In: Fibre Concrete 2011, 6th International Conference, Prague, Czech Republic

Deutscher Beton- und Bautechnik-Verein e.V. (2013) , Steel Fibre Reinforced Industrial Concrete Floors. Special Features of the Design and Detailing, Production and Conformity.

Deutscher Ausschuss für Stahlbeton e.V. (DAfStb) (2021). Stahlfaserbeton

Eligehausen R., Mallée R., Silva J.F. (2006) Anchorage in Concrete Construction. 1st ed.

European Committee for Standardization (CEN) (2018). Eurocode 2: Design of Concrete Structures - Part 4: Design of Fastenings for Use in Concrete.

fédération internationale du béton (fib).(2011) Bulletin 58: Design of Anchorages in Concrete - Guide to Good Practice.

Fuchs W., Eligehausen R., Breen J.E. (1995) Concrete Capacity Design (CCD) approach for fastening to concrete. ACI Structural Journal. 1995;92(1):73-94. https://doi.org/10.14359/1533

Gesoglu M., Ozturan T., Özel M., Güneyisi E. (2005) Tensile behaviour of post-installed anchors in plain and steel fibre-reinforced normal- and high-strength concretes. ACI Structural Journal. 102:224-231.

Holschemacher K., Dehn F., Müller T., Lobisch F. (2017) Grundlagen des Faserbetons - Fundamentals of Fibre Concrete. In: Beton-Kalender 2017: Spannbeton, Spezialbetone, Vol. 106. p. 381-472.

Klug Y., Holschemacher K., Wittmann F. (2002) Tragverhalten von Befestigungselementen in Stahlfaserbeton. In: Faserbeton: Innovationen im Bauwesen, Beiträge aus Praxis und Wissenschaft. p. 89-105.

Kurz C., Thiele C., Schnell J., Reuter M., Vitt G. (2012) Tragverhalten von Dübeln in Stahlfaserbeton. Bautechnik. 2012;89(8):545-552. https://doi.org/10.1002/bate.201200018

Mahrenholtz C., Ayoubi M., Müller S., Bachschmid S. (2019) Tension and shear performance of anchor channels with channel bolts cast in Fibre Reinforced Concrete (FRC). IOP Conference Series: Materials Science and Engineering. 2019;615:012089. https://doi.org/10.1088/1757-899X/615/1/012089

Maidl B. (1995) Steel Fibre Reinforced Concrete. Ernst.

Mechtcherine V. (2010) Rissbeherrschung durch Faserbewehrung. In: Müller H.S., Bosold D. (Eds.), Beherrschung von Rissen in Beton. Karlsruhe: KIT Scientific Publishing, p. 83-94.

Nilforoush R. (2017) Anchorage in Concrete Structures: Numerical and Experimental Evaluations of Load-Carrying Capacity of Cast-in-Place Headed Anchors and Post-Installed Adhesive Anchors. Dissertation, Luleå University of Technology, Sweden.

Nilforoush R., Nilsson M., Elfgren L.(2017) Experimental evaluation of tensile behaviour of single cast-in-place anchor bolts in plain and steel fibre-reinforced normal- and high-strength concrete. Engineering Structures. 2017;147:195-206. https://doi.org/10.1016/j.engstruct.2017.05.062

Reinhardt H.-W. (2010) Ingenieurbaustoffe. 2nd ed. Ernst & Sohn.

RILEM TC 162-TDF (2002). Test and design methods for steel fibre reinforced concrete - Design of steel fibre reinforced concrete using the sigma-w method: principles and applications. Materials and Structures. 2002;35:262-278.

Schnütgen B. (2005)Stahlfaserbeton. In: Stahlbetonbau aktuell: Praxishandbuch. Berlin: Bauwerk Verlag.

Spyridis P., Dreier J., Mellios N., Walter L., Biermann D. (2022) Multilateral assessment of anchorage bond characteristics in steel fibre reinforced concrete. Polymers. 2022; 14: 1411. https://doi.org/10.3390/polym14071411

Tóth M., Bokor B., Sharma A.(2019) Anchorage in steel fibre reinforced concrete - Concept, experimental evidence and design recommendations for concrete cone and concrete edge breakout failure modes. Engineering Structures. 2019;181:60-75. https://doi.org/10.1016/j.engstruct.2018.12.007

Vidyaranya K. (2019) Experimental Investigation of Concrete Breakout Strength of Anchor in Tension within Fibre Reinforced Concrete. Master's Thesis, The University of Texas at Arlington.

Vita N. (2024) Enhanced Performance of Anchorages in Uncracked Concrete with Steel Fibres or Post-Installed Reinforcement. Dissertation, University of Stuttgart, Germany; 2024. https://doi.org/10.18419/opus-15668

Vita N., Sharma A. (2021) Behaviour of single bonded anchors in non-cracked and cracked steel fibre reinforced concrete under short-time tensile loading. Engineering Structures. 2021; 245:112900. https://doi.org/10.1016/j.engstruct.2021.112900

Walter E., Ammann W.J. (1992) Fastening technology in fibre reinforced concrete. In: Fibre Reinforced Cement and Concrete, Proceedings of the 4th International RILEM Symposium. London: Spon; 1992. p. 659-675.

Wietek B. (2017) Faserbeton. Wiesbaden: Springer Vieweg. https://doi.org/10.1007/978-3-658-19079-8_1

Brief History and Defining Criteria of Strain Hardening FRC Composites

Antoine E. Naaman[1]

[1]: University of Michigan, Ann Arbor, USA

Abstract

The descriptors “strain-softening” and “strain-hardening” are now commonly used by researchers and practitioners to describe the tensile response of FRC composites. However, it took more than forty years for this terminology to become consolidated. Indeed, the first scientifically conducted experimental tensile tests on fiber reinforced concrete showed only “strain-softening” behavior, which was then considered typical. In these tests, only one major failure crack was observed. Later tests revealed another response in which more than one crack (multiple cracking) occurred, first reported in 1978. In subsequent years, researchers attempted to describe such behavior using terms such as “inelastic multiple cracking,” “desirable ductile response,” “high performance,” “kind of strain-hardening,” “pseudo strain-hardening,” “quasi strain-hardening,” and, finally, officially in 2003, “strain-hardening.” The consolidation of terminology for tensile response led directly to the characterization of bending response as either “deflection-softening” or “deflection-hardening.” The main objective of this paper is to document, for the record, key chronological milestones in the history of this development and to correlate the contributions of the “civil engineering–composite mechanics” community with those of the “materials science–fracture mechanics” community.

This paper is dedicated to the memory of Hans-Wolf Reinhardt (1939–2026), who, by organizing a series of international workshops on “High Performance Fiber Reinforced Cement Composites” from 1991 to 2015, helped lead the way to significant advances in the field, including the broader characterization of FRC composites as described here.

Keywords

Fiber reinforced concrete, tensile testing, strain-softening, strain-hardening, deflection-hardening, deflection-softening, multiple cracking, fracture energy

1 Introduction

Cement-based composites reinforced with discontinuous fibers can be conveniently classified according to their tensile response, namely, either strain-softening or strain-hardening; by correlation, the response of all FRC beams can be classified as either deflection-softening or deflection hardening. The behavior in tension dictates that in bending and the relationships are described in Figs. (1 and 2).

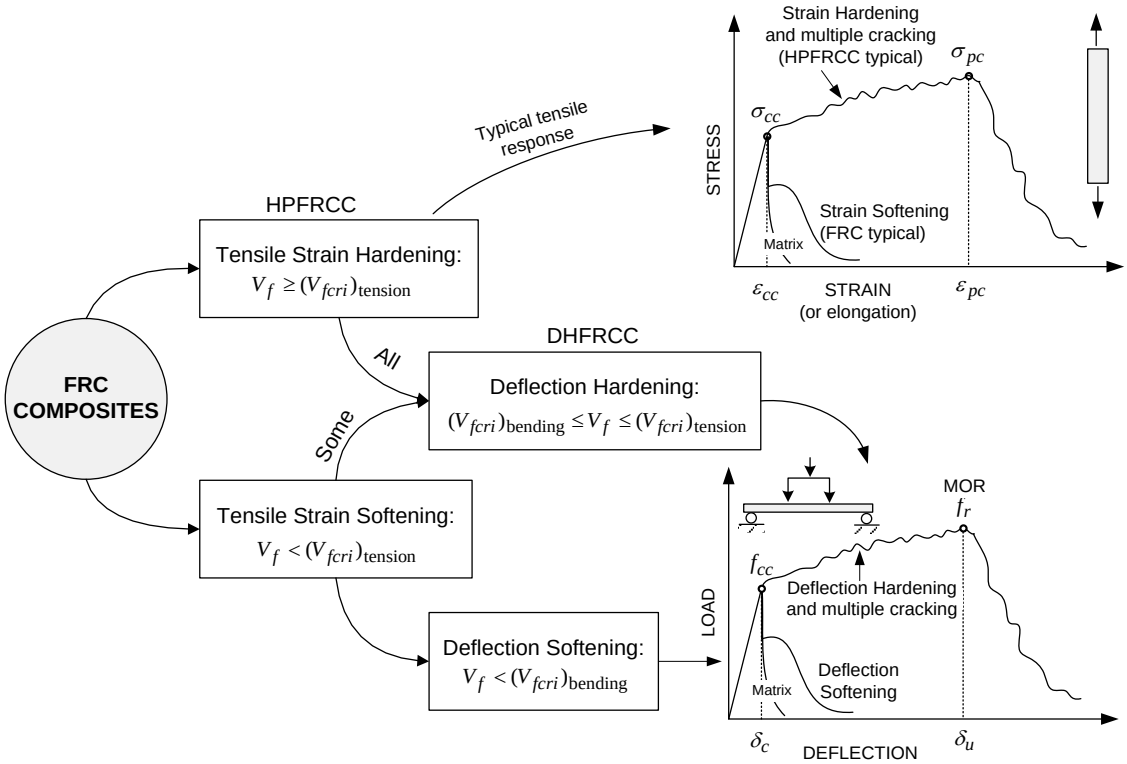


Figure 1: Classification of fiber reinforced cement composites based on their tensile response and implication for bending response of structural elements [Naaman and Reinhardt, Ref. 40].

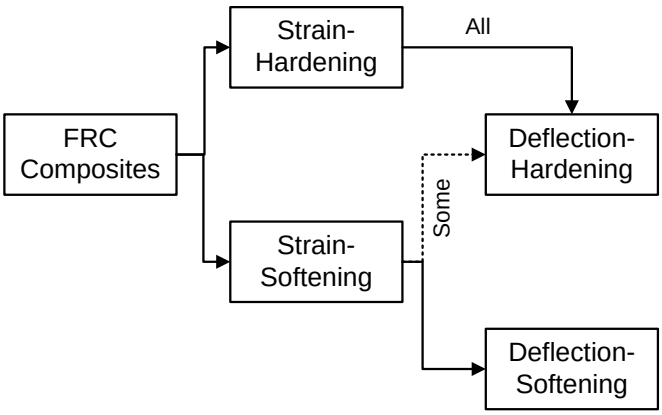


Figure: 2 General performance classification of FRC composites according to their behavior in tension and bending, as per Fig. 1. [42, 48]

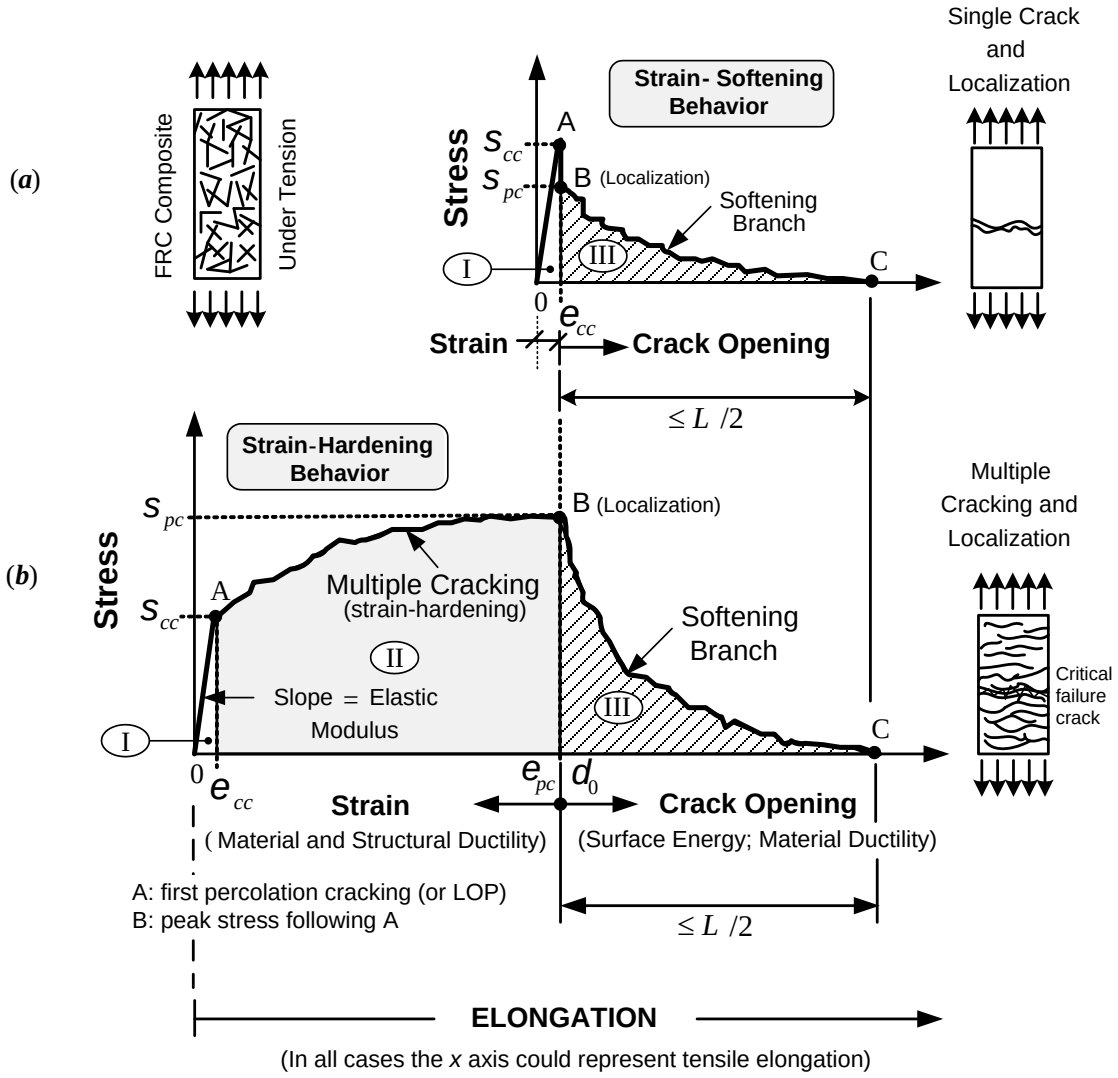


Figure: 3 Typical stress-strain or stress-elongation curve in tension up to complete separation. (a) Conventional strain-softening FRC composite. (b) Strain-hardening FRC composite [39].

While such a classification seems deceptively simple, it was not arrived at spontaneously and took more four decades to materialize. Two different groups of researchers, one in the field of "fracture mechanics and materials science" and the other in the field of "civil engineering and composite mechanics", working totally independently, formulated the criteria necessary to achieve such behavior. The two groups followed two entirely different approaches: one followed a composite mechanics approach leading to a stress criterion assuming a first crack has occurred, and one followed a fracture mechanics formulation leading to both an energy and a stress criterion. It is observed that the two groups, while following entirely different paths, solved in effect the same problem.

This paper describes some chronological developments since the 1960's and the related nomenclature that led to the special class of FRC composites which are characterized by a strain-hardening response after first cracking accompanied by multiple cracking up to relatively high strains (Fig. 1). Strain-hardening and deflection-hardening FRC composites are the composites of choice for use in advanced structural and non-structural applications.

2 Historical Background: Four Decades of Progress

The modern developments in fiber reinforced cement composites took off only during the early 1960's following studies by *Romualdi*, *Mandel* and *Batson* on the use of steel fibers in concrete [48 to 50]. This came at about the same time as a fundamental study of fiber reinforced concrete published in 1964 by *Krenchel* in Denmark [17]. In the U.K., *Majumdar* and *Ryder* [23, 24] as well as *Grimer* and *Ali* [8] evaluated the use of glass fibers as reinforcement of cement matrices. *Kelly and Davis [15, 16]* and *Aveston, Cooper,* and *Kelly* [1] published classical studies on brittle matrix composites which were applicable to cement-based matrices as well.

The work of *Romualdi*, *Mandel,* and *Batson* [50 to 52], while addressing tensile strength of fiber reinforced concrete from a fracture mechanics approach, gave little information on the tensile stress-strain or stress-elongation response of the composite in tension. They did not carry out direct tensile tests. They theorized that fibers arrest cracking in concrete and the average fiber spacing represents the length of the critical crack, interpreted from a fracture mechanics approach using *Griffith* theory; thus, they predicted a tensile strength of FRC to be inversely proportional to the square root of the fiber spacing [51]. In a related discussion, *Shah* and *Rangan* [54] showed the results of actual tensile tests of FRC to be significantly smaller that those predicted by *Romualdi* and co-workers. However, their tensile tests were load tests only with no elongation recorded; both studies were in effect referring to what we qualify today as the tensile strength at first cracking or first percolation crack.

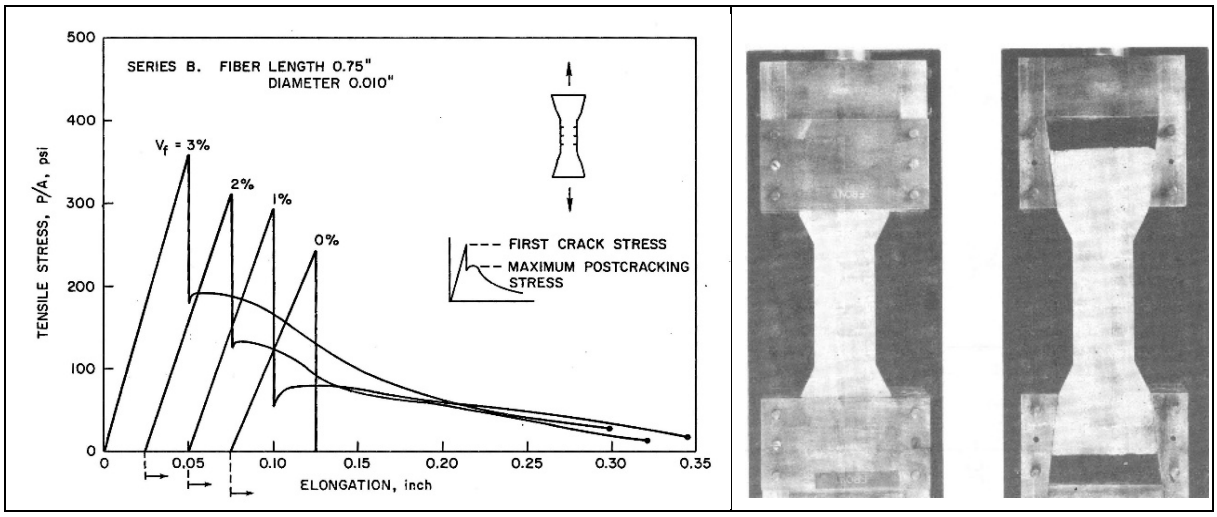


Figure: 4 Typical tensile stress versus machine elongation curves of steel FRC composites and tensile specimens as reported by Naaman, 1972 [27 to 29].

To the best of the author's knowledge the first in depth research to provide tensile stress-elongation curves of FRC was published by *Naaman* in 1972 [27 to 29] where the statistical nature of the tensile strength was also evaluated. *Naaman* used then a state-of-the-art Instron universal testing machine that provided a continuous record of load versus elongation (Fig. 4, left) on a chart. In the experimental part, the fibers used by *Naaman* were straight steel fibers, made from high strength wires, of aspect ratio less than 100, but the fibers were smooth and thus had relatively poor bond properties. Although the volume fraction of fibers evaluated varied from 1% to 3%, no multiple cracking was observed in these tests.

Figure 4 (left part) illustrates the typical response observed, where the elongation represents machine elongation. Essentially all the composites tested by *Naaman* showed strain-softening response after first cracking with localization at that cracked section. They belong to the "strain-softening" class of Figs. 1 and 2 and resemble the curve shown in Fig. 3a.

During the 1970's, numerous research investigations were undertaken on fiber reinforced cement and concrete (FRC) composites (*Shah [53], Kelly [16], Swamy [56], Neville [44], Hannant [9]*) as interest in the field grew worldwide. Better performance was generally being sought in terms of strength and deformation capacity. Several papers dealing with the tensile response of fiber reinforced concrete were presented at a 1978 RILEM Symposium on *Testing and Test Methods of Fiber Cement Composites* [54]. While researchers were clearly trying to exceed existing boundaries, no "strain-hardening" stress strain curve was described in these papers. However, in a discussion of the proceeding papers, *Kasperkiewickz* reported on some tensile tests carried out at the Institute of Fundamental Research in Poland in collaboration with the Cement and Concrete Institute in Stockholm, Sweden [14]; the tensile specimens were paddle shaped of section 28 $\times$100 mm, and containing 2% by volume of hooked-ends steel fibers of diameter 0.4 mm and length 25 mm. The fibers were aligned using an electromagnetic field. Strain was measured over a gage length of 245 mm. *Kasperkiewickz* reported clearly observing multiple cracking and some sort of strain hardening, but no figure for these results was given. He used the following sentence (page 495 of Ref. [56]): *"What is much more important is that the aligned fibers give quite substantial ductility and a kind of strain hardening characteristic to the composite."* To the author's knowledge, this was the first time that the term "strain hardening" was used to describe the related behavior of FRC composites. Later (in early 2000's) this author contacted Dr. *Kasperkiewickz* to get any written information on these tests but was essentially told that these were un-finished internal documents in Polish and were no longer available.

In a paper presented in 1978 at an ASTM Symposium on Fracture Mechanics and published in 1979 [30], *Naaman* and *Shah* reported on some tensile and bending tests where multiple cracking was observed. The tensile stress-elongation curve reproduced in the left part of Fig. 5, showed a strain-hardening response after first cracking, which was described by the authors as the "inelastic multiple cracking range" and represented a desirable "ductile" type of failure. The tensile specimen achieving such behavior contained 2.5% smooth steel fibers by volume, of length 25 mm. To the best of this author's knowledge and given the almost simultaneous time of *Kasperkiewicz* discussion [page 495 of Ref. 56], this was likely the first published "strain hardening like" response curve in tension for fiber reinforced concrete with steel fibers. Because the specimen had a small cross-section (25$\times$9 mm), the authors assumed that size effects and fiber alignment were significant to explain the desirable inelastic response. The authors did not use the attribute "strain hardening." However, they illustrated their vision of a general class of composites with multiple-cracking behavior by hypothetical load-elongation curves encompassing all fiber reinforced cement composites including those with continuous fibers; the corresponding figure is reproduced in Fig. 6. Surprisingly, this figure shows the qualitative response (curves 1 to 5) of both strain-softening and strain-hardening FRC composites as defined in Fig. 3, as well as the ideal response which is that of a composite with continuous fibers (curve 6) such as ferrocement.

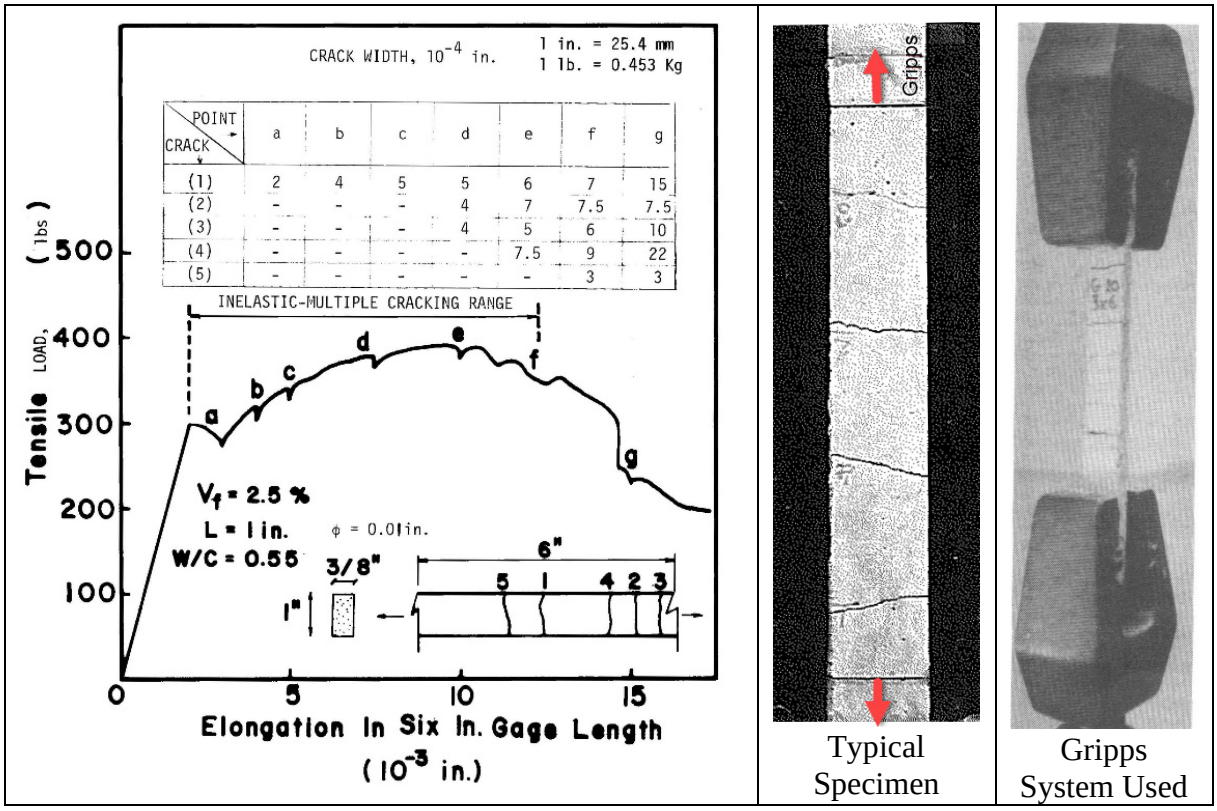


Figure: 5 Inelastic and multiple cracking response of some FRC composites in tension as observed by Naaman and Shah [30].

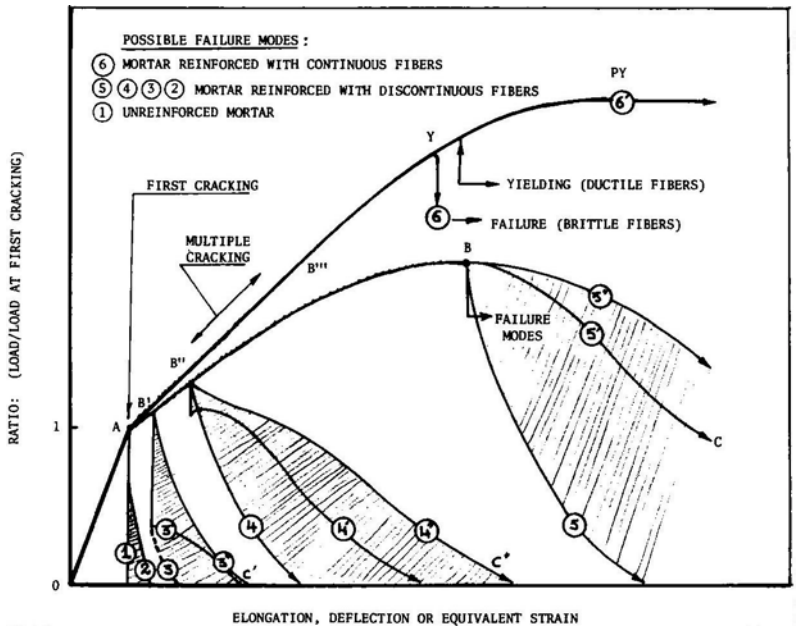


Figure: 6 Normalized hypothetical illustration of the response of fiber reinforced cement composites in tension as visualized by Naaman and Shah in 1979 [30].

Early in the 1980's, a new class of fiber reinforced cement composites identified as slurry infiltrated fiber concrete (or SIFCON) was first introduced by *Lankard* and co-workers [18, 19]. SIFCON is obtained by filling a mold to full capacity with fibers, then infiltrating the resulting fiber network by a cement-based slurry. Such a production process allowed the use of relatively high fiber volume contents, generally varying from 5% to 12% for commonly used steel fibers at the time. Extensive evaluation of the tensile and compressive properties of SIFCON composites was undertaken by *Naaman* and co-workers and *Balaguru* et al. during the 1980's leading to a number of publications [2, 12, 33 to 36]. The tensile stress-elongation curves reported in [34] described stresses up to 30 MPa and strains at peak stress of up to 1%. Figure 7 provides typical information from these tests. Extensive multiple cracking was observed. SIFCON demonstrated convincingly that FRC composites with strengths in tension (as high as normal concrete compressive strengths) can be developed with simultaneously very high ductility. SIFCON belongs mostly to the class of strain-hardening composites (Figs. 1 to 3). Note also that the strain axis in Fig. 7c is valid up to the peak stress only.

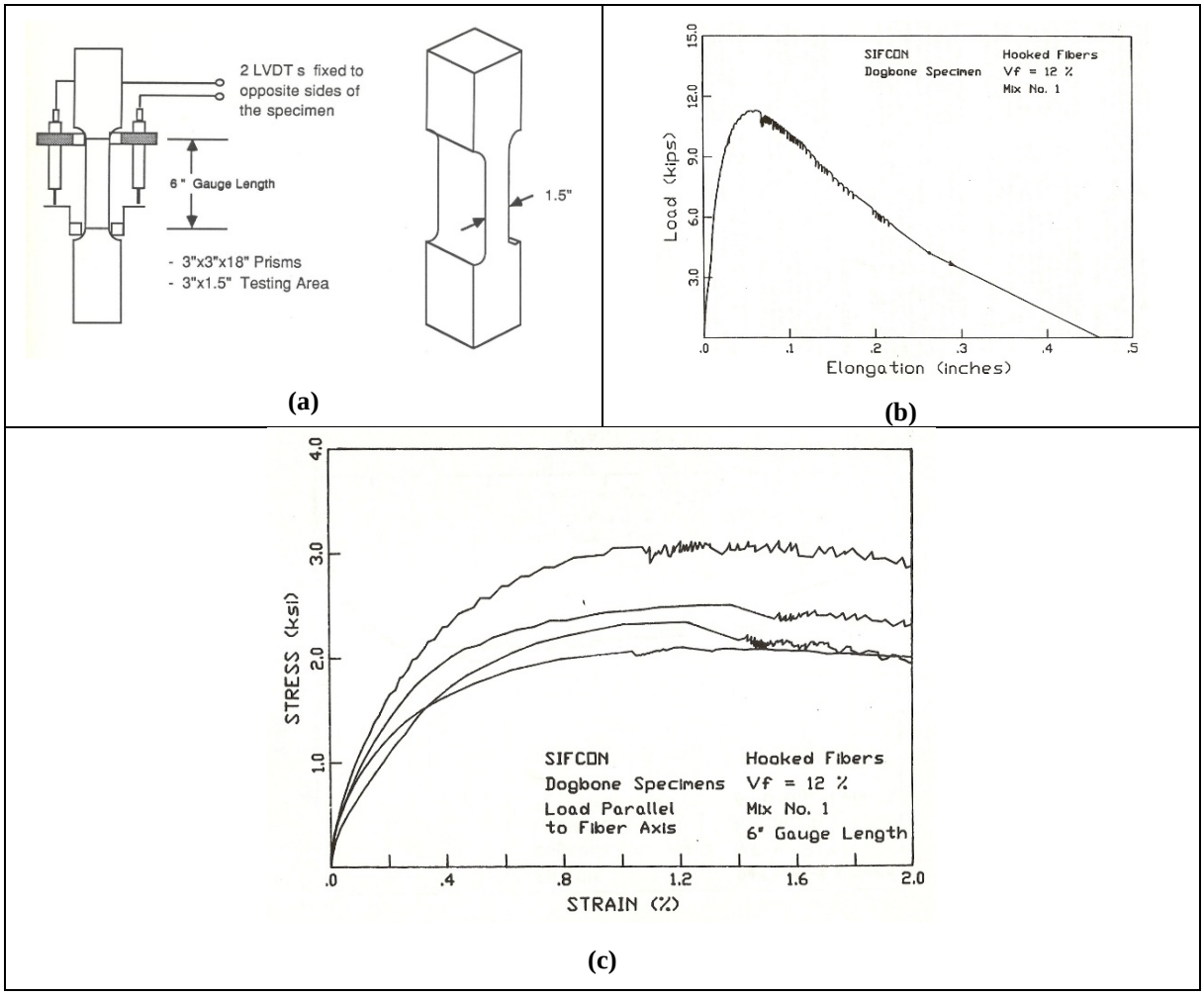


Figure: 7 Typical tensile response of SIFCON. (a) Test specimens. (b) Typical load-elongation response. (c) Typical stress-strain response of four identical specimens showing strains up to peak stress, ε_{pc}, up to about 2% (1 in = 25.4 mm; 1 ksi = 6.9 MPa; 1 kip = 4.448 kN) [12, 33].

In attempting to differentiate the behavior of SIFCON from other FRC composites at the time, *Naaman* suggested the use of the nomenclature "High Performance Fiber Reinforced Cement Composites" (HPFRCC) describing them as having a combination of high strength and toughness-ductility [31, 34]. In a 1987 paper [31] presented at an IABSE conference in Paris, *Naaman* described the typical tensile response of strain-softening and strain-hardening FRC composites, and provided a theoretical formulation to achieve strain-hardening behavior. The terms "strain-hardening" and "strain-softening" were not used but instead the terms "high-performance" and "conventional fiber" reinforced concrete were used. His figures are reproduced in Figs. 8 and 9; they correlate reasonably with Fig. 3.

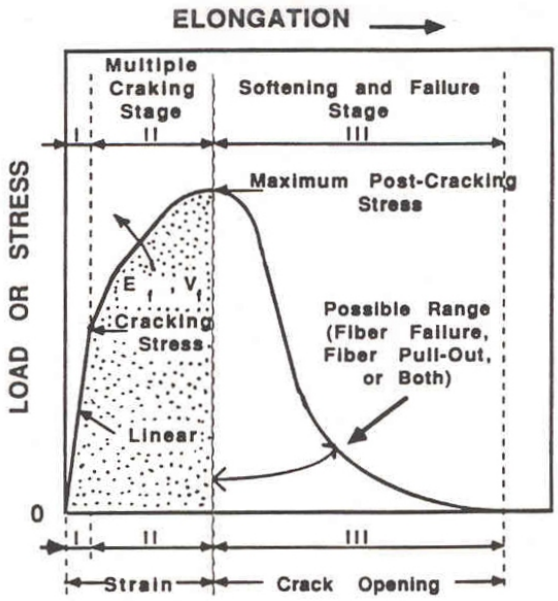


Figure: 8 Typical load-elongation response in tension of a High Performance FRC Composite such as SIFCON as defined by Naaman, 1987 [31].

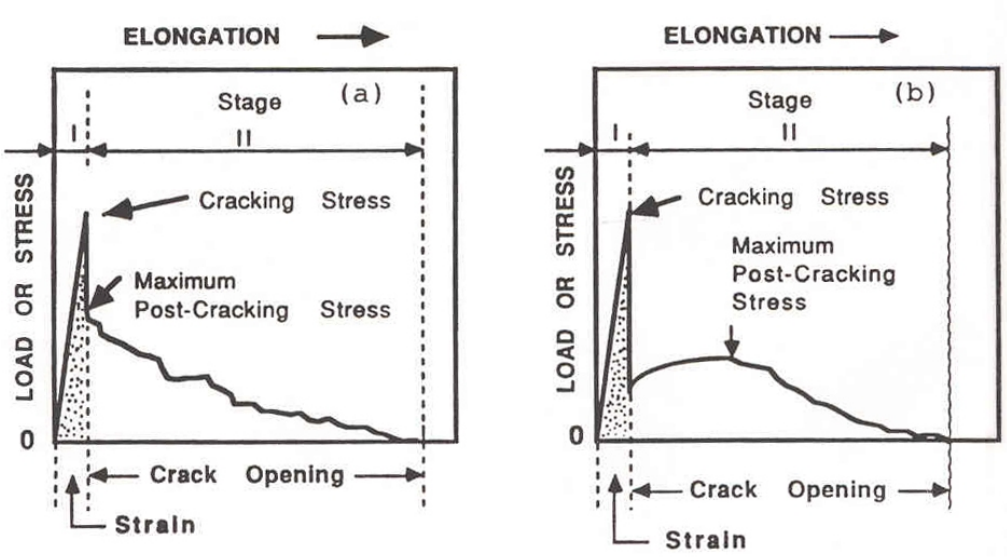


Figure: 9 Typical load elongation response in tension of conventional fiber reinforced concrete as described by Naaman, 1987 [31]. (a) Using premixed steel fibers. (b) Using premixed polypropylene fibers.

To develop a "high performance" stress-strain response similar to that in Fig. 8, Naaman [31] set the condition that, in order for multiple cracking to occur, the tensile post-cracking strength of the composite, σ_{pc} must be more than or equal to its first cracking strength, σ_{cc}, that is:

$$\sigma_{pc} \geq \sigma_{cc} \tag{1}$$

For σ_{cc} and σ_{pc}, *Naaman* used equations developed earlier in his doctoral thesis [27, 29], as follows:

$$\sigma_{cc} = \sigma_{mu}(1\text{-}V_f) + \alpha_1\alpha_2\overline{\tau}V_f\frac{\ell}{d} \tag{2}$$

$$\sigma_{pc} = \lambda_1\lambda_2\lambda_3\overline{\tau}V_f\frac{\ell}{d} \tag{3}$$

where σ_{mu} is the tensile strength of the matrix; V_f is the volume fraction of fibers; $\overline{\tau}$ is the average bond strength at the fiber-matrix interface; ℓ is fiber length; d is fiber diameter; α_1 is a coefficient representing the fraction of bond mobilized at matrix cracking; α_2 is the efficiency factor of orientation in the cracked state; λ_1 is the expected pull-out length ratio of a fiber (typically 1/4); λ_2 is the efficiency factor of orientation in the cracked state; and λ_3 is a group reduction factor associated with the number of fibers pulling out from the same area.

Using Eqs. (2 and 3) in Eq. (1) leads to the following condition for multiple cracking to occur [31]:

$$V_f\left(1+\frac{\overline{\tau}}{\sigma_{mu}}\frac{\ell}{d}(\lambda_1\lambda_2\lambda_3-\alpha_1\alpha_2\right)\geq 1 \tag{4}$$

For a given set of material variables and parameters, Eq. (4) can be used to derive a critical from which a critical volume fraction of fibers needed to achieve multiple cracking thus "strain hardening" in today's terminology [32, 35]:

$$(V_f)_{\text{cri-tension}} = \frac{1}{1+\frac{\overline{\tau}}{\sigma_{mu}}\frac{\ell}{d}\left(\lambda_1\lambda_2\lambda_3-\alpha_1\alpha_2\right)} \tag{5}$$

Equations (1 to 5) have been revised slightly in subsequent studies and are further explained in [32, 43] with additional factors added, but retained essentially the main parameters and variables. Equations (4 and 5) illustrate the influence of several parameters besides the volume fraction of fibers, including the aspect ratio of the fiber, the tensile strength of the matrix and the bond at the fiber matrix interface.

Shortly after *Naaman*'s paper, the term "HPFRCC" was adopted by *Reinhardt* and *Naaman* when organizing a series of RILEM-ACI international workshops on the subject (1991, 1995, 1999, 2003, 2007) with proceedings published under the auspices of RILEM in 1992, 1996, 1999, 2003 and 2007 [35, 36, 39, 45, 46, 47]. The workshop series continued in 2012 and 2015 (that is, HPFRCC 6 and 7) with additional organizers. A brief history of these workshops is described in a short paper in the prolog section of the proceedings of HPFRCC-7 [49]

The 1991 workshop [45] focused mostly on SIFCON type composites and CRC (compact reinforced concrete introduced by *H.H. Bache* [3], which could be described as a highly reinforced conventional reinforced concrete containing high volumes of steel fibers. The 1995 workshop [35] focused generally on HPFRCC and the history of their characterization was reviewed. Relevant to the above discussion, three existing models describing critical volume fraction of fibers to achieve strain-hardening and multiple cracking were discussed, the original model by *Naaman* [31] summarized in Eqs. (1 to 5), and two newer models, one by *Li* and *Wu* [20], and the other by *Tjibtobroto* and *Hansen* [57]. A thorough discussion related to similarities and differences between these models and other details can be found in [35, 36].

Besides the five international workshops mentioned above devoted to high performance fiber reinforced cement composites (HPFRCC), it is relevant to mention at least two related conferences. In 2002, the Japan Concrete Institute organized a symposium on deflection-hardening FRC composites (DHFRCC) which focused on "deflection-hardening" behavior in bending which requires a smaller amount of fiber reinforcement than strain-hardening FRC composites [13]. Also in 2005, an international workshop on Applications of HPFRCC was organized in Hawaii [7]; later a new series of workshops with the title "Strain Hardening Cement Composites" followed and, at time of this writing, it has become common to find international symposia or conferences on fiber reinforced concretes (such as the BEFIB [1] and the RILEM-ACI-FIB series, and the series on Brittle Matrix Composites organized by Brandt et al.) encompassing the subject of strain-hardening or deflection hardening.

3 Evolution of Nomenclature to Describe Strain Hardening Behavior

In the early 1990's attempts were made to use a better nomenclature to describe the strain-hardening and multiple cracking behavior of HPFRCC. This is because the term "high performance" [31, 41] was subjective and could be interpreted in different ways depending on relative levels of technical advances, the nature of the advance, and geographic location. Also, since the term "high performance" did not have the same meaning for all researchers it was often used to describe different properties such as strength, or durability, but not necessarily strain-hardening, ductility and multiple cracking. Some researchers focused on describing a particular composite formulation which could provide some specific properties for their product. So several acronyms were used such as SIFCON (early-1980's, as mentioned above), Densit (densified small particle composites, early 1980's), CRC (Compact Reinforced Concrete, (mid-1980's), then ECC (Engineered Cementitious Composites, early 1990's) by *Li* and co-workers, Ductal by researchers at Lafarge (mid-1990's) [5, 53], UHPFRC by Rossi and co-workers (2000) [53], etc…

While as mentioned earlier, *Kasperkiewickz* was first to describe in 1978 a "kind of strain hardening" behavior of some FRC composites [14], *Li* and co-workers were probably first to revive the terminology in 1992 using the term "pseudo strain-hardening" to illustrate the similarity in tensile behavior between this class of FRC composites and some steels [20, 21]. By 1995-1996, the terms "pseudo strain-hardening", "quasi strain-hardening" and "strain-hardening" became more widely used as evidenced by some of the papers published in the proceedings of the second international workshop on high performance fiber reinforced cement composites [35]. Thereafter, the descriptor "strain-hardening" was extensively used in five international workshops on HPFRCCs which took place in 1999, 2003, 2007, 2012 and 2015**.**

In the closing session of the 2003 fourth international workshop on HPFRCCs [39], a special discussion focused on the key characteristics of "strain-hardening" versus "strain-softening" and how they relate in particular to "deflection-hardening" and "deflection-softening" (Fig. 2). A summary of the workshop, where Fig. 1 was provided [40], *Naaman* and *Reinhardt* suggested the wide use of the classification and related nomenclature. While the first part of the classification dealing with tension (Fig. 2) is a fundamental classification, the second part, dealing with bending, is related to most common applications. Figure 10 illustrates some key milestones described in this paper.

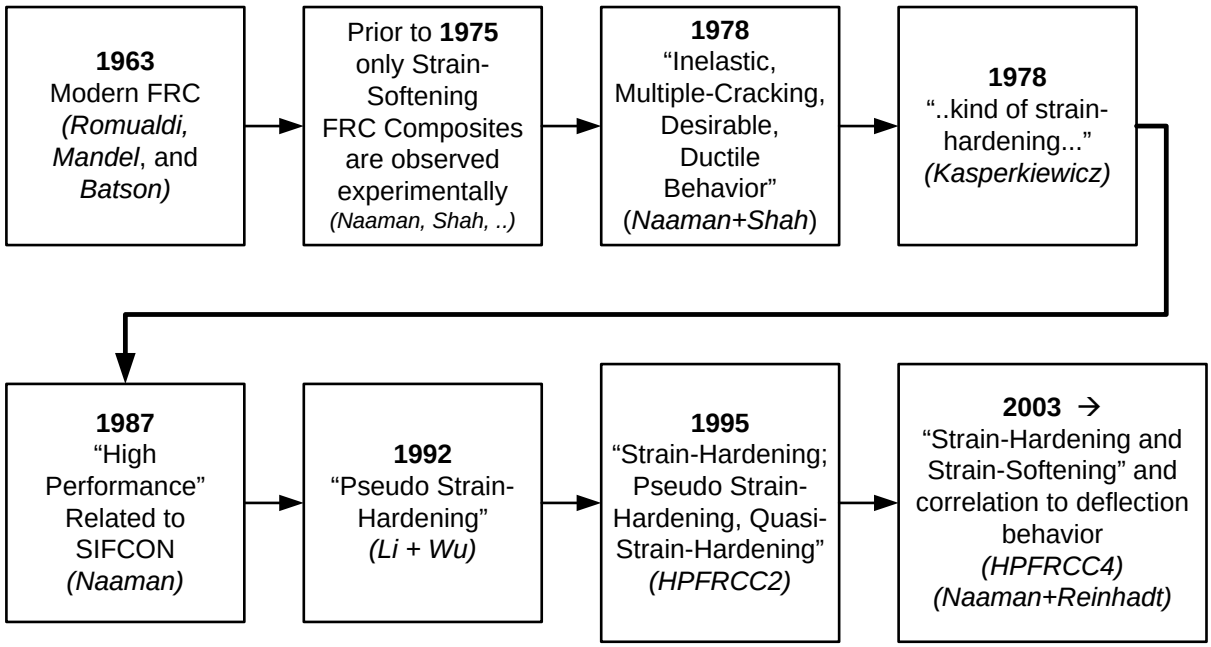


Figure 10 Evolution of terminology to describe strain-hardening behavior in tension, since modern theory of fiber reinforced concrete [32, 43].

5 Strain Hardening Behavior by Fracture Mechanics Approach

The civil engineering community has approached FRC not only from a composite mechanics viewpoint but also using fracture mechanics. As mentioned earlier the initial work of *Romualdi* and co-workers [49-50] was based on Griffith's fracture criterion assuming linear elastic materials; later several studies followed fracture mechanics principles to predict the response of FRC [4, 10, 11, 27, 28, 30, 58] but none addressed the "strain-hardening condition" before the late 1980's.

Classical references on research studies dealing with brittle matrix composites often start by the work of *Aveston*, *Cooper* and *Kelly* and *Kelly* [1, 15, 16] on the analysis of single and multiple fractures, the most commonly referred one published in 1971. In 1985, *Marshall*, *Cox*, and *Evans* published a paper on the mechanics of matrix cracking in fiber composites with brittle matrices [25]. They analysed in particular composites that exhibit multiple cracking prior to fiber failure and have purely frictional bonding between the fiber and the matrix. They distinguished between relatively short cracks and long cracks for which a steady-state cracking configuration develops. The term "steady state" crack is used to describe a flat crack along

which the fibers provide bridging forces resisting crack opening. In hindsight, such an analysis would have typically applied to fiber reinforced concretes of the time, using primarily steel fibers.

In 1988, *Marshall* and *Cox* published a paper describing the condition for "steady state" matrix cracking [26]. They wrote the following: " …*a steady state crack can be made to extend indefinitely in the matrix without ligaments (fibers) rupturing in the wake*." The condition for steady state cracking was formulated analytically using an energy balance criterion based on the J-integral in fracture mechanics; it stated that for a steady state crack to occur, the complementary energy must exceed the matrix crack tip toughness. In effect, this created the analytical condition for the occurrence of the first "percolation crack" or first "structural crack" or first "deviation from linearity crack" as described by the civil engineering community. Recall that Civil engineers considered first structural cracking primarily a stress controlled condition.

In a follow-up paper in 1989, a second condition to insure multiple cracking was formulated by *Cox*, *Marshall* and *Thouless* (1989, [6]), essentially stating that for multiple cracking to occur, first the condition for a steady state crack must be satisfied and, second, the maximum bridging stress must exceed the matrix cracking strength, $\sigma_{pc} \geq \sigma_{mu}$. This is very similar to *Naaman's* condition for multiple cracking that $\sigma_{pc} \geq \sigma_{cc}$ [31 and Eq. 1] for what he described as "high-performance FRC" (later strain-hardening) composites.

In two papers published in 1992 [20, 21], *Li* and *Leung* and *Li* and *Wu* (from the civil engineering community) used exactly the same energy condition originally developed by *Marshall*, *Cox* and *Evans* (1985 and 1988) [25, 26], to describe "pseudo-strain hardening" behavior in fiber reinforced cement composites; they named such materials "engineered cementitious composites" or ECCs. However, in characterizing ECCs, *Li* [22] and many of his co-workers often cited the steady-state cracking condition only, ignoring the stress condition stated by *Cox, Marshall* and *Thouless* (1989) [6]. According to this author the energy condition set forth for steady state cracking, is necessary but not sufficient [32, 43]; the stress condition is also needed. Most immediate conclusion is that successful ECCs are in effect "strain-hardening" FRC composites.

In summary, it can be said that while before 1990, the approach used by the "fracture mechanics – materials science community" and that used by the"civil engineering - composite mechanics community" have progressed along separate paths, independently of each other, they have merged thereafter for various analysis-design considerations of brittle matrix composites. The reader interested in the history of FRC composites will find additional details in [32, 43].

5 Disclosure

Thousands of studies have addressed the analysis of FRC composites. The author has attempted to identify as accurately as possible when, from a time stance, a "first" idea or terminology related to their "strain-hardening" behavior was published. No attempt was made to refer to related studies that occurred later. In some instances, the author has used his best recollection of the facts. Should a reader of this paper find some "inaccuracy" or a needed clarification as to the true origine of an idea, rest assured that it was not the author's intent to ignore it; more importantly feel free to publish a related discussion or an addendum to this paper in the future.

6 Dedication – Acknowledgments



This paper is dedicated to the memory of Professor Dr.-Eng Hans-Wolf Reinhardt (1939 – 2026). Professor Reinhardt and I first met in the mid-1980s, when I visited his laboratory at Delft University of Technology in the Netherlands to examine an impact testing machine he had developed. That visit gave us the opportunity to discuss our shared interests in fiber reinforced concrete, particularly SIFCON (Slurry Infiltrated Fiber Concrete), and marked the beginning of a long-term professional collaboration and personal friendship. Later, when Professor Reinhardt moved first to T.H. Darmstadt and then to the University of Stuttgart in Germany, he invited me to spend a sabbatical year (1990–1991) in Darmstadt and Stuttgart with support from the Alexander von Humboldt Foundation.

During that visit, we worked in particular on material tests of SIFCON and on the bending response of large SIFCON beams, with and without conventional reinforcing bars. Perhaps the most visible result of our collaboration was the co-organization of a series of seven Rilem-ACI international workshops on “High Performance Fiber Reinforced Cement Composites,” spanning the years 1991 to 2015. I am deeply grateful and honored to have been H. W. Reinhardt’s colleague and friend, and I remain humbled by his accomplishments. He was not only a unique leader in our field, but also a model of wisdom (technical and beyond), kindness, integrity, with a constant commitment to what is best and for the greater good. I personally feel that I have lost one of my pillars, but in hindsight I am immensely grateful that our paths have crossed in this life.

7 References

1. Aveston, J., Cooper, G.A., and Kelly, A., “Single and Multiple Fracture,” in *Properties of Fiber Composites*, Proceedings of Conference of the National Physical Laboratory, Guildford, U.K., IPC Science and Technology Press, 1971.
2. Balaguru, P., and Kendzulak, J., Mechanical Properties of Slurry Infiltrated Fiber Concrete (SIFCON), in *Fiber Reinforced Concrete Properties and Applications*, American Concrete Institute, SP-105, ACI, Detroit, 1987.
3. Bache, H.H., ” Principles of Similitude in Design of Reinforced Brittle Matrix Composites,’ in "*High Performance Fiber Reinforced Cement Composites - HPFRCC1,"* RILEM Publications 15, Edited by H.W. Reinhardt and A.E. Naaman, E. & FN Spon, London, 1992, pp. 39-56.
4. Brandt, A.M., “On the Calculation of Fracture Energy in SFRC Elements Subjected to Bending,” Proceedings of Conference on "*Bond in Concrete*", ed. P. Bartos, Paisley, U.K., June 1982, Appl.Science Publishers, London 1982, pp. 73-81.
5. Chanvillard, G., and Rigaud, S., “Complete Characterization of Tensile Properties of Ductal UHPFRC According to the French Recommendations,” in *High Performance Fiber*

Reinforced Cement Composites (HPFRCC-4), A.E. Naaman and H.W. Reinhardt, Editors, RILEM Publications, Pro. 30, June 2003, pp. 95-113.
6. Cox, B.N., Marshall, D.B., and Thouless, M.D., "Influence of Statistical Fiber Strength Distribution on Matrix Cracking in Fiber Composites," *Acta Metallica*, Vol. 37, No. 7, 1989, pp. 1933-1943.
7. Fischer, G., and Li, V.C., Editors, Proceedings of Rilem International Conference on "*Applications of High Performance Fiber Reinforced Cementitious Composites in Structural Applications*," Honolulu, Hawaii, 2005, RILEM Pro 049, 2006.
8. Grimer, E., and Ali, M.A., "The Strength of Cements Reinforced with Glass Fibers," *Magazine of Concrete Research*, March 1969.
9. Hannant, D.J., "*Fiber Cements and Fiber Concretes*," J. Wiley, 1978, 215 pp.
10. Hillerborg, A., Modeer, M., and Petersson, P-E., "Analysis of Crack Formation and Crack Growth in Concrete by Means of Fracture Mechanics and Finite Elements," *Cement and Concrete Research*, Vol. 6, 1976, pp. 773-782.
11. Hillerborg, A., "The Advanced Strip Method: a Simple Design Tool," *Magazine of Concrete Research*, Vol. 34, No. 121, 1982, pp. 175-181.
12. Homrich, J.R., and Naaman, A.E., "Stress-Strain Properties of SIFCON in Compression," in *Fiber Reinforced Concrete: Properties and Applications*, American Concrete Institute, SP-105, Detroit, Michigan, 1987, pp. 283-304.
13. Japan Concrete Institute, Proceedings of the JCI Workshop on Ductile Fiber Reinforced Cementitious Comp. (DFRCC) – Application and Evaluation, Tokyo, Japan, October 2002.
14. Kasperkiewicsz, J., discussion, in Proceedings of RILEM Symposium on *Testing and Test Methods of Fiber Cement Composites*, Edited by N. Swamy, The Construction Press, England, 1978, pp. 493-495, and private communication later.
15. Kelly, A., and Davis, G.J., "The Principles of Fiber Reinforcement of Metals," *Metallurgical Review*, Vol. 10, No. 37, 1965.
16. Kelly, A., "Reinforcement of Structural Materials by Long Strong Fibers," *ASM Symposium*, Boston, May 1972.
17. Krenchel, H., "*Fiber Reinforcement*," Akademisk Forlag, Copenhagen, Denmark, Eng. translation, 1964.
18. Lankard, D.R., "Slurry Infiltrated Fiber Concrete (SIFCON): Properties and Applications," in Proceedings of Symposium on *Very High Strength Based Materials*, Materials Research Society, Vol. 42, J.F. Young, Editor, Pittsburgh, 1985.
19. Lankard, D.R., and Newell, J.K., "Preparation of Highly Reinforced Steel Fiber Reinforced Concrete Composites," in *Fiber Reinforced Concrete – International Symposium*, American Concrete Institute, SP-81, Detroit, 1984, pp. 277-306.
20. Li, V.C., and Wu, H.C., "Conditions for Pseudo Strain Hardening in Fiber Reinforced Brittle Matrix Composites," *J. of Applied Mechanics Review*, Vol. 45, No. 8, 1992, pp. 390-398.
21. Li, V.C., and Leung, C.K.Y., "Theory of Steady State and Multiple Cracking of Random Discontinuous Fiber-Reinforced Brittle Matrix Composites," *ASCE Journal of Engineering Mechanics*, Vol. 118, No. 11, 1992, pp. 2246-2264.
22. Li, V.C., "On Engineered Cementitious Composites (ECC): A Review of the Material and its Implications," *Journal of Concrete Technology*, Japan Concrete Institute, Vol. 1, No. 3, November 2003, pp. 215-230
23. Majumdar, A.J., "Determining Bond Strength in Fiber Reinforced Composites," *Magazine of Concrete Research*, Vol. 20, Dec. 1968.
24. Majumdar, A.J., and Ryder, J.F., "Glass Fiber Reinforcement of Cement Products," *Glass Technology*, Vol. 9, No. 3, June 1968, pp. 78-84.

25. Marshall, D.B., and Cox, B.N., and Evans, A.G., "The Mechanics of Matrix Cracking in Brittle-Matrix Fiber Composites," *Acta Metallica*, Vol. 35, No. 11, 1985, pp. V2013-2021.
26. Marshall, D.B., and Cox, B.N., "A *J*-Integral Method for Calculating Steady-State Matrix Cracking Stresses in Composites," *Mechanics of Materials*, North-Holland, No. 7, 1988, pp. 127-133.
27. Naaman, A.E, "A Statistical Theory of Strength for Fiber Reinforced Concrete," Ph.D. Thesis, Massachusetts Institute of Technology, Sept. 1972, 196 pages.
28. Naaman, A.E., A. Argon and F. Moavenzadeh, "A Fracture Model for Fiber Reinforced Cementitious Materials," *Cement and Concrete Research*, Vol. 3, No. 4, 1973, pp. 397-411.
29. Naaman, A.E., F. Moavenzadeh and F.J. McGarry, "Probabilistic Analysis of Fiber Reinforced Concrete," *Journal of the Engineering Mechanic's Division, ASCE*, Vol. 100, No. EM2, April 1974, pp. 397-413.
30. Naaman, A.E., and Shah, S.P., "Fracture and Multiple Cracking of Cementitious Composites," in *Fracture Mechanics Applied to Brittle Materials*, ASTM STP 678, Part II, S.W. Frieman, Editor, 1979, 183-201. (Note: the related symposium was held in June 1978)
31. Naaman, A.E., "High Performance Fiber Reinforced Cement Composites," Proceedings of the IABSE Symposium on *Concrete Structures for the Future*, Paris, France, September 1987, pp. 371-376.
32. Naaman, A.E., A.E., "*Fiber Reinforced Cement and Concrete Composites*," Techno Press 3000, Sarasota, Florida, ISBN 978-0-9674930-3-0, 2018, 765 pages. www.foxpointprinting.com
33. Naaman, A.E., and Homrich, J.R., "Tensile Stress-Strain Properties of SIFCON," *ACI Materials Journal*, Vol. 86, No. 3, May-June 1989, pp. 244-251.
34. Naaman, A.E., "SIFCON: Tailored Properties for Structural Performance," in *High Performance Fiber Reinforced Cement Composites*, *HPFRCC1*, edited by H.W. Reinhardt and A.E. Naaman, RILEM Proceedings 15, E. and FN SPON, London, 1992, pp. 18-38.
35. Naaman, A.E., and Reinhardt, H.W., Co-Editors, "*High Performance Fiber Reinforced Cement Composites: HPFRCC 2"*, RILEM, No. 31, E. & FN Spon, London, 1996, 505 pages. Workshop occurred in 1995.
36. Naaman, A.E., and Reinhardt, H.W., "Characterization of High Performance Fiber Reinforced Cement Composites," in Proceedings of *High Performance Fiber Reinforced Cement Composites: HPFRCC 2*, RILEM, No. 31, E. & FN Spon, London, 1996, pp. 1-31.
37. Naaman, A.E., "Toughness, Ductility, Surface Energy and Deflection-Hardening FRC Composites," in Proceedings of the JCI Workshop on *Ductile Fiber Reinforced Cementitious Composites (DFRCC) – Application and Evaluation*, Japan Concrete Institute, Tokyo, Japan, October 2002, pp. 33-57.
38. Naaman, A.E., "Strain Hardening and Deflection Hardening Fiber Reinforced Cement Composites," in *High Performance Fiber Reinforced Cement Composites (HPFRCC-4),* A.E. Naaman and H.W. Reinhardt, Editors, RILEM Publ., Pro. 30, June 2003, pp. 95-113.
39. Naaman, A.E., and Reinhardt, H.W., Co-Editors, *"High Performance Fiber Reinforced Cement Composites - HPFRCC 4,"* RILEM Proc., PRO 30, RILEM Pbs., S.A.R.L., Bagneux, France, June 2003; 546 pages.
40. Naaman, A.E., and Reinhardt, H.W., "High Performance Fiber Reinforced Cement Composites (HPFRCC-4): International RILEM Report," *Materials and Structures*, Vol. 36, Dec. 2003, pp. 710-712. Also same report in *Cement and Concrete Composites*, Vol. 26, 2004, pp. 757-759.
41. Naaman, A.E., and Reinhardt, H.W., "Proposed Classification of FRC Composites Based on their Tensile Response " *Materials and Structures*, Vol. 39, page 547-555, 2006. Also,

Proceedings of symposium honoring S. Mindess, N. Banthia, Editor, University of British Columbia, Canada, August 2005. Electronic proceedings, 13 pages.
42. Naaman, A.E., "Deflection Softening and Deflection Hardening FRC Composites: Characterization and Modeling," in ACI special publication on *Deflection and Stiffness Issues in FRC and Thin Structural Elements*, P. Bischoff and R. Malhas, Editors, ACI SP-248, Electronic Proceedings, 2007, pp. 53-66.
43. Naaman, A.E., "Development and Evolution of tensile strain hardening FRC composites," in Fiber Reinforced Concrete: Design and Applications, *Proceedings of International Symposium, BEFIB 2008*, Edited by Ravindra Gettu, RILEM PRO 60, 2008, pp. 1-28.
44. Neville, A., Editor, Proceedings of the RILEM *International Symposium on Fiber Reinforced Cement and Concrete*, London, September, 1975.
45. Parra-Montecino, G.J., H.W. Reinhardt, H.W., and Naaman, A.E., Co-Editors "*High Performance Fiber Reinforced Cement Composites – HPFRCC 6,"* RILEM Publications, Springer, 2012, 559 pages.
46. Reinhardt, H.W., and A.E. Naaman, A.E., Co-Editors "*High Performance Fiber Reinforced Cement Composites - HPFRCC1,"* RILEM Publications 15, E. & FN Spon, London, 1992, 565 pages. Workshop occurred in 1991.
47. *Reinhardt, H.W., a*nd A.E. Naaman, A.E., Co-Editors, *"High Performance Fiber Reinforced Cement Composites - HPFRCC 3,"* RILEM Proceedings, PRO 6, RILEM Pbs., S.A.R.L., Cachan, France, May 1999; 666 pages.
48. Reinhardt, H.W., and A.E. Naaman, A.E., Co-Editors, *"High Performance Fiber Reinforced Cement Composites - HPFRCC 5,"* RILEM Proceedings, RILEM Pbs., Bagneux, France, 2007.
49. Reinhardt, H.W., Parra-Montesinos, G.J., and Garrecht, *"High Performance Fiber Reinforced Cement Composites – HPFRCC 7,"* RILEM Publications S.A.R.L., Bagneux, France, 2015, 510 pages.
50. Romualdi, J.P, and Batson, G.B., 'Mechanics of Crack Arrest in Concrete', *J. Engineering Mechanics, ASCE*. 89, 1963, 147–168.
51. Romualdi, J.P., and Mandel, J.A., "Tensile Strength of Concrete Affected by Uniformly Distributed Closely Spaced Short Length of Wire Reinforcement," *ACI Journal*, June 1964.
52. Romualdi, J.P., "Two Phase Concrete and Steel Materials," U.S. Patent No. 3,439,094, Feb. 25, 1969.
53. Rossi, P. and Chanvillard, G., Editors, Proceedings of Fifth RILEM Symposium on *Fiber Reinforced Concretes (FRC), BEFIB 2000*, September 2000, Rilem Publications, S.A.R.L., Cachan, France.
54. Shah, S.P., Ranjan, R.V., "Fiber Reinforced Concrete Properties," *ACI Journal*, Vol. 68, No. 2, Feb. 1971, pp. 126-135.
55. Shah, S.P., "Do Fibers Increase the Tensile Strength of Cement-Based Matrices?" *ACI Materials Journal*, Vol. 88, No. 6, Nov.-Dec. 1991, pp. 595-602.
56. Swamy, R.N., Editor, "*Testing and Test Methods of Fiber Cement Composites*," RILEM Symposium Proceedings, Sheffield, The Construction Press, England, 1978, 545 pages.
57. Tjiptobroto, P., and Hansen, W., "Model for prediction of the elastic strain of fiber reinforced composites containing high volume fractions of discontinuous fibers," *ACI Materials Journal*, V. 90, No. 2, March-April, 1993.
58. Visalvanich, K. and A.E. Naaman, "A Fracture Model for Fiber Reinforced Concrete," *Journal of the American Concrete Institute*, Vol. 80, No. 2, March/April 1983, pp. 128-138.

Influence of dispersed PVA fibers in the GFRP bar-concrete bond behavior

Veronica Bertolli[1], Tommaso D'Antino[1] and Christian Carloni[2]

[1]: Department of Architecture, Built Environment and Construction Engineering, Politecnico di Milano, Milan, Italy

[2]: Department of Civil and Environmental Engineering, Case Western Reserve University, Cleveland, OH, USA

Abstract

During the last few decades, fiber-reinforced concrete (FRC) has been widely used in the construction industry to increase strength and toughness of concrete structural members. Different types of dispersed fibers have been used in FRC, with different dimensions, shapes, and mechanical properties. Steel FRC (SFRC) is commonly used in specific structural applications (e.g., precast tunnel segments). The addition of synthetic fibers in concrete is becoming increasingly popular due to their ability to delay the occurrence of microcracks and/or provide post-cracking tensile residual strength. Furthermore, synthetic fibers have better durability than steel fibers. Among different synthetic fibers, polyvinyl alcohol (PVA) fibers have shown promising results.

This paper presents a preliminary experimental campaign aimed at assessing the bond behavior between thermoset GFRP bars and PVA FRC. Eight pull-out tests are performed, and the results obtained with PVA FRC specimens are compared with equivalent plain concrete (PC) specimens. Two different types of PVA fibers were used, namely 0.6 vol.%. PVA microfibers and 2.0 vol.% PVA macrofibers. The comparison between FRC and PC specimens shows that the addition of PVA fibers in concrete might have limited influence on the GFRP bar-concrete bond behavior.

Keywords

Fiber reinforced concrete, GFRP bars, PVA FRC, synthetic fibers.

1 Introduction

Glass fiber-reinforced polymer (GFRP) bars are increasingly adopted as internal reinforcement in reinforced concrete (RC) structures as an alternative to traditional steel bars, especially in aggressive environments where durability is a major concern (D'Antino et al., 2023). Owing to their high tensile strength, low density and resistance to chloride-induced corrosion, GFRP bars are widely used in marine structures, bridge decks, and infrastructures exposed to deicing salts (Aflakisamani et al., 2023; Cope et al., 2024). However, compared to steel reinforcement, GFRP bars exhibit a lower elastic modulus and a different bond behavior with concrete, often resulting in larger crack widths and higher deflections in service conditions. To mitigate these limitations, the use of fiber-reinforced concrete (FRC) structures (Vandewalle, 2000) combined with GFRP bars as internal reinforcement may provide an effective solution (Bertolli et al., 2026).

FRC has attracted increasing attention in the last three decades. Different types of fibers, including steel, glass, and synthetic fibers, have been used in concrete mixtures to improve tensile strength, toughness, and crack control (Martinelli et al., 2021; Naaman, 2018). Steel fiber-reinforced concrete (SFRC) is currently the most widely used type of FRC in structural applications (Conforti et al., 2019; Facconi et al., 2021). Among synthetic fibers, polyvinyl alcohol (PVA) fibers have shown promising results due to their high tensile strength, good bond with the cementitious matrix, and ability to promote multiple microcracking and strain-hardening behavior in cement-based composites (Plizzari, 2018). The combination of GFRP bars and PVA-FRC can therefore create a fully corrosion-resistant structural system with enhanced cracking control and improved post-cracking behavior (Bertolli et al., 2025). In particular, PVA fibers may compensate for the relatively low stiffness of GFRP-reinforced members by limiting crack opening and improving stress redistribution within the concrete matrix (Dopko et al., 2018). Nevertheless, some drawbacks still exist, including the higher material cost, potential reductions in workability associated with synthetic fibers, and the limited amount of experimental data currently available on the interaction between PVA-FRC and GFRP reinforcement (Signorini et al., 2020).

The presence of fibers in concrete might also influence the bond behavior of the GFRP bar-FRC interface. The bond behavior between bars and surrounding concrete is usually investigated through pull-out tests, in which the reinforcing bar embedded into a concrete specimen is pulled out while restraining the concrete block (Baena et al., 2009; Solyom et al., 2020). The local bond-slip relationship of the bar-concrete interface is influenced by different parameters, such as bar diameter and interface bonded length. The bar surface treatment and configuration were proven to play a crucial role (Rahman et al., 2025; Zhao et al., 2022). The bond behavior of GFRP bars may differ from that of traditional steel reinforcement because of the anisotropic nature of the material and the different surface geometries typically adopted for FRP bars. For this reason, the bond behavior of GFRP bar and concrete was extensively studied in the literature in the last few years.

On the other hand, very limited results are available in the literature on the bond behavior between GFRP bars and FRC. In particular, only two works investigated the stress transferred at the GFRP bar-FRC interface (Sun et al., 2021; Xie et al., 2018). In these works, pull-out tests were performed to investigate whether the ability of fibers of distributing stresses and cracks influence the bar-concrete bond behavior.

In this paper, the bond behavior of GFRP bar and concrete is investigated by means of eight pull-out tests performed on plain concrete and PVA fiber-reinforced concrete. Two different types of dispersed PVA fibers were used in all FRC specimens. Namely, micro- and macro-PVA fibers in a volume fraction of 0.6% and 2.0%, respectively. The pull-out specimens comprised a 12 mm-nominal diameter GFRP bar embedded in either PC or FRC cylinders. Tests were performed according to ASTM D7913 (ASTM International, 2020a), but concrete cylinders were used in place of concrete prisms and a bonded length equal to twenty times the bar nominal diameter was considered. The applied load – global slip curves of PC and FRC specimens are presented and discussed, and a comparison is made between the two specimen groups. The results obtained show that the addition of dispersed PVA fibers in concrete may have a limited influence on the GFRP bar-concrete interface bond behavior.

2 Materials and methods

This work presents the results of eight pull-out tests performed on thermoset GFRP bars embedded in concrete cylinders. The bars had 12 mm-nominal diameter (d_{nom} = 12 mm), and both PC and FRC concrete cylinders were used. The mechanical properties of the GFRP bars were taken from the literature, whereas PC and FRC mechanical properties were determined experimentally. The pull-out test specimens had bonded length ℓ_b equal to $\ell_b = 20d_{nom}$. These are the preliminary results of a broader experimental campaign on the use of GFRP bars as internal reinforcement of PVA-FRC structures.

2.1 Materials

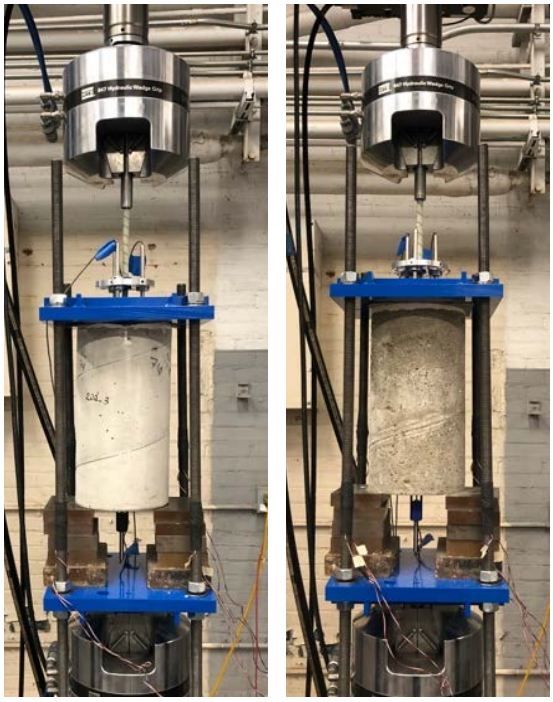
The thermoset GFRP bars used were made of E-CR glass long fibers and vinylester thermosetting resin. They had a sand-coated surface and a carbon yarn spirally wrapped around the bar surface with nominal spacing 20 mm. Their elastic modulus and cross-sectional area, computed by the Authors from the same type of bar in a previously published work, were E_{ft} = 54.46 GPa and A_{eff} = 126.7 mm^2, respectively (D'Antino et al., 2023; D'Antino and Pisani, 2023; Sireg Geotech Srl., 2022). Two batches of concrete were used to cast the PC and FRC specimens. The concrete used for PC specimens had a mixture proportion by weight of 1.8:1.0:0.4:3.0:4.2 (water-to-concrete ratio w/c = 0.55). Type IL cement was used, and superplasticizer was added in 5.0 %wt. of the cement. Two types of short, dispersed PVA fibers were added to this concrete to cast the FRC specimens. PVA microfibers had length and diameter of l_{nom} = 6 mm and ϕ_{nom} = 26 μm, and tensile strength and elastic modulus of $f_{ft,S}$ = 1600 MPa and $E_{f,S}$ = 39.0 GPa. PVA macrofibers had length and diameter of l_{nom} = 30 mm and ϕ_{nom} = 6000 μm, and tensile strength and elastic modulus of $f_{ft,S}$ = 900 MPa and $E_{f,S}$ = 23.0 GPa. The amount of PVA micro and macrofibers added in the mix design was 7.8 kg/m^3 and 26 kg/m^3, respectively, corresponding to fiber volume fractions of 0.6% and 2.0%, respectively. Concrete compressive strength was determined according to ASTM C39/C39M (ASTM International, 2020b) on three concrete cylinders with diameter of 150 mm and height of 300 mm, whereas concrete tensile strength was determined with ASTM C496/C496M (ASTM International, 2017). The tensile properties of FRC specimens were determined following the prescriptions of EN 14651 (European Committee for Standardization, 2007) and were published in a previous study (Bertolli et al., 2023). The results are reported in Table 1.

Table 1. PC and FRC mechanical properties at 28 days.

Properties	PC	FRC
Compressive strength, f'_c	32.3 MPa (CoV = 4.58%)	26.9 MPa (CoV = 10.06%)
Tensile strength, f_t	2.6 MPa (CoV = 2.28%)	3.0 MPa (CoV = 3.60%)
Nominal strength, f_L	-	6.27 MPa,
Tensile residual strength f_{R1}	-	5.66 MPa
Tensile residual strength f_{R2}	-	4.75 MPa
Tensile residual strength f_{R3}	-	2.68 MPa

2.2 Methods

Pull-out tests were performed on specimens consisting of GFRP bar with d_{nom} =12 mm embedded in a concrete cylinder. Cylindrical concrete specimens were adopted in place of the concrete cubes prescribed by ASTM D7913 (ASTM International, 2020a). Cylinders were used in order to have axial symmetry conditions during the tests, which entail for a uniform stress distribution along the whole bar-concrete bonded length. All bars had a total length of 740 mm, whereas the concrete cylinder height and diameter were 380 mm and 200 mm. Pull-out specimens were manufactured with a 50 mm-long protrusion at the free end, a bonded length $\ell_b = 20d_{nom} = 240$ mm and a 140 mm-long bond-breaker at the specimen loaded end. It is worth noting that ASTM D7913 (ASTM International, 2020a) prescribes a bonded length equal to $5d_{nom}$. In this work, a higher value of bonded length is used in order to check the non-uniform stress distribution along the interface. The results obtained in this work can be compared with works available in the literature where the same bar is used in pull-out specimens with different bonded lengths for PC specimens (i.e, $5d_{nom}$, $10d_{nom}$ (Zhao et al., 2022)). Hollows steel cylinders with length of 150 mm were epoxy-bonded to the top end of the bar to improve the load transfer between the bar and the machine jaws. The bar free length was 160 mm. Test were performed according to ASTM D7913 (ASTM International, 2020a), by pulling the bar top end while the concrete cylinder was restrained by two steel plates connected by four steel rods (see Figure 1). Tests were carried out on a 250 kN capacity servo-hydraulic testing machine, with a machine stroke rate of 0.88 mm/min. Three linear variable displacement transformers (LVDTs) were used to measure the relative displacement between concrete and GFRP bar at the concrete cylinder top surface, ξ, and one LVDT was attached to the bottom side of the concrete cylinder to measure the concrete-bar relative displacement at the free end, δ. Details of specimen preparation and casting, and details of the test setup and procedure can be found in Zhao et al. (Zhao et al., 2022). Specimens were named PO-20d-Y-N, where PO=pull-out test, 20d=joint bonded length as function of the bar nominal diameter ($20d_{nom}$), Y=PC (plain concrete) or FRC (fiber-reinforced concrete), and N=specimen number.



(a) (b)

Figure 1: Pull-out test setup: (a) PC and (b) FRC specimens.

3 Results

The results of the pull-out tests performed are reported in terms of applied load P – global slip g and applied load P – free-end slip δ in Figure 2a and b, respectively. The applied load P is the load measured by the testing machine, and the free-end slip δ is the value of slip measured by the LVDT positioned at the bar free-end. The global slip g is defined as the relative displacement between the bar and the top surface of the concrete cylinder (i.e., at the bar loaded end). It is computed as reported in Eq. (1).

$$g = \xi - \Delta L_{el} = \xi - L_c P / E_{ft} A_{eff} \quad (1)$$

where ξ is the slip at the loaded end computed as the average value of the three top LVDTs measurements, ΔL_{el} is the elastic elongation of the portion of the bar between the point at which the LVDTs were mounted and the beginning of the bonded area (ASTM International, 2020a). The elastic elongation is computed considering the elastic modulus in tension and the cross-sectional area of the GFRP bars. The distance between the top side of the bonded length and the position of the three LVDTs (i.e., where the bar-concrete displacement is measured during the tests) is L_c = 240 mm. Figure 2c and d report the call-out of the curves of Figure 2a and b.

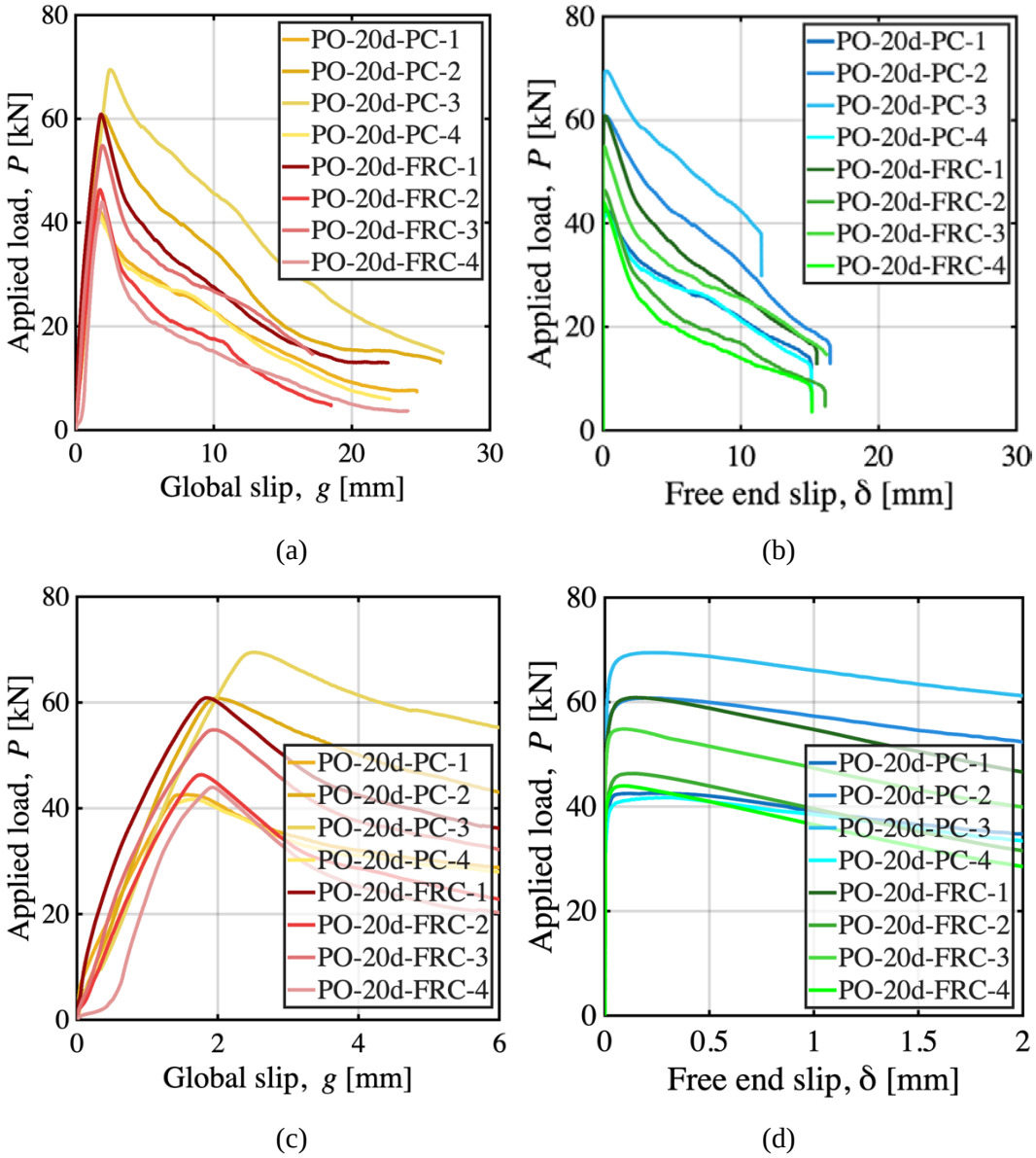


Figure 2. a) P – g curves and b) P – δ curves of pull-out tests for PC and FRC specimens. Call-out of c) P – g and d) P – δ curves.

The key values of the $P - g$ and $P - \delta$ curves are reported in Table 2. Namely, the peak applied load P^*, the global slip g^* and free end slip δ^* corresponding to P^* and the maximum average bond stress τ_{av}^*. As per ASTM D7913 (ASTM International, 2020a), the bond strength τ_{av}^* is defined as the average interfacial shear stress at the bar-concrete interface at peak load, and is computed as reported in Eq. (2).

$$\tau_{av}^* = \frac{P^*}{\pi d_b \ell_b} \tag{2}$$

The average value of τ_{av}^* was defined as $\overline{\tau}_{av}^*$ and was 5.29 MPa (CoV = 25.6%) and 5.08 MPa (CoV = 15.1%) for PC and FRC specimens, respectively. The box plot reported in Figure 3 show the median, the 25th–75th percentile range, and the overall distribution of the values in

the PC and FRC groups. The results obtained in the two specimen groups are quite similar, and the variability range of FRC was fully included within the wider variability range of PC. PC specimens attained values of peak load slightly higher than FRC specimens, but lower values of corresponding global slip g^* (Table 2 and Figure 3). It is worth noting that τ_{av}^* depends on the bar-concrete interface bonded length and hence is a conventional quantity that does not represent the actual bond behavior of the bar, which is governed by a local shear stress τ – slip *s* relationship (Focacci et al., 2000).

Considering that the bond strength of pull-out tests was proven to be influenced by the concrete compressive strength, it is worth noticing that f'_c = 32.2 MPa for PC and f'_c = 26.9 MPa for FRC specimens. However, this difference was considered limited and a direct comparison between the two set of specimens was performed. It is worth noticing that the bar-concrete bond behavior depends on different parameters, such as urface treatment, bar diameter, and bar-concrete bonded length. While the surface treatment is a specific characteristic of the bar investigated, the parametric evaluation of the bar-concrete bond behavior would require additional tests on bar with different diameter and with interfaces with different bonded lengths.

All values reported in Table 2 show high variability. In particular, PC specimens present a value of CoV = 25.6% in terms of P^* and τ_{av}^*, whereas for FRC specimens CoV = 15.1%. This variability is highlighted in Figure 3, where all values of τ_{av}^* obtained for FRC specimens fall between the 25th and 75th percentiles of PC specimens results. The variability observed in Table 2 and the high number of parameters influencing the bond behavior of the bar-concrete interface show that a higher number of tests should be performed on these types of specimens to better understand their bond behavior.

Table 2. Key parameters of the $P - g$ and $P - \delta$ curves.

Specimen	P^* [kN]	g^* [mm]	δ^* [mm]	τ_{av}^* [MPa]
PO-20d-PC-1	42.6	1.55	0.22	4.20
PO-20d-PC-2	60.8	2.00	0.22	6.00
PO-20d-PC-3	69.5	2.50	0.22	6.85
PO-20d-PC-4	41.7	1.67	0.30	4.12
Average	53.6	1.93	0.24	5.29
CoV	25.6%	22.0%	16.3%	25.6%
PO-20d-FRC-1	60.9	1.84	0.14	6.01
PO-20d-FRC-2	46.3	1.77	0.13	4.57
PO-20d-FRC-3	54.8	1.94	0.09	5.41
PO-20d-FRC-4	44.0	1.92	0.09	4.34
Average	51.5	1.87	0.11	5.08
CoV	15.1%	4.3%	25.0%	15.1%

PC and FRC specimens present similar load responses, both in terms of initial stiffness and post-peak behavior (Figure 2). All $P - g$ curves have an almost linear initial branch, followed by a non-linear branch that finishes in correspondence of the peak load P^*. Then, they have a narrow softening branch followed by a constant branch associated with friction between the bar and the surrounding concrete as the bar slips out from the concrete cylinder. The same trend can be observed in $P - \delta$ responses for both PC and FRC specimens, that present a brief ascending branch, followed by the softening and friction branches. Both specimen groups

present a certain value of residual load of the $P - g$, δ curves. The first ascending branch in the $P - \delta$ shows that after the stress-transfer zone has attained the free-end of the bonded interface, the load can still increase (up to P^*) (Focacci et al., 2000, 2024), suggesting a significant contribution of friction in the load responses of these interfaces. It is worth noting that $P - g$ and $P - \delta$ curves reported in Figure 2 are different from previous results reported in the literature for the same GFRP bar (Sireg Geotech Srl., 2022) but with a *thick* carbon yarn and less dense sand coating (Zhao et al., 2022). This comparison highlights the fundamental role of the physical and geometrical parameters of the surface treatment on the bar-concrete bond behavior.

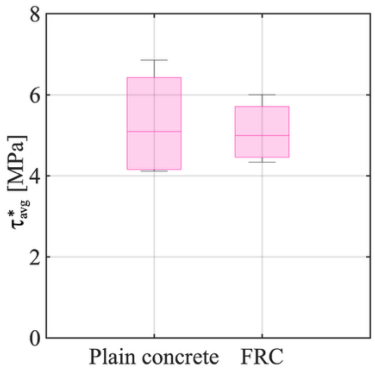


Figure 3. Box plot of the bond strength of GFRP bar-concrete interface for PC and FRC specimens.

All specimens tested failed due to debonding at the bar-concrete interface, with the detachment of a thin layer of concrete that remained attached to the bar sand coating (Figure 4). Failure modes were consistent within each specimen group, but in FRC specimens damage of the external layer of the GFRP bar was observed in some portions of the bonded interface for all specimens. Local damage of glass fibers was observed in these portions. In plain concrete specimens no damage was observed in the GFRP bars external surface. It is worth noting that since all FRC specimens comprised micro and macro PVA fibers, their individual contribution could not be determined.



(a) (b) (c)

Figure 4. Failure modes of pull-out test: a) PC and b) FRC specimens. c) Detail of the PVA fibers in concrete.

4 Concluding remarks

This paper investigated the bond behavior of thermoset GFRP bars embedded in either PC or PVA FRC cylindrical specimens. Pull-out tests were performed on eight specimens, four PC and four FRC, comprising a 12-mm nominal-diameter GFRP bar and concrete cylinders. The bonded length considered was function of the bar nominal diameter, $20d_{nom}$. Two different types of PVA fibers were added in concrete, micro-PVA and macro-PVA fibers, in a volume fraction of 0.6% and 2.0%, respectively. The applied load – global slip and applied load – free-end slip curves of pull-out tests on PC and FRC specimens show consistent behavior. They attained similar values of peak applied load and average interfacial shear stress, and similar values of slip at peak. They also showed the same failure mode, suggesting that the addition of dispersed fibers in concrete do not influence the bar-concrete interface bond behavior for the bars investigated in this study.

The results presented in this work provide useful insights on the bond behavior of GFRP bars and PVA FRC compared to GFRP bars and plain concrete. These preliminary results are part of a broader experimental campaign aimed at assessing the possible synergy between PVA-FRC and GFRP bars in enhancing the structural behavior of reinforced concrete structural elements.

5 Acknowledgements

The support of the RES515729 from National Center for Transportation (Washington State University) is gratefully acknowledged.

6 References

Aflakisamani, M., S. Mousa, H. M. Mohamed, E. A. Ahmed, and B. Benmokrane, 2023. “Design and Testing of Lightweight Self-Consolidating Concrete Bridge-Deck Slabs Reinforced with Glass Fiber- Reinforced Polymer Bars,” *ACI Structural Journal*, 120 (4). https://doi.org/10.14359/51738717.

ASTM International, 2017. *Test Method for Splitting Tensile Strength of Cylindrical Concrete Specimens. ASTM C496/C496M* ASTM International.

ASTM International, 2020. *Standard Test Method for Bond Strength of Fiber-Reinforced Polymer Matrix Composite Bars to Concrete by Pullout Testing. ASTM D7913/D7913M-14* ASTM International.

ASTM International, 2020. *Test Method for Compressive Strength of Cylindrical Concrete Specimens. ASTM C39/C39M-12* ASTM International.

Baena, M., L. Torres, A. Turon, and C. Barris, 2009. “Experimental study of bond behaviour between concrete and FRP bars using a pull-out test,” *Composites Part B: Engineering*, 40 (8): 784–797. https://doi.org/10.1016/j.compositesb.2009.07.003.

Bertolli, V., T. D’Antino, and C. Carloni, 2026. “Bending and Shear Behavior of Plain and PVA-Fiber Reinforced Concrete Beams with GFRP Reinforcing Bars,” In: *Proc. of the 12th International Conference on Fibre-Reinforced Polymer (FRP) Composites in Civil Engineering, CICE 2025*, 953–962 Springer Science and Business Media Deutschland GmbH.

Bertolli, V., M. A. Pisani, and T. D’Antino, 2025. “Use of thermoset- and thermoplastic-resin GFRP bars as internal flexural and shear reinforcement of concrete beams,” *Engineering Structures*, 343: 120986. https://doi.org/10.1016/j.engstruct.2025.120986.

Bertolli, V., M. M. Rahman, T. D'Antino, and C. Carloni, 2023. "Three-point bending tests of concrete notched beams with different sizes and contents of PVA fibers," In: *Proc. of the 3th fib Italy IMG Symposium on Concrete and Concrete Structures*, 409–416 fib. The International Federation for Structural Concrete.

Conforti, A., R. Zerbino, and G. A. Plizzari, 2019. "Influence of steel, glass and polymer fibers on the cracking behavior of reinforced concrete beams under flexure," *Structural Concrete*, 20 (1): 133–143. https://doi.org/10.1002/suco.201800079.

Cope, C. T., M. M. Rahman, F. Focacci, T. D'Antino, I. Abavisani, and C. Carloni, 2024. "Quasi-Static and Fatigue Behavior of GFRP Bars Embedded in Concrete: A Comparison Between Pull-Out Tests and Flexural Tests of Slabs," In: *Am. Concr. Inst. ACI Spec. Publ.*, 709–728 American Concrete Institute.

D'Antino, T., V. Bertolli, M. A. Pisani, and C. Poggi, 2023. "Tensile and interlaminar shear behavior of thermoset and thermoplastic GFRP bars exposed to alkaline environment," *Journal of Building Engineering*, 72: 106581. https://doi.org/10.1016/j.jobe.2023.106581.

D'Antino, T., and M. A. Pisani, 2023. "Tensile and compressive behavior of thermoset and thermoplastic GFRP bars," *Construction and Building Materials*, 366: 130104. https://doi.org/10.1016/j.conbuildmat.2022.130104.

Dopko, M., M. Najimi, B. Shafei, X. Wang, P. Taylor, and B. M. Phares, 2018. "Flexural Performance Evaluation of Fiber-Reinforced Concrete Incorporating Multiple Macro-Synthetic Fibers," *Transportation Research Record: Journal of the Transportation Research Board*, 2672 (27): 1–12. https://doi.org/10.1177/0361198118798986.

European Committee for Standardization, 2007. *Test method for metallic fibre concrete - Measuring the flexural tensile strength (limit of proportionality (LOP), residual). EN 14651:2007* Brussels, Belgium: CEN.

Facconi, L., F. Minelli, P. Ceresa, and G. Plizzari, 2021. "Steel fibers for replacing minimum reinforcement in beams under torsion," *Materials and Structures*, 54 (1): 34. https://doi.org/10.1617/s11527-021-01615-y.

Focacci, F., A. Nanni, and C. E. Bakis, 2000. "Local Bond-Slip Relationship for FRP Reinforcement in Concrete," *Journal of Composites for Construction*, 4 (1): 24–31. https://doi.org/10.1061/(ASCE)1090-0268(2000)4:1(24).

Focacci, F., M. M. Rahman, T. D'Antino, and C. Carloni, 2024. "FRP Strips Externally Bonded to Quasi-Brittle Substrates: Discussions and Advances of Open Research Topics," *Journal of Composites for Construction*, 28 (6) American Society of Civil Engineers (ASCE). https://doi.org/10.1061/JCCOF2.CCENG-4603.

Martinelli, P., M. Colombo, P. Pujadas, A. De La Fuente, S. Cavalaro, and M. Di Prisco, 2021. "Characterization tests for predicting the mechanical performance of SFRC floors: identification of fibre distribution and orientation effects," *Materials and Structures*, 54 (1): 3. https://doi.org/10.1617/s11527-020-01593-7.

Naaman, A. E., 2018. "Fiber reinforced concrete: five decades of progress," In: *Proceedings of the 4th Brazilian Conference on Composite Materials*, 35–56 Pontifícia Universidade Católica do Rio de Janeiro.

Plizzari, G., 2018. "Fiber Reinforced Concrete for repairing and strengthening RC structures: some recent advancements," *International Conference on Concrete Repair, Rehabilitation and Retrofitting (ICCRRR 2018)*, 199. https://doi.org/10.1051/matecconf/201819901004.

Rahman, M. M., C. T. Cope, I. Abavisani, T. D'Antino, F. Focacci, and C. Carloni, 2025. "Comprehensive Study of GFRP Bar-Concrete Bond Behavior Using Pull-out and Three-point Bending Tests," *Journal of Building Engineering*, 112819. https://doi.org/10.1016/j.jobe.2025.112819.

Signorini, C., A. Sola, B. Malchiodi, A. Nobili, and A. Gatto, 2020. "Failure mechanism of silica coated polypropylene fibres for Fibre Reinforced Concrete (FRC)," *Construction and Building Materials*, 236: 117549. https://doi.org/10.1016/j.conbuildmat.2019.117549.

Sireg Geotech Srl., 2022. "Glasspree® TS Round Bars (provided privately by the manufacturer)," (Italy).

Solyom, S., M. Di Benedetti, M. Guadagnini, and G. L. Balázs, 2020. "Effect of temperature on the bond behaviour of GFRP bars in concrete," *Composites Part B: Engineering*, 183: 107602. https://doi.org/10.1016/j.compositesb.2019.107602.

Sun, Q., Q. Jin, Y. Gao, H. Li, and Y. Cao, 2021. "Flexural behavior of PVA-FRC GFRP reinforced concrete beams," *Polymer Composites*, 42 (7): 3331–3348. https://doi.org/10.1002/pc.26062.

Vandewalle, L., 2000. "Cracking behaviour of concrete beams reinforced with a combination of ordinary reinforcement and steel fibers," *Materials and Structures*, 33 (3): 164–170. https://doi.org/10.1007/BF02479410.

Xie, T., M. S. Mohamed Ali, P. Visintin, D. J. Oehlers, and A. H. Sheikh, 2018. "Partial Interaction Model of Flexural Behavior of PVA Fiber–Reinforced Concrete Beams with GFRP Bars," *Journal of Composites for Construction*, 22 (5): 04018043. https://doi.org/10.1061/(ASCE)CC.1943-5614.0000878.

Zhao, X., M. Minhajur Rahman, T. D'Antino, F. Focacci, and C. Carloni, 2022. "Effect of bonded length on the load response and failure mode of pull-out tests of GFRP bars embedded in concrete," *Construction and Building Materials*, 347: 128425. https://doi.org/10.1016/j.conbuildmat.2022.128425.

Simplified Flexural Design of FRC Based on Integrated Residual Tensile Stress from Standard Beam Tests

Devansh Patel[1], Chidchanok Pleesudjai[1], Barzin Mobasher[1*]

[1]: School of Sustainable Engineering & the Built Env., Arizona State University, Tempe, AZ, USA

Abstract

This paper presents a simplified flexural design approach for fiber reinforced concrete derived directly from standard beam tests (ASTM C1609 and EN 14651). The method is based on inverse analysis of experimental load–deflection data to obtain full strain based and crack width based tensile models to compute stress distribution, neutral axis location, internal forces, and moment capacity. Compared to empirical conversion of residual flexural stresses into tensile model parameters, the proposed approach directly defines an average residual tensile stress by integrating the tensile stress distribution over the cracked tension zone. This average stress, combined with its resultant moment arm, reproduces the exact flexural response of the beam using a simplified formulation. The framework offers a direct, mechanics-based path to simplified flexural design while fully preserving the underlying tensile stress distribution. A large dataset of FRC beam tests, including quality control data from tunnel segment production and additional dosage studies, is used to evaluate the stress conversion factors and lever arm locations. While nominal flexural stresses show high scatter, the integrated tensile force and average tensile stress exhibit significantly lower variability. Both ASTM C1609 and EN 14651 are evaluated using consistent analytical flexure models. Clear conversion relationships between residual flexural stress and average tensile stress are established. The results confirm that flexural strength parameters correlate more closely with the average stress distribution regardless of whether strain based or crack width-based models are used.

Keywords

Flexural Design, Inverse-Analysis, Material Characterization, Test Methods, EN 14651, ASTM C1609

1 Introduction

The flexural response of fiber reinforced concrete (FRC) after cracking is dominated by the residual tensile stresses across the crack plane. Those stresses evolve continuously with deformation and are typically represented either in strain space, as σ(ε), or in crack-width space, as σ(w). In practice, two standard characterization tests for FRC are ASTMC1609 for unnotched beams under four-point bending and EN-14651 for notched beams under three-point bending CMOD control. Inverse-analysis approaches have been proposed for both types of test methods [1,2]. The ASTM test results can be interpreted through a smeared strain field [3] and plastic hinge length, whereas EN 14651 is interpreted in crack-width space through a localized hinge at the pre-determined notch location.

For routine design, however, the full nonlinear tensile law is inconvenient to use directly. A common engineering solution is to replace the nonlinear stress distribution with an equivalent stress block. This is analogous to the Whitney compression block in reinforced concrete, where a nonlinear compression profile is replaced by a uniform stress acting over an effective depth [4]. Current FRC design provisions [5–8] adopt an equivalent simplification through a rigid-plastic tensile blocks based on residual flexural strength. The tensile block is calibrated at a single large-deformation state and is applicable only to design of ultimate limit-state. This approach is restrictive as many practical applications of FRC are governed by serviceability. In that range, the governing crack widths are much smaller than the crack openings associated with residual flexural strengths at large crack widths (2.5 mm). The main simplification includes limitation of the conversion factor from nominal flexural stress to effective tensile stress and the tension resultant that is commonly placed at the center of the tension zone, even though the real post-crack stress profile is generally not uniform and its centroid need not lie at mid-depth.

Patel et al. (2025) proposed integrating the tensile stress distribution that is back-calculated via inverse-analysis across the cracked tension zone as an alternative simplified [9]. Results showed that the equivalent average tensile stress evolved with deformation converging to commonly used factors of 0.33-0.37. The objective of the present paper is to extend the approach proposed in [9] to EN 14651 by formulating an equivalent tension block for plain FRC along the full crack width range. The proposed method uses inverse analysis to back-calculate the tensile law, reconstructs the exact stress distribution through the cracked plane model, and then calculates the equivalent average tensile stress and the resultant lever arm location.

2 Analytical Modeling for Inverse-Analysis

ASTM C1609 uses an unnotched prism under four-point bending and reports load-deflection response. In the analytical inverse-analysis route developed previously by Mobasher and Group [10–12] the cracked region is represented by a smeared strain field over a plastic hinge length, so the recovered material law is expressed in strain space as σ(ε). Section response is obtained from strain compatibility, force equilibrium, and moment-curvature analysis, and the beam deflection is then reconstructed using a moment-area procedure.

EN 14651 uses a notched beam under three-point bending with CMOD control. The response is most described by a localized hinge at the notch. In the present study, inverse analysis is

performed directly in crack-width space using the analytical approach of σ(w) law presented in [2] that tracks neutral axis position, crack depth, and crack opening through the crack opening. Figure 1 illustrates comparison of the strain-based ASTM C1609 and the crack-width-based EN 14651 approach.

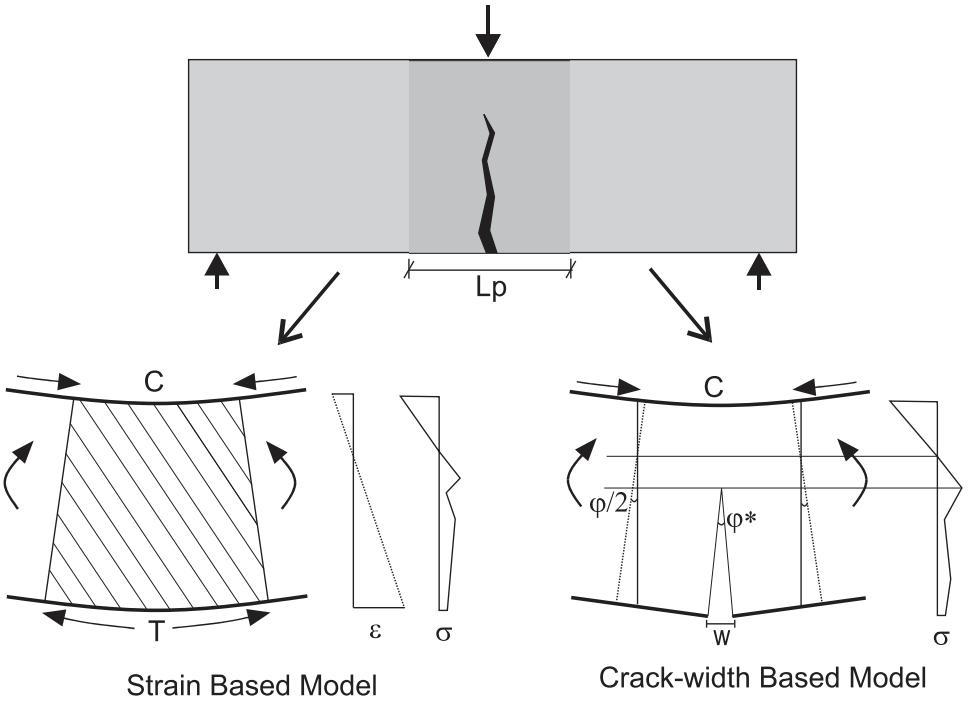
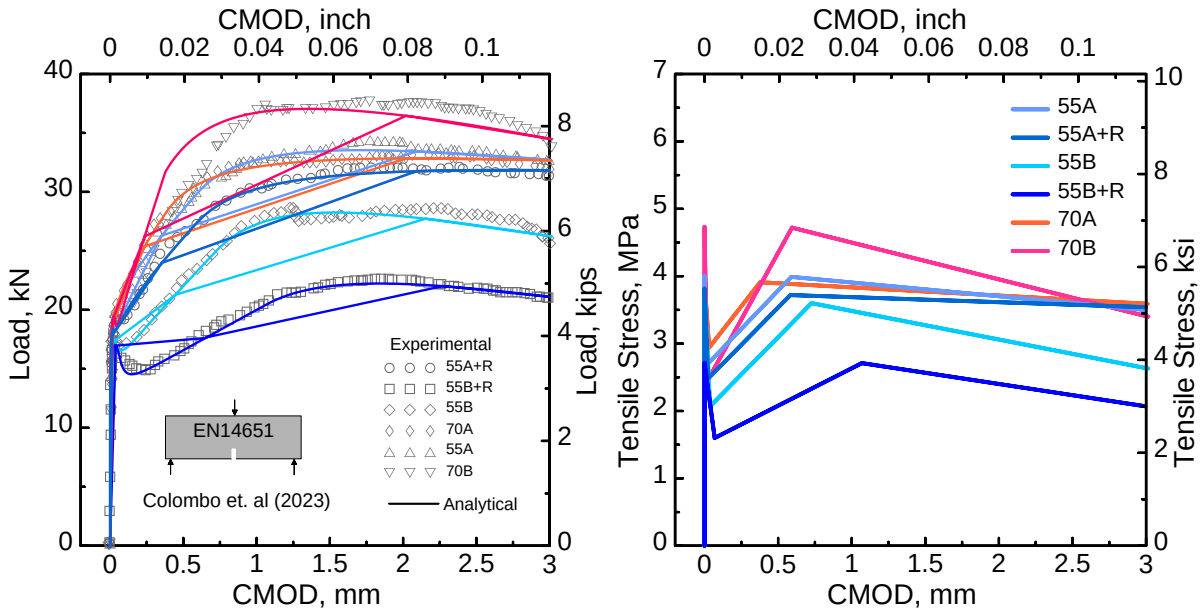


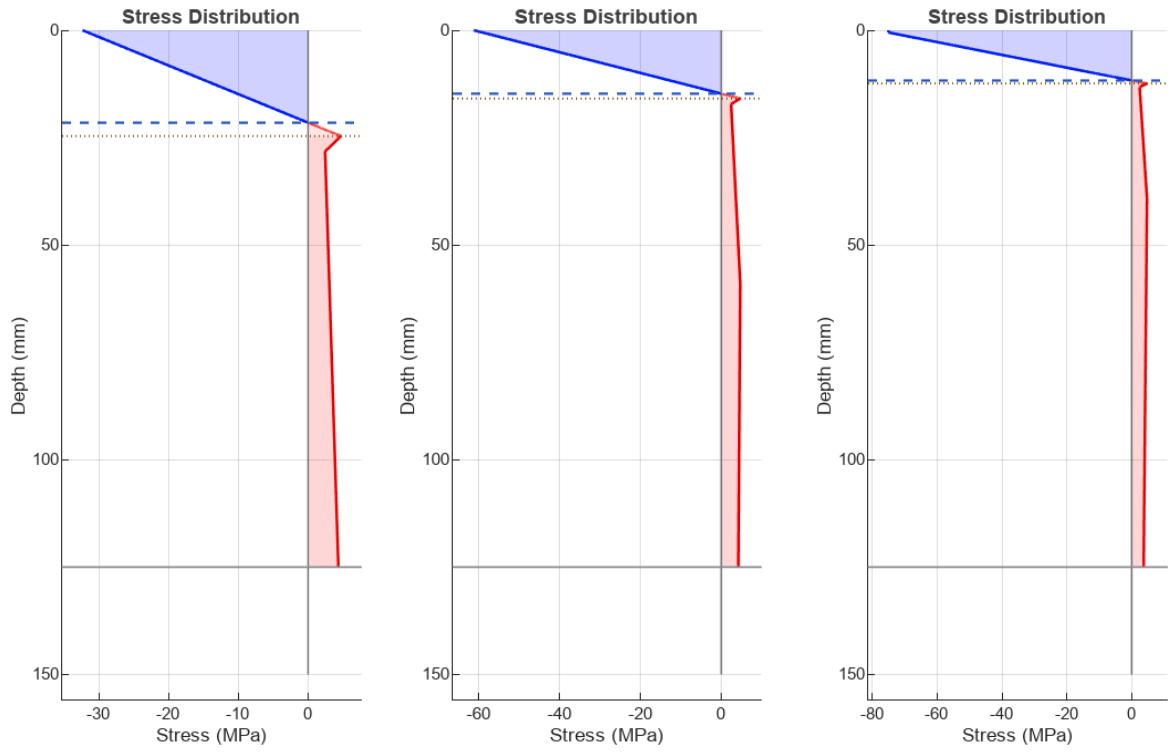
Figure 1: Schematic comparison of strain-based and crack-width-based.

An application of analytical model for inverse analysis is shown in the following section. Compared to iterative, analytical closed-form equations are used to solve the equilibrium equations at each deformation stage. Application of such use cases included fast inverse-analysis approaches that are convient for GUI based application for quick extraction of tension models. An GUI was developed by Mobasher and coworkers [13] and was used to conduct the inverse analysis. The inverse-analyis approach was applied to the Colombo et al. (2023) [14] datasets of EN14651 with two fiber dosage levels (55 kg/m^3 – 70 kg/m^3). Figure 2a shows that the analytical model fitting the experimental data that reproduces the measured load-CMOD response with good agreement. Figure 2b presents the corresponding tensile stress-crack width laws extracted from the inverse analysis. In this form, the experimental beam response is converted into a material law that can be directly used in the mechanics-based flexural analysis.

Figure 2c shows representative stress distributions along the depth at crack widths of w = 0.5 mm, 1.5 mm, and 2.5 mm. As crack width increases, the neutral axis shifts upward and the depth of the compression zone decreases, while the cracked tension zone occupies a larger portion of the depth.



(a) Inverse-analysis curve fitting (b) Extracted tension models



(c) Stress distribution stages at w=0.5mm, 1.5mm, and 2.5mm (70B)

Figure 2: Inverse-analysis for tension model extraction

3 Equivalent Stress Method

The equivalent stress method was first proposed by Patel et al. (2025) for the ASTM C1609 strain-based formulation and is extended here to the EN 14651 crack-width-based formulation. The basic idea is to replace the exact tensile stress distribution in the cracked zone by an equivalent average tensile stress that produces the same resultant force and moment. Figure 3 shows and illustration of the simplified approach that replaces the complex stress distribution along the depth into equivalent tensile and compression stress blocks. The lever arm and the stress is calculated by integration of the stress-distribution from inverse-analysis.

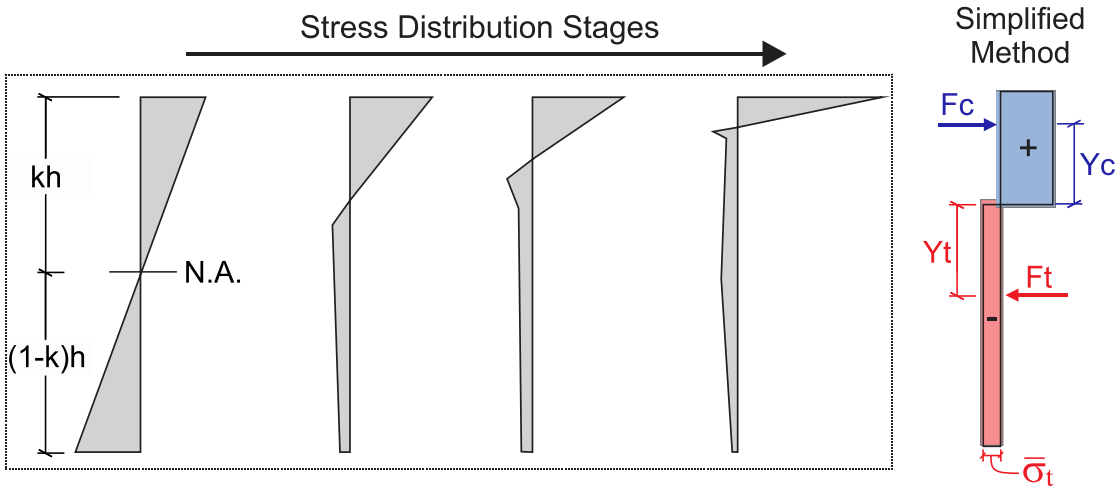


Figure 3: Exact section stress distribution and its replacement by an equivalent average tensile stress block with force- and centroid-consistent lever arms.

At any deformation state, the total tensile force is obtained by integrating the actual tensile stress profile over the cracked tension zone:

$$F_C = F_T = \sum_0^{(1-k)h} F_t(\varepsilon) = b\int_0^{(1-k)h} \sigma(\varepsilon)dy = bh\int_0^{\beta_i} \sigma_t(\beta_i)\left(\frac{(1-k)}{\beta_i}\right)d\beta_i \tag{1}$$

and the corresponding average tensile stress is defined as:

$$\bar{\sigma}_t = \frac{F_T}{A_t} = \frac{F_T}{(1-k)hb} \tag{2}$$

Where b, h are the width and depth respectively and (1-k)h is the depth of the tension zone. The location of the tensile resultant is not assumed at the centre of the cracked zone, but is calculated directly from the first moment of the stress distribution:

$$Y_t = \frac{b\int_0^{(1-k)h} y\sigma_t(y)dy}{F_T},\ Y_C = \frac{b\int_0^{kh} y\sigma_c(y)dy}{F_C} \tag{3}$$

The results produce the same internal moment as the full stress-distribution from:

$$M = F_T Y_T + F_C Y_C \tag{4}$$

The stress ratio, $\bar{\sigma}_t / f_n$ shows the precise conversion needed to calculate the tensile force along the cracked region using the flexure strength results from standard tests. For the EN 14651 formulation, the tensile stress is expressed directly in terms of crack width through σ(w(y)). The same integration procedure is then used to calculate $\bar{\sigma}_t$, Y_t and F_T.

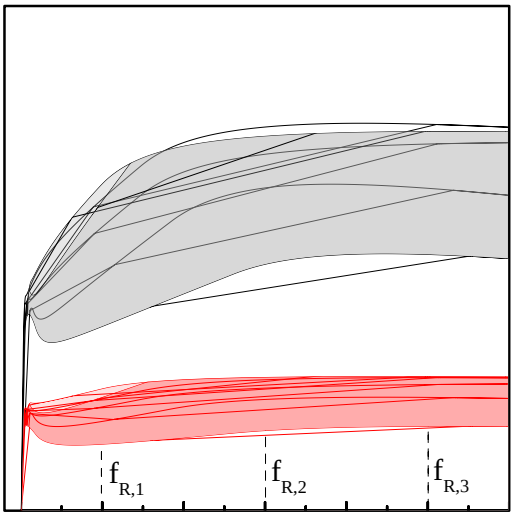
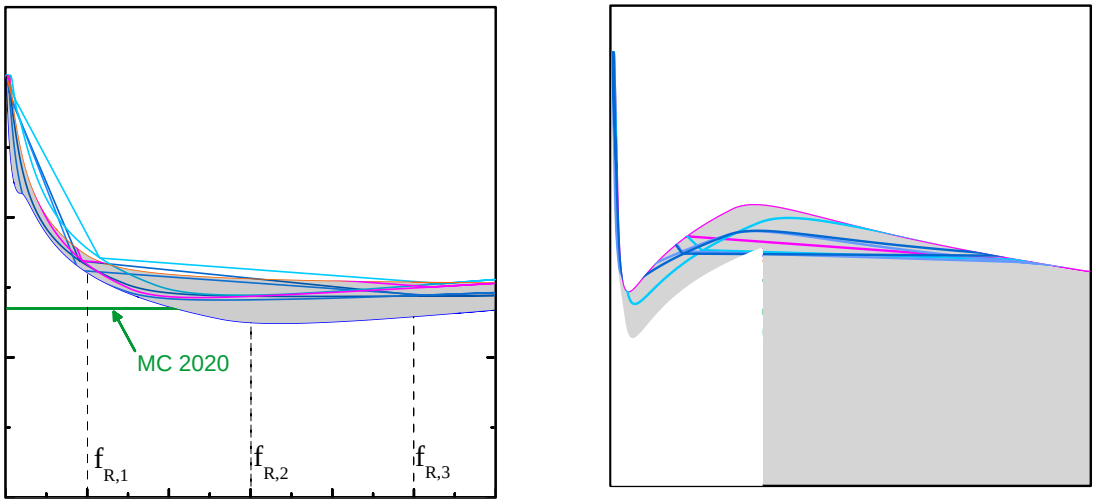


Figure 4: Nominal flexure stress compared to average tensile stress in EN14651



(a) (b)

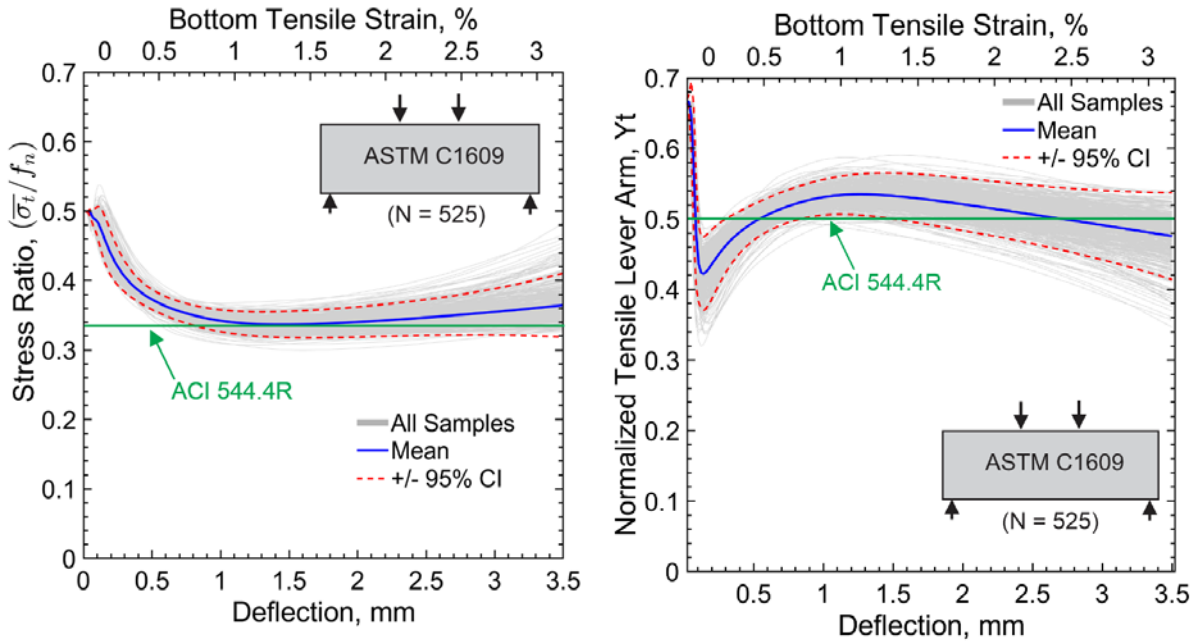
Figure 5: EN14651 design parameters: (a) stress ratio (b) normalized tensile lever arm

The nominal flexural stress and the integrated average tensile stress results for the example case from section 2 shown in figure 4. Figure 5 (a) shows the ration between the two values,

$\bar{\sigma}_t / f_n$. The stress-ratio curves show that the relation between average tensile stress and nominal flexural stress is not constant over the full deformation range. The stress ratio starts near 0.5 close to cracking, decreases rapidly in the early post-crack range, and then tends to stabilize around 0.32-3.6. This explains the constant conversion factors that appear reasonable at larger crack widths, while also showing that they do not represent the full response from first cracking through serviceability range. Note that at first-cracking the triangular stress distribution is represented as a rectangular block instead to give the 0.5 factor conversion.

A similar trend is observed for the normalized centroid location shown in figure 5 (c), where the centroid location of the tensile stress distribution is normalized to the height of the tension zone (1-k)h. The ratio Yt/[(1-k)h] approaches values close to 0.5 (centre of the tension block) over much of the post-crack regime, but it is not exactly constant. The actual lever arm depends on the evolving shape of the stress profile and therefore can be calculated from the integrated distribution. The Model Code 2020 recommended factors are also shown in the figures.

The ASTM C1609 results reported by Patel et al. (2025) of 500+ QC beam test data provide similar results (figure 6), explained in detailed in the prior work [9]. Using a large set of inverse-analyzed beam tests, that study showed that nominal flexural stress exhibits greater scatter than the corresponding integrated average tensile stress, and that the stress ratio evolves with deformation rather than remaining constant. The normalized centroid location also changes with deflection, showing that the lever can be calculated from the actual stress distribution rather than a prescribed assumption.



(a) Stress Ratio

(b) Normalized tension lever arm

Figure 6: Equivalent stress ratio and lever arm location for ASTM C1609 test data from [9]

4 Design Application & Future Scope

Design applications for such curves can be used to implement strain-basedd serviceability range values to better calculate the effect of addition of fibers on stiffness, load-capacity, crack-spacing etc. The current scope of this paper is however limited to the methodology itself. More practical use cases will involve deriving empirical nonlinear curve fitting equations as shown in [9], that calculates the average tensile stress as a function of crack-width or strain to apply at any deformation state. Key applications will include the design of serviceability states where the fibers make the most significant contribution to member performance. Such design curves will however require large data sets with varying dosage and fiber types to define strength class and its associated design curves. The authors are currently working on collecting data set for such design applications and how it can be scaled to hybrid members.

5 Conclusion

This paper extends the equivalent stress method from the strain-based ASTM C1609 formulation proposed in earlier work to the crack-width-based EN 14651 formulation. By integrating the actual tensile stress distribution, the method defines an average tensile stress and exact lever arms that preserve the sectional force and moment in simplified form. The results show that factors evolve systematically with deformation, marking a key application of the in the serviceability range, where fiber contribution to stiffness, load capacity, and crack control is most significant and where fixed ultimate-state stress blocks are not fully representative. Future work will focus on developing practical design curves as functions of crack width or strain using larger datasets covering different fiber dosages and types and extending the framework to hybrid members.

6 References

[1] σ-ε-Design method, Mater. Struct. 33 (2000) 75–81. https://doi.org/10.1007/BF02484159.

[2] Design of steel fibre reinforced concrete using the σ-w method: principles and applications, Mater. Struct. 35 (2002) 262–278. https://doi.org/10.1007/BF02482132.

[3] Z.P. Bažant, F. Lin, Nonlocal Smeared Cracking Model for Concrete Fracture, Journal of Structural Engineering 114 (1988) 2493–2510. https://doi.org/10.1061/(ASCE)0733-9445(1988)114:11(2493).

[4] C.S. Whitney, Design Of Reinforced Concrete Members Under Flexure Or Combined Flexure And Direct Compression, ACI Journal Proceedings 33 (1937). https://doi.org/10.14359/8429.

[5] ACI Committee 544, ACI 544.4R-18: Guide for Design with Fiber-Reinforced Concrete, ACI Standards and Committee Reports (2018) 1–33.

[6] M. Di Prisco, M. Colombo, D. Dozio, Fibre-reinforced concrete in fib Model Code 2010: Principles, models and test validation, Structural Concrete 14 (2013) 342–361. https://doi.org/10.1002/suco.201300021.

[7] fib - federation internationale du beton, fib Model code for concrete structures 2010, Ernst & Sohn (2013).

[8] M. di Prisco, (S)FRC in EC2 and in Model Code 2020, Concrete Structures 24 (2023) 36–41. https://doi.org/10.32970/CS.2023.1.6.

[9] D. Patel, C. Pleesudjai, M. Bakhshi, V. Nasri, B. Mobasher, Back-calculation of mechanical properties of fiber-reinforced concrete in tunnel lining segments, Structural Concrete (2025). https://doi.org/10.1002/suco.70052.
[10] C. Soranakom, B. Mobasher, Closed-Form Moment-Curvature Expressions for Homogenized Fiber-Reinforced Concrete, ACI Mater. J. 104 (n.d.). https://doi.org/10.14359/18824.
[11] C. Pleesudjai, ; Devansh, D. Patel, B. Mobasher, M. Asce, Generalized Nonlinear Moment-Curvature Model for Serviceability-Based Design of Hybrid Reinforced Concrete, (2023). https://doi.org/10.1061/JSENDH.
[12] D.D. Patel, C. Pleesudjai, N. Neithalath, B. Mobasher, Limit-state based design of hybrid reinforced UHPC flexural beams using parametric modeling, Eng. Struct. 357 (2026) 122353. https://doi.org/10.1016/j.engstruct.2026.122353.
[13] D. Patel, C. Pleesudjai, B. Mobasher, An Inverse Analysis and Design Software for FRC, UHPC, TRC, HRC Cement Composites, (n.d.). https://www.researchgate.net/publication/389270631_An_Inverse_Analysis_and_Design_software_for_FRC_UHPC_TRC_HRC_Cement_Composites
[14] M. Colombo, A. Conforti, M. di Prisco, B. Leporace-Guimil, G. Plizzari, G. Zani, The basis for ductility evaluation in SFRC structures in MC2020: An investigation on slabs and shallow beams, Structural Concrete (2023). https://doi.org/10.1002/suco.202300114.

Design aspects for long term and extreme loads

Long-Term Behavior of FRC with Hybrid Fibers

Sergio Carmona[1], Giovanni Plizzari[2], Jorge Barraza[3]

[1]: Dep. Obras Civiles, Universidad Técnica Federico Santa María, Valparaíso, Chile.

[2]: DICATAM, University of Brescia, Brescia, Italy.

[3]: Gestión Vial S.A., Santiago, Chile.

Abstract

The long-term behavior of cracked Fiber Reinforced Concrete (FRC) is a key aspect in tunnel lining applications, where primary shotcrete supports may remain under sustained loading for extended periods before the final lining becomes structurally effective. While the creep behavior of Steel Fiber Reinforced Concrete (SFRC) and Macro-Synthetic Fiber Reinforced Concrete (MSFRC) has been widely studied, limited information is available on Hybrid Fiber Reinforced Concrete (HFRC).

This paper presents the results of an experimental program performed on three FRC mixtures designed to satisfy class 2b performance according to fib Model Code 2020. The mixtures included SFRC, MSFRC, and a hybrid combination of steel and macro-synthetic fibers. Residual flexural strengths were determined according to EN 14651, and long-term tests were carried out according to RILEM TC 261 recommendation. Pre-cracked beams were subjected to sustained flexural loading corresponding to 50% of their residual strength and monitored for 360 days.

The results showed that SFRC exhibited the smallest instantaneous crack opening after load application, while HFRC and MSFRC developed progressively larger initial deformations as the proportion of macro-synthetic fibers increased. During the first 60 days, HFRC and MSFRC displayed a nonlinear increase in crack opening, whereas SFRC showed an approximately linear response. However, between 60 and 360 days, all mixtures exhibited nearly identical crack-opening rates. The results indicate that fiber type mainly affects the instantaneous and transient creep stages, while the long-term crack-opening rate appears largely independent of the fiber combination used.

Keywords

Fiber reinforced concrete, hybrid fibers, macro-synthetic fibers, steel fibers, creep, tunnel linings

1 Introduction

Fiber Reinforced Concrete (FRC) is widely used in structural applications such as industrial floors, precast elements, and tunnel linings because it provides residual load-bearing capacity after cracking and may partially or totally replace conventional reinforcement (Di Prisco et al. 2009). In underground construction, steel fibers and macro-synthetic fibers are the most widely used fiber types. Their mechanical response differs significantly due to their distinct stiffness, strength, and fiber–matrix interaction mechanisms. Steel fibers are more effective at small crack openings, providing high residual strengths and crack-bridging capacity, whereas macro-synthetic fibers contribute more significantly at larger crack widths due to their greater deformability and energy absorption capacity (Bernard, 2020).

The use of Macro-Synthetic Fiber Reinforced Shotcrete (MSFRC) has become widespread in Chile, both in mining projects—one of the country's most important economic sectors, involving the construction and operation of hundreds of kilometers of underground excavations—and in urban transportation infrastructure, including metro systems and highway tunnels excavated using the New Austrian Tunnelling Method (NATM; Amigo, 2023). The growing adoption of MSFRC is mainly associated with its corrosion resistance, ease of handling, reduced equipment wear, and lower operational costs as compared with traditional steel fiber reinforced shotcrete (Ballou, 2008). Furthermore, MSFRC can satisfy the structural requirements established by fib Model Code 2020 for load bearing FRC applications (*fib*, 2024).

Despite these advantages, concerns have recently emerged regarding the long-term behavior of MSFRC under sustained loading. Unlike steel fibers, macro-synthetic fibers exhibit a viscoelastic response that may lead to larger time-dependent deformations and progressive crack widening in cracked structural elements subjected to sustained stresses (Almusallam et al., 2013). Although several studies have investigated the creep behavior of Steel Fiber Reinforced Concrete (SFRC) and MSFRC, the available information remains limited, particularly for structural applications where long-term crack control is a critical design requirement.

The complementary behavior of steel and macro-synthetic fibers has led to the development of Hybrid Fiber Reinforced Concrete (HFRC), in which both fiber types are combined within the same cementitious matrix. Previous investigations have shown that hybridization may activate favorable multiscale crack-bridging mechanisms and improve post-cracking performance through synergistic interactions between fibers with different mechanical properties (Li et al., 2021). While the short-term mechanical behavior of HFRC has been extensively studied, its long-term response under sustained loading remains insufficiently documented.

This issue is particularly relevant for the Américo Vespucio Oriente II (AVO II) Project in Santiago, Chile, which comprises two 5.2 km long urban highway tunnels excavated beneath an operational metro line. The primary lining consists of a 250 mm thick fiber reinforced shotcrete shell designed to satisfy a compressive strength of 25 MPa and a post-cracking performance class 2b according to *fib* Model Code 2020 (AVO II, 2022). Although steel fibers constitute the reference solution for tunnel lining applications, alternative approaches based on macro-synthetic fibers and hybrid fiber combinations have been proposed to reduce equipment wear and improve construction efficiency. However, concerns regarding their long-term deformation under sustained loading motivated the present investigation.

Accordingly, the objective of this study is to evaluate the long-term behavior of SFRC, MSFRC, and HFRC subjected to sustained flexural loading. The experimental program follows the recommendations of RILEM TC 261 for pre-cracked beams under sustained loading (Llano-Torre and Serna, 2021), focusing on the evolution of Crack Mouth Opening Displacement (CMOD) and on the residual flexural performance after creep. The results contribute to a better understanding of the long-term behavior of SFRC, HFRC, and MSFRC, providing experimental evidence relevant to the design of tunnel linings where crack control under sustained loading is a critical requirement.

2 State of the art

The post-cracking behavior of FRC depends strongly on the type, geometry, mechanical properties, and dosage of the fibers used. Consequently, FRC may exhibit responses ranging from strain-softening to strain-hardening, including elastic-plastic behavior. Among the different fiber types available for structural applications, steel fibers and macro-synthetic fibers are currently the most widely used in tunnel linings and sprayed concrete support systems.

SFRC and MSFRC exhibit significantly different post-cracking mechanisms. In SFRC, the high stiffness and tensile strength of steel fibers provide efficient crack bridging at relatively small crack openings. After the first cracking peak, the load typically decreases and then increases again due to the pull-out resistance and mechanical anchorage of the fibers, reaching a second maximum at moderate CMOD values. Subsequently, the residual strength gradually decreases as fiber slip progresses and anchorage is progressively lost.

In contrast, MSFRC generally exhibits a deeper post-peak load drop followed by a progressive recovery of residual strength at larger crack openings. This behavior is associated with the greater deformability of polymeric fibers, their better pull-out response, and the larger number of fibers crossing the cracked plane. As a result, steel fibers are generally more effective in controlling crack opening during the early stages of crack propagation, whereas macro-synthetic fibers contribute more significantly at larger crack widths, providing enhanced ductility and energy absorption capacity.

The complementary nature of these mechanisms has motivated the development of Hybrid Fiber Reinforced Concrete (HFRC), in which steel and synthetic fibers are combined within the same concrete matrix. The objective of hybridization is to activate multiscale crack-bridging mechanisms capable of exploiting the advantages of each fiber type. Steel fibers contribute stiffness, crack control, and residual strength at small crack openings, while macro-synthetic fibers improve deformation capacity and stress transfer at larger crack widths. Several experimental studies have demonstrated that hybridization may generate synergistic effects, producing structural responses that exceed the simple combination of the individual fiber contributions (Banthia and Sappakittipakorn, 2007).

While the short-term performance of HFRC has been extensively studied, considerably less information is available regarding its long-term behavior under sustained loading. The long-term performance of concrete structures is strongly influenced by the behavior of the material after cracking, particularly when time-dependent phenomena such as shrinkage and creep are involved (Barpi and Valente, 2003). This issue has gained increasing attention during the last two decades because current structural design approaches generally account for compressive creep under service conditions, whereas tensile creep of cracked concrete and fiber reinforcement is rarely considered explicitly.

In cracked FRC elements subjected to flexural loading, creep results from several interacting mechanisms, including compressive creep of the concrete matrix, time-dependent debonding at the fiber–matrix interface, progressive fiber pull-out, stress redistribution within the cracked section, and tensile creep of the fibers (Del Prete et al., 2022). Due to the high modulus of elasticity of steel, creep deformation in SFRC is generally limited and the long-term response is mainly governed by fiber slip and anchorage degradation. Conversely, the behavior of MSFRC is strongly influenced by the viscoelastic properties of polymeric fibers, the stress level applied to the fibers, the number of fibers bridging the crack, and environmental conditions such as temperature and humidity (García-Taengua et al, 2014).

Recent studies suggest that HFRC may provide improved creep resistance compared with SFRC and MSFRC. After testing hybrid concrete reinforced with steel and synthetic fibers, Li et al. (2018) concluded that hybridization produces a positive synergistic effect that restrains creep deformation through multiscale reinforcement mechanisms and improved stress redistribution. However, research on the long-term behavior of HFRC remains limited, particularly for mixtures in which steel fibers are partially replaced by macro-synthetic fibers and for tunnel lining applications subjected to sustained loading.

The limited knowledge currently available on the long-term behavior of HFRC highlights the need for additional experimental evidence, particularly for tunnel lining applications where cracked fiber reinforced shotcrete may remain under sustained loading for extended periods. To contribute to this topic, the present study investigates the creep behavior of cracked SFRC, HFRC, and MSFRC beams designed to satisfy the same structural performance class. The experimental program was carried out in accordance with the RILEM TC 261 recommendation and focuses on the evolution of crack opening under sustained flexural loading. This paper reports the results obtained during the pre-cracking and creep stages of the test program, providing a comparative assessment of the influence of fiber type on the long-term deformation response of cracked FRC.

3 Materials properties

Three FRC mixtures were investigated. All mixtures were designed to satisfy the post-cracking performance class 2b specified for the AVO II tunnel project (AVO II, 2022) according to fib Model Code 2020 (*fib*, 2024), while maintaining adequate workability for shotcrete applications. The reinforcement systems consisted of: (i) Steel Fiber Reinforced Concrete (SFRC) containing 27 kg/m³ of steel fibers; (ii) Hybrid Fiber Reinforced Concrete containing 15 kg/m³ of steel fibers and 3.5 kg/m³ of macro-synthetic fibers; and (iii) Macro-synthetic Fiber Reinforced Concrete (MSFRC) reinforced with 7.0 kg/m³ of macro-synthetic fibers.

Each mixture was produced at industrial scale in 4 m³ batches at a ready-mix concrete plant in Santiago of Chile. The cementitious matrix consisted of high-strength pozzolanic Portland cement (ASTM, 2023), crushed gravel, natural sands, silica fume, and chemical admixtures. Hooked-end steel fibers were 35 mm long and 0.55 mm in diameter, with an aspect ratio of 65. The fibers had a tensile strength of 1345 MPa and an elastic modulus of 210 GPa. Macro-synthetic fibers, manufactured from virgin copolymer, were 65 mm long and had an equivalent diameter of 0.46 mm, resulting in an aspect ratio of 141. These fibers had a tensile strength of 613 MPa, an elongation at break of 10%, and an elastic modulus of 9.0 GPa. The complete mix proportions and fiber contents of the three FRC mixtures are presented in Table 1.

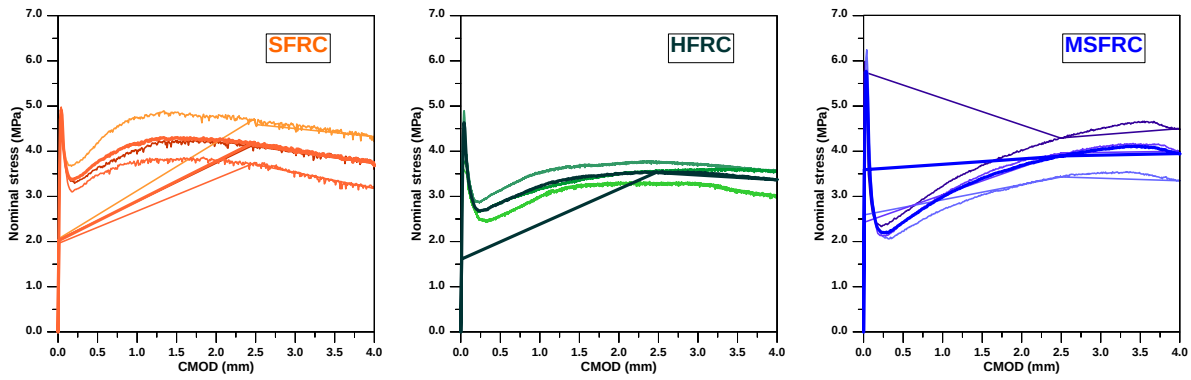
Table 1: Mix proportions and fiber contents of the FRC mixtures tested in this study.

Material (kg/m^3)	**SFRC**	**HFRC**	**MSFRC**
Cement	425		
Water	210		
Gravel 13 mm	120		
Coarse sand	1250		
Fine sand	247		
Plasticizer	2.0		
High-range water reducer	4.0		
Silica fume	21		
Fibers	S 27	S15 + MS 3.5	MS 7.0
Volume fraction of fibers V_f (%)	0.35	0.58	0.77
Theoretical density (kg/m^3)	2306	2298	2286

For each mixture, twelve 150×150×600 mm beams and six compression cylinders were cast. All the specimens remained at the production plant for 48 h under moisture protection and were subsequently cured in lime-saturated water at 23°C until testing at 28 days.

At the age of 28 days, the residual flexural strengths of each FRC mixture were determined according to EN 14651 (CEN, 2007) using a 100 kN closed-loop hydraulic testing machine under CMOD control. Three beams from each mixture were tested and the complete nominal stress–CMOD response was recorded up to a CMOD of 4.0 mm. During testing, load and CMOD were continuously recorded at a rate of 3 data/s.

The resulting nominal stress–CMOD curves are presented in Figure 1. All mixtures exhibited a stable transition from the pre-cracking to the post-cracking stage, characterized by a reduction in load after the first peak. In the case of SFRC, the nominal stress increased after the post-peak drop due to the high stiffness and crack-bridging capacity of the steel fibers, reaching a second peak equivalent to approximately 85% of the first peak at a CMOD of about 1.5 mm. Beyond this point, the residual strength gradually decreased as a result of progressive fiber pull-out and loss of anchorage (Laranjeira et al. 2010).



(a) (b) (c)

Figure 1: Nominal stress–CMOD responses obtained at 28 days for: (a) SFRC, (b) HFRC, (c) MSFRC.

In contrast, MSFRC exhibited a more pronounced post-peak load drop followed by a gradual recovery of residual strength, reaching a second peak equivalent to approximately 67% of the first maximum at a CMOD of about 3.5 mm. This behavior is associated with the greater deformability of the macro-synthetic fibers and their ability to transfer stress at larger crack openings.

The hybrid mixtures showed an intermediate response between SFRC and MSFRC. After the initial post-peak load reduction, the nominal stress increased to approximately 70% of the first peak at a CMOD close to 1.5 mm and then remained approximately constant until the end of the test. This response reflects the synergistic action of the two fiber types, whereby steel fibers provide effective crack bridging at small crack openings, while macro-synthetic fibers contribute to stress transfer and residual load-carrying capacity at larger CMOD values.

The main mechanical properties are summarized in Table 2. All mixtures satisfied the requirements of performance class 2b according to fib Model Code 2020. As the macro-synthetic fiber content increased, a reduction in the ratio f_{R3k}/f_{R1k} was observed, reflecting the larger post-peak load drop characteristic of synthetic fiber reinforced concretes.

Table 2: Mechanical properties of the FRC mixtures tested in this study.

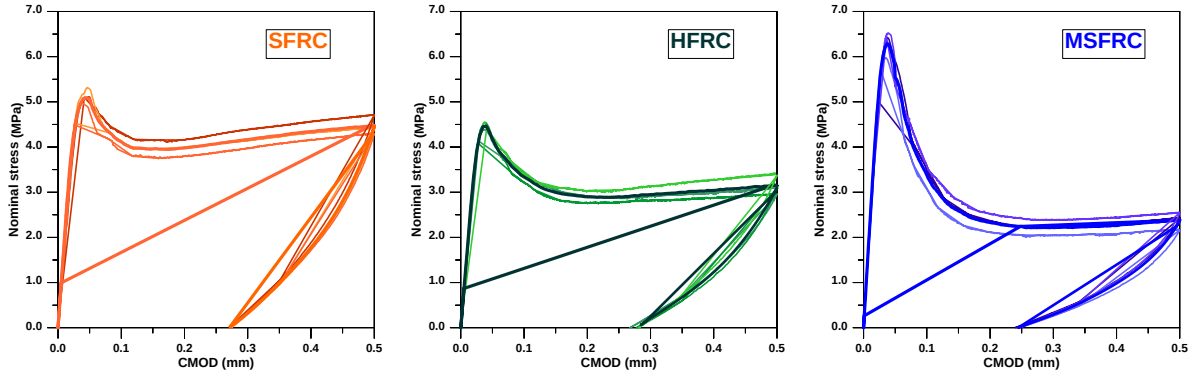
Parameter	**SFRC**	**HFRC**	**MSFRC**
Compressive strength, f_c (MPa)	49.6	33.6	60.0
Density (kg/m³)	2168	2108	2270
Slump (mm)	230	225	225
f_{Lk}(MPa)	4.9	4.5	5.6
f_{R1k} (MPa)	3.2	2.5	2.1
f_{R2k} (MPa)	3.4	2.5	2.8
f_{R3k} (MPa)	3.4	2.5	3.2
f_{R4k} (MPa)	3.0	2.1	2.8
f_{R1k}/f_{Lk}	0.7	0.6	0.4
f_{R3k}/f_{R1k}	1.1	1.0	1.5

As shown in Table 2, differences in compressive strength were observed among the mixtures despite the use of the same cementitious matrix composition. In particular, HFRC exhibited lower measured densities than the corresponding theoretical values reported in Table 1, suggesting the presence of macro-voids, likely associated with differences in compaction efficiency during casting. The presence of these macro-voids may partly explain the lower compressive strength observed in the hybrid mixtures. However, while macro-voids can significantly affect the compressive response of HFRC, its post-cracking tensile behavior is primarily governed by fiber bridging mechanisms and is therefore expected to be less sensitive to such defects. Consequently, the observed differences in matrix porosity are not expected to significantly affect the reliability of the subsequent long-term analyses or the interpretation of the effects associated with fiber type and hybridization.

4 Creep test program and results

The creep tests were carried out according to the recommendations of RILEM TC 261 for cracked FRC beams subjected to sustained flexural loading. The complete procedure consists of three consecutive stages: pre-cracking, sustained loading (creep), and post-creep characterization. However, this paper reports only the results obtained during the pre-cracking and creep stages. The post-creep characterization stage, involving the reloading of the specimens to determine their residual flexural strengths after sustained loading, will be conducted after completion of the two-year creep period and will be presented in a subsequent publication.

During the pre-cracking stage, three beams from each mixture were tested in accordance with EN 14651 and loaded under CMOD control until reaching $\mathrm{CMOD_p} = 0.5$ mm. The resulting nominal stress–CMOD curves are presented in Figure 2. Average results obtained during the pre-cracking stage are summarized in Table 3, which presents the load F_1 corresponding to $\mathrm{CMOD_p} = 0.5$ mm, the associated residual flexural strength $f_{\mathrm{R,p}}$, the residual crack opening after unloading, $\mathrm{CMOD_{pri}}$. The coefficients of variation (CoV), calculated from the three tested specimens, are given in brackets.



(a) (b) (c)

Figure 2: Nominal stress–CMOD responses obtained during the pre-cracking stage of the creep test for: (a) SFRC, (b) HFRC, (c) MSFRC.

Table 3: Average pre-cracking test results and corresponding creep loads. (CoV) is in the bracket

FRC	F_1 **(N)**	$f_{\mathrm{R,p}}$ **(MPa)**	$\mathrm{CMOD_{pri}}$ **(mm)**	F_c **(MPa)**
SFRC	13,992 (4.8)	4.48	0.272 (0.7)	11,660
HFRC	9,826 (6.7)	3.14	0.275 (2.7)	8,188
MSFRC	7,447 (8.2)	3.38	0.244 (3.6)	6,206

The results show a progressive reduction in the residual flexural strength $f_{\mathrm{R,p}}$ with increasing macro-synthetic fiber content. In addition, the residual crack opening after unloading, $\mathrm{CMOD_{pri}}$, was also influenced by the fiber type. Specimens reinforced with steel fibers exhibited higher $\mathrm{CMOD_{pri}}$ values, indicating lower elastic recovery, whereas mixtures

containing macro-synthetic fibers showed approximately 10% lower $\mathrm{CMOD}_{\mathrm{pri}}$ values, reflecting the greater recoverable deformation of the polymeric fibers.

Following the recommendations of RILEM TC 261, the pre-cracked specimens were stored for one week in the creep testing room under controlled conditions (20 ± 3°C and 50% relative humidity) before starting the sustained loading stage.

During the creep stage, the three pre-cracked specimens of each FRC mixture were subjected to sustained loading in multi-specimen four-point bending (4PBT) frames designed in accordance with the RILEM TC 261 recommendation (Figure 3). Each beam was instrumented with a ±10 mm LVDT connected to a data acquisition system. The applied load and CMOD were continuously monitored and recorded at hourly intervals throughout the one-year testing period.



Figure 3: View of the creep frames with the beams subjected to sustained loading.

Following the RILEM TC 261 recommendation, the sustained loading level was established through a creep index $I_c = f_{\mathrm{R,c}}/f_{\mathrm{R,p}} = 0.5$, where $f_{\mathrm{R,c}}$ is the sustained residual flexural stress applied during the creep stage and $f_{\mathrm{R,p}}$ is the residual tensile strength determined during the pre-cracking stage at a crack mouth opening displacement of $\mathrm{CMOD}_{\mathrm{p}} = 0.5$ mm. Consequently, the sustained load applied during the four-point bending creep test, F_c, corresponded to 50% of the residual pre-cracking strength. To ensure equivalent stress levels between the EN 14651 pre-cracking configuration and the four-point bending creep configuration, F_c was determined by equating the bending moments in the two configurations, yielding:

$$F_c = \frac{5}{6} \cdot F_1 \tag{1}$$

where F_1 is the load corresponding to $\mathrm{CMOD}_{\mathrm{p}} = 0.5$ mm during pre-cracking. The creep loads, F_c, determined for each FRC mixture are presented in Table 3.

The sustained loading period lasted 360 days. The corresponding average CMOD–time responses of the three FRC mixtures are shown in Figure 4. A comparison of the average curves reveals significant differences in the early-age creep behavior of the materials. The SFRC specimens exhibited an almost instantaneous crack opening of approximately 0.118 mm immediately after load application, followed by a nearly linear increase in CMOD throughout the monitoring period. In contrast, the HFRC and MSFRC specimens showed larger initial crack openings after 15 minutes of loading, reaching approximately 0.140 mm and 0.210 mm, respectively. Thereafter, both mixtures exhibited a nonlinear increase in CMOD during the first

60 days, after which crack opening evolved at an approximately linear rate until the end of the monitoring period.

To quantify and compare the long-term crack-opening behavior of the three FRCs, linear regressions were performed on the CMOD–time relationships over the 60–360 day interval. The lower bound of this interval was established based on a preliminary assessment of the temporal evolution and rate of change of each curve, which revealed transient responses of different durations at early ages. While SFRC exhibited an approximately linear evolution throughout most of the investigated period, HFRC reached a low-rate, quasi-linear regime after approximately 25 days, whereas MSFRC exhibited a later transition at approximately 45–50 days. Accordingly, 60 days was adopted as a common conservative threshold, ensuring that all three mixtures were compared beyond their respective transient regimes and over an identical time domain. This approach minimizes the influence of early-age transient behavior and enables the slopes of the linear regressions to be interpreted consistently as representative of the long-term crack-opening rates.

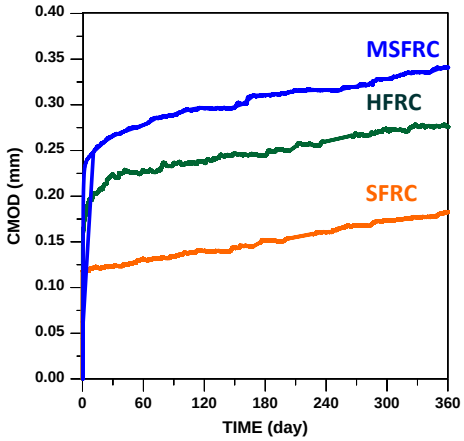


Figure 4: Average CMOD–time responses of the FRC mixtures subjected to sustained loading.

The regression parameters are summarized in Table 4. All three FRCs exhibited similar slopes, approximately 0.0002 mm/day, together with high coefficients of determination (R^2=0.9912, 0.9838, and 0.9783 for SFRC, HFRC and MSFRC, respectively), supporting the assumption of an approximately linear CMOD evolution within the selected interval. Despite their markedly different intercepts (0.117, 0.218, and 0.273, respectively), the comparable slopes indicate that the differences among the mixtures are primarily established during the instantaneous response and subsequent transient creep stage within the first two months of sustained loading. Once this transient stage has largely subsided, the three FRCs exhibit comparable rates of crack-opening evolution. These results therefore suggest that, under the investigated conditions, fiber type has a pronounced influence on the magnitude of the initial and early-age crack-opening response, whereas its influence on the subsequent long-term CMOD rate is comparatively limited.

Table 4: Linear regression parameters of the CMOD–time relationships for each FRC.

FRC	**Slope**	**Intercept**	R^2
SFRC	0.0002	0.117	0.9912
HFRC	0.0002	0.218	0.9838
MSFRC	0.0002	0.273	0.9783

5 Discussion

The results demonstrate that fiber type has a significant influence on the early-stage creep behavior of cracked FRC beams. The larger instantaneous crack openings observed in the HFRC and MSFRC specimens immediately after load application indicate a more compliant post-cracking response compared with SFRC. This behavior is consistent with the lower elastic modulus of macro-synthetic fibers and their greater deformability under tensile loading, which lead to larger fiber elongations and, consequently, greater crack-opening displacements for a given sustained load.

The differences among the three FRC systems became more pronounced during the first 60 days of sustained loading. While the SFRC specimens exhibited an approximately linear increase in crack opening from the early stages of the test, HFRC and MSFRC showed a marked nonlinear response, characterized by a comparatively rapid increase in CMOD followed by a progressive reduction in the crack-opening rate. This behavior is consistent with the greater sensitivity of macro-synthetic fibers to sustained loading, particularly due to the viscoelastic nature of the polymeric material. In addition, the time-dependent response of cracked FRC may involve other fiber-specific mechanisms, including progressive fiber–matrix slip and bond deterioration. In this context, the incorporation of steel fibers in the hybrid system appears to partially restrain the time-dependent deformation associated with the macro-synthetic fibers, resulting in an intermediate transient response between those of SFRC and MSFRC.

A distinctly different behavior emerged after approximately 60 days of sustained loading. Beyond this age, the CMOD–time curves became approximately linear and, more importantly, nearly parallel. Linear regressions performed over the common 60–360 day interval yielded essentially identical slopes for the three mixtures, despite the substantial differences in the absolute CMOD values accumulated during the preceding stages. The parallelism of the curves is particularly relevant from a mechanistic perspective, as it indicates that the incremental crack-opening rate at later ages becomes largely insensitive to fiber type. Consequently, fiber-specific time-dependent mechanisms—such as progressive slip and bond-related effects in steel fibers and viscoelastic deformation of macro-synthetic fibers—do not appear to produce markedly different contributions to the subsequent rate of crack opening. Although these mechanisms are likely responsible for a substantial part of the divergence among the mixtures during the instantaneous and transient stages, their differential influence appears to diminish as sustained loading progresses.

Therefore, the convergence toward a common crack-opening rate suggests an increasing relative contribution of time-dependent mechanisms shared by the three FRC systems. Among these, creep deformation of the cementitious matrix, particularly within the concrete compression zone, represents a plausible mechanism. Under sustained flexural loading, progressive compressive creep can increase the curvature of the cracked section and, through sectional compatibility, contribute to a continued increase in crack opening. Stress redistribution within the cracked section and time-dependent deformation of the fracture process zone may also contribute to this common long-term response. Accordingly, the results suggest that fiber type primarily controls the magnitude and duration of the instantaneous and transient crack-opening response, whereas, once this fiber-dependent transient stage has largely subsided, the subsequent CMOD evolution may become increasingly governed by mechanisms associated with the concrete matrix and the global response of the cracked section. Nevertheless, the present CMOD measurements alone do not allow the individual contributions of these mechanisms to be isolated, and the role of compression-zone creep should therefore be

regarded as a mechanically consistent interpretation rather than as a uniquely identified governing mechanism.

6 Concluding remarks

The experimental results demonstrate that fiber type has a marked influence on the early-stage creep response of cracked FRC under sustained flexural loading. SFRC exhibited the smallest instantaneous crack opening after load application, whereas HFRC and MSFRC showed progressively larger initial deformations as the proportion of macro-synthetic fibers increased.

During the first 60 days of sustained loading, HFRC and MSFRC exhibited a pronounced nonlinear increase in crack opening, while SFRC showed an approximately linear response from the early stages of the test. This behavior is consistent with the greater time-dependent deformability of macro-synthetic fibers and indicates that fiber type primarily governs the instantaneous and transient stages of the creep response.

Beyond approximately 60 days, the CMOD–time relationships of all mixtures became nearly linear and parallel. Linear regressions performed over the 60–360 day interval yielded essentially identical crack-opening rates, despite the substantial differences in the accumulated CMOD values. This result suggests that, once the initial fiber-dependent transient response has largely subsided, the subsequent long-term crack-opening rate becomes much less sensitive to fiber type and may be increasingly influenced by time-dependent mechanisms common to the cracked section.

HFRC consistently exhibited an intermediate response between SFRC and MSFRC, indicating that the incorporation of steel fibers can partially restrain the larger instantaneous and transient deformations associated with macro-synthetic fibers while preserving their contribution to post-cracking deformation capacity. These results suggest that HFRC may represent a suitable alternative for tunnel lining applications in which both post-cracking performance and control of long-term deformation are required.

7 Acknowledgements

The Author acknowledges the support provided by Gestion Vial S.A. in funding this work.

8 References

Almusallam, T.H., Ibrahim, S.M., Al-Salloum, Y.A., Abadel, A.A., and Abbas, H., 2016. “Analytical and experimental investigation on the fracture behavior of hybrid fiber reinforced concrete,” *Cement and Concrete Composites*, 74 pp201-217. Doi: 10.1016/j.cemconcomp.2016.10.002

Amigo, P., 2023. “Infrastructural residue: Construction through shafts and tunnels in the Santiago Metro,” *ARQ (Santiago)*, 114 pp138-145.

ASTM C595/C595M-23, 2023. *Standard Specification for Blended Hydraulic Cements*, ASTM International, USA.

AVO II (2022). *Proyecto Américo Vespucio Oriente II: Memoria Descriptiva y Antecedentes Técnicos del Proyecto*. Ministerio de Obras Públicas de Chile, Santiago, Chile.

Ballou, M., 2008. “Fibre-reinforced shotcrete for underground mines in the new millennium,” *Shotcrete Magazine*, Fall 2008 pp18-24.

Banthia, N., Sappakittipakorn, M., 2007. "Toughness enhancement in steel fiber reinforced concrete through fiber hybridization," Cement and Concrete Research, 37(9) pp1366-1372. Doi: 10.1016/j.cemconres.2007.05.005

Barpi, F., Valente, S., 2003. "Creep and fracture in concrete: a fractional order rate approach," *Engineering Fracture Mechanics*, 70 pp611-623.

Bernard, E.S., 2020. "Changes in long-term performance of fibre reinforced shotcrete due to corrosion and embrittlement," *Tunnelling and Underground Space Technology*, 98:103335. Doi: 10.1016/j.tust.2020.103335

EN 14651:2005+A1:2008, 2008. *Test method for metallic fibre concrete - Measuring the flexural tensile strength (limit of proportionality (LOP), residual)*, CEN, Belgium.

Di Prisco, M., Plizzari, G., and Vandewalle, L., 2009. "Fibre Reinforced Concrete: New Design Perspectives," *Materials and Structures*, 42(9) pp1261-1281.

Del Prete C., Buratti N., and Mazzotti C., 2022. "Experimental analysis of time dependent phenomena and temperature effects on macro-synthetic fibre reinforced concretes in different loading conditions," *Construction and Building Materials* 326:126904. Doi: 10.1016/j.conbuildmat.2022.126904

García-Taengua E., Arango S., Martí-Vargas J.R., and Serna P., 2014. "Flexural creep of steel fiber reinforced concrete in the cracked state," *Construction and Building Materials*, 65 pp321–329. Doi: 10.1016/j.cemconres.2010.05.005.

Fib, 2024. *Model Code for Concrete Structures 2020*, Fèdération Internationale du Béton, Lausanne

Laranjeira F., Molins C., and Aguado A., 2010. "Predicting the pullout response of inclined hooked steel fibers," *Cement and Concrete Research*, 40(10) pp1471-1487. Doi: 10.1016/j.cemconres.2010.05.005

Li B., Chi Y., Xu L., Shi Y., and Li C., 2018. "Experimental investigation on the flexural behavior of steel-polypropylene hybrid fiber reinforced concrete," *Construction and Building Materials*, 191 pp80-94. Doi: 10.1016/j.conbuildmat.2018.09.202

Li, K.F., Yang, C.Q., Huang, W, Zhao, Y.B., Wang, Y, Pan, Y and Xu, F., 2021 "Effects of hybrid fibers on workability, mechanical, and time-dependent properties of high strength fiber-reinforced self-consolidating concrete," *Construction and Building Materials* 277:122325. Doi: 10.1016/j.conbuildmat.2021.122325

Llano-Torre, A., and Serna, P. (2021). "Recommendation of RILEM TC 261-CCF: test method to determine the flexural creep of fibre reinforced concrete". *Materials and Structures*, 54:124. Doi: 10.1617/s11527-021-01675-0

Development of probabilistic cracking models for fiber reinforced concrete under static and dynamic loadings

Pierre Rossi[1]

[1] : Civil Engineering Department, COPPE, Federal University of Rio de Janeiro, Brazil.

Abstract

This article presents the fundamentals of a numerical model that is set to undergo subsequent algorithmic implementation. This model is a probabilistic semi-explicit cracking model dedicated to the dynamic behavior (loading range from 10^{-2} to 10^{3} GPa·s^{-1}) of structures made from steel fiber reinforced concrete (SFRC). It is based on the extension of the same model that has been previously proposed for static loading. This extension is presented after a detailed exploration of the physical mechanisms accompanying the cracking process of fiber-reinforced concrete under dynamic loading. The fact that the model is based on precise and detailed physical mechanisms allows proposing new theoretical relations concerning strain rate effect on the numerical model parameters. So, an innovative alternative to the experimental quantification of the model parameters is proposed. This alternative allows avoiding performing tests on sophisticated testing machine as, for example, the Hopkinson bar. It involves conducting only static uniaxial tensile tests on notched fiber-reinforced concrete specimens. It is a fully new and original proposal.

Keywords

Fiber reinforced concrete, dynamic behavior, cracking, finite elements, probabilistic model

1 Introduction

Dynamic loadings, as considered here, are what are referred to as impulsive-type loadings, caused, for example, by impacts or explosions. It is often emphasized that SFRCs (Steel Fiber Reinforced Concretes) perform particularly well under such impulsive loadings. The orders of magnitude of stress and strain rates generated by impulsive loadings in conventional civil engineering structures typically range from 10^{-2} to 10^{3} GPa·s^{-1}, which corresponds to strain rates ranging from 10^{-3} to 10 s^{-1}. Numerous experimental studies on this mechanical issue have shown a clear increase in energy dissipation (non-linear behavior) and load-bearing capacity in structural elements made with FRCs, compared to the same elements made with plain (non-fibered) concrete. Using fiber reinforced concretes in constructions therefore becomes an important issue when it is known that climate change is now leading to these constructions being subjected to increasingly violent impacts. To evaluate the specific performance of SFRCs under dynamic conditions (i.e., compared to their static performance), it is relevant to analyze whether, for a given mechanical property, denoted as P, the ratio P_{FRCs}/P_{CWF} (CWF: Concrete Without Fibers) increases as the stress rate increases, and what physical mechanisms govern the evolution of this ratio.

What follows is a description of the physical mechanisms specific to the behavior of fibers when an SFRC is subjected to high strain rates. In a composite material such as FRCs, sensitivity to strain rate effects can stem from the matrix (concrete), and/or the reinforcement (steel fibers). It is known that, within the aforementioned range of strain rates, steel is much less sensitive to rate effects than concrete. Therefore, in a first approximation, the rate effects in SFRCs can be attributed to those of the concrete. These are now well understood (Rossi, 1994) and are recalled in chapter 2.

Based on the description of the mechanisms of rate effects within SFRCs (Chapter 3), the basis of a numerical model for analyzing the cracking of SFRC constructions in dynamic is proposed. This numerical model is founded on the extension of the probabilistic semi-explicit cracking model proposed for static loadings (Rossi, 2023).

This paper is based on a previous and more detailed paper (Rossi, 2026).

2 Strain rate effects on plain concrete

One of the main findings from research conducted to date on strain rate effects is that, within a certain range of strain rates, these effects are primarily linked to the presence of evaporable water within the nanopores of the concrete's hydrates. A hypothesis has been proposed regarding the physical mechanism in which this evaporable water plays the central role. It is a mechanism akin to the Stefan effect, involving the viscosity of water (Rossi, 1994)

This effect can be summarized as follows: when a thin film of a viscous liquid is trapped between two perfectly flat plates that are being pulled apart at a certain velocity, the film exerts a restoring force on the plates that is proportional to the separation velocity. This mechanism is expressed by the following relationship:

$$F = (3\eta V^2/2\pi h^5) \times (dh/dt) \quad (1)$$

in which F is the restoring force, η, the viscosity of the liquid, h, the initial distance between the two plates, (dh/dt), the displacement rate of the two plates (> 0), V, the volume of the liquid.

If it is assumed that the free water present in the hydrates is responsible for a similar mechanism when the solid skeleton (here considered as a network of plates) undergoes tensile deformation, it can be understood why rate effects are significant in wet concrete.

To understand how the viscous mechanism, similar to the Stefan effect, can influence the tensile fracturing process, one must start from the quasi-static tensile cracking process in concrete. This cracking process proceeds as follows (Rossi, 1998):

Step 1: Formation and propagation of diffuse microcracking.
During this initial phase, the overall behavior appears linear elastic.

Step 2: Transition phase or onset of microcrack localization.
In this phase, some microcracks grow to form mesocracks. It is associated with the emergence of the nonlinear portion of concrete's tensile response, reflecting its low ductility.

Step 3: Localization of cracking.
During mesocrack development, one crack begins to dominate, leading to a macrocrack. The concrete's tensile strength is reached at this point.

Step 4: Macrocrack propagation.
This step concerns the structural behavior of the specimen. A reduction in force with increasing displacement is observed when the test is conducted at a fixed displacement rate, illustrating the structural softening behavior (the specimen being considering as a small structural element).

Based on knowledge of this static cracking process, the Stefan effect (viscous mechanism) intervenes before the crack localization **(**steps 1, 2, and 3) as follows: the formation of new microcracks and the propagation of initial microcracks are delayed. These two actions lead to a delay in the localization of microcracking and thus increase the peak load (So, the uniaxial tensile strength). After localization (step 4), the Stefan effect intervenes by acting on the microcracks of the process zone at the front tip of the macrocrack opposing its propagation (increase of the macrocrack propagation energy).

3 Strain rate effects on SFRC

Based on the dynamic cracking process in concrete, it can be analyzed how steel fibers intervene in this process. To do so, it must first be examined how fibers act in the quasi-static cracking process. Fibers' role in the static cracking process can be summarized as follows (Rossi, 1987): (1) In steps 1, 2, and 3, fibers can bridge micro- and meso-cracks, delaying the formation of a macrocrack. This improves the material's tensile strength and ductility; (2) In step 4, fibers bridge the macrocrack itself, opposing its propagation and increasing the energy required for crack growth. This step is related to a structural behavior (the specimen can be considered, mechanically, as a small structural element).

This paper does not delve into the specifics of how these bridging effects are achieved, such as fiber type, geometry, dosage, and orientation. For example, bridging effects in steps 1 to 3

can occur in UHPFRC (Ultra-High-Performance Fiber-Reinforced Concrete) when the fiber content is high (with small diameters) and fibers are well-oriented relative to the crack, usually obtained through uniaxial tensile testing or very high fiber volume fractions (exceeding 5%).

To influence the dynamic tensile cracking process, fibers must activate additional physical mechanisms compared to the static regime). It was demonstrated that the principal additional physical mechanism is related to the synergistic coupling between fibers and concrete**.**

Synergistic coupling between concrete and steel fibers: In chapter 2, fibers were shown to oppose displacement across crack faces and transfer stresses (bridging effect). Under impulsive loading, crack lips move at high velocity, and fibers are rapidly engaged. In transferring stress, fibers induce high strain rates in the surrounding matrix. Depending on fiber geometry and anchorage, these can be shear, tensile, or compressive stresses. For straight fibers, the transmitted stress is macroscopic shear. However, due to surface roughness and matrix heterogeneity, these become tensile stresses at the micro-scale, causing microcracking around the fiber, leading to nonlinear interface behavior. This microcracking near the fiber/matrix interface activates rate effects (as discussed in chapter 2), increasing macroscopic bond strength under dynamic vs. static loading. For mechanically anchored fibers (with hooks at their ends, as example), similar tensile stress concentrations arise, often greater than with bonded fibers. Rate effects here are localized near anchor points**,** increasing fiber effectiveness before pull-out.

In conclusion, both bonded and mechanically anchored fibers transmit higher forces dynamically than statically, for the same crack width (assuming fibers do not rupture).
Thus, whether fibers increase intrinsic strength, as in UHPFRC, or post-crack energy (any FRC), the strength ratio $K_R = R_{FRCs}/R_{Plain}$ or energy ratio $K_E = E_{FRCs}/E_{Plain}$ increases under dynamic loading. This effect scales with fiber content (Rossi, 1998).

4 Numerical model of cracking in SFRC structures in static

Existing diffuse cracking models (Fanella and Krajcinovic, 1985; Peng and Meyer, 2000; Barros and Figueras, 2001; De Montaignac et al. 2013) treat cracks as microcracked zones where the density of microcracks gradually increases until forming a void, at which point no further stress is transmitted. From a numerical perspective, within the framework of finite element theory, these microcracked zones are modeled using volume elements. Generally, these models follow a deterministic approach and describe the nonlinear mechanical behavior associated with microcracking.

Although these models are widely described in the literature and commonly used in practice, they have a significant drawback. Diffuse cracking models are not physically based since they transform a localized crack into diffused microcracked zone. This strong physical approximation results in an inaccurate representation of the cracking pattern in SFRC structures. Numerically, because G_f (the post-cracking energy values are significantly higher for FRCs than for conventional concretes, diffuse cracking models tend to overly spread the damaged (microcracked) zones and underestimate crack openings (Rossi, 2023).

The PSEC^f model for simulating the mechanical behavior of large-scale SFRC structures is a relatively recent development. It was originally introduced for static loading conditions (Rossi, 2023). The model is specifically intended to simulate macrocrack propagation, focusing on cracks with openings equal to or greater than 300 μm. It is based on the uniaxial tensile

behavior of SFRC (Rossi, 2023) and is only applicable to SFRCs exhibiting a strain-softening post-cracking response under uniaxial tension.

The main objective of this model is to address a key limitation in existing distributed cracking models from the literature, namely, the excessive dispersion of cracks, which results in underestimating the openings of larger cracks. Macrocrack initiation and propagation are simulated using linear volumetric elements, where cracks form when the tensile stress at the integration point of an element reaches the matrix's tensile strength (unreinforced concrete), assuming perfectly brittle matrix behavior. Concrete strength is modeled as a random variable following a Weibull distribution, with dependence on the finite element volume. As the finite element volume increases, both the mean and standard deviation of the matrix tensile strength decrease.

Previous experimental study (Rossi, 2012) has shown that the average post-cracking energy related to the bridging effect is independent of the tested material volume, although the standard deviation of this energy decreases with increasing volume. Aligning with the objectives of this model, a simplified approach is adopted where the fiber bridging energy G_{wf} is treated as a deterministic parameter, unaffected by the finite element volume.

The probabilistic semi-explicit model considers two key mechanical stages: initial macrocrack initiation (step 3 of chapter 2) and fiber bridging effect. These aspects are illustrated in Figure 1.

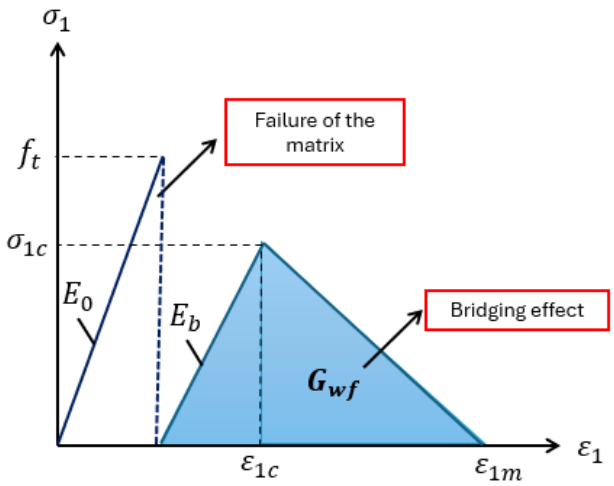


Figure 1: Aspects of the PSEC^f model for fiber-reinforced concrete – Mechanical behavior in uniaxial tension.

Crack initiation occurs when the maximum principal stress σ_1 in an element reaches the randomly assigned tensile strength f_t. At this point, the element's stiffness decreases sharply. During fiber bridging, as the maximum principal strain ε_1 increases, the bridging mechanism is activated, which increases the effective stiffness E_b but remains below the original material stiffness E_0. If ε_1 decreases, the element's stiffness remains low. During crack progression, once ε_1 reaches a critical value ε_{1c}, the stress σ_1 decreases linearly with ε_1 to simulate fiber pullout. When ε_1 attains its maximum value ε_{1m}, the fiber effect is considered negligible, and the element stiffness drops to zero. This softening behavior is modeled via a simple damage approach, where only the matrix values in the element related to the maximum principal stress-strain

relationship are modified, while other matrix entries remain zero. Consequently, the fiber bridging effect is treated as anisotropic.

Given the probabilistic nature of the model, Monte Carlo procedure is essential to ensure the results statistically reflect the variability inherent in both model parameters and material properties. For a given structural problem, the set of obtained results allows for a relevant statistical analysis, enabling a safety-oriented assessment of the structure's behavior.

It can be emphasized that, in the proposed model, the rupture of the matrix (the concrete) being perfectly brittle and its tensile strength a probabilistic parameter, this allows the cracks to be located much better than in the diffuse cracking models mentioned previously.

It is important to clarify that the proposed model is not valid for FRCs which have hardening behavior in uniaxial tension.

In this model, the bridging effect of the fibers is only considered when the matrix is fully cracked. This choice might appear overly simplistic given the macroscopic behavior observed during a direct tensile test on a notched specimen. Indeed, during such a test, a softening behavior emerges, resulting from the propagation of the macrocrack and the progressive bridging action of the fibers until the entire section of the specimen is fully cracked. However, as described in chapter 2, this macrocrack propagation phase is by no means a material behavior, but rather a structural behavior. In fact, this post-cracking softening behavior entirely depends on the dimensions of the direct tensile specimen, and more specifically on the cross-section where the cracking occurs (in the case of a notched specimen). As a result, the only stages of the cracking process of fiber-reinforced concrete under direct tension are considered in the model: (1) the behavior up to the initiation of the macrocrack (peak load) which is the material behavior of the uncracked FRC; and (2) the load transfer by the fibers when the specimen's cross-section is fully cracked (which is the material behavior of the fully cracked FRC). Indeed, for the latter stage, it has been experimentally demonstrated (Rossi, 2012) that the average behavior of the load transfer by the fibers is independent of the specimen's dimensions. The scattering related to this fibers load transfer behavior decreasing with the increasing specimen dimensions, it is important to adapt the number of specimens to be tested to get a correct information about the average behavior (Rossi, 2012).

The mean tensile strength of the matrix f_t and its standard deviation (which depends on the finite element volume) are computed from previously validated formulas (Rossi et al, 1994). These properties are randomly distributed across the mesh following a Weibull distribution. The fiber bond energy G_{wf} is derived from uniaxial tensile test on notched specimens (Casanova and Rossi, 1997; Rossi, 1998; Rilem TC 162, 2001). Since this uniaxial tensile test measure crack opening, a conversion to strain is necessary for modeling and numerical simulations. This conversion involves dividing the crack opening by a characteristic length of the finite elements, $l_e = V_e^{(1/3)}$, where V_e represents the volume of the finite element.

5 Numerical model of cracking in SFRC structures in dynamic

The majority of numerical models (finite elements models) related to the dynamic behavior of fiber-reinforced conte structures (Haido et al, 2011; Madhi et al, 2017; Arruda et Castro, 2021) exhibit the same issues as those concerning the static behavior of these structures. They

are not very relevant for providing a realistic representation of the cracking process (cracking is too diffuse compared to reality). This is due to the same inherent limitations of these models.

The proposed model is based on the development in dynamics of the PSEC^f model developed in statics (chapter 4). In this PSEC^f model, two parameters appear: the tensile strength f_t of concrete and the bridging effect energy of fibers G_{wf}. Chapter 3 shows that the rate effect on fiber-reinforced concretes have two main consequences: the increase, with the stain rate, of f_t, which is a probabilistic parameter and of G_{wf} which is a deterministic parameter.
Regarding the strain rate effect on f_t, studies (Rossi, 1994) led to the following generic relationship (Rossi, 2022):

$$f_{t,dyn} = f_{t,stat} + 2.8 + 0.3 \ln(\dot{\sigma}) \quad (2)$$

with strength (f_{tstat} and f_{tdyn}) given in MPa, while stress rate $\dot{\sigma}$ has units of GPa/s; f_{tstat} and f_{tdyn} are respectively the static and the dynamic tensile strengths.

As for the strain rate effect on G_{wf}, there is no generic relationship proposed in the literature. Therefore, it will need to be established from a very significant and costly experimental study (different concretes, geometries and percentage of fibers to be considered), or obtained for each specific FRC. In both cases, as with static tests, uniaxial tensile tests on notched specimens will need to be conducted at different loading rates, from low until high loading rates through intermediate loading rates. For the low and intermediate loading rates, a classic traction machine can be used, while for high loading rates the Hopkinson bar is the most effective testing method to be used (Wang et al, 2012; Hassan and Wille, 2022).

To enable the experimental determination of the evolution of the uniaxial tensile stress–strain law (Figure 1) – more specifically, the various parameters related to the fibers' bridging effect – with respect to the strain rate for a given FRC, it is essential to assume about this evolution.

Referring to chapters 3 and 4, the following assumption appears acceptable:

- The elastic modulus E_b is not a lot of affected by strain rate effects (this Young modulus is mainly linked to the one of the fibers which is not sensitive to the domain of strain rates considered).
- Due to the improvement of fiber anchorage or adhesion to concrete with increasing strain rate, the stress σ_{1C} increases with strain rate.
- Since, even when fibers start to slip within the concrete (descending branch of the bridging effect in Figure 1), few additional microcracks can appear around the fibers (the tensile stresses transmitted near the fibers decrease significantly), the viscous effects associated with this slipping can be neglected.
- The strain ε_{1m} (Figure 1), mainly related to the fiber's geometry and dimensions, can be assumed to be unaffected (or minimally affected, so no considered) by strain rate effects.

In consequence, the strain rate effects accompanying the proposed fiber bridging effect are primarily related to the enhancement of fiber adhesion or anchorage (increasing of σ_{1C} which becomes σ_{1Cdyn}).

Figure 2 summaries the PSEC^f model in dynamics.
Experimental studies to access the parameters of the proposed model are complex (especially the use of the Hopkinson bar, which is a relatively confidential experimental equipment) and

expensive. It is therefore relevant to propose an alternative to these studies by making a few assumptions. Thus, the only value to be determined in the dynamic bridging effect of fibers is that of the parameter (σ_{1Cdyn}). However, as proposed (hypothesis), the value of this parameter is linked to the improvement of the anchoring or adhesion of the fiber in the matrix (depending on the fiber type) with rate effects. Since this improvement can be attributed to the Stefan effect acting on the microcracking process in the vicinity of the fibers, and since this mechanism is similar to that governing the increase in the uniaxial tensile strength of concrete (Chapter 2), a new hypothesis may be proposed: the increase in the dynamic stress parameter (σ_{1Cdyn}) with strain rate follows the same law as the increase in the tensile strength of concrete. This assumption leads to the following relationship (Relation 3):

$$\sigma_{1Cdyn} = \sigma_{1Cstat} \, (f_{tdyn}/f_{tsta}) \tag{3}$$

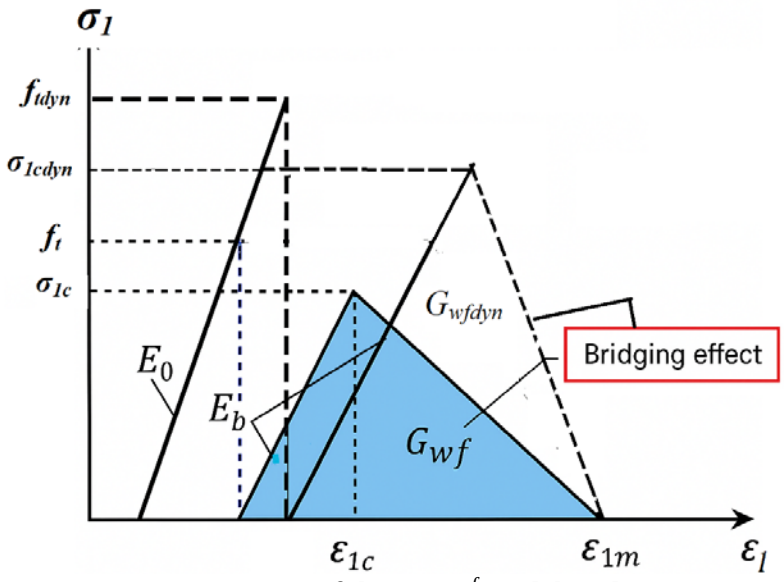


Figure 2: Aspects of the PSEC^f model in dynamics

From a numerical perspective, the influence of structural inertia should come automatically from a dynamic analysis (Jin et al, 2019), being a natural consequence of the inclusion of mass matrix and damping matrix in the equation of motion. Therefore, it should not be considered a priori either through Dynamic Increase Factor (DIF) or by sophisticated constitutive models. This choice is supported by thorough numerical simulations (Ozbolt et al, 2011; Ozbolt and Riedel, 2013).

Concerning the finite element procedure, before starting the numerical analysis, it is necessary to assign random property of f_t and deterministic one of σ_{1C} for each finite element according to a given probabilistic distribution concerning f_t. This type of procedure was originally described in (Rita, 2022) for the probabilistic semi-explicit cracking (PSEC) model related to concrete (it means without fibers). Once the probabilistic properties and the deterministic one have been assigned to the finite element mesh, boundary and initial conditions are provided, and a typical dynamic analysis is performed, usually adopting the Newmark-beta algorithm for the time-step integration.

6 Concluding remarks

This article presents the fundamentals of a numerical model that is set to undergo subsequent algorithmic implementation. This model is a probabilistic semi-explicit cracking model dedicated to the dynamic behavior of structures made from steel fiber reinforced concrete (SFRC). The proposed approach extends the original model and is based on its enhanced formulation. This extension is proposed after a detailed exploration of the physical mechanisms accompanying the cracking process of fiber-reinforced concrete under dynamic loading.

The fact that the model is based on precise and detailed physical mechanisms allows for an interesting alternative to the experimental quantification of the model parameters. This experimental quantification, which requires the use of a Hopkinson bar, is complex and costly. The proposed alternative involves conducting only uniaxial tensile tests in static on notched fiber-reinforced concrete specimens.

This work provides the scientific and engineering communities with a solid foundation to support such developments. Following a numerical implementation step and a validation work, based on available experimental data from the literature, will be necessary to confirm the accuracy and robustness of this model, which is therefore currently only theoretical.

7 References

Arruda, M.R.T. and Castro, L.M.S., 2021. “Non-linear dynamic analysis of reinforced concrete structures with hybrid mixed stress finite elements”, Advances in Engineering Software, Volume 153, 102965.

Barros, J. and Figueiras, J.A, 2001. “Model for the analysis of steel fiber reinforced concrete slabs on grade”, *Computers & Structures* 79(1): 97- 106.

Casanova, P. and Rossi, P., 1997. “Analysis and design of steel fiber reinforced concrete beams”, *ACI Structural Journal*, Vol. 94, No. 5, pp. 595-602.

De Montaignac, R., Massicotte, B. and Charron, J-P., 2013. “Finite-element modelling of SFRC members in bending”, *Magazine of Concrete Research* 65(19): 1133-1146.

Fanella, D. and Krajcinovic, D., 1985. “Continuum damage mechanics of fiber reinforced concrete” *J Eng Mech* 111(8): 995-1009.

Haido, J.H., Abu Bakar, B.H., Jayaprakash, J. and Abdul-Razzak, A.A., 2011. “Nonlinear Response of Steel-Fiber Reinforced Concrete Beams under Blast Loading: Material Modeling and Simulation”, *In: Ye, L., Feng, P., Yue, Q. (eds) Advances in FRP Composites in Civil Engineering. Springer*, Berlin, Heidelberg, https://doi.org/10.1007/978-3-642-17487-2_91.

Hassan, M. and Wille, K., 2022. “Direct tensile behavior of steel fiber reinforced ultra-high performance concrete at high strain rates using modified split Hopkinson tension bar”, *Composites*, Part B, 246, https://doi.org/10.1016/j.compositesb.2022.110259.

Jin, L. , Yu, W., Du, X. and Yang, W., 2019. “Dynamic size effect of concrete under tension: A numerical study”, *International Journal of Impact Engineering* 132,103318.

Mahdi, S., Kolbadi, S., Davoodian, H., Mohammad, S. and Kolbadi, S., 2017. “Evaluation of Nonlinear Behavior of Reinforced Concrete Frames by Explosive Dynamic Loading Using Finite Element Method”, *Civil Engineering Journal*, Vol. 3, No. 12.

Ozbolt, J., Sharma, A., and Reinhardt, H.-W., 2011. “ Dynamic fracture of concrete–compact tension specimen”, *International J. of solids and structures*, 48 (2011) 1534–15431.

Ozbolt, J. and Riedel, W., 2013. "Modelling the response of concrete structures from strain rate effects to shock induced loading", *Understanding the Tensile Properties of Concrete, Elsevier*, pp. 295–340.

Peng X and Meyer C, A continuum damage mechanics model for concrete reinforced with randomly distributed short fibers. *Comput Struct* 78: 505-515, 2000.

RILEM TC 162, 2001. "Test and design methods for steel fibre reinforced concrete: Uniaxial tension test for steel fibre reinforced concrete", *Mater Struct* : 34(235) : 3–6.

Rita, M.R., 2022. "Implementation of a macroscopic probabilistic model of cracking concrete using parallelization strategies", *PhD Thesis of Federal University of Rio de Janeiro.*

Rossi, P., 1994. "Dynamic behaviour of concrete: from material to the structure", *Materials and Structures* 27 319-323.

Rossi, P., 1998. "Les bétons de fibres métalliques", *Les presses de l'Ecole Nationale des Ponts et Chaussées* (in french).

Rossi P., 2012. "Experimental Study of Scaling Effect Related to Post- Cracking Behaviors of Metal Fibers Reinforced (MFRC)", *European Journal of Environmental and Civil Engineering* 16(10): 1261-1268.

Rossi, P., 2022. "Mode I Crack Propagation in Concrete Structures under Impact Loadings", *Cur Trends Civil & Struct Eng. 9(2):2022. CTCSE.MS.ID.000710. DOI: 10.33552/CTCSE.2022.09.000710.*

Rossi, P., 2023. "Basis of Probabilistic Semi-Explicit Cracking Model for Fiber Reinforced Concretes", *Cur Trends Civil & Struct Eng.* 10(1): 2023. CTCSE.MS.ID.000727. DOI: 10.33552/CTCSE.2023.10.000727.

Rossi, P., 2026. "Development of Probabilistic Cracking Models for Fiber Reinforced Concrete Under Static and Dynamic Loadings", *Cur Trends Civil & Struct Eng. 12(2): 2026. CTCSE.MS.ID.000778. DOI: 10.33552/CTCSE.2026.12.000778.*

Wang, Z., Zhou, N. and Wang, J., 2012. "Using Hopkinson pressure bar to perform dynamic tensile tests on SFRC at medium strain rates", *Magazine of Concrete Research*, 64(8), 657–664, 2012, http://dx.doi.org/10.1680/macr.11.00076.

Dual-Approach Verification of Enhanced Fatigue Life in Macro Synthetic Fibre Reinforced Concrete Sleepers

Christophe Camille[1,2], Olivia Mirza[2], Todd Clarke[1]

[1]: BarChip Australia Pty Ltd, Woolloongabba, Queensland, Australia

[2]: Western Sydney University, Locked Bag 1798, Penrith, NSW 2751, Australia

Abstract

The structural integrity of prefabricated railway sleepers is increasingly challenged by higher axle loads and extended maintenance intervals, requiring a shift toward performance-based design validation. This study investigates the structural behaviour and fatigue performance of prestressed concrete sleepers incorporating macro synthetic fibres reinforcement (PF), demonstrating a significant improvement in service life compared to conventional prestressed concrete (PO) sleepers without fibres. Fatigue testing was conducted under constant-amplitude cyclic loading with analysis focused on the stiffness degradation as a direct, performance-based measure of structural health and crack resistance. The experimental results were further validated against traditional stress-based fatigue assessment methods to ensure model reliability. The PF specimens exhibited a 34.8% higher initial stiffness and a subsequent 75.9% slower damage rate than the PO sleeper, indicating vastly superior resistance to damage accumulation and crack propagation. This enhanced structural behaviour translates directly into a life multiplier of 4.15 times before the 10% remaining stiffness serviceability limit is exceeded. The verified methodology and superior durability performance support the adoption of macro synthetic fibre technology in practice and future design codes, promoting more resilient, cost-effective and sustainable railway infrastructure. The strong correlation between the two validation approaches provides a robust foundation for performance-based modelling, confirming that fibre reinforcement offers a durable, high-performance alternative with demonstrated extension of service life in prestressed concrete sleepers.

Keywords

Fibre reinforced concrete, railway sleeper, fatigue design, post-crack performance

1 Introduction

Railway sleepers are subjected to a combination of static, dynamic and impact loading throughout their service life due to wheel-rail interactions. The magnitude of these repeated loads depends on train speed, track geometry and support conditions, all of which influence the mechanisms of fatigue damage. Fatigue failure in sleepers can occur at stress levels below material strength when subjected to cyclic loading and is characterised by the magnitude of the stress range and the number of load cycles (You et al., 2017). Under such conditions, fatigue in concrete initiates and propagates as micro-cracks that evolve into macro-cracks, accompanied by increasing permanent strains and a progressive reduction in structural stiffness. In prestressed concrete sleepers, repeated loading also induces micro-cracking in the prestressing wires, resulting in stress concentration and premature fracture.

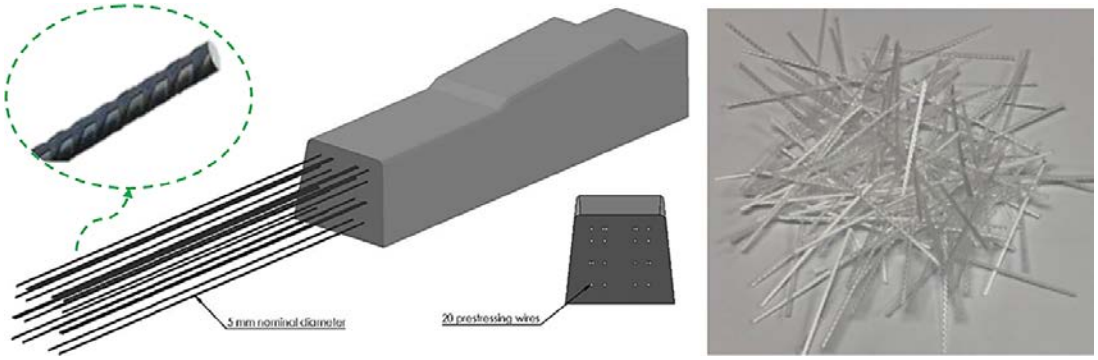
Current design approaches for prestressed concrete sleepers are primarily based on elastic analysis and permissible stress concepts, with fatigue resistance assessed through standard repeated load testing (Nairn & Stevens, 2010; Standard Australia Online, 2012). While uncracked sleepers generally exhibit adequate fatigue performance, cracking under service conditions is often unavoidable due to high-intensity impact loads (Parvez & Foster, 2017). The presence of cracks significantly increases the stress range in the prestressing steel, accelerating fatigue damage and reducing service life. Therefore, the fatigue life of prestressing steel becomes a critical indicator for determining maintenance and replacement intervals of concrete sleepers. This is particularly important for standards adopting partial prestress design, where tensile stresses are permitted in the concrete under service loading, increasing the likelihood of cracking and fatigue-related deterioration (Goto et al., 2018). Consequently, the development of reliable fatigue-life assessment methods for prestressed concrete sleepers is increasingly important.

In recent years, fibre reinforced concrete (FRC) has emerged as a promising solution for enhancing the performance of quasi-brittle materials. Advances in fibre technology have enabled the development of highly engineered macro synthetic fibres that enhance ductility, toughness, energy absorption and durability. An extensive experimental program conducted by the authors, including material characterisation, static testing and dynamic performance assessment, has demonstrated that macro synthetic fibres can significantly improve sleeper residual bending strength, energy absorption capacity and cracking resistance (Camille, 2021; Kahagala Hewage et al., 2024). This paper represents a continuation of this research program, focusing on the fatigue performance of macro synthetic fibre reinforced concrete (MSFRC) prestressed railway sleepers. To address the current gap in relating structural response to fatigue mechanisms, a dual-approach verification framework is proposed that combines stiffness- and stress-based assessments. The analytical results are validated against experimental fatigue data, enabling a comprehensive evaluation of the benefits of fibre reinforcement in reducing damage accumulation, lowering stress demand and extending service life. This work contributes to the development of more resilient and durable railway sleeper systems, supporting improved track performance and reduced maintenance requirements.

2 Experimental and Analytical Methodology

The experimental component of the investigation evaluated the fatigue performance of prestressed concrete sleepers incorporating macro synthetic fibres (PF) compared with

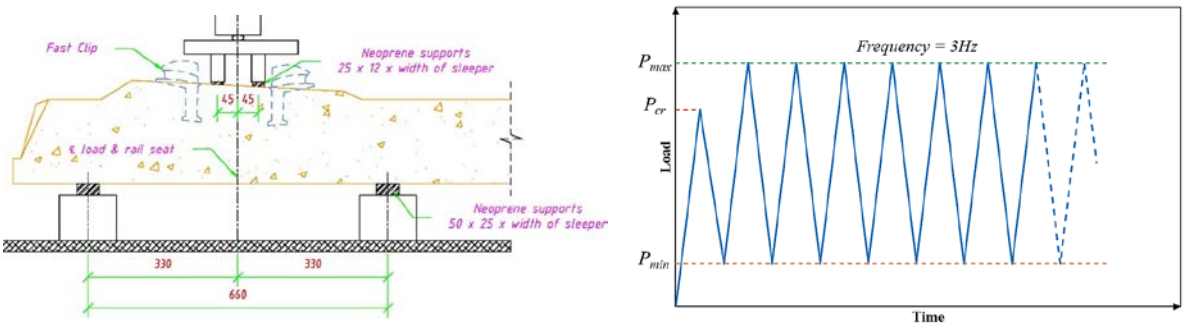
conventional prestressed sleepers without fibres (PO). All specimens were manufactured using identical geometry, prestressing configuration and base concrete mix to isolate the influence of fibre reinforcement. Fig. 1 illustrates the sleeper designed for heavy-haul applications, with a 30-tonne axle load and primarily reinforced with 20 chevron-patterned indented steel wires. PF sections were also reinforced with BarChip 48 (BC48) macro synthetic fibres made from a high-performance polypropylene material and classified as Class II fibres (i.e. $Ø \geq 0.3$ mm, (European Standard, 2006)). The dosage was representative of that used in structural applications (9.1 kg/m^3), with the aim of enhancing post-cracking behaviour and fatigue resistance, consistent with findings from previous studies by the authors (Camille, Kahagala Hewage, et al., 2022; Camille et al., 2021).



(a) (b)

Fig. 1: Reinforcement systems implemented in sleepers – (a) prestressing steel wire and (b) BC48 fibres

Prior to the sleeper's fatigue assessment, the fresh and hardened properties of concrete were tested and complied with the requirements of AS 1085.14, as reported in (Camille, Mirza, et al., 2022). The fatigue test generally followed the setup specified in AS 1085.14 (Fig. 2a), including the loading configuration, support conditions and cyclic procedure. However, given the inherently time-intensive nature of fatigue testing and the need to achieve failure within three million cycles, the upper fatigue load limit (P_{max}) was increased to approximately 45% above the standard-specified value. Prior to fatigue loading, the specimens were pre-cracked under static loading to approximately 235 kN (P_{cr}) at the rail seat, ensuring testing was conducted under representative cracked in-service conditions. These adjustments enabled an accelerated assessment of fatigue performance while maintaining consistency with the prescribed test methodology.



(a) (b)

Fig. 2: Repeated load test – (a) loading configuration and (b) loading protocol

Four sleepers were tested over a load range of 15 kN (P_{min}) to 285 kN (P_{max}) at 3 Hz (Fig. 2b). Note that P_{max} corresponds to approximately 68% of the ultimate static capacity of the sleeper, determined experimentally from monotonic rail seat testing. Accordingly, fatigue performance was assessed using a dual-approach methodology: (i) a stiffness degradation analysis derived from experimental measurements and (ii) a stress-based fatigue model based on effective stress range calculations.

2.1 Stiffness-Based Fatigue Assessment

Fatigue performance of the sleepers was quantified using a stiffness-degradation approach based on load-deflection responses measured under cyclic loading. For each selected cycle interval, the structural flexural stiffness (K_n) was calculated using the applied load amplitude ($P_{max} - P_{min}$) and the corresponding deflection range. This applied loading (15 – 285 kN) corresponds to approximately 61% of the sleeper's ultimate static capacity and an associated stress ratio $R \approx 0.05$, representing a highly aggressive and tensile-dominant regime followed by partial unloading. This promotes cyclic crack opening and closing, leading to progressive stiffness reduction. To establish a consistent reference state, the initial stiffness (K_0) was defined from the first stable fatigue cycles following pre-cracking, representing the in-service cracked condition at the onset of fatigue loading. The evolution of stiffness with increasing fatigue cycles was then used as a direct indicator of damage accumulation in the sleeper's structural response.

$$K_n = \frac{P_{max} - P_{min}}{\delta_{max,n} - \delta_{min,n}} \quad (1)$$

$$R = \frac{P_{min}}{P_{max}} \quad (2)$$

where:
K_n: Structural stiffness | R: Stress ratio

2.2 Analytical Stress-Based Fatigue Model

The analytical fatigue life of the prestressed concrete sleepers was evaluated using a stress-based model, where the cyclic stress range in the prestressing steel was taken as the governing fatigue parameter. The methodology follows a force-equilibrium sectional approach, similar to that adopted in You et al. (2017) for prestressed concrete sleepers and is extended herein to account for the presence of macro synthetic fibre reinforcement. Note that the fatigue life herein predicted was obtained using the parameters defined in Table 1, which are generally specified as lower-bound values for design purposes and are inherently conservative.

For a given bending moment, the internal force distribution was determined assuming plane sections remain plane, with equilibrium satisfied between internal forces and the applied moment. The internal force system consisted of concrete compression and prestressing steel tension, with an additional tensile force introduced for PF sections to represent the post-cracking bridging capacity of macro synthetic fibres. The applied fatigue loads (P_{min} & P_{max}) were converted into bending moments (Eq. 3) using the test configuration (Fig. 2a) at rail seat section to determine the corresponding steel stresses. Given that the specimens were pre-cracked prior to fatigue testing, the analysis was conducted assuming cracked section behaviour. That is, in the PO section, tensile concrete contribution was neglected and equilibrium was satisfied between the concrete compression block and prestressing steel force.

For PF, this equilibrium was extended by including an equivalent tensile force to represent fibre bridging, derived from residual strength parameters at ULS (i.e. f_{R3}). This enables the reduction in tensile demand on the prestressing steel due to fibre reinforcement to be captured within the sectional analysis. Note that the prestressing force, including effective losses, was incorporated as an initial internal force, enabling the interaction between external loading and prestress, particularly at low load levels where prestress governs crack closure behaviour.

Table 1: Material properties and model parameters

Material	Variable	Symbol	Value
Concrete	Mean compressive strength (MPa)	f_{cm}	68
	Flexural tensile strength (MPa)	f_{cf}	5.56
	Modulus of elasticity (GPa)	E_c	35.7
	Mean residual flexural strength (MPa) (for PF only)	f_{R3}	5.92
Prestressing wire	Ultimate tensile strength (MPa)	f_{pu}	1700
	Yield strength (MPa)	f_{py}	1410
	Nominal modulus of elasticity (GPa)	E_s	205
	Design stress range (MPa)	$\Delta\sigma_N$	300

$$M_{R+} = \frac{P_{max/min}}{2}(0.33 - 0.045) \tag{3}$$

$$\sigma_{s,eff} = \alpha.\sigma_{s,closed} + (1-\alpha).\sigma_{s,open}$$
$$\sigma_{s,open} = \psi.\sigma_{s,cr} \tag{4}$$

$$\log N_f = \begin{cases} \log N^* - k_1\left(\log \Delta\sigma_{s,eff} - \log \Delta\sigma_N\right), & \Delta\sigma_{s,eff} > \Delta\sigma_N \\ \log N^* + k_2\left(\log \Delta\sigma_N - \log \Delta\sigma_{s,eff}\right), & \Delta\sigma_{s,eff} \le \Delta\sigma_N \end{cases} \tag{5}$$

where:

M_{R+}: Positive bending moment at rail seat

$\sigma_{s,eff}$: Effective steel stress | $\sigma_{s,closed/open}$: Steel stress from close-open section equilibrium | $\sigma_{s,cr}$: Cracked section steel stress

α: Crack reopening factor | ψ: Average stress factor

N_f: Number of cycles to failure (for pre-tensioning steel k_1=5 & k_2=9)

Accordingly, a moderate nonlinear crack reopening model was introduced to describe the transition between closed and fully open crack states under cyclic loading, with fibre bridging influencing the post-reopening response. The effective steel stress at a given load level was therefore obtained by interpolating between closed-crack and cracked section responses, defined by Eq. (4). Note that an average stress factor (ψ) was introduced to convert the local peak steel stress obtained from cracked section equilibrium into an effective cyclic stress range that accounts for tension stiffening, crack spacing and stress redistribution. Separate values of ψ were adopted for PO and PF to reflect their different post-cracking performance, capturing the contribution of fibres in reducing stress concentration. Subsequently, the prestressing steel's fatigue life under constant-amplitude cyclic loading was estimated in accordance with the fib Model Code 2010, defined in terms of the stress range, with failure governed by a bilinear S-N relationship. The effective stress range in the prestressing steel ($\Delta\sigma_{s,eff}$) obtained from the

sectional analysis was adopted as the fatigue-driving parameter to determine the number of cycles to failure (N_f), as defined in Eq. (5). The resulting fatigue life predictions are subsequently compared with the mean experimental results to assess the accuracy and reliability of the adopted analytical approach. Therefore, the proposed methodologies provide a practical and physically interpretable framework for fatigue life prediction through a dual-approach verification framework, namely stiffness-based and stress-based analyses, each capturing different aspects of the sleeper response.

3 Results and Discussion

Fatigue testing was conducted under constant-amplitude cyclic loading in accordance with AS1085.14 and required an average of 35 days to reach 3 million load cycles. The fatigue performance of both PO and PF sleepers was evaluated and subsequently compared with analytical predictions from the stiffness- and stress-based approaches. Fig. 3 illustrates the experimental deflection-cycle results under maximum load (P_{max}) for all sleepers.

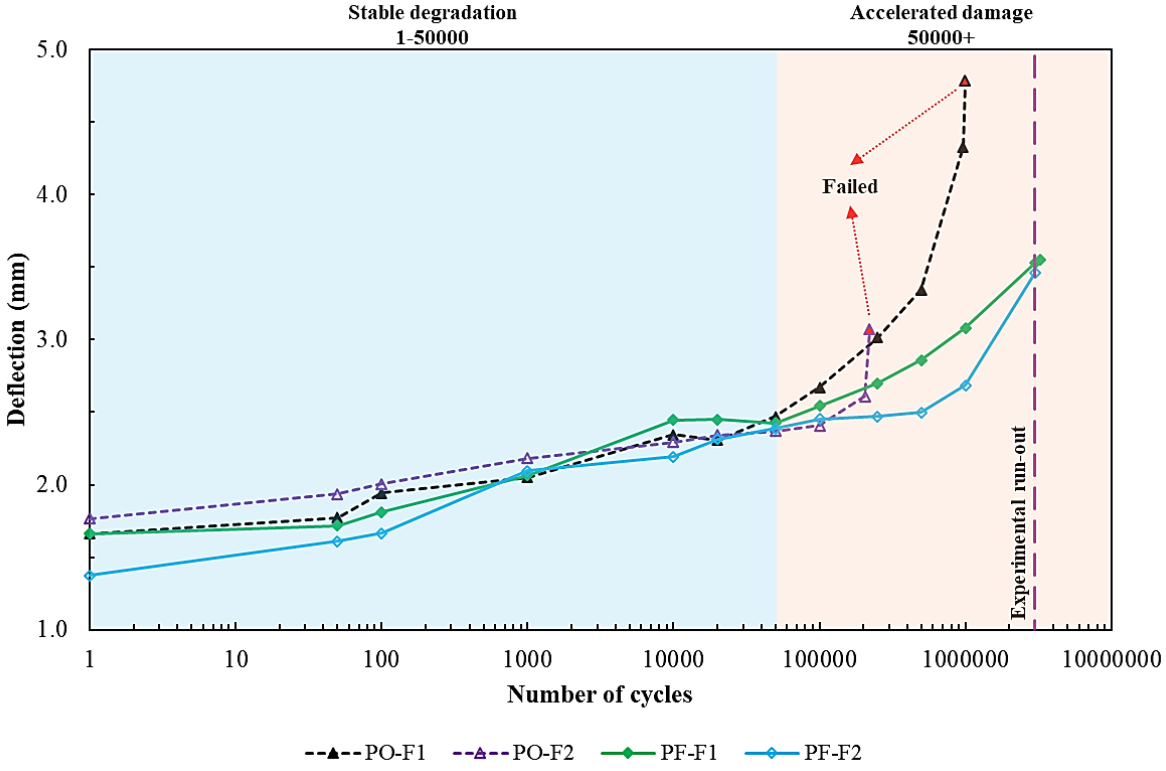


Fig. 3: Log deflection-cycle at maximum load

The experimental results showed that the conventional sleepers (PO-F1 & PO-F2) failed at approximately 222,472 and 991,400 cycles, both below one million cycles, indicating a relatively rapid accumulation of damage under cyclic loading. In comparison, the fibre reinforced sleepers (PF-F1 & PF-F2) exhibited significantly improved fatigue performance, achieving experimental run-out conditions by exceeding 3×10^6 cycles without failure. As the sleepers were pre-cracked prior to fatigue loading, initial deflections corresponding to early damage were observed, with PF exhibiting, on average, 11.5% lower deflections than PO, attributed to the contribution of fibre bridging in limiting crack opening and increasing post-cracking stiffness.

During cyclic loading, deflections increased progressively with the number of cycles due to stiffness degradation, with an initial stage of relatively low-rate deflection growth for all specimens, corresponding to stable crack development. Subsequently, an accelerated damage phase beyond 5×10^4 cycles led to the failure of PO sleepers, whereas PF exhibited a more progressive degradation response, with the average deflection being 19% lower. This behaviour indicates improved crack control and reduced stiffness loss, as further examined in the stiffness-degradation-based fatigue assessment that compares the evolution of stiffness for both PO and PF sleepers (Fig. 4).

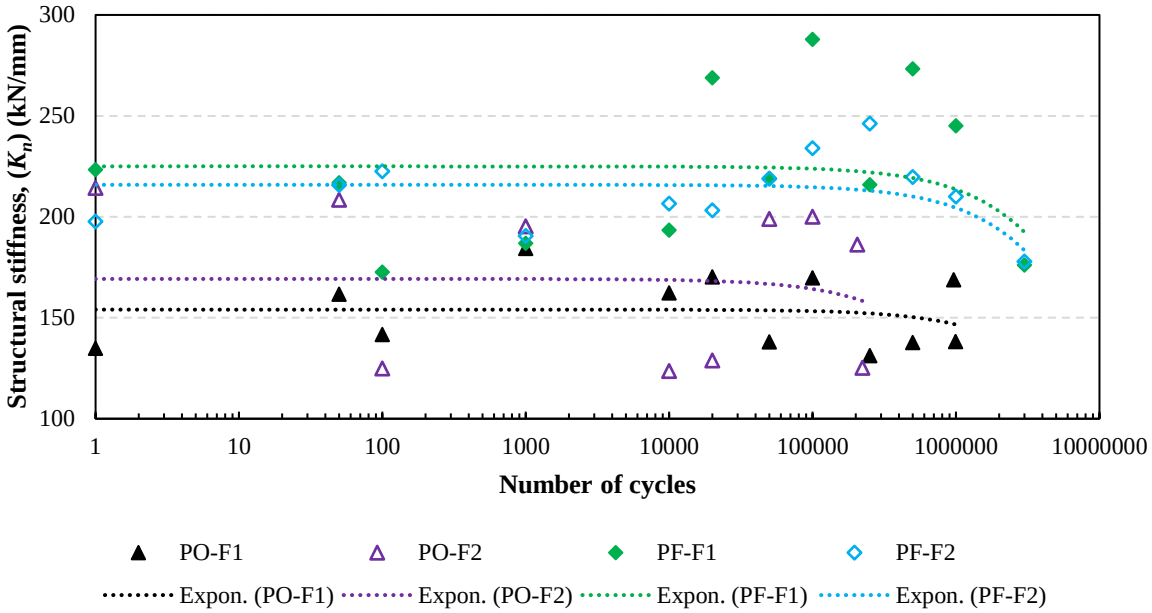


Fig. 4: Structural stiffness vs. load-cycles illustrating exponential degradation in PO and PF

The evolution of structural stiffness (K_n) with increasing load cycles was modelled using an exponential trendline, reflecting progressive, nonlinear damage accumulation. Based on the results, PO sleepers exhibited a steeper exponential decay, indicating faster stiffness degradation and earlier fatigue failure compared to PF, which maintained higher stiffness (i.e. flatter degradation) with a reduced rate of damage progression. The difference in exponential decay rates provides an empirical indicator of fatigue performance, with the lower degradation rate observed for PF corresponding to an increase in fatigue life of ~4.15 times that of PO sleepers. Note that apparent stiffness increases in PF are attributed to crack stabilisation, fibre engagement and sensitivity of stiffness calculations, rather than true material hardening, with overall behaviour governed by fatigue degradation. Accordingly, while this relationship offers a useful measure of the relative improvement in fatigue resistance, it should be interpreted as a comparative indicator rather than a direct predictive tool, with the stress-based approach providing a more rigorous assessment of fatigue life.

Based on the effective stress range calculated from the force-equilibrium model, the fatigue behaviour was interpreted in terms of cyclic stress demand in the prestressing steel. Accordingly, the analysis indicated that PO sleepers were subjected to a 15% higher effective stress range than PF, consistent with their earlier fatigue failure and reduced post-cracking load redistribution. This difference in stress demand explains the observed variation in fatigue performance and is further supported by analytical predictions that showed good agreement

with the experimental results, accurately estimating failure cycles (N_f) of approximately 8.8×10^5 for PO and 3.3×10^6 for PF. A comparison of the experimental results and analytical stress-based predictions is summarised in Table 2.

Overall, both approaches consistently capture the observed fatigue behaviour, with the stiffness response providing an empirical measure of damage progression and the stress assessment explaining the underlying mechanism controlling fatigue life. The agreement between these observations reinforces the dual-approach verification framework and highlights the role of fibre reinforcement in reducing damage accumulation and extending fatigue life in railway sleepers.

Table 2: Summary of experimental and analytical fatigue performance (Camille et al., 2025)

Specimen	**Avg. Static Capacity (kN)**		**Number of cycles to failure**	
	P_{cr}	P_u	**Experimental**	**Stress-based analytical**
PO-F1	220	453	222,472	883,341
PO-F2			991,400	
PF-F1	232	477	> 3×10^6 (run-out)	3,312,391
PF-F2				

4 Concluding remarks

In this study, the fatigue performance of prestressed concrete sleepers (i.e., PO & PF) was evaluated using a dual-approach framework that combined stiffness- and stress-based assessments and was validated against the experimental results. From the comparison herein, the following conclusions were drawn:

- PF sleepers demonstrated significantly improved fatigue behaviour, achieving experimental run-out beyond 3×10^6 cycles, while PO failed below 3×10^6 cycles.
- The stiffness-based assessment emphasised the progressive damage behaviour, showing reduced degradation rates in PF and an estimated life improvement factor of ~4.1.
- The mechanistic interpretation through the analytical stress-based approach calculated a reduced effective stress range (~15%) and a corresponding fatigue life increase of ~3.7, in good agreement with experimental results.

As a result, the consistency between stiffness and stress responses confirmed the reliability of the proposed dual-approach verification framework, demonstrating that macro synthetic fibre reinforcement enhances fatigue performance through improved crack control, stress redistribution and reduced stress concentration, ultimately enabling a more resilient and durable sleeper design with improved track performance and reduced maintenance requirements.

5 Acknowledgements

The authors gratefully acknowledge the Australian Research Council's Industrial Transformation Training Centres Scheme (ARC Training Centre for Advanced Technologies in Rail Track Infrastructure: IC170100006), which provided the catalyst for undertaking this research, as well as BarChip Inc and Western Sydney University for their support of the authors' work described herein.

6 References

Camille, C., Kahagala Hewage, D., Mirza, O., & Clarke, T. (2022). Full-scale static and single impact testing of prestressed concrete sleepers reinforced with macro synthetic fibres. *Transportation Engineering*, *7*, 100104. https://doi.org/https://doi.org/10.1016/j.treng.2022.100104

Camille, C., Kahagala Hewage, D., Mirza, O., & Clarke, T. (2025). *Enhancing the fatigue resistance of prestressed concrete sleepers using macro synthetic fibres* CORE 2025: Conference on Railway Excellence: Kaitiaki - Guarding the Future, Auckland. https://search.informit.org/doi/10.3316/informit.T202512090001530088184958 2

Camille, C., Kahagala Hewage, D., Mirza, O., Mashiri, F., Kirkland, B., & Clarke, T. (2021). Performance behaviour of macro-synthetic fibre reinforced concrete subjected to static and dynamic loadings for sleeper applications. *Construction and Building Materials*, *270*, 121469. https://doi.org/https://doi.org/10.1016/j.conbuildmat.2020.121469

Camille, C., Kahagala Hewage, D, Mirza, O, Mashiri, F, Kirkland, B, Clarke, T. (2021). Post-cracking strength classification of macro-synthetic fibre reinforced concrete for sleeper application.*Fibre Reinforced Concrete: Improvements and Innovations* RILEM-fib International Symposium on Fibre Reinforced Concrete: Improvements and Innovations, BEFIB 2020,

Camille, C., Mirza, O., Kirkland, B., & Clarke, T. (2022). Structural behaviour of prestressed concrete sleepers reinforced with high-performance macro synthetic fibres. *Engineering Failure Analysis*, *141*, 106671. https://doi.org/https://doi.org/10.1016/j.engfailanal.2022.106671

European Standard. (2006). Fibres for concrete - Part 2: Polymer fibres - Definitions, specifications and conformity, EN14889-2:2006. In. European Committee for Standardization (CEN).

Goto, K., Watanabe, T., Hosoda, M., & Minoura, S. (2018). Commentary: Fatigue Life Assessment Method for Prestressed Concrete Sleepers [General Commentary]. *Frontiers in Built Environment, Volume 4 - 2018*. https://doi.org/10.3389/fbuil.2018.00019

Kahagala Hewage, D., Camille, C., Mirza, O., Mashiri, F., Kirkland, B., & Clarke, T. (2024). Effect of post-peak flexural toughness on the residual performance of macro synthetic fibre reinforced concrete sleepers subjected to impact loading. *Engineering Structures*, *307*, 117913. https://doi.org/https://doi.org/10.1016/j.engstruct.2024.117913

Nairn, J., & Stevens, N. (2010). *Rational Design Method for Prestressed Concrete Sleepers* Conference on Railway Engineering - CORE 2010: Rail, Rejuvenation and Renaissance, Wellington, N.Z. https://search.informit.org/doi/10.3316/informit.761251021902120

Parvez, A., & Foster, S. J. (2017). Fatigue of steel-fibre-reinforced concrete prestressed railway sleepers. *Engineering Structures*, *141*, 241-250. https://doi.org/https://doi.org/10.1016/j.engstruct.2017.03.025

Standard Australia Online. (2012). Railway Track Materials - Part 14: Prestressed concrete sleepers, AS1085:14:2012. In. SAI Global database.

You, R., Li, D., Ngamkhanong, C., Janeliukstis, R., & Kaewunruen, S. (2017). Fatigue Life Assessment Method for Prestressed Concrete Sleepers [Review]. *Frontiers in Built Environment, Volume 3 - 2017*. https://doi.org/10.3389/fbuil.2017.00068

On the fatigue performance of ultra-high-performance and strain hardening cementitious composites

Rennan Liberato[1], Iranildo Silva Junior[1], Vitor Monteiro[2] and Flavio Silva[1]

[1]Department of Civil and Environmental Engineering (DEC), Pontifical Catholic University of Rio de Janeiro (PUC-Rio),

[2]Civil Engineering Program (PEC), Alberto Luiz Coimbra Institute for Graduate Studies and Research in Engineering (COP-PE/UFRJ)

Abstract

The comprehensive study of the fatigue deterioration of concrete structural members is vital when it comes to the design of elements under cyclic loading such as offshore platforms, pavements and wind towers. Although the use of fibers can dramatically enhance fatigue life of concrete elements and promote serviceability performance over the years, the latest development of ultra-high-performance concrete (UHPC) and strain hardening cementitious composites (SHCC) opens a new level of mechanical performance that can be exploited in the next generation of special construction works. The present research consequently assesses the superior fatigue service performance of UHPC and SHCC in comparison with conventional steel fiber reinforced concrete (SFRC). While SFRC and UHPC mechanical degradation were studied in terms of pre-cracked prims under continuous bending cycles, fatigue tensile tests in pre-cracked dogbone specimens (dogbone shape) were carried on for the strain-hardening composite. SHCC and UHPC offered superior fatigue life, reaching 1,000,000 cycles without failure when subject-ed to an upper load level 0.70 of the peak stress. Conventional pre-cracked steel fiber reinforced concrete, in turn, reached failure under the same fatigue load level conditions around 10^5 cycles. Moreover, stiffness remained almost constant along the 1,000,000 cycles for both special cementitious composites, indicating minimum mechanical decay throughout its fatigue life. The strain-hardening behavior provided by SHCC and UHPC formulations show great potential in terms of fatigue mechanical performance and a promising solution to fatigue sensitive structures.

Keywords

Fiber reinforced concrete, fatigue, ultra-high-performance concrete, strain hardening cementitious composites, mechanical degradation

1 Introduction

The increasing need for more reliable and sustainable structures in civil engineering fosters the development of new materials, methodologies and techniques. Typical examples include bridge decks (Lachance, 2016), offshore platforms (DNV-C502, 2012), pavements (Koorikkattil, 2022) and energy infrastructures, which are specially driven by global shift to renewable energy sources. Many of these infrastructures are subjected to repetitive (cyclic) loading along its service life, reaching from 10^3 cycles for low-cycle constructions (Nguyen, 2022) up to 10^9 for super-high-cycle installations, such as wind turbines (Chen, 2023). The cyclic loading can be caused by both natural (wind, waves and thermal variations) and anthropogenic actions (machine vibrations and traffic loads), leading to structural degradation and mechanical decay over time.

Traditionally, fatigue has been studied in the context of metal structures (Zenner, 2019), which have been linked to catastrophic failures when subjected to stress ranges significantly below the material strength. With the subsequent growth of structural applications subjected to cyclic loading made of (reinforced) concrete, fatigue has become a key aspect in the evaluation of the service life and mechanical deterioration over time (Wei, 2023). More recent studies have assessed the fatigue behavior of fiber reinforced concrete (FRC) in the post-cracked regime to verify the effect of fiber bridging after the fracture process zone has been formed (Bochino, 2025; Monteiro, 2023; Carlesso, 2019). The fatigue tests are generally carried out in two stages. First, the specimen is pre-cracked until a predetermined crack opening is reached. Thereafter, the specimen is subjected to cyclic loading until failure or a fixed number of cycles (around 10^6 and $2x10^6$ cycles) is achieved (Carlesso, 2019). Although part of the published papers assesses the fatigue performance in bending, direct tensile tests have also been applied to better capture the post-cracking response (Nagai, 2025; Isojeh, 2017).

Alongside the development of new methodologies and models to investigate FRC fatigue degradation, a new generation of high-performance cementitious materials has been proposed as alternatives for significantly enhancing the service life of infrastructure works (Yu, 2017; Wang, 2020; Makita, 2013). Strain-hardening cementitious composites (SHCC) are part of the group of highly ductile FRC materials with a promising capacity to withstand mechanical decay and multiple crack formation (Wang, 2020; Junger, 2025). Ultra-high-performance concrete (UHPC), in turn, is defined as cementitious composites with compressive strength greater than 150 MPa and enhanced durability, typically reinforced with steel fibers to provide post-crack strength and enhanced fracture properties (Makita, 2013; Zhou, 2018). Due to their capacity to provide pseudo-ductile behavior after matrix cracking, SHCC and UHPC can become effective candidates to improve the structure capacity to resist the mechanical decay associated with dynamic loadings, such as impact, traffic and ocean waves (Junger, 2025; Nagai, 2025; Cerqueira, 2023).

In the present work, fatigue life of steel fiber reinforced concrete (SFRC), UHPC and SHCC are compared aiming to verify the capacity of the new generation of cement composites to withstand mechanical degradation and control crack opening in service. Comprehensive experimental work was carried out to study SHCC and SFRC fatigue life in tension. Composite specimens were, first, pre-cracked under quasi-static loading and, thereafter, fatigue tests were initiated under distinct loading ranges. UHPC fatigue results were derived from past research carried out by Cerqueira (2023). The substantial increase in fatigue life was overall evaluated

with the purpose of investigating the application of the new generation of cementitious composites in structural applications.

2 Experimental program

2.1 Materials

2.1.1 Steel fiber reinforced concrete

The steel fiber reinforced concrete was formulated using Brazilian CPII F-32 Portland cement, supplemented with fly ash, silica fume, and silica flour (Mesh 325). The fine aggregates included two types of river sand (particle sizes: 0.15–0.85 mm for S_1 and 0.15–4.8 mm for S_2) and a coarse aggregate with a maximum diameter of 9.5 mm. MasterGlenium 51 superplasticizer (29% solid content) and MasterMatrix VMA 358 viscosity-modifying admixture were employed. Despite a relatively high superplasticizer dosage (5.5% by cement mass), the matrix and FRC compositions remained stable without visible segregation. Applied hooked-end steel fiber (SF) in the mix reported 35 mm of length, 0.75 mm of diameter of and 45 of aspect ratio. Fiber volume fractions were set at 20 (C20SF), 40 (C40SF), and 60 (C60SF) kg/m³. The resulting matrix achieved a 28-day compressive strength of 50 ± 3 MPa under saturated curing. More details on the mix compositions are displayed in Table 1. Matrix, C20SF, C40SF and C60SF reached a slump flow of 750 mm, 770 mm, 755 mm and 785 mm respectively.

Table 1: Mix compositions for SFRC

Constituent	Matrix	C20SF (0.25%)	C40SF (0.50%)	C60SF (0.75%)
Coarse aggregate (kg/m³)	492	478.57	465.04	438.04
Sand (S_1) (kg/m³)	827	827	827	827
Sand (S_2) (kg/m³)	100	100	100	100
Silica Mesh 325 (kg/m³)	70	70	70	70
Cement (kg/m³)	360	360	360	360
Fly Ash (kg/m³)	168	168	168	168
Silica Fume (kg/m³)	45	45	45	45
Water (kg/m³)	164	164	164	164
Superplasticizer (%)	5.50	5.50	5.50	5.50
Viscosity modifying admixture (%)	0.75	0.75	0.75	0.75
Steel fiber SF1 (kg/m³)	0	20	40	60
Steel fiber SF2 (kg/m³)	0	0	0	0

Sand S1: particle size between 0.15–0.85 mm
Sand S2: particle size between 0.15–4.8 mm

2.1.2 Strain-hardening cementitious composite

The SHCC matrix was formulated using CP-V ARI cement (ASTM Type III, 32 MPa at 28 days), natural river sand (0.075–0.212 mm), and POZOFLY fly ash. Rheological properties and fiber dispersion were optimized using BASF Glenium 51 (polycarboxylic ether superplasticizer) and ADITIBRAS VISCO-BRAS 200 (powdered VMA) to ensure cohesion and prevent segregation. Reinforcement consisted of ADMIXUS® UHMWPE fibers (length of 13 mm, diameter of 18 μm, tensile strength of 3000 MPa, and modulus of elasticity of 114 GPa) at a 2% volume fraction. Detailed proportions are provided in Table 2.

Table 2: Proportion of materials used in SHCC (kg/m³).

Cement	Fly Ash	Sand	Water	VMA	Superplasticizer	Fibers *(%)*
505	621	536	336	1.2	11.7	2

2.2 Fatigue tests

2.2.1 Flexural fatigue tests

The fatigue behavior of pre-cracked SFRC and UHPC was evaluated using prisms subjected to cyclic flexural loading following EN 14651 (CEN, 2005) standards. Failure was defined as CMOD > 4 mm or reaching a 1,000,000 cycles cycle limit. The complete test setup can be studied at Monteiro (2023) and Cerqueira (2023). A clip gauge was utilized to monitor Crack Mouth Opening Displacement (CMOD) and damage evolution across three stages:

Stage 1 (Pre-cracking): A static phase controlled by CMOD at a rate of 0.05 mm/min up to 0.10 mm, followed by 0.2 mm/min until reaching 0.5 mm.

Stage 2 (Unloading): Specimens were unloaded at 5 kN/min until the force on the loading cell reached 0.

Stage 3 (Fatigue): Sinusoidal loading was applied at 6 Hz, initiated from the mean load (P_{med}) between P_{low} and P_{upp}. Parameters included load ratio ($R = P_{low}/P_{upp}$) of 0.3 and stress levels ($S = P_{upp}/P_{R,1}$) of 0.70, 0.80, and 0.90. The fatigue test was divided into three stages as depicted in Figure 1.

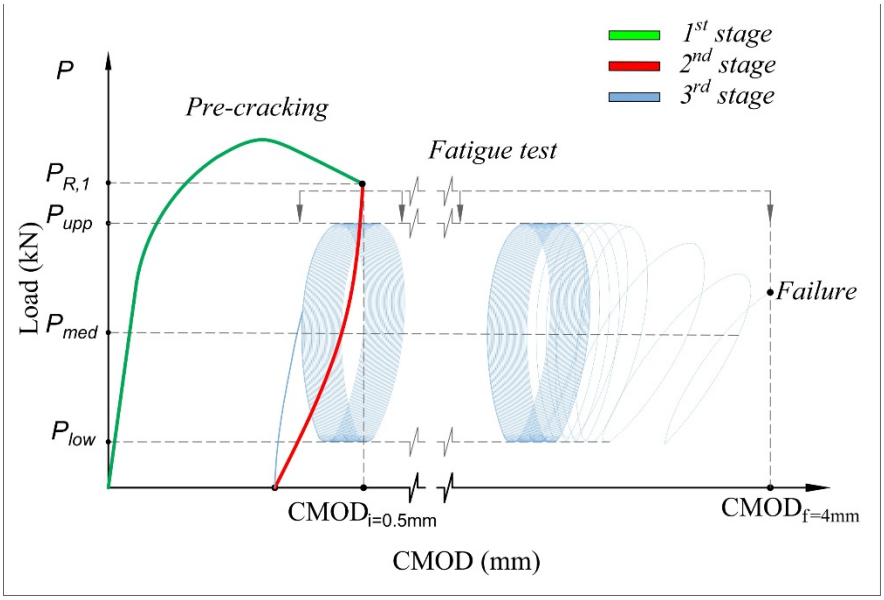


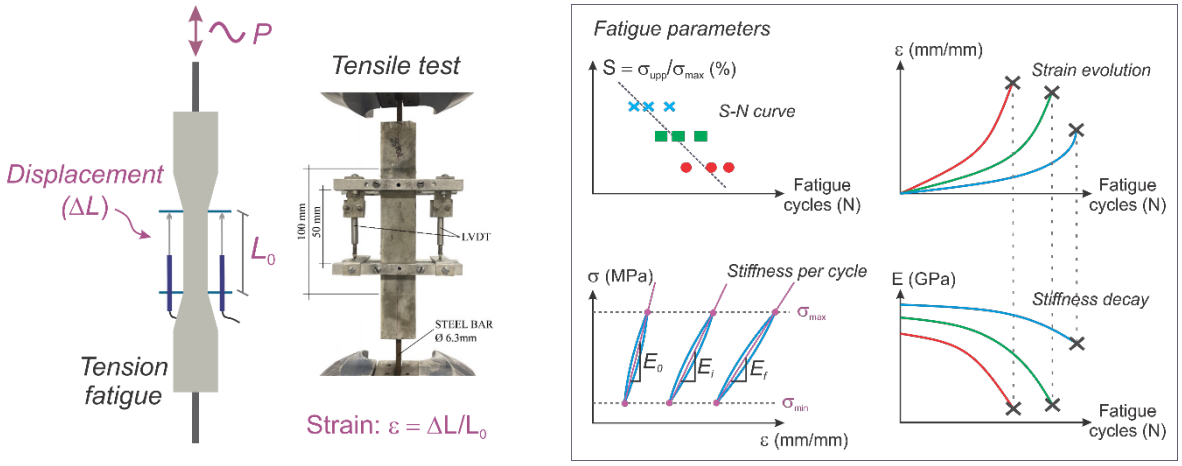
Figure 1: Flexural fatigue test procedure.Direct tensile fatigue test

Direct tensile fatigue tests were designed to evaluate the SHCC behavior under specific damage levels and structural integrity conditions. To achieve this, two distinct deformation states were established for the pre-cracking phase. During this stage, specimens were subjected to monotonic tensile loading until reaching average axial deformations of 1% and 3% (equivalent to axial strains of 0.01 and 0.03, respectively). These deformations were monitored using LVDTs over a 50 mm reference length. Once the target deformation was reached, the

specimens were unloaded, and the peak stress values at those specific strains were recorded. These values served as the reference tensile strength for determining the maximum and minimum cyclic load limits subsequently applied to the pre-cracked samples.

The fatigue loading program utilized three stress levels (S = 90%, 80%, and 70%) relative to the tensile strength recorded at the respective pre-crack deformation levels. The reference tensile stress for the fatigue tests (σ_{max}) was set as the recorded stress at 1% and 3% of average axial deformation aiming to simulate the fatigue behavior of the composite in service. Throughout the testing, the stress ratio ($\sigma_{min}/\sigma_{max}$) was maintained constant at 0.3. A sinusoidal loading frequency of 6 Hz was applied until specimen failure or until a limit of 10^6 cycles was reached. High-frequency data acquisition was performed at 512 Hz, specifically capturing the initial 100 cycles, intervals of every 1000 cycles, and the final 100 cycles of the fatigue life to monitor damage evolution. The experimental procedure for the SHCC tensile fatigue study is displayed in Figure 2a.

Fatigue degradation in cementitious materials is generally studies in terms stiffness decay, strain evolution and energy dissipation along the cycles. S-N curves, in turn, the sum of the load changes that the material can endure until it reaches fracture. Aiming to study the gain of service life of SHCC and UHPC under fatigue loading, and overall analysis of S-N curves is displayed. Figure 2b brings the main fatigue parameters applied in fatigue studies.



(a) (b)

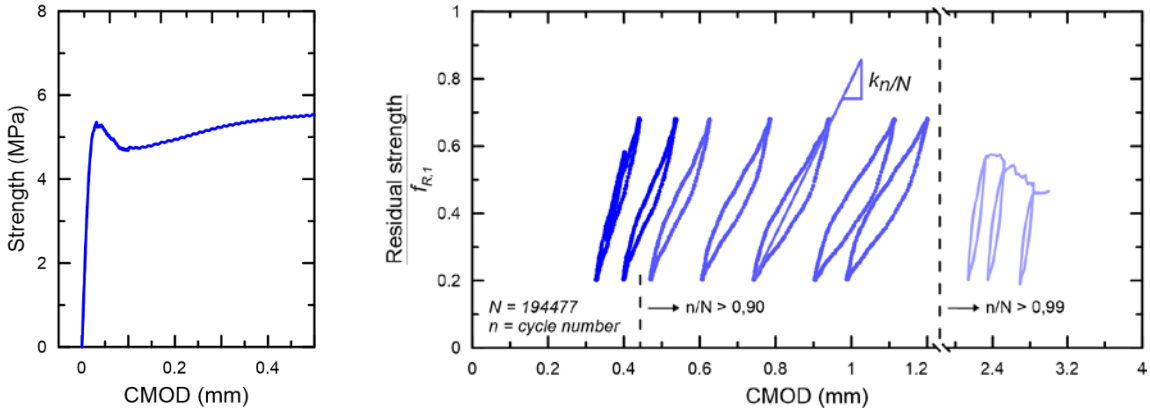
Figure 2: Direct tensile fatigue tests: (a) experimental setup and (b) governing parameters in fatigue analysis.

3 Test Results

Figure 3 displays the fatigue test results for one SFRC specimen at an upper stress level of 0.70 (S = 0.70). The load oscillations promote apparent decrease in bending stiffness along the cycles, defined as the inclination between cycle's maximum and minimum loads. The increase in the hysteresis cycles indicates prominent energy dissipation of the material, which is directly correlated with the mechanical decay and the fall of the fiber bridging capacity of the cracked section (Monteiro, 2023; Carlesso, 2019).

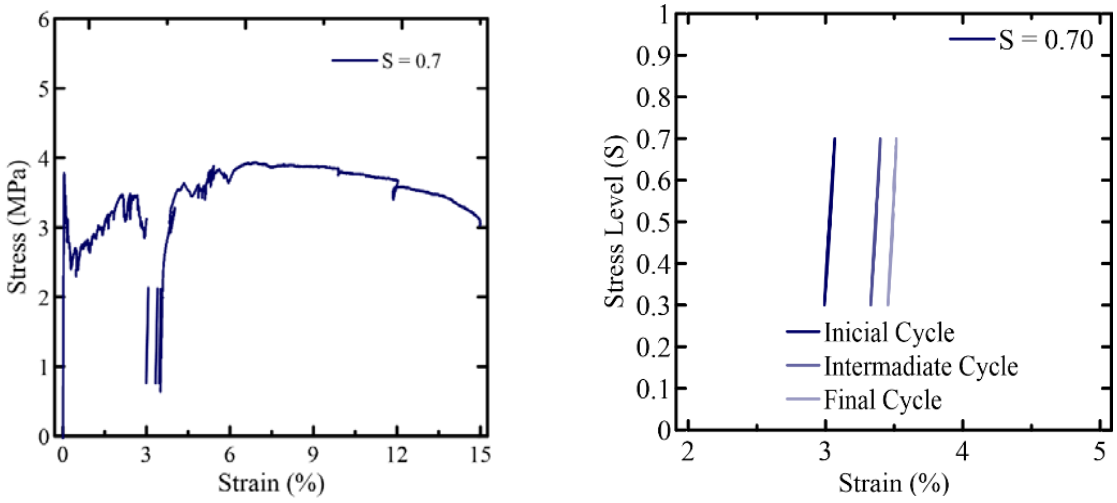
Figure 4 brings the mechanical degradation of the SHCC during and after the fatigue test in terms of the hysteretic cycles corresponding to the beginning, intermediate phases, and end of

the tests under S = 0.7. It is possible to verify a lower decrease in stiffness of the SHCC in relation to conventional SFRC. The strain-hardening composite can maintain its stiffness during fatigue loading even after 1% of strain prior the load reversals.



(a) (b)

Figure 3: Fatigue test on SFRC composite: (a) specimen pre-crack until reaching 0.50 mm of CMOD and (b) evolution of hysteresis cycles throughout the fatigue loading.



(a) (b)

Figure 4: Fatigue test results for SHCC composite after initial strain of 3%:(a) mechanical behavior before and after the fatigue test and (b) hysteresis cycles during the fatigue test.

Figure 5a show the fatigue life for the SFRC and SHCC after distinct initial strain values. SHCC-1% and SHCC-3% correspond to the fatigue tests after and initial strain of 1% and 3%, respectively. Figure 5 also displays the mean fatigue life curve through a linear regression analysis, which correlates load level S with the logarithm of the cycles before failure of the specimen (log10(N)). Since the majority of the results for SHCC-1% did not reach failure, it was not possible to estimate a linear regression for this case. A more comprehensive probabilistic analysis could not be developed since the predominance of run-outs restricted the development of more sophisticated probabilistic models of the fatigue life of the SHCC (Carlesso, 2019; Monteiro, 2023).

The increase in pre-damage shows a considerable reduction in fatigue life of the SHCC. While SHCC-1% reached 1,000,000 cycles without failure for a load level (S) of 0.80, the application of an initial strain of 3% significantly reduced the fatigue life of the composite. For this case failure occurred around 800,000 and 600,000 cycles. On the other hand, it is evident the major difference in fatigue life between SFRC and the studied strain-hardening composite.

Figure 5b compares the fatigue life observed in current experimental research with the one achieved by the developed 135 MPa UHPC composition from Cerqueira (2023). Table 3 summarizes the fatigue life reached by all compositions in terms of the applied stress level. Since the research for the assessed materials were carried out in distinct moments, each material presented a different number of fatigue tests. Similar to what was observed in Figure 5a, UHPC also promotes a significant gain in fatigue life in relation to SFRC. The number of cycles before failure for UHPC presents comparable results in relation to SHCC prior an initial strain of 3% (SHCC-3%) until a load level of 0.80. High result scatter is observed at S = 0.90.

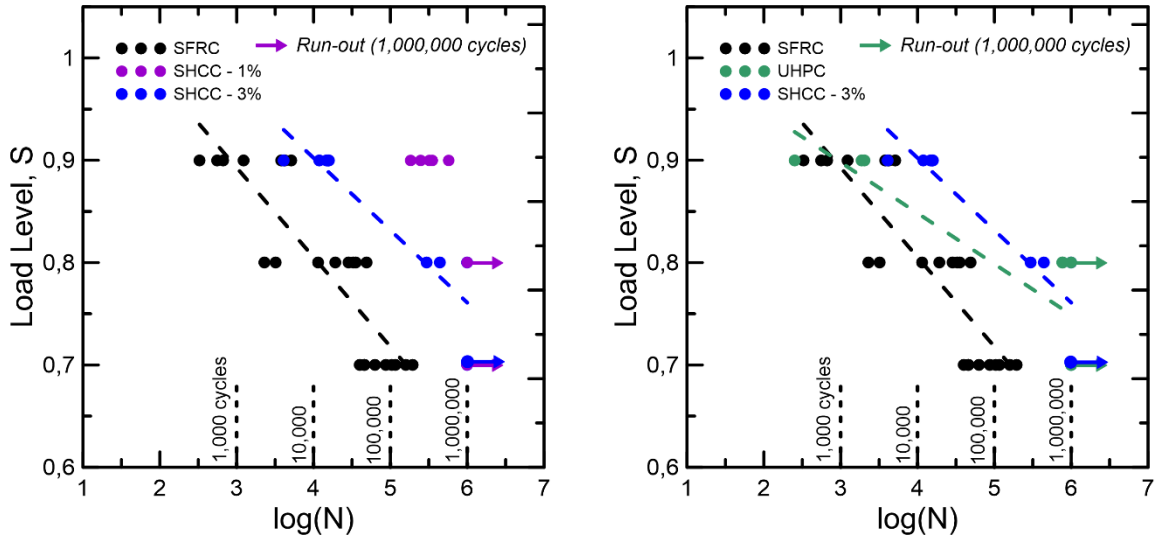


Figure 5: Comparison between the fatigue life of SFRC with (a) SHCC after initial strain of 1% (SHCC-1%) and 3% (SHCC-3%) and (b) UHPC and SHCC-3%

4 Analysis

When it comes to structural design for fatigue, restrictions are generally applied in terms of the applied stress ranges throughout the service life (Qiu, 2018). Fatigue limit state is directly linked to limit crack growth and mechanical deterioration during a pre-determined design life (Russel, 2006). While AASHTO LRFD Bridge Design Specifications (Russell, 2006) brings specific guidelines for fatigue analysis of structures with a 75-year design life for bridges, offshore structures (DNV-C502, 2012), a 25-year service life is correlated to endure up to 10^8 cycles without failure. For a material design perspective, present design guidelines demand $2x10^6$ cycles to evaluate the mechanical decay of materials in service under fatigue loading (DNV-C502, 2012).

For both regulations, damage evolution and stress intensity factor threshold are key, since both parameters are correlated with service and strength limit states, respectively. Therefore, SHCC and UHPC show promising capacity to withstand the mechanical decay in service, since

both can resist with mechanical decay at high loading level (S = 0.80). While SFRC presents failure around 10^5 for 0.70 load level, SHCC and UHPC do not reach rupture after 1,000,000 cycles.

Present research on pre-cracked FRC still interrupts fatigue tests around $1x10^6$. Nagai (2025), in turn, reached 6.4 million cycles under tensile fatigue of UHPC specimens at 40% strength level. The results achieved by Nagai (2025) suggest that strain hardening cementitious composites may also reach around $1x10^7$ cycles at low load levels. However, there is still a lack of information on the fatigue limit of the SHCC

Table 3: Fatigue life for each studied concrete composition

Concrete composition	**Load level (S)**		
	0.90	**0.80**	**0.70**
SFRC	557	2305	116114
	1222	3195	104000
	663	11491	87300
	5104	28459	194483
	4248	35584	157934
	3778	48712	40025
	329	19301	45739
SHCC-1%	572666	1000000*	1000000*
	349521	1000000*	1000000*
	246769	1000000*	1000000*
	321541	1000000*	1000000*
	184112	1000000*	1000000*
SHCC-3%	11889	1000000*	1000000*
	14806	1000000*	1000000*
	15449	441047	1000000*
	15801	296884	1000000*
	4095	1000000*	1000000*
UHPC	1880	1000000*	1000000*
	2028	760988	1000000*
	252	773780	1000000*

**Test run-out after 1000000 cycles*

5 Concluding remarks

Present research brought an overall analysis of the potential gain in fatigue life with the application of the new generation of fiber reinforced cementitious composites SHCC and UHPC. The study involved the evaluation of the number of cycles before failure of pre-cracked steel fiber reinforced concrete specimens as references for the evaluation of the potential gain fatigue life of special composites. Direct tensile fatigue tests were carried out to evaluate fatigue behavior of the SHCC. Initial strains of 1% and 3% were applied to the specimens to study the fatigue behavior after initial degradation of the material in service. The results for UHPC under fatigue loading were collected from previous research in the literature. The main conclusions achieved from the present study:

- Results clearly indicate that the SHCC and UHPC exhibit significantly superior fatigue performance in relation to SFRC. While SFRC failed between 10^2-10^5 cycles for the studied stress levels, UHPC and SHCC-1% reached the run-out limit of 10^6

cycles at high load levels (S = 0.70-0.80) for the majority of the tests. The advanced composites can substantially increase the fatigue service life of structures subjected to cyclic loading.

- The magnitude of the initial strain prior to the fatigue test significantly modifies the fatigue performance of the SHCC. While specimens with an initial damage of 1% generally survived the run-out test routine (10^6 cycles) without failure, the increase in pre-damage to 3% strain results in considerable fatigue life decrease. Despite this reduction, SHCC specimens can still reach the fatigue performance observed of UHPC and far superior to SFRC. Both SFRC and UHPC were also pre-cracked before the application of the fatigue test routine.
- The strain-hardening behavior of SHCC allows the material to maintain stiffness and structural integrity along the fatigue cycles. SHCC experienced very limited mechanical degradation during cyclic loading with almost constant stiffness. On the other hand, SFRC does exhibit more progressive stiffness decay and energy dissipation along the deterioration. The strain-hardening and multiple-cracking mechanisms in SHCC strongly contribute to the delay mechanical decay during service, which are key to the design of concrete structures under repetitive loading.

6 Acknowledgements

All testing was conducted at the Laboratory of Structures and Materials of the Pontifical Catholic University of Rio de Janeiro. This study was financed in part by the Conselho Nacional de Desenvolvimento Científico e Tecnológico – Brasil (CNPq). This research is part of the cooperation project Aneel PD-0394-1905/2019 (Furnas – PUC-Rio) named “Determinação de parâmetros para Ensaios Mecânicos do Concreto Reforçado com Fibras (CRF) sob Condições Extremas de Carregamento em Empreendimentos de Geração Hidrelétrica e Eólica”. For more details about the project, please access www.fadiga.civ.puc-rio.br.

7 References

Bocchino, G., Davolio, M., Gutierrez, A., Burello, N., Lo Monte, F., Zampini, D., and Ferrara, L., 2025. “Experimental investigation of the flexural fatigue behaviour of a High-Performance Fibre Reinforced Concrete (HPFRC),” *Construction and Building Materials*, 489.

Carlesso, D., de la Fuente, A., and Cavalaro, S., 2019. “Fatigue of cracked high performance fiber reinforced concrete subjected to bending,” *Construction and Building Materials*, 220, pp444-455.

CEN, 2005. *EN 14651: Test method for metallic fibre concrete – Measuring the flexural tensile strength (limit of proportionality (LOP), residual)*. European Committee for Standardization, Brussels.

Cerqueira, N., Monteiro, V., Souza, F., Cardoso, D., and Silva, F., 2023. “Mechanical degradation of ultra-high performance concrete under flexural fatigue loading,” *Construction and Building Materials*, 391.

Chen, C., Shen, X., Zhou, Z., and Hua, X., 2023. “Feasibility study of a steel-UHPFRC hybrid tower for offshore wind turbines,” *Ocean Engineering*, 288.

DNV-OS-C502, 2012. *Offshore Concrete Standard*, Norwegian standards body, Oslo.

Isojeh, B., El-Zeghayar, M., and Vecchio, F., 2017. "Fatigue Behavior of Steel Fiber Concrete in Direct Tension," *Journal of Materials in Civil Engineering*, 29(9).

Junger, D., and Mechtcherine, V., 2025. "Cyclic loading effects on high-strength strain-hardening cement-based composites with PE fibres (PE-SHCC): crack development and material degradation analysis," *Materials and Structures*, 58 (330).

Koorikkattil, A., Nayar, S., and Venudharan, V., 2022. "Flexural fatigue design of steel fibre reinforced concrete pavements: a comparative study," *Road Materials and Pavement Design*, 24(9), pp2301-2321.

Makita, T., and Brühwiler, E., 2013. "Tensile fatigue behaviour of ultra-high performance fibre reinforced concrete (UHPFRC)," *Materials and Structures*, 47, pp475-491.

Monteiro, V., Cardoso, D., and Silva, F., 2023. "A novel methodology for estimating damage evolution and energy dissipation for steel fiber reinforced concrete under flexural fatigue loading," *International Journal of Fatigue*, 166.

Nagai, Y., Ichinomiya, T., Kosaka, T., and Ferrara, L., 2025. "Investigating parameters governing UHPFRC tensile fatigue behaviour via direct tensile tests on dog-bone shaped specimens," *Construction and Building Materials*, 503.

Nguyen, D., Thai, D., and Lam, M., 2022. "Synergy in Flexure of High-Performance Fiber-Reinforced Concrete with Hybrid Steel Fibers," *Journal of Materials in Civil Engineering*, 34(6).

Qiu, J., Aw-Yong, W. L., and Yang, E. H., 2018. "Effect of self-healing on fatigue of engineered cementitious composites (ECCs)," *Cement and Concrete Composites*, 94, pp145-152.

Russell, H. G., Miller, R. A., Ozyildirim, H. C., and Tadros, M. K., 2006. "Compilation and Evaluation of Results From High-Performance Concrete Bridge Projects, Volume II: Final Report," *Report No. FHWA-HRT-05-056*.

Wang, Y., Liu, F., Yu, J., Dong, F., and Ye, J., 2020. "Effect of polyethylene fiber content on physical and mechanical properties of engineered cementitious composites," *Construction and Building Materials*, 251.

Wei, X., Makhloof, D., and Ren, X., 2023. "Analytical Models of Concrete Fatigue: A State-of-the-Art Review," *Computer Modeling in Engineering & Sciences*, 134(1).

Yu, K., Wang, Y., Yu, J., and Xu, S., 2017. "A strain-hardening cementitious composites with the tensile capacity up to 8%," *Construction and Building Materials*, 137, pp410-419.

Zenner, H., and Hinkelmann, K., 2019. "August Wöhler – founder of fatigue strength research," *Steel Construction*, 12(2), pp156-162.

Zhou, M., Lu, W., Song, J., and Lee, G., 2018. "Application of Ultra-High Performance Concrete in bridge engineering," *Construction and Building Materials*, 186.

Thermal Performance of Fibre-Reinforced Concrete with Different Aggregate Types Under Elevated Temperatures

Ahmed M. Seyam, Rita Nemes[1]

[1]: Construction Materials and Technology Department, Faculty of Civil Engineering, Budapest University of Technology and Economics, Műegyetem rkp. 3., H-1111 Budapest, Hungary

Keywords: polypropylene fibres; aggregate; elevated temperature; residual strength; fire exposure

1 Introduction

Concrete structures exposed to fire or elevated thermal environments undergo significant physicochemical changes that lead to deterioration of stiffness, strength, and durability. These changes are primarily associated with moisture evaporation, decomposition of cement hydrates, thermal incompatibility between aggregates and cement paste, and progressive micro-cracking. As fire resistance becomes an increasingly critical design requirement, understanding the residual mechanical performance of concrete after high-temperature exposure is essential for post-fire assessment and resilient structural design.

Polypropylene (PP) microfibres are widely used to mitigate explosive spalling because melting at approximately 150–170 °C creates pathways for vapour-pressure relief (Komonen & Penttala, 2003; Zhang & Tan, 2020). Their effect on residual strength is less consistent and depends on the concrete composition; therefore, this study distinguishes spalling mitigation from post-heating mechanical strength.

Aggregate mineralogy, density, porosity and thermal expansion affect thermal gradients, paste–aggregate incompatibility and cracking under heating. Comparative data for PP-fibre concrete made with natural, lightweight and recycled coarse aggregates remain limited, particularly at temperatures up to 1000 °C.

This study compares the residual compressive and flexural tensile strengths of five PP-fibre concretes made with different coarse aggregates after exposure to temperatures up to 1000 °C. Because every mixture contained PP fibres, the experimental comparison isolates aggregate-type and curing-age effects; fibre-specific effects are interpreted only with reference to established literature and the observed absence of explosive spalling.

2 Experimental program

This research program tested the effect on residual compressive strength and residual flexural strength when using different aggregates—specifically, when quartz gravel was replaced in a composition optimized for fire resistance with PP fibres. Simply put, from this perspective, is it permissible to substitute the aggregate? Attention was paid to waste-based aggregates (crushed clay brick - CB) and an aggregate produced from waste (expanded glass - EG). We used two type of natural stone and two waste-based aggregates. Since the waste-based aggregate resulted in lightweight concrete, a standard lightweight aggregate also had to be included in the test. Five PP-fibre mixtures were produced with quartz river gravel (QZ.P), andesite (AN.P), expanded clay (EC.P), expanded glass (EG.P) and recycled crushed clay brick

(CB.P). QZ and AN are natural aggregates, EC and EG are lightweight aggregates, it is produced from recycled waste material, and CB is recycled aggregate, and P denotes polypropylene fibre. All mixes used 450 kg/m³ cement, water-cement ratio (w/c) 0.38, a constant fine-aggregate volume and 3.375 kg/m³ PP microfibres (0.75% of cement mass).

Two testing periods were used. These were longer than the standard 28-day and 90-day periods. The reason for this is that concrete remains moist for a long time after it is poured. This difference is particularly significant when the additive is porous, such as lightweight aggregates. The goal was to rule out this effect. The load-bearing concrete in a building structure is not enclosed until it is about 4 months old, so it is not exposed to fire, and use begins at the earliest when the concrete is approximately 8–9 months old.

For each mixture and each test age (120 and 240 days), 18 cubes (100 × 100 × 100 mm) and 18 prisms (70 × 70 × 250 mm) were allocated across the ambient condition and five target temperatures, giving three specimens per condition. Compressive and three-point flexural tensile strengths were determined in accordance with EN 12390-3 and EN 12390-5, respectively. Specimens were heated in electric furnaces to 200, 400, 600, 800 or 1000 °C using the recorded furnace temperature–time regime, which was compared with the ISO 834 curve but did not fully reproduce it. Each target temperature was maintained for 2 h, followed by 24 h of natural air cooling before residual testing. The 2 h dwell was used to promote temperature uniformity; internal temperature measurements were not included in this extended abstract.
The assessment comprised residual compressive strength, residual flexural tensile strength, and visual damage assessment, including cracking, surface degradation and explosive spalling.

3 Results and Discussion

3.1 Compressive Strength at Elevated Temperatures

All mixtures showed progressive compressive-strength degradation, but the response depended on aggregate type. At 200 °C, residual strength ranged from 83.1% to 95.1% at 120 days. The curve does not show the exceptionally high value of 150–200 C reported in the literature. The reason for this is that this value is caused by water evaporation, but the concrete in our test specimen was already 120 days old and therefore dry. In this way, the effect of the additive was truly examined, eliminating any differences caused by the initial water content.

At 1000 °C, the 120-day values ranged from 13.3% (in the case of expanded glass aggregate - EG.P) to 28.6% (in case of the natural quartz aggregate - QZ.P), demonstrating substantial aggregate-dependent variation without a uniformly superior natural- or lightweight-aggregate category.
Beyond 400 °C, strength deterioration accelerated because of dehydration and thermally induced micro-cracking. At 1000 °C, most mixtures had lost more than 80% of their initial compressive strength; the exception was mix (QZ.P) at 120 days, which retained 28.6%.
Changing the curing age from 120 to 240 days produced comparatively small and mixture-dependent changes relative to the effect of temperature and aggregate type.

Andesite performed exceptionally well at 400°C, but overall, crushed brick is very good. It can be said that, in terms of fire resistance, it can be relied upon just as much as quartz gravel. This is a positive result.

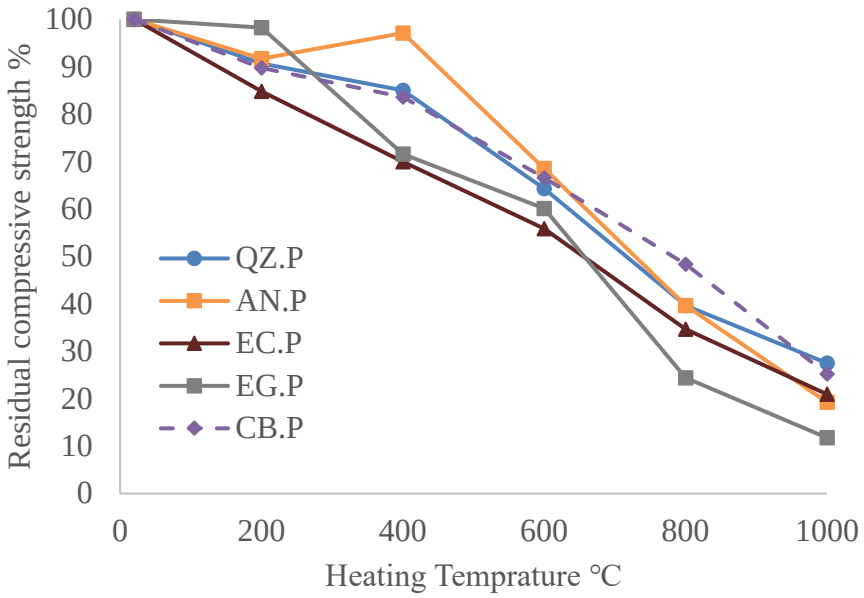


Figure 1: Relative residual compressive strength of PP-fibre concretes with different aggregate types at 120 days, – quartz river gravel (QZ.P), andesite (AN.P), expanded clay (EC.P), expanded glass (EG.P) and recycled crushed clay brick (CB.P).

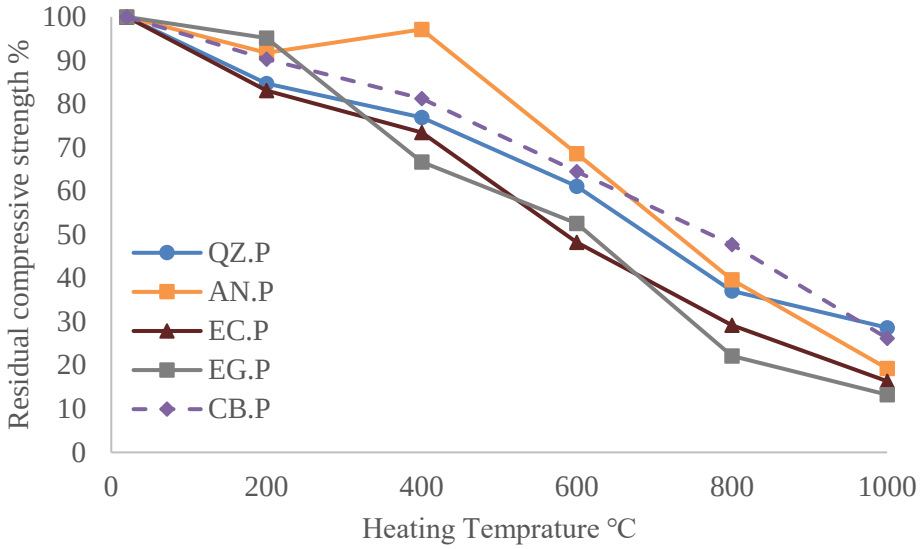


Figure 2: Relative residual compressive strength of PP-fibre concretes with different aggregate types at 240 days – quartz river gravel (QZ.P), andesite (AN.P), expanded clay (EC.P), expanded glass (EG.P) and recycled crushed clay brick (CB.P).

3.2 Flexural Strength Behaviour

Flexural tensile strength was generally more temperature-sensitive than compressive strength. At 1000 °C, the 240-day residual flexural strength ranged from 5.3% mix (AN.P) to 15.9% mix (QZ.P). Because no fibre-free control mixtures were included in this subset, the specific contribution of PP fibres to initial flexural performance cannot be quantified from these results.

Above the PP melting range, the fibres would not be expected to provide direct residual tensile reinforcement. Their established function is vapour-pressure relief and spalling mitigation rather than high-temperature strength retention (Zheng et al., 2014; Rawat et al., 2021).

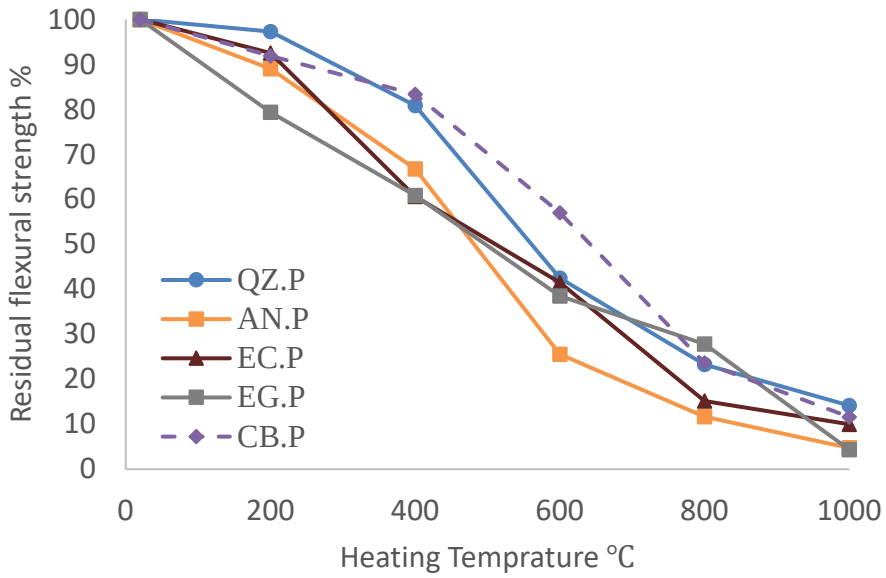


Figure 3: Relative residual flexural tensile strength of PP-fibre concretes with different aggregate types at 120 days – quartz river gravel (QZ.P), andesite (AN.P), expanded clay (EC.P), expanded glass (EG.P) and recycled crushed clay brick (CB.P).

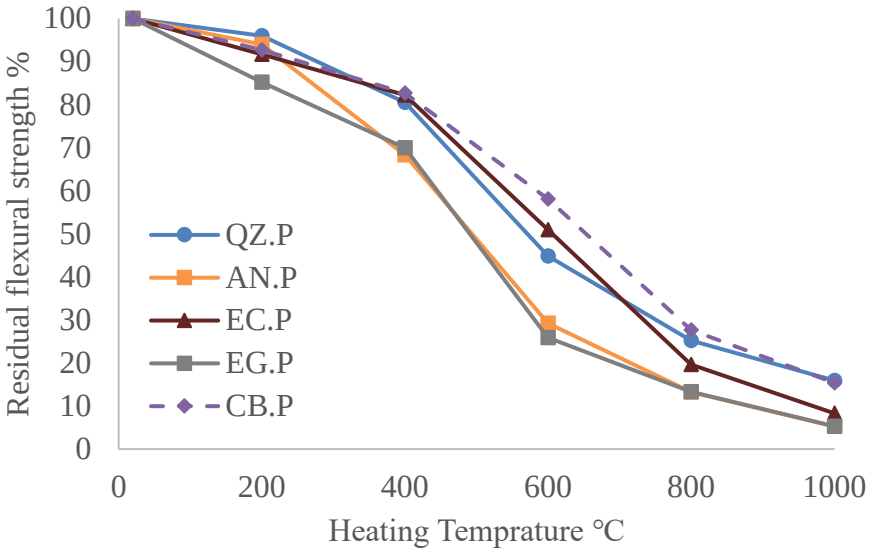


Figure 4: Relative residual flexural tensile strength of PP-fibre concretes with different aggregate types at 240 days – quartz river gravel (QZ.P), andesite (AN.P), expanded clay (EC.P), expanded glass (EG.P) and recycled crushed clay brick (CB.P).

4 Visual Damage Assessment

Visual inspection showed progressively greater cracking and surface degradation as temperature increased, particularly beyond 600 °C. Natural-aggregate mixtures generally

exhibited more visible surface cracking, while no explosive spalling was observed in the PP-fibre mixtures. These observations are qualitative and are not used as a substitute for the measured residual-strength results.

5 Key Findings and Implications

The experimental results show that:

Elevated temperatures caused severe mechanical degradation, particularly above 600°C.
Residual performance varied substantially with aggregate type; no single natural or lightweight category was superior at every temperature.
Aggregate-dependent differences were larger than the generally modest curing-age effect, although no statistical interaction analysis was undertaken.
No explosive spalling was observed in the PP-fibre mixtures; however, fibre-specific strength or crack-control benefits cannot be isolated without fibre-free controls but that was not the purpose of the study; it was chosen as the optimal approach based on the existing literature.

The results support aggregate-specific selection and assessment for concrete exposed to elevated temperatures, while avoiding broader claims about structural fire safety that were not directly measured.

6 Conclusions

The five PP-fibre concretes exhibited marked, aggregate-dependent differences in residual compressive and flexural strength after heating to 1000 °C. Temperature was the principal driver of degradation, while curing age from 120 to 240 days had a comparatively small and mixture-dependent influence. No explosive spalling was observed, consistent with the vapour-pressure-relief role associated with melting PP microfibres; however, the absence of fibre-free controls prevents attribution of strength or crack-control improvements to the fibres themselves. Accordingly, the results provide aggregate-specific evidence for post-heating material assessment rather than a direct measure of structural fire safety or a universally optimal mixture.

Crushed brick (CB) aggregate exhibited the most favourable performance. At both 120 and 240 days, it performed very similarly to the reference quartz gravel in terms of both compressive strength and tensile strength. Its use as a substitute does not require any modifications to the design.

When andesite (AN) is used, the compressive strength is favourable, outperforming quartz gravel up to 800 °C. However, the relative flexural strength is lower. This is not necessarily a problem because, given the composition of andesite, the flexural-to-compressive strength ratio is higher, so the actual value is already close to that of quartz gravel. This is worth noting during design if tensile strength must be explicitly calculated, especially at temperatures above 400 °C.

For typically lightweight aggregates such as expanded clay (EC) and expanded glass (EG), both the relative compressive strength and the relative flexural strength are significantly lower than the reference values. This is particularly true in the 400–600 °C range. For such highly porous, lightweight aggregates, the difference between the 120-day and 240-day results was the greatest. This may be due to the water initially present in the pores. In the case of EG, this effect is evident in the compressive strength at 200 °C.

When substituting EC and EG, fire resistance issues must be addressed differently than in the case of the reference quartz gravel aggregate concrete with PP microfibres.

7 Acknowledgements

The authors of the present manuscript are grateful to the Hungarian Scientific Research Fund (OTKA K 146724 project) for support.

8 References

Conforti, A., Zerbino, R., and Plizzari, G.A., 2018. “Influence of steel, glass and polymer fibers on the cracking behavior of reinforced concrete beams under flexure”, Structural Concrete, 1–11. doi: 10.1002/suco.201800079

Seyam, A.M., Shihada, S., and Nemes, R., 2020. “Effects of polypropylene fibres on ultra-high-performance concrete at elevated temperature”, Concrete Structures, 21, 11–16. doi: 10.32970/cs.2020.1.2

Nemes, R., Abed, M., Seyam, A.M., and Lublóy, É., 2022. “Behaviour of structural lightweight concrete produced with expanded clay aggregate after exposure to high temperatures”, Journal of Thermal Analysis and Calorimetry, 147, 8111–8118. doi: 10.1007/s10973-021-11167-6

Seyam, A.M., and Nemes, R., 2022. “Impacts of aggregate type and elevated temperature on flexural tensile strength of concrete”, in M. di Prisco, A. Meda and G.L. Balázs (eds), Proceedings of the 14th fib International PhD Symposium in Civil Engineering, Rome.

Seyam, A.M., and Nemes, R., 2023. “Age influence on compressive strength for concrete made with different types of aggregates after exposure to high temperatures”, Materials Today: Proceedings. doi: 10.1016/j.matpr.2023.06.403

Seyam, A.M., and Nemes, R., 2024. “Influence of elevated temperatures on the compressive strength of concrete made with different types of aggregate”, Periodica Polytechnica Civil Engineering doi: 10.3311/PPci.36784

Rawat, S., Lee, C.K., and Zhang, Y.X., 2021. “Performance of fibre-reinforced cementitious composites at elevated temperatures: A review”, Construction and Building Materials, 292, 123382. doi: 10.1016/j.conbuildmat.2021.123382

Zhang, D., and Tan, K.H., 2020. “Effect of various polymer fibers on spalling mitigation of ultra-high performance concrete at high temperature”, Cement and Concrete Composites, 114, 103815. doi: 10.1016/j.cemconcomp.2020.103815

Komonen, J., and Penttala, V., 2003. “Effects of high temperature on the pore structure and strength of plain and polypropylene fibre reinforced cement pastes”, Fire Technology, 39(1), 23–34.

Zheng, W., Luo, B., and Wang, Y., 2014. “Microstructure and mechanical properties of RPC containing polypropylene fibres at elevated temperatures”, Magazine of Concrete Research, *66(8), 397–408. doi: 10.1680/macr.13.00232*

European Committee for Standardization, 2006. EN 14889-2: Fibres for concrete - Part 2: Polymer fibres - Definitions, specifications and conformity.

Enhanced progressive collapse resistance in reinforced concrete frames using polypropylene fibers

Rutger Vrijdaghs[1], Krishnaa Subramanian[1]

[1]: Department of Civil Engineering, KU Leuven, Kasteelpark Arenberg 40, box 2448, Leuven, Belgium. Rutger.Vrijdaghs@kuleuven.be; Krishnaa.Subramanian@kuleuven.be

Abstract

Progressive collapse of reinforced concrete (RC) frame structures involves a disproportionate response following the loss of a primary load-bearing element, such as a column. Structural robustness in such scenarios depends on the development of alternate load paths through flexural action, compressive arch action (CAA), and catenary tensile action (CTA), which require significant ductility and deformation capacity. Although fiber-reinforced concrete (FRC) is known to enhance post-cracking behavior and energy dissipation, its influence on progressive collapse resistance in RC frames remains insufficiently quantified, particularly for polypropylene fibers.

This study experimentally evaluates the effect of polypropylene fiber-reinforced concrete on the progressive collapse behavior of RC beam–column sub-assemblages subjected to a middle column removal scenario. Four scaled specimens were tested under quasi-static displacement-controlled loading: two conventional RC frames and two FRC frames incorporating 0.5% polypropylene fibers by volume. The test setup provided strong boundary restraint, enabling the development of both CAA and CTA. Global and local responses were measured to capture damage evolution, axial deformation mechanisms, and failure modes.

The results demonstrate that polypropylene fibers lead to a modest increase in peak load capacity (approximately 6–9%) but, more importantly, a substantial enhancement in deformation capacity, ductility, and energy absorption. Fibers effectively delayed critical damage events such as transverse reinforcement failure and tensile rebar fracture, allowing significantly larger displacements and rotations. While the residual tensile contribution of the fiber matrix was limited due to the low strength class, improved concrete integrity at large deformations enhanced the development of alternate load paths.

A comparison with current Eurocode and Unified Facilities Criteria (UFC) provisions suggests that existing design rules may not fully reflect the robustness benefits provided by fiber-reinforced systems, highlighting the potential of polypropylene FRC as a complementary strategy for improving progressive collapse resistance.

Keywords

Fiber reinforced concrete, alternate load path, structural analysis, polypropylene fibers

1 Introduction

1.1 Progressive collapse resistance in reinforced concrete frames

Progressive collapse is characterized by a disproportionate propagation of structural damage following the local failure or removal of a primary load-bearing element, most commonly a column (Alshaikh et al, 2020). Once a column is lost, vertical loads are rapidly redistributed and the original bending moment distribution in the adjoining beams is changed, leading to significantly increased demands that are not explicitly considered in conventional design, see Figure 1 (Alshaikh et al, 2020).

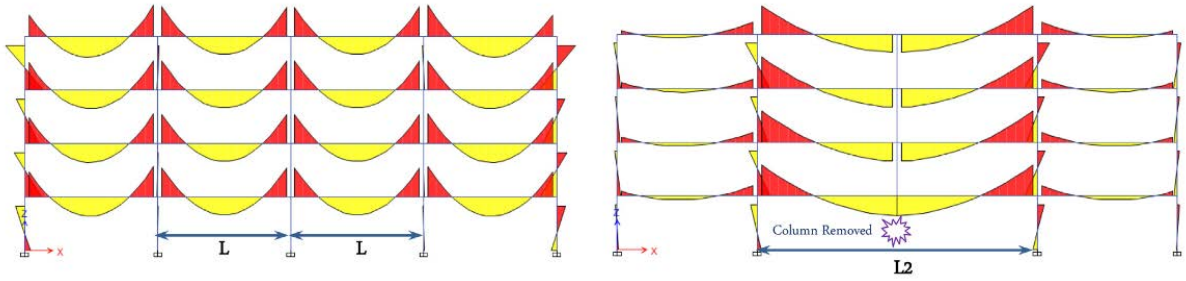


Figure 1: Bending moment distribution in frame buildings (left) under service (right) after central column loss, taken from (Alshaikh 2020)

To mitigate such scenarios, modern robustness design is based on the formation of Alternate Load Paths (ALPs), which enable the structure to redistribute actions through unintended but resilient resistance mechanisms (Adam et al, 2018). Experimental investigations on reinforced concrete (RC) beam–column frames subjected to column removal have consistently shown that ALP development occurs through a sequence of three mechanisms as deformation increases (Kim et al, 2012, Valipour et al, 2016). Initially, the system responds through flexural action, in which beams behave similarly to Vierendeel elements dominated by bending and shear with negligible axial force (Qian et al, 2023). As vertical deflection increases and beam elongation is restrained by the surrounding frame, compressive arch action (CAA) is activated, introducing axial compression that enhances resistance through moment–axial force interaction (Azim et al, 2020). At even larger deformations, typically when the vertical displacement approaches the beam depth, the axial force transitions from compression to tension and catenary tensile action (CTA) becomes the governing mechanism, with loads primarily resisted by the tensile capacity of the longitudinal reinforcement (Elkady et al, 2024).

The effectiveness of these mechanisms is strongly governed by ductility, reinforcement continuity and boundary stiffness. Low span-to-depth ratios favor CAA, while higher ratios allow larger rotations and facilitate CTA development (Yang et al, 2020). Similarly, increased longitudinal reinforcement improves flexural and arching capacity, while sufficient top and bottom reinforcement continuity is essential to sustain catenary forces (Alogla et al, 2016). Boundary conditions play a particularly critical role, as strong horizontal restraints are required to mobilize significant axial forces; weak or imperfect restraints often suppress CTA entirely (Lim et al, 2017). Material properties also influence ALP behavior, with higher concrete strengths generally enhancing flexural and compressive arch resistance but simultaneously reducing ductility and shortening the deformation range available for catenary action due to brittle cracking and premature reinforcement fracture (Deng et al, 2020). Observed failure

modes under progressive collapse loading include concrete crushing in beam–column joints, reinforcement pull-out or rupture, brittle shear failure and column instability, many of which can lead to sudden loss of load-carrying capacity once secondary resistance mechanisms are exhausted.

Current design standards address progressive collapse primarily through indirect measures such as tying force requirements and, in some cases, explicit ALP verification following hypothetical element removal. While these approaches aim to ensure a minimum level of continuity and robustness, significant discrepancies exist between codes regarding required tie forces, particularly for peripheral ties, and the material behavior assumed in such provisions remains largely limited to conventional reinforced concrete. As a result, secondary resistance mechanisms such as CAA and CTA are often conservatively or implicitly treated, despite their decisive role in preventing disproportionate collapse. An overview and comparison of various adopted design methodologies in different design codes is given in (Adam et al, 2018) and copied below as Figure 2.

Area	Code	1.Tying	2.ALP	3.Key	4.Risk
UK	Building Reg. 2010	✓	✓	✓	~
Europe	EN 1991-1-7	✓	✓	✓	✓
US (Civil)	ASCE/SEI 7-16	✓	✓	✓	~
US (Civil)	NYC BC 2014	✗	✓	✓	~
US (Civil)	IBC 2009	✓	✗	✗	✗
US (Gov.)	UFC 4-023-03	✓	✓	✓	~
US (Federal)	GSA 2013	✗	✓	✗	~
China	CECS 392:2014	✓	✓	✓	✗
Canada	NBCC 1995	✓	✓	✓	~
Australia	NCC 2016	✗	✓	✓	✓

✓ (method considered), ✗ (method not considered), ~ (method implicitly considered)

Figure 2: Overview of different design methodologies in codes, figure taken from (Adam et al, 2018)

1.2 Role of fiber reinforced concrete in ALP development

Fiber reinforced concrete (FRC) has been widely studied to enhance ductility, crack control and energy absorption, all of which are critical for structural performance under extreme loading conditions (di Prisco et al, 2009). Particularly, polypropylene fibers offer a combination of corrosion resistance, ease of incorporation and favorable post-cracking behavior. While polypropylene fibers have been shown to have little to no influence on compressive strength (Nataraja et al, 1999), their effect on post-cracking flexural behavior and energy dissipation is well established, especially at moderate to large crack openings.

In reinforced concrete elements, the interaction between conventional reinforcement and fibers leads to a more nuanced response. After cracking, fibers actively contribute by limiting crack width, delaying concrete crushing and reducing strain concentrations in the reinforcement. Experimental studies on reinforced steel fiber-reinforced concrete beams indicate that fibers can modestly increase peak flexural capacity (Ning et al, 2015) and, more importantly, significantly enhance post-peak deformation capacity and absorbed energy, particularly when sufficient reinforcement continuity is present (Conforti et al, 2019). These effects become increasingly relevant under progressive collapse scenarios, where large rotations and deformation-controlled behavior dominate, and where premature localization (Dancygier et al, 2016) or concrete degradation can prevent the successful mobilization of

compressive arch and catenary actions. Only limited studies are done on the interaction between steel FRC and progressive collapse resistances with some notable exceptions (Alshaikh et al, 2022, Valipour et al, 2016). In these papers, scaled-down frames were tested in laboratory conditions. The results showed that the inclusion of (steel) fibers increased both the ductility and deflection, but that fibers alone cannot completely substitute the transverse reinforcement.

The present study contributes to the state of the art by experimentally assessing the influence of polypropylene fibers on the progressive collapse behavior of reinforced concrete frames. By comparing conventional RC and fiber-reinforced specimens under identical column loss scenarios, the study provides insight into how fibers enhance peak resistance, energy absorption and ductility, and how they delay critical failure modes during CAA and CTA development. Furthermore, verification against multiple international design standards allows for an evaluation of whether current code provisions adequately reflect the enhanced robustness observed in fiber-reinforced systems, thereby highlighting both the potential and the limitations of existing design approaches.

2 Experimental program

2.1 Specimen design and scaling strategy

The experimental program was designed to investigate the progressive collapse response of reinforced concrete beam–column sub-assemblages subjected to a column loss scenario, with particular emphasis on the influence of polypropylene fiber reinforcement. The specimen design was derived from a realistic four-story office building with a regular plan grid of six by six meters. The full-scale structure was designed in accordance with EN 1991-1-1, assuming a characteristic live load of 3 kN/m² and a permanent load of 5 kN/m². Floor slabs were assumed to act in a one-way load transfer mechanism, resulting in a contributing width of six meters per beam. Applying the relevant partial safety factors led to a design line load of 67.5 kN/m on the beam. Fully restrained boundary conditions were assumed, producing both field and fixed-end moments that governed the beam design.

The full-scale beam section was designed as 220 × 500 mm and reinforced to resist these bending moments under ultimate limit state conditions. Three 18 mm diameter bars were provided in the bottom layer, while three 28 mm diameter bars were placed at the top. The top reinforcement was intentionally oversized relative to the required area to ensure that yielding and eventual failure would occur first in the bottom reinforcement at midspan. This design choice was critical to promote representative progressive collapse behavior dominated by beam deformation and to prevent premature failure at beam ends or in the columns.

To enable laboratory testing, the structure was scaled down while preserving the parameters most relevant to alternate load path development, particularly reinforcement ratios and moment capacity. Due to experimental constraints, the beam span was limited to 2.0 m. The resulting scaled beam had dimensions of 2000 × 240 × 100 mm with an effective depth of 215 mm, see Figure 3. The bottom reinforcement consisted of two 10 mm diameter bars, while the top reinforcement comprised two 16 mm diameter bars. Stirrups (diameter 8 mm, spacing 150 mm) were provided in the beam to ensure sufficient shear capacity and confinement of the compression zone. The supporting columns reinforcement consisted of four longitudinal bars, two 14 mm bars on the exterior faces and two 12 mm bars on the interior, combined with 10

mm diameter stirrups. All reinforcement detailing, including anchorage lengths and transverse reinforcement spacing, was done in accordance with EN 1992-1-1 requirements.

2.2 Boundary conditions and supports

To enable the full development of CAA and CTA, strong lateral restraint was required at the beam supports. A dedicated steel clamping system was therefore designed and fabricated. The system consisted of welded UPN180 profiles stiffened with additional steel plates and anchored to the test bench using preloaded high-strength bolts. During testing, bilateral clamping was applied to further enhance restraint stiffness and approximate fixed boundary conditions. A figure of the clamping setup is shown in Figure 3.

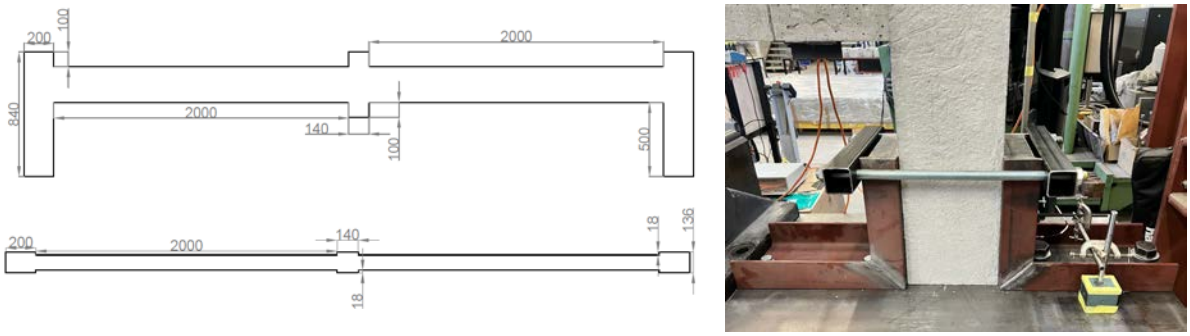


Figure 3: (left) Geometry in mm (right) Clamping setup at the bottom of the columns

2.3 Material characterization, fabrication, and test procedure

Four beam–column sub-assemblages were fabricated and tested, consisting of two conventional reinforced concrete specimens and two FRC specimens incorporating polypropylene fibers at a volume fraction of 0.5% (4.5 kg/m³). The polypropylene fibers had a modulus of elasticity of 6.87 GPa, an ultimate tensile strength of approximately 556 MPa, a diameter of 0.8 mm, and a length of 53.75 mm. Two separate concrete batches were produced for each material type to mitigate batch variability. The target concrete strength was C35/45, and the concrete composition is shown in Table 1. Superplasticizer (SP) was added in two different fractions: 0.2 kg/m³ for RC and 1 kg/m³ for FRC.

Table 1: Concrete composition

Component	CEM I 52.5R	Water	Sand 0/1	Sand 0/4	Gravel 4/16	SP
Weight [kg/m³]	335	193	324	505	996	0.2 / 1

Material characterization was performed using cubes (according to EN 12390) and prisms (according to EN 14651) cast from the same batch as the structural specimens. In total, fifteen cubes and fifteen prisms were tested for each concrete type. The specimens were cast into plywood formwork, compacted using needle vibration, and cured under plastic sheeting for two weeks before additional storage under laboratory conditions.

The progressive collapse tests were conducted using a quasi-static, displacement-controlled configuration. Each specimen was mounted on a rigid test bench with the clamping system enforcing restrained boundary conditions at the bottom of the columns. Vertical load was applied at the location of the removed middle column using a hydraulic press equipped with a

spherical hinge to avoid unintended moment transfer. Due to stroke limitations of the actuator, loading was applied in two phases, with unloading and repositioning between phases. A constant loading rate of 6 mm/min was adopted, corresponding to approximately 0.003 rad/min and consistent with values reported in previous experimental studies (Ning et al, 2015). A picture of the frame during testing is shown in Figure 4.

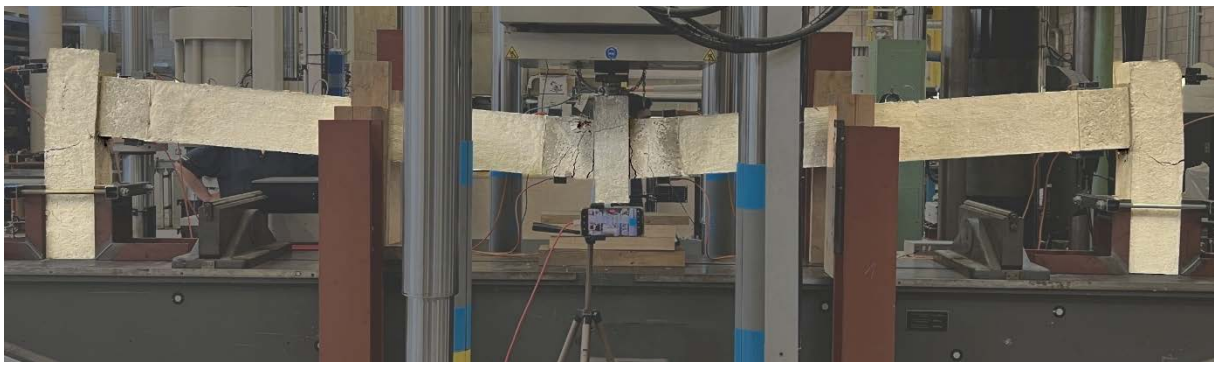


Figure 4: Concrete frame during testing (contrast enhanced photo)

Instrumentation was designed to capture both global and local response. Vertical displacement at the middle joint was used as the primary control and reference parameter. Additional sensors measured horizontal displacements at the column bases, axial deformation of the beam, joint rotations, crack openings, and concrete crushing. This extensive measurement setup enabled clear identification of damage evolution and transitions between flexural action, compressive arch action, and catenary tensile action, as well as a reliable assessment of the influence of polypropylene fibers on strength, ductility, and energy absorption.

3 Test Results

3.1 Material characterization

Cube tests yielded mean compressive strengths of 52.8 MPa for conventional reinforced concrete and 52.0 MPa for FRC, corresponding to characteristic cube strengths of 48.8 MPa and 47.7 MPa, respectively. Both mixtures were classified as C35/45. Prism tests were used to characterize the post-cracking behavior of the fiber reinforced concrete, the results are shown in Figure 5. Based on a lognormal distribution, the characteristic strengths $f_{Ri,k} = 1.94, 2.16, 2.29, 2.25$ MPa for $i = 1,2,3,4$ with coefficients of variation of 11.6, 12.7, 12.7 and 12.7 %, respectively. Based on residual strength parameters, the FRC was classified as 1.5d (according to fib Model Code 2020 (fib 2020)) or 1.5e (according to Eurocode 2 (2023), annex L (EC 2023)).

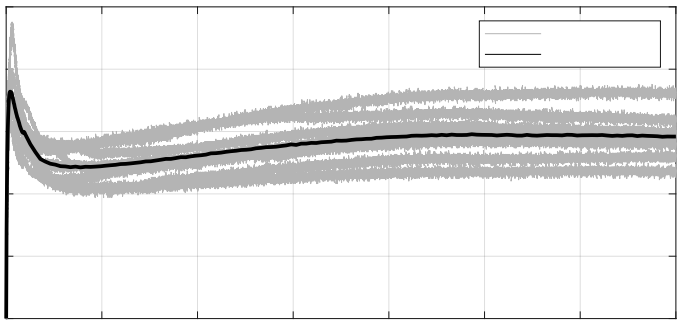


Figure 5: EN14651 results for FRC with 0.5 V% PP

3.2 Global structural response

The global structural response in terms of mid-joint displacement (MJD) and applied force (F) is shown in Figure 6 for all specimens. The frame undergoes various transitions throughout the test indicated by letters, ranging from first cracking (A) to peak load (B), column stirrup snapping (C-D), bottom rebar fracture (E-G) to final displacement (K) and unloading (L). The cycle H-I-J refers to the unloading-reloading cycle associated with 'resetting' the hydraulic actuator after reaching its maximum stroke.

The data in Table 2 is recorded for all specimens, together with the increase or decrease of the average FRC response to the average RC response:

$$\Delta = \left(\frac{P_{FRC1}+P_{FRC2}}{P_{RC1}+P_{RC2}} - 1\right) \cdot 100\%$$

Herein refer P_x to the parameter P (force or MJD) of test x ((F)RC(1/2)).

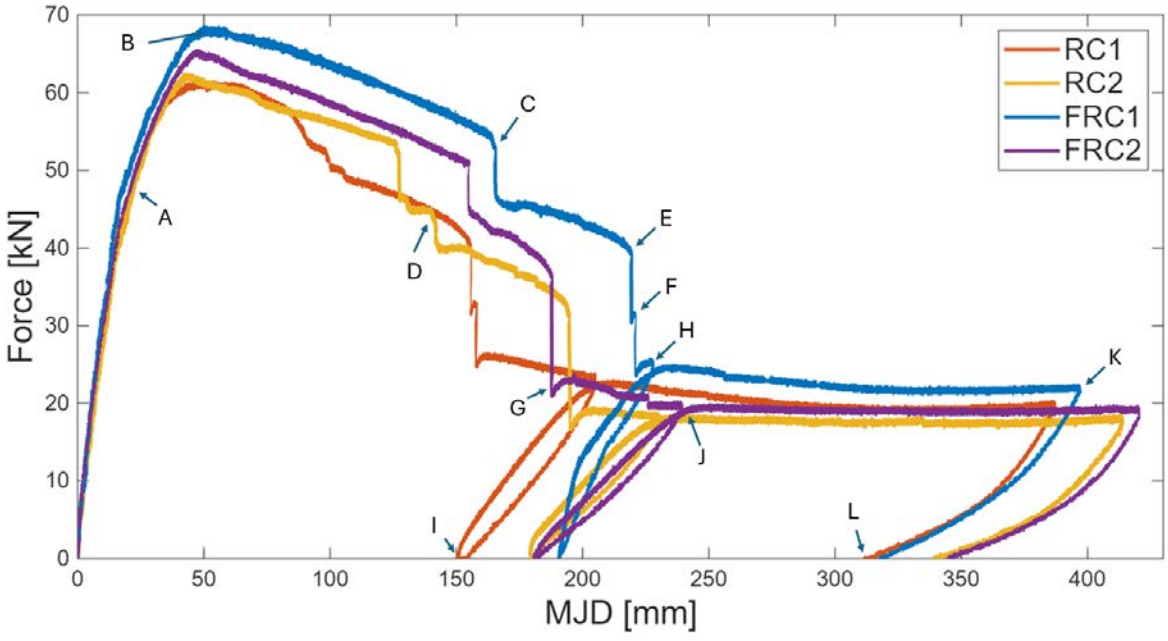


Figure 6: Force vs mid joint displacement (MJD) for all test specimens

Table 2: results of the MJD and force for all specimens at the predefined points A-L

	Force [kN]					MJD [mm]				
	RC1	**RC2**	**FRC1**	**FRC2**	**Δ**	**RC1**	**RC2**	**FRC1**	**FRC2**	**Δ**
A	42.6	40.3	46.5	42.7	7.6%	16.4	16.5	16.5	16.9	1.5%
B	61.5	62.4	68.2	65.4	7.9%	44.1	50.0	47.3	50.2	3.6%
C	52.6	52.2	54.2	50.8	0.3%	127.2	98.0	155.2	165.5	42.4%
D	50.1	46.4	46.2	44.5	-6.0%					
E	40.4	31.5	39.7	36.6	5.9%	194.2	155.9	187.8	219.4	16.3%
F		31.9		31.9	0 %		156.7		220.1	40.5%
G	24.8	16.8	23.9	21.3	8.7%	194.2	158.0	187.8	221.3	16.1%
H	23.3	18.4	25.6	19.7	8.6%	230.2	204.8	239.3	227.8	7.4%
I						179.6	154.3	181.3	190.7	11.4%
J	22.8	18.2	24.8	19.6	8.6%	234.8	209.3	244.2	230.8	7.0%
K	19.9	18.1	22.0	19.2	8.8%	413.9	387.0	420.2	396.9	2.0%
L						339.1	311.7	344.9	318.4	1.9%

Across all relevant points, the force improvement is around 6 – 9 %, which refers to the tensile capacity of the FRC matrix. Only at point D, corresponding to the first column stirrup snapping, is the force in the FRC frames lower. A larger difference/improvement is noted in the MJD, where the average increase in MJD is equal to 11 % (across all data points), but it can be as large at 42 % (point C).

3.3 Local measurement data

In support to the global response, LVDTs were also placed in the middle of the beam's height at the location where the bending moment would be equal to zero under simple flexural action (i.e. for a double fixed-ended beam with a point load at mid-span) as to prevent measuring axial deformation due to flexural actions. This is done for both FRC specimens, as well as for RC2. The LVDT data is shown in Figure 7.

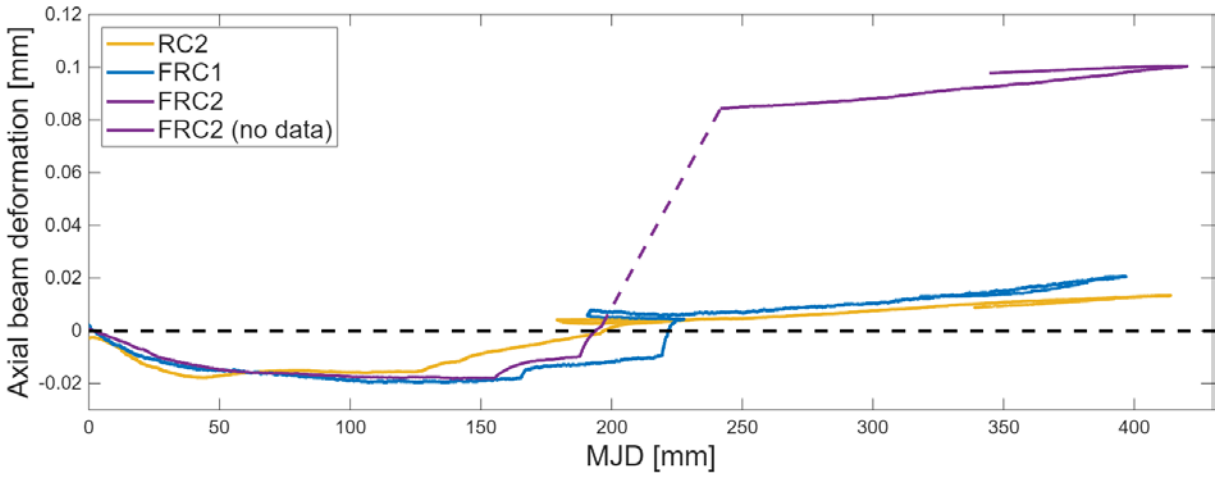


Figure 7: LVDT data of the axial deformation of the beams as a function of MJD.

The LVDT measurements should be interpreted as follows: negative values indicate compression, which would be the case under CAA, whereas positive values indicate tensile

elongation, typical for CTA. It is noted that all beams initially undergo compressive shortening, but from a MJD at around 200 mm (corresponding to a rotation of 0.1 rad, coinciding with the rupture of the tensile rebars), the deformation shifts into the tensile region. From that point onwards, the system is acting as a catenary, where all loads are transferred through tensile action of the beams along the top reinforcement.

4 Analysis

4.1 Failure mode analysis

The failure mode of all frames was similar, and unfortunately based on the local failure of the spot weld of the stirrups in the columns, indicated by the points (C) and (D) in Figure 6, despite providing sufficient anchorage in the transversal column reinforcement. In Figure 8, the failed stirrup in the column is shown after removing the concrete in the column after the test.



Figure 8: (left) Spot weld failure in the transversal reinforcement in the columns (right) middle joint of RC2 immediately after bottom reinforcement fracture (point G)

However, the system was able to redistribute forces such that at points (E) and (F) the bottom longitudinal reinforcement in the span of the frame fractured. In some cases, e.g. RC2 and FRC2, both bottom bars broke simultaneously, whereas for the other frames the rebars fractured one after the other. It is noted that even after complete loss of tensile reinforcement, the frames were still able to sustain a certain load though CAA and CTA mechanisms. At point K, the tests were stopped since the maximum deflection allowed in the test setup was reached, corresponding, at this point the average rotation was 0.2 rad (11.4°) which is often cited as a minimum required nodal rotation for the prevention of progressive collapse (UFC 4-023-03, 2009). At point K, the deformations in the mid joint localized on one side of the middle column, leading to the formation of a plastic hinge that either side of the column. Together with the two plastic hinges which formed in both columns, the frames developed in a triple-hinged system, albeit with hinges in the columns rather than at the beam-column nodes, as shown in Figure 9.

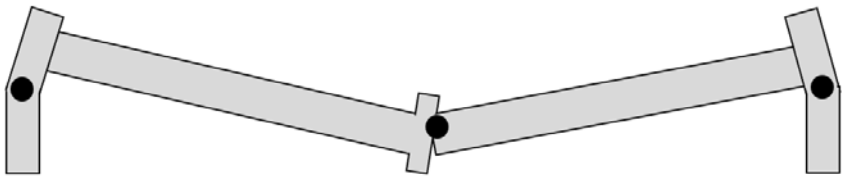


Figure 9: Development of a mechanism with triple hinges in all specimens (middle hinge location can be on either side of the middle column)

4.2 Comparison between RC and FRC

Given the relatively low FRC strength class (1.5d), the contribution of the residual tensile capacity of the matrix is quite limited (+8 % after tensile rebar fracture). Further work is being done to assess the influence of the FRC class on the structural capacity and behavior. Nevertheless, the fibers play a significant role in delaying the weld fracture (point C/D) and the tensile rebar fracture (point E/F). Relative to the MJD at peak load (point B), the weld failed at an MJD which is 2.4x higher for RC and 3.3x the MJD at peak load for FRC frames. Similarly, the average MJD for RC frames at point E (first tensile rebar fracture) is 3.7x the MJD at peak load, and 4.2x the MJD at peak load for FRC. These values can be understood as deformation-based ductility values up to predefined events. The major contribution of the fibers lies in ensuring the integrity of the crushed or cracked concrete at large MJDs. This is shown in Figure 10, where the local damage is shown for an RC and FRC frame, left and right respectively, at point G, i.e. immediately after all tensile rebars have fractured.



Figure 10: Local damage at the column at point G for (left) RC frame and (right) FRC frame.

As concrete integrity improved, the load carrying and redistribution capacity of the frame increased. Consequently, the energy absorption capacity of the FRC frames is also greater than for RC frames, a result which is also found in literature. Assessing the energy absorption capacity as the integration of the force-MJD curve up to certain points - in this case, B (peak load), C (weld failure), E (first tensile rebar fracture) and K (minimum of the highest MJD for all specimens, here $K_{RC2} = 387$ mm), the average values are shown in Table 3, together with Δ, the improvement from the average energy absorption capacity of RC to that of FRC.

Table 3: Energy absorption capacity in MJ for various maximum MJDs for RC and FRC frames

E [MJ]	RC1	RC2	FRC1	FRC2	Δ
Up to B	2,3	1,9	2,4	2,2	9,9%
Up to C	5,1	6,7	9,6	8,4	53,8%
Up to E	8,5	9,6	12,1	10,4	24,2%
Up to $(\min K_i) = 387$ mm	12,7	12,7	15,8	13,7	15,9%

Here, the fibers significantly impact structural performance, with greater energy absorption capacities across the entire test range. Also note that the last row does not correspond to the full failure of the frame, i.e. after exhaustion of the tensile tie capacity in the catenary phase. It is very likely that at even higher MJD, the FRC matrix would be providing even greater improvements than the 16 % noted here at point K.

4.3 Comparison with design rules

In Eurocode 2 (2005), peripheral and internal reinforcement is needed to take up the tensile forces T_p and T_i. These amounted to 70 and 60 kN respectively, or according to Eurocode 1-7 102 kN and 204 kN, respectively. In the full-scale design, sufficient reinforcement is provided to take up these forces. In the design according to UFC 4-023-03, the tie force that should be safely taken up is equal to 504 and 135 kN for T_p and T_i, respectively in the full-scale structure. Again here, the provided reinforcement exceeds this required value. Both the requirements in EC1/2 and UFC are there to ensure that the structure has sufficient deformation capacity to activate ALPs and to prevent progressive collapse. Based on the experimental results, it seems that these values are indeed sufficient, although it must be underlined that especially the Eurocode requirements lead to – in practice – very lightly reinforced structures. This is also noted in literature, where different researchers have indicated that the provisions in design codes can be unconservative (Valipour et al, 2016, Izzuddin et al, 2022).

5 Concluding remarks

This study experimentally assessed the influence of polypropylene fiber-reinforced concrete on the progressive collapse response of reinforced concrete frame sub-assemblages subjected to a column loss scenario. While the direct contribution of the fiber matrix to peak resistance was relatively limited, the inclusion of polypropylene fibers substantially improved the deformation-controlled response of the system. As a result, fiber-reinforced frames exhibited increased ductility, delayed critical damage mechanisms, and greater energy absorption capacity, highlighting the effectiveness of PP fibers as a complementary measure for improving structural robustness under extreme loading conditions. The following conclusions are drawn:

- Polypropylene fibers resulted in a moderate increase in peak load capacity (approximately 6–9%) under column loss conditions.
- The primary benefit of fibers was observed in the deformation domain, with significantly larger mid-joint displacements and attainable rotations compared to conventional RC frames.
- Fiber reinforcement delayed critical failure events, including transverse reinforcement failure in the columns and fracture of tensile longitudinal reinforcement.
- Improved concrete integrity at large deformations enhanced the development of alternate load paths during both compressive arch action and catenary tensile action.
- The energy absorption capacity of fiber-reinforced frames exceeded that of conventional RC frames across all deformation stages considered.
- Comparison with current design provisions suggests that existing robustness requirements may not fully capture the enhanced deformation capacity provided by FRC, indicating potential for more performance-based consideration of fibers in progressive collapse design.

6 Acknowledgements

The fiber materials were provided by MasterBuilders Solutions, whose contribution is generously acknowledged. The experimental work was carried out by master thesis student Brent Dossaert.

7 References

Adam, J. M., Parisi, F., Sagaseta, J., and Lu, X., 2018. “Research and practice on progressive collapse and robustness of building structures in the 21st century,” Engineering Structures, 173, pp. 122–149.

Alogla, K., Weekes, L., and Augusthus-Nelson, L., 2016. “A new mitigation scheme to resist progressive collapse of RC structures,” Construction and Building Materials, 125, pp. 533–545.

Alshaikh, I. M., Bakar, B. A., Alwesabi, E. A., and Akil, H. M., 2020. “Experimental investigation of the progressive collapse of reinforced concrete structures: An overview,” Structures, 25, pp. 881–900.

Alshaikh, I. M. H., Abu Bakar, B. H., Alwesabi, E. A. H., Abadel, A. A., Alghamdi, H., and Wasim, M., 2022. “An experimental study on enhancing progressive collapse resistance using a steel fiber-reinforced concrete frame,” Journal of Structural Engineering, 148(7), 04022073.

Azim, I., Yang, J., Bhatta, S., Wang, F., and Liu, Q. F., 2020. “Factors influencing the progressive collapse resistance of RC frame structures,” Journal of Building Engineering, 27, 100986.

Conforti, A., Zerbino, R., and Plizzari, G. A., 2021. “Assessing the influence of fibers on the flexural behavior of reinforced concrete beams with different longitudinal reinforcement ratios,” Structural Concrete, 22, pp. 1892–1893.

Dancygier, A. N., and Berkover, E., 2016. “Cracking localization and reduced ductility in fiber-reinforced concrete beams with low reinforcement ratios,” Engineering Structures, 111, pp. 411–424.

Deng, X.-F., Liang, S.-L., Fu, F., and Qian, K., 2020. “Effects of high-strength concrete on progressive collapse resistance of reinforced concrete frame,” Journal of Structural Engineering, 146(1).

Di Prisco, M., Plizzari, G., and Vandewalle, L., 2009. “Fibre reinforced concrete: new design perspectives,” Materials and Structures, 42, pp. 1261–1281.

DoD (Department of Defense), 2009. “UFC 4-023-03: Design of buildings to resist progressive collapse,” Unified Facilities Criteria, Change 3, November 2016, Washington, D.C., USA.

Elkady, N., Nelson, L. A., Weekes, L., Makoond, N., and Buitrago, M., 2024. “Progressive collapse: Past, present, future and beyond,” Structures, 62, 106195.

European Committee for Standardization, 2004. “EN 1992-1-1: Eurocode 2: Design of concrete structures – part 1-1: General rules and rules for buildings,” Brussels, Belgium.

European Committee for Standardization, 2023. “EN 1992-1-1:2023: Eurocode 2: Design of concrete structures – part 1-1: General rules, rules for buildings, bridges and civil engineering structures,” Brussels, Belgium.

fib (International Federation for Structural Concrete), 2020. “fib Model Code 2020 for Concrete structures”, Lausanne, Switzerland.

Izzuddin, B. A., and Sio, J., 2022. “Rational horizontal tying force method for practical robustness design of building structures,” Engineering Structures, 252, 113676.

Kim, J., and Yu, J., 2012. “Analysis of reinforced concrete frames subjected to column loss,” Magazine of Concrete Research, 64(1), pp. 21–33.

Lim, N. S., Tan, K., and Lee, C., 2017. “Effects of rotational capacity and horizontal restraint on development of catenary action in 2-d RC frames,” Engineering Structures, 153, pp. 613–627.

Nataraja, M., Dhang, N., and Gupta, A., 1999. “Stress–strain curves for steel-fiber reinforced concrete under compression,” Cement and Concrete Composites, 21(5–6), pp. 383–390.

Ning, X. L., Ding, Y. N., Zhang, F. S., and Zhang, Y. L., 2015. “Experimental study and prediction model for flexural behavior of reinforced SCC beam containing steel fibers,” Construction and Building Materials, 93, pp. 644–653.

Qian, K., and Fang, Q., 2023. Progressive Collapse Resilience of Concrete Structures: Mechanisms, Simulations and Experiments, Springer Nature Singapore.

Valipour, H., Vessali, N., and Foster, S., 2016. “Fibre-reinforced concrete beam assemblages subject to column loss,” Magazine of Concrete Research, 68(6), pp. 305–317.

Yang, T., W. Chen, and Z. Han, 2020. “Experimental investigation of progressive collapse of prestressed concrete frames after the loss of middle column,” Advances in Civil Engineering, 2020, pp. 1–12.

High temperature behaviour of strain-hardening ultra-high performance fibre reinforced concretes

Péter Ludvig[1]; Anna Szijártó[2]; Bruno A. Bacelar[3]; Thiago M. Viana[3]; Salem Nehme[2]

[1]: Department of Civil Engineering, Federal Center for Technological Education of Minas Gerais (CEFET-MG), Brazil.

[2]: Department of Construction Materials and Technologies, Budapest University of Technology and Economics (BME), Hungary.

[3]: Graduate Program in Civil Engineering, Federal Center for Technological Education of Minas Gerais (CEFET-MG), Brazil.

Abstract

Ultra-High-Performance Concretes (UHPCs) are at the forefront of research interest, as they offer durable and robust solutions to meet the growing demands of modern engineering The incorporation of short fibres (resulting in UHPFRCs – Ultra-hight-performance fiber reinforced concrete) can mitigate the inherently brittle mechanical behaviour of UHPCs and impart a certain level of ductility, which may lead to strain-hardening behaviour depending on the type and dosage of fibres used. Due to their extremely low porosity, UHPCs are particularly sensitive to exposure to elevated temperatures. Consequently, investigating the residual mechanical properties of these materials is of paramount importance for estimating the service life of UHPFRC structures. In this study, structural Polyvinyl Alcohol (PVA) fibres were added to UHPC matrices at dosages ranging from 1 to 35 kg/m³. The specimens were subjected to furnace heating up to 800 °C, after which the residual mechanical properties – including compressive strength, flexural strength, and fracture energy – were evaluated. The results indicate a progressive deterioration of mechanical properties with increasing exposure temperature. Although well-defined strain-hardening behaviour was not observed beyond the melting point of the PVA fibres, a significant increase in strain capacity was recorded, suggesting that the fibres still contributed to the stress-transfer mechanisms within the UHPC matrix.

Keywords

Ultra-high performance fibre reinforced concrete; Strain-hardening; High temperature behaviour; Residual mechanical properties

1 Introduction

Ultra-High-Performance Concretes (UHPCs) can be considered materials capable of meeting many of today's increasing demands for outstanding mechanical performance and durability. With the addition of structural fibres, ultra-high-performance fibre-reinforced concrete (UHPFRC) is obtained. While plain UHPC typically exhibits a very brittle post-cracking response, fibre reinforcement can significantly enhance its deformation capacity and may lead to strain-hardening behaviour.

The exposure of UHPCs or UHPFRCs to elevated temperatures, such as during a fire, still represents a challenge. The low porosity of these materials contributes to the development of high pore pressure upon heating (Nassar et al., 2024; Viana et al., 2020). This internal pressure can easily reach the tensile strength of the concrete, leading to cracking or even (explosive) spalling. The use of structural fibres in UHPCs provides clear advantages in terms of mechanical behaviour at normal ambient temperatures. However, these fibres – especially polymeric ones – have lower thermal stability compared to the concrete matrix and are therefore particularly vulnerable to exposure to elevated temperatures (Lyzwa and Zehfuss, 2021).

On the other hand, non structural polymer fibres, such as polypropylene (PP), are often used to mitigate the negative effects of pore pressure in concretes, as they melt and create additional pathways for vapour release once the temperature exceeds their melting point. However, these fibres do not contribute to strain-hardening behaviour. Conversely, structural Polyvinyl Alcohol (PVA) fibres are not so effective to reduce the damages caused by elevated temperatures (Lin et al., 2024).

Several attempts were made to combine the effects of different types of fibres to address the challenges associated with elevated temperatures. However, this trade-off (i.e. partially replacing structural fibres with PP ones) often has negative effects on ambient temperature behaviour (Zhang et al., 2021).

This paper presents an experimental investigation on strain-hardening UHPFRC specimens exposed to temperatures of up to 800 °C with varying PVA fibre dosages. Residual mechanical parameters, including compressive and flexural strength and fracture energy and toughness were evaluated.

2 Experimental program

The UHPC compositions were made up with the following constituents: CEM I 52.5 N grade Portland cement (Duna-Dráva Cement), silica fume (Elkem), metakaolin (Metaver-N), FL-30 (30 μm maximum particle size) and FL-100 (100 μm maximum particle size) quartz powders and quartz sand with 0.2-0.6 and 0.8-1.2 mm fractions (both Üveg-Ásvány Kft.). Normal potable water was used for hydration at a water-to-cement ratio of 0.29. Two types of admixtures were employed: Sika Control 40 shrinkage reducer (1.5 % by weight of cement) and MasterBuilders Glenium 300 superplasticizer (3.0 % by weight of cement). The fibres employed were MasterBuilders MasterFiber 401 (PVA). The fibre parameters can be seen in Table 1, meanwhile the exact composition of the UHPC mixes are given in Table 2.

Table 1: Characteristics of the fibres used in UHPC mixes.

Parameter	**Value**
Material	PVA
Length	12 mm
Diameter	0.6 mm
Melting point	200-230 °C
Tensile strength	800 MPa
Elastic modulus	29 GPa
Shape	straight

Table 2: UHPC mix proportions.

Material	**Quantity (kg/m^3)**
Cement CEM I 42.5 N	700
Water	203
Quartz sand 0.2-0.6 mm	556
Quartz sand 0.8-1.2 mm	556
Quartz powder FL-30	75
Quartz powder FL-100	75
Silica fume	36
Metakaolin	106
Shrinkage reducer	10.5
Superplasticizer	21

The concrete was mixed in a planetary blender with a capacity of 10 liters. First, the dry constituents were mixed for 30 sec, then the mixing water was added together with the admixtures. After 10 min of mixing, the fibres were slowly added and mixing continued for further 5 min. Table 3 indicates the fibre content of the mixes. The concretes were poured in steel moulds to prepare prismatic specimens of 40 × 40 × 160 mm^3 size. The specimens were demoulded after 24 hours and kept in lime saturated water until 7 days of age. They were kept in laboratory environment until the day of testing.

Table 3: Fibre content of UHPC mixes.

Notation	**Fibre content (kg/m^3)**
PVA-01	1
PVA-02	2
PVA-05	5
PVA-10	10
PVA-20	20
PVA-35	35

Reference values of mechanical parameters were determined at 28 days of age. First a notch was made in the middle of the prismatic specimens with a diamond saw at around 25 % of the total depth. Three-point bending tests were conducted controlled by the Crack Mouth Opening Displacement (CMOD) at a constant rate of 0.001 mm/sec in an Instron universal testing

machine equipped with a 600 kN load cell. Flexural tensile strength σ_{max} of the specimens was calculated using the following formula:

$$\sigma_{max} = \frac{3P_{max}S}{2b(h-a)^2}; \quad (1)$$

where P_{max} is the peak load, S is the span (100 mm), b and h are the width and the height of the cross-section, respectively and a is the depth of the notch. Fracture energy was calculated using the area under the load versus mid-span deflection curve based on the following equation:

$$G_{F,max} = \frac{mg\delta + W_{max}}{b(h-a)}; \quad (2)$$

where m is the specimen mass, g is the gravitational acceleration, δ_{max} is the mid-span deflection under maximum load, and W_{max} is the area of the load-displacement curve until maximum load. The mid-span deflection was calculated according to the equations 3 and 4 that were based on the analytical solutions of Tada, Paris and Irwin (2000) for an S/h relation of 3:

$$\delta = k \cdot CMOD; \quad (3)$$

$$k = 0.215 \cdot \left(\frac{a}{h}\right)^{-1.21} \quad (4)$$

where CMOD is the crack mouth opening displacement. It is important to note, that the energy calculated corresponds to the peak of the load-deflection diagram. Fracture toughness was calculated using equation 5:

$$K_{IC} = \frac{P_{max}S}{bh^{3/2}} f\left(\frac{a}{h}\right); \quad (5)$$

where the geometry factor f(a/h) was calculated according to the following formula based on Dally and Riley (1991):

$$f\left(\frac{a}{h}\right) = 2.9\left(\frac{a}{h}\right)^{\frac{1}{2}} - 4.6\left(\frac{a}{h}\right)^{\frac{3}{2}} + 21.8\left(\frac{a}{h}\right)^{\frac{5}{2}} - 37.6\left(\frac{a}{h}\right)^{\frac{7}{2}} + 38.7\left(\frac{a}{h}\right)^{\frac{9}{2}}. \quad (6)$$

The average values obtained from three specimens of each type of concrete were considered.

The exposure to elevated temperatures occurred in an electric resistance furnace. The heat-up ramp followed an average heating rate of 10 °C/min. The specimens were kept at the specific temperature for 2 hours and slow air-cooling was applied thereafter. The tests to determine residual parameters were performed on room-temperature specimens. The following parameters were determined: mass loss, residual compressive and flexural tensile strengths, residual fracture energy and fracture toughness. The case of loss of a specimen due to explosive spalling was also registered.

3 Test Results

Typical load-displacement curves of the UHPFRCs are shown in the top-left diagram of Figure 1. The effect of increasing fibre content is clearly visible, with higher fibre contents attributing a strain-hardening behaviour. PVA-35 and PVA-20 concretes presented a slight increase in stress after the first peak. On the other hand, concretes with PVA fibre content up to 10 kg/m^3 (PVA-01, 02, 05, 10) did not show this feature, despite having an increasing strain capacity with increasing fibre contents.

The other diagrams in Figure 1 presents the load-displacement relationship of the UHPFRCs before and after exposure to 300, 450 and 600 °C. The strain-hardening behaviour is not detectable anymore. At the same time, higher fibre contents show less fragile fracture.

Explosive spalling that caused the loss of specimens happened more likely with the UHPFRC that has the lowest fibre content (1 kg/m^3), as it is shown in Table 4. At 450 and 600 °C 2 out of 3 specimens were lost in each case, meanwhile none of the 3 specimens survived the exposure at 800 °C of the PVA-01 concrete. Other occurrences of spalling were witnessed for PVA-05 composition (1 of 3 specimens exploded during the experiments at 600 and 800 °C each) and for PVA-10 (1 out of 3 specimens exploded after exposure at 300 °C).

Table 4: Number of specimens lost due to explosive spalling at different peak temperatures.

Notation	**Number of specimens exploded / total number of specimens**			
	300 °C	**450 °C**	**600 °C**	**800°C**
PVA-01	0/3	2/3	2/3	3/3
PVA-02	0/3	0/3	0/3	0/3
PVA-05	0/3	0/3	1/3	1/3
PVA-10	1/3	0/3	0/3	0/3
PVA-20	0/3	0/3	0/3	0/3
PVA-35	0/3	0/3	0/3	0/3

Compressive strength of the UHPFRC specimens at 28 days and the residual values after exposure to elevated temperatures is shown in Figure 2. An increase in compressive strength was observed for most mixtures exposed to 300 and 450 °C when compared to non-heated samples, although the magnitude of this effect varied with fibre content. This increase is well documented and is due to the additional formation of hydration products. The phenomenon is more likely to occur in concretes with low water to binder ratio and with elevated content of supplementary cementitious materials – like in this case. The increase was more pronounced in UHPFRCs with low fibre content. When the temperatures exceeded 450 °C, the compressive strength showed a progressive decline. Explosive spalling caused loss of all specimens with the lowest (1 kg/m^3) fibre dosage at 800 °C. The residual compressive strength values are therefore zero for this composition.

Flexural strength of the UHPFRC specimens at 28 days and the residual values after exposure to elevated temperatures is shown in Figure 3. The behaviour was similar to that observed for compressive strength. An increase in flexural strength was observed after exposure to 300 and 450 °C; however, the extent of this improvement varied among the mixtures depending on fibre content. Higher temperatures resulted in gradual losses of strength.

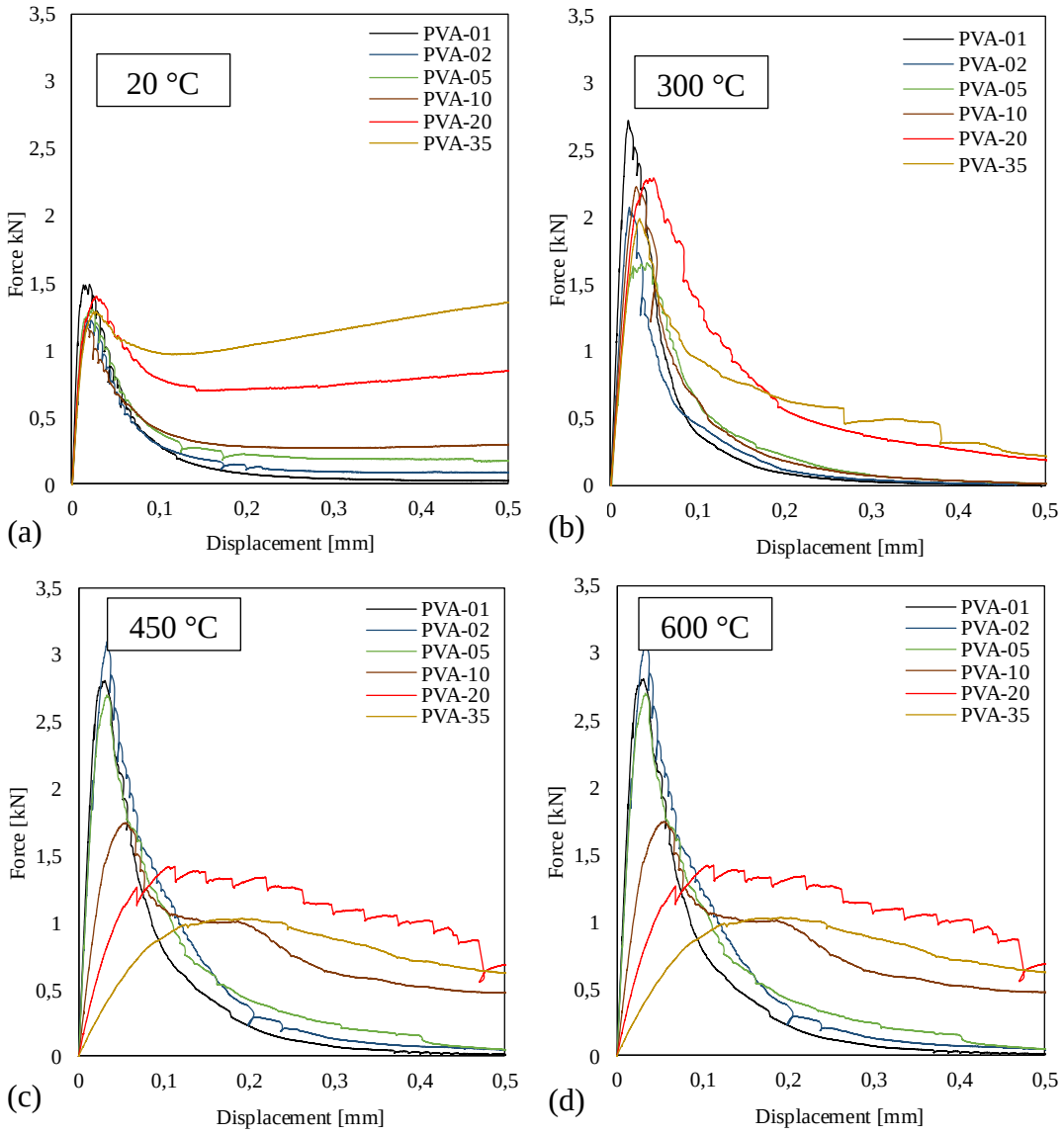


Figure 1: Load-displacement curves of UHPFRCs with different fibre contents before and after exposure to elevated temperatures. (a): 20 °C (reference); (b): 300 °C; (c): 450 °C; (c): 600 °C.

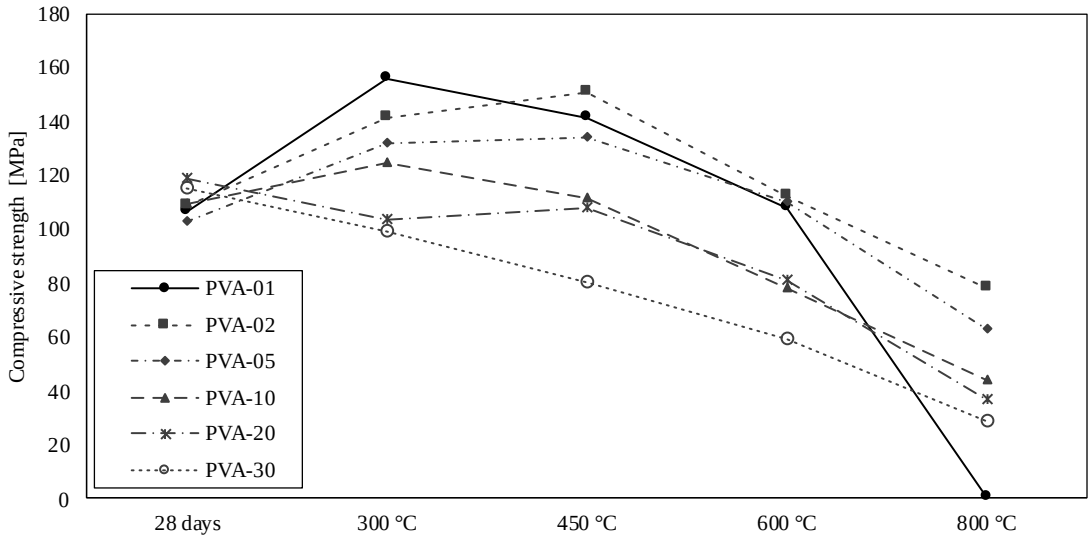


Figure 2: Compressive strength of the UHPC mixes before and after exposure to elevated temperatures.

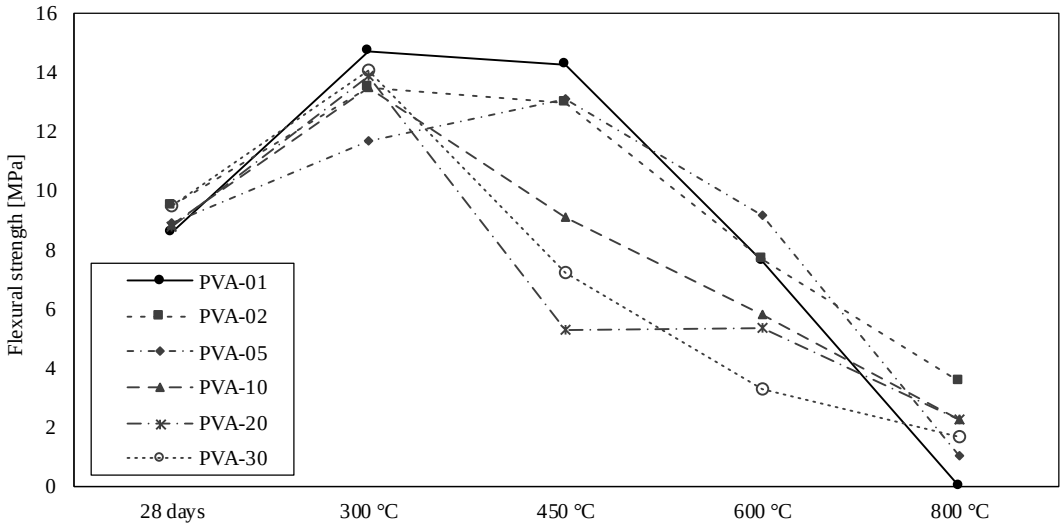


Figure 3: Flexural strength of the UHPC mixes before and after exposure to elevated temperatures.

The effect of the exposition to elevated temperatures on the fracture energy and fracture toughness are presented in Figures 4 and 5 respectively. For mixtures with more elevated fibre contens, fracture energy values increased after exposure up to 600 °C compared to the reference condition, whereas a decline was generally observed at higher temperatures. The magnitude of these changes depended on the fibre dosage. The compositions with lower fibre content (up to 10 kg/m^3) behaved in similar pattern compared to the reference. The increase of temperature had a different effect on the fracture toughness. The curves show a similar pattern to compressive or flexural strengths, where temperatures of 300 and 450 °C caused an increase of the initial values with a decrease at higher temperatures. The effect of fibre dosage had a negative effect on the fracture tougness. Regarding the fracture energy and toughness curves, it is important to note, that the energy calculated corresponds to the peak of load-deflection diagram.

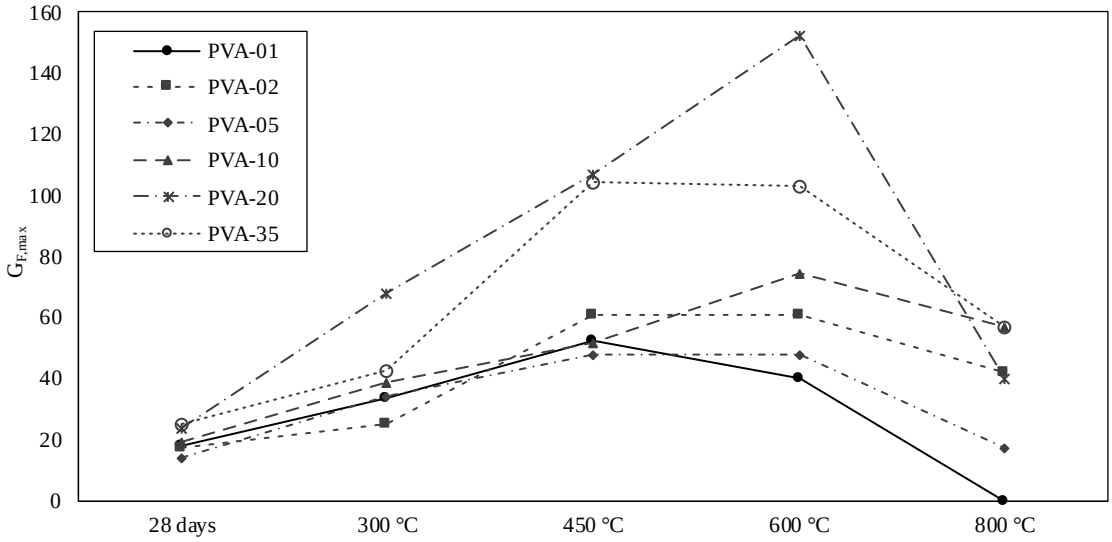


Figure 4: Fracture energy of the UHPC mixes before and after exposure to elevated temperatures.

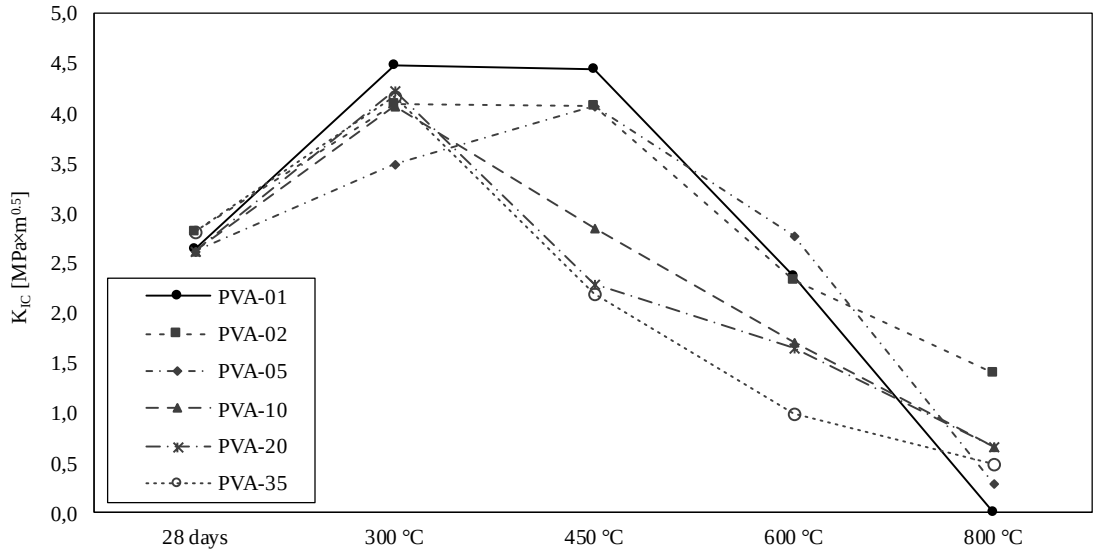


Figure 5: Fracture toughness of the UHPC mixes before and after exposure to elevated temperatures.

Figure 6 shows the mass loss of the UHPC specimens upon heating. As expected, increasing temperatures cause higher mass losses. On the other hand, the mass loss seems to be proportional to the fibre content, however this relationship is not so well established.

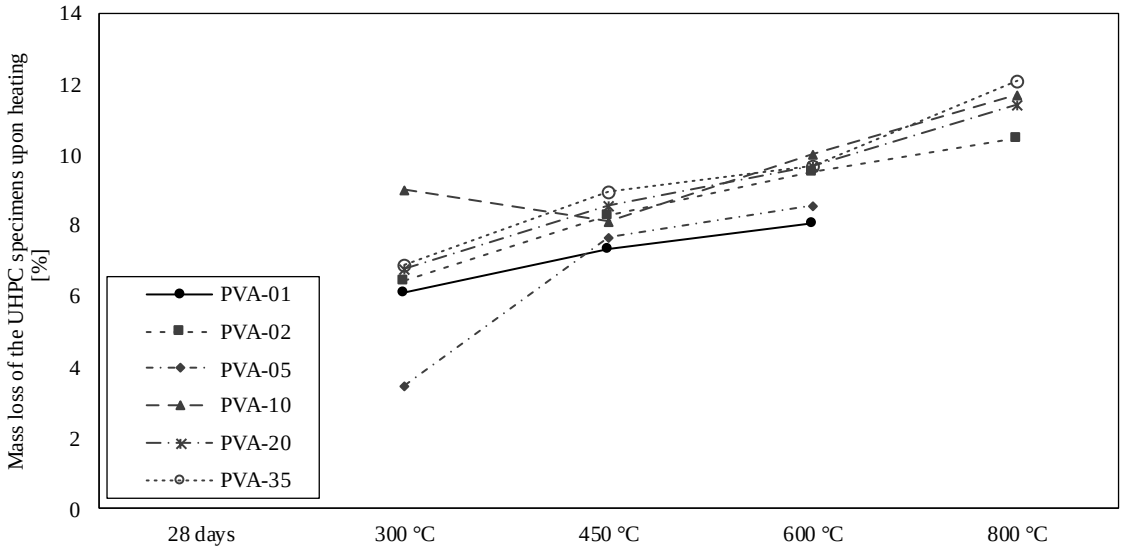


Figure 6: Mass loss of the UHPC mixes before and after exposure to elevated temperatures.

4 Analysis

UHPCs with higher fibre dosages exhibited clear strain-hardening behaviour, whereas lower fibre content UHPCs showed stress-strain relationship similar to the brittle fracture of fibre-free concretes. For intermediate fibre contents, the strain-hardening component increased progressively: the post-peak branch of the curve first showed a steep descending trend, then became less steep with increasing fibre content, and eventually changed into an ascending branch for higher fibre contents. These observations are in good agreement with previous results reported in the literature (Dehghanpour et al., 2022; Zhang et al., 2023). In the strict meaning of the term, strain-hardening happened at fibre dosages of 20 and 35 kg/m^3.

The compressive and flexural strengths of UHPCs with different fibre content did not differ remarkably. This is consistent with previous findings showing that structural fibre addition does not substantially increase peak strength values (Agrawal et al., 2025; Zhang et al., 2023). However, at temperature exposures up to 450 °C, the UHPC with the lowest fibre content (PVA-01) exhibited higher compressive and flexural strengths than the concretes with higher fibre content. This may be explained by the fact that PVA fibres primarily improve post-cracking behaviour rather than peak strength. Furthermore, higher fibre dosages may increase porosity and the number of fibre–matrix interfaces, which can adversely affect the mechanical strength of the composite. Besides that, higher fibre contents may result in higher porosity after the complete melting of those fibres, which is well known to have a negative effect on mechanical strength (Dehghanpour et al., 2022).

Spalling is a phenomenon that affects concretes with lower porosity. When fibres in a higher volume were added to UHPCs, the additional pores resulted from their melting created an additional porosity to the matrix that effectively mitigated the occurrence of spalling. According to the results, it can be seen, that the minimum fibre content for this to happen is somewhere above 10 kg/m^3, as no specimen was lost during the experiments with higher fibre dosages. The mass loss of the UHPFRCs is more affected by the dehydration and decomposition of hydration products, than the melting of the fibres, therefore the results of this method does not give a good

correlation with the increase of porosity, more especially the connected pores that help to reduce internal pore pressures that would cause explosive spalling.

An enhancement in the mechanical performance of UHPCs due to heating has already been observed and documented (Li et al., 2019), including for steel fibre reinforced UHPCs (Agrawal et al., 2025). This effect is mainly attributed to further hydration of unhydrated cement particles and supplementary cementitious materials activated by heat. In the present study, this phenomenon affected the investigated mechanical parameters, namely compressive strength, flexural strength fracture energy and fracture toughness, with the exception of compressive strength of UHPCs with fibre content over 20 kg/m^3, where the trend was strictly descending. No significant differences were observed among these parameters in the magnitude of heat-induced enhancement. The increase of fibre content had a positive effect on facture energy, but on the other hand, fracture toughness exhibited an opposite tendency. This may be explained by the UHPCs becoming less rigid and showing a larger strain capacity for the peak stress value. With the degradation of the matrix, plastic deformations increase, which have the capacity to absorb more energy. At the same time, with the lower peak load, the fracture toughness values also decrease. These findings suggest that the relationship between mechanical performance and the hydration of the cementitious matrix as an effect of heating and the amount of structural fibres follow the above described phenomena and the contribution to the investigated mechanical parameters is not universal (Agrawal et al., 2025).

5 Concluding remarks

The presence of fibres prior to heating had an overall positive effect on the mechanical behaviour of the UHPCs. Although the strength values did not change significantly, the post-peak strain capacity was markedly enhanced. This improvement is associated with enhanced post-cracking behaviour and higher energy absorption at failure, making the material more suitable for demanding structural applications and loading conditions.

When exposed to elevated temperatures, UHPCs containing PVA fibres lost their strain-hardening behaviour due to fibre melting. Nevertheless, specimens with higher fibre dosages retained some residual strain capacity. In contrast, mixtures with lower fibre contents exhibited higher residual compressive and flexural strengths after exposure to temperatures between 300 °C and 450 °C. However, low PVA fibre contents proved insufficient to mitigate explosive spalling.

With regard to strain-hardening behaviour, PVA fibres are not suitable for maintaining these characteristics beyond approximately 200-230 °C, as they melt and no longer contribute structurally. This limitation should be carefully considered in scenarios requiring both high energy absorption and resistance to elevated temperatures, such as fire events following seismic actions.

6 Acknowledgements

The Authors acknowledge the support provided by CEFET-MG, CNPq, CAPES and FAPEMIG in funding this work. This study received funding from CNPq Call 18/2024, grant number 308573/2025-0. The Authors also express their gratitude to the Hungarian National Research, Development and Innovation Office for supporting the project 2021-1.2.4-TÉT-2021-00062 (Support to bilateral science and technology cooperations).

References

Agrawal, S., Yulianti, E., Amran, M., Hung, C.-C. (2025) Behavior of unconfined steel-fiber reinforced UHPC post high-temperature exposure, Case Studies in Construction Materials, v. 22, pp. e04173, https://doi.org/10.1016/j.cscm.2024.e04173.

Dally, J.W. & Riley, W.F. Experimental stress analysis, 3rd ed. McGraw-Hill, 1991, pp 639.

Dehghanpour, D., Subasi, S., Guntepe, S., Emiroglu, M., Marasli, M. (2022) Investigation of fracture mechanics, physical and dynamic properties of UHPCs containing PVA, glass and steel fibers, Construction and Building Materials, v. 328, pp. 127079, https://doi.org/10.1016/j.conbuildmat.2022.127079.

Li, Y., Yang, E.-H., Tan, K. H. (2019) Effects of heating followed by water quenching on strength and microstructure of ultra-high performance concrete. Construction and Building Materials, v. 207, pp. 403-411, https://doi.org/10.1016/j.conbuildmat.2019.02.123.

Lin, J., Zhang, Y., Guo, Z., & Du, H. (2024) Impact of synthetic fibers on spalling and intrinsic pore structure of ultra-high performance concrete (UHPC) under elevated temperatures. Construction and Building Materials, v. 439, pp. 137325, https://doi.org/10.1016/j.conbuildmat.2024.137325.

Lyzwa, J., Zehfuss, J. (2021) Experimental investigations of ultra-high performance concrete exposed to natural fires. Fire Safety Journal. https://doi.org/10.1016/j.firesaf.2021.103399

Nassar, R.U.D., Zaid, O., Althoey, F., Abuhussain, M. A., Alashker, Y. (2024) Spalling behavior and performance of ultra-high-performance concrete subjected to elevated temperature: A review. Construction and Building Materials, v. 411, pp. 134489, https://doi.org/10.1016/j.conbuildmat.2023.134489.

Tada, H., Paris, P. C., & Irwin, G. R. (2000). The Stress Analysis of Cracks Handbook (3rd ed.). ASME Press. https://doi.org/10.1115/1.801535.

Viana, T.M., Bacelar, B.A., Coelho, I.D., Ludvig, P., & Santos, W.J. (2020) Behaviour of ultra-high performance concretes incorporating carbon nanotubes under thermal load. Construction and Building Materials, v. 263, pp. 120556, https://doi.org/10.1016/j.conbuildmat.2020.120556.

Zhang, D., Liu, Y., & Tan, K.H. (2021). Spalling resistance and mechanical properties of strain-hardening ultra-high performance concrete at elevated temperature. Construction and Building Materials, v. 266, pp. 120961, https://doi.org/10.1016/j.conbuildmat.2020.120961.

Zhang, K., Ni, T., Zhang, J., Wang, W., Chen, X., Zaccariotto, M., Yin, W., Zhu, S., & Galvanetto, U. (2023). Experimental and Hybrid FEM/Peridynamic Study on the Fracture of Ultra-High-Performance Concretes Reinforced by Different Volume Fractions of Polyvinyl Alcohol Fibers. Polymers, 15(3), 501. https://doi.org/10.3390/polym15030501.

Fatigue Behaviour of High-Performance Fibre Reinforced Concrete (HPFRC): from Experimental Investigations to Design Provisions

Gabriele David Bocchino[1], Nicholas Sergio Burello[2], Alfredo Alan Flores Gutierrez[3], Davide Zampini[2], Liberato Ferrara[1]

[1]: Department of Civil and Environmental Engineering, Politecnico di Milano, Milan, Italy.

[2]: CEMEX Innovation Holding AG Brügg Branch, Brügg, Switzerland.

[3]: CEMEX, Mexico City, Mexico.

Abstract

The advancements in concrete materials, such as High-Strength Concrete (HSC), are enabling designers to conceive increasingly ambitious structures with more slender and optimised sections. However, when such structures serve mobility infrastructures (e.g., airport pavements, highway and railway pavements and bridges) or energy-harvesting and energy-storage systems (e.g., windmills, gravity-based energy storage systems), they may be subjected to millions or billions of load cycles over their service life. This can lead to damage accumulation and premature deterioration or failure, making fatigue a potentially governing design criterion.

Fibre-Reinforced Concrete (FRC) and High-Performance Fibre-Reinforced Concrete (HPFRC) can represent possible solutions to the problem of fatigue, as the bridging effect of fibres provides the material with increased toughness and non-negligible tensile strength, enabling it to better withstand cyclic actions.

This work presents the outcomes of several fatigue campaigns conducted by the authors over multiple years, including cyclic tests up to 10^6 cycles in compression and uniaxial flexure, as an ongoing campaign on biaxial flexure of a deflection-hardening HPFRC.

The experimental results—specifically, the cycles to failure—are used to evaluate the validity of fatigue formulations in current design codes, namely Model Code 2020 and Eurocode 2. Relative to code predictions, no enhancement was observed in compression, whereas flexural performance was markedly improved.

Keywords

High-Performance Fibre-Reinforced Concrete (HPFRC), S-N curve, fatigue, flexure, compression

1 Introduction

Advancements in concrete technology have resulted in improved concrete material with denser matrices, higher compressive strengths, reduced permeability and, consequently, enhanced durability, as well as improved fresh properties. These materials, which include High-Strength Concrete (HSC) and High-Performance Concrete (HPC), are allowing designers to conceive thinner sections and more slender elements, also in response to growing attention in the efficient use of materials for sustainability purposes.

However, when such structural elements are used as part of systems which by their nature are subjected to repeated loads, cycles might induce damage accumulation and lead to premature degradation and failure (Lee and Barr, 2004; Kachkouch et al., 2022), making fatigue a primary design concern.

Fatigue can be significant both in compression and in flexure. In compression, an example is provided by concrete wind turbine towers (Chen et al., 2023; Dolan et al., 2016; Harte and Van Zijl, 2007; Loraux, 2018), which, due to self-weight and precompression, are mainly subjected to compressive stresses. These stresses, however, are not constant in time, as wind loads, temperature gradients, and the nacelle rotation introduce cyclic variations (Harte and Van Zijl, 2007). Other fatigue-prone applications (Hsu, 1981; Makita and Brühwiler, 2014; Nguyen et al., 2022) include bridges and other mobility and transportation infrastructures—including, e.g., highways, mass rapid transit systems, and railways—as well as airport pavements and industrial floors (Nayar and Gettu, 2020; Koorikkattil et al., 2023, 2026). These are often subjected to cyclic loading in flexure, which may be even more critical than compression due to the brittle behaviour of concrete in tension.

The inclusion of fibres is widely regarded as a possible solution to fatigue in concrete (Koorikkattil et al., 2023), as they can delay crack initiation, slow down damage propagation (Stephen and Gettu, 2020), and, in general, confer to the material improved toughness and better tensile behaviour. Therefore, Fibre-Reinforced Concrete (FRC) and High-Performance Fibre-Reinforced Concrete (HPFRC) represent promising candidates for fatigue-sensitive applications.

However, for designers to fully exploit the enhanced capabilities of these materials and achieve more optimised yet safe designs, suitable code formulations are required (Brandt, 2008). In general, fatigue provisions are based on S-N curves (also known as Wöhler curves, named after the researchers who originally developed them for fatigue in metals (Wöhler, 1858; Zenner and Hinkelmann, 2019)) which relate a stress level (S), to the number of cycles (N) that a material can sustain at that level. Most formulations in current design codes—namely Eurocode 2 (*EN 1992-1-1:2023 – Eurocode 2: Design of concrete structures. Part 1-1: General rules and rules for buildings, bridges and civil engineering structures*, 2023) and Model Code 2020 (International Federation for Structural Concrete, 2023)—were developed for Plain Concrete (PC), and their applicability to FRC remains to be assessed.

In this work, the validity of current design formulations in both compression and flexure is evaluated by comparing them to an extensive database of fatigue tests on a deflection-hardening HPFRC, conducted at Politecnico di Milano and Cemex Innovation Holding. The experimental programme includes tests in compression, flexure, and biaxial flexure. Where appropriate,

updated formulations are proposed, and suggestions for improvement are provided, contributing to future developments of fatigue design provisions.

2 Experimental Programmes and Monotonic Characterisation

The material used in the fatigue campaigns presented herein belongs to a family of HPFRC with a steel-based hybrid reinforcement system, commercialised under the name of Cemex© Resilia©, whose mix design is covered by patent EP3307692 B1 (Zampini et al., 2016).

A first series of experimental tests was conducted to investigate the fatigue behaviour of the material under compressive and uniaxial flexural loading. Prior to fatigue testing, the material was fully characterised under monotonic loading in compression and flexure, as described in (Bocchino et al., 2025).

Six monotonic compressive tests were performed on cylinders according to EN 12390-3 ("EN 12390-3:2019 – Testing hardened concrete. Part 3, Compressive strength of test specimens," 2019). The specimens were also instrumented with three Linear Variable Displacement Transducers (LVDTs) to measure vertical displacements and obtain the full stress-strain response. The material exhibited an average compressive strength $f_{cm} = 91.64\ MPa$ and a characteristic compressive strength $f_{ck} = 83.22\ MPa$, resulting in class C80 according to Model Code 2020 (or class C80/95 according to Eurocode 2).

In a similar fashion, six notched beams were tested monotonically, while recording the Crack Mouth Opening Displacement (CMOD) in a Three-Point Bending (3PB) configuration according to EN 14651 ("EN 14651," 2005). The obtained average values of the flexural parameters of interest were $f_{Lm} = 5.78\ MPa$, $f_{R1m} = 12.16\ MPa$ and $f_{R3m} = 11.92\ MPa$, while the corresponding characteristic values were $f_{Lk} = 4.83\ MPa$, $f_{R1k} = 9.23\ MPa$; whileand $f_{R3k} = 8.03\ MPa$. The FRC under study can thus be classified as 8b according to Model Code 2020 (or 8c according to Eurocode 2).

The results of the monotonic characterisation of the material—hereafter referred to as HSFRC-1, where "HS" denotes "High Strength" and "1" refers to the first series of experimental tests—are summarised in Table 1.

Table 1: Monotonic characterisation of mix HSFRC-1.

	$\mathbf{f_c}$[MPa]	$\mathbf{f_L}$[MPa]	$\mathbf{f_{R1}}$[MPa]	$\mathbf{f_{R2}}$[MPa]	$\mathbf{f_{R3}}$[MPa]	$\mathbf{f_{R4}}$[MPa]
average	91.64	5.78	12.16	13.39	11.92	10.36
standard deviation	4.75	0.53	1.65	1.59	2.19	2.40
characteristic	83.22	4.83	9.23	10.57	8.03	6.12

For the fatigue tests, each specimen was subjected to sinusoidal cycles between two load levels defined as a percentage of f_{ck} for compression and f_{R1k} for uniaxial flexure. Across all tests, the lower load level (S_{low}) was set to 10% of the reference stress, while the upper load level (S_{upp}) was selected among four values: 45% and 60%, representative of design limit states, and 80% and 90%, chosen to induce significant and observable damage in the material during the tests. In the following, load levels are denoted with a superscript indicating the

reference quantity used in their definition. For example, $S_{low}^{(f_{R1k})}$ denotes the lower load level defined as a percentage of f_{R1k}. The specimens were cycled at a frequency of 3 Hz, up to a predefined number of cycles—10^2, 10^4, 10^6—or until failure, whichever occurred first, and three nominally identical tests were performed for each case. Specimens that did not fail upon reaching the predefined number of cycles were unloaded and subsequently tested monotonically to assess the possible degradation in residual strength.

More recently, a further campaign was initiated to investigate the fatigue behaviour of FRC under biaxial flexure. In this case, two variations of the previous mix were considered. In terms of compressive strength, the first mix exhibited $f_{cm} = 63.38\ MPa$ and $f_{ck} = 58.83\ MPa$, corresponding to class C50 according to Model Code 2020 (or C55/67 according to Eurocode 2), whereas the second mix exhibited $f_{cm} = 86.29\ MPa$ and $f_{ck} = 83.39\ MPa$, corresponding to class C80/95 according to Model Code 2020 (or C80 according to Eurocode 2). Throughout this work, the two mixes are designated as NSFRC-2 and HSFRC-2, where "NS" and "HS" denote "Normal Strength" and "High Strength", respectively, and "2" refers to the second series of experimental tests. In terms of flexural behaviour, NSFRC-2 exhibited $f_{Lm} = 5.34\ MPa$, $f_{R1m} = 7.31\ MPa$ and $f_{R3m} = 7.22\ MPa$, and the corresponding characteristic values were $f_{Lk} = 4.88\ MPa$, $f_{R1k} = 5.02\ MPa$ and $f_{R3k} = 5.42\ MPa$, corresponding to class 5c both according to Model Code 2020 and Eurocode 2. Conversely, HSFRC-2 exhibited $f_{Lm} = 6.17\ MPa$, $f_{R1m} = 12.74\ MPa$ and $f_{R3m} = 11.51\ MPa$, and $f_{Lk} = 5.06\ MPa$, $f_{R1k} = 10.45\ MPa$ and $f_{R3k} = 8.01\ MPa$, resulting in class 10b according to Model Code 2020 (or class 8c according to Eurocode 2). All results for the two mixes are summarised in Tables 2 and 3. It should be noted that, despite the difference in classification, mixes HSCFRC-1 and HSCFRC-2 exhibit very similar behaviour, as it can be seen by directly comparing Table 1 and Table 3.

Table 2: Monotonic characterisation of mix NSFRC-2.

	f_c[MPa]	f_L[MPa]	f_{R1}[MPa]	f_{R2}[MPa]	f_{R3}[MPa]	f_{R4}[MPa]
average	63.38	5.34	7.31	7.86	7.22	6.50
standard deviation	2.77	0.26	1.30	1.22	1.02	0.87
characteristic	58.83	4.88	5.02	5.70	5.42	4.96

Table 3: Monotonic characterisation of mix HSFRC-2.

	f_c[MPa]	f_L[MPa]	f_{R1}[MPa]	f_{R2}[MPa]	f_{R3}[MPa]	f_{R4}[MPa]
average	86.29	6.17	12.74	12.41	11.51	10.46
standard deviation	1.77	0.63	1.30	1.83	1.98	2.05
characteristic	83.39	5.06	10.45	9.17	8.01	6.84

Using the two mixes, Round Determinate Panels (RDPs) with a nominal thickness of 75 mm and a nominal diameter of 800 mm were cast. They were first tested monotonically in accordance with ASTM C1550 (C09 Committee, 2020), with the RDPs supported on three supports spaced 120° apart and loaded by applying a point load at the centre of the panel. Panels are expected to fail by forming three radial cracks (hereafter referred to as "panel failure"). However, occasionally, failure occurred in a beam-like manner ("beam failure"), with a single crack splitting the entire panel. For both mixes, three tests were performed; in each case, two out of three specimens failed in the desired mode. According to the standard, at least two tests

exhibiting panel failure are required for proper characterisation. Therefore, the average peak load associated to panels made of each material was computed excluding the result corresponding to the beam-like failure. The panels made of NSFRC-2 exhibited an average peak load $P_m = 39.75\,kN$, while those made of HSFRC-2 exhibited $P_m = 59.97\,kN$. All results in terms of peak loads are summarised in Table 4, while additional considerations regarding these tests are reported in (Bocchino et al., 2026).

Table 4: Flexural characterisation of RDPs. Averages computed disregarding beam-like failures "(b.f.)".

	P [kN]	
	NSFRC-2	**HSFRC-2**
A	38.20	60.83
B	44.56(b.f.)	67.04(b.f.)
C	41.31	59.12
average (excluding b.f.)	39.75	59.97

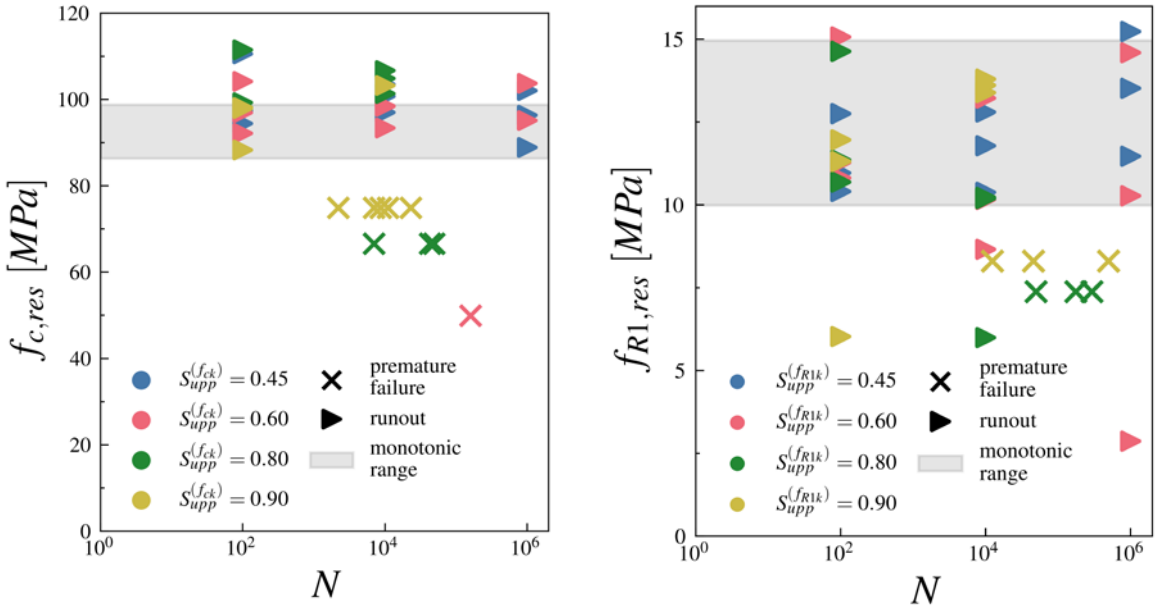
The associated fatigue campaign is still ongoing at the time of writing this paper. Fatigue tests on RDPs followed a procedure analogous to that of previously described campaigns, but with load levels defined as a percentage of the average peak loads obtained from the monotonic tests. To accommodate the limitations of the testing machine (which was the same used for the corresponding monotonic characterisation), the loading frequency was reduced to $0.5 \div 1.5\,Hz$ (instead of the $3\,Hz$ employed for the previous campaigns), and different combinations of cyclic loading histories and load ranges were used. Throughout the tests, the central deflection was measured using an LVDT, while crack development over one-third of the panel was monitored using a custom-built Digital Image Correlation (DIC) system.

3 Experimental Results

A first way to interpret the fatigue test results is by relating the residual strength to the number of applied cycles, N. Figure 1 summarises these results for compression and uniaxial flexure. To construct the plots, which contain data points corresponding to both runouts (unloaded and subsequently tested monotonically to directly assess their residual strength) and premature failures, it was assumed that, when specimens failed during testing, failure occurred because the degradation of the material caused the residual strength to reach the applied upper stress level.

With reference to Figure 1(a), it can be observed that, in compression, for $S_{upp}^{(f_{ck})} = 0.45$, no specimens failed and all were able to withstand 10^6 cycles. For $S_{upp}^{(f_{ck})} = 0.60$, two out of the three specimens intended to be tested up to 10^6 cycles resulted in runouts, while one failed at 1.7×10^5 cycles. For $S_{upp}^{(f_{ck})} = 0.80$, considering testes aimed at 10^4 and 10^6, some specimens endured 10^4 cycles without failing, whereas others failed in the range $7 \times 10^3 \div 5 \times 10^4$. A similar trend was also observed for $S_{upp}^{(f_{ck})} = 0.90$, with most specimens failing in the range $7 \times 10^3 \div 2.3 \times 10^4$.

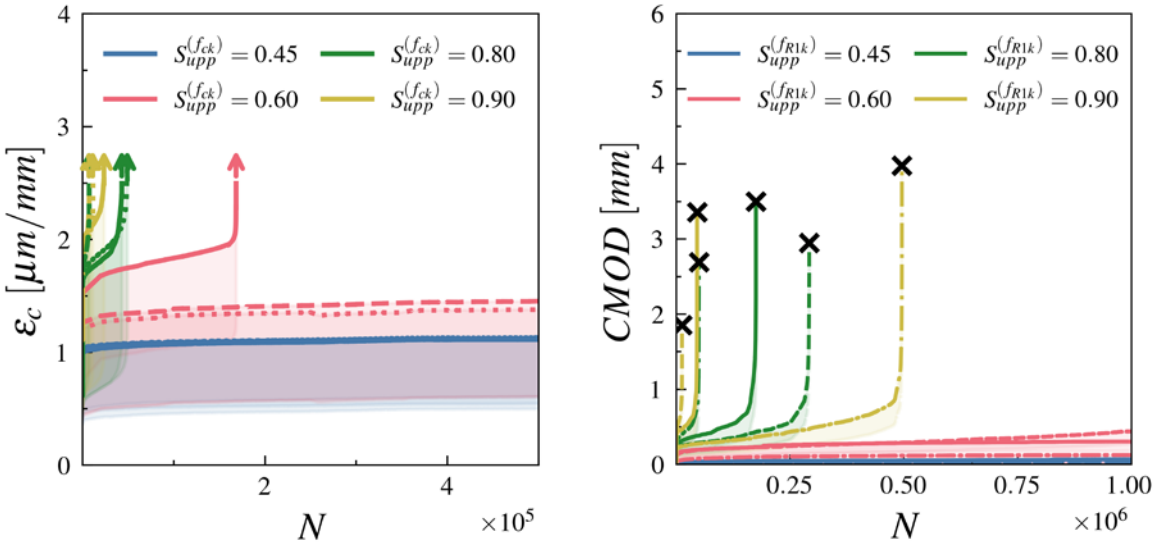
Regarding flexure (Figure 1(b)), none of the specimens tested at $S_{upp}^{(f_{R1k})} = 0.45$ and $S_{upp}^{(f_{R1k})} = 0.60$ failed. Conversely, for the two higher upper load levels, $S_{upp}^{(f_{R1k})} = 0.80$ and $S_{upp}^{(f_{R1k})} = 0.90$, none of the tests intended to reach 10^6 cycles resulted in runouts, with specimens failing in the range $1.2 \times 10^4 \div 5 \times 10^5$.



(a) Compression *(b) Uniaxial flexure*

Figure 1: Residual strength with respect to number of applied cycles N.

As mentioned in Section 2, during the fatigue tests, the evolution of suitably identified kinematic parameters was also recorded to have an indication of damage progression alongside the applied cycles. It is well known that the evolution of fatigue tests is usually characterised by three phases in terms of kinematic parameters, stiffness and even dissipated energy (Do et al., 1993; Hümme et al., 2016; "ACI 215-21," 2022; Martinello Carlesso et al., 2025). For example, in terms of kinematic parameters, the first phase is characterised by a rapid increase—e.g., longitudinal strain ε_c in compression or $CMOD$ in uniaxial flexure—at a decreasing rate, followed by a second phase of steady increase at an approximately constant rate, and a final third phase or rapid increase at an accelerated rate, leading to failure. Figure 2 presents the obtained curves: ε_c with respect to N for the compression tests, and $CMOD$ with respect to N for uniaxial flexure tests (for tests originally intended to reach 10^6 cycles). It can be observed that specimens that failed prematurely progressed to the third phase, whereas runouts were stopped somewhere during the second phase and do not exhibit the accelerated increase.



(a) Compression *(b) Uniaxial flexure*

Figure 2:Evolution of kinematic parameters with respect to the cycles performed N.

For specimens that did fail during testing, these kinematic quantities can also be plotted against the normalised cycle number n, defined as the ratio of the number of cycles N to the number of cycles at failure N_R for each specific test. For instance, Figure 3 shows the evolution of $CMOD$ against n for the six specimens that failed during testing. A tentative subdivision between the three phases is highlighted, keeping in mind that the evolution is continuous and no sharp boundaries exist. As reported in literature (Martinello Carlesso et al., 2019; Kachkouch et al., 2022; "ACI 215-21," 2022), the second phase typically spans the majority of the fatigue life, both in compression and in flexure, usually starting at about $n = 0.10 \div 0.20$ and ending at about $n = 0.80 \div 0.90$.

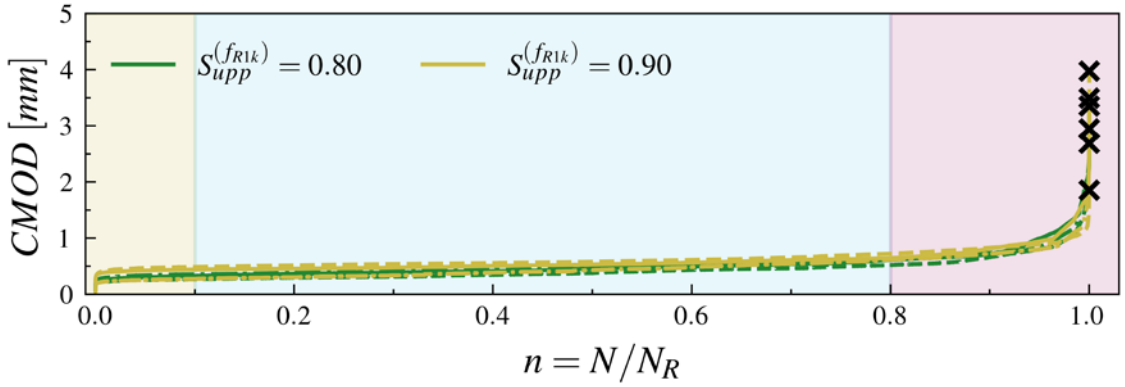
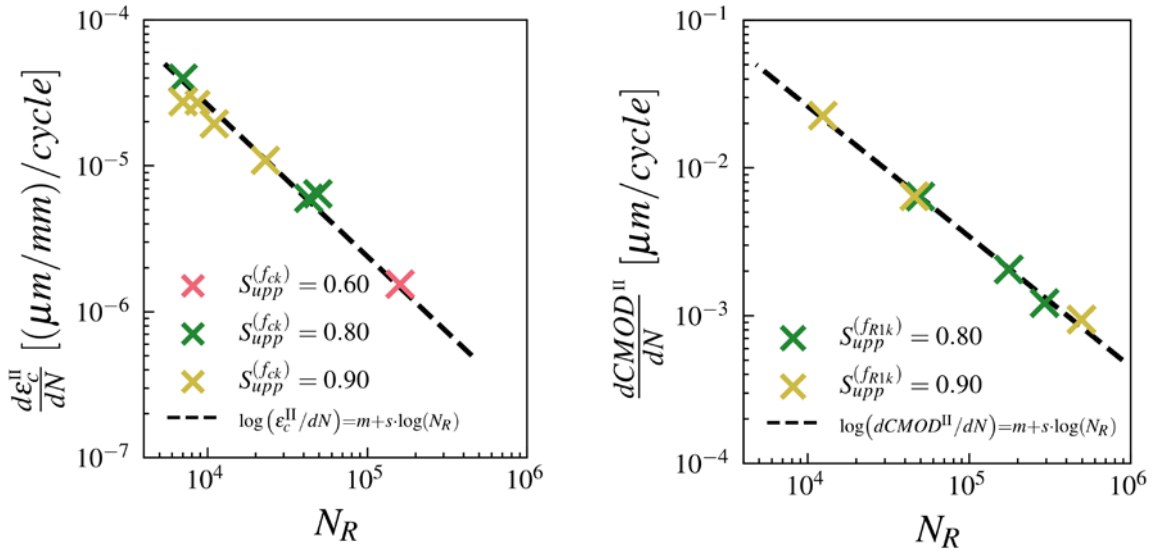


Figure 3: Evolution of $CMOD$ with respect to the normalised number of cycles n.

The second phase of the curves can be considered approximately linear, with its slope corresponding to the rate of increase of $CMDO$ in flexure, $dCMOD^{(II)}/dN$, or, analogously, the rate of increase of strain in compression, $\varepsilon_c^{(II)}/dN$.

Sparks and Menzies (1973) originally observed, for compression fatigue in PC, a strong linear correlation between the logarithm of the strain rate in the secondary phase, $\log(\varepsilon_c^{(II)}/dN)$, and the logarithm of the number of cycles to failure, $\log(N_R)$. Many researchers have since empirically shown that this relationship is also valid for FRC (Do et al., 1993; Cachim et al., 2002; Poveda et al., 2017; Blasón et al., 2022; González et al., 2023). For example, Figure 4 shows that Sparks-Menzies's law appears to hold for the material under study in compression as well as in uniaxial flexure. Once the coefficients of the Sparks-Menzies's law are obtained for a given material and type of loading, they can be used to predict the number of cycles to failure for runout tests, as will be shown in Section 4.



(a) Compression *(b) Uniaxial flexure*

Figure 4: Validation of Sparks-Menzies's law for the studied material.

4 Comparison Between Experimental Results and Design Formulations

The experimental results presented in Section 3 can be organised in S-N diagrams, with each test represented as a pair consisting of the number of cycles to failure, N_R, and the corresponding upper stress level S_{upp}, enabling comparison with fatigue formulations from current design codes. For specimens that failed during testing, these points are readily obtained. Conversely, to include also runouts, it is necessary to estimate the cycles to failure that they would have reached, had the test not been interrupted. Several methods have been proposed in literature, often based on the evolution of kinematic parameters, stiffness, dissipated energy or residual strength. A reasonable approach consists in using the relationship derived from Sparks-Menzies's law calibrated on the prematurely failed specimens (see Figure 4). Assuming that the runout tests have reached the stable rate of increase characteristic of the second phase, this rate can be estimated and, using Sparks-Menzies's law, the corresponding number of cycles to

failure N_R can be estimated, under the assumption that the relationship remains valid beyond the region used for calibration (i.e. usually the low-cycle fatigue region). In the present work, fatigue life estimations relied exclusively on the Sparks-Menzies method and were applied only to runout tests at 10^6 cycles, disregarding those at 10^2 and 10^4 cycles (which might not be sufficient to reliably estimate the rate of increase of the secondary phase, particularly when considering tests performed at low load levels. These shorter tests might not be sufficient to reliably estimate the rate of increase of the secondary phase, particularly for tests performed at low load levels, leading to an overestimation of the rate and consequently to an underestimation of fatigue life.

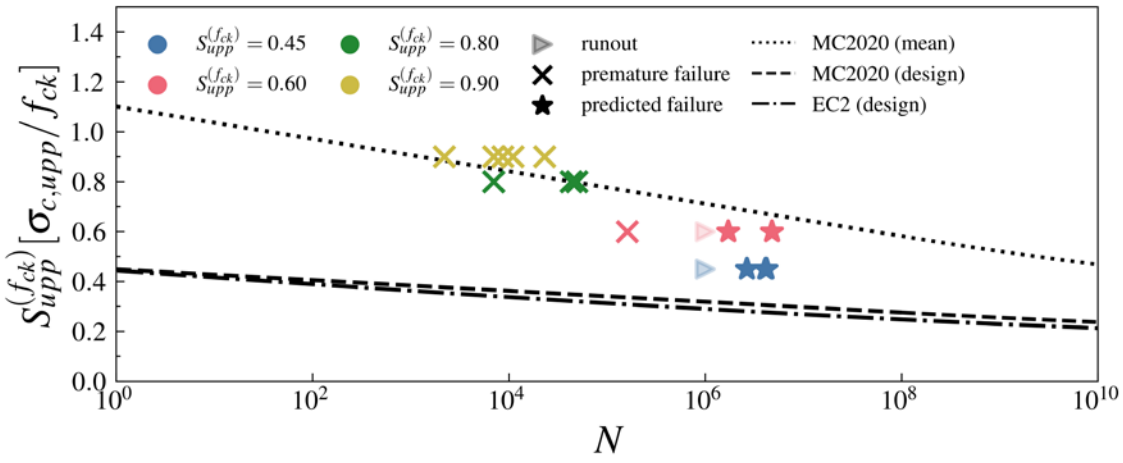


Figure 5: Comparison between experimental results and S-N curves from current design codes in compression.

Starting with compression, Figure 5 compares the experimental points—including both premature failures and predictions obtained from runouts—to design formulations from Model Code 2020 and Eurocode 2. As a general remark, Model Code 2020 provides two mathematically analogous formulations. The first one (Model Code 2020, §14.6.2), referred to here as the "mean" formulation, aims to capture the actual material behaviour, while the second (Model Code 2020, §30.2.2), referred to as the "design" formulation, is intended for design purposes. Specifically, the mean formulation defines stress levels based on the average compressive strength of the material, f_{cm}, whereas the design formulation defines stress levels based on the characteristic strength, f_{ck}, and introduces appropriate safety coefficients and load factors. In contrast, Eurocode 2 provides a single formulation for design, which despite having a different mathematical expression, is based on the same principles as the Model Code 2020 design formulation, resulting in very similar curves in cases such as the present one.

From Figure 5, it can be observed that the behaviour at high stress levels seems to be well captured by the mean formulation of Model Code 2020, whereas behaviour at lower stresses levels is overestimated compared to the experimental data. In any case, when considering the design curves from both Model Code 2020 and Eurocode 2, the experimental points lie well above both curves, thereby ensuring safety in design. It can thus be concluded that, in compression, fibres do not appear to provide improved fatigue performance, and current design formulations do not require updating. Other researchers have also reported similar observations, and in general, there is no consensus in the literature on the role of fibres in the fatigue behaviour

of FRC in compression (Cachim et al., 2002; Lee and Barr, 2004; Lohaus et al., 2012; Schäfer and Breitenbücher, 2023). It should be notated that this lack of improvement might be expected, as in compression fibres are typically not activated (Lee and Barr, 2004), except by the tensile strains induced by Poisson's effect in the transverse direction. However, these strains might generally be too small to activate the fibres—at least until advanced degradation has already occurred—thereby explaining why fibres might not be effective in retarding damage progression.

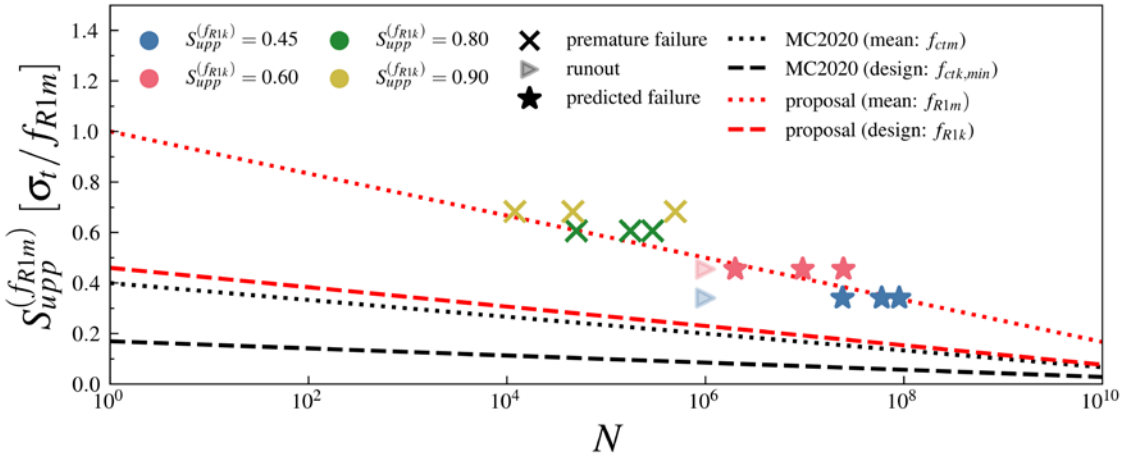


Figure 6: Comparison between experimental results and S-N curves from current design codes in uniaxial flexure.

Similarly to what has been shown for compression, Figure 6 compares the experimental results in flexure with relevant design formulations. It should be noted that for flexure, the relevant stress to be considered is the maximum tensile stress, σ_t, occurring in the specimen, and it is therefore necessary to employ S-N curves established for concrete in tension. While Model Code 2020 provides such curves, Eurocode 2, only provides S-N curves in compression. Therefore, in the following, reference is made only to Model Code 2020. As an additional note, the reference stress level used in the S-N diagram of Figure 6, is $S_{upp}^{(f_{R1m})}$, defined as the ratio between the upper applied tensile stress, $\sigma_{t,upp}$, and f_{R1m} of the considered material. To compare experimental points and different S-N curves, all values have been renormalised accordingly, using simple mathematical transformations as explained in (Bocchino et al., 2024).

From the plot, it can be observed that the experimental points (again including both premature failures and predictions obtained from runouts) lie markedly above both the design curve (as expected) and the mean curve intended to capture the material behaviour. This indicates that, for FRC materials like the ones under study, Model Code 2020 underestimates the material performance, suggesting that a tailored formulation could better exploit the improved capabilities of the material. The gap between experimental results and the Model Code 2020 formulations arises because these formulations define stress levels based on the tensile strength of concrete, namely f_{ctm} for the mean curve and $f_{ctk,min}$ for the design curve. While this approach is appropriate for PC, the tensile and flexural behaviour of FRC is not governed by the strength of the matrix, but by its residual flexural strengths, primarily f_{R1} and f_{R3}. However, for FRCs such as those under study, the values of f_{ctm} and, even more so, $f_{ctk,min}$ (determined on the basis of f_{ck} according to Model Code 2020 §14.6.1.2) are much

lower than f_{R1k}, leading to overly conservative maximum admissible stress levels. For instance, the design curve from Model Code 2020 represented in Figure 6 (and appropriately renormalised) shows a maximum admissible stress level smaller than $S_{upp}^{(f_{cm})} = 0.20$, approximately half the stress level for which all specimens survived 10^6 cycle with no recorded loss of residual strength. Therefore, for FRC materials like the one herein investigated, with deflection-hardening behaviour, it would be more suitable to define stress levels either based on the actual tensile strength determined experimentally for each case, or more conveniently directly on f_{R1} or possibly also f_{R3} (to take into account different types of post-peak behaviours), which are parameters already required in FRC design.

As an example, still with reference to Figure 6, maintaining the same mathematical formulation of the mean curve of Model Code 2020 and simply replacing f_{ctm} with f_{R1m} yields a curve that closely captures the observed experimental behaviour. Likewise, for the design curve, replacing $f_{ctk,min}$ with f_{R1k} (while retaining the same safety coefficients and load factors) leads to a new curve that appears to strike a better balance between safety and optimisation, lying well below all experimental points while remaining above the current design formulation from Model Code 2020.

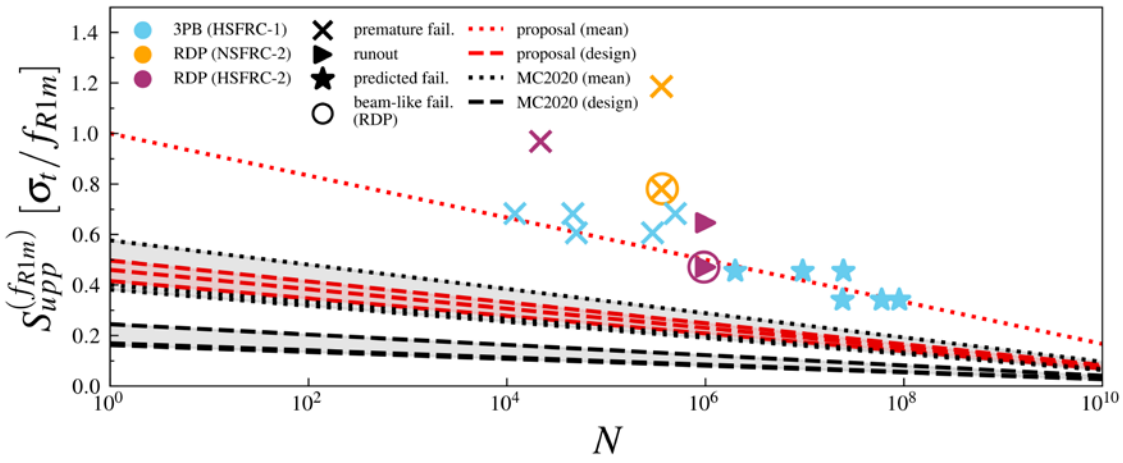


Figure 7: Comparison between uniaxial and biaxial flexure.

Finally, referring to Figure 7, it is interesting to compare the current formulations and the proposed one with the preliminary results obtained under biaxial flexure. As stated in Section 2, two different mixes were used for the RDPs. It is still possible to compare results between different mixes, however, except for the curve corresponding to the proposed formulation, which already uses the same stress definition adopted for the entire plot (i.e. based on f_{R1m}), all other curves are replicated once per considered mix (three in this case), as they must be normalised with respect to the specific value of f_{R1m} of each mix.

For the fatigue tests on RDPs, load levels were initially defined with respect to peak loads. The corresponding stress levels were estimated a posteriori, assuming elastic behaviour (as it is customarily done also in the case of notched 3PB tests). Figure 7 reports both points referring to panels that failed in the expected three-crack pattern as well as those that failed in a beam-like manner. For the former, the maximum tensile stress was estimated using a formula obtained by Minelli and Plizzari (2015) from elastic Finite Element Method (FEM) analysis, whereas for

the latter, the panel was assimilated to a beam in an asymmetric 3PB configuration, and the maximum tensile stress was computed according to Navier's beam formula, with an adequate choice of section and span lengths.

It can be seen that two out of the three specimens that failed in the desired three-crack pattern lie markedly above even the proposed improved formulation, with levels close or even exceeding 1. The third specimen was a runout, and thus no conclusions can be drawn about its final position relative to the curve, had the test continued until failure (in this case, Sparks-Menzies's law could not be applied for predictions, due to insufficient available data). However, it is reasonable to accept that it would have fallen further to the right and thus further above the proposed curve. At first glance, stress levels greater than unity may seem paradoxical, but several factors must be considered. First, it should be recalled that load levels in the RDP tests were defined with respect to peak loads, rather than directly in terms of stress levels occurring in the panels. Therefore, stress levels greater than 1 are possible, even disregarding experimental variability, since f_{R1m} does not generally correspond to the peak strength of the material. Additionally, the maximum tensile stress was computed from an elastic analysis; however, when the panel develops biaxial behaviour, due to redistribution, the actual stresses might be lower than the estimated values.

Conversely, the two remaining points corresponding to beam-like failures lie closer to the proposed curve, even though, also in this case, the runout specimen might have ended slightly above the curve had the test continued.

These preliminary results seem to suggest that when the specimen failed in a beam-like manner, its behaviour was similar to that of a beam, with results close to the proposed improved formulation. In contrast, specimens that were able to develop biaxial behaviour, particularly the two that failed prematurely, performed even better than the proposed updated formulation.

While the observed difference between the two types of behaviour likely reflects a physical reality, the effect may have been magnified by the way in which stresses were estimated in the two cases. The fatigue campaign on RDPs is still ongoing, and if further results confirm the observed behaviour, they may help support an improved formulation that also accounts for the redistribution effect in biaxial fatigue by integrating a redistribution factor into the definition of the stress level.

5 Conclusions

This works has presented and summarised the main outcomes of several fatigue campaigns performed on a deflection-hardening HPFRC material, encompassing tests in compression, uniaxial flexure and biaxial flexure.

In compression, fibres do not appear to improve fatigue behaviour. Fibres are effective when bridging cracks under tensile loading; however, in compression, tensile stresses may develop transversely due to Poisson's effect, although the corresponding strain levels might generally be insufficient to activate the fibres. Therefore, current design formulations from Eurocode 2 and Model Code 2020—which were already calibrated for HSC—do not require updating

Under flexure, fibres are active from the beginning and can significantly enhance fatigue performance compared with PC. In fact, experimental results lie markedly above the design curve proposed in Model Code 2020 (Eurocode 2 does not include a design formulation in

tension) for PC. Based on the observed behaviour, a tailored design formulation was proposed, aimed at better balancing safety and optimisation, using f_{R1} as a reference parameter. Future updates of the codes should include formulations specifically calibrated on FRC materials, potentially based on f_{R1} and also f_{R3}, to account for different post-peak behaviours.

6 Acknowledgements

The first author acknowledges the support of the Italian National Plan of Recovery and Resilience Mission 4, component 1 “Enhancement of the offer of educational services: from nurseries to universities”; Investment 3.4 “Advanced teaching and university skills” and Investment 4.1 “Extension of the number of research doctorates and innovative doctorates for public administration and cultural heritage” for the co-funding of his PhD scholarship.

M.Arch. Giuseppe Pappadà, Mr. Paolo Broglia, Arch. Maria Santangelo, Mr. Francesco Pillai, and M.Eng. Giacomo Vazzana technicians from the Laboratory for Testing Materials, Buildings and Structures (LPMSC) Politecnico di Milano, are gratefully acknowledged for their support during the execution of the original experimental campaign.

B.Sc. Mateusz Kusmierek, Mr. Lorenzo Fontana, M.Sc. Samuele Cimini, and Mr. Pablo Hoffmann de Buen, technicians and interns at Cemex Innovation Holding, are also kindly acknowledged for their support during the execution of the ongoing experimental campaign on Round Determinate Panels.

7 References

ACI 215-21, 2022.

Blasón, S., Fernández Canteli, A., Poveda, E., Ruiz, G., Yu, R.C., Castillo, E., 2022. Damage evolution and probabilistic strain-lifetime assessment of plain and fiber-reinforced concrete under compressive fatigue loading: Dual and integral phenomenological model. Int. J. Fatigue 158, 106739. https://doi.org/10.1016/j.ijfatigue.2022.106739

Bocchino, G.D., Burello, N.S., Flores Gutierrez, A.A., Zampini, D., Ferrara, L., 2026. Experimental Investigation of the Biaxial Fatigue Behaviour of a High-Performance Fibre Reinforced Concrete (HPFRC), in: Accepted for Publication in the Proceedings of the 7th Fib Congress (Lisbon, 2026). Lisbon, Portugal.

Bocchino, G.D., Davolio, M., Flores Gutierrez, A.A., Burello, N.S., Lo Monte, F., Zampini, D., Ferrara, L., 2025. Experimental Investigation of the Flexural Fatigue Behaviour of a High-Performance Fibre Reinforced Concrete (HPFRC). https://doi.org/10.1016/j.conbuildmat.2025.141826

Bocchino, G.D., Davolio, M., Gutierrez Flores, A.A., Burello, N.S., Lo Monte, F., Ferrara, L., 2024. High-Performance Steel Fibre Reinforced Concrete (HPFRC) Flexural Fatigue Design with Upgraded S-N Curves, in: Mechtcherine, V., Signorini, C., Junger, D. (Eds.), Transforming Construction: Advances in Fiber Reinforced Concrete, RILEM Bookseries. Springer Nature Switzerland, Cham, pp. 372–380. https://doi.org/10.1007/978-3-031-70145-0_46

Brandt, A.M., 2008. Fibre reinforced cement-based (FRC) composites after over 40 years of development in building and civil engineering. Compos. Struct. 86, 3–9. https://doi.org/10.1016/j.compstruct.2008.03.006

C09 Committee, 2020. ASTM C1550-20, Standard Test Method for Flexural Toughness of Fiber Reinforced Concrete (Using Centrally Loaded Round Panel). https://doi.org/10.1520/C1550-20

Cachim, P.B., Figueiras, J.A., Pereira, P.A.A., 2002. Fatigue behavior of fiber-reinforced concrete in compression. Cem. Concr. Compos. 24, 211–217. https://doi.org/10.1016/S0958-9465(01)00019-1

Chen, C., Shen, X., Zhou, Z., Hua, X., 2023. Feasibility study of a steel-UHPFRC hybrid tower for offshore wind turbines. Ocean Eng. 288, 116140. https://doi.org/10.1016/j.oceaneng.2023.116140

Do, M., Chaallal, O., Aïtcin, P., 1993. Fatigue Behavior of High-Performance Concrete. J. Mater. Civ. Eng. 5, 96–111. https://doi.org/10.1061/(ASCE)0899-1561(1993)5:1(96)

Dolan, C.W., Morgan, K.B., Kuchma, D.A., 2016. Report on Design of Concrete Wind Turbine Towers. American Concrete Institute, Farmington Hills, MI.

EN 1992-1-1:2023 – Eurocode 2: Design of concrete structures. Part 1-1: General rules and rules for buildings, bridges and civil engineering structures, Definitive. ed, 2023.

EN 12390-3:2019 – Testing hardened concrete. Part 3, Compressive strength of test specimens, 2019.

EN 14651: Test method for metallic fibered concrete - Measuring the flexural tensile strength (limit of proportionality (LOP), residual), 2005.

González, D.C., Mena, Á., Ruiz, G., Ortega, J.J., Poveda, E., Mínguez, J., Yu, R., De La Rosa, Á., Vicente, M.Á., 2023. Size effect of steel fiber–reinforced concrete cylinders under compressive fatigue loading: Influence of the mesostructure. Int. J. Fatigue 167, 107353. https://doi.org/10.1016/j.ijfatigue.2022.107353

Harte, R., Van Zijl, G.P.A.G., 2007. Structural stability of concrete wind turbines and solar chimney towers exposed to dynamic wind action. J. Wind Eng. Ind. Aerodyn. 95, 1079–1096. https://doi.org/10.1016/j.jweia.2007.01.028

Hsu, T.T.C., 1981. Fatigue of Plain Concrete. ACI J. Proc. 78. https://doi.org/10.14359/6927

Hümme, J., Von Der Haar, C., Lohaus, L., Marx, S., 2016. Fatigue behaviour of a normal-strength concrete – number of cycles to failure and strain development. Struct. Concr. 17, 637–645. https://doi.org/10.1002/suco.201500139

International Federation for Structural Concrete (Ed.), 2023. fib Model Code for concrete structures (2020), Version 1. ed. International Federation for Structural Concrete (fib), Lausanne.

Kachkouch, F.Z., Noberto, C.C., De Albuquerque Lima Babadopulos, L.F., Melo, A.R.S., Machado, A.M.L., Sebaibi, N., Boukhelf, F., El Mendili, Y., 2022. Fatigue behavior of concrete: A literature review on the main relevant parameters. Constr. Build. Mater. 338, 127510. https://doi.org/10.1016/j.conbuildmat.2022.127510

Koorikkattil, A., Nayar, S.K., Venudharan, V., 2026. Design of steel fibre reinforced concrete pavements with experimentally validated fatigue models. Mater. Struct. 59, 26. https://doi.org/10.1617/s11527-025-02910-8

Koorikkattil, A., Nayar, S.K., Venudharan, V., 2023. Flexural fatigue design of steel fibre reinforced concrete pavements: a comparative study. Road Mater. Pavement Des. 24, 2301–2321. https://doi.org/10.1080/14680629.2022.2139285

Lee, M.K., Barr, B.I.G., 2004. An overview of the fatigue behaviour of plain and fibre reinforced concrete. Cem. Concr. Compos. 26, 299–305. https://doi.org/10.1016/S0958-9465(02)00139-7

Lohaus, L., Oneschkow, N., Wefer, M., 2012. Design model for the fatigue behaviour of normal-strength, high-strength and ultra-high-strength concrete. Struct. Concr. 13, 182–192. https://doi.org/10.1002/suco.201100054

Loraux, C.T., 2018. Long-term monitoring of existing wind turbine towers and fatigue performance of UHPFRC under compressive stresses. École Polytechnique Fédérale De Lausanne.

Makita, T., Brühwiler, E., 2014. Tensile fatigue behaviour of ultra-high performance fibre reinforced concrete (UHPFRC). Mater. Struct. 47, 475–491. https://doi.org/10.1617/s11527-013-0073-x

Martinello Carlesso, D., Cavalaro, S.H.P., Bairán, J.M., De La Fuente, A., 2025. Flexural fatigue performance of pre-cracked steel fibre reinforced concrete: Experimental program and design-oriented approach. Constr. Build. Mater. 467, 140308. https://doi.org/10.1016/j.conbuildmat.2025.140308

Martinello Carlesso, D., De La Fuente, A., Cavalaro, S.H.P., 2019. Fatigue of cracked high performance fiber reinforced concrete subjected to bending. Constr. Build. Mater. 220, 444–455. https://doi.org/10.1016/j.conbuildmat.2019.06.038

Minelli, F., Plizzari, G., 2015. Derivation of a simplified stress–crack width law for Fiber Reinforced Concrete through a revised round panel test. Cem. Concr. Compos. 58, 95–104. https://doi.org/10.1016/j.cemconcomp.2015.01.005

Nayar, S.K., Gettu, R., 2020. Mechanistic-empirical design of fibre reinforced concrete (FRC) pavements using inelastic analysis. Sādhanā 45, 19. https://doi.org/10.1007/s12046-019-1255-1

Nguyen, D.-L., Thai, D.-K., Lam, M.N.-T., 2022. Synergy in Flexure of High-Performance Fiber-Reinforced Concrete with Hybrid Steel Fibers. J. Mater. Civ. Eng. 34, 04022090. https://doi.org/10.1061/(ASCE)MT.1943-5533.0004232

Poveda, E., Ruiz, G., Cifuentes, H., Yu, R.C., Zhang, X., 2017. Influence of the fiber content on the compressive low-cycle fatigue behavior of self-compacting SFRC. Int. J. Fatigue 101, 9–17. https://doi.org/10.1016/j.ijfatigue.2017.04.005

Schäfer, N., Breitenbücher, R., 2023. Microcrack And Fatigue Behavior Of High-Performance Fiber-Reinforced Concrete Under Cyclic Compressive Loading, in: Proceedings of the 11th International Conference on Fracture Mechanics of Concrete and Concrete Structures. Presented at the 11th International Conference on Fracture Mechanics of Concrete and Concrete Structures, IA-FraMCoS. https://doi.org/10.21012/FC11.092343

Sparks, P.R., Menzies, J.B., 1973. The effect of rate of loading upon the static and fatigue strengths of plain concrete in compression*. Mag. Concr. Res. 25, 73–80. https://doi.org/10.1680/macr.1973.25.83.73

Stephen, S.J., Gettu, R., 2020. Fatigue fracture of fibre reinforced concrete in flexure. Mater. Struct. 53, 56. https://doi.org/10.1617/s11527-020-01488-7

Wöhler, A., 1858. Bericht über die Versuche, welche auf der Königl. Niederschlesisch-Märkischen Eisenbahn mit Apparaten zum Messen der Biegung und Verdrehung von Eisenbahnwagen-Achsen während der Fahrt angestellt wurden. Z. Für Bauwes. 8, 641–652.

Zampini, D., Guerini, A., Volpatti, G., Esser, J., 2016. Advanced Fiber Reinforced Concrete Mix Designs. EP3307692A1.

Zenner, H., Hinkelmann, K., 2019. August Wöhler – founder of fatigue strength research: On the 200th anniversary of August Wöhler's birth. Steel Constr. 12, 156–162. https://doi.org/10.1002/stco.201900011

Compressive Fatigue Behaviour of Concrete Incorporating Recycled Aggregates and Recycled Glass Fibres from Wind Turbines

Nadia Quijano Arteaga[1], Samantha Hidalgo Astudillo[1], Débora Martinello Carlesso[2], Stanislav Aidarov[3] and Albert de la Fuente[1].

[1]: Civil and Environmental Engineering Department, Universitat Politècnica de Catalunya (BarcelonaTECH), Barcelona, Spain, nadia.quijano@upc.edu, samantha.elizabeth.hidalgo@upc.edu, and albert.de.la.fuente@upc.edu.

[2]: Civil Engineering Department, Universidade Federal de Santa Catarina, Florianópolis, Brazil, d.carlesso@ufsc.br

[3]: Department of Project and Construction Engineering, Universitat Politècnica de Catalunya (BarcelonaTECH), Barcelona, Spain, stanislav.aidarov@upc.edu

Abstract

The decommissioning of wind turbines is expected to generate large volumes of concrete from foundations and composite materials from blades. These materials may be reused in the construction of new wind energy infrastructure, where structural components are subjected to cyclic loading conditions. In this context, recycled aggregates and fibres derived from wind turbine components represent a potential resource for structural concrete applications, provided that their mechanical performance is adequately assessed. This study investigates the influence of recycled glass fibres, obtained from wind turbine blades, on the compressive fatigue behaviour of concrete incorporating recycled aggregates (RCA). Two mixtures were evaluated: a reference natural aggregate concrete (NAC-0) and a recycled aggregate concrete with 100 % replacement of coarse natural aggregates and incorporating 3 % recycled glass fibres (RAC100-3). Cylindrical specimens were subjected to cyclic compressive loading with a minimum stress of $0.10 \cdot f_{cm}$ and maximum stress levels of $0.60 \cdot f_{cm}$ and $0.70 \cdot f_{cm}$, where f_{cm} is the mean compressive strength of each mixture. A run-out limit of $2 \cdot 10^6$ cycles was adopted. The results show that NAC-0 exhibits the typical cyclic creep behaviour of conventional concrete, with several specimens reaching run-out. RAC100-3 displayed a more heterogeneous response, while maintaining a comparable fatigue performance under the investigated conditions. These results indicate that recycled materials derived from wind turbine components could be incorporated into structural concrete without compromising compressive fatigue behaviour, although the specific contribution of fibres under the studied conditions remains limited and further studies are required to prove structural reliability of these concretes.

Keywords

Recycled aggregate concrete, compressive fatigue, wind turbine foundations, and recycled glass fibres.

1 Introduction

Concrete components such as wind turbine towers and foundations are predominantly subjected to cyclic compressive actions during service, arising from wind loading, rotor imbalance and operational variability. These repeated fluctuations induce progressive microcracking and stiffness degradation, meaning that fatigue failure may occur well before the static compressive strength is reached. For this reason, understanding compressive fatigue is fundamental for evaluating the long-term performance and safety of wind turbine support structures[1], [2], [3].

Fatigue in concrete is characterised by progressive internal damage driven by the growth of microcracks under repeated loading, leading to irreversible strain and a reduction in mechanical properties. This process depends on several factors, including stress level, material properties and environmental conditions, and is typically classified according to the number of load cycles. As shown in Table 1, fatigue behaviour can be categorised into low-cycle, high-cycle and super high-cycle fatigue each associated with different loading conditions and structural applications [4]. In the case of wind turbine structures, fatigue is generally associated with high-cycle to super high-cycle regimes.

Table 1. Fatigue cycles spectrum with corresponding structures. [4]

Low-cycle fatigue (0–10^3 cycles)	**High-cycle fatigue** (10^3–10^7 cycles)	**Super high-cycle fatigue** (10^7–10^9 cycles)
• Structures subjected to earthquakes • Structures subjected to storms	• Bridges • Airport runways • Wind turbines • Highway pavement • Concrete railroad ties	• Mass rapid transit structures • Sea structures • Machine foundations • Wind turbines

In this context, the incorporation of fibres has been investigated as a strategy to enhance the mechanical performance of concrete, particularly in terms of crack control and post-cracking behaviour. In fibre reinforced concrete (FRC), fibres can bridge microcracks and delay their propagation, which may improve fatigue performance, especially under tensile or flexural loading conditions [11]. However, their effectiveness under compressive fatigue remains less understood, particularly when non-conventional fibres such as recycled glass fibres are used.

Furthermore, recycled fibres obtained from wind turbine blades present additional challenges related to their irregular geometry, variable size and potentially reduced fibre–matrix bond, which may influence their contribution to crack control under cyclic loading[1], [12].

Within this framework, the present study investigates the compressive fatigue behaviour of concrete incorporating recycled materials derived from wind turbine components. In particular, the study evaluates the influence of recycled glass fibres on the fatigue response of recycled aggregate concrete, considering aggregates obtained from previously loaded structural elements under cyclic compressive loading.

2 Experimental programme

2.1 Materials and mixtures

Two mixtures were studied: a reference natural aggregate concrete (NAC-0) and a recycled aggregate concrete with 100 % replacement of coarse natural aggregates and incorporating 3 % recycled glass fibres (RAC100-3). The RCA were obtained from a dismantled wind turbine foundation and processed into two size fractions (4/10 mm and 10/20 mm), as shown in Figure 1. The aggregates presented densities of 2,355 and 2,250 kg/m³, with water absorption values of 4.75% and 4.15%, respectively.



Figure 1. Crusned blocks from sample of the foundation block (a), crushing process (b), crushed aggregates obtained of 4/10 (c) and 10/20 (d).

The recycled glass fibres were classified into four length-based categories (long, medium, short and powder), as shown in Figure 2. Their geometric properties were highly variable, with lengths ranging from 5.7 to 77.0 mm (mean 31.6 mm), widths from 0.1 to 48.5 mm (mean 7.0 mm), and thicknesses from 0.1 to 17.8 mm (mean 2.16 mm), resulting in aspect ratios between 1.6 and 241.0 (mean 15.8). These fibres can be classified as macrofibres; however, their variability exceeds the limits typically specified for structural macrofibres in relevant standards [8]. The fibre density was determined according to EN 1097-6[13], yielding a value of 1,840 kg/m³.

Concrete production was carried out using CEM II/A-L 42.5 N cement, with an effective water-to-binder ratio of 0.40. The recycled blade fibres were incorporated only in the RAC100-3 mixture. The selected dosage was chosen to achieve a relatively high fibre content while maintaining acceptable workability of the mix. The mix proportions are summarised in Table 2.

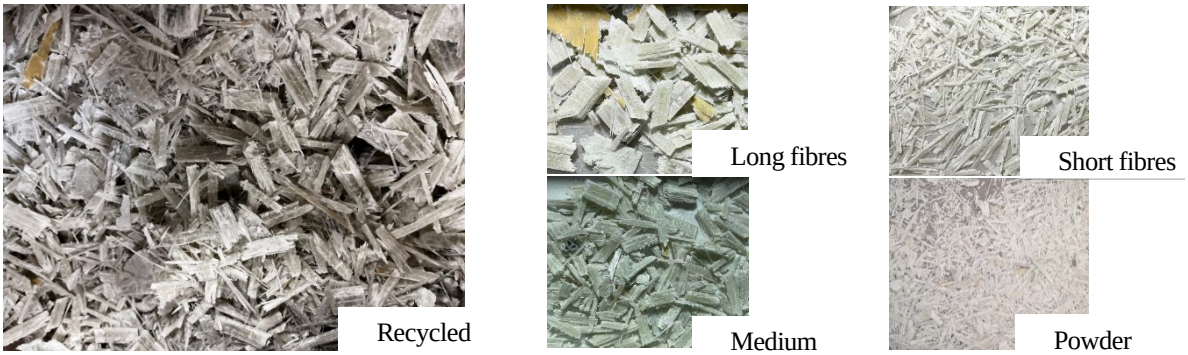


Figure 2. Categorization of the recycled fibres according to size.

Table 2. Compositions for the different concretes, the mixture proportions are expressed as mass ratios relative to the cement content (CEM II/A-L 42,5R = 1.00).

Component	NAC-0	RAC100-3
CEM II/A-L 42.5R	1.0	1.0
Fine aggregate 0/2 mm (NA)	0.4	0.3
Fine aggregate 0/4 mm (NA)	1.4	1.1
Coarse aggregate 4/10 mm (NA)	0.6	-
Coarse aggregate 4/10 mm (**RCA**)	-	0.7
Coarse aggregate 10/20 mm (NA)	1.8	-
Coarse aggregate 10/20 mm (**RCA**)	-	1.6
w/c	0.4	0.4
Fibres	0.0 (0%)	0.1 (3.0%)
Plasticizer	(1.0%)	(1.0%)
Superplasticizer	(0.6%)	(0.7%)
Air	<2%	<2%

2.2 Fatigue testing procedure

Static compressive characterisation was performed on 150 mm cubes, whereas compressive fatigue testing was conducted on 100 × 200 mm cylinders. The specimens were demoulded after 24 hours, cured for 28 days in a standard curing room and tested at 28 days. Dynamic testing was conducted using an INSTRON hydraulic servo-controlled machine. Fatigue tests were load-controlled with sinusoidal loading at a frequency of 6 Hz, ensuring a practical testing duration (Figure 3). Load and displacement were recorded throughout the tests.

Simulated stress data from selected sections of a wind turbine foundation were analysed to define representative stress levels for the fatigue assessment. The maximum and minimum compressive stress ratios ($S_{c,max}$ and $S_{c,min}$) were evaluated considering typical fatigue criteria, including limits associated with infinite fatigue life and stress ratio constraints reported in the literature [14]. Based on this analysis, representative values of $S_{c,max}$ and $S_{c,min}$ were identified and used to define the loading conditions for the experimental programme.

The selected stress levels were defined based on analysed stress histories of wind turbine towers. These data indicate that approximately 13% of load cycles exceed 0.70·fcm, around 30% fall within the range 0.60–0.70, and the majority (56%) occur below 0.60. Accordingly, the selected stress levels allow the evaluation of both representative and extreme loading conditions.

To ensure consistency with laboratory testing conditions, the relationship between the maximum stress level and the number of cycles to failure was analysed using a logarithmic S–N representation. A regression analysis (Eq. 1) was used to estimate the fatigue endurance limit, which was found to occur at approximately $S_{c,max} \approx 0.57$, below which specimens are expected to reach the maximum number of cycles without failure. It should be noted that this relationship is derived from simulated compressive fatigue data for natural aggregate concrete, under loading conditions representative of wind turbine foundations, and is not calibrated for recycled aggregate concrete [4] [10].

$$S_{c,max} = 0.897 - 0.053\, logN \quad (1)$$

Under cyclic compressive loading, concrete typically exhibits a cyclic creep response characterised by progressive strain development, which forms the basis for interpreting damage evolution in this study.

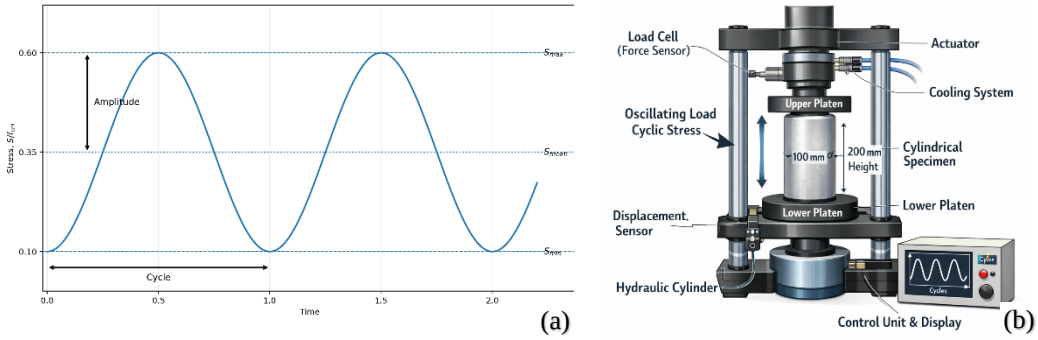


Figure 3. Schematic representation of fatigue test (a) and compressive fatigue setup (b).

Considering the frequency of data, the typical dispersion observed in fatigue tests, and the need for laboratory representativeness, the fatigue tests were conducted with $S_{c,max}$ set at 0.60 and 0.70 and $S_{c,min}$ at 0.10 of the respective sample f_{cm}. At these stress levels, microcracking was expected to occur, allowing the evaluation of fatigue behaviour under cyclic loading. Fatigue test was stopped at specimen failure or if the test reached $2 \cdot 10^6$ cycles, whichever occurred first. If the specimen did not fail after $2 \cdot 10^6$ cycles, it was reloaded under the same configuration as the compressive test, and the post-fatigue strength was assessed.

The collected data include the load applied by the testing machine during both static and fatigue tests, the relative displacement between the upper and lower platens (Figure 3), and the displacement measured using LVDTs. The analysis focuses on the evaluation of fatigue performance and damage progression of the tested concretes.

3 Test Results

3.1 Fatigue loading parameters and test outcomes

The static mechanical characterisation of the tested concretes is summarised in Table 3. The mean compressive strength f_{cm}, estimated as the average of three specimens, is reported together with the corresponding standard deviation of the sample (σ), coefficient of variation (CoV), and secant modulus of elasticity E_{cm}. These parameters describe both the strength level and the variability of each mix prior to fatigue. Lower elastic modulus values were obtained for the recycled mixture compared to NAC-0; however, given the limited sample size, no definitive conclusions can be drawn regarding the significance of this difference. The corresponding load levels, amplitudes and mean values are summarised in Table 4.

Tests performed at $S_{c,max}=0.70 \cdot f_{cm}$ resulted in premature and sudden compressive failure of several specimens, indicating that this stress level was excessively severe and did not allow the development of progressive fatigue damage. Consequently, the maximum stress level was reduced to $S_{c,max}=0.60 \cdot f_{cm}$ to promote stable cyclic behaviour and enable fatigue characterisation within a practical testing duration.

Specimens that reached the run-out condition maintained a high proportion of their reference compressive strength, whereas specimens tested at $S_{c,max} = 0.70 \cdot f_{cm}$ exhibited a higher likelihood of premature failure. Figure 4 shows the experimental setup for both the fatigue and post-fatigue compressive tests.

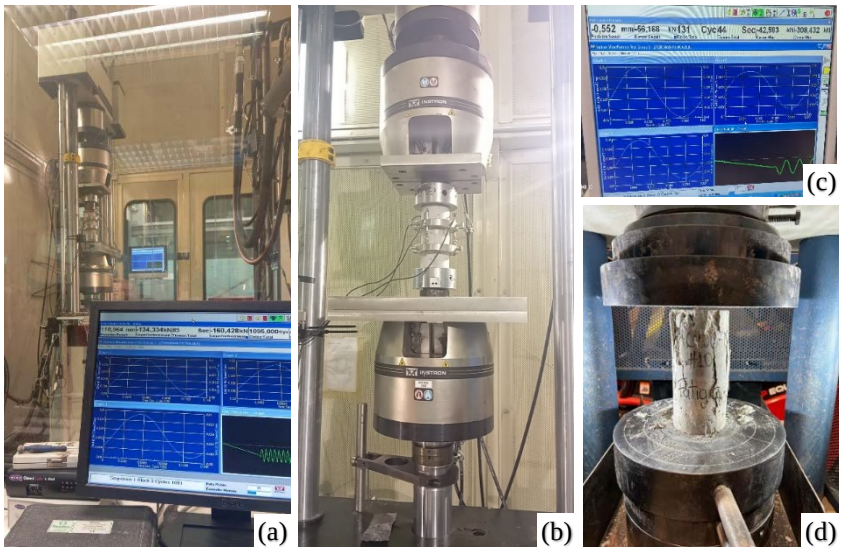


Figure 4. (a), (b), (c) Compression fatigue test setup and (d) post-fatigue compressive test.

Table 3. Static characterisation values.

Type	**E_{cm} (N/mm²)**	**f_{cm} * (N/mm²) [95% C.I.]**	**σ (N/mm²)**	**CoV**
NAC-0	35,232	55.9 [52.3–59.5]	2.5	4.2%
RAC100-3	30,472	51.7 [47.5–55.9]	2.9	5.5%

* Mean compressive strength of three specimens at the test age.

It should be noted that the fibre dosage used (3% by volume) represents an upper bound, selected to challenge the mixing and casting procedures under the target consistency conditions rather than to define an optimised mixture. Under these conditions, difficulties in fibre dispersion and workability are expected, which may affect the internal structure of the material and contribute to the lower elastic modulus values obtained. Therefore, this result should be interpreted within this experimental context and is not necessarily representative of mixtures with lower fibre contents.

Table 4. Fatigue load levels for each concrete mix.

Type	**F_{cm} (kN)**	**$S_{c,min}$ = 0.1·F_{cm} (kN)**	**$S_{c,max}$ = 0.6·F_{cm} (kN)**	**$S_{amplitude}$ (kN)**	**$S_{c,mean}$ (kN)**	**$S_{c,max}$ = 0.7·F_{cm} (kN)**	**$S_{Amplitude}$ (kN)**	**$S_{c,mean}$ (kN)**
NAC-0	439.0	43.9	263.4	109.8	153.7	307.3	131.7	175.6
RAC100-3	406.1	40.6	243.6	101.5	142.1	284.2	121.8	162.4

Concrete subjected to compressive fatigue typically exhibits a cyclic creep response, characterised by the evolution of the maximum strain per cycle (ε_{max}) with the number of

loading cycles (N). This approach is widely used to interpret fatigue damage, as the accumulation of strain is associated with microcrack development and progressive stiffness degradation [15].

The normalised representation $\varepsilon_{max}/\varepsilon_{max,f}$ versus N/N_f was used to analyse the fatigue behaviour of the tested mixtures, allowing a consistent comparison of deformation evolution independently of absolute strain levels.

The results show that both mixtures exhibit the characteristic cyclic creep response, with an initial stage of relatively rapid strain development followed by a more stable phase with gradual strain accumulation. No clear tertiary stage was observed for specimens reaching run-out, indicating that the applied stress levels were generally within a stable fatigue regime.

3.2 Results of fatigue tests – NAC-0

Table 5 presents the pre- and post-fatigue compressive strength parameters for the tested NAC-0 specimens. For each specimen, the f_{cm} of the mix, N_f, and $S_{c,max}$ are reported. The table also shows the post-fatigue compressive strength (f_{cf}) of each specimen. The values in parentheses indicate the residual strength expressed as a percentage of f_{cm}.

Table 5. Summary of fatigue testing – NAC-0

Specimen	**f_{cm*} (N/mm^2)**	**Specimen**	**N_f**	**$S_{c,max}$**	**f_{cf} (N/mm^2)**
NAC-0	**55.9** σ= 2.5 CoV=4.2% [52.3–59.5]	N_5	2,000,000	0.7·f_{cm}	54.3 (97%)
		N_7	2,000,000		52.7 (94%)
		N_9	194,500		Failed
		N_{10}	144,000		Failed
		N_{11}	107,500		Failed
		N_{12}	2,000,000	0.6·f_{cm}	50.29 (90%)
		N_{13}	2,000,000		52.70 (94%)

* Mean compressive strength of three specimens at the test age

The results for the NAC-0 specimens confirm a strain evolution consistent with compressive fatigue in concrete, characterised by a rapid increase during the early cycles followed by a more gradual progression towards run-out. In the normalised representation Figure 5, the averaged NAC-0 response (for run-out specimens) reaches $\varepsilon_{max}/\varepsilon_{max,f} = 0.437$ at 500 cycles ($N/N_f = 0.0003$) and 0.857 at $N/N_f = 0.10$, indicating a pronounced primary stage.

For specimens completing $2{\cdot}10^6$ cycles, ratcheting (accumulated plastic strain) remained limited ($\Delta\varepsilon_{max} \approx 4.79\times10^{-4}$), although NAC-0 a certain degree of dispersion in the measured strain response, due to one specimen showing a substantially higher accumulated strain. This dispersion can be attributed to the presence of two subgroups of specimens tested at different maximum stress levels ($S_{c,max}$=0.60·f_{cm} and 0.70·f_{cm}), leading to variations in the effective stress ratio depending on the individual specimen strength.

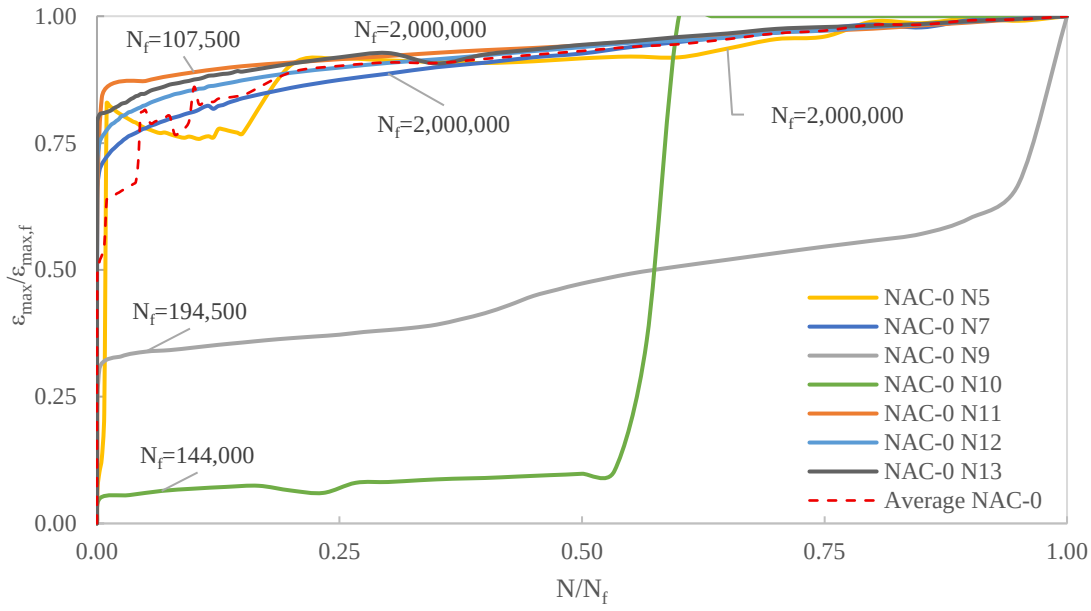


Figure 5. Evolution of the normalised strain (εmax/εmax,f) with N/Nf (NAC-0)

3.3 Results test Fatigue – RAC100-3

Table 6 presents the pre- and post-fatigue compressive strength parameters for the tested RAC100-3 specimens.

Table 6. Summary of fatigue testing – RAC100-3

Specimen	**f_{cm*} (N/mm^2)**	**Specimen**	**N_f**	**$S_{c,max}$**	**f_{cf} (N/mm^2)**
RAC 100-3	**51.7** σ= 2.9 CoV=5.5% [47.5–55.9]	N_4	1,734,385	0.7·f_{cm}	Failed
		N_5	6,500		Failed
		N_6	2,000,000	0.6·f_{cm}	47.7 (92%)
		N_7	2,000,000		47.3 (91%)

* Mean compressive strength of three specimens at the test age

Figure 6 presents the $\varepsilon_{max}/\varepsilon_{max,f}$ – N/N$_f$ curves for the RAC100-3 specimens tested. The average curve shows a relatively high degree of early strain development, reaching $\varepsilon_{max}/\varepsilon_{max,f}$=0.627 at 500 cycles.

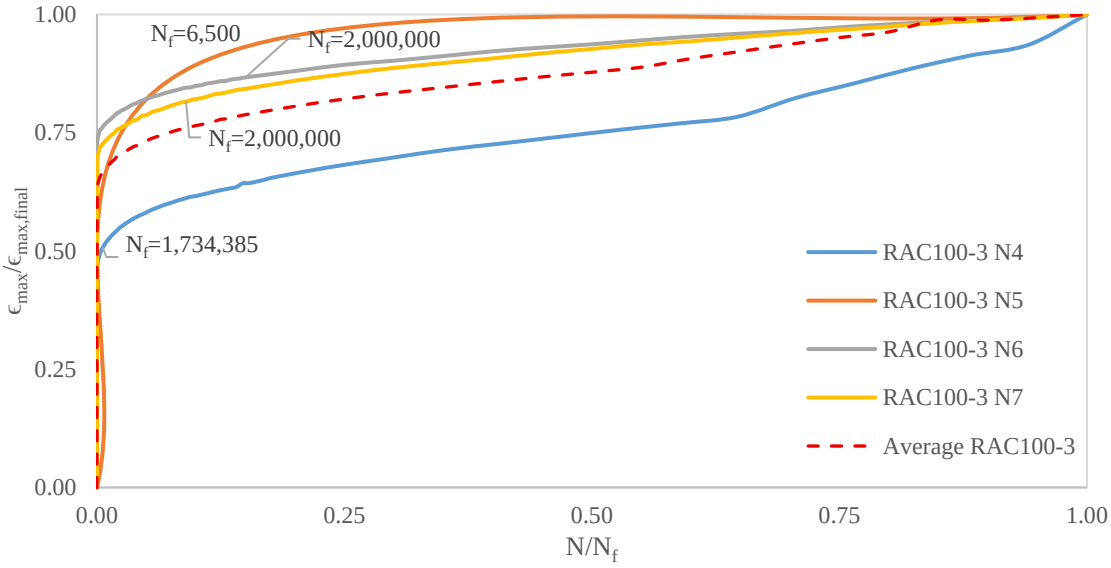


Figure 6. Evolution of the normalised strain ($\varepsilon_{max}/\varepsilon_{max,f}$) with N/N_f (RAC100-3)

With respect to the potential contribution of the recycled fibres to the fatigue performance, no clear enhancement is observed under the investigated conditions. However, no clear reduction in fatigue performance is identified when compared to NAC-0. At the highest stress level $0.7 \cdot f_{cm}$ none of the specimens reached $2 \cdot 10^6$ cycles. Similar failures were also observed in NAC-0, indicating that this loading condition is inherently severe and may govern the fatigue response independently of fibre addition. For specimens tested at $0.60 \cdot f_{cm}$, post-fatigue compressive strength values remained within the expected range of variability. Overall, these results suggest that the incorporation of recycled fibres at the studied dosage does not lead to a clear improvement in fatigue behaviour, but also does not significantly compromise it under the investigated conditions.

4 Analysis

The fatigue response of the investigated concretes was evaluated in terms of fatigue life, post-fatigue compressive strength and strain evolution under cyclic loading.

Both NAC-0 and RAC100-3 exhibited the typical compressive fatigue behaviour of concrete, characterised by an initial phase of relatively rapid strain development followed by a stable secondary stage with gradual strain accumulation. No clear tertiary stage was observed in specimens reaching run-out, indicating that the selected stress levels were within a stable fatigue regime.

At material level, NAC-0 showed a consistent behaviour, with several specimens reaching the run-out limit. However, premature failures were observed at the higher stress level ($S_{c,max} = 0.70 \cdot f_{cm}$), highlighting the sensitivity of compressive fatigue to stress level and specimen-level variability. It should be noted that this stress level corresponds to an extreme loading condition, representing only a limited proportion of cycles in the analysed stress histories.

In contrast, RAC100-3 presented a more heterogeneous response. None of the specimens tested at $S_{c,max} = 0.70 \cdot f_{cm}$ reached run-out, while those tested at $S_{c,max} = 0.60 \cdot f_{cm}$

showed residual compressive strength values slightly lower than f_{cm}, although within the expected variability of the material.

This behaviour may be associated with the increased material heterogeneity introduced by the incorporation of recycled fibres; however, the limited number of specimens does not allow a definitive assessment of their influence on fatigue performance.

From a deformation perspective, RAC100-3 exhibited higher strain levels compared to NAC-0, consistent with its lower stiffness. While normalised strain curves allow comparison of fatigue behaviour, absolute strain levels are also relevant, as they are directly related to stiffness degradation and serviceability performance.

Overall, both mixtures exhibit comparable compressive fatigue behaviour under the investigated conditions, although RAC100-3 shows a higher dispersion of results.

5 Concluding remarks

This study investigated the compressive fatigue behaviour of concrete incorporating recycled materials derived from decommissioned wind turbines, focusing on a reference concrete (NAC-0) and a recycled aggregate concrete with 100 % replacement and 3 % recycled fibres (RAC100-3).

Based on the experimental results, the following conclusions can be drawn:

- Both concretes exhibited the classical cyclic creep behaviour under compressive fatigue, with primary and secondary stages clearly identified within the investigated stress range.
- NAC-0 showed stable fatigue performance, with several specimens reaching run-out. Premature failures at the highest stress level ($S_{c,max} = 0.70 \cdot f_{cm}$) highlight the sensitivity of compressive fatigue behaviour to stress magnitude and specimen variability.
- RAC100-3 exhibited a more heterogeneous response. Under the investigated conditions, its fatigue behaviour was comparable to NAC-0, although with a higher dispersion of results and no clear improvement associated with the incorporation of recycled fibres at the studied dosage.
- Importantly, no reduction in fatigue life or post-fatigue compressive strength was identified within the investigated stress levels and number of cycles.

6 Acknowledgements

The authors gratefully acknowledge the financial support provided by the project Revalorization of Blades and Concrete (C-12696), funded by RWE Offshore Wind GmbH. Additional funding was provided by the Agencia Estatal de Investigación (AEI), Ministerio de Ciencia, Innovación y Universidades (Gobierno de España), through the HEAT project (PID2023-149321OB-C32).

7 References

[1] V. Revilla-Cuesta, M. Skaf, V. Ortega-López, and J. M. Manso, “Raw-crushed wind-turbine blade: Waste characterization and suitability for use in concrete

production," *Resour. Conserv. Recycl.*, vol. 198, Nov. 2023, doi: 10.1016/j.resconrec.2023.107160.

[2] N. Hurtado-Alonso, J. Manso-Morato, V. Revilla-Cuesta, V. Ortega-López, and M. Skaf, "Optimization of concrete containing wind-turbine wastes following mechanical, environmental and economic indicators," *Cleaner Materials*, vol. 16, Jun. 2025, doi: 10.1016/j.clema.2025.100317.

[3] V. Ortega-López, F. Faleschini, N. Hurtado-Alonso, J. Manso-Morato, and V. Revilla-Cuesta, "Analysis of raw-crushed wind-turbine blade as an overall concrete addition: Stress–strain and deflection performance effects," *Compos. Struct.*, vol. 340, Jul. 2024, doi: 10.1016/j.compstruct.2024.118170.

[4] f. TG4.7, "Recycled Aggregate Concrete Structures - State-of-the-art report (In print)," 2024.

[5] F. You, S. Luo, J. Zheng, and K. Lin, "Analysis of Compressive Fatigue Failure of Recycled Aggregate Concrete," *Materials 2021, Vol. 14, Page 4620*, vol. 14, no. 16, p. 4620, Aug. 2021, doi: 10.3390/MA14164620.

[6] C. Thomas, J. Setién, J. A. Polanco, I. Lombillo, and A. Cimentada, "Fatigue limit of recycled aggregate concrete," *Constr. Build. Mater.*, vol. 52, pp. 146–154, Feb. 2014, doi: 10.1016/j.conbuildmat.2013.11.032.

[7] C. Thomas, I. Sosa, J. Setién, J. A. Polanco, and A. I. Cimentada, "Evaluation of the fatigue behavior of recycled aggregate concrete," *J. Clean. Prod.*, vol. 65, pp. 397–405, Feb. 2014, doi: 10.1016/j.jclepro.2013.09.036.

[8] Q. Peng, L. Wang, and Q. Lu, "Influence of recycled coarse aggregate replacement percentage on fatigue performance of recycled aggregate concrete," *Constr. Build. Mater.*, vol. 169, pp. 347–353, Apr. 2018, doi: 10.1016/j.conbuildmat.2018.02.196.

[9] E. A. B. Koenders, M. Pepe, and E. Martinelli, "Compressive strength and hydration processes of concrete with recycled aggregates," *Cem. Concr. Res.*, vol. 56, pp. 203–212, Feb. 2014, doi: 10.1016/J.CEMCONRES.2013.11.012.

[10] F. You, S. Luo, and J. Zheng, "Experimental Study on Residual Compressive Strength of Recycled Aggregate Concrete Under Fatigue Loading," *Front. Mater.*, vol. 9, Jan. 2022, doi: 10.3389/fmats.2022.817103.

[11] Walraven *et al.*, "fib Bulletin 65. Model code 2010 Volume 1," Mar. 2012, doi: 10.35789/fib.BULL.0065.

[12] V. Revilla-Cuesta, A. B. Espinosa, R. Serrano-López, M. Skaf, and J. M. Manso, "Mechanical Properties of Concrete Mixes with Selectively Crushed Wind Turbine Blade: Comparison with Raw-Crushing," *Materials*, vol. 17, no. 24, Dec. 2024, doi: 10.3390/ma17246299.

[13] Asociación Española de Normalización y Certificación, "UNE-EN 1097-6 Tests for mechanical and physical properties of aggregates. Part 6: Determination of particle density and water absorption," Madrid, 2014. [Online]. Available: www.aenor.es

[14] D. G. As, “DNVGL-ST-C502 Offshore concrete structures,” 2018, Accessed: Mar. 18, 2026. [Online]. Available: http://www.dnvgl.com,

[15] J. M. Chandra Kishen, A. Ramaswamy, S. Ray, R. Vidyasagar, F. M. Weber, and S. Anders, “Fatigue damage versus creep deformation-differentiation using the development of stiffness”, doi: 10.21012/FC11.092386.

Investigation of different polypropylene fiber contents in ultra-high-performance concrete under temperature increase.

Péter Ludvig[1], Thiago Marques Viana[1], Bruno Athaíde Bacelar[1], Isabela Domingues Coelho[1]

[1] : Graduate Program in Civil Engineering, Federal Center for Technological Education of Minas Gerais, Amazonas, Belo Horizonte 30510-000, Brazil.

Abstract

Ultra-high-performance concrete (UHPC) is a cement composite with enhanced properties and represents a growing trend in civil construction. With high compressive strength, often exceeding 120 MPa, the material allows for smaller structural elements under the same applied load, resulting in lower material consumption and a sustainable use. Despite its superior mechanical performance, some weaknesses still need to be addressed to expand its use, such as its performance under high temperatures. Due to its very dense structure, the material exhibits explosive spalling at elevated temperatures. An important strategy to reduce this effect is the application of polypropylene fibers (PPF), which can prevent this occurrence, motivating research to investigate the modifications promoted by the presence of PPF in UHPC.
In this sense, the present research aimed to investigate different levels of PPF incorporation in UHPC under heating (up to 320 ºC and 660 ºC), analyzing the occurrence of spalling, mass loss, density modification, and residual compressive strength. Cubic reference specimens and with incorporations of 1.25 kg/m³ and 2.5 kg/m³ of PPF were prepared and subjected to heating in a muffle furnace at a rate of 5ºC/min, with plateaus at 320 ºC and 660 ºC, for 30 minutes, to observe the effects of thermo-hygral and thermo-mechanical spalling, respectively. It is noticeable that the presence of fibers at 1.25 kg/m³ does not cause a loss of compressive strength without heating and is already capable of preventing explosions in both heating ranges. At 320 ºC, the survival rate of the reference sample is 80%, while that of the samples containing PPF is 100%. In the 660 ºC range, the survival rate of the reference sample drops to 0 %, while the samples containing PPF remain at 100 %. About residual compressive strength, it decreases with increasing temperature, which may be related to the occurrence of stress, even if not capable of causing an explosion, cracking, mass loss, or chemical reactions in the material's compounds due to the temperature increase.

Keywords

Ultra-high-performance concrete (UHPC), High temperatures, Spalling, Polypropylene fibers.

1 Introduction

Ultra-high performance concretes (UHPCs) are cement composites that represent an innovative and growing material with great potential for the construction industry, due to their improved mechanical properties and increased durability, which relates to greater sustainability (Mo et al., 2026; Teoh., 2026; Kravanja et al., 2024; Amran et al., 2022). These characteristics can be explained by the very dense macrostructure, which enhances compressive strength and hinders the entry of harmful agents into the concrete, increasing durability (Amran et al., 2022). Although densification of the macrostructure can be beneficial, this aspect is related to the frequent occurrence of explosive spalling when these materials are subjected to elevated temperatures, therefore, it is necessary to investigate its behavior, as well as prevention and performance strategies after heating, to expand its safe use (Hernández-Figueirido et al., 2024; Viana et al., 2020).

The frequent observation of spalling explosions in UHPC is associated with a series of mechanisms, the predominant idea being that, during heating, the moisture still present inside the material evaporates, but the very dense porous structure does not allow this vapor to be carried out of the element, so that a large internal pressure is formed, which causes the explosion (Lin et al., 2024; Viana et al., 2020). The process in question can be called thermo-hygral spalling and is frequently observed at temperatures ranging between 220 ºC and 320 ºC. Other processes related to spalling are attributed to mechanical stresses during heating (thermo-mechanical), typically occurring between 430 ºC and 660 ºC; as well as the decomposition of hydrated products and calcite, and rehydration of calcium oxide (thermo-chemical), occurring from 700 ºC (Liu et al., 2018).

The use of polypropylene fibers is a technique that can be used to prevent spalling, since the presence of the fibers, which melt during heating, creates a network of channels to relieve stresses resulting from the presence of steam inside the test specimen (Rui et al., 2025). This occurs due to the melting of the fibers, which happens near 165 ºC, but also due to the thermal incompatibility of the fiber with the cementitious matrix, which generates microcracking, so that these effects modify the pore structure and relieve the water vapor pressure during heating (Zaid et al., 2024; Abdel et al., 2023; Zhang et al., 2020; Li et al., 2019). Despite this, the predicting spalling in UHPC containing PPF remains a challenge (Jiang et al., 2024) and the generation of research data in this regard proves to be something important.

In addition to the occurrence of spalling itself, evaluating the material's performance after heating is also of great importance. After exposure to high temperatures, the losses in compressive strength are significant, on the order of 80 %, which generates an additional cause for concern (Aljabbri et al., 2021; Viana et al., 2020). Various fiber incorporation levels have been investigated, and the effects of increases or decreases on spalling and mechanical performance could be better delineated with the generation of more data on the subject (Christ et al., 2023; Shen et al., 2022; Zhang et al., 2020). Furthermore, it is important to emphasize that, although PPF is frequently cited as a solution for spalling, the optimal dosage still needs to be investigated, so residual performance may be an important factor in this evaluation (Du et al., 2020). Considering all the above, the present research aims to investigate the effects of incorporating PPF in two different proportions to a UHPC mixture regarding the occurrence of spalling and its performance after heating.

2 Experimental program

The experimental program of this research consists of molding 40 mm side cubic specimens of reference UHPC, according to the proportions shown in Table 1, and incorporating 1.25 kg/m³ of polypropylene fibers (PPF) and 2.5 kg/m³ of PPF. Seventeen test specimens were produced for each variation of UHPC, for characterization and subsequent heating.

Table 1: Mix proportion (kg/m³).

Identification	Cement	Sand	Silica Fume	SP1	SP2	Water	PP fibers
Reference	818	1122	123	41	8	196	---

The abbreviations SP1 and SP2 in Table 1 refer to the two superplasticizers used in the mixture, both based on polycarboxylate, namely MasterGlenium 51 and Viscocrete, respectively. The specifications of the PPFs used can be found in Table 2.

Table 2: Polypropylene fibers specifications.

---	Information
Composition	100 % Virgin polypropylene
Type	Monofilament
Length	12 mm
Diameter	30 μm
Density	910 kg/m³
Flash point	330 ºC
Melting point	160 ºC

The process for producing the test specimens followed the procedure shown in Figure 1, in which 17 test specimens of 40x40x40 mm³ were produced from each mixture, that is, from the reference and from each incorporation of fiber, since 3 specimens were used to determine the moisture content, 4 for compressive strength and evaluations without heating and 5 for submission to each temperature (320 ºC and 660 ºC). Before the actual molding process took place, the consistency was assessed using the flow table test, following the prescriptions of NBR 13276 (2016). The use of the aforementioned standard is appropriate due to the similarity between mortars and UHPC, as they are cement composites in which coarse aggregates are absent. After demolding, the specimens were cured by submerged curing for 28 days, then measured, weighed and stored in a laboratory environment (with natural air circulation) for 8 months in order to evaluate the material under conditions closer to those of UHPC in service. Subsequently, all specimens were again measured, weighed and packaged, except for 3 units of each variation, which were dried and used for analysis of their degree of saturation. The information is also useful in assessing apparent density and mass loss.

The test specimens were then subjected to two heating regimes in a DigiMec brand FHMP type muffle furnace with microprocessor-controlled temperature control, both with a heating

rate of 5 ºC/min, but with target temperatures of 320 ºC and 660 ºC, in order to track the typical ranges for the occurrence of hygral-thermo spalling and thermo-mechanical spalling. The procedure takes place in into a metal cage (with each space containing approximately 55 mm of edge) to prevent explosive spalling fragments from reaching other test specimens, this also ensures identification after heating, since the identification ink fades with temperature. The temperatures at which explosions occurred were recorded through acoustic identification, with the temperature recorded on the equipment display at the time of the explosions. Due to the inertia of the equipment in reaching the target temperature, which was maintained for 30 minutes, the maximum temperatures observed were 360 ºC and 690 ºC. The specimens were cooled at a rate of 0.6 ºC/min, still inside the equipment.

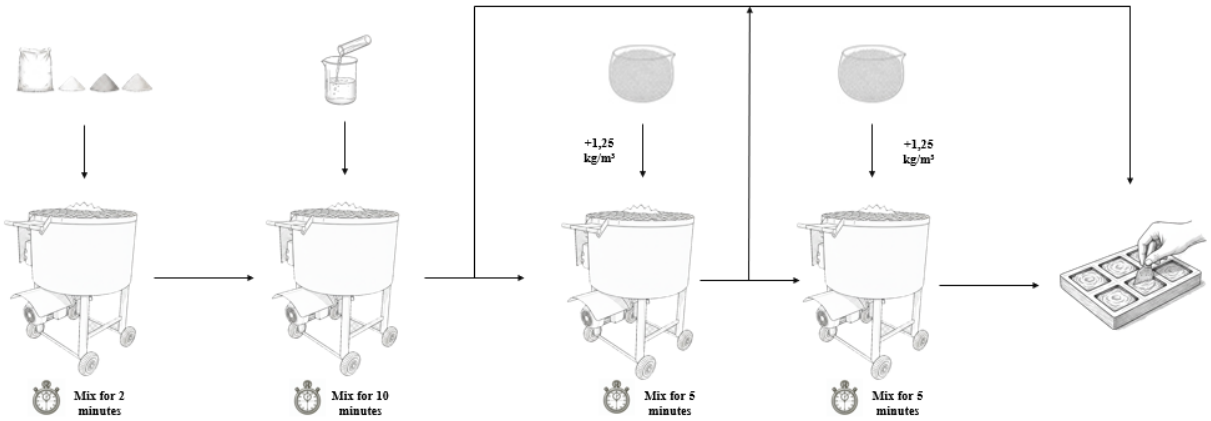


Figure 1: Mix procedure.

The mechanical performance of the material was determined through compression strength tests without heating and after each heating cycle. The cubic specimens were tested in a universal testing machine with load cell of 2000 kN using a load increment rate of 2400 N/s, observing the prescriptions of EN 196-1 (2016). As already discussed in this research, a standard specific to mortars is used here again, due to its similarity to UHPC.

3 Test Results

Regarding the consistency assessment, the test results are presented in Figure 2. It can be seen that the insertion of PPF caused a reduction in the spreading value, such that workability may be impaired by the presence of the material even at the lowest percentage of 1.25 kg/m³. It is also noted that increasing the fiber content exacerbates this reduction, with decreases in relation to the reference of 7.25 % and 15.75 % at insertions of 1.25 kg/m³ and 2.5 kg/m³, respectively. It is worth noting that the results were analyzed using the ANOVA statistical test at a significance level of 5 %, which indicated that there is a difference within the group, since an F value of 39.36 was obtained, higher than the critical F value of 2.51. Additionally, Tukey's test was performed to verify statistically significant differences between the groups, with differences found in all combinations, as shown in Figure 2.

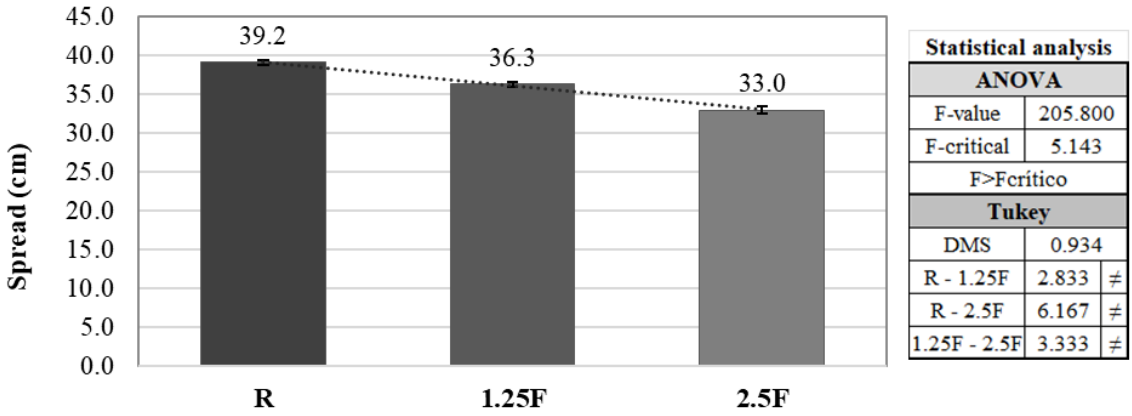


Figure 2: Effect of PPF insertion on consistency as measured by the flow table test.

About the effects of PPF insertion on compressive strength, the results are presented in Figure 3, and it can be seen that the absolute values decrease as the amount of fiber increases, with decreases of 6.71 % and 11.52 % for fiber contents of 1.25 kg/m³ and 2.5 kg/m³, respectively. Despite this, the statistical analysis does not indicate a significant difference between the groups, as the ANOVA test showed an F-value lower than the critical value, rejecting any difference between the groups, which was confirmed by Tukey's test, as can be seen in the figure. These results are important because maintaining compressive strength in the presence of PPF is valuable for maximizing the benefit of spalling prevention without compromising other properties.

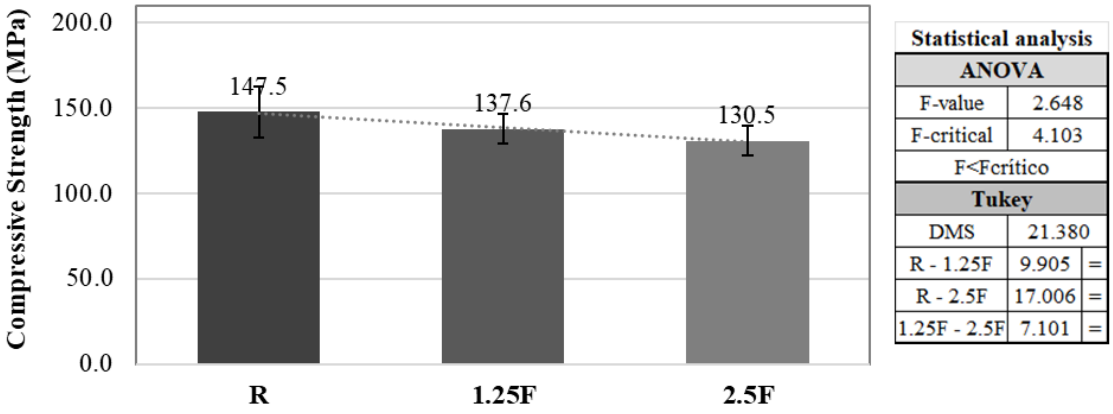
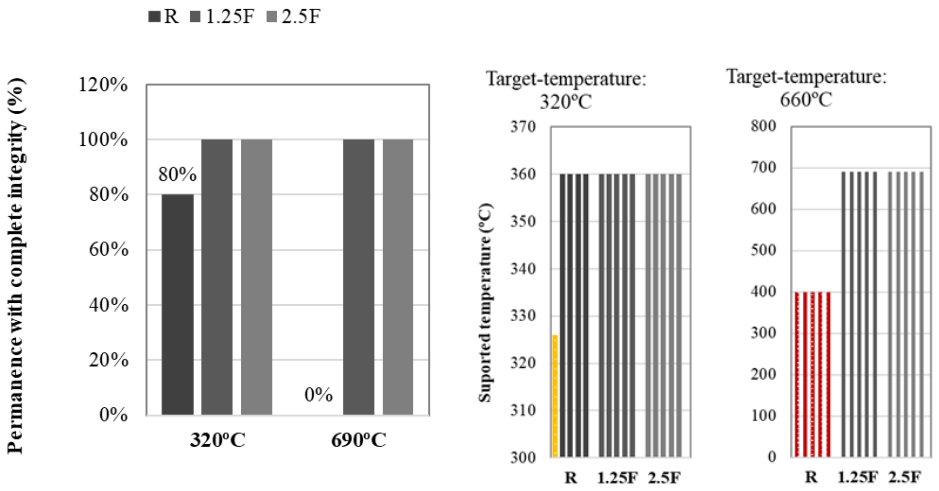


Figure 3: Effect of PPF insertion on compressive strength without heating.

Once the heating cicles have been carried out, it is important to assess the occurrence of the spalling phenomenon, which is shown in Figure 4. Figure 4a indicates the percentage of specimens that remained intact after heating, meaning that spalling did not occur. Figure 4b shows the temperature withstood by the specimens, highlighting the average temperature at which spalling occurred.



(a) (b)

Figure 4: Performance during heating, (a) percentage of specimens that remained intact, and (b) temperature withstood by the specimens.

Considering the spalling occurrence temperatures recorded in Figure 4, it is possible to affirm that both investigated occurrence processes took place (thermo-hygral and thermo-mechanical), since temperatures close to 320 ºC and above 430 ºC were observed (Liu et al., 2018). It can be seen that the presence of PPF was able to prevent spalling at both target temperatures and both incorporation percentages, demonstrating the effectiveness of the strategy. At 660 ºC, the range in which the worst performance for reference occurred, all reference samples exploded, while none of the samples containing PPF exploded. Considering these findings, an important contribution can be made to the current discussion regarding the optimal PPF content for spalling prevention, since incorporating 1.25 kg/m³ of PPF was sufficient to prevent spalling and maintain residual compressive strength compatible with the highest content (2.5 kg/m³). This information emerges amidst a wide range of dosages found in research, thus supporting studies aimed at determining optimal contents.

Another important performance parameter to consider is residual compressive strength, that is, the portion that remains after heating. This data is presented in Figure 5, where it can be observed that, at 320 ºC, the percentage drop is similar between the reference and the material containing 1.25 kg/m³ of PPF, while it is mitigated in the material with 2.5 kg/m³. At 660 ºC, the drop in strength could not be measured for the reference, since all specimens exploded; however, it is possible to see that the loss of mechanical performance is quite pronounced for the two mixtures containing fibers, in practically equivalent percentages of 70.06 % and 71.16 %. This indicates that the higher the exposure temperature, the greater the drop in compressive strength.

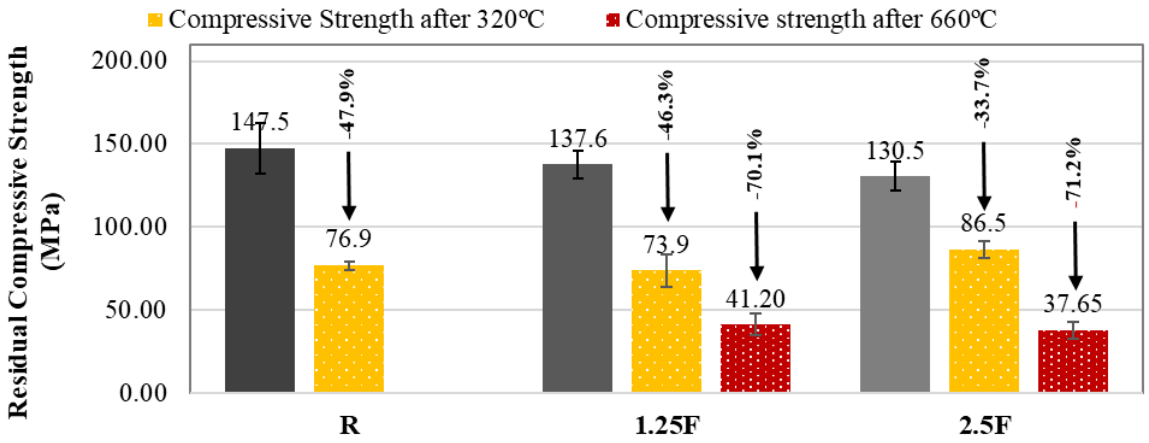
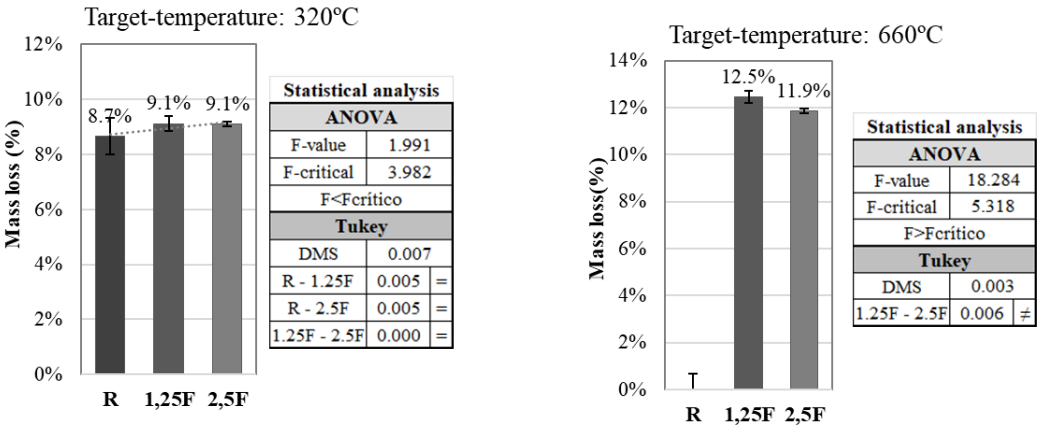


Figure 5: Effect of PPF insertion on residual compressive strength after heating.

Regarding mass loss, the results of which are presented in Figure 6, it can be seen that there is a tendency for an increase in the percentage of mass lost at 320 ºC. This is reflected in the increase in the average percentage loss value, which increases by 5.31 % for the material with an increase of 1.25 kg/m³ and 5.19% for the material with 2.5 kg/m³. However, considering the statistical tests, there is no significant difference. At 660 ºC, it was not possible to evaluate the reference, because all the specimens exploded; however, it is possible to see that the material with the higher fiber content (2,5 kg/m³) has a greater mass loss, which proved to be statistically valid by the ANOVA and Tukey tests, as can be seen in Figure 6b.



(a) (b)

Figure 6: Average mass loss of specimens, (a) after 320ºC and (b)after 660ºC.

The variation in apparent density is also an important parameter for analyzing the performance of UHPC after heating, as well as providing useful information in the analysis of other parameters, such as mass loss and compressive strength. The drops in apparent density can be analyzed using Figure 7. It can be observed that the density losses are similar for all mixtures at 320 ºC, as well as for the mixtures containing 1.25 kg/m³ and 2.5 kg/m³ at 660ºC, since the reference sample did not withstand that temperature.

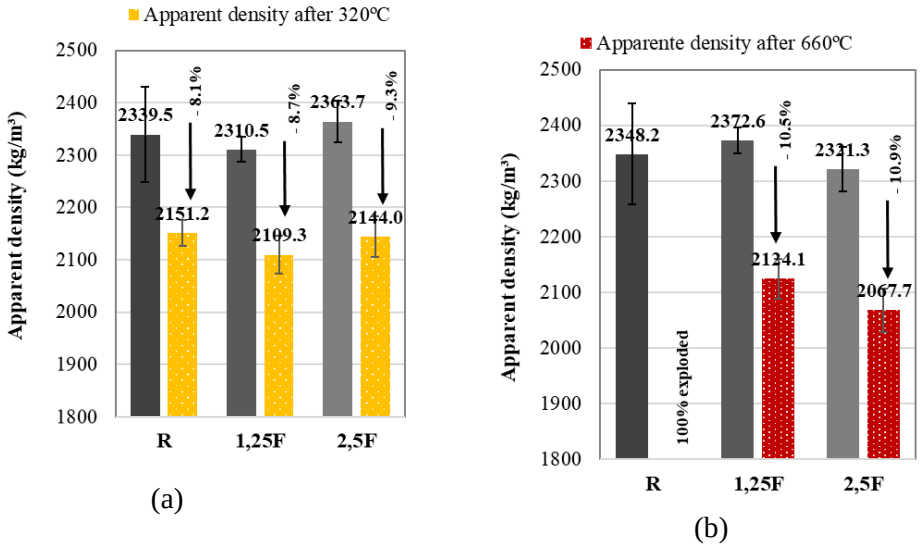


Figure 7: Average mass loss of specimens, (a) after 320ºC and (b)after 660ºC.

The density modification results are consistent with the mass loss. It should be mentioned that the apparent density may not exactly reflect the same trend as the mass loss due to volumetric stability, since, in this study, different levels of volumetric stability were verified at 660 ºC, being -2.21 % for 1.25 kg/m³ and -0.98 % for 2.5 kg/m³, which helps to explain the fact that the 1.25 kg/m³ mixture showed the greatest mass loss, but did not show the greatest density loss.

4 Discussion

The flowability results indicated losses on the order of 7.25 % and 15.75 % at insertions of 1.25 kg/m³ and 2.5 kg/m³. The loss of flowability of UHPC with the addition of PPF is expected due to its specific surface area, which absorbs water, in addition to the increased internal friction in the mixture. These results are expected and consistent with several studies showing that the fluidity of UHPC decreases with increased incorporation of PPF (Shen et al., 2023; Du et al., 2020). In terms of magnitude, Du et al (2020) found similar losses, of 6.25 % compared to the reference with an incorporation of 1.385 kg/m² and 20.35 % with an incorporation of 2.0 kg/m³.

Regarding compressive strength, although the averages show a slight downward trend, from 6.7 % to 1.25 kg/m³ and from 11.5 % to 2.5 kg/m³, statistically, these differences are not significant. Even so, it is worth mentioning that Xiong and Liew (2015) found strength losses of around 13 % with the addition of 1 % PPF by volume, which corresponds to approximately 0.86 kg/m³. This finding was attributed by the same authors to the consequences of the loss of workability on mechanical strength. Shen et al. (2023) found similar results, in which small decreases (from 1.5 % to 4.8 %) were identified when incorporating different percentages of PPF (from 1 % to 3 %). However, in many cases, the presence of PPF at dosages of approximately 2 kg/m³ does not significantly alter compressive strength, as was the case identified in this study (Du et al., 2020).

When analyzing the heating performance results regarding spalling, it is observed that the presence of PPF was able to completely prevent the phenomenon at both tested contents (1.25 kg/m³ and 2.5 kg/m³). The fact that spalling can be prevented from 1.25 kg/m³ onwards

is especially important, since it is necessary to understand the optimum fiber content, as a significant increase can have negative consequences on compressive strength (Xiong and Liew, 2015). In the research developed by Du et al. (2020), a content of 0.91 kg/m³ was not able to prevent spalling, so the cited result becomes even more important in the search for the optimum PPF content. Spalling prevention is achieved by creating a network of pressure relief channels resulting from the melting of the PPF (Rui et al., 2025; Le et al., 2025).

When it comes to the temperature at which spalling occurs, the range found and shown in Figure 4 is consistent with the literature (Rui et al., 2025; Liu et al., 2018). Considering that the explosions were detected at approximately 320 ºC and 400 ºC, it can be inferred that thermo-hygral and thermo-mechanical processes may be occurring. It should be noted that the recorded temperature was that displayed on the instrument's screen, so the temperature inside the specimen may be lower, strengthening the theory of that the thermo-hygral phenomenon may be present, even in cases where the explosion was observed at temperatures higher than its typical detection range.

Analyzing the residual compressive strength data shown in Figure 5, it can be seen that, at 320 ºC, the smallest loss of resistance is identified at a fiber content of 2.5 kg/m³, which may be associated with the higher content of fibers that melted (at around 160 ºC), so that the specimen was subjected to a lower vapor pressure. Additionally, it becomes evident that the second target temperature (660 ºC) presented a much greater potential for strength loss, as expected, since, from 400 ºC onwards, a more pronounced drop in mechanical performance is observed (Chen et al., 2024).

Regarding mass loss, although the average values are close and without statistically significant difference, it is noticeable that, at 320 ºC, the average losses are greater in the mixtures containing polypropylene fibers. This may occur due to the melting and decomposition of the polypropylene fibers, which have already occurred after the maximum temperature reached in this heating range (Jin et al., 2024; Tsuchiya, Sumi, 1969). It should be emphasized, however, that the amounts of PPF by mass correspond to 0.055 % and 0.11 %, which corroborates the fact that the differences observed are quite small and statistically irrelevant. As expected, due to the decomposition of substances, which is continuous with the addition of heat, it is observed that the mass loss increases when comparing the losses at the 320 ºC target with the 660 ºC target, with an increase of 36.5 % for the mixture containing 1.25 kg/m³ and 30.2 % for 2.5 kg/m³. These data are well associated with the results of the residual compression resistance tests, shown in Figure 5, since a sharp drop in resistance is observed when comparing the two target temperatures, in addition to being aligned with the literature (Qian et al., 2023).

Finally, the apparent density variation of the mixtures corroborates the data on residual compressive strength and mass loss. Analyzing the variations shown in Figure 7, it is noticeable that the variations between the mixtures are small at both target temperatures. Additionally, it is possible to observe an accentuation in the density drop when the target temperature is 660 ºC, which corresponds to the increased mass loss and resistance observed. The density changes may be associated with the evaporation of water inside the bodies, the melting and decomposition of fibers, as well as eventual cracking during the process and chemical changes that occur in the substances at high temperatures. In this context, it is worth noting that this study did not identify significant volumetric variations in the tested specimens.

5 Concluding remarks

This study investigated the effects of adding polypropylene fibers to a UHPC blend to evaluate its heating behavior. Fibers were incorporated at concentrations of 1.25 kg/m³ and 2.5 kg/m³, and the material was heated to two target temperatures: 320 °C and 660 °C. The results showed that the presence of fibers negatively impacted the workability of the material in its fresh state, with decreasing spread as the amount of fiber increased. The compressive strength without heating showed decreases in average values; however, these decreases were not statistically significant.

The presence of fibers proved effective in preventing the spalling phenomenon, especially when related to the thermo-hygral mechanism, considering the temperatures at which the explosions of the reference test specimens occurred (between 320 ºC and 500 ºC as read on the muffle furnace display). It is important to emphasize that prevention occurs even at the lowest incorporation level used in this research (1.25 kg/m³) and without any statistically significant loss in compressive strength being observed, thus strengthening the discussions about the optimal PPF content. Additionally, it can be inferred that residual compressive strength decreases with increasing application temperature, which may be related to the material weakening process after undergoing stresses, even if not capable of causing an explosion, cracking, mass loss, among other effects. This scenario can be explained by the progressive and sharp decreases in mass loss with heating, as well as in apparent density.

6 Acknowledgements

The authors acknowledge the support provided by the Federal Center for Technological Education of Minas Gerais (CEFET-MG) for the support. We are also grateful for the agencies CNPq, CAPES, FAPEMIG and CEFET-MG for providing financial support, LIASA and Sika for the supply of materials.

7 References

Abadel, A. A., Khan, M. I., & Masmoudi, R. (2023). Influence of elevated temperature on the engineering properties of ultra-high-performance fiber-reinforced concrete. Materials Science-Poland, 41(1), 140-160.

Aljabbri, N. A. S., Hussein, M. N., & Khamees, A. A., 2021. Performance of Ultra High Strength Concrete Expose to High Rise Temperature. In Annales de Chimie Science des Matériaux (Vol. 45, No. 4).

Amran, M., Huang, S. S., Onaizi, A. M., Makul, N., Abdelgader, H. S., & Ozbakkaloglu, T., 2022. Recent trends in ultra-high performance concrete (UHPC): Current status, challenges, and future prospects. Construction and Building Materials, 352, 129029.

Associação Brasileira de Normas Técnicas, *Argamassa para Assentamento e Revestimento de Paredes e Tetos – Preparo da Mistura e Determinação do Índice de Consistência*, ABNT NBR 13276, 2016.

Chen, M., Yang, F., Zhang, T., & Zhou, L., 2024. Effect of elevated temperatures on behaviour of recycled steel and polypropylene fibre reinforced ultra-high performance concrete under dynamic splitting tension. Journal of Building Engineering, 84, 108586.

Christ, R., Lerner, L. R., Ehrenbring, H. Z., Pacheco, F., Bolina, F. L., Poleto, G., ... & Tutikian, B. F., 2023. Evaluation of ultra-high-performance concrete columns at high temperatures after 180 days of curing. Buildings, 13(9), 2254.

Du, Y., Qi, H. H., Huang, S. S., & Liew, J. R., 2020. Experimental study on the spalling behaviour of ultra-high strength concrete in fire. Construction and Building Materials, 258, 120334.

European Standards, EN-196-1: *Methods of testing cement - Part 1: Determination of strength*, 2016.

Hernández-Figueirido, D., Reig, L., Melchor-Eixea, A., Roig-Flores, M., Albero, V., Piquer, A., & Pitarch, A. M., 2024. Spalling phenomenon and fire resistance of ultrahigh-performance concrete. Construction and Building Materials, 443, 137695.

Jiang, J., Wu, M., & Ye, M., 2024. Prediction of fire spalling behaviour of fibre-reinforced concrete. Magazine of Concrete Research, 76(5), 229-244.

Jin, Z., Tian, H., Liang, B., Li, M., Du, S., Ma, G., ... & Zhao, X., 2024. Exploring the synthesis effects of glazed hollow beads and polypropylene fibers on the strength retention of ultra-high performance concrete after fire exposure using X-Ray computed tomography. Case Studies in Construction Materials, 21, e03782.

Kravanja, G., Mumtaz, A. R., & Kravanja, S., 2024. A comprehensive review of the advances, manufacturing, properties, innovations, environmental impact and applications of ultra-high-performance concrete (UHPC). Buildings, 14(2), 382.

Le Lee, K. J., Zhang, Z., & Tan, K. H., 2025. Multiscale investigation of sustainable spalling-resistant ultra-high performance concrete containing sludge-derived slag derivates and recycled polypropylene fibre. Cement and Concrete Composites, 106289.

Li, Y., Pimienta, P., Pinoteau, N., & Tan, K. H., 2019. Effect of aggregate size and inclusion of polypropylene and steel fibers on explosive spalling and pore pressure in ultra-high-performance concrete (UHPC) at elevated temperature. Cement and Concrete Composites, 99, 62-71.

Lin, J., Zhang, Y., Guo, Z., & Du, H., 2024. Impact of synthetic fibers on spalling and intrinsic pore structure of ultra-high performance concrete (UHPC) under elevated temperatures. Construction and Building Materials, 439, 137325.

Liu, J. C., Tan, K. H., & Yao, Y., 2018. A new perspective on nature of fire-induced spalling in concrete. Construction and Building Materials, 184, 581-590.

Mo, Z., Qian, L., Xiao, Y., Zhuang, W., & Gao, X., 2026. Review of Mechanical Properties and Hydration for Eco-Friendly UHPC—Role of Reactive Powders and Supplementary Cementitious Materials. Sustainability, 18(4), 1804.

Qian, Y., Yang, D., Xia, Y., Gao, H., & Ma, Z., 2023. Properties and improvement of ultra-high performance concrete with coarse aggregates and polypropylene fibers after high-temperature damage. Construction and Building Materials, 364, 129925.

Rui, Z. Q., Chu, Y., Guo, L. P., & Qing, Y. Y., 2025. Enhancing high-temperature spalling resistance and residual mechanical properties of UHPC: The combined role of polypropylene fibers and metakaolin. Journal of Building Engineering, 114305.

Shen, D., Liu, C., Luo, Y., Shao, H., Zhou, X., & Bai, S, 2023. Early-age autogenous shrinkage, tensile creep, and restrained cracking behavior of ultra-high-performance concrete incorporating polypropylene fibers. Cement and Concrete Composites, 138, 104948.

Shen, Y., Dai, M., Pu, W., & Xiang, Z., 2022. Effects of content and length/diameter ratio of PP fiber on explosive spalling resistance of hybrid fiber-reinforced ultra-high-performance concrete. Journal of Building Engineering, 58, 105071.

Teoh, K. B., Hiew, S. Y., Banthia, N., & Yoo, D. Y., 2026. Machine Learning in Ultra-High-Performance Concrete (UHPC): A Multiscale Review of Applications, Challenges, and Prospects. Archives of Computational Methods in Engineering, 1-56.Abrishami, H. H., and Mitchell, D., 1997. “Influence of Steel Fibres on Tension Stiffening,” *ACI Structural Journal*, 94(6) pp769-776.

Tsuchiya, Y., & Sumi, K., 1969. Thermal decomposition products of polypropylene. Journal of Polymer Science Part A-1: Polymer Chemistry, 7(7), 1599-1607.

Viana, T. M., Bacelar, B. A., Coelho, I. D., Ludvig, P., & Santos, W. J., 2020. Behaviour of ultra-high performance concretes incorporating carbon nanotubes under thermal load. Construction and Building Materials, 263, 120556.

Xiong, M. X., & Liew, J. R., 2015. Spalling behavior and residual resistance of fibre reinforced Ultra-High performance concrete after exposure to high temperatures. Materiales de Construcción, 65(320), e071-e071.

Zaid, O., Althoey, F., Abuhussain, M. A., & Alashker, Y., 2024. Spalling behavior and performance of ultra-high-performance concrete subjected to elevated temperature: A review. Construction and Building Materials, 411, 134489.

Zhang, W., Zeng, W., Zhang, Y., Yang, F., Wu, P., Xu, G., & Gao, Y., 2020. Investigating the influence of multi-walled carbon nanotubes on the mechanical and damping properties of ultra-high performance concrete. Science and Engineering of Composite Materials, 27(1), 433-444.

Effect of Polymer-Fibre-Containing Recycled Concrete Aggregate on the High-Temperature Resistance of Recycled Concrete

Viktor Hlavička[1]

[1]: Budapest University of Technology and Economics, Faculty of Civil Engineering, Department of Construction Materials and Technologies, Műegyetem rkp 3, Budapest H-1111, Hungary

Abstract

This study investigates the high-temperature performance of recycled aggregate concrete (RAC) produced with recycled concrete aggregates (RCA) derived from conventional and polypropylene (PP) microfiber-reinforced parent concretes. Three types of RCA were considered, originating from a reference concrete (N1) and two fiber-reinforced concretes with different fiber dosages (P1: 1 kg/m³, P2: 2 kg/m³). RAC mixtures were prepared with 25%, 50%, and 75% RCA replacement ratios and subjected to thermal exposure up to 800 °C.

Residual compressive strength, flexural-tensile strength, and spalling behavior were evaluated. RAC exhibited typical temperature-dependent strength evolution, with significant degradation above 450 °C. The use of RCA from PP fiber-reinforced concretes improved thermal resistance and reduced strength degradation; however, increasing RCA content accelerated deterioration. Spalling resistance was also enhanced by fiber-containing RCA, although less effectively than by direct fiber addition.

Keywords

Fibre reinforced concrete, PFRC, RCA, RAC, heat load, compressive strength, flexural-tensile strength, spalling.

1 Introduction

Concrete is one of the most extensively utilized materials in the construction industry, being employed in large volumes across structural, utility, and infrastructure applications. According to the Global Cement and Concrete Association, global concrete production reached approximately 14 billion m³ in 2020 (Global Cement and Concrete Association, 2023). Concrete is fundamentally composed of cement, water, and aggregates; consequently, the annual production of such vast quantities necessitates substantial cement manufacturing and extensive aggregate extraction. As a result, aggregates used in concrete production have become among the most intensively exploited natural resources worldwide (UEPG, 2022).

Through appropriate selection and rigorous testing of aggregates, it is now feasible to produce concretes incorporating recycled concrete aggregates (RCA) that achieve mechanical performance comparable to, or even exceeding, that of conventional aggregate concretes (McNeil & Kang, 2013; Nemes, 2026; Wang et al., 2021). However, beyond mechanical strength, concrete must also satisfy durability requirements, including adequate resistance to elevated temperatures, such as those encountered during fire exposure.

In response, an increasing number of studies have investigated the thermal performance of recycled aggregate concrete (RAC) (Fernandes et al., 2021; Zheng et al., 2023). Nevertheless, the findings reported in the literature are sometimes contradictory, indicating that several factors influencing the thermal resistance of RAC remain insufficiently understood. Therefore, further experimental investigations are required to achieve a more comprehensive understanding of the governing mechanisms.

At elevated temperatures, concrete undergoes irreversible physicochemical changes that degrade its mechanical properties and alter its microstructure and mineralogical composition. The deterioration process is governed by both chemical transformations and spalling, which is influenced by factors such as mixture composition, moisture content, and thermal exposure conditions (Thielen, 1994). Thermal effects include moisture evaporation and dehydration processes below 200 °C, followed by the decomposition of portlandite between 450–550 °C. At 573 °C, quartz phase transformation induces volumetric expansion and internal stresses, while above 700 °C, the decomposition of C–S–H phases lead to further structural damage and significant strength reduction (Alonso & Schneider, 2019; Ma et al., 2015; Malik et al., 2021).

Spalling is a critical phenomenon in concrete subjected to elevated temperatures, characterized by the detachment of surface layers due to pore pressure buildup and thermal stresses. This process can significantly reduce structural integrity, especially under fire exposure. The incorporation of polypropylene (PP) microfibers is an effective method to mitigate spalling. At approximately 160–170 °C, the fibers melt, forming a network of microchannels that increases permeability and facilitates vapor pressure release. Although PP microfibers substantially improve spalling resistance, their melting-induced porosity may contribute to reduced residual mechanical properties at high temperatures (Balázs & Lublóy, 2012; Bošnjak, 2014).

2 Experimental program

The aim of the study was to determine the effect of recycled concrete aggregate (RCA) containing polymer fibres on the heat resistance of new concrete. Three different parent concrete mixtures were used for this study. One of these mixtures (N1) had a water-cement ratio of 0.5 and did not contain polymer fibres. The other two mixtures had a water-cement ratio of 0.45 and contained polymer microfibres in varying amounts: the fibre dosage was 1 kg/m³ for mixture P1 and 2 kg/m³ for P2. The fibre-containing mixtures were prepared using polypropylene (PP) microfibres. The PP fibers were 18 mm long and had a diameter of 0.032 mm (Figure 1). In all three base mixtures, quartz gravel and sand from river dredging were used. The composition of the initial mixtures is summarized in the Table 1.



Figure 1: PP fibers

Part of the parent concrete mixes was used to make crushed concrete aggregate for further concrete mixes. A jaw crusher was used to crush the concrete elements. The un-crushed specimens were used in strength tests. The research also determined the particle size distribution, the body density, and water absorption of the RCA made from the original mixtures. The results of the measurements were used to design the recipes for recycled concrete.

The composition of recycled aggregate concrete (RAC) mixes is summarized in Table 1. For the recycled concrete mixes, only one w/c ratio (0.45) was used. For the RAC, the RCA proportions were 25, 50, and 75%, which collectively included both the fine (0/4 mm) and coarse (4/11 mm) aggregate fractions. Therefore, a total of 9 recycled concrete mixes were produced using RCA from the original three concrete mixes. In the case of recycled concrete mixtures, the water absorption of the RCA was also taken into account. The recipes were corrected by adding extra water calculated from the 30 minutes water absorption of the aggregate.

For both the parent and recycled mixtures, the concrete test specimens were stored underwater for 6 days after demolding, in accordance with the Hungarian standard (MSZ 4798, 2016), and then stored under laboratory conditions.

For both the original and the recycled concrete mixes, the superplasticizer was dosed so that the mixes were of consistency class F2 (EN 12350-5:2019, 2019).

The specimens of the parent concrete mixes and the recycled mixes were heat-loaded at 28 days of age. Electric furnaces were used for heating. The heating rate of the furnaces was close to, but below, the heating rate of the standard ISO fire curve (ISO 834-1, 1999). The test

specimens were tested at the ambient temperature (20 °C) and after 5 different heat loads (150, 300, 450, 600, 800 °C). In all cases, the heat exposure time was 2 h. The specimens were then cooled slowly back to the initial temperature together with the furnace. In each case, 3 specimens were tested per heat load.

Table 1: Concrete mix designs for 1 m^3

		Concrete mix code											
		N1	P1	P2	RN1-25	RN1-50	RN1-75	RP1-25	RP1-50	RP1-75	RP2-25	RP2-50	RP2-75
Aggregate [kg/m^3]	sand 0/4	760.2	781.3	780.1	727.8	582.3	454.9	727.8	582.3	454.9	636.8	491.3	454.9
	natural coarse 4/11	1007.7	1035.6	1034.1	636.8	327.5	0.0	636.8	327.5	0.0	727.8	418.5	0.0
	RCA N1 0/11	-	-	-	429.9	859.9	1289.8	-	-	-	-	-	-
	RCA P1 0/11	-	-	-	-	-	-	426.5	853.0	1279.5	-	-	-
	RCA P2 0/11	-	-	-	-	-	-	-	-	-	429.9	859.9	1279.5
	RCA ratio	*0%*	*0%*	*0%*	*25%*	*50%*	*75%*	*25%*	*50%*	*75%*	*25%*	*50%*	*75%*
Cement (CEM I 32,5 N-LH) [kg/m^3]		390.0	390.0	390.0	390.0	390.0	390.0	390.0	390.0	390.0	390.0	390.0	390.0
Water [kg/m^3]		195.0	175.5	175.5	175.5	175.5	175.5	175.5	175.5	175.5	175.5	175.5	175.5
w/c		*0.50*	*0.45*	*0.45*	*0.45*	*0.45*	*0.45*	*0.45*	*0.45*	*0.45*	*0.45*	*0.45*	*0.45*
Extra water [kg/m^3]		-	-	-	6.45	12.90	19.35	4.27	8.53	12.80	9.46	18.82	28.15
PP fiber [kg/m^3]		-	1.00	2.00	-	-	-	-	-	-	-	-	-
Superplasticizer [kg/m^3]		0.9	3.3	2.1	0.8	0.8	1.4	1.6	0.8	0.8	1.4	1.6	1.2

The concrete mixtures were used to make 70x70x250 cm slab specimens. After the thermal loading (in cooled state), the slabs were first subjected to a crack-controlled bending test (EN 14651:2005+A1, 2007) and then to a compressive strength test on the remaining two half-slabs (Figure 2). The compressive strength tests used were different from the standard tests (EN 12390-3, 2019). However, previous research (Alimrani & Balazs, 2020; Hlavička, 2021) has shown that for a maximum aggregate size of 11 mm, the results of the compressive strength tests on the half-slabs are close to the compressive strength values obtained on the standard 150 mm edge length cubes. The flexural-tensile strength values calculated from the crack-controlled test are below the results of the pure flexural test due to the stress peak resulting from the notch. However, this is not relevant to the present experiment, as the temperature-induced degradation tendency can be determined.

The research project also aims to investigate the fracture energy of recycled concrete after heat loading. This is the reason why the flexural-tensile strength was investigated in a notched specimen test. However, the fracture energy results will be presented in a later publication. These results are not discussed in this paper.



Figure 2: Crack-controlled bending test (left), compressive strength tests on half-slab (right)

3 Test Results and Discussion

3.1 Strength of concretes in ambient temperature

The compressive and flexural-tensile strengths of the concretes (without heat loading) measured at 28 days of age are shown in Figure 3 and Table 2.

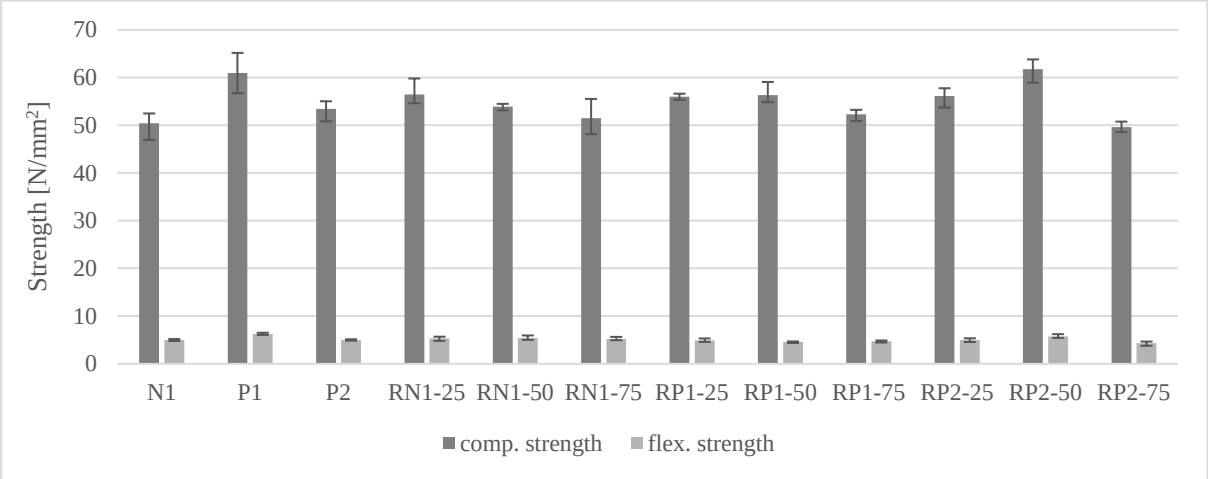


Figure 3: Compressive and flexural-tensile strength of concretes

Among the base mixtures, the P1 and P2 concretes, which were prepared with a lower water-to-cement ratio (w/c = 0.45), exhibit higher compressive strength than the conventional N1 mixture (w/c = 0.5), which is consistent with the denser microstructure of the cement stone. This is also confirmed by the results of the body density (Table 2) measurements on the test specimens. It can be seen that the body density of the P1 mixture, despite the addition of PP fibers, exceeds that of the N1 mixture. The body density of the N1 mixture is nearly identical to that of the P2 mixture, which has a higher fiber content but a lower water-cement ratio. At the same time, increasing the fiber content from 1 kg/m³ to 2 kg/m³ resulted in a slight decrease in compressive strength, which can also be explained by the mixture's increasing porosity.

In mixtures containing recycled aggregates, there is a general trend for compressive strength to decrease as the replacement ratio increases, which can be attributed to the less favorable properties of the recycled aggregates and a weaker interface zone (ITZ). This decrease is particularly pronounced in the case of N1-based recycled concrete (RN1). In contrast, aggregates derived from higher-quality, lower water-cement ratio, and fiber-reinforced base concrete (RP1, RP2) provide better mechanical performance, highlighting the decisive role of the base concrete's quality.

Based on the results, it can be concluded that the addition of microfibers had no effect on the flexural-tensile strength of the base concretes. The compressive strength to flexural-tensile strength ratio is nearly identical for all three base concretes: 9.7–10.7. For the recycled concretes, the compressive strength to flexural-strength ratio when using RCA N1 is the same as that observed for the base concretes (9.9–10.5). However, when using RCA containing PP fibers, the compressive strength to flexural-tensile strength ratio increased in all cases (10.7–12.3). This means that the flexural-tensile strength deteriorated relative to the compressive strength.

Table 2: Average values of properties of the concrete before and after heat load

Mix.	Temp. [°C]	Spalling [piece]	Density [kg/m^3]	Comp. Strength [N/mm^2]	Flex. Strength [N/mm^2]
N1	20	0	2279.49	50.40	4.99
	150	0	2266.82	46.83	4.27
	300	0	2232.39	45.20	5.50
	450	0	2217.91	49.23	4.76
	600	2	2122.57	35.31	2.60
	800	1	2133.41	16.30	0.41
P1	20	0	2301.92	60.95	6.25
	150	0	2292.50	52.96	4.92
	300	0	2249.66	66.00	7.08
	450	0	2222.50	67.15	5.08
	600	0	2189.49	49.15	1.83
	800	0	2144.77	23.74	0.57
P2	20	0	2247.70	53.42	5.01
	150	0	2196.91	51.18	5.29
	300	0	2209.97	53.64	6.02
	450	0	2156.46	59.61	4.76
	600	0	2132.71	32.24	1.27
	800	0	2119.36	16.78	0.55
RN1-25	20	0	2247.95	56.44	5.36
	150	0	2231.30	49.79	4.97
	300	0	2159.55	51.67	5.30
	450	0	2162.04	55.73	5.40
	600	0	2111.09	33.95	1.57
	800	3	-	-	-
RN1-50	20	0	2151.35	53.92	5.39
	150	0	2150.57	42.13	4.41
	300	0	2082.95	49.80	5.47
	450	0	2075.15	49.43	5.27
	600	1	2052.48	38.71	2.77
	800	3	-	-	-
RN1-75	20	0	2183.04	51.52	5.20
	150	0	2144.58	42.38	3.64
	300	0	2064.65	49.98	4.62
	450	0	2051.69	49.54	4.69
	600	1	2008.28	34.00	2.14
	800	3	-	-	-

Mix.	Temp. [°C]	Spalling [piece]	Density [kg/m^3]	Comp. Strength [N/mm^2]	Flex. Strength [N/mm^2]
RP1-25	20	0	2252.87	56.00	4.95
	150	0		45.93	4.40
	300	0	2145.82	63.23	5.75
	450	0	2153.70	60.77	5.39
	600	1	2125.70	48.44	2.52
	800	3	-	-	-
RP1-50	20	0	2191.33	56.36	4.57
	150	0	2181.58	48.76	4.14
	300	0	2099.38	60.79	5.33
	450	0	2117.44	57.24	4.76
	600	1	2048.52	41.14	2.43
	800	3	-	-	-
RP1-75	20	0	2190.21	52.31	4.70
	150	0	2132.34	43.88	3.85
	300	0	2105.85	54.08	5.00
	450	0	2032.61	53.14	4.61
	600	0	2011.97	35.16	1.86
	800	3	-	-	-
RP2-25	20	0	2269.29	56.14	5.00
	150	0	2235.78	48.45	4.73
	300	0	2188.54	58.26	5.60
	450	0	2162.86	58.66	5.16
	600	1	2125.32	43.83	2.36
	800	3	-	-	-
RP2-50	20	0	2222.44	61.75	5.74
	150	0	2192.07	49.02	4.56
	300	0	2123.11	63.78	5.60
	450	0	2121.40	63.58	5.62
	600	0	2064.64	46.98	2.70
	800	3	-	-	-
RP2-75	20	0	2145.05	49.63	4.31
	150	0	2105.01	38.96	4.64
	300	0	2038.64	46.94	4.44
	450	0	2045.72	48.05	4.51
	600	0	1999.42	28.37	1.89
	800	0	1949.13	14.75	0.44

3.2 High-temperature resistance of original concretes

The results for the compressive strength and flexural-tensile strength of the parent concrete specimens after heat loading are summarized in Table 2, while the values for the relative residual compressive strength and relative residual flexural-tensile strength after heat loading are illustrated in Figure 4.

The results obtained after heat loading show that the compressive strength and flexural-tensile strength values reach a local minimum at 150 °C. This is followed by an increase in the strength values. For compressive strength, the local maximum is observed at 450 °C for all three concrete mixtures, and then, as the temperature continues to rise, the compressive strength

decreases rapidly. For flexural-tensile strength, the local maximum is observed at 300 °C for all three initial mixtures, after this point the flexural-tensile strength decreases.

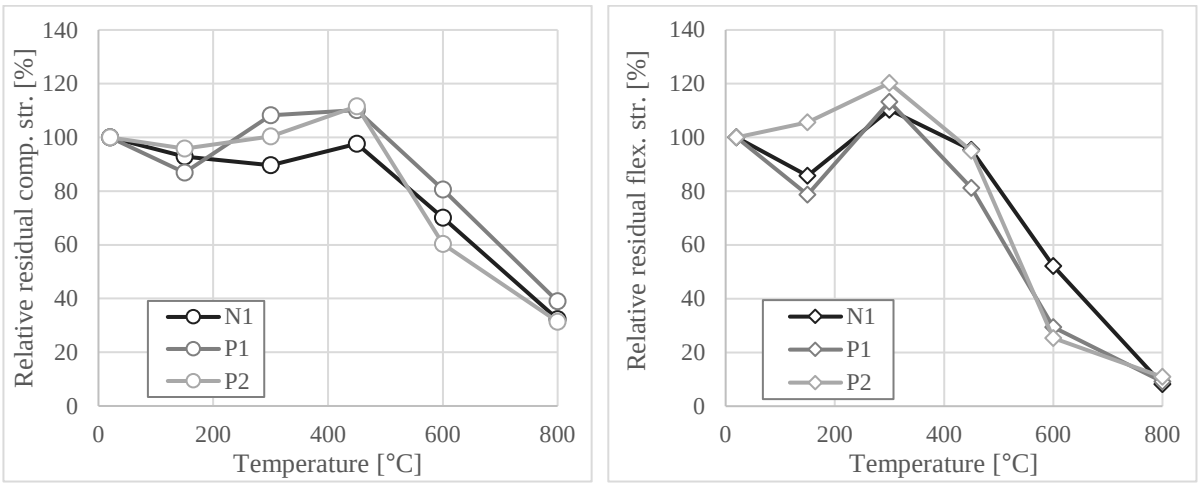


Figure 4: Relative residual compressive strength (left) and Relative residual flexural-tensile strength (right) of original concretes as a function of temperature

According to the literature, there are several reasons for the increase in strength after 150 °C. As a result of thermal expansion, the aggregate particles are compressed more tightly, resulting in aggregate interlock (Ali & Lublóy, 2022; Sólyom et al., 2019; Zhang & Bicanic, 2006). In this temperature range, the cement gel layers displace, resulting in an increase in the Van der Waals force (Malik et al., 2021; Naus, 2006). Furthermore, several studies have shown that between 100 and 300 °C the evaporation of pore water generates high internal steam pressure, creating internal autoclaving conditions that promote the additional hydration of previously unhydrated cement grains (Ma et al., 2015).

The results show that the addition of PP microfibers had a positive effect on the residual compressive strength of the concrete mixtures. The residual compressive strength of mixtures P1 and P2 exceeded that of mixture N1 at both 300 and 450 °C. However, this effect is not observed in the case of flexural-tensile strength. In this case, at the local peak observed at 300 °C, only the results of the P2 mixture exceed those of the N1 mixture. Then, as the temperature continued to rise, the non-fibre-reinforced N1 mixture exhibited a slower rate of degradation between 300 and 800 °C than the PP fibre-reinforced concretes.

3.3 High-temperature resistance of recycled concrete

Using RCA from the three original concretes, we produced a total of 9 recycled concretes. The RCA ratio was 25, 50 and 75%. The results for the compressive strength and flexural-tensile strength of the RAC specimens after heat loading are summarized in Table 2, while the values for the relative residual compressive strength and relative residual flexural-tensile strength after heat loading are illustrated in Figure 5, Figure 6 and Figure 7.

A similar trend can be observed in recycled concrete regarding changes in residual compressive strength and residual flexural-tensile strength as in base concrete. Initially, both compressive strength and flexural-tensile strength decrease as the temperature rises. A local minimum is observed at 150 °C, after which the strength increases. For all RACs, both compressive strength and flexural-tensile strength begin to decrease significantly after 450 °C. This is caused by the decomposition of cement stone and the deterioration of the ITZ.

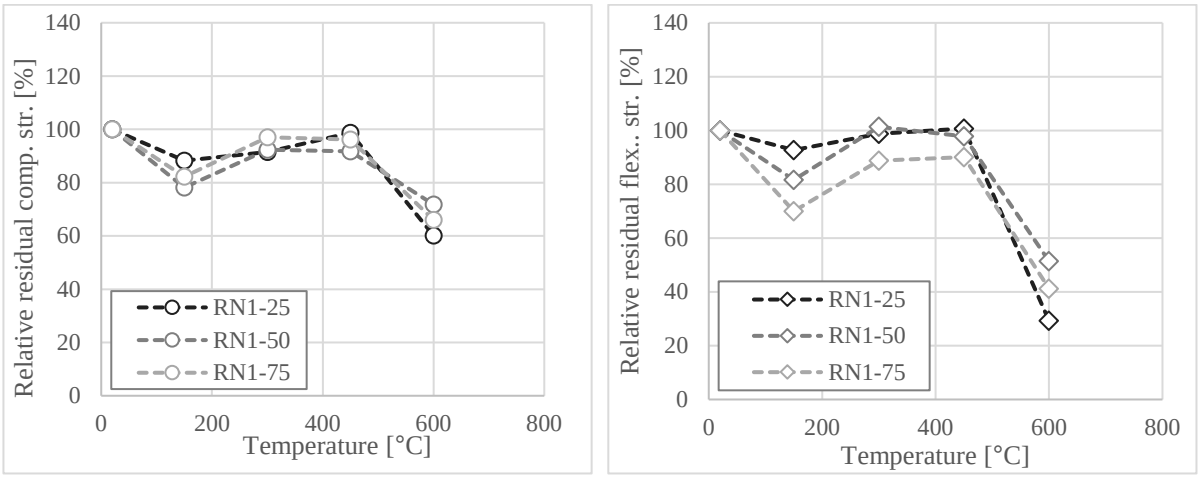


Figure 5: Relative residual compressive strength (left) and the Relative residual flexural-tensile strength (right) of RAC whit RCA N1 as a function of temperature

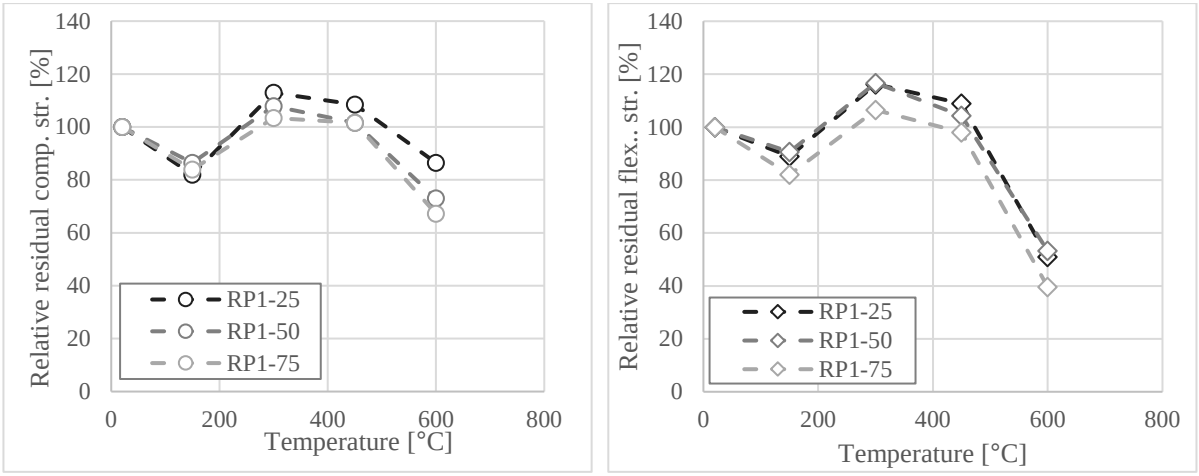


Figure 6: Relative residual compressive strength (left) and the Relative residual flexural-tensile strength (right) of RAC whit RCA P1 as a function of temperature

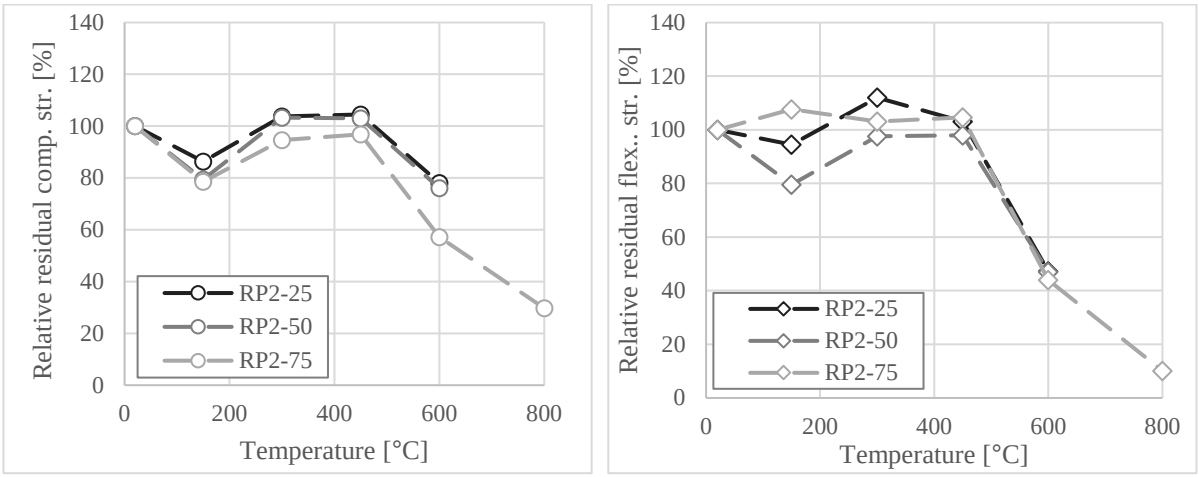


Figure 7: Relative residual compressive strength (left) and the Relative residual flexural-tensile strength (right) of RAC whit RCA P2 as a function of temperature

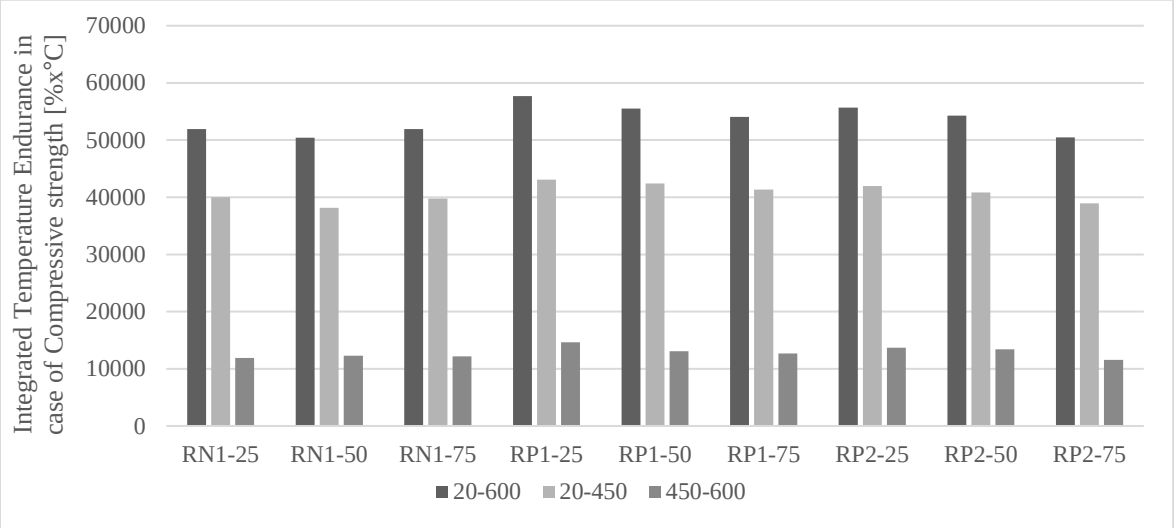


Figure 8: Integrated Temperature Endurance of RACs in case of compressive strength

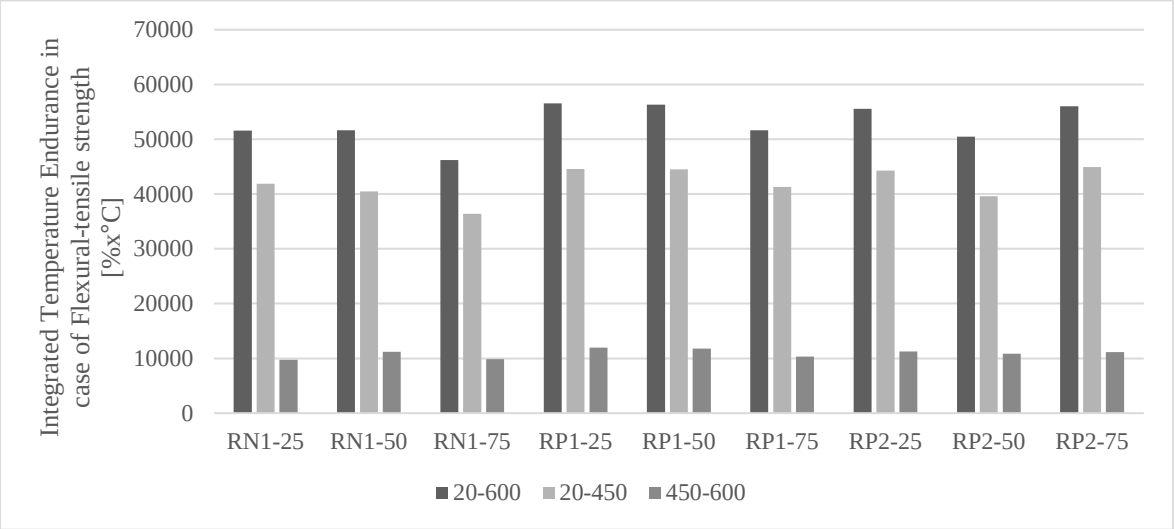


Figure 9: Integrated Temperature Endurance of RACs in case of flexural-tensile strength (right)

To compare the deterioration tendency of concretes of different strengths, the area under the relative stress - temperature curves was examined. This integrated area (Integrated Temperature Endurance - ITE) gives a good characterisation of the rate of degradation (Fehérvári, 2023). If the integrated area is large, the rate of degradation is slow, and if the integrated area is small, the rate of degradation is fast. The integrated temperature resistance values are summarised in Figure 8 and Figure 9, where we examined the entire range (20–600 °C), the range up to the local maximum (20–450 °C), and the descending range (450–600 °C).

When examining the entire range of residual compressive strength, the results show that the ITE values for the RP1 and RP2 mixtures exceeded those of the RN1 mixtures. This means that the use of RCA containing PP fibers slowed the thermal degradation of the compressive strength of the RAC mixtures. When examining the initial section between 20 and 450 °C and the sections beyond 450 °C separately, it is also evident that the RP1 and RP2 mixtures have higher ITE values than the RN1 mixture. Therefore, the effect of fiber content cannot be separated into the sections before and after the local maximum. The values also show that as the RCA content

increases, the ITE value decreases for all three RCA types. Consequently, as the RCA content increases, the rate of degradation due to heat loading accelerates.

In the case of residual flexural-tensile strength, the same effect can be observed as with residual compressive strength. In this case as well, the RP1 and RP2 mixtures had higher ITE values than the RN1 mixtures. Furthermore, it is also true for residual flexural-tensile strength that as the RCA content increases, the degradation caused by heat loading accelerates, and the ITE value decreases.

3.4 Spalling

The Table 2 also includes the number of test specimens that exploded during heat loading (Figure 10). In the case of the base concretes, the effect of adding PP fibers is clearly visible. For the N1 mixture, 2 test specimens failed at a heat load of 600 °C, and 1 test specimen failed at a heat load of 800 °C. In contrast, in the case of mixtures containing PP microfibers, no test specimens were destroyed by spalling at either 600 °C or 800 °C.



Figure 10. Test specimens destroyed by spalling under heat load

In the case of recycled aggregate concretes, it can be concluded that their resistance to spalling was generally inferior to that of the reference P1 and P2 mixtures incorporating polypropylene (PP) microfibers. Under exposure to 800 °C, nearly all specimens experienced spalling across the investigated mixtures.

A comparison among the recycled aggregate concretes indicates that, for mixtures produced with recycled concrete aggregates (RCA) derived from PP microfiber-reinforced concretes, spalling resistance improved with increasing RCA content. Specifically, in mixtures incorporating RCA P1, the number of specimens failing due to spalling at 600 °C decreased as the RCA replacement ratio increased, and a similar trend was observed for mixtures containing RCA P2.

Furthermore, in the case of mixtures with 75% RCA P2, no explosive spalling occurred even at 800 °C. This enhanced performance can be attributed to the higher initial fiber content of the P2 base concrete, which likely promoted the formation of a more effective pore network upon thermal degradation of the fibers, thereby facilitating vapor pressure release and mitigating spalling.

Overall, it can be concluded that the use of RCA containing PP microfibers contributes to improving the spalling resistance of RAC mixtures. However, this effect is less pronounced

than in cases where PP microfibers are directly incorporated into the concrete mixtures during production.

4 Concluding remarks

The present study investigated the high-temperature performance of recycled aggregate concrete (RAC) produced with recycled concrete aggregates (RCA) derived from both conventional and polypropylene (PP) microfiber-reinforced base concretes. Based on the experimental results, several key conclusions can be drawn:

- The results confirmed that RAC exhibits a thermal degradation behavior similar to that of conventional concrete, characterized by an initial reduction in strength up to approximately 150 °C, followed by a temporary recovery and a subsequent significant decrease beyond 450 °C. Both compressive and flexural-tensile strengths were strongly affected by elevated temperatures; however, flexural-tensile strength proved to be more sensitive to thermal damage.
- The quality and composition of the parent concrete used to produce RCA were found to play a decisive role in the thermal performance of RAC. Mixtures incorporating RCA derived from PP fiber-reinforced concretes (RP1 and RP2) consistently showed improved resistance to thermal degradation, as reflected by higher Integrated Temperature Endurance (ITE) values compared to mixtures containing conventional RCA (RN1). This indicates that the beneficial effects of fibers can be partially preserved through the recycling process.
- At the same time, increasing the RCA replacement ratio resulted in a systematic reduction in ITE values for all aggregate types, indicating an accelerated rate of strength degradation at higher RCA contents. This highlights the importance of optimizing RCA content when designing RAC for applications involving elevated temperatures.
- The spalling behavior further emphasized the role of PP fibers. While RAC generally exhibited lower resistance to spalling than the original fiber-reinforced concretes, the use of RCA containing PP microfibers improved spalling resistance compared to conventional RCA. The effectiveness of this mechanism increased with higher RCA contents and was most pronounced in mixtures containing RCA derived from higher fiber dosage (P2), where no explosive spalling was observed even at 800 °C. Nevertheless, the results also demonstrate that this indirect fiber effect is less efficient than the direct incorporation of PP fibers into the concrete mixture.

Overall, the findings highlight that the thermal performance of RAC can be significantly enhanced by using RCA derived from fiber-reinforced parent concretes. However, the combined effects of RCA quality and replacement ratio must be carefully balanced to ensure adequate mechanical performance and durability under high-temperature exposure.

5 Acknowledgements

I would like to thank my colleagues Krisztián Takács and Balázs Burai for their help in the laboratory measurements. I would also like to thank Viktor Cseri and Duna-Dráva Cement Kft. for providing the cement needed for the tests. Project no. PD 146109 has been implemented with the support provided by the Ministry of Culture and Innovation of Hungary from the National Research, Development and Innovation Fund, financed under the OTKA PD_23 funding scheme.

6 References

Ali, S. I. A., & Lublóy, É. (2022). Fire resistance properties of heavyweight magnetite concrete in comparison with normal basalt- and quartz-based concrete. *Journal of Thermal Analysis and Calorimetry*, *147*(21), 11679–11691. https://doi.org/10.1007/s10973-022-11407-3

Alimrani, N. S., & Balazs, G. L. (2020). Investigations of direct shear of one-year old SFRC after exposed to elevated temperatures. *Construction and Building Materials*, *254*, 119308. https://doi.org/10.1016/j.conbuildmat.2020.119308

Alonso, M. C., & Schneider, U. (2019). *Degradation Reactions in Concretes Exposed to High Temperatures* (pp. 5–40). https://doi.org/10.1007/978-3-319-95432-5_2

Balázs, G. L., & Lublóy, É. (2012). Post-heating strength of fiber-reinforced concretes. *Fire Safety Journal*, *49*, 100–106. https://doi.org/10.1016/J.FIRESAF.2012.01.002

Bošnjak, J. (2014). *Explosive spalling and permeability of high performance concrete under fire – numerical and experimental investigations* [PhD Thesis]. Institut für Werkstoffe im Bauwesen der Universität Stuttgart.

EN 12350-5:2019. (2019). *Testing fresh concrete - Part 5: Flow table test*.

EN 12390-3. (2019). *Testing hardened concrete – Part 3: Compressive strength of test specimens*.

EN 14651:2005+A1. (2007). *Test method for metallic fibre concrete - Measuring the flexural tensile strength (limit of proportionality (LOP), residual)*.

Fehérvári, S. (2023). The Effect of Elevated Temperature on Ordinary Portland Cements. *Periodica Polytechnica Civil Engineering*, *67*(1), 224–231. https://doi.org/10.3311/PPci.20519

Fernandes, B., Carré, H., Mindeguia, J.-C., Perlot, C., & La Borderie, C. (2021). Effect of elevated temperatures on concrete made with recycled concrete aggregates - An overview. *Journal of Building Engineering*, *44*, 103235. https://doi.org/10.1016/j.jobe.2021.103235

Global Cement and Concrete Association. (2023). *CEMENT AND CONCRETE AROUND THE WORLD*. https://gccassociation.org/concretefuture/cement-concrete-around-the-world/

Hlavička, V. (2021). Comparison of the result of notched three point bending test with Model Code 2010 formulas. *Concrete Structures*, *22*, 5–12. https://doi.org/10.32970/cs.2021.1.2

ISO 834-1. (1999). *Fire-resistance Tests – Elements of building construction, Part 1: General requirements*.

Ma, Q., Guo, R., Zhao, Z., Lin, Z., & He, K. (2015). Mechanical properties of concrete at high temperature-A review. In *Construction and Building Materials*. https://doi.org/10.1016/j.conbuildmat.2015.05.131

Malik, M., Bhattacharyya, S. K., & Barai, S. V. (2021). Thermal and mechanical properties of concrete and its constituents at elevated temperatures: A review. *Construction and Building Materials*, *270*, 121398. https://doi.org/10.1016/j.conbuildmat.2020.121398

McNeil, K., & Kang, T. H. K. (2013). Recycled Concrete Aggregates: A Review. In *International Journal of Concrete Structures and Materials* (Vol. 7, Number 1, pp. 61–69). Korea Concrete Institute. https://doi.org/10.1007/s40069-013-0032-5

MSZ 4798. (2016). *Concrete. Specification, performance, production, conformity, and rules of application of EN 206 in Hungary* .

Naus, D. J. (2006). *The Effect of Elevated Temperature on Concrete Materials and Structures - a Literature Review*. https://doi.org/10.2172/974590

Nemes, R. (2026). Utilization of Demolition Waste for Concrete Aggregate. *Buildings*, *16*(3), 526. https://doi.org/10.3390/buildings16030526

Sólyom, S., Di Benedetti, M., Guadagnini, M., & Balázs, G. L. (2019). Effect of temperature on the bond behaviour of GFRP bars in concrete. *Composites Part B: Engineering*, 107602. https://doi.org/10.1016/j.compositesb.2019.107602

Thielen, K. Ch. (1994). Strength and Deformation of Concrete Subjected to high Temperature and Biaxial Stress-Test and Modeling. *Deutscher Ausschuss Für Stahlbeton*, *437*.

UEPG. (2022). *Sustainable Supply of Aggregates in Europe (Final Report 12/2022)*.

Wang, B., Yan, L., Fu, Q., & Kasal, B. (2021). A Comprehensive Review on Recycled Aggregate and Recycled Aggregate Concrete. In *Resources, Conservation and Recycling* (Vol. 171). Elsevier B.V. https://doi.org/10.1016/j.resconrec.2021.105565

Zhang, B., & Bicanic, N. (2006). Fracture energy of high-performance concrete at high temperatures up to 450°C: the effects of heating temperatures and testing conditions (hot and cold). *Magazine of Concrete Research*, *58*(5), 277–288. https://doi.org/10.1680/macr.2006.58.5.277

Zheng, Y., Xi, X., Zhang, Y., Zhang, P., & Du, C. (2023). Review of mechanical properties and strengthening mechanism of fully recycled aggregate concrete under high temperature. *Construction and Building Materials*, *394*, 132221. https://doi.org/10.1016/j.conbuildmat.2023.132221

Comparative Fatigue Behaviour of Steel Fibre Reinforced Concrete under Flexural and Traffic-Type Loading

Sheila Bisika[1] and Humaira Fataar[1]

[1]: Department of Civil Engineering, Stellenbosch University, Cnr Banghoek Road & Joubert Street, Stellenbosch 7600, South Africa.

Abstract

The fatigue behaviour of steel fibre reinforced concrete (SFRC) is commonly evaluated using three or four-point flexural beam tests under cyclic loading. While these tests provide insight into fatigue life and crack mouth opening displacement (CMOD), they may not replicate traffic-induced stress states in pavement applications. Accelerated Pavement Testing (APT) simulates repeated wheel loading and is typically applied to slabs and full-scale pavement sections. This study adopts a beam-scale approach to evaluate material-level fatigue behaviour under traffic-representative loading. However, beam-scale APT remains limited and no clearly established framework links conventional beam fatigue testing with traffic-type loading. Consequently, it remains unclear how conventional beam testing relates to fatigue under traffic.
This study experimentally investigated the CMOD evolution and fatigue response under both typical three-point flexural fatigue loading and traffic-type wheel loading. The wheel loading regime was applied through development of a preliminary beam-based APT methodology using the Model Mobile Load Simulator (MMLS3). Progressive CMOD growth was observed under both load regimes, indicating fatigue damage progression. The response under MMLS3 loading was more complex, with regions of crack stabilisation, reduction, and gradual CMOD evolution observed over repeated cycles. Crack behaviour under traffic-type loading was found to be influenced by the evolving bending moment distribution, support conditions, and local stress state associated with the moving wheel load, rather than the applied load magnitude alone. These findings demonstrate fundamental differences between conventional laboratory-based flexural fatigue and traffic-representative loading conditions.

Keywords

Steel fibre reinforced concrete, fatigue, fibre bridging, MMLS3, accelerated pavement testing, crack mouth opening displacement

1 Introduction

The use of concrete pavements has increased considerably over recent decades due to their extended structural service life, high durability, and low maintenance requirements (Vishwakarma and Ingle, 2018). For highways subjected to heavy and repetitive traffic loading, concrete pavements are often preferred to asphalt alternatives because of their superior long-term structural performance (Wtaife et al., 2018). However, despite these advantages, cracking remains the predominant distress mechanism governing the structural capacity and serviceability of concrete pavement systems (Huang, 2004).

Concrete exhibits high compressive strength but relatively low tensile and flexural capacity, resulting in brittle behaviour once cracking initiates. In pavement applications, repeated traffic loading induces fatigue cracking that progressively reduces structural capacity and may ultimately lead to failure (Vishwakarma and Ingle, 2018). Consequently, improving the tensile strength and post-cracking performance of concrete is critical for enhancing pavement durability and fatigue resistance. Fibre-reinforced concrete (FRC) has been widely adopted to address this limitation. Discrete fibres enhance ultimate load capacity, increase toughness, improve load transfer efficiency across cracks, and reduce crack widths through crack-bridging mechanisms (di Prisco et al., 2009). Steel fibres are the most widely used fibre type in structural concrete due to their ability to enhance residual tensile strength and post-cracking flexural performance (Elsaigh et al., 2005, Wtaife et al., 2018).

In concrete pavement systems, steel fibres improve crack control and post-cracking behaviour through enhanced toughness, ductility, and load transfer across cracks, resulting in improved flexural performance under loading (Wtaife et al., 2018). Since concrete pavements are continuously subjected to repeated traffic loading throughout their service life, pavement design and performance assessment remain largely governed by flexural response, as fatigue behaviour is primarily influenced by stress levels and load repetitions (Mandal et al., 2018, Ramakrishnan and Josifek, 1987). In practice, fatigue behaviour is typically evaluated using adaptations of the EN 14651:2005+A1:2007 notched prism tests, where fatigue performance is assessed through laboratory-scale flexural beam testing under three-point or four-point bending. In these tests, the crack mouth opening displacement (CMOD) is used as a key indicator of damage progression. However, these test methods impose idealised bending stress conditions that may not fully capture the complex stress states experienced by concrete pavements under wheel loading.

Accelerated Pavement Testing (APT) has been developed to simulate traffic-type loading under controlled conditions and better represent in-service pavement behaviour. It is commonly applied at slab or full-scale level (Cai and Wang, 2013). The Model Mobile Load Simulator (MMLS3) applies repeated rolling wheel loads to replicate traffic-induced stresses (Hugo and Steyn, 2015). However, its application at beam scale remains largely unexplored. As a result, no clear framework exists to link conventional flexural fatigue testing with wheel-induced fatigue loading at the material level, limiting the interpretation of laboratory results in relation to pavement in-service behaviour.

This study aims to address this gap by developing a preliminary beam-scale APT methodology using the MMLS3 and comparing fatigue response under (i) conventional three-point cyclic flexural loading and (ii) traffic-type wheel loading. CMOD evolution is evaluated under both

regimes to identify differences in damage progression and to provide insight into the relationship between laboratory-based and traffic-representative fatigue behaviour in SFRC.

2 Experimental Programme

2.1 Mix Design and Specimen Preparation

The experimental programme consisted of steel fibre reinforced concrete (SFRC) beam specimens prepared for static flexural, flexural fatigue, and MMLS3 testing. A total of six SFRC beam specimens with dimensions of 150 × 150 × 700 mm were cast for static flexural and flexural fatigue testing. An additional three SFRC specimens with dimensions of 150 × 75 × 600 mm were prepared for MMLS3 testing. The reduced dimensions of the MMLS3 specimens were due to size constraints on the developed testing rig.

The experimental component of this investigation utilised a previously validated SFRC mix design adapted from Fataar (2022). Although originally developed for general SFRC applications, the mix design complied with the requirements of the Standard Specifications for Road and Bridge Works for South African Road Authorities (Committee of Transport Officials (COTO), 2020) in terms of aggregate grading, cement content, and workability. The mix proportions used for all specimens are presented in Table 1. The steel fibres used in this study were DRAMIX 3D 65/60 BG hooked-end fibres supplied by Bekaert and were incorporated at a dosage of 0.8% by volume for all SFRC specimens. In addition, a high-range water-reducing superplasticiser, Chryso®Fluid Optima 206, was incorporated into the concrete mix to improve workability while maintaining the desired water-to-cement ratio.

The workability of each batch was verified using a slump test conducted in accordance with EN 12350-2:2009, with an average slump of approximately 150 mm obtained for all the SFRC mixes. The concrete was cast into the moulds, compacted, and left to set before demoulding. Following demoulding, the specimens were water-cured for 28 days prior to testing. Prior to testing, all specimens were notched at mid-span using a wet saw blade in accordance with EN 14651:2005+A1:2007. A notch depth of 25 mm was used for the 150 × 150 × 700 mm beams, while a reduced notch depth of 12.5 mm was adopted for the MMLS3 specimens due to their reduced dimensions. Steel knife edges were bonded on either side of the notch using epoxy adhesive on specimens requiring CMOD measurements to allow attachment of the clip gauge during testing.

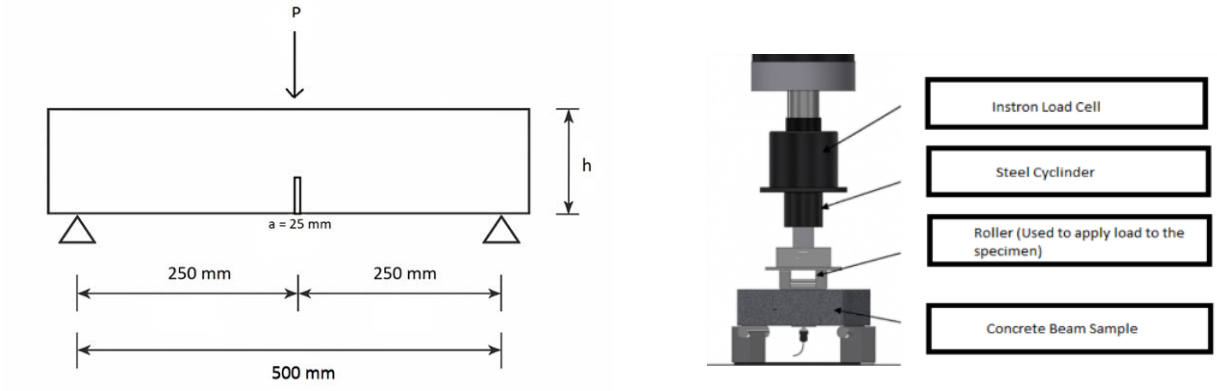
Table 1: Mix design for SFRC concrete mix used in all specimens (Fataar, 2022)

Type of Material	**Mix proportion (kg/m^3)**
Cement (CEM II/A-S 52.5 N)	450
Sand (Malmesbury)	880
Stone (Greywacke 13 mm)	820
Water	194
Superplasticiser (Dosage of 1.4% by mass of the binder)	6.3
Steel fibres (Dosage of 0.8% of the total volume)	65

2.2 Conventional Three-point bending Testing

Three-point bending tests were conducted in accordance with EN 14651:2005+A1:2007, as shown in Figure 1 (a), to evaluate the flexural performance of the SFRC specimens. Loading was applied under displacement control using an Instron servo hydraulic testing machine, as illustrated in Figure 1 (b). The loading procedure followed the same standard.

During testing, the applied load and CMOD were continuously recorded. The average maximum flexural force obtained from the static tests was subsequently used to define the loading levels for fatigue testing.



(a) (b)

Figure 1:(a) Three-point loading on each beam specimen (b) Schematic representation of the experimental flexural loading arrangement used for static and fatigue testing of SFRC specimens

The fatigue protocol followed the framework developed by Fataar (2022), with modifications to the pre-cracking procedure. Specimens were initially pre-cracked under displacement control at a rate of 0.05 mm/min until a CMOD of 0.1 mm was achieved. This level of pre-cracking was selected to ensure consistent crack initiation while activating fibre engagement and limiting excessive fibre deformation prior to cyclic loading. Following pre-cracking, cyclic loading was applied using a sinusoidal waveform at a frequency of approximately 5 Hz. The maximum load was set at 34.4 kN, corresponding to 85% of the average peak load obtained from static flexural testing, while the minimum load was maintained at 3 kN to ensure continuous compressive loading (Fataar, 2022). Testing was continued until a CMOD of 3.5 mm or until 2 million cycles was reached. Throughout testing, the applied load and CMOD were continuously monitored to evaluate fatigue damage progression and crack propagation. The cyclic fatigue loading procedure was repeated on three specimens.

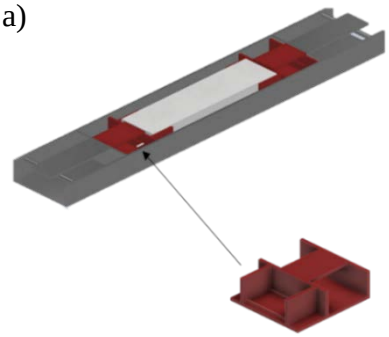
2.3 Preliminary MMLS3 Test Setup Development

One of the primary objectives of this study was to develop a preliminary beam-scale testing methodology using the MMLS3 to evaluate the fatigue behaviour of SFRC beams under traffic-type loading. Existing applications of the MMLS3 are primarily limited to flexible pavements, with no established methodology for beam-scale concrete testing. Consequently, a new experimental configuration was required.

A custom support system consisting of steel beam holders was designed to replicate a three-point bending configuration within the MMLS3 setup as presented in Figure 2 (a). This

configuration was selected due to its widespread use in conventional flexural fatigue testing of SFRC, allowing comparison with standard laboratory methods.

a)



b)



Figure 2: (a) Schematic representation of the beam-scale MMLS3 support system showing the custom steel holder configuration; (b) physical implementation of the support system within the MMLS3 test setup

The final MMLS3 support system consisted of steel beam support fixtures positioned at either end of the specimen to provide a simply supported boundary condition during loading. Additional steel rod supports were incorporated to accommodate flexural deformation under the moving wheel loads, while a wheel ramp extension was included to accommodate the elliptical motion of the MMLS3 wheels. The setup remained stable throughout testing, with minimal movement observed under loading. The MMLS3 was positioned in accordance with established MMLS3 testing procedures, with tyre contact verified through suspension gap measurements (Walubita, 2000). The system was operated with four tyres inflated to 800 kPa, corresponding to approximately 2.7 kN per tyre, based on manufacturer specifications, and a loading frequency of 2 Hz (7,200 cycles per hour) (Walubita, 2000). Each specimen was subjected to 40,000 load cycles, with 20,000 cycles per run. Testing was conducted with reference to SANS 3001:2016, adapted for the current experimental configuration. The final MMLS3 beam test setup incorporating all modifications is presented in Figure 2 (a) and (b).

2.4 Testing of uncracked SFRC specimens under MMLS3 loading

Initial MMLS3 testing was conducted on uncracked SFRC beam specimens using the setup illustrated in Figure 3 to evaluate whether repeated traffic-type loading could initiate cracking within the concrete matrix. No visible crack initiation was observed under the applied wheel loads, indicating that the loading level was insufficient to exceed the limit of proportionality (LOP) determined from the static flexural tests as defined in EN 14651:2005+A1:2007. Consequently, pre-cracking of the specimens was required prior to MMLS3 testing to activate fibre bridging behaviour. Surface deformation measurements were subsequently taken at three stages prior to loading 0, 20,000 cycles and lastly at 40,000 cycles. Measurements were obtained using an XY scanner (Figure 4 (a)), which is typically used to assess rutting and surface deformation in asphalt pavements. While the system does not directly measure beam deflection under load, the recorded surface profiles were used as an approximate indicator of vertical deflection behaviour. This approximation was considered acceptable for this preliminary investigation, given the high stiffness and rigidity of concrete.



Figure 3: Model Mobile Load Simulator (MMLS3) used for Accelerated pavement testing (Ozdemir, 2016)

a)



b)

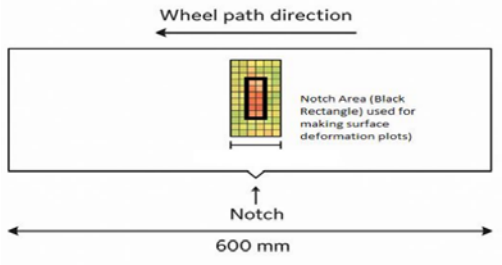


Figure 4: (a) MMLS3 testing setup with XY scanner for deformation measurements; (b) beam schematic indicating wheel path direction and measurement region

For each measurement a scanning region was defined within the XY scanner system, focusing on the mid-span region where the notch is located, as this is where maximum flexural response was expected as illustrated in Figure 4 (b). A scan area of approximately 130 mm in the transverse (x) direction and 52 mm in the longitudinal (y) direction was selected to capture the critical deformation beneath the wheel path. The scanner first performed a jog scan to establish the measurement area, followed by measurement of deformation progression over the loading cycles. No visible crack initiation was observed, indicating that the applied wheel loads were insufficient to exceed the first-crack strength of the concrete. This highlights a limitation of beam-scale accelerated pavement testing under low-magnitude wheel loading, where crack initiation may not occur within practical loading durations. Consequently, conventional crack monitoring techniques such as CMOD measurement were not applicable under these conditions.

2.5 Testing of pre-cracked SFRC specimens under MMLS3 loading

To investigate the post-cracking behaviour of the SFRC specimens under traffic-type loading, the beams were pre-cracked under controlled conditions using the Instron testing machine prior to MMLS3 testing. Specimens were pre-cracked to a CMOD of approximately 0.10 mm to ensure activation of the fibre bridging mechanisms before cyclic loading. Crack opening behaviour was monitored using two Linear Variable Differential Transformers (LVDTs) mounted symmetrically across the notch to measure the CMOD as illustrated in Figure 5. The pre-cracked specimens were subjected to repeated loading using the MMLS3, with each of the three specimens subjected to 40,000 loading cycles. Throughout testing, CMOD was continuously monitored to evaluate crack propagation and fatigue behaviour under traffic-representative loading

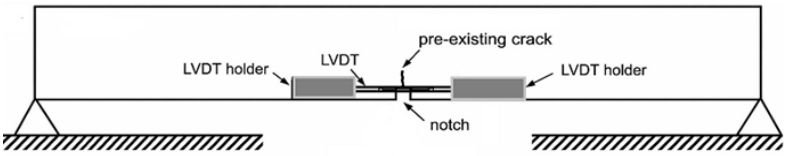


Figure 5: Experimental setup of a notched concrete beam instrumented with LVDTs to measure crack opening at a pre-existing notch.

3 Test Results

3.1 Instron Three-Point Bending Results

The fatigue behaviour of the pre-cracked SFRC specimens with an initial CMOD of 0.10 mm was evaluated using three-point bending tests on the Instron machine. As shown in Figure 6, all specimens exhibit a progressive increase in CMOD with increasing number of load cycles. The response exhibits two distinct stages, an initial phase of stable and gradual crack growth, followed by a rapid increase in CMOD at approximately 80–120 cycles, indicating the onset of unstable crack propagation.

Some variation between specimens was observed. While Samples 1 and 3 show a relatively sharp increase in CMOD following this transition, Sample 2 exhibits a more gradual increase indicating more stable crack propagation. This variation suggests differences in the effectiveness of fibre bridging between specimens. While steel fibres initially control crack growth by transferring stresses across the crack, continued cyclic loading leads to progressive fibre slip and debonding, reducing crack-bridging effectiveness and allowing increased crack opening over time (Vicente et al., 2019, Stephen and Gettu, 2020).

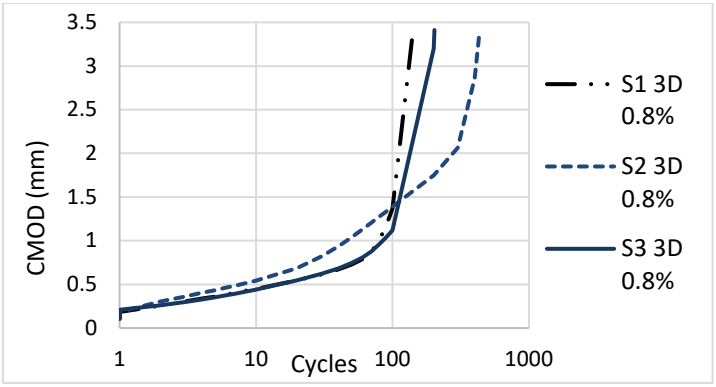


Figure 6: CMOD vs cycles for 3D 0.8% specimens under 3PBT Instron loading

3.2 MMLS3 Results: Uncracked SFRC Specimens

The surface deformation behaviour of the uncracked SFRC specimens was evaluated using heatmap visualisation. Figure 7 presents the deformation distribution for Sample 1 at (a) 20,000 cycles and (b) 40,000 cycles under MMLS3 loading. The colour gradient indicates the magnitude of deformation, with red–orange representing higher deformation and yellow–green indicating lower deformation. Between 20,000 and 40,000 cycles, deformation spreads across a larger area in all specimens, as shown by the expansion of the red–orange regions in Figure 7. This indicates progressive vertical displacement under repeated loading. This trend is further

supported by the deformation profile shown in Figure 8, where Sample 1 exhibits a progressive increase in vertical surface deformation between 20,000 and 40,000 cycles. Similar behaviour was observed for the remaining specimens.

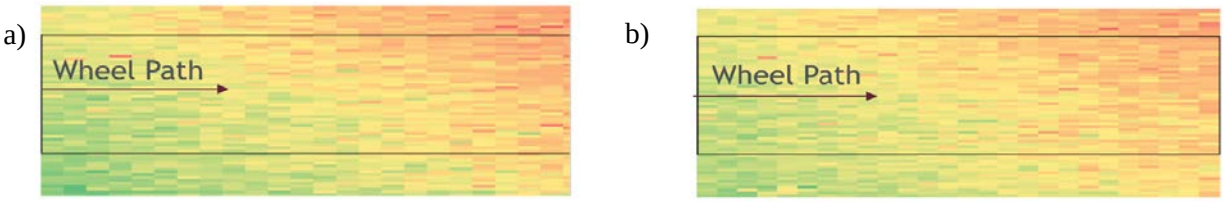


Figure 7: Heat map of surface deformation for SFRC Sample 1 under MMLS3 loading at 20,000 (a) and 40,000 (b) cycles

A consistent non-uniform deformation distribution is observed across all specimens particularly Samples 2 and 3, with higher deformation concentrated toward one side of the beam and lower deformation on the opposite side. This behaviour is likely influenced by slight misalignment or offset of the wheel path relative to the beam centreline. This asymmetrical pattern continues with increasing load cycles, indicating a stable and repeatable deformation trend across the tested specimens. Overall, the results confirm progressive and non-uniform deformation under repeated MMLS3 loading along the wheel path.

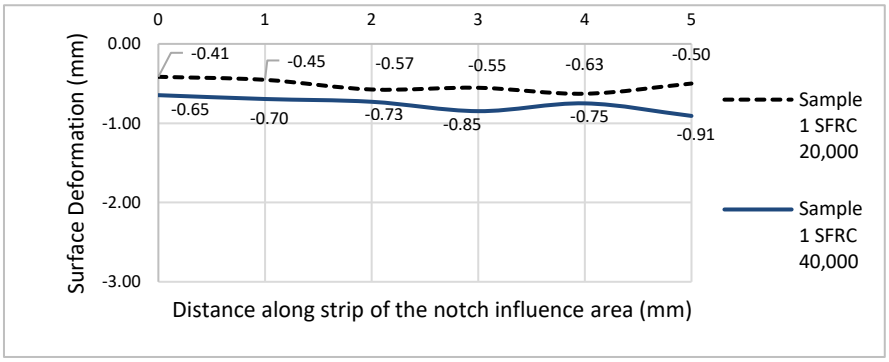


Figure 8: Surface deformation profile along the notch influence area for Sample 1 at 20,000 and 40,000 cycles

3.3 MMLS3 Results: Pre-Cracked Specimens

During the pre-cracking stage using the Instron machine, the unloading CMOD was not recorded, and therefore the residual CMOD could not be determined directly for each specimen. To address this, the unloading CMOD obtained from the instrumented three-point bending tests (3PBT) of three specimens were averaged and used as an estimate of the residual crack width once the load was removed, which was calculated to be 0.055 mm. Consequently, the recorded displacement represents only the opening and closing of the pre-existing crack relative to the zeroed position. To obtain the total crack width, the estimated residual crack width from the pre-cracking stage was added to the measured LVDT displacement.

The MMLS3 system did not directly measure the applied load; therefore, the load history was estimated based on its operating characteristics. The device applies a cyclic wheel load at approximately 2 Hz, varying from 0 kN to a peak of 2.7 kN and back to 0 kN. Assuming a consistent loading pattern, the load within each cycle was approximated using linear interpolation between these points. The interpolation was aligned with the LVDT time steps,

allowing a corresponding load value to be assigned to each displacement measurement and enabling construction of representative load–CMOD curves.

The CMOD at the maximum load was observed at selected cycle intervals for each specimen, as shown in Figure 9. For Sample 1, the CMOD at peak load remains relatively stable, with only minor variation across cycles, indicating consistent crack opening behaviour under repeated loading. Sample 2 exhibits a comparatively larger initial crack opening at early cycle stages, followed by a consistent reduction in CMOD with increasing number of cycles. One possible explanation for this behaviour is an initial adjustment of the crack faces and fibre-bridging mechanism during the early loading cycles. As the fibres engage and facilitate stress transfer across the crack faces, increased resistance to crack opening may develop, resulting in the observed reduction in CMOD (Stephen and Gettu, 2020). However, additional investigation is required to confirm whether this mechanism contributed to the observed behaviour.

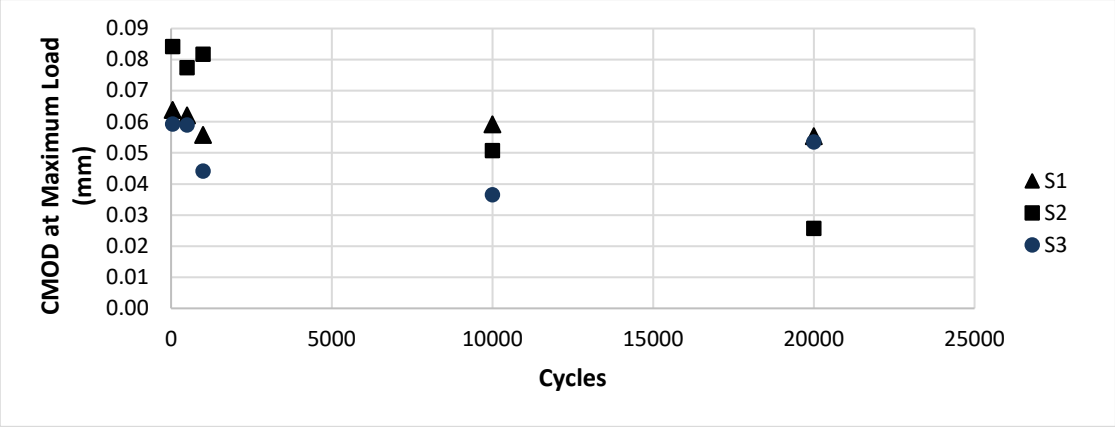


Figure 9: Variation of CMOD at maximum load with increasing number of cycles for Samples 1–3 under MMLS3 loading

In contrast, Sample 3 shows a different trend, where the CMOD initially decreases up to approximately 10,000 cycles, followed by a gradual increase at higher cycle counts. This behaviour indicates a transition in crack response, where initial stabilisation or closure is followed by progressive crack opening, potentially due to reduced effectiveness of fibre bridging or local damage accumulation. These differing trends highlight variability in fatigue response between specimens and demonstrate that the crack behaviour under MMLS3 loading evolves with increasing cycle count. The results further support that the crack response is influenced not only by the magnitude of the applied load, but also by the evolving structural and material interaction under repeated moving loading. Further investigation is required to determine whether this behaviour is a consequence of fibre bridging variability or test set up implications.

The load–CMOD response obtained from the MMLS3 testing exhibits a non-linear relationship, with regions where CMOD decreases despite increasing load, as illustrated in Figure 10 for Sample 1. In contrast to conventional three-point bending tests, where CMOD typically increases with load, the MMLS3 results show reductions in CMOD during the loading phase. This trend was observed across all specimens, indicating that crack response is influenced by factors beyond the applied load.

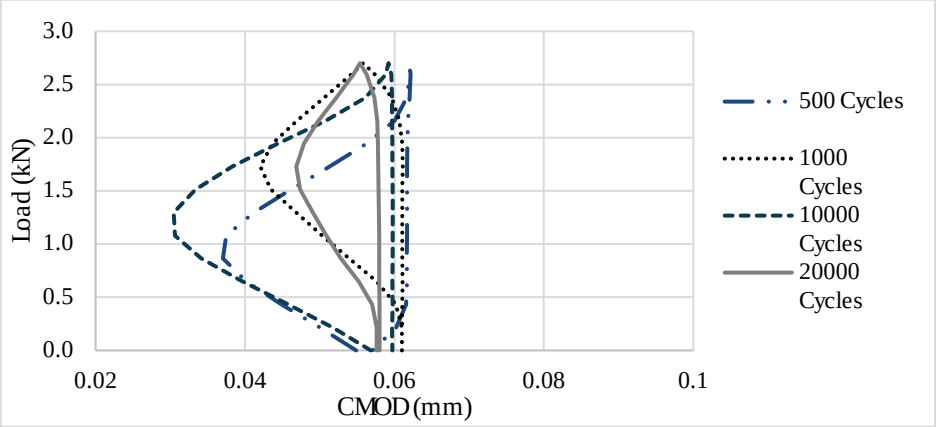


Figure 10: Load–CMOD response at selected loading cycles for Sample 1 during MMLS3 testing

The load–CMOD curves presented in Figures 10 and 11 indicate complex unloading behaviour following peak loading, suggesting that the post-peak response requires further investigation. This suggests that once the wheel load has passed the crack location, the response is dominated by elastic recovery and crack closure. In contrast, the loading paths exhibit noticeable curvature and variation between cycles, indicating changes in the interaction between structural response and material behaviour during loading.

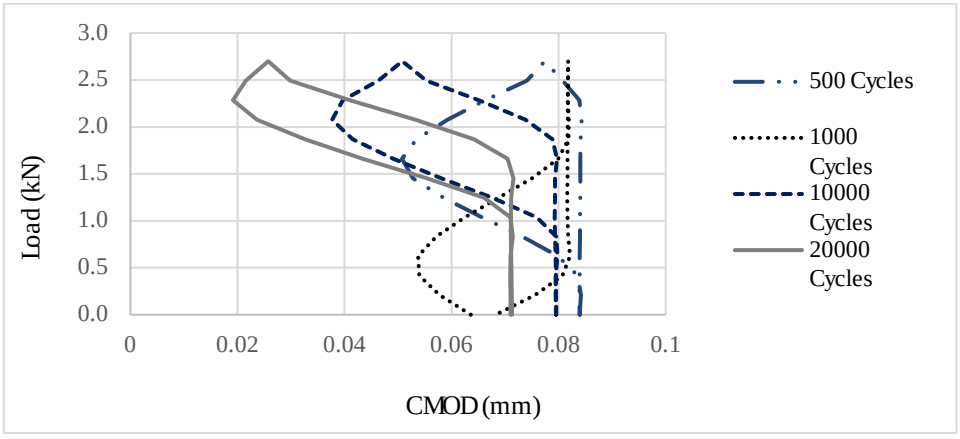


Figure 11: Load–CMOD response at selected loading cycles for Sample 3 (representative of the behaviour observed in Samples 2 and 3) during MMLS3 testing

Across cycles, differences in behaviour are observed between the specimens. In Samples 2 and 3, a distinct change in response occurs at higher cycle counts, where the loading path shows a more pronounced reduction in CMOD during loading, followed by recovery beyond the mid-point of the cycle. In contrast, Sample 1 exhibits a more consistent response, with less distinct changes in curve shape across cycles.

Variability is also observed in the unloading behaviour. For some cycles, the CMOD returns to approximately the same value after unloading, while in others it returns to a different value, as observed in Figures 10 and 11. This suggests that in certain instances, residual deformation or crack growth may be occurring while in others the response is largely recoverable.

The initially substantially higher crack growth observed in Sample 3, as shown in Figure 11 may be attributed to local material variability, such as fibre distribution and orientation, which influence the effectiveness of crack bridging. In contrast, Samples 1 and 2 exhibit comparatively smaller crack width ranges initially (approximately 0.03–0.065 mm) indicating more stable crack development. However, the overall trends remain consistent and do not indicate measurement instability. Overall, the results show that the relationship between load and CMOD is influenced by factors beyond the applied load alone, with variations observed as the wheel moves along the beam.

4 Analysis

The load–CMOD response under MMLS3 loading reflects the strong influence of structural behaviour under moving load conditions. The reduction in CMOD observed during portions of the loading phase indicates that crack opening is governed by the evolving structural response of the beam, rather than the applied load magnitude alone. In particular, the local stress state at the crack is influenced by the bending moment distribution, which varies as the wheel load moves across the beam.

This behaviour can be attributed to the combined effects of the moving load and the support configuration. The presence of the welded rollers and additional steel rod supports modifies the structural response of the beam relative to a conventional simply supported configuration. The MMLS3 wheel contact length was calculated to be approximately 42 mm using the nominal MMLS3 specifications (MLS Test Systems (Pty) Ltd, 2016). As this contact length is smaller than the 80 mm spacing between the supports (Figure 2 (b)), the wheel contact patch remains entirely within the support region as the wheel passes between the supports. This results in continuous beam behaviour, producing a hogging (negative) bending moment at the midpoint. This hogging moment induces local compression at the crack location, leading to temporary crack closure during specific wheel positions. As the load approaches, passes over, and moves away from the crack, the resulting bending moment distribution and local stress state at the crack change accordingly, leading to variations in stress. This behaviour suggests that the crack response is influenced by the evolving bending moment distribution associated with the moving wheel load, resulting in periods of crack closure and crack opening, as shown in Figures 10 and 11. This interpretation is further supported by the observed reduction in CMOD during portions of the loading phase, a response that differs from conventional three-point bending fatigue tests where crack opening generally increases with increasing load.

In contrast to conventional beam fatigue testing, where the loading position is fixed and the bending moment distribution remains constant, the moving load in the MMLS3 system produces a continuously evolving moment profile. Conventional beam fatigue testing primarily captures the material fatigue response, whereas the MMLS3 loading system captures the interaction between the moving wheel load, support conditions, and crack evolution. These observations suggest that the fatigue response of SFRC beams under MMLS3 loading is influenced by a combination of moving load effects, support conditions, and material behaviour. This behaviour is not captured in standard EN 14651 testing, where the loading position remains fixed and does not account for moving load effects.

5 Concluding remarks

A series of fatigue tests were conducted on pre-cracked SFRC beams using both Instron three-point bending and MMLS3 loading to investigate crack development under different loading conditions. The results showed that, while conventional three-point bending fatigue testing produced a progressive increase in CMOD, the response under MMLS3 loading was more complex, with regions of stabilisation, reduction, and gradual evolution in crack opening observed over repeated load cycles. The proposed mechanical interpretation provides a plausible explanation for the experimentally observed CMOD reductions and suggests that the measured response is influenced not only by material mechanisms, such as fibre bridging, but also by the interaction between the moving wheel load and the support arrangement.

Overall, the results suggest that crack behaviour under traffic-type loading may be influenced by the evolving bending moment distribution and local stress state associated with the moving wheel load, rather than the applied load magnitude alone. The findings highlight fundamental differences between conventional flexural fatigue testing and traffic-type loading and provide preliminary insight into the relationship between laboratory-based fatigue testing and wheel-induced fatigue behaviour in SFRC pavements.

6 References

CAI, M. & WANG, S. 2013. Accelerated Pavement Testing in Chinese Mainland. *Procedia - Social and Behavioral Sciences,* 96**,** 104-113.

COMMITTEE OF TRANSPORT OFFICIALS (COTO) 2020. Standard Specifications for Road and Bridge Works for South African Road Authorities: Draft Standard (DS), Chapter 6: Concrete Layers. Pretoria, South Africa: Committee of Transport Officials (COTO).

DI PRISCO, M., PLIZZARI, G. & VANDEWALLE, L. 2009. Fibre reinforced concrete: new design perspectives. *Materials and Structures,* 42**,** 1261-1281.

ELSAIGH, W. A., ROBBERTS, J. M. & KEARSLEY, E. P. 2005. Steel fibre reinforced concrete for road pavement applications. *24th Annual Southern African Transport Conference.* Pretoria, South Africa.

EUROPEAN COMMITTEE FOR STANDARDISATION 2005. EN 14651:2005. Test method for metallic fibre concrete – Measuring the flexural tensile strength (limit of proportionality (LOP), residual). BSI London.

EUROPEAN COMMITTEE FOR STANDARDISATION 2009. BS EN 12350-2: 2009: Testing fresh concrete. Part 2: Slump test. BSI London.

FATAAR, H. 2022. *Fatigue Behaviour of Steel Fibre Reinforced Concrete.* PhD dissertation, Stellenbosch University.

HUANG, Y. H. 2004. *Pavement Analysis and Design,* Upper Saddle River, New Jersey, USA, Pearson Prentice Hall.

HUGO, F. & STEYN, W. 2015. A Synthesis of Applications of the MLS as an Innovative System for Evaluating Performance of Asphalt Materials in Pavement Engineering. *11th Conference on Asphalt Pavements for Southern Africa (CAPSA 2015).*

MANDAL, T., EDIL, T. & TINJUM, J. 2018. Study on flexural strength, modulus, and fatigue cracking of cementitiously stabilised materials. *Road Materials and Pavement Design,* 19**,** 1546-1562.

MLS TEST SYSTEMS (PTY) LTD. 2016. *MMLS3 – Model Mobile Load Simulator* [Online]. Available: https://academic.sun.ac.za/mls/mmls3.htm [Accessed June 2026].

OZDEMIR, U. 2016. *An Acceptance Test for Chip Seal Projects Based on Image Analysis.* Master of Science, Michigan State University.

RAMAKRISHNAN, V. & JOSIFEK, C. 1987. Performance characteristics and flexural fatigue strength of concrete steel fiber composites. *International Symposium on Fibre Reinforced Concrete.* Madras, India.

SOUTH AFRICAN BUREAU OF STANDARDS 2016. SANS 3001-PD1:2016. Civil engineering test methods Part PD1: Determination of permanent deformation and moisture sensitivity in asphalt mixes with the MMLS3.

STEPHEN, S. & GETTU, R. 2020. Fatigue fracture of fibre reinforced concrete in flexure. *Materials and Structures,* 53.

VICENTE, M. A., MÍNGUEZ, J. & GONZÁLEZ, D. C. 2019. Computed tomography scanning of the internal microstructure, crack mechanisms, and structural behavior of fiber-reinforced concrete under static and cyclic bending tests. *International Journal of Fatigue,* 121**,** 9-19.

VISHWAKARMA, R. J. & INGLE, R. K. 2018. Effect of Panel Size and Radius of Relative Stiffness on Critical Stresses in Concrete Pavement. *Arabian Journal for Science and Engineering,* 43**,** 5677-5687.

WALUBITA, L. F. 2000. *Accelerated pavement testing using the third-scale model mobile load simulator (MMLS3).* MEng, Stellenbosch University.

WTAIFE, S., ALSABBAGH, A., EISSA, T., ALSHAMMARI, E., SHABAN, A. & SUKSAWANG, N. 2018. Analysis of Flexural Capacity of Fiber Reinforced Concrete Pavements. *International Journal of Technology and Engineering Studies,* 4**,** 203-210.

Flexural Performance of Low-Carbon UHPCs Exposed to Elevated Temperatures

M. Mirza Abdillah Pratama[1,2], Ravi Ranade[3], Doo-Yeo Yoo[4], Behzad Nematollahi[1]

[1]: School of Mechanical, Aerospace and Civil Engineering, University of Sheffield, UK.

[2]: Universitas Negeri Malang, Malang, 65145 Indonesia.

[3]: Department of Civil, Structural, and Environmental Engineering, University at Buffalo, State University of New York, USA.

[4]: Department of Architecture and Architectural Engineering, Yonsei University, Seoul, South Korea

Abstract

This study investigates the flexural performance of low-carbon ultra-high performance concrete (UHPC) incorporating high-volume supplementary cementitious materials (SCMs) exposed to elevated temperatures. Effects of replacing 60 wt% of cement with either GGBS or fly ash and incorporating polypropylene (PP) fibres, in addition to steel fibres, on thermal damage, residual flexural strength, flexural stress–deflection behaviour, and flexural toughness of specimens after exposure to temperatures ranging from 200°C to 1000°C were evaluated. The results showed that the incorporation of high-volume SCMs improved the thermal performance of UHPC at 200–400°C. Specimens containing only steel fibres experienced severe explosive spalling at and above 400°C due to vapour pressure accumulation within the dense matrix. In contrast, the incorporation of PP fibres effectively mitigated explosive spalling and enabled all mixtures to remain intact up to 1000°C. Specimens containing PP fibres exhibited enhanced residual flexural strength and flexural toughness at 200–400°C, particularly for the mixture containing fly ash, which demonstrated the highest performance improvement. However, all mixtures exhibited progressive deterioration beyond 600°C due to thermal degradation of the matrix and fibre–matrix interface. Overall, the combined use of high-volume SCMs and PP fibres improved the thermal stability and residual flexural behaviour of UHPC exposed to elevated temperatures.

Keywords

Ultra-high performance concrete; Supplementary cementitious materials; Elevated temperature; Residual flexural strength; Flexural toughness.

1 Introduction

Ultra-high performance concrete (UHPC) has gained considerable attention due to its exceptional mechanical properties, superior durability, and dense microstructure compared to conventional concrete. The use of a low water-to-binder ratio, optimized particle packing, and steel fibre reinforcement enables UHPC to achieve compressive strengths exceeding 150 MPa together with enhanced ductility and durability. However, the high cement contents required in UHPC contribute to high production costs and significant environmental impacts associated with ordinary Portland cement (OPC) production (Al-Tam et al, 2026).

To improve sustainability, supplementary cementitious materials (SCMs) such as ground granulated blast-furnace slag (GGBS) and fly ash have been widely investigated as partial OPC replacements in UHPC. Previous studies reported that SCMs can improve particle packing, refine pore structure, and enhance long-term durability through pozzolanic and latent hydraulic reactions (J. Song et al, 2025). In addition to reducing the environmental footprint, SCM incorporation may also improve the thermal resistance of cementitious materials (Q. Song et al, 2022).

Despite its superior mechanical performance, UHPC is highly vulnerable to explosive spalling under elevated temperatures due to its dense microstructure and low permeability, which restrict vapour pressure release during heating. Exposure to high temperatures can cause dehydration of hydration products, thermal cracking, and severe deterioration of mechanical properties. To mitigate explosive spalling, polypropylene (PP) fibres are commonly incorporated into UHPC. The melting of PP fibres at approximately 160–170°C creates interconnected pore channels that facilitate vapour pressure release and reduce thermal damage (Nassar et al, 2024).

Limited studies have comprehensively evaluated the residual flexural performance of UHPC containing high-volume SCMs and PP fibres after elevated-temperature exposure (Ashteyat et al, 2025; Prakash et al, 2022). In particular, the combined influence of SCM-modified microstructure and PP fibre-induced pore formation on post-heating flexural behaviour remains insufficiently understood.

Therefore, this study investigates the flexural performance of UHPC incorporating high-volume GGBS and fly ash after exposure to elevated temperatures up to 1000°C. UHPC mixtures with and without PP fibres were evaluated in terms of thermal damage, residual flexural strength, stress–deflection behaviour, and flexural toughness. The findings contribute toward the development of more sustainable and thermally durable UHPC for structural applications exposed to elevated-temperature conditions.

2 Experimental programme

2.1 Materials and mix proportion

The proportions of UHPC mixtures are presented in Table 1. Cement, silica fume (SF), GGBS, and FA were used as binder materials. Two types of cement, namely OPC and calcium sulphoaluminate (CSA) cement, were used, with a CSA/(OPC+CSA) mass ratio of 0.05 in all mixtures. 60 wt% of the total (OPC+CSA) content was replaced by GGBS in the S60 and S60-PP mixtures and by FA in the F60 and F60-PP mixtures. Silica sands with two different sizes: finer sand (FS) and coarser sand (CS), with average particle sizes of 186.13 μm and 418.32 μm,

respectively, were used with FS:CS of 50 wt%:50 wt%. A polycarboxylate-based superplasticiser (SP) was used. Copper-coated straight steel fibres (length = 6 mm, diameter = 0.2 mm, and tensile strength = 2850 MPa) were incorporated in all mixtures at 2 vol%. In addition, PP fibres with a length of 6 mm and a melting point ranging from 160°C to 170°C were added at 0.3 vol% in selected mixtures.

Table 1: Proportions of UHPC mixtures

Mix ID	Binder				Sand	Water	SP	Steel fibre	PP fibre
	Cement[1]	SF	GGBS	FA					
S0F0	0.75	0.25	0	0	1.0	0.17	0.04	0.02	0
S60	0.30	0.25	0.45	0	1.0	0.17	0.04	0.02	0
F60	0.30	0.25	0	0.45	1.0	0.17	0.04	0.02	0
S0F0-PP	0.75	0.25	0	0	1.0	0.17	0.04	0.02	0.3%
S60-PP	0.30	0.25	0.45	0	1.0	0.17	0.04	0.02	0.3%
F60-PP	0.30	0.25	0	0.45	1.0	0.17	0.04	0.02	0.3%

Note: All values are mass ratios of the total binder mass, except for fibres (volume fraction).
[1]Cement is composed of OPC+CSA with CSA/(OPC+CSA) mass ratio of 0.05 in all mixtures.

2.2 Specimen preparation

Initially, all dry materials were dry mixed for 1 min. Subsequently, 95% water was gradually added while mixing for 2 min. After that, SP and the remaining water were added to the mixture while continuous mixing was maintained for 11 min until a homogeneous mixture was achieved. Steel fibres were then gradually added to the mix and mixed for 4 min to minimise fibre agglomeration and ensure uniform dispersion throughout the matrix. The PP fibres (if any) were added together with the steel fibres during the final stage of mixing.

Fresh UHPC was cast into 40 × 40 × 160 mm^3 prism moulds for three-point bending tests, with an effective span of 120 mm and a deflection rate of 0.5 mm/min. The moulded specimens were covered with a plastic sheet to prevent moisture loss for 24 h. The specimens were then demoulded and covered with the plastic sheet for another 24 h at room temperature (20 ± 2°C). After that, the specimens were heat-cured by immersing them in water inside sealed steel boxes and placing them in an oven at 90°C for 48 h. After completion of heat curing, the specimens were removed from the oven and kept immersed in water in the sealed steel boxes at room temperature until reaching an age of 7 days after casting.

2.3 Heating configuration

Before elevated-temperature exposure, all specimens were air-dried at room temperature (20 ± 2°C) for 72 h to reduce free moisture content and minimise the risk of explosive spalling during heating. Elevated-temperature exposure was conducted using an electric furnace under controlled heating conditions. The specimens were exposed to target temperatures of 200°C, 400°C, 600°C, 800°C, and 1000°C. Before heating, the specimens were placed inside steel boxes to provide protection and minimise direct thermal shock during the heating process. The heating regime consisted of a constant heating rate of 4°C/min until the target temperature was reached. Subsequently, the specimens were maintained at the target temperature for 2 h to ensure thermal equilibrium throughout the specimen volume. After completion of the holding period, the furnace was switched off, and the specimens were allowed to cool down naturally inside the furnace to room temperature.

3 Results and discussion

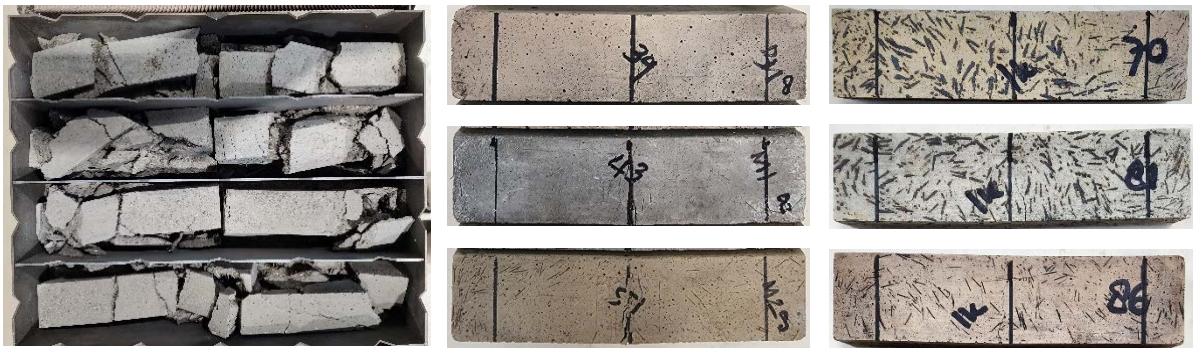
3.1 Thermal damage type

Table 2 presents the thermal damage types of UHPC mixtures after exposure to elevated temperatures. The results show that PP fibres significantly improved the spalling resistance of UHPC. For the mixtures containing only steel fibres, no visible damage was observed up to 200°C. However, severe explosive spalling occurred at 400°C (Figure 1a). This behaviour was associated with vapour pressure accumulation within the dense UHPC matrix during heating (Zhang et al, 2024). In contrast, all mixtures containing PP fibres remained intact up to 1000°C without explosive spalling. The results indicate that SCM incorporation alone was insufficient to prevent explosive spalling, whereas the use of PP fibres effectively preserved the structural integrity of UHPC under elevated temperatures. At 800°C, a progressive colour change to greyish brown was observed, which may be attributed to chemical reactions within the matrix, moisture loss, and oxidation reactions (Zheng et al, 2012). At 1000°C, oxidation of the steel fibres became more pronounced, contributing to the darker surface appearance of the specimens (Figures 1b and 1c).

Table 2: Thermal damage type

Mix ID	Thermal damage type				
	200°C	400°C	600°C	800°C	1000°C
S0F0	ND	S	n/t	n/t	n/t
S60	ND	S	n/t	n/t	n/t
F60	ND	S	n/t	n/t	n/t
S0F0-PP	ND	ND	ND	ND	ND
S60-PP	ND	ND	ND	ND	ND
F60-PP	ND	ND	ND	ND	ND

Note: “ND” means “No Damage”; “S” means “Spalled”; “n/t” means “not tested”. As the specimens containing steel fibres only were already spalled at 400°C, other specimens at higher temperatures (600°C, 800°C, and 1000°C) were not tested.



(a) S0F0, S60 and F60 after heating at 400°C

(b) S0F0-PP, S60-PP, and F60-PP (from top to bottom) after heating at 800°C

(b) S0F0-PP, S60-PP, and F60-PP (from top to bottom) after heating at 1000°C

Figure 1: Visual appearance of specimens after elevated-temperature exposure

3.2 Residual flexural strength

Table 3 presents the residual flexural strength of UHPC mixtures after exposure to elevated temperatures. Figure 2 illustrates the corresponding residual flexural strength ratio relative to the strength at ambient temperature. The mixtures containing only steel fibres exhibited reduced flexural strength after exposure to 200°C. Furthermore, severe explosive spalling prevented these mixtures from surviving beyond 200°C due to the dense and low-permeability microstructure of UHPC, which restricted vapour pressure release during heating (Yao et al, 2024).

In contrast, all mixtures containing PP fibres remained intact up to 1000°C. As shown in Figure 2, the mixtures containing SCMs and PP fibres (i.e., S60-PP and F60-PP) achieved residual flexural strength ratios greater than 1.0 at 200-600°C, showing their enhanced flexural strength compared to their strength at 20°C, which may be attributed to continued hydration and thermal activation of GGBS and FA reactions, which promoted additional C-S-H formation and microstructure densification and improved fibre-matrix bond performance (Arunothayan and Sanjayan, 2023). The S60-PP mixture exhibited the highest residual flexural strength at 200°C, while the F60-PP mixture exhibited the highest residual flexural strength at 400°C.

Table 3: Residual flexural strength

Mix ID	20°C	Residual flexural strength (MPa)				
		200°C	400°C	600°C	800°C	1000°C
S0F0	21.3 ± 1.5	16.6 ± 0.4	n/a	n/a	n/a	n/a
S60	17.6 ± 0.3	15.1 ± 0.1	n/a	n/a	n/a	n/a
F60	17.6 ± 0.3	14.9 ± 0.3	n/a	n/a	n/a	n/a
S0F0-PP	21.5 ± 3.0	19.4 ± 0.2	20.1 ± 0.9	17.2 ± 0.9	7.0 ± 0.3	7.1 ± 0.2
S60-PP	15.9 ± 1.2	21.7 ± 0.3	19.7 ± 1.0	16.4 ± 1.4	7.9 ± 0.1	5.8 ± 0.4
F60-PP	15.4 ± 2.0	21.1 ± 1.9	25.7 ± 0.6	17.8 ± 0.2	7.9 ± 0.1	5.2 ± 0.2

Note: "n/a" denotes that the residual flexural strength could not be measured due to explosive spalling of specimens containing steel fibres only at 400°C and above (see caption of Table 2).

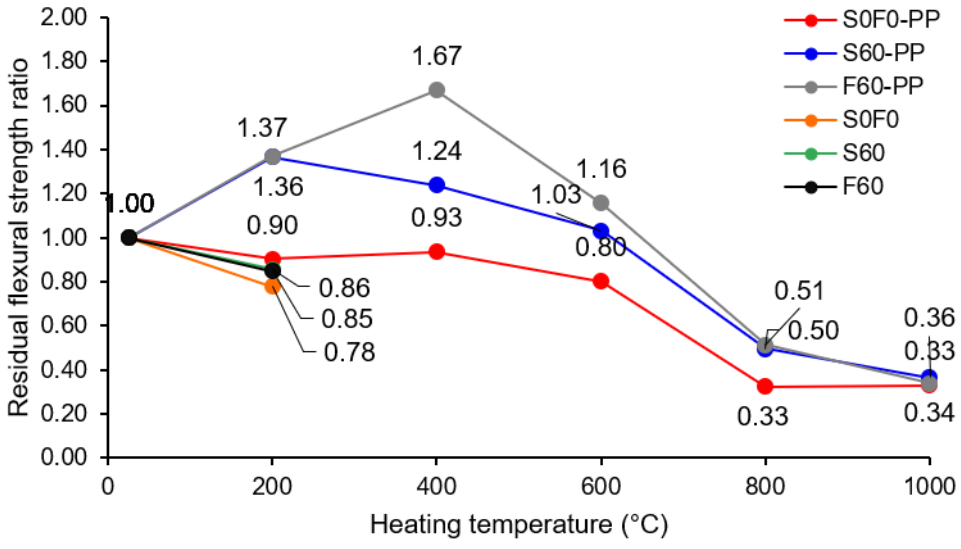


Figure 2: Residual flexural strength ratio

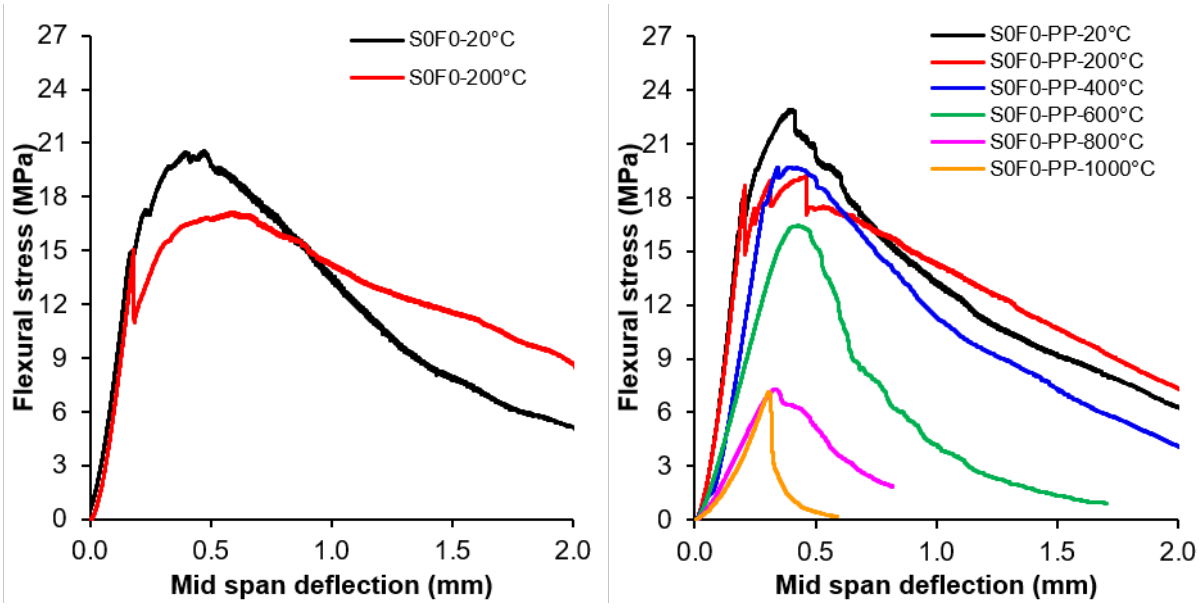
The incorporation of PP fibres further improved thermal stability by forming interconnected pore channels after melting at approximately 160–170°C, thereby relieving internal vapour pressure and reducing thermal cracking (Li et al, 2019). Consequently, the PP-fibre mixtures maintained structural integrity throughout the heating programme.

However, all mixtures exhibited progressive deterioration beyond 600°C, with significant reductions in residual flexural strength and strength index observed at 800°C and 1000°C. The strength indices decreased below 0.5 at these temperatures. This deterioration was associated with decomposition of hydration products, fibre–matrix debonding, and oxidation of steel fibres, which collectively reduced the residual flexural resistance of UHPC (Serafini et al, 2020; Sundin et al, 2023).

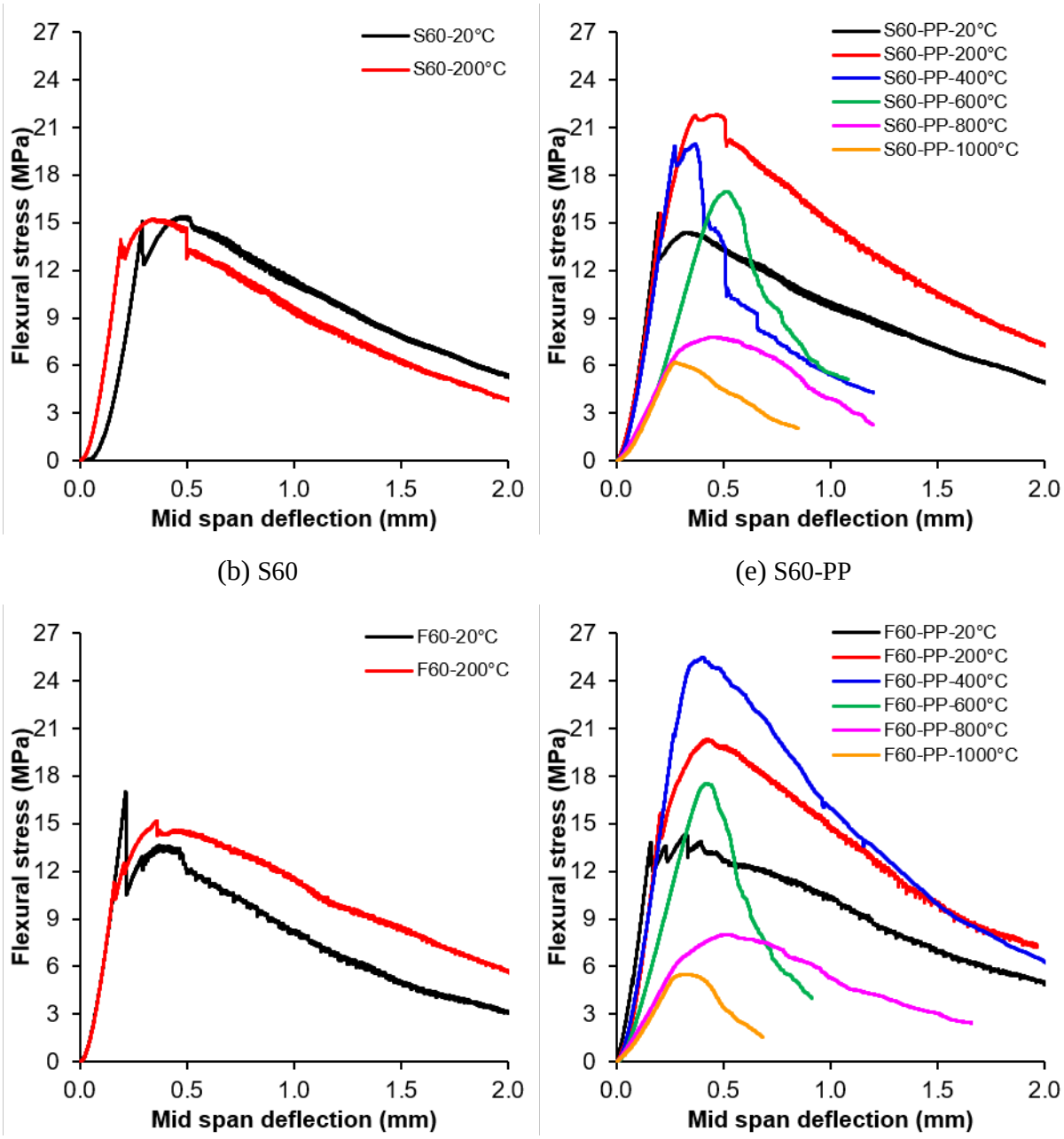
3.3 Flexural stress vs. mid-span deflection relationship

Figure 3 shows the flexural stress vs mid-span deflection relationship of all UHPC mixtures. For mixtures containing only steel fibres, deflection-hardening behaviour was observed at ambient temperature, indicating effective crack bridging by the steel fibres (Yoo et al, 2024). The control mixture exhibited the highest peak stress and the most extended post-peak response. After exposure to 200°C, all steel-fibre-only mixtures showed lower peak stress and steeper post-peak softening.

In contrast, all mixtures containing PP fibres remained intact up to 1000°C and exhibited more stable flexural behaviour after heating. At 200°C and 400°C, the PP-fibre mixtures showed enhanced deflection-hardening response and improved post-cracking behaviour, particularly for the F60-PP mixture (containing FA). However, all mixtures exhibited progressive deterioration beyond 600°C, characterised by reduced peak stress, loss of deflection-hardening behaviour, and steeper post-peak softening. At 800°C and 1000°C, the curves indicate severe reduction in ductility and energy absorption capacity due to decomposition of hydration products and degradation of the fibre–matrix interface (Sundin et al, 2023).



(a) S0F0 (d) S0F0-PP



(b) S60 (e) S60-PP

(c) F60 (f) F60-PP

Figure 3: Representative flexural stress vs mid-span deflection curves

3.4 Flexural toughness

Table 4 presents the flexural toughness of UHPC mixtures exposed to elevated temperatures. Flexural toughness was determined from the area under the stress–deflection curve up to a mid-span deflection of 2.0 mm. ASTM C1609 (ASTM International, 2024) specifies that toughness should be determined at a minimum net deflection equal to 1/150 of the span length (equal to 0.8 mm in this study). However, because most specimens in this study exhibited deflection-hardening behaviour with higher deflection levels, the toughness was calculated based on 1/60 of the net span deflection, which equals 2.0 mm in this study (Kim et al, 2008; Nematollahi et

al, 2014). At ambient temperature, the control mixture (S0F0) exhibited the highest flexural toughness among mixtures without PP fibres, while the incorporation of high-volume GGBS and FA reduced the flexural toughness due to lower flexural strength. After exposure to 200°C, both the control and the FA-incorporated mixtures showed improved flexural toughness, indicating improved ductility and more stable post-cracking behaviour.

Table 4: Flexural toughness

Mix ID	Flexural toughness (J/mm^2)					
	20°C	**200°C**	**400°C**	**600°C**	**800°C**	**1000°C**
S0F0	22.1 ± 1.7	20.7 ± 4.5	n/a	n/a	n/a	n/a
S60	18.4 ± 1.9	14.6 ± 3.1	n/a	n/a	n/a	n/a
F60	17.0 ± 1.1	20.6 ± 3.4	n/a	n/a	n/a	n/a
S0F0-PP	24.1 ± 2.8	20.8 ± 4.5	19.2 ± 1.7	10.8 ± 1.8	2.9 ± 0.6	1.1 ± 0.1
S60-PP	16.9 ± 1.8	28.3 ± 1.9	12.5 ± 1.4	8.9 ± 1.3	5.9 ± 0.4	2.8 ± 0.4
F60-PP	20.6 ± 3.4	24.6 ± 6.2	27.7 ± 1.7	8.8 ± 0.5	8.2 ± 0.5	2.4 ± 0.3

Note: “n/a“ denotes that the residual flexural strength could not be measured due to explosive spalling of specimens containing steel fibres only at 400°C and above (see caption of Table 2).

The incorporation of PP fibres further enhanced the residual flexural toughness behaviour of UHPC. The PP-fibre mixtures, particularly with the FA incorporation, exhibited higher flexural toughness at 400°C, demonstrating improved post-cracking behaviour and load-carrying capacity after heating. Similarly, the GGBS mixture containing PP fibres showed improved toughness retention at 200°C. This behaviour is beneficial for structural applications requiring higher toughness and impact resistance under elevated-temperature conditions. However, significant reductions in flexural toughness were observed beyond 600°C, indicating increased brittleness and reduced ductility at very high temperatures (He et al, 2025).

4 Concluding remarks

This study investigated the effects of high-volume SCM replacement (i.e., replacing 60 wt% of cement with either fly ash or GGBS) and the addition of PP fibres (0.3 vol%), in addition to 2 vol% of steel fibres, on the flexural performance of UHPC subjected to elevated temperatures. The following conclusions were drawn:

- All mixtures containing only steel fibres experienced severe explosive spalling at and above 400°C due to vapour pressure build-up within the dense matrix. The incorporation of PP fibres effectively mitigated explosive spalling and enabled all mixtures to remain intact up to 1000°C by facilitating vapour pressure release during heating.
- At 200–400°C, the PP-fibre mixtures incorporating 60 wt% GGBS (S60-PP) and 60 wt% fly ash (F60-PP) exhibited higher residual flexural performance than the control mixture (S0F0-PP) at the same temperatures. Among the PP-fibre mixtures, F60-PP showed the highest residual flexural strength and flexural toughness, particularly at 400°C, indicating superior thermal resistance and post-cracking behaviour after elevated-temperature exposure.
- All mixtures exhibited progressive deterioration beyond 600°C, characterised by reduced flexural strength and lower flexural toughness due to thermal degradation.

- At room temperature, replacing 60 wt% OPC with either fly ash or GGBS reduced the flexural strength of UHPC. The flexural strengths of the mixtures containing either GGBS or fly ash were comparable. This is true regardless of the addition of PP fibres.
- At room temperature, the addition of PP fibres did not change the flexural strength of the control mixture but reduced the flexural strengths of the mixtures containing either GGBS or fly ash.

5 Acknowledgements

The first author acknowledges the Indonesia Endowment Fund for Education (LPDP), Ministry of Finance of the Republic of Indonesia, for providing financial support through its scholarship programme under contract number SKPB-6581/LPDP/LPDP.3/2023.

6 References

Al-Tam, S.M., Youssf, O., Mahmoud, M.H., and Tahwia, A.M., 2026. "Towards Greener Construction: A Comprehensive Evaluation of Eco-Friendly UHPC Reinforced with Hybrid Fibers." *Scientific Reports* 16(1), pp7196. doi: 10.1038/s41598-025-33711-2.

Arunothayan, A.R., and Sanjayan, J.G., 2023. "Elevated Temperature Effects on 3D Printed Ultra-High Performance Concrete." *Construction and Building Materials* 367, pp130241. doi: 10.1016/j.conbuildmat.2022.130241.

Ashteyat, A., Shhabat, M., Alkhalaileh, A., Al-Zu'bi, M., and Abdel-Jaber, M., 2025. "Behavior of Ultra-High-Performance Concrete under Elevated Temperatures: A Comprehensive Review of Mechanical, Physical, Thermal, and Microstructural Properties." *Results in Engineering* 26. doi: 10.1016/j.rineng.2025.104960.

ASTM International, 2024. *ASTM C1609/C1609M-24 Test Method for Flexural Performance of Fiber-Reinforced Concrete (Using Beam With Third-Point Loading)*. West Conshohocken, PA: ASTM International.

He, J., Wang, H., and Yu, Q., 2025. "Flexural Fracture Behavior of Ultra-High Performance Concrete after High-Temperature Exposure." *Construction and Building Materials* 481, pp141544. doi: 10.1016/J.CONBUILDMAT.2025.141544.

Kim, D. joo, Naaman, A.E., and El-Tawil, S., 2008. "Comparative Flexural Behavior of Four Fiber Reinforced Cementitious Composites." *Cement and Concrete Composites* 30(10), pp917–28. doi: 10.1016/J.CEMCONCOMP.2008.08.002.

Li, Y., Tan, K.H., and Yang, E.H., 2019. "Synergistic Effects of Hybrid Polypropylene and Steel Fibers on Explosive Spalling Prevention of Ultra-High Performance Concrete at Elevated Temperature." *Cement and Concrete Composites* 96, pp174–81. doi: 10.1016/J.CEMCONCOMP.2018.11.009.

Nassar, R.U.D., Zaid, O., Althoey, F., Abuhussain, M.A., and Alashker, Y., 2024. "Spalling Behavior and Performance of Ultra-High-Performance Concrete Subjected to Elevated Temperature: A Review." *Construction and Building Materials* 411. doi: 10.1016/j.conbuildmat.2023.134489.

Nematollahi, B., Sanjayan, J., and Shaikh, F.U.A., 2014. "Comparative Deflection Hardening Behavior of Short Fiber Reinforced Geopolymer Composites." *Construction and Building Materials* 70, pp54–64. doi: 10.1016/J.CONBUILDMAT.2014.07.085.

Prakash, S., Kumar, S., Biswas, R., and Rai, B., 2022. "Influence of Silica Fume and Ground Granulated Blast Furnace Slag on the Engineering Properties of Ultra-High-Performance Concrete." *Innovative Infrastructure Solutions* 7(1). doi: 10.1007/s41062-021-00714-7.

Serafini, R., Mendes, L.M., Salvador, R.P., and De Figueiredo, A.D., 2020. "The Effect of Elevated Temperatures on the Properties of Cold-Drawn Steel Fibres." *Magazine of Concrete Research* 73(18), pp936–44. doi: 10.1680/JMACR.19.00498.

Song, J., Banthia, N., and Yoo, D.Y., 2025. "Effect of Supplementary Cementitious Materials on Durability of Ultra-High-Performance Concrete: A Review." *Cement and Concrete Composites* 163, pp106198. doi: 10.1016/j.cemconcomp.2025.106198.

Song, Q., Guo, M.Z., and Ling, T.C., 2022. "A Review of Elevated-Temperature Properties of Alternative Binders: Supplementary Cementitious Materials and Alkali-Activated Materials." *Construction and Building Materials* 341. doi: 10.1016/j.conbuildmat.2022.127894.

Sundin, M., Hedlund, H., and Cwirzen, A., 2023. "Eco-Concrete in High Temperatures." *Materials* 16(12), pp4212. doi: 10.3390/MA16124212.

Yao, X., Han, Y., Shen, L., and Zhu, D., 2024. "Experimental Study on the Effect of Polypropylene Fiber on Compressive Strength and Fracture Properties of High-Strength Concrete after Elevated Temperatures." *Journal of Building Engineering* 86, pp108860. doi: 10.1016/J.JOBE.2024.108860.

Yoo, D.Y., Soleimani-Dashtaki, S., Oh, T., Chun, B., Banthia, N., Lee, S.J., and Yoon, Y.S., 2024. "Strain-Hardening Effect on the Flexural Behavior of Ultra-High-Performance Fiber-Reinforced Concrete Beams with Steel Rebars." *Developments in the Built Environment* 17, pp100343. doi: 10.1016/J.DIBE.2024.100343.

Zhang, Y., Zhang, S., Zhao, W., Wang, Y., Ju, J.W., Yan, Z., and Zhu, H., 2024. "Spalling Behavior in Ultra-High Performance Concrete: Multi-Technique Insights and Multi-Scale Fiber-Rubber Mitigation Strategies." *Journal of Building Engineering* 98, pp111333. doi: 10.1016/J.JOBE.2024.111333.

Zheng, W., Li, H., and Wang, Y., 2012. "Compressive Behaviour of Hybrid Fiber-Reinforced Reactive Powder Concrete after High Temperature." *Materials & Design* 41, pp403–9. doi: 10.1016/J.MATDES.2012.05.026.

Sustainability, Durability, Serviceability

Durability of cracked, SFRC beams in outdoor conditions

György L. Balázs[1], Ronny Ramiro Almeida Vasquez[1], Jorge Luis Campoverde Abril[1], Imre Kovács[2], Katalin Kopecskó[3]

[1] : Department of Construction Materials and Technologies, Faculty of Civil Eng., Budapest University, of Technology and Economics, Műegyetem rkp. 3, 1111 Budapest, Hungary

[2] : University Debrecen, Civil Engineering Department, Ótemető street 2., Debrecen

[3] : Department of Engineering Geology and Geotechnics, Faculty of Civil Eng., Budapest University, of Technology and Economics, Műegyetem rkp. 3, 1111 Budapest, Hungary

Abstract

This study presents a unique long-term durability assessment of reinforced concrete beams incorporating both conventional reinforcement and steel fiber reinforcement (SFRC). The original experimental program, conducted approximately 30 years ago, focused on the shear capacity of beams reinforced with hooked-end and undulated steel fibers at volume fractions of 0; 0.5 and 1.0%. The test series included 18 beam specimens (Kovács and Balázs, 2003). Following load testing, the cracked beam specimens were stored under natural outdoor exposure conditions for approximately 25 years (July 1999 - January 2026), without the use of de-icing salts. The specimens were subjected to cyclic wetting and drying, as well as freeze-thaw action, within an annual temperature range of approximately -10 to +40 °C.

The present study evaluates the durability performance of these previously loaded and cracked SFRC beams, with particular focus on carbonation penetration both from exposed surfaces and along structural cracks. In addition, the condition of the fiber-matrix interfacial zone, the spatial distribution of fibers (including their position relative to the main reinforcement), and the state of fibers located in different regions of the cross-section are investigated. The results provide new insights into the long-term behavior of SFRC under realistic environmental exposure, including the corrosion risk of steel fibers and the evolution of fiber-related deterioration mechanisms over time. The findings contribute to a better understanding of the durability and sustainability of SFRC structural elements subjected to combined mechanical loading and environmental actions.

Keywords

Steel fiber-reinforced concrete (SFRC), durability, long-term exposure, carbonation ingress, fiber corrosion, cracked concrete

1 Introduction

The integration of discrete steel fibers into cementitious matrices has become a cornerstone of modern civil engineering, offering significant enhancements in ductility, flexural strength, and crack control compared to traditional concrete (Bauwens et al., 2021). Unlike conventional continuous reinforcement, steel fiber reinforced concrete (SFRC) relies on a mechanism where fibers bridge cracks providing substantial post-cracking resistance and energy absorption (Kovács & Balázs, 2004). These properties are essential for the structural safety and serviceability of infrastructure, particularly in elements that almost completely replace conventional stirrups with steel fibers.

A fundamental challenge in the production of SFRC structural elements is the achievement of a homogeneous fiber distribution. Research has shown that fiber spatial arrangement is governed by the material's properties, vibration time, and gravitational settling (Kobaka, 2021). Furthermore, the presence of conventional reinforcement often induces a *blocking effect* or *sieve effect*, where fibers become entangled in the upper layers of stirrups and longitudinal bars during casting (Bauwens et al., 2021). Such irregularities result in vertical anisotropy, which can lead to sectional deficits in fiber density in critical tension zones, potentially compromising the intended mechanical reliability of the element (Laranjeira et al., 2011).

The long-term durability of the concrete cover is primarily threatened by carbonation, a diffusion-driven process where atmospheric CO_2 reacts with hydration products to reduce the alkalinity of the matrix (Belda Revert et al., 2018). While carbonation typically leads to a denser pore structure, it also triggers the depassivation of steel reinforcement once the pH drops below approximately 9.0 (Wang et al., 2014). Experimental evidence suggests that an optimal steel fiber content of around 1.5% can retard the carbonation rate by refining the micropore structure; however, excessive fiber volume can facilitate deeper CO_2 penetration by creating weak interfacial transition zones (ITZ) and macro-voids (Bauwens et al., 2021; Wang et al., 2014).

Within the carbonated zone, the interaction between fiber corrosion and the surrounding matrix presents a unique *durability paradox*. Although the volumetric expansion of iron oxides can exert internal pressure leading to spalling, minor oxidation of fibers has been observed to increase the frictional bond strength at the fiber-matrix interface (Marcos-Meson, Fischer, et al., 2021). Because steel fibers have heterogeneous distribution, they primarily undergo micro-cell corrosion, which limits the large-scale structural damage typically associated with macro-cells in conventional reinforced concrete (Hansson et al., 2006). This mechanism, often supported by autogenous healing within cracks, allows SFRC elements to retain significant residual structural capacity even after decades of weathering (Marcos-Meson, Solgaard, et al., 2021).

In the present work, a comprehensive investigation is conducted on three steel fiber reinforced concrete beams designated as Beam 1 (FRC-B9), Beam 2 (FRC-B5), and Beam 3 (FRC-B2) to evaluate the long-term effects of 25 years of natural environmental exposure in Europe. Building upon the original experimental data from testing, this study utilizes a detailed methodology involving longitudinal and transversal sectioning to expose the internal state of the concrete matrix and the reinforcement cage, which consists of 16 mm bottom bars, 6 mm top bars, and 4 mm stirrups. The analysis specifically focuses on the interaction between pre-existing structural macro-cracks and environmental degradation, employing phenolphthalein-based chemical diagnostics to map carbonation depths and visual inspections to categorize the corrosion state of both conventional steel and bridging fibers. Furthermore, the research

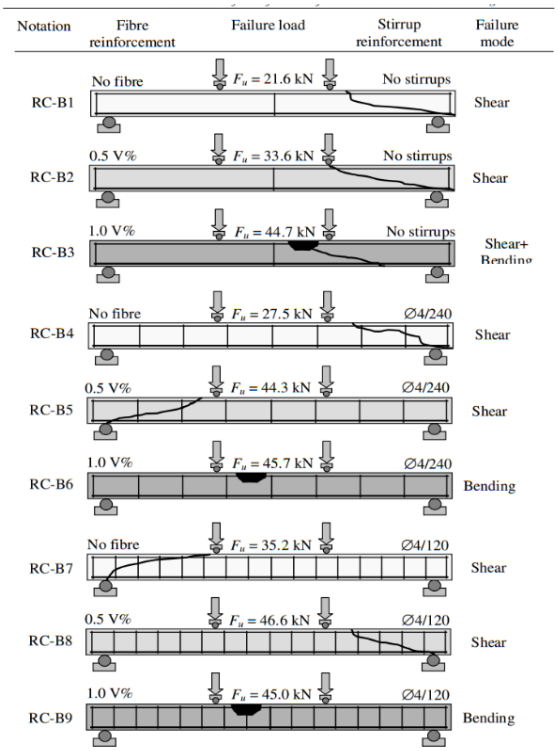
investigates the evolution of fiber distribution and aims to synthesize these findings to obtain a clear understanding of the residual structural integrity and the shift in failure kinematics of the elements after more than two decades of weathering.

2 Experimental program

2.1 Sampling and sectioning strategy

The research project entitled “Increasing toughness of concrete by application of steel fibers” (Grant No. MKM 150/94, 1994-1996), funded by the Hungarian Ministry of Education and coordinated by G.L. Balázs, included a test series of 2 x 9 fiber-reinforced concrete (FRC) beams. The main objective of the project was to investigate the influence of steel fibers on both the material behavior of concrete and the structural response of beams in bending and shear. Two types of fibers were considered: hooked-end and undulated steel fibers.

The experimental program of the project between 1994 and 1996 revealed distinctive structural behavior and failure modes. At the end of the project, nine of the tested beams were preserved and stored under outdoor conditions from 1999 to 2025, where they have been used as demonstration specimens for students and visitors (Fig. 1). The experimental results and main conclusions were published by Kovács and Balázs (2003), and later presented in greater detail in the monograph Structural Performance of Steel Fiber Reinforced Concrete (Kovács and Balázs, 2004), based on the PhD theses of Imre Kovács.



To assess the long-term durability and internal degradation mechanisms of SFRC, a destructive testing approach was adopted. Three representative beam specimens were selected from the original experimental program. The beams, originally 2.0 m in length with a cross-section of 100 × 150 mm, had been stored under outdoor conditions in Budapest for approximately 25 years.

The sectioning strategy was designed to distinguish between carbonation effects in the intact concrete matrix and those associated with pre-existing structural cracks. Specimens were cut using a water-cooled diamond saw in order to minimize heat-induced microcracking and to obtain smooth, planar surfaces suitable for both chemical analysis and digital image processing.

Figure 1. Identification of the selected experimental beams compared to the original test series (Kovács and Balázs, 2003; Kovács and Balázs, 2004)

The present 25-year durability analysis focuses specifically on a subset of 3 beams selected for their representative failure modes and reinforcement configurations The identification and original properties of the beams are as follows (Fig. 1): FRC-B9, FRC-B2 and FRC-B5.

The selection of these three specific beams allows for a comparative analysis of how different failure types specifically the differences between flexural and shear macro-cracks influence the rate of carbonation and the subsequent corrosion of both the steel fibers and the conventional stirrups over two decades of exposure.

2.2 Longitudinal cuts (crack path analysis)

Longitudinal sections were extracted by cutting the beams parallel to their longitudinal axis, deliberately intersecting the primary failure zones generated during the load tests 25 years ago. Especially for beams FRC-B5 and FRC-B2, which failed in shear, the cuts were executed in the outer thirds (shear spans) to capture the diagonal shear cracks.

The primary objective of this longitudinal sectioning was to conduct analysis of the internal crack morphology, the extent of carbonation, and the resulting corrosion state of the reinforcement within the beam's core. By exposing the internal profiles of the 25-year-old macro-cracks, it becomes possible to evaluate how these structural damages acted as preferential ingress channels for CO_2 and moisture, directly influencing the chemical environment and degradation rates near the original failure zones. This approach provides a clear view of the zone of interaction where the effects of the environment on both the steel fibers and the conventional reinforcement can be mapped in relation to the pre-existing damage (Fig. 2).



Figure 2. Detail of the carbonation front revealed by the 1% phenolphthalein indicator (top: before, bottom: after application of indicator). The sharp boundary distinguishes the highly alkaline uncarbonated core (purple, pH ≥ 9) from the carbonated outer layer (colorless/grey, pH ≤ 9)

2.3 Transversal cuts (uncracked matrix assessment)

In contrast to the crack path analysis, transversal cuts were performed perpendicular to the longitudinal axis in areas visually identified as uncracked. These sections were deliberately taken away from the primary failure zones (Fig. 3).



This transversal sectioning served two critical purposes. First, it provided a baseline to assess the natural carbonation penetration depth from the four exposed orthogonal faces into the dense, uncracked concrete matrix. Second, it yielded flat, 2D cross-sectional surfaces necessary for the stereological assessment of the fibers. These smooth faces are essential to accurately count the fiber intersections per unit area, map their spatial distribution, and mathematically correlate them to the original volumetric fiber fractions (V_f) of 0.5% and 1.0% used in the initial mixtures.

Figure 3. Transversal cut of the SFRC beam taken from an uncracked region, displaying the natural progression of the carbonation front from the exposed edges after 25 years

2.4 Crack morphology and surface diagnostic procedures

The diagnostic phase of the internal analysis was designed to systematically map and characterize the crack networks exposed during the sectioning process. This step is essential to differentiate between mechanical damage originating from the structural tests and the secondary, environment-induced degradation over the 25-year exposure period.

Macro-crack profiling methodology

High-resolution visual inspections were conducted on the longitudinal sections to trace the path of the primary macro-cracks. This profiling allows for the identification of how these structural *hinges* functioned as preferential paths, allowing carbonation and moisture to bypass the concrete cover.

Assessment of the crack-interface

The analysis focused on the interfaces of these cracks, specifically examining the oxidation state of the bridging steel fibers. By observing the presence of rust staining and the accumulation of corrosion products within the crack voids, the *interfacial zone* can be mapped to determine how environmental ingress has affected localized material integrity.

2.5 Chemical diagnostics: carbonation and corrosion

To accurately assess the chemical degradation of the concrete matrix and the physical state of the steel reinforcement after 25 years of environmental exposure, standardized diagnostic protocols were applied to the freshly sectioned surfaces.

Phenolphthalein method

Immediately following the sectioning of the SFRC beams, the freshly cut surfaces were cleared of cutting dust and subjected to chemical diagnostics to determine the penetration depth of the carbonation front. A 1% phenolphthalein solution dissolved in ethyl alcohol was sprayed evenly across both the transversal and longitudinal cross-sections.

This technique is the universal standard method for revealing the carbonation profile in concrete structures. The chemical indicator undergoes a distinct color transition based on the alkalinity of the cementitious matrix. Areas that turn a deep magenta or purple indicate a highly alkaline, uncarbonated environment (pH > 9.0), where the natural passivating layer protecting the steel is expected to be intact. On the other hand, areas that remain colorless retaining the natural light grey tone of the weathered concrete indicate a significant drop in pH (typically ≤ 9.0). This pH reduction is caused by the ongoing reaction between atmospheric carbon dioxide (CO_2) and calcium hydroxide ($Ca(OH)_2$) over the 25-year period, marking the fully carbonated zones.

Visual inspection of corrosion

To evaluate the long-term durability of the steel fiber reinforcement, a systematic visual inspection of the fibers exposed on the cut surfaces was conducted. A qualitative, three-tier visual grading criterion (Grade 1 to Grade 3), adapted from established methodologies in SFRC durability literature was established to classify the severity of corrosion for the individual fibers (Marcos-Meson et al., 2018) (Fig. 4.a – 4.c). The physical condition of each evaluated fiber was strictly cross-referenced with its exact topographical location within the concrete member. It was recorded whether the specific fiber was situated within the uncarbonated highly alkaline zone (purple), the fully carbonated solid matrix (colorless/grey), or directly bridging a macroscopic structural crack. This spatial correlation is essential to isolate the primary vector of corrosion in SFRC elements exposed to long-term outdoor conditions.



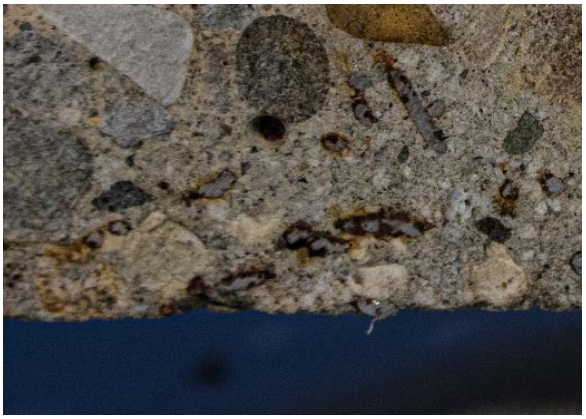
Grade 1 (Intact/Shiny): No visible signs of oxidation; the fiber retains its original metallic luster and smooth surface.

Figure 4.a Visual grading of steel fiber corrosion on exposed cross-sections: Grade 1 - Intact/Shiny



Grade 2 (Surface Rust): Presence of superficial oxidation, localized brown staining, or minor pitting, without a significant loss of cross-sectional area.

Figure 4.b Visual grading of steel fiber corrosion on exposed cross-sections: Grade 2 - Surface Rust



Grade 3 (Severe Corrosion): Heavy oxidation, flaking, rust-induced volumetric expansion, or a noticeable reduction in the effective cross-section of fibers.

Figure 4.c Visual grading of steel fiber corrosion on exposed cross-sections: Grade 3 - Severe Corrosion

2.6 Digital Image Processing for fiber distribution

To quantitatively evaluate the spatial distribution of the steel fibers and identify the specific batches from the original casting, a digital image analysis methodology was implemented on the transversal cuts.



High-resolution photographs of the 100 × 150 mm cross-sections were processed using image analysis software. The exposed metallic fibers were digitally tagged to calculate the total fiber count per section. To assess potential gravitational segregation and flow effects caused by the reinforcement cage during casting, a grid method was applied. The 150 mm depth of each cross-section was divided into three equal horizontal strips: Top (0–50 mm), Middle (50–100 mm), and Bottom (100–150 mm). The fibers within each strip were counted to determine their relative vertical distribution and correlate it with the original 0.5% and 1.0% volume fractions.

Figure 5. Digital tagging of exposed steel fibers on the transversal cross-section for spatial distribution and segregation analysis

3 Test Results

3.1 Quantitative fiber spatial distribution

The digital image processing of the four transversal cross-sections per beam yielded precise fiber counts, allowing for the empirical identification of the fiber distribution (Fig. 6). The total fiber counts and their relative spatial distribution across the three horizontal strips are summarized in Table 1.

Table 1. Total fiber counts and spatial distribution across the transversal sections per beam

#	Beam FRC-B9			Beam FRC-B5			Beam FRC-B2		
	Top	**Middle**	**Bottom**	**Top**	**Middle**	**Bottom**	**Top**	**Middle**	**Bottom**
1	110	111	82	76	49	37	51	40	64
2	93	111	75	78	47	49	76	65	56
3	73	36	14	81	38	34	51	45	29
4	123	120	105	61	26	35	48	51	38

The FRC-B9 beam exhibited nearly double the total fiber count (1053 fibers) compared to beams FRC-B5 and FRC-B2 (611 and 614 fibers, respectively). This confirms that FRC-B9 corresponds to the mixture with a 1.0% fiber volume fraction, while beams FRC-B5 and FRC-B2 correspond to the 0.5% batches. Furthermore, the data reveals a non-homogeneous distribution of the fibers. Contrary to typical gravitational settling expectations, all three beams demonstrated a noticeable agglomeration in the top third of the cross-section. FRC-B5 exhibited the most extreme segregation, with 48% of its total fibers concentrated in the upper 50 mm.

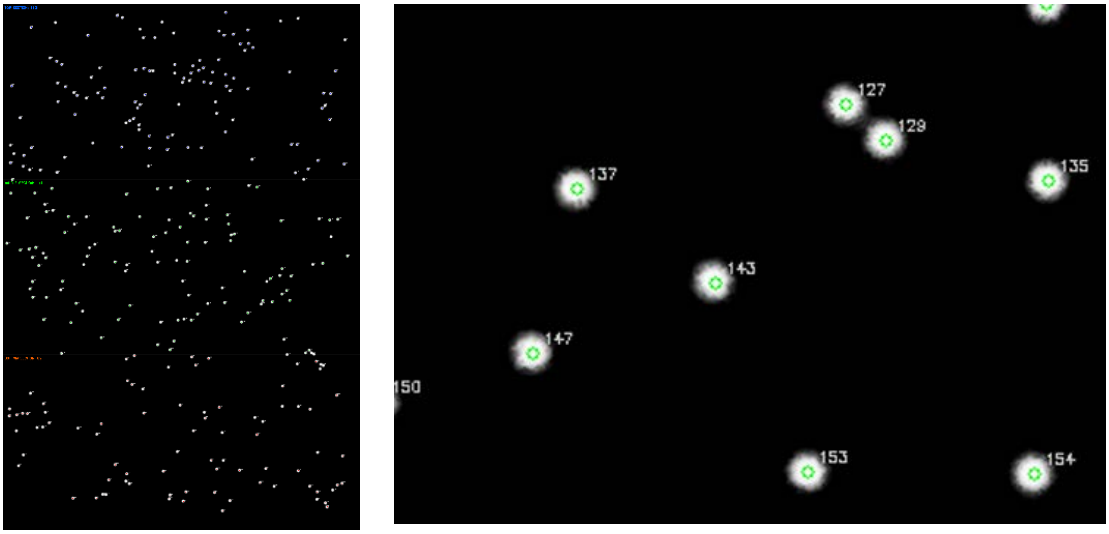


Figure 6. Software recognition and automated counting of steel fibers divided across the Top, Middle, and Bottom horizontal strips

3.2 Visual and chemical assessment of carbonation

The progression of the natural carbonation front over the 25-year outdoor exposure period for SFRC beams was evaluated through direct visual inspection and chemical diagnostic verification. Even before the application of the chemical indicator, the carbonation front was visually identifiable. The cross-sections displayed a distinct boundary separating the outer perimeter from the inner core (Fig. 7).



This visible carbonated perimeter roughly corresponded to the concrete cover; the matrix located outside the conventional stirrups appeared visually altered, while the concrete core confined within the stirrups appeared unaffected.

To confirm this visual assessment, a 1% phenolphthalein solution was applied to the freshly cut surfaces. The chemical reaction perfectly matched the initial macroscopic observations. The outer concrete cover turned a colorless/grey hue, confirming a fully carbonated state with a significantly reduced pH. In contrast, the internal core within the conventional reinforcement cage turned deep purple, confirming that the highly alkaline environment (pH > 9.0) was successfully preserved deep inside the structural SFRC member.

Figure 7. Transversal cross-section illustrating the exact alignment of the carbonation front (colorless) with the concrete cover. The highly alkaline core (purple) is effectively preserved within the boundaries of the conventional stirrups

3.3 Corrosion state at structural cracks

A critical visual inspection was conducted on the longitudinal sections of FRC-B9 (flexural failure), and FRC-B5 and FRC-B2 beams (shear failures) to assess the condition of the steel fibers directly exposed to the 1999 structural macro-cracks.

Fibers located within the failure zones and large structural cracks primarily exhibited *Grade 2 (Surface Rust)* or, in the most exposed areas, *Grade 3* (Severe Corrosion), but crucially, the majority were not fully consumed. They largely retained their structural cross-section and physical integrity. In the fully carbonated outer cover (colorless/grey), the embedded steel fibers were overwhelmingly found in an intact, pristine state (*Grade 1*). Oxidation (*Grade 2*) in these carbonated regions was exclusively observed on fibers that were intersected by local micro-cracks. Fibers embedded in uncracked, carbonated concrete, as well as the conventional stirrups and longitudinal rebars located away from the primary failure zones, showed absolutely no signs of oxidation (*Grade 1*).

4 Analysis

4.1 Fiber segregation and its impact on durability

The quantitative distribution data highlights a significant internal architectural feature of the tested SFRC members: a pronounced agglomeration of fibers in the top section. This unexpected distribution can be attributed to the interaction between the fiber suspension and the conventional reinforcement cage during the original casting and vibration process. The top longitudinal reinforcement bars and the upper corners of the conventional stirrups likely acted as a physical barrier. As fresh concrete was poured into the narrow 100 × 150 mm formwork, the steel fibers became entangled in the upper reinforcement, preventing a uniform downward flow.

This top-heavy distribution has direct, long-term durability consequences. The bottom part of a simply supported beam is the primary tension zone where flexural macro-cracks initiate. The data reveals that the bottom 50 mm strip suffered from a critical lack of fibers. Because there were fewer fibers available to bridge the tensile stresses at the bottom of the member, the resulting structural cracks likely opened wider than intended. These wider cracks functioned as paths for moisture and atmospheric CO_2, accelerating the localized environmental degradation observed at the crack interfaces.

4.2 Concrete cover efficacy and carbonation profiling

The cross-sectional analysis highlights the effectiveness of the concrete cover over 25-year period. The alignment of the carbonation front with the exterior boundary of the conventional stirrups demonstrates that Fickian diffusion progressed predictably from the exposed faces. The concrete cover successfully acted as a sacrificial layer, absorbing the atmospheric CO_2 and protecting the main reinforcement cage. The internal core remained highly alkaline, completely shielding the conventional rebars and the internal fibers from chemically induced depassivation.

However, pre-existing macroscopic cracks fundamentally altered these CO_2 ingress mechanisms. In beams FRC-B5 and FRC-B2, once the diagonal shear cracks compromised the concrete cover, their internal walls effectively became new *external* surfaces. This allowed carbon dioxide to penetrate laterally from the crack walls, neutralizing the highly alkaline protection precisely where the bridging fibers are structurally most critical (Fig. 8).



Figure 8. Longitudinal sections of beams FRC-B5 and FRC-B2, *demonstrating how severe diagonal shear cracks acted as new, unprotected "external" surfaces for environmental ingress*

4.3 Crack-assisted carbonation and the durability paradox

The assessment revealed a nuanced *durability paradox* regarding the fibers embedded within the fully carbonated concrete matrix. For active corrosion to propagate, three conditions must be met simultaneously: depassivation of the steel fibers, available oxygen, and sufficient free moisture to act as an electrolyte. While carbonation successfully lowered the pH and destroyed the passive film on the steel within the cover zone, the fibers generally did not corrode unless accompanied by a physical fissure.

Where the carbonated matrix remained physically intact, the fibers were largely preserved in their original state. Unlike continuous conventional rebars that can span across zones of varying moisture and pH to form highly destructive galvanic macro-cells, the short, discontinuous nature of the steel fibers prevents this phenomenon. Both the anodic and cathodic sites must exist on the same micro-scale fiber. Thus, carbonation alone, in the absence of a continuous water supply through open microcracks, is insufficient to induce severe active corrosion in SFRC elements. Oxidation was exclusively observed on fibers that were intersected by local micro-cracks, which provided the necessary capillary pathway for moisture.

4.4 Long-term resilience of bridging action

The most significant finding of this investigation is the physical state of the fibers bridging the primary structural cracks. It is a common concern that wide macro-cracks in SFRC elements exposed to outdoor weathering will lead to rapid and complete corrosion of the exposed metallic fibers, rendering them structurally useless. However, the 25-year data contradict this assumption.

Because the fibers at the flexural and shear failure planes generally suffered from *Grade 2* surface oxidation rather than full cross-sectional loss (*Grade 3*), they physically continue to bridge the cracks. This proves that even after two decades of harsh weathering without the protection of an alkaline matrix, the fibers successfully fulfill their structural purpose, maintaining residual tension-stiffening and post-crack ductility. If the remaining cross-section of a corroded fiber is reduced beyond a critical threshold, it will rupture rather than pull out, compromising the ductile failure mechanism.

5 Conclusions

This paper presents an extraordinary chance to check requirements for SFRC beams, with conventional reinforcements and steel fibers that were tested until maximum loading in flexure or shear, then kept in outdoor conditions for 25 years in Budapest with continental climate (cyclically wet and dry, temperature from -10 to +40 degrees Celsius). Longitudinal and transversal saw cuts were analyzed thoroughly and the following conclusions can be drawn from the observations:

- The presence of a conventional reinforcement cage may influence the distribution of steel fibers, which might become entangled in the upper layers of stirrups and longitudinal bars, leading to a top agglomeration and a deficit of fibers in the bottom tension zone.
- After 25 years of natural weathering, the carbonation front typically aligns with the exterior boundary of the conventional stirrups. The uncracked concrete cover successfully protects the structural core, maintaining a highly alkaline environment (pH > 9.0) that prevents the depassivation of internal reinforcement and steel fibers.

- Carbonation depassivation alone is insufficient to initiate severe corrosion in steel fibers. In uncracked but fully carbonated concrete, fibers remain in an uncorroded state because the absence of physical fissures starves the electrochemical reaction of a continuous moisture supply.
- Pre-existing structural macro-cracks act as the primary cause of degradation. These cracks bypass the sacrificial cover and allow carbon dioxide to penetrate laterally from the crack walls into the alkaline core, neutralizing protection precisely where bridging fibers are most structurally critical.
- Despite 25 years of exposure, steel fibers bridging flexural and shear cracks largely maintain their mechanical integrity. While surface oxidation is common in these zones, full cross-sectional loss is rare, allowing the fibers to continue fulfilling their purpose by providing residual tension-stiffening and post-crack ductility.
- While the composite behavior is primarily governed by ductile fiber pull-out, severe localized corrosion in wide macro-cracks can reduce a fiber's tensile capacity below the force required for pull-out, eventually shifting the failure mode toward brittle rupture.

6 References

Bauwens, T., Grünewald, S., & De Schutter, G. (2021). Simulation of Fibre Orientation in Self-compacting Concrete: Case Studies. In P. Serna, A. Llano-Torre, J. R. Martí-Vargas, & J. Navarro-Gregori (Eds.), *Fibre Reinforced Concrete: Improvements and Innovations* (Vol. 30, pp. 64–74). Springer International Publishing. https://doi.org/10.1007/978-3-030-58482-5_6

Belda Revert, A., De Weerdt, K., Hornbostel, K., & Geiker, M. R. (2018). Carbonation-induced corrosion: Investigation of the corrosion onset. *Construction and Building Materials*, *162*, 847–856. https://doi.org/10.1016/j.conbuildmat.2017.12.066

Hansson, C. M., Poursaee, A., & Laurent, A. (2006). Macrocell and microcell corrosion of steel in ordinary Portland cement and high performance concretes. *Cement and Concrete Research*, *36*(11), 2098–2102. https://doi.org/10.1016/j.cemconres.2006.07.005

Kobaka, J. (2021). A Statistical Model of Fibre Distribution in a Steel Fibre Reinforced Concrete. *Materials*, *14*(23), 7297. https://doi.org/10.3390/ma14237297

Kovács, I., & Balázs, G. L. (2003). Structural behaviour of steel fibre reinforced concrete. *Journal Structural Concrete Vol 4. 2003/2, pp. 58-64.*

Kovács, I., & Balázs, G. L. (2004). *Structural behaviour of steel fibre reinforced concrete*. Comp. of Budapest University of Technology and Economics. http://fib.bme.hu/konyvek/steel-fiber-.pdf

Laranjeira, F., Grünewald, S., Walraven, J., Blom, C., Molins, C., & Aguado, A. (2011). Characterization of the orientation profile of steel fiber reinforced concrete. *Materials and Structures*, *44*(6), 1093–1111. https://doi.org/10.1617/s11527-010-9686-5

Marcos-Meson, V., Fischer, G., Solgaard, A., Edvardsen, C., & Michel, A. (2021). Mechanical Performance of Steel Fibre Reinforced Concrete Exposed to Wet–Dry Cycles of Chlorides and Carbon Dioxide. *Materials*, *14*(10), 2642. https://doi.org/10.3390/ma14102642

Marcos-Meson, V., Michel, A., Solgaard, A., Fischer, G., Edvardsen, C., & Skovhus, T. L. (2018). Corrosion resistance of steel fibre reinforced concrete—A literature review. *Cement and Concrete Research*, *103*, 1–20. https://doi.org/10.1016/j.cemconres.2017.05.016

Marcos-Meson, V., Solgaard, A., Skovhus, T. L., Jakobsen, U. H., Edvardsen, C., Fischer, G., & Michel, A. (2021). Pull-out behaviour of steel fibres in cracked concrete under wet–dry cycles – deterioration phenomena. *Magazine of Concrete Research*, *73*(16), 843–852. https://doi.org/10.1680/jmacr.19.00448

Wang, Y., Niu, D., & Dong, Z. (2014). Experimental Study on Carbonation of Steel Fiber Reinforced Concrete. *Proceedings of the 4th International Conference on the Durability of Concrete Structures*, 55–59. https://doi.org/10.5703/1288284315382

Mechanical and environmental performance of SFRC using fibres made of recycled and renewably produced steel and Limestone Calcined Clay Cement LC^3

Beatrice Malchiodi[1], Lionel Sofia[1], Sébastien Wolf[2], Karen Scrivener[1]

[1]: Laboratory of Construction Materials - EPFL, CH-1015 Lausanne, Switzerland

[2]: ArcelorMittal Fibres, Route de Finsterthal, L-7769 Bissen, Luxembourg

Abstract

Steel Fibre Reinforced Concrete (SFRC) is widely used for structural applications due to its superior post-cracking performance and ability to replace fully or partially conventional reinforcement. However, its environmental impact remains significant, driven by high-clinker binders and carbon-intensive steel production. Although low-carbon binders and steel fibres made of recycled steel are available, their combined impact on the structural performance of SFRC remains insufficiently documented.

In response to the growing demand for sustainable and circular construction materials, this study investigates the technical viability of a low-carbon SFRC incorporating Limestone Calcined Clay Cement (LC^3) and fibres made from Recycled and Renewably Produced Steel (RRPS), aiming to significantly reduce CO_2 emissions while maintaining structural performance.

A comprehensive experimental program was conducted to evaluate compressive strength, flexural behaviour, and post-cracking performance. The results show that LC^3-based mixes enhance energy absorption capacity and residual strengths, particularly when combined with longer fibres, leading to improved post-cracking behaviour. At the same time, the embodied carbon footprint is reduced by up to 16% compared to the reference mix.

These findings demonstrate that high mechanical performance and reduced environmental impact can be achieved simultaneously. The proposed approach provides a robust pathway for integrating low-carbon binders and circular steel into structural SFRC and supports ongoing developments in performance-based design within the fib and ACI communities.

Keywords

Fibre reinforced concrete, Limestone Calcined Clay Cement, SFRC, post-cracking performance, residual flexural strength, Recycled and Renewably Produced Steel, sustainability, low carbon.

1 Introduction

Steel Fiber Reinforced Concrete (SFRC) is a mature material widely used in structural and non-structural applications. Over more than four decades, it has proven to be an efficient and high-performing alternative to traditional Reinforced Concrete (RC), with steel fibres partially or fully replacing conventional reinforcement. However, SFRC is not simply RC without rebars; it constitutes a distinct material requiring specific mix designs and dedicated design provisions, particularly for bending, shear, and crack control. Its growing relevance is reflected in European standards, where the forthcoming Eurocode 2 includes Annex L for SFRC design, and in the United States through extensive guidance from the ACI 544 committee, including applications in elevated slabs.

Unlike RC, where tensile forces are carried by discrete rebars, SFRC relies on a distributed network of steel fibres to enhance tensile resistance and control cracking. Fibre performance depends on key parameters such as geometry, aspect ratio, mechanical properties, and anchorage behavior within the cementitious matrix. Proper interaction between fibres and binder is essential to ensure ductility and optimize post-cracking performance by balancing fibre pull-out and rupture mechanisms.

In parallel with performance requirements, the construction industry faces increasing pressure to reduce the environmental impact of materials while maintaining structural efficiency. In this context, the choice of reinforcement plays a key role. By replacing conventional rebar with steel fibres, SFRC can significantly lower the carbon footprint of widely used applications such as industrial floors for warehouses, data centers, and gigafactories. Compared to traditional rebar-reinforced solutions, SFRC floors typically achieve reductions exceeding 20%. This benefit is further enhanced when using fibres produced from recycled and renewably produced steel (RRPS), enabling overall emission reductions of up to 35%, while maintaining structural performance.

Complementing these advances in reinforcement, the development of low-carbon binders further enhances the sustainability potential of SFRC. While Portland cement (CEM I) has traditionally been used, blended cements such as CEM II and CEM III are increasingly adopted to improve environmental impact. However, binder selection remains critical, as alternative compositions can significantly influence fibre efficiency and overall mechanical performance. Limestone calcined clay cement (LC^3) has emerged as a promising solution by enabling up to 50% clinker substitution through the synergistic use of calcined clay and limestone. This significantly reduces CO_2 emissions while maintaining mechanical performance and durability. LC^3 is now standardized (e.g., EN 197-5, ASTM C595) and increasingly adopted in practice due to its environmental and economic benefits.

This study investigates the feasibility of combining LC^3 with steel fibres produced from recycled and renewable sources to develop a more sustainable SFRC. The objective is to quantify the reduction in environmental impact while ensuring that the required mechanical performance is maintained, based on experimental characterization following EN 14651.

2 Experimental program

To assess the performance of LC³-based SFRC, two types of hooked-end, unglued steel fibres were investigated. A long fibre (60 mm length, 0.9 mm diameter) typically used in industrial floors and lightly loaded rafts, and a shorter fibre (35 mm length, 0.75 mm diameter) commonly applied in low-duty slabs and crack-control applications were selected to cover a broad performance range. Both fibres were manufactured from low-carbon steel with a tensile strength of 1200 MPa. The fibres were produced entirely from recycled steel using an electric arc furnace (EAF) powered by renewable energy (wind and solar). This process, based on melting scrap steel, significantly reduces CO_2 emissions compared to the conventional blast oxygen furnace (BOF) route, which relies on primary raw materials such as iron ore and coke.

Table 1: Fibre types and properties.

Properties	**RRPS HE 90/60**	**RRPS HE 75/35**
Length (mm)	60	35
Diameter (mm)	0.9	0.75
V_f (%)	0.5	0.5
Wire Tensile strength (MPa)	1200	1200

Three binders were used: (i) a CEM II/A-LL cement as a conventional reference, (ii) a commercial LC³ cement classified as CEM II/C-M (Q-LL) according to EN 197-5, and (iii) a laboratory-produced LC³ blend (LC^3-50) composed of 50% clinker, 30% calcined clay (39% kaolinite), 15% limestone, and 5% gypsum.

All mixtures were designed for a compressive strength class C30/37, with a target spread of 630 mm without fibres and 420 mm with fibres. To isolate the effects of fibre type and binder, a constant binder content (310 kg/m³) and fibre dosage (40 kg/m³) were used. Six concrete formulations were investigated (see Tables 2 and 3).

Mixing was performed in a 180 L laboratory mixer over 10 minutes. Cement, aggregates, and water were first mixed for 2 minutes, followed by the addition of superplasticizer and gradual incorporation of fibres to ensure uniform dispersion. The spread of the concrete mix before and after incorporation of the fibres was measured according to EN 12350-5. Flexural specimens (150 × 150 × 600 mm³) were cast in steel moulds and compacted by vibration in accordance with EN 14651. After 24 hours of curing at 20 ± 1°C and ~95% relative humidity, specimens were stored in water at 20 ± 1°C until testing at 28 days.

Table 2: C30/37 Concrete mix design.

Ingredient	**Quantity (kg/m^3)**
0/4 mm sand	720
4/8 mm aggregate	740
8/16 mm aggregate	390
Binder	310
RRPS-Fibres (RRPS HE 90/60 or RRPS HE75/35)	40
Water	158
Superplasticizer	variable
Target spread without/with fibres [Class EN 206-1]	F5/F3

Table 3: Concrete mix design and fibre characteristics for all the sets of specimens tested.

Mix	Cement type	Fibre type	SP (kg/m^3)	Spread (mm)	Spread (class)
Ref. – 90/60	CEM II/A-LL	RRPS HE 90/60	2.45	630 / 420	F5/F3
LC^3Com. – 90/60	CEM II/C-M (Q-LL)	RRPS HE 90/60	1.63	630 / 420	F5/F3
LC^3-50 – 90/60	LC^3-50	RRPS HE 90/60	2.47	630 / 420	F5/F3
Ref. – 75/35	CEM II/A-LL	RRPS HE 75/35	0.96	590 / 480	F5/F3
LC^3Com. – 75/35	CEM II/C-M (Q-LL)	RRPS HE 75/35	1.58	630 / 490	F5/F3
LC^3-50 –75/35	LC^3-50	RRPS HE 75/35	1.84	630 / 490	F5/F3

Flexural performance was evaluated using three-point bending tests on notched beams (span 500 mm, notch depth 25 mm) following EN 14651:2005+A1:2007. Six specimens per mix were tested. Residual flexural tensile strengths were derived from load–CMOD and load–deflection responses. Tests were displacement-controlled (0.05 mm/min up to CMOD = 0.1 mm, then 0.2 mm/min), with CMOD measured by extensometer and data recorded at 5 Hz up to 3.5 mm. Deflection was calculated from CMOD using the following Eq. 1 by EN 14651 (1):

$$\delta = 0.85\, CMOD + 0.04 \quad (1)$$

After flexural testing, the resulting prisms (150 × 150 × 300 mm^3) were tested in compression according to EN 12390-3 using a 5000 kN machine. Characteristic compressive strength was determined following EN 13791:2019:

$$f_{ck} = f_m - k_n \cdot s \quad (2)$$

where $f_m$is the mean compressive strength, s the standard deviation, and k_n a coefficient dependent on the number of specimens tested.

The environmental assessment focused on Global Warming Potential (GWP) over stages A1–A3 (raw material production), which dominate total emissions. Steel production via EAF can reduce emissions by up to 90%, from approximately 3000 $kgCO_2eq/t$ (BOF) to about 350 $kgCO_2eq/t$ with high scrap content. In addition, replacing conventional rebar with steel fibres reduces the carbon footprint of typical SFRC floor applications by more than 20%, and up to 35% when using recycled and renewable steel fibres.

Table 4: GWP of the concrete components.

Component	GWP ($kgCO_2eq/t$)	Source
RRPS HE 90/60	346	EPD ArcelorMittal – XCarb® Fibres
RRPS HE 75/35	346	EPD ArcelorMittal – XCarb® Fibres
CEM II/A-LL	460	EPD Cement supplier
CEM II/C-M (Q-LL)	390	EPD Cement supplier
LC^3-50	365	Calculated from EPD cement supplier
0/4 sand	2.51	EPD Swiss aggregate supplier
4/8 mm aggregate	2.76	EPD Swiss aggregate supplier
8/16 mm aggregate	2.76	EPD Swiss aggregate supplier
Superplasticizer	1870	Walach et al. (2019), EPD supplier

The Global Warming Potential (GWP) of the binders was assessed using Environmental Product Declarations (EPDs) for CEM II/A-LL and CEM II/C-M (Q-LL), in accordance with EN 15804 (A1–A3). For the LC3-50 blend, GWP values were estimated based on equivalent constituent data consistent with EPD assumptions to enable a representative comparison.

3 Test Results

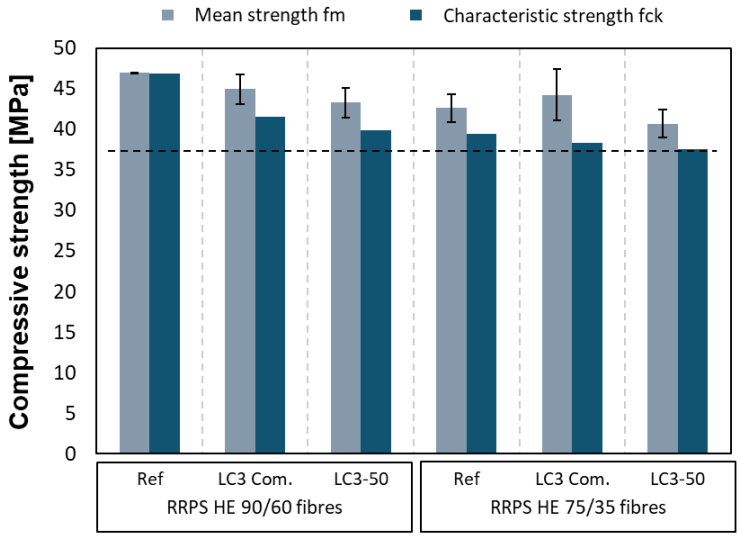
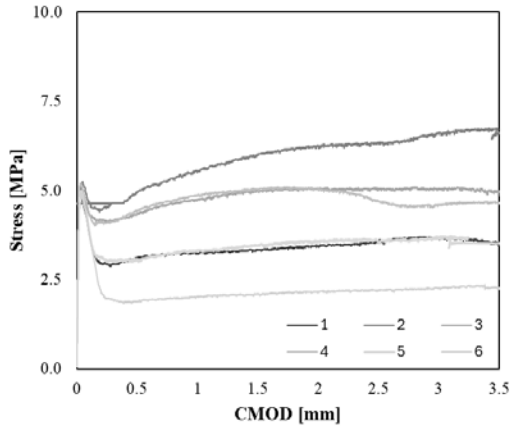


Figure 1: Mean (f_m) and characteristic (f_{ck}) compressive strengths of the six concrete mixes. Error bars indicate standard deviation, and the horizontal dashed line represents the minimum characteristic compressive strength requirement for strength class C30/37.

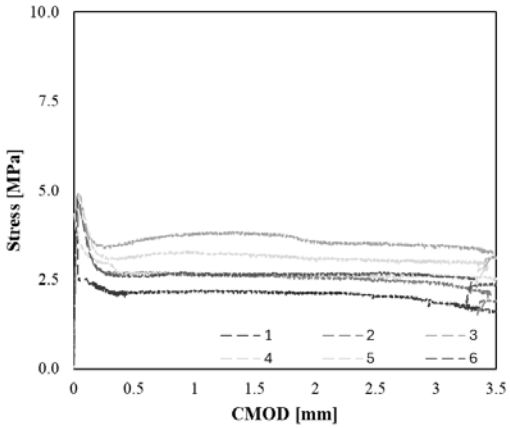
Figure 1 presents the mean compressive strength $f_m$and the characteristic compressive strength f_{ck}(determined according to EN 13791:2019 based on the number of specimens) for three concrete mixes (Ref, LC^3 Com., LC^3-50) reinforced with two fibre types (RRPS HE 90/60 and RRPS HE 75/35).

Overall, while LC^3 incorporation results in a slight reduction in mean compressive strength, the values remain sufficiently high for structural applications, supporting the viability of LC^3 as a sustainable alternative binder. A slightly larger gap between mean and characteristic values is observed for LC^3 concretes, indicating increased variability.

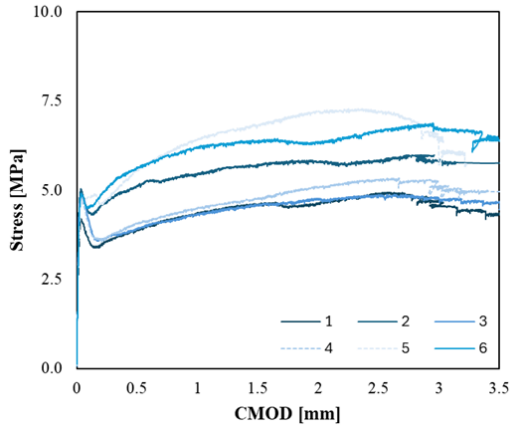
The influence of fibre type on compressive strength is minor compared to that of the binder composition. Slight differences are observed between the RRPS HE 90/60 and RRPS HE 75/35 fibres, indicating a marginal effect, likely related to fibre distribution and matrix interaction, without altering the overall trends.



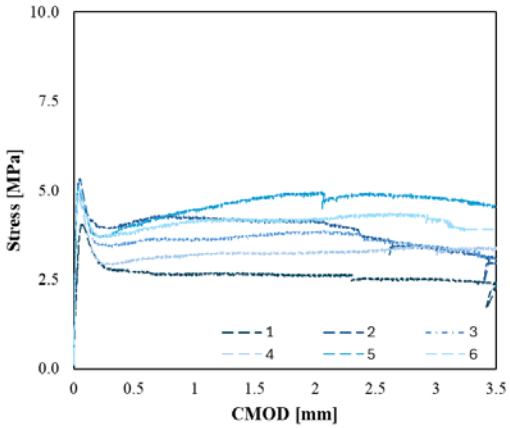
(a) Ref. – 90/60



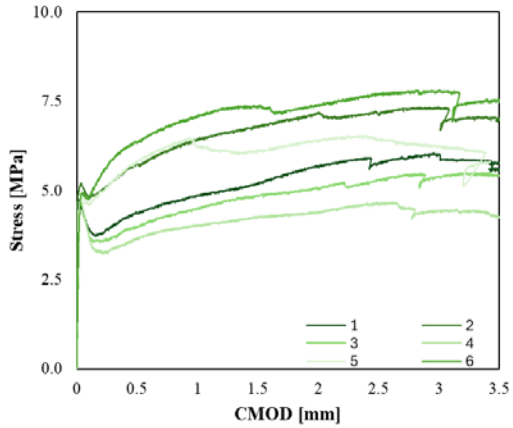
(b) Ref. – 75/35



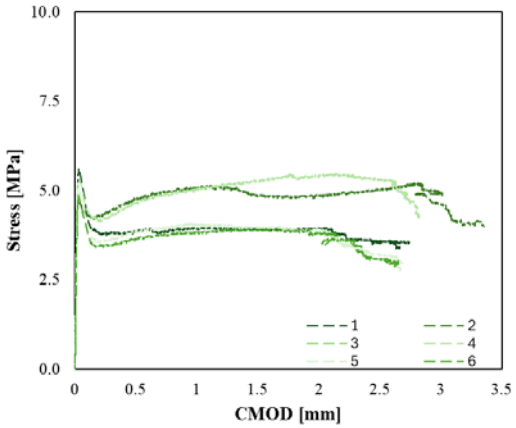
(c) LC^{3}Com. – 90/60



(d) LC^{3}Com. – 75/35



(e) LC^3-50 – 90/60



(f) LC^3-50 – 75/35

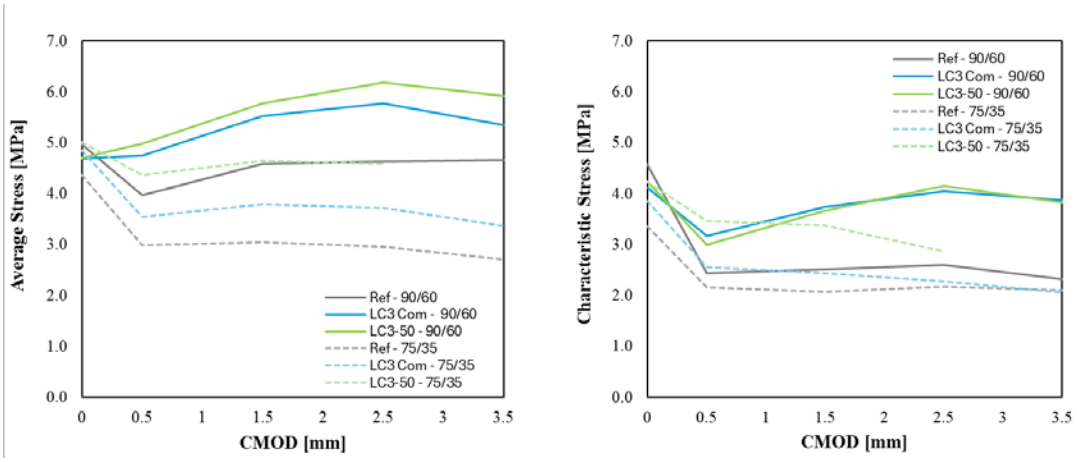
Figure 2: Comparison of stress–CMOD curves for six specimens: (a)Ref – 90/60 *(b) Ref.* – 75/35 *(c)* LC^{3}Com. – 90/60 *(d)* LC^{3}Com. – 75/35 *(e)* LC^3-50 – 90/60 *(f)* LC^3-50 – 75/35

The full stress–CMOD curves highlight the influence of both binder type and fibre geometry on the post-cracking behaviour of the concretes.

For all mixes, an initial peak (Limit Of Proportionality, LOP) is observed at low CMOD values, followed by a drop corresponding to crack initiation and matrix cracking. Beyond this point, the residual behaviour is governed by fibre bridging. The reference mix (Figure 2.a and 2.b) exhibits lower residual stresses and a more pronounced softening response, particularly for short fibres, indicating less post-cracking capacity compared to long-fibres for high CMOD and same dosage.

In contrast, the LC^3-based mixes (Figure 2c, 2d, 2d, 2e) show significantly improved post-cracking performance. Both LC^3 Com. and LC^3-50 exhibit higher residual stress levels and a more stable or even hardening response at increasing CMOD, especially with long fibres. This indicates enhanced fibre–matrix interaction and improved load transfer after cracking. The enhanced post-cracking behaviour of LC3-based SFRC compared to CEM II A-LL can be attributed to the refined microstructure of the binder. LC^3 systems are known to promote the formation of additional carboaluminate phases and a denser C–S–H network, resulting in reduced porosity and a more homogeneous matrix (Scrivener et al., 2018; Bishnoi and Scrivener, 2019). This densification is expected to improve the interfacial transition zone, which is known to be more porous than the bulk matrix (Scrivener et al., 2004), thereby enhancing the fibre–matrix bond. Such behaviour is consistent with established relationships between matrix quality and fibre pull-out mechanisms in SFRC (Denarié and Brühwiler, 2006; 2011). A denser matrix thus improves fibre anchorage and increases residual stresses. This effect is further amplified with decreasing clinker content from LC^3 Com. to LC^3-50, as the higher calcined clay content increases alumina availability and promotes additional hydrate formation, leading to further microstructural refinement and improved fibre–matrix interaction.

The effect of fibre geometry is clearly visible. Long fibres (Figure 2a, 2c, 2e) provide higher residual stresses and better stress retention at large CMOD values compared to short fibres (Figure 2b, 2d, 2f), which show earlier softening and lower residual capacity. This difference is consistent across all binder types. Between the LC^3 mixes, LC^3-50 (Figure 2e, 2f) generally exhibits the highest residual stresses and the most pronounced strain-hardening behaviour, particularly at large crack openings. Overall, the combination of LC^3 binders and longer fibres results in the most favourable post-cracking response.



(a) (b)

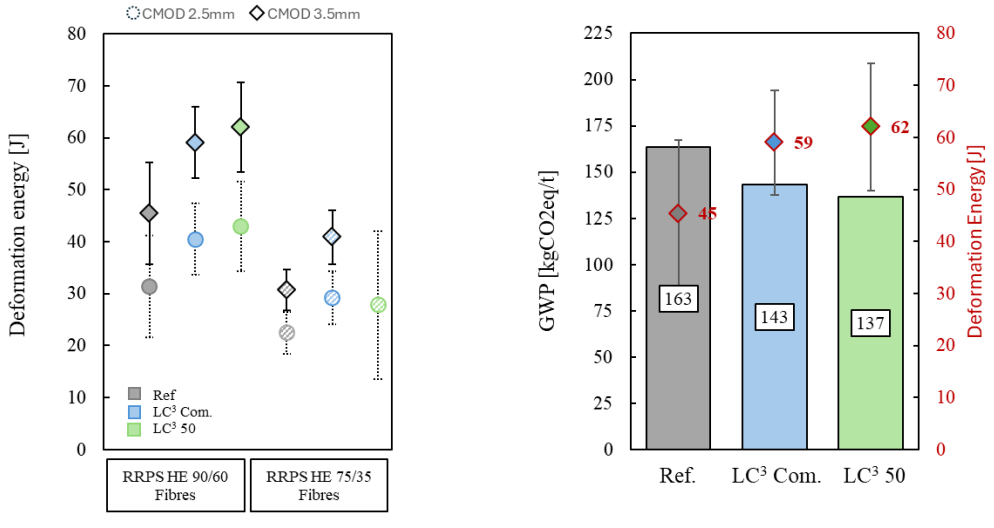
Figure 3: (a) Average stress-CMOD curves for all concrete mixes and different fibres (b) Characteristic stress-CMOD curves for all concrete mixes and different fibres.

Analysis of the beam test results with RRPS HE 90/60 fibres shows that LC³-based mixes consistently exhibit higher average residual flexural tensile strengths $f_{r,i,m}$than the reference mix (Figure 3a). The improvement is particularly pronounced at larger crack openings (CMOD ≥ 2.5 mm), corresponding to $f_{r3,m}$and $f_{r4,m}$, which are critical for structural design. These gains are structurally relevant, as they may enable a reduction in element thickness in applications governed by residual strength, in line with recommendations such as Technical Report 34.

The analysis of characteristic values (Figure 3b) confirms the same trend. LC³-based concretes achieve significantly higher characteristic residual strengths than the reference mix, especially at larger CMOD. While LC³ Com. and LC³-50 show comparable performance, LC³-50 tends to provide slightly higher values at larger crack openings. The difference with the reference mix is substantial (on the order of 1–1.5 MPa for $f_{r3,k}$), which can translate into reduced slab thickness at the ultimate limit state, according to Eurocode 2 Annex L or similar design approaches.

Results obtained with RRPS HE 75/35 fibres confirm these trends, although with lower absolute values and reduced sensitivity to binder type. LC³ mixes still demonstrate improved residual strengths compared to the reference, but the magnitude of improvement is less pronounced than with longer fibres.

Finally, the influence of fibre geometry is clearly reflected in both figures: longer fibres (90/60) provide superior performance compared to shorter fibres (75/35) across all CMOD levels, particularly at larger crack openings, due to improved crack-bridging capacity and anchorage. Overall, LC³-based concretes combined with longer fibres deliver the most favorable structural performance.



(a) (b)

Figure 4: a) Deformation energy calculated until CMOD 2.5 and 3.5 mm for all SFRC, b) Total GWP of the SFRC with RRPS HE 90/60 (bar chart, primary axis) and corresponding deformation energy (red markers, secondary axis).

Deformation energy was used as an additional performance indicator, defined as the mean integral of the load–CMOD curves for each mix. It was evaluated up to CMOD levels of 3.5

mm and 2.5 mm, the latter adopted due to limitations in the test setup for the LC3-50 – 75/35 series, which did not allow measurements beyond this level. Figure 4a shows the deformation energy at CMOD = 2.5 mm and 3.5 mm for the different binders and fibre geometries. LC³-based concretes consistently exhibit higher deformation energy than the reference mix, indicating improved ductility and post-cracking performance. This enhancement is more pronounced at larger crack openings (CMOD = 3.5 mm), where fibre–matrix interaction dominates. Among the binders, LC³-50 generally provides the highest energy values, confirming its superior load-carrying capacity after cracking. Fibre geometry also resulted in having a strong influence: longer fibres (90/60) yield significantly higher deformation energy than shorter fibres (75/35), particularly at large CMOD, due to improved anchorage and crack-bridging efficiency. However, increased scatter is observed for LC³ mixes, especially at higher CMOD levels, indicating greater variability in the post-cracking response. Overall, the results demonstrate that both LC³ binders and longer fibres contribute positively to energy absorption capacity, with their combination providing the most favorable post-cracking behaviour.

Figure 4b compares the deformation energy and total GWP of the three concrete formulations incorporating long fibres (RRPS HE 90/60), selected due to their superior post-cracking performance in bending. The total GWP of all concrete mixes was calculated as the summary of the products between the component content and component GWP and using the GWP value of Table 4. The total GWP of mixes with the same binder type and different fibre type resulted in having the same value. A clear reduction in GWP is observed when replacing the reference mix (163 $kgCO_2eq/t$) with LC³-based binders, decreasing to 143 $kgCO_2eq/t$ for LC³ Com. and 137 $kgCO_2eq/t$ for LC³-50, corresponding to reductions of approximately 12% and 16%, respectively.

Simultaneously, mechanical performance, represented by dissipated energy, improves with LC³ incorporation, increasing from 45 J (Ref.) to 59 J (LC³ Com.) and 62 J (LC³-50). This indicates enhanced post-cracking behavior and ductility, likely due to improved fibre–matrix interaction.

Overall, LC³-based concretes not only enhance mechanical performance, particularly in terms of post-cracking behavior and ductility, but also allows reducing CO_2 emissions. This dual benefit directly supports the development of structural materials that are both higher performing and more sustainable, with LC³-50 offering the most advantageous combination.

4 Concluding remarks

SFRC is a well-established alternative to conventional reinforced concrete, offering enhanced structural performance through fibre reinforcement. At the same time, the construction industry faces increasing pressure to reduce CO_2 emissions without compromising mechanical efficiency. A key gap remains in combining low-carbon binders with sustainable reinforcement to achieve both objectives simultaneously. This study addressed this challenge by evaluating SFRC made with LC³ binders and recycled and renewably produced steel (RRPS) fibres through mechanical testing and GWP assessment. The results show that LC³ significantly enhances post-cracking behaviour, with higher residual strengths, increased dissipated energy, and improved ductility—especially with longer fibres. Simultaneously, LC³ enabled GWP reductions of up to 16%, demonstrating that improved mechanical performance can be achieved alongside lower environmental impact. These findings confirm the strong potential of

combining LC³ and RRPS fibres to develop structural SFRC that is high-performing and low-carbon, particularly for applications such as slabs and foundations where post-cracking behaviour is critical. Remaining challenges include controlling variability, extending validation to a wider range of strength classes and structural conditions, and facilitating integration into design standards and practices. Nevertheless, the proposed approach provides a technically viable and scalable solution for advancing low-carbon, high-performance structural concrete.

5 Acknowledgements

The Author acknowledges the support provided by ArcelorMittal in funding this work.

6 References

CEN – EN14651:2005+A1- "Test Method for metallic fibre concrete – Measuring the flexural tensile strength (limit of proportionality (LOP), residual)", September 2007.ACI 544 6R-15

Tiberti, G., Germano, F., Mudadu, A., Plizzari, G., "An overview of the flexural post–cracking behavior of steel fibre reinforced concrete*, Structural Concrete 19 (2018) 695–718.

Ruiz, G., De La Rosa, A., Wolf, S., Poveda, S., "Model for the compressive stress-strain relationship of steel fibre-reinforced concrete for non-linear structural analysis", Hormigón y Acero 69-Suppl. 1 (2018) 75–80.

Wolf, S., Ruiz, G., De La Rosa, A., Poveda, E., Schäfer, M., Zanon, R., 2023 "Ductility in compression of SFRC and its use with low CO_2 emissions green steel fibres", *Proceedings of the ACI-fib-RILEM International Workshop 2023*, Tempe, Arizona, USA

Parmentier B., Van Itterbeeck P., Skowron A. "The flexural behaviour of SFRC flat slabs: the Limelette full-scale experiments for supporting design model codes". *FRC 2014 Joint ACI-fib International Workshop Fibre Reinforced Concrete: from Design to Structural Applications, Montreal, Canada; 2014*

fib, 2012. Model Code 2010, Bulletin 65, Fédération Internationale du Béton, Lausanne

Concrete Society – Technical Report TR34 4th Edition "Concrete industrial ground floors – a guide to design and construction" 2013 – amended March 2016.

CEN, EuroCode 2, Design of concrete structures. Part 1-1: General rules — Rules for buildings, bridges and civil structures, prEN 1992-1-1: 2022, version of November 10, 2022, available at CEN websites (2022).

EPD-ArcelorMittal Fibres – Steel Fibres Low Emissions (2023)

Flooring Brochure. ArcelorMittal Fibres

K.L. Scrivener et al., Calcined clay limestone cements (LC3), 2018, Cement and Concrete Research, 114, 49–56, 10.1016/j.cemconres.2017.08.017

S. Bishnoi, K.L. Scrivener, Impacting factors and properties of limestone calcined clay cement (LC3), 2019, Cement and Concrete Research, 121, 1–14, 10.1016/j.cemconres.2019.03.014

K.L. Scrivener et al., The interfacial transition zone (ITZ) between cement paste and aggregate in concrete, 2004, Interface Science, 12(4), 411–421, 10.1023/B:INTS.0000042339.92990.4c

E. Denarié, E. Brühwiler, Structural behavior of fiber-reinforced concrete beams under bending, 2006, Engineering Structures, 28(10), 1450–1460, 10.1016/j.engstruct.2005.12.002

E. Denarié, E. Brühwiler, Structural response of SFRC slabs on grade, 2011, Engineering Structures, 33(2), 547–555, 10.1016/j.engstruct.2010.11.012

Mechanical Performance of Recycled PET Fibre-reinforced Concrete

Muhammad Ali[1], Olivia Mirza[1], Christophe Camille[1], Fidelis Mashiri[1]

[1] : School of Engineering, Design and Built Environment, Western Sydney University, Sydney, Australia.

Abstract

Plastic waste, particularly discarded bottles, poses a significant environmental threat worldwide, affecting both terrestrial and aquatic ecosystems. Among these, non-biodegradable plastics such as polyethylene terephthalate (PET) are especially problematic. Reusing and recycling plastic waste presents an effective strategy to mitigate its environmental impact, particularly non-biodegradable plastics like PET. This study explores the use of shredded recycled PET fibre in concrete. A 24 mm length of PET fibre is incorporated in concrete with varying fibre volume fractions (V_f) of 0%, 0.2%, 0.4%, and 0.6%, to investigate the fresh and hardened properties of concrete. A total of 44 specimens were cast and tested to assess their compressive strength, split tensile strength, flexural behaviour, and peak load capacity under bending. The results indicated a significant improvement in concrete performance due to the enhancement of compressive and tensile strengths. In addition, the inherent hardness and plastic nature of PET fibres provided effective flexural properties by acting as a bridging mechanism within the concrete matrix, promoting uniform dispersion. This study highlights the dual benefits of incorporating recycled PET fibres in concrete: enhancing mechanical performance and advancing sustainable construction practices by reducing plastic waste and supporting a circular economy.

Keywords

Recycling, plastic waste, PET fibre, fibre-reinforced concrete, mechanical performance

1 Introduction

Concrete is the most widely used construction material, primarily due to its excellent compressive strength, high durability (Patil & Shukla 2017). However, its inherently low tensile strength, brittle behaviour, and less resistance to cracking constrain its structural efficiency. The inclusion of short discrete fibres enhances the mechanical properties of hardened concrete, particularly by improving its crack resistance (Blanco, A et al. 2016; Pujadas et al. 2012). Fibre reinforcement contributes to increased residual tensile strength and helps to control crack propagation by transferring the stresses across the crack planes (Blanco, Ana et al. 2013; Pujadas et al. 2014). This enhancement is primarily influenced by the number of fibres intersecting the crack, fibre distribution within the matrix, and the quality of the fibre-matrix bond (Pujadas et al. 2014).

Researchers have proposed the use of plastic waste material to reinforce the concrete, forming fibre-reinforced concrete (FRC). The potential of plastic fibres to enhance the concrete's durability and improve its pre- and post-cracking properties has increasingly drawn the attention of researchers (Blanco, Ana et al. 2013; Camille 2021; Camille et al. 2022; Camille et al. 2021; Camille et al. 2024; López-Carreño et al. 2017; Pujadas et al. 2014). Plastics are non-biodegradable materials that persist in the environment and may take 100 to 1000 years to decompose in landfills (Galloway 2008). The annual plastic waste generation has been recorded as 31.5 million tons in the USA (Gu & Ozbakkaloglu 2016), 6.7 million tons in the Asian region (Kim et al. 2010), 4.7 million tons in the UK (Siddique, Khatib & Kaur 2008) and 2.6 million tons in Australia (Joe et al. 2022). The global recycling rate of plastic remains very low. It was reported that 6.4 billion tons of plastic waste were produced globally from 1950 to 2017, of which only 9% was recycled or reused, 12% was incinerated, and the majority of plastic waste 79% was either dumped or sent to landfills (Ali et al. 2025). Therefore, a significant push exists to utilise this plastic waste to form new products rather than in landfills.

PET fibres are derived from plastic drinking bottles and offer high durability, low cost and a favourable strength-to-weight ratio, making them widely applicable in the construction industry and various other engineering applications (Orset, Barret & Lemaire 2017). Marthong and Sarma (2016) reported an increase of up to 24% in the compressive strength of concrete with 0.5% PET fibre inclusion, compared to reference concrete. Al-Hadithi, AI, Noaman and Mosleh (2019) reported that the compressive strength of self-compacting concrete can increase by up to 45% with a 1.5% V_f of PET fibres due to better confinement to concrete with a 35 mm length of fibres. In contrast, Khalid et al. (2018) and de Oliveira and Castro-Gomes (2011) reported negligible changes in the compressive strength of PET fibre concrete, compared to control specimens without PET fibre, due to the large length of the PET fibre causing bulging and failing to resist the stress within the concrete matrix. However, some studies have observed a detrimental impact on the compressive strength of PET fibre-reinforced concrete. Alani, A et al. (2019) reported a 1-2.6% decline in compressive strength of PET fibre-reinforced concrete compared to the control specimens. Similarly, Borg, Baldacchino and Ferrara (2016) observed an 8.6% reduction in compressive strength with a 1.5% addition of straight PET fibre. Kim et al. (2010) also reported a similar reduction of about 9% with a lower PET fibre volume of 1%. In general, the reduction of compressive strength can be attributed to the poor distribution of PET fibres within the concrete mix with a high-volume fraction of PET fibres of more than 1%, leading to inadequate consolidation of the concrete mix.

Alani, AH et al. (2022) investigated the flexural properties of PET fibre concrete and concluded that flexural strength increased by 18% with the use of high aspect ratio PET fibres at a 1% *Vf*. Borg, Baldacchino and Ferrara (2016) also observed an increase of approximately 20% with the addition of 1% shredded PET fibres. Pelisser et al. (2012) observed an increase of over 18% with a lower PET fibre content than 1%. The addition of PET fibres in concrete acts as a reinforcement that provides a path to transfer the stress through the crack surface (Kim et al. 2010). The inclusion of PET fibres in concrete significantly influences its mechanical performance, depending on the *Vf* and fibre size. However, further research is needed to determine the optimal ratio of PET fibres that provides the most effective performance for engineering applications in the construction industry, which forms the basis of this study. Therefore, this study was conducted to evaluate the effectiveness of 24 mm long PET fibres at varying *Vf* to reinforce the concrete, which is effective in improving the mechanical properties of concrete for civil engineering applications.

2 Experimental program

A locally available ordinary Portland cement (OPC) was used in this study. Crushed blue metal aggregates with a maximum size of less than 10 mm, and well-graded coarse sand were used to prepare the concrete mixes. The PET fibres were obtained from recycled PET drinking bottles and extruded to a length of 24 mm and a diameter of 0.3 mm, as shown in Fig. 1, and possessed a tensile strength of 950 ± 10 MPa, an elastic modulus of 12 ± 2 GPa, and a density of 1.38–1.40 g/cm³.



Figure 1: Recycled PET fibres (24 mm length)

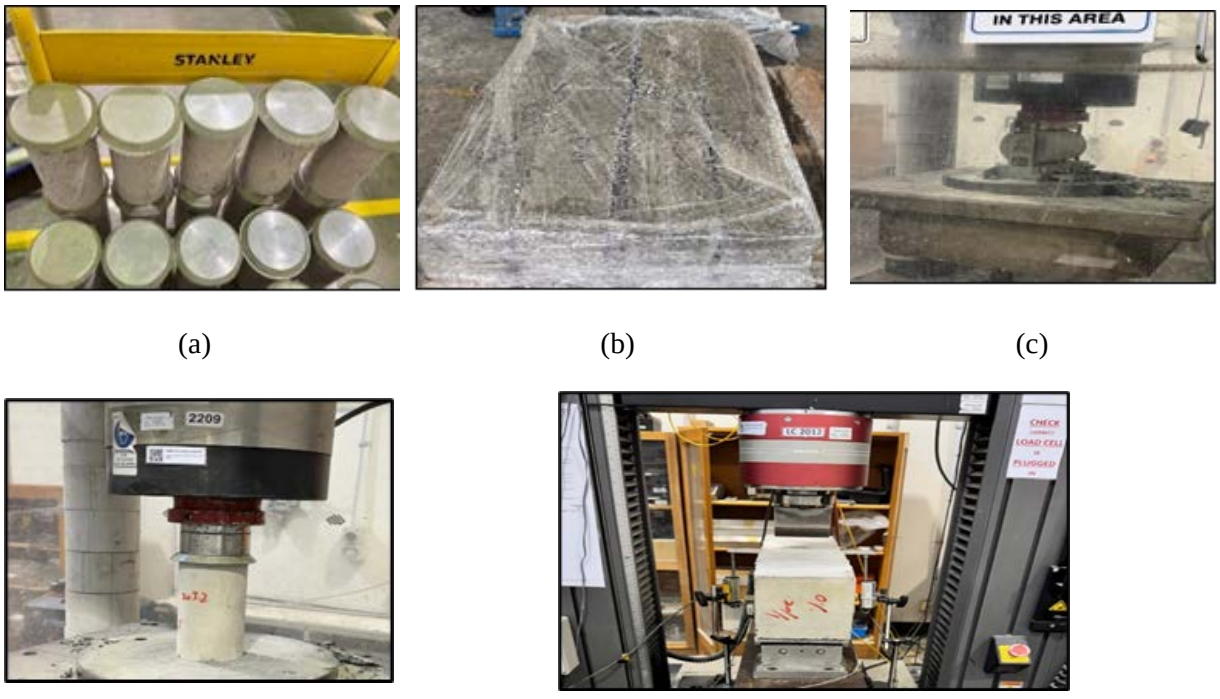
The concrete mix designed in this study corresponds to M35-grade concrete, which denotes a characteristic 28-day compressive strength of 35 MPa. Four concrete mixes were prepared using a concrete mix ratio: cement 1: sand 1.5: aggregate 3.0, with a water-to-cement ratio (w/c) of 0.38. Additionally, a high-range water reducer (HRWR) was added at a dosage of 3.33 L/m^3 to maintain the workability of fresh concrete mixes. Four different PET fibre ratios, 0%, 0.2%, 0.4%, and 0.6%, were used to reinforce the concrete. The details of each concrete mix are presented in Table 1.

Table 1: Mix design for 35 MPa concrete mix used in all trials

Mix ID	**Mix proportions (kg/m^3)**			**PET fibre dosage (%)**	**rPET fibre content (kg/m^3)**
	Cement	Sand	Aggregates		
M-1	418	627	1255	0	0
M-2				0.2	2.5
M-3				0.4	5.0
M-4				0.6	7.5

A total of 36 specimens were prepared to evaluate the compressive, splitting tensile, and flexural properties of PET fibre-reinforced concrete, as presented in Fig. 2(a) and (b). The fresh and hardened concrete properties were evaluated in accordance with relevant Australian and European standards. The slump test was conducted following AS1012.3.1 (2014), while compressive and splitting tensile strengths were determined in accordance with AS1012.9 (2014) and AS1012.10 (2000), respectively. For compressive strength testing, three cylindrical specimens (Ø100 mm × 200 mm) were tested for each mixture after capping the specimen ends to ensure smooth loading surfaces, as shown in Fig. 2(a). The splitting tensile strength was evaluated using three cylindrical specimens for each mixture, as presented in Fig. 2(c) and (d).

Flexural strength was evaluated using 12 notched beam specimens (150 mm × 150 mm × 575 mm) subjected to three-point bending over a span length of 525 mm at a displacement-controlled loading rate of 0.08 mm/min, as shown in Fig. 2(e). A 25 mm deep notch was introduced at the beam mid-span to promote controlled crack initiation. The beam geometry and loading configuration were based on EN14651 (2005). The flexural strength was calculated using the following formula: $f_r = PL/2bh_{sp}^2$, where (f_r) is the flexural strength (MPa), (P) is the peak load (N), (L) is the span length (mm), (b) is the specimen width (mm), and (h_{sp}) is the specimen depth above the notch (mm). All specimens were cured in a water tank at room temperature (27 ± 5°C) for 7 days and subsequently wrapped in plastic until testing at 28 days, as shown in Fig. 2(b). Three specimens were tested for each concrete mix, and the average values are reported in Section 3.



(a) (b) (c)

(d) (e)

Figure 2: Preparation and testing of PET fibre-reinforced concrete specimens (a) capping of cylinders for compressive strength test, (b) beams rapping after 7-days of water curing, (c) tensile strength testing, (d) compressive strength testing, (e) flexural strength testing on notched beams

3 Results and Discussion

3.1 Slump test

The incorporation of PET fibres led to a reduction in the workability of concrete mixes at all fibre dosages, as presented in Fig. 3. A slight decrease of approximately 9% was observed with the inclusion of a lower PET ratio of 0.2% PET fibres. However, further increasing the amount of PET fibres resulted in a workability reduction of 24% and 31%, with 0.4% and 0.6% additions of PET fibres in fresh concrete, respectively. The reduction in slump values is primarily attributed to the addition of PET fibres in concrete, which increases the internal friction within the concrete mix (Irwan et al. 2013). As the fibre content increased, fibre interaction became more pronounced, restricting the mobility of aggregates and reducing the flowability of the fresh concrete. This reduction in workability may also contribute to fibre clustering and reduced matrix homogeneity at higher fibre dosages, which can adversely affect the mechanical performance of hardened concrete.

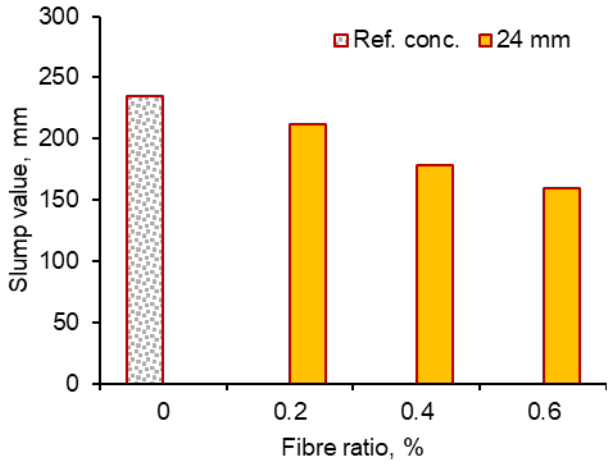


Figure 3: Slump values of fresh concrete with PET fibres

3.2 Compressive strength

Three cylindrical specimens were tested for each ratio, and the average values of compressive strength of PET fibre concrete are illustrated in Fig. 4. The incorporation of PET fibres at *Vf* between 0.2% and 0.6% led to an overall improvement in the compressive strength of concrete. The optimal performance can be seen at 0.2% dosage of PET fibre, which improves the compressive strength by about 31%, compared to the control concrete without PET fibre. However, increasing the amount of PET fibre by 0.4% and 0.6% resulted in a decreasing trend, which still demonstrated 21% and 17% improvement in the compressive strength of concrete, respectively, compared to the control specimens. Thus, the optimum percentage was found at 0.2% *Vf* of PET fibres. The improvement in compressive strength may be attributed to the ability of the PET fibres to restrain the initiation and propagation of microcracks within the cementitious matrix, thereby delaying crack coalescence under compressive loading. At this dosage, the fibres were sufficiently dispersed, providing effective crack restraint without adversely affecting matrix homogeneity. The reduction in compressive strength observed at higher fibre dosages may be attributed to increased fibre interaction and reduced workability, which can promote fibre clustering and increase the likelihood of entrapped air voids within the concrete matrix.

The incorporation of PET fibres changed the failure pattern of the concrete specimens, as shown in Fig. 5. PET fibre-reinforced concrete exhibited a more ductile response and a smaller number of vertical surface cracks compared with the control specimens, which failed predominantly in shear, as shown in Fig. 2. This indicates that PET fibres contribute to a more controlled failure mode under compressive loading.

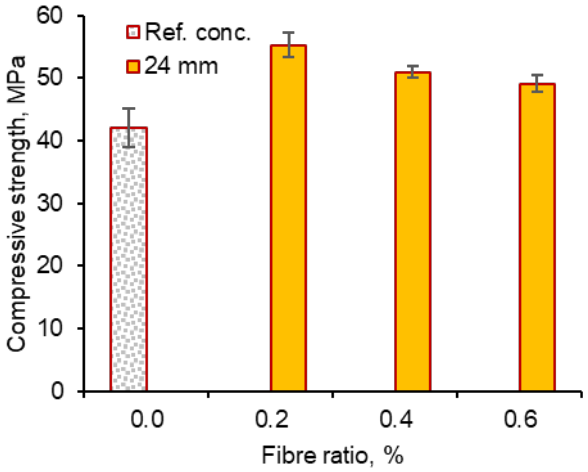


Figure 4: Compressive strength of PET fibre-reinforced concrete



Figure 5: Failure mode of concrete cylindrical specimens

3.3 Tensile strength

Three cylindrical specimens were tested at 28 days for each PET fibre dosage, and the average tensile strength values are illustrated in Fig. 6. The tensile strength of concrete improved with the addition of PET fibres ranging from 0.2-0.6% *Vf*. A significant improvement can be observed at 0.2% and 0.4% dosage of PET fibre, which increases the tensile strength by about 32% and 20%, respectively, compared to the control concrete without PET fibre. However, increasing the amount of PET fibre by 0.6% resulted in a reduction of the tensile strength of concrete, which is about 7%, compared to the control specimens. Thus, the optimum percentages were found at 0.2% of 24 mm PET fibres. The improvement in tensile strength may be attributed to the ability of PET fibres to bridge developing cracks and delay crack propagation, thereby enhancing the load-carrying capacity of the concrete after crack initiation (Kim et al. 2010). At higher fibre dosages, fibre

clustering, reduced workability, and increased entrapped air voids may have reduced reinforcement efficiency, resulting in lower tensile strength gains.

The incorporation of PET fibres altered the failure mode of tensile specimens, as shown in Fig. 7. The plain concrete failed into two separate pieces, whereas the PET fibre-reinforced concrete exhibited multiple surface cracks and formed fibre bridges across the crack planes.

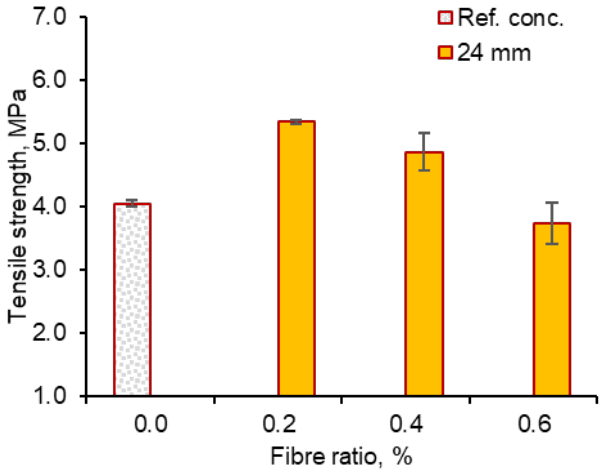


Figure 6: Tensile strength of PET fibre-reinforced concrete



Figure 7: Failure mode of the tested split tensile strength concrete

3.4 Flexural strength

Fig. 8 shows the average values of flexural strength of PET fibre-reinforced concrete at 28 days. The incorporation of PET fibres at dosages between 0.2% and 0.6% resulted in only marginal changes in flexural strength. The optimum performance was observed at 0.2% dosage of PET fibre, which increases the flexural strength by about 4%, as compared to the reference concrete without PET fibre. However, increasing the amount of PET fibre by 0.4% and 0.6% resulted in a reduction of the flexural strength of concrete by 8% and 11%, respectively, compared to the reference concrete beam specimens. Thus, the optimum percentages were found at 0.2% of 24 mm PET fibres.

The flexural strength of hardened concrete is improved with the low addition of PET fibre due to the development of a better bond and bridge mechanism, which prevents crack propagation within the concrete (Al-Hadithi, A, Abdulrahman & Al-Rawi 2020; Nkomo,

Masu & Nziu 2022). The relatively small improvement observed in flexural strength suggests that the fibres contributed primarily to crack control rather than increasing the peak load-carrying capacity of the concrete. At higher fibre contents, reduced workability, increased fibre interaction, and potential fibre clustering may have reduced the effectiveness of fibre reinforcement, resulting in lower flexural performance.

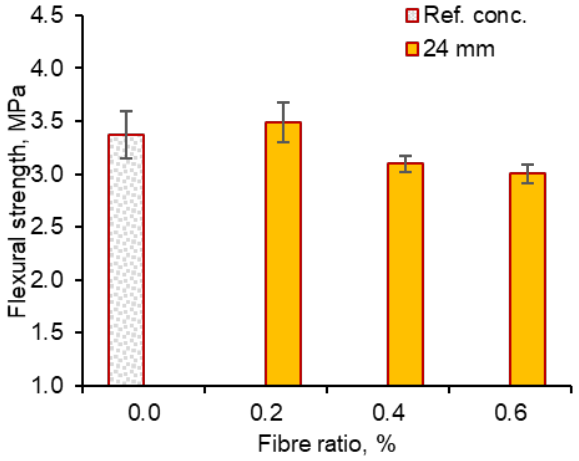


Figure 8: Flexural strength of PET fibre-reinforced concrete

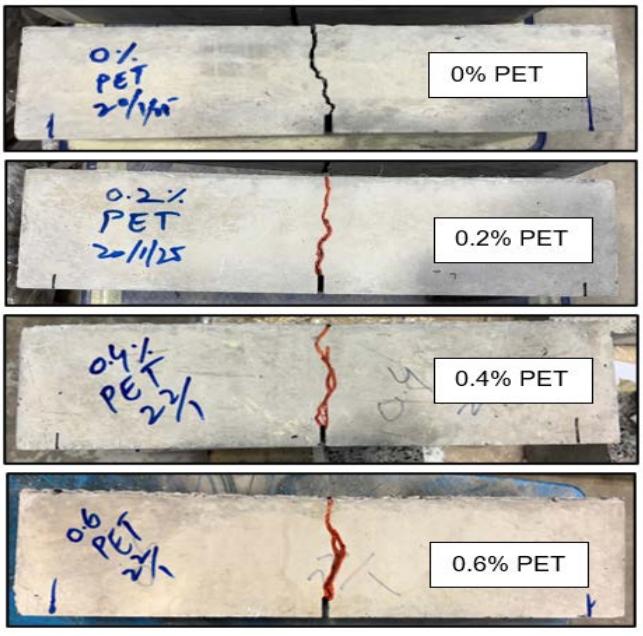


Figure 9: Failure pattern of flexural strength beams

The crack pattern of flexural beam specimens is shown in Fig. 9. The control beam specimens exhibited sudden and brittle failure at 0.79mm crack width, characterised by cracks throughout the specimens. In contrast, the PET fibre-reinforced concrete beams demonstrated fibre bridge behaviour, which enabled stresses to be transferred across developing cracks and delayed crack propagation before failure. Thus, the incorporation of PET fibres enhanced the post-cracking behaviour of concrete, allowing crack widths of up to 3mm to be sustained. However, the ultimate flexural strength of PET fibre-reinforced concrete did not improve significantly, which may be attributed to fibre pulled-out occurring before the full tensile

capacity of the fibres was utilized, as shown in Fig. 10. Similar observations have been reported by De Silva and Prasanthan (2019), who found that longer PET fibres were more effective in improving crack-bridging performance and post-cracking behaviour.

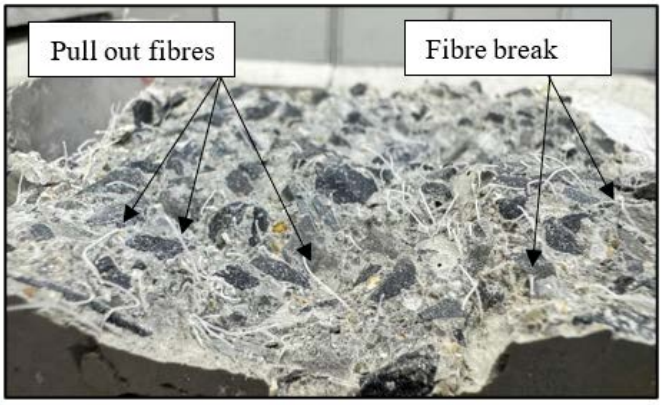


Figure 10: Pull out of fibres from the concrete after failure

4 Conclusions

For civil engineering applications, it is essential to understand the behaviour of plastic fibres. The mechanical properties of concrete serve as a key indicator for assessing the effectiveness of PET fibre reinforcement before its application in the construction industry. Based on the experimental research, the following conclusions were drawn.

- The workability of concrete decreases with the inclusion of PET fibres by 0.2-0.6%, due to internal friction between the constituents of concrete.
- A minor decrease in workability (~9%) is observed at 0.2%, whilst a more pronounced reduction (~31%) occurs at 0.6%.
- PET fibre length of 24 mm demonstrated to be more effective at 0.2% and 0.4% dosages in improving the compressive and tensile strength of concrete.
- The compressive strength of concrete improved by 31% with 0.2% PET fibre but decreased with increasing the amount of PET fibre.
- The tensile strength of concrete improved by 32% with a lower PET fibre ratio of 0.2%, but decreased with higher fibre content.
- A lower PET fibre ratio of 0.2% improves the flexural strength of concrete, while a higher PET fibre content is better for enhancing the pre-cracking behaviour of concrete.

5 Recommendations

Future research should focus on optimising fibre dispersion and workability at higher fibre dosages and investigating the influence of fibre geometry on the pre- and post-cracking behaviour of concrete. Comparative studies with steel fibre-reinforced concrete are also recommended to evaluate the structural applicability of PET fibres.

6 Acknowledgements

The authors would like to thank Western Sydney University for providing financial support

through the RTP scholarship and CSF funds, as well as the structural lab staff at WSU.

7 References

Al-Hadithi, A, Abdulrahman, M & Al-Rawi, M 2020, 'Flexural behaviour of reinforced concrete beams containing waste plastic fibers', IOP Publishing, vol. 737, no. 1, p. 012173.

Al-Hadithi, AI, Noaman, AT & Mosleh, WK 2019, 'Mechanical properties and impact behavior of PET fiber reinforced self-compacting concrete (SCC)', *Composite structures*, vol. 224, DOI doi:10.1016/j.compstruct.2019.111021.

Alani, A, Bunnori, N, Noaman, A & Majid, T 2019, 'Durability performance of a novel ultra-high-performance PET green concrete (UHPPGC)', *Construction and Building Materials*, vol. 209, pp. 395-405, DOI doi:10.1016/j.conbuildmat.2019.03.088.

Alani, AH, Bunnori, NM, Noaman, AT & Majid, T 2022, 'Mechanical characteristics of PET fibre-reinforced green ultra-high performance composite concrete', *EUROPEAN JOURNAL OF ENVIRONMENTAL AND CIVIL ENGINEERING*, vol. 26, no. 7, pp. 2797-818.

Ali, M, Mirza, O, Camille, C & Mashiri, F 2025, 'Incorporation of recycled PET fibre as a reinforcement in structural and Non-Structural concrete: A systematic literature review', *Innovative Infrastructure Solutions*, vol. 10, no. 12, p. 578.

AS1012.3.1 2014, *2014 Methods of testing concrete, Slump test*, Standards Australia, Sydney.

AS1012.9 2014, *Methods of testing concrete, Compressive strength of concrete specimens*, Standards Australia, Sydney.

AS1012.10 2000, *Methods of testing concrete, Determination of indirect tensile strength of concrete specimens*, Standards Australia, Sydney.

Blanco, A, Pujadas, P, De la Fuente, A, Cavalaro, S & Aguado, A 2013, 'Application of constitutive models in European codes to RC–FRC', *Construction and Building Materials*, vol. 40, pp. 246-59.

Blanco, A, Pujadas, P, De la Fuente, A, Cavalaro, S & Aguado, A 2016, 'Influence of the type of fiber on the structural response and design of FRC slabs', *Journal of Structural Engineering*, vol. 142, no. 9, p. 04016054.

Borg, R, Baldacchino, O & Ferrara, L 2016, 'Early age performance and mechanical characteristics of recycled PET fibre reinforced concrete', *Construction and Building Materials*, vol. 108, pp. 29-47, DOI doi:10.1016/j.conbuildmat.2016.01.029.

Camille, C 2021, *Feasibility study on macro synthetic fibre reinforced concrete for sleeper applications*, Western Sydney University.

Camille, C, Hewage, DK, Mirza, O & Clarke, T 2022, 'Full-scale static and single impact testing of prestressed concrete sleepers reinforced with macro synthetic fibres', *Transportation Engineering*, vol. 7, p. 100104.

Camille, C, Hewage, DK, Mirza, O, Mashiri, F, Kirkland, B & Clarke, T 2021, 'Performance behaviour of macro-synthetic fibre reinforced concrete subjected to static and dynamic loadings for sleeper applications', *Construction and Building Materials*, vol. 270, p. 121469.

Camille, C, Mirza, O, Kirkland, B & Clarke, T 2024, 'Numerical investigation of prestressed concrete sleepers reinforced with high-performance macro synthetic fibres', *Engineering Failure Analysis*, vol. 159, p. 108149.

de Oliveira, LAP & Castro-Gomes, JP 2011, 'Physical and mechanical behaviour of recycled PET fibre reinforced mortar', *Construction and Building Materials*, vol. 25, no. 4, pp. 1712-7.

De Silva, S & Prasanthan, T 2019, 'Application of recycled PET fibers for concrete floors', *Engineer*, vol. 52, no. 01, pp. 21-7.

EN14651 2005, *Test method for metallic fibre concrete – Measuring the flexural tensile strength (limit of proportionality, residual)*, European standards.

Galloway, T 2008, 'Plastic bottles and moral codes', *Marine pollution bulletin*, vol. 56, no. 2, pp. 163-5.

Gu, L & Ozbakkaloglu, T 2016, 'Use of recycled plastics in concrete: A critical review', *Waste management*, vol. 51, pp. 19-42, DOI doi:10.1016/j.wasman.2016.03.005.

Irwan, J, Asyraf, R, Othman, N, Koh, H, Annas, M & Faisal, S 2013, *The Mechanical. Properties of PET Fiber Reinforced Concrete From Recycled Bottle Wastes*, vol. 795, Univ Tun Hussien Onn Malaysia UTHM, Batu Pahat, Malaysia PU - Trans Tech Publications Ltd PI - Durnten-Zurich PA - Kreuzstrasse 10, 8635 Durnten-Zurich, Switzerland.

Joe, P, Christine, W, Kyle, OF, Lara, S, Piya, N, Sabrina, G et al. 2022, *National Waste Report 2022*, The Department of Climate Change, Energy, the Environment and Water; Blue Environment Pty Ltd.

Khalid, F, Irwan, J, Ibrahim, M, Othman, N & Shahidan, S 2018, 'Performance of plastic wastes in fiber-reinforced concrete beams', *Construction and Building Materials*, vol. 183, pp. 451-64, DOI doi:10.1016/j.conbuildmat.2018.06.122.

Kim, S, Yi, N, Kim, H, Kim, J & Song, Y 2010, 'Material and structural performance evaluation of recycled PET fiber reinforced concrete', *CEMENT & CONCRETE COMPOSITES*, vol. 32, no. 3, pp. 232-40, DOI doi:10.1016/j.cemconcomp.2009.11.002.

López-Carreño, R-D, Pujadas, P, Cavalaro, SH & Aguado, A 2017, 'Bond strength of whitetoppings and bonded overlays constructed with self-compacting high-performance concrete', *Construction and Building Materials*, vol. 153, pp. 835-45.

Marthong, C & Sarma, DK 2016, 'Influence of PET fiber geometry on the mechanical properties of concrete: An experimental investigation', *EUROPEAN JOURNAL OF ENVIRONMENTAL AND CIVIL ENGINEERING*, vol. 20, no. 7, pp. 771-84, DOI doi:10.1080/19648189.2015.1072112.

Nkomo, NZ, Masu, LM & Nziu, PK 2022, 'Effects of Polyethylene Terephthalate Fibre Reinforcement on Mechanical Properties of Concrete', *Advances in Materials Science and Engineering*, vol. 2022, DOI doi:10.1155/2022/4899298.

Orset, C, Barret, N & Lemaire, A 2017, 'How consumers of plastic water bottles are responding to environmental policies?', *Waste management*, vol. 61, pp. 13-27.

Patil, V & Shukla, V 2017, 'Use of PET fibre as constituent of concrete', *IJARIIE*, vol. 3, no. 2, pp. 280-4.

Pelisser, F, Montedo, O, Gleize, P & Roman, H 2012, 'Mechanical Properties of Recycled PET Fibers in Concrete', *MATERIALS RESEARCH-IBERO-AMERICAN JOURNAL OF MATERIALS*, vol. 15, no. 4, pp. 679-86, DOI doi:10.1590/S1516-14392012005000088.

Pujadas, P, Blanco, A, Cavalaro, S & Aguado, A 2014, 'Plastic fibres as the only reinforcement for flat suspended slabs: Experimental investigation and numerical simulation', *Construction and Building Materials*, vol. 57, pp. 92-104.

Pujadas, P, Blanco, A, De la Fuente, A & Aguado, A 2012, 'Cracking behavior of FRC slabs with traditional reinforcement', *Materials and Structures*, vol. 45, pp. 707-25.

Siddique, R, Khatib, J & Kaur, I 2008, 'Use of recycled plastic in concrete: A review', *Waste management*, vol. 28, no. 10, pp. 1835-52.

Effect of Residual Tensile Strength on Drying Shrinkage Cracking in Fiber Reinforced Concrete Pavements

Chidchanok Pleesudjai[1], Devansh Patel[2], Barzin Mobasher[3*]

[1] Graduate Research Assistant, School of Sustainable Engineering & the Built Env., Arizona State University, Tempe, AZ, 85281, USA, email: cpleesud@asu.edu

[2] Graduate Research Assistant, School of Sustainable Engineering & the Built Env., Arizona State University, Tempe, AZ, 85281, USA, email: dpatel52@asu.edu

[3] Professor, School of Sustainable Engineering & the Built Env., Arizona State University, Tempe, AZ, 85281, USA, email: barzin@asu.edu

Abstract

Drying shrinkage is a major contributor to early-age cracking in concrete elements subjected to restraint. In fiber reinforced concrete (FRC), discrete fibers provide post-cracking residual tensile strength that can significantly prevent crack development and influence stress redistribution. However, conventional shrinkage analysis methods do not explicitly account for the influence of residual tensile strength on cracking behavior. This paper presents a numerical simulation approach for evaluating drying shrinkage cracking in restrained plain concrete and FRC elements, consistent with the material characterization framework recommended in ACI 544. Time-dependent shrinkage strain is imposed as a prescribed deformation, and a section equilibrium analysis evaluates the curling moment of pavementthat develops with post-crack stress redistribution. The tensile behavior of FRC is represented by a quadrilinear stress-strain relationship derived from residual strength parameters obtained from ASTM C1609 testing. The simulation results highlight the role of retained residual tensile stress in mitigating shrinkage-induced damage, providing mechanistic insight into the benefits of FRC for crack control in restrained concrete elements. This proposed framework provides a mechanics-based tool for controlling shrinkage-induced cracking and supports performance-based design of FRC elements in accordance with ACI 544 provisions.

Keywords

drying shrinkage, rigid pavement, fiber reinforced concrete, curling moment, residual tensile strength

1 Introduction

In the United States, approximately 98% of pavements were surfaced with hot-mix asphalt (HMA), while concrete pavements accounted for only a small portion of the overall network (A. Williams et al., 2024). This distribution is mainly due to the higher initial construction cost of concrete. However, under specific traffic, climate, and maintenance conditions, concrete pavements may provide improved durability and life-cycle performance (Concrete Sustainability Hub, 2014). In rural or remote regions where access to bituminous materials is limited or where long-term durability is the primary design consideration, concrete pavements offer a practical and economical alternative. In recent years, the use of fiber-reinforced concrete (FRC) and conventional reinforced concrete incorporating with fibers (Hybrid RC) in roadway applications has become increasingly common to reduce pavement thickness or eliminate the need for traditional rebar reinforcement (Foliard et al., 2006; Ramakrishnan et al., 1990). The inclusion of fiber enhances first crack strength and significantly improves serviceability performance, while conventional reinforcement provides crack control and improves ductility (Pleesudjai et al., 2025).

Over the past several decades, rigid pavement design has evolved from purely empirical procedures to more advanced mechanistic-empirical approaches. Early design methods, such as the AASHTO 1993 Guide for Design of Pavement Structures (AASHTO, 1993), which were based on empirical correlations from the AASHO Road Test conducted in Ottawa, Illinois, from 1958 to 1960. Modern methodologies, including the Mechanistic-Empirical Pavement Design Guide (MEPDG), integrate structural mechanics with calibrated performance models that account for traffic loading, climatic conditions, and material behavior. However, despite these advancements, the MEPDG does not explicitly account for material post-crack behavior, stress redistribution, or the effective modulus of the composite when considering the combined behavior of concrete, rebar, and fiber as a single material system. As a result, the sequence of crack initiation, propagation, and stress redistribution in concrete is not adequately represented in the current MEPDG framework.

Drying shrinkage in a concrete pavement is not uniform through the slab depth, because the exposed surface loses moisture faster than the protected interior. The surface contracts more than the bottom, so the slab tends to curl and lift at its edges. When this curling is restrained by the slab self weight, by the dowels at the transverse joints, and by the friction of the subbase, the differential shrinkage is converted into an internal bending moment through the depth, in addition to the in-plane tension that the average shrinkage produces. Both actions drive early-age cracking and reduce serviceability. The residual tensile strength of FRC is central to this response, because it lets the cracked section keep carrying tension across the crack and sustain the curling moment rather than shedding it.

This study presents a potential methodology for the early-age response of concrete pavements under drying shrinkage. The differential shrinkage through the slab depth is restrained and analyzed by a section equilibrium method that resolves the curling bending moment about its neutral axis. The average shrinkage also produces an in-plane restrained tension, the companion mechanism presented alongside the curling response in the sections that follow. The curling moment and the in-plane tension act on the same slab, and combining them into a single coupled analysis is identified as the next step.

2 Material Characterization by Inverse Analysis

For a restrained pavement slab the governing limit state is serviceability rather than ultimate capacity. Differential drying shrinkage through the slab depth produces curling and restrained-shrinkage stress, and the resulting crack width and joint spacing control long term performance. These serviceability quantities are governed by the post-crack tensile response of the material, that is the stress the section retains after first cracking and the way that stress redistributes as cracking develops. A characterization that captures the full post-crack response, rather than a single residual value, is therefore required for pavement design.

The post-crack tensile capacity of fiber reinforced concrete (FRC) is characterized in practice by residual strength indices measured in a standard flexural test. The four-point bending test defined in ASTM C1609 reports the residual flexural strength at several deflection levels, namely L/600 and L/150, together with the first-crack strength and the flexural toughness (ASTM C1609/C1609M, 2019). For the standard 450 mm span, these deflection levels correspond to 0.75 mm and 3.0 mm. For ultimate limit state design, ACI 544.4R-18 converts the residual flexural strength at L/150, denoted $f_{D,150}$, to an equivalent residual tensile stress through a single fixed factor of 0.37 (ACI Committee 544.4R-18, 2018). The fib Model Code ("Fib Model Code for Concrete Structures (2020)," 2024) similarly classifies the material by the residual strengths measured in standardized bending.

The 0.37 factor is an average relationship valid only at the L/150 deflection under the standardized configuration. Back-calculation of 525 ASTM C1609 beam tests shows that the ratio of equivalent tensile stress to residual flexural strength is not constant (Patel et al., 2025). It decreases from 0.50 in the elastic range to between 0.33 and 0.35 in the stabilized post-cracking regime, as the neutral axis migrates toward the tension face. A single residual value therefore collapses a stress distribution that evolves from a triangular elastic profile at first crack to a quasi-uniform residual block at large crack openings. It cannot represent the strain, the curvature, or the crack width at the intermediate states that govern serviceability. The same index is measured under one specimen geometry and one boundary condition. The peak load and post-cracking response of a member that differs in depth, span-to-depth ratio, or support condition are therefore not captured by that single value.

The full tensile stress-strain response is recovered instead by inverse analysis of the measured load-deflection record. The procedure fits a closed-form moment-curvature solution to the experimental beam response and returns the complete tensile envelope that reproduces it (Pleesudjai et al., n.d.; Soranakom & Mobasher, 2008). The recovered response is represented by a quadrilinear tensile stress-strain model, with a linear elastic branch to first cracking followed by three post-crack branches that capture the residual stress carried by fiber bridging. Figure 1(b) presents the back-calculated tensile response for the tested groups. The measured responses fall into two categories defined by their post-crack behavior. The lower bound group, denoted #2A, exhibits deflection-softening, in which the residual stress decays after first cracking. The upper bound group, denoted #2B, exhibits deflection-hardening, in which the section sustains stress above the first-crack level. The compressive response is taken as equivalent for plain concrete and FRC, because the fiber dosages considered do not materially change compressive strength. The complete back-calculated quadrilinear envelope is the constitutive input carried into the shrinkage and curling analysis in the sections that follow.

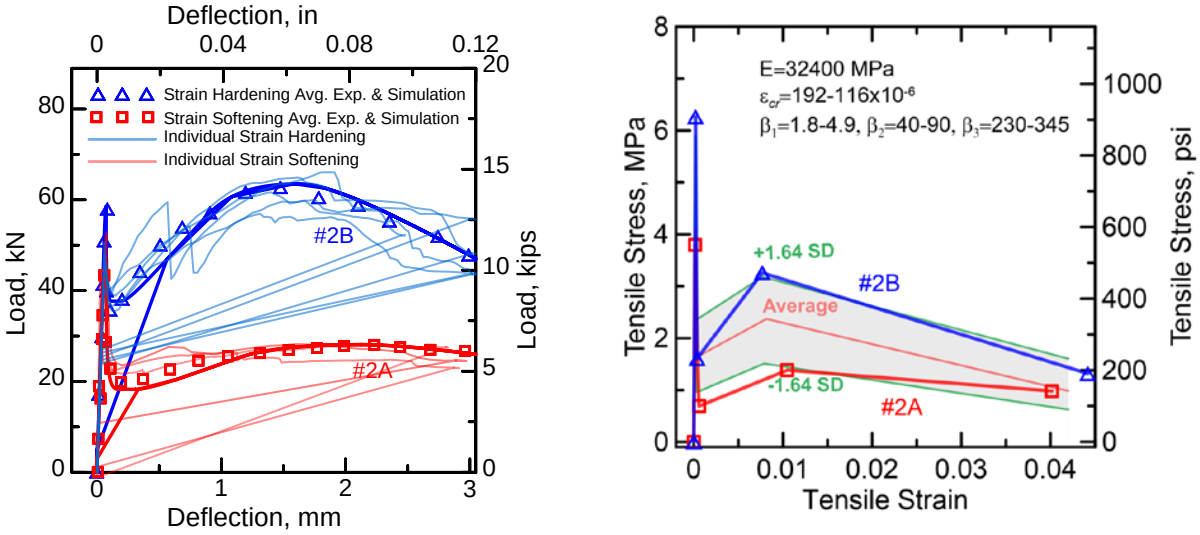


Figure 1: Results categorization based on deflection softening and hardening responses (a) Two sample groups of ASTM C1609 test at 28 days, (b) The corresponding tensile stress-strain by inverse analysis results (Patel et al., 2025).

3 Drying Shrinkage in Concrete Element

Drying shrinkage is the time-dependent volume contraction of hardened concrete caused by the loss of moisture from the capillary pore system to the surrounding environment under drying exposure. Under restrained conditions, tensile stress builds up and results in cracking once the tensile strength of concrete is reached. This volume change is driven by moisture transport through the cementitious matrix and is commonly modeled as a diffusion-controlled process.

3.1. Drying Shrinkage Strain

The free-shrinkage strain is expressed as a function of the internal humidity profile through the slab thickness. The humidity profile follows the error-function solution of Fick diffusion given in Eq. (3), and the free-shrinkage strain at each depth is related to it through the cubic function in Eq. (1). The time-dependent free-shrinkage strain in Eq. (1) is the product of the ultimate shrinkage strain and a time-development function. The ultimate shrinkage strain follows an empirical relationship for drying at infinite time, and the time development follows the ACI 209R-92 formulation given in Eq. (2), where *t* is the time after the end of initial moist curing in days.

Bakhshi and Mobasher (Bakhshi & Mobasher, 2011) performed free-shrinkage tests according to ASTM C157-04 on plain concrete and on glass FRC (see Figure 2). They found that the measured free-shrinkage development can be represented by a modified ACI 209R model. The ACI 209R formulation recommends a value of 35 days for *f* and an exponent of 1.0 for the time function. Fitting the measured curves gave the calibrated parameters of 28 days for *f* and 1.5 for the exponent, together with a best-fit ultimate shrinkage that decreases with fiber content, from 2160 microstrain for the plain control to 1836 microstrain at the highest glass fiber dosage. These calibrated parameters are what allow the ACI 209 model to represent the difference in free shrinkage between plain concrete and FRC.

Free shrinkage strains of about 400 to 900 microstrain have been reported across various materials and conditions, and average strains of 200 to 500 microstrain are used for shrinkage modelling (Destrée et al., 2016). For the present pavement analysis, an ultimate shrinkage strain of 500 microstrain is adopted, which falls within these reported ranges.

$$\varepsilon_{sh}(z,t) = \varepsilon_{sh}(t)\left[1 - h(z)^3\right] \tag{1}$$

$$\varepsilon_{sh}(t) = \varepsilon_{sh,ult}\left(\frac{t}{35+t}\right) \tag{2}$$

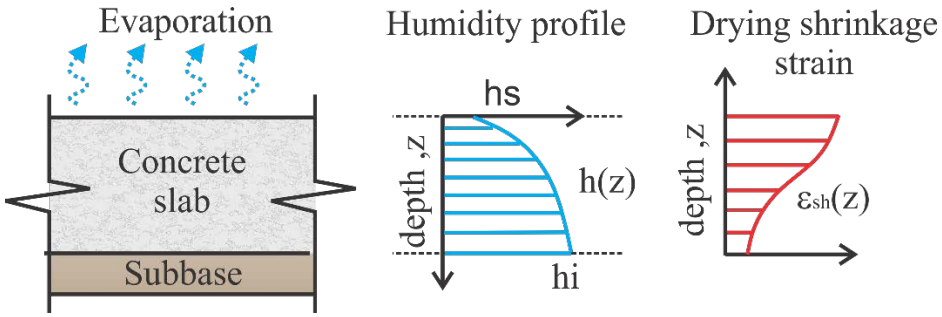


Figure 2: Humidity profile and corresponding drying shrinkage strain along pavement depth

When the internal relative humidity profile h(z) from the moist interior toward the drying surface of a concrete is simplified to follow the Fick's law of diffusion as in Eq. (3). In this equation, h_s is the humidity at the exposed surface, h_i is the higher humidity deep inside the material, and *erf(z)* is the mathematical error function (Tuma, 1970) that arises as the solution to Fick's law of diffusion. Because moisture moves through concrete primarily by diffusion, the error-function shape provides a realistic representation of the gradual transition from dry conditions at the surface to wet conditions inside. When *z* is small (near the surface), *erf(z)* is small, and the humidity remains close to h_s. As *z* increases by means of moving inward, *erf(z)* approaches 1, therefore the humidity approaches the interior value h_i.

$$h(z) = h_s - (h_s - h_i)erf(z) \tag{3}$$

The through-depth drying shrinkage strain from 14 to 365 days computed from Eq. (1) to Eq. (3) is presented in Figure 3, with the humidity differential set by the exposed surface RHs = 50 percent and the protected bottom in contact with the subbase RHi = 95 percent. The surface shrinkage exceeds the bottom shrinkage, therefore the free shrinkage varies through the depth and the section carries both an average contraction and a through-depth gradient. These two parts act through two different restraints, and the slab cannot move in both ways at once, so the two restraint conditions are shown separately in the two panels of Figure 3.

Figure 3(a) is the fully restrained condition. The slab is held in plane by friction with the subbase and by continuity with the adjacent sections, so it cannot shorten, and the full free shrinkage strain is restrained and converted into tension. The solid lines are the restrained strain at each age and the dashed lines are the depth average from Eq. (4), which reaches 134 microstrain at 28 days, 217 microstrain at 90 days, and 275 microstrain at 365 days. This average is largest at the drying surface, and it is the in-plane restraint that drives the transverse cracking, the companion in-plane mechanism to the curling analyzed in Section 4. These

average values are of the same order as the early age shrinkage range of 50 to 200 microstrain reported for rigid pavements (Nam et al., 2006; Wells et al., 2006).

$$\overline{\varepsilon_R}(z,t) = \frac{1}{h}\int \varepsilon_{sh}(z,t)dz \tag{4}$$

Figure 3(b) is the axial free condition solved with the section equilibrium for the FRC, the same neutral-axis solver used in Section 4. The transverse joint is free to shorten, so the average contraction is relieved by axial movement and the stress producing mechanical strain is the free shrinkage measured from this relief. The mechanical strain is tension near the drying surface and compression near the bottom and crosses zero at the neutral axis. Before the surface cracks this neutral axis is the elastic location at 75.4 mm, and the fiber reinforced section holds it near mid-depth at 76.4 mm at 365 days because the residual law keeps the cracked surface band carrying tension. This mechanical strain is the part that bends the section and generates the curling moment analyzed in Section 4. The same free shrinkage field therefore produces two distinct responses, an in-plane tension set by the average that drives cracking and a curling bending set by the gradient that drives the moment, and the two panels make the difference between the restraint conditions explicit. The same free shrinkage strain is applied to the plain and FRC. Fiber can modestly reduce the free shrinkage magnitude through internal restraint, on the order of 10%-15% for the low dosage glass fiber concrete measured by Bakhshi and Mobasher (Bakhshi & Mobasher, 2011), but this reduction is specific to the fiber system and is conservatively neglected here.

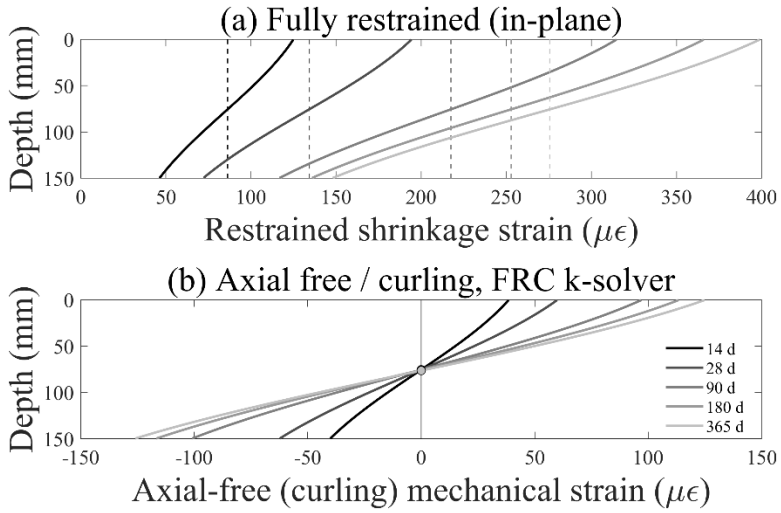


Figure 3: Drying shrinkage strain through the 150 mm pavement thickness at five ages (14, 28, 90, 180, 365 days); (a) the fully restrained in-plane strain, (b) the axial free curling mechanical strain.

3.2. Drying Shrinkage Stress

The fully restrained in-plane stress of Figure 3(a) builds an average tension whose depth average follows Eq. (5). This average, together with the average strain of Eq. (4), is the in-plane restraint that drives the transverse cracking, the companion in-plane mechanism whose coupling with the curling response is left to future work. The remainder of this subsection treats the axial free curling stress that sets up Section 4.

The concrete properties are an elastic modulus of 24,855 MPa, a compressive strength of 27.5 MPa, and a tensile strength of 2.49 MPa, with first cracking when the tensile strain reaches the cracking strain of 100 microstrain. The FRC tensile response is the quadrilinear law of Figure 4, which follows the linear segment approach recommended in (ACI Committee 544.4R-18, 2018) and is characterized in (Pleesudjai, 2021; Pleesudjai et al., 2023), and the plain concrete loses its tensile capacity at cracking. Figure 5 shows the axial free curling response through the 150 mm thickness from 14 to 365 days, the mechanical strain in the top row and the stress in the bottom row, with plain concrete in the left column and FRC in the right column. The strain is tension at the drying surface and compression at the bottom, and crosses zero at the neutral axis, and the stress follows the strain through the constitutive law.

Before the curling surface crack at 105 days the plain and fiber reinforced sections are identical and elastic, with the neutral axis at mid-depth at 75.4 mm. After 105 days the surface cracks. In the plain section the cracked surface band loses all tensile stress, the cracked depth reaches 39 mm at 365 days, and the neutral axis migrates downward to 92.6 mm. In the FRC the fibers bridge the crack and retain a residual stress that reaches 2.4 MPa at the surface at 365 days, the cracked depth reaches only 19.5 mm, and the neutral axis stays near mid-depth at 76.4 mm. The axial free curling stress carries no net axial force, so its depth average is zero and its first moment about the neutral axis is the curling moment developed in Section 4. The residual stress retained in the fiber reinforced cracked band, and the neutral axis that stays near mid-depth, are the reason the fiber reinforced section sustains the larger curling moment.

$$\overline{\sigma_R}(z,t) = \frac{1}{h}\int \sigma_{sh}(z,t)dz \tag{5}$$

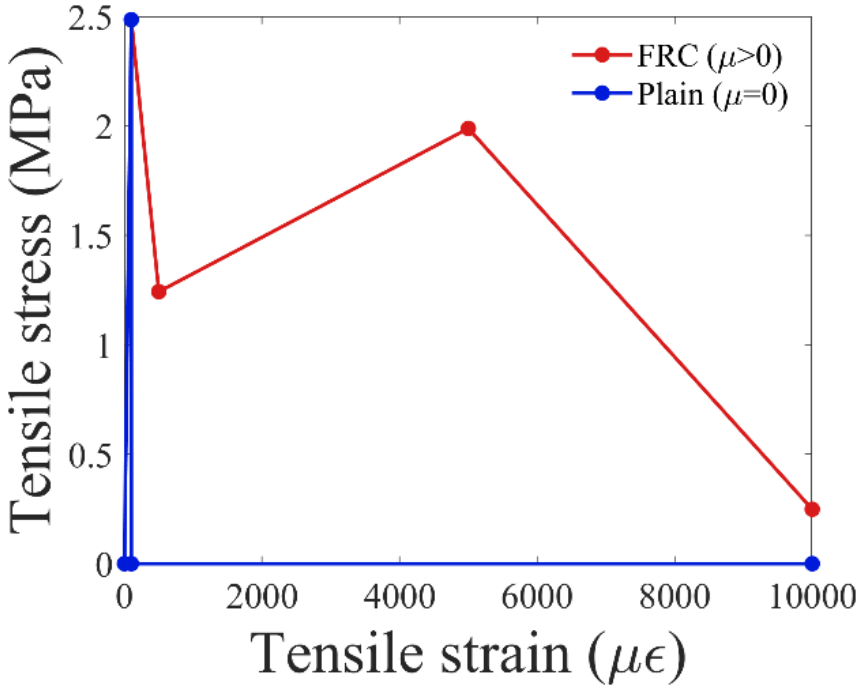


Figure 4: Quadrilinear tensile stress-strain model

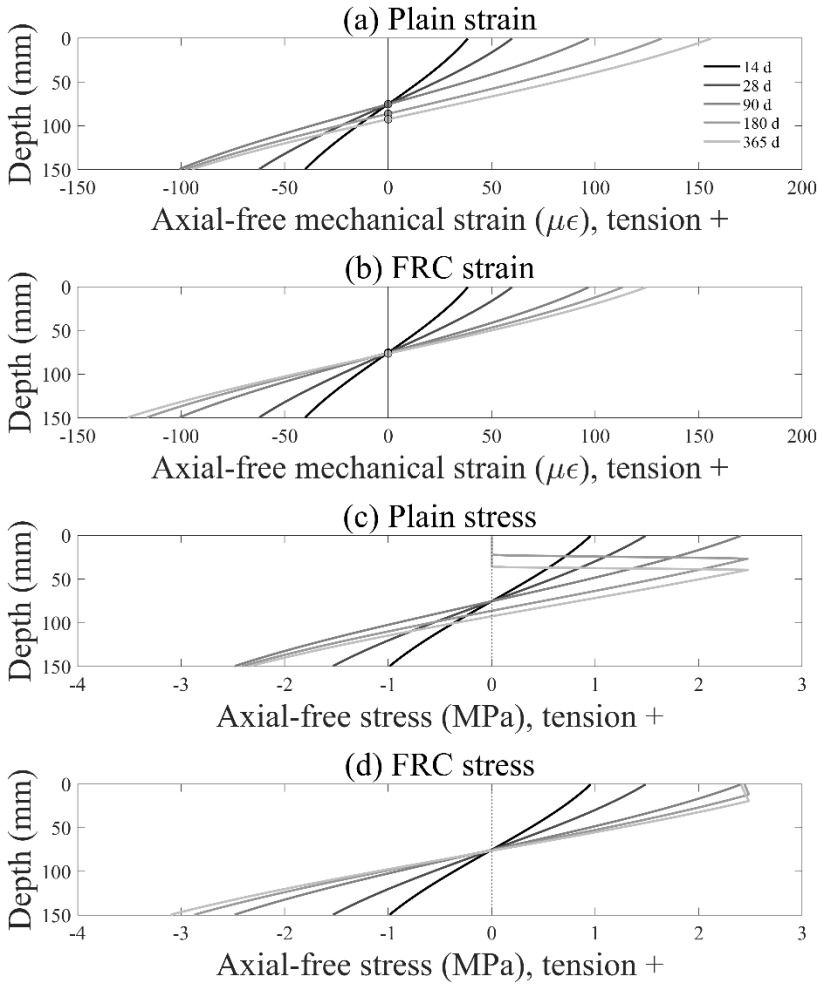


Figure 5: Axial free curling response through the 150 mm thickness at five ages (14, 28, 90, 180, 365 days).

4 Moment Generation from Curling in Pavement Section

Drying shrinkage develops faster at the exposed surface than in the protected interior, which makes the free shrinkage strain vary through the slab depth as described by Eq. (1). A slab that is free to deform would curl and lift at its edges because the surface contracts more than the bottom. At a doweled transverse joint the dowel restrains the vertical movement between adjacent slabs and holds the section against curling, while the joint remains free to open in the plane of the slab. Under this restraint condition the differential shrinkage is converted into an internal bending moment that the section carries about its neutral axis. The restraint is therefore axial free and curvature restrained, the joint opens in plane, the net axial force is zero, and the curling curvature is held to zero. Figure 6 illustrates this curling moment, the slab curling under the drying gradient while the dowel restrains the curl, which generates the bending moment carried about the neutral axis.

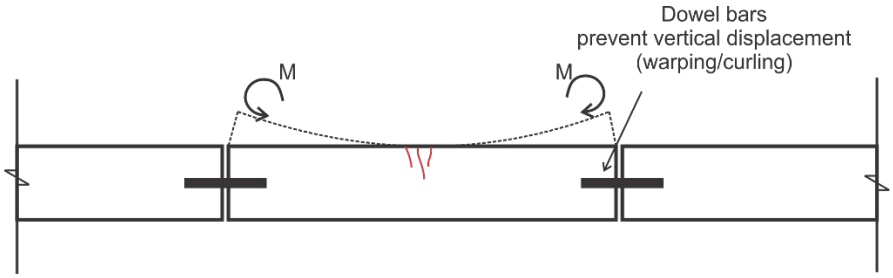


Figure 6: Curling moment generated by differential shrinkage in a pavement section.

This axial-free curling is evaluated by a plane-section analysis of the cross-section. Plane sections remain plane, and the total strain through the depth is the sum of a uniform strain and a curvature term. Because the dowel holds the curvature to zero, the total strain reduces to the uniform value ε_0, and the stress producing mechanical strain at each depth is the total strain minus the free shrinkage eigenstrain as given in Eq. (6).

$$\varepsilon_{mech}(z) = \varepsilon_0 - \varepsilon_{sh}(z) \tag{6}$$

Each layer stress follows the full multilinear constitutive law, the elastic branch below the cracking strain and the post-crack branch above it, written as $\sigma(z) = f_t G\left(\varepsilon_{mech}(z)/\varepsilon_{cr}\right)$ where G is the normalized stress-strain function. The uniform strain ε_0 is solved from the condition of zero net axial force in Eq. (7), the joint being free to shorten.

$$N = b\int_0^h \sigma(z)dz = 0 \tag{7}$$

The neutral axis is the depth z_{na} where the mechanical strain changes sign, $\varepsilon_{mech}(z_{na}) = 0$ and the developed moment is the first moment of the layer stress about this axis as given in Eq. (8). This layer stress is the curling stress distribution presented in Figure 5, and the developed moment is therefore the first moment of that distribution about the neutral axis.

$$M = b\int_0^h \sigma(z)(z - z_{aa})dz \tag{8}$$

Before cracking the neutral axis sits at the section mid depth and the moment is the elastic curling moment. Once the surface stress exceeds the cracking strength the tension and compression stiffness differ, the neutral axis leaves the mid depth, and the moment is recomputed from equilibrium at every drying step. This neutral axis formulation replaces the bottom surface pivot used in the earlier work, which fixed the lever arm at the full slab depth and therefore overstated the moment.

The section was evaluated for the pavement material defined in Section 3, with elastic modulus E = 24855 MPa, tensile strength ft = 2.49 MPa, and cracking strain ε_{cr} =100 microstrain, over a slab thickness of 150 mm, with the free shrinkage growing in time through Eq. (2). Figure 7(a) presents the developed curling moment about the real neutral axis over one year for the plain and the fiber reinforced sections. The two responses are identical until the surface reaches the cracking strain at 105 days, where the moment magnitude is 10091 N mm per mm width. After this point the two materials diverge. In the plain section the cracked surface band loses all tensile stress, the neutral axis migrates downward from the mid depth to a ratio k = z_{na}/h = 0.617, and the moment magnitude falls to 5304 N mm per mm at 365 days, a reduction of 47 percent from the value at first crack. In the fiber reinforced section the fibers bridge the

crack and sustain a residual stress, the neutral axis remains near the mid depth at k = 0.509, and the moment magnitude continues to grow to 11849 N mm per mm at 365 days. The fiber reinforced section carries 2.23 times the curling moment of the plain section at one year.

Figure 7(b) presents the neutral axis location through the depth over the same period. The two sections share a neutral axis at the mid depth, z_{na} = 75.4 mm, until first cracking, after which the plain neutral axis descends to 92.6 mm while the fiber reinforced neutral axis holds at 76.4 mm. The plain neutral axis migrates because the cracked face loses tension and the resisting area shifts toward the bottom. The fiber reinforced neutral axis barely moves because the bridged crack keeps the tension block active on the drying face.

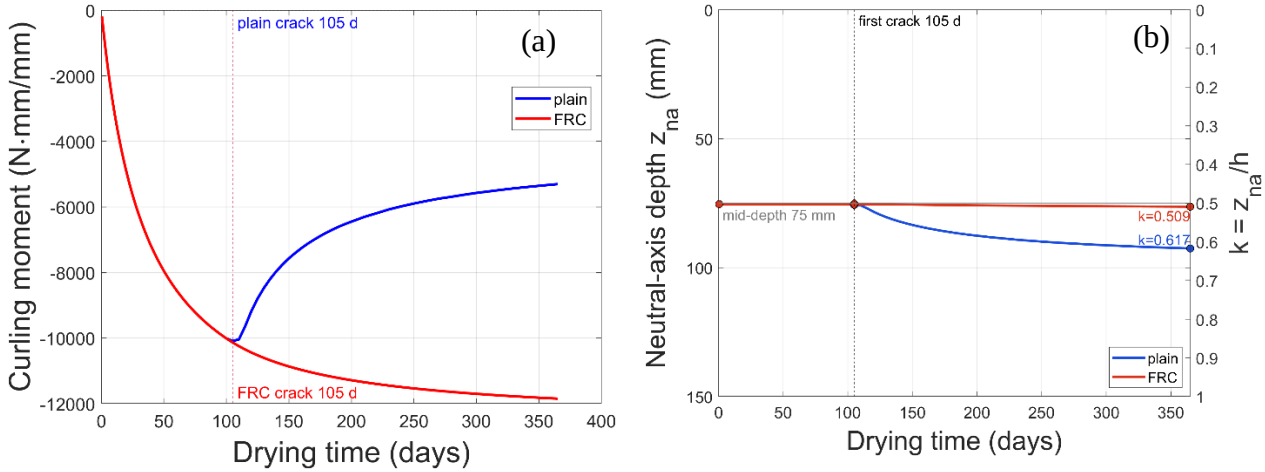


Figure 7: Curling response over one year for plain and FRC under the axial free curling condition; (a) developed moment about the real neutral axis, (b) neutral-axis depth migration.

5 Conclusions

A neutral-axis section method was developed for the curling moment that drying shrinkage generates through the depth of a concrete pavement, with the section carrying the bending about a neutral axis solved from equilibrium.

The benefit of the retained residual moment is the preservation of flexural continuity across the shrinkage crack. The plain section behaves as a hinge once the surface cracks, it sheds the curling moment by opening a crack that reaches 39 mm while the neutral axis drops toward the compression face. The fiber reinforced section keeps the crack shallow at 19.5 mm and tight through fiber bridging, and it continues to act as a continuous flexural member that transfers the moment across the crack. This retained continuity carries three practical consequences. First, the shallower and tighter crack limits the ingress of moisture and chloride, which protects the subbase and any embedded reinforcement and improves long term durability. Second, the retained section stiffness reduces the curling deflection at the slab edges and corners, which lowers the corner and edge stresses that combine with wheel loads and extends the fatigue life. Third, the retained post crack moment capacity indicates a potential for reduced slab thickness and longer joint spacing at equal serviceability, consistent with field reports of improved performance in fiber reinforced pavements. The benefit is realized only after cracking, because both sections reach first crack at the same 105 days.

6 References

A. Williams, B., Willis, R., & Shacat, J. (2024). *Asphalt Pavement Industry Survey on Recycled Materials and Warm-Mix Asphalt Usage: 2022*.

AASHTO. (1993). *AASHTO Guide for Design of Pavement Structures*.

ACI Committee 544.4R-18. (2018). Guide for Design with Fiber-Reinforced Concrete. In *American Concrete Institute*.

ASTM C1609/C1609M. (2019). Standard Test Method for Flexural Performance of Fiber-Reinforced Concrete (Using Beam With Third-Point Loading). In *ASTM International*.

Bakhshi, M., & Mobasher, B. (2011). Experimental observations of early-age drying of Portland cement paste under low-pressure conditions. *Cement and Concrete Composites*, *33*(4), 474–484. https://doi.org/10.1016/j.cemconcomp.2011.01.009

Concrete Sustainability Hub. (2014). *Supplementary Information for Comparative Pavement Life Cycle Assessment and Life Cycle Cost Analysis* (Issue July 2014).

Destrée, X., Yao, Y., Mobasher, B., & Asce, M. (2016). *Sequential Cracking aTheir Openings in Steel-Fiber-Reinforced Joint-Free Concrete Slabs*. *28*(4), 1–11. https://doi.org/10.1061/(ASCE)MT.1943-5533.0001377

fib Model Code for Concrete Structures (2020). (2024). In *Structural Concrete* (2024th ed.). International Federation of Structural Concrete (fib).

Foliard, K., Sutfin, D., Turner, R., & Whitney, D. P. (2006). *Use of Fibers in Concrete Pavement*. *7*. www.ntis.gov

Nam, J., Kim, S., & Won, M. C. (2006). Measurement and Analysis of Early-Age Environmental Loading. *Journal of the Transportation Research Board, No. 1947*, 79–90.

Patel, D., Pleesudjai, C., Bakhshi, M., Nasri, V., & Mobasher, B. (2025). Back-calculation of mechanical properties of fiber-reinforced concrete in tunnel lining segments. *Structural Concrete*. https://doi.org/10.1002/suco.70052

Pleesudjai, C. (2021). *Generalized modeling and Experimental Validation of Flexural Response in Cement Based Composites*. Arizona State University.

Pleesudjai, C., Oliveira, C. A. S., Araujo, D. L., Patel, D., de Andrade, M. A. S., Filho, R. T., & Mobasher, B. (2025). Efficiency of hybrid reinforced concrete beams with low reinforcement ratios. *Materials and Structures*, *58*(6), 218. https://doi.org/10.1617/s11527-025-02736-4

Pleesudjai, C., Patel, D. D., & Mobasher, B. (n.d.). *Analytical Solutions for Serviceability Based Flexural Design of Hybrid Reinforced Concrete*.

Pleesudjai, C., Patel, D. D., & Mobasher, B. (2023). Generalized Nonlinear Moment–Curvature Model for Serviceability-Based Design of Hybrid Reinforced Concrete. *Journal of Structural Engineering*, *149*(12). https://doi.org/10.1061/JSENDH.STENG-12235

Ramakrishnan, V., Balaguru, P., Kostaneski, L., & Johnston, D. (1990). *Field performance of fiber reinforced concrete highway pavements* (Issue April).

Soranakom, C., & Mobasher, B. (2008). Correlation of tensile and flexural responses of strain softening and strain hardening cement composites. *Cement and Concrete Composites*, *30*(6), 465–477. https://doi.org/10.1016/j.cemconcomp.2008.01.007

Tuma, J. J. (1970). *Engineering mathematics handbook* (McGraw-Hill (ed.)). McGraw-Hill.

Wells, S. A., Phillips, B. M., & Vandenbossche, J. M. (2006). Characterizing strain induced by environmental loads in jointed plain concrete pavements: Immediately after paving and throughout first 10 months. *Transportation Research Record*, *1947*, 36–48. https://doi.org/10.3141/1947-04

Modeling the compressive behavior and cracking process of plain concrete (PC) and fiber reinforced concrete (FRC)

Pierre Rossi[1]

[1]: Civil Engineering Department, COPPE, Federal University of Rio de Janeiro, Brazil.

Abstract

This paper investigates the complex cracking process of plain concrete (PC) and fiber reinforced concrete (FRC) under compression. It outlines a six-step mechanism describing crack evolution, highlighting the role of heterogeneity, Poisson's effect, and friction. The study also analyzes the impact of boundary conditions on the experimental compressive behavior related to these materials. Probabilistic Semi-Explicit Cracking models for PC (PSEC) and FRC ($PSEC^f$) are proposed to capture the distinct behaviors observed in compression and more especially the oblique cracks creation**.**

Keywords

Concrete, Fiber-Reinforced Concrete, Compression, Cracking Process, Boundary Conditions, Probabilistic Models, Finite Element Modeling

1 Introduction

The compressive behavior of concrete, along with its Young's modulus, is a fundamental mechanical property. Compressive strength has long been standardized and is widely used in both design codes and nonlinear finite element modeling. However, the cracking behavior of plain concrete (PC), and particularly fiber reinforced concrete (FRC), is significantly more complex than typically assumed. This paper presents a detailed examination of this cracking process and introduces Probabilistic Semi-Explicit Cracking models for PC (PSEC) and FRC ($PSEC^f$). These models aim to analyze the propagation of macrocracks in structures subjected to predominantly compressive stresses. The present paper is based on a previous and more detailed paper (Rossi, 2025).

2 PC cracking process under compression

The cracking process of PC and FRC under compression has been the subject of very detailed descriptions in the past (Rossi, 1998; Rossi, 2023). It can be summarized as follows:

- **Step 1: Initiation and propagation of diffuse microcracking**

Tensile stresses, induced by Poisson's effect and the material's heterogeneity, lead to microcracks parallel to the loading direction. These small openings do not affect the specimen's elastic behavior.

- **Step 2: Formation of long vertical cracks**

Microcracks evolve into long vertical cracks, which segment the specimen into slender columns. Despite this segmentation, the material remains quasi-linear elastic due to the elastic behavior of these columns.

- **Step 3: Formation of oblique microcracks**

Irregular geometries and local bending within columns create oblique microcracks (due to local tensile stresses insides the columns). These remain small and do not significantly alter global mechanical behavior.

- **Step 4: Onset of oblique mesocrack propagation**

Microcracks coalesce into oblique mesocracks (always due to local tensiles stresses). Tangential displacements and resulting friction introduce non-linear strain and energy dissipation.

- **Step 5: Localization of an inclined macrocrack**

One mesocrack dominates, forming an inclined macrocrack. This process consumes energy through friction and corresponds to the peak load of the compression test.

- **Step 6: Propagation of the inclined macrocrack**

Macrocrack propagation defines post-peak behavior. Friction during sliding leads to less brittle response compared to tension. Visible vertical cracks propagation and opening result from tangential displacements (due to the inclined macrocrack propagation). It is important to specify that the propagation of the inclined macrocrack is governed by local tensile stresses (mode I propagation), because, in concrete, cracks creation and propagation are always governed by local tensile stresses (due to the high material heterogeneity).

If standard compression tests are concerned, it can be pointed out that the test results are influenced by the boundary conditions.

Frictional restraint at the specimen-press interface can distort stress fields and increase shear near the ends. This leads to excessive mesocrack formation, increased confinement, and artificially elevated compressive strength and ductility. This point was experimentally studied and demonstrated in the past (Torrenti et al, 1991; Torrenti et al, 1993). Such artifacts must be carefully considered to avoid overestimating concrete performance.

Fibers act by bridging active cracks with mode I or II displacements. Their effectiveness begins at Step 5 of the cracking process and is most pronounced during Step 6. Under ideal conditions, fibers enhance post-peak behavior but do not significantly raise compressive strength. However, in the presence of boundary condition artifacts, the apparent contribution of fibers is exaggerated due to increased crack formation near platens.

3 Modeling the compressive behavior: existing approaches

However, if the findings from previous chapters are considered, several important observations emerge (Rossi, 1998; Rossi, 2023): (1) the post-peak behavior is not an intrinsic material property, but rather a structural one; (2) the boundary conditions imposed by experimental setups related to standard compression test tend to overestimate both the compressive strength and the ductility of concrete; (3) only the quasi-linear elastic portion of the experimental stress-strain curve, obtained from a compression test influenced by boundary effects, can be reliably considered as an intrinsic material property.

The issue lies in the fact that most compression tests used to characterize the compressive behavior of concrete, particularly the standard tests, are affected by the boundary conditions. As a result, the current methods for modeling compressive behavior are highly questionable.

Two main modeling approaches are commonly found in the literature:

- Analytical formulations in design codes (e.g., Eurocode 2)
- Finite element models

The first approach is based on the well-established concept of cracked section equilibrium. In this case, a simplified model curve is arbitrarily derived from the experimental curve, incorporating safety factors that significantly underestimate the compressive response observed in tests. Consequently, up to the peak load, this standard approach can generally be considered conservative.

The second category includes smeared cracking models and damage models (Mazars, 1984; Rots et al, 1985; Pijaudier-Cabot and Bazant, 1987; Jirasek and Zimmermann, 1998; Bazant and Jirasek, 2002; Jirasek, 2011), which are more widely used in numerical simulations. These models typically rely on stress–strain laws calibrated directly from experimental data, including the post-peak portion of the curve. However, if the findings from previous chapters are considered, this method of fitting model parameters is fundamentally flawed, as it misrepresents the material's true behavior.

4 PSEC and PSEC^f numerical models

PSEC model

In this proposed model, macrocrack propagation is governed by two key criteria:

- Macrocrack initiation is associated with the uniaxial tensile strength f_t,
- Macrocrack propagation is governed by the mode I critical fracture energy G_{IC}, as defined in the well-known Linear Elastic Fracture Mechanics (LEFM) framework.

A macrocrack propagates when the entire G_{IC} is dissipated, and the crack is numerically represented as a sequence of fully damaged finite elements. The novelty of this approach lies in its use of volume elements, rather than singular elements typically employed in conventional LEFM-based numerical models. Therefore, the proposed model does not fall under the category of classical damage or smeared crack models.

In classical damage models, damaged zones are treated as physically real, and crack openings are derived from these zones. In contrast, the proposed model does not consider physically existing damaged zones. Instead, a damage parameter is introduced arbitrarily as a mechanism to dissipate G_{IC}, without representing a physically observable phenomenon.

The mechanical properties f_t and G_{IC} are treated as random variables that depend on the size of the mesh elements. Previous experimental and numerical studies (Rossi et al, 1994; Rita et al, 2024) have established and validated their probabilistic behavior. These properties are linked to the element heterogeneity ratio, r_e, defined by:

$$r_e = V_e/V_a \tag{1}$$

in which, V_a is the volume of the greatest aggregate size of concrete and V_e is the volume of the mesh element.

The probabilistic properties of f_t and G_{IC}, it means the mean value, μ, and σ, the standard deviation, are given by the following relations (Rita et al, 2024):

$$\mu(f_t(r_e)) = a(r_e)^{-y} \tag{2}$$

in which a = 6.5 MPa and y is given by Equation (3), where f_c represents the concrete compressive strength determined by performing a standard test on 160 x 320 mm cylinder specimen.

$$y = 0.25 - 3.6 \times 10^{-3}\, f_c/\alpha + 1.3 \times 10^{-5}\, (f_c/\alpha) \tag{3}$$

in which $\alpha = 1$

$$\sigma/\mu(f_t(r_e)) = c(r_e)^{-d} \tag{4}$$

In Equation (4), c = 0.35 and d is given by Equation (5), as follows:

$$d = 4.5 \times 10^{-2} + 4.5 \times 10^{-3} f_c/\alpha - 1.8 \times 10^{-5} (f_c/\alpha)^2 \tag{5}$$

$$\sigma(G_{IC}) = (A\, ln(r_e) + B) \times \mu(G_{IC}) \tag{6}$$

In Equation (5) A = - 8.538 and B = 70.88

$$\frac{\sigma}{\mu}\left(G_{IC}(r_e)\right) = A\left[\frac{1}{y}\ln\left(\frac{a\mu(f_t(r_e))}{\sigma(f_t(r_e))}\right) + \frac{B}{A}\right] \quad (7)$$

A schematic overview of the model is provided in Figure 1. The introduction of a damage parameter in the theoretical approach is arbitrary and serves solely as a method to dissipate G_{IC}. It means that, in the proposed model, there is no relation between the non-linear strain (softening branch of the stress-strain curve in tension) and real crack propagation.

Finally, it is important to point out that it has been demonstrated that the 3D probabilistic semi-explicit cracking model is mesh independent in static if $r_e > 1$ (Rita et al, 2024).

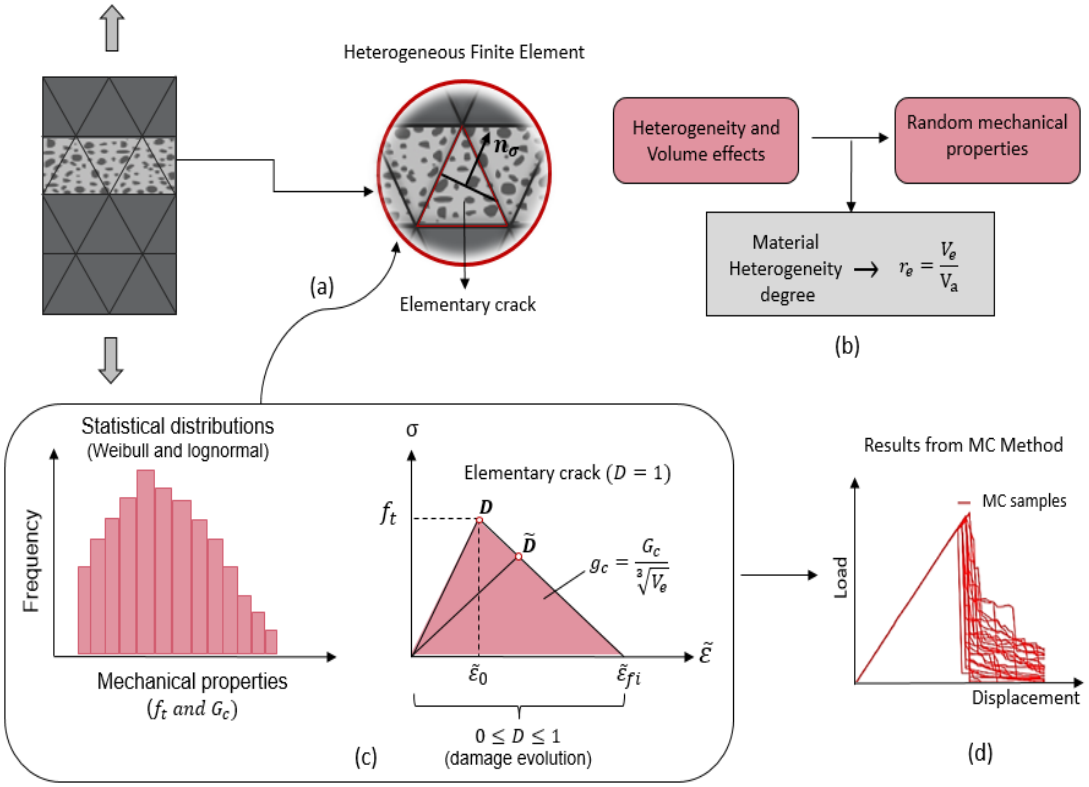


Figure 1: General aspects of the 3D probabilistic semi-explicit cracking model of concrete [15]

PSEC^f model

The basis of the PSEC^f model was initially introduced for the simulation of large-scale FRC structures under static loading conditions (Rossi, 2023). This model is specifically developed to simulate the propagation of macrocracks and is grounded in the uniaxial tensile behavior of FRCs. It applies only to FRCs that exhibit softening behavior in post-cracking uniaxial tension.

The primary aim of the PSEC^f model is to overcome a significant limitation of conventional distributed cracking models (Fanella and Krajcinovic, 1985; Li F. and Li Z., 2000; Peng X and Meyer C, 2000; Barros and Figueiras, 2001; De Montaignac et al, 2013), namely their tendency to generate overly dispersed crack patterns. This dispersion often leads to a substantial underestimation of dominant crack openings (Rossi, 2023). The PSEC^f model addresses this issue by simulating macrocrack initiation and propagation through linear volumetric finite elements. A crack is assumed to form when the tensile stress at an element's integration point

(there is only one point of integration in the finite tetrahedron element used, located at the centroid of the element) exceeds the matrix tensile strength (i.e., the tensile strength of the unreinforced concrete), under the assumption of a perfectly brittle matrix.

The matrix tensile strength is treated as a random variable that follows a Weibull distribution (as for the PSEC model), with its statistical properties depending on the volume of the finite element. As the element volume increases, both the mean and standard deviation of the tensile strength decrease, reflecting the size effect observed in quasi-brittle materials.

Experimental results (Rossi, 2012) indicate that the average post-cracking energy associated with fiber bridging is independent of the tested material volume, although its standard deviation decreases with increasing volume. To reflect this behavior and simplify implementation, the PSEC^f model treats the fiber bridging energy, denoted G_f, as a deterministic parameter, assumed to be independent of the finite element volume.

The model distinguishes two key mechanical stages (Figure 2):

- Macrocrack initiation, governed by the tensile strength of the matrix.
- The fiber bridging effect, which controls the post-crack energy dissipation.

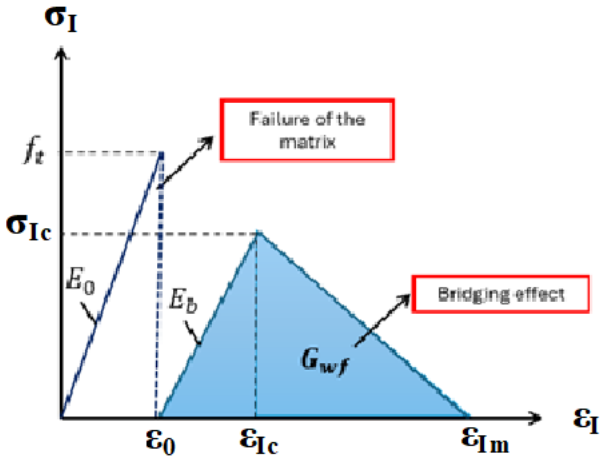


Figure 2: Aspects of the PSEC^f model for fiber-reinforced concrete – Mechanical behavior in uniaxial tension.

Crack initiation in the PSEC^f model occurs when the maximum principal tensile stress σ_I in a finite element reaches (at the center of gravity of the element) its tensile strength f_t. At this point, the element's stiffness undergoes a sharp reduction, indicating the onset of cracking. During the fiber bridging phase, as the maximum principal strain $\varepsilon_I$increases, the bridging mechanism becomes active. This results in an increase in effective stiffness E_b, though it remains below the original undamaged stiffness E_0. As crack opening continues and ε_I reaches a critical strain ε_{Ic}, the stress σ_I begins to decrease linearly with further strain, representing the fiber pullout process. When the strain reaches a maximum value ε_{Im}, the bridging effect of the fibers is considered negligible, and the element stiffness is reduced to zero.

This softening behavior is modeled through a simplified damage-based approach, wherein only the entries of the stiffness matrix associated with the direction of σ_I (i.e., the maximum principal stress-strain relation) are modified. All other matrix components remain unchanged.

As a result, the fiber bridging effect is treated as anisotropic, reflecting the directional nature of crack propagation.

A key advantage of this approach is the improved localization of cracks. Since the concrete matrix is assumed to behave as perfectly brittle, and its tensile strength is treated as a random variable, the model is able to represent crack initiation and propagation more realistically than smeared (diffuse) cracking models, which tend to artificially spread damage over large areas.

It is important to note that the PSEC^f model is not applicable to FRCs that exhibit hardening behavior in uniaxial tension.

In this model, the fiber bridging effect is only activated when the matrix is fully cracked. While this simplification may seem restrictive in light of the macroscopic response observed in direct tensile tests on notched specimens, it is deliberately chosen for physical consistency. In such tests, a softening response is observed, attributed to the propagation of a macrocrack and the gradual engagement of fibers across the cracked section. However, this macrocrack propagation phase does not reflect an intrinsic material property, but rather a structural effect, which depends on specimen geometry, particularly the cross-sectional area at the crack location (Rossi, 1998).

It is important to emphasize that, due to the probabilistic nature of both the PSEC and PSEC^f models, a Monte Carlo simulation procedure is essential to generate results that accurately capture the inherent variability in both model parameters and material properties. For a given structural configuration, the resulting ensemble of simulations enables statistically robust analyses**,** supporting reliability-based or safety-oriented assessments of structural performance.

One must finally point out that the PSEC model has been the subject of a numerical implementation validated by experimental results, whereas the PSEC^f model remains a proposed approach, for which numerical implementation and validation are yet to be carried out**.**

However, in their current formulations, the PSEC and PSEC^f models are limited to simulating crack propagation under predominantly tensile stress states. They do not account for cracking driven by compressive stresses, which is the primary focus of the present work. This limitation necessitates further model development, which is addressed in the following chapter.

5 PSEC and PSEC^f models for macrocracks propagation under predominant compressive stress

It is clear that the PSEC and PSEC^f models, which are macroscopic in nature, are neither intended nor capable of representing all the stages of the cracking process in concrete and fiber reinforced concrete described in Chapters II, III, and IV. However, it is important that they are able to account for the onset of the inclined macrocrack that leads to the ultimate compressive strength of concrete.

Although the initiation of this inclined macrocrack results from the presence of local tensile stresses at various scales within the compressive cracking process, it is essential that both models incorporate the initiation of this inclined macrocrack.

At the macroscopic scale of a finite element volume, this inclined crack can be interpreted as a shear crack. Therefore, introducing a shear-based criterion to initiate this inclined crack in concrete is a relevant and justified approach.

Referring to the Mohr-Coulomb failure criterion, it appears evident that the shear strength should be equal to $f_c/2$. This shear strength is thus treated as a deterministic parameter, in contrast to the tensile strength, which is considered a random variable dependent on the finite element volume. This choice of using a deterministic parameter is consistent with the cracking process of concrete under compression described in Chapter II. Unlike the tensile cracking process, the compressive cracking process is not governed by the presence of the weakest element, as suggested by Weibull's weakest link theory (Weibull, 1939; Weibull, 1951).

Consequently, both models incorporate two criteria for macrocrack initiation: a tensile criterion, and a shear criterion.

For the shear criterion, as with the tensile one, the model considers the maximum principal shear stress τ_I (always at the centroid of the finite element). The two initiation criteria are therefore expressed as:

$$\begin{cases} \sigma_I - f_t \geq 0 \; macrocrack\; initiation\; in\; tension \\ \tau_I - \frac{f_c}{2} \geq 0 \; macrocrack\; initiation\; in\; shear \end{cases} \quad (8)$$

Of course, it is possible for both criteria to be satisfied simultaneously within the same element. However, only one macrocrack should be initiated per element. Therefore, a selection rule must be applied to determine which criterion governs the crack initiation. One way to make this decision is to consider the dominant criterion, defined as follows:

$$\begin{cases} [(\sigma_I - f_t)/f_t] - [(\tau_I - 0.5\, f_c)/0.5\, f_c] \geq 0, \; tension\; is\; dominant \\ [(\sigma_I - f_t)/f_t] - \left[\frac{\tau_I - 0.5\, f_c}{0.5} f_c\right] \leq 0, \; shear\; is\; dominant \end{cases} \quad (9)$$

In the unlikely case where:

$$[(\sigma_I - f_t)/f_t] - \left[\frac{\tau_I - 0.5\, f_c}{0.5} f_c\right] = 0, \text{ the tensile criterion is selected} \quad (10)$$

If the macrocrack is initiated in shear, its evolution is linked to the maximum principal tensile stress. This choice, which is open to criticism, is guided by what the proposed model is able to represent of the compressive cracking process in concrete, as presented in Chapter 2.

In the case of the PSEC model, the propagation of the crack occurs in Mode I following the model behavior proposed in Figure 1.

In the case of the PSEC^f model, the propagation phase of the macrocrack is not considered, as the matrix is assumed to be elastic perfectly brittle. Only the bridging effect of the fibers is considered. The tensile stiffness of the fibers being significantly higher than their shear stiffness, only the bridging effect in tension is modeled (Figure 2).

It is important to clarify that this choice differs from that proposed in the previous article (Rossi, 2025). Indeed, in that previous article, it was proposed that, after its initial shear initiation, the evolution of the macrocrack is linked to the tensile stress perpendicular to the direction of the maximum principal shear stress.

The numerical implementations of both probabilistic models, as well as their experimental validation, remain to be carried out concerning the cracking behavior of PCs and FRCs.

6 Concluding remarks

This work focuses on the modeling of macrocrack propagation in Plain Concrete (PC) and Fiber Reinforced Concrete (FRC) structures when this propagation is governed by predominantly compressive stresses. The modeling is based on two probabilistic models: the PSEC model (for PC structures), which has already been numerically implemented and experimentally validated, and the PSEC^{f} model (for FRC structures), which is currently under numerical implementation and validation. In their current state, both probabilistic models only account for macrocrack propagation governed by predominantly tensile stresses. This paper presents, in detail, their planned extension to compressive stress-driven cracking. These extensions are grounded in a precise and comprehensive analysis of the compression-induced cracking process in PC and FRC.

7 References

Barros, J. and Figueiras, J.A, 2001. “Model for the analysis of steel fiber reinforced concrete slabs on grade”, *Computers & Structures* 79(1): 97- 106.

Bazant Z. and Jirasek M., 2002. “Nonlocal integral formulations of plasticity and damage: survey of progress”, *J Eng Mech* 128:1119-1149.

Casanova, P., Rossi, P., Analysis and design of steel fiber reinforced concrete beams. *ACI Structural Journal*, Vol. 94, No. 5, pp. 595-602, 1997.

Cunha, V., Barros, J., Sena-Cruz, J. A finite element model with discrete embedded elements for fiber reinforced composites. *Computers & Structures* 94-95: 22-33, 2012.

De Montaignac, R., Massicotte, B. and Charron, J-P., 2013. “Finite-element modelling of SFRC members in bending”, *Magazine of Concrete Research* 65(19): 1133-1146.

Fanella, D. and Krajcinovic, D., 1985. “Continuum damage mechanics of fiber reinforced concrete”, *J. Eng. Mech.* 111(8): 995-1009.

Jirasek, M. and Zimmermann T., 1998. “Rotating crack model with transition to scalar damage”, *Journal of engineering mechanics* 124(3):277–284.

Jirasek, M., 2011. “Damage and smeared crack models”, *G. Hofstetter, G. Meschke (Eds.), Numerical modeling of concrete cracking, Springer*, p. 1–49.

Li F. and Li Z., 2000. “Continuum damage mechanics-based modeling of fiber reinforced concrete in tension”, *Int J Solids Struct* 38: 777-793.

Mazars, J., 1984. “Application de la mécanique de l’endommagement au comportement non-linéaire et la rupture du béton de structure“, *Ph.D. thesis, Ecole Normale Supérieure de Cachan* (in french).

Peng X and Meyer C, 2000. “A continuum damage mechanics model for concrete reinforced with randomly distributed short fibers”, *Comput Struct* 78 : 505-515.

Pijaudier-Cabot, G., and Bazant, Z. P., 1987. “Nonlocal damage theory”, *J. Eng. Mech. ASCE*, 113: 1512–1533.

Rita, M.R, Rossi, P., Fairbairn, E.d.M and Ribeiro, F.L.B., 2024. “Determination of the Probabilistic Properties of the Critical Fracture Energy of Concrete Integrating Scale Effect Aspects”, *Appl. Sci. 2024,14, 462, https://doi.org/10.3390/app14010462*.

Rossi, P., Wu, X, Le Maou, F. and Belloc, A., 1994. “Scale effect on concrete in tension”, *Mater. Struct.* 27 437–444.

Rossi, P., 1998. “ Les bétons de fibres métalliques“, *Les presses de l’Ecole Nationale des Ponts et Chaussées* (in french).

Rossi P., 2012. “Experimental Study of Scaling Effect Related to Post- Cracking Behaviors of Metal Fibers Reinforced (MFRC)”, *European Journal of Environmental and Civil Engineering* 16(10) : 1261-1268.

Rossi, P., 2023. “True Compression Behavior of Concretes and Fiber Reinforced Concretes”, *Cur Trends Civil & Struct Eng. 10(2):2023*, CTCSE.MS.ID.000731.

Rossi, P., 2023. “Basis of Probabilistic Semi-Exlicit Cracking Model for Fiber Reinforced Concretes”, *Cur Trends Civil & Struct Eng.* 10(1): 2023. CTCSE.MS.ID.000727. DOI: 10.33552/CTCSE.2023.10.000727.

Rossi, P., 2025. “Modeling the Compressive Behavior and Cracking Process of Plain Concrete (PC) and Fiber Reinforced Concrete (FRC)”, *Cur Trends Civil & Struct Eng.* 12(2): 2025. CTCSE.MS.ID.000778.

Rots, J., Nauta P., Kuster G. and Blaauwendraad, J., 1985. “Smeared crack approach and fracture localization in concrete”, HERON 30(1).

Torrenti, J.M., Desrues, J., Benaija, E. H. and Boulay, C., 1991. “Stereo-photogrammetry and localization in concrete under compression”, *J. Eng. Mech.*, 117(7): 1455-1465.

Torrenti, J. M., Benaija, E. H. and Boulay, C., 1993. “Influence of boundary conditions on strain softening in concrete compression test”, *J. Eng. Mech.*, 1993, 119(12): 2369-2384.

Weibull, W., 1939. “A Statistical Theory of the Strength of Materials”, *Royal Swedish Institute for Engineering Research*: Stockholm, Sweden.

Weibull, W., 1951. “A statistical distribution function of wide applicability”, *J. Appl. Mech.*, 18, 293–297.

Performance of Date Palm Pedicel and Coir Fibre in Natural Fibre Reinforce Concrete for Sustainable Construction

Abdallah Al Abri[1]; Kazi Md Abu Sohel[1]; Sherif El-Gamal[1]; Khalifa Al-Jabri[1]

[1]: Department of Civil and Architectural Engineering, Sultan Qaboos University, Muscat, Oman.

Abstract

The development of high-performance materials made from natural resources is increasing globally due to environmental and sustainability concerns. Palm fibre is one of the natural smart materials that can be used to produce fibre-reinforced concrete, eliminating synthetic, glass and metal fibre. A significant amount of agricultural waste is produced and dumped in landfills, including palm date parts such as leaves, trunks, fruit bunches and surface fibres. However, these fibres are a great source of natural fibre for the concrete. Several studies show that the natural fibres in concrete enhance the mechanical properties of concrete. In this study, two types of natural fibre namely date palm pedicel fibre and coconut shell (coir) fibre are considered to compare their performance in concrete. Date palm pedicel fibre (DPPF) and coconut shell fibre *i.e.* coir fibre (CF) were prepared in four conditions: raw, alkaline treatment, boiled, and boiled with alkaline treatment. The tensile behaviour of each fibre type was examined using a universal testing machine, following ASTM D3822 guidelines. Measurements included tensile strength, Young's modulus, breaking distance, and elongation at failure. Once the fibres were characterized, they were incorporated into concrete mixes to produce natural fibre reinforced concrete (NFRC) and tested for mechanical performances. Compressive strength, splitting tensile strength, and flexural strength for the NFRC were evaluated after 7 and 28 days of curing for both coir- and pedicel-reinforced concrete. It was found that alkaline treatment, especially when boiling followed by alkaline treatment, substantially improved the strength and stiffness of the fibres. Generally, coir fibres experienced higher elongation under tensile force compared to that of date palm pedicel fibre. Similarly, the tensile strength of date palm pedicel fibre showed higher tensile strength than coir fibre for both treated and untreated cases. However, both fibres achieved sufficient strength after statement making them very much appropriate be used for reinforcing brittle cement-based materials. The NFRC test results showed noticeable improvements in tensile and flexural performance, confirming the crack-bridging ability and energy absorption characteristics imparted by the natural fibres.

Keywords

Fibre reinforced concrete, Natural fibre, Date palm fibre, Coir fibre, Natural fibre treatment

1 Introduction

Metallic, synthetic, and glass fibre have been used in concrete and cement mortar mixes for many years to improve tensile and other mechanical properties. However, the production of these fibres was costly, resulted in CO_2 emissions, and required the use of non-renewable materials (Tonoli et al. 2010). Therefore, over the past few years, efforts have been made to replace the manufactured fibres with natural fibres. The use of natural fibres in cementitious matrix is gaining attraction among the researchers around the world because of its affordability and sustainability (Bendahane et al., 2023).

Table 1: Characterization of typical plant fibres

Type of Fibre	Density (g/ cm^3)	Fibre Length (mm)	Diameter (µm)	Tensile Strength (MPa)	Young's Modulus (GPa)	Elongation at breakage (%)	References
Alfa	1.40	0.2-30	6.0-22.0	18–25	18-58	1.4-2.4	Ajouguim et al. 2023; Al Abri and Sohel 2024
Bamboo	0.6-1.1	0.8	19.8	540–630	11-17	4.3-9.7	Correia et al. 2014; Zhang et al. 2021, Abri and Sohel 2024
Bagasse	1.25	10.1-16.09	180-390	197.8-290	17-27	1.1	Nazir et al. 2021; Abri and Sohel 2024
Banana	1-1.5	12	45	550	5-20	4.5-6.5	Palanisamy and Ramasamy 2022; Abri and Sohel 2024
Coconut/ coir	0.88-1.36	200-300	12 - 35	170-275	3-26	18.0-36.7	Hasan et al. 2021; Abri and Sohel 2024
Cotton	1.5-1.6	25-37	12-35	5.5-12.6	287-597	7.0-8.0	Mahdi and Dean 2020; Abri and Sohel 2024
Flax	1.4-1.5	6-80	12.4-23.9	800-1500	60-80	2.0-3.0	Olivito et al. 2014; Abri and Sohel 2024
Hemp	1.4-1.6	5-55	10.9-42	550-900	70	1.0-6.0	Liu et al. 2017; Abri and Sohel 2024
Jute	1.46	1-6	5-25	393-770	10-30	1.5-1.8	Ramakrishna and Sundararajan 2005; Abri and Sohel 2024
Kenaf	1.2-1.4	40-300	55-60	230-1000	14.5-73	9.1-12.3	Fiore et al. 2015; Abri and Sohel 2024
Oil palm	0.7-1.55	25	19.4	65-220	0.44-1.9	3.2	Raut and Gomez 2016; Abri and Sohel 2024
Pineapple leaf	1.32	10-90	50-150	159	11.84	2.0-2.8	Sivasubramanian et al. 2022; Abri and Sohel 2024
Sisal	1.45	0.5-8	10-20	600-700	9.4-22.0	2.0-2.5	Sahu and Gupta 2017
Date palm turn surface fibre	0.917 ± 0.127	71-290	100-1000	58–203	2–7.5	5–15.5	Alawar et al. 2009; Al-Khanbashi et al. 2005; Kriker et al. 2005; Adamu et al. 2022

Natural fibres are typically categorized into two main types: primary and secondary fibres. Primary fibres refer to fibres that are cultivated for their fibre content, and this category includes jute, sisal, kenaf, palm, and hemp fibres. On the other hand, secondary fibres are fibres that are obtained from byproducts of plant cultivation, and this category includes agroresidues, coir fibres, and pineapple fibres. There are six main types of natural fibres, which can be further

classified based on the part of the plant from which they are derived. The six types are bast fibres (such as flax and jute), leaf fibres (such as sisal and pineapple leaf fibres), seed fibres (such as cotton and coconut), kernel fibres (such as hemp and kenaf), grass and reed fibres (such as wheat, maize, and rice), and all other types (such as wood and roots) (Karthi et al. 2020, Aravindh et al., 2022, Bendahane et al., 2023). Table 1 summarizes common plant fibres and their common mechanical properties, as described in the literature. Tensile strength and elongation at break are crucial for determining the mechanical properties of plant fibre-reinforced concrete. However, previous research works highlighted that the variations in plant fibre extraction and processing methods can lead to significant differences in experimental results. Therefore, it is critical to consider the relevant characteristics and composition of plant fibres, along with local climatic conditions, when developing standards or guidelines for their extraction processes and testing methodologies.

Adamu et al. (2022) studied the possibility of adding date palm surface fibres (DPF) to the concrete matrix. Date palm fibre (DPF) offers several benefits when considered as a natural reinforcement material: it is abundant, inexpensive, environmentally friendly, and sourced directly as a by-product of palm date trees. Despite these benefits, its incorporation into cement composites poses challenges, most notably a slight decrease in mechanical strength and an increase in porosity. To effectively use DPF in concrete applications, it needs to be combined with an additive that can mitigate these drawbacks of the NFRC-based cement composites. Consequently, it is proposed to use Silica fume to partially replace the cement and accordingly reduce the porosity and minimize the undesirable effect of the DPF on the strength of the composite. Numerous studies were conducted on the use of different parts of the date palm tree (*e.g.*, palm trunk fibre and leaf sheath fibre or turn surface fibre) in the concrete mixture to produce fibre-reinforced concrete (Dhakal et al., 2018, Benaimeche et al., 2018). Similar to the date palm fibre, many studies have investigated extensively the precise mix proportions to achieve the optimal mix of coir-fibre reinforced concrete. Varghese and Unnikrishnan (2023) explained the production process of coir fibre reinforced concrete. All of these studies described the improvement of mechanical properties of the concrete or mortar reinforced with date palm fibres. However, none of the studies considered different treatment options of the fibres.

In the present work, the effect of different chemical and treatment processes on the strength and morphological properties of the date palm pedicel fibre and coir fibre was carried out. The strength properties of the concrete with the treated fibre were determined experimentally.

2 Experimental program

2.1 Fibre Extraction and Preparation

The extraction of natural fibres both date palm pedicel fibre (DPPF) and coir fibre (CF) was successfully carried out using fibre extraction machine. Coir fibres were obtained from coconut husk waste collected from local market, while date palm pedicel fibres were extracted from locally sourced Omani date palm residues after collecting the ripped dates. The fibre extraction process included mechanical separation, cleaning, and controlled drying in an oven for 24 hours. These processes ensure that the fibres are uniform and reproducible. Because standardized methods for processing pedicel fibres are largely absent in the literature, several extraction trials were carried out. Through repeated refinement, an optimized procedure was developed that produced fibres with consistent length, clean surfaces, and uniform physical appearance. This optimization is an important outcome of this study because it provides a

practical methodology for utilizing locally available agricultural waste fibres in cementitious applications while also improving the reproducibility of experimental results. Figure 1 illustrates the date palm pedicel branches and mechanically extracted forms date palm pedicel fibres. Finally, both pedicels and coir were then cut into uniform length of 50 mm using a band saw machine.



Figure 1: Raw and extracted pedicel fibre

2.2 Fibre Treatment Procedures

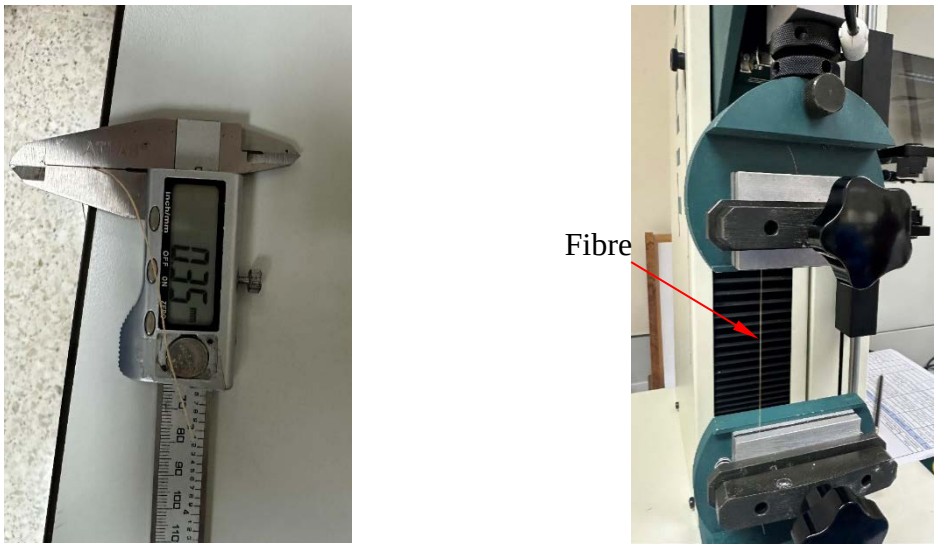
Three types of treatment processes were conducted to purify and improve their compatibility with the concrete matrix and their long-term durability. The first process was direct chemical treatment, where both coir and pedicel fibres were treated with 5% sodium hydroxide (NaOH) for an hour to remove surface impurities, lignin, and hemicellulose, increasing surface roughness and improving interfacial bonding with the cement matrix. Following that, a 30-minute secondary treatment with 2% acetic acid was used to neutralize residual alkalinity and stabilize the fibre surface. In the second type of treatment process was boiling the fibres for 3 hours. This process makes it easy to sperate the raw fibre with less impurities on the surface. The third process is the combination of boiling and alkaline treatment with 5% NaOH followed by washed with 2% acetic acid. This approach was chosen to increase fibre durability while reducing degradation in the alkaline concrete environment. Figure 2 depicts the chemical treatment of pedicel fibre in sodium hydroxide (NaOH) solution. The colour change observed in the NaOH solution during chemical treatment is due to the extraction of lignin, hemicellulose, waxes, and phenolic compounds from the fibres, confirming the alkaline treatment process's effectiveness.

2.3 Characterization of Natural Fibres

A comprehensive characterisation program was carried out to determine the suitability of extracted date palm pedicel fibre and coir fibre as concrete reinforcement materials in terms of physical and strength properties. The physical and mechanical properties of the fibres were investigated through tensile strength testing and water absorption measurement. Tensile tests were performed using Universal Testing Machine (UTM) to determine ultimate tensile strength, elastic modulus, elongation at break, and failure modes of the fibres. Figure 3 shows the diameter measurement and the setup for tensile test.



Figure 2: Colour change of the NaOH solution during alkaline treatment of date palm pedicel fibres



(a) (b)

Figure 3: (a) diameter measurement (b) tensile test using UTM

2.4 Natural fibre reinforced concrete design

The mix design of the concrete was followed by the ratio of 1:1.6:2.5 (cement : fine aggregate : coarse aggregate). The water cement ratio was 0.485 and superplasticizer was used to increase the workability of concrete, and the dosage was 0.45% of cement. The target design compressive strength was 35 MPa. To produce natural FRC, 0.5% and 1.0% fibres by weight of cement were added to the concrete mixture. Length of the fibre was 50 mm. The selected fibre length and dosage were based on preliminary experimental investigations conducted by the authors to optimize the use of coir and date palm pedicel fibres in concrete. In those trials, fibre lengths of 25, 50, and 75 mm were evaluated, and the 50 mm length showed the most effective balance between crack-bridging capacity, strength enhancement, and fibre dispersion.

Similarly, fibre contents ranging from 0.5% to 1.0% by weight of cement provided the most favourable mechanical response without causing excessive reduction in workability or compaction quality. Therefore, the present study adopted 50 mm fibre length with 0.5% and 1.0% fibre contents to further evaluate the comparative performance of coir and date palm pedicel fibres in concrete. Various concrete specimens were prepared at different coir and pedicel fibres content (0.5% and 1% by weight of cement). Based on the fibre characterization results, the concrete mixtures were prepared using coir and date palm pedicel fibres that had been alkaline-treated and subsequently washed with acetic acid. This treatment condition was selected because it enhanced the tensile strength and stiffness of both fibres while improving surface roughness, which is beneficial for fibre-matrix interaction in cementitious composites. Therefore, the mechanical performance reported in the following sections corresponds to concrete reinforced with alkaline-treated treated coir and date palm pedicel fibres at 0.5% and 1.0% by weight of the cement. In addition, a standard specimen without fibre reinforcement was prepared to serve as a benchmark. Cylinders with dimensions of 200 mm by 100 mm diameter and prism with dimensions of 500×100×100 mm were prepared in accordance to ASTM C78.

Table 1: Mix design for 35 MPa cast concrete mix used in all trials.

Ingredient	**Quantity (kg/m^3)**
Cement	442
Fine aggregate	711
Coarse aggregate	1067
Water	214.4 kg/m^3
Super plasticizer	2 liter/ m^3
Target slump	80 to 120 mm

The concrete cylinders were tested after 28 days of water curing under compressive load using an automatic concrete compression testing machine. The split tensile test on cylinder specimens was conducted using the same machine. Four point bending test was conducted on prism specimen to determine the flexural strength of the FRC concrete cast 28 days before.

3 Test Results

3.1 Fresh-state behaviour of concrete mixtures

The fresh-state behaviour of the concrete mixtures was evaluated using the slump test. The control mixture achieved a slump of 118 mm, which is considered medium to high range workable concrete. The incorporation of natural fibres reduced the slump, indicating a decrease in workability. The slump decreased to 107 mm and 103 mm for PED-0.5% and PED-1.0%, respectively, and to 105 mm and 101 mm for CF-0.5% and CF-1.0%, respectively. Although all fibre-reinforced mixtures remained within the target slump range of 80 to 120mm (medium to high workability), the reduction became more evident as the fibre content increased from 0.5% to 1.0%. This behaviour can be attributed to the hydrophilic nature and high surface area of the natural fibres, which increase water demand and internal friction during mixing. In addition, the presence of discrete fibres may restrict aggregate movement and reduce compactability. The slightly lower slump observed in the coir fibre mixtures may be related to their higher aspect ratio, which can increase fibre interaction and resistance to flow.

3.2 Physical and mechanical properties of coir and date palm pedicel fibre

Tensile strength testing was performed on pedicel and coir fibres subjected to four different treatment conditions, namely raw, only chemical treatment, boiled, and boiled with subsequent chemical treatment. The tensile test results are shown in Figure 4. The tensile strength of raw date palm pedicel fibre (DPPF) and coir fibre (CF) are 302 and 98 MPa, respectively. It can be seen that chemical (alkaline) treatment significantly enhances the mechanical performance of both type of fibres. When coir fibre was treated with alkaline, its tensile strength and Young's modulus increased by 17% and 56%, respectively, compared to the raw condition. This increase in strength and stiffness can be attributed to the removal of surface impurities, waxes, and lignin by alkaline media, which results in improved fibre integrity and load transfer mechanism. However, this strength improvement was accompanied by a reduction in elongation at break from 4.13% to 3.76%. This indicate that the chemical treatment makes the fibre stiffer and less ductile compared to that of the raw fibre.

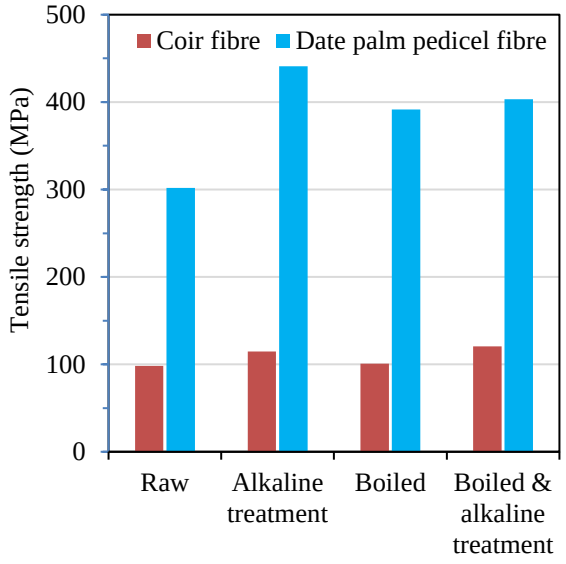
Boiling treatment alone had a slight effect on the tensile strength of coir fibres, though it did in a noticeable reduction in stiffness. This is likely because some of the amorphous regions underwent partial thermal breakdown. However, when the fibres were boiled and then treated with an alkaline solution, their tensile strength increased by 6% over that of only chemically treated fibre. This suggests a synergistic effect of thermal cleaning and chemical modification in increasing fibre strength while maintaining moderate ductility.

Date palm pedicel fibres (DPPF) had significantly higher tensile strength and stiffness than coir fibres across all treatment conditions, demonstrating their superior reinforcing potential. When subjected to alkaline treatment, both tensile strength and Young’s modulus increase remarkably, as can be seen in Figures 4(a) and 4(b). This strength enhancement demonstrates how chemical processing improves cellulose exposure and fibre crystallinity. Similar to coir fibres, alkaline treated pedicel fibres showed lower elongation at break from 39.15% to 30.57% compared to the raw state, indicating that alkaline treatment increases stiffness and reduces ductility of natural fibres.

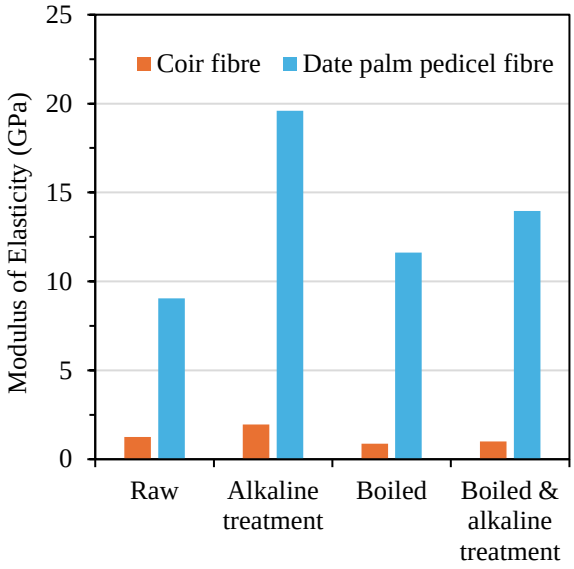
Overall, the findings show that alkaline treatment is the primary factor influencing fibre mechanical performance, while boiling serving as a secondary modification step. The treated fibres' increased strength and stiffness indicate their suitability for crack-bridging and load-transfer mechanisms in fibre-reinforced concrete applications.

Water absorption tests were carried out to determine the hydrophilic characteristics of both types of fibres and their potential impact on concrete workability. Figure 5 depicts the results of a water absorption test on DPPF and CF fibres before and after different treatment conditions, such as raw, raw with chemical treatment, boiled, and boiled with subsequent chemical treatment.

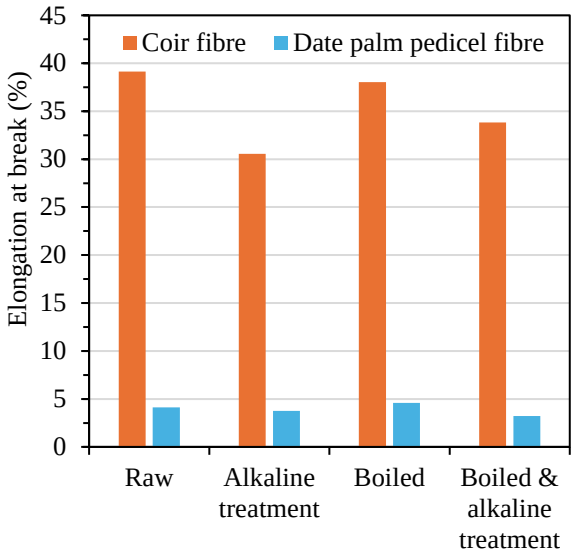
The water absorption test results for both DPPF and CF fibres show that all applied treatment methods have a significant impact on their hydrophilic characteristics. For DPPF fibres, the raw fibres absorbed water approximately 97% of their dry state weight. After chemical treatment, this water absorption slightly increased to 107%, while in case of only boiling treatment, the absorption increased to 111%. However, in case of the combined application of boiling and chemical treatment, the absorption rate increased significantly to 156%. This sharp increase indicates that removing surface waxes and impurities, as well as loosening the fibre's internal structure, significantly improved its ability to absorb water.



(a): Tensile strength



(b): Young's modulus



(c): Elongation at breakage

Figure 4: results of tensile test.

Coir fibres (CF) followed a similar trend of DPPF fibre, as can be seen in Figure 5. However, the raw fibres absorbed less water (~54%) than DPPF fibre (97%). The only chemical and boiling treatments increased absorption by 99% and 109%, respectively. Furthermore, the combined boiling and chemical treatment resulted in the highest water absorption of 128% for CF fibre. Overall, both fibres demonstrate that treatment processes make them more hydrophilic. The DPPF fibres typically absorbed more water than CF fibres. These findings are significant for the application of natural fibres to produce fibre reinforced concrete, because increased water absorption may affect fibre-matrix bonding and overall water demand of the concrete mix.

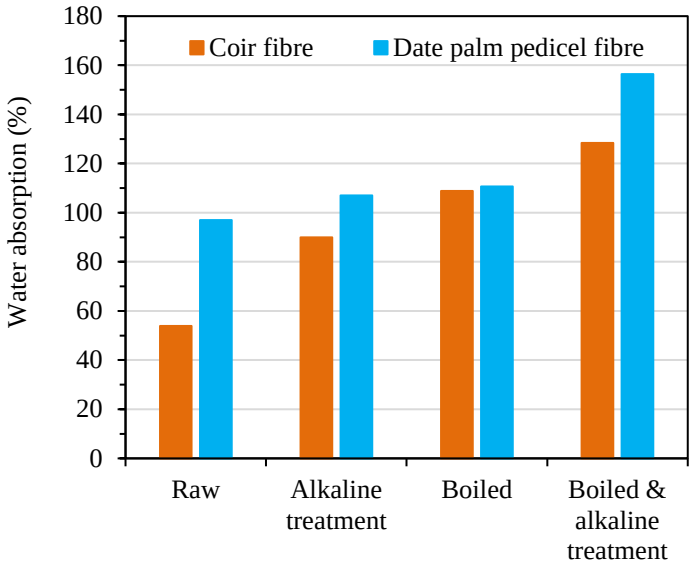


Figure 5: results of water absorption test.

3.3 Performance of Coir and Pedicels Fibre Reinforced Concrete

This section describes the experimental study on concrete reinforced with coir and date palm pedicel fibres at concentrations of 0.5% and 1.0% of the cement weight. The results are compared to a standard control mix (conventional concrete), with emphasis on compressive strength, splitting tensile strength, and flexural strength. For each mix variation, three specimens were tested, and the reported values are the average of the three test results. The variability of the test results is presented using error bars corresponding to the standard deviation of the three tested specimens for each mixture

3.3.1 Compressive Strength

The compressive strength results at 7 and 28 days are presented in Figure 6. After 7 days, the control mix achieved 37.53 MPa. Introducing 0.5% and 1.0% dosages of coir fibre (CF) led to a slight decrease in the compressive strength, with values of 36.71 MPa and 34.38 MPa, respectively, which are 2.2% and 8.4% lower than the control mix strength. The mixes containing pedicel fibres showed more pronounced decreases, measuring 32.27 MPa at 0.5% dosage and 28.73 MPa at 1.0% dosage, respectively, which are 14% and 23.5% lower than the control mix strength.

After 28 days of curing, the compressive strength of the control mix reached 40.92 MPa. The strength of the coir fibre blended mix was similar to that of the control mix, with 40.39 MPa at 0.5% dosage and 39.51 MPa at 1.0% dosage, which were 1.3% and 3.4% lower than the control mix strengths, respectively. The strength of the DPPF fibre blended mix also improved significantly after 28 days of curing. The strength of DPPF bladed mixes was 38.67 MPa at 0.5% dosage and 37.40 MPa at 1.0% dosage, which were 5.5% and 8.6% less than the control mix strengths, respectively.

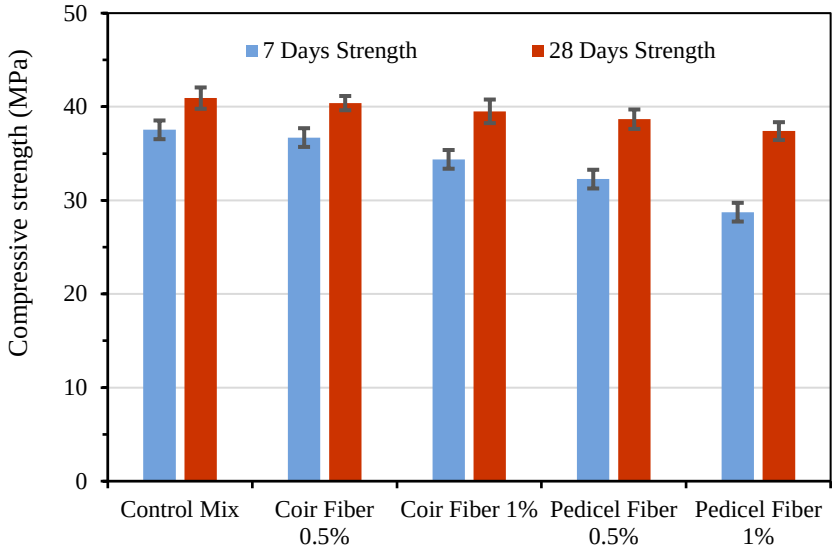


Figure 6: Compressive strength of 3 mix types at 7 and 28 days.

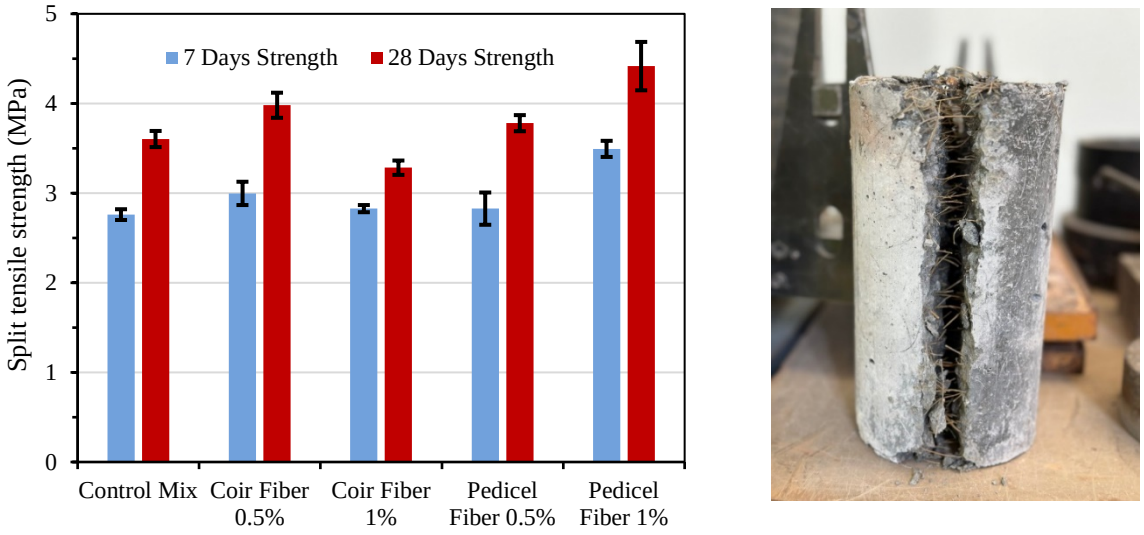
The findings are consistent with the general expectation that incorporating natural fibres causes a slight drop in concrete compressive strength, particularly when higher fibre amounts are used. This reduction is most likely caused by fibre agglomeration (fibre balling effect), the formation of additional voids, and continuity interruption in the cement matrix. The effect was more noticeable in mixes with DPPF than in those with CF, demonstrating how fibre type and shape influence performance. Generally, the diameter of DPPF is higher than that of CF. Despite these reductions, the compressive strength remains within acceptable limits for structural use, especially at 0.5% fibre dosage. Overall, the findings highlight a trade-off: a minor decrease in strength is compensated for by increases in ductility and crack resistance, both of which are highly important in real-world applications.

The reduction in compressive strength due to fibre addition was more evident at 7 days than at 28 days, particularly at the higher fibre dosage. This behaviour can be attributed to the early-age condition of the cementitious matrix, where hydration is still progressing and the fibre–matrix interfacial transition zone has not fully developed. The hydrophilic nature of natural fibres also absorbed part of the mixing water and disturbed local compaction, leading to additional voids and weaker interfacial regions at early age. With continued curing, further hydration improves matrix densification and fibre–matrix bonding, thereby reducing the strength difference between the control and fibre-reinforced mixtures at 28 days. The larger early-age reduction observed in the pedicel fibre mixtures may be related to their higher water absorption and larger diameter compared with coir fibres.

3.3.2 Split Tensile Strength

Figure 7(a) shows results of splitting tensile strength tests at 7 and 28 days of curing. At the age of 7 days, the control mix achieved a split tensile strength of 2.76 MPa. The addition of 0.5% and 1% dosages of coir fibres resulted in a slight increase in split tensile strength of 2.997 MPa and 2.83 MPa, respectively, which were 8.6% and 2.4% higher than the control mix strength. The pedicel fibre mixes performed similarly or better than the coir fibre mixes. At the age of 7days, the concrete mixes with 0.5% and 1% degases of DPPF achieved split tensile strength of 2.83 MPa and 3.49 MPa, respectively, which were 2.4% and 26.5% higher than the control mix strength, respectively. At 28 days, the control mix achieved split tensile strength of 3.60

MPa. The coir fibre mixes produced 3.98 MPa (0.5% coir, 10.5% higher than control mix) and 3.28 MPa (1.0% coir, 9.0% lower than the control). The poor performance of the 1.0% coir mix at 28 days is most likely due to poor fibre dispersion within the concrete matrix, which can result in fibre balling and weak zones that impair tensile strength development. The pedicel mixes demonstrated significant enhancement: 3.78 MPa (0.5% pedicel, 4.9% higher than control) and 4.42 MPa (1.0% pedicel, 22.6% higher than the control mix strength).



(a) (b)

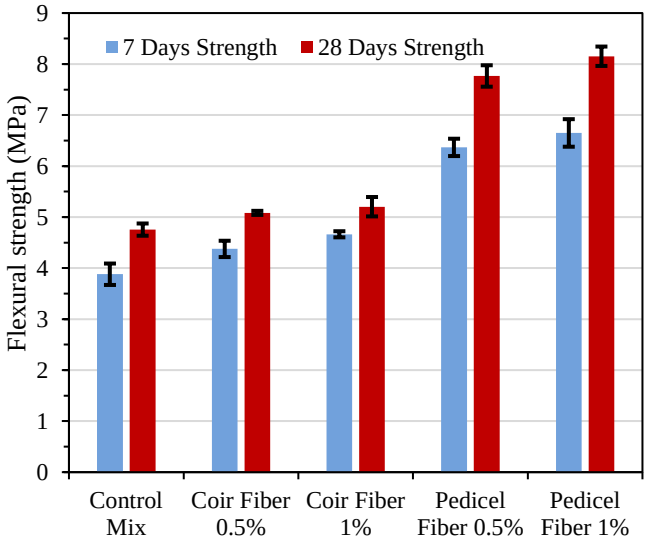
Figure 7: (a) Split tensile strength of 3 mix types at 7 and 28 days (b) Crack-bridging effect of date palm pedicel fibres during splitting tensile testing.

These findings show that incorporating natural fibres, particularly pedicel fibres, at a 1.0% dosage significantly increases the splitting tensile strength of concrete. The fibres' bridging effect improves crack prevention property under tensile loading, as shown in Figure 7(b) especially, while coir fibres increased tensile strength at lower dosages, challenges such as fibre clumping and poor dispersion at higher dosages may limit their effectiveness, as demonstrated by the 1.0% coir mix performance. The pedicel fibres, on the other hand, showed consistent and significant improvements over both curing periods, indicating their potential role in improving the tensile performance of fibre-reinforced concrete.

3.3.3 Flexural Strength

The flexural strength of the concrete mixes was evaluated using prism specimens measuring 500 × 100 × 100 mm and tested under a four-point loading setup in accordance with ASTM C78/C78M - Standard Test Method for Flexural Strength of Concrete (using simple beam with third-point loading). Figure 8(a) shows the results for the 7- and 28-day curing periods. Figure 8(b) shows the fibre pull out at flexural crack in the beam. The close inspection showed that some of the fibres were fractures along with the pull-out fibres.

After 28 days of curing, the control mix had attained 4.76 MPa, as flexural strength. The coir fibre mixes performed slightly better than the control, with 5.08 MPa (0.5% coir, 6.7% improvement) and 5.20 MPa (1.0% coir, 9.2% improvement). The pedicel fibre mixes demonstrated significant gains, reaching 7.77 MPa (0.5% pedicel, 63% higher than control) and 8.15 MPa (1.0% pedicel, 71% higher than the control mix strength).





(a) (b)

Figure 8: (a) Flexural strength of 3 mix types at 7 and 28 days, and (b) Crack bridging by pedicel fibres under flexural loading.

The results clearly show that adding natural fibres, particularly pedicel fibres, significantly increases the flexural strength of FRC concrete. This improvement is due to high tensile strength of the fibres and ability to bridge cracks effectively (see Figure 8(b)), which improves both crack resistance and energy absorption under bending loads. Coir fibres also helped to increase flexural strength, but not as much as the DPPF. This is most likely due to their lower tensile strength and stiffness than the pedicel fibres.

In addition to fibre tensile properties, fibre geometry should also be considered when interpreting the flexural response. Based on the measured diameter ranges and a fibre length of 50 mm, the aspect ratio was approximately 556-625 for coir fibre and 357-417 for date palm pedicel fibre. Although coir fibre had a higher aspect ratio, the superior flexural performance of the pedicel fibre mixtures cannot be attributed to aspect ratio alone. In fibre-reinforced concrete, crack-bridging efficiency depends on the combined effect of fibre aspect ratio, tensile strength, elastic modulus, interfacial bond, and dispersion quality. The higher tensile strength and elastic modulus of pedicel fibre enabled more effective stress transfer across flexural cracks. In contrast, the exceptionally high aspect ratio of coir fibre may have promoted greater fibre interaction and less uniform dispersion, especially at higher fibre contents. As a result, the lower aspect ratio of pedicel fibre did not reduce its reinforcing effectiveness, since its superior mechanical properties played the dominant role in governing the flexural behaviour.

4 Concluding remarks

This study presents a thorough approach to evaluating the properties of DPPF and CF fibres under different treatment conditions, as well as their performance when used in a concrete mix to produce NFRC. From the experimental works following conclusions can be drawn:

- Both fibres benefit from alkaline treatment, which enhances surface bonding and mechanical properties. Boiling with alkaline treatment resulted in cleaner surfaces with increased fibrillation and cellulose content of coir and pedicel fibres.
- Date pedicel fibre achieved the highest tensile strength when subjected to boiling and alkaline treatment. Its higher tensile strength and stiffness make it suitable for load-bearing and structural rigidity applications, which can be more effective at improving cementitious composites for structural purposes. In contrast, coir fibre demonstrated a higher ductility in tensile testing, making it ideal for applications that require flexibility and crack-bridging.
- Mechanical testing of pedicel and coir fibre reinforced concrete revealed significant improvements in splitting tensile and flexural strength at a 1.0% dosage, resulting in consistent strength gains that are ideal for structural performance. Similarly, adding coir fibres improves flexural strength and splitting tensile strength but in lower extent than date palm pedicel fibre.

Overall, both coir and date palm pedicel fibres show promise in terms of concrete tensile and flexural strength, as well as a balance of strength and increased ductility, crack resistance, and energy absorption capability.

5 Acknowledgements

The author gratefully acknowledges the support received through IG funding from Sultan Qaboos University for this work, under grant number IG/ENG/CAED/24/01.

6 References

Adamu, M., Marouf, M.L., Ibrahim, Y.E., Ahmed, O.S., Alanazi, H. and Marouf, A.L., 2022. "Modeling and optimization of the mechanical properties of date fiber reinforced concrete containing silica fume using response surface methodology," *Case Studies in Construction Materials*, *17*, p.e01633.

Al Abri, A. and Sohel, K.M.A., 2024. "Sustainable Fiber Reinforced Concrete: Coir and Date Palm Fiber in Concrete – A Review," *Proceedings of the 5th International Conference on Advanced Engineering Technologies 2024*, Bayburt University, Turkey, September 25-27.

Alawar, A., Hamed, A.M. and Al-Kaabi, K., 2009. "Characterization of treated date palm tree fiber as composite reinforcement," *Composites Part B: Engineering*, *40*(7), pp.601-606.

Ajouguim, S., Page, J., Djelal, C. and Saadi, L., 2023. "Effect of treated Alfa fibers on hydration kinetics, mechanical, and adhesion properties of fiber cement composite," *Journal of Building Engineering*, *71*, p.106558.

Aravindh, M., Sathish, S., Ranga Raj, R., Karthick, A., Mohanavel, V., Patil, P.P., Muhibbullah, M. and Osman, S.M., 2022. "A Review on the Effect of Various Chemical Treatments on the Mechanical Properties of Renewable Fiber-Reinforced Composites," *Advances in Materials Science and Engineering*, *2022*(1), p.2009691.

Benaimeche, O., Carpinteri, A., Mellas, M., Ronchei, C., Scorza, D. and Vantadori, S., 2018. "The influence of date palm mesh fibre reinforcement on flexural and fracture behaviour of a cement-based mortar," *Composites Part B: Engineering*, *152*, pp292-299.

Bendahane, K., Belkheir, M., Mokaddem, A., Doumi, B. and Boutaous, A., 2023. "Date and doum palm natural fibers as renewable resource for improving interface damage of cement composites materials," *Beni-Suef University Journal of Basic and Applied Sciences, 12:37.*

Correia, V. da C, Santos, S.F., Mármol, G., Curvelo, A.A. da S. and Savastano, H., 2014. "Potential of bamboo organosolv pulp as a reinforcing element in fiber–cement materials," *Construction and Building Materials*, *72*, pp.65-71.

Dhakal, H., Bourmaud, A., Berzin, F., Almansour, F., Zhang, Z., Shah, D.U. and Beaugrand, J., 2018. "Mechanical properties of leaf sheath date palm fibre waste biomass reinforced polycaprolactone (PCL) biocomposites," *Industrial crops and products*, *126*, pp394-402.

Fiore, V., Di Bella, G. and Valenza, A.J.C.P.B.E., 2015. "The effect of alkaline treatment on mechanical properties of kenaf fibers and their epoxy composites," *Composites Part B: Engineering*, *68*, pp14-21.

Hasan, K.F., Horváth, P.G., Kóczán, Z. and Alpár, T., 2021. "Thermo-mechanical properties of pretreated coir fiber and fibrous chips reinforced multilayered composites," *Scientific Reports*, *11*(1), p.3618.

Al-Khanbashi, A., Al-Kaabi, K. and Hammami, A., 2005. "Date palm fibers as polymeric matrix reinforcement: fiber characterization," *Polymer composites*, *26*(4), pp.486-497.

Karthi, N., Kumaresan, K., Sathish, S., Gokulkumar, S., Prabhu, L. and Vigneshkumar, N., 2020. "An overview: Natural fiber reinforced hybrid composites, chemical treatments and application areas," *Materials today: proceedings*, *27*, pp2828-2834.

Kriker, A., Debicki, G., Bali, A., Khenfer, M.M. and Chabannet, M., 2005. "Mechanical properties of date palm fibres and concrete reinforced with date palm fibres in hot-dry climate," *Cement and Concrete Composites*, *27*(5), pp554-564.

Mahdi, E. and Dean, A., 2020. "The effect of filler content on the tensile behavior of polypropylene/cotton fiber and poly (vinyl chloride)/cotton fiber composites," *Materials*, *13*(3), p.753.

Nazir, M.H., Ayoub, M., Zahid, I., Shamsuddin, R.B., Yusup, S., Ameen, M. and Qadeer, M.U., 2021. "Development of lignin based heterogeneous solid acid catalyst derived from sugarcane bagasse for microwave assisted-transesterification of waste cooking oil," *Biomass and Bioenergy*, *146*, p.105978.

Olivito, R.S., Cevallos, O.A. and Carrozzini, A., 2014. "Development of durable cementitious composites using sisal and flax fabrics for reinforcement of masonry structures," *Materials & Design*, *57*, pp258-268.

Palanisamy, E. and Ramasamy, M., 2022. "Dependency of sisal and banana fiber on mechanical and durability properties of polypropylene hybrid fiber reinforced concrete," *Journal of Natural Fibers*, *19*(8), pp3147-3157.

Ramakrishna, G. and Sundararajan, T., 2005. "Impact strength of a few natural fibre reinforced cement mortar slabs: a comparative study," *Cement and concrete composites*, *27*(5), pp547-553.

Raut, A.N. and Gomez, C.P., 2016. "Thermal and mechanical performance of oil palm fiber reinforced mortar utilizing palm oil fly ash as a complementary binder," *Construction and Building Materials*, *126*, pp476-483.

Sahu, P. and Gupta, M.K., 2017. "Sisal (Agave sisalana) fibre and its polymer-based composites: a review on current developments," *Journal of Reinforced Plastics and Composites*, *36*(24), pp1759-1780.

Sivasubramanian, P., Mayandi, K., Santulli, C., Alavudeen, A. and Rajini, N., 2022. "Effect of fiber length on curing and mechanical behavior of pineapple leaf fiber (PALF) reinforced natural rubber composites," *Journal of Natural Fibers*, *19*(11), pp.4326-4337.

Tonoli, D., Henrique, G. and de Souza Almeida, A.E.F., 2010. "Surface properties of eucalyptus pulp fibres as reinforcement of cement-based composites," *Holzforschung*, *64*(5), pp595-601.

Zhang, W., Wang, C., Gu, S., Yu, H., Cheng, H. and Wang, G., 2021. "Physical-mechanical properties of bamboo fiber composites using filament winding," *Polymers*, *13*(17), p.2913.

Time-Dependent Deflection and Crack Width in Polypropylene Fibre Reinforced Concrete Beams: A Review and Preliminary Experimental Results

Krishnaa Subramanian[1], Tom Molkens[2], Rutger Vrijdaghs[3]

[1,2,3]: Department of Civil Engineering ,KU Leuven, Belgium. Krishnaa.Subramanian@kuleuven.be; Rutger.Vrijdaghs@kuleuven.be; Tom.Molkens@kuleuven.be

Abstract

Fibre reinforced concrete (FRC) has gained increasing acceptance as a structural material. Design frameworks such as fib Model Code 2010 and the upcoming revision of Eurocode 2 provide provisions for material classification, ultimate limit state design, and serviceability crack control, primarily developed for steel fibre reinforced concrete (SFRC). For polypropylene fibre reinforced concrete (PPFRC), equivalent guidance is currently under development and requires extensive experimental evidence for validation. To date, experimental knowledge on the creep behaviour of PPFRC remains particularly limited. While polypropylene fibres are known from material-level studies to undergo viscoelastic creep under sustained tensile stress, their structural-level behaviour requires further investigation.

Against this background, this paper reviews the current state of knowledge on long-term studies of FRC members with conventional steel reinforcement. Given the limited number of PPFRC studies available, SFRC is also included to provide a comparative baseline for future work. Most existing analytical models have been developed for SFRC and are assessed in terms of their applicability and current validation range. Reviewing them provides a basis for extension to other fibre types. The paper also introduces an ongoing experimental programme on PPFRC beams with minimum steel reinforcement ratios, with preliminary results at six months discussed in terms of time-dependent deflection and crack width evolution.

Keywords

Polypropylene fibre reinforced concrete, Long-term serviceability, Creep and shrinkage, Time-dependent deflection, Crack width, Minimum reinforcement.

1 Introduction

The use of fibre reinforced concrete (FRC) in structural applications has grown significantly over the past decade, driven by its ability to enhance post-cracking tensile response, reduce crack widths, and improve member stiffness and durability (Cardoso et al., 2019; Conforti et al., 2021; Di Prisco et al., 2009). FRC has found particular application in lightly reinforced structural members where serviceability, rather than strength, typically governs design. Among available fibre types, steel fibre reinforced concrete (SFRC) has dominated structural applications. Extensive experimental research and constitutive modelling have established reliable material characterisation through residual flexural strength testing in accordance with EN 14651:2005. This research foundation enabled the incorporation of SFRC into fib Model Codes and, more recently, as an informative annex in the revised Eurocode 2 (EN 1992-1-1:2023), covering material classification, ultimate limit state resistances, and serviceability crack control. With formal code recognition now in place, the structural application of SFRC is set to expand further.

Alongside SFRC, polypropylene fibre reinforced concrete (PPFRC) is increasingly being explored as a structurally and economically viable alternative for lightly reinforced structural members. Recent studies (Conforti et al., 2021; Pakravan and Ozbakkaloglu, 2019) have demonstrated promising short-term flexural performance and crack control, while offering corrosion resistance, lower cost, and reduced environmental impact compared to steel fibres. However, the long-term behaviour of PPFRC under sustained loading remains a critical and largely unresolved challenge. Unlike steel fibres which undergo negligible creep at ambient temperatures, polypropylene fibres are viscoelastic and elongate under sustained tensile load when the stress level is incompatible with the time-dependent properties of the polymer (Tošić et al., 2020). At the fibre–matrix interface, both fibre types are subject to progressive bond creep and pull-out under sustained tensile stress (Tošić et al., 2020). At the structural level, the presence of conventional reinforcement introduces time-dependent load redistribution between the fibres and the rebar. The extent to which fibre creep at this scale translates into crack widening and deflection in lightly reinforced PPFRC members remains insufficiently established by experimental evidence. This lack of knowledge represents a fundamental barrier to the inclusion of PPFRC in future design frameworks and to its wider structural adoption.

In this context, the objective of this paper is twofold. First, to examine the structural-level experimental evidence on the long-term serviceability of FRC members together with the analytical models developed to predict time-dependent deflection and crack width, considering key parameters such as fibre type and dosage, reinforcement ratio, and load level. Second, to present an experimental programme that addresses these gaps for lightly reinforced members at commonly used PP fibre dosages subjected to sustained loading corresponding to the serviceability deflection limit of L/250, together with the preliminary findings. The lever-arm loading frame used for the test setup is described in detail.

2 State of the Art on Long-Term Serviceability of FRC Structural Members

The experimental programmes reviewed herein cover full-scale FRC beams and slabs under sustained flexural loading, with observations on time-dependent deflection and crack width evolution over periods ranging from several months to ten years. The analytical models

discussed operate at the structural level, addressing time-dependent curvature, tension stiffening decay, and crack width prediction for FRC flexural members.

2.1 Experimental Studies on FRC Structural Members

The earliest structural-level investigation into the long-term behaviour of SFRC beams was conducted by Tan and his group (Tan et al., 1994, 1995; Tan and Saha, 2005). Time-dependent deflections and crack widths were monitored over ten years, a duration unique in the literature. Simply supported beams with a longitudinal reinforcement ratio of 1.59% and steel fibre content varying from 0 to 2% by volume fraction were tested under simulated UDL at sustained load levels ranging from 0.35 to 0.80 times the ultimate load (P_u). The results confirmed that fibres became progressively more effective with time, with the long-term to instantaneous deflection ratio reducing from 1.3 for plain RC to 1.03 at 2% fibre content at ten years. This effect was more pronounced at sustained load levels above the service load of 0.58 P_u. Notably, the long-term to instantaneous crack width ratio stabilised after approximately 140 days.

Nakov et al. (2016) further contributed to the limited body of SFRC long-term studies by investigating creep effects under both sustained and cyclic loading. Twelve beams with a longitudinal reinforcement ratio of approximately 0.43% in three concrete types (plain RC and SFRC with 30 and 60 kg/m³ hooked-end steel fibres) were tested over 360 days under two regimes: sustained loading at the permanent moment after pre-cracking, and a daily cyclic variable load (8 hours on, 16 hours off). The service moment corresponded to 0.58 times the ultimate. Fibres reduced long-term deflections by approximately 15–22% and crack widths by 40–50% compared to plain RC. The cyclic loading regime substantially amplified the creep response: the creep ratio for plain RC increased from 2.00 under sustained loading to 3.34 under cyclic loading (a 1.67× amplification). Fibres partially mitigated this amplification, reducing the amplification factor to 1.28× for 30 kg/m³ (1.72 → 2.20) and 1.47× for 60 kg/m³ (1.76 → 2.58).

While the above studies focused on SFRC, polypropylene (PP) fibres have also been examined in long-term structural investigations, alone or in combination with steel (Aslani et al., 2014; Watts et al., 2022; Tošić et al., 2024). Aslani et al. (2014) investigated eight one-way self-compacting concrete (SCC) slabs ($\rho = 0.87\%$) over 240 days under sustained loads of 30% and 50% of the ultimate design load. The slabs were cast in four mixes: plain SCC, SCC with 30 kg/m³ hooked-end steel fibres, SCC with 5 kg/m³ PP fibres, and a hybrid with 15 kg/m³ steel and 3 kg/m³ PP fibres. Steel fibres produced the lowest long-term deflection ratios at 240 days (2.21-2.32), while PP fibres alone produced the highest (3.47-6.95), exceeding plain SCC (2.04-3.07). The hybrid mix showed intermediate deflection ratios (2.37-3.08) but the minimum crack widths, indicating that deflection control was best with steel fibres alone and crack width control was best with the hybrid combination.

Watts et al. (2022) conducted a comprehensive experimental investigation simultaneously monitoring both time-dependent deflections and crack widths. Six large-scale beams with longitudinal reinforcement ratios of 0.69% and 0.78% in three concrete types (plain RC, SFRC with 30 kg/m³ hooked-end steel fibres, and PPFRC with 5 kg/m³ polypropylene fibres) were subjected to a sustained UDL of approximately 50% of the ultimate moment over 630 days. Both fibre types reduced instantaneous deflections relative to plain RC, with average reductions of 36% for steel and 15% for PP. At later ages, the time-dependent deformation of all FRC beams exceeded that of plain RC, reflecting the progressive decay of fibre tension across the cracks with time. Steel fibres achieved an average 32% reduction in mean crack width at 630

days, while PP fibres produced only a marginal effect. Tošić et al. (2024) recently investigated minimum-reinforcement PPFRC beams ($\rho \approx 0.20\%$) under one year of sustained loading, with two PP fibre types at dosages of 3 and 9 kg/m³ alongside a plain RC reference. Time-dependent deflection monitoring revealed that beams with lower PP fibre dosage (3 kg/m³) exhibited a normalised deflection ratio significantly higher than plain RC, while higher dosage (9 kg/m³) performed comparably. Following the one-year sustained loading period, beams were tested to failure to assess residual flexural capacity — no loss of ductility or moment capacity was observed.

2.2 Analytical Models for Time-Dependent Deflection and Crack Width in FRC Members

Existing design codes provide no specific equations or guidance for the prediction of time-dependent deflection and crack width in FRC structural members. For crack width specifically, this limitation was demonstrated by Vasanelli et al. (2014), who showed that EC2, RILEM TC 162-TDF, and MC2010 (all of which account for time-dependent effects through a single empirical factor on concrete strain with no FRC-specific provision) predict a time-dependent increase in crack width for FRC beams that is not observed experimentally, while ACI 224R provides no long-term formulation at all.

Alongside the experimental programme described in Section 2.1, Tan and his group also developed analytical models for long-term deflection and crack width in SFRC beams (Tan et al., 1994; Tan et al., 1995; Tan and Saha, 2005). Three approaches for long-term deflection were adapted to SFRC: a modified ACI long-term multiplier with a fibre-volume-dependent correction factor α, the Effective Modulus Method (EMM), and the Age-Adjusted Effective Modulus Method (AEMM), with the latter two incorporating fibre-modified creep coefficients and shrinkage strains. For crack width, Tan et al. (1995) proposed a semi-empirical formula for the long-term crack widths in reinforced SFC beams under sustained loads, derived from a correlation analysis, with the long-term to instantaneous crack width ratio observed to become constant after 140 days. Tan and Saha (2005) validated these formulations against ten-year data from nine SFRC beams covering fibre contents from 0 to 2% and sustained load levels of 0.35 to 0.80 P_u. The modified ACI approach gave conservative predictions, with the largest deviation at ten years of approximately 17% for the plain RC beam and closer agreement at higher fibre contents. The EMM also yielded conservative predictions with a maximum deviation of approximately 16%. The AEMM predicted slightly lower deflections than the EMM, with experimental values generally above the predicted, a deviation attributed by the authors to the progressive loss of fibre stress transfer capability with age, which is not accounted for in the formulation. The crack width regression was refitted against the ten-year data.

Later studies by Sturm and his group (Sturm et al., 2018; Visintin et al., 2018; Sturm et al., 2019) introduced mechanics-based approaches founded on partial interaction (PI) theory. The local bond-slip behaviour at the crack face is used directly to derive crack spacing, crack widths, and tension stiffening from material properties. Creep of the concrete is incorporated through an age-adjusted effective modulus, and shrinkage enters as an offset in strains between the reinforcement and the concrete. The framework was first developed for plain RC (Sturm et al., 2018; Visintin et al., 2018) and later extended to FRC and UHPFRC by Sturm et al. (2019), where the fibre contribution is captured through the tensile stress–crack width relationship of the composite and bond properties taken from pull-out tests on the fibrous material. In Visintin et al. (2018), predicted crack widths were in good agreement with measurements from a single plain RC beam under 400 days of sustained loading, with predicted deflections within the range

obtained for different shrinkage assumptions. The FRC and UHPFRC extension in Sturm et al. (2019) was validated against 26 beams with accurate predictions of the instantaneous load-deflection behaviour, but long-term validation on FRC or UHPFRC beams with reinforcement is not provided.

Watts et al. (2020) extended the instantaneous tension chord-based deflection model of Amin et al. (2017), originally developed for SFRC, to time-dependent behaviour by adding creep- and shrinkage-induced curvature components. The creep curvature uses an empirical modification factor on the instantaneous curvature and considers only compressive creep of the concrete. Shrinkage is treated separately for the cracked and uncracked portions of the section. Fibre tensile creep is not included. Watts et al. (2021) then extended the formulation to crack width as the product of crack spacing and the extreme tensile strain of the section computed from the time-dependent curvature, with crack spacing taken from the Amin et al. model. The two models were validated by Watts et al. (2022) on six large-scale beams containing plain RC, steel fibres (30 kg/m³), and polypropylene fibres (5 kg/m³) at reinforcement ratios of 0.69% and 0.78%, loaded to approximately 50% of the ultimate over 630 days. The deflection model gave an average experimental-to-predicted ratio of 1.06 with a CoV of 6%, and the crack width model gave 0.97 with a CoV of 2%.

2.3 Critical Research Gaps

The current review shows that structural-level experimental evidence on the long-term serviceability of FRC members remains limited in both volume and scope. Most studies cover longitudinal reinforcement ratios between 0.40% and 0.90%, with only one study at near-minimum reinforcement; steel fibre dosages range from 20 to 60 kg/m³, PP fibre dosages are mostly 3, 5, and 9 kg/m³, and sustained loads are typically around 50% of the ultimate. For SFRC, the studies collectively show that steel fibres reduce both time-dependent deflection and crack width, with the effect increasing with fibre dosage and more pronounced at higher load levels. For PPFRC, the results are inconsistent: some configurations show comparable or beneficial performance while others show larger time-dependent deflections than plain RC. This points to the need for systematic investigation across reinforcement ratio, fibre dosage, and load level. Experimental evidence is lacking for near-minimum reinforcement ratios under service-level loading, a regime which Tošić et al. (2020) identify as a priority for future structural-level research.

On the analytical side, despite the progress represented by the models reviewed in Section 2.2, none have been incorporated into design codes, and their validation remains confined to narrow experimental datasets. The creep coefficient in these models is mostly taken to represent compressive creep of the concrete, while tensile creep of the cracked composite is largely neglected. This reflects the scarcity of experimental data on cracked FRC under sustained tensile stress, with no standardised test method established for measuring it. The wide variability of test parameters across studies has limited the development of general analytical models, and Tošić et al. (2020) identify the broadening of current models to PPFRC and the incorporation of time-dependent polymeric fibre properties as priorities for future analytical work.

3 Experimental Program

3.1 Materials, Specimens, and Test Matrix

CEM I 52.5 R cement was used with sand (0/4 mm) and gravel (4/16 mm) as fine and coarse aggregates, with mix proportions by mass of cement : coarse aggregate : fine aggregate : water = 1 : 3.22 : 2.15 : 0.45 and 0.1% superplasticiser by mass of cement. Embossed monofilament polypropylene fibres of 54 mm length and 0.8 mm diameter, supplied by Master Builder Solutions, were incorporated at two dosages: 4.5 kg/m³ (0.5% by volume) and 9 kg/m³ (1% by volume). Both dosages fall within the range most commonly investigated in structural-level PPFRC studies (3–9 kg/m³, e.g., Aslani et al., 2014; Watts et al., 2022; Tošić et al., 2024), and were selected so the present results extend that body of evidence to near-minimum reinforcement ratios. Steel reinforcement had a mean yield strength of 550 MPa.

Full-scale beams of 2600 mm total length with a 200 mm × 350 mm cross-section were cast. Two longitudinal reinforcement ratios were considered: the minimum reinforcement ratio, achieved with two 8 mm diameter bars ($A_{s,prov}$ = 100 mm²), and twice the minimum, achieved with two 10 mm and one 8 mm diameter bars ($A_{s,prov}$ = 207 mm²). Shear reinforcement comprised 8 mm diameter stirrups at 100 mm spacing in the shear zones, with a clear cover of 30 mm. Companion cylinders were cast simultaneously to measure the free shrinkage strain throughout the test duration.

Two series were investigated. Series A combined $A_{s,min}$ with 1% PP fibre dosage, and Series B combined $2A_{s,min}$ with 0.5% PP fibre dosage. Two nominally identical specimens were cast and tested in each series, designated A1, A2 and B1, B2 respectively.

3.2 Test Setup and Instrumentation

A cantilever-based lever arm system, shown in Figure 1, was developed to apply sustained loads to reinforced concrete specimens under flexural creep conditions. The lever arm, a 2500 mm hollow steel section, rotates about a fixed fulcrum positioned 150 mm from one end, enabling mechanical amplification of applied dead weights. Two nominally identical specimens from each test series were arranged in a vertically stacked configuration, with the lower beam positioned in an inverted orientation. The upper beam, supported at its ends on a 2400 mm span, receives concentrated loads at two points spaced 600 mm apart through a spreader beam contacted by the lever arm, creating a four-point bending configuration. Two intermediate rollers transmit the applied forces and the self-weight of the upper beam to the inverted lower specimen, which is supported from below at the same 600 mm spacing. This arrangement produces four-point bending conditions in both specimens simultaneously: the upper beam deflects downward while the lower beam, being inverted, deflects upward. The rollers between the upper and lower specimens allow free rotation and accommodate the relative vertical displacement between the two beams as they deflect. The lower beam carries the applied load plus the self-weight of the upper beam, and each beam responds independently to its own stiffness, so the configuration does not introduce boundary stresses or measurement interference between the upper and lower beams.

The mechanical amplification is achieved through the lever arm geometry, with dead weights applied 2200 mm from the fulcrum and the beam loading point positioned 100 mm from the fulcrum, yielding an initial amplification factor of 22. As sustained loading causes progressive beam deflection, the lever arm rotates about the fixed fulcrum, altering the effective lever arm

lengths and consequently increasing the amplification factor and the applied load over time. Dead weights were removed whenever the applied load reached a ±5% tolerance band, monitored continuously through the lever arm rotation. The band was set from short-term load–deflection tests carried out on companion specimens prior to sustained loading, keeping the upper bound within the serviceability regime and below the yield load of the reinforcement. Fluctuations within this band are small relative to the mean sustained load, so the measured creep response is effectively governed by it.

Six LVDTs, positioned as shown in Figure 1 (L1 to L6), were used to capture deformation: three on the upper beam at mid-span and the two loading points, and three on the lower beam at mid-span and the two support locations. Two laser displacement sensors measured the vertical deflection of the lever arm at two locations (one at the loading point, 100 mm from the fulcrum, and one at 1460 mm from the fulcrum), from which the rotation and amplification factor were continuously monitored, triggering weight removal when the tolerance limit was approached. Long-term crack evolution was tracked using Demec points installed at major crack locations identified during pre-cracking. All instrumentation was connected to a data acquisition system operating at 2 Hz throughout the test duration. The creep testing programme is designed for a 12-month duration; the data reported here correspond to the first six months of sustained loading.

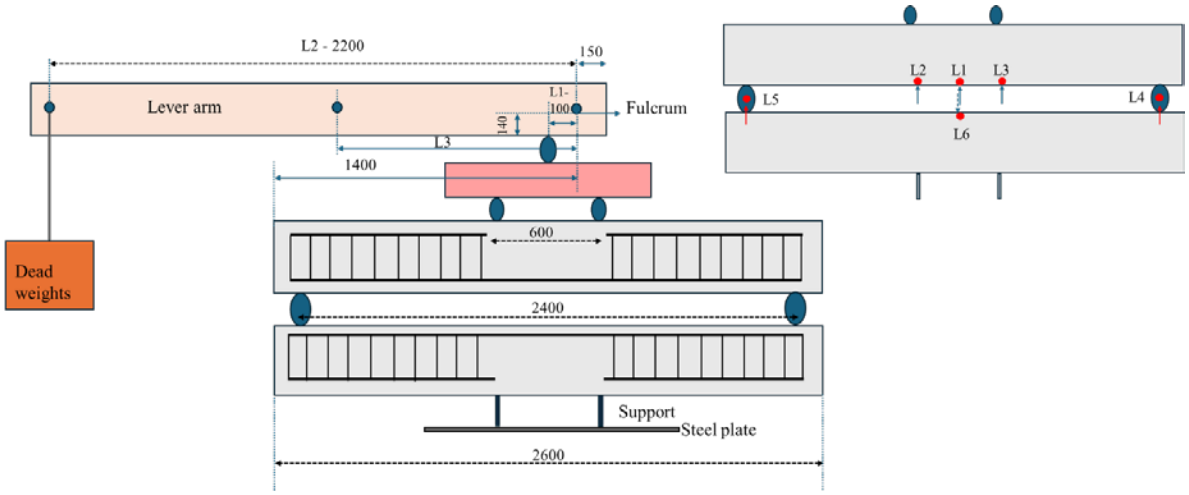


Figure 1: Lever arm test setup and instrumentation for sustained loading

4 Experimental Procedure and Preliminary Observations

This section presents the experimental observations from the testing programme. The pre-cracking response, including load-deflection behaviour and crack formation, is first described, followed by a discussion of the sustained loading conditions and the time-dependent evolution of deflection and crack width over six months.

4.1 Pre-Cracking Loading Response

All specimens were initially tested under four-point bending up to a mid-span deflection of 4.8 mm, corresponding to the span/500 serviceability limit state deflection limit per Eurocode 2. At this stage the specimens were unloaded, and the load-deflection response is shown in Figure 2. Crack widths, heights, and spacing were recorded at the deflection limit prior to unloading. Seven flexural cracks formed in Series A specimens, with an average crack width

of 0.22 mm and a maximum of 0.4 mm. Nine flexural cracks formed in Series B specimens, with an average crack width of 0.18 mm and a maximum of 0.3 mm (Figure 3a).

4.2 Sustained Loading

Following pre-cracking, a sustained load corresponding to 50% of the load at the span/500 deflection limit was applied to each series — 26 kN for Series A and 33 kN for Series B. The load was applied in a single step by stacking steel plates simultaneously using the lever arm system (Figure 3c). Monitoring of deflection and crack width began immediately after load application, with crack width evolution tracked using Demec points installed at major crack locations (Figure 3c). Throughout the sustained loading period, the temperature and relative humidity were maintained constant at 20°C and 60% respectively.

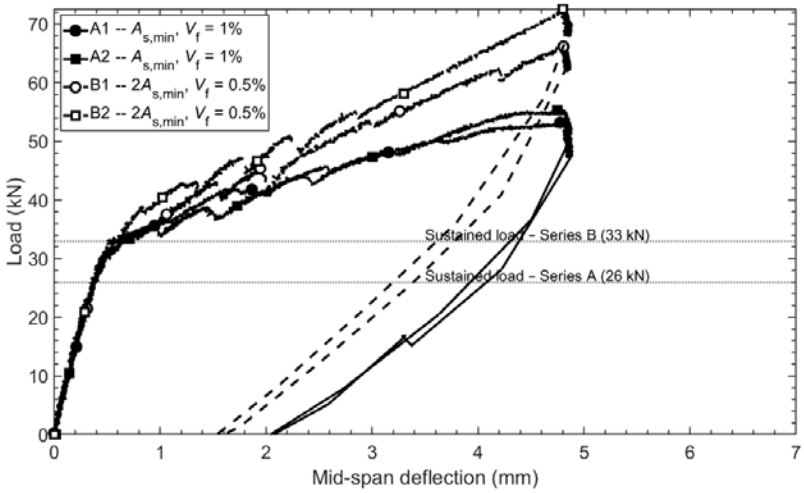


Figure 2 : Load (kN) versus midspan deflection (mm) during pre-cracking loading for specimens A1, A2 (Series A) and B1, B2 (Series B)

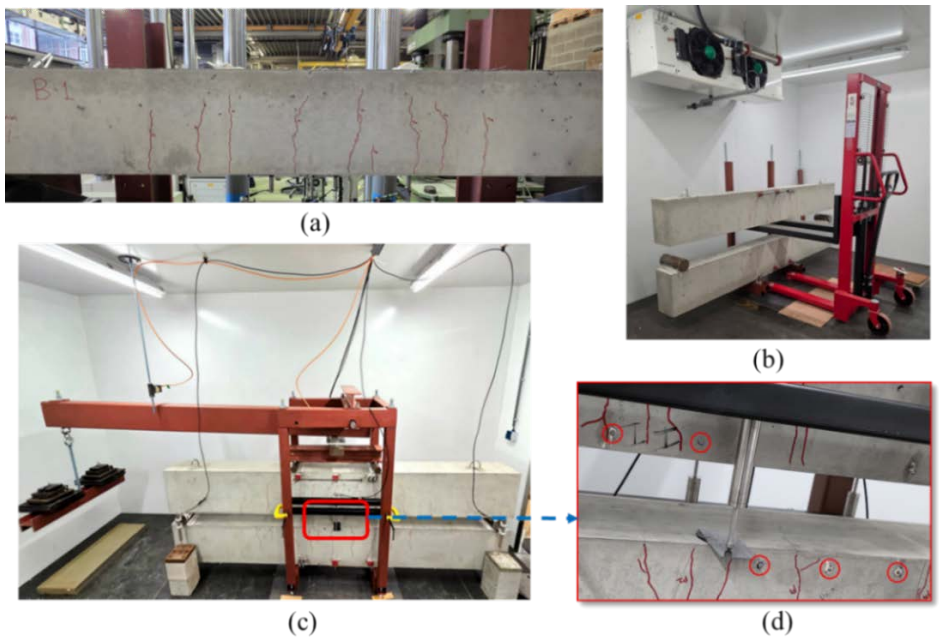


Figure 3: (a) Crack pattern after pre-cracking; (b) stacking of beam specimens; (c) sustained loading using lever arm system; (d) Demec point monitoring at crack locations

4.3 Time-Dependent Deflection and Crack Width Evolution

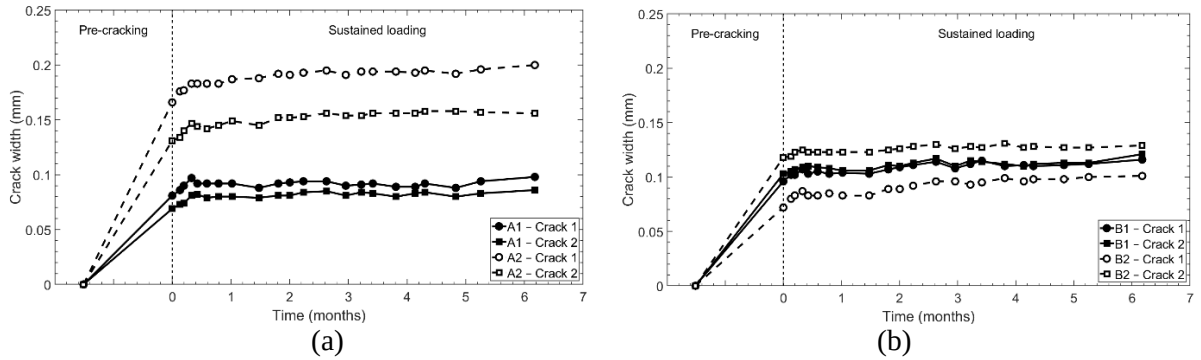
The time-dependent crack width evolution measured using Demec points is shown in Figure 4 for both series. In each plot, the time axis is referenced to the start of sustained loading (t = 0), with the pre-cracking phase shown to its left. Both series exhibit a gradual increase in crack width following the application of sustained load, growing slowly over the six-month monitoring period. A similar trend has been reported for FRC beams under sustained loading in the literature (Vasanelli et al., 2014; Watts et al., 2022). The midspan deflection for both beams was obtained from the LVDT readings positioned as shown in Figure 1, with a chord correction applied to isolate the individual deflection of each beam. The time-dependent midspan maximum deflection for all specimens is shown in Figure 5, where A1 and B1 are the top beams deflecting downward and A2 and B2 are the bottom beams deflecting upward. For ease of comparison, all deflections are plotted as negative values.

All specimens exhibit a rapid initial deflection upon loading followed by a gradual increase with time, consistent with the expected creep behaviour. The creep deflection is obtained from the measured total deflection by removing the instantaneous and shrinkage components. The shrinkage strain is taken as the average measured on the companion cylinders, and the corresponding shrinkage deflection at member level is calculated following the procedure of Watts et al. (2020). The deflection-based creep coefficient (φ_δ) for each series, calculated as the average of the two specimens, is reported in Table 1. While deflection-based creep coefficients for steel fibre reinforced concrete beams have been reported in the literature (Tan et al., 1994; Nakov et al., 2016), corresponding numerical values for PPFRC beams remain absent, with the available studies on PPFRC (Watts et al., 2022; Tošić et al., 2024) reporting time-dependent deflection only qualitatively. The values reported here provide an initial numerical indication of the deflection-based creep coefficient for PPFRC beams at near-minimum reinforcement, with further values to be reported as the programme continues.

Table 1: Deflection components and creep coefficient for each series

Series	Δ_o (mm)	Δ_{total} (mm)	Δ_{sh} (mm)	Δ_{cr} (mm)	φ_δ
A	0.65	1.29	0.64	1.28	1.94
B	1.13	1.65	0.65	1.18	1.08

Note: Δ_o - instant deflection ; Δ_{sh} – shrinkage deflection ; Δ_{cr} – creep deflection ; φ_δ – creep coefficient



(a) (b)

Figure 4: Time-dependent crack width evolution under sustained loading: (a) Series A; (b) Series B

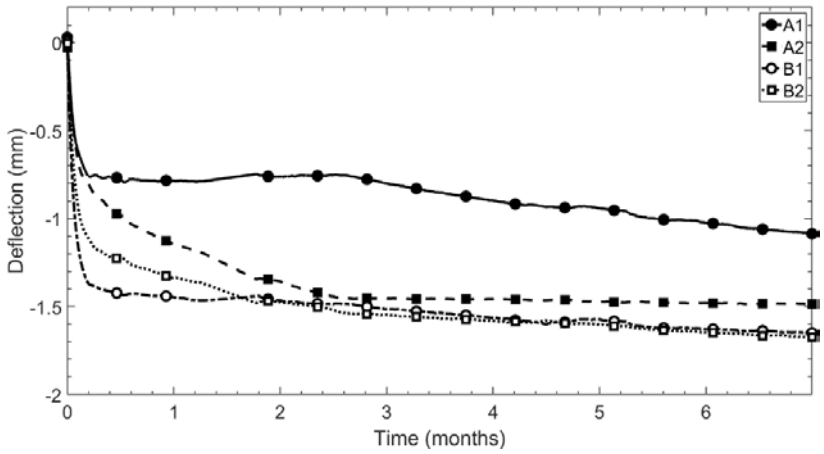


Figure 5 : Time-dependent midspan deflection (mm) versus time (months) under sustained loading

5 Concluding remarks

This paper reviewed the limited structural-level evidence on long-term serviceability of FRC members and highlighted the lack of data for PPFRC, particularly in lightly reinforced sections. To address this gap, a long-duration experimental programme was developed using a lever-arm sustained loading setup. The preliminary results, covering the first six months of sustained loading, show gradual increases in deflection and crack width with a decreasing growth rate over time. The deflection-based creep coefficients obtained at this stage provide an initial numerical reference for PPFRC beams at near-minimum reinforcement, where such values have not previously been reported. These observations are preliminary and reflect only the early portion of the planned monitoring period. Continued monitoring is expected to provide a longer-term dataset against which existing analytical models can be assessed in due course.

6 References

Amin, A., Foster, S.J., and Kaufmann, W., 2017. "Instantaneous deflection calculation for steel fibre reinforced concrete one way members," Engineering Structures, 131, pp. 438–445.

Aslani, F., Nejadi, S., and Samali, B., 2014. “Long-term flexural cracking control of reinforced self-compacting concrete one-way slabs with and without fibres,” Computers and Concrete, 14, pp. 419–443.

Cardoso, D.C.T., Pereira, G.B.S., Silva, F.A., et al., 2019. “Influence of steel fibers on the flexural behavior of RC beams with low reinforcing ratios: Analytical and experimental investigation,” Composite Structures, 222.

CEN (2005). EN 14651:2005+A1:2007 — Test method for metallic fibre concrete — Measuring the flexural tensile strength (limit of proportionality (LOP), residual). European Committee for Standardization, Brussels, Belgium

Conforti, A., Zerbino, R., and Plizzari, G.A., 2021. “Assessing the influence of fibers on the flexural behavior of reinforced concrete beams with different longitudinal reinforcement ratios,” Structural Concrete, 22, pp. 347–360.

Di Prisco, M., Plizzari, G., and Vandewalle, L., 2009. “Fibre reinforced concrete: New design perspectives,” Materials and Structures, 42, pp. 1261–1281.

Nakov, D., Markovski, G., Arangjelovski, T., and Mark, P., 2016. “Creeping effect of SFRC elements under specific type of long-term loading.”

Pakravan, H.R., and Ozbakkaloglu, T., 2019. “Synthetic fibers for cementitious composites: A critical and in-depth review of recent advances,” Construction and Building Materials, 207, pp. 491–518.

Sturm, A.B., Visintin, P., and Oehlers, D.J., 2018. “Time-dependent serviceability behavior of reinforced concrete beams: Partial interaction tension stiffening mechanics,” Structural Concrete, 19, pp. 508–523.

Sturm, A.B., and Visintin, P., 2019. “Local bond slip behavior of steel reinforcing bars embedded in ultra-high-performance fibre reinforced concrete,” Structural Concrete, 20, pp. 108–122.

Tan, K.H., Paramasivam, P., and Tan, K.C., 1994. “Creep and shrinkage deflections of RC beams with steel fibers,” Journal of Materials in Civil Engineering, 6(4), pp. 474–494.

Tan, K.H., Paramasivam, P., and Tan, K.C., 1995. “Cracking characteristics of reinforced steel fiber concrete beams under short- and long-term loadings.”

Tan, K.H., and Saha, M.K., 2005. “Ten-year study on steel fiber-reinforced concrete beams under sustained loads,” ACI Structural Journal, 102(3), pp. 472.

Tošić, N., Aidarov, S., and de la Fuente, A., 2020. “Systematic review on the creep of fiber-reinforced concrete,” Materials, 13.

Tošić, N., Bokern, J., Hunger, M., and de la Fuente Antequera, A., 2024. “Effect of fibre type and quantity on the short- and long-term behaviour of polypropylene fibre reinforced concrete beams,” RILEM Bookseries, Springer, pp. 440–447.

Vasanelli, E., Micelli, F., Aiello, M.A., and Plizzari, G., 2014. “Crack width prediction of FRC beams in short and long term bending condition,” Materials and Structures, 47, pp. 39–54.

Visintin, P., Sturm, A.B., and Oehlers, D.J., 2018. “Long- and short-term serviceability behavior of reinforced concrete beams: Mechanics models for deflections and crack widths,” Structural Concrete, 19, pp. 489–507.

Watts, M.J., Amin, A., Gilbert, R.I., Kaufmann, W., and Minelli, F., 2020. "Simplified prediction of the time-dependent deflection of SFRC flexural members," Materials and Structures, 53(3), p. 48.

Watts, M.J., Amin, A., Gilbert, R.I., Kaufmann, W., and Minelli, F., 2021. "Simplified time-dependent crack width prediction for fiber reinforced concrete flexural members," Structural Concrete, 22(3), pp. 1549–1560.

Watts, M.J., Amin, A., and Gilbert, R.I., 2022. “Time-dependent deformation and cracking behaviour of FRC beams,” Engineering Structures, 268.

Eco-Resilient (ECORE) FRC Constructions

Pierre Rossi[1]

[1]: Civil Engineering Department, COPPE, Federal University of Rio de Janeiro, Brazil.

Abstract

This paper presents a new concept concerning the development of eco-resilient concrete constructions, that is to say constructions with a reduced carbon footprint and which can withstand mechanical stress and physico-chemical attacks worsened by climate change. After a critical analysis of current research and development policies in the field of concrete construction, a new global approach is proposed which should allow this concrete construction profession to better respond to the challenges caused by global warming. This approach is based on two strong ideas: 1) The use of fiber in combination with passive or active reinforcements in all constructions susceptible to crack; 2) The use of numerical models based on non-linear finite element calculations in order to optimize the design of eco-resilient concrete constructions.

Keywords

Concrete constructions, Fiber reinforced concretes, Ecological, Resilient, Design optimization, Finite Element Models

1 Introduction

Climate change has various causes and consequences. Concrete structures both contribute to these causes and suffer from their consequences. Due to the poor carbon footprint of cement, the main constituent of concrete, they are a major contributor to global warming (not to mention the consumption of natural resources). As the most widely used material in the construction industry, concrete structures also become victims of climate change. Indeed, this disruption leads to exceptional and frequent natural hazards. Among these hazards, one may cite, non-exhaustively, floods, coastal overflows, earthquakes, and fires. All of them subject concrete structures to severe mechanical and physical aggressions to which they must resist. Among these aggressions, the most significant are dynamic loadings (impacts and earthquakes), temperature variations (day/night, summer/winter), humidity variations (rain/drought), water penetration (flooding), and very high temperatures (fires).

Concrete structures must therefore demonstrate increasing resilience. The main aspect of this resilience is linked to the design of these structures, which must enable them to withstand such aggressions with minimal damage. This last point is important because rapid repair, at the lowest possible cost and with minimal consumption of natural resources, is the best candidate for sustainable development.

In conclusion, today's and tomorrow's concrete structures must be both ecological and resilient, or eco-resilient (ECORE structures). Achieving these two objectives is far from simple. The current shortcomings of research and development clearly illustrate this difficulty.

This paper expands upon and develops the content of a previous article on the same topic (Rossi, 2024).

2 Critical analysis of research in the field of concrete structures

2.1. Research at the Material Scale

Research and development, considered at the international level, has in recent years focused mainly and heavily on the ecological aspects of concrete, with the primary objective of reducing its carbon footprint. To achieve this, studies have concentrated on developing concrete mixtures containing less cement by replacing part of the cement with powders having lower carbon footprints and/or derived from recycled materials. Consequently, these studies have focused on rheology (workability), durability, and elementary mechanical behavior (compressive and tensile strengths) of these new so-called "ecological" or alternative concretes.

However, it should not be forgotten that the sole purpose of a construction material is to be used in the erection of a structure (a self-evident truth). Therefore, it is the structure itself that must be ecological, while concrete is merely a means to achieve this objective.

A concrete structure thus becomes "ecological" by reducing the amount of cement it contains while still fulfilling the functions required of it.

As previously mentioned, due to climate change, concrete structures are subjected to increased mechanical stresses and physicochemical aggressions. Understanding the cracking process of these structures is therefore a major issue in relation to such aggressions because:

- The cracking process of concrete subjected to impulsive loadings (such as impacts) or seismic-type loading (which falls within the framework of plastic fatigue) is very different from that associated with quasi-static loading.
- So-called service cracking (crack openings normally not exceeding 300 µm) greatly accelerates the penetration of aggressive liquids (water containing aggressive ions) into both the concrete itself and the reinforcements present in load-bearing structures, such as passive reinforcement in reinforced concrete or active reinforcement in prestressed concrete.

However, determining the tensile and compressive strengths of concrete does not provide relevant information about the cracking process under static loading, and even less under seismic or dynamic loading (impacts) of a structure made of this concrete.

Only the use of fracture mechanics makes it possible to obtain such relevant information.

Consequently, current research on alternative concretes is insufficient to address the challenges posed by climate change.

2.2. Research at the Structural Scale

As previously stated, it is the concrete structure itself that must be ecological. In other words, the structure must minimize, for given functions, the quantity of cement it contains. Achieving this minimization necessarily depends on the design method chosen for the structure.

Nowadays, concrete structures are predominantly designed using design codes (Eurocodes in Europe). These codes emerged at the beginning of the 20th century in order to enable numerous engineering firms around the world to design concrete structures rapidly and with the highest possible level of safety.

These design codes are based on simplified approaches that remain rather rudimentary compared to the real mechanical and physicochemical behavior of concrete structures. This is one of the main reasons why they incorporate numerous so-called safety coefficients, whose purpose is to compensate for the deficiencies and uncertainties inherent in these approaches.

The problem, in view of current challenges, is that these safety coefficients generally lead to significant overdesign of concrete structures, without necessarily making them safer.
In other words, design codes result in excessive consumption of concrete and therefore cement.

Today, a large majority of national and international working groups dealing with the design of concrete structures are working on the announced improvement of these design codes.

Improving a conceptually unsuitable tool will not produce a suitable tool, but may only reduce its inadequacy.

3 Proposal for a global design approach for ECORE concrete structures

In order for concrete structures to improve their resistance to the mechanical and physicochemical aggressions associated with climate change, they must improve their resistance to cracking under such aggressions.

It is now well known and accepted that fibers, particularly steel fibers, greatly contribute to controlling this cracking process (research on this topic is now fully clear and mature). Thus:

- Fibers are more effective than conventional reinforced concrete bars in controlling service cracks. Under the same service loading, cracks are narrower, more tortuous in their propagation path, and often discontinuous in the presence of fibers. Concrete structures therefore become much more resistant to liquid penetration.
- Fibers combined with reinforced concrete bars provide significant improvement in the impact and seismic behavior of concrete structures.

These positive contributions of fibers are linked to the fact that they act at a different scale of the concrete cracking process and complement conventional reinforcements (passive and active reinforcements).

Today, fibers must be considered just as indispensable as these conventional reinforcements.

Fibers should be used in all concrete structures whose functions are impaired by cracking.

The addition of fibers therefore improves the resilience of concrete structures, but it does not necessarily achieve the objective of improving the ecological performance of these structures.

To achieve this, their design must lead to a significant reduction not only in the quantity of cement used, but also in the quantity of reinforcement bars and fibers.

Structures with hyperstatic mechanical behavior are those that provide greater safety when cracking occurs. This is due to a much less localized cracking process (because of stress redistribution) than that associated with mechanically isostatic structures, especially in the case of service cracking.

As previously mentioned, current structural design rules for concrete structures are too rudimentary to realistically account for the multiple-cracking mechanisms of hyperstatic structures, whether they are made of reinforced concrete, fiber-reinforced concrete, or hybrid reinforcement combining bars and fibers. They cannot lead to an optimized design of these structures.

The only possible solution lies in the use of nonlinear finite element analysis, that is, analysis capable of accounting for the cracking processes of concrete structures.

A number of numerical models pursuing this objective already exist in the scientific literature.

The main problem in using these models for optimized design (in terms of shape, geometry, and dimensions) is that they are currently insufficiently validated at the scale of real structures.

In the past, numerous experimental studies were carried out internationally on full-scale structures or structural elements. The main objective of these studies was to demonstrate that design codes were sufficiently reliable with regard to ultimate structural behavior, particularly ultimate strength.

Today, similar experimental campaigns must be conducted again. However, this time, their objective should be the validation of numerical models regarding their ability to account, both qualitatively and quantitatively, for cracking processes at serviceability and ultimate limit states of structures.

If this objective is not considered a priority in the field of concrete structures, it is highly unlikely that the concept of eco-resilient structures will develop.

4 Existing numerical models for cracking analysis of concrete structures

In the framework of this paper, it has been chosen to consider only models relevant for performing simulations of real structures.

In the literature, there exist two main model families for analyzing the cracking process of FRC structures: the diffused cracking models and the explicit cracking models.

It is important to focus on the fact that, for all of these numerical models, the main mechanical property of FRC used is its behavior in uniaxial tension and, more especially, the mechanical relationship between the uniaxial tensile strength and a crack opening.

This relationship can be obtained directly by performing a uniaxial tensile test on notched specimens]; or, indirectly, by performing bending tests on small beams or on small slabs and by using inverse approaches.

The first type of test is the best one for directly and precisely obtaining the mechanical data (Rossi, 2024); however, this test is unfairly considered difficult to perform (Rossi, 2024). This is the reason why many researchers prefer to perform the second family of tests even though these tests are indirect and less precise.

4.1. Diffused Cracking Models

These models do not consider cracks as real cinematic discontinuities but as microcracked zones in which the density of the microcracks continuously increases until they create a kind of hole (no more stresses are transmitted). Numerically speaking, in the framework of finite elements theory, the microcracked zones are modeled by using volume elements. This means that the volume of the holes corresponds to the volume elements adopted.

In these models, which are generally determinist, the non-linear mechanical behavior (related to the microcracking process) of the volume elements is linked to the post-peak behavior in the tension of the FRC. This post-peak behavior is generally characterized by two material parameters:

- The shape of the post-peak (this means after the linear elastic part of the tensile behavior of the FRC) behavior of the tensile stress-strain curve.

- The post-peak energy dissipation related to the tensile stress-strain curve. This dissipation energy is very often called G_f.

To summarize, the diffuse cracking models, applied to FRC, are based on the use of the non-linear finite elements method with volume elements. The non-linear behavior considered is that of the FRC in tension, in the form of a relationship between the tensile stress and the tensile strain.

Experimentally speaking, the post-peak behavior of FRCs corresponds to the post-localization cracking; this means after it progresses from diffused microcracking to a localized macrocrack. Then, it clearly appears that the diffuse cracking models are not physically based.

The post-peak behavior in tension, used as the main mechanical characteristic in the diffused cracking models, comes from the experimental tensile stress-crack opening–tensile strain used in the model requires the introduction of a length that permits the division of the crack's opening value to obtain the "equivalent" tensile strain.

In the majority of the diffused cracking models, this length is linked to the volume element size of the finite element mesh.

This length chosen and used in the numerical simulation is very important because it permits, during the simulation, the transformation of the non-linear strains observed in crack openings.

These models, which at the present time are the most commonly described in the literature and used in practice, have a large drawback where the determination of crack openings that are less or equal to 300 microns is concerned.

Indeed, the diffused cracking models are not physically based because they "transform" a localized crack in a diffused microcracking zone. This strong physical approximation leads to a strong approximation of the cracking pattern of a given FRC structure being obtained, especially at the service limit state. The cracks are always more numerous and less spaced out at the service limit state than at the ultimate limit state. Being that the G_f values are a lot larger for FRCs than for normal concretes, the diffused cracking models result in a greater spread of the damaged (microcracked) zones and an underestimation of crack openings. Therefore, these models do not lead to a fairly reliable and secure response to the durability of FRC structures.

However, at the ultimate limit state, whereby cracks are localized with larger openings, the diffused cracking models are less approximate.

The more well-known diffused cracking models for FRC are damaged models (Fanella and Krajcinovic, 1985; Li and Li, 2000; Peng X and Meyer C, 2000) and smeared crack models (Barros and Figueiras, 2001; Cunha et al., 2012; De Montaignac et al., 2013), which are mechanically equivalent.

4.2. Explicit Cracking Models

Contrary to the diffused cracking models, the explicit cracking models have the objective of treating the cracks as "real" cracks, which means as cinematic discontinuities and not as non-linear strains.

There mainly exist two families of explicit cracking models that can analyze cracking at the scale of the structure: the cohesive crack models and the probabilistic explicit cracking models.

4.2.1. The Cohesive Crack Models

These models were the first to be used to analyze crack propagation in FRCs (Hillerborg, 1980; Forbes, 2001; Carpinteri et al., 2015).

In these models, the propagation of existing cracks is modelled by using interface elements. These interface elements are located at the front tip of the existing cracks.

The interface elements are interesting because their behavior (linear or non-linear) is not considered via a stress–strain relationship but via a stress–displacement relationship. This means that the experimental post-peak behavior of the FRC linking the tensile stress to the crack opening can be directly used as the non-linear behavior of the interface elements. This is a large advantage compared to the diffused cracking models. Indeed, the fact that these models are more physically based allows them to avoid the use of a “numerical length”, which is not physically based (so leads to some approximations), to transform a strain in a displacement (so in a kind of equivalent crack opening).

There is nevertheless a large problem concerning the field of utility and therefore of the use of these models.

Indeed, as mentioned before, they are models related to crack propagation and not to crack initiation. This means that it is important to know the initial position of the cracks to study their propagation by using the numerical model. This is not very effective when the structure has many cracks at the service limit state.

So, these models are more effective at following one crack propagation until the rupture of the FRC structure.

4.2.2. The Probabilistic Explicit Cracking Model

The probabilistic explicit cracking model (Rossi et al., 2016; Rossi et al., 2018) is based on the following physical assumptions:

- The material being considered is heterogeneous and its local mechanical characteristics are randomly distributed.
- These mechanical characteristics are scale effect dependent. This means that they depend on the volume of the material considered.

From the mechanical and numerical points of view, this can be summarized as follows:

- Each volume element of the mesh represents a volume of the heterogeneous material.
- The tensile and shear strengths are distributed randomly over all elements of the mesh.
- Cracks are simulated by using non-linear interface elements (quadratic elements). Failure criteria of Rankin in tension and Tresca in shear are used. Once one of these failure criteria is reached, the interface element is considered as opened, simulating a crack’s creation. The tensile and shear strengths, as well as the normal and tangential stiffness values of the element, are then set equal to zero.

The complete bridging action of fibers inside the cracks is simulated as follows:

- The normal and tangential stresses in the interface element linearly increase with the normal and tangential displacements to simulate the elastic bridging action.

- This elastic action of the fibers exists until a threshold value related to the normal displacement is reached. From this threshold value, the normal stress linearly decreases with the normal displacement. This is to consider the damage of the bond between the concrete and the fiber. This decreasing evolution is considered through a damage model.
- Finally, when the normal displacement reaches a second threshold, the action of the fibers is considered negligible, and so, the interface element is considered definitively broken. Its normal and tangential rigidities are then set to zero.
- The post-cracking energy, dissipated during all of the bridging action of the fibers, is randomly distributed over the finite element mesh. This random distribution is a log-normal distribution function with a mean value independent of the mesh elements' size and a standard deviation that increases as the mesh elements' size decreases. This choice is in perfect agreement with the experimental results.

4.3. Critical comments

The main problem in using these above models for optimized design is that they are currently not enough validated at the scale of real structures, especially when the cracking process at the service life is concerned.

In the past, numerous experimental studies were carried out internationally on full-scale structures or structural elements. The main objective of these studies was to demonstrate that design codes were sufficiently reliable with regard to ultimate structural behavior, particularly ultimate strength.

Today, similar experimental campaigns must be conducted again. However, this time, their objective should be the validation of numerical models regarding their ability to account, both qualitatively and quantitatively, for cracking processes at serviceability and ultimate limit states of structures.

In this context, the second Blind Simulation Competition (BSC) organized by fib WG 2.4.1 aimed to evaluate the predictive performance of finite element method (FEM)-based models for the analysis and design of hybrid-strengthened structures. The chosen structure was a shallow beam for which two models were tested up to failure. Performed measurements include the applied loads, crack widths, material deformations in critical zones and the overall structural behavior (Barros et al., 2023).

Although the work carried out as part of this Fib blind competition was significant and original, it presented a limitation regarding the conclusions that can be drawn about the prediction of cracks opening at Service Limit State. Indeed, during the experimental tests, only the average cracks opening in specific zones of the beam were measured. However, what matters for the durability of the beam is not the average cracks opening but the widest cracks, which is very different (the same average can result from very different cracks opening distributions).

It will therefore be necessary, in the future, to repeat this type of blind competition with access to these widest cracks opening.

It is important to point out and emphasize that, to date, very few numerical models have been developed and validated to analyze the cracking of fiber-reinforced concrete structures subjected to impact or seismic loading.

To address the challenges associated with the development of resilient eco-structures

subjected to climate change-related hazards, it is urgent to develop these numerical models.

5 Concluding remarks

This paper addresses the response of the concrete construction industry to the challenge posed by global warming and the disruptions it generates.

It indicates that a relevant, efficient, and accessible approach to meeting this challenge consists in developing the concept of eco-resilient (ECORE) structures.

This concept is based on two major ideas: 1) Using fiber-reinforced concretes in combination with passive or active reinforcements in all structures likely to crack when subjected to loadings intensified by climate disruption: 2) Using numerical models based on nonlinear finite element analysis in order to optimize the design of these eco-resilient concrete structures.

The main challenge in using these models for optimized design (in terms of shape, geometry, and dimensions) is to sufficiently validate them at the scale of real structures.

In the past, numerous experimental studies were carried out internationally on full-scale structures or structural elements to demonstrate that design codes were sufficiently reliable with regard to ultimate structural behavior, particularly ultimate strength. Today, similar experimental campaigns must be conducted again to validate the numerical models related to FRC regarding their ability to account (both qualitatively and quantitatively) for cracking processes at serviceability and ultimate limit states of structures submitted to static, seismic and impact loadings.

If this objective and challenge are not considered a priority in the field of concrete structures, it is highly unlikely that the concept of ECORE structures will develop.

6 References

Barros, J., Figueiras, J.A, 2001. “Model for the analysis of steel fiber reinforced concrete slabs on grade”, *Computers & Structures* 79(1): 97- 106.

Barros J. A. O. et al., 2023. “Blind competition on the numerical simulation of continuous shallow steel-fiber reinforced concrete beams failing in bending.” *fib Structure Concrete Journal*, vol. 24, no. 3, pp. 1–31.

Carpinteri, A., Cadamuro, E. and Ventura, G., 2015. “Fiber-reinforced concrete in flexure: A cohesive/overlapping crack model application.” *Mater. Struct*, 48, 235–247.

Cunha, V., Barros, J., Sena-Cruz, J. A finite element model with discrete embedded elements for fiber reinforced composites. *Computers & Structures* 94-95: 22-33, 2012.

De Montaignac, R., Massicotte, B. and Charron, J-P., 2013. “Finite-element modelling of SFRC members in bending”, *Magazine of Concrete Research* 65(19): 1133-1146.

Fanella, D. and Krajcinovic, D., 1985. “Continuum damage mechanics of fiber reinforced concrete”, *J. Eng. Mech.* 111(8): 995-1009.

Forbes, O. J., 2001. “Fictitious Crack Propagation in Fiber-Reinforced Concrete Beams.” *J. Eng. Mech.*, 127, 272–280.

Hillerborg, A., 1980. “Analysis of fracture by means of the fictitious crack model, particularly for fibre reinforced concrete.” *Int. J. Cem. Compos*, 2, 177–184.

Li F. and Li Z., 2000. “Continuum damage mechanics-based modeling of fiber reinforced concrete in tension”, *Int J Solids Struct* 38: 777-793.

Peng X and Meyer C, 2000. “A continuum damage mechanics model for concrete reinforced with randomly distributed short fibers.”, *Comput Struct* 78: 505-515.

Rossi, P., Tailhan, J.L. and Daviau-Desnoyers, D., 2016. “Numerical models for designing steel fiber reinforced concrete structures: Why and which ones?” *FRC 2014: ACI-fib International Workshop*; Massicotte, Charron,, Plizzari and Mobasher (Eds).; *FIB Bulletin 79—ACI SP-310*; *American Concrete Institute*: Farmington Hills, MI, USA, V. 310, pp. 289–300.

Rossi, P., Daviau-Desnoyers, D. and Tailhan, J.L., 2018. “Probabilistic Numerical Model of Ultra-High-Performance Fiber Reinforced Concrete (UHPRFC) Cracking Process.” *Cem. Concr. Compos.*, 90, 119–125.

Rossi, P, 2024. “Experimental Test for Characterizing the Tensile Behavior of Fiber Reinforced Concretes (FRCs): Uniaxial Tensile Test Versus Bending Test.”, *Transforming Construction: Advances in Fiber Reinforced Concrete; BEFIB 2024; RILEM Book series*, Mechtcherine, Signorini, Junger, D. (eds), vol. 54.. https://doi.org/10.1007/978-3-031-70145-0_18.

Rossi, P., 2024. “Eco-resilient (ECORE) concrete constructions: a new challenge and a new concept.”, *Current Trends in Eng Sci.* 4: 1052

Ultra-High-Performance Concrete (UHPC) as a sustainable alternative

Hudd, R.W.[1], Kumar, D.[1], Winterberg, R.[2]

[1]: School of Engineering, University of Waikato, New Zealand.

[2]: Managing Director, Ductil GmbH, Essen, Germany.

Abstract

UHPC is renowned for its superior strength and durability, offering substantial improvements over traditional concrete in terms of structural integrity and design flexibility. These developments facilitate the creation of longer, slenderer, and more aesthetically appealing structures, while simultaneously ensuring increased resilience and longevity.

This paper reports on research with UHPC as an alternative to conventional concrete for lower strength applications. Experimental investigations undertaken on lightly reinforced concrete beams showed that 'I'- and 'T' section UHPC beams yield comparable load bearing capacity to a reference beam with square cross section. The material and environmental costs have been analysed. The reduced material quantities in the UHPC specimens show that the I-beam material cost and GWP were only about 30% higher than the reference. The T-beam costs were both about 5% less than the reference. A new type of micro steel fibre was also investigated which allowed significant reduction of fibre dose rate while giving the same flexural and shear performance. This in turn further reduces the environmental impact.

Keywords

UHPC, micro steel fibre, fibre reinforced concrete, post-crack performance, shear performance, sustainability

1 Introduction

UHPC is a high strength cementitious material, usually consisting of cement, fine aggregates and fillers often reinforced with steel fibres. While definitions vary, a compressive strength of at least 150 MPa is typically used as an indicator. The high compressive strengths are achieved primarily by adopting low water-to-binder ratios typically below 0.25. Early research aimed to achieve this through optimised particle packing (Bache, 1981) or applied high pressures and temperatures after casting to densify the mixes and activate reactive filler components (Richard & Cheyrezy, 1995). Modern high-performance super plasticising admixtures allow very workable mixes to be obtained at very low water-to-binder ratios.

The high strength performance of UHPC lends itself to applications such as bridges and high-rise structures which require these high compressive strengths to support the loads. A pedestrian bridge was designed and constructed using UHPC due to the architectural limitation on the height vs. span rate (Matupayont & Winterberg, 2024). Using pre-stressed UHPC allowed for a shallow height vs. span rate of 1:22 only.

When compared to conventional concrete, UHPC is an expensive material. High cement contents, admixtures, steel fibres and selected aggregates and fillers all result in higher raw material cost. As a result, it is not generally considered to be cost-effective for conventional applications. The high binder content also contributes to a larger environmental footprint.

The research presented in this paper investigated the potential to use UHPC as a means of reducing material cost and environmental impact. The properties of the UHPC mixtures using a small aggregate size and a flowing consistency allowed it to be placed into narrow sections. The aim was to determine if the cost and environmental impact of thin UHPC elements would be comparable to that of a conventional concrete section with the same performance properties.

2 Experimental program

The test programme evaluated the effect of varying section dimensions on flexural and shear performance of simple reinforced concrete beams. The different beam sections made are shown in Figure 1.

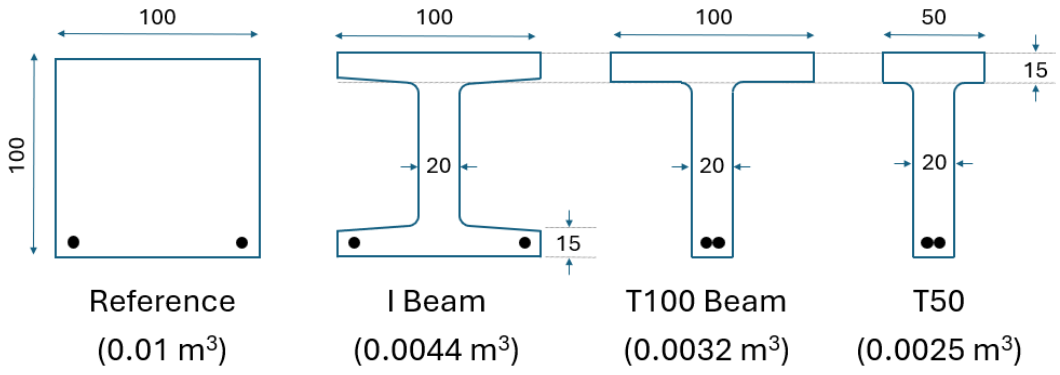


Figure 1: Reference and UHPC beam sections.

Reference beams with a 100 mm square section were made using a 40 MPa concrete mix with a 10mm maximum aggregate size. Beams were reinforced with two 500 grade 6 mm diameter rebars. The UHPC mix used for these tests used locally available Portland cement (Standards New Zealand, 2009), a locally sourced greywacke aggregate (<2.36mm), polycarboxylate superplasticiser and 13mm steel fibres (2800 MPa, aspect ratio = 65). Superplasticising admixture and fibre quantities were varied to meet specific beam requirements. Approximate mix quantities are shown in Table 1:

Table 1: Concrete Mix Quantities.

	Reference		**UHPC**	
Material	kg/m^3	% by weight	kg/m^3	% by weight
Portland Cement	370	16	1000	43
Fine Aggregate	740	31	1000	43
Coarse aggregate	1110	47		
Water	165	7	250	11
Admixture			10 – 12	0.5
13 mm steel fibres			0 – 160	0 – 7

Comparison of material usage based on cross sectional area showed the I-beam used 44% of the concrete in the reference while T-beams with initial and reduced flange widths had 32 and 25% of the volume respectively. Beams were tested using a four-point bending rig with the arrangement shown in Figure 2.

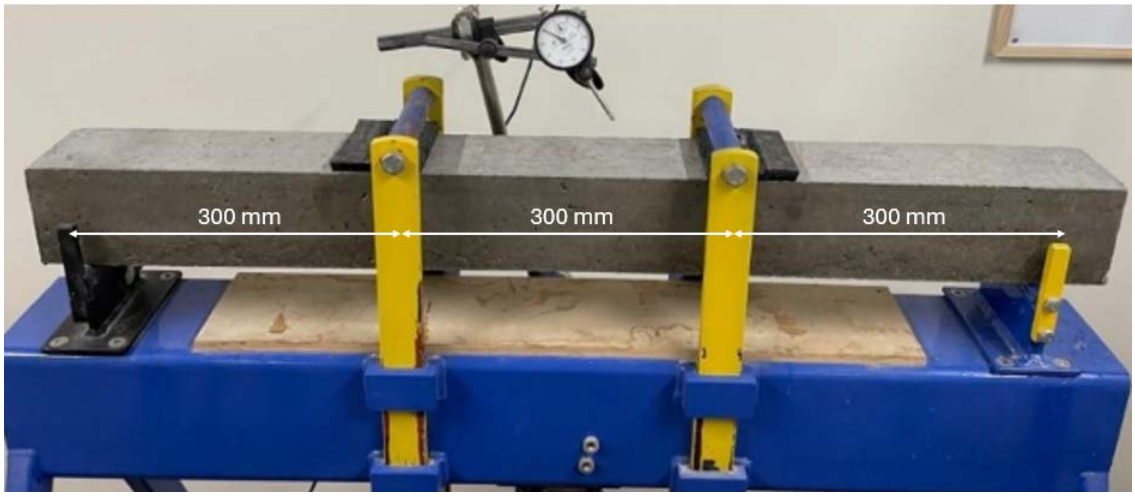


Figure 2: Four Point Testing Assembly.

Load was applied vertically downwards at the two third points using a manually operated hydraulic jack. Load was determined using a 100 kN load cell connecting the jack to the frame. Beam deflection was recorded using a dial gauge positioned at mid-span. Load was applied at approximately 5 kN per minute with deflections recorded at 1 kN intervals. Crack development was monitored visually and subsequently linked to the load and deflection behaviour.

2.1 Behaviour under Loads

Consistent load deflection behaviour was observed in the majority of cases (Figure 3). The curves show an initial linear behaviour attributed to the tensile strength of the concrete. This typically occurred at an applied load of 6 – 7 kN for the reference beams and 10 – 12 kN for the UHPC beams. This was followed by a flatter portion of the curve attributed to the elastic response of the steel reinforcement. Finally, at higher loads the curves flattened off indicating the increased extensions associated with the steel yielding.

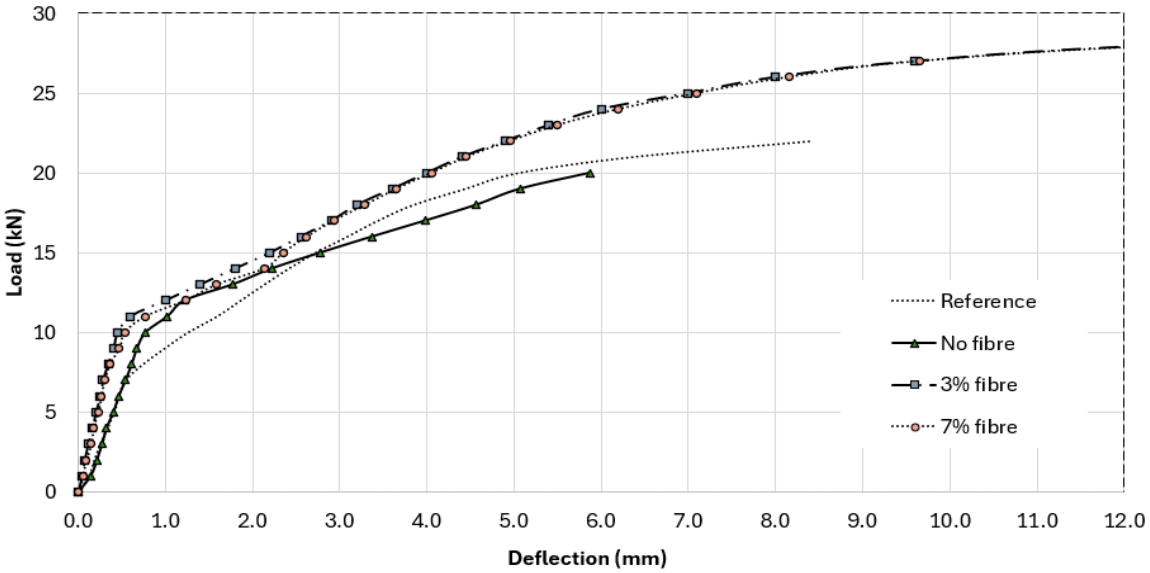


Figure 3: Relationship between load and deflection for I-beams with different fibre contents, reference beam included for comparison.

The reference beam exhibited a conventional balanced failure mode with increasing deflection at constant load followed by compression failure in the concrete (Figure 4, left).

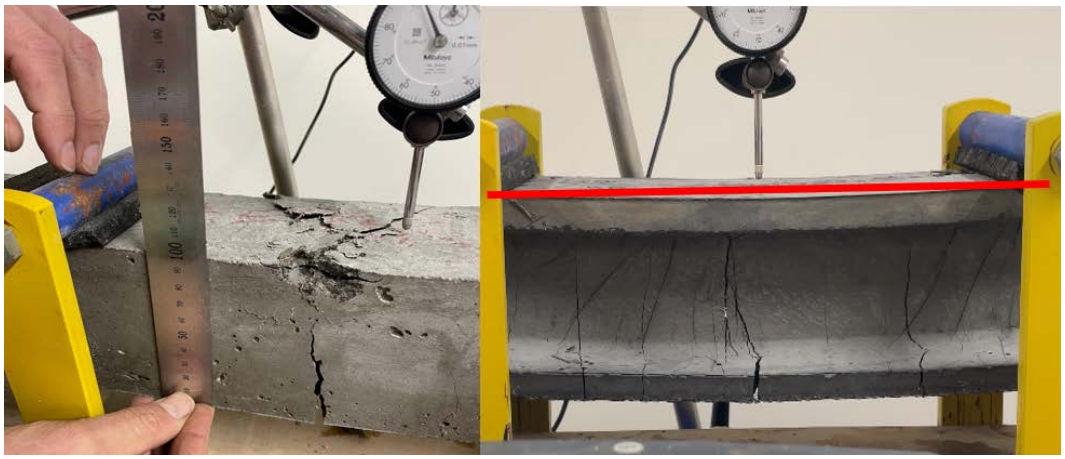


Figure 4: Reference (left) and UHPC I-beam Failure Modes (right).

Several different failure modes were observed in the UHPC beams:

1. Increased deflection with constant load, however no concrete compression failure was observed (Figure 4, right).
2. Shear failure adjacent to one support accompanied by formation of a large shear crack, with a large associated deflection and loss of load capacity
3. Gradual shear failure associated with development of numerous inclined cracks, increase in load capacity and deflection

Assessment of the different failure modes allowed the UHPC sections to be optimised.

With the initial I-section it was identified that while the bending performance was comparable with the reference, the beam exhibited a shear failure. Inclusion of 3% by weight of fibres improved both the shear and flexural capacity.

Adopting a T-beam reduced the material quantity required for the beam but required an increase in fibre quantity to give sufficient shear strength. It was noted that with higher fibre contents, shear cracking was evident, but the failures were gradual without loss of load carrying capacity. Tests showed that while the compressive strength was improved by adding fibres this additional strength did not contribute to the beam performance.

2.2 UHPC beam development

The main objective of this project was to demonstrate that beams made using UHPC could provide comparable strength performance to conventional beams using less material. The absence of coarse aggregate in the UHPC allowed thin sections to be cast giving substantial reductions in material volumes.

Preliminary testing used UHPC to make an I-section beam. These beams exhibited similar load capacity to the reference beams but exhibited a shear failure at maximum load. This was attributed to the reduced concrete area in the section (Figure 1). Incorporating steel fibres is frequently reported in UHPC mix designs with quantities up to 2% by volume (~7% by weight). Adding 3% by weight of fibres to the mix proved to be effective for the I-sections giving increased load capacity and shear strength. Beams were tested with fibre contents up to 7% by weight but there was no additional increase in the load capacity.

The change to an I-section represented a 56% reduction in concrete volume. However, except at the supports, analysis showed that the concrete in the tensile face flange was not contributing to the performance. To evaluate the effect of this a T-section was adopted with the same web thickness and compression flange as the I-section. This section achieved the same load capacity as the I beam. However, with only 3% fibre content substantial shear cracking was observed. The failure was gradual with multiple shear cracks opening up along the end sections of the beams. Increasing the fibre content to 5% fibre was effective for controlling this behaviour.

It was noted that there was minimal or no visible concrete crushing in the compressive face of the section indicating that the concrete was not failing. To further optimise the sections the flange width in the T-section was reduced to 50 mm. This provided further material savings without any observed reduction in load capacity (Figure 5).

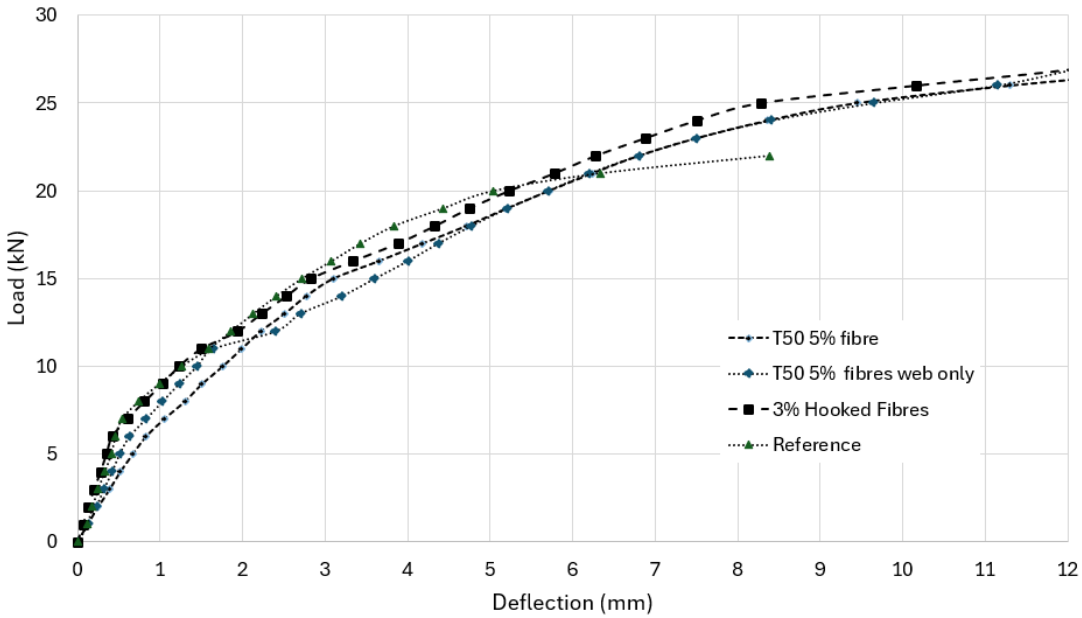


Figure 5: Relationship between load and deflection for 50 mm T-beams with different fibres.

Inclusion of fibres added to the material cost so a test was conducted to determine whether the strategic placement of fibres could achieve the same load capacity but at a reduced cost. A beam was cast with fibres in the web only. This beam had comparable performance to the beam with fibres throughout.

Further tests were carried out to evaluate if hooked fibres gave better performance. Tests showed that 3% by weight of 14 mm hooked fibres (2800 MPa, aspect ratio = 70) was sufficient to control shear in a T-beam.

3 Economic impact

A key objective of this research was to determine whether UHPC could be a more cost effective than conventional concrete in low strength applications. The high cement, fibre and admixture content gives UHPC a high material cost. Additionally, utilising selected aggregates and fillers further contributes to the high cost. In this study, costs were minimised by using commonly available fine aggregates and not including fillers.

Material costing was evaluated for the mix constituents shown in Table 2 using bulk material costings from local retail suppliers where available. These were used to compare the costs of the elements being produced which allowed comparison on a like-for-like performance basis rather than a bulk material cost (Table 2).

As can be seen, UHPC without fibres is double the cost of the same volume of the reference concrete. The cost increased progressively as the fibre content increased. However, as can be seen from the table as material quantities are reduced the individual unit cost is reduced. While smaller sections required higher fibre percentages to give adequate overall performance the values show that optimal fibre dosage and application give comparable or better cost performance than the reference beam.

Table 2: Material and unit costs for reference and UHPC beams.

	Reference		UHPC	I-beam	T100	T50	T50 Web
Fibres ($5/kg)	$/m^3	$/beam	$/m^3	$/beam	$/beam	$/beam	$/beam
0%	$376	$3.76	$720	$3.17 (-16%)	-	-	-
3%			$1100	$4.87 (+29%)	$3.54 (-6%)	$2.71 (-28%)	$2.45 (-35%)
5%			$1350	$5.99 (+59%)	$4.35 (+16%)	$3.33 (-11%)	$2.90 (-23%)
7%			$1570	$6.96 (+85%)	$5.06 (+34%)	$3.87 (+3%)	$3.27 (-13%)

While the reduced sections enable considerable volume savings and base material costs, the inclusion of fibres for shear performance offsets some of the cost benefits. Selective application of fibres, for example only including them in the webs, did give a cost benefit. While this will increase complexity when casting the cost savings might be justified. A test using hooked fibres demonstrated that the same performance was achievable with a 40% reduction in fibre quantity.

4 Environmental impact assessment

An environmental assessment was carried out using equivalent carbon dioxide emission (CO2e) values obtained from environmental product declarations (EPDs) for the different materials. The results of these comparisons are shown in the Table 3.

Table 3: CO2 equivalent values for reference and UHPC beams (values in parentheses are percentages relative to the reference beam).

Cement GWP (CO2e.)		40MPa		UHPC		
	kg/tonne	kg/m^3	Beam	kg/m^3	I-beam 3% fibre	T-50 5% fibre
GP Cement	848	318	3.2	837	4.3 (+34%)	2.8 (-12%)
Eco Cement 1	704	265	2.7	696	3.6 (+33%)	2.2 (-18%)
Eco Cement 2	557	211	2.1	553	3.0 (+43%)	1.8 (-14%)

As with economic cost, these values show that the environmental impact of UHPC is more than double of the reference concrete with a conventional cement. Emission values for three cements were compared. As with the economic cost, the reduction in material for the UHPC beams results in emissions reductions for each unit with the 50 mm flanged T-beam having lower emissions than the reference.

Additional cost and environmental benefits are achievable. However, the present analysis only considered material quantities for comparable structural performance. While further

refinement of the mix designs and elements is expected to give further reductions in materials, the reduced UHPC sections offers potential for greater savings at a project level.

These will result from the following:

- Lower beam weights will reduce the size of supporting elements including columns and foundations. This will give further direct material reductions throughout the structure.
- Reducing structural loads will reduce the reinforcement requirement in these supporting elements.
- Reduced foundations size will reduce the amount of ground preparation or ground improvement works.
- Reductions in size and weight of elements will have a direct effect on logistics costs. For example, the number of precast UHPC elements that can be carried within proscribed weight limits for delivery vehicles will be increased. This will have a direct environmental benefit by reducing the number of vehicle movements required.

5 Concluding remarks

This research has demonstrated that utilising the high strength of UHPC significant reductions in materials quantities can be achieved while giving equivalent strength performance to a 40 MPa reference beam. Comparing the performance of I- and T- section beams made from UHPC showed that while smaller sections required increased fibre dose rates, it was still possible to obtain elements with comparable strength performance.

The reductions in material quantities gave direct savings in unit costs with reduced environmental impact. Comparison with the test beams showed that these were equivalent to or better than the reference beams. Furthermore, it can be argued that using smaller beam sections has cumulative benefits at a project level reducing overall structural load, foundation and logistical requirements.

6 References

Bache, H., 1981. “Densified Cement / Ultra-fine Particle-Based Materials”. *The Second International Conference on Superplasticisers in Concrete*, (pp. 1 - 34). Ottawa, Canada.

Matupayont, S., & Winterberg, R., 2024. “SCG-CPAC Ultra High Performance Fiber-Reinforced Concrete Bridge”. *fib Symposium 2024*. Christchurch, New Zealand.

Richard, P., & Cheyrezy, M., 1995. “Composition of reactive powder concrete”. *Cement & Concrete Research*.

Standards New Zealand, 2009. NZS 3122:2009 *Specification for Portland and blended cements*. Standards New Zealand, Wellington, New Zealand.

Evaluation of cracking localization and its effect on load and displacement capacities of R/SFRC beams

Yuri S. Karinski[1] and Avraham N. Dancygier[2]

[1] National Building Research Institute, Technion – Israel Institute of Technology, Technion City, Haifa 3200003, Israel

[2] Engineering Faculty, Kinneret Academic College on the Sea of Galilee, Zemach, Israel & Faculty of Civil and Environmental Engineering, National Building Research Institute, Technion – Israel Institute of Technology, Haifa, Israel.

Abstract

This work presents a model to evaluate the deflection capacity of R/SFRC beams, considering the effect of cracking localization phenomenon. This is a model, which is applicable to a wide range of reinforcement ratios: relatively low - when CL is significant, as well as relatively larger ratios, when cracking localization is negligible. The limit between these two ranges is set by a transition point that can be determined experimentally. The model employs a simplified curvature distribution along the beam at the ultimate limit state, which includes a part of the beam that has increased curvature, representing the 'weak sections' where CL develops. The ultimate deflection is calculated by performing cross-sectional analysis, where for the weak sections (if exist) the calculations are done with values of the SFRC residual strengths that are reduced by a factor proposed in the model. The model was validated against reported results of 4-point-bending tests of normal strength concrete within a relatively wide range of reinforcement ratios and 40 kg/m^3 of steel fibers. The comparison shows reasonable agreement between the calculated and test results for both deflection and moment capacities.

Keywords

Deflection capacity, R/SFRC beams, Cracking localization

1 Introduction

Reinforced concrete (RC) beams containing steel fibers are expected to show increased flexural ductility. However, steel fiber reinforced concrete beams with rebars (R/SFRC beams) that have relatively small reinforcement ratios (ρ) exhibit a phenomenon of 'cracking localization' (CL), which causes decrease of the displacement capacity, in contrast to plain RC beams (Dancygier et al, 2016; Yoo et al, 2018; Mahmood et al, 2024; Pleesudjai et al, 2025). Conversely, for larger reinforcement ratios R/SFRC beams behave similarly to plain RC beams (Hasgul et al, 2018; Küsel et al, 2019). This behavior depends on both fiber and reinforcement contents and the rebars' stress hardening (Gebreyesus et al, 2025; Shao et al, 2019). The transition from the two types of behavior - at lower and larger reinforcement ratios - corresponds to a transition point (TP) beyond which the effect of CL is negligible (Gebreyesus et al, 2023, 2025). Moreover, it has been shown that this phenomenon is characterized by a non-uniform widening of the flexural cracks, and it can be explained by the non-uniform distribution of the fibers along the beam (Dancygier et al, 2014). This non-uniform widening leads to strain (and stress) localization in the rebars that bridge the widened cracks and consequently - to decreased displacement capacity (Markic et al, 2020; Dancygier et al, 2019). Consideration of steel stress hardening is relevant because it can restrain the larger crack widening where CL occurs.

The reduction of displacement capacity is the reason for the EC2 requirement to increase the minimum reinforcement ratio in elevated R/SFRC beams and slabs when "plastic analysis is performed without direct check of the rotation capacity" (EN 1992-1-1, 2023). It is therefore important to develop analytical or numerical methods to evaluate R/SFRC beams' displacement capacity. Such methods are based on Finite Element analysis where each element takes into consideration the fibers and micro-crack distributions (Carvalhoa et al, 2020) or an analytical sectional analysis with moment-curvature relations (Yao et al, 2020; Mobasher et al, 2015). However, the CL phenomenon, which causes the non-uniform curvature distribution along the beam, is not included in these methods.

This paper presents an analytical model to evaluate the load and deflection capacities of R/SFRC beams for all ranges of the tension reinforcement, considering both cases when the effect of cracking localization affects the behavior and when it is insignificant.

2 The proposed model

The deflection capacity (at the ultimate limit state) of R/SFRC beams is proposed to be calculated by the model presented herein. For the cases when CL occurs, it is assumed that all wide cracks are located in the central part of the beam's span. This leads to the simplified curvature distribution $\phi(x)$, which is illustrated in Fig. 1c for a 4-point-bending setup. It can be seen in the figure that when there is cracking localization the curvature in the constant moment zone includes two parts: one with increased curvature ϕ_{cl} along a length denoted L_{cl} (also denoted in the following text as 'weak'), and the other with "ordinary" curvature ϕ_u. When CL is negligible (at certain, large enough reinforcement ratios), the curvature is constant. ϕ_y in the Fig. 1 is the curvature at yield at "ordinary" cross-sections of the beam, and M_y and M_u are the yield ultimate moments. Note that the curvatures ϕ_u and ϕ_{cl} correspond to ordinary and weak cross-sections under the same external moment M_u.

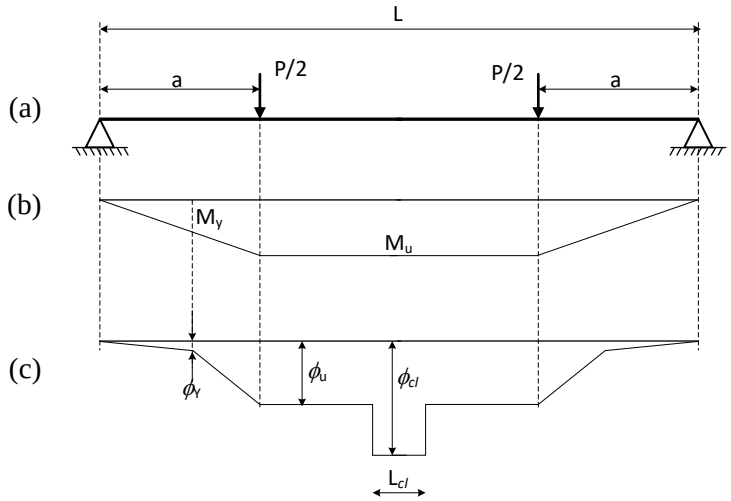


Figure 1: Illustration of the simplified curvature distribution for a 4-point-bending setup

The length L_{cl} is proposed in the model to be given by the following expression:

$$L_{cl} = \frac{L/2 - a}{n/m} \cdot CLF \leq L/2 - a \quad (1)$$

where n and m are the total number of cracks and the number of wide cracks, respectively, L and a are shown in Fig. 1a, and the coefficient CLF is given by:

$$CLF = 1 + (CLF_{max} - 1)\left(\frac{n/m - 1}{n - 1}\right)^{1/3} \quad (2)$$

Note that when n = m (no CL and $\phi_{cl} = \phi_u$) CLF = 1.0 and $L_{cl} = L/2 - a$, while when m = 1 (maximum level of cracking localization) CLF = CLF_{max} which should be calibrated.

As noted in the Introduction, there exists a transition point (TP) of reinforcement ratio above which cracking localization is negligible. Thus, in the model, n/m was set to 1.0 (and accordingly, CLF = 1.0) for the beam specimens with reinforcement ratios above the TP.

The SFRC residual strengths f_{R1} and f_{R3} are incorporated into sectional analysis, for the two types of cross-sections – 'weak' (reduced f_{R1} and f_{R3} values) and 'ordinary'. The resulting moment-curvature relations of these sections are then used to construct the curvature diagram along the beam (see Fig. 1c), which is then (twice) integrated to yield the ultimate displacement δ_u.

The material models of the SFRC and the reinforcing steel, used for the sectional analysis are based on the models proposed in EC2 (EN 1992-1-1, 2023) and Model Code 2020 (*fib*, 2023): The reinforcement steel is represented by an elastic-plastic material model with a linear hardening; The SFRC tensile behavior follows the bi-linear relationship specified in EC2, with the ascending branch neglected. For the concrete under compression, the EC2 non-linear constitutive relation was used. This relation includes a descending branch defined by a coefficient 'k_2', which, due to the action of the fibers, is expected to be larger than the coefficient 'k_1' that defines the ascending branch. Yet, for low values of f_{R1} and relatively low mean-compressive strengths, f_{cm}, the EC2 expression of k_2 can lead to $k_2 < k_1$. Therefore, the

corrected expression of k_2 employed in the model is set to the maximum between the formula in EC2 and k_1:

$$k_2 = max\left\{1 + \frac{20}{\sqrt{82-2.2f_{R,1k}}}, k_1\right\} \quad (3)$$

Note that both coefficients, k_1 and k_2, depend on the characteristic value of the residual tensile strength $f_{R,1k}$ and that f_{cm} and E_{ci} (used to calculate k_1 in EC2) remain unchanged (while the strain at the peak stress ε_{c1} depends on $f_{R,1k}$).

The sectional analysis of the weak sections was performed using values of $f_{R1,k}$ and $f_{R3,k}$ that were reduced by a factor denoted k_{cl}:

$$k_{cl} = \frac{1}{V_f} \cdot {'V_{f,cl}}' = \frac{1}{V_f} \cdot \frac{\xi_{cr}[\rho_{r,ef} + V_f(1-\rho_{r,ef})] - \rho_{r,ef}}{1-\rho_{r,ef}} \quad (4)$$

where V_f is the mean volumetric fiber content, $\rho_{r,ef} = \rho_r \cdot f_u/f_y$, ρ_r is the effective tension reinforcement ratio (relative to the effective tension cross-sectional area) and f_u and f_y are the ultimate and yield steel strengths. ξ_{cr} is a calibrated critical value of a random variable (ξ) that represents the distribution of the fibers along the beam, as defined by Karinski et al (2024):

$$\xi = \frac{\rho_{r,ef} + V'_f(1-\rho_{r,ef})}{\rho_{r,ef} + V_f(1-\rho_{r,ef})} \quad (5)$$

where V'_f is a random variable, which is the actual fibers volumetric ratio in a specific "slice" (a portion of the beam's length around a crack), noting that the mean value of V'_f is equal to V_f.

In cases when the effect of CL is negligible, i.e., beyond the transition point, k_{cl} is set to 1.0 along the entire span.

3 Computational procedure and model validation

The cross-sectional analysis was performed to evaluate M_u and M_y (see Fig. 1b) and their corresponding curvatures, ϕ_u, ϕ_{cl} and ϕ_y. For a 4-point-bending setup these calculations are done as explained in the following text.

For the cases that include the CL effect the cross-sectional analysis is performed for both reduced and non-reduced SFRC characteristic residual tensile strengths. First, the M-ϕ_{cl} relation is calculated for the weak cross-sections with the reduced parameters. The critical value ξ_{cr} was set in this work as the average of the theoretical, minimum and limit values of ξ (see 'ξ_{min}' and 'ξ_w' in Karisnki et al, 2024). This M-ϕ_{cl} curve is indicated in Fig. 2 by a solid line.

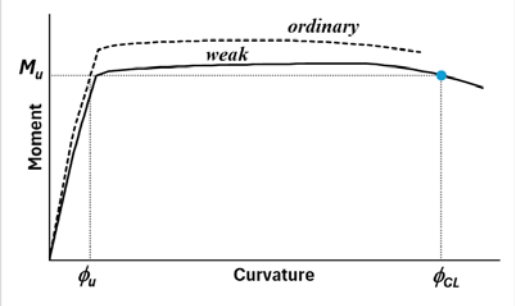


Figure 2: M-ϕ curves of weak and ordinary cross-sections

The ultimate moment M_u is defined as 95% of the maximum moment, at the post-peak branch, following Park (1989) and Gebreyesus et al (2025)).

Next, a similar analysis is carried out for an ordinary cross-section (k_{cl} = 1), where the curvature ϕ_u is obtained for the same moment capacity M_u that was calculated for the weak cross-section (because the moment is the same for all cross-sections along the constant moment zone, Fig. 1b). It is evident that the *M-ϕ* curve for this case (dashed line in Fig. 2) is stiffer than that obtained for the weak cross-sections. Consequently, when the weak part of the beam reaches its ultimate capacity, the *M-ϕ* curve of the ordinary cross-sections is at its ascending branch from which ϕ_u is obtained.

When CL is insignificant (beyond the TP) the above calculation is performed only once with the non-reduced characteristic SFRC residual strengths.

Validation of the model is presented by comparison of the model's predictions with results of 4-point-bending tests of R/SFRC beam specimens with 40 kg/m^3 steel fibers (V_f = 0.5%), reported in (Dancygier et al, 2016; Karinski et al, 2024 and Gebreyesus et al, 2025) with reinforcement ratios that varied from 0.15 to 1.26%. The span L was 3.2 m (with a constant moment zone equal to 1.5 m, Fig. 1a), and a rectangular cross-section with a width and height of 240 mm and 300 mm. The length of the hooked end fibers was 35 mm with an aspect ratio of 64. The SFRC characteristic tensile residual strengths (of the ordinary cross-sections) were $f_{R,1k}$ = 2.89 MPa and $f_{R,3k}$ = 2.94 MPa, and the corresponding strengths that were used in the SFRC material model (EN 1992-1-1, 2023) were f_{Ft1} = 1.07 MPa, f_{Ft3} = 0.92 MPa. Young's Modulus of the steel was taken as 200 GPa for all rebars and the concrete mean cube compressive strength varied from 29 to 34 MPa. For the data of these specimens the value of k_2 (Eq. 3) of the ordinary cross-sections was equal to 3.30 and for the weak cross sections – it was calculated by Eq. (3) using k_{cl} to reduce $f_{R,1k}$ as explained above. Other parameters are given in Table 1. The number of cracks, n and m, are given in the table (up to the transition point, set at ρ = 0.73%, for V_f = 0.5%, according to the experimental data presented and analyzed in Gebreyesus et al, 2023), where the number m is the average value of the wide cracks counted on the two sides of the beam. Note that according to the proposed model, beyond the transition point, when CL is insignificant, n/m is not relevant to the calculations. The calibrated value of CLF_{max} was 2.75.

Table 1: Parameters of the tests with V_f = 0.5%.

ρ (%)	d{1} (mm)	Tensile steel		Concrete		Number of cracks	
		f_y (MPa)	f_u (MPa)	k_1 {3} (-)	k_{cl} (-)	n	m
0.15	271	503	677	3.09	0.41	12, 10	2, 1
0.39	270	503, 409{2}	677, 579{2}	3.11	0.46	14, 15	2, 4
0.53	269	481	599	3.20	0.48	18, 17	5.5, 5
0.63	269	481	599	3.13	0.53	17, 18	7.5, 8
0.72	267	529	687	3.00	0.55	20, 19	12, 12.5
0.94	268	423	607	3.14	1.00	-	-
1.26	267	529	687	3.10	1.00	-	-

{1} Effective depth
{2} Of the 8- and 10-mm rebars (respectively) that were used in the "0.39" specimens
{3} Of the ordinary cross-sections

The ultimate deflections and moment capacities calculated by the proposed model are compared with the experimental results in Tables 2 and 3, respectively. Note that the experimental results of each specimen type (i.e., reinforcement ratio) were obtained from two specimens.

Table 2: Ultimate deflections.

ρ (%)	Experiment{1}			Calculated			Absolute Error (%)
	δ_{u1} (mm)	δ_{u2} (mm)	Mean (mm)	δ_{u1} (mm)	δ_{u2} (mm)	Mean (mm)	
0.15	38	33	36	43	34	39	8
0.39	99	113	106	107	156	132	24
0.53	98	88	93	96	103	100	7
0.63	122	142	132	130	129	129	2
0.72	164	193	179	134	139	136	24
0.94	108	119	114	87	87	87	23
1.26	85	81	83	76	76	76	8
						MAPE (%)	14

{1} For each ρ - 2 specimens were tested

Table 3: Moment capacities.

ρ (%)	Experiment{1}			Calculated	Absolute Error (%)
	M_{u1} (kN·m)	M_{u2} (kN·m)	Mean (mm)	M_u (kN·m)	
0.15	20.4	20.0	20.2	18.6	8
0.39	38.7	40.4	39.5	36.3	8
0.53	57.7	63.0	60.4	47.0{2}	22
0.63	70.8	75.8	73.3	61.0	17
0.72	65.2	70.3	67.7	55.9	17
0.94	97.7	99.9	98.8	87.3	12
1.26	127.2	123.9	125.6	110.6	12
				MAPE (%)	14

{1} For each ρ - 2 specimens were tested
{2} Average value of 46.9 and 47.1 kN·m

Tables 2 and 3 show that there is a reasonable agreement between the calculated and test results for both deflection and moment capacities with mean absolute percentage errors of 14%. For the displacement capacity the absolute error ranged from 2% to 24% and for the moment capacity – from 8% to 22%.

4 Concluding remarks

This work presents a model to evaluate the deflection capacity of R/SFRC beams, considering the effect of cracking localization (CL) phenomenon. This is a model, which is applicable to both cases when CL is significant (at low reinforcement ratios) and when it is insignificant (at relatively larger ratios). The limit between these two ranges of reinforcement ratios is set by a transition point that can be determined experimentally. The model employs a simplified

curvature distribution along the beam at the ultimate limit state, which includes a part of the beam that has increased curvature, representing the 'weak sections' where CL develops. The ultimate deflection is calculated by performing cross-sectional analysis, where for the weak sections (if exist) this analysis was performed using values of the SFRC residual strengths, reduced by a factor proposed in the model. The model was validated against reported results of 4-point-bending tests of normal strength concrete with reinforcement ratios that varied from 0.15 to 1.26% and 40 kg/m^3 of steel fibers (V_f = 0.5%). The comparison shows reasonable agreement between the calculated and test results for both deflection and moment capacities with mean absolute percentage errors of 14%.

The proposed model can provide a useful way to evaluate a minimum reinforcement ratio for R/SFRC flexural elements (e.g., slabs) to ensure their adequate deflection capacities.

5 Acknowledgements

This work was partly supported by a joint grant from the Centre for Absorption in Science of the Ministry of Immigrant Absorption and the Committee for Planning and Budgeting of the Council for Higher Education under the framework of the KAMEA Program.

6 References

Carvalhoa, M. R., Barros, J. A. O., Zhang, Y. and Dias-da-Costa, D., 2020. "A computational model for simulation of steel fibre reinforced concrete with explicit fibres and cracks", *Computational Methods in Applied Mechanics and Engineering*, 363 pp 112879.

Dancygier, A. N. and Karinski, Y. S., 2014. "Probabilistic model of the crack localization in axially loaded fibrous reinforced concrete bars", *Engineering Structures*, 79 pp 417–26.

Dancygier, A. N. and Berkover, E., 2016. "Cracking localization and reduced ductility of fiber-reinforced concrete beams with low reinforcement ratios", *Engineering Structures*, 111 pp 411-24.

Dancygier, A. N. and Karinski, Y. S., 2019. "Effect of cracking localization on the structural ductility of normal strength and high strength reinforced concrete beams with steel fibers", *International Journal of Protective Structures*, 10(4) pp 457–469.

EN 1992-1-1:2023, Eurocode 2: Design of concrete structures - Part 1-1: General rules - Rules for buildings, bridges and civil engineering structures (CEN)

fib, 2023. *Model Code for Concrete Structures (2020)*. Fèdération Internationale du Béton, Lausanne

Gebreyesus, Y. Y., Karinski, Y. S., Dancygier, A. N. and di Prisco, M., 2023. "Experimental investigation of cracking localization in RC beams with steel fibers", *Structural Concrete*, 24 pp 1386–1401.

Gebreyesus, Y. Y., Karinski, Y. S. and Dancygier, A. N., 2025. "An enhanced approach to assess the reduction of flexural ductility of R/SFRC beams and slabs", *International Journal of Protective Structures*, 16(4) pp 933-946.

Hasgul, U., Turker, K., Birol, T. and Yavas, A., 2018. "Flexural behavior of ultra-high-performance fiber reinforced concrete beams with low and high reinforcement ratios", *Structural Concrete*, 19(6) pp 1577–1590.

Karinski, Y. S., Dancygier, A. N. and Gebreyesus, Y. Y., 2024. "Probabilistic model for cracking localization in reinforced fibrous concrete beams", *Journal of Engineering Mathematics*, 144(1) pp 23.

Küsel, F. and Kearsley, E., 2019. “Effect of steel fibres in combination with different reinforcing ratios on the performance of continuous beams”, *Construction and Building Materials*, 227 pp 116553.

Mahmood, S. M. F., Akter, T., Foster, S. J. and Valipour, H., 2024. “Minimum tensile reinforcement ratio for conventionally reinforced-SFRC beams and slabs”, *Structures*, 63 pp 106320.

Markic, T., Amin, A., Kaufmann, W. and Pfyl, T., 2020. “Strength and deformation capacity of tension and flexural RC members containing steel fibers”, *ASCE Journal of Structural Engineering*, 146(5) pp 04020069.

Mobasher, B., Yao, Y. and Soranakom, C., 2015. ”Analytical solutions for flexural design of hybrid steel fiber reinforced concrete beams”, *Engineering Structures*, 100 pp 164–177.

Park, R., 1989. “Evaluation of ductility of structures and structural assemblages from laboratory testing”, *Bulletin of New Zealand National Society of Earthquake Engineering*, 22

Pleesudjai, C., Oliveira, C. A. S., Araujo, D. L., Patel, D., de Andrade, M. A. S., Filho, R. T. and Mobasher, B., 2025. “Efficiency of hybrid reinforced concrete beams with low reinforcement ratios”, *Materials and Structures*, 58 pp 218.

Shao, Y. and Billington, S. L., 2019. “Predicting the two predominant flexural failure paths of longitudinally reinforced high-performance fiber-reinforced cementitious composite structural members”, *Engineering Structures*, 199 pp 109581.

Yao, Y., Mobasher, B., Wang, J. and Xu, Q., 2020. “Analytical approach for the design of flexural elements made of reinforced ultra-high performance concrete”, *Structural Concrete*, 22(1) pp 298–317.

Yoo, D. Y. and Moon, D. Y., 2018. “Effect of steel fibers on the flexural behavior of RC beams with very low reinforcement ratios”, *Construction and Building Materials*, 188 pp 237–54.

Recycling of Steel Fiber Reinforced Concrete

Klaus Holschemacher[1], Stefan Bau[1], Wladislaw Polienko[1]

[1]: Structural Concrete Institute, HTWK Leipzig, Germany.

Abstract

The favorable impact of steel fibers in concrete is well known. Worldwide, extensive research has been conducted to describe and to analyze these phenomena. Recently, steel fiber reinforced concrete (SFRC) is used extensively in industrial floors, but also in walls and ceiling constructions. Beside the beneficial impact of steel fibers, the recycling of SFRC and, in particular, the separation of crushed concrete and steel fibers should be in focus, too. Only a few research programs are described in literature and comprehensive suggestions or guidelines for this topic are missed completely.

Therefore, an experimental program was carried out to evaluate the usual procedures for breaking SFRC with jaw crusher and subsequently to separate the steel fibers using magnetic technology. Two different types of steel wire fibers with end hooks in combination with two concrete strength classes were investigated within the test program. The fiber amount was in the range between 20 and 80 kg/m^3. In the result of the crushing process, the number of fibers separated from recycled concrete grains increased with higher initial fiber content and lower concrete strength. For recycled concrete with grain size up to 8 mm the majority of steel fibers could be separated from concrete. The separated steel fibers were almost never broken but, in most cases strongly deformed. Nevertheless, the application of such recycled steel fibers in SFRC resulted in surprisingly high efficiency, measured in three-point bending tests.

It is intended to study the influence of the crusher type in a following research step, where an impact mill is included in the experimental program.

Keywords

Recycling, steel fibers, industrial floors, crushing technology, jaw crusher, fiber separation, post-cracking behavior

1 Introduction

1.1 Increasing importance of sustainability and circular economy

Steel fiber reinforced concrete (SFRC) is a well approved construction material. It is well known and proved by an almost uncountable number of research papers that the addition of steel fibers to a cementitious matrix results in many advantages. Especially, the post cracking behavior is significantly improved by the presence of fibers. After first cracks have occurred, the fibers are bridging the cracks and transfer tensile forces from one side of the crack to the other one. In simplified terms, it means that a post-cracking tensile stress in SFRC is available and can be used to transfer loads (Holschemacher 2010). This phenomenon has already been taken into account in numerous codes, standards and recommendations today, which are more or less legally binding, e.g. ACI 360R-10 (2013), ACI 544.4R-18 (2018), ACI 544.6R-15 (2015), DAfStb (2021), EN 1992-1-1 (2023), *fib* Model Code (2022).

While in past construction costs and construction time were the decisive parameters for design of structures, sustainability issues must be additionally considered in modern building industry. In this context, aspects of the circular economy, especially the recycling of building materials, are of increasing importance (Schönborn and Junge 2021).

In Germany, SFRC is used for the production of about 10 million m^2 of industrial floors every year (AST 2023). Worldwide, 60% of all industrial floors are currently made from SFRC (Krampeharex 2026). These numbers illustrate that an enormous amount of SFRC has been used in the past for industrial floors alone and will continue to be used in future. Therefore, problems related to the recycling of SFRC are moving into the focus of scientific interest.

1.2 Recycling of mineral waste

During the construction and as the result of the demolition of buildings, streets and ways, and other structures, a huge amount of mineral waste is produced. By application of appropriate recycling methods, the mineral waste can be transferred to recycled construction material that may be used as gravel, paving stones, concrete aggregates or filler material. In this way, raw materials are saved and the circular economy in construction industry is strengthened.

The recycling process of mineral construction waste consists of various successive steps, e.g.: Selective deconstruction and sorting, multiple crushing, screening and classification, magnetic separation, cleaning, and optional wet-mechanical processing, accompanied by appropriate quality management (Neupane et al. 2025), (Wang et al. 2021), (Mulder, de Jong and Fox 2021). For breaking and de-sizing of concrete blocks, there are different types of shredders available, e.g. jaw crusher, impact mill, and cone crusher. The available technology has generally proven in construction practice for ordinary reinforced concrete. However, there are only few reports on recycling of SFRC.

There are many research reports about the application of recycled waste tire steel fibers in SFRC, e.g. (Domski et al. 2017), (Frazao et al. 2022), (Oan and Attia 2025). Also, the application of recycled aggregates for production of SFRC or other types of fibre reinforced concrete was reported in many papers, e.g. (Sarvanan and Nirmala 2025), (Xie at al. 2021). In contrast, there are only very few publications on recycling of SFRC and reuse of recovered fibers.

(Kunieda et al. 2014) used a jaw crusher for recycling of normal strength fiber reinforced concrete mixes containing steel fibers or polypropylene fibers. Regardless of the fiber type, a large amount of fibers could not be separated from the matrix, especially for larger grain sizes of crushed concrete. Most of polypropylene fibers were broken in the result of the crushing process, whereas the steel fibers were only deformed, but not ruptured. Recycling of ultra high-performance steel fiber reinforced concrete (UHPFRC) was topic of the paper from (Sedran et al. 2009) indicating that crushing with jaw crusher was inefficient because the steel fibers mostly remained in contact to crushed concrete. With an impact mill, better results were achieved. A very special method for separation of steel fibers and crushed concrete is the electric-pulse fragmentation (Bru et al. 2018), a process which has not yet been scaled up beyond the laboratory level. (Tosic et al. 2023) and (Liu at al 2023) reported that addition of recovered polypropylene fibers to the concrete mix and the presence of fibers in the recycled aggregates may result in even improved residual tensile strength.

The results of the literature review clearly show the necessity of further investigations on recycling of SFRC. The research should be focused on the most effective crushing technology, the best possible separation of steel fibers from the matrix, and the ability of recovered steel fibers to contribute to structural behavior of SFRC members when reused again.

2 Experimental program

2.1 General remarks

SFRC can be produced using very different mix compositions. There are various commercially produced steel fibers available, the fiber amount can vary widely, and compressive strength and post-cracking tensile strength of SFCR can cover a large range. Furthermore, as reported previously, various crushing technologies are widespread in construction technology. For these reasons, it was necessary to take some initial decisions for the structure of the research program. Because of the described diversity of SFRC, it was obvious that the intended research program could only identify first trends.

2.2 Materials

At the time, when the first stage of the experimental program was carried-out, there was no construction site where SFRC was being demolished under practical conditions. Thus, the required amount of SFRC was produced in the lab and cast in specimens that were subsequently subjected to the recycling procedure.

Within the experimental program two different concrete mixes in combination with two different steel fiber types were used. The concrete mixes had water-cement ratios of w/c = 0.5 and w/c = 0.4. As aggregate, ordinary river sand and gravel were used. The maximum grain size was 16 mm. Two commercial end hooked steel fibers with different fiber diameter and aspect ratio were utilized within the experimental program. The steel fiber amount varied between 20 and 80 kg/m^3. Besides the commercial steel fibers, also recovered fibers were used in a following test series. The recovered fibers were obtained from the test specimens that were crushed in the previous test series.

Details of the applied concrete mixes are provided in Table 1. The originally used steel fibers are shown in Figure 1.

Table 1. Mix design of tested SFRC.

Test series	**Cement Content**	**w/c-ratio**	**Fibre Type**	**Fibre Amount**
	(in kg/m^3)			(in kg/m^3)
F1/0.5/20	320	0.5	1	20
F1/0.5/50	320	0.5	1	50
F1/0.5/80	320	0.5	1	80
F2/0.5/50	320	0.5	2	50
F1/0.4/50	360	0.4	1	50
F_{rec}/0.5/50	320	0.5	recovered	50
F_{rec} – Test series with recovered steel fibers.				

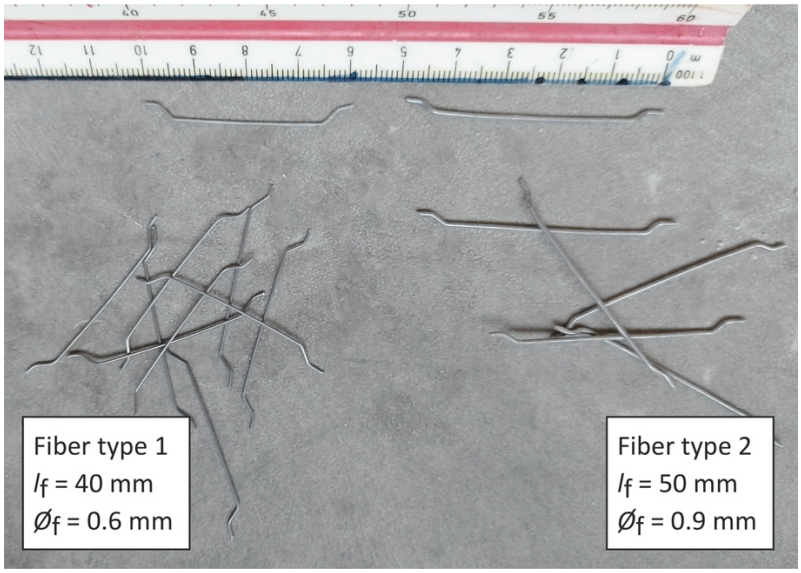


Figure 1. Applied steel fibers.

2.3 Test program

For each test series, six concrete cubes measuring 150 mm x 150 mm x 150 mm and beam-like specimens with cross-section 100 mm x 100 mm and 700 mm length were produced. The specimens were stored in a climate chamber at a temperature of 20°C and 60% relative humidity, and subsequently tested in the concrete age of 28 days.

After testing the material properties, the specimens were manually fractured in small pieces that could be subsequently processed by a laboratory jaw crusher (Figure 2). The jaw crusher's mouth opening was adjusted to 30 mm. The crushing process was performed only once. This means that the procedure was not repeated for material that had already passed through the crusher. The following step was a magnetic separation where detached steel fibers where removed from crushed concrete grains. The magnetic separation was carried out in three passes. This measure allowed to separate almost all detached steel fibers from the concrete grains.

The crushed concrete was sieved then to determine the grain distributions. Finally, the weight of the retrieved steel fibers was measured.



a) Jaw crusher b) Retrieved steel fibers c) Recycled concrete grains

Figure 2. Recycling procedure: Jaw crusher, retrieved steel fibers, and recycled concrete grains.

3 Results

3.1 Material properties

The mean value of the concrete compressive strength was 38 MPa for concrete with w/c = 0.5, respectively 55 MPa for concrete with w/c = 0.4. The results of the three-point bending tests were as expected and are shown in Figure 3. It is obvious that the first crack load corresponds to the increased concrete tensile strength for concrete with w/c = 0.4 and comparable fiber content. The post-cracking behavior is improved by increased fiber content and higher concrete strength.

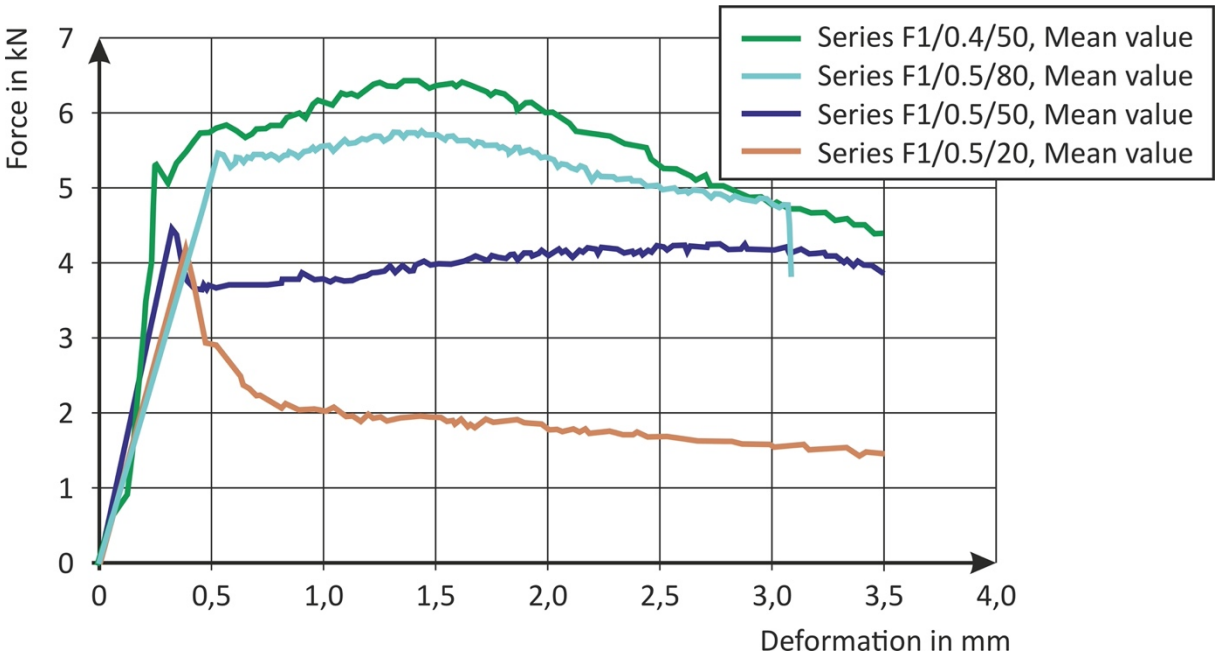


Figure 3. Load-deflection curves of tested SFRC beams. Mean values of six tested specimens for each test series.

3.2 Recycling efficiency

As result of the crushing procedure, the most steel fibers could be retrieved if the grain size of crushed concrete was not bigger than 8 mm. For grain size of 16 mm and larger, the vast majority of steel fibers was still fixed in the concrete and could not be separated (Figure 4). Nevertheless, it can be stated, that, in average over all performed test, around 50% of the originally in SFRC present steel fibers could be retrieved. The percentage of retrieved steel fibers increased with lower concrete strength (w/c-ratio) and lower fiber length, because of the worse bond between fiber and concrete in these situations (Kaeseberg et al. 2024).



Figure 4. Examples for crushed SFRC particles.

3.3 Application of recycled steel fibers

The retrieved steel fibers were apparently characterized regarding their damage degree in three levels: ruptured, deformed, undeformed. In average, 69% steel fibers were deformed and, surprisingly, 24% steel fibers were almost or completely undeformed (Figure 5).



Figure 5. Examples for retrieved steel fibers.

To prove the possibility that retrieved steel fibers can be reapplied for structural applications, three-point bending tests were performed again. For this reason, only retrieved fibers and

concrete with w/c = 0.5 were used, see test series F_{rec}/0.5/50 in Table 1. In comparison to SFRC specimens with original steel fibers, the SFRC with retrieved fibers had similar load-deflection curves for low deformations up to 1.5 mm. For higher deflections, there is a clear reduction of the residual tensile strength (Figure 6).

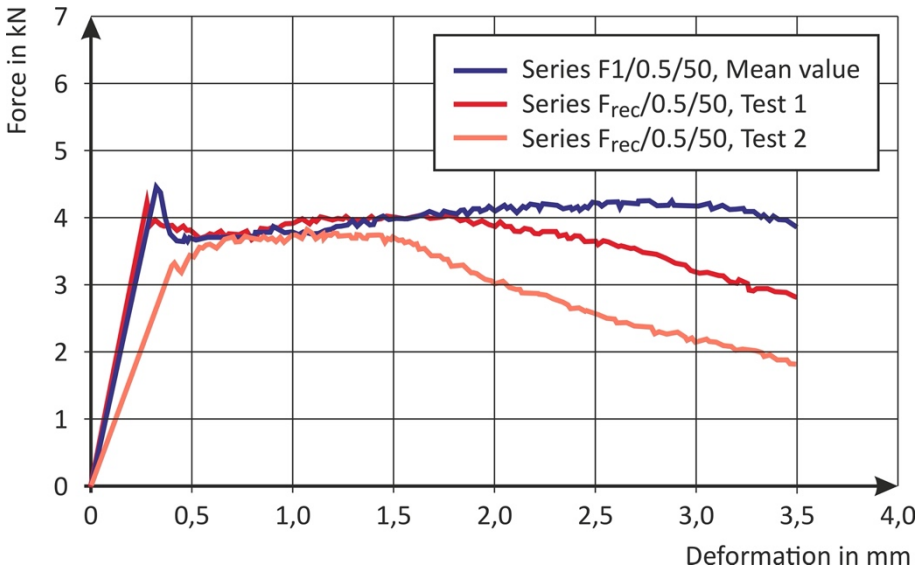


Figure 6. Comparison of load-deflection curves for specimens with original and retrieved steel fibers.

4 Concluding remarks

The carried out experimental investigation showed that the separation of steel fibers from crushed concrete is possible for grain sizes up to 8 mm. For larger grain sizes, the majority of steel fibers cannot be detached from concrete.

Application of retrieved steel fibers in SFRC seems to be possible, especially for limited crack opening in the serviceability states. However, due to the limited number of tests, no definitive conclusions can yet be drawn.

5 Acknowledgement

This work was supported by the European Regional Development Fund (EFRE) and the Free State of Saxony as part of the EFRE Validation Funding 2021-2027, Project No. 100689166.

6 References

ACI 360R-10 (2013). Guide to Design of Slabs-on-Ground. American Concrete Institute (ACI), Farmington Hills, USA.

ACI 544.4R-18 (2018). Guide to Design with Fiber-Reinforced Concrete. American Concrete Institute (ACI), Farmington Hills, USA.

ACI 544.6R-15 (2015). Report on Design and Construction of Steel Fiber-Reinforced Concrete Elevated Slabs. American Concrete Institute (ACI), Farmington Hills, USA.

AST (2023). Leaflet Steel fibre reinforced concrete mix design for industrial floors in Germany. Association Steel Fibre Technology (AST), Hamm, Germany.

Biswas, W., Zhang, X., Matters, C., and Maboud, M. (2024). Techno-Eco-Efficiency Assessment of Using Recycled Steel Fibre in Concrete. Sustainability 2024, 16, 3717. https://doi.org/10.3390/su.16093717.

Bru, K. et al. (2018). Investigation of lab and pilot scale electric-pulse fragmentation systems for the recycling of ultra-high performance fibre-reinforced concrete Minerals Engineering, 2018, 128, 187-194. https://doi.org/10.1016/j.mineng.2018.08.040.

DAfStb (2021). DAfStb Guideline Steel Fibre Reinforced Concrete (in German). Deutscher Ausschuss für Stahlbeton, Berlin, Germany.

Domski, J., Katzer, J., Zakrzewski, M., and Ponikiewski, T. (2017). Comparison of the mechanical characteristics of engineered and waste steel fiber used as reinforcement for concrete. Journal of Cleaner Production 2027, 158, 18-28. https://doi.org/10.1016/j.jclpro.2017.04.165.

EN 1992-1-1 (2023). Eurocode 2: Design of concrete structures – Part 1-1: General rules and rules for buildings.

fib Model Code (2022). Model Code for Concrete Structures. Fédération Internationale du Béton (*fib*), Lausanne, Switzerland.

Frazao, C., Barros, J., Bogas, J., Garcia-Cortes, V., and Valente, T. (2022). Technical and environmental potentialities of cycled steel fiber reinforced concrete for structural applications. Journal of Building Engineering, 2022, 45, 103579. https://doi.org/10.1016/j.jobe.2021.103579.

Holschemacher, K., Mueller, T., and Ribakov, Y. (2010). Effect of steel fibres on mechanical properties of high-strength concrete. Material & Design 2010, 31, 5, 2604-2616. https://doi.org/10.1016/j.jmatdes.2009.11.025.

Kaeseberg, S., Schmidt, E., and Holschemacher, K. (2024). Recycling methods for steel fiber reinforced concrete. Proceedings of the International Engineering and Construction, 11, 2. https://doi.org/10.14455/ISEC.2024.11(2).MAT-04.

Krampeharex (2026). https://www.krampeharex.com/en/fibres/applications/industrial-floors/#:~:text=True%20natural%20resources,production%20halls%2C%20or%20logistics%20centres.

Kunieda, M., Ueda, N., and Nakamura, H. (2014). Ability of recycling on fiber reinforced concrete. Construction and Building Materials 2014, 677, 315-320. https://dx.doi.org/10.1016/j.conbuildmat.2014.01.060.

Liu, G., Tosic, N., and de la Fuente, A. (2023). Recycling of Macro-Synthetic Fiber-Reinforced Concrete and Properties of New Concretes with Recycled Aggregate and Recovered Fibers. Applied Sciences 2023, 13, 2029. htpss://doi.org/10.3390(app13042029.

Mulder, E., de Jong, T., and Feenstra, L. (2007). Closed Cycle Construction: An integrated process for the separation and reuse of C&D waste. Waste Management 2007, 27, 1408-1415. https://doi.org/10.1016/j.wasman.2007.03.013.

Neupane, R.P., Devi, N.R., Imjai, T., Rajout, A., and Noguchi, T. (2025). Cutting-edge technologies and environmental insights in recycled concrete aggreagate production: A comprehensive review. Resources, Conservation & Recycling Advances, 2025, 25, 200241. https://doi.org/10.1016/j.rcadv.2024.200241.

Oan, A.F. and Attia, F. (2025). Evaluation of the mechanical behavior of concrete reinforced with waste tire steel fibers. Scientific reports, 2025, 15, 35398. https://doi.org/10.1038/s42598-025-07615-0.

Sarvanan, M., Nirmala, R. (2025). Steel fibre-reinforced concrete with fully recycled coarse and partially recycled fine aggregates. Scientific reports 2025, 15, 43479. https://doi.org/10.38/s41597-025-24351-7.

Schönborn, A. and Junge, R. (2021). Redefining Ecological Engineering in the Context of Circular economy and Sustainable Development. Circular Economy and Sustainability, 2021, 1, 375-394. https://doi.org/10.1007/s43615-021-00023-2.

Sedran, T., Durand. C, and de Larrard, F. (2009). An example of UHPFRC recycling. International Workshop 'Designing and Building with Ultra-High Performance Fibre-Reinforced Concrete (UHPFRC), Marseille, France.

Tosic, N., Martinez, D.P., Hafez, H., Reynvart, I., Ahmad, M., Liu, G., and de la Fuente, A. (2023). Multi-recycling of polyproylene fibre reinforced concrete: Influence of recycled aggregate properties on new concrete. Construction and Building Materials 2022, 346, 128458. https://doi.org/10.1016/j.conbuildmat.2022.128458.

Wang, B., Yan, L., Fu, Q., and Kasal., B. (2021). A Comprehensive Review on Recycled Aggregate and recycled Aggregate Concrete. Resources, Conservation & Recycling, 2021, 171, 105565. https://doi.org/10.1016/j.reconrec.2021.105565.

Xie, J., Kou, S., Ma, H., Long, W.-J., Ye, T.-H. (2021). Advances on properties of fiber reinforced recycled aggregate concrete: Experiments and models. Construction and Building Materials 2021, 277, 122345. https://doi.org/10.1016/j.conbuildmat.2021.122345.

Fracture model double-K - Concrete with a dose of recycled and industrially produced steel fibers

Jaroslav Prokop[1], Petr Frantík[2], Ivan Hollý[1,3]

[1]: Institute of Constructions and Architecture, Slovak Academy of Sciences, Dúbravská cesta 9, 845 03 Bratislava, Slovakia.

[2]: Faculty of Civil Engineering, Brno University of Technology, Veveří 331/95, 602 00 Brno, Czech Republic.

[3]: Faculty of Civil Engineering, Slovak University of Technology, Radlinského 2766/11, 810 05 Bratislava, Slovakia.

Abstract

Waste tire landfills are a potential source of diseases and fire, and they occupy valuable land suitable for construction or agriculture. A partial solution to reducing or even eliminating landfill waste is to find suitable applications for recycled products from waste tires. Recycled steel fibers (RSF) appear to be suitable for use in concrete to partially eliminate low tensile strength and brittle behavior. In this paper, the cubic compressive strength of concrete according to the STN EN 12390-7 standard, the secant modulus of elasticity according to the STN EN 12390-3 standard, and the bending test of the sample with a stress concentrator in the middle of the sample span in accordance with the STN EN 14651+A1 standard was experimentally tested. The aim was to compare the values of the modulus of elasticity obtained using two different methodologies and to determine the fracture-mechanical parameters characterizing crack formation and propagation. It was found that RSF significantly improved the fracture toughness of concrete by 40.9% compared to fiber-free concrete and even surpassed that of concrete with type A fibers by 0.037 MPa·m$^{1/2}$. The value of resistance to stable crack propagation was increased by about three times in all fiber-concretes compared to concrete without fibers. Based on the results presented in this paper, it can be assumed that fiber-concrete with an RSF dosage has good prospects for use in building structures prone to brittle fracture.

Keywords

Fracture model double-K, recycled steel fibers, industrial steel fibers, compression strength, modulus of elasticity, fracture toughness

1 Introduction

Concrete, the most widely used building material in the world, is characterized by high compressive strength. On the other hand, tensile strength represents only about 10% of the compressive strength. Concrete can be classified as a quasi-brittle material, meaning that after reaching the maximum recorded force, a gradual decrease in load is observed as deformation increases. The described behavior can be attributed to bridging effects in the fracture process zone of the crack. A crack can propagate in the concrete matrix stably or unstably, depending on the fracture energy required for crack propagation, fracture toughness, and resistance to stable crack propagation. The values of the aforementioned parameters can be increased by using steel fibers in concrete.

Currently, the use of recycled components in concrete is a very topical and important issue, including recycled steel fibers (RSF) obtained from processed waste tires. Unlike industrial steel fibers (ISF), RSF does not have the same shape, dimensions, and tensile strength. According to previous research, RSF is a competitive alternative to ISF.

The use of ISF and RSF dosage in concrete composites has been the subject of many studies (Pająk et al, 2021; Zia et al, 2023; Pawelska-Mazur and Kaszynska 2021). Unfortunately, these studies lack emphasis on evaluating the toughness of fiber-reinforced concrete. In 1999, a new approximate Double-K model was proposed by the research group around Reinhardt and Xu (1999). Using the Double-K fracture-mechanical model, it is possible to determine the elastic modulus of fiber-reinforced concrete, fracture toughness, and resistance to stable crack propagation based on the results of a bending test of a fiber-reinforced concrete prism with a stress concentrator. Xu and Reinhardt (2000) later proposed a simplified procedure for obtaining the Double-K fracture parameters. In this procedure, two empirical formulas were proposed to determine the crack opening and the stress intensity factor induced by the cohesive stress around the crack opening.

The aim of this paper is to demonstrate the competitiveness of RSF compared to ISF in terms of fracture-mechanical parameters characterizing crack initiation and propagation. The research focuses on the influence of RSF and ISF use on the elastic modulus, fracture toughness, and resistance to stable crack propagation. The mentioned parameters were obtained from the double-K fracture model, while the input values were evaluated from the results of a three-point bending test of a beam with a stress concentrator.

2 Experimental program

2.1 Materials and sample preparation

The concrete was made from cement, water, aggregate, plasticizers, and fibers. CEM II/A- LL 42.5 R cement was used as a binder with a dosage of 350 kg/m³. Drinking water was used to start hydration with a dosage of 165 kg/m³. The ratio between the mass dose of water and cement, which is expressed by the water coefficient, was 0.47. Natural river aggregate in fractions 0-4, 4-8, and 8-16 was used as a filler with a dosage of 1010 kg/m^3, 320 kg/m^3, and 540 kg/m^3 per unit volume of finished concrete. The plasticizer-to-cement ratio was 0.005, corresponding to a dose of 1.75 L/m^3. For mix designs 4B and 4C, it was necessary to increase workability to ensure sufficient placement and compaction of the fresh concrete. For this reason, plasticizer dosages of 1.93 L/m^3 and 2.48 L/m^3 were used in mix designs 4B

and 4C, respectively. The reference concrete, marked S0, was produced without fiber. In mix designs 4R, 4A, 4B, and 4C, steel fibers were used in concrete marked R, A, B, and C at a dosage of 40 kg/m^3, added to the fresh concrete as the last component. This method of adding fibers represents the procedures used on construction sites. A summary of the fiber types used is presented in Table 1. Type R fibers were obtained by magnetic separation with a fibers from steel cords, the final purity of which reached a steel content of more than 99% by weight and less than 1% of the attached rubber, requiring new fibers, which are essential components of tires.

Table 1: Type of fibers

Name	*Recycled steel fibers*	*ArcelorMIttal HE 1/60*	*Dramix 3D 65/35*	*Dramix 4D 65/35*
Abbreviation	R	A	B	C
Group	RSF	ISF	ISF	ISF
Figure				

Samples were produced at 25 °C and 60% relative humidity. Mixing was carried out in a gravity concrete mixer. In the first step, aggregate fractions were mixed with cement. After the dry ingredients were properly mixed, water and a plasticizing additive were added and mixed for 5 minutes. Due to unwanted, random bonds between the fibers, manual separation was performed, followed by the addition to the mixer and subsequent mixing for 3 minutes. The concrete was placed in layers into the molds, with each layer being compacted using a vibrator. After the pouring was completed, the samples were covered with a plastic sheet to prevent microcrack formation caused by the rapid drying of the concrete. After demolding, the samples were covered with a plastic sheet until the experimental testing.

2.2 Testing and evaluation of results

The workability of fresh concrete was determined using the slump test in accordance with STN EN 12350-2. The compressive strength of concrete was tested for each mix design using three 150 mm edge-length cubes, in accordance with STN EN 12390-7, at a compressive stress rate of 0.5 MPa/s. The secant modulus of elasticity was determined in accordance with STN EN 12390-3 as the average of three prisms measuring 100 mm × 100 mm × 400 mm. The input values for the double-K fracture model were determined from a three-point bending test on a notched beam. The preparation of the sample and test set for three-point bending was in accordance with STN EN 14651+A1. The experimental setup for the bending test with a crack mouth opening displacement (*CMOD*) gauge is shown in Fig. 1.

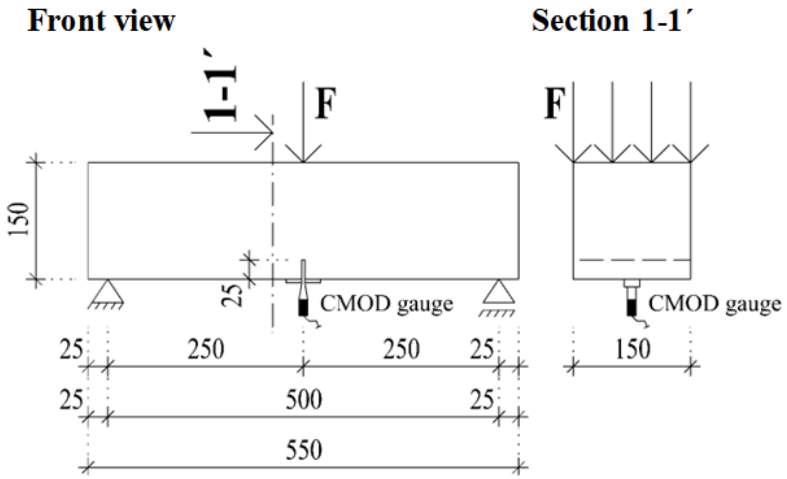


Figure 1 Experimental setup for the bending test

Fig. 2 shows the resulting curve of *P-CMOD* or *P-δ*, which can be obtained from a three-point bending fracture test, with a stress concentrator created in the middle of the sample span. Between points B and C, there is an observable deviation of the tangent from the initial tangent (starting from point O). It is known that point B represents the formation of a fracture process zone (FPZ), and microcracks begin to appear in the concrete matrix. Between points O and B, the body behaves linearly elastically, and the initial notch depth does not grow. With this assumption, the load acting at point B is considered initial, denoted P_{ini}, and the corresponding stress intensity factor is called the initial fracture toughness of the material, K_{Ic}^{ini}. The most unstable state is reached at point C, where the maximum recorded load P_{max} acts, at which the crack length a and the crack tip opening displacement (*CTOD*) reach the critical values of the crack width (a_c) and $CTOD_c$, respectively. The name of the double-K model arose from the fact that the result of the input analysis is the results of the values of the initiation fracture toughness K_{Ic}^{ini} and the (total) fracture toughness K_{Ic}^{un}, i.e., two fracture toughnesses. Fig. 2 provides a graphical representation of the points described above. To obtain the results from the double-K fracture model, the given points were inserted into the macro *TPBT_G_F* (Havlíková, 2016).

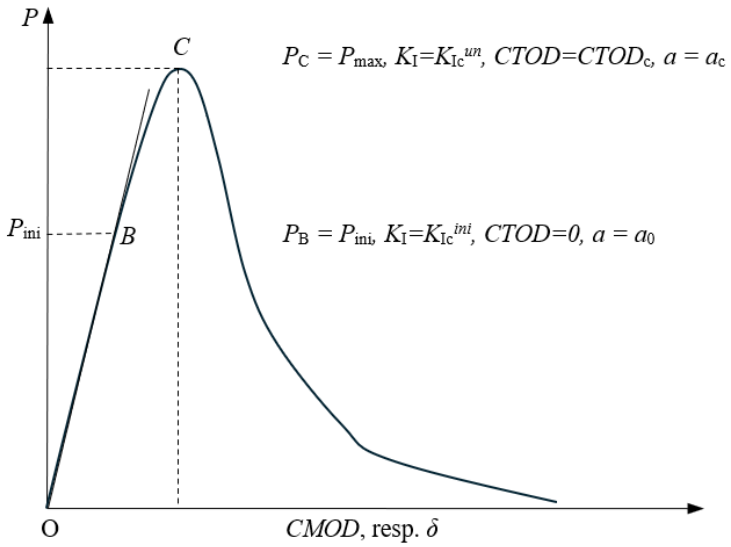


Figure 2 Graphical representation of characteristic points for the Double-K model (Havlíková, 2016)

Other input data that needed to be entered into the *TPBT_G_F* macro were the dimensions of the body (span *S*, length *L*, notch depth a_0, depth *D*, height of CMOD blades H_0), body mass *m*, compressive strength of concrete f_c, yield function (1), and shape function (2), which can be calculated as follows:

$$V_1\left(\alpha_{0k} = \frac{a_0 + H_0}{D + H_0}\right);\ V_1\left(\alpha_c = \frac{a_c + H_0}{D + H_0}\right); \tag{1}$$

$$F_1\left(\alpha_{0k} = \frac{a_0}{D}\right); F_1\left(\alpha_{0k} = \frac{a_0}{D}\right) \tag{2}$$

From the above inputs, the concrete density γ_{con}, the concrete weight q and the ligament cross-sectional modulus W were calculated. Based on these inputs and the results in the TPBT_G_F macro, the values of the elastic modulus $E_{c,2k}$ and the fracture toughness K_{Ic}^{un} were calculated. The elastic modulus (3), (4) and the fracture toughness (5), (6), (7) were determined based on the following formulas, where P_i represents the force at the proportionality line and a_c represents the value of the critical crack length:

$$E_{2K} = \frac{P_i \cdot S \cdot a_0}{W \cdot CMOD} \cdot V_1(\alpha_{0k}); where\ \alpha_{0k} = \frac{a_0 + H_0}{D + H_0} \tag{3}$$

$$V_1(\alpha_{0k}) = 0.76 - 2.28 \cdot \alpha_{0k} + 3.87 \cdot {\alpha_{0k}}^2 - 2.04 \cdot {\alpha_{0k}}^3 + \frac{0.66}{(1 - \alpha_{0k})^2} \tag{4}$$

$${K_{\mathrm{Ic}}}^{\mathrm{un}} = \frac{M_{\max}}{W} \cdot \sqrt{a_c} \cdot \mathrm{F}_1(\alpha_{\mathrm{ck}}); where\ \alpha_{\mathrm{ck}} = \frac{a_c}{D} \tag{5}$$

$$M_{max} = \frac{(q \cdot L + P_{max}) \cdot S - 0.5 \cdot q \cdot L^2}{4} \tag{6}$$

$$\mathrm{F}_1(\alpha_{\mathrm{ck}}) = \frac{1.99 - \alpha_{\mathrm{ck}} \cdot (1 - \alpha_{\mathrm{ck}}) \cdot (2.15 - 3.93 \cdot \alpha_{\mathrm{ck}} + 2.7 \cdot {\alpha_{\mathrm{ck}}}^2}{(1 + 2 \cdot \alpha_{\mathrm{ck}})(1 - \alpha_{\mathrm{ck}})^{\frac{3}{2}}} \tag{7}$$

3 Analysis of Results

3.1 Experimentally obtained results

3.1.1 Concrete slump and compressive strength

Table 2 shows the resulting slump values of fresh concrete and the average cube compressive strengths. In mix design 4C, the plasticizer dosage was increased by 42%, resulting in a higher slump. In the case of samples with type B and C fibers, the deterioration of workability was more pronounced than in the case of samples with type R and type A fibers, respectively.

In the case of fiber concrete with a fiber dosage of 40 kg per unit volume of finished fresh concrete (hereinafter referred to as 40 kg per m³), the average compressive strength ($f_{cm,cube}$) of 67.1 MPa was achieved with the 4C mix design, which represents a difference from 4R +8.2 MPa. All investigated mix designs (except 2R, which showed a 3.6% decrease in strength)

exhibited higher compressive strength than the reference concrete without fibers, marked S0. Based on the cube compressive strength results, the mix design marked R achieved the lowest compressive strength among fiber concretes. Based on the results obtained, the sample standard deviation (St. Dev.) is relatively low, indicating low dispersion in the partial results.

Table 2: Slump and cubic compressive strength of concrete results

Mix design	Slump (mm)	Comparison of results (%)	$f_{cm,cube}$ (MPa)	$f_{c,cube,St.Dev.}$ (MPa)	Comparison (%)
S0	200	100.0	56.7	1.2	100.0
4R	115	57.5	58.9	0.5	103.9
4A	140	70.0	59.8	0.2	105.5
4B	45	22.5	60.8	1.6	107.3
4C	55	27.5	67.1	0.8	118.4

3.1.2 Secant modulus of elasticity

Table 3 shows the average values of the secant modulus of elasticity of concrete $E_{c,EXP}$. In the case of fiber concretes with a fiber dosage of 40 kg per m^3, the lowest value of the modulus of elasticity was recorded for mix design 4A with a value of 38.4 GPa, while the highest average value of the modulus of elasticity was recorded for recipe 4C with a value of 40.5 GPa. Based on the obtained results, it can be stated that the addition of RSF or ISF to concrete had no significant effect on the change in the sectional modulus of elasticity of the tested concretes.

Table 3 Secant modulus of elasticity results

Mix design	$E_{c,EXP}$ (GPa)	$E_{c,EXP,St.Dev}$ (GPa)	Comparison (%)
S0	38.7	0.2	100.0
4R	39.1	0.3	101.1
4A	38.4	0.4	99.1
4B	40.7	0.8	105.0
4C	40.5	0.4	104.6

3.1.3 Flexural test results

Figure 3 shows the resulting *F-CMOD* dependences obtained from experimental verification of bent specimens with a notch. From the results, it can be observed that in the case of the receptor without fibers marked S0, a brittle fracture occurred after reaching the maximum load due to the inability of the simple concrete matrix to transmit the stress in the crack. In the case of the sample marked S0-CM-3, it was possible to capture almost the entire descending branch due to the slowdown of the increase by one third of the *CMOD* speed compared to the data given in the methodology section. Concrete specimens with fibers showed a tensile failure mode with increasing *CMOD* value due to the ability of the fibers to create a bridging effect between the crack surfaces. In the case of using fibers of type B and C at a dosage of 40 kg per m^3 of concrete, a slight decrease in the recorded load was observed after the first crack, however, after a short increase in *CMOD*, the force continued to increase.

This behavior can be attributed to the end termination of the fibers and the number of fibers that crossed the controlled crack.

The *F-CMOD* dependence was experimentally measured until a *CMOD* of 5 mm was reached. After this value, the *F-CMOD* curves for fiber-reinforced concrete specimens were approximated and identified using 2D FEM, in which a coherent function boundary condition was assigned to the axis of symmetry of the specimen (Prokop et al. 2026).

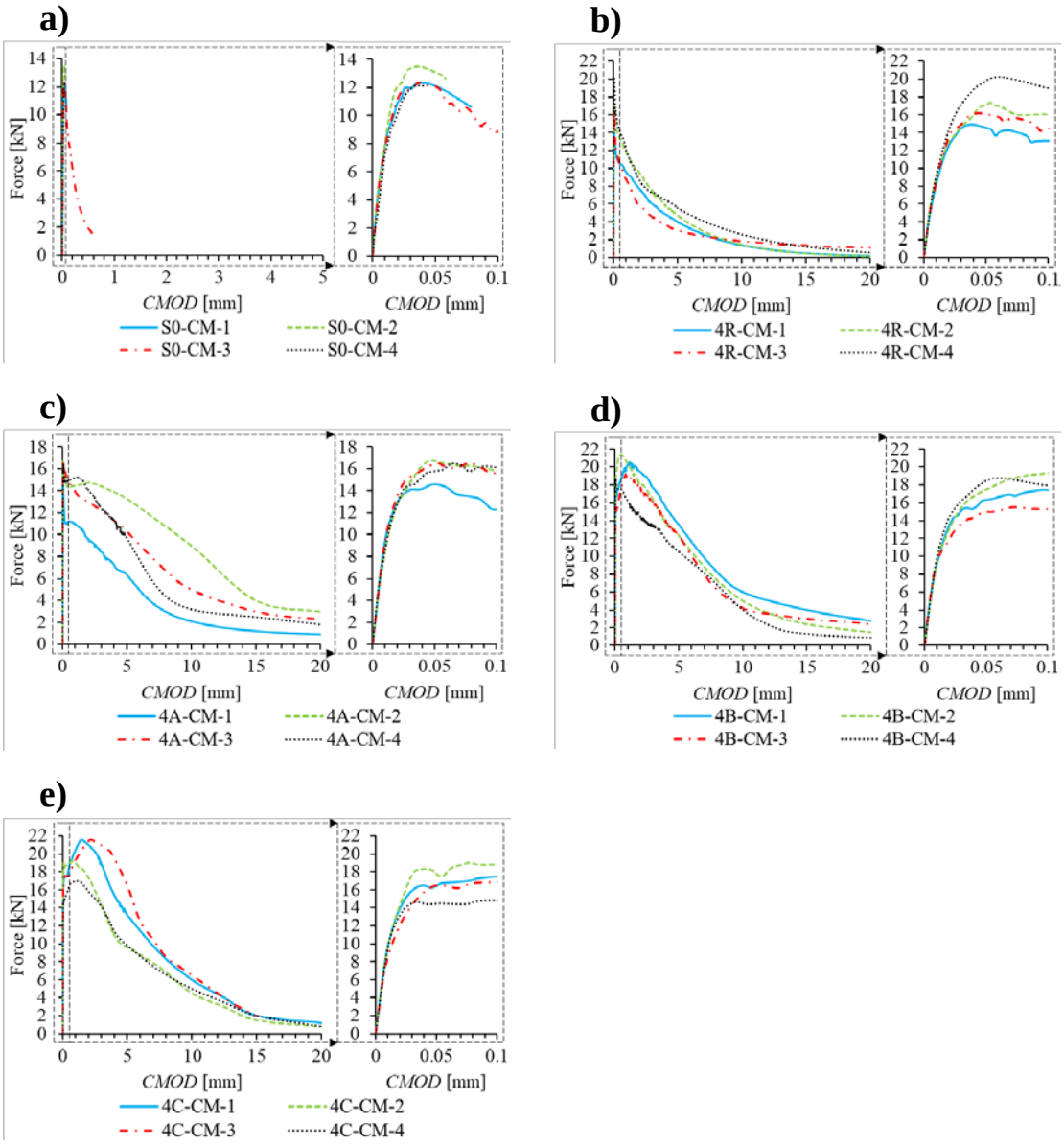


Figure 3 F-CMOD behavior

3.2 Results from the double-K fracture model

Table 4 shows the results for the Double-K model, obtained using the TPBT_GF macro, in which the necessary functional values from the force-crack mouth opening displacement (*F- CMOD*) dependence and the test specimen geometry were inserted. The resulting values of the elastic modulus $E_{c,2K}$, the fracture toughness (K_{Ic}^{un}), the ratio between the initiation

and peak fracture toughness (K_{Ic}^{ini}/K_{Ic}^{un}), which is a characteristic of the resistance to stable crack propagation, were obtained from the above macro.

From the above results, it can be observed that the type of fibers, or rather their dose, did not significantly affect the elastic modulus $E_{c,2K}$. This phenomenon can be explained by the fibers not being sufficiently activated at the *CMOD*s where the functional values were read. For this reason, it can be stated that the elastic modulus is mainly contributed by the properties of the cement composite without fibers. The fracture toughness values, K_{Ic}^{un}, increased with increasing fiber dose in the concrete. In the case of fiber concretes with a fiber dosage of 40 kg per m^3, the highest K_{Ic}^{un} was recorded for mix design 4C, at 2.943 MPa·m$^{1/2}$. Compared to the reference mix design S0, the K_{Ic}^{ini}/K_{Ic}^{un} parameter showed the greatest improvement, reaching 0.409 at a fiber dosage of 40 kg per m^3 in mix design 4B. From the above results obtained using the fracture model double-K, it can be stated that the highest toughness and the most stable crack propagation were achieved in fiber-concrete mixtures with fibers of types B and C. In the comparison of mix designs with doses of RSF and ISF, it can be concluded that recycled fibers have a slightly more positive effect on the K_{Ic}^{un} and K_{Ic}^{ini}/K_{Ic}^{un} values compared to ISF with fiber type A. ISF types B and C significantly increase the values of these parameters for both selected fiber dosages. Normalized results, based on the values from the mix design S0, are shown in Fig. 4.

Table 4 Results from fracture model double-K

Mix design	$E_{c,2K}$ (GPa)	$E_{c,2K,St.Dev}$ (GPa)	$K_{Ic}^{un}{}_{avg}$ (MPa·m$^{1/2)}$	$K_{Ic}^{un}{}_{St.Dev.}$ (MPa·m$^{1/2}$)	$K_{Ic}^{ini}/K_{Ic}^{un}{}_{avg}$ (-)	$K_{Ic}^{ini}/K_{Ic}^{un}{}_{St.Dev.}$ (-)
S0	39.5	6.9	1.372	0.16	0.136	0.03
4R	39.2	1.1	1.933	0.30	0.377	0.07
4A	37.7	2.4	1.896	0.20	0.342	0.04
4B	38.5	3.2	2.943	0.87	0.409	0.10
4C	36.7	2.0	2.731	0.69	0.336	0.06

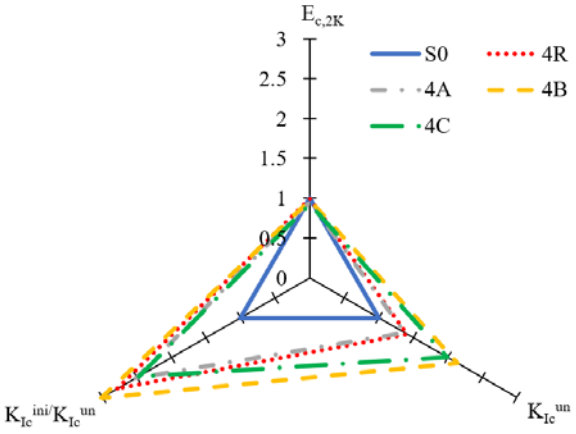


Figure 4 Normalized results from the fracture model double-K

3.3 Comparison of the modulus of elasticity according to the methodologies used

The average results determined from the secant modulus of elasticity (applied compressive stress) and the values of the elastic modulus determined by substituting the functional values of the *F-CMOD* dependence into the *TPBT_G_F* macro is shown in Fig. 5. Based on a comparison of the secant modulus of elasticity obtained from the sample's bending stress and the modulus of elasticity $E_{c,2K}$ obtained from concrete bending tests, the results are in good agreement. The exception is the fiber-free mix design labeled S0, for which a 15.5% difference between the two methodologies is observed. This percentage difference can be attributed to the initial instability of the fiber-free samples during the bending test. To reduce this percentage difference in the future, the bending test should be performed with a *CMOD* increment of less than 0.04 mm/min.

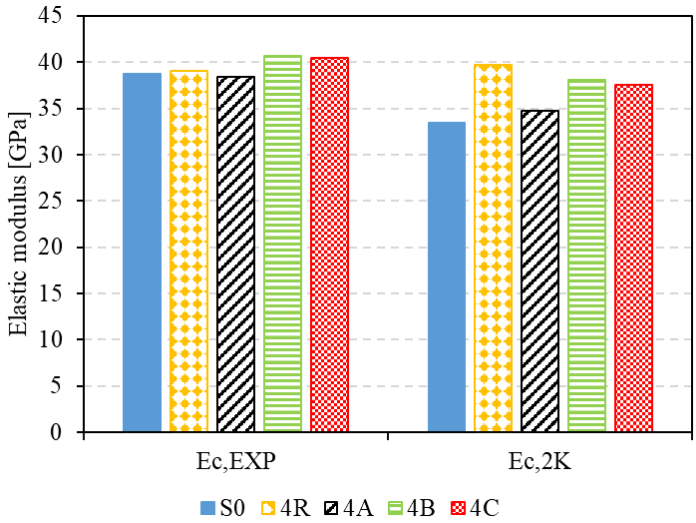


Figure 5 Comparison of elastic modulus results according to the methods

4 Concluding remarks

In this paper, the fracture mechanical properties of concrete without fibers, with a dose of recycled steel fibers (RSF), or industrially produced fibers (ISF) were compared. The most important findings from the experimental testing of concrete samples can be summarized in the following points:

- Despite the deteriorated workability, concrete marked 4C achieved the highest recorded average cube compressive strength of 67.1 MPa, which represented a percentage increase of 18.4% compared to the S0 mix design.
- In the secant modulus of elasticity, the fibers had a minimal effect on the result. In the case of the $E_{c,2K}$ results, a difference was observed in the S0 mix design in the rate of increase of *CMOD*.
- In concrete mix designs with a large number of short fibers with hook ends (4B, 4C), a higher increase in fracture toughness K_{Ic}^{un} was observed compared to mix designs 4R and 4A, where the fibers were absent from the hook end, or the number of fibers per unit volume of concrete was lower than in mix designs 4B and 4C.

- The resistance to stable crack propagation, defined by the ratio K_{Ic}^{ini}/K_{Ic}^{un}, increased by about three times in all fiber-concrete mix designs.

Considering the favorable results from concretes with a fiber dosage of 40 kg per m^3 on the formation and propagation of cracks in the concrete matrix, it is recommended for further research to experimentally investigate and analyze the results obtained from concrete mixtures with variable fiber dosages, or with hybridized fibers consisting of RSF and ISF.

5 Acknowledgements

This research was supported by the Interreg CENTRAL EUROPE 2021–2027 CE0100390 – ReBuilt initiative, projects APVV-23-0193, APVV-23-0383, and Project 101112386 — H2GEO.

6 References

Pająk, M., Krystek, M., Zakrzewski, M., and Domski, J., 2021. Laboratory Investigation and Numerical Modelling of Concrete Reinforced with Recycled Steel Fibers, *Materials*, 14(8), doi: 10.3390/ma14081828

Zia, A., Zhang, P., and Holly, I., 2023. Experimental investigation of raw steel fibers derived from waste tires for sustainable concrete, *Construction and Building Materials*, 368, doi: 10.1016/j.conbuildmat.2023.130410

Pawelska-Mazur, M., and Kaszynska, M., 2021. Mechanical Performance and Environmental Assessment of Sustainable Concrete Reinforced with Recycled End-of-Life Tyre Fibres, *Materials*, 14(2), doi: 10.3390/ma14020256.

Xu, S., and Reinhardt, H. W., 1999. Determination of double-K criterion of crack propagation in quasibrittle fracture, *International Journal of Fracture*, 98, pp. 111–149.

Xu, S., and Reinhardt, H. W., 2000. A simplified method for determining double-K fracture meter parameters for three-point bending test, *International Journal of Fracture*, 104, pp. 181–209.

STN EN 12350-2 (731312), 2020. Testing fresh concrete. Part 2: Slump test.

STN EN 12390-7 (731302), 2020. Testing hardened concrete. Part 7: Density of hardened concrete.

STN EN 12390-3 (731302), 2020. Testing hardened concrete. Part 3: Compressive strength of test specimens.

STN EN 14651+A1 (731306), 2008. Test methods for concrete reinforced with metal fibers. Measurement of tensile strength in bending (limit of proportionality (LOP), residual strength).

Havlíková, I., 2016. Vyhodnocení lomových testu těles z vybraných stavebních materiálu pomoci modelu Dvojí-K. Brno.

Prokop, J., Frantík, P., Hollý, I., and Hussein, K., 2026. Application of the double-K fracture model and identification to evaluate the fracture-mechanical properties of concrete with a dose of recycled and industrially produced fibers, 24:e06032, doi: 10.1016/j.cscm.2026.e06032.

The role of recycled steel fibers in the sustainability of cementitious composites

Alessandro P. Fantilli[1], Andrea Garda[1]

[1:] Politecnico di Torino, DISEG, Torino, Italy

Abstract

The use of recycled materials in cement-based composites, especially rubber granulates from end-of-life tires (ELTs), is an effective way to satisfy green public procurement. As the optimal amount of rubber that can replace natural aggregates remains undefined, three-point bending and compression tests were performed on different cement-based mortars. Through these tests, mechanical properties (i.e., flexural and compressive strength) were measured and correlated with the ecological impact, measured through the Life Cycle Assessment (LCA). The eco-mechanical analysis of the mortars reveals that only with suitable amounts of supplementary cementitious materials (SCM), rubber, and steel fibers from ELTs, both mechanical and environmental performances of cementitious composites improve. This is true not only when the material properties are considered, but also when the structural behavior of beams, with and without fibers, are compared.

Keywords

End-of-life tires (ELTs); rubberized concrete; sustainable construction materials; eco-mechanical analysis.

1 Introduction

This article analyzes the possible integration of rubber and steel fibers from end-of-life tires (ELTs) into cement-based mixtures. It is motivated by the significant quantity of end-of-life tires that are generated every year [1], which produce significant environmental concerns. In this context, the use of recycled rubber as aggregate of mortars and concretes allows the reuse of already available resources, and reduces landfill disposal, while limiting the extraction and processing of raw materials [1]. Also, the development of fiber-reinforced mortars and concretes with recycled steel fibers from ELTs represents a strategic approach for the construction sector. Indeed, it contributes to the reduction of new steel production and enhances the global structural behavior of concrete elements [2].

Although material recycling may appear very sustainable at first glance, it does not always lead to a reduction of the Global Warming Potential (GWP) of cement-based composites [3]. For this reason, in addition to the mechanical characterization of mortars containing ELTs materials, this study includes a quantitative evaluation of the environmental impact. It is reported in terms of the equivalent CO_2 associated with the production and processing of mortar and concrete components. The aim is to identify the best mixture containing ELTs to be used in structural elements with a reduced environmental impact.

2 Experimental program

2.1 Materials and mixtures

As it is well known, mortar is composed of cement, water and sand. With respect to the mortar mixture of the UNI EN 196-1 [4], herein assumed as a reference, it is possible to obtain new mortars by using alternative aggregates, chemical additives (including supplementary cementitious materials), and fibers.

Concerning cements, CEM II/A-LL 42.5 R and CEM III/A 42.5 N are herein considered. They have 6.6% and 42.7% of recycled materials, respectively. As aggregate, UNI EN 196-1 [4] suggests the use of CEN Silica Sand (hereafter called as Sand A), having the size fractions shown in Table 1.

Table 1: Granulometric fraction of Sand A – sieve residue.

2.00 mm	**1.60 mm**	**1.00 mm**	**0.50 mm**	**0.16 mm**	**0.08 mm**
silica	silica	silica	silica	silica	silica
0 g	95 g	378 g	431 g	270 g	176 g

To use ELTs materials, 15% by mass of Sand A was substituted by rubber. Accordingly, in the composition of the new Sand B (see Table 2), 200 g of the stone fraction at 0.5 mm was substituted by the same volume (about 130 ml) and fraction of rubber (the total weight of the rubber was 50 g). As reinforcement, recycled steel fibers from ELTs, with high tensile strength (≈2700 MPa) and a Young's modulus of about 210 GPa, provide an effective contribution to both strength and toughness of concrete.

Table 2: Granulometric fraction of Sand B – sieve residue.

2.00 mm	**1.60 mm**	**1.00 mm**	**0.50 mm**	**0.50 mm**	**0.16 mm**	**0.08 mm**
silica	silica	silica	silica	rubber	silica	silica
0 g	95 g	378 g	229 g	50 g	270 g	176 g

The average length (≈20 mm) and diameter (≈0.27 mm), and therefore a high aspect ratio (l/d ≈ 74), ensure a dense fiber distribution, improving crack control and post-cracking behavior. Additionally, the origin from end-of-life tires makes these fibers a sustainable solution with very low environmental impact.

By means of these materials, the following cement-based mixtures were tailored:

- Mortar M1 is the standard mortar of UNI EN 196-1 [4], composed of 450 g of CEM II/A-LL 42.5 R, 225 g of water, and 1350 g of CEN Silica Sand (Sand A).
- Mortar M2 is similar to Mortar M1 except for the type of cement, which has been substituted with CEM III/A 42.5 N.
- In Mortar M3, material fractions do not change with respect to M2, but Sand A has been substituted with Sand B.
- Finally, in Mortar M4 only 95 g of recycled steel fibers (RSF) from ELTs have been added with respect to the composition of Mortar M3. In this case, the common mixing procedure is sufficient to achieve the proper fiber distribution.

The composition of all these 4 mortars is reported in Table 3.

Table 3: Composition 1 liter of the mortars used in this research project.

Mortar	**Water**	**CEM II**	**CEM III**	**Type of Sand**	**RSF**	**Super Plasticizer**	**Content of Recycled material**
-	(g)	(g)	(g)	-	(g)	(g)	(%)
M1	225	450	0	Sand A	0	2.25	1.46
M2	225	0	450	Sand A	0	2.25	9.47
M3	225	0	450	Sand B	0	2.25	12.90
M4	225	0	450	Sand B	95	2.25	17.10

2.2 Samples and test setup

In accordance with UNI EN 196-1 [4], a compartmented steel mold was used to produce three prismatic specimens (40 × 40 × 160 mm^3) for each mortar (see Fig.1a). All the 12 prisms (3 specimens times 4 mortars) were removed from the formwork the day after casting, cured for 27 days at laboratory conditions (22 °C and RH = 50%), and appropriately measured and weighed. The main properties of the prisms are reported in Table 4.

In accordance with UNI EN 196-1 [4], the samples were first tested in three-point bending (Fig.1a) by imposing the displacement η in midsection, which increased at a velocity of 0.05 mm/min up to the failure. This test was followed by the uniaxial compression test on the remaining halves of the specimens (Fig.1b). Each test piece was inserted between two metal

plates having an area of 40 × 40 mm^2. The load is increased continuously at a rate of 200 N/min, and the test was stopped when the specimen reached the failure.

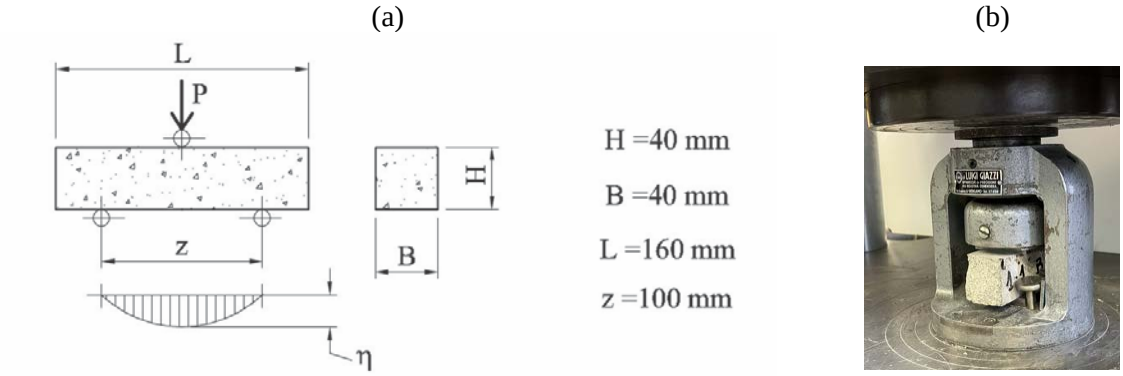


Figure 1:Mechanical tests on mortar [4]: (a) geometry of the prisms and setup of the three-point bending test; (b) uniaxial compression tests.

Table 4: Weight and dimensions of the mortar samples.

		B	***H***	***L***	**Weight**
Mortar	**specimen**	**(mm)**	**(mm)**	**(mm)**	**(N)**
M1	M1-1	39.85	39.87	160.06	5.66
	M1-2	39.95	40.18	160.16	5.74
	M1-3	39.77	39.89	160.16	5.67
M2	M2-1	39.91	39.80	159.93	5.65
	M2-2	39.93	39.62	159.96	5.58
	M2-3	39.89	39.85	159.98	5.68
M3	M3-1	39.84	40.14	160.69	5.52
	M3-2	39.97	40.71	160.42	5.57
	M3-3	39.94	39.61	160.22	5.45
M4	M4-1	39.98	39.89	160.03	5.75
	M4-2	39.85	40.67	159.86	5.79
	M4-3	39.82	40.16	159.84	5.77

2.3 LCA evaluation

To comprehensively assess the environmental impact associated with the cementitious mortars previously described, an approach based on Life Cycle Assessment (LCA) was adopted in accordance with ISO 14040 [5] and ISO 14044 [6] standards. More precisely, a simplified form of LCA focused exclusively on climate-changing emissions, expressed in terms of kilograms of equivalent carbon dioxide (kg CO_2 eq), is herein used to quantify the global warming potential (GWP).

When available, these data can be obtained from the Environmental Product Declarations (EPDs) of the materials, which report the CO_2 eq referred to a specific unit (e.g., 1 kg or 1 m^3). In the other cases, LCA model was implemented using SimaPro 9.6 software and Ecoinvent 3.10 database, in order to ensure the traceability and consistency of material and energy flows throughout the entire life cycle.

The environmental impact assessment was conducted using the Environmental Footprint 3.1 (EF 3.1) method, in accordance with the latest European standards for product-level analysis. The analysis carried out for the mixtures of Table 3 provides the values of CO_2 eq per 1 liter of mortar, as reported in the histograms of Fig.2.

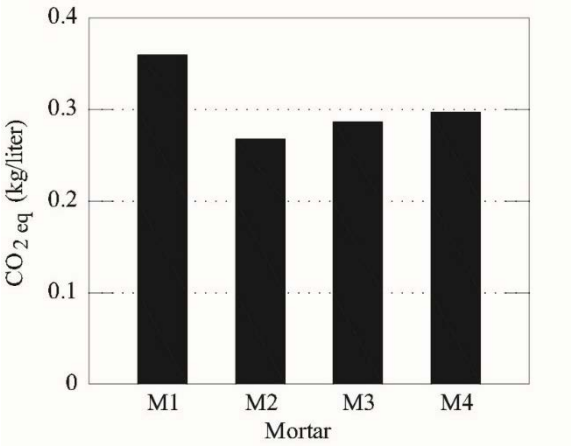


Figure 2: GWP of the mortars investigated in this project.

Mortar M1 has the highest environmental impact. This is due to the CEM II/A which contains a low percentage of recycled materials. Mortars M2, M3 and M4 are significantly less impactful than M1, as they were made with low carbon cement containing SCM. In particular, M2 has the lowest impact (see Fig.2). M3 is slightly more impactful than M2 due to the presence of rubber, which contributes to the environmental impact, although it is recycled. Finally, M4 is a bit more impactful than M3 because of the combined presence of rubber and steel fibers.

3 Test results

3.1 Three-point bending tests

The results of the three-point bending tests are reported in Table 5, where the values of the maximum load P_{max} are listed. From these values, it is possible to measure the corresponding flexural strength (f_{ctf}) of the mortars:

$$f_{ctf} = \frac{3}{2}\frac{P_{max}\,L}{B\,H^2} \tag{1}$$

where, L = 100 mm = span of the beam (in Fig. 1b); B and H = width and depth of the beams as reported in Table 4. The values of f_{ctf} are also reported in Table 5, whereas the average values are compared in the histogram of Fig.3.

Mortar M2, which has the same composition of mortar M1 except for the type of cement, shows a slight decrease (of about 8%) in flexural strength. This reduction becomes more significant, and equals approximately 15%, in the case of mortar M3, because rubber substituted silica aggregate. Mortar M4, which has the same composition as M3 but incorporates recycled steel fibers from ELTs, shows a significant increment of flexural strength (equal to 138%) with respect to the reference mortar M1.

Table 5: Results of the three-point bending tests.

		P_{max}	f_{ctf}
Mortar	**specimen**	**(N)**	**(MPa)**
M1	M1-1	2009	4.76
	M1-2	1981	4.61
	M1-3	1969	4.67
M2	M2-1	2228	5.29
	M2-2	1401	3.35
	M2-3	1811	4.29
M3	M3-1	1495	3.49
	M3-2	1908	4.32
	M3-3	1730	4.14
M4	M4-1	2911	6.86
	M4-2	4529	10.31
	M4-3	7008	16.37

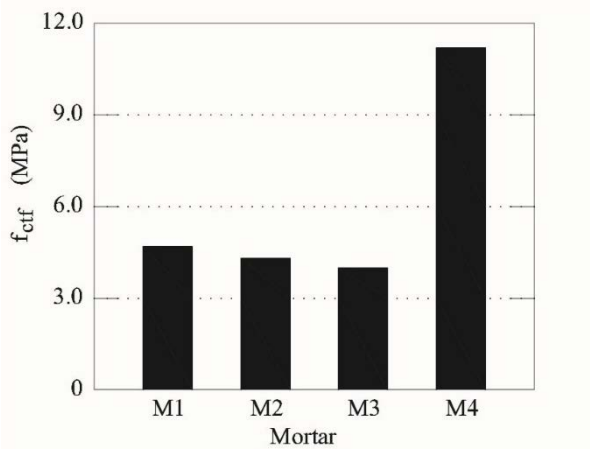


Figure 3: Average flexural strength of the mortars.

As expected, the mere presence of rubber in the cementitious composite reduced the load-bearing capacity [7]. The causes of the lower strength are certainly linked to the lower elastic modulus of the rubber and the poor rubber-matrix adhesion. However, the introduction of fibers from ELTs significantly increased the flexural strength, as shown in Fig.3.

3.2 Uniaxial Compression

The values of maximum load F_{max}, measured with of the uniaxial compression tests on 24 halves of the prisms, are listed in Table 6. From these values, the compressive strength, f_c, of all mortars can be computed as follows:

$$f_c = \frac{F_{max}}{40 \times 40} \tag{2}$$

where F_{max} is in N, and f_c in MPa.

The values of f_c are listed in Table 6, whereas their average values are compared in the histogram of Fig.4.

Contrarily to the flexural strength, mortar M2 shows a compressive strength higher than that of mortar M1. Nevertheless, if rubber substitutes silica sand, as in the mortar M3, the strength decreases. This result is consistent with the study by Gregori et al. [8], in which the compressive strength of rubber-modified concrete reduces with the increment of the substitution rate of aggregate with rubber. Concerning mortar M4, which has the same composition as mortar M3, but with the addition of RSF from ELTs, an increment of 5% and of 23% of compressive strength can be observed with respect to mortar M1 and mortar M3, respectively. In other words, the use of fibers improves not only the mechanical response in bending, as expected, but also in compression.

Table 6: Results of compression tests (A and B are two halves obtained from bending test).

		Maximum load		**Compressive strength**	
Mortar	**specimen**	$F_{max,A}$ **(kN)**	$F_{max,B}$ **(kN)**	$f_{c,A}$ **(MPa)**	$f_{c,B}$ **(MPa)**
M1	M1-1	93.10	94.20	58.20	58.90
	M1-2	94.00	96.20	58.80	60.10
	M1-3	91.40	87.20	57.10	54.50
M2	M2-1	108.00	110.00	67.50	68.80
	M2-2	103.00	109.00	64.40	68.10
	M2-3	105.00	109.00	65.60	68.10
M3	M3-1	79.50	76.00	49.70	47.50
	M3-2	79.50	80.40	49.70	50.30
	M3-3	81.00	78.60	50.60	49.10
M4	M4-1	100.00	96.30	62.50	60.20
	M4-2	98.00	101.00	61.20	63.10
	M4-3	91.70	96.60	57.30	60.50

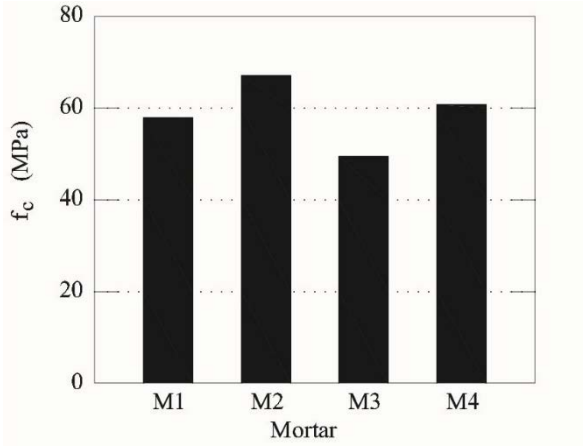


Figure 4: Average compressive strength of mortars.

4 Analysis of results

4.1 Eco-mechanical analysis at material level

The ecological and mechanical analyses previously described can be combined within the non-dimensional diagram shown Fig.5 [9]. This analysis allows engineers and architects to determine the best mortars.

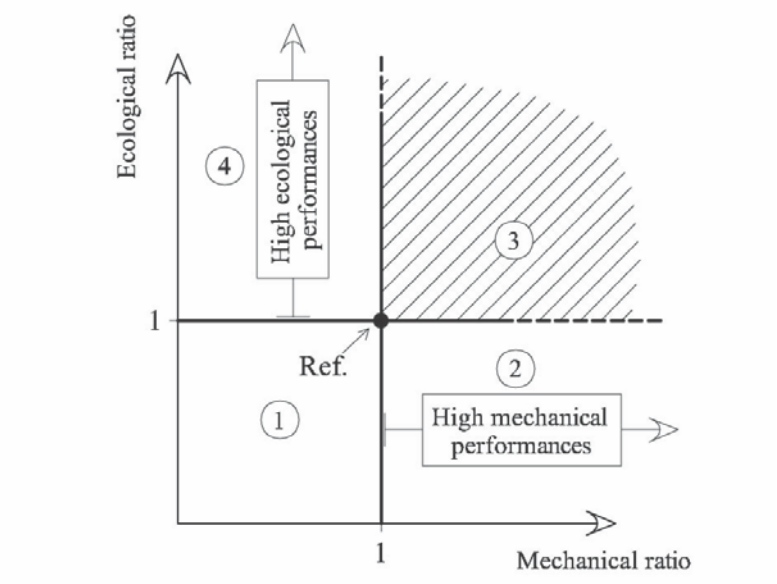


Figure 5: The non-dimensional eco-mechanical chart for comparative analyses of mortars [9].

In this diagram, the y-axis shows the dimensionless ecological ratio, whose expression varies depending on the nature of the ecological index (EI). If EI is a parameter to be minimized (e.g., GWP in terms of CO_2 eq.), the ratio is defined as the upper limit value of the ecological impact (EI_{sup}) divided by EI. The x-axis, on the other hand, represents the dimensionless mechanical ratio, defined as the ratio between the mechanical performance under consideration (MI) and the corresponding reference value (MI_{ref}).

Once the axes have been defined, the reference sample must be identified (mortar M1 in this case), which provides the values of both MI_{ref} and EI_{sup} . With respect to the coordinates (1;1) of this reference mortar, four areas that can be defined within the non-dimensional diagram of Fig.5: only the mortars which fall in the sector 3 show higher mechanical and ecological performances than the reference mortar.

Fig.6 shows the eco-mechanical analyses performed considering EI = GWP (as reported in Fig. 2), whereas MI is the flexural and compressive strengths in Fig.6a and Fig.6b, respectively. When the flexural strength is the functional unit, only the mixture M4 shows a significant improvement in the mechanical performance, combined with a lower environmental impact, both considered with respect to the reference sample M1. This is due to the presence of fibers. The mortars M2 and M3, on the other hand, show a reduced mechanical performance, despite the environmental performances are better than in mortar M1.

This result is similar to that obtained when compressive strength is the functional unit (see Fig.6b). However, in this case also mortar M2 falls in sector 3, and only mortar M2 showed a lower compressive strength than mortar M1.

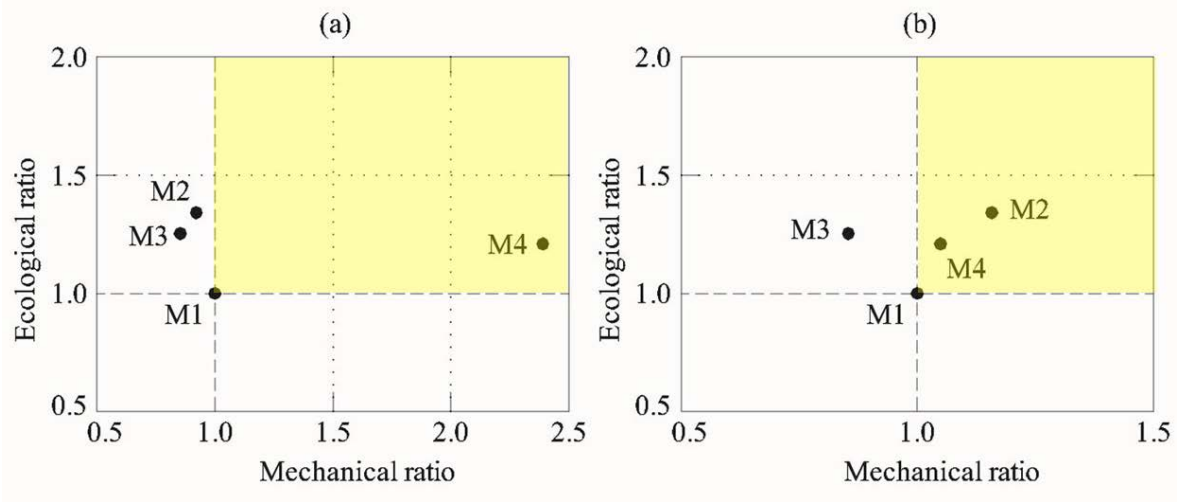


Figure 6: Eco-mechanical analyses of the mortars performed at material level considering EI = GWP and MI as (a) flexural strength and (b) compressive strength.

4.2 Eco- mechanical analysis at structural level

To carry out the analysis at structural level, starting from the statical configuration shown in Fig.1b and maintaining both *H* and *L* equal to 40 mm and 100 mm, respectively, the width *B* is computed in order to have P_{max} = 20 kN. This geometrical size can be computed by means of an inverse formula from Eq.(1):

$$B = \frac{3}{2}\frac{P_{max}\,L}{f_{ctf}\,H^2} \tag{3}$$

where f_{ctf} is the average flexural strength shown in Fig.4. The values of *B*, the total volume, and the total GWP of the beams are reported in Table 7. The latter parameter is computed by multiplying the total volume with the corresponding with the unitary GWP (see Fig.2). From values of Total GWP listed in the last column of Table 7, and compared in Fig.7, it is possible to argue that, if a structural element is mainly working in bending, M4 is the most convenient mortar for casting the beams, because the capacity of P_{max} = 20 kN can be obtained with the lowest Total GWP. This result is also consistent with that illustrated in Fig.6a. However, referred to mortar M1, all the other mortar can reduce the environmental impact and maintaining the same performance (i.e., P_{max} = 20 kN) although they require larger sizes than M1 and M4.

Table 7: the total GWP of beams designed to resist to Pmax = 20 kN.

Mortar	**GWP**	f_{ctf}	***H***	***L***	***B***	**Volume**	**Total GWP**
	(kg $CO_{2\,eq}$ /l)	**(MPa)**	**(mm)**	**(mm)**	**(mm)**	**(l)**	**(kg $CO_{2\,eq}$)**
M1	0.359	4.68	40	100	401	1.60	0.58
M2	0.268	4.31	40	100	435	1.74	0.47
M3	0.286	3.99	40	100	470	1.88	0.54
M4	0.297	11.2	40	100	168	0.67	0.20

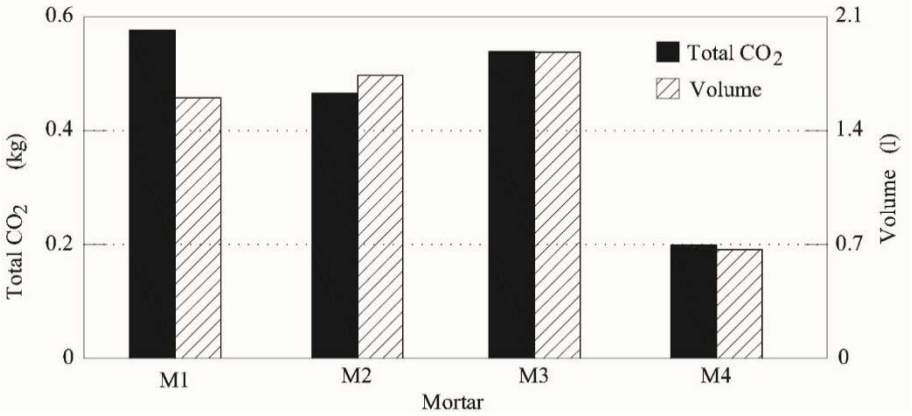


Figure 7: Total GWP and volume of the beams having a bearing capacity P_{max} = 20 kN.

Therefore, at structural level, the presence of recycled fibers contributes not only to reduction of the environmental impact (maintaining the same performance of the beam), but also the final volume of the structural elements reduces.

Similarly, if a column must have a load-bearing capacity of F_{max} = 80 kN, the same height (L = 100 mm), and size H = 40 mm, the size B of the cross-section can be calculated assuming the compressive strength of the mortars (see Fig.4):

$$B = \frac{P}{f_{cm}\, H} \tag{4}$$

As shown in Table 8, all the sizes were used to evaluate the total volume and, by multiplying by the unitary GWP (kg CO_2 eq /l) of each mixture, it was possible to estimate the Total GWP.

Table 8: Total GWP of columns designed to resist to P_{max} = 80 kN

Mortar	**GWP**	f_{cm}	***H***	***L***	***B***	**Volume**	**Total GWP**
n°	**(kg $CO_{2\,eq}$ /l)**	**(MPa)**	**(mm)**	**(mm)**	**(mm)**	**(l)**	**(kg $CO_{2\,eq}$)**
M1	0.359	57.93	40	100	34.5	0.14	0.050
M2	0.268	67.08	40	100	29.8	0.12	0.032
M3	0.286	49.48	40	100	40.4	0.16	0.046
M4	0.297	60.79	40	100	32.9	0.13	0.039

Also in this case, the comparison among all the Total GWP is illustrated in Fig.8. If structural element is mainly under compression, it is more convenient to use mortar M2. With the same load-bearing capacity, this mixture requires less material, resulting in a reduction of the Total GWP. The same conclusion is also valid for mortar M4. However, to achieve the same load-bearing capacity as M2, it is necessary to increase size B (and the volume) by approximately 10%. Referring to mortar M1, all the other mortars can reduce the environmental impact of the columns, although they require larger dimensions.

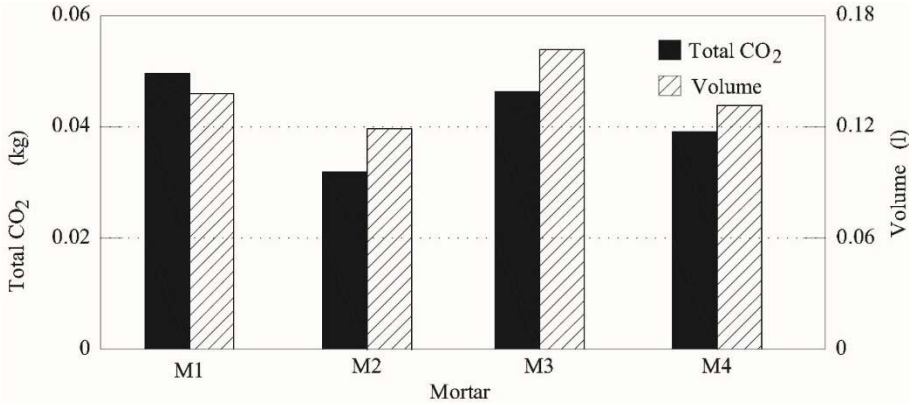


Figure 8: Total GWP and volume of the columns having a bearing capacity F_{max} = 80 kN.

5 Conclusions

According to the results of the experimental investigation described in the previous sections, the following conclusion can be drawn:

1. If they are properly used, recycled material from ELTs can improve the mechanical properties of cement-based mortars and reduce the environmental impact.
2. In terms of flexural strength, the mixture of mortar M4, containing cement with a lower environmental impact, rubber, and recycled steel fibers from end-of-life tires, showed the best performance
3. Due to the presence of fibers, beams made with mortar M4 can reduce both the Total GWP and volume with respect to traditional unreinforced mortars, without reducing the strength.
4. Also, in compression mortar M4 shows good performance, however the presence of fibers is not as effective as in bending.

6 Acknowledgements

The present study has been developed within the European project LIFE20 GIE FR 282 - RE-PLAN CITY LIFE (RElevant Audience Plan Leading to Awareness Network for CIrcular Economy Use of Recycled TYre materials in CITY LIFE). This manuscript reflects only the authors' views and opinions. Neither the European Union nor the European Commission can be considered responsible for them.

7 References

[1] Hashamfirooz, M., Dehghani, M. H., Khanizadeh, M., Aghaei, M., Bashardoost, P., Hassanvand, M. S., Hassanabadi, M., Momeniha, F. (2025). A systematic review of the environmental and health effects of waste tires recycling. *Heliyon* 11, e41909 https://doi.org/10.1016/j.heliyon.2025.e4190

[2] Qin, X., Kaewunruen S. (2022). Environment-friendly recycled steel fibre reinforced concrete. *Construction and Building Materials* 327, 126967 https://doi.org/10.1016/j.conbuildmat.2022.126967

[3] Bennett, B., Visintin, P., & Xie, T. (2022). Global warming potential of recycled aggregate concrete with supplementary cementitious materials. *Journal of Building Engineering*, *52*, 104394. https://doi.org/10.1016/j.jobe.2022.104394

[4] European Committee for Standardization (CEN) (2005). EN 196-1 Methods of testing cement - Part 1: Determination of strength.

[5] International Organization for Standardization (ISO) (2006). ISO 14040:2006 Environmental management — Life cycle assessment — Principles and framework. Geneva.

[6] International Organization for Standardization (ISO) (2006). ISO 14044:2006 Environmental management — Life cycle assessment — Requirements and guidelines. Geneva.

[7] Fantilli, A. P., Bianco, I., Blengini, G. A., & Chiaia, B. (2025) The contribution of tire recycled materials in the circular economy of cement-based composites. In Concrete and Circular Economy, RILEM Bookseries. https://doi.org/10.1007/978-3-032-06802-6

[8] Gregori, A., Castoro, C., Marano, G. C., & Greco, R. (2019). Strength Reduction Factor Concrete with Recycled Rubber Aggregates from Tires. *Journal of Materials in Civil Engineering*, 31(8), 04019146. https://doi.org/10.1061/(ASCE)MT.1943-5533.0002783

[9] Chiaia, B., Fantilli, A. P., Guerini, A., Volpatti, G. and Zampini, D. (2014). Eco-mechanical index for structural concrete. *Construction and Building Materials* 67, 386-392. https://doi.org/10.1016/j.conbuildmat.2013.12.090

Retrofitting and strengthening

UHPFRC strengthening of bridge slabs - Towards a better understanding and prediction of failure mode under shear load

Jean-Philippe Charron[1], Espoir Kahama[1], Martin Pharand[1]

[1]: Polytechnique Montreal, Montreal, Canada.

Abstract

Ultra-High Performance Fibre Reinforced Concrete (UHPFRC) has become a widely adopted solution for strengthening aging reinforced concrete (RC) structures due to its high strength and durability. When used as an overlay on bridge slabs, UHPFRC significantly enhances shear performance while preserving the original geometry. Experimental studies have shown that UHPFRC-strengthened slabs exhibit a two-stage action under shear loading: an initial monolithic response followed by a composite action characterized by a double-hinge mechanism and structural hardening. This composite action evolves through shear and bending cracking, hinge formation, and interface delamination, leading to three potential failure modes: concrete crushing in the substrate (strut failure), tensile failure of the UHPFRC layer (tie failure), or shear failure at the interface. Existing analytical models typically address only one failure mechanism and rely on different assumptions, limiting their general applicability.

To address this limitation, a group of complementary analytical models based on a global strut-and-tie model is proposed. It includes three complementary models to predict the ultimate shear resistance associated with each failure mode. A preliminary calibration using three experimental slab tests demonstrates the combined use of the models accurately identifies the governing failure mechanism and provides reliable predictions of shear capacity. However, further validation on a broader experimental database, particularly for tie and interface failures, remains necessary to improve the robustness and applicability of the proposed approach.

Keywords

Ultra-high performance fibre reinforced concrete (UHPFRC), bridge slabs, shear strengthening, analytical model, shear strength, failure mode.

1 Introduction

Over the last twenty years, Ultra-High Performance Fibre Reinforced Concretes (UHPFRC) have undergone significant development and are now commercially available worldwide. Compared to conventional normal-strength concrete (NSC), UHPFRC exhibit superior mechanical and durability properties, including compressive strength exceeding 120 MPa (according to North-American standards CSA-S6 2025 and AASHTO 2024), tensile strength greater than 7 MPa accompanied by strain-hardening behavior (Russell & Graybeal, 2013), and enhanced durability resulting from its extremely low permeability to water, chloride ingress, and carbonation (Charron and Desmettre, 2013).

These characteristics make UHPFRC particularly suitable for the rehabilitation of aging reinforced concrete (RC) structures. Typical repair strategies involve combining the existing RC substrate with a UHPFRC overlay, with or without additional reinforcement. Such repairs improve watertightness, increase stiffness, and enhance both flexural and shear capacities, while often preserving the original cross-sectional dimensions of the structure (Pharand & Charron, 2023). These repairs have been successfully implemented in a wide range of infrastructure, including bridges, buildings, dams, and underground structures.

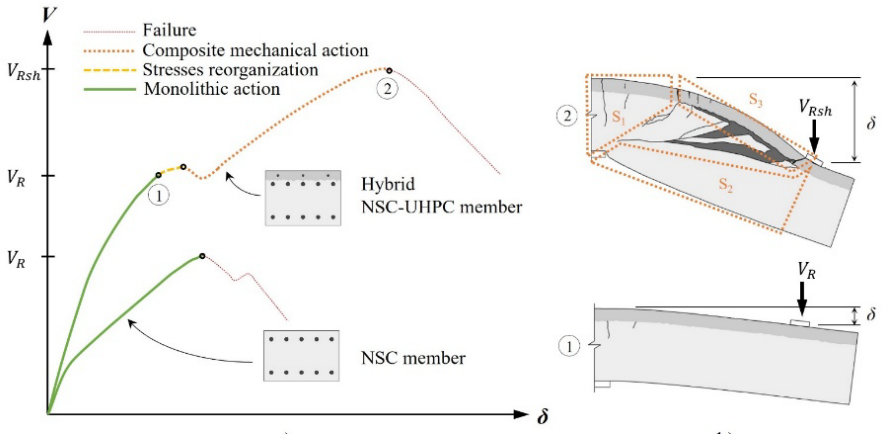
This paper focuses on the shear strengthening of bridge slabs with UHPFRC overlays. Several experimental campaigns have been conducted to evaluate the shear behavior of UHPFRC strengthened slabs (Hussein and Amleh, 2015; Ji and Liu, 2020; Noshiravani and Brühwiler, 2013; Sine et al. 2022; Pharand et Charron, 2023a). Experiments have shown that complex shear behavior takes place up to failure, where shear cracks develop in the NSC substrate, delamination occurs close to or at the repair interface, and tensile cracks form in the UHPFRC layer. As most shear failure occurrences involved concrete strut crushing at the shear crack tips, some analytical models were proposed to evaluate shear capacity for this failure mode (Bastien-Masse and Brühwiler, 2016; Pharand and Charron, 2023b; Sine et al., 2022). Models were also suggested to predict shear capacity when the failure involves significant crack localization in the UHPRC overlays (Ji et Liu, 2020) and a severe interface delamination (Yin et al, 2018). However, most models are based on different design philosophies and assumptions, making difficult the evaluation of the shear strength of UHPFRC strengthened slabs for various failure modes on a common basis.

The paper describes a group of complementary analytical models developed at Polytechnique Montreal to predict the failure mode and the shear resistance of bridge slabs strengthened with UHPFRC overlays.

2 Mechanical behavior of UHPFRC strengthened bridge slabs under shear loads

Experimental studies on the shear response of UHPFRC-strengthened slabs have demonstrated a two-stage structural behavior prior to failure. In the first stage, shear forces are primarily resisted through a monolithic action similar to that of conventional NSC slabs (solid green line in Figure 1a). During this phase, the UHPFRC overlay enhances the shear transfer mechanisms within the NSC substrate and delays the initiation of diagonal shear cracks (Noshiravani and Brühwiler, 2013; Sine et al., 2022; Pharand and Charron, 2022; Yin et al., 2017). The maximum shear resistance reached in this stage is denoted V_R.

Following the formation of diagonal shear cracks, the second stage takes place characterized by a composite action between the NSC substrate and the UHPFRC layer (bold dotted orange line in Figure 1a), often referred to as the double-hinge mechanism (Noshiravani and Brühwiler, 2014). The development of two plastic hinges in the UHPFRC releases stress in the NSC substrate and enables a strain-hardening action in the strengthened slabs (Noshiravani and Brühwiler, 2013; Pharand and Charron, 2022; Sine et al., 2022; Bastien-Masse and Brühwiler, 2016). The ultimate shear capacity corresponding to this stage is denoted V_{Rsh} (Figure 1a).

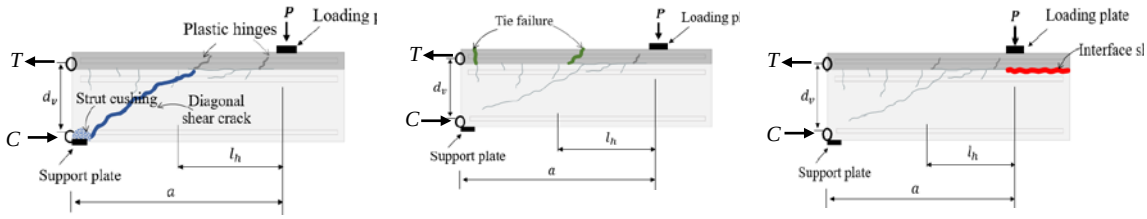


(a) Load-displacement curve (b) Crack pattern and amplified deformed shape

Figure 1: Behavior of hybrid NSC-UHPFRC members under shear load (Pharand and Charron, 2023)

The composite mechanical action develops through four successive steps (Pharand and Charron, 2023a) (dashed yellow line in Figure 1a): (I) initiation of diagonal shear cracks in the NSC; (II) formation of the first plastic hinge within the UHPFRC layer; (III) delamination at the NSC–UHPFRC interface accompanied by stabilization of the compression strut in the NSC; and (IV) formation of a second plastic hinge in the UHPFRC layer. Once this mechanism is established, the slab can be divided into three subsections (② in Figure 1b). Subsection S1 is a hybrid zone primarily subjected to bending stresses. Subsection S2 corresponds to a portion of the NSC where compressive stresses dominate, ensuring direct load transfer from the point of application to the support. Subsection S3 represents the delaminated UHPFRC layer with a plastic hinge at each end; it mainly carries tensile stresses with a portion of the shear forces.

The composite action of UHPFRC strengthened slabs can lead to three shear failure modes (Figure 2). First, the most frequent failure mode observed is the concrete crushing of subsection S2 at the tip of the diagonal shear cracks (Ji and Liu, 2020; Noshiravani and Brühwiler, 2013; Pharand and Charron, 2023a; Sine et al., 2022; Yin et al., 2017) (Figure 2a). Second, complete interface delamination of subsection S3 beyond the loading plate can occur (Figure 2c), especially when the NSC-UHPFRC interface properties are weak (limited roughness of the NSC substrate) as observed by Houdoin (2022). Third, the tensile resistance of subsection S3 can be reached with limited reinforcement ratio in the UHPFRC overlays (Pharand and Charron, 2022a; Houdoin, 2022). These two later shear failure modes have received much less attention in literature.



(a) Stut failure in substrate (b) Tie failure in UHPFRC (c) Interface failure

Figure 2: Shear failure modes of UHPFRC-strengthened slabs (Kahama et al. 2025)

3 Analytical models for UHPFRC strengthened slabs under shear loads

Polytechnique Montreal is developing a group of complementary analytical models allowing evaluation of the structural hardening resistance V_{Rsh} of UHPFRC strengthened slabs for all types of shear failure modes. For that purpose, a global strut and tie model (Figure 3) was developed to replicate the mechanical hardening behavior of the slabs based on digital image correlations and strain gauges measurements (Pharand & Charron, 2023b). In the strut and tie model, ties T_1 and T_2 carry tensile stresses from the applied load P, reduced by the plastic hinges H_1 and H_2 reactions. Both ties' strength is defined from the combined properties of the tensile cord: NSC rebars, UHPFRC rebars as well as the UHPFRC layer. Bending plastic moment M_U of hinges is defined using UHPFRC layer cross-section properties, which includes the UHPFRC and its rebars. Strut C_1 at angle θ_1 carries compression stresses from plastic hinge H_1 reaction, while strut C_2 at angle θ_2 carries compression stresses from the applied load P, reduced by the plastic hinge H_2 reaction. Both struts' strength is defined by the NSC substrate properties. All node locations, except for hinge H_1, are geometrically determined. The analytical models in the next sections are proposed to evaluate the ultimate shear strength of the system (V_{Rsh}) when the weak element in the structural system is the NSC strut, the UHPFRC tie or the NSC-UHPFRC interface.

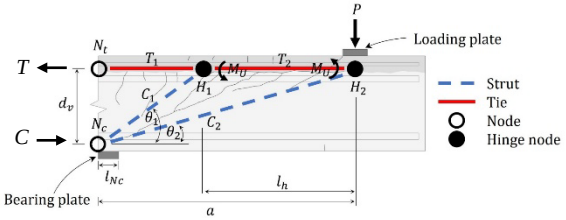


Figure 3: Shear failure modes of UHPFRC strengthened slabs (Pharand & Charron, 2023b)

3.1 Strut failure model

The strut failure model was developed and validated in Pharand's thesis (2022). In this case, the NSC struts are considered the weak element of the global strut and tie model, the ties and NSC-UHPFRC interface are considered stable. The two struts *C1* and *C2* (Figures 2a and 3) are combined into a single strut. The resistance of the combined NSC strut at node N_c is computed based on forces' equilibrium and the Canadian code recommendations (CSA, 2014) for node regions bound by struts and bearing areas (CCC zone). Assumptions and details of development of the model are available in Pharand & Charron (2023b). The ultimate force P, named $V_{Rsh\ strut}$, that can be resisted by the combined NSC strut at node N_c is computed by Equation 1. Geometrical parameters are illustrated in Figure 3. M_u represents the plastic bending moment of

the reinforced UHPFRC layer and R_{Nc} is the resistance of the node-to-strut interface. Most influent parameters in this model are the NSC compression strength, the shear-to-span ratio *a/d*, and the UHPFRC overlay characteristics (f_t, A_{sU}).

$$V_{\substack{Rsh \\ strut}} = \frac{(4\,a\,M_U/{d_v}^2) + \sqrt{(-4\,a\,M_U/{d_v}^2)^2 - 4(1 + {a^2}/{{d_v}^2}) \cdot (4{M_U}^2/{d_v}^2 - {R_{Nc}}^2)}}{2\,(1 + {a^2}/{{d_v}^2})} \quad (1)$$

3.2 Tie failure model

The tie failure model is developed in Kahama's thesis (Kahama et al., 2025). The model focuses on the behaviour of ties *T1* and *T2*, more particularly on tie *T1* the most solicited in the strut and tie model (Figures 2b and 3). The NSC strut and the NSC-UHPFRC interface are considered stable for this failure mode. The ultimate shear strength of the strengthened slab is reached when the tensile force acting through the tie *T1* equals its ultimate tensile strength, calculated as the sum of the tensile contribution of the rebars in the NSC substrate and UHPFRC layer, and of the UHPFRC layer. The maximal force *P* that can be sustained by tie *T1*, named $V_{Rsh\ tie}$, is computed with Equation 2. The parameters influencing the most the resistance in this model are the shear-to-span ratio *a/d*, and the UHPFRC overlay characteristics (f_t, A_{sU}).

$$V_{rsh\ tie} = \frac{T_1 d_v}{a} + 2\frac{M_U}{a} \quad (2)$$

3.3 Interface failure model

An interface failure model is proposed by Kahama et al. (2025). For this failure mode, the NSC strut and UHPFRC ties are considered stable. The slab's ultimate resistance is triggered by the shear stress at the NSC-UHPFRC interface under the loading point (Figures 2c and 3) achieving the shear strength of the interface estimated by the Mohr-Coulomb's law ($\tau = c + \mu\,\sigma$). The maximal force *P* that can be sustained by the NSC-UHPFRC interface, named $V_{Rsh\ int}$, is given by Equation 3, where *c* is the cohesion and μ the friction coefficient. α represents the ratio of the tie *T1* strength provided by the reinforced UHPFRC layer on the total strength of the tie. In this model, the interface length under compression l_c, the cohesion *c* at interface, as well as *a/d* and α ratios are important parameters for evaluating the strength. Higher roughness of the substrate surface favor greater cohesion at the interface and increases the shear strength, it is thus important to characterize the cohesion for various substrate surface preparation.

$$V_{rsh\ int} = (c\,b\,l_c + \alpha\frac{2M_u}{d_v}\frac{a}{l_h} - \frac{2M_u}{l_h}\mu)/(\frac{\alpha\,a}{d_v} - \mu) \quad (3)$$

4 Preliminary calibration of analytical models for UHPFRC strengthened slabs under shear loads

The first calibration of the models was done with shear tests carried out on UHPFRC strengthened slabs of previous research projects at Polytechnique Montreal. Table 1 describes the configurations of three slabs, each of them underwent one of the shear failure modes described previously. Variables presented are the shear-to-span ratio (a/d_{eq}), the slab width (*b*),

the substrate and UHPFRC layer thicknesses (h_c and h_U), rebars' area in the substrate and the UHPFRC layer (A_{sU} and A_{sc}), the ultimate shear capacity evaluated in laboratory (V_{exp}), and the shear failure mode identified with DIC and strain gauges measurements during the tests. More details on experimental programs such as materials' properties and slab test configurations are available in references.

Table 1: Database of shear tests conducted on UHPFRC strengthened slabs for model calibration.

Slab ID	Ref.	a/d_{eq}	b (mm)	h_c (mm)	h_U (mm)	A_{sc} (mm^2)	A_{sU} (mm^2)	V_{exp} (kN)	Failure mode
US-S	*	3.33	400	240	50	1500	300	220	Strut failure
H-4B	#	2.48	660	220	50	387	600	342	Tie failure
H-5B	#	2.94	660	213	50	387	600	249	Interface failure

* : Pharand and Charron J.-P. (2023b), # : Houdoin (2022)

Figure 4 shows the experimental resistance for each slab (V_{exp} in black). Then, theoretical shear strengths obtained with the strut failure model ($V_{Rsh\ strut}$ in blue), the tie failure model ($V_{Rsh\ tie}$ in green), and the interface shear failure model ($V_{Rsh\ int}$ in red) described in Section 3 are shown. Calculations were done according to the characteristics of slabs cross-section and materials' properties measured in each project.

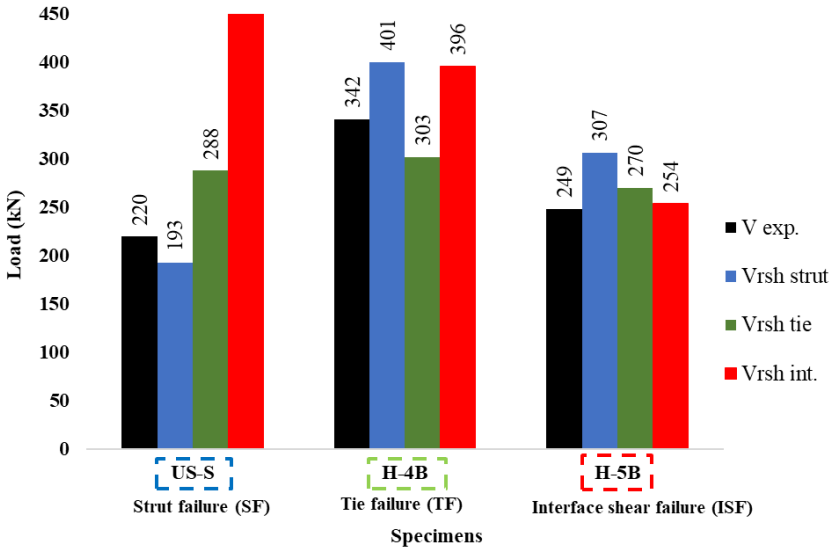


Figure 4: Preliminary calibration of analytical models for shear resistance

The US-S slab failed experimentally due to the NSC strut crushing. For this specimen, the strength predicted by the strut failure model ($V_{rsh\ strut}$, Figure 4) is the lowest among those obtained by other models, meaning that strut resistance controls the ultimate shear strength. Furthermore, the prediction provided by the strut failure model is closest to the experimental value, with a deviation of 12%. The models developed for tie failure or interface shear failure overestimate the actual slabs' strength. Indeed, the high bond properties of the interface (substrate roughness of CSP9) and the significant rebar area in tie T1 (A_{sU} and A_{sc}) provided greater resistances for these failure modes.

The H-4B slab failed experimentally in the UHPFRC tie. The resistance obtained by the proposed tie failure model ($V_{rsh\ tie}$, Figure 4) yields the lowest value and the closest match to the experimental values, with a deviation of 11%. This confirms that the ultimate shear capacity of this slab is controlled by the tie strength. The large width (660 mm) of the H-4B slab and the high compressive strength of the substrate (70 MPa) have increased the strut strength and prevented its crushing. The interface failure was also avoided because the slab had moderate interface bond properties (substrate roughness of CSP6) with a large portion (83%) of the tie's tensile force transferred through the reinforced UHPFRC layer, which favored interface resistance.

The H-5B slab failed experimentally due to the interface shear. For this slab, the proposed model for interface shear failure provides the lowest value and the closest to the experimental results, with a deviation of 2%. The shear strength of the interface was achieved because significant shear stresses had developed below the loading plate with the greater shear-to-span ratio combined with a large portion (83%) of the tie's tensile force transferred through the reinforced UHPFRC layer. This configuration has reduced the tensile stress in the tie in comparison to the H-4B slab, avoiding that failure. Also, the large width (650 mm) of the H-5B slab combined with the high compressive strength of the substrate (70 MPa) prevented the strut failure.

5 Discussion

The theoretical predictions of the complementary analytical models proposed for estimating the shear capacity of UHPFRC strengthened slabs for various shear failure modes are reliable for the very small test database considered. The models must now be calibrated on a larger group of shear tests, particularly with slabs showing tie and interface failures that are very limited in the literature. These tests must include variation of important parameters described in Sections 3.2 and 3.3, such as materials properties (c, f_t), overlay characteristics (A_{sC}, h_U, A_{sU}), and testing configurations (a/d ratio).

Currently no design provisions consider all three types of shear failure modes observed in UHPFRC strengthened slabs. The Swiss code (SIA 2016) is one of the few provisions applicable to NSC-UHPFRC structures, it integrates a model describing the strut failure mode only. Other models proposed in literature for the tie failure and interface failure modes were not adopted in design provisions as they require more validation. Moreover, their integration in a design code would be difficult as they are based on different design philosophies and assumptions.

The complementary analytical models described in the paper are based on a global strut-and-tie model and share the same assumptions. Their combined utilization allows the evaluation of the shear strength of UHPFRC strengthened slabs for all three types of shear failure, the identification of the critical failure mode and thus the optimization of a safer design for the UHPFRC repair.

Once the validation of the complimentary analytical models will be completed with experimental campaigns described previously, the next steps of development for integration in code provisions will be to carry out sensibility studies of the models, provide typical values for some parameters unavailable at design process, and integrate safety factors in models.

6 Conclusions

The assessment of the shear behavior of UHPFRC strengthened slabs requires a thorough understanding of the composite action developing before failure. A better characterization of the composite action enables the development of analytical models for all shear failure modes. The findings of the research conducted at Polytechnique Montreal is summarized as follows:

- The composite action taking place under shear loads can lead to three failure modes involving either compression crushing of the NSC substrate, tensile failure of the UHPFRC overlay, or delamination of the NSC-UHPFRC interface.

- Based on a global strut and tie model, three analytical models were proposed to predict the shear resistance of UHPFRC strengthened slabs showing NSC strut failure, UHPFRC tie failure and NSC-UHPFRC interface shear failure.

- Combined utilization of the three models allowed identification of the actual shear failure mode (the one with the lowest resistance) and accurate predictions of the shear strength for UHPFRC strengthened slabs considered.

New analytical models proposed still require further calibration and validation to improve their robustness and accuracy. The data collected during upcoming experimental programs will enable deeper validation and/or refinement of the assumptions considered in the proposed models.

7 Acknowledgements

The Authors acknowledge the support provided by the Fonds de Recherche du Quebec Nature et Technologies (FRQNT) and Quebec Ministry of Transportation (QMT) in funding this work.

8 References

ASSHTO, 2024. "Guide Specifications for Structural Design with Ultra-High Performance Concrete", *ASSHTO Publications*, 97 p.

Bastien-Masse, M., Brühwiler, E., 2016. "Contribution of R-UHPFRC Strengthening layers to the shear resistance of RC elements", *Structural Engineering International*, 26(4), 365-374.

Charron, J.-P., Desmettre, C., 2013. "Intérêt de l'utilisation des bétons renforcés de fibres pour la construction d'ouvrages d'art durables", *Report SR13-01 Polytechnique Montreal*, Canada, 45 p.

CSA-S6, 2025. "Canadian Highway Bridge Design Code. CSA Standard S6-25". *Canadian Standard Association*, Rexdale (Ontario), Canada.

Houdoin, A., 2022. "Évaluation expérimentale et numérique de la capacité résiduelle de dalles prélevées sur un pont existant et de l'effet d'un renforcement en BFUP sur leur résistance en cisaillement", *PhD thesis, Polytechnique Montreal*.

ICRI, 2020. "Guide for the Preparation of Concrete Surfaces for Repair Using Hydrodemolition Methods", *International Concrete Repair Institute*, Report 310.3R-2014.

Ji H., Liu C., 2020. “Ultimate shear resistance of ultra-high performance fiber reinforced concrete-normal strength concrete beam”. *Engineering structures*, 203, 109825.

Kahama, E., Charron, J.-P., Desmettre, C., 2025. “Strengthening of bridge slabs with UHPC overlays”, *Research report SR25-02 submitted to Quebec Ministry of Transportation*, Polytechnique Montreal, Canada, 121 p.

Noshiravani, T., Brühwiler, E., 2013. “Experimental investigation on reinforced ultra-high-performance fiber-reinforced concrete composite beams subjected to combined bending and shear”, *ACI Structural Journal*, 110, pp. 251-261.

Pharand, M., Charron, J.-P., 2023a. “Experimental Investigation of the Shear Resistance Mechanism on Hybrid NSC-UHPFRC Predamaged and Undamaged Unidirectional Bridge Slabs”, *ASCE Journal of Structural Engineering*, 149 (9), pp. 1-14.

Pharand M., Charron J.-P., 2023b. “Shear resistance and structural hardening resistance models for hybrid NSC-UHPC elements”. *Advances in Structural Engineering*, 26(6), 1027-1041.

Pharand, M., 2022. “Comportement structural et dimensionnement en flexion et à l’effort tranchant d’éléments hybrides en béton ordinaire et en béton fibré à ultra-hautes performances”. *PhD thesis of Polytechnique Montreal*.

Russel, H.G., Graybeal, B., 2013. “Ultra-High Performance Concrete: State-of-the-Art Report for the Bridge Community”, *FHWA Technical report FHWA-HRT-13-060*, USA, 171 p.

SIA 2016. UHPFRC: materials, design and application, SIA 2052 code.

Sine A., Pimentel M., Nunes S., (2022). “Shear behaviour of RC-UHPFRC composite beams without transverse reinforcement”. *Engineering Structures*, 257, 114053.

Yin H., Shirai K., Teo W., 2018. “Prediction of shear capacity of UHPC–concrete composite structural members based on existing codes”. *Journal of civil engineering and management*, 24(8), 607-618.

Enhancing the Service Life of Historical Bridge Structures: Experimental Assessment of a CFRP–FRM Retrofit System

Anna Bontempi[1], Nico Di Stefano[1], Giulio Morandini[2], Giuseppe Melcangi[2], Luca Albertario[2], Fausto Minelli[1].

[1] University of Brescia, Department of Civil, Environmental, Architectural Engineering and Mathematics (DICATAM), Via Branze, 43, Brescia, 25123, Italy.

[2] MAPEI.

Abstract

The rehabilitation of historical bridges requires solutions capable of preserving cultural heritage while ensuring adequate structural performance and durability. This study aims to experimentally evaluate the effectiveness of a hybrid CFRP–FRM retrofit system for extending the service life of severely deteriorated bridge elements. The investigation was conducted on a full-scale reinforced concrete bridge girder that had been in service for nearly 90 years and exhibited extensive corrosion damage, including concrete cover loss and corrosion of longitudinal reinforcement and stirrups.

The experimental programme consisted of two phases. First, the original girder was tested to assess its residual load-bearing capacity under four-point loading in displacement control. The test was interrupted after the yielding of the existing bars. Subsequently, the girder was strengthened using two 12 mm CFRP bars to enhance flexural capacity and a 50 mm fibre reinforced mortar overlay with polypropylene fibres to improve confinement and crack control. Finally, it was retested under the same loading configuration up to failure.

The paper discusses the implementation of the strengthening technique and presents the experimental results, comparing the unstrengthened and strengthened states. The findings demonstrate the effectiveness of hybrid CFRP–FRM systems as a practical and efficient solution for extending the service life of deteriorated bridge elements, while also providing valuable insights into their application on full-scale structural components.

Keywords

RC bridge girder; CFRP bars; fibre reinforced mortar; strengthening; corrosion; full-scale testing; service life extension.

1 Introduction

A large portion of the existing reinforced concrete (RC) and prestressed concrete (PC) bridge infrastructure currently in service was designed during the early and mid-twentieth century according to design approaches primarily focused on ultimate safety and serviceability requirements, while durability-related aspects and long-term performance received comparatively limited attention. After decades of exposure to aggressive environmental conditions, many of these structures now exhibit significant deterioration phenomena, demonstrating the limitations of such design assumptions in terms of service-life performance (Walraven, 2021). Consequently, the assessment, maintenance, and preservation of aging bridge infrastructure have become increasingly critical issues for modern transportation networks, particularly in Europe, where a large percentage of bridges have already exceeded their nominal design life (Di Prisco, 2019).

Among the different deterioration mechanisms affecting existing bridge structures, reinforcement corrosion is widely recognized as one of the most critical and pervasive causes of structural degradation in RC and PC bridges. Corrosion processes may induce cracking and spalling of the concrete cover (Higgins et al., 2010), reduction of the steel reinforcement area, deterioration of bond properties between steel and concrete (Coronelli and Gambarova, 2004), and progressive losses in strength, stiffness, and ductility (Imperatore et al., 2017; Almusallam, 2001; Zhang et al., 2009). Such effects considerably increase the uncertainty associated with residual capacity assessment and complicate maintenance and intervention planning for existing infrastructure (Lupoi et al., 2022; Adey et al., 2019). In this scenario, the availability of reliable experimental evidence and robust assessment methodologies becomes essential for supporting risk-informed bridge management strategies and prioritising interventions according to structural condition and safety requirements.

Although the topic has received increasing attention in recent years, experimental investigations performed on real-scale bridge members subjected to long-term natural corrosion are still relatively scarce. Opportunities to test full-scale structural elements removed from existing bridges remain uncommon, and much of the currently available knowledge is still derived from laboratory specimens subjected to artificially accelerated deterioration processes. Some studies have nevertheless investigated the residual behaviour of naturally deteriorated RC and PC bridge beams, providing useful information on the influence of corrosion on structural response, strength degradation, and failure mechanisms (Rogers et al., 2012; Belletti et al., 2020; Savino et al., 2023; Lupoi et al., 2022). However, a significant lack of experimental data concerning full-scale bridge elements exposed to decades of natural environmental degradation still persists.

Within this context, strengthening interventions may represent an effective and sustainable alternative to bridge replacement. Besides the direct costs associated with demolition and reconstruction, replacement strategies often involve substantial indirect consequences, including traffic disruption, detours, environmental impacts, and broader socioeconomic costs, especially in the case of strategic transportation infrastructure (Frangopol and Liu, 2007). When feasible, retrofit solutions can therefore provide a more efficient approach for extending the service life of existing bridges while preserving acceptable structural safety levels.

Among the different strengthening approaches currently available, fibre reinforced polymer (FRP)-based systems have been extensively adopted because of their high mechanical performance, corrosion resistance, and relatively simple installation procedures (Täljsten,

2006). Nevertheless, externally bonded or near-surface mounted FRP systems may exhibit limitations when applied to deteriorated concrete substrates, particularly with regard to bond durability, compatibility with existing materials, and long-term performance under environmental exposure (De Lorenzis and Teng, 2006). Furthermore, investigations involving real-scale bridge members strengthened with FRP systems remain limited, and premature debonding phenomena have frequently been reported as governing failure mechanisms that restrict the achievable increase in structural capacity (Aidoo et al., 2006). These aspects highlight the need for strengthening solutions capable of ensuring reliable stress transfer mechanisms and improved compatibility with existing deteriorated concrete members.

In recent years, cement-based fibre reinforced composites have attracted increasing interest as strengthening materials for existing concrete infrastructure due to their combined structural and durability related benefits. In particular, fibre reinforced cementitious overlays and jackets can provide not only additional protection against environmental deterioration, but also a direct mechanical contribution through post-cracking tensile resistance, crack-bridging capacity, and stress redistribution mechanisms. High-performance FRC systems, including ultra high performance fibre reinforced concrete (UHPFRC), have demonstrated promising results in strengthening applications for RC members, leading to improvements in structural response, crack control, and durability performance (Lampropoulos et al., 2016; Huang et al., 2022). Nevertheless, most available studies are still mainly based on small-scale specimens or numerical investigations, while experimental evidence involving full-scale bridge members remains comparatively limited.

The effectiveness of cementitious FRC strengthening systems is strongly dependent on the stress transfer mechanisms developing at the interface between the existing substrate and the newly applied overlay. Surface preparation, substrate roughness, and interface shear characteristics play a fundamental role in achieving adequate composite interaction and in mobilizing the tensile post-cracking behaviour of the FRC layer (Mansour et al., 2017; Iavarone et al., 2024).

Against this background, the present study examines the strengthening of an historical RC bridge girder that remained in service for approximately 90 years and exhibited severe corrosion induced deterioration. The experimental programme involved a full-scale T-shaped girder removed from an existing bridge and tested under four point bending conditions. The investigation was conducted in two phases. First, the residual structural response of the unstrengthened member was experimentally assessed. Subsequently, the girder was retrofitted using a hybrid strengthening system composed of two 12 mm diameter CFRP bars integrated within a sprayed polypropylene fibre reinforced cementitious composite (PP-FRC) overlay. Beyond its durability-enhancing function, the PP-FRC layer was intended to provide distributed crack control and post-cracking tensile contribution, promoting stress redistribution and improving the interaction between the existing substrate and the externally added reinforcement. After strengthening, the beam was tested up to failure under the same loading configuration.

2 Experimental programme

2.1 Full-Scale Bridge Girder and Initial Assessment

The experimental investigation was carried out on a reinforced concrete (RC) bridge girder approximately 90 years old, removed during the demolition of the Fiume Garza overpass in

Brescia (Italy). The original bridge consisted of a simply supported structural system composed of T-shaped RC girders. During the replacement intervention, the existing structure was substituted with new precast prestressed reinforced concrete (PRC) beams, while two of the original girders were preserved and donated by the Municipality of Brescia to the University of Brescia for research purposes. The present study focuses on one of these full-scale specimens and investigates the applicability of an innovative strengthening solution potentially suitable as an alternative to replacement for deteriorated existing bridge members.

The bridge exhibited severe degradation associated with long-term environmental exposure. Figure 1a shows the deterioration state observed in part of the original structure, characterized by widespread concrete cover losses and reinforcement corrosion. The investigated girder presented extensive concrete cover loss together with advanced corrosion affecting both longitudinal reinforcement and stirrups, as illustrated in Figure 1b.

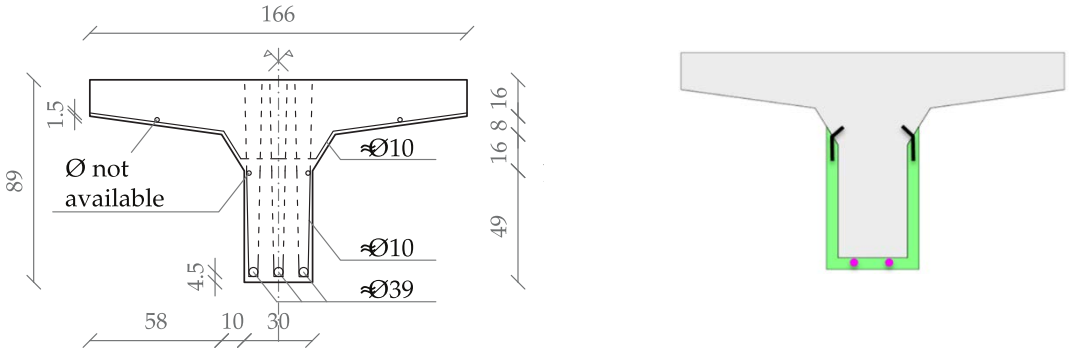


(a) (b)

Figure 1: (a) degradation conditions of the bridge in situ and (b) of the specimen considered in the experimental programme.

The geometry of the specimen cross section is reported in Figure 2a. The tested element was a full-scale bridge girder with an overall length of approximately 8.8 m and a total self weight close to 12.4 t. The member exhibited a T-shaped cross section representative of early twentieth-century bridge construction practice. The total section depth was approximately 890 mm, while the flange width was about 1660 mm. The web thickness was approximately 300 mm, whereas the flange thickness varied along the transverse direction, reaching approximately 150–160 mm near the outer edges. Figure 2b shows the adopted hybrid strengthening system, consisting of two 12 mm diameter CFRP bars embedded within a sprayed polypropylene fibre reinforced cementitious composite (PP-FRM) overlay. The configuration and structural role of the strengthening intervention are discussed in detail in the following sections.

The longitudinal tensile reinforcement consisted of a single layer with three smooth steel bars, each with a nominal diameter of 39 mm. Transverse reinforcement was provided by six-legged stirrups with a nominal diameter of 10 mm, designed to confine both the web and the lower flange region. The stirrup spacing was not constant along the beam length; within the shear critical regions, the spacing was approximately 190 mm. The reinforcement configuration is representative of historical RC bridge construction practice, with large diameter smooth longitudinal reinforcement distributed with relatively wide spacing. At the time of construction, less emphasis was generally placed on crack-width control and durability oriented detailing concepts, which in modern RC design are commonly addressed through the use of smaller diameter and more closely distributed bars.



(a) (b)

Figure 2: (a) existing cross section and (b) strengthened girder.

2.2 Existing section materials

The mechanical characterization of the existing materials was based on the results of a previous extensive experimental investigation carried out on a similar girder removed from the same bridge structure (Di Stefano, 2022). Although the previously investigated beam had a different geometry, it belonged to the same original construction phase and was manufactured using comparable materials and construction techniques. Due to the severe surface deterioration of the concrete and the presence of very large coarse aggregates, with maximum dimensions approaching 50 mm, direct core extraction was considered potentially unreliable for material characterization purposes. Consequently, the concrete properties were estimated through non-destructive testing techniques. Initial assessments were performed using rebound hammer tests, while the final values adopted for the structural evaluation were derived from Windsor probe testing.

The mean compressive strength of the existing concrete was estimated to be approximately 44 MPa. Prior to testing, the girder exhibited widespread cracking, localized concrete cover detachment, and clear evidence of advanced corrosion induced deterioration, confirming the degraded condition of the original materials. Since the elastic modulus of the concrete was not experimentally measured, it was estimated from the measured compressive strength through the ACI-based formulation reported in Equation 1, resulting in an approximate value of 28.9 GPa.

$$E_c = 3320\sqrt{f_c} + 6900 \qquad \textit{Equation 1}$$

The existing reinforcement consisted of smooth steel bars, representative of construction practice typical of the early twentieth century. The mechanical properties of the reinforcement were determined through tensile tests performed on extracted steel samples. The longitudinal reinforcement showed an average yield strength of 287 MPa, an average ultimate tensile strength of 412 MPa, and an elastic modulus close to 203 GPa. The measured ultimate strain was approximately 22%, while the average corrosion induced mass loss was about 4%.

The transverse reinforcement, consisting of 10 mm diameter stirrups, exhibited considerably more severe corrosion damage. Tensile tests provided an average yield strength of approximately 268 MPa, an ultimate strength of about 344 MPa, and an elastic modulus of roughly 185 GPa. The average mass loss due to corrosion reached approximately 35%,

indicating substantial deterioration of the transverse reinforcement. Nevertheless, despite the advanced corrosion level, the structural response of the tested girder was not governed by shear mechanisms. No critical shear deficiencies were observed, and the original transverse reinforcement arrangement, characterized by multiple stirrup legs and relatively large diameters, still ensured a residual shear capacity higher than the corresponding flexural resistance. Since the present investigation focuses primarily on flexural strengthening, the mechanical properties of the stirrups are reported mainly for completeness.

The main mechanical properties of the existing materials are summarized in Table 1.

Table 1: Mechanical properties of the existing material.

Existing steel reinforcement	Yielding stress [MPa]	287
	Ultimate stress [MPa]	412
	Young modulus [GPa]	203
	Ultimate strain [%]	22
Existing concrete	Cylindrical compressive strength [MPa]	44
	Young Modulus [GPa]	28.9

2.3 Strengthening materials

The mechanical characterization of the sprayed polypropylene fibre reinforced cementitious composite (PP-FRM) adopted for the strengthening overlay was carried out on specimens produced through spray application in order to reproduce, as closely as possible, the actual installation conditions (Figure 3a,b).



(a) (b)

Figure 3: (a) spraying of the specimens and (b) specimens after demoulding.

This approach was adopted because the mechanical properties reported in the manufacturer's technical documentation refer to cast and vibrated specimens, which are not fully representative of sprayed applications.

The compressive strength of the sprayed PP-FRM was evaluated through monotonic compression tests on 150 mm cube specimens. The average equivalent cylindrical compressive

strength obtained from the tests was approximately 41.2 MPa, confirming the good mechanical performance of the material even under the adopted spray application conditions.

The post-cracking tensile behaviour of the strengthening material was investigated through three-point bending tests on notched prisms according to UNI EN 14651 (Figure 4a). Residual tensile strengths were determined at the prescribed CMOD levels for the six specimens and are summarized in Table 2. The results highlighted a pronounced post-cracking contribution provided by the polypropylene fibres, with a residual strength ratio f_{R3}/f_{R1} equal to 1.45. This behaviour indicates progressive fibre engagement after matrix cracking and confirms the capability of the material to sustain increasing crack openings while maintaining significant load transfer capacity (Figure 4b).



Figure 4: (a) FRM-PP notched beam test set-up and (b) detail of the crack bridging mechanism.

Table 2: Results of three-point bending tests on notched FRM beams.

	f_L [MPa]	f_{R1} [MPa]	f_{R2} [MPa]	f_{R3} [MPa]	f_{R4} [MPa]
#1	2.93	3.36	4.50	4.79	4.49
#2	2.99	3.67	5.07	5.30	4.85
#3	3.06	3.28	4.40	4.55	4.19
#4	1.67	3.22	4.28	4.50	4.13
#5	2.74	2.83	4.25	4.62	4.28
#6	2.43	2.31	3.08	3.34	3.30
Average [MPa]	**2.64**	**3.11**	**4.26**	**4.52**	**4.21**
St. Dev.	0.52	0.48	0.65	0.65	0.52
cov [%]	19.86	15.30	15.28	14.32	12.27

Based on the measured residual strengths, the investigated material was classified as class 3e FRM, characterized by high ductility and stable residual tensile capacity at large crack openings. The experimental results also showed satisfactory repeatability, with coefficients of variation comparable to those commonly reported for EN 14651 testing. The nominal stress–CMOD curves (Figure 5) exhibited an initial stress drop associated with matrix cracking, followed by a recovery phase governed by fibre bridging mechanisms and a relatively stable

residual response up to large crack openings. Such behaviour confirms the effectiveness of the PP fibres in promoting distributed cracking and post-cracking stress redistribution within the cementitious composite.

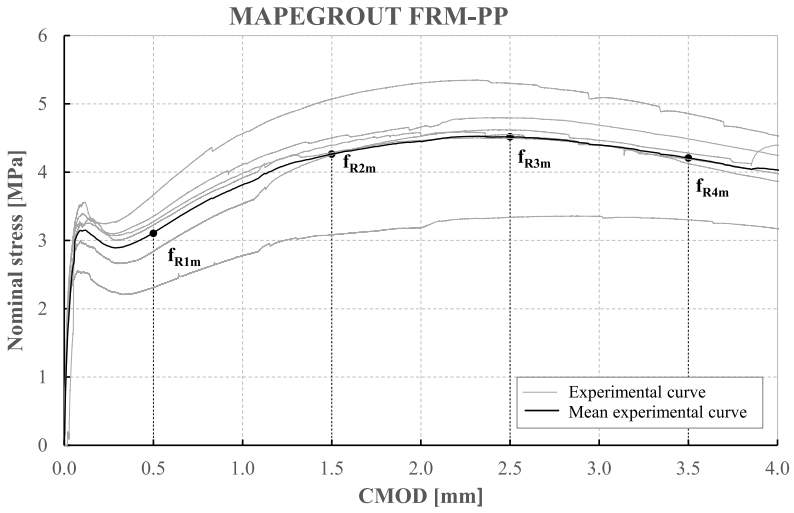


Figure 5: Nominal stress – CMOD curves of the FRM-PP specimens.

Following the bending tests, the number of fibres crossing the fracture surfaces was counted in order to estimate the actual fibre content of the material through the procedure proposed by Enfedaque et al. (2019). This approach allowed an indirect evaluation of the equivalent fibre volume fraction, which was not explicitly provided by the manufacturer, resulting in an estimated value of approximately 0.44%.

The elastic modulus of the sprayed PP-FRM was not directly measured experimentally because the cylindrical specimens originally intended for this purpose were discarded due to casting defects and incomplete filling. Therefore, the elastic modulus was estimated through numerical calibration. A finite element model developed in DIANA (DIANA FEA B.V., 2022) was used to reproduce the experimental load–displacement response of the notched prisms, and the elastic modulus was iteratively adjusted until satisfactory agreement with the experimental curves was achieved. The calibrated elastic modulus was approximately 28 GPa, slightly lower than empirical estimates derived from code-based relationships (shown in Table 3), likely reflecting the effective stiffness of the sprayed material under the adopted application conditions.

Table 3: calculation of the elastic modulus of the FRM-PP according to different standards.

NTC2018	$E_C = 22000\left(\frac{f_c}{10}\right)^{0.3}$	33.7 GPa
ACI 318	$E_C = 4700\sqrt{f_c[MPa]}$	30.6 GPa

Table 4 summarizes the main mechanical properties of the FRM-PP.

Table 4: Mechanical properties of the FRM strengthening material.

f_c [MPa]	41.2
E_c [GPa]	28
Fibres' shape	straight
V_f [%]	0.44
Fibres' length [mm]	24
Class [UNI EN 14651]	3e

The strengthening system included two 12 mm diameter CFRP bars, characterized by a linear elastic behaviour up to brittle failure, without yielding phenomena, as typical of FRP reinforcement systems. Due to the experimental complexity associated with direct tensile testing of CFRP bars, the mechanical properties adopted in the present study were derived from tensile tests previously performed by an external accredited laboratory on CFRP bars produced using the same material system, although with a smaller nominal diameter (10 mm). The experimental tests provided an average tensile strength of approximately 2540 MPa, an elastic modulus of 168 GPa, and an ultimate tensile strain of about 1.5%.

2.4 Strengthening procedure and test set-up

The experimental programme was conducted in two consecutive phases. Initially, the girder was tested under four-point bending in its original unstrengthened condition. The test was interrupted after yielding of the longitudinal reinforcement, at an applied load of 846 kN, in order to evaluate the residual structural capacity while limiting excessive damage to the specimen. A residual midspan deflection equal to 13.8 mm was measured. The maximum crack widths recorded during the unstrengthened test were approximately 0.78 mm and 2.65 mm for shear and flexural cracks, respectively. After unloading, the strengthening intervention was applied.

The adopted retrofit system consisted of two 12 mm diameter CFRP bars installed at the intrados of the beam and embedded within a 50 mm thick sprayed polypropylene fibre reinforced cementitious mortar (PP-FRM) overlay, as previously shown in Figure 2b. The strengthening materials were selected considering the aggressive exposure conditions affecting the original bridge environment. In particular, the use of CFRP reinforcement together with a sprayed PP-FRM overlay was intended to provide a corrosion-resistant strengthening solution capable of enhancing both structural performance and long-term crack control. Furthermore, the spray application technique allowed installation without the need for conventional formwork, which would have been difficult to implement under the original bridge. Figure 6 shows the bridge during the original construction phase and during dismantling operations approximately 90 years later.

Prior to strengthening, local restoration of damaged concrete cover was carried out using a thixotropic repair mortar. The same mortar was also used to fill the main and most evident cracks generated during the first loading phase. In addition, dowel connectors bonded with epoxy resin were installed to improve shear transfer between the strengthening layer and the existing flange. The beam surface was subsequently roughened mechanically to achieve an interface roughness of approximately ±5 mm, improving stress transfer and composite interaction between the existing concrete and the FRM structural layer. The existing longitudinal reinforcement and the CFRP bars were instrumented with strain gauges before application of the overlay.



(a) (b)

Figure 6: (a) pictures of the bridge location at the moment of casting and (b) during the dismantling process.

The CFRP bars were positioned at the beam intrados, while temporary wooden guides were installed to control the thickness of the sprayed overlay during application (Figure 7a,b). The FRM overlay was mainly applied by spraying, with limited manual finishing in localized areas after removal of the temporary guides to ensure continuity of the strengthening layer (Figure 7c).



(a) (b) (c)

Figure 7: (a) CFRP strengthening bars; (b) temporary wooden reference guide for the overlay thickness; (c) detail of the overlay application at a location where the wooden guides were removed.

The strengthening overlay extended approximately 250 mm beyond the support regions adopted in the experimental set-up.

After 28 days of curing, the strengthened girder was tested under four-point bending using the same loading configuration previously adopted for the unstrengthened condition in order to allow direct comparison between the two tests. The loading scheme and the instrumentation layout are shown in Figure 8. It should be noted that EB1, EB2, WB1, and WB2 were potentiometric displacement transducers specifically installed to monitor the interface behaviour. The instruments, with a measurement resolution of 10^{-5} mm, were positioned at the top surface of the overlay within the regions of maximum shear force, approximately 48 cm from the overlay ends, and were used to measure the slip between the existing concrete substrate and the PP-FRM overlay.

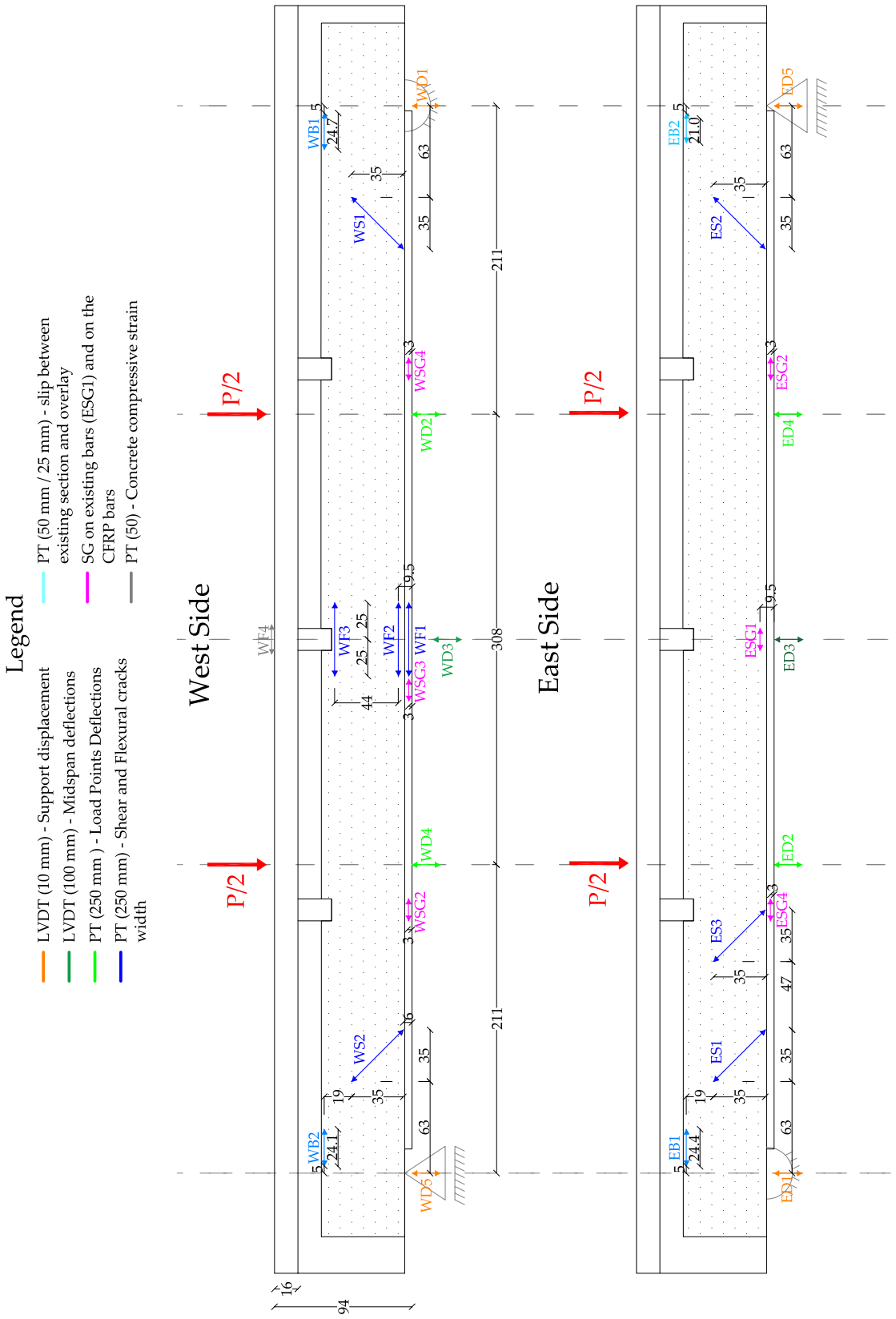


Figure 8: instrumentation layout and loading scheme.

3 Test Results

Figure 9 compares the load–midspan deflection responses of the unstrengthened girder and of the strengthened specimen. The reported loads include the self-weight contribution of the beam, strengthening overlay, and steel distribution beam. The strengthened configuration exhibited an approximately 33% increase in ultimate load compared to the original condition. It should be noted that this comparison refers to two consecutive tests performed on the same girder, which had experienced yielding and cracking during the first loading phase and was locally repaired before strengthening. Therefore, the possible influence of the pre-existing damage and subsequent repair on the strengthened response cannot be independently quantified from the present experimental programme.

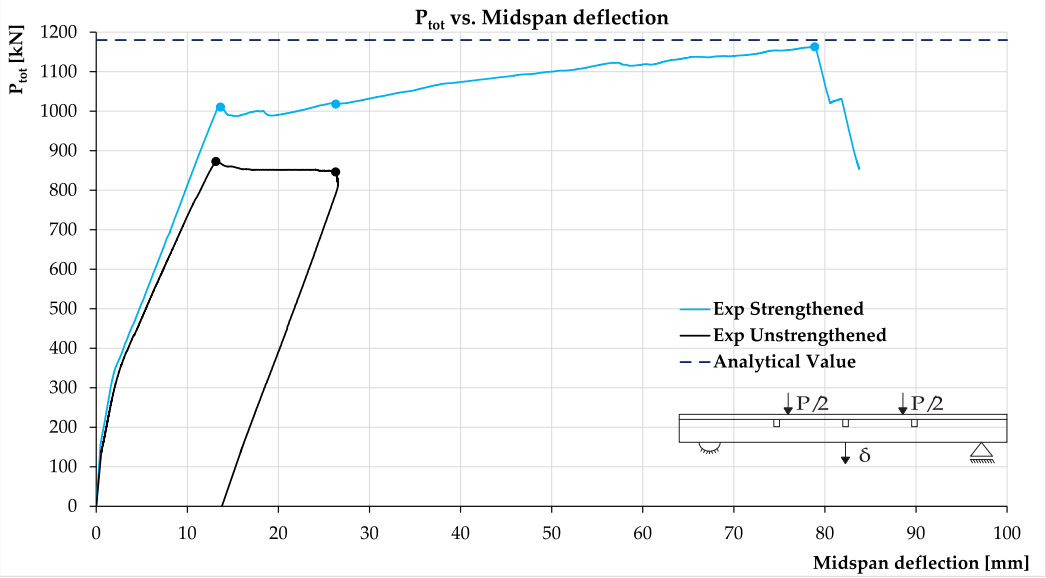


Figure 9: Load - Midspan deflection curve of the unstrengthened and strengthened (black and light blue) tests.

The response of the strengthened girder showed an initial uncracked stage followed by the cracked behaviour typical of reinforced concrete members. After yielding of the existing longitudinal reinforcement, the structural response did not exhibit the horizontal plateau observed in the unstrengthened test. Instead, the load–deflection curve maintained a residual stiffness up to failure due to the elastic contribution provided by the CFRP bars. Although CFRP reinforcement is characterized by elastic–brittle behaviour, the presence of the existing steel reinforcement ensured a globally ductile response of the structural element, with a ductility in terms of displacement of approximately 6.

Collapse occurred following the sequential rupture of the two CFRP bars. After rupture of the first bar, a limited additional load increase was observed before failure of the second reinforcement bar. Following CFRP rupture, the load returned approximately to the unstrengthened plateau, confirming that the flexural capacity increase was primarily associated with the CFRP reinforcement. Analytical sectional calculations indicated that the contribution of the PP fibres to the flexural resistance of the strengthened section was approximately 7% of the total flexural capacity.

The observed crack pattern is reported in Figure 10. The critical crack developed near loading point 4, where the widest crack opening was recorded, while an additional significant

flexural crack formed close to loading point 2. Consistently, the displacement measurements indicated larger deflections in the region corresponding to loading point 4.

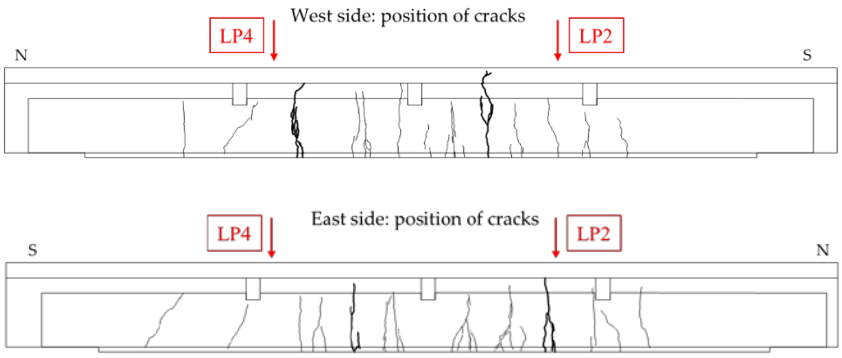


Figure 10: crack pattern of the strengthened test.

Slip measurements showed extremely limited relative displacements between the existing concrete and the FRM overlay throughout loading, with no sudden increase indicative of interface slip or debonding. The maximum recorded displacement was approximately 0.01 mm, confirming an almost perfect composite interaction. Although no direct measurements were performed near major cracks or at the overlay ends, visual inspection revealed no evidence of slip or debonding in these regions. These results also support the effectiveness of the adopted surface preparation in ensuring stress transfer and composite action.

The strain measurements recorded on the CFRP bars within the constant bending moment region showed generally consistent trends, with local variations mainly associated with crack localization effects. Some strain gauges were damaged during the test, resulting in premature signal interruption before collapse. Nevertheless, the recorded values confirmed the progressive activation of the CFRP reinforcement up to failure.

The strain measured in the existing longitudinal steel reinforcement at midspan was about 5071 με at maximum load. The recorded strain values significantly exceeded the corresponding yielding strain, confirming the development of extensive plastic deformations in the original steel reinforcement. This result explains the satisfactory global ductility observed for the strengthened girder despite the brittle tensile failure mechanism associated with the CFRP bars.

4 Concluding remarks

The main findings of the experimental investigation can be summarized as follows:

- The proposed hybrid strengthening system provided a significant enhancement of the structural response, leading to an increase in ultimate load of approximately 33% compared to the unstrengthened configuration;
- Despite the brittle tensile behaviour of CFRP reinforcement, the strengthened girder exhibited satisfactory global ductility, in terms of displacement close to 6;
- The sprayed PP-FRM overlay ensured effective composite interaction with the existing concrete substrate, as confirmed by the extremely limited interface slip recorded during the tests. In addition to its durability-related function, the PP-FRM layer contributed to distributed crack control;

- The study contributes to the limited experimental evidence on the strengthening of full-scale RC bridge girders subjected to long-term natural degradation;
- From a practical perspective, the proposed retrofit technique may represent a promising alternative to bridge replacement, potentially allowing strengthening interventions with reduced impact on traffic interruption and infrastructure serviceability;
- The adopted strengthening materials, consisting of CFRP reinforcement and a sprayed cementitious PP-FRM overlay, are particularly suitable for aggressive exposure conditions due to their corrosion-resistant characteristics and their potential contribution to long-term durability enhancement.

The experimental programme was limited to a single strengthened specimen. Further experimental investigations should extend the application of the proposed strengthening technique to additional specimens, including members with different geometries, to further assess its effectiveness and applicability under different structural configurations.

Overall, the experimental results support the feasibility of hybrid CFRP–PP-FRM strengthening systems as an effective retrofit solution for existing deteriorated bridge girders within sustainable bridge management and life extension strategies.

5 Acknowledgements

The authors gratefully acknowledge Eng. Eleonora Frusca, Eng. Franco Gregorini and Giovanni Bergomi for their valuable contribution to the experimental programme, the data processing activities, and the interpretation of the experimental results through their thesis work. The authors also acknowledge Andrea Del Barba, technician of the Laboratorio Pisa at the University of Brescia, for his valuable assistance during the laboratory testing activities.

6 References

- Adey, B.T. (2019). A Road Infrastructure Asset Management Process: Gains In Efficiency And Effectiveness. Infrastructure Asset Management, 6(1), 2–14. Https://Doi.Org/10.1680/Jinam.17.00018
- Aidoo, J., Harries, K.A., & Petrou, M.F. (2006). Full-Scale Experimental Investigation Of Repair Of Reinforced Concrete Interstate Bridge Using Cfrp Materials. Journal Of Bridge Engineering, 11(3), 350–358.
- Almusallam, A.A. (2001). Effect Of Degree Of Corrosion On The Properties Of Reinforcing Steel Bars. Construction And Building Materials, 15(8), 361–368.
- Belletti, B., Rodríguez, J., Andrade, C., Franceschini, L., Sánchez Montero, J., & Vecchi, F. (2020). Experimental Tests On Shear Capacity Of Naturally Corroded Prestressed Beams. Structural Concrete, 21(5), 1777–1793.
- Coronelli, D., & Gambarova, P. (2004). Structural Assessment Of Corroded Reinforced Concrete Beams: Modeling Guidelines. Journal Of Structural Engineering (Asce), 130(8), 1214–1224.
- De Lorenzis, L., & Teng, J.G. (2006). Near-Surface Mounted Frp Reinforcement: An Emerging Technique For Strengthening Structures. Composites Part B: Engineering, 37(2–3), 119–143.

- Di Prisco, M. (2019). Critical Infrastructures In Italy: State Of The Art, Case Studies, Rational Approaches To Select Intervention Priorities. In: Fib Symposium Proceedings.
- Di Stefano, N. (2022). Assessment Of Existing Bridges With Special Emphasis On Corrosion. Phd Thesis, University Of Brescia, Curriculum “Rehabilitation Of Historical And Modern Buildings”.
- DIANA FEA B.V. (2022). DIANA Finite Element Analysis, Release 10.6. Delft, The Netherlands.
- Enfedaque, A., Alberti, M.G., & Gálvez, J.C. (2019). Influence of fiber distribution and orientation in the fracture behavior of polyolefin fiber-reinforced concrete. Materials, 12(2), 220. https://doi.org/10.3390/ma12020220
- Frangopol, D.M., & Liu, M. (2007). Maintenance And Management Of Civil Infrastructure Based On Condition, Safety, Optimization, And Life-Cycle Cost. Structure And Infrastructure Engineering, 3(1), 29–41.
- Higgins, C., Et Al. (2010). Influence Of Corrosion On Cracking And Spalling Of Reinforced Concrete. Aci Materials Journal, 107(2), 179–187.
- Huang, Y., Grünewald, S., Schlangen, E., & Luković, M. (2022). Strengthening Of Concrete Structures With Ultra-High Performance Fiber Reinforced Concrete (Uhpfrc): A Critical Review. Construction And Building Materials, 336, 127398.
- Imperatore, S., Rinaldi, Z., & Coccia, S. (2017). Influence Of Corrosion On The Ductility Of Reinforced Concrete Beams. Engineering Structures, 146, 28–37.
- Iavarone, F., Di Ludovico, M., Prota, A., Et Al. (2024). Shear Bond Between Existing Concrete And High-Strength Fiber-Reinforced Overlay: Influence Of Substrate Strength And Interface Roughness. Structural Concrete, 25, 526–536.
- Lampropoulos, A.P., Tsioulou, O., & Dritsos, S.E. (2016). Strengthening Of Reinforced Concrete Beams Using Uhpfrc Layers Or Jackets. Construction And Building Materials, 106, 103–112.
- Lupoi, A., Belletti, B., Vecchi, F., Et Al. (2022). Experimental Assessment Of Naturally Corroded Reinforced Concrete Bridge Elements. Structural Concrete, 23(4), 2501–2516.
- Mansour, M., Bakhoum, M.M., & El-Salakawy, E. (2017). Effect Of Substrate Surface Roughness On The Flexural Performance Of Concrete Slabs Strengthened With An Sfrc Overlay. Pci Journal, 62(1), 44–61.
- Rogers, R.A., Wotherspoon, L., Scott, A., & Ingham, J.M. (2012). Residual Strength Assessment And Destructive Testing Of Decommissioned Concrete Bridge Beams With Corroded Pretensioned Reinforcement. Pci Journal, 57(3), 100–118.
- Savino, P., Tondolo, F., Sabia, D., Et Al. (2023). Large-Scale Experimental Static Testing On 50-Year-Old Prestressed Concrete Bridge Girders. Applied Sciences, 13(2), 834.
- Täljsten, B. (2006). Strengthening Of Concrete Structures With Frp Composites. Journal Of Composites For Construction (Asce), 10(3), 187–194.
- Walraven, J. (2021). Assessment Of Concrete Structures With Corroded Reinforcement: Development Of Recommendations. In: Proceedings Of The 3rd Cacrcs Workshop – Capacity Assessment Of Corroded Reinforced Concrete Structures, Delft University Of Technology.
- Zhang, R., Castel, A., & François, R. (2009). Concrete Cover Cracking With Reinforcement Corrosion Of Rc Beams. Cement And Concrete Research, 39(5), 371–382.

Tensile Behavior of Fe-SMA Reinforced UHPFRC under Different Activation Methods

XiuJiang Shen[1]; YuLin Li[2]; Tamás Mészöly[1]; Norbert Randl[1]

[1]: Faculty of Civil Engineering and Architecture, Carinthia University of Applied Sciences, Austria

[2]: College of Civil and Environmental Engineering, Changsha University of Science & Technology, China

Abstract

Iron-based shape memory alloy (Fe-SMA) bars can introduce prestress into ultra-high-performance fibre-reinforced concrete (UHPFRC) through thermal activation. This study investigated the influence of different activation methods on the tensile behaviour, elastic-limit stress, effective recovery stress, and crack-control performance of Fe-SMA-bar-reinforced UHPFRC. Three activation methods were considered: steam-curing activation at 95 ± 5 °C, autoclave-curing activation at 175 ± 5 °C, and resistive-heating activation at 400 °C.

Direct tensile tests were conducted on dumbbell-shaped specimens with two reinforcement ratios of 1.96% and 3.93%. The cracking process and maximum crack-width development were monitored using digital image correlation (DIC) system. The results showed that the activation method strongly affected the tensile response of the composite specimens. A higher activation temperature increased the recovery stress generated in the Fe-SMA bars and therefore increased the elastic-limit stress. However, the crack-control performance was not governed only by activation temperature. Autoclave-curing activation provided the best overall crack-control performance because it combined improved UHPFRC properties with effective activation of the Fe-SMA bars. In contrast, resistive heating produced the highest estimated recovery stress, but the local high temperature around the bars may have weakened the bar–UHPFRC interface, resulting in lower crack-control efficiency.

An analytical evaluation considering both the increase in elastic-limit stress and the compensation of shrinkage-induced stress was used to estimate the effective recovery stress. The results indicate that although higher activation temperatures can increase the effective recovery stress, the utilization efficiency decreases with increasing activation temperature and reinforcement ratio. These findings provide guidance for selecting suitable activation methods for Fe-SMA-bar-reinforced UHPFRC elements.

Keywords

UHPFRC; Fe-SMA bar; elastic-limit strength; effective recovery stress; crack-width control

1 Introduction

Iron-based shape memory alloys (Fe-SMAs) have attracted increasing attention as cost-effective alternatives to conventional Ni-Ti-based SMAs for civil engineering applications. Because of their favourable mechanical properties (high yielding & ultimate strength) and shape memory effect, Fe-SMA bars are particularly suitable for strengthening concrete structures, where they can introduce prestress while also functioning as conventional reinforcement, thereby enhancing structural performance.

Numerous studies have shown that Fe-SMA bars can be combined with concrete or UHPFRC to form a composite reinforcement system in which heating activates the shape memory effect and introduces prestress into the structure. Such composite systems have improved flexural, shear, and compressive performance (Yeon et al, 2022; Zhao et al, 2025; Czaderski, 2021; Cui et al, 2025).

A growing body of research has examined Fe-SMA-reinforced concrete structures, using activation methods such as resistive heating, gas-torch or hot-air-gun heating, oven heating, and autoclave heating (Dong et al, 2023; Rojob and El-Hacha, 2017; Schleiting et al, 2023; Choi et al, 2021; Cui et al, 2025). Although these methods can activate the shape memory effect and generate prestress in concrete structures, their influence on the SMA-UHPFRC composite system remains insufficiently understood.

This study aims to investigate the influence of different activation methods on the tensile behaviour of Fe-SMA-bar-reinforced UHPFRC (SMA-UHPFRC). Steam-curing activation, autoclave-curing activation, and resistive-heating activation were compared in terms of tensile response, effective recovery stress, and crack-control performance.

2 Experimental program

The tensile tests were conducted using dumbbell-shaped specimens. Three activation methods were considered: steam-curing activation, autoclave-curing activation, and resistive-heating activation. For each type of test, two reinforcement ratios of 1.96% and 3.93% were adopted, resulting in a total of 6 groups and 18 specimens (3 specimens per group). Additionally, specimens for the tensile and compressive testing of UHPFRC were prepared simultaneously. The specimen designations and test parameters for the tensile tests are presented in Table 1.

The Fe-SMA bars were pre-stretched up to 6% in strain. After pre-straining, the elastic modulus was 142 GPa, and the tensile strength and nominal yield strength were 915 MPa and 777 MPa, respectively. The recovery stresses of the bare Fe-SMA bar at 100°C, 200°C, 300°C, and 400°C reached 176 MPa, 328 MPa, 378 MPa, and 472 MPa, respectively. Each tensile specimen had a total length of 600 mm, with a constant cross-section of 80 mm × 50 mm over 200mm in the middle. At both ends of specimen, 30 mm of the Fe-SMA bar was exposed to allow resistive heating. The specimen dimensions and reinforcement layout are illustrated in Figure 1.

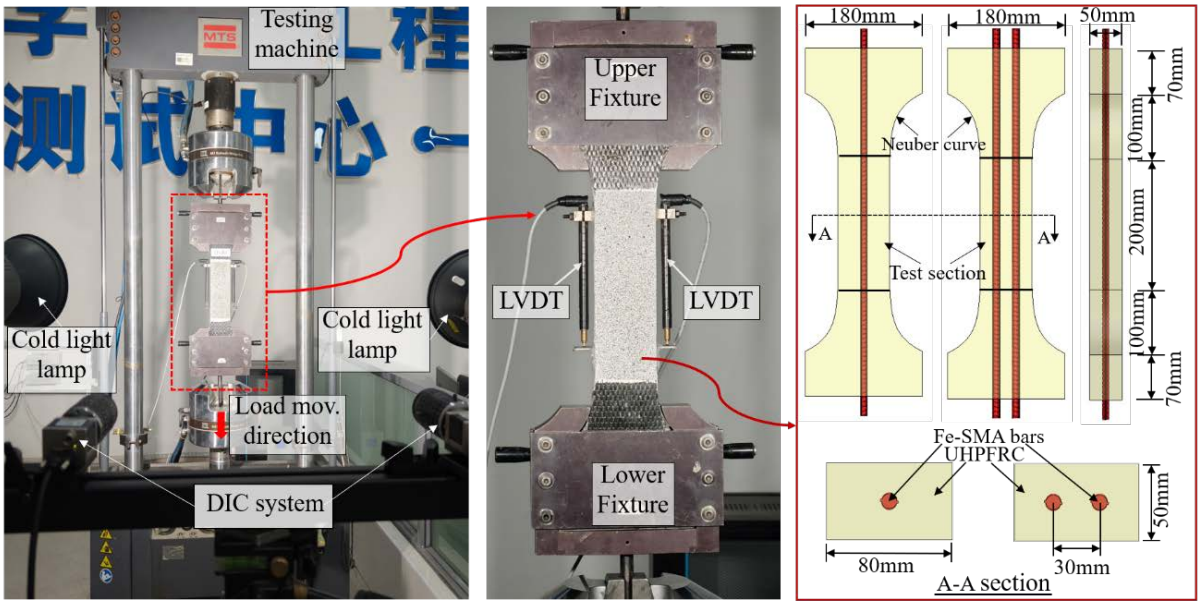


Figure 1: Direct tensile test setup and dumbbell specimen dimensions.

The specimens were fabricated using a commercial UHPFRC premix with a volume fraction of 2% straight steel fibers. The steel fibers had a length of 13 mm and a diameter of 0.2 mm, and the water-cement ratio was 0.19-0.20. The compressive strengths of UHPFRC under natural curing, steam curing, and autoclave curing were measured to be 136.18 MPa, 150.54 MPa, and 188.97 MPa using 100 × 100 × 100 mm cubes, respectively.

After casting the fresh UHPFRC mixture into custom-made molds, the specimens were covered with PVC plates and cured at room temperature with moisture retention for 48 hours before demolding. Five days after demolding, the specimens were subjected to either 48 hours of steam curing (95 ± 5 °C and RH ≥ 95%) or 3 hours of autoclave curing under supersaturated steam conditions (1.8~1.9 MPa and 175 ± 5 °C). The heat treatment during curing also served as the activation process.

For resistive heating, after a total of 28 days of natural curing, the specimens were heated to 400°C using a custom-built high-current generator, with a current density of 6.3 A/mm² applied for 115 seconds. The required current density and heating time were determined using test specimens of the same dimensions, with thermocouples attached to the surface of the Fe-SMA bars.

Prior to the tensile tests, the transition zone of each dumbbell specimen was reinforced by bonding carbon fiber sheets, and the casting surface of specimen was painted white and sprayed with black speckles of approximately 0.5 mm in diameter for DIC measurement.

As shown in Figure 1, the dumbbell specimen was fixed on a universal tensing machine using an anchoring system. Two linear variable differential transformers (LVDTs) were mounted on both narrow sides of specimen to measure the deformation over a gauge length of 180 mm in the constant section zone. Meanwhile, DIC system was employed to record the micro/macro-crack initiation and evolution over the entire 200 mm × 80 mm area on specimen surface during testing. The tensile loading protocol consisted of an initial force-controlled stage

at a rate of 1.0 kN/min up to 5.0 kN, followed by a displacement-controlled stage at a rate of 0.5 mm/min until complete separation of UHPFRC or rupture of rebar.

Table 1: Test parameters and number of specimens.

No.	**Activation method**	***T* (°C)**	***ρ* (%)**	***Ns***
T-U_N	Natural curing	-	0	0
T-RU_R-1.96	Resistive heating activation	400	1.96	1
T-RU_R-3.93	Resistive heating activation	400	3.93	2
T-U_S	Steam curing	-	0	0
T-RU_S-1.96	Steam curing activation	100	1.96	1
T-RU_S-3.93	Steam curing activation	100	3.93	2
T-U_H	Autoclave curing	-	0	0
T-RU_H-1.96	Autoclave curing activation	180	1.96	1
T-RU_H-3.93	Autoclave curing activation	180	3.93	2

3 Test Results

The representative fracture characteristics of each group at failure point is shown individually in Figure 2, where the fine black lines refer to the microcracks and the thick lines represent macrocracks. The average tensile stress-strain curves for all groups are summarized in Figure 3.

As shown in Figure 2, the unreinforced specimens generally exhibited single localized macrocracking followed by final separation. The curing condition influenced the cracking pattern and tensile response of the UHPFRC. Compared with natural curing and steam curing, autoclave curing resulted in a more pronounced improvement in the multiple microcracking. This is consistent with the compressive strength results, where the compressive strength increased from 136.18 MPa under natural curing to 150.54 MPa under steam curing and 188.97 MPa under autoclave curing. The average tensile stress–strain curves in Figure 3 further indicate that the autoclave-cured UHPFRC specimen showed the highest elastic-limit stress σ_A (initiation of microcrack) among the unreinforced specimens.

In comparison with the unreinforced specimens, the reinforced specimens developed a more distributed cracking pattern with uniformly distributed microcracks and multiple-macrocrack phenomena (Figure 2). This could be attributed to the composite effect of longitudinal reinforcement and recovery stress from Fe-SMA rebars.

As shown in Figure 3, the tensile stress–strain response of the reinforced specimens was affected by both activation method and reinforcement ratio. For the same reinforcement ratio, the autoclave-curing activation group generally showed a favourable overall tensile response, which can be attributed to the combined effect of improved UHPFRC properties and recovery stress generated in the Fe-SMA bars. The resistive-heating group showed a high elastic-limit stress σ_A because of the higher activation temperature and corresponding higher recovery stress.

However, its post-cracking crack-control performance was not always superior, indicating that the efficiency of prestress transfer was affected by the local heating process.

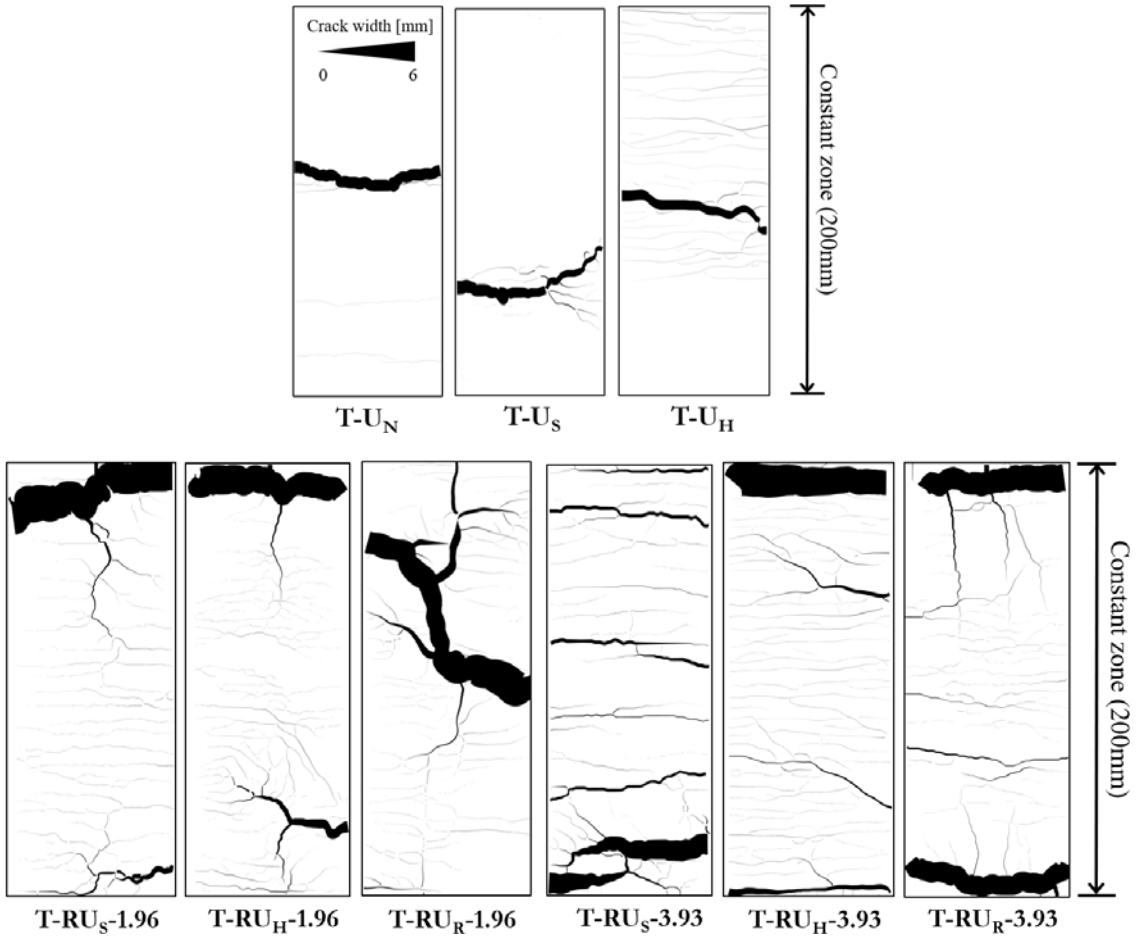


Figure 2:Representaive failure modes at failure point.

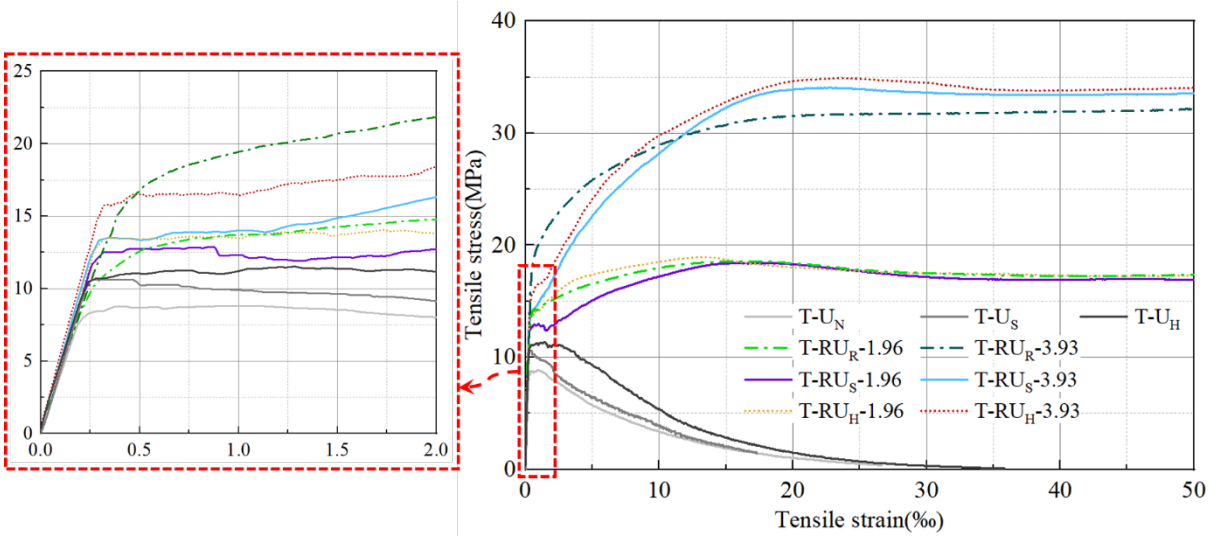
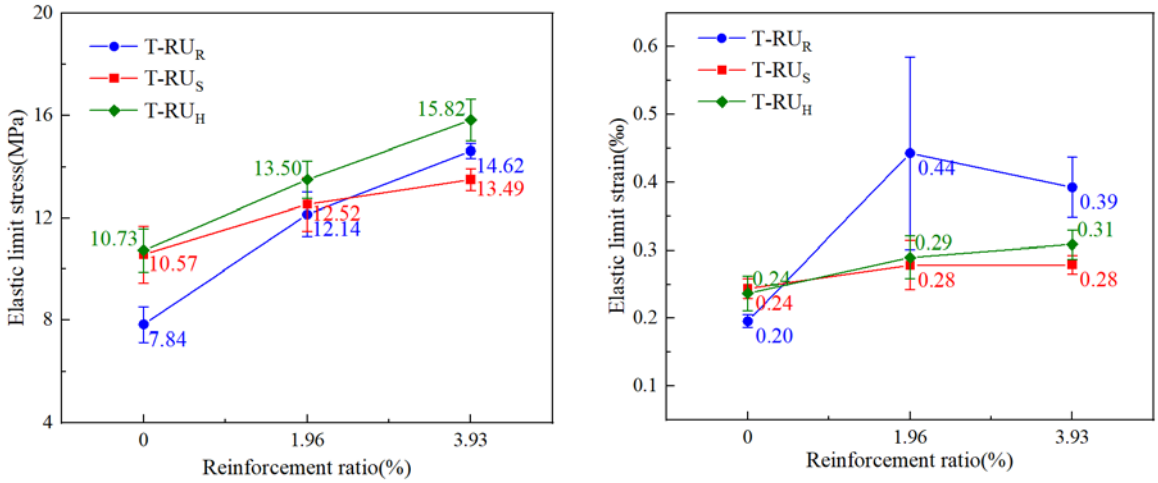


Figure 3: Comparison of average stress-strain curves for different activation methods.

Figure 4 compares the elastic-limit stress σ_A and elastic-limit strain ε_A of specimens subjected to different activation methods. The elastic-limit stress increased with increasing activation temperature and reinforcement ratio. For reinforcement ratios of 1.96% and 3.93%, respectively, σ_A increased by 18.5% and 27.7% for the steam-curing activation group, by 25.8% and 47.5% for the autoclave-curing activation group, and by 54.9% and 86.5% for the resistive-heating activation group. These results indicate that a higher activation temperature can generate larger recovery stress in the Fe-SMA bars, thereby increasing the elastic-limit stress of the composite specimen.



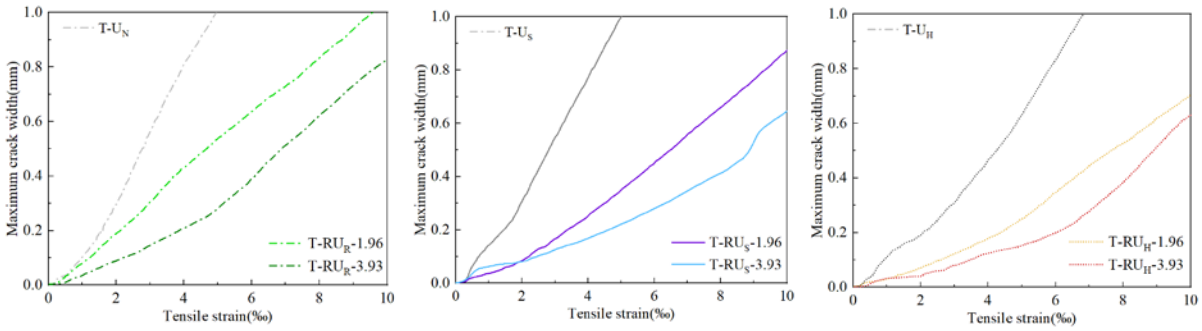
(a) (b)

Figure 4: Influence of activation method on (a) elastic-limit stress and (b) elastic-limit strain.

Figure 5 compares the influence of reinforcement ratio on the maximum crack-width development under different activation methods. The maximum crack width was obtained from the DIC results by identifying the largest crack opening within the monitored region at each tensile strain level. It is clear that, at the same strain level, reinforcement significantly reduced the maximum crack width compared with unreinforced UHPFRC, and the crack width decreased continuously as the reinforcement ratio increased.

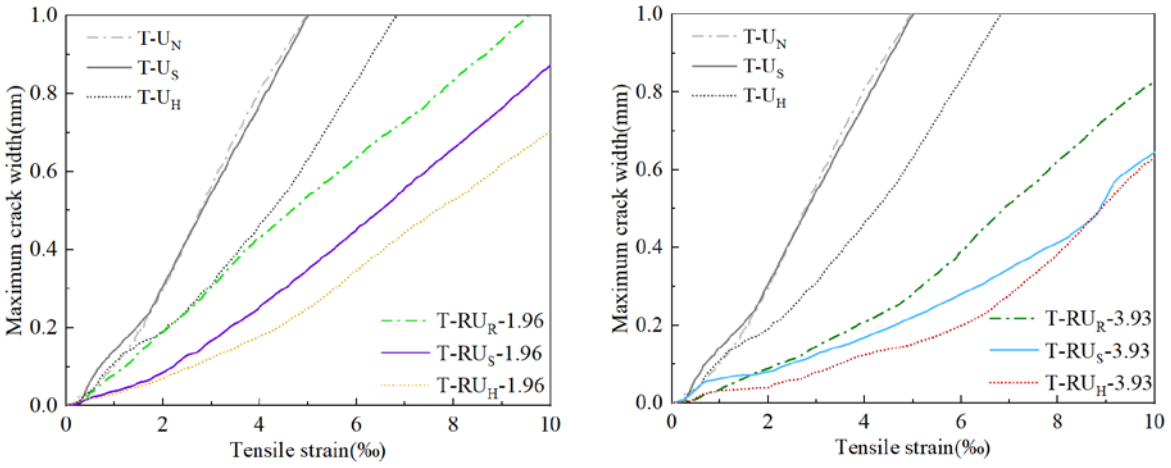
Figure 6 compares the influence of activation method at the same reinforcement ratio. For both reinforcement ratios, the autoclave-curing activation group exhibited the best overall crack-control performance. This behaviour can be explained by two combined effects: first, autoclave curing improved the mechanical properties of the UHPFRC; second, the activation temperature was sufficient to generate effective recovery stress in the Fe-SMA bars without causing severe local damage at the bar–UHPFRC interface.

In contrast, although resistive heating produced the highest expected recovery stress because of the 400 °C activation temperature, the local heating may have induced temperature gradients and strain incompatibility between the Fe-SMA bars and the surrounding UHPFRC. This may have weakened the bar–UHPFRC interface and reduced the efficiency of stress transfer after the elastic limit.



(a) (b) (c)

Figure 5: Effect of reinforcement ratio on crack width under (a) resistive heating, (b) steam curing, and (c) autoclave curing.



(a) (b)

Figure 6: Effect of activation method on crack width at reinforcement ratios of (a) 1.96% and (b) 3.93%.

4 Effective recovery stress analysis

By comparing the increase in elastic-limit stress between unreinforced UHPFRC and Fe-SMA-bar-reinforced UHPFRC, the effective recovery stress provided by the Fe-SMA bars through the shape memory effect can be estimated. Based on force equilibrium, the effective recovery stress can be expressed by Equation (1):

$$\sigma_{re} = \frac{F_{re}}{A_s} = \frac{F_{RU,A} - F_{U,A}}{A_s} = \frac{\sigma_{RU,A}(A_U + A_s) - \sigma_{U,A}A_U}{A_s} \quad (1)$$

where $F_{RU,A}$ and $\sigma_{RU,A}$ are the elastic-limit force and elastic-limit stress of the Fe-SMA-bar-reinforced UHPFRC, respectively; $F_{U,A}$ and $\sigma_{U,A}$ are the elastic-limit force and elastic-limit stress of the UHPFRC, respectively; A_U is the cross-sectional area of the UHPFRC excluding the Fe-SMA bars; and A_s is the cross-sectional area of the Fe-SMA bars.

Previous studies on the tensile behavior of ordinary steel rebar reinforced concrete or UHPFRC have shown that: due to the shrinkage effect of concrete, the addition of rebar restricts the free shrinkage process of the concrete, thereby inducing initial tensile stress in the reinforced

concrete member and reducing the tensile elastic limit strength. Since the shrinkage strain of UHPFRC is larger than that of ordinary concrete, this phenomenon becomes more pronounced. The same issue exists in Fe-SMA bar reinforced UHPFRC before activation. Consequently, part of the actual effective recovery stress is consumed to compensate for the reduction in elastic limit strength caused by shrinkage.

Previous research (Yoo et al, 2018) reported that hygrothermal curing methods such as steam curing accelerate the shrinkage process of UHPFRC but do not alter the total shrinkage strain compared with natural curing. They also proposed that the free shrinkage strain of UHPFRC can be calculated using the following equations:

$$\varepsilon_{sh}(t) = \varepsilon_{sh,\infty}\beta(t) \tag{2}$$

$$\varepsilon_{sh,\infty} = -2300\, exp[-7.2(w/b)] \tag{3}$$

$$\beta(t) = 1 - exp\left(-0.65\sqrt{t}\right) \tag{4}$$

where t is the age of the UHPFRC, $\varepsilon_{sh,\infty}$ is the total free shrinkage strain, and w/b is the water to cement ratio. The calculated total shrinkage strain of the UHPFRC was $545\ \mu\varepsilon$, and the free shrinkage strain at the age of 90 days was calculated to be $544\ \mu\varepsilon$.

The initial compressive strain in the reinforcement ($\Delta\varepsilon_{s,sh}$) and the initial tensile strain in the UHPFRC ($\Delta\varepsilon_{U,sh}$) induced by shrinkage can be calculated using the following equations:

$$\Delta\varepsilon_{s,sh} = \frac{1}{1+n\cdot\rho'}\cdot\varepsilon_{sh} \tag{5}$$

$$\Delta\varepsilon_{U,sh} = \frac{n\cdot\rho'}{1+n\cdot\rho'}\cdot\varepsilon_{sh} \tag{6}$$

where n is the ratio of the elastic modulus of the reinforcing bar to that of the UHPFRC, $n = E_s/E_U$; ρ' is the net-section reinforcement ratio, $\rho' = A_s/A_U$; and ε_{sh} is the free shrinkage strain of the UHPFRC.

The recovery stress required to compensate for the compressive strain in the Fe-SMA bars ($\sigma_{re,sh}$) is calculated using the following equation:

$$\sigma_{re,sh} = \Delta\varepsilon_{s,sh}E_s = \frac{1}{1+n\cdot\rho'}\varepsilon_{sh}E_s \tag{7}$$

Table 2 : Effective recovery stress calculated considering shrinkage effect.

No.	$\Delta\varepsilon_{s,sh}$ **(**$\mu\varepsilon$**)**	$\sigma_{re,el}$ **(MPa)**	$\sigma_{re,sh}$ **(MPa)**	$\sigma_{re,eff}$ **(MPa)**	$\sigma_{re,eff}/\sigma_{re,the}$
T-RU$_S$-1.96	511	110.30	72.73	183.0	1.04
T-RU$_S$-3.93	481	85.09	68.36	153.4	0.87
T-RU$_H$-1.96	513	151.76	72.94	224.7	0.76
T-RU$_H$-3.93	483	140.50	68.74	209.2	0.70
T-RU$_R$-1.96	508	227.02	72.19	299.2	0.63
T-RU$_R$-3.93	475	180.46	67.53	248.0	0.53

Therefore, the total effective recovery stress consists of two components: the contribution to increasing the elastic-limit stress and the contribution to compensating for the initial tensile stress caused by shrinkage. The effective recovery stress is $\sigma_{re,eff} = \sigma_{re,el} + \sigma_{re,sh}$. The calculation results are presented in Table 2.

With increasing activation temperature and reinforcement ratio, the effective recovery stress increased, but the ratio of effective recovery stress to theoretical recovery stress decreased, indicating the utilization efficiency of the recovery stress decreased.

5 Concluding remarks

Tensile tests were conducted on Fe-SMA-bar-reinforced UHPFRC specimens to investigate the influence of activation method on tensile response, elastic-limit stress, effective recovery stress, and crack-width control. Three activation methods were considered: steam-curing activation, autoclave-curing activation, and resistive-heating activation. Based on the experimental results and analytical evaluation, the following conclusions can be drawn:

- The curing condition affected the mechanical performance of UHPFRC. Autoclave curing produced the highest compressive strength and the highest elastic-limit stress of the unreinforced UHPFRC specimens.
- Higher activation temperature increased the recovery stress generated in the Fe-SMA bars and therefore increased elastic-limit stress of the reinforced UHPFRC specimens. The increase in elastic-limit stress reached 18.5%–27.7% for steam-curing activation, 25.8%–47.5% for autoclave-curing activation, and 54.9%–86.5% for resistive-heating activation.
- Autoclave-curing activation provided the best overall crack-control performance because it combined improved UHPFRC properties with effective activation of the Fe-SMA bars. In contrast, resistive heating generated the highest recovery stress but showed lower crack-control efficiency, probably due to local bond deterioration and strain incompatibility caused by the high activation temperature.
- The effective recovery stress increased with activation temperature but its utilization efficiency decreased with increasing activation temperature and reinforcement ratio. This indicates that a higher theoretical recovery stress is not necessarily fully transferred to the UHPFRC member.

6 Acknowledgements

The authors gratefully acknowledge funding provided by the Austrian Research Promotion Agency (FFG) within the framework of the SCORE project (No. FO999920335).

7 References

Yeon, Y.-M., Hong, K.-N., and Ji, S.-W., 2022. “Flexural Behavior of Self-Prestressed RC Slabs with Fe-Based Shape Memory Alloy Rebar”, *Applied Sciences*, 12(3), pp1640 doi: 10.3390/app12031640.

Zhao, Y., Zhao, X.-L., Dong, Z., Cui, C., Zhao, Z., and Shi, C., 2025. “Flexural behavior of thin-walled UHPC plates reinforced with self-prestressed Fe-SMA rebars”, *Thin-Walled Structures*, 216, pp113704 doi: 10.1016/j.tws.2025.113704.

Czaderski, C., 2021. “Iron based shape memory alloys as shear reinforcement for bridge girders”, *Construction and Building Materials*, 274, pp121793 doi: 10.1016/j.conbuildmat.2020.121793.

Cui, C., Dong, Z., Zhu, H., Zhao, Y., Han, T., Pan, Y., and Ghafoori, E., 2025. “Axial compressive behavior of UHPC columns reinforced with self-prestressed Fe-SMA spiral stirrups”, *Structures*, 77, pp109107 doi: 10.1016/j.istruc.2025.109107.

Dong, Z., Liu, Z., Ji, J., Zhu, H., Wu, G., and Sun, C., 2023. “Characterization of self-prestressing iron-based shape memory alloy bars for new structures”, *Construction and Building Materials*, 371, pp130795 doi: 10.1016/j.conbuildmat.2023.130795.

Rojob, H. and El-Hacha, R., 2017. “Self-Prestressing Using Fe-SMA for Flexural Strengthening of Reinforced Concrete Beams”, *ACI Structural Journal*, 14(2), pp523–532 doi: 10.14359/51689455.

Schleiting, M., Wetzel, A., Bauer, A., Frenck, J.-M., Niendorf, T., and Middendorf, B., 2023. “Potential of Fe-Mn-Al-Ni Shape Memory Alloys for Internal Prestressing of Ultra-High Performance Concrete”, *Materials*, 16(10), pp3816 doi: 10.3390/ma16103816.

Choi, E., Ostadrahimi, A., Kim, W.J., and Seo, J., 2021. “Prestressing effect of embedded Fe-based SMA wire on the flexural behavior of mortar beams”, *Engineering Structures*, 227, pp111472 doi: 10.1016/j.engstruct.2020.111472.

Yoo, D.-Y., Kim, S., and Kim, M.-J., 2018. “Comparative shrinkage behavior of ultra-high-performance fiber-reinforced concrete under ambient and heat curing conditions”, *Construction and Building Materials*, 162, pp406–419 doi: 10.1016/j.conbuildmat.2017.12.029.

Izadi, M.R., Ghafoori, E., Shahverdi, M., Motavalli, M., and Maalek, S., 2018. “Development of an iron-based shape memory alloy (Fe-SMA) strengthening system for steel plates”, *Engineering Structures*, 174, pp433–446 doi: 10.1016/j.engstruct.2018.07.073.

Extended abstracts

Rethinking Wearing Surfaces (WS) for Orthotropic Steel Deck Bridges – SFRC WS for Extending the Bridge Service Life

Vellore S. Gopalaratnam[1]

[1]: Professor Emeritus, University of Missouri-Columbia, Columbia, Missouri 65203, USA.

1 Introduction

Traditionally, wearing surfaces (WS) on orthotropic steel deck (OSD) bridges serve several essential functions, including providing skid resistance, improving ride quality, protecting the deck plate from corrosion, and smoothing deck and weld irregularities. OSD bridges were economical for long-span applications in the 1960s, and many constructed during that period in the US and globally are now reaching the end of their service lives, requiring replacement or retrofits. In this context, this presentation reexamines the role of wearing surface systems as integral composite structural components rather than mere protective layers. When designed with this structural function in mind, steel fiber reinforced concrete (SFRC) WS, it is demonstrated, can reduce post-retrofit fatigue stresses in the deck plate for the range of service temperatures, thereby significantly extending the remaining fatigue life of these aging bridges.

2 Wearing Surfaces Investigated – Materials and Types

The prevailing knowledge base for WS design in the 1960s, when OSD bridges were widely constructed, emphasized minimizing WS thickness to reduce dead loads on the bridge. In the ensuing decades, traffic volumes increased substantially, and tire contact pressures rose to accommodate significantly heavier truck loads. These evolving functional demands placed unrealistic stresses on the WS, often resulting in premature failures characterized by tensile cracking over stiffening ribs and delamination at the steel–WS interface due to elevated interfacial shear stresses.

Through investigations of WS of varying thickness (10 mm to 100 mm) and material types - including polymer concrete, polyurethane, epoxy asphalt, polyester concrete, and lightweight SFRC - across several OSD bridges between 1988 and 2015, the University of Missouri team developed a comprehensive understanding of WS performance under service temperatures ranging from −10°C to 50°C. These bridges included the Poplar Street Bridge (St. Louis, Missouri), the Bronx–Whitestone Bridge (Bronx, New York), and the San Mateo–Hayward Bridge (Bay Area, California).

The combined insights from field performance monitoring, instrumentation data, temperature-varying laboratory flexural fatigue tests, and companion analytical studies have been documented in multiple publications (Gopalaratnam et al., 1994, 2012, 2013a–c). Based on these investigations, the author was invited to serve as the primary author of the Wearing Surfaces chapter of the authoritative Federal Highway Administration manual, Design, Construction, and Maintenance of Orthotropic Steel Deck Bridges (Gopalaratnam, 2012).

The presentation at the joint ACI–fib–RILEM International Workshop, FRC 2026, will summarize the key findings from these research efforts, with particular emphasis on the most recent recommendation: the use of a 100 mm thick lightweight SFRC wearing surface system (40 MPa, 1,750 kg/m³ design mix incorporating expanded shale aggregates, and 1.5% volume fraction of 38 mm long crimped steel fibers of aspect ratio 40) to extend the post-retrofit service life of the Poplar Street Bridge deck by an estimated 30–40 years. Lightweight (expanded shale aggregates) SFRC has been shown to enhance the composite deck plate stiffness for the entire

range of service temperatures, thus greatly reducing the fatigue stress levels in the steel deck plate. This is unlike Epoxy Asphalt and Polymer Concrete wearing surfaces which exhibit elastic modulus that vary with temperature (Fig.1). Fig. 2 highlights the effect of thin and thick wearing surfaces on reductions in the steel stress with varying modular ratios ($n=E_{ws}/E_s$). The 100 mm thick lightweight SFRC wearing surface recommended was placed on the 660 m long, continuous five-span, nine-lane Mississippi River crossing in 2013. The wearing surface has since provided excellent performance with minimal maintenance. The presentation will also address materials design, laboratory material and structural testing, and the practical challenges encountered during field placement of SFRC.

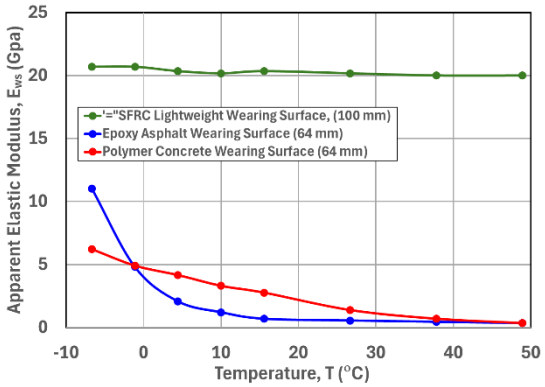


Fig. 1 Back-calculated wearing surface modulus ("apparent" modulus) from composite steel-WS flexural tests.

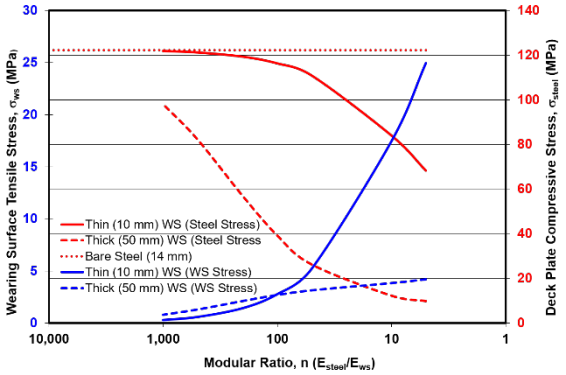


Fig. 2 Reduction in stress in the steel deck plate when thin and thick wearing surfaces are used. The stresses are plotted versus the modular ratio

3 Concluding remarks

The lightweight SFRC wearing surface system designed for the Poplar Street Bridge and placed in 2013 has provided excellent composite action, reducing stress in the 14 mm steel-deck plate to enhance the post-retrofit service life of the bridge by an estimated 30-40 years. The temperature independent elastic modulus of the lightweight SFRC allows for reliable composite action in the entire rage of service temperatures.

4 References

Gopalaratnam, V.S., Baldwin, J.W., Hartnagel, B.A., and Rigdon, R.A., "Evaluation of Wearing Surface Systems for Orthotropic Steel-Plate-Bridge Decks," Report 89-2, Missouri Highway and Transportation Department, January 1994, 64 pp.

Gopalaratnam, V. S., "Wearing Surfaces"' Primary Author for Chapter 9 of the FHWA Manual for the Design, Construction and Maintenance of Orthotropic Steel Deck Bridges, Publication No. FHWA-IF-12-027, 2012, pp. 166-189.

Gopalaratnam, V. S., Chamarthi, R. and Maggenti R., "Wearing Surface Performance on Orthotropic Steel Deck -- Implications of Composite Action", Proceedings of the 3rd Orthotropic Bridge Conference, Sacramento, CA, June 2013a, 8 pp.

Gopalaratnam, V. S. and Chamarthi, R. "Challenges in Designing Wearing Surfaces for Orthotropic Bridge Decks", Proceedings of the 3rd Orthotropic Bridge Conference, Sacramento, CA, June 2013b, 8 pp.

Gopalaratnam, V.S., "Lightweight SFRC Wearing Surface Recommendations for the Poplar Street Bridge Widening Project", Research Report, HDR, Inc., 2013c, 10 pp.

Hybrid Steel Fibre Reinforced Concrete based on calcium sulfoaluminate binder for precast tunnel segment production

Giulia Brentana[1], Ivan Trabucchi[1], Stefano Guanziroli[2], Giuseppe Tiberti[1] and Giovanni A. Plizzari[1]

[1]: Università di Brescia, DICATAM, via Branze 43, Brescia, 25123, Italy

[2]: Hinfra, Casale Monferrato, Italy.

1 Introduction

Nowadays many Governments promote the development of new transport networks to improve people and goods exchanges in a more sustainable way. The main projects currently ongoing are the Trans-European Transport Network (TEN-T), the Belt and Road Initiative (BRI) and India-Middle East-Europe Economic Corridor (IMEC). The success of these projects also depends on the construction of new tunnels, which increasingly involve the use of mechanized tunnelling techniques and, consequently, the adoption of precast elements. Then, research in the field of new solutions for precast segments remains highly relevant. Generally, these elements are made of reinforced concrete, although Fibre Reinforced Concrete (FRC) is becoming increasingly popular. This work intends to continue along this path with the aim of evaluating, by means of an experimental program, the use of a special FRC developed and patented by the company HINFRA together with its partner BUZZI, based on the adoption of a binder with sulfoaluminate cement and a hybrid fibre system (45 + 15 kg/m^3 of macro and micro steel fibres, selected from a preliminary mechanical characterization phase). The use of this material introduces a major novelty relative to conventional segments manufacturing. In fact, due to its fast setting and hardening characteristics a dual optimization can be achieved: simplifying and accelerating the production process, and enabling short-term assembly and loading of the segments.

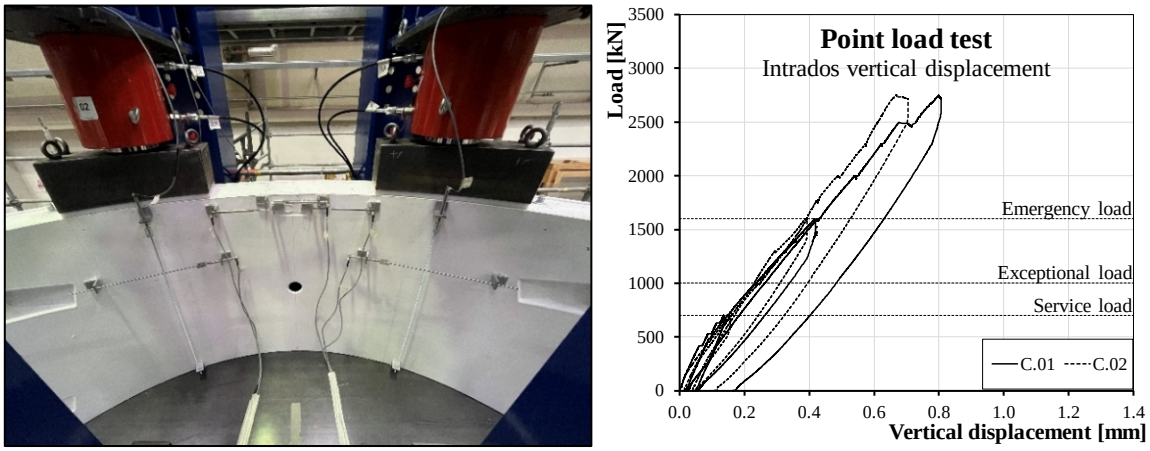
2 Experimental program

The experimental program involves the production of two full-scale tunnel segments using steel molds from a real case study, the Scilla Tunnel, to evaluate the feasibility of using a concrete characterized by rapid setting and hardening. In addition, samples for the material mechanical characterization were prepared alongside each segment. The Scilla Tunnel has an internal diameter of 3.50 m and a thickness of 0.20 m. The tests were performed on trapezoidal segments. A reaction frame available at the “Pietro Pisa” Laboratory of the University of Brescia was used to simulate the loads applied by the boring machine. The equipment consists of a concrete beam and two steel frames. Figure 1a shows the sample in the frame, evidencing how it was fully supported by the beam and loaded by two plates. The test was carried out under load-control, following a loading protocol consisting of three cycles. For each loading shoe, after reaching 700 kN, 1600 kN and 2750 kN, the segment was subsequently unloaded. To monitor the test, several transducers were applied on intrados (Figure 1a) and extrados sides.

Sensors were placed vertically under the loading shoes, in between the loading point (spalling zone) and transducers were applied horizontally 0.30 m under the loading area (splitting zone).

3 Test Results

According to preliminary evaluations the minimum compressive strength to safely un-mold the segment must be higher than 20 MPa. The batches produced to cast two segments (ID: C.01 and C.02, respectively) reached, after six hours from casting, a concrete compressive strength of 22.3 and 23.9 MPa. The full-scale tests on segments started after 48 hours of curing, when the compressive strength for both was around 55 MPa. However, it is worth noting that the "demolding time" and "experimental time" can be further reduced by adjusting the amount of retarder used in the mix design. The first crack was detected in between the loading point at 1600 kN (C.01) and 1750 kN (C.02). The crack propagates along the segment depth until a second type appears under the loading shoes: the splitting crack; the latter was observed at 2500 kN and 2750 kN for C.01 and C.02, respectively. The maximum crack opening was measured by a digital microscope and was 0.35 mm for C.01 and 0.15 mm for C.02. Figure 1b shows load vs. vertical displacement curves measured on the two segments at the intrados side. Table 1 reports the main mechanical properties measured at 28 days.



(a) (b)

Figure 1: (a) Intrados view of the segment with transducers; (b) load-vertical displacement curves.

Table 1: Main mechanical properties determined according to EN 12390-3 and EN 14651.

	$f_{cm,cube}$ [MPa]	f_{Lm} [MPa]	f_{R1m} [MPa]	f_{R2m} [MPa]	f_{R3m} [MPa]	f_{R4m} [MPa]
C.01	65.8	6.31	10.96	10.78	9.96	8.27
C.02	77.2	7.19	13.33	13.01	11.65	10.99

4 Concluding remarks

Experimental results showed that the use of calcium sulfoaluminate binder in concrete production enables fast demolding (<6 h) without the need for accelerated curing. In addition, the development of compressive strength and the toughness provided by the hybrid fibre system allows the segment to withstand TBM loads just 48 hours after casting, with an effective control of cracking induced by load diffusion up to high contact pressure. While these promising findings were obtained from two full-scale elements, further validation is desirable.

Reinforcing 3D-Printed Concrete with Sprayed SHCC Overlay: A Post-Printing Reinforcement Method

Min Zhou[1], Maurizio Guadagnini[1], Behzad Nematollahi[1*]

[1]: School of Mechanical, Aerospace and Civil Engineering, University of Sheffield, UK.

1 Introduction

Three-dimensional printed concrete (3DPC) reduces construction time and cost but suffers from anisotropy and weak interlayer interfaces, leading to brittle failure without reinforcement (Mechtcherine et al., 2020). Although various reinforcement strategies have been investigated, most existing reinforcement strategies interrupt the automated printing workflow or constrain geometrical freedom (Lloret-Fritschi et al., 2020). Sprayed strain-hardening cementitious composite (SHCC) overlays have been used to improve shear resistance, crack control, and seismic energy dissipation capacity in conventional reinforced concrete and masonry structures (He et al., 2023; van Zijl & de Beer, 2019). This study proposes using sprayed SHCC as a 'post-printing' reinforcement method for 3DPC subjected to out-of-plane bending. This method does not interrupt the printing process or limit geometrical freedom. The thickness of the 3DPC substrate was held constant, while the thickness of the sprayed SHCC overlay was varied to 10, 20, and 30 mm as a design parameter.

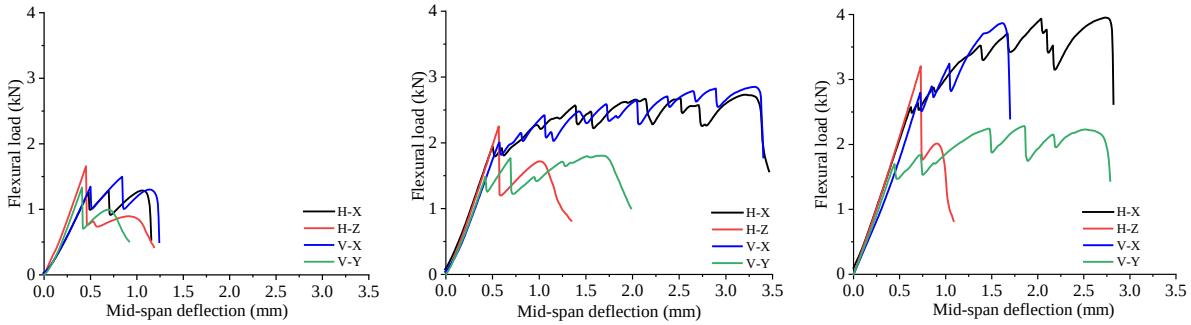
2 Experimental

The binder of 3DPC mixture comprised cement, fly ash, and silica fume (0.7:0.2:0.1 wt.% of binder), equal proportions of finer and coarser silica sands (0.75 wt.% each), a water-to-binder ratio of 0.34, superplasticizer (0.75 wt.%), consistency retention admixture (0.3 wt.%), and nano-clay (0.65 wt.%). The sprayed SHCC binder comprised cement, fly ash, and silica fume (0.43:0.5:0.07 wt.% of binder), finer sand only (0.35 wt.%), water-to-binder ratio of 0.26, and superplasticizer (1 wt.%). Polypropylene fibers (0.1 vol.%) were added to the 3DPC mixture, while polyvinyl alcohol fibers (2 vol.%) were used in the sprayed SHCC mixture. Printed wall panels (370 mm x 400 mm x 30 mm) were water-cured for 28 days, after which substrate surfaces were conditioned to saturated surface-dry conditions before spraying. Two cutting orientations (H: parallel; V: perpendicular to printing direction) and three testing directions (X, Y, Z) were adopted to account for 3DPC anisotropy. Four-point bending tests were conducted at 0.5 mm/min on specimens T10, T20, and T30, corresponding to overlay thicknesses of 10, 20, and 30 mm.

3 Test Results

Figure 1 presents flexural load-deflection curves of plain and reinforced 3DPC. Plain 3DPC specimens exhibited brittle failure with peak flexural loads and corresponding deflections ranging from 0.3–1.7 kN and 0.3–0.6 mm, respectively. T10 specimens in H-X and V-X directions only exhibited deflection-hardening behaviour. The P_{MOR} and deflection ranged from 1.2–1.7 kN and 0.4–1.1 mm. T20 and T30 specimens demonstrated superior performance, with H-X, V-X, and V-Y directions exhibiting deflection-hardening behaviour, while the H-Z direction showed deflection-softening. As overlay thickness increased from 10 to 30 mm, the

overlay progressively became the dominant load-bearing component, with flexural performance exhibiting a non-linear growth relationship with overlay thickness.



(a) Reinforced 3DPC-T10 (b) Reinforced 3DPC-T20 (c) Reinforced 3DPC-T30

Figure 1: Flexural load-deflection curves of 3DPC specimens reinforced with different sprayed SHCC overlay thicknesses.

4 Concluding remarks

Sprayed SHCC overlays effectively reinforced 3DPC under out-of-plane bending without interrupting printing. Increasing overlay thickness from 10 to 30 mm shifted the load-bearing role to the overlay, transforming brittle failure into deflection-hardening behavior, with flexural capacity increasing non-linearly with thickness.

5 Acknowledgements

The authors gratefully acknowledge the Engineering and Physical Sciences Research Council (EPSRC), the University of Sheffield, and COBOD International for funding this research through the EPSRC DTP CASE Conversion scheme (EP/W524360/1).

6 References

He, S., Mustafa, S., Chang, Z., Liang, M., Schlangen, E., & Luković, M. (2023). Ultra-thin Strain Hardening Cementitious Composite (SHCC) layer in reinforced concrete cover zone for crack width control. Engineering Structures, 292, 116584. doi: https://doi.org/10.1016/j.engstruct.2023.116584

Lloret-Fritschi, E., Wangler, T., Gebhard, L., Mata-Falcón, J., Mantellato, S., Scotto, F., Flatt, R. (2020). From Smart Dynamic Casting to a growing family of Digital Casting Systems. Cement and Concrete Research, 134, 106071. doi: https://doi.org/10.1016/j.cemconres.2020.106071

Mechtcherine, V., Bos, F. P., Perrot, A., da Silva, W. R. L., Nerella, V. N., Fataei, S., . . . Roussel, N. (2020). Extrusion-based additive manufacturing with cement-based materials – Production steps, processes, and their underlying physics: A review. Cement and Concrete Research, 132, 106037. doi: https://doi.org/10.1016/j.cemconres.2020.106037

van Zijl, G. P., & de Beer, L. (2019). Sprayed strain-hardening cement-based composite overlay for shear strengthening of unreinforced load-bearing masonry. Advances in Structural Engineering, 22(5), 1121-1135. doi: https://doi.org/10.1177/136943321880768

Energy-based evaluation of ductility and toughness in fibre-reinforced self-compacting natural hydraulic lime concrete

Ángel De La Rosa [1]

Gonzalo Ruiz [2]

Jesús Rodríguez [1]

[1]: DIMME, Grupo de Durabilidad e Integridad Mecánica de Materiales Estructurales, Universidad Rey Juan Carlos, C. Tulipán s/n, 28933 Móstoles, Madrid, Spain,

[2]: ETSI Caminos, C. y P., Universidad de Castilla-La Mancha, Av. Camilo José Cela 2, 13071 Ciudad Real, Spain

1 Introduction

This study investigates the mechanical and fracture behavior of sustainable lime-based concrete reinforced with fibers, with particular emphasis on an energy-based characterization of its post-cracking response. The research is motivated by the need for low-carbon construction materials capable of ensuring adequate structural performance. In this context, lime-based binders emerge as a viable alternative to Portland cement, especially when combined with fiber reinforcement to enhance ductility and crack resistance [1,2]. The main objective is to evaluate the influence of fibers on ductility, toughness, and load-bearing capacity under compression and bending.

2 Experimental or modelling program

Different mixtures (w/ℓ = 0.4 and 0.3) with steel (SF-1,2: 23.6-11.8 kg/m³) and polyvinyl alcohol fibers (PVA-1,2: 3.9-2.0 kg/m³), corresponding to volume fractions of 0.0015–0.003, were tested in flexure to determine residual strengths and work of fracture. Steel fiber concretes showed slightly higher post-cracking capacity ($f_{R1} = 0.9$ MPa; $f_{R3} = 0.5$–0.4 MPa) than PVA mixes ($f_{R1} = 0.8$–0.7 MPa; $f_{R3} = 0.7$–0.3 MPa). The work of fracture at $15.5\delta_m$ (δ_m is the peak-load displacement) was similar for SF-1 (2.864 N·m), SF-2 (2.695 N·m), and PVA-1 (2.807 N·m), but lower for PVA-2 (2.129 N·m), indicating reduced toughness at the lowest fiber content.

3 Test Results

The compressive response (Fig. 1(a), (b)) shows that both steel and PVA fibers have limited influence on peak strength but improve post-peak stability by reducing abrupt load loss, with steel fibers providing slightly greater stabilization and PVA fibers promoting a more uniform stress distribution. Under flexural loading (Fig. 1(c), (d)), fiber reinforcement markedly enhances the response, promoting a transition from brittle to quasi-ductile behavior with smoother post-peak softening; steel fibers increase residual capacity at large crack openings, while PVA fibers favor more distributed cracking at early stages. In all cases, fibers delay crack propagation and increase energy dissipation, improving overall toughness.

Figure 1: Mechanical response of the studied mixtures: (a), (b) compressive behavior; (c), (d) flexural behavior (results corresponding to the highest fiber dosage, SF-1 and PVA-1).

4 Concluding remarks

Fiber reinforcement enhances fracture performance and energy absorption, leading to more ductile behavior and improved crack control in lime-based concrete, while supporting the development of sustainable, low-carbon composites with better structural performance.

5 Acknowledgements

Funded by MCIU (PID2023-147971OB-C31), JCCM (SBPLY/24/180225/000003), and UCLM–ERDF (2025-GRIN-38445); materials supplied by Cal El Tigre, Master Builders Solutions, Omya Clariana, and Bekaert.

6 References

[1] Almeida, J.A.P.P., Barros, J.A.O., and Pereira, E.N.B. (2024) *Toughness of natural hydraulic lime fibre-reinforced mortars for masonry strengthening overlay systems, Applied Sciences*, 14(5):1947. https://doi.org/10.3390/app14051947

[2] De La Rosa, Á., Ruiz, G., and Moreno, R. (2025) *Design of eco-sustainable self-compacting lime-based concretes with pozzolanic and hydraulic additions for structural use, International Journal of Architectural Heritage: Conservation, Analysis, and Restoration*. https://doi.org/10.1080/15583058.2025.2559177

Simultaneous Optimization of Fiber Scheme and Structural Design for UHPC Structures

Naser S. Alimrani – Postdoctoral Scholar, Department of Civil Engineering, McGill University, Montreal, Quebec, Canada, Email: naser.alimrani@mcgill.ca

Jian Zhan – Postdoctoral Scholar, Department of Civil Engineering, McGill University, Montreal, Quebec, Canada, Email: jian.zhan@mail.mcgill.ca

Yi Shao* (*corresponding author) – Assistant Professor, Department of Civil Engineering, McGill University, Montreal, Quebec, Canada, Email: yi.shao2@mcgill.ca

1. Introduction

Ultra-high performance concrete (UHPC) is an advanced concrete with superior mechanical properties and durability. Its high packing density and very low water-to-cement ratio result in high compressive strength, elastic modulus, and negligible permeability. The addition of short steel fibers (typically 1–4% by volume) further enhances strength and ductility in both tension and compression.

Due to these properties, UHPC has seen increasing global use, with over 500 projects in the United States, Switzerland, and China, covering both rehabilitation and new construction. Several countries have issued design standards, including France (2016), Switzerland (2016), the United States (2024), and China (2024), supporting its wider adoption.

In current design practice, UHPC material properties are usually fixed, while variables focus on geometry and reinforcement. However, a mix with 2% steel fibers can account for up to 75% of total material cost, with fibers alone contributing up to 50%. As a result, studies have explored reducing fiber volume (e.g., from 4% to 1%) while increasing reinforcement to lower costs. This approach is practical since UHPC components are often supplied separately, allowing easy adjustment of fiber content.

Although studies confirm the feasibility of partially replacing fibers with reinforcement, fiber volume is often selected arbitrarily. The optimal combination of fiber content, geometry, and reinforcement remains unclear, as fiber volume strongly affects tensile behavior, which governs strength, serviceability, and durability. Trial-and-error methods are also costly and inefficient. Therefore, a systematic numerical optimization framework is needed to identify optimal UHPC designs, which is currently lacking

This study aims to build a generalized optimization framework to explore the optimized design of UHPC structures at both material and structural levels. This extended abstract will introduce the generalized framework while the rest of the results will be shown in the presentation. We will demonstrate the feasibility and advantages of the proposed optimization framework by applying it to optimizing prestressed UHPC beams that are reported in literature and adopted in practice. A sensitivity analysis is conducted to reveal how different UHPC and reinforcement prices affect the optimized design.

2. A generalized formwork

This section presents a generalized optimization framework for designing UHPC cross-sections at both material and structural levels. To maintain flexibility across regions, structure types, and evolving design practices, detailed equations are omitted. Sections 3 to 5 demonstrate the framework using current methods for prestressed UHPC beams.

Equations (1)–(6) define the optimization problem, with design variables denoted by x~\tilde{x}x~. At the material level, these include reinforcement type and UHPC composition (e.g., fiber type and volume). At the structural level, they include geometric parameters (e.g., beam height and web thickness) and reinforcement configuration (amount and location).

$$\min_{\tilde{x}} S(\tilde{x}) = Cost(\tilde{x}) + \lambda Carbon(\tilde{x}) \quad (1)$$

Subject to

$$\phi M_n(\tilde{x}) \geq M_u \quad (2)$$

$$\phi V_n(\tilde{x}) \geq V_u \quad (3)$$

$$\sigma_s(\tilde{x}) \leq \sigma_{s,limit} \quad (4)$$

$$\varepsilon_s(\tilde{x}) \leq \varepsilon_{s,limit} \quad (5)$$

$$Stiffness\ (\tilde{x}) \geq Stiffness_limit \quad (6)$$

$$\tilde{x}_{upper_bound} \geq \tilde{x} \geq \tilde{x}_{lower_bound} \quad (7)$$

The design variables xxx include material parameters (e.g., reinforcement type, fiber type and volume) and structural parameters (e.g., beam geometry and reinforcement layout). Equation (1) minimizes cost and carbon footprint. Costs include materials, labor, transportation, and foundations, while carbon depends on the selected life-cycle assessment. The parameter λ controls the weight of carbon (e.g., λ=0 ignores carbon). Equations (2)–(3) enforce ultimate limit states, ensuring moment and shear capacities exceed required demands. Equations (4)–(6) represent serviceability constraints on stress, strain, and stiffness, ensuring adequate performance and crack control. These may be reformulated (e.g., cracking moment or span-to-depth limits). Equation (7) bounds the variables to ensure constructability, durability, and ductility (e.g., minimum web thickness or fiber volume). The variables and constraints can be adapted to different standards. As the framework targets initial optimization, simplified formulations are used, with final designs verified using more detailed methods

3. References

AFNOR (Association Française de Normalisation). National addition to eurocode 2–Design of concrete structures: Specific rules for ultra-high performance fibre-reinforced concretes (UHPFRC). NF P18-710, La Plaine Saint-Denis, France: AFNOR., 2016.

E. Brühwiler, Swiss UHPFRC Model Standard: Ultra-High Performance Fibre Reinforced Cementitious composite (UHPFRC) – Materials, dimensioning and execution (adapted and translated version of the Technical Leaflet SIA 2052), 2024.

SIA (Swiss Society of Architects and Engineers). UHPFRC— Materials, design and construction. Technical Leaflet SIA 2052, Zurich, Switzerland: SIA, 2016.

Federal Highway Administration. Structural Design with Ultra-High Performance Concrete, Washington, DC, 2023.

Behaviour Of Reinforced Concrete Structural Elements Under Fire Exposure – An Integrated Structural Interpretation

Éva Lublóy[1], András Biró[1], György L. Balázs[1] Viktor Hlavička[1]

[1]: Budapest University of Technology and Economics, Faculty of Civil Engineering, Department of Construction Materials and Technologies, Műegyetem rkp 3, Budapest H-1111, Hungary

1 Introduction

Recent design strategies have focused on optimizing the concrete mix composition to enhance fire performance without compromising structural capacity. This study evaluates the effectiveness of such an approach through a series of large-scale laboratory tests conducted on prefabricated wall panels and TT slab elements.

Previous investigations have shown that steel fibres can limit crack development in the temperature range of approximately 400–600 °C (Hertz, 2003), thereby reducing the likelihood of surface spalling. Even more effective spalling mitigation has been reported for short, small diameter polypropylene fibres. Upon heating, these fibres melt and generate an interconnected pore network within the concrete matrix, facilitating vapour release and reducing internal pressure build up. Adjustments to cement type and aggregate type were also investigated.

2 Experimental program

The experimental campaign comprised fire resistance tests on two prefabricated reinforced concrete structural elements: a wall panel and a TT slab element (Lublóy *et al.*, 2019; Lubloy, 2024). In both cases, the objective of the investigations was to enhance the fire resistance limit state of the elements through the addition of polypropylene fibres.

Thermal loading of the specimens was applied following the standard fire curve prescribed in EC1. Fire tests were performed in compliance with EN 1365-2:2014 and EN 1365-1:2013 standards.

3 Test Results

For the single-layer wall panel models, the modified concrete mix led to a substantial reduction in both the surface area and depth of spalling. As a consequence, lower and more uniform temperature rises were measured on the unexposed surfaces of the lower, middle and upper panels. This more favourable high-temperature behaviour directly translated into an increase of the fire resistance rating from REI 90 to REI 120, fulfilling the most stringent regulatory requirement prescribed for walls in the highest risk category according to Hungarian National Fire Protection Regulations (OTSZ, 2021).

Similarly, for the TT slab elements, the modified concrete composition resulted in a markedly reduced spalling depth on the fire-exposed soffit and lower temperature increases on the slab upper surface. Although the timing of spalling initiation was similar in both tests, the reduced loss of concrete cover in the modified element enabled a higher fire resistance classification, increasing the fire resistance limit from REI 60 to REI 90, which corresponds to the regulatory requirement for slabs in buildings with the highest risk category.

4 Concluding remarks

Overall, the results confirm that concrete mix optimization is an effective and practical means of improving fire resistance of prefabricated high-strength reinforced concrete elements. The findings highlight that spalling mitigation and thermal insulation capacity of the residual concrete cross-section are key governing factors of structural fire performance. From an engineering perspective, the presented approach allows improved fire resistance to be achieved without increasing element thickness or modifying reinforcement, making it particularly attractive for precast applications where production efficiency and geometric constraints are critical.

The outcomes of this study support the broader conclusion that fire-resistant design of high-strength concrete structures should not rely solely on material strength considerations, but must account for high-temperature damage mechanisms, especially spalling, through targeted concrete composition design.

5 Acknowledgements

Authors acknowledge the support by the Hungarian Research Grant NVKP_16-1-0019 ‘‘Development of concrete products with improved resistance to chemical corrosion, fire or freeze-thaw”.

6 References

Hertz, K.D. (2003) “Limits of spalling of fire-exposed concrete,” *Fire Safety Journal*, 38(2), pp. 103–116. Available at: https://doi.org/https://doi.org/10.1016/S0379-7112(02)00051-6.

Lublóy, É. *et al.* (2019) “CT and laboratory test of the wall panels after fire load,” *Construction and Building Materials*, 211, pp. 1105–1116. Available at: https://doi.org/10.1016/j.conbuildmat.2019.03.148.

Lubloy, E. (2024) “The relationship between conctere composition and structural stability in case of fire,” *Construction and Building Materials*, 431, p. 136545. Available at: https://doi.org/10.1016/j.conbuildmat.2024.136545.

OTSZ (2021) *54/2014. (XII. 5.) BM rendelet az Országos Tűzvédelmi Szabályzatról - Hatályos Jogszabályok Gyűjteménye*. Available at: https://net.jogtar.hu/jogszabaly?docid=a1400054.bm (Accessed: November 21, 2020).

Fatigue in compression and indirect tension in a high-tech steel-fiber reinforced concrete

Ángel De La Rosa[1], Gonzalo Ruiz[2*], Vaibhav W. Masih[2], Riccardo Zanon[3]

[1]: Grupo de DIMNE, Universidad Rey Juan Carlos, Móstoles, Spain.
[2]: ETSI Caminos, C. y P., Universidad de Castilla-La Mancha, Ciudad Real, Spain
[3]: Department of Engineering, University of Luxembourg, Luxembourg

1 Introduction

Fatigue behavior in concrete, particularly in steel fiber reinforced concretes (SFRC), is influenced by stress levels, microstructural characteristics, and loading modes. Recent advancements in engineered concretes prompt a reassessment of fatigue laws and the applicability of traditional models to high-performance materials.

This study investigates the fatigue response of a highly engineered SFRC, focusing on compressive and indirect tensile fatigue behavior, fatigue life distributions, and crack evolution using Digital Image Correlation (DIC). The study seeks to validate Sparks and Menzies' law [1] for tensile cyclic loading and identify common fatigue mechanisms across different loading modes.

2 Experimental program

The used SFRC composition contains 0.6% in volume of hooked steel fibers (ArcelorMittal HE ++ 75/35). The mix was designed to ensure self-compaction and stable rheology even in the presence of fibers. Mechanical characterization at six months revealed a compressive strength f_c of 67 MPa and an elastic modulus of 34 GPa. Furthermore, the residual flexural strengths were 6.4 MPa and 5.0 MPa at crack-mouth openings of 0.5 mm and 2.5 mm, respectively [2].

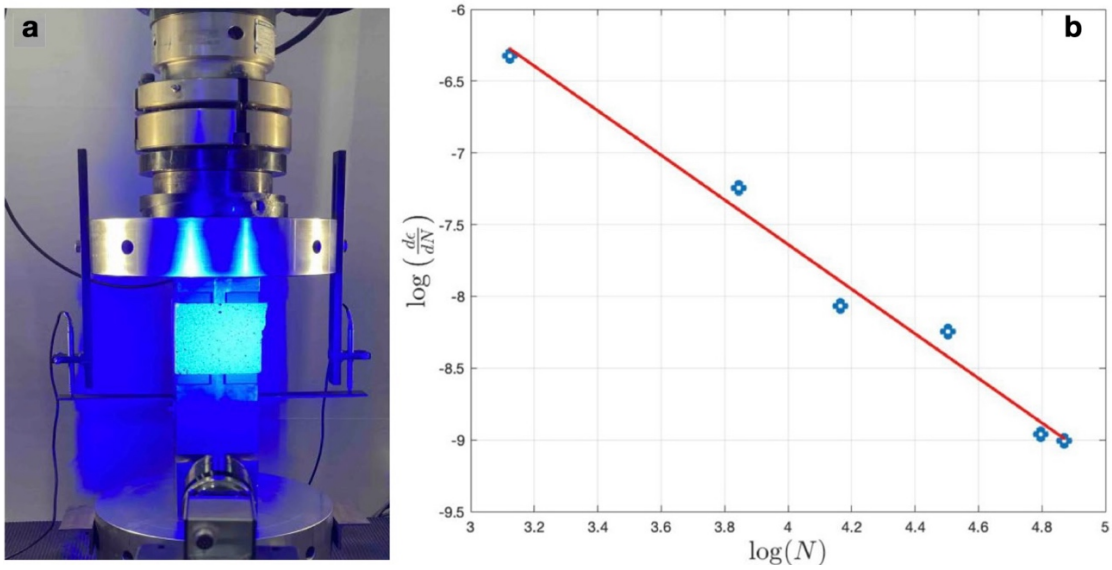


Figure 1 (a) Indirect tensile test setup, (b) Sparks and Mezies' law in phase 1 of tensile tests.

Compression fatigue tests were performed on 100 mm-edge cubes using a hinge-based loading system. Fatigue tests were conducted at 2 Hz with maximum stresses of 0.80 f_c and 0.90 f_c. No runouts were observed.

Indirect tensile fatigue was evaluated using a modified Brazilian configuration [2]. The test setup and DIC instrumentation are shown in Fig. 1a. The fatigue protocol consisted of two phases: phase 1 – 86400 cycles at 0.85 of the first-crack stress (determined through DIC); phase 2 – Cyclic loading at 0.85 of the tensile strength until failure. DIC enabled continuous monitoring of strain concentrations, crack initiation, and crack-growth patterns.

3 Results

The fatigue lives of cubes tested in compression followed Weibull distributions whose parameters depended strongly on stress range. At 0.80 f_c, fatigue lives were generally an order of magnitude longer than at 0.90 f_c. Strain–cycle histories exhibited a transient primary regime followed by a secondary linear strain-rate regime. The slope of this secondary regime correlated linearly with fatigue life in a log–log plot, confirming the validity of the Sparks and Menzies law [1] for this advanced SFRC.

Specimens in phase 1 completed the required cycles under tension, maintaining stable crack propagation. In contrast, phase 2 exhibited rapid deformation and failure. Both first cracking and fatigue lives followed Weibull distributions, with a secondary strain rate regime displaying a log-log linear correlation with fatigue life (as shown in Fig. 1b for phase 1).

4 Concluding remarks

The experimental campaign demonstrates that the fatigue behavior of highly engineered SFRC in both compression and indirect tension can be effectively described using probabilistic life models and secondary strain rate analysis. The main findings are: (1) fatigue lives under both loading modes follow Weibull distributions; (2) secondary strain rate regimes are strongly correlated with fatigue life; (3) the modified Brazilian test provides a controlled mode I cracking mechanism, which, combined with DIC, allows precise tracking of crack initiation and propagation; (4) the two-phase tensile fatigue protocol clearly distinguishes between stable damage accumulation and instability onset; and (5) the engineered SFRC exhibits significant sensitivity to stress range, with notably longer fatigue lives under lower stress amplitudes.

5 Acknowledgements

This research work was supported by ArcelorMittal Global R&D and ArcelorMittal Fibres, Luxembourg. The authors also acknowledge additional funding from the MICU (Spain) through grant PID2023-147971OB-C31, the JCCM through grant SBPLY/24/180225/000003, and the UCLM and the ERDF through grant 2025-GRIN38445.

6 References

[1] Sparks P.R., Menzies J.B. The effect of rate of loading upon the static and fatigue strength of plain concrete in compression. *Magazine of Concrete Research* 25(83) (1973) 73–80.

[2] De La Rosa Á., Ruiz G., Masih V.W., Zanon R. Innovative high-technology concrete mix-design method integrating rheological properties and fracture mechanics. *Construction and Building Materials* 458 (2025) 139538.

Extension of the Simplified Modified Tension Chord Model to predict cracking and deformation in fibre reinforced concrete

Guillem Rojas[1], Reignard Tan[2] & Terje Kanstad[2]

[1]: University of Stavanger (UiS), Stavanger, Norway.
[2]: Norwegian University of Science and Technology (NTNU), Trondheim, Norway

1 Introduction

Cracking is inherent to reinforced concrete (RC) under tension, making crack width a vital factor for durability and serviceability. To control performance, design codes impose strict limits. Adding steel fibers to the concrete improves post-cracking tensile capacity and tension stiffening, typically reducing both crack spacing and width. However, predicting these widths remains complex due to the intricate interactions between concrete, reinforcement, and fibers.

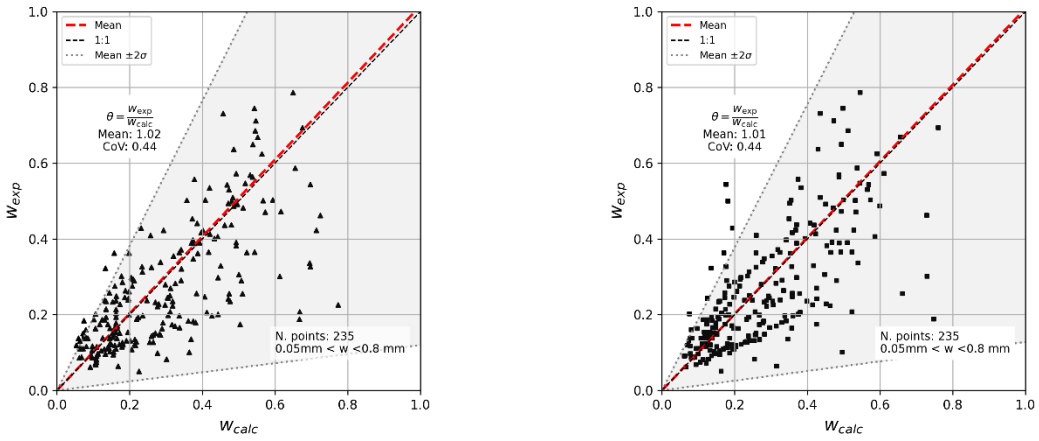
This method extends the **Simplified Modified Tension Chord Model (SMTCM)** and is proven to predict crack widths accurately and consistently for Fiber Reinforced Concrete (FRC). The extended SMTCM for FRC is a mechanical model based on solving the second order differential equation (SODE) for the slip. Hence, the formulation makes it more applicable for generic use as opposed to the current semi-empirical formulations in the codes, which relies on experimental calibration further limiting its range of application.

2 Extension of the Simplified Modified Tension Chord Model to FRC

The **MTCM** and more specifically its simplified version **SMTCM** for the calculations of crack widths, included in (Rojas et al., 2026), has been extended to FRC members. The model incorporates the contribution of fibres through residual tensile stresses and is formulated to allow practical application in engineering design. Fibers' effect is considered by taking a constant value of the post-cracking tensile stress $\sigma(w)$ –to provide explicit solutions to the equations– as well as an orientation factor considering the casting procedure and element geometry.

The proposed model was used to reproduce the complete force–elongation response of RC and FRC ties and to compare predicted vs. experimentally obtained crack widths –ranging from 0.05 to 0.80 mm– for a published experimental database. The database included 55 specimens, with reinforcement ratios from 1.24% to 8.72%, with hook-end steel fibres (V_f = *0.25–1.5%, 20–118 kg/m³, fibre lengths 6–50 mm, aspect ratios* l_f/d_f = *40–100*). The accuracy of crack width predictions was assessed using the concept of modelling uncertainty, defined as the ratio between experimental and calculated crack widths ($\theta = w_{exp} / w_{cal}$). The proposed SMTCM method was also compared with the crack width formulation included in the revised Eurocode

2 – Annex L. The modelling uncertainty is graphically presented in Figure 1, for both RC and FRC.



(a) (b)

Figure 1: Modelling uncertainty (θ) for maximum crack width for the experimental database. w_{exp} is the crack width measured reported in the experiments and w_{cal} is the calculated crack width, while the mean and the CoV represents the mean value and the coefficient of variation of the θ a) SMTCM, b) EN1992-1-1 (2023).

3 Concluding remarks

This study presents an extension of the SMTCM to predict cracking behaviour in FRC members and applies this model to a broad database of published data on concrete ties.

For the analyzed database, the mean modelling uncertainty for the SMTCM method was approximately equal to 1.0 –coefficient of variation (CoV) of 0.44– for both RC and FRC. The accuracy and statistical dispersion of the predictions was comparable to that obtained using the Eurocode 2 formulation. The analytical results show satisfactory agreement with experimental observations and confirm the capability of the model to capture the main mechanisms governing cracking behaviour.

The complete development of the SMTCM extended to FRC can be found in (Rojas et al., 2026).

4 Acknowledgements

The authors acknowledge the support provided by the '*FiberCon*' industrial research project, led by Dr.techn. Olav Olsen AS and funded by the Norwegian Research Council.

5 References

Rojas, G., Tan, R., & Kanstad, T. (2026). Simplified modified tension chord model extended to predict cracking and deformation of fiber reinforced concrete. *Structural Concrete*.

Fiber orientation effects in thin layers of HPFRC jacketing: a critical discussion of Model Code 2020 provisions.

Ivan Beltracchi[1], Adriano Reggia[1], Giovanni Metelli[1], Giovanni A. Plizzari[1]

[1]: Università di Brescia, DICATAM - Department of Civil, Environmental, Architectural Engineering and Mathematics, via Branze 43, Brescia, 25123, Italy.

1 Introduction

The assessment and rehabilitation of existing transport infrastructure represent one of the major engineering challenges of the 21st century. Across Europe, a significant proportion of reinforced and prestressed concrete (RC and PRC) bridges currently in service were designed between the 1950s and 1980s, according to design assumptions that no longer reflect present-day conditions. These structures are now subjected to increased traffic demands, heavier vehicle loads, material ageing, all of which progressively reduce their residual service life and compromise their structural reliability within more stringent durability and safety requirements.

In this context, advanced rehabilitation solutions based on HPFRCs are growing for their achieved toughness, enhanced durability and reduced environmental impact, making them a promising strategy for extending the service life of ageing infrastructures. This research started from an experimental campaign conducted at the University of Brescia on 1:2 scaled bridge piers retrofitted with thin HPFRC jacketing layers, subjected to quasi-static cyclic loading to reproduce seismic conditions. Experimental results highlighted the contribution of HPFRC in terms of strength enhancement and ductility (Reggia et al.,2024).

By following, an in-depth study on the influence of fibre dispersion and orientation within these layers has been performed. Three scaled specimens, with the same jacketing thicknesses (3-5 cm), were casted. Subsequently, 30 beams extracted along different sides and directions, were tested according to 3PBT procedure to investigate the response of the material throughout the retrofitting and compare it with 6 standard EN-14651 specimens, conventionally adopted for material characterization. The outcomes highlighted an anisotropic distribution of fibres along jacketing, affected by casting procedures and wall effects, amplified for the reduced layers thicknesses. This experimental approach aims to extract a generic constitutive law, which takes into account the different behavior of the material within jacketing by using new orientation coefficients derived for all the extracted samples and by relating them with thicknesses, aspect ratios and with reference EN-14651 values $f_{R,i}$. This proposed law was then implemented within a non-linear FE model and compared with average experimental response (pushover) of the retrofitted columns and with the design procedure suggested within Model Code 2020, which adopts standardized orientation coefficients on mechanical properties of reference beams, not directly related to thin layers of jacketing.

2 Experimental or modelling program

The following pic shows the 3 samples (25x55x1 m) casted and the respective 30 beams extracted horizontally and vertically from different sides and direction of jacketing.

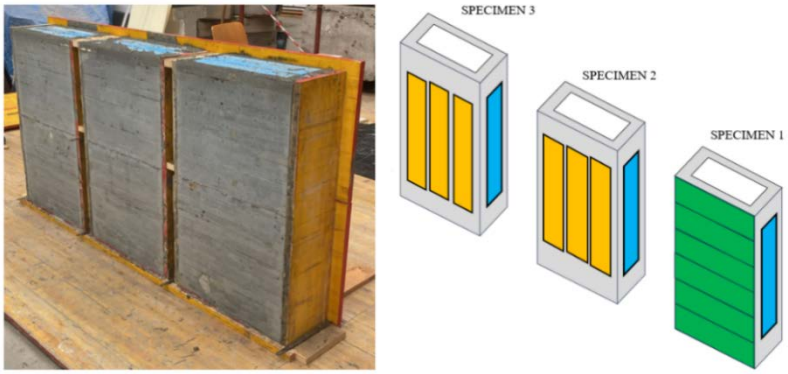
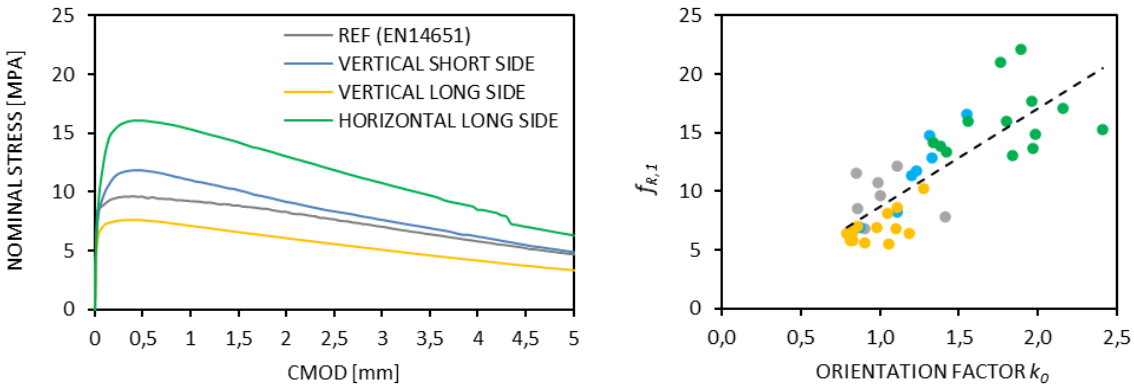


Figure 1 Scheme of extracted beams along different directions of HPFRC specimens.

Following 3PBT, Image analysis was employed to characterize fibre distribution and orientation along cutting sections for all beams near midspan. Orientation and out-of-plane inclination coefficients (k_0,k_θ) were were correlated with jacketing thickness, fibre arrangement, and post-cracking performance measured through $f_{R,i}$ values of EN-14651 beams. Based on these observations, an empirical Power-law model was developed to predict the flexural behaviour of thin HPFRC layers. The model was subsequently enhanced using a Neural Network optimization framework, capturing non-linear interactions between fibre orientation, casting effects, and thickness to fibre length ratio (t/l_f). This reduced prediction error from 25% to less than 7%, thus improving the representation of material mechanical response.

3 Test Results



(a) (b)

Figure 2 (a) Average curves extracted from 3PBT performed on 30 beams and reference EN-14651 ones; (b) orientation factors derived from samples with Image Analysis, related to $f_{R,1}$ (and $f_{R,I}$) values.

Average experimental curves are presented in *Figure 2* a, thus proving the different behavior of HPFRC within jacketing (orange and green curves derived from beams both belonging to long side 3 cm thick, with the first ones extracted vertically while the latter ones horizontally) for different fibers orientation, dispersion and thicknesses (blue curve related to short side vertical beams, 5 cm thick), compared to standard beams (grey curve from EN-14651).
From experimental values, a general strain softening law has been also derived, used in parallel with the analytical law implement in non-liner FE analyses (red curve):

$$f_I = 0.7 f_{ref,i} \left(\frac{t}{l_f}\right)^{0.14} (k_\theta)^{2.1} (k_0)^{0.43} \;\; and \;\; f_{R,i} = f_{R,1} * e^{-0.18(i-1)} \;\; (strain\ softening) \qquad (1)$$

with *t* jacketing thicknesses, l_f fibers length, $k_0 = 1.2$ (short side) and $k_0 = 1.6$ (long side).

Therefore, the analytical model was performed and compared with the design method described in Model Code 2020 (dotted red curve), which suggest to adopt orientation factor equal to $k_0 = 0.86 = \frac{a_f(=0.5)}{0.58}$ in the case of 3D random orientation of fibers, applied on $f_{R,i}$ values.

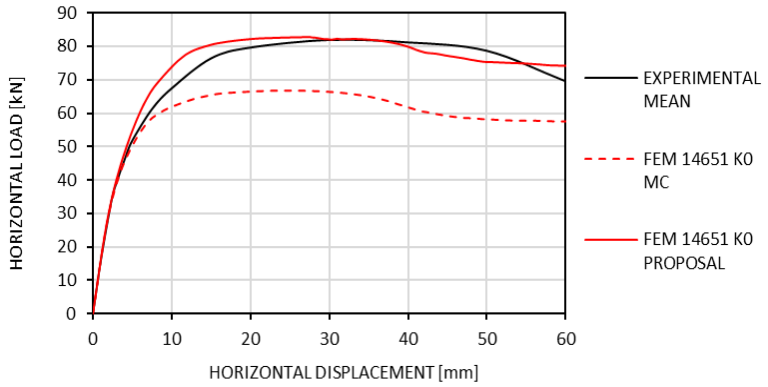


Figure 3 Average experimental curves of 1:2 scaled columns compared with FE analyses.

4 Concluding remarks

The proposed methodology demonstrated a significantly improved agreement with the experimental results compared to the current provisions of Model Code 2020. In particular, the latter underestimated the global structural response by approximately 20-30%, mainly because MC proposed orientation factors, applied to EN-14651 samples, were calibrated for horizontal slabs and vertical walls rather than for HPFRC jacketing. The findings of this study therefore suggest that dedicated orientation factors should be introduced for jacketing applications, accounting for thickness-dependent fibre alignment and casting-induced anisotropy. This approach would allow to a more realistic prediction of global structural performance, thus leading to more reliable strengthening designs for infrastructures.

5 Acknowledgements

The authors wish to thank HEIDELBERG Cement Group for supporting this research work. A special acknowledgement goes to Dr. Eng. Bruno Leporace, Eng. Michele Rossini, Mr. Augusto Botturi, Mr. Andrea Del Barba and Mr. Luca Martinelli for their support into the experimental project.

6 References

Beltracchi I., Reggia A., Trabucchi I., Metelli G., Plizzari G., Effect of Fiber Orientation in Ultra-thin HPFRC Repair, Fib Young Italy, Naples 2026.

Reggia, A., Trabucchi, I., Beltracchi, I., Morbi, A., & Plizzari, G. A. (2024, November). Structural Reinforcement of Specimen Bridge Columns with HPFRC. In International Conference on Concrete Repair, Rehabilitation and Retrofitting (pp. 300-309). Cham: Springer Nature Switzerland.

Matthews, S. L. (2023). fib Model Code 2020: Enabling advances for new and existing concrete structures. Structural Concrete, 24(4), 4341-4351.

Numerical Study on the Strengthening of Pitting-Corroded Reinforced Concrete Dapped-End Beams

Elisa Carleschi[1], Jean-Philippe Charron[2], Giovanni Plizzari[1]

[1]: University of Brescia, Brescia, Italy.

[2]: Polytechnique de Montréal, Montreal, Canada.

1 Introduction

Bridge infrastructure built during the last century is progressively dealing with issues related to material ageing, increased traffic volumes and stricter safety requirements. Rather than replacement, rehabilitation has become the preferable method for preserving existing structures while minimizing economic costs and environmental impacts. In this context, reinforced concrete half-joints (Gerber girders) deserve particular attention because their discontinuous geometry and their complicated stress fields, making these regions especially vulnerable to deterioration and brittle failure mechanisms. Among the different sources of degradation, pitting corrosion of reinforcing bars is one of the most critical, as localized steel loss can significantly reduce the structural capacity. So strengthening interventions must be designed to account the corrosion damage. However, many existing bridge elements need to be upgraded even in the absence of significant deterioration, since current service loads frequently exceed those considered in the original design. Ultra-high-performance fiber-reinforced concrete (UHPFRC) offers an attractive solution for these applications because it combines very high mechanical strength, excellent durability and superior crack control, allowing efficient strengthening with limited additional thickness and weight.

2 Modelling program

This study presents the development of a validated nonlinear finite element model for reinforced concrete dapped-end beams, aimed at supporting the design of effective strengthening solutions. The proposed retrofit strategies are intended for both corrosion-damaged structures and undamaged members requiring capacity enhancement due to increased service demands. The numerical model was calibrated against experimental results obtained from ten girders exhibiting different locations and severities of pitting corrosion in the reinforcing steel, ensuring an accurate representation of the initial damage condition. The tested beams had an overall length of 5500 mm, a depth of 1000 mm, and a width of 240 mm, while the dapped-end region measured 500 mm in length, 450 mm in depth, and 240 mm in width. The validated modelling framework is employed to predict the structural response of strengthened dapped-end beams, optimize the retrofit design, and support the planning of a forthcoming experimental campaign. Two identical strengthening solutions were designed, one for the reference girder and one for the corroded specimen, using ATENA software by Červenka Consulting.The proposed retrofit consists of a 50 mm thick UHFRC overlay applied locally in the critical half-joint region, where shear stresses and stress concentrations are highest. The intervention is designed to avoid removing the existing concrete cover, thereby simplifying on-site application. The UHFRC mixture contains 3% steel fibres by volume, and its constitutive behaviour was calibrated using experimental data reported by Liu (2023) at Polytechnique Montréal.

3 Test Results

The results obtained from the numerical analyses are presented through load–displacement curves. The curves compare the reference configurations (black: experimental uncorroded beams) with the corroded experimental beams (red experimental uncorroded beams), the corresponding numerical simulations of the corroded beams (brown), and the strengthened solutions in both cases corroded and not corroded (green: UHFRC overlay). In particular the selected corroded girder, called “L30”, is characterized by -30% of reduction in cross-section area in the longitudinal reinforcements close to the main crack.



(a) (b)

Figure 1: retrofitting on Dapped-end beam without corrosion (a) and with corrosion (b).

The application of UHFRC overlay increases the peak load capacity by 43% (686 kN) in the uncorroded girders and by +21% for L30 (582 kN) for the corroded beams. This significant enhancement can be attributed to the fiber-induced confinement provided by UHFRC, which effectively delays shear failure at the nib and produces an extended post-peak plateau, indicating an improvement in ductility.

4 Concluding remarks

The obtained numerical results reveal how UHFRC overlays improve the load-carrying capacity of corroded dapped-end beams. UHFRC not only compensates for corrosion losses but also enhances overall strength, making it the more effective strengthening solution. This confirms the significant contribution of fiber composites to improving bridge safety and extending the remaining service life of existing bridges.

5 Acknowledgements

The project was funded by the PNRR through the PRIN 2022 project “New perspectives for the assessment, control and retrofitting of damaged reinforced concrete bridges” and by the European Union-NextGeneration EU, Mission 4, Component 1 (CUP D82B23003170001).

6 References

Liu, T. (2023). “Shear Strengthening of Reinforced Concrete Beams Using Ultra High Performance Fiber Reinforced Concrete (UHPC)“ Phd thesis, Polytechnique Montréal, Canada.

Systemizing UHPFRC intervention for existing bridges : environmental and economic benefits at the network scale

Numa Bertola[1], Célia Küpfer[2] and Eugen Brühwiler[3]

[1] Department of Engineering, University of Luxembourg, Luxembourg
[2] Peter Guo-hua Fu School of Architecture, McGill University, Canada
[3] Institute of Civil Engineering, EPFL, Lausanne, Switzerland

1 Introduction

Replacing bridges at the end of their intended service duration or due to structural deterioration incurs high environmental and financial costs. Another strategy is to regenerate their structural performance and improve their durability using ultra-high-performance fiber-reinforced cementitious composite (UHPFRC). A 50-100 mm reinforced UHPFRC layer bonded to the bridge deck can simultaneously increase bending and shear capacities and protect the existing underlying concrete thanks to the UHPFRC waterproofing qualities. This approach can lead to a significant increase in service duration, even for already-damaged structures [1].

More than 120 bridges have received UHPFRC structural intervention since 2004 in Switzerland [2]. This study quantifies the environmental and economic savings for the 3,903 bridges in the Swiss Federal Road network over the next 80 years if UHPFRC strengthening is systematically applied, rather than the conventional solution of demolition and reconstruction.

2 Bridge-scale impact analyses and network applicability

We quantified life-cycle assessment and costing for 17 UHPFRC interventions for an 80-year service extension and compared them with conventional costs and environmental impacts (Figure 1). Across 17 interventions, mean global warming potential was 165 $kgCO_{2,eq}/m^2$ (range 120-226), compared with 1,000 $kgCO_{2eq}/m^2$ for best-practice replacement and 2,250 $kgCO_{2eq}/m^2$ for the mean benchmark. Direct emissions therefore fall by 84.0- 92.9%, while the project-level cost is approximately 75% lower.

Applicability of the UHPFRC strengthening strategy was assessed by comparing six network attributes with completed UHPFRC projects: material, structural type, deck area, span count, condition grade, and construction year [3]. The study showed that UHPFRC intervention can be performed on 99.7% of bridges in the Swiss Federal Road network. Removed bridges correspond to extraordinary structures (i.e., long-span cable-stayed bridges,..):

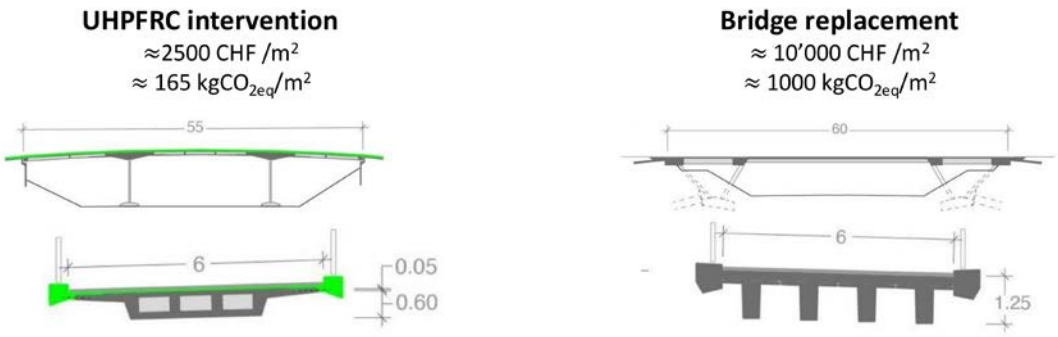


Figure 1: Typical UHPFRC strengthening and bridge-replacement alternatives.

3 Network-scale savings

The results at the bridge-element scale were then extrapolated to Switzerland's network of 3,903 national road bridges to quantify benefits over the next 80 years. A key assumption is the number of bridges that will be replaced yearly in the future. The presented scenario is based on predictions [4] for the bridge owner (the Swiss Confederation) combining inspection reports, degradation-based scenarios, computational tools, and machine learning. Over the next 80 years, owner predictions indicate that 3,208 (77.5%) bridges will need to be replaced. Systematically applying the UHPFRC-intervention strategy would result in 9.06 BCHF in economic savings and 2.55 $MTCO_{2eq}/m^2$ in environmental savings.

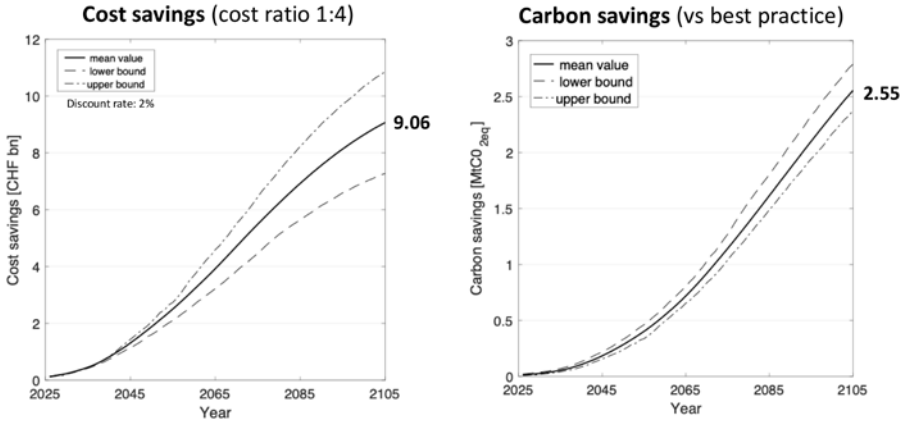


Figure 2: Cumulative economic and environmental savings for the 3,903-bridge network.

4 Concluding remarks

Using the Swiss Federal Road network as a case study, it was demonstrated that cost and environmental savings are very significant when systematically using the UHPFRC intervention strategy compared with conventional demolition-reconstruction solutions. Systematic UHPFRC strengthening can avoid the burden of demolition and align bridge-owner budget and carbon objectives. Transfer to other countries requires local cost, carbon, and bridge-replacement estimations. Future work should include preventive maintenance scenarios and indirect traffic impacts in the comparison.

5 References

[1] Brühwiler E. UHPFRC technology to enhance the performance of existing concrete bridges. Structure and Infrastructure Engineering 2020;16:94–105. https://doi.org/10.1080/15732479.2019.1605395.

[2] Bertola N, Schiltz P, Denarié E, Brühwiler E. A Review of the Use of UHPFRC in Bridge Rehabilitation and New Construction in Switzerland. Frontiers in Built Environment 2021;7:155. https://doi.org/https://doi.org/10.3389/fbuil.2021.769686.

[3] Bertola N, Küpfer C, Brühwiler E. Environmental and economic benefits of UHPFRC intervention in bridge management for the Swiss Network. Nature Communications 2026;17. https://doi.org/https://doi.org/10.1038/s41467-026-69103-x.

[4] Marsili F, Diederich H, Ralbovsky M, Hajdin R, Vorwagner A, Kessler S. Abschätzung der Restnutzungsdauer von Brückenbauwerken durch Entwicklung und Erprobung hybrider Modelle - ENDURE. 2024.